NANOMATERIALS HANDBOOK

NANOMATERIALS HANDBOOK

EDITED BY

YURY GOGOTSI

Taylor & Francis
Taylor & Francis Group
Boca Raton London New York

A CRC title, part of the Taylor & Francis imprint, a member of the
Taylor & Francis Group, the academic division of T&F Informa plc.

The upper left image on the cover is a colored SEM micrograph of a nano-lamina of graphite produced by chlorination of iron carbide. The upper right image is a colored SEM micrograph of a graphite polyhedral crystal (GPC) with its Raman spectra in the foreground. Both images are by S. Dimovski, Drexel University. The lower image is a molecular dynamics simulation of zipping of a graphene edge (by S.V.Rotkin, Lehigh). Similarities between a sleeve formed at the edge of graphite and a single-wall nanotube can be clearly seen. The background (by J. Libera) is a TEM image of the GPC edge. Artist view by B. Grosser, ITG, Beckman Institute, UIUC). See chapters 6 and 8 for more information.

Published in 2006 by
CRC Press
Taylor & Francis Group
6000 Broken Sound Parkway NW, Suite 300
Boca Raton, FL 33487-2742

Printed in the United States of America on acid-free paper
10 9 8 7 6 5 4 3 2 1

International Standard Book Number-10: 0-8493-2308-8 (Hardcover)
International Standard Book Number-13: 978-0-8493-2308-9 (Hardcover)
Library of Congress Card Number 2005053105

Library of Congress Cataloging-in-Publication Data

Nanomaterials handbook / [edited by] Yuri Gogotsi.
p. cm.
Includes bibliographical references and index.
ISBN 0-8493-2308-8
1. Nanostructured materials--Handbooks, manuals, etc. I. Gogotsi, IU. G., 1961-

TA418.9.N35H357 2006
620.1'1--dc22 2005053105

informa
Taylor & Francis Group
is the Academic Division of Informa plc.

Visit the Taylor & Francis Web site at
http://www.taylorandfrancis.com

and the CRC Press Web site at
http://www.crcpress.com

This book is dedicated to my family — the source of my inspiration

Preface

Nanomaterials Handbook is designed specifically to provide an overview of nanomaterials for today's scientists, graduate students, and engineering professionals. The study of nanomaterials, which are materials with structural units (grains or particles) on a nanometer scale in at least one direction, is the fastest growing area in material science and engineering. Material properties change on the nanoscale; for example, the theoretical strength of materials can be reached or quantum effects may appear. Thus, nanomaterials may have properties different from those of single crystals or conventional microstructured, monolithic, or composite materials.

Man has been taking advantage of nanomaterials for a long time. Roman glass artifacts (e.g., the famous Lycurgus cup located in the British Museum in London) contained metal nanoparticles, which provided beautiful colors. In medieval times, metal nanoparticles were used to color glass for cathedral windows. For example, the famous gold ruby glass contains nanometer-size gold particles that impart the glass its red color. Currently, nanomaterials play a role in numerous industries, e.g., (1) carbon black particles (about 30 nm in size) make rubber tires wear-resistant; (2) nano phosphors are used in LCDs and CRTs to display colors; (3) nanofibers are used for insulation and reinforcement of composites; (4) nano-size alumina and silica powders are used for fine polishing of silicon wafers; (5) nanoparticles of iron oxide create the magnetic material used in disk drives and audio/video tapes; (6) nano-zinc oxide or titania is used in sunscreens to block UV rays from the sun; and (7) nanoscale-platinum particles are crucial to the operation of catalytic converters. Many new nanomaterials, such as nanotubes, fullerenes, and quantum dots, have emerged recently and many others are under development.

The handbook uses terms familiar to a materials scientist or engineer and describes nanomaterials, but not nanotechnology in general. The nanomaterials area alone is so broad that it is virtually impossible to cover all materials in a single volume. Carbon-based materials receive special attention in this book, because carbon is as important to nanotechnology as silicon is to electronics. The materials will not only be divided into traditional classes such as ceramics, semiconductors, metals, biomaterials, and polymers; but also will be treated based on their dimensionality, processing methods, and applications. A variety of applications, ranging from drug delivery systems and field-emission displays to machine tools and bioimplants will be described. Both commercially available and emerging materials will be covered. The handbook consists of 27 chapters written by leading researchers from academia, national laboratories, and industry, and covers the latest material developments in America, Asia, Europe, and Australia.

Finally, I would like to acknowledge all people who have been helpful in making this book possible. My family has been very patient and understanding. My students and postdocs helped me concentrate on the book project and Taylor & Francis staff helped me immensely.

Editor

Yury Gogotsi is professor of materials science and engineering at Drexel University, Philadelphia, Pennsylvania. He also holds appointments in the Departments of Chemistry and Mechanical Engineering at Drexel University and serves as director of the A.J. Drexel Nanotechnology Institute and associate dean of the College of Engineering. He received his M.S. (1984) and Ph.D. (1986) degrees from Kiev Polytechnic and a D.Sc. degree from the Ukrainian Academy of Science in 1995. His research group works on carbon nanotubes, nanoporous carbide-derived carbons, and nanofluidics. He has also contributed to the areas of structural ceramics, corrosion of ceramic materials, and pressure-induced phase transformations. He has coauthored 2 books, edited 7 books, obtained 20 patents, and authored more than 200 research papers. He has advised a number of M.S., Ph.D., and postdoctoral students at Drexel University and University of Illinois at Chicago.

Gogotsi received several awards for his research, including I.N. Frantsevich Prize from the Ukrainian Academy of Science, S. Somiya Award from the International Union of Materials Research Societies, Kuczynski Prize from the International Institute for the Science of Sintering, and Roland B. Snow Award from the American Ceramic Society. He has been elected a fellow of the American Ceramic Society, academician of the World Academy of Ceramics, and full member of the International Institute for the Science of Sintering.

Contributors

Rostislav A. Andrievski
Institute of Problems of Chemical Physics
Russian Academy of Sciences
Chernogolovka, Russia

Michel W. Barsoum
Department of Materials Science and Engineering
Drexel University
Philadelphia, Pennsylvania

François Béguin
Centre de Recherche sur la Matière Divisée
CNRS-Université
Orléans, France

J.D. Carey
Advanced Technology Institute
University of Surrey
Guildford, United Kingdom

A.K. Cheetham
University of California
Santa Barbara, California

I-Wei Chen
University of Pennsylvania
Philadelphia, Pennsylvania

Mingwei Chen
Tohoku University
Sendai, Japan

Ying Chen
Department of Electronic Materials Engineering
Research School of Physical Science and Engineering
The Australian National University
Canberra, Australia

D. Davis
Louisiana State University
Baton Rouge, Louisiana

Svetlana Dimovski
Department of Materials Science and Engineering
Drexel University
Philadelphia, Pennsylvania

Mildred S. Dresselhaus
Massachusetts Institute of Technology
Cambridge, Massachusetts

Fangming Du
Department of Chemical and Biomolecular Engineering
University of Pennsylvania
Philadelphia, Pennsylvania

Ali Erdemir
Argonne National Laboratory
Argonne, Illinois

Osman Levent Eryilmaz
Argonne National Laboratory
Argonne, Illinois

John E. Fischer
Department of Materials Science and Engineering
University of Pennsylvania
Philadelphia, Pennsylvania

Elzbieta Frackowiak
Institute of Chemistry and Technical Electrochemistry
Poznań University of Technology
Poznań, Poland

Yury Gogotsi
Department of Materials Science and Engineering
Drexel University
Philadelphia, Pennsylvania

Z. Guo
Louisiana State University
Baton Rouge, Louisiana

Meredith L. Hans
Department of Materials Science and Engineering
Drexel University
Philadelphia, Pennsylvania

Kevin Hemker
Johns Hopkins University
Baltimore, Maryland

Joseph P. Heremans
The Ohio State University
Columbus, Ohio

Q. Huang
Louisiana State University
Baton Rouge, Louisiana

Pavel E. Kazin
Moscow State University
Moscow, Russia

Kursat Kazmanli
Istanbul Technical University
Istanbul, Turkey

Frank K. Ko
Department of Materials Science and Engineering
Drexel University
Philadelphia, Pennsylvania

Y. Li
Louisiana State University
Baton Rouge, Louisiana

Anthony M. Lowman
Department of Materials Science and Engineering
Drexel University
Philadelphia, Pennsylvania

A. Lozano-Morales
Louisiana State University
Baton Rouge, Louisiana

En Ma
Johns Hopkins University
Baltimore, Maryland

R.A. Masumura
Naval Research Laboratory
Washington, D.C.

Aurelio Mateo-Alonso
Dipartimento di Scienze Farmaceutiche
Università degli Studi di Trieste
Piazzale Europa, Italy

Gary McGuire
International Technology Center
Research Triangle Park, North Carolina

Nikhil Mehta
Auburn University
Auburn, Alabama

A. Nikitin
Department of Materials Science and Engineering
Drexel University
Philadelphia, Pennsylvania

I.A. Ovid'ko
Institute of Problems of Mechanical Engineering
Russian Academy of Sciences
Moscow, Russia

Giuseppe R. Palmese
Department of Materials Science and Engineering
Drexel University
Philadelphia, Pennsylvania

A. Panda
Louisiana State University
Baton Rouge, Louisiana

C.S. Pande
Naval Research Laboratory
Washington, D.C.

Nicholas A. Peppas
University of Texas
Austin, Texas

E.J. Podlaha
Louisiana State University
Baton Rouge, Louisiana

Maurizio Prato
Dipartimento di Scienze Farmaceutiche
Università degli Studi di Trieste
Piazzale Europa, Italy

Barton Prorok
Auburn University
Auburn, Alabama

Eduard G. Rakov
D.I. Mendeleev University of Chemical Technology
Moscow, Russia

Vijay I. Raman
Department of Materials Science and Engineering, Drexel University
Philadelphia, Pennsylvania

C.N.R. Rao
Jawaharlal Nehru Centre for Advanced Scientific Research
Bangalore, India

Michiko Sato
Purdue University
West Lafayette, Indiana

Olga Shenderova
International Technology Center
Research Triangle Park, North Carolina

S.R.P. Silva
Advanced Technology Institute
University of Surrey
Guildford, United Kingdom

Amit Singhal
NEI Corporation
Piscataway, New Jersey

Ganesh Skandan
NEI Corporation
Piscataway, New Jersey

Jonathan E. Spanier
Department of Materials Science and Engineering
Drexel University
Philadelphia, Pennsylvania

Nikos Tagmatarchis
Dipartimento di Scienze Farmaceutiche
Università degli Studi di Trieste
Piazzale Europa, Italy

R. Tenne
Department of Materials and Interfaces
Weizmann Institute
Rehovot, Israel

J. Brock Thomas
University of Texas
Austin, Texas

Yuri D. Tretyakov
Moscow State University
Moscow, Russia

Mustafa Urgen
Istanbul Technical University
Istanbul, Turkey

Xiao-Hui Wang
Tsinghua University
Beijing, China

Thomas J. Webster
Purdue University
West Lafayette, Indiana

Karen I. Winey
Department of Materials Science and Engineering
University of Pennsylvania
Philadelphia, Pennsylvania

G. Yushin
Department of Materials Science and Engineering
Drexel University
Philadelphia, Pennsylvania

Hongzhou Zhang
Department of Electronic Materials Engineering
Research School of Physical Sciences and Engineering
The Australian National University
Canberra, Australia

J. Zhang
Louisiana State University
Baton Rouge, Louisiana

Table of Contents

1 Materials Science at the Nanoscale

C.N.R. Rao
Jawaharlal Nehru Centre for Advanced Scientific Research, Bangalore, India

A.K. Cheetham
University of California, Santa Barbara, California

CONTENTS

1.1 INTRODUCTION

Nanoscience and nanotechnology primarily deal with the synthesis, characterization, exploration, and exploitation of nanostructured materials. These materials are characterized by at least one dimension in the nanometer ($1\,nm = 10^{-9}\,m$) range. Nanostructures constitute a bridge between molecules and infinite bulk systems. Individual nanostructures include clusters, quantum dots, nanocrystals, nanowires, and nanotubes, while collections of nanostructures involve arrays, assemblies, and superlattices of the individual nanostructures [1,2]. Table 1.1 lists typical dimensions of nanomaterials. The physical and chemical properties of nanomaterials can differ significantly from those of the atomic-molecular or the bulk materials of the same composition. The uniqueness of the structural characteristics, energetics, response, dynamics, and chemistry of nanostructures constitutes the basis of nanoscience. Suitable control of the properties and response of nanostructures can lead to new devices and technologies. The themes underlying nanoscience and nanotechnology are twofold: one is the bottom-up approach, that is, the miniaturization of the components, as articulated by Feynman, who stated in the 1959 lecture that "there is plenty of room at the bottom" [3]; and the other is the approach of the self-assembly of molecular components, where each nanostructured component becomes part of a suprastructure. The latter approach is akin to that of Jean-Marie Lehn [4].

TABLE 1.1
Nanostructures and Their Assemblies

Nanostructure	Size	Material
Clusters, nanocrystals Quantum dots	Radius, 1–10 nm	Insulators, semiconductors, metals, magnetic materials
Other nanoparticles	Radius, 1–100 nm	Ceramic oxides
Nanobiomaterials, Photosynthetic reaction center	Radius, 5–10 nm	Membrane protein
Nanowires	Diameter, 1–100 nm	Metals, semiconductors, oxides, sulfides, nitrides
Nanotubes	Diameter, 1–100 nm	Carbon, layered Chalcogenides, BN, GaN
Nanobiorods	Diameter, 5 nm	DNA
Two-dimensional arrays of nanoparticles	Area, several nm^2–μm^2	Metals, semiconductors, magnetic materials
Surfaces and thin films	Thickness, 1–100 nm	Insulators, semiconductors, metals, DNA
Three-dimensional superlattices of nanoparticles	Several nm in three dimensions	Metals, semiconductors, magnetic materials

Some of the important concerns of materials scientists in the nanoscience area are:

- Nanoparticles or nanocrystals of metals and semiconductors, nanotubes, nanowires, and nanobiological systems.
- Assemblies of nanostructures (e.g., nanocrystals and nanowires) and the use of biological systems, such as DNA as molecular nanowires and templates for metallic or semiconducting nanostructures.
- Theoretical and computational investigations that provide the conceptual framework for structure, dynamics, response, and transport in nanostructures.
- Applications of nanomaterials in biology, medicine, electronics, chemical processes, high-strength materials, etc.

Nanoscience and nanotechnology have grown explosively in the last decade, because of the increasing availability of methods of synthesis of nanomaterials as well as tools of characterization and manipulation (Table 1.2). Several innovative methods of synthesizing nanoparticles and nanotubes and their assemblies are now available. The size-dependent electrical, optical, and magnetic properties of individual nanostructures of semiconductors, metals, and other materials are better understood. Besides the established techniques of electron microscopy, crystallography, and spectroscopy, scanning probe microscopies have provided powerful tools for the study of nanostructures. Novel methods of fabricating patterned nanostructures as well as new device concepts are being constantly discovered. Nanostructures also offer opportunities for meaningful computer simulation and modeling since their size is sufficiently small to permit considerable rigor in treatment. In computations on nanomaterials, one deals with a spatial scaling from 1 Å to 1 μm and temporal scaling from 1 fs to 1 s, the limit of accuracy going beyond 1 kcal/mol. There are many examples to demonstrate current achievements in this area: familiar ones are STM images of quantum dots (e.g., germanium pyramid on a silicon surface) and the quantum corral of 48 Fe atoms placed in a circle of 7.3-nm radius. Ordered arrays or superlattices of nanocrystals of metals and semiconductors have been prepared by several workers. Nanostructured polymers formed by the ordered self-assembly of triblock copolymers and nanostructured high-strength materials (e.g., Cu/Cr nanolayers) are other examples. Prototype circuits involving nanoparticles and nanotubes for nanoelectronic devices have been fabricated.

Remember that some of the established technologies, such as catalysis and photography, already employ nanoscale processes. The capability to synthesize, organize, and tailor-make

TABLE 1.2
Synthesis and Methods of Characterization of Nanomaterials

Scale (approx.)	Synthetic Methods	Structural Tools	Theory and Simulation
0.1–10 nm	Covalent synthesis	Vibrational, spectroscopy, NMR, diffraction methods, scanning probe microscopies (SPM)	Electronic structure, molecular dynamics, transport
<1–100 nm	Self-assembly techniques	SEM, TEM, SPM	Molecular dynamics and mechanics
100 nm–1 μm	Processing	SEM, TEM	Coarse-grained models for electronic interactions, vibronic effects, transport.

materials at the nanoscale is, however, of recent origin. The present goals of the science and technology of nanomaterials are to master the synthesis of nanostructures (nano-building units) and their assemblies of desired properties; to explore and establish nanodevice concepts; to generate new classes of high-performance nanomaterials, including biology-inspired systems; and to improve techniques for the investigation of nanostructures [5–7]. One potential applications of nanotechnology is the production of novel materials and devices in nanoelectronics, computer technology, medicine, and health care.

1.2 THE NANOWORLD IS UNIQUELY DIFFERENT

The physical and chemical properties of nanostructures are distinctly different from those of a single atom (molecule) and bulk matter with the same chemical composition. These differences between nanomaterials and the molecular and condensed-phase materials pertain to the spatial structures and shapes, phase changes, energetics, electronic structure, chemical reactivity, and catalytic properties of large, finite systems, and their assemblies. Some of the important issues in nanoscience relate to size effects, shape phenomena, quantum confinement, and response to external electric and optical excitations of individual and coupled finite systems.

Size effects are an essential aspect of nanomaterials. The effects determined by size pertain to the evolution of structural, thermodynamic, electronic, spectroscopic, and chemical features of these finite systems with increasing size. Size effects are of two types: one is concerned with specific size effects (e.g., magic numbers of atoms in metal clusters, quantum mechanical effects at small sizes) and the other with size-scaling applicable to relatively larger nanostructures. The former includes the appearance of new features in the electronic structure. In Figure 1.1, we show how the electronic structures of metal and semiconductor nanocrystals differ from those of bulk materials and isolated atoms. In Figure 1.2, we show the size dependence of the average energy level spacing of sodium in terms of the Kubo gap (E_F/N) in Kelvin. In this figure, we also show the effective percentage of surface atoms as a function of particle diameter. Note that at small sizes, we have a high percentage of surface atoms.

The structure of nanoparticles of CdS, CdSe, and such materials is affected by size. Melting point, electronic absorption spectra, and other properties show marked size effects. In Figure 1.3 and Figure 1.4, we show some of the size effects graphically. It should be noted that metals show nonmetallic band gaps when the diameter of the nanocrystals is in the 1 to 2 nm range. Hg clusters show a nonmetallic band gap that decreases with increase in cluster size. Approximately 300 atoms appear to be necessary to close the gap. Metal nanoparticles of 1 to 2 nm diameter exhibit unexpected catalytic activity, as exemplified by nanocatalysis by gold particles.

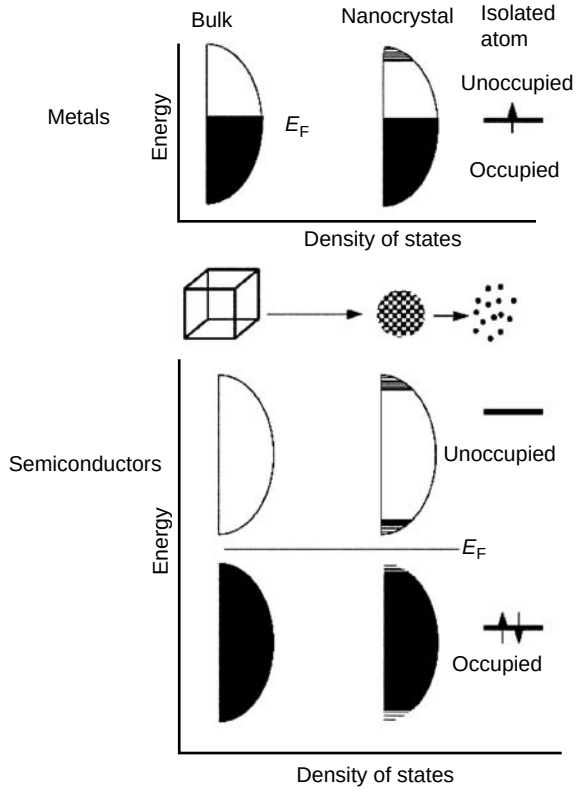

FIGURE 1.1 Density of states for metal and semiconductor nanocrystals compared to those of the bulk and of isolated atoms. (Reproduced from Rao, C.N.R. et al., *Chem-Eur. J.*, 8, 29, 2002.)

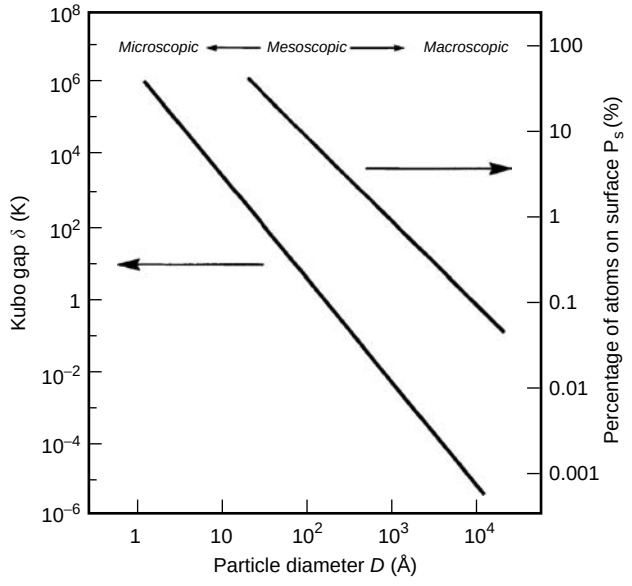

FIGURE 1.2 A plot of the average electronic level spacing (Kubo gap, δ) of sodium as a function of nanoparticle diameter. Also shown as the percentage of atoms at the surface. (Reproduced from Edwards, P.P., et al., in *Metal Clusters in Chemistry*, Braunstein, P., et al., Ed., John Wiley & Sons, New York, p. 1454, 1999.)

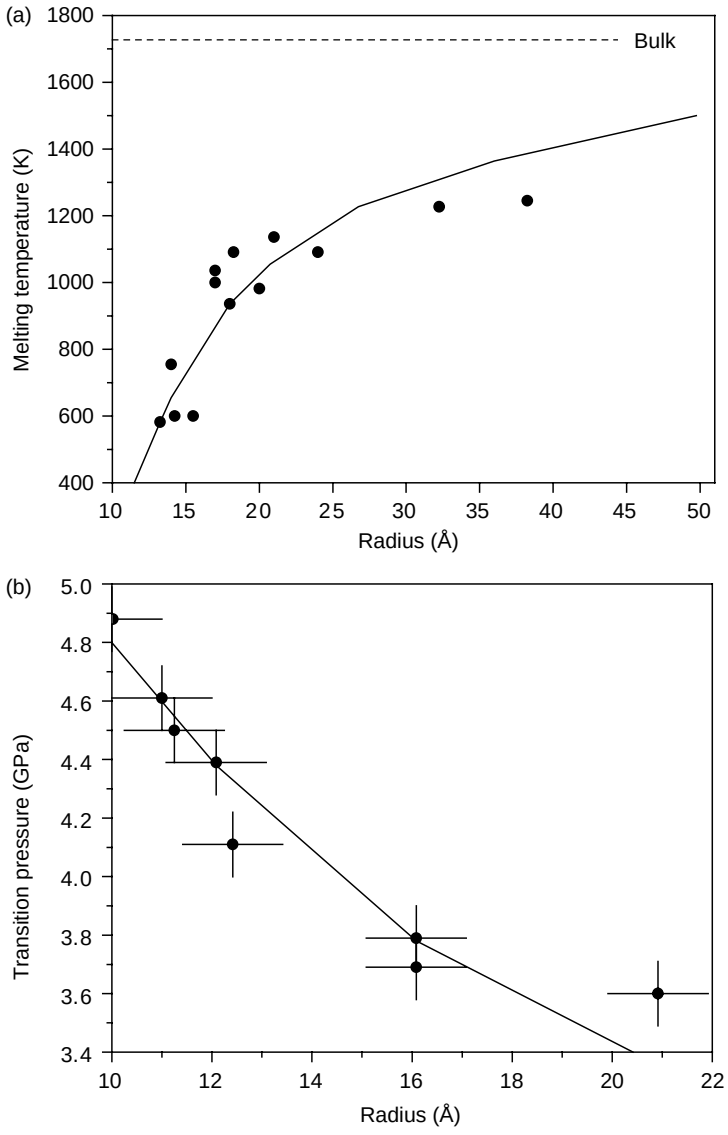

FIGURE 1.3 Size dependence of the (a) melting temperature of CdS nanocrystals and (b) the pressure induced transformation of the wurtzite-rock salt transformation in CdSe nanocrystals. (Reproduced from Alivisatos, A.P., *J. Phys. Chem.*, 100, 13226, 1996.)

Shapes of nanoparticles also play a role in determining properties, such as reactivity and electronic spectra. For example, the position of the plasmon band of metal nanorods is sensitive to the aspect ratio.

1.3 SYNTHESIS AND CHARACTERIZATION

The growth of nanoscience and nanotechnology in the last decade has been possible because of the success in the synthesis of nanomaterials in conjunction with the advent of tools for characterization and manipulation. The synthesis of nanomaterials spans inorganic, organic, and biological systems on manipulation (Table 1.2). The subsequent assembling of the individual nanostructures into

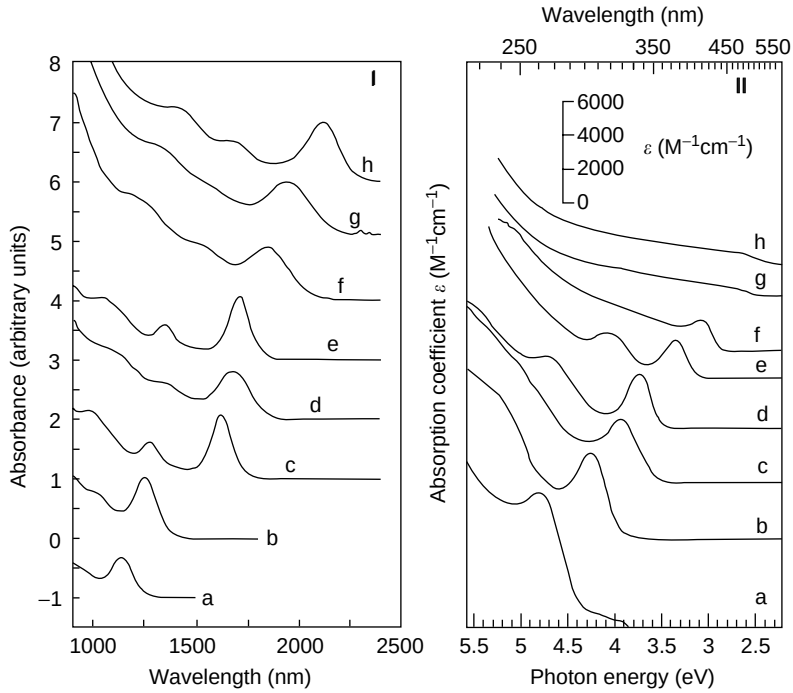

FIGURE 1.4 Electronic absorption spectra of (I) PbSe, (II) CdS nanocrystals. I, a.3, b.3.5, c.4.5, d.5, e.5.5, f.7, g.8, h.9 nm II, a.64, b.0.72, c.0.8, d.0.93, e.1.94, f.2.8, g.4.8 nm. (Reproduced from Vossmeyer, T., et al., *J. Phys. Chem.*, 98, 7665, 1994 and Murray, R.W., et al., *IBM J. Res. Dev.*, 45, 47, 2001.)

ordered arrays is often imperative. Notable examples of the synthesis of novel nanobuilding units are:

- Nanocrystals of metals, semiconductors and magnetic materials, employing colloid chemistry methods
- The use of physical and chemical methods for the synthesis of nanoparticles of ceramic materials
- Surface deposition of clusters and nanocrystals on graphite and other metallic or semiconducting surfaces to obtain novel three- or two-dimensional nanosystems
- Single- and multi-walled carbon nanotubes as well as nanotubes of inorganic materials, such as metal oxides, chalcogenides, and nitrides
- Nanowires of metals, semiconductors, oxides, nitrides, sulfides, and other materials
- New polymeric structures involving dendrimers and block copolymers
- Nanobiological structures (e.g., bacterial and plant photosynthetic reaction centers and segments of DNA). Mutagenesis of the protein structure as well as chemical modifications of the DNA double strand, enable the control of the response of these systems

The synthesis of nanomaterials includes control of size, shape, and structure. Assembling the nanostructures into ordered arrays often becomes necessary for rendering them functional and operational. In the last decade, nanoparticle (powders) of ceramic materials have been produced in large scales by employing both physical and chemical methods. There has been considerable progress in the preparation of nanocrystals of metals, semiconductors, and magnetic materials by employing colloid chemical methods [2]. Nanocrystals of materials with narrow size distributions have been

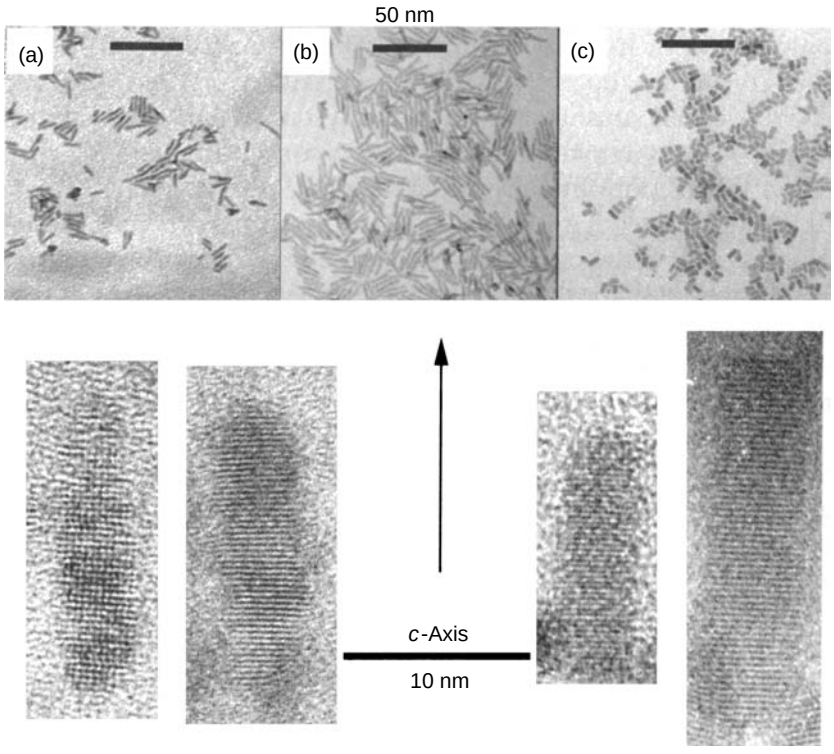

FIGURE 1.5 TEM images of CdSe quantum rods (a, b) low-resolution images of quantum rods of different aspect ratios; (c) three-dimensional orientation. High resolution images are also shown. (Reproduced from Peng, X. et al., *Nature*, 404, 59, 2000.)

prepared by controlling the shape in some instances. To illustrate this aspect, we show transmission electron microscope (TEM) images of CdSe nanorods in Figure 1.5.

Since the discovery of carbon nanotubes [11], there has been considerable progress in the synthesis of multi- and single-walled nanotubes (MWNTs and SWNTs) and bundles of aligned nanotubes [12,13]. In Figure 1.6, we show electron microscope images of MWNTs and SWNTs. Typical methods employed to synthesize SWNTs are an arc discharge with carbon electrodes containing suitable catalysts, laser ablation, pyrolysis of precursors, and decomposition of CO. Carbon nanotubes have been doped with nitrogen and boron. Especially noteworthy is the synthesis of Y-junction carbon nanotubes, which could become vital components in nanoelectronics. Nanotubes of inorganic materials, in particular those of layered metal chalcogenides (e.g., MoS_2, WS_2, $MoSe_2$, NbS_2), have been synthesized by various methods [14,15].

The construction of ordered arrays of nanostructures by employing techniques of organic self-assembly provides alternative strategies for nanodevices. Two- and three-dimensional arrays of nanocrystals of semiconductors, metals, and magnetic materials have been assembled by using suitable organic reagents. Strain-directed assembly of nanoparticle arrays (e.g., of semiconductors) provides the means to introduce functionality into the substrate that is coupled to that on the surface. We show TEM images of self-assembled Pd nanocrystals capped with alkanethiols in Figure 1.7. Assembly of nanocrystals is carried out by various means. Besides the use of alkane thiols and such reagents, DNA-directed assembly has been accomplished.

The area of nanoporous solids has witnessed many major advances. A constant quest for crystalline solids with giant pores has resulted in the recent synthesis of several novel materials [2]. The pore size in zeolites and other nanoporous materials can be controlled and the shape-selective

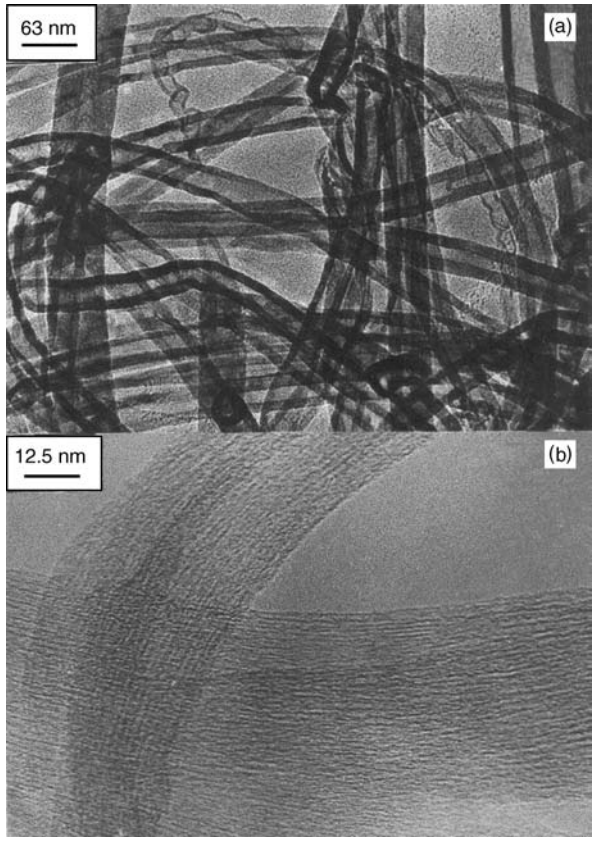

FIGURE 1.6 Transmission electron microscopic images of (a) multi- and (b) single-walled carbon nanotubes.

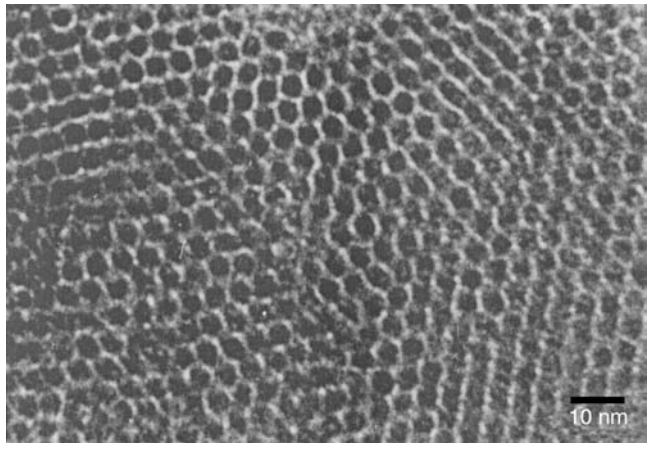

FIGURE 1.7 Two-dimensional arrays of Pd nanocrystals.

catalysis afforded by nanoporous solids continues to motivate much of the work in catalysis. Since Mobil chemists discovered mesoporous MCM 41, a variety of mesoporous inorganic solids with pore diameters in the 2 to 20 nm range have been prepared and characterized. Mesoporous fibers and spheres of silica and other materials have also been prepared. A variety of inorganic, organic,

and organic–inorganic hybrid open-framework materials with different pore architectures have been synthesized in the last few years.

Typical examples of self-assembly are:

- Two- and three-dimensional structures of nanocrystals of semiconductors, metals, and magnetic materials self-assembled using suitable organic solvents.
- Polymer-coated nanocrystals assembled to form giant nanoparticles.
- Self-assembled carbon nanotubes forming single crystals.
- Self-assembly of colloid nanostructures.
- Self-assembly induced by Lithography.
- Utilization of the unique features of recognition, assembly, and specific binding of nucleobases in DNA duplexes for the construction of blocks or templates for the assembly of other nanoelements.
- Decoration of viral particles with metal nanoparticles, with the aim of allowing the viruses to assemble themselves into arrays to create networks of the nanoparticles.

1.4 EXPERIMENTAL METHODS

While the standard methods of measurement and characterization are constantly employed for the investigation of nanostructures, the use of scanning probe microscopies (spatial resolution, ~1 nm), combined with high-resolution electron microscopy, has enabled direct images of the structures and the study of properties. For example, scanning tunneling spectroscopy and conduction atomic force microscopy provide information on the electronic structure and related properties. Scanning probe microscopies are employed at low temperatures, under vacuum or in magnetic fields. Magnetic force microscopy directly images magnetic domains, and magnetic resonance microscopes can detect nuclear or electron spin resonance with submicron spatial resolution. Computer-controlled scanning probe microscopy is useful in nanostructure manipulation in real time, and nanomanipulators are being used with scanning and TEMs. Newer versions of nanomanipulators will have to be developed by using technologies such as nanoelectromechanical systems (NEMS).

Near-field scanning optical microscopy allows optical access to sub-wavelength scales (50 to 100 nm) by breaking the diffraction limit. Optical tweezers provide an elegant means to investigate the mechanical properties and dynamics of particles and molecules. Thus, force measurement of complementary DNA binding provides a sensitive sensor.

Nanomechanics performed using the atomic force microscope enables the study of single molecules, and is valuable in understanding folding and related problems in biological molecules. Cantilever probes have been developed to enable high-speed nanometer scale imaging.

Microfabricated chips for DNA analysis and polymerase chain reactions have been developed. It would be of great benefit if improved tools for three-dimensional imaging and microscopy, as well as for chemical analysis of materials in nanometric dimensions, become available.

1.5 COMPUTER SIMULATION AND MODELING

Several computational techniques have been employed to simulate and model nanomaterials. Since the relaxation times can vary anywhere from picoseconds to hours, it becomes necessary to employ Langevin dynamics besides molecular dynamics in the calculations. Simulation of nanodevices through the optimization of various components and functions provides challenging and useful task. There are many examples where simulation and modeling have yielded impressive results, such as nanoscale lubrication. Simulation of the molecular dynamics of DNA has been successful to some extent. Quantum dots and nanotubes have been modeled satisfactorily. First principles calculations of nanomaterials can be problematic if the clusters are too large to be treated by Hartree–Fock methods and too small for density functional theory.

1.6 APPLICATIONS

By employing sol–gels and aerogels, inorganic oxide materials of high surface areas with improved absorptive, catalytic, and other properties are being produced. Consolidated nanocomposites and nanostructures enable production of ultrahigh strength, tough structural materials, strong ductile cements, and novel magnets. Significant developments are occurring in the sintering of nanophase ceramic materials and in textiles and plastics containing dispersed nanoparticles. Nanostructured electrode materials could improve the capacity and performance of the Li-ion batteries. Shipway et al. [16] have reviewed nanoparticle-based applications. Known and new types of nano-, meso- and macroporous materials can be put to use for inorganic synthesis and in industrial catalysis. The chemical industry may indeed get involved to a greater extent in the design of catalysts containing different types of nanometric particles, since nanoscale catalysis could provide great selectivity.

Techniques of nanoimprint lithography and soft lithography are sufficiently developed and a combination of self-assembly with tools of patterning can enable new nanolithographic patterns. Thin-film electrets patterned with trapped charge provides another method of patterning that may be useful in high-density charge-based data storage and high-resolution printing. Dip-pen lithography [17] employing nanomaterials has made progress (Figure 1.8).

Potential applications of carbon nanotubes are many [12,18]. Carbon nanotubes are being used as tips in scanning microscopes and also as efficient field emitters for possible use in display devices. Since SWNTs can be metallic or semiconducting, we would expect many applications exploiting the electronic structure of these materials [2]. Thus, the supercapacitance of the nanotubes can be used for applications in various ways, such as electrochemical actuators. Field-effect transistors have been fabricated using nanotubes. We show typical *I–V* curves in an FET configuration in Figure 1.9. Three- and four-terminal devices seem possible. The Y-junction nanotubes can become useful chips for fabrication of novel circuits.

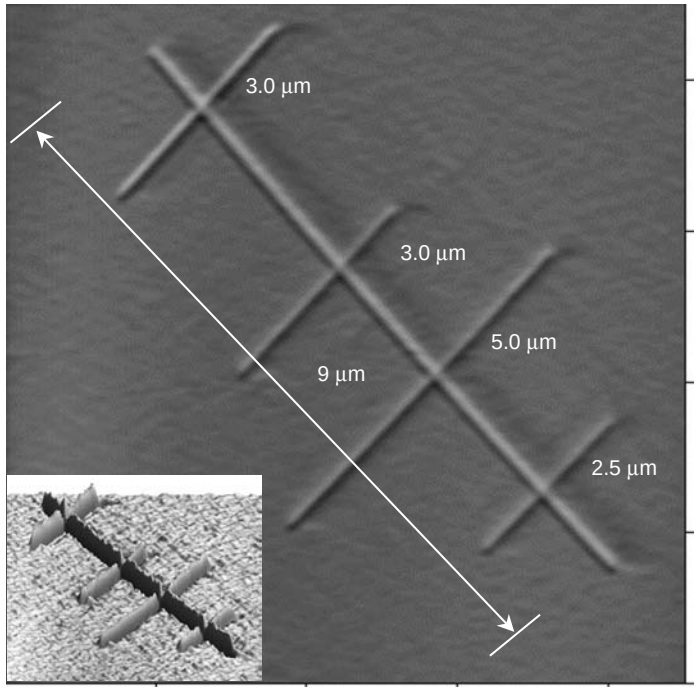

FIGURE 1.8 Dip-pen lithography using Fe_2O_3 nanoparticles. (Reproduced from Gundiah, G. et al., *Appl. Phys. Lett.*, 84, 5341, 2004.)

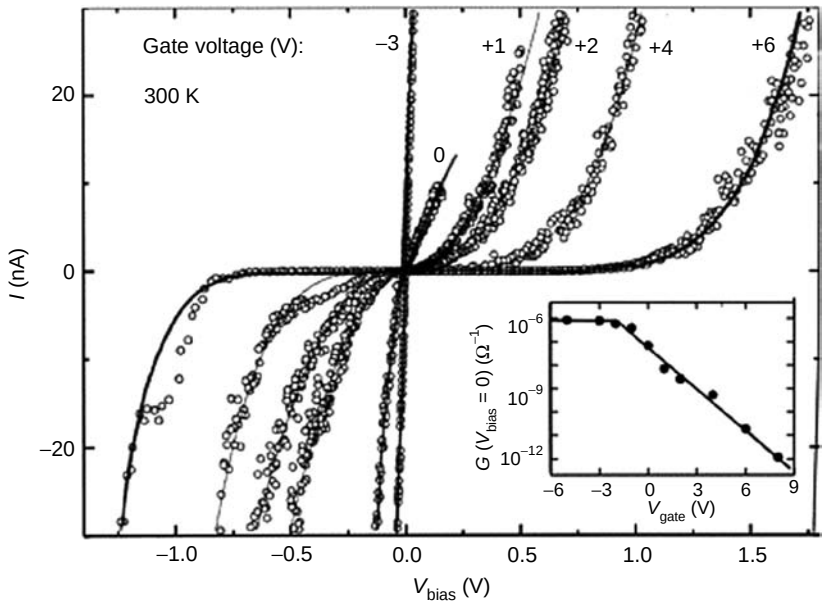

FIGURE 1.9 *I–V* characteristics of a single-walled nanotube at different gate voltages showing field-effect transistor behavior. (Reproduced from Tans, S.J., Veresheuren, A.R.M., and Dekker, C., *Nature*, 393, 49, 1998.)

Chemical and biochemical sensors have been fabricated with nanotubes. Although carbon nanotubes were expected to be good for hydrogen storage, recent measurements have negated this possibility. Surface properties of carbon nanotubes are being explored for catalytic applications, specially after deposition of metal nanoparticles on the surface. While we limit ourselves to carbon nanotubes here, remember that potential uses of inorganic nanotubes have not been explored. Similarly, the use of inorganic nanowires for various applications has yet to be investigated fully.

Colloidal gold particles attached to DNA strands can be employed to assay specific complementary DNAs. There are many examples where semiconductor or metal nanocrystals or quantum dots have been tagged for use as biological sensors. The technology of DNA microchip arrays, involving lithographic patterning, is bound to see further improvement. Drug and gene delivery will become increasingly more effective with the use of nanoparticles and nanocapsules. Molecular motors, such as the protein F_1-AT phase, are already known, but it may become practical to power an inorganic nanodevice with such a biological motor. Other areas of biology in which nanomaterials can have an impact are the monitoring of the environment and living systems by the use of nanosensors and the improvement of prosthetics used to repair or replace parts of the human body.

The most significant applications of nanomaterials may be in nanodevices and nanoelectronics [1,12,18]. There are already some important advances in these areas to justify such an expectation. Typical of the advances made hitherto are the demonstration of single-electron memory. Coulomb blockade and quantum effects, scanning probe tips in arrays, logic elements, and sensors. Applications of semiconductors nanostructures, in particular those of the III–V nitrides (e.g., InGaN) as LEDs and laser diodes, have been impressive, and quantum dots and wires of these materials will have many uses. Resonant tunneling devices in nanoelectronics deserve special mention since they have already demonstrated success in multivalued logic and memory circuits. Functional devices based on quantum confinement would be of use in photonic switching and optical communications.

1.7 OUTLOOK

The preceding sections provide a glimpse of the present status of nanostructured materials. There is great vitality in this area and immense opportunities. Nanoscience is a truly interdisciplinary area covering physics, chemistry, biology, materials, and engineering. Interaction among scientists with different backgrounds will undoubtedly create new materials and a new science with novel technological possibilities.

Nanoscience and nanotechnology are likely to benefit various industrial sectors, including chemical and electronic industries, as well as manufacturing. Health care, medical practice, and environmental protection will benefit from nanoscience. One of the difficult problems facing the design of nanostructures-based systems is understanding how to interconnect and address them. The success of nanoscience will depend on the development of new device and manufacturing technologies. There is every reason to believe that there will be much progress in the coming decade.

REFERENCES

1. Rao, C.N.R., Muller, A., and Cheetham, A.K., Eds., *Chemistry of Nanomaterials*, Wiley-VCH, Weinheim, 2004.
2. Rao, C.N.R. and Cheetham, A.K., Science and Technology of Nanomaterials, *J. Mater. Chem.*, 11, 2887, 2001.
3. Feynmann, R.P., *Miniaturization*, Reinhold, New York, 1961.
4. Lehn, J.M., *Supramolecular Chemistry*, VCH, Weinheim, 1995.
5. Seigel, R.W., Hu, H., and Roco, M.C., Eds., *Nanostructure Science and Technology*, Kluwer Academic Publishers, Boston, 1999.
6. Roco, M.C., William, R.S., and Alivisatos, A.P., *Nanotechnology Research Directions*, Kluwer Academic Publishers, Boston, 2000.
7. National Nanotechnology Initiative, National Science and Technology Council, Washington DC, 2002.
8. Jortner, J. and Rao, C.N.R., *Pure Appl. Chem.*, 74, 1491, 2002.
9. Alivisatos, P., *Science*, 271, 933, 1996.
10. (a) Goldstein, A.N., Echer, C.M., and Alivisatos, A.P., *Science*, 256, 1425, 1992; (b) Tolbert, S.H., and Alivisatos, A.P., *Science*, 265, 373, 1994; (c) Alivisatos, A.P., *J. Phys. Chem.*, 100, 13226, 1996.
11. Iijima, S., Nature, 363, 603, 1993.
12. Rao, C.N.R., and Govindaraj, A., Nanotubes and Nanowires, *Royal Soc. Chem.* (London), 2005.
13. *Accounts Chem. Res.*, (Special issue), 35, 997–1113, 2002.
14. Tenne, R., and Rao, C.N.R., Inorganic Nanotubes, *Phil. Trans. Royal Soc*. (London), 362, 2099, 2004.
15. Rao, C.N.R., Deepak, F.L., Gundiah, G. and Govindaraj, A., Inorganic nanowires, *Prog. Solid State Chem.*, 31, 5, 2003.
16. Shipway, A.N., Katz, E., and Willner, I., *Chem. Phys. Chem.*, 1, 18, 2001.
17. Piner, R.D., Zhu, J., Xu, F., Hong, S., and Mirkin, C.A., *Science*, 283, 601, 1999.
18. Baughman, R.H., Zakhidov, A.A., and de Heer, W.A., *Science*, 297, 787, 2002.

2 Perspectives on the Science and Technology of Nanoparticle Synthesis

Ganesh Skandan and Amit Singhal
NEI Corporation, Piscataway, New Jersey

CONTENTS

2.1 INTRODUCTION

Nanostructured materials, particularly those derived from nanoparticles, have evolved as a separate class of materials over the past decade. The most remarkable feature has been the way in which completely disparate disciplines have come together with nanomaterials as the theme. The breadth of the field is enormous, ranging from the use of nanoparticles of zinc oxide in hygiene products, such as diapers [1], to altering the characteristics of solid rocket propellants by the addition of nanoparticle fillers [2]. The enthusiasm is justified for the most part, as the fundamental materials' properties appear to be different at the nanoscale. For example, according to Qi and Wang [3], when the ratio of the size of the atom to that of the particle becomes less than 0.01 to 0.1, the cohesive energy begins to decrease, which in turn reduces the melting point. In a related report, Nanda and co-workers [4] have shown that the surface energy of free nanoparticles is higher than that of

embedded nanoparticles, and is substantially higher compared to that of the bulk. There is also ample evidence that nanoparticles display characteristics that are distinctly different from their microcrystalline counterparts. For example, Reddy and co-workers [5] have shown that nanoparticles of anatase TiO_2, synthesized by a precipitation technique, show direct bandgap semiconductor behavior, whereas microcrystalline TiO_2 is an indirect bandgap material.

The field has matured so rapidly and so fast that it is probably hard to find a segment of any technical subject where the implications of nanomaterials have not been explored at least to a preliminary extent. Studies are being conducted on the potential use of nanomaterials in diverse applications, including hydrogen storage [6,7], ion-sensing and gas sensing [8], surface-modified nanoparticles for enhanced oil recovery [9], adsorption of chemical and biological agents on to nanoparticles (website of Nanoscale Materials Inc.), active electrode materials for lithium-ion batteries [10], light-emitting devices [11] and dental compositions [12], to name a few.

The purpose of this chapter is to examine the progress to date in the science and technology of the production of ultrafine particles, which form the building blocks for nanostructured materials. While high surface area inorganic materials of a few compositions, such as supported metal catalysts, carbon black, and nanoparticulate silica, have been in use for several decades; it was not until the 1970s and 1980s that new techniques were developed in a deliberate attempt to synthesize tailored nanoparticles [13–16] of different compositions. However, these efforts were few and far apart. Further, the implications of materials at such a fine scale were at best poorly appreciated. Some 10 to 15 years later, in the late 1980s and early 1990s, several new nanoparticle synthesis techniques began to be developed, most of them at university and national research laboratories. These processes targeted for the most part, nanoparticles of single phase (e.g., TiO_2, SiC) and multicomponent ($BaTiO_3$, Y_2O_3–ZrO_2) materials. With the availability of nanoparticles, albeit in relatively small quantities, applications began to be developed, which in turn provided the impetus to scale the production processes to commercially accepted levels, and at the same time, develop lower cost approaches to nanoparticles synthesis. Sometime thereafter, the emphasis shifted to synthesis of "designer" nanoparticles, often with a complex structure as well. These were aimed at specific applications, where either the nanoparticles when added to a matrix would provide a desired functionality, or the nanoparticles themselves were processed into a film or a coating. In contrast, despite a massive global effort, processing nanoparticles into large bulk nanostructured objects has remained a laboratory curiosity. This chapter is an attempt to outline the progression of the field of nanoparticulate materials from both a fundamental research as well as a commercial standpoint. The discussion here is restricted to metal and ceramic nanoparticles and their corresponding inorganic–organic hybrids.

2.2 CLASSIFICATION OF NANOPARTICLE SYNTHESIS TECHNIQUES

All particle synthesis techniques fall into one of the three categories: vapor-phase, solution precipitation, and solid-state processes. There are a handful of processes that combine aspects of one or more of these broad categories of processes. Although vapor-phase processes have been in vogue during the early days of nanoparticles development, the last of the three processes mentioned above is the most widely used in the industry for production of micron-sized particles, predominantly due to cost considerations. One of the most established powder producers, Ferro Corporation, uses the solid-state synthesis method almost exclusively; hundreds of tons of lithium cobalt oxide, which is the commonly used cathode material in lithium-ion batteries, is produced using solid-state synthesis. A description of nanoparticles synthesis techniques that fall into one of the above categories follows.

2.2.1 Solid-State Synthesis of Nanoparticles

Solid-state synthesis generally involves a heat treatment step (in order to achieve the desired crystal structure), which is followed by media milling. While it is generally believed that it is difficult

for the lower limit of the average particle size to be much below 100 nm, recent innovations by established companies in the industry may prove otherwise. In particular, the Netzsch LMZ-25 ZETA II System and the Dyno-Mill ECM may push the envelope on what mechanical attrition can do to reduce the particle size. It is claimed that nanoparticles as small as 30 nm can be produced using milling media of a very small size, i.e., 200 μm [17].

Judging by the contents of publications, the scientific community has not shown much enthusiasm for mechanical attrition processes for nanoparticles synthesis, perhaps due to issues pertaining to impurity pick up, lack of control on the particle size distribution, and inability to tailor precisely the shape and size of particles in the 10 to 30 nm range, as well as the surface characteristics. Nonetheless, in several instances a modified version of mechanical attrition has been used to synthesize oxide nanoparticles. In the mid-1990s, Advanced Powder Technology in Australia [18] pioneered a solid-state process with a postmilling operation. Dry milling was used to induce chemical reactions through ball-powder collisions that resulted in forming nanoparticles within a salt matrix. Particle agglomeration was minimized by the salt matrix, which then was removed by a simple washing procedure. One of the major products was cerium oxide, which generally has been an expensive material and scarcely available in a nanopowder form. There continues to be reports on the so called mechanochemical processing of nanoparticles, albeit in various different forms; for example, in a recent publication Todaka et al. [19] synthesized ferrite compounds with a spinel structure (e.g., Fe_3O_4, $CoFeO_4$) by ball-milling aqueous solutions of metal chlorides and NaOH.

It should be noted, however, that mechanical milling is a versatile technique to produce metallic nanocrystalline micropowders, as opposed to high surface area nanoparticles. One of the earliest efforts on nanocrystalline metals was by researchers at Exxon Mobil [20], where aluminum and its alloys were ball-milled in liquid-nitrogen atmosphere. In addition to refining the grain size, the milling process introduced ultrafine dispersion, which improved the high temperature creep resistance. The work was subsequently expanded to other materials' systems by Lavernia and co-workers [21]. In conventional high-energy ball milling, the creation and self-organization of dislocations to high-angle grain boundaries within the powder particles during the milling process leads to a reduction in the grain size by a factor of about 10^4. In keeping with the focus of the chapter on nanoparticulate materials, the reader is referred to the article written by Koch [22], where detailed descriptions of milling processes have been provided. Accordingly, no further discussion on solid-state processes used to synthesize nanoparticles will be made in this chapter.

2.2.2 Vapor-Phase Synthesis of Nanoparticles

Gas condensation, as a technique for producing nanoparticles, refers to the formation of nanoparticles in the gas phase, i.e., condensing atoms and molecules in the vapor phase. Oddly enough, it had been practiced in the industry long before it became the subject of research in institutions worldwide. For example, Cabot Corporation in the United States and Degussa in Germany, have been using atmospheric flame reactors for decades to produce megatons of such diverse nanoparticles as carbon black (used in tires and inks), silicon dioxide (used in myriad applications including additives in coffee creamers and polymers), and titanium dioxide (used in scores of applications including UV-protecting gels). The generic process involves hydrolysis of gaseous metallic chlorides under the influence of water, which develops during the oxyhydrogen reaction, which in turn, leads to a high-temperature reaction zone [23]. The reaction products include the oxide powder and hydrochloric acid, which are recycled. The powders have relatively high surface area (e.g., 50 m^2/g for TiO_2; primary particle size: 21 nm) and disperse to the extent necessitated by the application. Figure 2.1 shows a TEM micrograph of TiO_2 nanoparticles.

2.2.2.1 Inert Gas Condensation of Nanoparticles

The general perception was that considerable control could be exercised on the particle size, shape, and extent of aggregation if gas condensation processes could be carried out either in a low-pressure

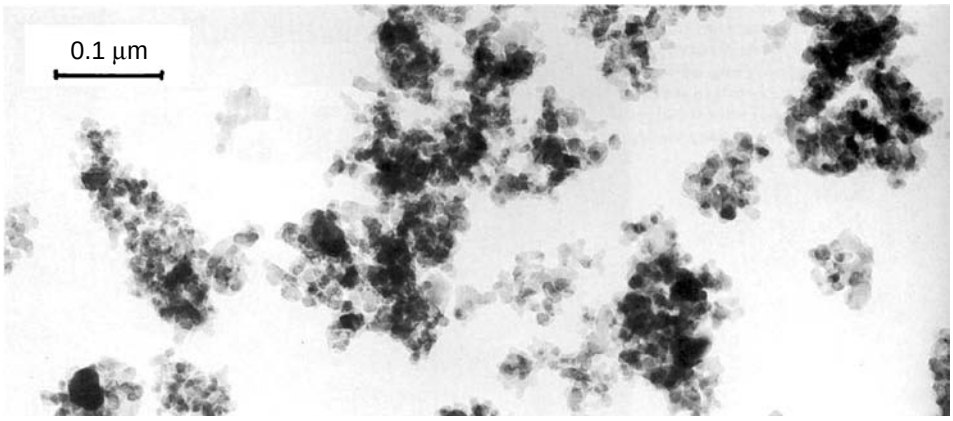

FIGURE 2.1 TEM image of Degussa's titanium dioxide powder.

environment, or the nanoparticles were quenched rapidly as soon as they were formed. Accordingly, Granquist and Buhrmann initially synthesized metal nanoparticles by the inert gas condensation (IGC) process. The nanoparticles, some of them with a mean size of 10 nm and smaller were formed when metal atoms effusing from a thermal source rapidly lost their energy by collisions with gas atoms. Figure 2.2 is a schematic of the setup used by the authors to produce metal nanoparticles. A number of metal nanopowders, including Al, Co, Cr, Cu, Fe, Ga, Mg, and Ni, were synthesized by this technique. A large glass cylinder (diameter, 0.34 m; height, 0.45 m) fitted to water-cooled stainless-steel endplates was evacuated to a pressure of approximately 2×10^{-6} torr by an oil diffusion pump. An alumina crucible, placed on a stand-off, was slowly heated via radiation from a graphite heater element. After appropriate outgassing, the pump line was closed and a reduced atmosphere of an inert gas, usually 0.5 to 4 torr of high-purity argon, was introduced into the cylinder. The crucible was now heated rapidly under quasi-equilibrium conditions (constant temperature and inert-gas pressure). The nanoparticles, which nucleate and grow in the gas phase, were collected on a water-cooled copper surface. The production rate was about 1 g per run.

The short collision mean free path, e.g., 10^{-7} m for aluminum at 1 torr of argon, resulted in efficient cooling, producing a high supersaturation of metal vapor, leading to homogeneous nucleation. It was shown that the dominant mechanism of particle growth was by coalescence of clusters into nanoparticles, which resulted in the formation of nanoparticles with a log normal size distribution. Glieter [24] introduced a modification to the process by carrying it out in an ultrahigh vacuum chamber (backfilled with 1 to 10 torr of inert gas) and condensing the nanoparticles on the so-called 'cold-finger,' which was a liquid-nitrogen-filled rotating cylinder. Figure 2.3 shows a schematic of the process; nanoparticles develop in a thermalizing zone just above the evaporative source due to interactions between the hot vapor species and the much colder inert gas atoms in the chamber. The process was versatile as both metals and oxides could be synthesized, the latter being enabled by the introduction of oxygen [25]. It is worth noting that much of the initial efforts of these and other researchers [26] were aimed at being able to consolidate the nanoparticles into a bulk material, and investigate the novel characteristics of grain boundaries in nanocrystalline materials [27]. As such, the "cold-finger" was convenient to deposit the nanoparticles, scrape off and pack into a die, all under quasi ultrahigh-vacuum conditions. This process was subsequently used by Weertman and co-worker [28].

The early gas condensation processes were soon replicated and improved upon by scores of researchers; a few are described below. By and large, the primary objective of the subsequent studies was to increase the rate of evaporation of the metal species thereby increasing the production rate. As such, several variants of the original IGC process began to emerge. For example, the Fraunhofer Institute of Materials developed a closed-loop IGC system (private communication),

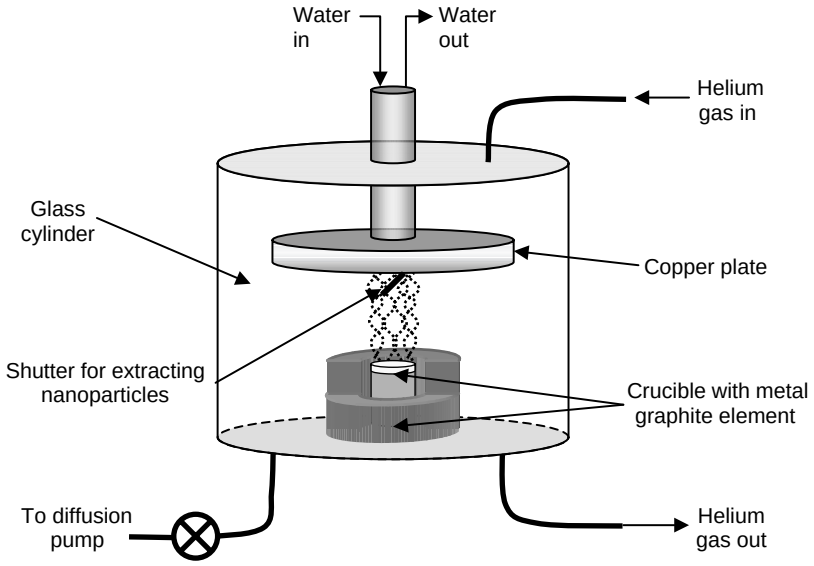

FIGURE 2.2 Schematic of the IGC setup.

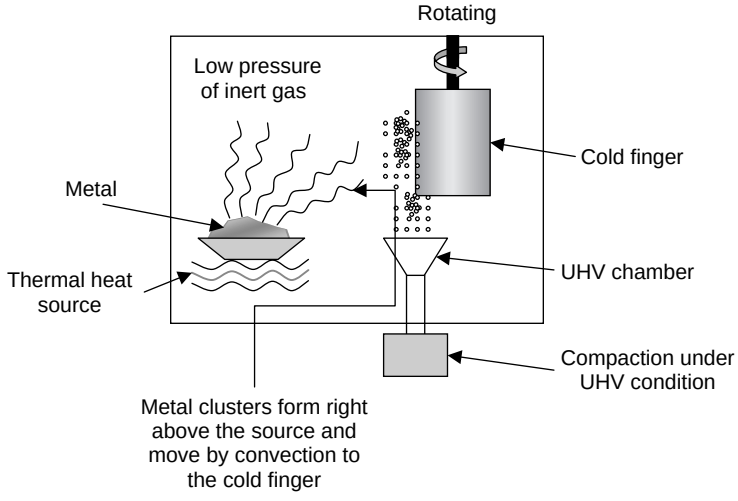

FIGURE 2.3 Schematic of the setup used by Gleiter [24].

and is shown in Figure 2.4. The system was primarily used for production of silver and copper nanoparticles, but could also be used to produce nanopowders of other elements. The metal was fed in the form of a wire into a Joule-heated tungsten boat at a background pressure of 2 to 4 kPa. Filter deposition was used to collect the nanoparticles. High evaporation rates were sustained by a cross-flow of carrier gas. In general, gas condensation synthesis is an expensive proposition due to the high-energy cost for evaporating elements and compounds. The only exceptions are those materials that sublime. Capitalizing on the ability of certain materials to sublime, Khan and co-workers [29] have used a sublimation furnace in a controlled environment to vaporize and condense MoO_3 nanoparticles with a high surface area, ~50 m^2/g. Amongst other uses, nanoparticles of MoO_3 show promise for increasing the efficacy of a thermite reaction used in explosives.

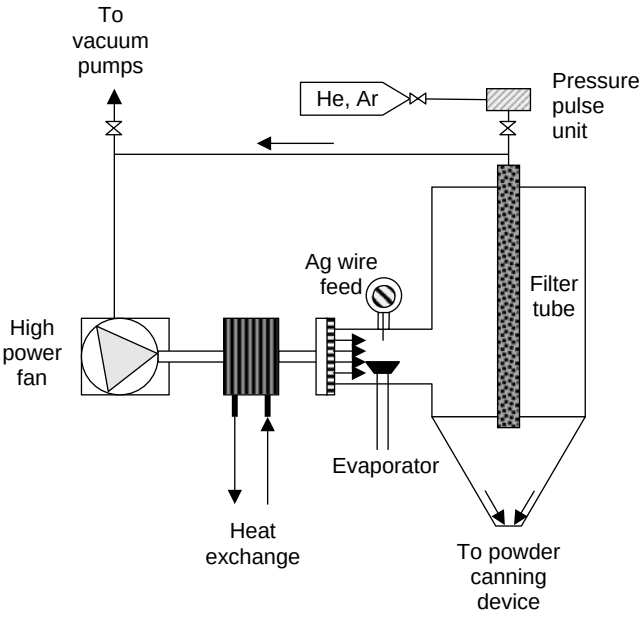

FIGURE 2.4 The modified IGC system developed by the Fraunhofer Institute in Germany.

2.2.2.2 Plasma-Based Synthesis of Nanoparticles

A thermal plasma (i.e., ionized gases), as a heat source for melting materials had been gaining prominence for quite some time in the materials community. In fact, plasma spraying of materials on to substrates to form protective coatings has been a well-established industrial practice for decades. So it was natural for researchers to begin using a thermal plasma as a heat source for evaporating materials, both metals and ceramics. Incidentally, much work along these lines appears to have been done in Japan, before it became established in the United States and other parts of the world. Among the early adopters of the plasma approach was Wada [30] and the process was subsequently scaled by Kashu et al. [31]. A piece of metal was mounted on a water-cooled copper hearth and heated by a plasma jet flame. The gas atmosphere was helium (a few hundred torr), mixed with about 15% hydrogen. The evolving smoke flowed into a cold cone onto which the ultrafine particles deposited. They were collected in an ampoule, which could be sealed off without exposing the collected sample to air. Using a 10 kW plasma gun, ultrafine particles of Al, Co, Cu, Fe, Ti, and Ta were produced with the scaled equipment. The mean diameter was ~20 nm and the production rate was as high as 50 g/h for some metals. However, problems, such as not being able to focus the plasma at a pressure lower than 200 torr and deterioration of the plasma in long runs, led to curtailment of further development of the process.

Uda [32,33] at Nisshin Steel Co. developed a direct current arc plasma method to produce metal nanoparticles. Essentially, a metal block was placed on a water-cooled copper anode plate or a graphite anode crucible. The equipment was evacuated to about 100 Pa and then backfilled with a hydrogen–argon mixture gas at 0.1 MPa pressure, at which point the sample was melted by the arc. Metal vapors were formed and condensed in the gas phase, and subsequently removed by circular gas flow. Hydrogen gas, free of any entrained powder, was reintroduced into the generation chamber by a gas circulation pump. It was found that the presence of hydrogen increased the rate of formation of nanoparticles by a factor of 10 to 10,000 compared to conventional evaporation. The enhanced evaporation mechanism was explained as follows: in arc melting under a hydrogen atmosphere, the molten metal comes into contact with both atomic as well as molecular hydrogen. The former is substantially more soluble in the metal and reaches a supersaturated state rapidly. A supersaturated hydrogen

beyond the arc evolves into non-arc gas phase. The extensive dissolution and subsequent evolution of hydrogen gas from the molten metal leads to enhanced evaporation of metal.

A number of variations of the plasma approach began to emerge in development work across the globe, each improving upon the previous work. Rao et al. [34] argued that the high temperatures in a plasma lead to cold boundary layers and nonuniformities in processing conditions, especially during condensation. They developed a modified process wherein nonuniformities were minimized by expanding the plasma containing the vapor-phase precursors through a subsonic nozzle with a hot ceramic wall. This arrangement approached a configuration of one-dimensional flow with one-dimensional temperature gradients in the direction of the flow in the nozzle, leading to high uniformity of the quench rate. Furthermore, the nozzle provided much higher quench rates than would have been obtainable otherwise.

The plasma system developed by Rao et al. [34] is shown in Figure 2.5. The reactor consisted of a water-cooled chamber with an assembly consisting of a plasma torch, a reactant injection system, and a converging nozzle mounted on the top flange of the chamber. The torch was a Miller SG-1B plasma gun with a special tungsten-lined nozzle for argon–hydrogen operation. The 25 mm-long injection section was immediately downstream of the anode, and consisted of a water-cooled nickel

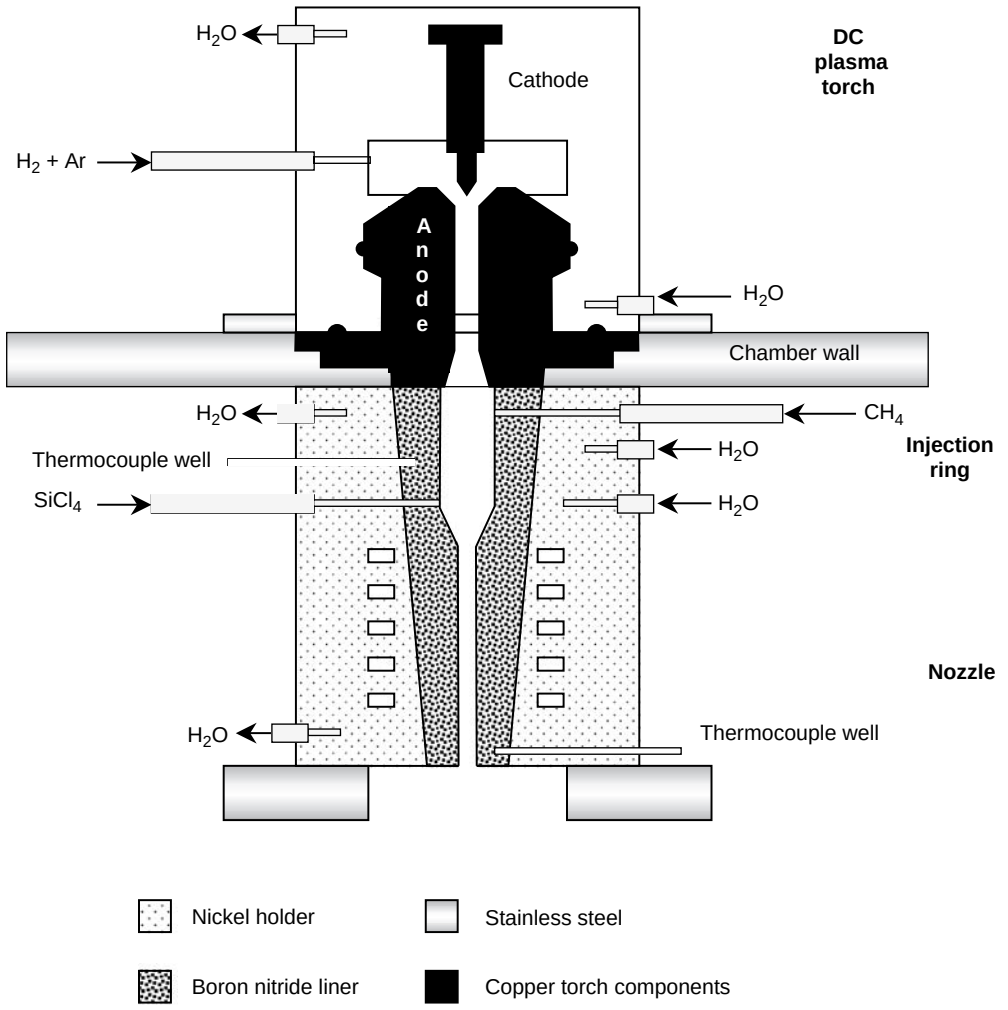

FIGURE 2.5 Plasma process with expanding nozzle to produce nanoparticles.

ring with a ceramic liner and holes at two axial locations, which are connected to the reactant supplies. Precursor vapors were introduced through heated lines, and immediately following the injection section is the 50 mm-long converging nozzle held in place by a water-cooled nickel holder. The nozzle and the liner for the injection ring were made of one piece of boron nitride.

In yet another variation of the plasma process, Phillips and co-workers [35] aerosolized micron-sized particles and delivered them into a hot microwave plasma, wherein the particles evaporated and reacted downstream to form the corresponding oxide nanoparticles by condensation from the gas phase.

Perhaps the greatest stride in plasma processes for nanoparticles synthesis from a commercial standpoint was made by researchers and engineers at Nanophase Technologies Corp. Figure 2.6 is a schematic of the process as practiced by the company. A high-purity metal was vaporized and allowed to condense in a chamber via an arc generated by a water-cooled tungsten inert gas torch driven by a power supply. The cathode, which is nonconsumable, was shielded by a stream of an inert working gas from the environment. The working gas then became ionized to a concentration large enough to establish an arc. The interior of the chamber was maintained at a pressure of 250 to 1000 torr. The consumable precursor material, which was a metal rod up to 2″ diameter, was fed either vertically or horizontally, maintaining a stable arc and continuous production of nanoparticles. Metal clusters were oxidized in flight to the respective oxides. It should be noted that while in principle the process at Nanophase Technologies resembles that practiced by Granquist and Buhrmann more than three decades ago, the extent of engineering that has gone into the process allows Nanophase Technologies to offer tonnage quantities of oxide ceramic powders [36].

Apart from Nanophase Technologies, several other companies in the United States have developed processes based on the use of a thermal or arc plasma to convert either coarse particles into vapors and condense into nanoparticles, or pyrolyze precursor compounds in the gas phase into nanostructured powders. Notable among them are Nanotechnologies Inc. and NanoProducts Corp. Supplying plasma-based nanoparticle production systems also appears to be a burgeoning business. For example, Tekna Plasma Systems Inc. [37], based in Canada, is a manufacturer of integrated turn-key transferred arc plasma systems.

2.2.2.3 Flame-Based Synthesis of Nanoparticles

The use of a hydrocarbon (or hydrogen)–oxygen flame to pyrolyze chemical precursor species and produce nanoparticles is attractive in principle due to the fact that flame processes are already in use on a commercial scale. Over the past decade and a half, research has been directed predominantly

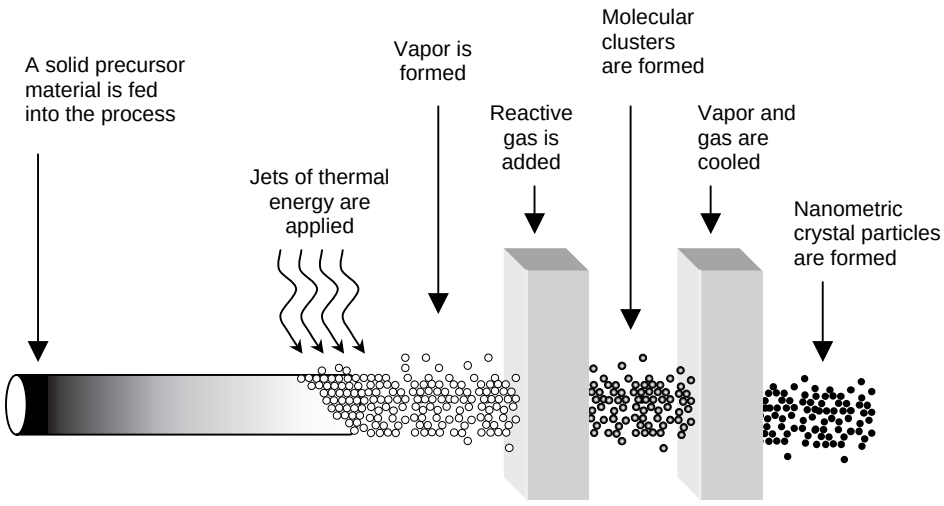

FIGURE 2.6 Schematic of the vapor condensation process practiced by Nanophase Technologies.

toward introducing uniformity and control over the pyrolysis process in a flame, with the anticipation of forming nanoparticles with a narrow size distribution and minimal aggregation. This included developing flames with a flat geometry, as opposed to the traditional Bunsen burner conical flames. There were predominantly two variations to the theme of nanoparticle synthesis using combustion flames. On the one hand, researchers such as Pratsinis et al. [38] and Katz and Hung [39] worked extensively on *atmospheric flames*, including studies on the effect of an electric field on the flame itself as well as on the nanoparticles [40]. This led to an increased understanding of cluster formation and particle growth in a flame. While the traditional flame processes involved mixing reactants along with the combustibles, a variation of the process was the counter-current flow scheme, in which reactants were fed independently through a separate tube into the flame. A further variation on the theme of separating the reactant stream from the fuel/oxidizer stream was a multi-element diffusion flame burner. Wooldridge and co-workers [41] have described one such design, where the flat flame diffusion burner consists of an array of hypodermic needles set in a honeycomb matrix: the fuel is mixed with the precursor reactant and flowed through individually sealed tubes that are less than a millimeter in diameter, and the oxidizer flows through the surrounding channels in the honeycomb. Modifications continue to be made to the basic flame process as evidenced by work done by Jang and Kim [42], who developed a five-piped turbulent diffusion flame reactor for producing $<$50 nm size particles of TiO_2 from $TiCl_4$ precursor.

Recognizing the need for a rarefied atmosphere to inhibit collision of hot nanoparticles in a flame reactor (thereby reducing the propensity of nanoparticles to aggregate), Glumac et al. [43] (including the lead author of this chapter), developed *low pressure flame* synthesis, which was known as the combustion flame-chemical vapor condensation (CF-CVC) process [44]. The forerunner to the CF-CVC process was the CVC process, which utilized a hot-wall reactor in a low pressure environment [45]. Distinct differences in the nanoparticle size distribution and degree of aggregation were observed in subsequent studies [46]. As with many vapor-phase processes, it is a challenge to produce high quality nanoparticles at commercially viable production rates in low-pressure flame processes.

The processes described above utilized precursor vapors, and so were restricted to oxide ceramics that could be derived from metalorganic or organometallic precursors with ambient pressure boiling points of ~200°C or lower. As such, acetates and nitrates were not utilized. Laine and coworkers [47] atomized nonvolatile precursors dissolved in a solvent and directed them through a combustion flame. Powders with high surface area were formed as a result of rapid pyrolysis. The range of compositions of nanopowders could now be expanded to multicomponent oxide materials. It should be noted that the mechanism of nanoparticle formation is unlike that of vapor condensation when nonvolatile species are pyrolyzed in the flame. While this chapter was being written, a spin-off company, TAL Materials, was scaling the flame process for commercial applications.

A majority of the vapor-phase processes have until now been directed toward the synthesis of oxide ceramics, since they form the bulk of the ceramics industry. Reduced pressure hot-wall reactors such as those employed by H.C. Starck in Germany, were exceptions. Hot-wall reactors have also been employed to synthesize nanostructured SiC and Si_3N_4 powders [48]. The relatively slow kinetics of nitridation and carburization reactions has been the fundamental issue with the ability to synthesize nitride and carbide nanoparticles in the gas phase. The short residence at high temperatures in any vapor-phase process is just not enough to complete the reaction. Panchula and Ying [49] have addressed this issue by evaporating nitriding aluminum nanoparticles *in situ* in a forced-flow reactor with a microwave plasma downstream, which dissociates nitrogen molecules in the gas stream and reheats the particles to promote complete conversion of Al to AlN.

2.2.2.4 Spray Pyrolysis of Nanoparticles

Spray pyrolysis, which combines aspects of gas-phase processing and solution precipitation, has been in use for quite some time. A company by the name Seattle Specialty Ceramics, and subsequently acquired by Praxair, employed spray pyrolysis to produce specialty powders. The technique, shown schematically in Figure 2.7, involves the formation of precursor aerosol droplets that

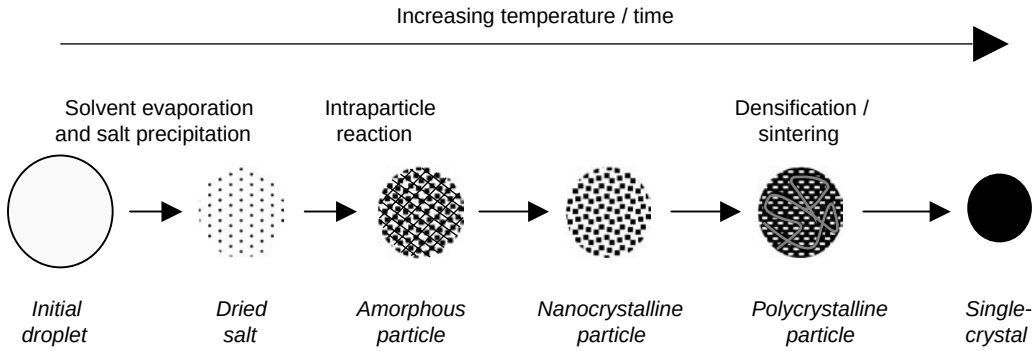

FIGURE 2.7 Sequence of events during the spray pyrolysis process. (Adapted from J. Dimeler, *SID Digest*, 1022, 1999.)

are delivered by a carrier gas through a heating zone [50]. Precursor solutions of metal nitrates, metal chlorides, and metal acetates are atomized into fine droplets and sprayed into the thermal zone. Inside the heating zone, the solvent evaporates and reactions occur within each particle to form a product particle. Spherical, dense particles in the 100 to 1000 nm range can easily be formed in large volume by this method. The principal advantage of the spray pyrolysis method is the ability to form multicomponent nanoparticles as solutions of different metal salts can be mixed and aerosolized into the reaction zone.

Over the years, much emphasis has been given to being able to reduce the precursor droplet size during spray pyrolysis as this in turn would reduce the particle size. Tsai et al. [51] pushed the limit on the particle size by using precursor drops that were 6 to 9 μm in diameter. They obtained uniformly sized dense and spherical particles of ~150 nm of yttria-stabilized zirconia by reducing the precursor concentration by about an order of magnitude.

In a modified version of the spray pyrolysis method, Che et al. [52] synthesized SiO_2-encapsulated Pd nanoparticles. These composite nanoparticles were formed from a Pd-nitrate solution containing ultrafine SiO_2 particles by ultrasonic spray pyrolysis. A precursor particle, formed below 700°C in the drying stage, was composed of a homogeneous mixture of nanoparticles of SiO_2 and $PdO \cdot H_2O$. When PdO was decomposed above 700°C, metallic Pd nanoparticles were formed in the SiO_2 matrix. Because of the high surface free energy, the Pd particles coalesced and condensed in the interior of the composite particle. As a result of the relocation within the composite particle, SiO_2 was forced out of the particle toward the surface, and an SiO_2-encapsulated Pd particle was formed.

2.3 SOLUTION PROCESSING OF NANOPARTICLES

Precipitating clusters of inorganic compounds from a solution of chemical compounds has been an attractive proposition for researchers, primarily because of the simplicity with which experiments can be conducted in a laboratory. This is especially true if the goal is to just have a nanocrystalline powder, instead of a "dispersible" nanoparticulate powder. For example, Kim and Maier [53] synthesized high ionic conductivity nanocrystalline CeO_2 with consummate ease by precipitating Ce and Gd nitrates in dilute ammonia solution at room temperature. Scaling the process to production of tonnage quantities of powders is, however, anything but straightforward. A major advantage of solution processing is the ability to form encapsulated nanoparticles, specifically with an organic molecule, for providing functionality to the nanoparticles, improving their stability in a medium, or for controlling their shape and size. Solution processing can be classified into five major categories: (1) sol–gel processing, (2) precipitation method, (3) water–oil microemulsions (reverse micelle) method, (4) polyol method, and (5) hydrothermal synthesis.

2.3.1 Sol-Gel Processing

Sol–gel technique is one of the most popular solutions processing method for producing metal oxide nanoparticles. This process is well described in several books [54,55] and reviews. Over the years, solution precipitation and sol–gel processing have come to be used interchangeably, mostly by people on the fringes of the technical community. There are distinct differences between the two methods, as will be made clear below. In sol–gel processing, a reactive metal precursor, such as metal alkoxide, is hydrolyzed with water, and the hydrolyzed species are allowed to condense with each other to form precipitates of metal oxide nanoparticles. The precipitate is subsequently washed and dried, which is then calcined at an elevated temperature to form crystalline metal oxide nanoparticles.

The hydrolysis of metal alkoxides involves nucelophilic reaction with water, which is as follows:

$$M(OR)_y + xH_2O \rightarrow M(OR)_{y-x}(OH) + xROH$$

Condensation occurs when either hydrolyzed species react with each other and release a water molecule, or a hydrolyzed species reacts with an unhydrolyzed species and releases an alcohol molecule. The rates at which hydrolysis and condensation reactions take place are important parameters that affect the properties of the final product. For example, slower and more controlled hydrolysis typically leads to smaller particles, and base-catalyzed condensation reactions form denser particles.

2.3.2 Solution Precipitation

In the precipitation method, an inorganic metal salt (e.g., chloride, nitrate, acetate, or oxychloride) is dissolved in water. Metal cations in water exist in the form of metal hydrate species, such as $Al(H_2O)^{3+}$ and $Fe(H_2O)_6^{3+}$. These species are hydrolyzed by adding a base solution, such as NaOH or NH_4OH. The hydrolyzed species condense with each other to form either a metal hydroxide or hydrous metal oxide precipitate on increasing the concentration of OH^- ions in the solution. The precipitate is then washed, filtered, and dried. The dried powder is subsequently calcined to obtain the final crystalline metal oxide phase. The major advantage of this process is that it is relatively economical and is used to synthesize a wide range of single-and multicomponents oxide nanopowders. Additionally, nanocomposites of metal oxides are also produced by coprecipitation of corresponding metal hydroxides. One of the major drawbacks of the process as described above is the inability to control the size of particles and their subsequent aggregation.

In the recent past, significant efforts have been made to control particle characteristics, such as surface area and aggregate size, by precipitating in the presence of a surfactant or an organic molecule. Hudson and Knowles [56] synthesized mesoporous, high surface area zirconium oxide by incorporating cationic quaternary ammonium surfactants in the hydrous oxide and subsequent calcination of the inorganic/organic intermediate. Surfactants were incorporated by cation exchange at a pH that was above the isoelectric point of the hydrous oxide. The pore size distribution and surface area of zirconium oxide nanopowders were modified by changing the length of the hydrophobic chain from C_8 to C_{18}. The BET surface area of powders ranged between 240 and 360 m^2/g. Fokema et al. [57] demonstrated that changing the precipitating agent from ammonium hydroxide to tetraalkylammonium hydroxide results in a decrease in the primary particle size of yttrium oxide. The reason for the decrease in the particle size was attributed to the higher pH that can be achieved with tetraalkylammonium hydroxide in comparison to ammonium hydroxide and the steric effect of tetraalkylammonium cation to reduce the diffusion of soluble precursors to the particle surface.

One often comes across nuances in the precipitation method, where perhaps there is at most a small deviation from the conventional steps outlined above. For example, in order to synthesize nanoparticles of indium tin oxide (used in thin film form as the conducting layer in all electronic displays), Lu et al. [58] employed conventional steps of dissolving salts of indium and tin and precipitating the hydroxide,

followed by washing, drying, and calcinations. The key to the formation of nanoparticles was an intermediate peptization step, wherein the particle size of the precipitate is reduced by adjusting the pH to acidic values.

2.3.3 Water–Oil Microemulsion (Reverse Micelle) Method

Uniform and size-controlled nanoparticles of metal, semiconductor, and metal oxides can be produced by the water-in-oil (W/O) microemulsion (also called reverse micelle) method. In a W/O microemulsion, nanosized water droplets, stabilized by a surfactant, are dispersed in an oil phase. A schematic of a W/O microemlusion is shown in Figure 2.8. Nanosized water droplets act as a microreactor, wherein particle formation occurs and helps to control the size of nanoparticles. A unique feature of the reverse micelle process is that the particles are generally nanosized and monodisperse [59]. This is because the surfactant molecules that stabilized the water droplets also adsorb on the surface of the nanoparticles, once the particle size approaches that of the water droplet.

A common way to practice the reverse micelle technique is by mixing two microemulsions that carry appropriate reactants. Water droplets of two microemlusions are allowed to collide with each other and the particle formation reaction takes place inside the water droplet. Nanoparticle synthesis inside reverse micelles is accomplished by one of the two different chemical reactions: (i) hydrolysis of metal alkoxides or precipitation of metal salts with a base, in case of metal oxide nanoparticles, and (ii) reduction of metal salts with a reducing agent, such as $NaBH_4$, in case of metal nanoparticles. Particles are either filtered or centrifuged and then washed with acetone and water to remove any residual oil and surfactant molecules adsorbed on the surface of nanoparticles [60]. Subsequently, the powders are calcined to form the final product. One of the issues in this process is being able to remove efficiently the nanoparticles from the organic phase and simple washing is not sufficient. One way of removing metal and semiconductor nanoparticles from the oil phase is to immobilize them on stable supports. For example, Hirai et al. [61] separated CdS nanoparticles with thiol-modified mesoporous silica and thiol-modified polystyrene particles via a chemical bonding between nanoparticles and the thiol functional group. Another method to overcome the particle separation issue is using water-in-super critical CO_2 microemlusion, since CO_2 can be easily removed by decreasing the pressure.

Harutyunyan and co-workers [62] have disclosed a seemingly simple method for forming metal nanoparticles, wherein metal acetates or other suitable salts are thermally decomposed in the presence of a passivating solvent, such as glycol ether. When the acetate–solvent mixture is refluxed for a prolonged period of time at a temperature above the melting point of the acetate, metal ions come together

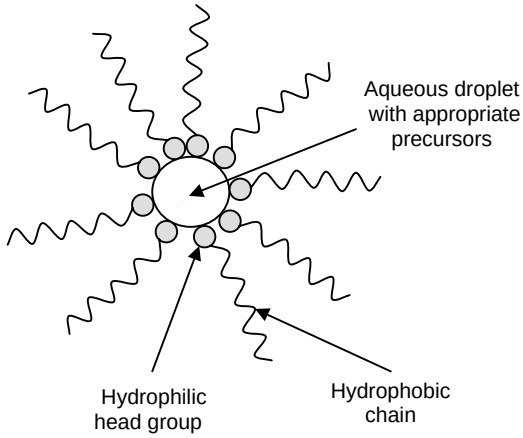

FIGURE 2.8 Schematic of a reverse micelle.

to form nanoparticles. The authors believe that the solvent binds to the surface of the metal clusters, thereby retarding growth and aggregation into larger particles. As expected, the nanoparticle characteristics are dependent on the concentration of the salt in the solvent. Miyao and co-workers [63] extended the technique to include catalytically active silica–alumina nanocomposite particles.

A technique, which in some ways combines the aspects of different solution precipitation techniques, is the hydrodynamic cavitation process. Nanocrystalline oxide ceramic particles in the range 100 nm to a few microns have been produced by hydrodynamic processing in a microfluidizer. The method of producing oxide nanoparticles by the hydrodynamic cavitation process begins with the co-precipitation of the metal oxide components. The precipitated slurry stream is then drawn into a device where it is immediately elevated to high pressures within a small volume. The precipitated gel experiences ultrashear forces and cavitational heating. These two aspects lead to the formation of nanophase particles and high-phase purity in complex metal oxides [64].

2.4 COMMERCIAL PRODUCTION AND USE OF NANOPARTICLES

Over the past 5 years or so, nanoparticle producers have been working hard to differentiating themselves from their competitors, by either providing nanopowders with varied particle characteristics or by developing nanoparticles of proprietary compositions. In many instances, the ability to supply tonnage quantities of nanopowders has also been established. The selling price (which in many cases is a function of the manufacturing cost) has also come down over the years. Good quality alumina nanoparticles, that can be dispersed in a polymer matrix without substantially compromising the optical clarity, sell for ~$100.00/kg. It should be noted that this is still an order of magnitude higher than what submicron size alumina sells for, which is ~$10/kg. For obvious reasons, there has been no widespread replacement of micrograined materials by nanomaterials in applications. On the other hand, applications where a small amount, say approximately 10 wt%, of nanoparticle addition has been able to change substantially the properties and performance of the end-product, are becoming increasingly popular. A number of such examples can be found in the area of functional coatings.

2.5 FUTURE PERSPECTIVES

It is too premature to identify the winners and the losers of the “battle for supremacy in nanopowder production.” If history in other materials’ fields is any indication, those processes that can benefit from economies of scale will likely to be the winners. Further, companies in other regions of the world are a source of inexpensive raw materials, such as China, are likely to become the supplier of choice of raw nanopowders.

If the number of conferences on nanomaterials worldwide is any hint of the level of activity in this field, one can only conclude that there is plenty of uncovered ground. In all probabilities, we are yet to see a peak in the research output in nanomaterials. Increase in synergy between computation and experimental work will lead to new discoveries and new materials’ structures at the nanoscale, which in turn will spawn new process technologies.

Despite years of effort in reducing the product development cycle, there continues to be a disconnect between nanoscale research and penetration in the commercial market. There still exists a substantial gap between basic research and its application in real life, in spite of efforts by academia to bridge effectively this gap and hasten the utilization of their intellectual property in commercial products. Several commercialization models have been tried, only a few of which have met with a modicum of success.

All said and done, interest in value-added nanomaterials that utilize high-quality nanoparticles is growing. As alluded to above, those products where the addition of a relatively small amount of functionalized nanoparticles leads to a major change in the properties and performance, will likely be the winners.

ACKNOWLEDGMENT

The authors thank Krista D. Martin, Engineering Asst. at NEI Corporation, for assistance in gathering technical information and in preparing the schematics.

REFERENCES

1. C. Kropf, C. Hundeiker, M. Heller, and C. Wild, Nano-sized Zinc Oxide in Hygeine Products, U.S. Patent Application, US 2004/0033270 A1, 2004.
2. B. Palaszewski, http://sbir.grc.nasa.gov/launch/RACNanotechnologyGelledFuelsDastoorHQ05-2001_brief.pdf
3. W.H. Qi, and M.P. Wang, Size effects on the cohesive energy of nanoparticles, *J. Mat. Sci. Lett.*, 21, 1743–1745, 2002.
4. K.K. Nanda, A. Maisels, F.E. Kruis, H. Fissan, and S. Strappert, Higher surface energy of free nanoparticles, *Phys. Rev. Lett.*, 91, 106102, 2003.
5. K.M. Reddy, S.V. Manorama, and A.R. Reddy, Bandgap studies on anatase TiO_2 nanoparticles, *J. Solid State Chem.* 158, 180–186, 2001.
6. J. Lawrence, and G. Xu, Hydrogen storage capacity improvement of nanostructured materials, *Mat. Res. Soc. Symp. Proc.*, 704, 219–224, 2002.
7. D. Snow, and C. Brumlik, Nanoparticles for Hydrogen Storage, Transportation and Distribution, U.S. Patent 6,589,312 B1, 2003.
8. M.-I. Baraton, L. Merhari, J. Wang, and K. Gonsalves, Investigation of TiO_2/PPV nanocomposite for gas sensing applications, *Nanotechnology*, 9, 356–359, 1998.
9. J. Baran, Jr., and O. Cabrera, Use of Surface-Modified Nanoparticles for Oil Recovery, U.S. Publ., US 2003/0220204 A1, 2003.
10. A. Singhal, G. Skandan, F. Badway, N. Ye, A. Manthiram, H. Ye, and J.J. Zhu, Nanostructured electrode materials for next generation electrochemical devices, *J. Power Sources*, 129, 38, 2004.
11. G.O. Mueller, and R. Mueller-Mach, Lumileds Lighting US, LLC, Light-emitting devices utilizing nanoparticles, European Patent Application, Appl. 03076772.7.
12. C. Angelerakis, and M.-D.S. Nguyen, U.S. Patent 6,593,395 B2, Kerr Corporation, 2002.
13. C. G. Granquist, and R.A. Buhrman, *J. Appl. Phys.*, 47, 2200, 1976.
14. R. Birringer, H. Gleiter, H.P. Klein, and P. Marquardt, *Phys. Lett.*, 102A, 8, 365, 1984.
15. H. Gleiter, *Prog. Mat. Sci.*, 33, 4, 1990.
16. R. Uyeda, *Prog. Mat. Sci.*, 15, 5, 1991.
17. http://www.inkworldmagazine.com/Feb042.htm.
18. www.apt-powders.com
19. Y. Todaka, M. Nakamura, S. Hattori, K. Tsuchiya, and M. Umemoto, Synthesis of ferrite nanoparticles by mechanochemical processing using a ball mill, *Mat. Trans.*, 44, 277–284, 2003.
20. M. Luton, R. Iyer, R. Petkovic-Luton, J. Vallone, and S. Matra, Method of extruding oxide dispersion strengthened Alloys, U.S. Patent 4,818,481, 1989.
21. J. Lee, F. Zhou, K. Chung, N. Kim, and E. Lavernia, Grain growth of nanocrystalline Ni powders prepared by cryomilling, *Metall. Mater. Trans. A*, 32A, 3109, 2001.
22. C.C. Koch, Mechanical and thermal processing methods, *Rev. Adv. Mater. Sci.*, 5, 91–99, 2003.
23. Cabot and Degussa Technical, Literature, Personal communication, 2000.
24. H. Gleiter, *Prog. Mat. Sci.*, 33, 223, 1989.
25. H. Hahn, R.S. Averback, *J. Am. Ceram. Soc.*, 74, 1991.
26. G. Thomas, R.W. Seigel, and J. Eastman, Grain boundaries in nanocrystalline Pd by high resolution electron microscopy and image simulation, *Scr. Metall. Mater.*, 24, 201–206, 1990.
27. P.G. Sanders, J. Weertman, and J. Eastman, Pore size distribution in nanocrystalline metals from small angle neutron scattering, *Acta Mater.*, 46, 4195–4202, 1998.
28. J.R. Weertman, D. Farkas, H. Kung, M. Mayo, R. Mitra, and H. Van Swygenhoven, MRS Bulletin, 24, 44–50, 1999.
29. M. Khan, J. Cole, and J. Taube, Nanoparticles of Molybdenum Oxide, U.S. Patent Application, Pub. US 2002/0192149 A1.
30. N. Wada, *Jap. J. Appl. Phys.*, 8, 551, 1969.

31. S. Kashu, M. Nagase, C. Hayashi, R. Uyeda, N. Wada, and T. Tasaki, *Proceedings of the 6th International Congress, Jap. J. Appl. Phys. Supp.*, 2, 492, 1974.
32. R. Uyeda, *Prog. Mat. Sci.*, 35, 1, 1991.
33. M. Uda, *Nanostruct. Mater.*, 1, 101, 1992.
34. N. Rao, S. Girshick, J. Heberlin, P. McCurry, S. Jones. D. Hansen, and B. Micheel, *Plasma Chem. Plasma Process.*, 15, 581, 1995.
35. J. Phillips, D. Mendoza, and C. Chen, Method for Producing Metal Oxide Nanoparticles, U.S. Patent Appl. US 2004/0009118 A1, 2004.
36. H. Sarkas, and J. Piepenbrink, Process for preparing nanostructured materials of controlled surface chemistry, U.S. Patent 6,669,823 B1.
37. http://www.tekna.qc.ca/
38. S.E. Pratsinis, W. Zhu, and S. Vemury, *Powder Technol.*, 86, 87, 1996.
39. J.L. Katz, and C-H. Hung, *Twenty-third Symposium (International) on Combustion*, The Combustion Institute, Pittsburgh, PA, 1990.
40. Unpublished work, NEI Corporation.
41. M.S. Wooldridge, P.V. Torek, M.T. Donovan, D.L. Hall, T.A. Miller, T.R. Palmer, and C.R. Schrock, An experimental investigation of gas-phase combustion of SiO_2 nanoparticles using a multi-element diffusion flame burner, *Combust. Flame*, 131, 98–109, 2002.
42. H-D. Jang, and S-K. Kim, Method for producing nanometer sized ultrafine titanium dioxide, U.S. Patent 6,613,301 B2, 2003.
43. N.G. Glumac, Y-J. Chen, and G. Skandan, Diagnostics and modeling of nanopowder synthesis in low pressure flames, *J. Mater. Res.*, 13, 2572–2579, 1998.
44. N. Glumac, G. Skandan, Y.-J. Chen, and B.H. Kear, Combustion Flame Synthesis of Nanophase Materials, U.S. Patent 5,876,683, 1999.
45. W. Chang, G. Skandan, H. Hahn, and B.H. Kear, Apparatus for Making Nanostructured Powders and Whiskers, U.S. Patent 5,514,350, 1996.
46. A. Singhal, G. Skandan, and B.H. Kear, On nanoparticle aggregation during vapor phase synthesis, *Nanostruct. Mater.*, 11, 545, 1999.
47. C. Bickmore, K. Waldner, R. Baranwal, T. Hinklin, D. Treadwell, and R. Laine, *J. Europ. Ceram. Soc.*, 18, 287, 1998.
48. W. Chang, G. Skandan, H. Hahn, S.C. Danforth, and B.H. Kear, Chemical vapor synthesis of nanostructured ceramics, *Nanostruct. Mater.*, 4, 345, 1994.
49. M. Panchula, and J. Ying, Nanocrystalline aluminum nitride: vapor phase synthesis in a forced flow reactor, *J. Am. Ceram. Soc.*, 86, 1114–1120, 2003.
50. G. Messing, S. Zhang, and V. Jayanthi, *J. Amer. Ceram. Soc.*, 76, 2707, 1993.
51. S. Tsai, Y. Song, Ch.Y. Chen, T. K. Tseng, C.S. Tsai, and H.M. Lin, Nanoparticles synthesis by air-assisted ultrasonic spray pyrolysis, *Mat. Res. Soc. Symp. Proc.*, 704, 85–90, 2002.
52. S. Che, D. Sakurai, T. Yasuda, K. Shimozaki, and N. Mizutani, *J. Ceram. Soc. Jap.*, 105, 269, 1997.
53. S. Kim, and J. Maier, On the conductivity mechanism of nanocrystalline ceria, *J. Electrochem. Soc.*, 149, J73–J83, 2002.
54. C.J. Brinker, and C.W. Scherer, *Sol–Gel Science*, Academic Press, San Diego, CA, 1990.
55. L.V. Interrante, and M.J. Hampden-Smith, Eds., *Chemistry of Advanced Materials — An Overview*, Wiley-VCH, New York, 1998.
56. M.J. Hudson, and J.A. Knowles, *J. Mater. Chem.*, 6, 89, 1996.
57. M.D. Fokema, E. Chiu, and J.Y. Ying, *Langmuir*, 16, 3154, 2000.
58. H. Lu, C. Hsu, I. Lin, and C. Weng, Method for Preparing ITO Nanometer Powders, U.S. Patent Application, US 2003/0211032 A1, 2003.
59. I. Capek, *Adv. Colloid Interface Sci.*, 110, 49, 2004.
60. H. Huang, G.Q. Xu, W.S. Chin, L.M. Gan, and C.H. Chew, *Nanotechnology*, 13, 318, 2002.
61. T. Hirai, T. Saito, and I. Komasawa, *J. Phys. Chem. B*, 105, 9711–9714, 2001.
62. A. Harutyunyan, L. Grgorian, and T. Tokune, Method for Synthesis of Metal Nanoparticles, U.S. Patent Publication, US 2004/0099092 Al, 2004.
63. T. Miyao, T. Sawaura, and S. Naito, Preparation of silica-alumina ultra fine particles possessing nanopore structure by means of reversed micelle technique, *J. Mat. Sci. Lett.*, 21, 867–870, 2002.
64. W.R. Moser, Process for the preparations of Solid State Materials, U.S. Patent 5,466,646, Assigned to Worcester Polytechnic Institute, 1995.

3 Fullerenes and Their Derivatives

Aurelio Mateo-Alonso, Nikos Tagmatarchis, and Maurizio Prato
Dipartimento di Scienze Farmaceutiche, Università degli Studi di Trieste, Piazzale Europa, Italy

CONTENTS

3.1 INTRODUCTION

Since the discovery[1] and the bulk production[2,3] of fullerenes an integrated research field involving organic transformations of these all-carbon hollow-cluster materials has emerged. C_{60} has been the most thoroughly studied member of fullerenes because it (1) is produced abundantly in the carbon soot by the arc discharge of graphite electrodes, (2) has high symmetry (icosahedral I_h with all 60 carbons chemically equivalent), (3) is less expensive, (4) is relatively inert under mild conditions, and (5) shows negligible toxicity. Electronically, C_{60} is described as having a closed-shell configuration consisting of 30 bonding molecular orbitals with 60 p electrons,[4] which give rise to a completely full fivefold degenerate h_u highest occupied molecular orbital that is energetically located approximately 1.5 to 2.0 eV lower than the corresponding antibonding lowest unoccupied molecular orbital (LUMO) one.[5,6] The first electron in the reduction of C_{60} is added to a triply degenerate

t_{1u} unoccupied molecular orbital and is highly delocalized.[7] This threefold-degeneracy, together with the low-energy possession of the LUMO, make C_{60} a fairly good electron acceptor with the ability of reversibly gaining up to six electrons upon reduction.[8,9] The facile reduction contrasts with its difficult oxidation. Only the first three reversible oxidation waves have been observed.[10] This high degree of symmetry in the arrangement of the molecular orbitals of C_{60} provides the foundation for a plethora of intriguing physicochemical, electronic, and magnetic properties. Semiconducting,[11] magnetic,[12–16] and superconducting[17–19] properties of unmodified C_{60} have been intensively investigated; however, these properties remain to be explored for functionalized fullerenes. On the other hand, nonlinear optical and photophysical properties of functionalized fullerene materials have been already under investigation.

The skeleton of C_{60} consists of 20 hexagonal and 12 pentagonal rings fused all together. The chemical reactivity of C_{60} is that of a strained electron deficient polyalkene, with rather localized double bonds. Cycloaddition reactions have been widely applied for the functionalization of fullerenes. Usually, addition occurs across [6,6] ring junctions where electron density is much higher than at the [6,5] ones. Other reactions that take place on the spherically shaped carbon core of fullerenes involve additions of nucleophiles, free radicals, and carbenes as well as η^2-complexation with various transition metal elements. In such fullerene adducts, the functionalized carbon atoms change their hybridization from a trigonal sp^2 to a less strained tetrahedral sp^3 configuration; thus, the primary driving force for addition reactions is the relief of strain in the fullerene cage. Furthermore, the regiochemistry of the addition is governed by the minimization of the 5,6-double bonds within the fullerene skeleton. Therefore, any 1,2-addition reactions occur to produce ring-closed 6,6-adducts, having two sp^3 carbon atoms on the fullerene framework. However, sometimes ring-opened 6,5-adducts (fulleroids) are formed, keeping all fullerene carbon atoms sp^2-hybridized.

The main advantage gained upon functionalization of fullerenes is a substantial increase in their solubility. The existence of a great diversity of synthetic protocols combined with the high number of chemical reactions that have been mainly applied to C_{60} has led to the formation of a wide variety of functionalized fullerenes.

The special characteristics of the added groups, coupled with the unique structural, physicochemical, and electronic properties of fullerenes (which in most of the cases are retained after functionalization), have aided the development of new materials with tremendous potential in fascinating and widespread technological applications such as electronic and optoelectronic devices, light-emitting diodes , photovoltaics, and thermotropic liquid crystals. This chapter highlights the rapid progress made in the above scientific areas by the syntheses and applications of some novel functionalized fullerene materials.

3.2 FUNCTIONALIZATION OF FULLERENES

3.2.1 CYCLOADDITIONS

Fullerenes behave as a 2π electron-deficient dienophiles and dipolarophiles and, therefore undergo cycloaddition reactions such as [2+2], [3+2], and [4+2]. These have been carried out either thermally or photochemically, and they typically take place on the 6,6-ring junctions of the fullerene skeleton.

3.2.1.1 [2+2] Cycloadditions

Four-membered rings fused to 6,6-ring junctions are formed upon [2+2] cycloadditions. The first example of this procedure was the [2+2] thermal addition of benzyne to C_{60}.[20,21] Schuster and coworkers[22–25] reported photochemical [2+2] cycloadditions of cyclic enones and 1,3-diones, while Liou and Cheng[26] reported the addition of electron-deficient alkenes. It can be concluded from their experiments that (1) photocycloadditions cannot proceed at wavelengths where only C_{60} absorbs light (i.e., 532 nm); (2) better yields are obtained either by increasing the concentration of the enone or by

decreasing the concentration of the fullerene; (3) the [2+2] cycloaddition takes place between the ground state of the C_{60} and the enone triplet excited state via an intermediate triplet 1,4-biradical.

The addition of diethylaminopropyne to C_{60} resulted in a [2+2] adduct that can be ring-opened under acidic conditions. Then, novel fullerene lactones were obtained under oxidative cyclization conditions in the presence of activated carbon.[27]

Recently, the interest in the synthesis of fullerene dimers has increased,[28] as they can be used as building blocks for nanotechnological applications (Scheme 3.1). The first procedure was published by Komatsu and coworkers;[29,30] the experiments yielded the dimer when carried out using high-speed vibration milling (HSVM) in the presence of potassium cyanide, while in solution[31] only C_{60}-cyanated derivatives were obtained. This technique has also been applied to the reaction between C_{60} and pentanocene[32] and to the dimerization of C_{70}[33] and C_{60}–C_{70} cross-dimers.[34]

3.2.1.2 [3+2] Cycloadditions

Five-membered rings fused to 6,6-junctions can be formed upon [3+2] cycloadditions to fullerenes. The 1,3-dipolar cycloaddition of azomethine ylides has shown as one of the most versatile tools for functionalization of fullerenes and has been widely used.[35–38] Azomethine ylides are reactive intermediates that can be generated *in situ* by one of the following protocols: (1) decarboxylation of immonium salts derived from thermal condensation of α-amino acids (Scheme 3.2) and aldehydes (alternatively ketones), or (2) thermal ring opening of aziridines. 1,3-Dipolar addition of azomethine ylides to C_{60} yields fulleropyrrolidines that are formed across the 6,6-junction of the fullerene core. The key features of this type of reaction are summarized as: (1) utilization of functionalized aldehydes leads to the formation of 2-substituted fulleropyrrolidines, whereas utilization of *N*-substituted glycines affords *N*-substituted fulleropyrrolidines (Scheme 3.2); and (2) mono-fulleropyrrolidines are formed by controlling the stoichiometry of the reagents and the reaction conditions. Therefore, through this methodology, structurally different fullerene derivatives for different

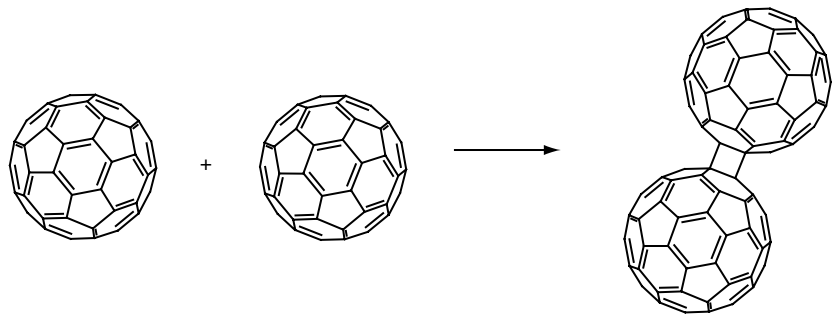

SCHEME 3.1 [2+2] Cycloaddition C_{60} dimer.

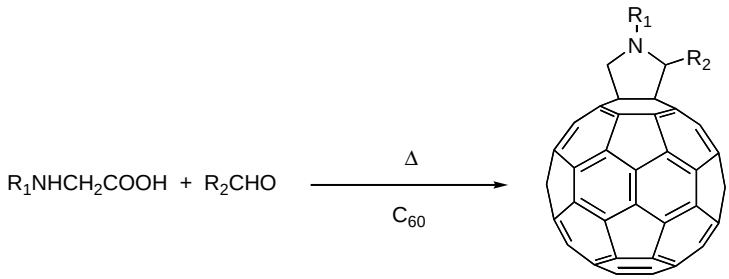

SCHEME 3.2 [3+2] Cycloaddition using azomethine ylides.

applications are obtained, either by using properly functionalized azomethine ylides or by modifying a fulleropyrrolidine intermediate. The characteristics of the fullerene skeleton combined with the properties of the substituents introduced, leads to the construction of fullerene-based materials with novel properties.

When the highly hydrophobic fullerenes are derivatized with hydrophilic residues, fullerene-based amphiphilic derivatives are obtained. Such materials are suitable for the construction of Langmuir–Blodgett (LB) films. Amphiphilic fulleropyrrolidines bearing suitable hydrophilic addends (Figure 3.1) have been found to form true monolayers that can be eventually transferred onto solid substrates while the formation of LB films could not be equally realized with their corresponding hydrophobic analogs.[39–55]

N-substituted fulleropyrrolidines can be *N*-alkylated to give fulleropyrrolidinium salts. The insertion of positive charges increases substantially the solubility of such compounds in aqueous media, which have been used for the construction of supramolecular architectures. *N*-functionalization with oligoethylene glycol chains bearing terminal ammonium salts enhanced the solubility in water, while the fullerene–fullerene interactions were responsible for aggregation due to hydrophobicity. The combination of these properties led to the formation of spheres, nanorods, or nanotubules in water (Figure 3.2).[56] When porphyrins were inserted, the molecules assembled in nanotubules, but the removal of the porphyrin fragment generated nanometer level structures characterized by long uniform bundles of tens of aligned parallel nanotubules with

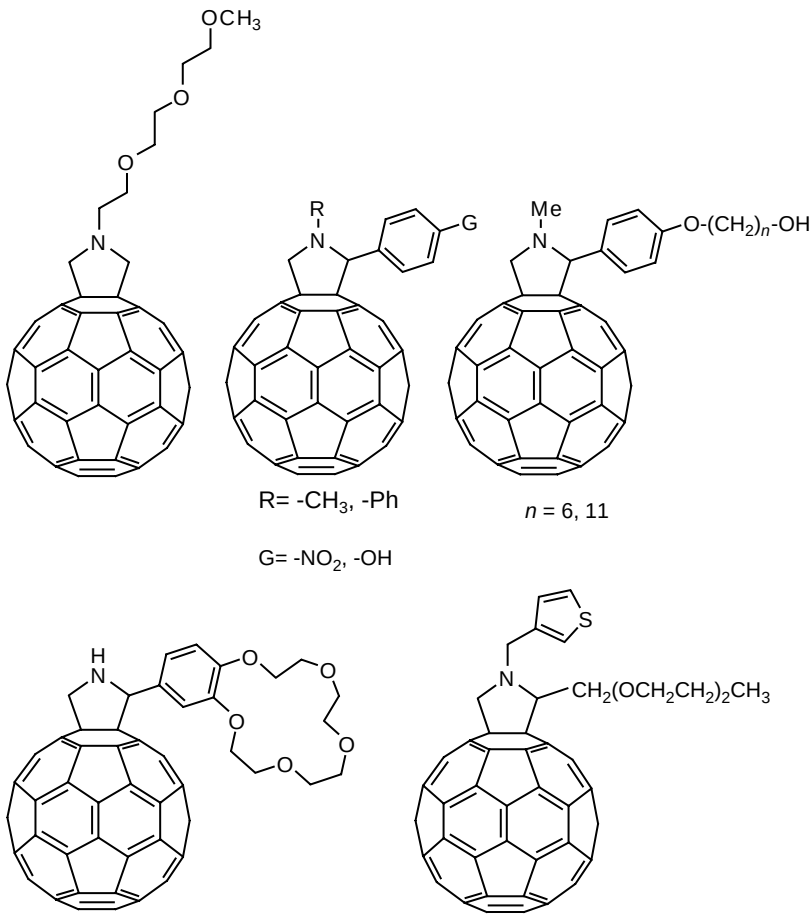

FIGURE 3.1 Fullerenes functionalized with hydrophylic addends.

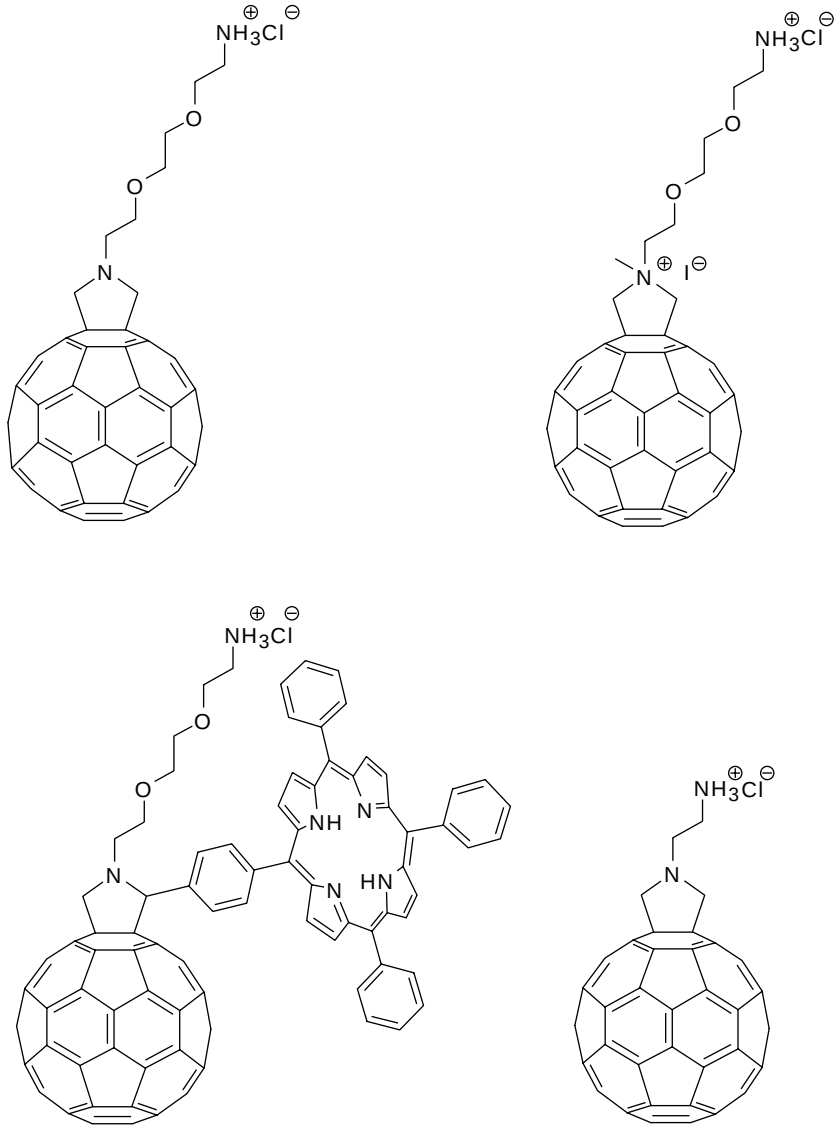

FIGURE 3.2 Fulleropyrrolidine salts.

diameters of about 4 nm and lengths of several microns. If the porphyrin fragment is removed, the driving force for the formation of well-defined nanotubules is less favorable, resulting in one-dimensional linear structures, which are rather different from the relatively common spherical systems obtained by fullerenes derivatives. Removal of the long oligoethylene glycol chains in favor of a short aliphatic chain results in spherical aggregates, thereby recovering the supramolecular topology of C_{60} mesoscopic aggregates. Therefore, it is reasonable to assume that molecular tailoring or different solution treatment of such amphiphilic organofullerene materials induces different kinds of assembly.[57]

The solubility in water of this type fulleropyrrolidine derivatives allowed its insertion into the interlayer space of smectite clays leading to a new family of organic–inorganic nanocomposites.[58] The positively charged fulleropyrrolidines were introduced into the clay galleries by cation exchange, replacing the charge-balancing cations such as Na^+ (Figure 3.3).

The solubilization of fullerenes in water allows the possibility to explore their properties in different fields such as medicinal chemistry and biotechnology. Again the functionalization with polar side-chains[59] and with positively charged groups[60] enhanced the solubility to sufficiently high concentrations (10^{-4} to 10^{-5} *M*) to study the biological activity of fulleropyrrolidines.[61]

In another very recent report, a fulleropyrrolidine–mercaptophenyl hybrid material was synthesized and self-assembled in two-dimensional arrays.[62] The self-assemblies of this novel material have shown reversible electrochemistry and intriguing electronic properties suitable for constructing well-ordered nanostructural morphologies and thin film functional materials.

1,3-Dipolar additions have been also used in the preparation of novel compounds such as fulleroproline, the biggest unnatural amino acid[63] that comprises a natural α-amino acid proline condensed to a 6,6 ring junction of C_{60}.[64] When glycine *t*-butyl ester was condensed with formaldehyde in refluxing toluene, followed by removal of the protecting group under acidic conditions, fulleroproline was generated that turned out to be insoluble in any kind of solvent (Scheme 3.3). However, derivatization of the pyrrolidine nitrogen with either an acylating agent (i.e., acetic anhydride) or a protecting group (i.e., Fmoc fluorenylmethyloxycarbonyl or Boc, *tert*-butyloxycarbonyl) affords a compound that can be easily characterized for further peptide synthesis.

Alternatively, fulleroprolines can be obtained via the thermal ring opening of aziridines (Scheme 3.4).[65] In this case, the fulleroproline results orthogonally protected at the *N*- and *C*-termini. In addition, di- and tripeptides have already been prepared by incorporating fulleroproline at their *N*- or *C*-terminal parts.[66–68]

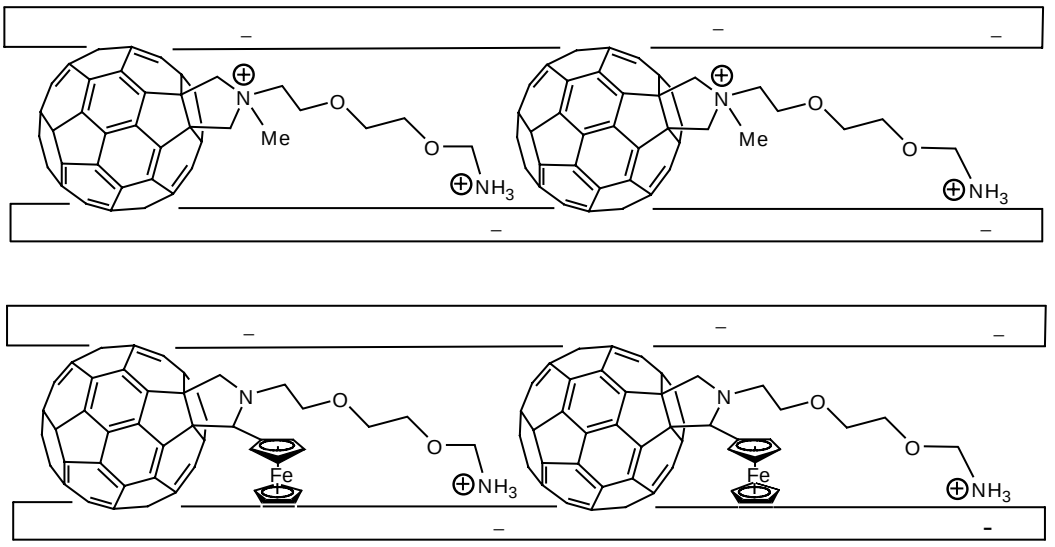

FIGURE 3.3 Fullerenes inserted in clay galleries.

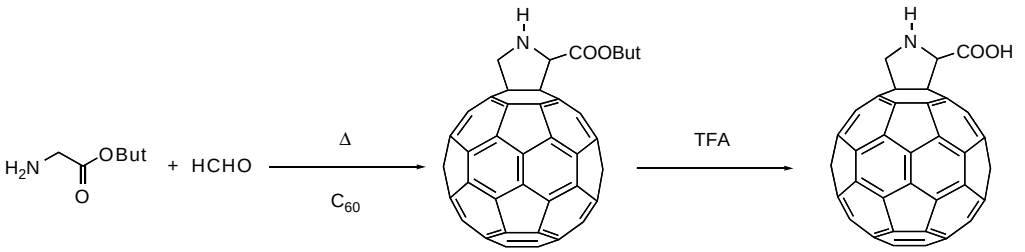

SCHEME 3.3 Synthesis of fulleroproline.

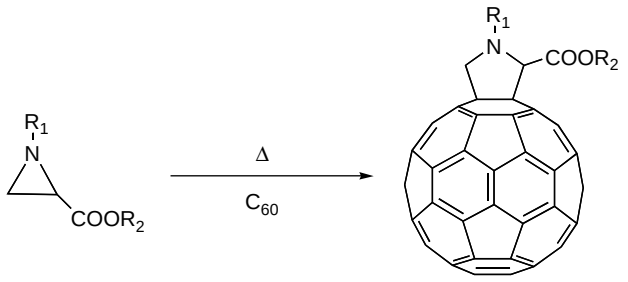

SCHEME 3.4 [3+2] Cycloaddition by thermal opening of azyridines.

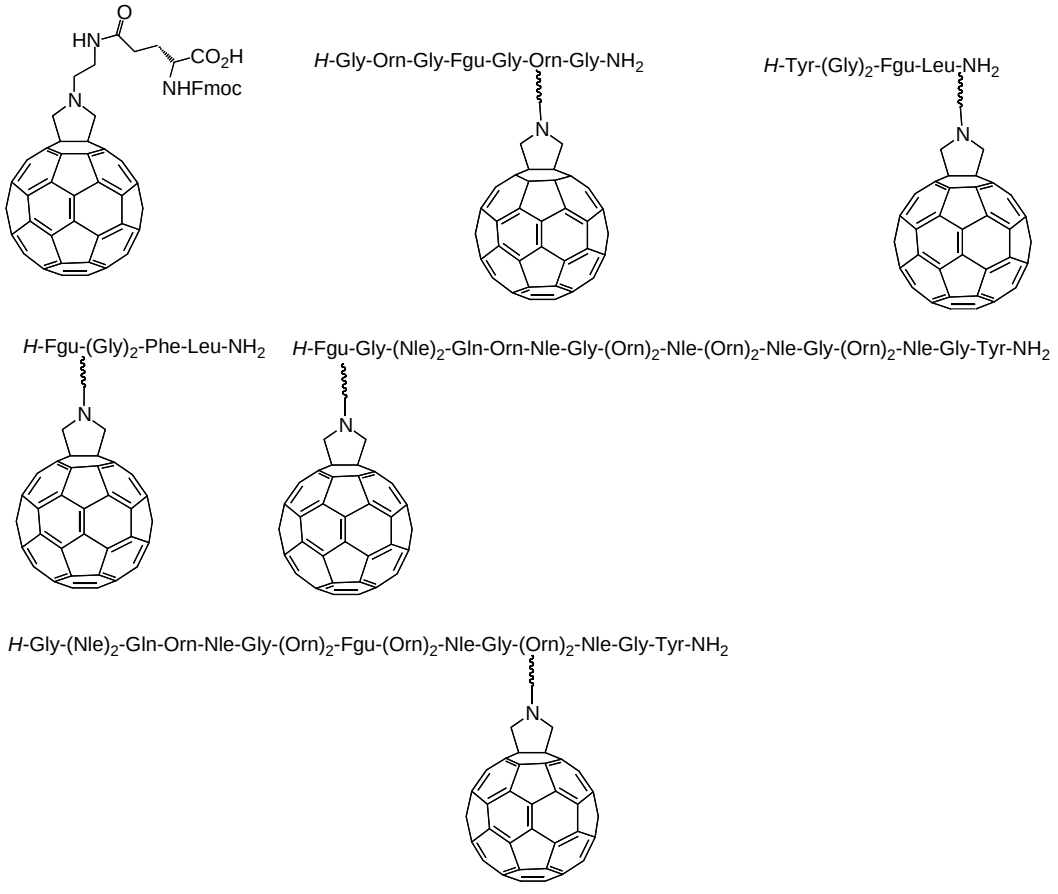

FIGURE 3.4 Fullerene peptides.

For more complex fullerene-modified peptides, a protocol for the solid phase using the fulleropyrrolidino-glutamic acid, was developed. Such protocol was used to insert a series of different peptides, including Leu-enkephalins analogs and antimicrobial sequences (Figure 3.4).[69]

Dendrimers can serve as building blocks for the construction of organized materials with nanosize precision due to the well-defined three-dimensional structure they possess. An issue of great importance is to incorporate photoactive and/or redox-active units at the center of the dendrimer in order to establish this type of materials as molecular devices. Through 1,3-dipolar addition, a wide

variety of fullerodendrimers containing oligoethylene glycol as well as with oligophenylenevinylene have been synthesized.[70–72]

Recently, the synthesis of a functionalized fullerene having a DNA minor groove binder and an oligonucleotide chain covalently linked to a fullerene cage via a fused pyrrolidine ring was reported.[73–75] The design of the latter synthesis was based on an already established idea that coupling of fullerenes to a minor groove binder leads to higher affinity and specificity of the derivatives toward target DNA.[76] The construction of fullerene–DNA hybrid materials allows transmission electron microscopy (TEM) imaging of deoxyribonucleic acid without the use of any heavy metal. Recently, such compounds became available and showed to bind to DNA through electrostatic interactions with the phospharylated groups providing excellent contrast for imaging individual DNA molecules.[77]

Fulleropyrrolidine-based steroid hybrids were synthesized and found to decrease both the ATP hydrolysis and Ca^{2+} uptake activity of sarcoplasmic reticulum Ca^{2+}-ATPase while the inhibitions were concentration-dependent.[78] Recently, a range of fullerene–flavanoid dyads were synthesized.[79–81] The idea of preparing such systems stemmed from the fact that flavanoids possess significant antioxidant activity, can act as anticarcinogens, and express beneficial effects in inflammatory and immunomodulatory systems.

Bisadducts can also be produced using [3+2] cycloaddition methodology (Figure 3.5). The isolation and full characterization of the whole series of the pyrrolidine bisadducts (*trans*-1, -2, -3, -4, equatorial, *cis*-3, -2, and -1).[82] Although some of these patterns had been partly characterized before,[83–85] the isolation and full characterization of the never observed *cis*-3, -2, and -1 fulleropyrrolidine isomers were achieved.

In a recent paper,[86] the bisadducts were prepared and separated by high-performance liquid chromatography (HPLC), following the previous procedure. It should be noted that *trans*-2, *trans*-3, and *cis*-3 enatiomers display C_2 symmetry and are chiral due to their addition pattern. Then, each couple of these enantiomers was separated by chiral HPLC. The resulting enantiomerically pure isomers were transformed into fulleropyrrolidinium salts. The *trans*-3 enantiomers were used successfully to induce chiral helicity, in opposite directions of negatively charged polymer backbones.

In a different work[87] that focused on the biological and medicinal application of fullerenes, different C_{60} bisadducts containing polyethyleneglycol chains and ammonium salts were prepared to prevent aggregation and increase the solubility in water. Only *trans*-2, -3, -4 and equatorial isomers were completely purified by HPLC, showing an increase of solubility in water by 100 times compared with the corresponding monoadducts, and also exhibited high solubility on a phosphate-buffered solution.

The influence on the reduction potentials of the different substitution patterns in fulleropyrrolidines and fulleropyrrolidinium salts have been studied.[88] This concept has been extended efficiently to the preparation of molecules in other applications, such as cation recognition.[89] Bisfunctionalized crown ethers have been attached very close to the fullerene sphere using 1,3-dipolar additions. An electrochemical signal is obtained from the variation of the redox potentials of the fullerene when different cations are binded. The responses were favorable showing reduction potential shifts between 15 and 38 mV depending on the cation.

Among other examples, the thermal [3+2] cycloaddition of azides to C_{60}[90–92] should be highlighted as it is the first step toward [60]azafullerenes (Scheme 3.5).[93–95] When the reaction is carried out at temperatures $<80°C$, the cycloaddition takes place preferentially in the 6,6-ring junctions, affording thermically labile triazolines. Owing to the lower symmetry D_{5h} of C_{70} as compared with I_h symmetrical C_{60}, the regiochemistry of [3+2] cycloadditions of azides gives isomeric mixture of [70]triazolines that can be eventually separated and serve as precursors in the synthetic route to [70]azafullerenes.[96–98]

Diazo compounds are added to fullerenes across a 6,6-double bond yielding fulleropyrrazolines, which decompose to mixtures of methanofullerenes and methanofulleroids either thermally or photochemically.[99]

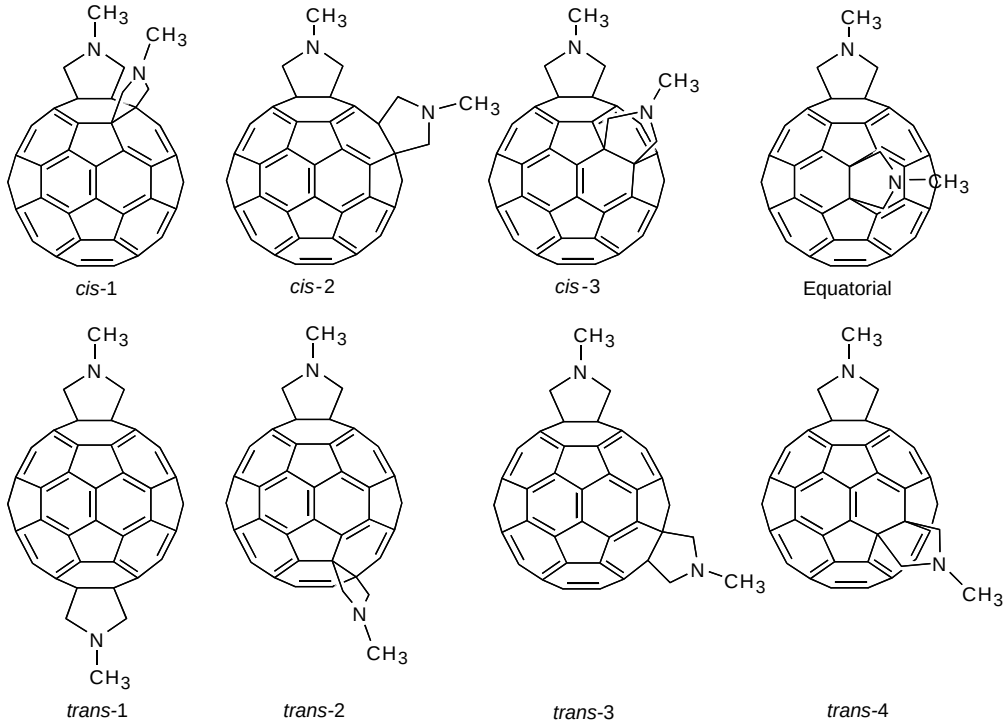

FIGURE 3.5 All fullerene bisadducts.

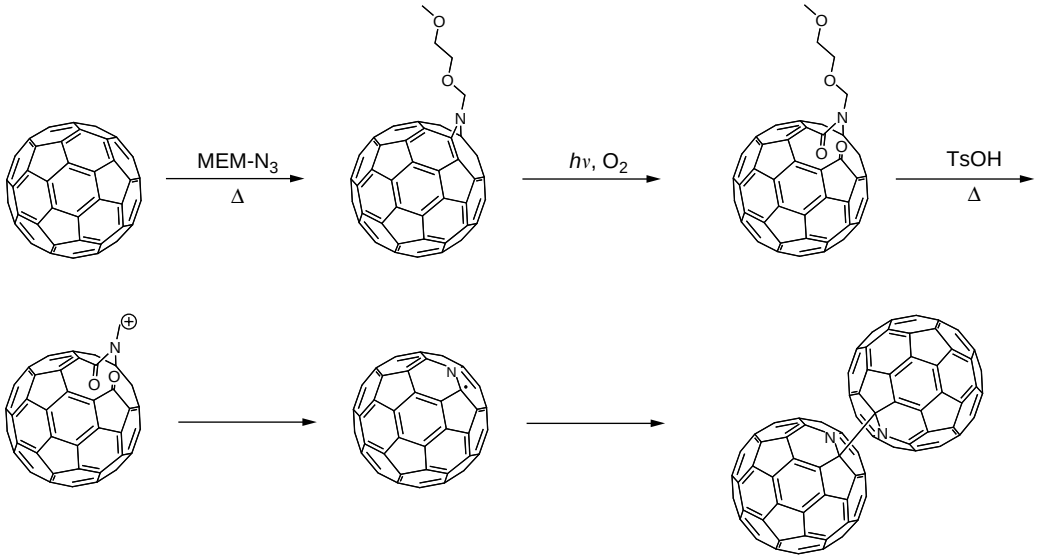

SCHEME 3.5 Synthesis of [60]azafullerene.

Buta-2,3-dienoates and buta-2-ynoates, in the presence of phosphine as catalyst have been found to react with C_{60} in a [3+2] fashion,[100,101] contrary to the early observations of yielding [2+2] cycloadducts.[102]

3.2.1.3 [4+2] Cycloadditions

In the [4+2] Diels–Alder cycloaddition, 1,3-dienes are added to 6,6-junctions of fullerenes. This type of cycloaddition offers the great advantage of controlling the degree of functionalization as well as the site of addition. However, it also offers the disadvantage of being reversible in most cases. Therefore, the cycloadditions are normally unstable. There are several examples of these cycloadditions reported in the literature, which can be divided into two main categories: (1) those in which the 1,3-dienes are cycloadded directly to the fullerene skeleton and (2) those in which the 1,3-dienes are generated *in situ* from the used reactants (Scheme 3.6).

In the first category, the addition of several analogs of Danishefsky dienes is highlighted, yielding fullerene-fused cyclohexanones.[103] The presence of the carbonyl group makes this system suitable for further chemical transformations on the carbonyl group leading to useful materials in nanotechnological areas.

A different example showed the reversible addition of a water-soluble fullerodendrimer with biotechnological applications.[104] A dendrimeric anthracene unit was successfully attached to C_{60} using the Diels–Alder cycloaddition, providing solubility to the whole system in water. The reversibility of the reaction allows the possibility of removal of the solubilizing group that could release C_{60} intracellularly.

Solid state reactions between C_{60} and aromatic compounds such as anthracene, tetracene, pentacene, and naptho[2,3-a]pyrene were carried out under HSVM conditions, to yield the corresponding [4+2]cycloadducts.[32] When the reaction was carried out with anthracene, the same product as in solution was obtained,[105–107] but with better yields. While in the case of pentacene, the reaction gave a different adduct to the one obtained in solution, in which pentacene was attached to two C_{60}

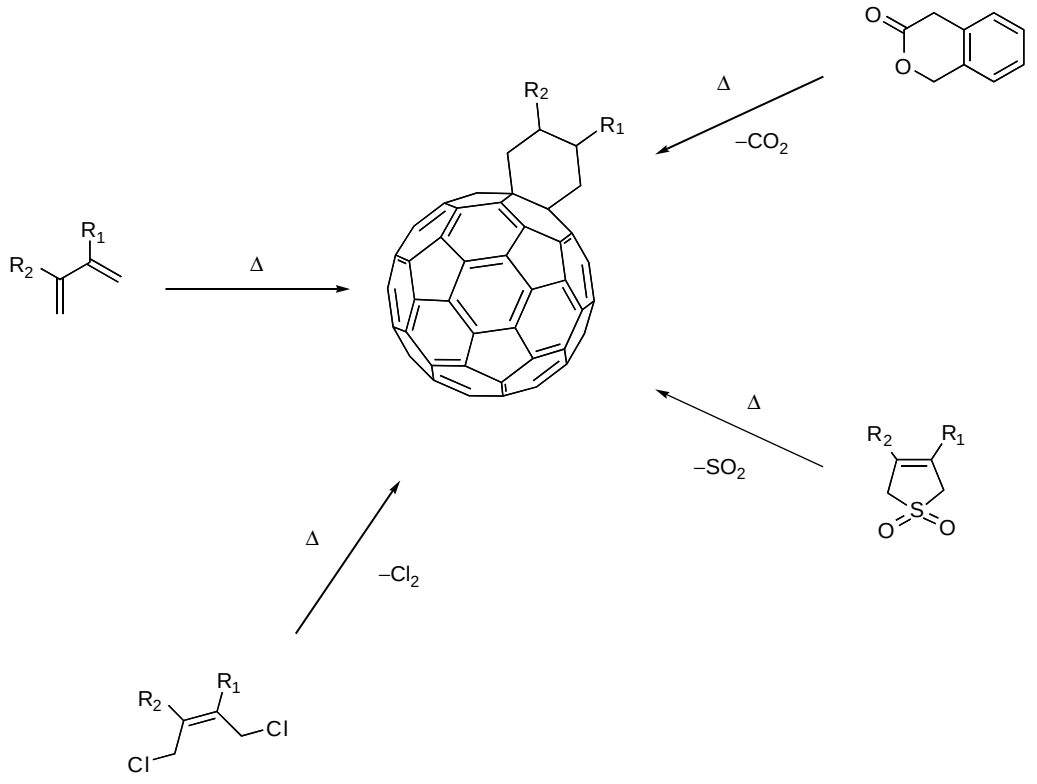

SCHEME 3.6 [4+2] Cycloaddition to C_{60}.

molecules. Moreover, the reaction with tetracene and naptho[2,3-a]pyrene afforded the expected [4+2] cycloadducts, similar to the case when the reactions were carried out in solution. Other Diels–Alder reactions between electron-deficient dienes with fullerenes involved tropones,[108] 1,3-butadienes substituted with electron-withdrawing groups[109] as well as 2-pyrone.[110]

The second category of [4+2] cycloadditions, which involves the *in situ* generation of the diene, has been applied to prepare novel organofullerene materials bearing fused furan and thiophene rings,[111,112] which are suitable for nanoelectronics and photovoltaics applications. Other examples include reactive *o*-quinodimethanes species created *in situ* by thermolysis of cyclic sulfones,[113] substituted cyclo-[113,114] or benzocyclo-butanes[115] and 1,4-elimination of dibromides.[115]

The reaction of "masked" *o*-benzoquinone[116] with C_{60} was also studied.[117] The [4+2] cycloaddition reaction of such electron-deficient dienes with fullerenes resulted in the formation of highly functionalized bicyclo[2.2.2] octenone-fused fullerenes. The reactants were generated *in situ* by oxidation of the readily available 2-methoxy phenols.

Heterocyclic analogs of *o*-quinodimethane have become increasingly popular for Diels–Alder functionalization of C_{60}, since methods for generating these highly reactive species have been developed. However, most attention has been paid to their generation via chelotropic elimination of SO_2 from heteroaromatic-fused 3-sulfolenes and 1,4-elimination from the corresponding α,α'- dihalides.[118–122]

Some novel C_{60}-based [4+2] adducts were recently synthesized through 1,4-dihalide elimination, giving fused tetrathiafulvalene–C_{60} dyads and C_{60}–tetrathiafulvalene–C_{60} dumbbell triads, in which the fullerene acceptor is doubly tethered to the donor tetrathiafulvalene through a rigid cyclohexene ring.[123] With this novel approach, control of the relative orientation as well as the distance between the donor and acceptor units was achieved. Thereby, through-space interactions were expected to dominate because of the special topology of the constructed molecules. More examples of such donor–acceptor hybrid systems are discussed in following sections.

All the work cited in this section refers to monoaddition of dienes to fullerenes. By using an excess of a diene the formation of multi-adducts is increased. Following these conditions, hexakisadducts fullerenes has been prepared upon cycloaddition of 2,3-dimethyl-1,3-butadiene to C_{60}.[124,125] Different bisadducts[126] containing crown ethers have been prepared by 1,4-dihalide elimination depending on the size of the crown ether used. Various properties of these derivatives with potential applications in the field of molecular sensors, including complexation, electrochemical, and fluorescence emission behaviors have been studied.

A few examples of [4+2] cycloadditions to higher fullerenes have been described, which lead to isomeric mixtures due to their lower molecular symmetry. Such works involved cycloadditions of *in situ* created reactive *o*-quinodimethane to C_{70} and C_{76}[127,128] as well as pentamethylcyclopentadiene[129] to C_{70}.

3.2.2 Cyclopropanation Reactions

Cyclopropanation reactions are considered among the widely used methods for regioselective functionalization of fullerenes. In general, cyclopropanated fullerenes (methanofullerenes) can be synthesized either by (i) generation of carbon nucleophiles from α-halo esters and their subsequent addition to C_{60} (Bingel method), (ii) thermal addition of diazo compounds followed by thermolysis or photolysis, or (iii) addition of free carbene species.

In the Bingel cyclopropanation reaction[130] (addition–elimination), the addition of anions of α-haloesters to fullerenes is followed by an intramolecular substitution of the halide by the intermediate fullerene anion to give the corresponding methanofullerene derivative (Scheme 3.7). The addition takes place exclusively on double bonds between two six-membered rings of the fullerene skeleton. The versatility of the reaction is justified in terms of the ready availability of the starting ester compounds. Furthermore, additional chemical transformations to the ester addend group of an already synthesized methanofullerene could occur. For example, activation of malonic acid

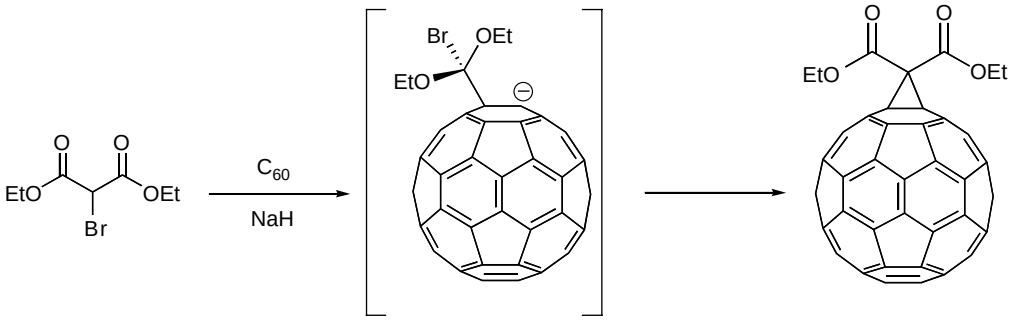

SCHEME 3.7 Bingel reaction.

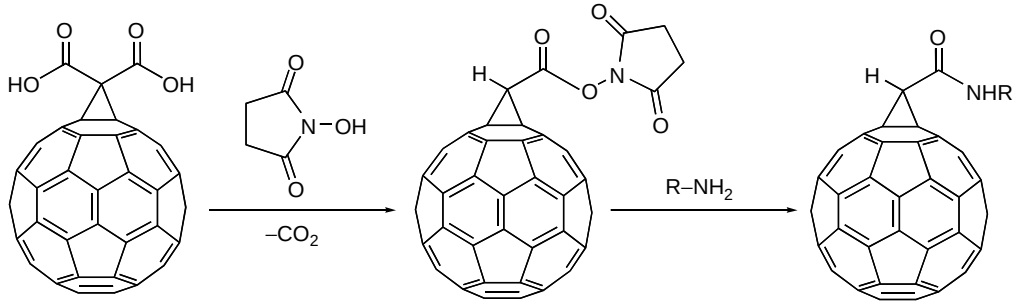

SCHEME 3.8 Chemical modification of Bingel adducts.

methanofullerene material with *N*-hydroxysuccinimide and subsequent reaction with amines furnishes the corresponding methanofullerene amides, as shown in Scheme 3.8.

It is worth mentioning that during the activation of malonic acid on the methanofullerene material with N-hydroxysuccinimide, decarboxylation occurs. Therefore, to prevent decarboxylation a spacer was introduced between the bridging carbon atom of the methanofullerene and the reacting carboxylic acid unit in such systems. This route ultimately provides access to the construction of methanofullerene derivative bearing a free carboxylic acid moiety as a versatile building block as shown in Scheme 3.9. In this instance, the reaction has been used for the construction of a novel structure consisting of alternating C_{60}–C_{70} methanofullerene units. The novel features of this material are summarized in its electronic absorption spectrum that shows the characteristic absorptions of both C_{60} and C_{70} subunits as well as in the cyclic voltammogram which indicates that each fullerene unit behaves as an independent redox center.[131]

Recently, modifications of the original Bingel cyclopropanation have been performed, thereby expanding the use and applicability of the reaction and increasing the construction of novel fullerene-based materials. For example, alternative pathways generation *in situ* of the reactive halomalonate intermediate have been developed.[132,133] Additionally, a series of phosphonium[134] and sulfur[135] ylides have been reacted with C_{60}, following a similar addition–elimination pathway, yielding the corresponding methanofullerenes. However, the yields of these reactions can vary significantly depending on the nature of the ylide used.

A different way to synthesize methanofullerene materials is upon addition of diazo compounds to fullerenes via formation of unstable pyrazoline derivatives,[136,137] where nitrogen is thermally or photochemically released (Scheme 3.10). Two different compounds were formed: thermally the [5,6]-open fulleroid is obtained upon addition on a 5,6-junction;[138] while photochemically a mixture of the 5,6-open fulleroid as well as the methanofullerene upon addition to a 6,6-ring junction is

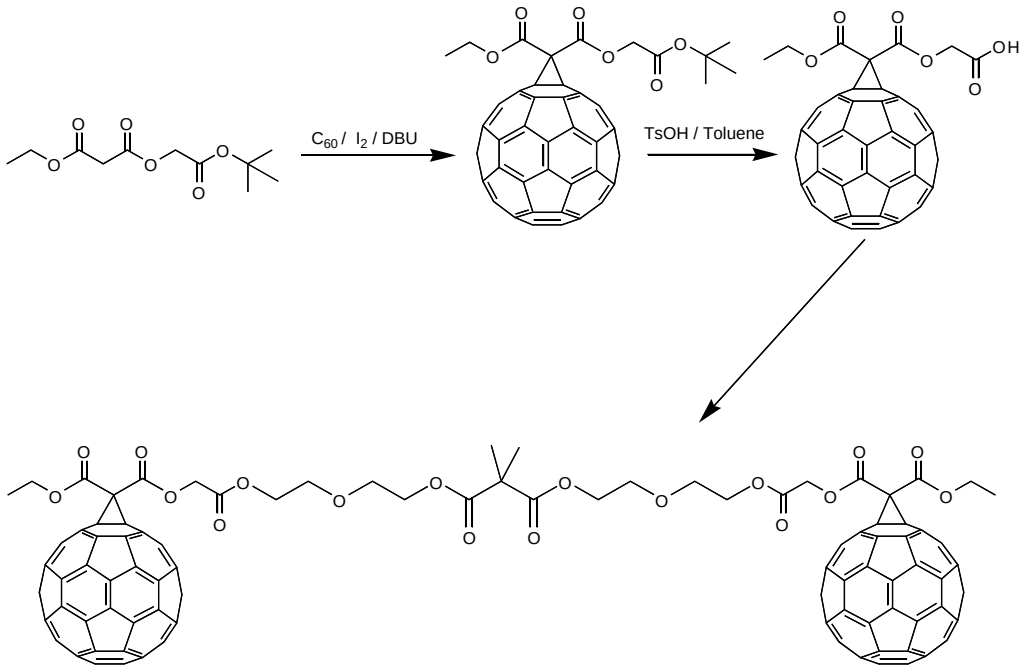

SCHEME 3.9 Bingel building blocks.

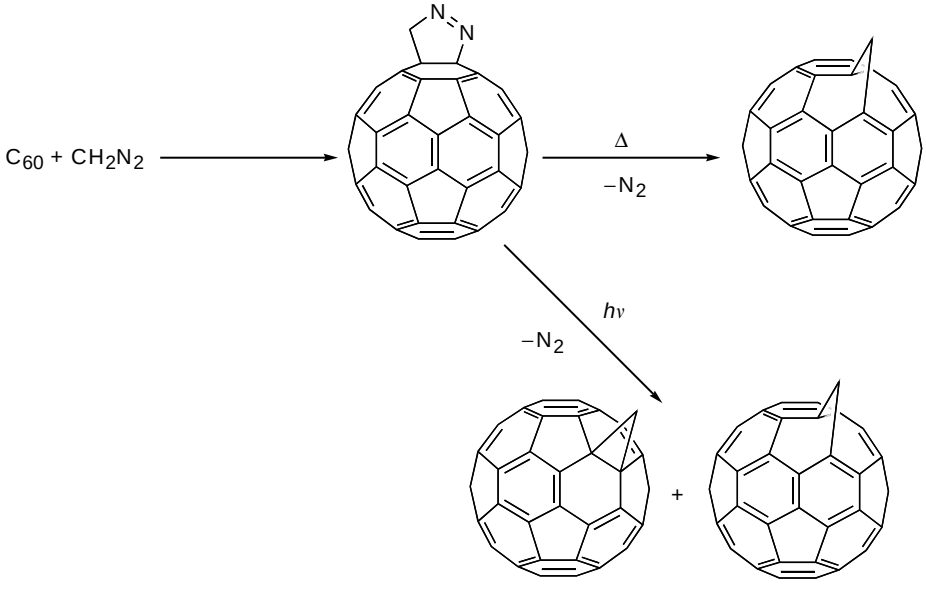

SCHEME 3.10 Synthesis of methanofullerenes by addition of diazocompounds.

formed.[138,139] The ratio of the 5,6-fulleroid and 6,6-methanofullerene formed is highly dependent on the starting diazo compound used.[140–143]

Given the wide variety of substituted diazomethanes that can be used[144–149] as well as other chemical methods for *in situ* generation of diazo compounds,[146,150–152] a variety of ethanofullerene materials with diverse functional groups has been synthesized and studied. A representative

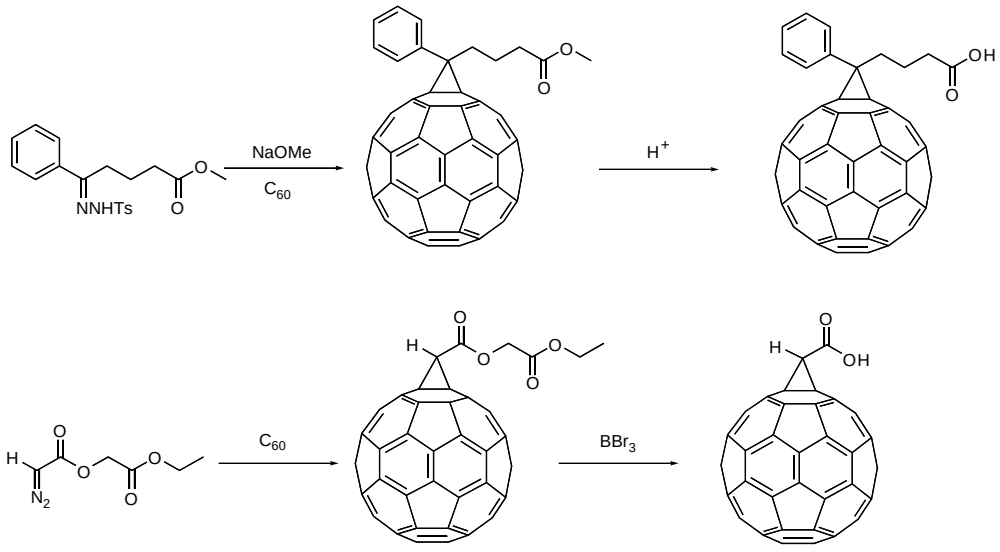

SCHEME 3.11 Addition of tosyl hydrazones and diazomalonates.

example of base-induced decomposition of tosylhydrazones and immediate entrapment by C_{60} of the *in situ* generated diazo compounds and electron-deficient diazomalonates is presented in Scheme 3.11. In the former case, the methyl ester of the corresponding methanofullerene material can be further transformed to the carboxylic acid giving access to a variety of methanofullerene-based derivatives,[153–155] while in the latter case a methanofullerene-carboxylic acid material is generated.[141,156] In either case, esterification or amidation condensation reactions can be easily performed in order to construct useful methanofullerene-based materials for LB films, electron-donor hybrids for technological applications.[157–161]

In an intriguing example based on the Bingelyclopropanation reaction, diethylmalonate in the presence of an auxiliary base was reacted with $(C_{60})_2$ dimer to yield a mixture of monoadducts. The monoaddition reaction can be considered as "bisfunctionalization" of one of the C_{60} cages explaining the formation of isomers. The same reaction was also carried out on dimeric material encapsulating ^{3}He in one of the C_{60} cages. However, functionalization was more complicated with regio-isomeric products arising from addends either on an empty C_{60} cage or a ^{3}He-encapsulating one.[162]

At this point it should be mentioned that an important field, where the cyclopropanation has been widely used, is the construction of fullereno-dendrimers,[71,72,163–165] possessing fullerenes as either functional cores[51,131,166–171] or branches.[50,172–175] An example of an organofullerene material that has the potential to serve as a core building block for the construction of dendrimeric compounds (as well as a precursor to a C_{2v} symmetrical pentakisadducts) has been recently synthesized. Thus, utilizing Bingel cyclopropanation reaction under template activation conditions, a highly symmetrical decakisadduct of $(C_{60})_2$ was produced.[176] Furthermore, several cyclopropanated organofullerene materials have been synthesized for the preparation of fullerene-containing thermotropic liquid crystals. A wide variety of such liquid-crystalline materials was synthesized possessing mono-,[177–179] hexa-addition pattern[180] or even dendritic addends.[181–183]

Finally, the third way that gives access to methanofullerene materials is based on the addition of highly reactive free carbenes to fullerenes. A representative example is the reaction under pyrolytic conditions of sodium trichloroacetate that generates dichlorocarbene, which effectively adds to C_{60} furnishing the corresponding methanofullerene derivative.[184] Another interesting example concerns the all-carbon fullerene dimers C_{121} and C_{122} which have been synthesized via an intermediate methanofullerene carbene[185,186] as shown in the following Scheme 3.12.

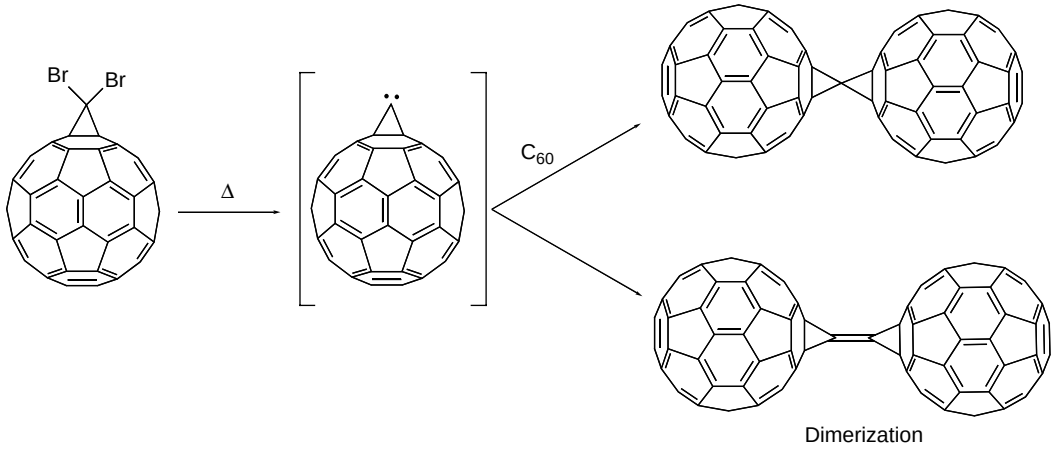

SCHEME 3.12 Generation and reactivity of fullerenecarbenes.

Cyclopropanation reaction has been successfully applied for the functionalization of endohedral metallofullerenes.[187–190] Gd@C_{60} endohedral metallofullerene has been derivatized with multiple malonate ester units to increase the solubility.[191] The decakisadduct of Gd@C_{60}[C(COOCH$_2$ CH$_3$)$_2$]$_{10}$ was easily converted into the water-soluble Gd@C_{60}[C(COOH)$_2$]$_{10}$ material which was medicinally evaluated and suitable for future biotechnological applications. In another recent example, the isolation and crystallographic characterization of a paramagnetic endohedral metallofullerene cyclopropanated derivative based on *in situ* generated carbene attack from 2-adamantene-2,3-[3H]-diazirine onto the π-spherical network of La@C_{82} was reported.[192]

It should be mentioned that cyclopropanations can be also achieved in the solid state with active methylene compounds in the presence of a base under HSVM conditions.[193]

Bisadducts can also be obtained through this procedure. Tether-directed remote multifunctionalization is probably one of the most effective means for controlling multiple additions. It was introduced in 1994 by Isaacs et al.[194] and reviewed in 1999 by Diederich and Kessinger.[195] By controlling the length and geometry of the tether, bis- and trisadduct structures can be almost exclusively obtained. Recent examples appeared in the literature showing the regio- and stereoselective synthesis of bisadducts using bismalonates connected to different carbazol moieties[196] or Tröger bases.[197] The success of the latter relied on the existence of two chiral nitrogen centers, the rigidity and the folded geometry of the Trögger base.

An independent study[198] showed how bis-α-halophenylacetates of the same length produced almost exclusively *trans*-2 or equatorial bisadducts depending on the halogen used. It could be concluded that the nature of the leaving group as well as that of the tether part also plays an important role on the regioselectivity.

3.3 SELF-ASSEMBLED FULLERENE ARCHITECTURES

Supramolecular architectures containing fullerenes have attracted a lot of attention.[199,200] Fullerenes can be incorporated into well-ordered arrays by means of different intermolecular interactions, including hydrogen bonding, π-stack interactions, and metal templates. In recent years, novel supramolecular systems have been developed with a wide variety of architectures with very interesting properties.

3.3.1 ROTAXANES, CATENANES, PSEUDOROTAXANES

[2]Rotaxanes are interlocked molecules formed by a macrocycle and a thread (Figure 3.6). The macrocycle is trapped within the thread by two terminal bulky stoppers. These can be obtained by

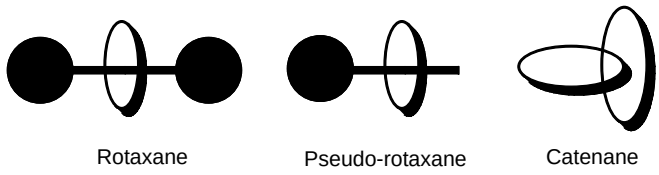

FIGURE 3.6 Different interlocked architectures.

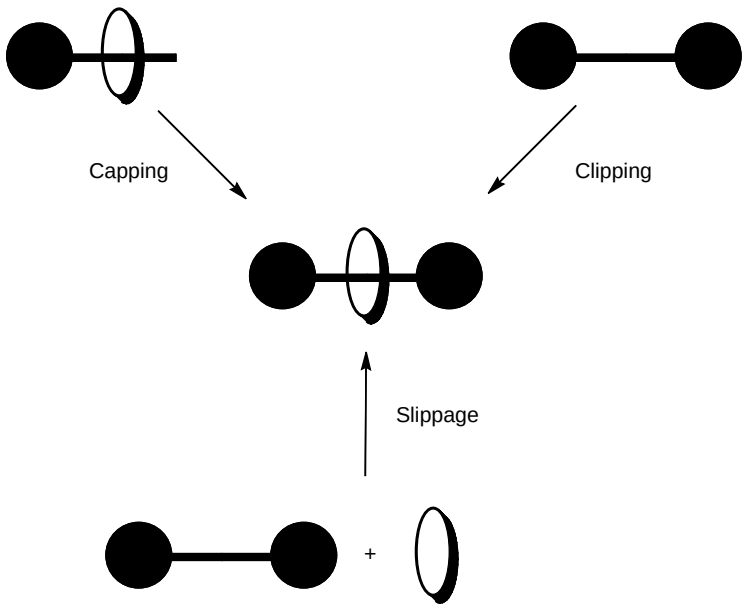

FIGURE 3.7 Strategies for the preparation of rotaxanes.

different strategies, such as clipping, capping, or slippage (Figure 3.7). The applications of these systems have generated a lot of expectation as they can be used as different molecular devices with applications in energy conversion and storage, information storage, and nanosenoring.

Fullerenes have been incorporated into these supramolecular structures as stoppers or as units in the macrocycle, in order to exploit their photo- and electrochemical properties.

The very first example of a rotaxane, including two fullerenes as stoppers, was reported by Diederich and collaborators[201] (Figure 3.8). It was obtained by the capping strategy where the thread contained a phenanthroline unit and a fullerene as a stopper. Then, by coordination of the two phenanthroline units with copper, the macrocycle was introduced into the thread and was locked by the addition of another fullerene stopper.

More recently, Schuster and coworkers[202] have successfully used this metal-templated strategy to build similar structures containing fullerenes as stoppers but including a porphyrin unit into the macrocycle. The fullerenes were functionalized using the Bingel reaction. These systems containing porphyrins are used to transmit and process solar energy into other energy sources. This topic will be analyzed in depth in forthcoming sections.

In a different article from Schuster's laboratory,[203] an analogous rotaxane was prepared. The fullerene unit was contained in the macrocycle and the porphyrins were used as stoppers. The macrocycle was threaded following metal-templated capping strategy. The structural distribution allowed the preparation of novel catenane systems by complexation of the two terminal Zn-porphyrins when one equivalent of a bidentate ligands, such as 1,4-Diazabicyclo[2.2.2]octane

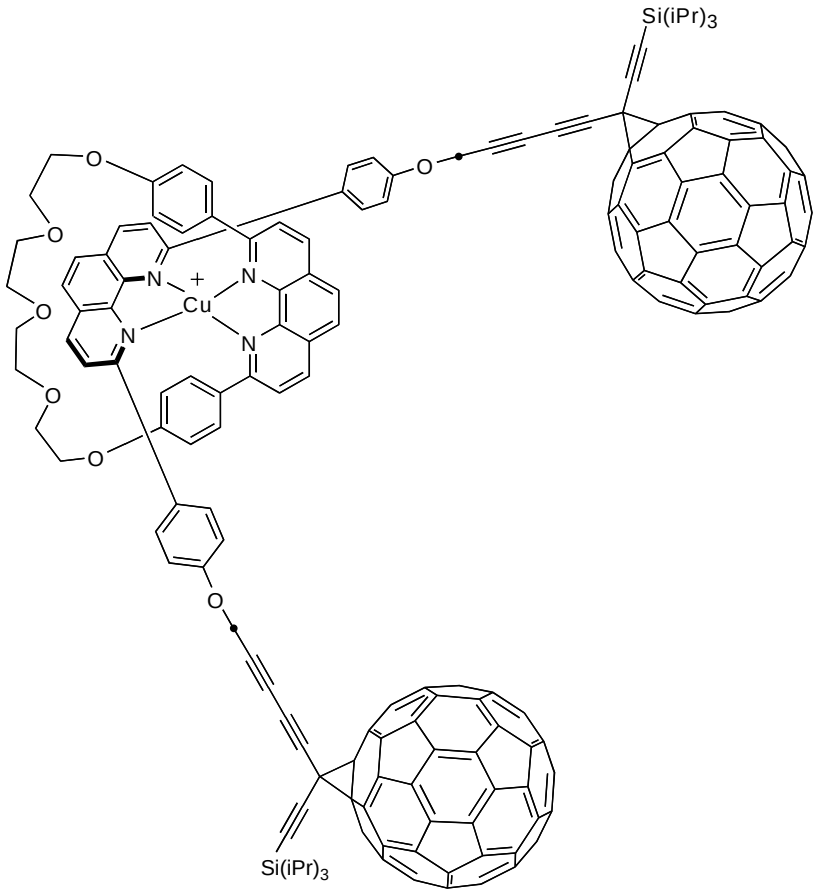

FIGURE 3.8 Phenantroline based fullerene rotaxane.

(DABCO) and 4,4′-bipyridine, were used. A subsequent addition of one extra equivalent of the bidentate ligand converted the 1:1 catenane supramolecular complex into a 2:1 rotaxane complex.

Catenanes consist of two or more interlocked macrocycles (Figure 3.6). The first example of a catenane containing a fullerene was first reported in a collaborative work between Stoddard and Diederich[204] (Figure 3.9). The [2]catenane was obtained by molecular recognition between π-electron-rich aromatic and π-electron-deficient aromatic units. A bisfunctionalized fullerene prepared by tether addition, contained the π-electron-rich aromatic unit. Then the π-electron-deficient aromatic unit was used to clip the second macrocycle.

Following this methodology, rotaxanes and catenanes have been prepared.[205] A thread was synthesized with one fullerene as a stopper, a naphthalenetetracarboxylic diimide moiety and a 1,3-dicarboxylic acid unit at the other end. The electron-deficient diimide was capable to recognizing an electron-rich naphthocrown ether. When the reaction was carried out in the presence of 1,8-Diazabicyclo[5.4.0]undec-7-ene (DBU) and an excess of C_{60} a [2]rotaxane was obtained. But if the experiment was carried out only with DBU, a [2]catenane was obtained by the formation of a Bingel bisadduct.

Rotaxanes can be assembled using other molecular interactions, such as hydrogen bonds. In a collaborative work between Prato and Leigh groups,[206] C_{60} was functionalized following the 1,3-dipolar fashion (Figure 3.10). A glycylglycine template was introduced into the molecule, as well as a long alkyl chain and a phenolic stopper. Macrocyclization of *p*-xylylenediamine and isophthaloyl

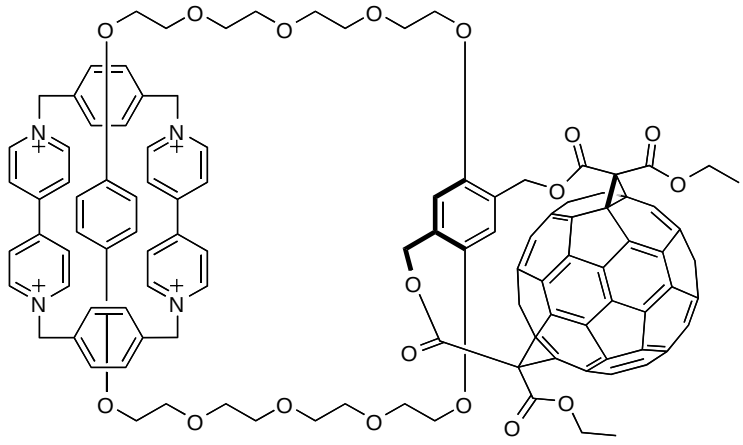

FIGURE 3.9 Fullerene catenane.

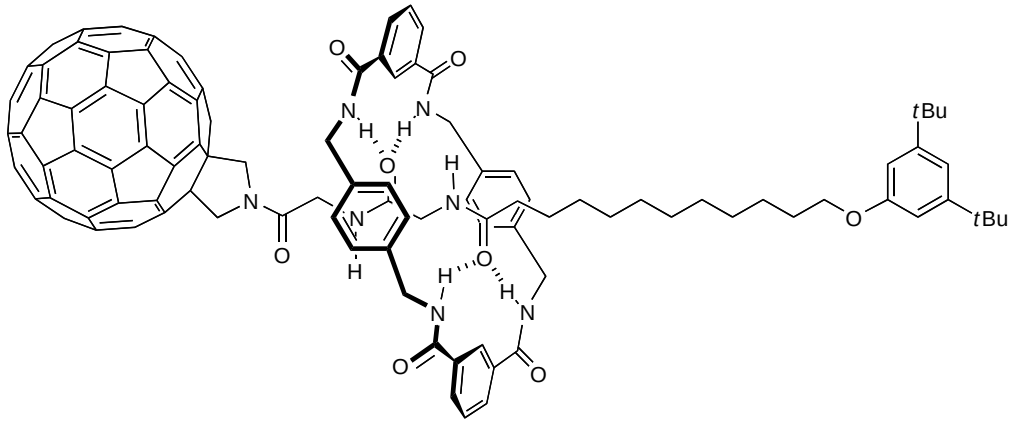

FIGURE 3.10 Hydrogen bond assembled rotaxane.

dichloride templated by hydrogen bond clipped the rotaxane around the glycylglycine residue. The importance of this work relied on the possibility of switching the macrocycle within the thread. The macrocycle bonds to the peptide residue in solvents such as chloroform or dichloromethane. In highly polar solvents such as Dimethylsulfoxide (DMSO), the hydrogenbonds were disrupted and the macrocycle was preferentially located over the alkyl chain. The location of the macrocycle can be monitored by means of NMR spectroscopy and time-resolved spectroscopy.

In another example of rotaxanes assembled by hydrogen bonding, the thread was capped in the macrocycle and stoppered by two porphyrins.[207] The macrocycle functionalized with the hydrogen bond template and butadiene sulfone. Then, C_{60} was added to the macrocycle using Diels–Alder cycloaddition, as 1,3-butadiene was generated *in situ* from butadiene sulfone.

Other structures known as pseudorotaxanes, analogous to rotaxanes but with none, or only one stopper, have also generated a lot of interest (Figure 3.6). These assemblies are not interlocked, so both the thread and the macrocycle are free to dissociate. The first pseudorotaxane bearing a fullerene was published in 1999.[208] It was prepared by complexation between two C_{60} units functionalized via Bingel. One of them was functionalized with a crown ether, while the other one was functionalized with a secondary amine. The secondary amine was transformed into an ammonium salt. Then the fullerene crown ether bound the ammonium salt and the association constant was

determined by NMR as $K_a = 970\ M^{-1}$. An interesting feature regarding the reversibility of these systems should be highlighted. When the fullerene ammonium salt was complexed with dibenzo-24-crown-8, the fluorescence of the macrocycle was quenched by proximity of the fullerene. Then, in the presence of a base the ammonium salt was transformed in the free base and the two units disassembled switching "on" the fluorescence of the system.

Similar systems have been successfully prepared by coordination of fullerene ammonium salts with phthalocyanine[209,210] (Figure 3.11) and porphyrin[211] crown ethers. The association constants, respectively, were $K_a = 153{,}000$ and $K_a = 375{,}000\ M^{-1}$, such high values can be associated with the stabilization of the supramolecular complex by π-stacking interactions between the heterocycles and C_{60}. The quenching of the fluorescence of both the phthalocyanine and the porphyrin was observed.

3.3.2 Nanorings, Peapods

New supramolecular motifs of fullerenes with concave–convex structures have been developed very recently by π-stack interactions. It comprises interactions between fullerenes and different curved carbon structures, such as nanorings or nanotubes. Both structures have π-orbitals oriented radially, as well as the fullerenes.

Nanorings are closed loops formed by conjugated π-orbitals. They are very interesting from the point of view that they can host different molecules depending on the size of the ring. Fullerenes can be hosted by nanorings as shown by Kawase and Oda.[212] They prepared [6]- and [8]paraphenyleneacetylene and studied their complexation with C_{60} and with *bis*(ethoxycarbonyl)methanofullerene. The experiments with C_{60} showed the formation of a 1:1 supramolecular complex with [6]paraphenyleneacetylene (Figure 3.12) and the association constant was determined ($K_a = 16{,}000\ M^{-1}$). The same measurements were attempted with *bis*(ethoxycarbonyl)methanofullerene but the changes in absorption were too small to measure a reliable association constant. On the other hand, it was possible to obtain an X-ray structure from the fullerene monoadduct and [6]paraphenyleneacetylene, confirming the structure of the complex. The experiments with [8]paraphenyleneacetylene showed none or very small complexation with C_{60}.

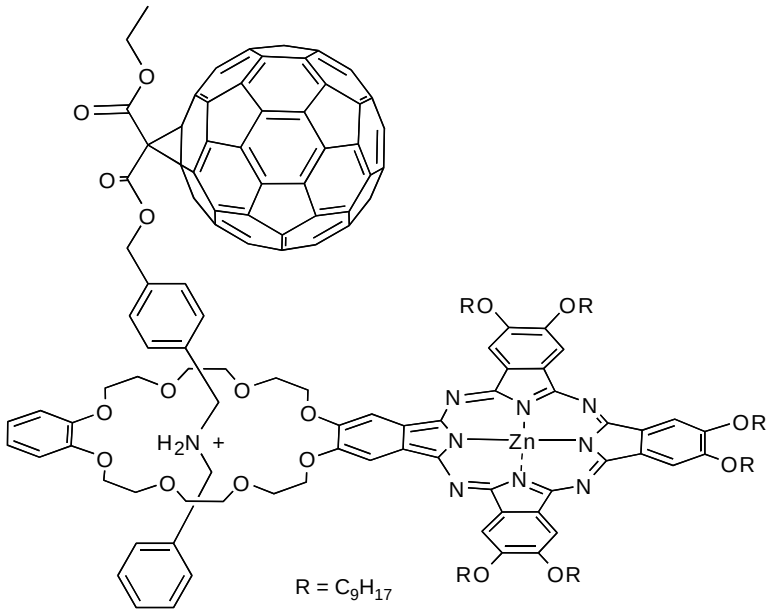

FIGURE 3.11 Phthalocyanine–fullerene pseudorotaxane.

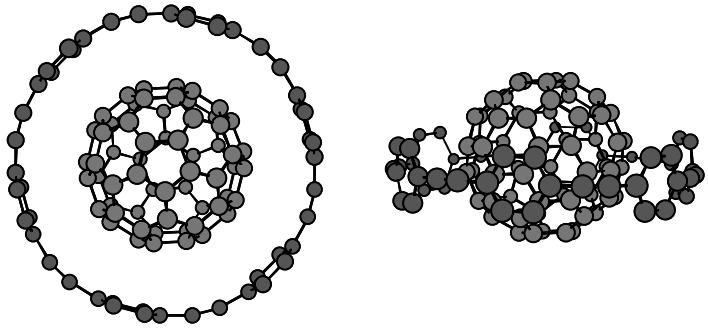

FIGURE 3.12 C_{60}-nanoring complex.

In a different article from the same authors,[213] the complexation of C_{60} and C_{70} with [6]- and [7]paraphenyleneacetylene was studied. Also other complexation studies were carried out with the novel isomers of [7]paraphenyleneacetylene that have 1,4- or 2,6-naphtylene units diametrically opposed. The calculation of the association constants was attempted but they were too large to be determined precisely ($>5 \times 10^4$), which indicated that very stable complexes were formed. Fluorescent measurements were carried out from these complexes, providing a lot of information about the estimated relative stability of the whole series of rings with C_{60} and C_{70}. The results were consistent with the values of the association constants and also showed that the new naphtylene nanorings are very efficient fluorescent sensors for fullerenes.

During the synthesis and purification of the different paraphenyleneacetylene and 1,4-naphtyleneacetylene nanorings, it was found that big rings could form inclusion complexes with smaller rings.[214] [6]Paraphenyleneacetylene could be inserted within the larger [9]paraphenyleneacetylene, the association constant could only be determinated at –60°C ($K_a = 340 \pm 45\ M^{-1}$). The same behavior was observed with the analogous 1,4-naphtyleneacetylene nanorings showing much higher association constants at –60°C ($K_a = 11{,}000 \pm 1400\ M^{-1}$) because of the larger contact area. In order to prepare complexes including fullerenes, C_{60} was first included within the smaller ring as done in previous experiments and subsequently these complexes were then assembled with the larger ring. NMR experiments proved the formation of these onion-type complexes (Figure 3.13). The association constants could only be calculated for the [9]paraphenyleneacetylene⊃([6]paraphenyleneacetylene⊃C_{60}) complex at –60°C ($K_a = 410 \pm 80\ M^{-1}$).

Other interesting structures known as carbon peapods have been developed in the last years. Carbon peapods are single-walled carbon nanotubes (SWCNTs) that are filled with fullerenes (Figure 3.14). They are considered as a new supramolecular carbon allotrope. Carbon peapods were first reported in 1998[215] when they were detected by high-resolution transmission electron microscopy (HRTEM) as side products during the production of carbon nanotubes. Since then, several methods for the efficient filling of empty SWCNTs have been developed.

The first production method was reported by Luzzi and Smith in 2000.[216] Carbon peapods were prepared from raw nanotubes produced by pulsed laser vaporization. Several defects (such as sidewall holes and open ends) were introduced on the surface of the nanotubes by refluxing the material in nitric acid, thus facilitating the insertion of fullerenes. Subsequently they were annealed at high temperatures and low pressures. C_{60} was only inserted in 1.3 to 1.4 nm diameter SWCNTs that are the only ones that permit the preferred graphitic 0.3 nm van der Waals separation between the fullerene and the nanotube.

Endohedral fullerenes such as $Ce@C_{82}$,[217,218] $Gd@C_{82}$,[219] $Dy@C_{82}$,[220] $La@C_{82}$,[221] $Sm@C_{82}$,[221] $Ti_2@C_{82}$,[222] $La_2@C_{82}$,[223] and $Gd_2@C_{82}$,[224] have been introduced in carbon nanotubes. Different motions have been observed by HRTEM of peapods containing $Ce@C_{82}$.[217] The images showed the translational motion of the fullerenes inside the nanotubes, as well as rotation of the fullerene units.

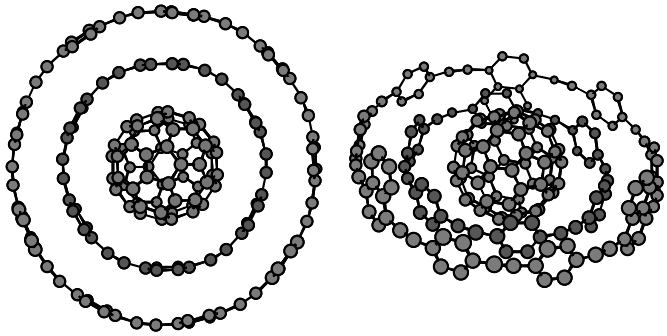

FIGURE 3.13 C_{60} Onion type complex.

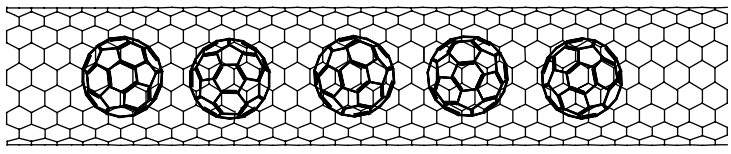

FIGURE 3.14 Carbon peapods.

Yudasaka and coworkers[225] introduced two very interesting and simple methods that do not require extreme conditions for the preparation of carbon peapods. These processes are known as nano-extraction and nano-condensation and are easy to apply and require no special skills. First, commercial SWCNTs were treated under extreme condition to open holes in sidewalls and ends. In nano-extraction, C_{60} crystallites were sonicated in ethanol, then the nanotubes were added to the solution and left at room temperature for 1 day. TEM images showed $(C_{60})n$@SWCNTs in a 50 to 70 filling percentage. The success of this method relies on the high affinity of the fullerenes for the nanotubes that was enhanced by the medium, due to the low affinity of the SWCNTs and C_{60} to ethanol. In nano-condensation, SWCNTs were deposited on a grid surrounded by filter paper. After the addition of a saturated solution of C_{60} in toluene the SWCNTs were filled in a 50 to 70% as estimated by TEM, in only a few seconds. The mechanism of this process was not completely understood. These two methods demonstrated that high temperatures are not needed for filling SWCNTs, therefore other molecules that are not stable to sublimation or evaporation temperatures could also be inserted.

Briggs and coworkers[218,226] have discovered that SWCNTs can be filled with fullerenes in supercritical fluids using low temperatures (30 to 50°C). These low-temperature conditions allowed to fill the SWCNTs with empty, endohedral, and functionalized fullerenes. Nanotubes were produced by the arc discharge method. During purification, the ends were opened and also sidewall holes were introduced. Then a mixture of nanotubes and C_{60} was exposed to pressurized supercritical CO_2 to 150 bar at 50°C and the cycle was repeated six times yielding $(C_{60})n$@SWCNTs in an ~70% filling factor. The general applicability to this filling procedure has been demonstrated by the introduction of different functionalized fullerenes such as $C_{61}(COOEt)_2$ or $Er_3N@C_{80}$. However, experiments[226] carried with $C_{61}(COOH)_2$ showed that the fullerene derivative was preferentially coordinated outside the SWCNTs rather than forming peapods. Supercritical CO_2 showed to facilitate the penetration of the fullerene derivatives inside the nanotubes by different factors. These include (1) low solvation of both fullerenes and SWCNTs, (2) low viscosity and lack of surface tension that promote the solvent to flow through the nanotubes without being encapsulated, thus leaving free room for the insertion of fullerenes, and (3) clean the surface and the holes as well as separates the nanotube bundles.

3.3.3 Supramolecular Assemblies with Porphyrins

Surprisingly, fullerene derivatives can form complexes with planar electron-rich macrocycles, such as porphyrins. The association between fullerenes and porphyrins was first observed by x-ray crystallography in a covalently linked fullerene–porphyrin.[227,228] Since then, a variety of x-ray structures from co-crystals of different fullerenes and porphyrins have been reported.[229,230] The nature of the supramolecular interactions between these two units is not fully understood. It has been suggested that the association can be due to van der Waal interactions[229,231] to electrostatic interactions,[232] and to charge-transfer interactions.[233,234] Theoretical calculations[235] showed that the electrostatic interactions contribute approximately with 50 to 60% of the total attractive interactions. Also, a charge transfer contribution of about 0.10 to 0.14 electrons from the porphyrin to the fullerene was observed. More importantly, the high affinity of fullerenes and porphyrins was not only observed in the solid state, but also in solution as shown by upfield shifts in both ^{1}H-and ^{13}C-NMR experiments in toluene.[229]

These results stimulated furthermore, and new porphyrin hosts were designed and synthesized for binding fullerenes. A type of bis-porphyrin systems, known as "porphyrin jaws," were prepared by Reed and coworkers.[236] The complexation of several "jaws" with fullerenes was studied both in solid state and in solution. The most successful binding was obtained with a palladium-based "jaw" (Figure 3.15) as observed by MALDI mass spectrometry. Also, mass spectrometry experiments with mixtures of fullerenes were carried out, showing the different affinities. Association constants around 490 to 5200 M^{-1} were determined between bis-metalated porphyrin "jaws" and C_{60} using NMR. The highest association constant was obtained for the free bis-porphyrin.

Novel supramolecular peapod systems[237] have been developed using dendrimeric "jaws." Once the porphyrin "jaws" complexed with C_{60} or C_{70}, the hexacarboxylic porphyrins polymerized unidirectionally through hydrogen bond dimerization of the side acid functionalization affording the supramolecular peapods with the dendrimeric envelope. The fibers observed by TEM displayed a constant diameter of 12 to 15 nm, which agreed with the diameter estimated from the molecular model.

Cyclic porphyrin dimers show high affinity for C_{60} (K_a = 670,000 M^{-1}) (Figure 3.16).[238] Dendrimeric systems containing this cyclic bis-porphyrin dimers have also been prepared.[239] The high affinity of this system for fullerenes was observed even with the high branched dendrimers for both C_{60} (K_a = 15,000 M^{-1}) and C_{70} (K_a = 230,000 M^{-1}). Different lengths with bis-porphyrin cyclic hosts have been investigated[240] in order to separate different fullerenes from fullerene mixtures obtained directly from the carbon-soot method. The extraction experiments showed that the different size bis-porphyrin hosts extracted selectively the higher fullerenes as was verified by HPLC–MS. The association constants were calculated by spectroscopic titration showing 118 and 16 times larger affinities for C_{96} ($K_a = 3.0 \times 10^7$ M^{-1}) that those obtained for C_{60} ($K_a = 5.1 \times 10^5$ M^{-1}) and C_{70} ($K_a = 1.3 \times 10^7$ M^{-1}).

3.3.4 Complementary Hydrogen Bonded Supramolecular Systems

Complex supramolecular architectures can be prepared by complementary hydrogen-bond donor–acceptor systems. Hydrogen bonds not only provide a high directionality and selectivity, but also introduce the possibility of multiple bonding in complementary donor–acceptor patterns, thus increasing the stability and the selectivity of the supramolecular system.

Hummelen[241] and Martin[242] pioneered the introduction of self-complementary hydrogen bond patterns in functionalized fullerenes. Quadrupole hydrogen bond motifs based on 2-uridopyrimidin-4-ones, were used to prepare self-assembled fullerene dimers (Figure 3.17). The dimers were successfully assembled and a high association constant was measured ($K_a = 1 \times 10^6$ M^{-1}).[241] Moreover, a fluorescence quench of 50% was observed in the assembled dimer.[242] On the other hand, an enhancement of the fluorescence was detected when disrupting hydrogen bond solvents were added. These results evidenced the strong electronic coupling occurring through the hydrogen bond.

More sophisticated systems have been prepared following the quadrupole hydrogen bond strategy. Fullerenes were assembled with oligo(*p*-phenylenevinylene)s (OPVs), the photo- and electrochemical properties of these new materials with applications in the field of plastic solar cells, were

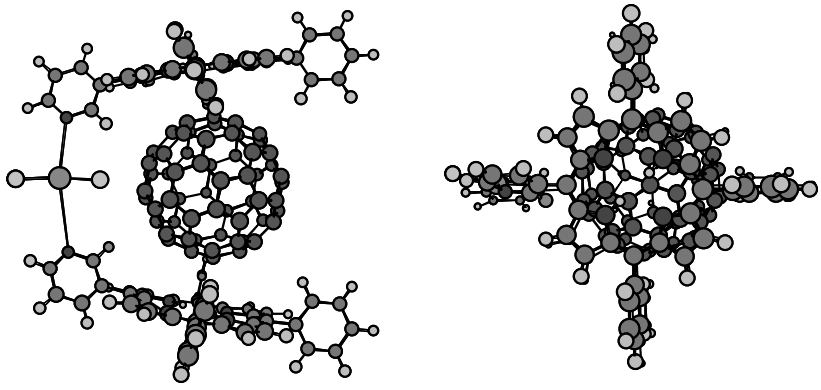

FIGURE 3.15 Porphyrin jaws. Left: Side view. Right: Top view.

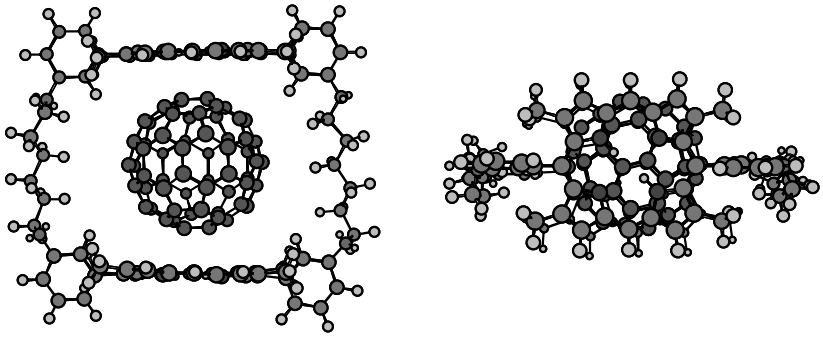

FIGURE 3.16 C_{60}–porphyrin dimer complex. Left: Side view. Right: Top view.

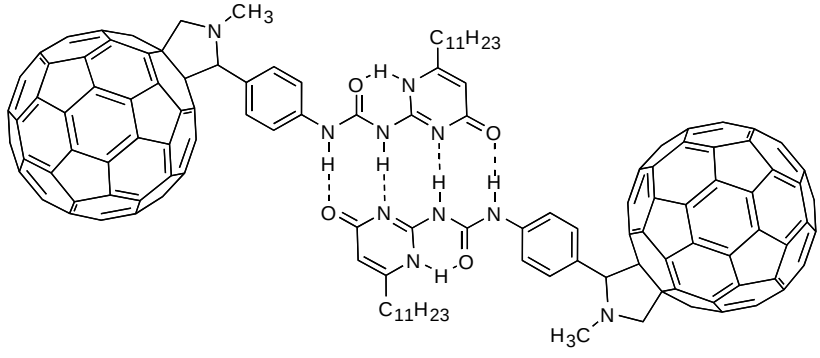

FIGURE 3.17 Self assembled fullerene dimer.

studied (Figure 3.18).[243,244] Additionally, C_{60} was functionalized with two 2-uridopyrimidin-4-one moieties, which self-assembled as a linear supramolecular fullerene polymer[245] as well as other motifs with bis-functional OPVs.[246]

Hydrogen bond assemblies are not restricted to 2-uridopyrimidin-4-ones motifs. In an elegant example from Martin and collaborators,[247] a wide variety of fullerene–tetrathiafulvalene systems was prepared through complementary recognition between carboxylates and guanidinium salts by donor–donor/acceptor–acceptor hydrogen bond motifs (Figure 3.19).

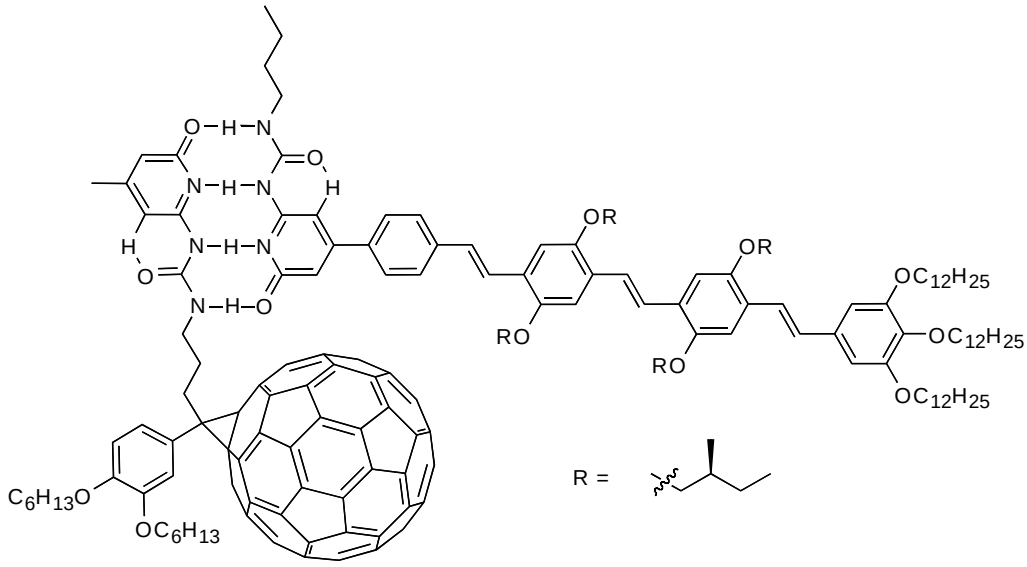

FIGURE 3.18 OPV-C_{60} hydrogen bond assembly.

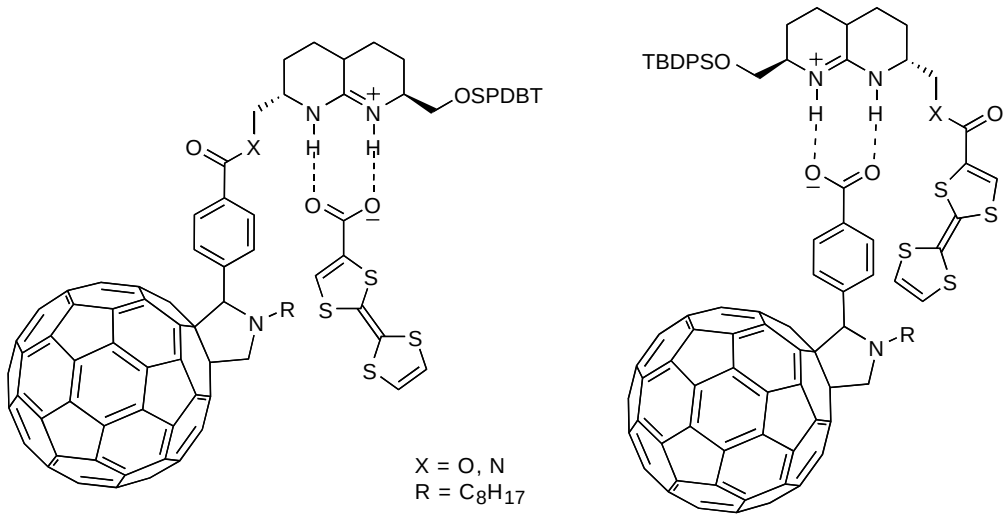

FIGURE 3.19 Recognition between carboxylates and guanidinium salts.

3.4 APPLICATIONS

In the last few years, scientists have employed the different methodologies for the functionalization of fullerenes, as well as the different types of supramolecular interactions to build a variety of very interesting molecular architectures with efficient applications. In the next section, some of the most promising fields of application of fullerene-containing systems will be summarized. The inherent photo- and electrochemical properties of fullerenes have played an active role in the performance of the system.

3.4.1 Donor–Acceptor Systems

The research on donor–acceptor systems involving fullerenes has attracted a lot of attention, as they can be used as artificial photosynthetic systems to transform light into chemical energy.

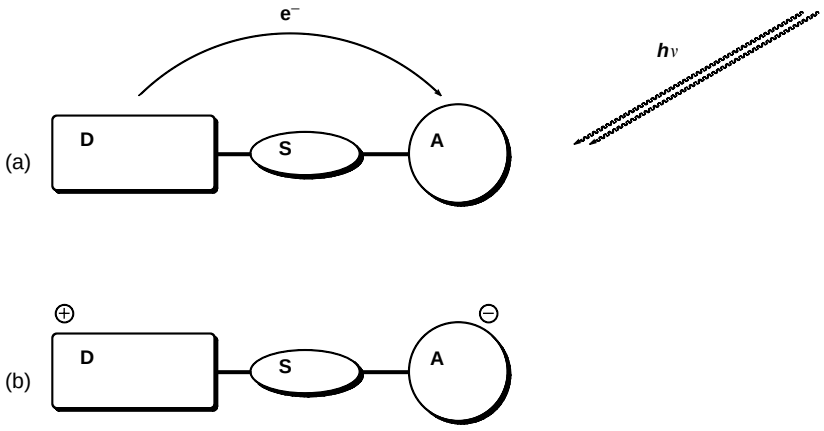

FIGURE 3.20 (a) Photoinduced electron transfer; (b) radical pair formed.

The simplest systems, known as dyads, can be described as the result of two units, an electron donor (D) and an electron acceptor (A), linked together through covalent or noncovalent interactions. After photostimulation,[248] the charge transfer is induced between the two units leading to a charge-separated state where the energy is stored (Figure 3.20).

An important feature that should be taken into account is the lifetime of the charge-separated state formed. The excited state should be sufficiently long-lived to be converted into chemical energy. In order to increase the lifetimes, C_{60} has been widely used as an electron-acceptor unit, not only because of the high electron affinity[7–9] but also because of the high delocalization of the electron in the three-dimensional π-system and its small reorganization energy.[249] Other factors such as the rate of charge recombination, affect directly the lifetime of the charge-separated state. Therefore, the selection of the linker (or spacer) between the two units is very important. It controls the distance, the orientation, and the electronic coupling between the two units, and thus the electron transfer and the rate of charge recombination. Depending on the nature of the linker, covalent or noncovalent, both the electron transfer and the charge recombination can occur through bond or through space.

Additionally, a wide range of electron donors has been explored and they will be reviewed in the following sections.

3.4.1.1 Dyads Containing Photoactive Electron Donors

Electron transfer takes place easily between fullerenes and heterocycles that absorb light in the visible region of the spectrum, such as porphyrins, phthalocyanines, and subphthalocyanines.

Porphyrin dyads have been by far the most investigated systems.[250–253] Dyads linked through covalent spacers have been constructed and investigated. In some architectures, the porphyrin was linked close to the fullerene[254–262] or forced apart.[159,263–265]

1,3-Dipolar addition was used to prepare architectures bearing porphyrins in position 2 of fulleropyrrolidines.[254–256] These systems have shown the longest lifetimes reported in dyads to the moment (230 μsec at 25°C)[255] and have been highlighted for their simplicity and effectiveness (Figure 3.21).[266]

Strapped and parachute-like fullerene–porphyrin architectures have been prepared via Bingel with flexible linkers that allow the porphyrin to get very close to the fullerene.[258–262]

Other systems have been assembled by means of supramolecular interactions in rotaxane architectures,[202,203,207,211] in sandwiched π-stack complexes[229–234,236–240] or by metal coordination.[267–271]

A zinc tetraphenyl porphyrin (Zn(TPP)) was noncovalently linked to a C_{60} derivative via axial pyridine coordination to the metal (Figure 3.22).[267–270,272] Photoexcitation of the Zn-complex led to electron transfer with very long lifetimes of the charge-separated pairs as revealed by optical

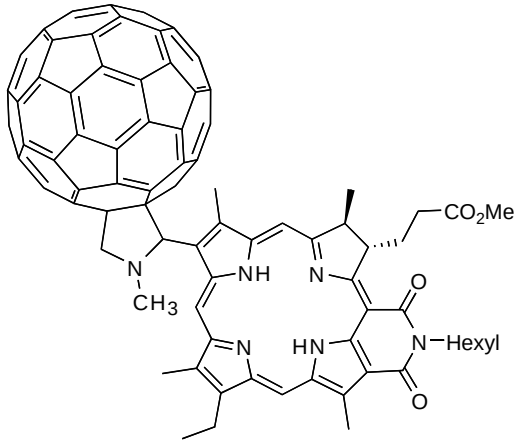

FIGURE 3.21 Simple fullerene–porphyrin dyad.

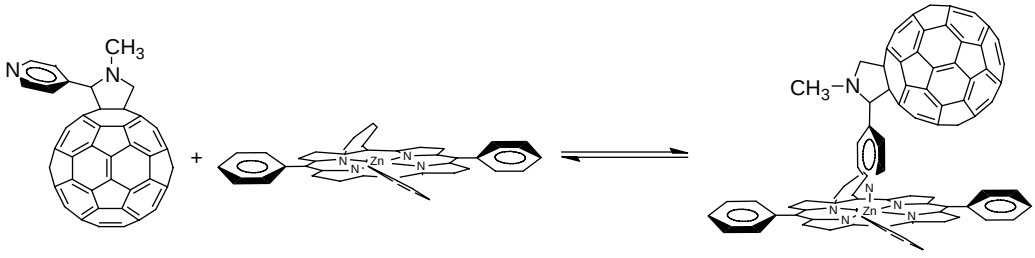

FIGURE 3.22 Preparation of dyads by metal complexation.

spectroscopy and confirmed by time-resolved electron paramagnetic resonance spectroscopy. Similar fulleropyrrolidine complexes, including also porphyrins covalently linked have been reported.[269–271]

Phthalocyanines and subphthalocyanines have been used for the construction of different efficient dyads. Once more, the most straightforward approach involved 1,3-dipolar addition yielding fulleropyrrolidines substituted with phthalocyanines in position 2.[154,273,274] Various pseudorotaxane architectures were prepared by Torres and collaborators[209,210] (Figure 3.11, see Section 3.3.1). The most notorious properties of these systems relied on the possibility of switching "on" and "off" the electron transfer by the addition of acid or base. Under acidic conditions the fullerene ammonium salt complexed with the phthalocyanine crown ether allowing photoinduced electron transfer between the two units. While under basic conditions the two units are apart and no electron transfer took place.

A wide variety of substituted suphthalocyanines[275,276] has been assembled by complexation with 2-phenony-substituted fulleropyrrolidines. The peripheral substitution in the subphthalocyanine moiety led to the tuning of the electron-donating properties of the dyads.

3.4.1.2 Dyads Containing Nonphotoactive Electron Donors

Donor–acceptor systems can be also prepared using nonphotoactive electron donors such as tetrathiafulvalene[277] (TTF) and ferrocene units. In this case, the fullerene unit (electron acceptor) gets excited by light irradiation to its singlet state, while the electron donor does not absorb light and remains in its ground state, this is followed by electron transfer.[248]

The first synthesis of C_{60}–tetrathiafulvalene dyads was done via 1,3-dipolar cycloaddition by using the appropriate azomethine ylides substituted with a tetrathiafulvalene unit as electron donor

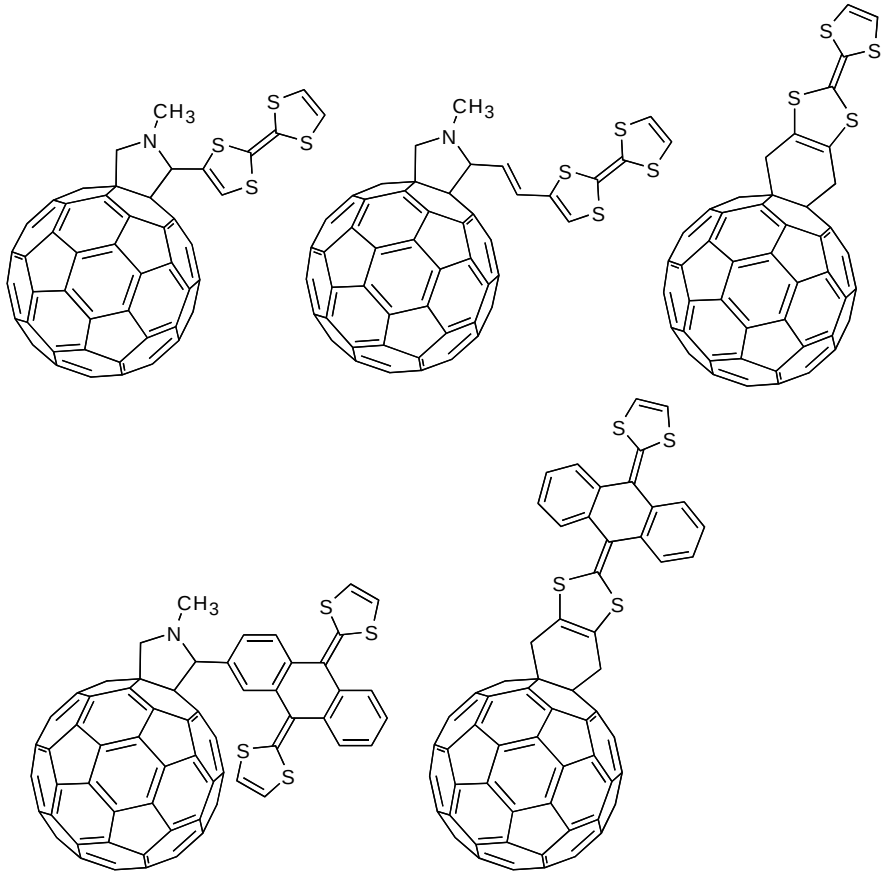

FIGURE 3.23 Fullerene–TTF dyads.

(Figure 3.23).[278,279] These were followed by more sophisticated approaches that had highly conjugated tetrathiafulvalene units linked to C_{60} skeleton (Figure 3.23).[280] The idea for synthesizing such π-extended-tetrathiafulvalenes stemmed from their ability to form stable dication species that introduced electrical and magnetic properties, in sharp contrast with simple tetrathiafulvalenes that are known to form only stable radical cations.[281,282] However, in the early dyads, no electronic interactions between the donor–acceptor units were observed.[283]

When the redox units were attached via Diels–Alder cycloaddition,[284–286] efficient electron- and energy transfer took place between the active units of the system by a through-bond coupling mechanism (Figure 3.23).

Electron transfer events were also detected when C_{60} was functionalized by 1,3-dipolar addition, using azomethine ylides[283,287] with vinyl spacers bearing TTF moieties, along with azides bearing TTF [288] and π-extended-TTF units (Figure 3.23).[289]

Other examples of active dyads bearing TTFs functionalized by Bingel-type adducts were reported.[290]

Recently, a variety of supramolecular C_{60}–TTF dyads have been assembled through complementary recognition between guanidinium salts and carboxylic acids, through donor–donor–acceptor–acceptor hydrogen bond motifs.[247] Eight different dyads were prepared and studied displaying different functional groups and spacers (Figure 3.19, see Section 3.3.4). Intramolecular electron transfer occurred between the two units but this was not observed when solvents that disrupt hydrogen bonds were added. Alternatively, intermolecular electron transfer was detected.

Ferrocene (Fc) is another good example of electron donor that is not excited upon light irradiation. Some fullerene–ferrocene dyads have been synthesized following the methodology of 1,3-dipolar cycloaddition to C_{60}, with either variable spacing building blocks or rigid linkers, in order to tune the redox properties of the system.[177,279,291–294] Another novel dyad that contained two covalently bound ferrocene units was recently synthesized via cyclopropanation of the fullerene core.[295]

Recently, liquid-crystalline fullerene–ferrocene dyads[296] were prepared by 1,3-dipolar additions leading to fulleropyrrolidines bearing functionalized fullerene unit and a mesomorphic dendrimer. Photoinduced intramolecular electron transfer was observed (Figure 3.24).

3.4.1.3 Polyads

More complicated systems bearing more than two electroactive units have been built and studied.[252,297] In this case, the donor–acceptor systems are called triads, tetrads, pentads, hexads, etc., depending on the number of electroactive units that can work both as donors and acceptors. The objective is to build an optimal distance for long-lived charge-separated states by means of a series of short distance and efficient electron transfer events.

A variety of triads and tetrads displaying combinations of fullerenes, porphyrins, Zn-porphyrins, and ferrocenes were synthesized and studied by Imahori and collaborators. In a very elegant work, ZnP–H_2P–C_{60} (Figure 3.25) was synthesized and investigated.[298,299] After photostimulation, energy transfer took place from the ZnP to the H_2P followed by an electron transfer from the excited H_2P to C_{60} giving a long distance charge-separated state.

Analogous Fc–ZnP–C_{60} and Fc–H_2P–C_{60} (Figure 3.25) triads that contain a terminal ferrocene unit[299,300] were prepared and examined. When irradiated, two consecutive electron transfers took place. First from the porphyrin to C_{60} and then from the ferrocene to the porphyrin leading to the charge-separated state. By combination of these two systems, a tetrad was reported,[301] which showed the longest charge-separated state to date, as the product of a sequence of energy and multistep electron transfer events (Figure 3.25).

Novel multicomponent polyads have been prepared and analyzed, based on linear[302,303] and branched[304] multiporphyrin polyads (Figure 3.26), including a ferrocene–multiporphyrin pentad.[305]

Multiple donor–acceptor systems containing TTF have been also explored. These include porphyrin–C_{60} triads bearing terminal TTF[306] and π-extended-TTF[307] moieties (Figure 3.27).

Series of triads based on a terminal π-extended-TTF unit linked to C_{60} through a polyphenylenevinylene (PPV) molecular wire have been recently reported.[308] After light irradiation, electron transfer occurred leading to a 40 Å charge-separated state (Figure 3.28).

3.4.2 Plastic Solar Cells

Fullerenes participate in the formation of charge-transfer complexes with weak electron donors, such as conjugated polymers. Upon photoexcitation, electron transfer takes place between the S_1 excited state of the polymer and the more electronegative C_{60}.[309] The addition of C_{60} to conjugated polymers increased the photoconductivities[310,311] to a large extent, as a result of the photoinduced electron transfer. Due to these properties, fullerene-based plastic solar cells have shown as one of the most promising applications of these composite materials. This field has been extensively reviewed.[312,313]

In the first example,[309] C_{60} was added to PPV and electron transfer occurred from the excited state of the polymer to C_{60}. It was observed that the charged-separated state was long-lived enough to allow the charges to migrate to the anode and the cathode, and thus the first fullerene-based photodiode was constructed.[314] Nevertheless, the interactions between the acceptor and the donor were limited by the flat geometry of the interface. When functionalized fullerenes were adopted, the photodiodes displayed better photoconversions.[146,315–317] The use of functionalized fullerenes decreased the aggregation and increased the interaction with the soluble conjugated polymer

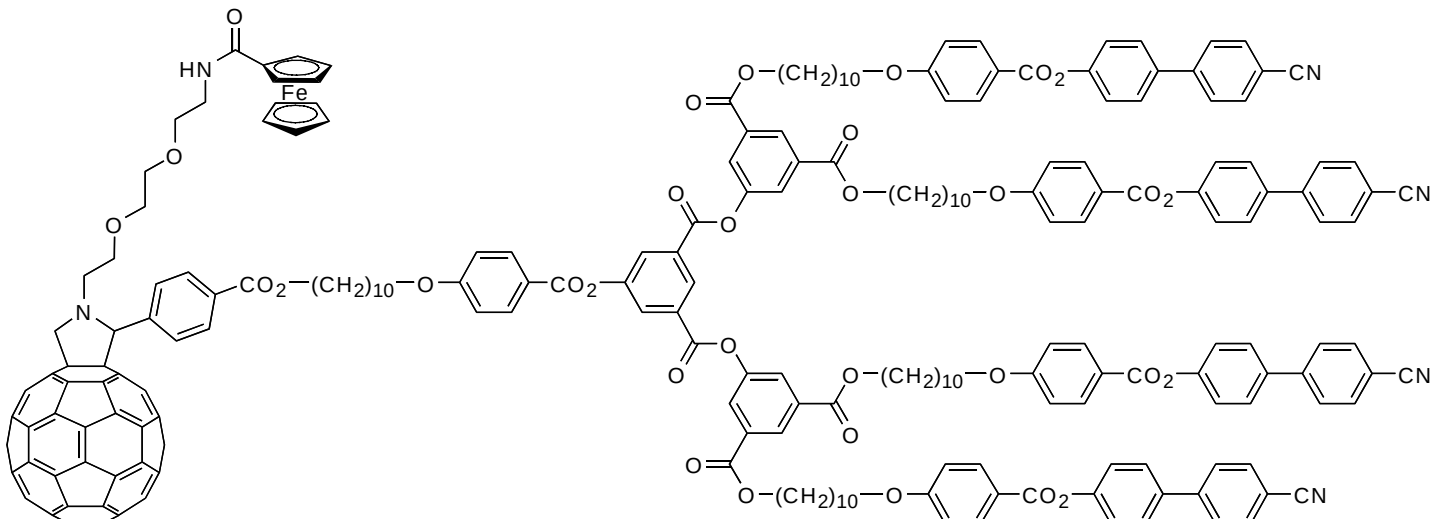

FIGURE 3.24 Liquid crystalline fullerene–ferrocene dyad.

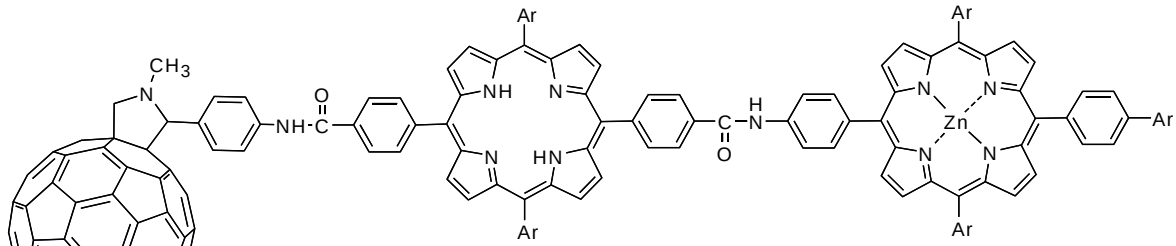

C_{60}-H_2P-ZnP

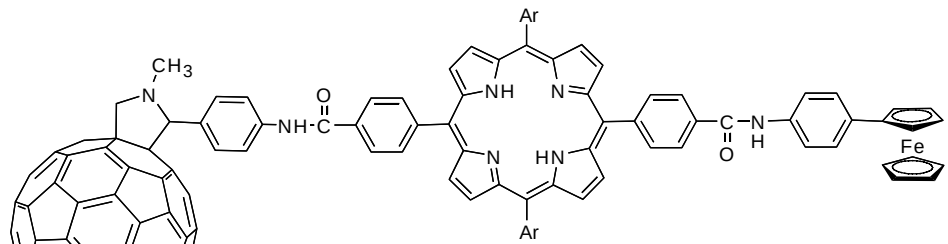

C_{60}-H_2P-Fc

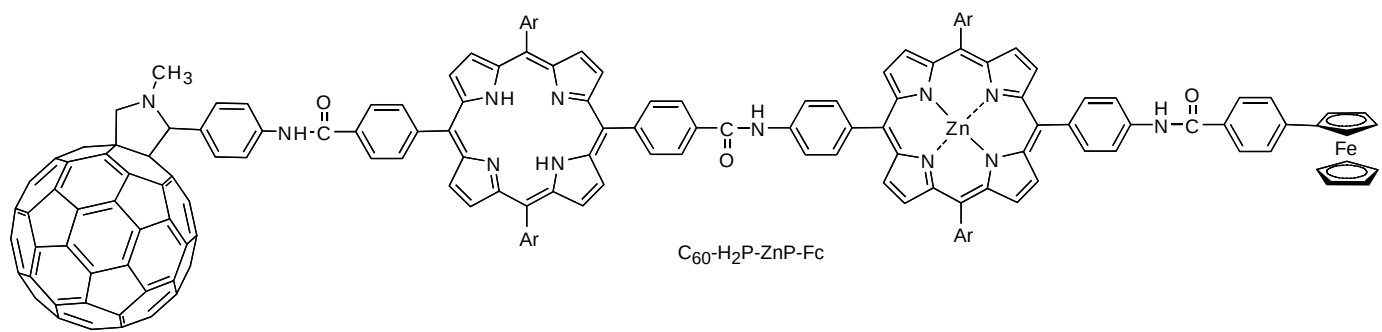

C_{60}-H_2P-ZnP-Fc

FIGURE 3.25 C_{60}-porphyrin–ferrocene polyads.

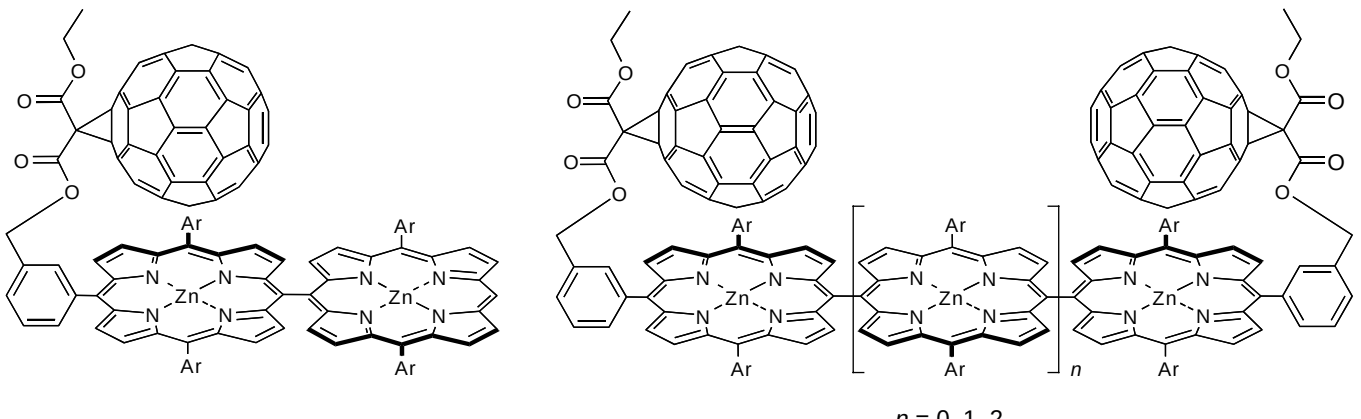

FIGURE 3.26 Olygoporphyrin polyads.

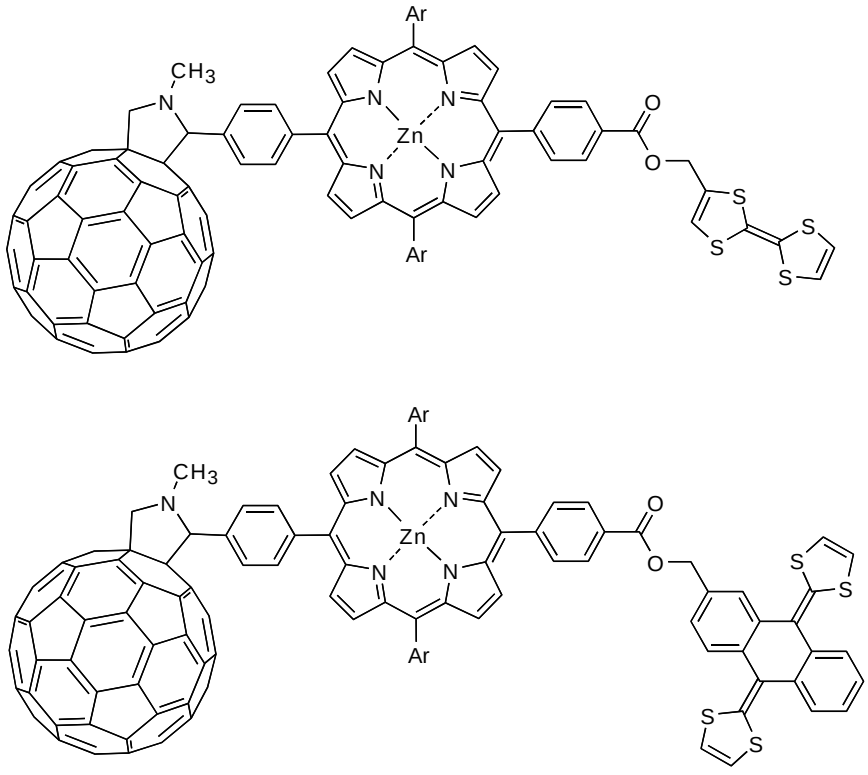

FIGURE 3.27 TTF-porphyrin–C_{60} triads.

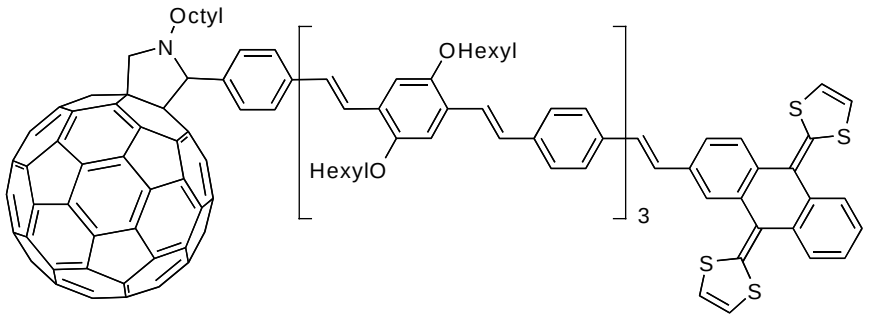

FIGURE 3.28 Molecular wire.

enhancing the generation of a photocurrent circuit.[312,315] Also, it has been shown that the morphology of the so called "bulk heterojunction" has a very important influence in the power conversion efficiency.[317] Hence, diverse strategies have been proposed to improve the processibility of functionalized fullerene materials and obtain their intimate mixing with conjugated polymers to control both electronic and morphological properties.

1-(3-methoxycarbonyl)-propyl-1-1-(6′6)C_{61} (PCBM) has been widely used as acceptor in multiple bulk heterojunction solar cells. More recently, new fullerenes acceptors were studied including DPM-12[318] and mixtures of isomers of [70]PCBM.[319]

In more detail, the following systems have already been designed and tested to a great extent as useful photodiodes: (1) diblock-copolymers (i.e., conjugated donor block polymer plus fullerene-bearing

block)[320] and (2) conjugated oligomer–fullerene dyads with different conjugation length of the donor moiety.[321–328]

Novel hybrid materials have been realized in which fullerenes participate in composite films with π-conjugated polymer-electron donors such as oligothiophenes. Established studies have already shown that the photoinduced electron transfer is rather enhanced between π-conjugated polymers and fullerenes, while back electron transfer is considerably slower.[309,316,329,330] Electrosynthesized polythiophene with pendant fullerene substituents was recently obtained from the corresponding bithiophene–fulleropyrrolidine dyad.[331] The novel described material has the potential of a double-cable polymer, heavily loaded with fullerene electron-conducting moieties.

Studies dealing with the incorporation of conjugated oligomeric units in fullerene dyads systems have been increased, especially after the observation of electron transfer from conducting oligomers (or polymers) to C_{60}.[309,332] Some further examples on such materials involved the construction of organofullerene materials in which two oligo-phenylenevinylene,[333] or two oligo-thienyleneviylenes[334] units, have been attached on the skeleton of C_{60} via a fused pyrrolidine ring. Further works utilizing oligo-phenylenevinylenes[335,336] and oligo-naphthylenevinylenes[337–339] in fullerene hybrids systems have been performed and found to possess intriguing physicochemical properties including singlet–singlet energy transfer as well as intramolecular electron-transfer interactions.

Recently, self-assembly of complementary hydrogen bond motifs have been introduced in both fullerenes and conjugated oligo(*p*-phenylenevinylene)s in order to control the morphology of the fullerene–oligomer mixture and obtain better photoconversions.[243,244,246]

3.5 CONCLUSIONS

The organic functionalization of C_{60} has produced a wide range of derivatives, which retain the basic properties of pristine fullerene. Among the many possible reactions available, cycloadditions have been most widely used, along with cyclopropanation (nucleophilic) reactions. The products have now improved the solubility and processibility and can be used in several applications including electron-transfer reactions, liquid crystals, polymers, dendrimers, and solar cells. The continuous evolution of fullerene science and technology, accompanying the progress obtained in the functionalization chemistry, has led to the production of more and more compounds that open new horizons in the potential applications of these fascinating molecules.

ACKNOWLEDGMENTS

Part of the work described in this chapter was supported by the European Union through grants HPRN-CT-2002-00168 and HPRN-CT-2002-00177, and by MIUR (PRIN 2004, prot. 2004035502).

REFERENCES

1. Kroto, H.W., et al., *Nature*, 318, 162, 1985.
2. Krätschmer, W., et al., *Nature*, 347, 354, 1990.
3. Haufler, R.E., et al., *J. Phys. Chem.*, 94, 8634, 1990.
4. Haddon, R.C., Brus, L.E., and Raghavachari, K., *Chem. Phys. Lett.*, 125, 459, 1986.
5. Haddon, R.C., Brus, L.E., and Raghavachari, K., *Chem. Phys. Lett.*, 131, 165, 1986.
6. Yang, S.H., et al., *Chem. Phys. Lett.*, 139, 233, 1987.
7. Echegoyen, L, Diederich, F., and Echegoyen, L.E., Electrochemistry of Fullerenes, in *Fullerenes: Chemistry, Physics, and Technology*, Kadish, K.M. and Ruoff, R.S., Eds., Wiley, New York, 2000, p. 1.
8. Echegoyen, L. and Echegoyen, L.E., *Acc. Chem. Res.*, 31, 593, 1998.
9. Arias, F., et al., *J. Am. Chem. Soc.*, 117, 1422, 1995.
10. Bruno, C., Doubitski, I., Marcaccio, M., Paolucci, F., Paolucci, D., and Zaopo, A., *J. Am. Chem. Soc.*, 125, 15738–15379, 2003.

11. Haddon, R.C., et al., *Appl. Phys. Lett.*, 67, 121, 1995.
12. Allemand, P.M., et al., *Science*, 253, 301, 1991.
13. Makarova, T.L., et al., *Science*, 253, 301, 2001.
14. Lappas, A., et al., *Science*, 267, 1799, 1995.
15. Narymbetov, B., et al., *Nature*, 407, 883, 2000.
16. Mizoguchi, K., et al., *Phys. Rev. B*, 6314, 2001.
17. Hebard, A.F., et al., *Nature*, 350, 600, 1991.
18. Grant, P., *Nature*, 413, 264, 2001.
19. Dagotto, E., *Science*, 293, 2410, 2001.
20. Hoke II, S.H., et al., *J. Org. Chem.*, 57, 5069, 1992.
21. Tsuda, M., et al., *Chem. Lett.*, 2333, 1992.
22. Wilson, S.R., et al., *J. Am. Chem. Soc.*, 115, 8495, 1993.
23. Wilson, S.R., et al., *J. Org. Chem.*, 58, 6548, 1993.
24. Schuster, D.I., et al., *J. Am. Chem. Soc.*, 118, 5639, 1996.
25. Jensen, A.W., et al., *J. Am. Chem. Soc.*, 119, 7303, 1997.
26. Liou, K.-F. and Cheng, C.-H., *J. Chem. Soc. Chem. Commun.*, 2473, 1995.
27. Bernstein, R. and Foote, C.S., *Tetrahedron Lett.*, 39, 7051, 1998.
28. Segura, J.L. and Martin, N., *Chem. Soc. Rev.*, 29, 13, 2000.
29. Wang, G.W., et al., *Nature*, 387, 583, 1997.
30. Komatsu, K., et al., *J. Org. Chem.*, 63, 9358, 1998.
31. Keshavarz-K., M., et al., *J. Am. Chem. Soc.*, 117, 11371, 1995.
32. Murata, Y., et al., *J. Org. Chem.*, 64, 3483, 1999.
33. Forman, G.S., Tagmatarchis, N. and Shinohara, H., *J. Am. Chem. Soc.*, 124, 178, 2002.
34. Tagmatarchis, N., et al., *Synlett*, 235, 2002.
35. Wilson, S., et al., Organic chemistry of Fullerenes, in *Fullerenes: Chemistry, Physics, and Technology*, Kadish, K.M. and Ruoff, R.S., Eds., Wiley, New York, 2000, chap. 3.
36. Maggini, M., Scorrano, G., and Prato, M., *J. Am. Chem. Soc.*, 115, 9798, 1993.
37. Prato, M. and Maggini, M., *Acc. Chem. Res.*, 31, 519, 1998.
38. Tagmatarchis, N. and Prato, M., *Synlett*, 768, 2003.
39. Wang, P., et al., *J. Mater. Chem.*, 7, 2397, 1997.
40. Wang, P., Metzger, R.M. and Chen, B., *Thin Solid Films*, 329, 96, 1998.
41. Guo, Z., et al., *Synth. Commun.*, 28, 1957, 1998.
42. Murakami, H., et al., *Chem. Lett.*, 815, 1999.
43. Ge, Z.X., et al., *Tetrahedron Lett.*, 40, 5759, 1999.
44. Guo, Z., et al., *Synth. Met.*, 102, 1567, 1999.
45. Leo, L., et al., *Langmuir*, 16, 4599, 2000.
46. Zhang, S., Gan, L., and Huang, C., *Chem. Phys. Lett.*, 331, 143, 2000.
47. Guo, Z.,et al., *Appl. Phys. B*, 70, 257, 2000.
48. Ge, X.Z., *Thin Solid Films*, 368, 147, 2000.
49. Carano, M., et al., *Electrochim. Acta*, 46, 265, 2000.
50. Nierengarten, J.F., *Chem. Eur. J.*, 6, 3667, 2000.
51. Rio, Y., et al., *Tetrahedron Lett.*, 41, 10207, 2000.
52. Guo, Z., *Appl. Phys. B*, 71, 545, 2001.
53. Angelini, G., et al., *Langmuir*, 17, 6404, 2001.
54. Hernandez, M.P., *Langmuir*, 17, 2001.
55. Nakashima, N., et al., *Chem.Eur. J.*, 7, 1766, 2001.
56. Georgakilas, V., et al., *Proc. Natl. Acad. Sci. U.S.A.*, 99, 5075, 2002.
57. Cassell, A.M., Asplund, C.L., and Tour, J.M., *Angew. Chem. Int. Ed. Engl.*, 38, 2403, 1999.
58. Gournis, D., et al., *J. Am. Chem. Soc.*, 126, 8561, 2004.
59. Tomberli, V., et al., *Carbon*, 38, 1551, 2000.
60. Bosi, S., et al., *Bioorg. Med. Chem. Lett.*, 10, 1043, 2000.
61. Kordatos, K., et al., *J. Org. Chem.*, 66, 4915, 2001.
62. Kang, S.H., et al., *Angew. Chem. Int. Ed. Engl.*, 43, 1512, 2004.
63. Holmes, A.B. and Stephenson, G.R., *Chem. Ind.*, 303, 1994.
64. Maggini, M., et al., *J. Chem. Soc. Chem. Commun.*, 305, 1994.

65. Bianco, A., et al., *J. Am. Chem. Soc.*, 119, 7550, 1997.
66. Bianco, A., et al., *J. Am. Chem. Soc.*, 118, 4072, 1996.
67. Bianco, A., et al., *J. Pept. Res.*, 50, 159, 1997.
68. Bianco, A., et al., *J. Pept. Sci.*, 4, 364, 1998.
69. Pantarotto, D., et al., *J. Am. Chem. Soc.*, 124, 12543, 2002.
70. Nierengarten, J.F., et al., *Chem.-Eur. J.*, 9, 37, 2003.
71. Nierengarten, J.F., *Top. Curr. Chem.*, 228, 87, 2003.
72. Nierengarten, J.F., *C. R. Chim.*, 6, 725, 2003.
73. Bergamin, M., et al., *Chem. Commun.*, 17, 2001.
74. Da Ros, T., et al., *Aus. J. Chem.*, 54, 223, 2001.
75. Da Ros, T., et al., *Eur. J. Org. Chem.*, 405, 2002.
76. Nakamura, E., et al., *Bull. Chem. Soc. Jpn.*, 69, 2143, 1996.
77. Cassell, A.M., Scrivens, W.A., and Tour, J.M., *Angew. Chem. Int. Ed. Engl.*, 37, 1528, 1998.
78. Li, H.S., et al., *J. Chem. Soc. Perkin. Trans.* 1, 617, 2000.
79. de la Torre, M.D.L., et al., *Tetrahedron Lett.*, 43, 2002.
80. de la Torre, M.D.L., et al., *Tetrahedron Lett.*, 43, 4617, 2002.
81. de la Torre, M.D.L., et al., *Tetrahedron*, 60, 3581, 2004.
82. Kordatos, K., et al., *J. Org. Chem.*, 2802, 2001.
83. Lu, Q., Schuster, D.I., and Wilson, S.R., *J. Org. Chem.*, 61, 4764, 1996.
84. Pasimeni, L., et al., *J. Am. Chem. Soc.*, 119, 12896, 1997.
85. Schick, G., et al., *J. Am. Chem. Soc.*, 121, 3246, 1999.
86. Nishimura, T.T., et al., *J. Am. Chem. Soc.*, 126, 11711, 2004.
87. Bosi, S., et al., *Eur. J. Org. Chem.*, 4741, 2003.
88. Carano, M., et al., *J. Am. Chem. Soc.*, 125, 7139, 2003.
89. Smith, P.M., et al., *Chem. Commun.*, 1754, 2003.
90. Prato, M., et al., *J. Am. Chem. Soc.*, 115, 1148, 1993.
91. Hummelen, J.C., Prato, M., and Wudl, F., *J. Am. Chem. Soc.*, 117, 7003, 1995.
92. Grösser, T., et al., *Angew. Chem. Int. Ed. Engl.*, 34, 1343, 1995.
93. Hummelen, J.C., et al., *Science*, 269, 1554, 1995.
94. Hummelen, J.C., Bellavia-Lund, C., and Wudl, F., Heterofullerenes, in *Fullerenes and Related Structures*, Springer-Verlag, GmbH, 1999, p. 93.
95. Lamparth, I., et al., *Angew. Chem. Int. Ed. Engl.*, 34, 2257, 1995.
96. Nuber, B. and Hirsch, A., *Fullerene Sci. Technol.*, 4, 715, 1996.
97. Bellavia-Lund, C., and Wudl, F., *J. Am. Chem. Soc.*, 119, 943, 1997.
98. Tagmatarchis, N., et al., *Synlett*, 1761, 2001.
99. Smith, A.B., et al., *J. Am. Chem. Soc.*, 115, 5829, 1993.
100. Shu, L.H., et al., *Chem. Commun.*, 79, 1997.
101. O'Donovan, B.F., et al., *Chem. Commun.*, 81, 1997.
102. Zhang, C.L.X., *J. Org. Chem.*, 60, 2906, 1997.
103. Ohno, M., et al., *Tetrahedron*, 52, 4983, 1996.
104. Takaguchi, Y., et al., *Angew. Chem. Int. Ed. Engl.*, 41, 817, 2002.
105. Komatsu, K., et al., *Tetrahedron Lett.*, 34, 8473, 1993.
106. Schlueter, J.A., et al., *J. Chem. Soc., Chem. Commun.*, 972, 1993.
107. Tsuda, M., et al., *J. Chem. Soc., Chem. Commun.*, 1296, 1993.
108. Mori, A., Takamori, Y., and Takeshita, H., *Chem. Lett.*, 395, 1997.
109. Ohno, M., Shirakawa, Y., and Eguchi, S., *Synthesis*, 1812, 1998.
110. Mori, S., et al., *Synth. Commun.*, 27, 1475, 1997.
111. Jonas, U., et al., *Chem. Eur. J.*, 1, 243, 1995.
112. Ohno, M., et al., *Tetrahedron*, 53, 9075, 1997.
113. Walter, M., et al., *Fullerene Sci. Technol.*, 4, 101, 1996.
114. Mattay, J., et al., *J. Phys. Chem. Solids*, 58, 1929, 1997.
115. Nakamura, Y., et al., *J. Chem. Soc., Perkin Trans.* 2, 2351, 1995.
116. Liao, C.C. and Peddinti, R.K., *Acc. Chem. Res.*, 35, 856, 2002.
117. Yen, C.F., Peddinti, R.K., and Liao, C.C., *Org. Lett.*, 2, 2909, 2000.
118. Tome, A.C., et al., *Tetrahedron Lett.*, 38, 2557, 1997.

119. Boulle, C., et al., *Tetrahedron Lett.*, 38, 81, 1997.
120. AlHariri, M., et al., *J. Org. Chem.*, 62, 405, 1997.
121. Segura, J.L. and Martin, N., *Chem. Rev.*, 99, 3199, 1999.
122. Liu, J.H., et al., *J. Org. Chem.*, 65, 3395, 2000.
123. Kreher, D., et al., *J. Mater. Chem.*, 12, 2137, 2002.
124. Kräutler, B. and Maynollo, J., *Angew. Chem. Int. Ed. Engl.*, 34, 87, 1995.
125. Krautler, B. and Maynollo, J., *Tetrahedron*, 52, 5033, 1996.
126. Nakamura, Y., et al., *J. Am. Chem. Soc.*, 124, 4329, 2002.
127. Hermann, A., et al., *Helv. Chim. Acta*, 77, 1689, 1994.
128. Seiler, P., Herrmann, A., and Diederich, F., *Helv. Chim. Acta*, 78, 344, 1995.
129. Meidine, M.F., et al., *J. Chem. Soc. Perkin Trans.* 2, 1189, 1994.
130. Bingel, K., *Chem. Ber.*, 126, 1957, 1993.
131. Nierengarten, J.-F., et al., *Helv. Chim. Acta*, 80, 2238, 1997.
132. Nierengarten, J.-F., et al., *Angew. Chem. Int. Ed. Engl.*, 35, 2101, 1996.
133. Camps, X. and Hirsch, A., *J. Chem. Soc. Perkin Trans.* 1, 1595, 1997.
134. Bestmann, H.J., et al., *Tetrahedron Lett.*, 35, 9017, 1994.
135. Wang, Y., et al., *Tetrahedron Lett.*, 36, 6843, 1995.
136. Wudl, F., *Acc. Chem. Res.*, 25, 157, 1992.
137. Suzuki, T., et al., *Science*, 254, 1186, 1991.
138. Suzuki, T., et al., *J. Am. Chem. Soc.*, 114, 7301, 1992.
139. Smith, A.B., III, et al., *J. Am. Chem. Soc.*, 115, 5829, 1993.
140. Diederich, F., Isaacs, L., and Philp, D., *Chem. Soc. Rev.*, 23, 243, 1994.
141. Isaacs, L. and Diederich, F., *Helv. Chim. Acta*, 76, 2454, 1993.
142. Hall, M.H., Lu, H.J., and Shevlin, P.B., *J. Am. Chem. Soc.*, 123, 1349, 2001.
143. Janssen, R.A.J., Hummelen, J.C., and Wudl, F., *J. Am. Chem. Soc.*, 117, 544, 1995.
144. Osterodt, J., et al., *Chem. Ber.*, 126, 2331, 1993.
145. Wilson, S.R. and Wu, Y., *J. Chem. Soc., Chem. Commun.*, 784, 1993.
146. Hummelen, J.C., et al., *J. Org. Chem.*, 60, 532, 1995.
147. Tomioka, H. and Yamamoto, K., *J. Chem. Soc., Perkin Trans.* 1, 63, 1996.
148. Knol, J. and Hummelen, J.C., *J. Am. Chem. Soc.*, 122, 3226, 2000.
149. Meijer, M.D., et al., *Tetrahedron Lett.*, 39, 6773, 1998.
150. An, Y.-Z., et al., *J. Org. Chem.*, 59, 2927, 1994.
151. Anderson, H.L., et al., *Angew. Chem. Int. Ed. Engl.*, 33, 1366, 1994.
152. Li, Z., Bouhadir, K.H., and Shevlin, P.B., *Tetrahedron Lett.*, 37, 4651, 1996.
153. Ravaine, S., et al., *New J. Chem.*, 19, 1, 1995.
154. Sastre, A., et al., *Org. Lett.*, 1, 1807, 1999.
155. Ravaine, S., et al., *J. Phys. Chem.*, 99, 9551, 1995.
156. Isaacs, L., Wehrsig, A., and Diederich, F., *Helv. Chim. Acta*, 76, 1231, 1993.
157. Safonov, I.G., Baran, P.S., and Schuster, D.I., *Tetrahedron Lett.*, 38, 8133, 1997.
158. Baran, P.S., et al., *J. Am. Chem. Soc.*, 119, 8363, 1997.
159. McMahon, S., et al., *J. Org. Chem.*, 66, 5449, 2001.
160. Jonas, U., et al., *Chem. Eur. J.*, 1, 243, 1995.
161. Cardullo, F., et al., *Langmuir*, 14, 1955, 1998.
162. Fujiwara, K., et al., *J. Am. Chem. Soc.*, 123, 10715, 2001.
163. Even, M., et al., *Chem.Eur. J.*, 7, 2595, 2001.
164. Guillon, D., et al., *Macromol. Symp.*, 192, 63, 2003.
165. Hirsch, A. and Vostrowsky, O., *Top. Curr. Chem.*, 217, 51, 2001
166. Camps, X., Schönberger, H., and Hirsch, A., *Chem. Eur. J.*, 3, 561, 1997.
167. Catalano, V.J. and Parodi, N., *Inorg. Chem.*, 36, 537, 1997.
168. Brettreich, M. and Hirsch, A., *Tetrahedron Lett.*, 39, 2731, 1998.
169. Camps, X., et al., *Chem. Eur. J.*, 5, 2362, 1999.
170. Herzog, A., Hirch, A., and Vostrowsky, O., *Eur. J. Org. Chem.*, 171, 2000.
171. Schwell, M., et al., *Chem. Phys. Lett.*, 339, 25, 2001.
172. Nierengarten, J.F., Felder, D., and Nicoud, J.F., *Tetrahedron Lett.*, 40, 269, 1999.
173. Nierengarten, J.F., Felder, D., and Nicoud, J.F., *Tetrahedron Lett.*, 40, 273, 1999.

174. Nierengarten, J.F., Felder, D., and Nicoud, J.F., *Tetrahedron Lett.*, 41, 41, 2000.
175. Felder, D., et al., *New J. Chem.*, 24, 687, 2000.
176. Fujiwara, K. and Komatsu, K., *Chem. Commun.*, 1986, 2001.
177. Chuard, T. and Deschenaux, R., *Helv. Chim. Acta*, 79, 736, 1996.
178. Deschenaux, R., Even, M., and Guillon, D., *Chem. Commun.*, 537, 1998.
179. Dardel, B., et al., *Macromolecules*, 32, 5193, 1999.
180. Chuard, T., et al., *Chem. Commun.*, 2103, 1999.
181. Tirelli, N., et al., *J. Chem. Soc. Perkin Trans.* 2, 193, 2000.
182. Campidelli, S. et al., R., *Helv. Chim. Acta*, 84, 589, 2001.
183. Dardel, B., et al., *J. Mater. Chem.*, 11, 2814, 2001.
184. Tsuda, M., et al., *Tetrahedron Lett.*, 34, 6911, 1993.
185. Osterodt, J. and Vögtle, F., *Chem. Commun.*, 547, 1996.
186. Dragoe, N., et al., *Chem. Commun.*, 85, 1999.
187. Chai, Y., et al., *J. Phys. Chem.*, 95, 7564, 1991.
188. Bethune, D.S., et al., *Nature*, 366, 123, 1993.
189. Nagase, S., Kobayashi, K., and Akasaka, T., *Bull. Chem. Soc. Jpn.*, 69, 2131, 1996.
190. Shinohara, H., *Rep. Prog. Phys.*, 63, 843, 2000.
191. Bolskar, R.B., et al., *J. Am. Chem. Soc*, 123, 5741, 2001.
192. Maeda, Y., et al., *J. Am. Chem. Soc.*, 126, 6858, 2004.
193. Zhang, T.H. et al., *Org. Biomol. Chem.*, 2, 1698, 2004.
194. Isaacs, L., Haldimann, R.F., and Diederich, F., *Angew. Chem. Int. Ed. Engl.*, 33, 2339, 1994.
195. Diederich, F. and Kessinger, R., *Acc. Chem. Res.*, 32, 537, 1999.
196. Nakamura, Y., et al., *Org. Lett.*, 6, 2797, 2004.
197. Sergeyev, S. and Diederich, F., *Angew. Chem. Int. Ed. Engl.*, 43, 1738, 2004.
198. Hino, T. and Saigo, K., *Chem. Commun.*, 402, 2003.
199. Diederich, F. and Gomez-Lopez, M., *Chem. Soc. Rev.*, 28, 263, 1999.
200. Guldi, D.M. and Martin, N., *J. Mater. Chem.*, 12, 1978, 2002.
201. Armaroli, N., et al., *Chem. Eur. J.*, 4, 406, 1998.
202. Li, K., et al., *J. Am, Chem. Soc.*, 126, 3388, 2004.
203. Schuster, D.I., et al., *Org. Lett.*, 6, 1919, 2004.
204. Ashton, P.R., et al., *Angew. Chem. Int. Ed. Engl.*, 36, 1448, 1997.
205. Nakamura, Y., et al., *Angew. Chem. Int. Ed. Engl.*, 42, 3158, 2003.
206. Da Ros, T., et al., *Org. Lett.*, 5, 689, 2003.
207. Watanabe, N., et al., *Angew. Chem. Int. Ed. Engl.*, 42, 681, 2003.
208. Diederich, F., et al., *J. Chem. Soc. Perkin Trans.* 2, 1577, 1999.
209. Martinez-Diaz, M.V., et al., *J. Mater. Chem.*, 12, 2095, 2002.
210. Guldi, D.M., et al., *Chem. Commun.*, 2774, 2002.
211. Solladie, N., et al., *Chem. Commun.*, 2412, 2003.
212. Kawase, T., et al., *Angew. Chem. Int. Ed. Engl.*, 42, 1624, 2003.
213. Kawase, T., et al., *Angew. Chem. Int. Ed. Engl.*, 43, 1722, 2004.
214. Kawase, T., et al., *Angew. Chem. Int. Ed. Engl.*, 42, 5597, 2003.
215. Smith, B.W., Monthioux, M., and Luzzi, D.E., *Nature*, 396, 323, 1998.
216. Luzzi, D.E. and Smith, B.W., *Carbon*, 38, 1751, 2000.
217. Khlobystov, A.N., et al., *Angew. Chem. Int. Ed. Engl.*, 43, 1386, 2004.
218. Khlobystov, A.N., et al., *J. Mater. Chem.*, 14, 2852, 2004.
219. Hirahara, K., et al., *Phys. Rev. Lett.*, 85, 5384, 2000.
220. Chiu, P.W., et al., *Appl. Phys. Lett.*, 79, 3845, 2001.
221. Okazaki, T., et al., *J. Am. Chem. Soc.*, 123, 9673, 2001.
222. Debarre, A., et al., *Chem. Phys. Lett.*, 380, 6, 2003.
223. Smith, B.W., Luzzi, D.E., and Achiba, Y., *Chem. Phys. Lett.*, 331, 137, 2000.
224. Suenaga, K., et al., *Nano Lett.*, 3, 1395, 2003.
225. Yudasaka, M., et al., *Chem. Phys. Lett.*, 380, 42, 2003.
226. Britz, D.A., et al., *Chem. Commun.*, 176, 2004.
227. Drovetskaya, T., Reed, C.A., and Boyd, P., *Tetrahedron Lett.*, 36, 7971, 1995.
228. Sun, Y.P., et al., *J. Org. Chem.*, 62, 3642, 1997.

229. Boyd, P.D.W., et al., *J. Am. Chem. Soc.*, 121, 10487, 1999.
230. Konarev, D.V., et al., *Chem. Eur. J.*, 7, 2605, 2001.
231. Schuster, D.I., et al., *J. Mater. Chem.*, 12, 2041, 2002.
232. Sun, D., et al., *Proc. Natl. Acad. Sci. U. S. A.*, 99, 5088, 2002.
233. Guldi, D.M., et al., *J. Am. Chem. Soc.*, 123, 9166, 2001.
234. Guldi, D.M., et al., *Chem. Commun.*, 373, 2000.
235. Wang, Y.-B.L., et al., *J. Am. Chem. Soc.*, 125, 6072, 2002.
236. Sun, D.Y., et al., *J. Am. Chem. Soc.*, 124, 6604, 2002.
237. Yamaguchi, T., et al., *J. Am. Chem. Soc.*, 125, 13934, 2003.
238. Tashiro, K., et al., *J. Am. Chem. Soc.*, 121, 9477, 1999.
239. Nishioka, T., et al., *Macromolecules*, 33, 9182, 2000.
240. Shoji, Y., Tashiro, K., and Aida, T., *J. Am. Chem. Soc.*, 126, 6570, 2004.
241. Rispens, M.T., et al., *Chem. Commun.*, 161, 2001.
242. Gonzalez, J.J., et al., *Chem. Commun.*, 163, 2001.
243. Beckers, E.H.A., et al., *J. Mater. Chem.*, 12, 2054, 2002.
244. Rispens, M.T., et al., *Synth. Met.*, 135, 801, 2003.
245. Sanchez, L., Rispens, M.T., and Hummelen, J.C., *Angew. Chem. Int. Ed. Engl.*, 41, 838, 2002.
246. Beckers, E.H.A., et al., *Chem. Commun.*, 2888, 2002.
247. Segura, M., et al., *J. Am. Chem. Soc.*, 125, 15093, 2003.
248. Guldi, D.M. and Prato, M., *Acc. Chem. Res.*, 33, 695, 2000.
249. Guldi, D.M., *Chem. Commun.*, 321, 2000.
250. Imahori, H. and Sakata, Y., *Adv. Mater.*, 9, 537, 1997.
251. Imahori, H. and Sakata, Y., *Eur. J. Org. Chem.*, 2445, 1999.
252. Guldi, D.M., *Chem. Soc. Rev.*, 31, 22, 2002.
253. Guldi, D.M., *Pure Appl. Chem.*, 75, 1069, 2003.
254. Kashiwagi, Y., et al., *Org. Lett.*, 5, 2719, 2003.
255. Ohkubo, K., et al., *Angew. Chem. Int. Ed. Engl.*, 43, 853, 2004.
256. Guldi, D.M., et al., *J. Mater. Chem.*, 14, 303, 2004.
257. Bourgeois, J.P., et al., *Helv. Chim. Acta*, 81, 1835, 1998.
258. Dietel, E., et al., *Chem. Commun.*, 1981, 1998.
259. Cheng, P., Wilson, S.R., and Schuster, D.I., *Chem. Commun.*, 89, 1999.
260. Schuster, D.I., et al., *J. Am. Chem. Soc.*, 121, 11599, 1999.
261. Sutton, L.R., et al., *J. Am. Chem. Soc.*, 126, 10370, 2004.
262. Schuster, D.I., et al., *J. Am. Chem. Soc.*, 126, 7257, 2004.
263. Maggini, M., et al., *Chem. Eur. J.*, 4, 1992, 1998.
264. Bell, T.D.M., et al., *Chem. Phys. Lett.*, 268, 223, 1997.
265. Fong, R., Schuster, D.I., and Wilson, S.R., *Org. Lett.*, 1, 729, 1999.
266. Harriman, A., *Angew. Chem. Int. Ed. Engl.*, 43, 2, 2004.
267. Da Ros, T., et al., *Chem. Commun.*, 635, 1999.
268. Da Ros, T., et al., *Chem. Eur. J.*, 7, 816, 2001.
269. D'Souza, F., et al., *Chem. Commun.*, 267, 2001.
270. D'Souza, F., et al., *Inorg. Chem.*, 38, 2157, 1999.
271. D'Souza, F., et al., *J. Am. Chem. Soc.*, 123, 5277, 2001.
272. Wilson, S.R., et al., *Chem. Commun.*, 226, 2003.
273. Guldi, D.M., et al., *Chem. Commun.*, 2056, 2002.
274. Loi, M.A., et al., *J. Mater. Chem.*, 13, 700, 2003.
275. Gonzalez-Rodriguez, D., et al., *Org. Lett.*, 4, 335, 2002.
276. Gonzalez- Rodriguez, D., et al., *J. Am. Chem. Soc.*, 126, 6301, 2004.
277. Segura, J.L. and Martin, N., *Angew. Chem. Int. Ed. Engl.*, 40, 1372, 2001.
278. Martin, N., et al., *Tetrahedron Lett.*, 37, 5979, 1996.
279. Prato, M., et al., *Tetrahedron*, 52, 5221, 1996.
280. Martin, N., et al., *J. Org. Chem.*, 62, 5690, 1997.
281. Yamashita, Y., Kobayashi, Y., and Miyashi, T., *Angew. Chem. Int. Ed. Engl.*, 28, 1052, 1989.
282. Bryce, M.R., et al., *Angew. Chem. Int. Ed. Engl.*, 29, 1450, 1990.
283. Martin, N., et al., *J. Phys. Chem. A*, 104, 4648, 2000.
284. Llacay, J., et al., *Chem. Commun.*, 659, 1997.

285. Llacay, J., et al., *J. Org. Chem.*, 63, 5201, 1998.
286. Mas-Torrent, M., et al., *J. Org. Chem.*, 67, 566, 2002.
287. Martin, N., et al., *Carbon*, 38, 1577, 2000.
288. Guldi, D.M., et al., *J. Org. Chem.*, 65, 1978, 2000.
289. Gonzalez, S., et al., *Org. Lett.*, 5, 557, 2003.
290. Gonzalez, S., Martin, N., and Guldi, D.M., *J. Org. Chem.*, 68, 779, 2003.
291. Maggini, M., et al., *J. Chem. Soc. Chem. Commun.*, 589, 1994.
292. Guldi, D.M., et al., *J. Am. Chem. Soc.*, 119, 974, 1997.
293. Guldi, D.M., et al., *Nano Lett.*, 2, 775, 2002.
294. Guldi, D.M., et al., *Chem. Commun.*, 2320, 2002.
295. Kay, K.Y., Kim, L.H., and Oh, I.C., *Tetrahedron Lett.*, 41, 1397, 2000.
296. Campidelli, S., et al., *J. Mater. Chem.*, 14, 1266, 2004.
297. Imahori, H., *Org. Biomol. Chem.*, 2, 1425, 2004.
298. Luo, C., et al., *J. Am. Chem. Soc.*, 122, 6535, 2000.
299. Imahori, H., et al., *J. Am. Chem. Soc.*, 123, 2607, 2001.
300. Fujitsuka, M., et al., *Chem. Lett.*, 721, 1999.
301. Imahori, H., et al., *J. Am. Chem. Soc.*, 123, 6617, 2001.
302. Bonifazi, D. and Diederich, F., *Chem. Commun.*, 2178, 2002.
303. Bonifazi, D., et al., *Angew. Chem. Int. Ed. Engl.*, 42, 4966, 2003.
304. Kuciauskas, D., et al., *J. Am. Chem. Soc.*, 121, 8604, 1999.
305. Imahori, H., et al., *Chem. Eur. J.*, 10, 3184, 2004.
306. Liddell, P.A., et al., *Helv. Chim. Acta*, 84, 2765, 2001.
307. Kodis, G., et al., *J. Mater. Chem.*, 12, 2100, 2002.
308. Giacalone, F., et al., *J. Am. Chem. Soc.*, 126, 5340, 2004.
309. Sariciftci, N.S., et al., *Science*, 258, 1474, 1992.
310. Lee, C.H., et al., *Phys. Rev. B*, 48, 15425, 1993.
311. Morita, S., Zakhidov, A.A., and Yoshino, K., *Solid State Commun.*, 82, 249, 1992.
312. Cravino, A. and Sariciftci, N.S., *J. Mater. Chem.*, 12, 1931, 2002.
313. Hoppe, H. and Sariciftci, N.S., *J. Mater. Res.*, 19, 1924, 2004.
314. Sariciftci, N.S., et al., *Appl. Phys. Lett.*, 62, 585, 1993.
315. Janssen, R.A.J., et al., *J. Chem. Phys.*, 103, 788, 1995.
316. Yu, G., et al., *Science*, 270, 1789, 1995.
317. Shaheen, S.E., et al., *Appl. Phys. Lett.*, 78, 841, 2001.
318. Riedel, I., et al., *Thin Solid Films*, 451–52, 43, 2004.
319. Wienk, M.M., et al., *Angew. Chem. Int. Ed. Engl.*, 42, 3371, 2003.
320. Stalmach, U., et al., *J. Am. Chem. Soc.*, 122, 5464, 2000.
321. Martin, N., et al., *Chem. Rev.*, 98, 2527, 1998.
322. Liu, S.G., et al., *J. Org. Chem.*, 64, 4884, 1999.
323. Knorr, S., et al., *J. Chem. Phys.*, 110, 3502, 1999.
324. Yamashiro, T., et al., *Chem. Lett.*, 443, 1999.
325. Nierengarten, J.F., et al., *Chem. Commun.*, 617, 1999.
326. van Hal, P.A., et al., *J. Phys. Chem. A*, 104, 5974, 2000.
327. Peeters, E., et al., *J. Phys. Chem. B*, 104, 10174, 2000.
328. Martini, I.B., et al., *Chem. Phys. Lett.*, 327, 253, 2000.
329. Roman, L.S., et al., *Adv. Mater.*, 9, 1164, 1997.
330. Fromherz, T., et al., *Sol. Energy Mater. Sol. Cells*, 63, 61, 2000.
331. Cravino, A., et al., *Chem. Commun.*, 2487, 2000.
332. Pasimeni, L., et al., *Chem. Commun.*, 429, 1999.
333. Armaroli, N., et al., *Chem. Commun.*, 599, 2000.
334. Martineau, C., et al., *Adv. Mater.*, 14, 283, 2002.
335. Gu, T. and Nierengarten, J.F., *Tetrahedron Lett.*, 42, 3175, 2001.
336. Gu, T., et al., *Chem. Phys. Chem.*, 3, 124, 2002.
337. Segura, J.L. and Martin, N., *Tetrahedron Lett.*, 40, 3239, 1999.
338. Segura, J.L., et al., *Chem. Commun.*, 701, 2000.
339. Guldi, D.M., et al., *J. Org. Chem.*, 67, 1141, 2002.

4 Carbon Nanotubes: Structure and Properties

John E. Fischer
Department of Materials and Engineering,
University of Pennsylvania, Philadelphia, Pennsylvania

CONTENTS

4.1 INTRODUCTION

Carbon nanotubes were discovered in 1991 as a minor byproduct of fullerene synthesis [1]. Remarkable progress has been made in the ensuing 14 years, including the discovery of two basic types of nanotubes (single-wall and multiwall); great strides have been taken in their synthesis and purification, elucidation of the fundamental physical properties, and important steps are being taken toward realistic practical applications.

Carbon nanotubes are long cylinders of 3-coordinated carbon, slightly pyramidalized by curvature [2] from the pure sp^2 hybridization of graphene, toward the diamond-like sp^3. Infinitely long in principle, a perfect tube is capped at both ends by hemi-fullerenes, leaving no dangling bonds. A single-walled carbon nanotube (SWNT) is one such cylinder, while multiwall tubes (MWNT) consist of many nested cylinders whose successive radii differ by roughly the interlayer spacing of graphite (see Figure 4.1 in the chapter by Du and Winey [3]). The minimum diameter of a stable freestanding SWNT is limited by curvature-induced strain to ~0.4 nm [4]. MWNT may have outer shells >30 nm

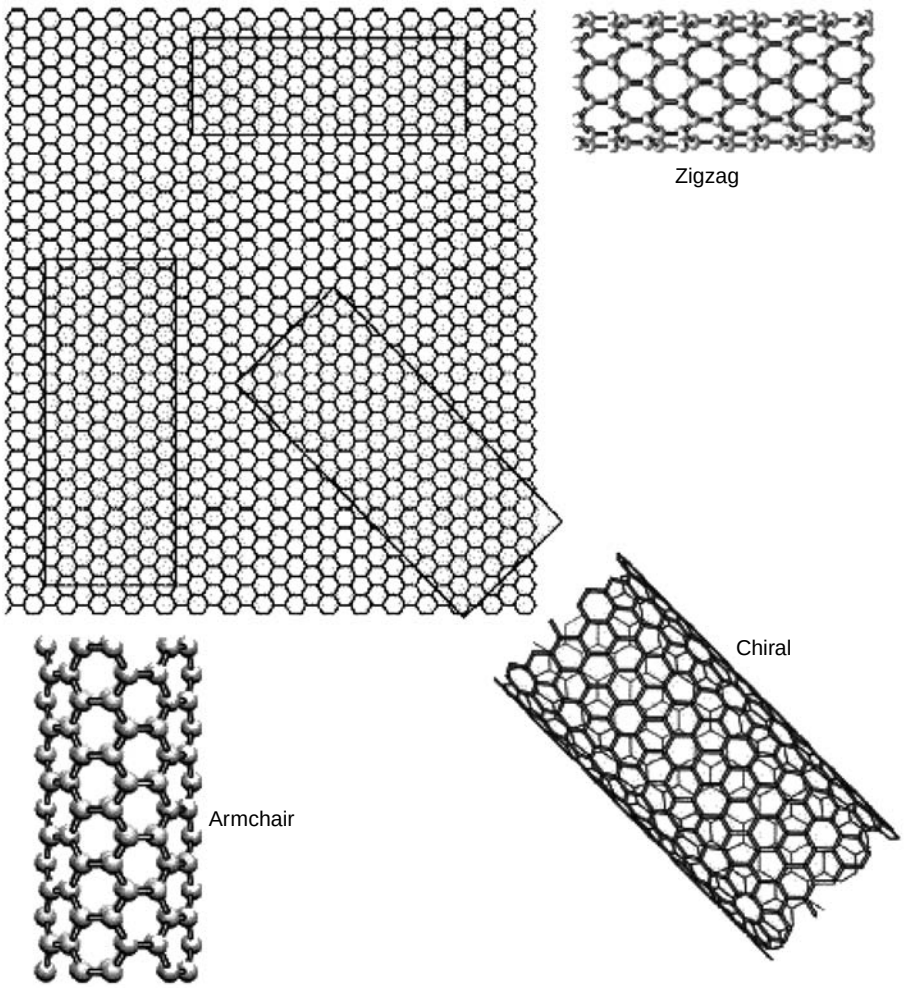

FIGURE 4.1 Schematic representation of the relation between nanotubes and graphene. The three rectangles can be rolled up into seamless nanotubes; the short side, referred to as the roll-up vector **R**, becomes the circumference. $\mathbf{R} = n\mathbf{a}_1 + m\mathbf{a}_2$, is a graphene 2D lattice vector, where $\mathbf{a}_1$ and $\mathbf{a}_2$ are unit vectors. Integers *n* and *m* uniquely define the tube: diameter, chirality, metal vs. semiconducting nature, and band gap, if semiconducting. In a bulk polydisperse sample consisting of a distribution of diameters, the larger the average diameter, the greater the number of *n*, *m* pairs that will satisfy the seamless roll-up condition.

in diameter, with varying numbers of shells, affording a range of empty core diameters. Lengths up to 3 mm have been reported [5]. Nanotubes are distinguished from less-perfect quasi-one-dimensional carbon materials by their well-developed parallel wall structure. Other elements too can be made into nanotubes, so one often encounters the term "SWCNT" to distinguish them from noncarbon tubes, i.e., BN, BCN, metal dichalcogenides [6]. The unique feature of carbon nanotubes is that they exist in both metallic and semiconducting varieties, a blessing or a curse depending on the context.

SWNTs can be conceptualized as seamless cylinders rolled up from graphene rectangles (cf. Figure 4.1), or as cylindrical isomers of large fullerenes. C_{70} is the smallest nanotube; compared with C_{60} it contains an extra belt of hexagons normal to the fivefold axis of the hemi-C_{60} caps. Adding more belts leads to longer tubes of the metallic (5,5) armchair category as defined later. According to theory, cylindrical fullerene isomers are less stable than the more nearly spherical ones because the 12 pentagons necessary to ensure closure are localized on the two caps. This

results in strain concentrations at the ends of closed tubes, which in turn makes it easier to perform additional chemistry on the ends than on the sidewalls [7].

There exist many quasi-one-dimensional all-carbon structures, which are neither SWNT nor MWNT. Composite materials reinforced with carbon or graphite fibers are often used in sporting goods, high-performance aircraft, and other applications where high stiffness and lightweight are required. Companies such as Hyperion sell commodity quantities of vapor-grown carbon fibers as conductivity additives for paints and plastics. Carbon nanohorns have received a good deal of attention lately as catalyst supports, fuel cell, and battery electrodes [8]. Such materials lack the atomic perfection of nanotubes, but are nonetheless crucially important in science and industry.

The discovery and rapid evolution of carbon nanotubes has played a major role in triggering the explosive growth of R & D in nanotechnology. Many of the early lessons learnt carried over to rapid developments in inorganic semiconductor nanowire science and engineering, in particular, field effect transistor (FET)-like switching devices, and chemical and biological sensors. The nanotube field *per se* has fanned out to encompass molecular electronics, multifunctional composites, flat-panel display technology, high-strength lightweight structural materials, nanoscale metrology (mass, heat, functional scanning probe tips, etc.), and others. In this chapter, I attempt to provide a broad-brush introduction to the materials responsible for all this excitement. My selection of sources is personal. Apologies in advance to friends, colleagues, and others whose work I fail to mention.

This chapter is a survey of the physical properties of carbon nanotubes, with emphasis on macroscopic assemblies of engineering interest. The important subjects of synthesis, purification, and composite materials are covered elsewhere in this volume [3,7]. Contact is made with single-tube properties where appropriate; an obvious issue is the extent to which properties of macroscopic material approach those of ideal individual tubes. Materials scientists will immediately note with dismay the paucity of information relating to defects and their influence on properties. In this important arena theory and simulations are far ahead of experiments. Atomic-scale defects may be at the resolution limit of high-resolution transmission electron microscopy (HRTEM). Their presence can be inferred from the breakup of individual tube device characteristics into multiple quantum dots defined by defect-related internal barriers [9].

4.2 STRUCTURE

We start the discussion by considering a single isolated tube. Is it a molecule? If so, we might be able to dissolve it in order to perform high-resolution ^{13}C NMR, the method which proved that the carbons in C_{60} were all equivalent, thus confirming the soccer-ball structure. So far, no true solvent for pristine nanotubes has been found. The surfactants, or chemical functionalization, necessary to obtain stable suspensions must perturb the intramolecular structure however slightly. Worse yet, we still lack even minute samples consisting of a single type of nanotube, so even if we had an NMR spectrum, it would be impossible to interpret. HRTEM is a borderline technique for resolving individual carbon atoms 0.14 nm apart. Electron diffraction from a single tube is possible in principle. The most convincing images are from scanned probe microscopy at low temperatures. The example shown in Figure 4.2(a) has a screw axis and "handedness" like DNA, and is referred to as a chiral SWNT.

4.2.1 Single-Wall Tubes, Bundles, and Crystalline Ropes

An SWNT can be envisioned as a narrow rectangular strip of nanoscale graphene "chicken wire" with carbon atoms 0.14 nm apart at each apex, rolled up into a seamless cylinder 1–10 nm in diameter and as long as several micrometers. "Graphene" refers to a monolayer of sp^2-bonded carbon atoms. Several possibilities for legal strips, those that will roll up seamlessly, are shown in Figure 4.1. Because the length and width of legal strips are "quantized," so too are the lengths and diameters of the tubes. The short side of the rectangle becomes the tube diameter and therefore is "quantized" by the requirement that the rolled-up tube must have a continuous lattice structure. Similarly,

the rectangle must be properly oriented with respect to the flat hexagonal lattice, which allows only a finite number of roll-up choices. The longer the short side, the larger the tube diameter *and* the larger the number of choices. Two of them correspond to high-symmetry SWNT; in "zigzag" tubes (top), some of the C–C bonds lie parallel to the tube axis, while in "armchair" tubes (bottom left), some bonds are perpendicular to the axis. Intermediate orientations of the rectangle produce chiral tubes when wrapped, as in Figure 4.2(a).

The different wrappings have profound consequences on the electronic properties. The allowed electron wave functions are no longer those of the unwrapped infinite two-dimensional graphene; the rolling operation imposes periodic boundary conditions for propagation around the circumference, the consequences of which depend on the symmetry. This is the reason why SWNT can either be metallic or insulating.

SWNT in close proximity can self-assemble into more or less close-packed parallel arrays, referred to as ropes or bundles according to whether the arrays are well ordered or not, respectively. These can be directly visualized in the electron microscope when a rope accidentally curves upward from the grid such that the focal plane cuts normally through the rope, as shown in Figure 4.2(b). The driving force is the van der Waals (vdW) attraction, amplified by the considerable lengths involved. Figure 4.2(b) shows a well-ordered rope consisting of ~100 tubes with similar diameters. In principle there is no limit to the number of tubes per rope, while the perfection of the 2D organization is directly related to the diameter polydispersity and thus to the synthesis method. The 2D triangular lattice implied by Figure 4.2(b) has been studied quantitatively using x-ray, neutron, and electron diffraction. Data analysis for materials containing highly ordered ropes has advanced to the point that diameter dispersivity, finite size, and the filling of the interior lumen can all be accounted for.

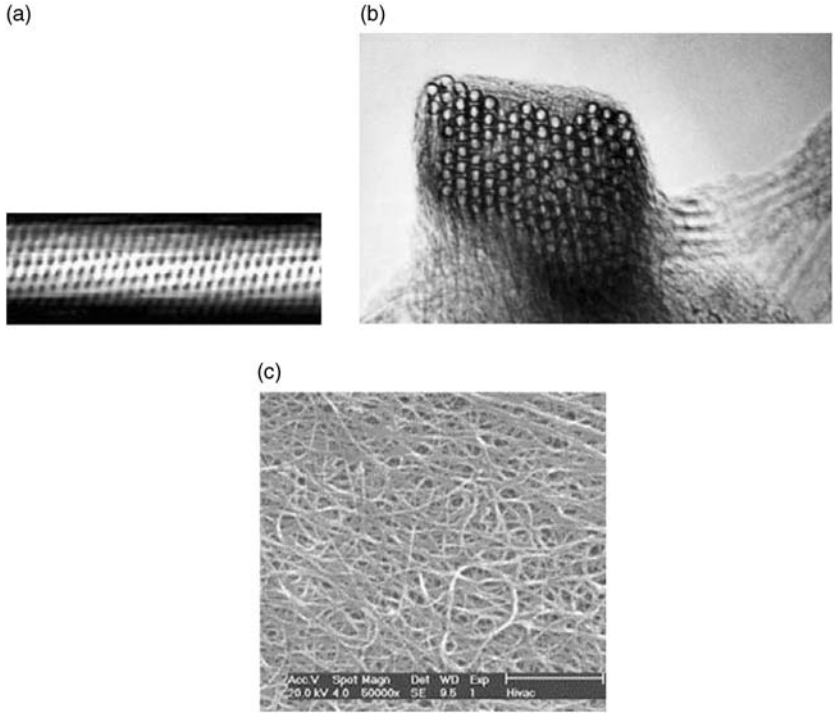

FIGURE 4.2 Single-wall carbon nanotube images at different length scales. (a) Scanning tunneling microscope image of a chiral SWNT (image by Clauss, W.); (b) HRTEM image of a nanotube rope (from Thess, A. et al., *Science* **273**, 483 (1996), with permission); (c) tangled spaghetti of purified SWNT ropes and bundles (Smalley, R. E., website).

Long-range order in three dimensions is generally frustrated. The 2D close-packed lattice imposes threefold rotational symmetry, while the point symmetry normal to the molecular axes will be modulo 3 only in special cases. This observation has important consequences for the nature of electronic tube–tube interactions in macroscopic materials.

Crystalline ropes are observed in some raw nanotube soots; others show TEM evidence for bundles, but with little or no 2D diffraction intensity. Crystallinity can often be improved by anaerobic thermal annealing, which is generally interpreted as minor rearrangements of misaligned tubes in a bundle, as opposed to grain growth by long-range migration of individuals accreting onto a small primordial rope. Purified bulk material resembles a spaghetti of nanotube ropes depicted in the SEM image in Figure 4.2(c).

Van der Waals bonding among the tubes in a rope implies that the equation of state should be closely related to those of graphite and solid C_{60} (similar bonding in 2, 1, and 3 directions, respectively [10]). The compressibility in a hydrostatic diamond anvil-cell environment, as determined by x-ray diffraction, is not consistent with the trend established by the other two carbon isomorphs, suggesting that the tubes become polygonalized into hexagonal cross sections at rather modest pressures [11]. The volume compressibility has been measured up to 1.5 GPa as 0.024 GPa^{-1}. The deformation of the nanotube lattice is reversible up to 4 GPa, beyond which the nanotube lattice is destroyed. Similarly, the thermal expansion of the 2D triangular lattice [12] of the rope does not follow the pattern of interlayer graphite and FCC C_{60}. One possibility is that the circular cross section of a tube is only an idealization, with the time-averaged cross-sectional shape changing with temperature due to thermally driven radial fluctuations.

4.2.2 Multiwall Tubes

Multiwall tubes have two advantages over their single-wall cousins. The multishell structure is stiffer than the single-wall one, especially in compression. Large-scale syntheses by enhanced chemical vapor deposition (CVD) processes are many, while for single-wall tubes, only the Rice HiPco process appears to be scaleable. The special case of double-wall tubes is under intense investigation; the coaxial structure of two nested tubes is well defined by the synthesis conditions, and large enhancement in stiffness over the single wall has already been achieved [13]. Multiwall structures are intrinsically frustrated since it is impossible to satisfy epitaxy simultaneously, or compatibility of wrapping indices (n, m) on adjacent shells, with the very strong tendency to maintain the intershell spacing close to that of the graphite interlayer spacing of 3.35 Å. Experimentally, the intershell correlations in MWNT are characteristic of turbostratic graphite in which the ABAB stacking order is severely disrupted [14].

Are multiwall tubes really concentric "Russian doll" structures, or are they perhaps scrolled? A minority of TEM studies suggests scrolling by virtue of observing n and $n+1$ graphene layers on opposite sides of the MWNT. One such example [14] is shown in Figure 4.3. On the other hand, attempts to intercalate bulk MWNT samples result in destruction of the cylindrical morphology, which would not be the case if the MWNT were a continuous graphene sheet rolled into a seamless scroll [15].

Several unique features of multiwall tubes should be noted here. Hydrothermal synthesis results in water-filled tubes, a natural model system for studying 1D nanofluidics and exploiting these as nanoreactors [16]. Synthetic methods can be adapted to allow direct fiber production from the primordial soot or the hot reactor plume [17,18], or by twisting fibers from vertically aligned MWNT grown as a carpet-like array on a substrate [19,20]. Current pulses, through individual MWNT, controllably remove one shell at a time, permitting the custom construction of devices to order, with metallic or semiconducting outer shells [21].

4.2.3 Macroscopic Nanotube Materials

Individual nanotubes can be used to construct electronic devices, gas and biosensors, sensitive nanobalances, NEMS resonators, scanning probe tips, etc. [22]. As the cost of production decreases

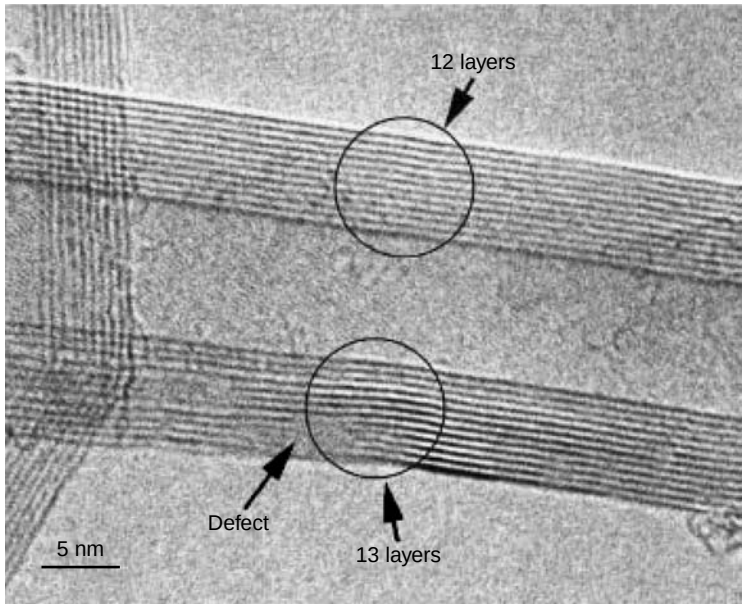

FIGURE 4.3 HRTEM image of an MWCNT. The number of graphene layer images on the two edges of the tube differs by 1, implying a scroll structure rather than the assumed-to-be-universal Russian doll morphology. (From Lavin, J. G. et al., *Carbon* **40**, 1123–1130 (2002), with permission.)

with time, applications involving macroscopic nanotube-derived materials become feasible. Such materials should obviously be strong and lightweight. Prospects for replacing traditional materials rest on opportunities to design in multifunctional combinations of mechanical, electrical, thermal, dielectric, magnetic, and optical properties.

Macroscopic nanotube materials are available in many forms: compressed random mats of raw or purified soot, filter-deposited foils ("buckypaper") [23], spin-coated or solvent-cast films [24], and various forms of all-nanotube [25,26], or composite [3,27] fibers. Property optimization for these complex materials depends on many factors. For example, the degree of preferred nanotube orientation within a macroscopic body determines the extent to which one takes advantage of the excellent but anisotropic intrinsic nanotube properties. Another major factor is the macroscopic density. This is important from several aspects. Empty space means missing material in the body, such that most properties will never be optimal. On the other hand, porosity on different length scales can be useful, e.g., for perm-selective membranes, fast diffusion for ionic conduction in electrochemical devices [28], and tailored nanoporosity for filtering, storage, or sequestration of specific molecular-scale analytes.

Materials of SWNT can be partially aligned by mechanical shear [15], anisotropic flow [3,26], gel extrusion [29], filter deposition from suspension in strong magnetic fields [30], or the application of electric fields during or after growth [31]. Fibers exhibit axially symmetric alignment with mosaic spreads of a few degrees in composites [3], and as low as 20° for all-SWNT post-stretched gel fibers [25]. Ordinary filter-deposited or solvent-cast films exhibit substantial adventitious alignment of tube axes in the film plane due simply to the rather gentle landing of rigid sticks on a flat surface [32].

The most complete characterization of the degree of alignment is obtained by combining the best features of Raman scattering [33] and traditional x-ray fiber diagrams [34]. With two independent experimental parameters, texture can be modeled as a "two-phase" system consisting of an aligned fraction, characterized by the angular distribution of tube axes about the preferred direction, plus a completely unaligned fraction to account for SWNT aggregates, which are insufficiently dispersed

to respond to the aligning field. The model distribution function, shown schematically in Figure 4.4, is represented by a Gaussian "bugle horn" for the axially aligned fraction sitting atop a right-circular cylinder, which accounts for the unaligned fraction. X-ray two-dimensional fiber diagrams unambiguously give the Gaussian width from the azimuthal dependence of either a Bragg intensity or form factor diffuse scattering if the material is not sufficiently crystalline. A similar method was previously applied to texture studies of oriented films and fibers of conjugated polymers [35]. This approach can be applied to thin films cut into strips and carefully stacked in a capillary as well as to fibers. Both geometries are shown schematically in Figure 4.5. Angle-dependent polarized Raman scattering, using the x-ray-derived distribution width as input unambiguously gives the unaligned fraction. This is because the resonantly enhanced Raman contribution from the SWNT contribution dominates over all the other constituents of the sample [36], even at the 1% loading level [37]. An example of this combined fitting approach is shown in Figure 4.6 for nanotube fibers extruded from strong acid solution with no post stretching [34]. Here we deduce a mosaic distribution width of 55° full-width at half-maximum (FWHM) and an aligned fraction of 90%. In the case of magnetically aligned buckypapers, these parameters can be correlated with measurements of electrical resistivity ρ and thermal conductivity κ parallel and perpendicular to the alignment direction [30]. Differences between 7 and 26 T aligning magnetic fields give some clues about the alignment mechanism and strategies for improving the process.

4.2.4 Fibers

The best alignment achieved so far is in polymer–SWNT composites [3,27]. Here the "dope" consists of either a polymer melt with SWNT dispersed at concentrations up to 10 wt%, or mixtures of polymer and SWNT in the same organic "solvent." This is extruded through a small orifice after twin-screw mixing and then stretched by take-up spindles. The extensional flow through the orifice, combined with shear flow during stretching, combine to yield FWHMs of the order of a few degrees in the best cases [3]. SWNT–(poly)vinyl alcohol (PVA) composite fibers exhibit modest alignment as extruded, but this can be greatly improved by controlled elongation prior to removal of the PVA by heat treatment [25,38]. Nanotube fibers consisting mainly of MWNT can be obtained directly during carbon arc synthesis [18], or by agglomeration as the tubes are pulled off a substrate [19]. Nothing quantitative is known yet about the degree of alignment in these and related materials [20].

4.2.5 Filled Tubes

Carbon soot produced by arcing in helium or laser ablation contains both fullerenes (mainly C_{60}) and nanotubes, the proportions varying with the amount of transition metal catalysts in the graphite

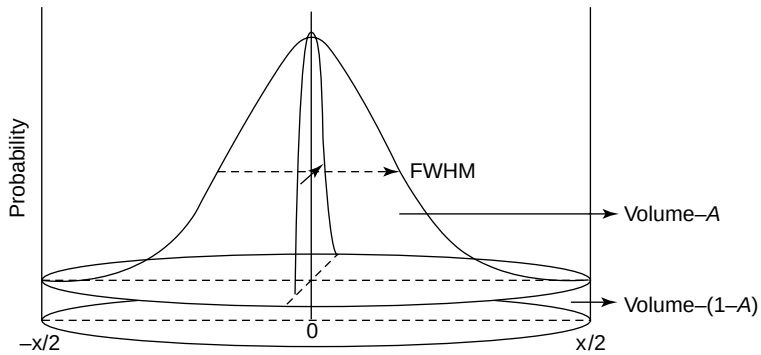

FIGURE 4.4 Two-phase model for the axially symmetric distribution of nanotube axes in oriented fibers. The inverted horn is the aligned fraction, characterized by an FWHM. The pillbox on top of which the horn is positioned is the unaligned fraction, characterized by its volume relative to the total.

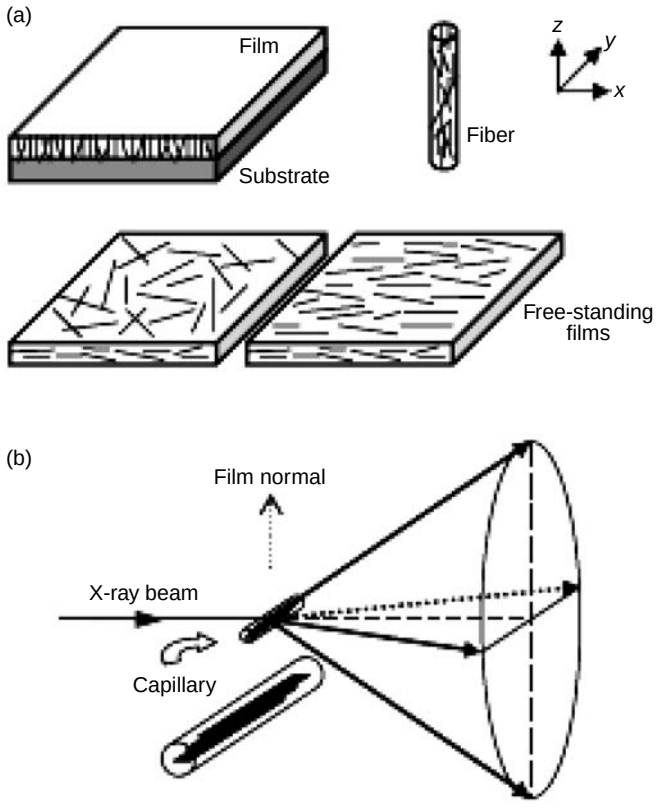

FIGURE 4.5 Schematic of the experimental setup for measuring out-of-plane mosaic. The film plane is parallel to the incident x-ray beam. Out-of-plane preferred orientation results in azimuth (χ)-dependent anisotropic scattering within the 2D detector plane, (a) and (b) refer to films and fibers, respectively.

electrode or target, as discussed previously. Acid purification of nanotube-rich soot reveals the presence of "peapods" — SWNT with chains of C_{60} inside [39], in substantial amounts [40], denoted by "C_{60}@SWNT." It is now understood that acid etching opens holes in the SWNT, either by decapitation or creation of sidewall defects. Fullerenes and other species can diffuse in and be trapped by annealing after filling [41]. Rational synthesis now achieves >80% filling routinely [42]. The process has been extended to higher fullerenes [43], endofullerenes [44] and other substances [7]. We speculated early on that host–guest interactions might favor commensurate packings, in which case the ideal container for C_{60} would be the (10,10) tube. The interior lumen is a good fit for C_{60} (vdW diameter ~1 nm), and, with armchair symmetry, exactly four "belts" of hexagons would be commensurate with one C_{60} [45]. This turned out not to be important after all, implying very weak interactions between the pea and the pod. There are indeed strong steric constraints on the tube diameter, which will accept a perfect 1D chain [46], while there seems to be no effect of symmetry on filling probability. Global filling fractions depend strongly on diameter dispersivity; HiPco tubes have broad diameter distributions and generally give at best 50–60% filling.

Films of crystalline peapods exhibit unique "fiber diagrams" using the 2D detector (cf. Figure 4.5). Figure 4.7 shows an example of a detector image from such a film. Diffraction peaks from the 1D lattice of close-packed C_{60} peas are concentrated in the horizontal direction, perpendicular to those from the 2D pod lattice. This separation is a consequence of the out-of-plane preferred orientation; the sample is neither a "perfect powder" nor a single crystal, but rather a "mosaic crystal" with identical orientation distributions exhibited by [0 0 L] and [H K 0] families of reflections [32]. The absence of mixed [H K L] indicates that the peas in different pods "float" along the tube axis

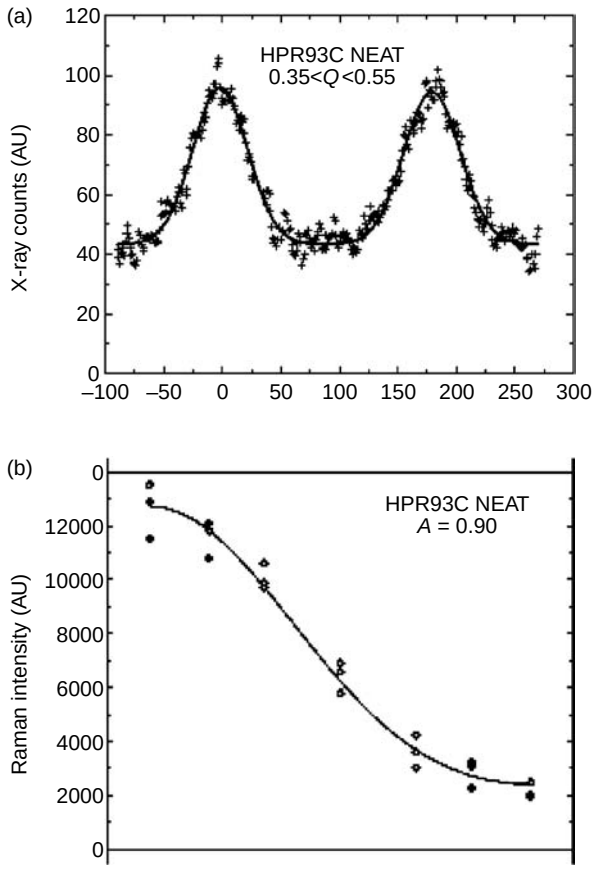

FIGURE 4.6 Combining x-ray fiber diagrams and angle-dependent polarized Raman scattering to solve the texture problem in SWNT materials. (a) Background-subtracted X-ray counts, summed over different Q intervals, every 1° in χ. Symbols represent data; smooth curves are fits to two Gaussians plus a constant. (b) Angle-dependent polarized Raman data (open circles) and fits (solid curves). A two-parameter model was used, with one (FWHM) fixed at the value determined from (a). (From Zhou, W. et al., *J. Appl. Phys.* **95**, 649 (2004), with permission.)

with respect to each other; there are no 3D correlations among peas in different pods [32,41]. Also shown are radial cuts through 2D images of an unfilled control sample [0 0 L] I, the filled sample [0 0 L] II, and [H K 0] III. Note that the filling of C_{60} into nanotubes significantly changes the diffraction profile. The (0 0 1) and (0 0 2) peaks from the 1D C_{60} chains are easily detected. Filling fractions can be obtained from detailed curve fits; these seem to be limited only by the diameter dispersion of the starting material, i.e., a real-world sample will always contain some tubes which are too small to be filled [42,46].

One of the most significant developments in the peapod arena is their exploitation as precursors to the formation of highly perfect double-wall nanotubes [13]. Thermal decomposition inside the original SWNT container leads to rearrangement of broken bonds on near-neighbor tubes into a smaller seamless cylinder whose diameter respects the usual vdW spacing requirement. This process takes place at a temperature considerably below those of the amorphization of FCC C_{60} [47] and enormously below the gas-phase decomposition temperature [48]. Clearly, the coordination and packing environment in the condensed phase leads to facile destruction of the icosahedral molecule by rather violent near-neighbor collisions, more effective in the 12-coordinated 3D solid than in the 2-coordinated chain structure of the "peas."

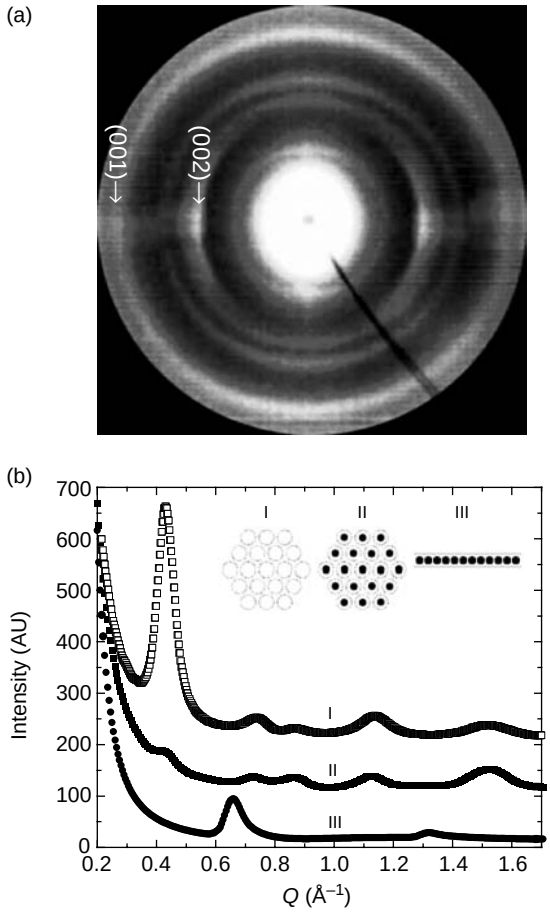

FIGURE 4.7 (a) Detector image from a C_{60}@SWNT peapod film. Diffraction peaks from the 1D C_{60} lattice are concentrated in the direction perpendicular to those from the 2D pod lattice, a consequence of the out-of-plane preferred orientation. (b) X-ray diffraction patterns from starting SWNT film (control sample), and C_{60}@SWNT film (peapod sample). Note that the filling of C_{60} into nanotubes significantly changes the diffraction profile. The (0 0 1) and (0 0 2) peaks from the 1D C_{60} chains are easily detected. (From Zhou, W. et al., *Appl. Phys. Lett.* **84**, 2172 (2004), with permission.)

The extent to which nanotube properties are affected by the endohedral doping is controversial and will be discussed later.

4.2.6 Nanotube Suspensions

It is appropriate to conclude our discussion of structure in nanotube materials with a few words about tubes in solution or suspension. These are important for fundamental and technological reasons. Absorption spectroscopy of isolated tubes [49] reveals important aspects of their presumed simple electronic structure and its dependence on tube diameter and symmetry as well as the importance of excitonic and other higher order effects [50]. Nanotube suspensions also provide a unique system in which to study rigid rod-phase behavior [51] and network formation at higher concentrations. Furthermore, an improved understanding of suspension structure should lead to better control of solution processes such as phase separation, chemical derivatization, control and improvement of polymer/nanotube composite properties, and optimization of the "dope" from which fibers are spun.

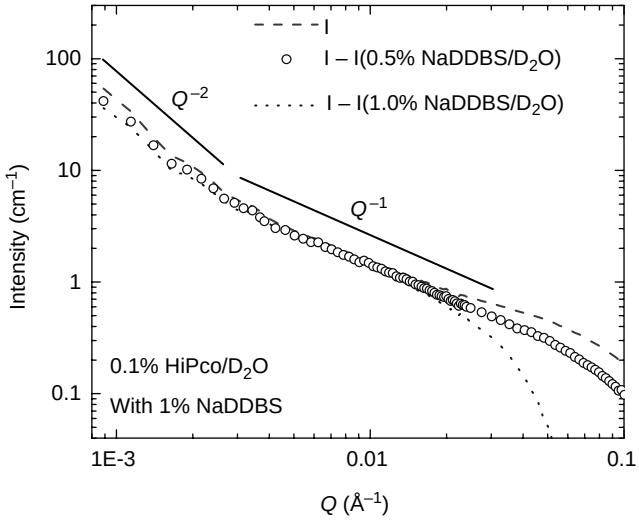

FIGURE 4.8 Analysis of SANS data from nanotubes in surfactant/heavy water suspension. Subtraction of surfactant contribution from total intensity for HiPco tubes. Dashed and dotted lines correspond to the extreme assumptions of no excess surfactant and no surfactant on the tubes, respectively. A Q^{-1} slope is clearly visible from 0.003 to 0.02 A^{-1}, no matter what fraction of surfactant intensity is subtracted. There is also a crossover to -2 exponent at 0.004 A^{-1}, suggesting the formation of a dilute network with a mesh size ~160 nm. (From Zhou, W. et al., *Chem. Phys. Lett.* **384**, 185–189 (2004), with permission.)

Individual SWNTs with diameters 1–2 nm and lengths 100 nm to several micrometers can be envisioned as rigid rods, and if sufficiently dilute, should display a correspondingly simple structure factor in scattering experiments (light, x-rays, neutrons, etc.). In particular, the scattered intensity, I, from a suspension of isolated rigid rods with diameter D and length L should follow a Q^{-1} law for scattering wave vectors $2\pi/L < (Q = 4\pi \sin\theta/\lambda) < 2\pi/D$ [52]. This is generally not observed; suggesting that even at very low concentrations, the SWNTs tend to form loose networks with node spacings of the order of the tube length. One exception is the dilute suspensions using the ionic surfactant sodium dodecylbenzene sulfonate (NaDDBS) and its relatives [52]. It is believed that the benzenoid moiety provides π stacking interactions with the graphene-like tube wall structure, of sufficient strength to adhere to single tubes and thus preventing them from aggregating. Figure 4.8 shows small-angle neutron scattering data for HiPco SWNT in 1% NaDDBS/D_2O suspensions. After correcting for scattering from NaDDBS micelles and incoherent proton background, one indeed observes a linear regime at intermediate values of Q. There is a crossover from Q^{-1} to Q^{-2} behavior at about 0.004 A^{-1}, corresponding to average tube length ~160 nm. This is precisely what is found from atomic force microscopy (AFM) image analysis of >1000 tubes, confirming that we have truly isolated tubes at this very low concentration, i.e., 10^{-3} wt%. Linear regimes are not observed at any practicable concentration using Triton-X, polymer melts, or superacids. Fiber spinning requires much higher concentrations, so we must accept some degree of aggregation as the dope is being extruded out of the orifice or spinneret. How this limits the properties of the ensuing fibers has not been determined as yet.

4.3 PHYSICAL PROPERTIES

We focus on the properties of macroscopic nanotube materials. These ultimately derive from the intrinsic attributes of single tubes, vastly complicated by defects, impurities, preferred orientation, network connectivity, large-scale morphology, etc. Theory does a reasonable job of predicting, rationalizing, and explaining single-tube properties, while structure–property relations in macroscopic

assemblies are still in a rudimentary state. For composites in particular, properties of the simplest materials show large deviations from the rule of mixture behavior.

To achieve viability in practice, any class of new materials must have some property that surpasses the state of the art sufficiently to justify replacement. Alternatively, new materials may provide some new capability otherwise unavailable. It seems likely that the first large-scale applications for nanotubes will arise from multifunctionality, for example, stiff lightweight structural parts, which also conduct electricity and have low thermal expansion.

4.3.1 Mechanical Properties

The strength of the carbon–carbon bond gives rise to the extreme interest in the mechanical properties of nanotubes. Theoretically, they should be stiffer and stronger than any known substance. Simulations [53] and experiments [54] demonstrate a remarkable "bend, don't break" response of individual SWNT to large transverse deformations; an example from Yakobson's simulation is shown in Figure 4.9. The two segments on either side of the buckled region can be bent into an acute angle without breaking bonds; simulations and experiments show the full recovery of a straight perfect tube once the force is removed.

Young's modulus of a cantilevered individual MWNT was measured as 1.0 to 1.8 TPa from the amplitude of thermally driven vibrations observed in the TEM [55]. At the low end, this is only ~20% better than the best high-modulus graphite fibers. Exceptional resistance to shock loads has also been demonstrated [56]. Both the modulus and strength are highly dependent on the nanotube growth method and subsequent processing, due no doubt to variable and uncontrolled defects. Values of Young's modulus as low as 3 to 4 GPa have been observed in MWNT produced by pyrolysis of organic precursors [57]. TEM-based pulling and bending tests gave more reasonable moduli and strength of MWNT of 0.8 and 150 GPa, respectively [58].

Multiwall nanotubes and SWNT bundles may be stiffer in bending but are expected to be weaker in tension due to "pullout" of individual tubes. In one experiment, 15 SWNT ropes under tension broke at a strain of 5.3% or less. The stress–strain curves suggest that the load is carried primarily by SWNT on the periphery of the ropes, from which the authors deduce breaking strengths from 13 to 52 GPa [59]. This is far less than that reported for a single MWNT [58]. On the other hand, the mean value of tensile modulus was 1 TPa, consistent with near-ideal behavior. Clearly, the effects of nonideal structure and morphology have widely different influences on modulus and strength. There is always some ambiguity in choosing the appropriate cross-sectional area to use in evaluating stress–strain data. On a density-normalized basis the nanotubes look much better [22]; modulus and strength are, respectively, 19 and 56 times better than steel.

Figure 4.10 shows the formation of a remarkable nanotube yarn by pulling and (optionally) twisting material from a "forest" of vertically aligned MWNT grown by a CVD process [19]. The untwisted yarns are very weak; if they accidentally touch a surface while being pulled off the substrate, they immediately break. On the other hand, twisted single-strand yarns exhibited strengths in the range 150 to 300 MPa; this improved to 250 to 460 MPa in the two-ply yarns. Further gain

FIGURE 4.9 MD simulation of a large-amplitude transverse deformation of a carbon nanotube, apparently beyond the elastic limit. In fact, the tube snaps back once the computer-generated force is removed, and there is no plastic deformation or permanent damage. (From Yakobson, B. I., *Appl. Phys. Lett.* **72**, 918–920 (1998), with permission.)

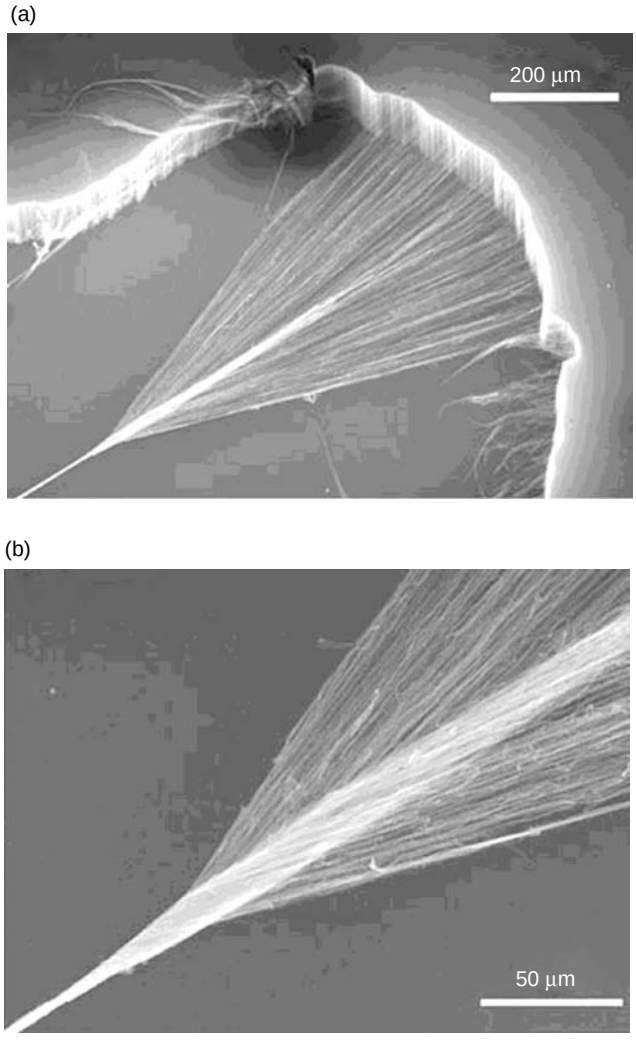

FIGURE 4.10 *Ex situ* SEM snapshots of a carbon nanotube yarn in the process of being drawn and twisted. The MWNTs, ~10 nm in diameter and 100 μm long, form small bundles of a few nanotubes each in the forest. Drawing fiber normal (a) and parallel (b) to the edge of the forest of nanotubes. (From Zhang, M. et al., *Science*, **306**, 1358 (2004), with permission.)

to 850 MPa was achieved by infiltration with PVA [19], which also improved the strain-to-failure to 13%. Toughness, the so-called "artificial muscle" [60], is a major issue in the optimization of nanotube actuators, where the figure of merit is the work done per cycle.

Another form of nanotube material useful for sensors and actuators are thin films or buckypapers. A typical result for solution-cast film with random SWNT orientations in the plane [32] is described in [61]. The tensile modulus, strength, and elongation-to-break values are 8 GPa (at 0.2% strain), 30 MPa, and 0.5%, respectively, much lower than what can be routinely achieved in fibers. This suggests that failure in the films occurs via interfibrillar slippage rather than fracture within a fibril.

4.3.2 Thermal Properties

The thermal conductivity κ of carbon materials is dominated by atomic vibrations or phonons. Even in graphite, a good electrical conductor, the electronic density of states is so low that thermal transport via

"free" electrons is negligible at all temperatures. Thus, roughly speaking, $\kappa(T)$ is given by the product of (1) the temperature-dependent lattice specific heat C_p, a measure of the density of occupied phonon modes at a given temperature; (2) the group velocity of the phonon modes (speed of sound V_s for acoustic branches, not strongly T-dependent); and (3) a mean free path accounting for elastic and inelastic, intrinsic and extrinsic phonon-scattering processes. It was conjectured early on that nanotubes would be excellent heat conductors [62]; the axial stiffness conduces to large V_s, the 1D structure greatly restricts the phase space for phonon–phonon (Umklapp) collisions, and the presumed atomic perfection largely eliminates elastic scattering from defects. Calculations of the lattice contribution to κ, pioneered by the Tomanek group [63], yield values in the range of 2800 to 6000 W/mK.

Experiments on individual tubes are extremely difficult, and so far have been limited to MWNT [64]. Figure 4.11 shows the temperature-dependent thermal conductance of a 14-nm-diameter, 2.5-μm-long MWNT; $\kappa(T)$ based on an effective cross-sectional area is shown in the inset. The salient features are a peak value ~3000 W/mK at 320 K, in good agreement with the perfect-tube calculations, and a roll-off in κ above 320 K signaling the onset of Umklapp scattering. For bulk MWNT foils, κ is only 20 W/mK [65], suggesting that thermally opaque junctions between tubes severely limit the large-scale diffusion of phonons. The temperature dependence below 150 K reflects the effective dimensionality of the phonon dispersion, a subtlety that is more pronounced in SWNT and will be discussed later. The onset of Umklapp scattering at 320 K is highly significant. Knowing C_p and V_s from other experiments and theoretical estimates, the mean free path is ~500 nm, comparable to the length of the sample. This means that phonon transport at low T is essentially ballistic; on average a phonon scatters only a few times as it traverses the sample. There is no corresponding rollover in the data from bulk nanotube samples.

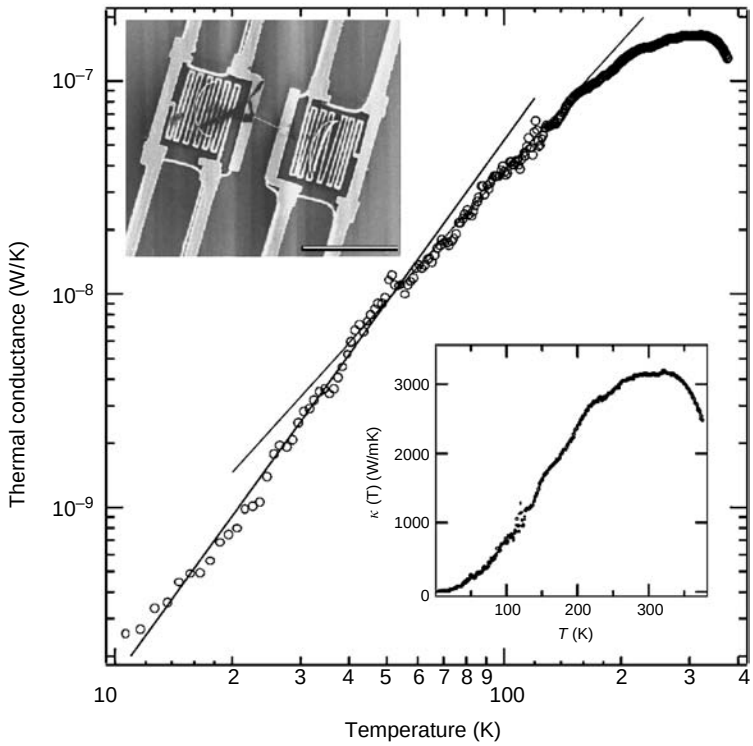

FIGURE 4.11 Thermal conductance of an individual MWNT of 14 nm diameter. The power law slope decreases from ~2.5 to ~2.0 above ~5 K. Saturation occurs at 340 K, the thermal conductance decreasing at higher T. Lower inset shows the thermal conductivity, for which some assumptions about effective area are required. (From Kim et al., *Phys. Rev. Lett.* **87**, 215502 (2001), with permission.)

One of the most important concepts in nanotube physics is quantization of the electronic states by the restricted 1D geometry. Analogous 1D phonon quantization is difficult to observe because of the far smaller energy/temperature scale. In general, the smaller the object, the higher the temperature at which quantum confinement effects can be detected, so SWNT with radii ~2 nm raise the temperature to practicable values. Temperature-dependent heat capacity of purified SWNT shows direct evidence for 1D quantized phonon subbands [66] (see Figure 4.12). The sample is ~40 mg of purified HiPco SWNT, for which the 2D triangular lattice is not well developed. This material was chosen in the hope that the 1D physics would not be obscured by tube–tube coupling. However, a good fit to the data (solid dots) requires an anisotropic, weakly 3D Debye model, shown in the inset, which accounts for weak coupling between SWNT in a rope (black curve). Below 8 K, only the acoustic branch contributes (blue curve), while above 8 K the first optic subband becomes significant (red curve). The key point is that this subband "turns on" at a temperature high enough to be detected, yet low enough not to be buried by graphene-like 2D contributions. The relevant fitting parameters are 4.3 meV for the $Q = 0$ subband energy (in reasonable agreement with predictions for this diameter) and 1.1 meV for the transverse Debye energy, signaling very weak intertube coupling. It would be of interest to repeat this experiment on samples with weaker or stronger tube–tube coupling, the former, for example, by intercalation with large dopant ions [67]. Above 25 K, C_p of bulk SWNT is indistinguishable from that of graphite. Extension of the measurement on the same sample down to the milliKelvin regime [68], confirmed the importance of 3D effects at the lowest temperatures; a definitive analysis was impeded by a strong nuclear hyperfine contribution from residual Ni catalyst.

Both SWNT and MWNT materials and composites are being actively studied for thermal management applications, either as "heat pipes" or as alternatives to metallic or alumina particle additives to low thermal resistance adhesives. The individual MWNT results are promising; similar data for SWNT are not yet available. In the case of polymer composites, the important limiting factors are quality of the dispersion and interphase thermal barriers [3]. What limits κ in all-nanotube

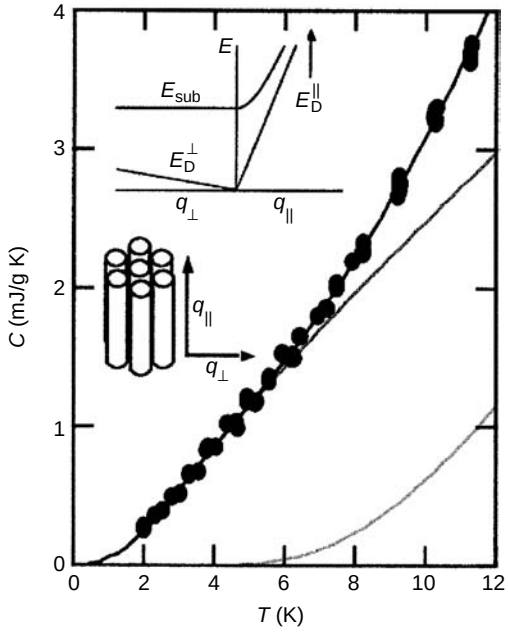

FIGURE 4.12 Specific heat vs. T of SWCNTs (dots) fitted to an anisotropic two-band Debye model that accounts for weak coupling between SWNT in a rope (solid curve). The rope structure and ensuing phonon dispersion are shown as insets. (From Hone, J. et al., *Science* **289**, 1730 (2000), with permission.)

fibers, sheets, etc.? Tube wall defects can be minimized by avoiding long sonication and extended exposure to acids in the fabrication process. In one example, partial alignment of nanotube axes in buckypaper yielded anisotropic thermal conductivities, with $\kappa_{//}/\kappa_{\perp}$ ~5 to 10 [69].

Experimental determinations of κ are subject to many pitfalls, one of which is the problem of defining the cross-sectional area through which the heat is flowing. This is similar to the dimensional ambiguity we encountered with Young's modulus. There are many well-tested methods for measuring thermal conductance G, but translating that into thermal conductivity κ is not straightforward. This is illustrated by two different results from the magnetic field-aligned buckypaper mentioned above. In the first method, sample dimensions were deduced from a measurement of electrical resistance of the κ sample and scaling to the resistivity of a different sample, with well-defined geometry, taken from the same batch. This assumed that the resistivity is uniform over centimeter length scales in the original piece of buckypaper, and gave κ parallel to the average tube axis ~250 W/mK. A second measurement in which the actual dimensions were carefully measured gave a more modest 60 W/mK.

Figure 4.13 shows the effect of stretch alignment on the thermal conductivity of SWNT fibers gel extruded from water/PVA suspensions [25]. Here the fibers are statically stretched in a PVA/water bath by suspending a weight on the end of a length of pristine fiber. Vacuum annealing after elongation eliminates the PVA, so the fiber properties are entirely due to aligned nanotubes. Reducing the mosaic by increasing the elongation, form 23° to 15° FWHM, gives an almost threefold increase in κ (300 K). In contrast to the individual MWNT data (Figure 4.11), there is no evidence for $\kappa(T)$ saturation or rolloff at high temperature. This almost certainly means that κ is limited by interparticle barriers and not by the Umklapp mean free path.

Figure 4.14 shows $\kappa(T)$ for similar fibers extruded from superacid suspension but not stretched [34]. Here the correlations are with nanotube concentration and syringe orifice diameter. Concentration dictates the phase of the rigid rod suspension [26] and controls the viscosity, while the orifice diameter affects the degree of flow-induced alignment. From the three examples shown, and from other observations, the authors find that (1) annealing to remove acid residues and the attendant p-type metallic doping (see below) has no effect on κ at any temperature; (2) reducing the

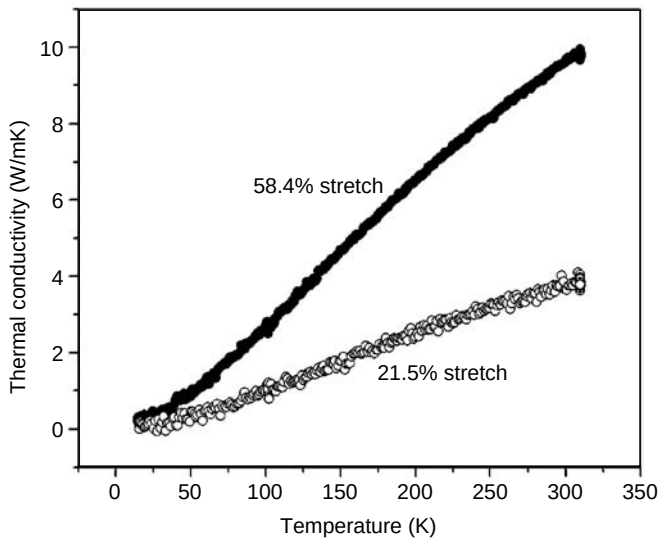

FIGURE 4.13 Thermal conductivity vs. temperature for annealed nanotube fibers, which have been stretch-aligned to 21% (lower curve) and 58% (upper curve). Additional alignment of the latter yields a factor of ~2 further enhancement of κ. The temperature dependence is dominated by that of the lattice specific heat, as is generally observed. (From Badaire, S. et al., *J. Appl. Phys*. **96**, 7509 (2004), with permission.)

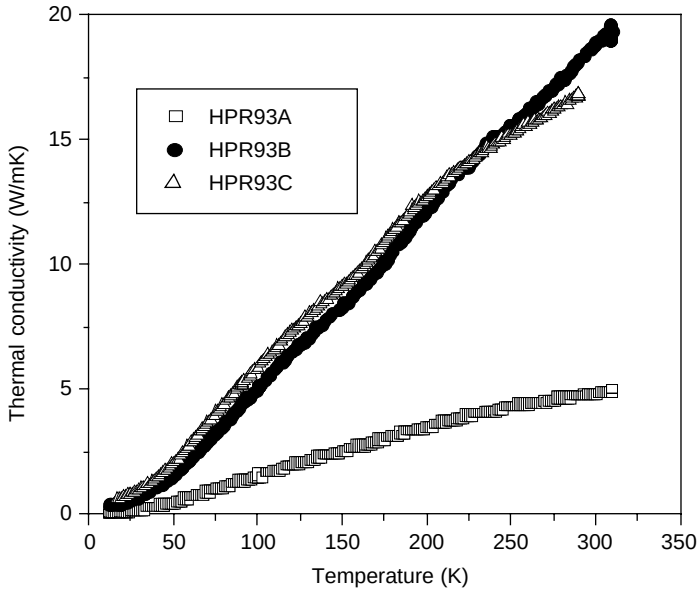

FIGURE 4.14 Thermal conductivity κ vs. temperature of three HiPco fibers. HPR93 exhibits the broadest mosaic distribution of nanotube axes, as determined from the x-ray fiber diagrams.

concentration from 8 to 6%, or reducing the syringe diameter from 500 to 250 μm improves κ(300 K) fourfold; and (3) further syringe diameter reduction to 125 μm yields no further improvement. The syringe diameter effects are clearly due to improved alignment; the smallest orifice gives the smallest mosaic, 45° FWHM compared to 65° with the 500 μm one. The best κ value is still orders of magnitude below graphite and ideal MWNT, most probably due to thermal barriers. It may be significant that the highest macroscopic κ was obtained for materials made from pulsed laser vaporization (PLV) SWNT without extended exposure to strong acids. PLV tubes made thus are known to be highly perfect, while acid immersion can lead to defects and ultimately to very short tubes. Either way, the phonon mean free path in such materials may be quite low.

Thermal conductivity of peapods is enhanced relative to that of empty tubes, and the enhancement exhibits interesting temperature dependence [70,71]. Difference data, κ(filled)-κ(empty), from 10 to 285 K are shown in Figure 4.15. Three distinct regions are evident. Region I is dominated by the contribution from the very soft C_{60}–C_{60} acoustic modes. A 1D Debye temperature of 90 K is estimated for these modes using a Lennard–Jones potential. At T_D all the LA modes are excited, the excess heat capacity saturates and $\Delta\kappa$ levels off to a constant value (region II). The filling fraction of this sample is well below 50%, and the theory predicts the existence of C_{60} capsules separated by lengths of empty tubes to account for the unfilled sites [46]. We imagine the onset of a new thermal transport mechanism (region III), beginning at temperatures sufficiently high to break the weak vdW bond between a terminal C_{60} and its capsule. This will happen more efficiently at the hot end, and, once liberated, the free C_{60} will thermally diffuse to, and join, the end of a cold capsule, as shown schematically in the inset. The internal degrees of freedom represent an additional thermal transport process accompanying the mass transport inside the tube. The rate of this process increases with increasing T and will saturate at a very high T, which transforms the assembly of capsules to a 1D gas. This scenario is speculative at this point since it has been observed only in one sample. A rigorous test of the mechanism would be to find out if the effect disappears in a completely filled sample. Other endohedral species may give larger enhancements, and these materials may then become candidates for thermal management applications such as additives to conducting adhesives.

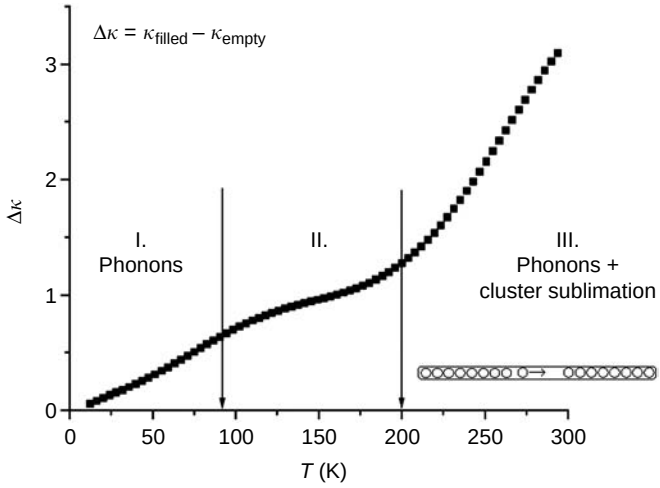

FIGURE 4.15 Excess thermal conductivity in a partially filled C_{60}@SWNT buckypaper. Enhancement in regime I attributed to the 1D LA phonons on the C_{60} chains. Saturation in regime II after $T > T_{Debye} \sim 90$ K of the 1D molecular modes. Further enhancement in regime III assigned to hot C_{60} molecules subliming off the end of a capsule, diffusing to the end of a colder capsule while carrying internal vibrations as a combined heat and mass transfer.

4.3.3 Electronic Properties

At the last count Google.scholar gave 4400 hits on this rubric, so this section will be highly selective.

Theory led experiment in this important aspect of nanotube properties, and the most important results emerge from a simple idea. One monolayer of graphene has two energy bands $E_n(k)$ which cross at the Fermi energy E_F, so the system is on the cusp of a metal–insulator (MI) transition. The electronic ground state can therefore be described either as a zero-gap semiconductor or as a metal with infinitesimal density of states at the Fermi energy $N(E_F)$. In 3D graphite, the interlayer interaction causes a transition to a semimetal which conducts well, because the $\sim 10^{18}$ charge carriers/cm^3 have very high mobility. On the other hand, rolling a single sheet into a tube is a symmetry-breaking transition, which leads to semiconducting or metallic ground states, depending on the choice of wrapping (Figure 4.1). The band structure of a single tube consists of unusual 1D subbands resulting from the requirement that the radial wave function be commensurate with the circumference of the tube. The larger the tube, the smaller the subband spacing; in the 2D graphene limit, there are only the two bands mentioned above. The longitudinal dispersion is linear for a range of energies close to zero.

As noted earlier, bulk properties are generally dominated by extrinsic effects, although some of the 1D subtleties remain, especially in oriented material. The properties of the principal techniques are resistivity and its temperature dependence, density of states spectroscopy using electron energy loss and photoemission, optical absorption, and reflectivity. In a few cases, thermoelectric power and conduction electron spin resonance have also been applied to nanotube physics.

The electrical properties of bulk nanotube materials have evolved considerably since the first experiments 10 years ago. Early samples consisted of pressed "mats" of nanotube soots from carbon arc or laser ablation processes, which contained only 10 to 30 wt% tubes. Major impurities were amorphous carbon, metal catalyst particles, and fullerenes, mainly C_{60}. Mat densities were as low as 1% of the crystallographic value computed from a triangular lattice of 1.4 nm diameter SWNT. On the other hand, long high-quality tubes could be found in these soots. This is because they had not been subjected to acid treatment or sonication in attempts to remove impurities, both of which are now known to create sidewall defects and ultimately to cut tubes into shorter lengths.

The prevailing attitude at the time was that only single-tube measurements would give useful information. Nevertheless, some valuable information, still valid today, was obtained from four-probe measurements on these mats. First, correcting for the missing material, ρ (300 K) values within 1–2 decades of in-plane graphite were obtained, suggesting that bulk SWNT materials could be developed into strong, lightweight synthetic metals [72]. Second, the very modest temperature dependence in the range 80 K $< T <$ 350 K changed from nonmetallic to weakly metallic at ~200 K, suggesting a phonon-scattering mechanism at high temperatures. Third, experiments extended to very low T showed a strong divergence in ρ (T) as $T > 0$, indicating strong localization of carriers [73]. Finally, chemical doping with bromine or potassium [67,74] showed that like graphite, bulk SWNT material acted as an amphoteric host for redox doping. All of these phenomena have since been revisited using purified samples with SWNT content approaching 100%.

Figure 4.16 shows the anisotropy of ρ (T) measured parallel and perpendicular to the alignment direction for the case of buckypaper deposition in a magnetic field [30]. The temperature dependence is weakly nonmetallic and quite similar for both orientations. Furthermore, the anisotropy is independent of temperature. These observations indicate that we are not observing the intrinsic anisotropy of aligned SWNT; transport in the perpendicular direction is dominated by misaligned bundles or fibrils, which short out the larger intertube/interbundle resistance. The nonmetallic T-dependence is consistent with previous results on unoriented buckypaper after similar acid purification and high-temperature vacuum annealing. These processes are presumed to reduce the mean free path for electron–phonon scattering via defect creation or tube cutting, and thus eliminate the high-temperature regime of positive dρ/dT. At 295 K, the measured $\rho_{//}$ for 7 T field alignment is 0.91 mΩ cm. Accounting for gross porosity raises this to 0.41 mΩ cm.

The weak anisotropy can be accounted for by a simple model of 1D paths in the plane of the sample, each sample containing on average n elements (ropes, tubes) of fixed length and resistance. The resistance of each path is linearly proportional to n and, since for a fixed number of elements, the number of paths is inversely proportional to n, the resistance of the ensemble of paths in parallel is

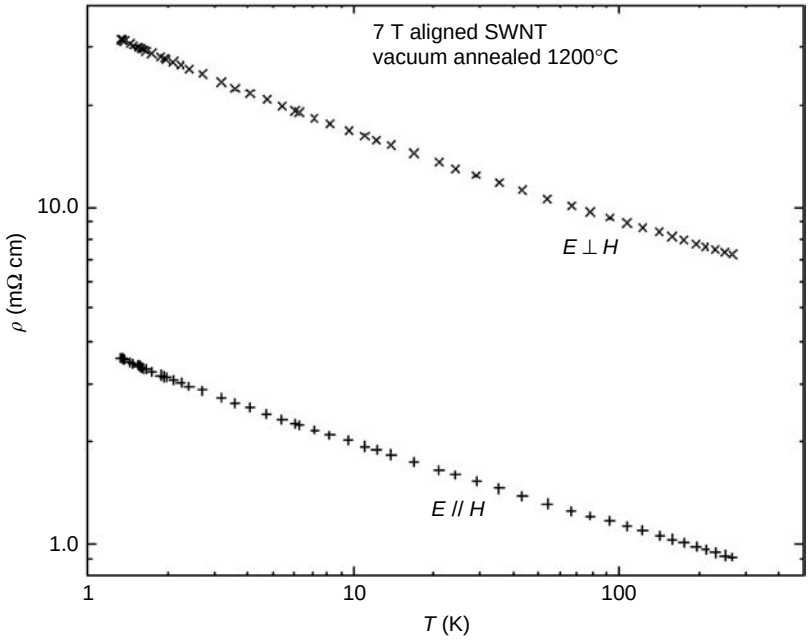

FIGURE 4.16 Resistivity vs. temperature for annealed 7 T-aligned buckypaper, measured with current perpendicular and parallel to the average alignment axis on two different samples with in-line four-probe contacts. (From Fischer, J. E. et al., *J. Appl. Phys.* **93**, 2157 (2003), with permission.)

proportional to n^2. The average number of elements n required for current to flow through the sample is equal to L/λ, where L is the length of the sample and λ is the mean projection of the element length in the current direction: λ depends on the distribution width and aligned fraction. Using x-ray and Raman data as input, very good agreement is obtained between predicted and measured $\rho_{//}/\rho_{\perp}$ for 7 and 26 T data.

How does the experimental $\rho_{//}$ (300 K) compare with that of an assembly of ballistic conductors? Assume that each metallic tube in a perfectly aligned sample is comprised of finite-length ballistic conductors in series, the length being the mean free path λ for electron–phonon backscattering. Each tube has two transport channels corresponding to the two bands degenerate at E_F. Taking $\lambda = 300$ nm [75], $\rho_{//}$ = (area/tube)/($2G_o \times 300$ nm) $= 1.5 \times 10^{-5}\ \Omega$ cm, where G_o is the conductance quantum 12.6 K $\Omega)^{-1}$. Assuming further that tube growth is stochastic with respect to wrapping indices, only one third of the tubes will be metallic at 300 K and so $\rho_{//} \sim 50\ \mu\Omega$ cm, roughly twice the value for graphite. This is a surprising result because there are many factors which will increase this number in real samples: finite distribution width of tube axes, unaligned tubes, empty volume (porosity), junction resistance between tube segments and between ropes, incoherent intertube scattering within a rope, and elastic scattering from tube ends, defects and impurities. These may be partially offset by p doping of the semiconducting tubes by acid residues from purification and by atmospheric oxygen.

Pure nanotube fibers offer the prospect of even lower resistivities since they are readily aligned during extrusion and can be further aligned by stretching. We discuss next the results of transport measurements on the two sets of fibers described above: syringeextruded from oleum suspensions and PVA/water mixtures.

Figures 4.17(a) and (b) show the effects of extrusion conditions and post-extrusion annealing on the temperature-dependent resistivity of fibers extruded from anhydrous sulfuric acid, or oleum [34]. Varying degrees of alignment were obtained from HPR93 fibers extruded using three different combinations of SNWT concentration and orifice diameter. The texture results of these have been discussed above. Annealing was carried out in vacuum or flowing argon at 1100°C for 24 h. In the neat state, all three fibers exhibit low resistance with metallic temperature dependence above 200 K, as shown in Figure 4.17(a). The best alignment is obtained for HPR93B, which correlates nicely with the lowest ρ (300 K) = 0.24 mΩ cm, about a factor 10 less than graphite. For all three neat fibers, both the small values and the weak temperature dependence are due to the strong redox doping effect of bisulfate from the acid suspension. The nondivergent low-T behavior in the neat state can be ascribed to interparticle tunneling induced by thermal fluctuations [76].

The effect of annealing on ρ (T) is shown in Figure 4.17(b), which displays the results of a series of successively higher annealing temperatures at constant time intervals. All three annealed samples show large increases in resistivity at all T, in addition to notably steeper nonmetallic temperature dependence. In general, annealing removes dopant molecules and the fibers become more resistive with higher annealing temperatures. This effect is more pronounced at low T. Note that for HPR93B, dρ/dT still becomes more negative with decreasing T at our lower limit of 1.3 K, unlike the nondivergent behavior of the neat fibers. These results suggest that removing dopant molecules leads to localization of charge carriers within the ropes.

A similar study of fibers spun from PVA–water–surfactant [29] focused on the effect of post-extrusion stretching while the green "gel" fiber still contained ~50% PVA. The effect on ρ (300 K) is shown in Figure 4.18 [25]. An initial decrease by a factor ~4 up to 21% stretch is followed by saturation beyond ~35% stretch. Surprisingly, the x-ray-derived-distribution width is narrowing continuously over the whole range of stretching (up to 80%), suggesting that above an intermediate degree of alignment, ρ (297 K) is limited by some other factor which does not improve with further stretching. Note also that for these composite gel fibers, ρ (300 K) is 20 to 30 times larger than for the neat oleum-based fibers. Here, the insulating PVA impedes long-range transport while the presence of trace p-type dopants enhances the neat conductivity of the oleum fibers.

Selected fibers were annealed in H_2 at 1000°C after stretching, to remove the insulating PVA and thereby obtain more highly conducting material. This process leads to a strong reduction in

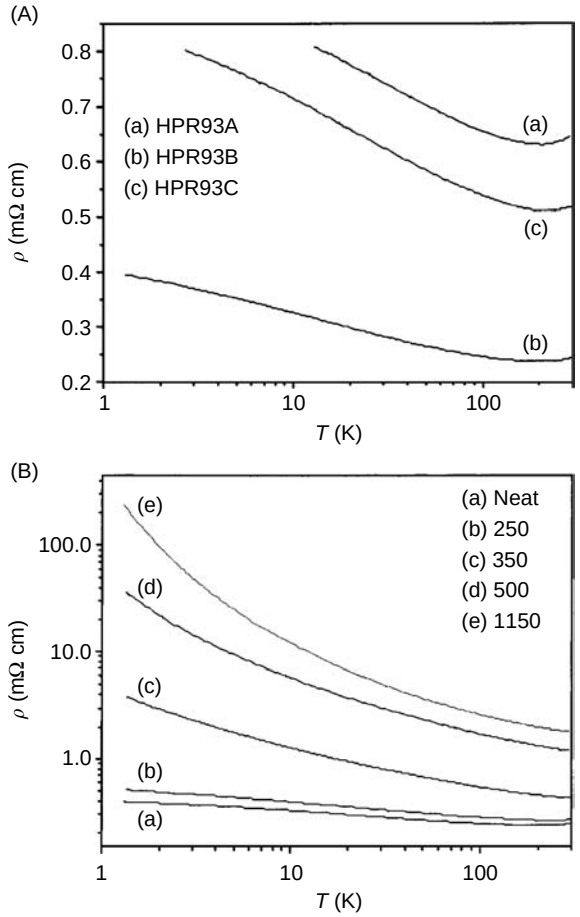

FIGURE 4.17 (a) Four-point resistivity vs. temperature for three neat SWNT fibers extruded from oleum suspension. ρ decreases at all T as alignment improves. Nonmetallic behavior at low T levels off as $T \rightarrow 0$ (non-divergent behavior) while metallic behavior is observed above 200 K. (b) Effect of vacuum annealing on ρ (T) for HPR93B; note log–log scale. ρ increases as the bisulfate p-dopants are removed, especially at very low T (factor ~500 at 1.3 K). Metallic behavior is lost, and the slope $d\rho/dT$ continues to increase as $T \rightarrow 0$ (divergent behavior). (From Zhou, W. et al., *J. Appl. Phys.* **95**, 649 (2004), with permission.)

ρ (300 K) and a flattening of the ρ (T) curve to a much weaker T dependence than in the green gel fiber. The data for green PVA/SWNT composite fiber and for the PVA-free annealed one are shown in Figure 4.19. Both have been stretch-aligned as indicated in the figure legend; note the log–log scale. At 300 K, ρ for the composite fiber exceeds that of the annealed one by 40 to 50 times. Here, the elimination of PVA removes high-resistance interbundle contacts so the macroscopic carrier transport is more efficient. At low temperature the difference is more dramatic, suggesting that the presence of PVA enhances the effects of carrier localization by disorder. The composite fiber resistance becomes too high to measure at the lowest temperature. Extrapolating to 2 K, we deduce a resistance ratio of at least 11 decades, strongly suggesting totally different conduction mechanisms in the two morphologies. It is obvious from the data that disorder dominates charge transport in both states. Furthermore, the disorder is most likely to encompass all three dimensions since the fibers consist of coupled and intertwined objects. In particular, we expect that the disorder is neither limited to 1D carrier localization on individual tubes or bundles, nor to defect scattering/trapping on single tubes. The huge effect of PVA, which permeates the interbundle volumes in the composite

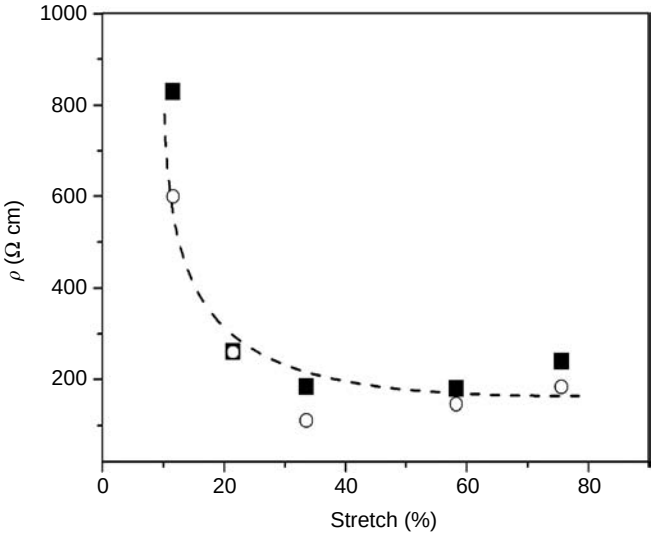

FIGURE 4.18 Four-probe electrical resistivity at room temperature vs. stretch ratio for PVA composite nanotube fibers. The experiments have been conducted on two series of samples (black squares, open circles). Accurate cross-sectional areas were obtained from SEM image analysis. The resistivity decreases with stretch ratio by a factor between three and four for the two sets of data. The absolute value is intermediate between all-SWNT fibers and polymer composites. The dashed line is a guide to the eye. (From Badaire, S. et al., *J. Appl. Phys*. **96**, 7509 (2004), with permission.)

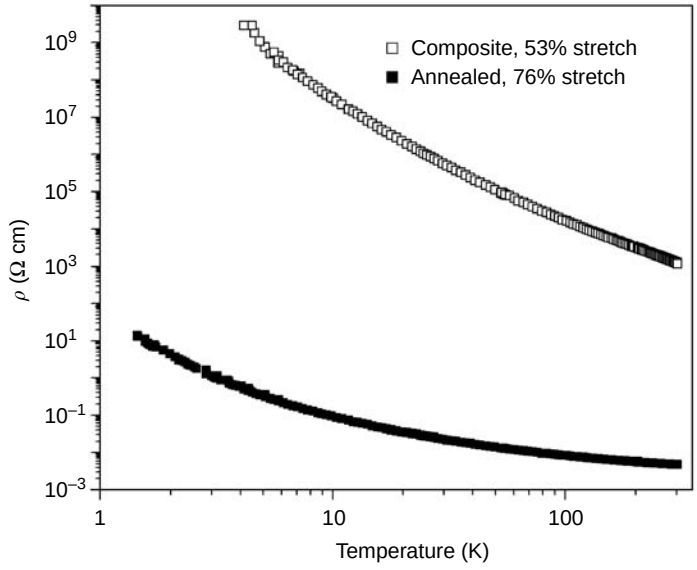

FIGURE 4.19 Resistivity vs. temperature for composite (53% stretch) and annealed (76% stretch) nanotube fibers (note log–log scale). Note that $\rho(T)$ for the composite fiber is more strongly divergent as $T \to 0$ as compared to the annealed one. (From Badaire, S. et al., *J. Appl. Phys.* **96**, 7509 (2004), with permission.)

fibers, cannot possibly be 1D. It is interesting to note that for both fiber series, one ends up with about the same ρ (300 K) after annealing, whereas this value is approached from opposite directions in the two different processes.

The qualitatively different $\rho(T)$ behaviors in the two sets of fibers can be attributed to an MI transition as a function of doping level [77]. On the metallic side for heavily doped tubes, ρ tends

to a finite value as T approaches zero, and the effective band gap, $-\mathrm{d}\ln\rho/\mathrm{d}T$, vanishes as T approaches zero; examples of this behavior are shown in Figure 4.20. On the insulating side for PVA-rich gel fibers or annealed oleum fibers, ρ diverges as T approaches zero, and the exponential T dependence can be ascribed to strong localization and either 3D Mott or Coulomb gap variable-range hopping [77]. The MI transition is revealed by systematic measurements of resistivity and transverse magnetoresistance (MR) in the ranges 1.9 to 300 K and 0 to 9 T, as a function of p-type redox doping. The observed changes in transport properties are explained by the effect of doping on semiconducting SWNTs and tube–tube coupling.

How does the presence of endohedral C_{60} affect the electronic properties of peapods? Despite predictions based on work function differences between peas and pod, there is no evidence for charge transfer redox doping by the endofullerenes. Figure 4.21 shows $\rho\,(T)$ data for a peapod sample and an unfilled control [70,71]. Near 300 K the resistivities are the same within experimental error, and the peapod temperature dependence is steeper suggesting stronger disorder effects compared with the empty tubes.

More fundamental than electron transport properties is the spectrum of allowed electron energies or density of states $N(E)$. This can be measured on individual tubes using scanning tunneling spectroscopy, which yields much important information. For bulk materials, one measures the related quantities such as electron energy loss function, using electron energy loss spectroscopy (EELS), absorption spectroscopy using thin films, or reflection spectroscopy if flat and reasonably smooth surfaces are available. We close this section by giving a few examples.

Figure 4.22 shows the loss function of a 100-nm-thick film of ~60% SWNT deposited on a TEM grid [78]. Both energy and momentum of the transmitted electrons can be determined, so the observed transitions can be separated into dispersing and nondispersing, which correspond to "collective" (plasmon) and "localized" interband processes, respectively. The inset shows the loss function over a wide energy range, in which the plasmons representing collective excitations of the π and $\pi + \sigma$ electrons can be clearly seen at 5.2 and 21.5 eV, respectively, in agreement with the theory. Features in the loss function at 0.85, 1.45, 2.0, and 2.55 eV are independent of q and are therefore assigned to interband transitions. Their nature is revealed by a Kramers–Kronig transform

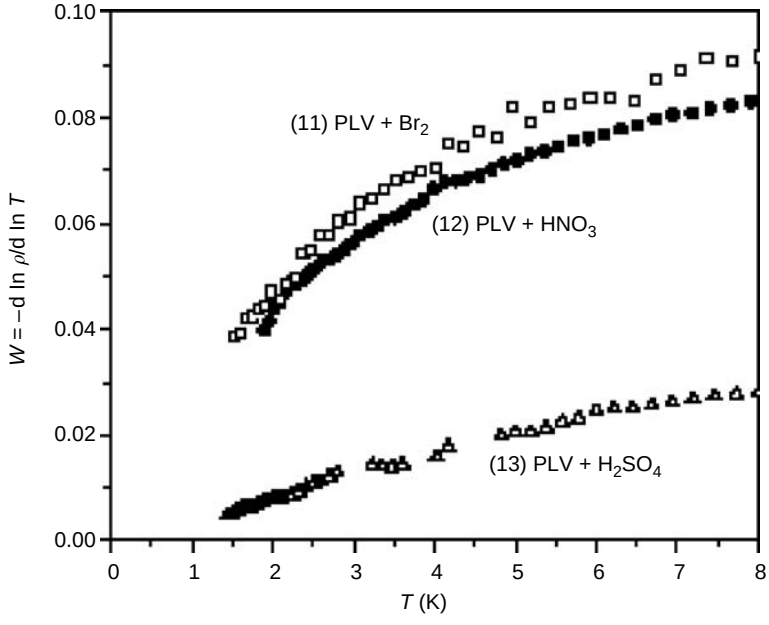

FIGURE 4.20 Reduced activation energy W vs. T for the most conductive p-doped SWNT samples. Extrapolating from the lowest data point 1.3 K to $T = 0$ shows that W, and any possible energy gap, vanishes, signaling a true metallic state. (From Vavro, J. et al., *Phys. Rev. B* **71**, 155410 (2005), with permission.)

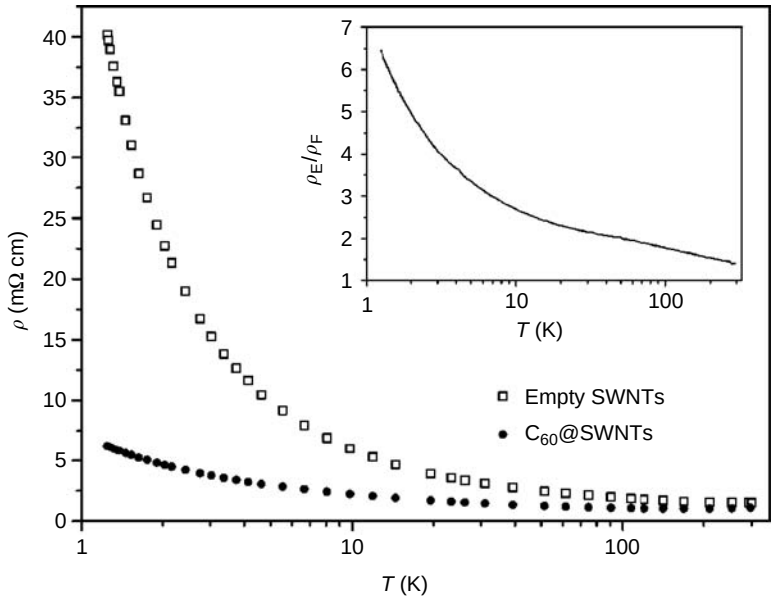

FIGURE 4.21 Four-point resistivity vs. *T* for C60@SWNT (filled circles) and empty nanotubes (open squares). The ratio empty/filled is shown in the inset. At ambient temperature the resistivities are indistinguishable. (From Vavro, J. et al., *Appl. Phys. Lett.* **80**, 1450 (2002), with permission.)

to obtain real and imaginary parts of the dielectric function, ε_2 being directly proportional to the optical absorption coefficient. The results are shown in Figure 4.23, which reveals three interband transitions at 0.65, 1.2, and 1.8 eV. These are the energy separations of the 1D van Hove singularities, slightly broadened by diameter dispersivity in bulk samples. We now understand the sequence of transitions as E_{11}^S, E_{22}^S, and E_{11}^M where *n* is the band index and Sand M denote semiconducting and metallic tubes, respectively.

EELS also gives important information about the effects of redox doping on electronic properties [79]. Figure 4.24 shows how the loss function evolves with potassium concentration. The upshift in the π plasmon near 6.5 eV is due to the gradual addition of an extra electron per *n* carbons to the previously empty π^* conduction band. The extra delocalized electron is charge-compensated by K^o oxidizing to K^+ during intercalation. Figure 4.24(b) shows this relation explicitly, with K/C determined from core-level spectroscopy. The disappearance of fine structure below 2 eV signals the upshift in E_F, which quenches the van Hove interband transitions since the final states in the neutral material (Figure 4.23) are now occupied by doping.

Optical absorption and reflectance are complementary to EELS. The energy resolution is higher, polarization and selection rule information is accessible, and the spectra extend to lower energies which would otherwise be obscured in EELS by the tail of the ~100 kV incident electron beam. The lower energy cutoff permits accurate measurements of the so-called Drude plasmon, a collective excitation of the delocalized electrons, and how it evolves with doping.

Figure 4.25 shows the reflectance of an unoriented undoped film [80]. The solid curve is a model fit, including a free carrier Drude term and several interband Lorentz oscillators. These results confirm that undoped material consists of a mixture of conducting and semiconducting nanotubes, typical for bulk samples. The interband transition energies are consistent with electronic structure calculations for 1.4-nm-diameter tubes, and with EELS described above. The theory predicts that because these transitions involve 1D van Hove singularities, they should be completely polarized along the nanotube axis, i.e., they should vanish when the incident and transmitted beams are cross polarized. This was proved in a clever experiment on magnetically aligned SWNT suspensions with

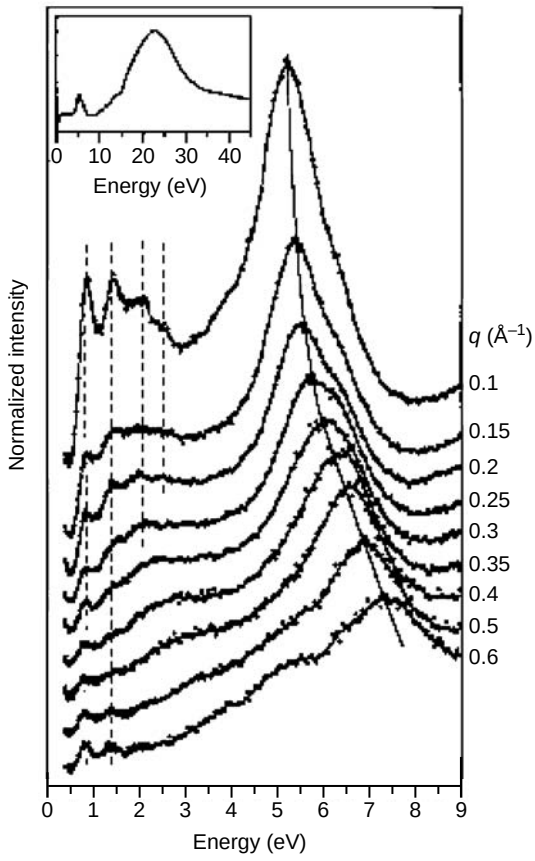

FIGURE 4.22 The loss function of purified SWNT from EELS in transmission for the different q values is shown. The contributions from the elastic peak have been subtracted. The inset contains the loss function over an extended energy range, showing the π plasmon and the $\pi + \sigma$ plasmon at around 5 and 22 eV, respectively. (From Pichler, T. et al., *Phys. Rev. Lett.* **80**, 4729 (1998), with permission.)

the alignment locked in place by gelation [81]. Polarized Raman scattering was used to quantify the degree of alignment. Combined with absorbance data from the partly aligned sample, the intrinsic polarized absorbance is recovered. The fitted Drude plasma frequency ω_P is 0.29 eV, characteristic of a small concentration of conduction electrons or holes.

Chemical doping is revealed in absorption and reflectance spectroscopy by several mechanisms. The higher concentration of free carriers shifts the Drude edge to higher energy. The Drude scattering time may be affected by doping-induced disorder or dimensional crossover. Low-energy interband transitions may be quenched by the E_F shift through valence or conduction band singularities. Examples of these phenomena are evident in the reflectance spectra shown in Figure 4.26 for potassium-doped purified SWNT buckypaper [82]. These experiments were performed in sealed quartz tubes to avoid air exposure; consequently, the results differ significantly from those quoted in an earlier publication in which such precautions were not taken [83]. Data recorded in the range 0.07 to 4 eV show clearly that with increasing K concentration, the 1D van Hove transitions disappear and the Drude edge shifts progressively to higher energies into the visible spectrum [84]. Colors from purple to golden-brown, reminiscent of alkali graphite compounds, are observed as the K concentration increases to saturation. The Drude edge blue-shifts strongly, signaling a large increase in conduction electron concentration after doping. Now the fitted value of σ_P is 1.85 eV. In the free-electron model for metals, the DC conductivity is proportional to ω_P^2. This implies a ~40×

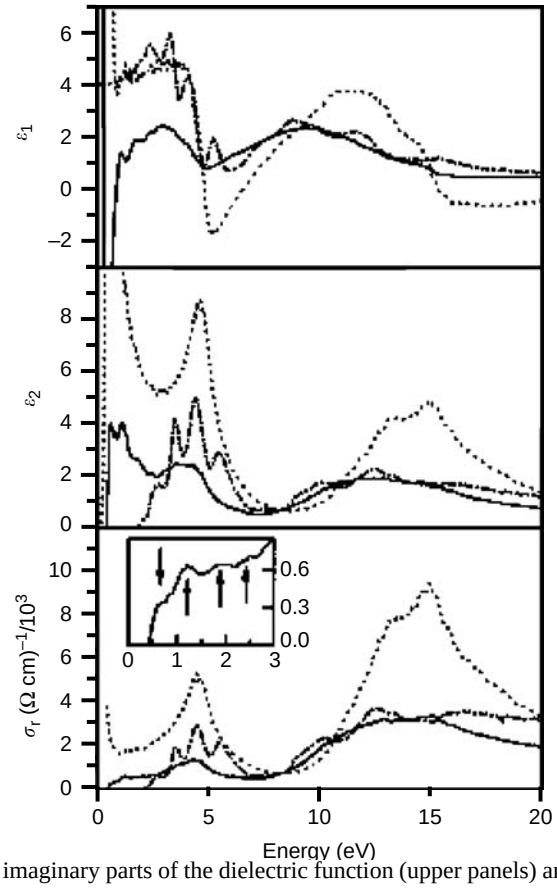

FIGURE 4.23 Real and imaginary parts of the dielectric function (upper panels) and the real part of the optical conductivity for SWNT (solid curves), C_{60} (dot–dash curves) and graphite (dotted curves). (From Pichler, T. et al., *Phys. Rev. Lett.* **80**, 4729 (1998), with permission.)

enhancement in σ by saturation doping, in excellent agreement with direct measurements. Reference [83] reports a much smaller enhancement, underscoring the importance of avoiding air exposure. Similar experiments with electron acceptor doping show a maximum upshift to only 1.2 eV. The weaker effect on ω_p with acceptors is again familiar from graphite intercalation compounds, in which the fraction of a free hole per intercalated molecule is considerably less than the fraction of a free electron per alkali ion.

A key parameter in characterizing doped bulk SWNT samples is the position of the Fermi energy, above or below the neutrality point for donors and acceptors, respectively. This is straightforward in electrochemical experiments, in which temperatures are limited to near ambient and the sample is not optically accessible at all wavelengths. An alternative is provided by the phonon drag, or electron–phonon scattering contribution to the thermopower. The basic idea is quite simple [85], and is shown schematically in Figure 4.27(a). The Fermi surface of a 1D metal consists of two points separated in k by a wave vector of amplitude $|Q|$. Momentum-conserving (inelastic) electron–phonon scattering thus requires participation of acoustic phonons with wave vector Q, which are absorbed or emitted as electrons scatter from the left- to right-moving branch of $E(k)$. Thus, the temperature dependence will reflect the temperature dependence of the heat capacity, and phonon drag is quenched below a characteristic temperature T_o given approximately by $0.2\pi\hbar\omega_Q/k_B$ (cf. Figure 4.27(a)). $|Q|$ is set by the chemical potential μ, which in turn is controlled by the doping level; h and k_B are the Planck and Boltzmann constants, respectively. Operationally (Figure 4.27(b)), one records thermopower vs. temperature, locates T_o from the peak in the derivative, and backs out E_F from the

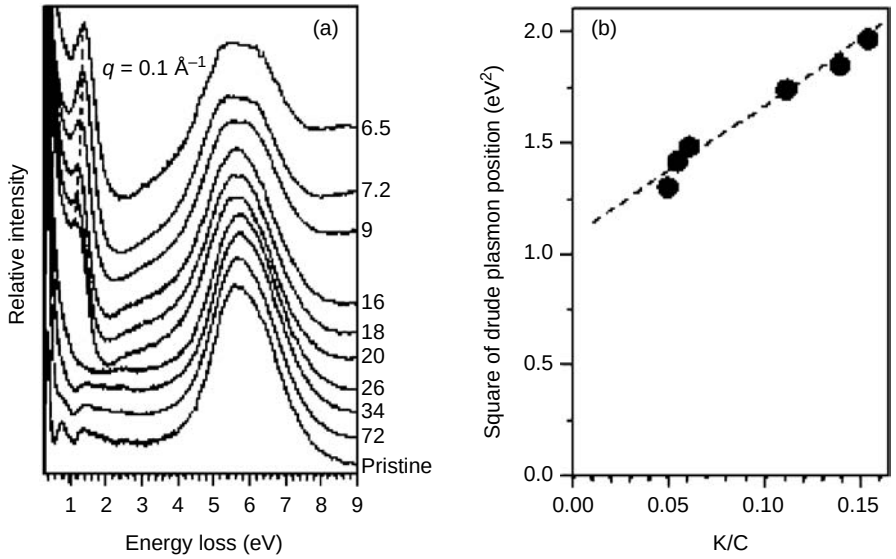

FIGURE 4.24 (a) The loss function of pristine and potassium-intercalated SWNT; the potassium concentration increases from bottom to top. The dashed line indicates the shift of the position of the charge carrier plasmons with increasing concentration. (b) The quantitative relation between the square of the energy position of the charge carrier plasmon and the relative potassium concentration. (From Liu, X. et al., *Phys. Rev. B* **67**, 125403 (2003), with permission.)

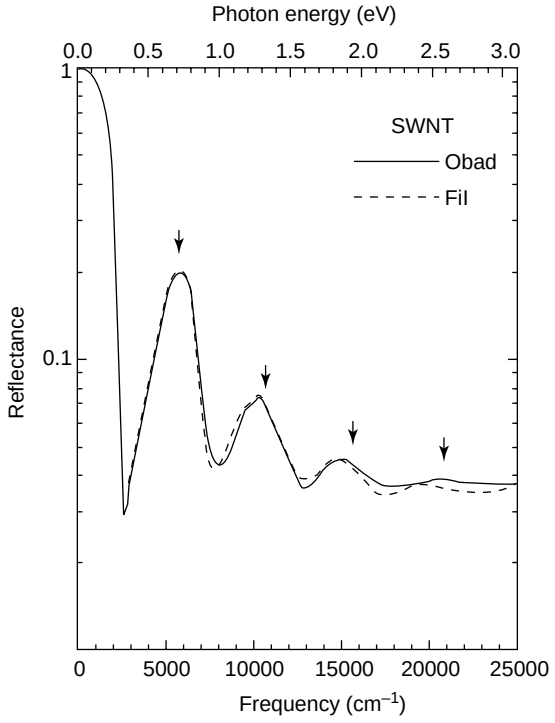

FIGURE 4.25 Reflectance of an unaligned SWNT mat measured from 25 to 25,000 cm^{-1} (lower scale), corresponding to the energy interval 0.003–3 eV (upper scale). R approaches 1 at $E = 0$, characteristic of a metal. Four interband transitions involving 1D van Hove singularities are identified by the downward arrows. (From Hwang, J. et al., *Phys. Rev. B* **62**, R13310 (2000), with permission.)

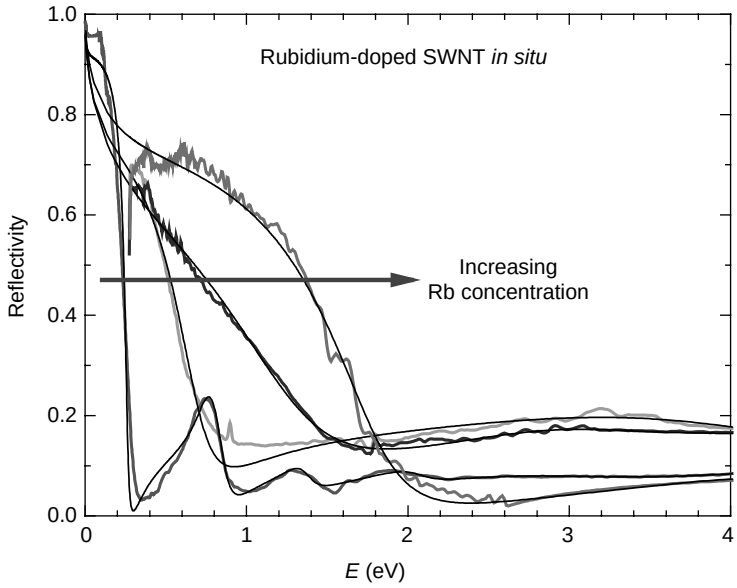

FIGURE 4.26 Reflectance vs. photon energy for four SWNT buckypaper samples with increasing carrier concentration from alkali doping. Leftmost curve is for undoped SWNT. Doping causes a strong blueshift of the free carrier Drude edge, and quenches the interband transitions as E_F increases through the first two-conduction band van Hove singularities. (From Zhou, W. et al., *Phys. Rev. B* **71**, 205423 (2005), with permission.)

relevant dispersion relations. In the example shown, we see the sharp contrast between undoped and sulfuric acid-doped data from which a Fermi level depression of 0.5 eV is obtained.

The phonon drag method for locating E_F suffers one major drawback — it relies on a model for the energy band dispersion $E(k)$. The original one-electron tight-binding models have been extremely useful [86], while the importance of higher order effects is becoming evident [87]. For studies of the metallic state of doped nanotube materials, it would be helpful to have a characterization technique which directly measures the free carrier concentration (Hall effect), or at least the density of states at the Fermi energy $N(E_F)$. The Pauli paramagnetism of conduction electrons provides one option. This is difficult to observe directly in magnetization measurements due to strong diamagnetic corrections, which are not well quantified. This limitation is overcome by conduction electron spin resonance (CESR), which in essence is the Zeeman effect of delocalized electrons. Evidence for Pauli spins in raw SWNT soot was reported 10 years ago [88]. This was controversial because (1) it was believed that the random orientation combined with anisotropic metallic properties would broaden the CESR beyond recognition, and (2) assuming stochastic growth such that only approximatelyone third of the tubes is metallic, and given the theoretical result that $N(E_F)$ per mole is only approximately one fourth that of 3D graphite, these few intrinsic metallic spins might be undetectable. The original interpretation was supported by subsequent measurements of the temperature dependence of integrated CESR linewidth [89]. While the more typical paramagnetic resonance associated with localized spins obeys a Curie law temperature dependence, susceptibility $\chi \sim 1/T$, the nanotube χ was independent of T in the range 70 to 300 K. The same sample exhibited the aforementioned shallow minimum in resistivity vs. T at about 200 K, so the T independence of χ_{Pauli} ruled out an MI transition in the undoped material.

CESR was extended to alkali-doped buckypaper using *in situ* electrochemical doping to follow the resonance vs. K concentration [90]. Figure 4.28(a) shows the evolution of the full profile, which consists of a narrow Pauli contribution, magnified in Figure 4.28(b), superposed on a broad antiferromagnetic resonance (AFMR) associated with residual transition metal catalyst. The Pauli

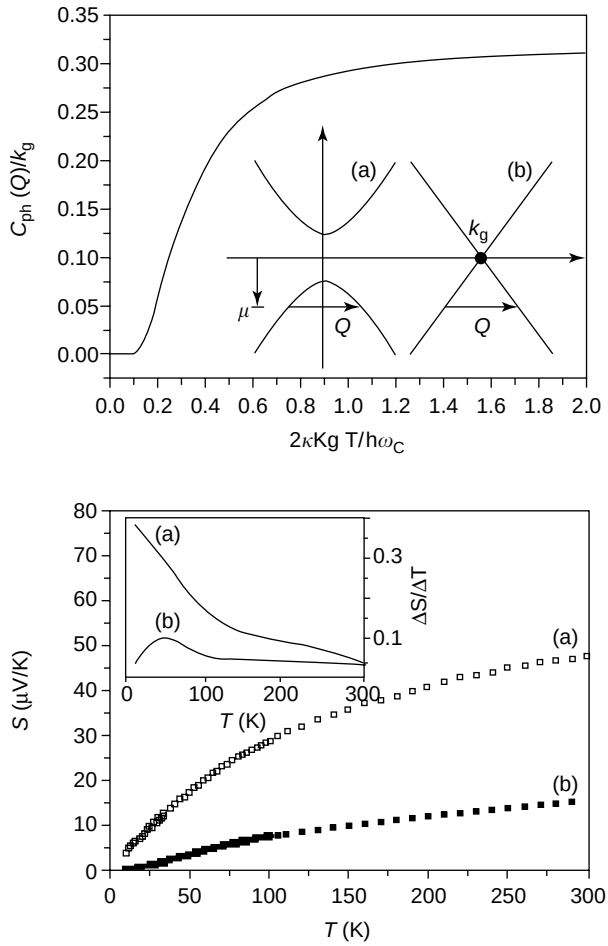

FIGURE 4.27 Phonon drag in SWNT. Top: calculated phonon heat capacity vs. T for a p-type doped nanotubes with chemical potential μ applicable to semiconducting or metallic tubes is shown in the inset. The cutoff in occupied phonon energies leads to a weak threshold in thermopower S. Bottom: S (T) and its derivative for SWNT fibers extruded from sulfuric acid (b) and after annealing to remove the acid and return μ toward zero. The peak in the derivative (b) is a measure of the doping-induced downshift in E_F. (From Vavro, J. et al., *Phys. Rev. Lett.* **90**, 065503 (2003), with permission.)

CESR grows in intensity with increasing K concentration, while the position and width are constant. The AFMR intensity diminishes as the sample becomes more conducting and the microwave skin depth decreases. Figure 4.28(b) shows that χ_{Pauli}, proportional to the double integral of the CESR line, increases monotonically with K/C. Now that an absolute scale is established, the absence of CESR in this undoped material is surprising since there is ample sensitivity.

It also calls into question the origin of the T-independent signal observed previously in unpurified soot [89]. Figure 4.29 shows that χ_{Pauli} is independent of T for two saturation-doped samples, from 30 to 290 K. This proves beyond doubt that alkali-doped SWNTs are true metals. The absolute value 5×10^{-8} emu/g translates to $N(E_F) = 0.015$ states/eV per carbon per spin, approximately five times smaller than a theoretical estimate [91]. The anomalously small value in doped material, and the absence of a true ESR signal in clean undoped material, remain to be resolved.

The independence of the CESR linewidth on temperature is unusual. The inverse of the width is proportional to the spin relaxation rate, which is usually dominated by spin–orbit interaction with

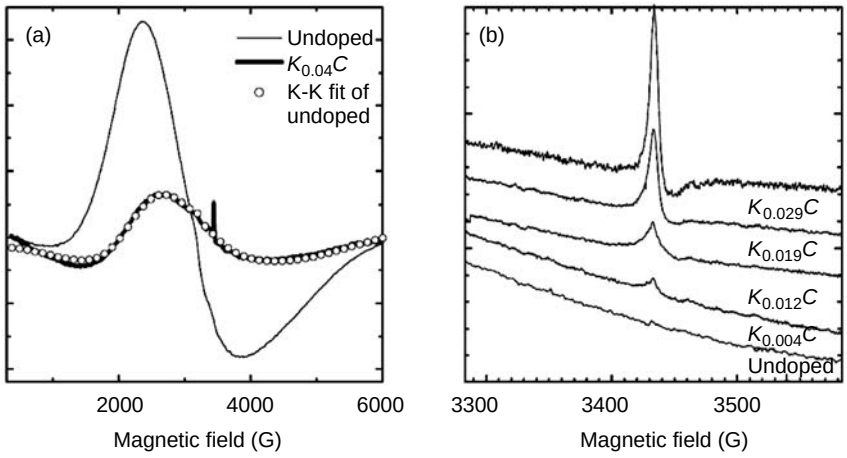

FIGURE 4.28 Conduction electron spin resonance in K-doped SWNT. (a) Ferromagnetic resonance of Ni catalyst particles in undoped and fully doped SWNT (light and heavy curves, respectively). The narrow CESR peak is not seen in the undoped sample, and the Ni resonance changes line shape as the sample becomes more conducting and the skin depth decreases. (b) The CESR line grows continuously with increasing K concentration, while the spin relaxation rate (line width) and *g* factor (position) remain constant. (From Claye, A. S. et al., *Phys. Rev. B* **62**, R4845 (2000), with permission.)

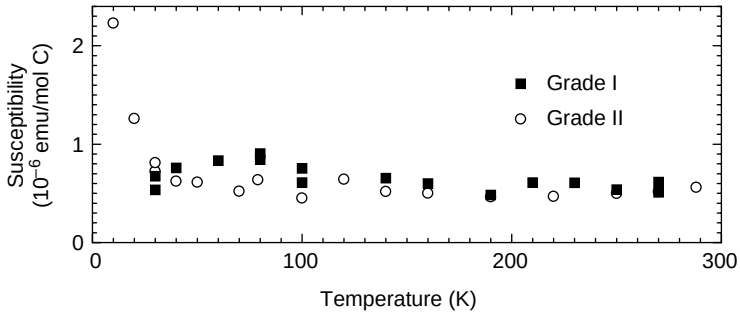

FIGURE 4.29 The Pauli spin susceptibility vs. *T* for saturation-doped SWNT is independent of *T* above 30 K, characteristic of a metallic state. (From Claye, A. S. et al., *Phys. Rev. B* **62**, R4845 (2000), with permission.)

the dopants. The only explanation is inhomogeneous doping; small saturation-doped regions are created at the outset, and their number density increases with global K/C without affecting their size. This model is supported by accompanying x-ray diffraction data [90].

4.3.4 Magnetic and Superconducting Properties

We close with a brief mention of these collective phenomena in bulk nanotube materials. An excellent entrée to the magnetism controversy is the recent paper by Cesvedes et al. and references therein [92]. The authors prove convincingly that there is no bulk magnetism in a clean multiwall nanotube sample. On the other hand, when placed on a flat ferromagnetic substrate, fringing fields can be observed by magnetic force microscopy. Thus, the prospect for "contact-induced magnetism" and the application of carbon nanotubes to nanoscale spintronic devices remain open. Magnetic contrast is observed for carbon nanotubes placed on cobalt or magnetite substrates, but is absent on silicon, copper, or gold. Spin transfer of about 0.1 μB per contact carbon atom is obtained.

The dialog about nanotube superconductivity began with a very simple argument [93]: if one could tune the chemical potential to the peak of a van Hove singularity, either chemically or electrostatically,

one should have a high $N(E_F)$ value, a prerequisite for BCS superconductivity. The obvious problem in applying this to bulk material is the diameter dispersivity. Even in single tubes, higher order interactions will broaden the square-root energy divergences. This has not prevented some from conjecturing T_c above 400 K for nanotube superconductors. Super-current flow through an SWNT with low-resistance contacts was reported in 1999 [94]; analogous to contact-induced magnetism, no claims were made for bulk nanotube superconductivity. Evidence for a bulk anisotropic Meissner effect below 20 K in aligned 0.4-nm-diameter SWNT was claimed and justified by the argument that small-diameter tubes will be the stiffest, and thus, the average phonon energy in the BCS equation will be favorable [95]. This dramatic result has not been reproduced by other researchers since it appeared 4 years ago. As with bulk magnetism, it would appear that the jury is still out concerning bulk superconductivity in carbon nanotubes and other nanostructures.

4.4 SUMMARY AND PROSPECTS

It is difficult to counter the argument that carbon is the most amazing element in the Periodic Table. In the space of a mere 30 years, we have experienced the discovery of (or renaissance in) three material families: graphite intercalation compounds (GICs), fullerene solids, and nanotubes. GICs provided a wealth of detailed chemical and physical information, while immediate applications were frustrated by cost, lack of air stability, and most importantly, the lack of new or greatly improved applications and properties. Though the foundations of physics and chemistry remain unshaken, the Li ion battery industry has certainly benefited greatly from this store of knowledge. Fullerene solids fared better, and may yet surprise us in the practical world; while no large volume application has yet emerged, the elucidation of electronic properties in this highly correlated system has made invaluable contributions to fundamental science. Nanotubes may offer the best prospects yet; money is already being made on some small-scale applications. The combination of enhanced properties encourages the drive to multifunctional materials, and also affords an excellent laboratory for studying 1D phenomena. Extensions to other tubular and nanowire-like materials provide ample scope for new discoveries.

ACKNOWLEDGMENTS

The nanotube phase of my research life has been enriched by delightful interactions with numerous students, postdocs, colleagues and collaborators. This chapter draws heavily from the work of recently awarded theses of Roland Lee, Zdenek Benes, Agnes Claye, Norbert Nemes, Juraj Vavro, and Marc Llaguno, and soon to be awarded theses of Wei Zhou and Csaba Guthy. Funding from the National Science Foundation, the Office of Naval Research, and especially the Department of Energy are gratefully acknowledged. I am grateful as well to Linda Fischer for a most thorough proofreading.

REFERENCES

1. S. Iijima, Helical microtubules of graphitic carbon, *Nature* **354**, 56–58 (1991).
2. R. C. Haddon and S.-Y. Chow, Hybridization as a metric for the reaction coordinate of the chemical reaction: concert in chemical reactions, *Pure Appl. Chem.* **71**, 289–294 (1999).
3. F. Du and K. I. Winey, this volume.
4. N. Wang, G. D. Li and Z. K. Tang, Mono-sized and single-walled 4 Å carbon nanotubes, *Chem. Phys. Lett.* **339**, 47 (2001).
5. G. Eres, A. A. Puretzky, D. B. Geohegan and H. Cui, In situ control of the catalyst efficiency in chemical vapor deposition of vertically aligned carbon nanotubes on predeposited metal catalyst films, *Appl. Phys. Lett.* **84**, 1759–1761 (2004).
6. R. Tenne, this volume.

7. E. G. Rakov, this volume.
8. T. Yoshitake, Y. Shimakawa, S. Kuroshima, H. Kimura, T. Ichihashi, Y. Kubo, D. Kasuya, K. Takahashi, F. Kokai, M. Yudasaka and S. Iijima, Preparation of fine platinum catalyst supported on single-wall carbon nanohorns for fuel cell application, *Physica B* **323**, 124–126 (2002).
9. M. Freitag, A. T. Johnson, S. V. Kalinin and D. A. Bonnell, Role of single defects in electronic transport through carbon nanotube field-effect transistors, *Phys. Rev. Lett.* **89**, 216801 (2002).
10. J. E. Fischer, P. A. Heiney, A. R. McGhie, W. J. Romanow, A. M. Denenstein, J. P. McCauley Jr. and A. B. Smith III, Compressibility of solid C_{60}, *Science* **252**, 1288 (1991).
11. J. Tang, L.-C. Qin, T. Sasaki, M. Yudasaka, A. Matsushita and S. Iijima, Compressibility and polygonization of single-walled carbon nanotubes under hydrostatic pressure, *Phys. Rev. Lett.* **85**, 1887 (2000).
12. Y. Maniwa, R. Fujiwara, H. Kira, H. Tou, H. Kataura, S. Suzuki, Y. Achiba, E. Nishibori, M. Takata, M. Sakata, A. Fujiwara and H. Suematsu, Thermal expansion of single-walled carbon nanotube (SWNT) bundles: X-ray diffraction studies, *Phys. Rev. B* **64**, 241402 (2001).
13. S. Bandow, G. Chen, G. U. Sumanasekera, R. Gupta, M. Yudasaka, S. Iijima and P. C. Eklund, Diameter-selective resonant Raman scattering in double-wall carbon nanotubes, *Phys. Rev. B* **66**, 075416 (2002).
14. J. G. Lavin, S. Subramoney, R. S. Ruoff, S. Berber and D. Tomanek, Scrolls and nested tubes in multiwall carbon nanotubes, *Carbon* **40**, 1123–1130 (2002).
15. L. Jin, C. Bower and O. Zhou, Alignment of carbon nanotubes in a polymer matrix by mechanical stretching, *Appl. Phys. Lett.* **73**, 1197 (1998).
16. Y. Gogotsi, J. A. Libera, A. Güvenç-Yazicioglu, and C. M. Megaridis, In-situ multiphase fluid experiments in hydrothermal carbon nanotubes, *Appl. Phys. Lett.* **79**, 1021–1023 (2001).
17. H. W. Zhu, C. L. Xu, D. H. Wu, B. Q. Wei, R. Vajtal and P. M. Ajayan, Direct synthesis of long single-walled carbon nanotube strands, *Science* **296**, 884 (2002).
18. Y.-L. Li, I. A. Kinloch and A. H. Windle, Direct spinning of carbon nanotube fibers from chemical vapor deposition synthesis, *Science* **304**, 276 (2004).
19. M. Zhang, K. R. Atkinson and R. H. Baughman, Multifunctional carbon nanotube yarns by downsizing an ancient technology, *Science* **306**, 1358 (2004).
20. K. Hata, D. N. Futaba, K. Mizuno, T. Namai, M. Yumura and S. Iijima, Water-assisted highly efficient synthesis of impurity-free single-walled carbon nanotubes, *Science* **306**, 1362 (2004).
21. P. G. Collins, M. S. Arnold and P. Avouris, Engineering carbon nanotubes and nanotube circuits using electrical breakdown, *Science* **292**, 706–709 (2001).
22. R. H. Baughman, A. A. Zakhidov and W. A. De Heer, Carbon nanotubes — the route toward applications, *Science* **297**, 787–792 (2002).
23. A. G. Rinzler, J. Liu, P. Nikolaev, C. B. Huffman, F. J. Rodriguez-Macias, P. J. Boul, A. H. Lu, D. Heymann, D. T. Colbert, R. S. Lee, J. E. Fischer, A. M. Rao, P. C. Eklund and R. E. Smalley, Large-scale purification of single-wall carbon nanotubes: process, product, and characterization, *Appl. Phys. A* **67**, 29 (1998).
24. T. V. Sreekumar, T. Liu, S. Kumar, L. M. Ericson, R. H. Hauge and R. E. Smalley, Single-wall carbon nanotube films, *Chem. Mater.* **15**, 175 (2003).
25. S. Badaire, C. Zakri, P. Poulin, V. Pichot, P. Launois, J. Vavro, M. Chen and J. E. Fischer, Correlation of properties with preferred orientation in extruded and stretch-aligned single wall carbon nanotubes, *J. Appl. Phys.* **96**, 7509 (2004).
26. L. M. Ericson, H. Fan, H. Peng, V. A. Davis, J. Sulpizio, Y. Wang, R. Booker, W. Zhou, J. Vavro, C. Guthy, S. Ramesh, C. Kittrell, G. Lavin, H. Schmidt, W. W. Adams, M. Pasquali, W.-F. Hwang, R. H. Hauge, J. E. Fischer and R. E. Smalley, Macroscopic, neat, single-walled carbon nanotube fibers, *Science* **305**, 1447 (2004).
27. R. Haggenmueller, W. Zhou, J. E. Fischer and K. I. Winey, Production and characterization of polymer nanocomposites with highly aligned single-walled carbon nanotubes, *J. Nanosci. Nanotech.* **3**, 105 (2003).
28. A. S. Claye, J. E. Fischer, C. B. Huffman, A. G. Rinzler and R. E. Smalley, Solid-state electrochemistry of the Li single-wall carbon nanotube system, *J. Electrochem. Soc.* **147**, 2845 (2000).
29. B. Vigolo, A. Penicaud, C. Coulon, C. Sauder, R. Pallier, C. Journet, P. Bernier and P. Poulin, Macroscopic fibers and ribbons of oriented carbon nanotubes, *Science* **290**, 1331 (2000).

30. J. E. Fischer, W. Zhou, J. Vavro, M. C. Llaguno, C. Guthy, R. Haggenmueller, M. J. Casavant, D. E. Walters and R. E. Smalley, Magnetically aligned single wall carbon nanotube films: preferred orientation and anisotropic transport properties, *J. Appl. Phys.* **93**, 2157 (2003).
31. S. Huang, X. Cai and J. Liu, Growth of millimeter-long and horizontally aligned single-walled carbon nanotubes on flat substrates, *J. Am. Chem. Soc.* **125**, 5636–5637 (2003).
32. W. Zhou, K. I. Winey, J. E. Fischer, S. Kumar and H. Kataura, Out-of-plane mosaic of single-wall carbon nanotube films, *Appl. Phys. Lett.* **84**, 2172 (2004).
33. H. H. Gommans, J. W. Alldredge, H. Tashiro, J. Park, J. Magnuson and A. G. Rinzler, Fibers of aligned single-walled carbon nanotubes: polarized Raman spectroscopy, *J. Appl. Phys.* **88**, 2509 (2000).
34. W. Zhou, J. Vavro, C. Guthy, K. I. Winey, J. E. Fischer, L. M. Ericson, S. Ramesh, R. Saini, V. A. Davis, C. Kittrell, M. Pasquali, R. H. Hauge and R. E. Smalley, Single wall carbon nanotube fibers extruded from super-acid suspensions: preferred orientation, electrical, and thermal transport, *J. Appl. Phys.* **95**, 649 (2004).
35. J. E. Fischer, Q. Zhu, X. Tang, E. M. Scherr, A. G. MacDiarmid and V. B. Cajipe, Polyaniline fibers, films, and powders — X-ray studies of crystallinity and stress-induced preferred orientation, *Macromolecules* **27**, 5094 (1994).
36. M. A. Pimenta, A. Marucci, A. Empedocles, M. G. Bawendi, E. B. Hanlon, A. M. Rao, P. C. Eklund, R. E. Smalley, G. Dresselhaus and M. S. Dresselhaus, Raman modes of metallic carbon nanotubes, *Phys. Rev. B* **58**, R16 016 (1998).
37. R. Haggenmueller, H. H. Gommans, A. G. Rinzler, J. E. Fischer and K. I. Winey, Aligned single-wall carbon nanotubes in composites by melt processing methods, *Chem. Phys. Lett.* **330**, 219 (2000).
38. P. Launois, A. Marucci, B. Vigolo, A. Derre and P. Poulin, Structural characterization of nanotube fibers by x-ray scattering, *J. Nanosci. Nanotechnol.* **1**, 125–128 (2001).
39. B. W. Smith, M. Monthioux and D. E. Luzzi, Encapsulated C-60 in carbon nanotubes, *Nature* **396**, 323 (1998).
40. B. Burteaux, A. Claye, B. W. Smith, M. Monthioux, D. E. Luzzi and J. E. Fischer, Abundance of encapsulated C-60 in single-wall carbon nanotubes, *Chem. Phys. Lett.* **310**, 21 (1999).
41. B. W. Smith, R. M. Russo, S. B. Chikkannanavar and D. E. Luzzi, High-yield synthesis and one-dimensional structure of C_{60} encapsulated in single-wall carbon nanotubes, *J. Appl. Phys.* **91**, 9333 (2002).
42. X. Liu, T. Pichler, M. Knupfer, M. S. Golden, J. Fink, H. Kataura, Y. Achiba, K. Hirahara and S. Iijima, Filling factors, structural, and electronic properties of C_{60} molecules in single-wall carbon nanotubes, *Phys. Rev. B* **65**, 045419 (2002).
43. P. M. Rafailov, C. Thomsen and H. Kataura, Resonance and high-pressure Raman studies on carbon peapods, *Phys. Rev. B* **68**, 193411 (2003).
44. T. Okazaki, K. Suenaga, K. Hirahara, S. Bandow, S. Iijima and H. Shinohara, Electronic and geometric structures of metallofullerene peapods, *Physica B: Cond. Matt.* **323**, 97–99 (2002).
45. B. W. Smith and J. E. Fischer, unpublished.
46. M. Hodak and L. A. Girifalco, Ordered phases of fullerene molecules formed inside carbon nanotubes, *Phys. Rev. B* **67**, 075419 (2003).
47. M. R. Stetzer, P. A. Heiney, J. E. Fischer and A. R. McGhie, Thermal stability of solid C60, *Phys. Rev. B* **55**, 127 (1997).
48. E. Kolodny, B. Tsipinyuk and A. Budrevich, The thermal stability and fragmentation of C_{60} molecule up to 2000 K on the milliseconds time scale, *J. Chem. Phys.* **100**, 8542 (1994).
49. S. M. Bachilo, M. S. Strano, C. Kittrell, R. H. Hauge and B. R. Weisman, Structure-assigned optical spectra of single-walled carbon nanotubes, *Science* **298**, 2361–2366 (2002).
50. C. L. Kane and E. J. Mele, Ratio problem in single-carbon nanotube fluorescence spectroscopy, *Phys. Rev. Lett.* **90**, 207401 (2003).
51. V. A. Davis, L. M. Ericson, A. N. G. Parra-Vasquez, H. Fan, Y. Wang, V. Prieto, J. A. Longoria, S. Ramesh, R. K. Saini, C. Kittrell, W. E. Billups, W. W. Adams, R. H. Hauge, R. E. Smalley and M. Pasquali, Phase behavior and rheology of SWNTs in superacids, *Macromolecules* **37**, 154–160 (2004).
52. W. Zhou, M. F. Islam, H. Wang, D. L. Ho, A. G. Yodh, K. I. Winey and J. E. Fischer, Small angle neutron scattering from single-wall carbon nanotube suspensions: evidence for isolated rigid rods and rod networks, *Chem. Phys. Lett.* **384**, 185–189 (2004).
53. B. I. Yakobson, Mechanical relaxation and "intramolecular plasticity" in carbon nanotubes, *Appl. Phys. Lett.* **72**, 918–920 (1998).

54. M. R. Falvo, G. J. Clary, R. M. Taylor II, V. Chi, F. P. Brooks, J. R. Washburn and R. Superfine, Bending and buckling of carbon nanotubes under large strain, *Nature* **389**, 582–584 (1997).
55. M. Treacy, T. W. Ebbesen and J. M. Gibson, Exceptionally high Young's modulus observed for individual carbon nanotubes, *Nature* **381**, 678–680 (1996).
56. Y. Q. Zhu, T. Sekine, T. Kobayashi, E. Takazawa, M. Terrones and H. Terrones, Collapsing carbon nanotubes and diamond formation under shock waves, *Chem. Phys. Lett.* **287**, 689–693 (1998).
57. F. Li, H. M. Cheng, S. Bai, G. Su and M. S. Dresselhaus, Tensile strength of single-walled carbon nanotubes directly measured from their macroscopic ropes, *Appl. Phys. Lett.* **20**, 3161–3163 (2000).
58. Z. L. Wang, R. P. Gao, P. Poncharal, W. A. De Heer, Z. R. Dai and Z. W. Pan, Mechanical and electrostatic properties of carbon nanotubes and nanowires, *Mater. Sci. Eng. C* **16**, 3–10 (2001).
59. M.-F. Yu, B. S. Files, S. Arepalli and R. S. Ruoff, Tensile loading of ropes of single-wall carbon nanotubes and their mechanical properties, *Phys. Rev. Lett.* **84**, 5552 (2000).
60. O. Inganäs and I. Lundström, Carbon nanotube muscles, *Science* **284**, 1281–1282 (1999).
61. T. V. Sreekumar, Tao Liu, S. Kumar, L. M. Ericson, R. H. Hauge and R. E. Smalley, Single-wall carbon nanotube films, *Chem. Mater.* **15**, 175–178 (2003).
62. J. Hone, M. Whitney, C. Piskoti, and A. Zettl, Thermal conductivity of single-walled carbon nanotubes, *Phys. Rev. B* **59**, R2514 (1999).
63. S. Berber, Y. K. Kwon and D. Tomanek, Unusually high thermal conductivity of carbon nanotubes, *Phys. Rev. Lett.* **84**, 4613 (2000).
64. P. Kim, L. Shi, A. Majumdar and P. L. McEuen, Thermal transport measurements of individual multiwalled nanotubes, *Phys. Rev. Lett.* **87**, 215502 (2001).
65. W. Yi, L. Lu, D. L. Zhang, Z. W. Pan and S. S. Xie, Linear specific heat of carbon nanotubes, *Phys. Rev. B* **59**, R9015 (1999).
66. J. Hone, B. Batlogg, Z. Benes, A. T. Johnson and J. E. Fischer, Quantized phonon spectrum of single-wall carbon nanotubes, *Science* **289**, 1730 (2000).
67. J. E. Fischer, Chemical doping of single-wall carbon nanotubes, *Acc. Chem. Res.* **35**, 1079 (2002).
68. J. C. Lasjaunias, K. Biljaković, Z. Benes, J. E. Fischer and P. Monceau, Low-temperature specific heat of single-wall carbon nanotubes, *Phys. Rev. B* **65**, 113409 (2002).
69. J. Hone, M. C. Llaguno, N. M. Nemes, J. E. Fischer, D. E. Walters, M. J. Casavant, J. Schmidt and R. E. Smalley, Electrical and thermal transport properties of magnetically aligned single-wall carbon nanotube films, *Appl. Phys. Lett.* **77**, 666 (2000).
70. J. Vavro, M. C. Llaguno, B. C. Satishkumar, D. E. Luzzi and J. E. Fischer, Electrical and thermal properties of C-60-filled single-wall carbon nanotubes, *Appl. Phys. Lett.* **80**, 1450 (2002).
71. J. Vavro, M. C. Llaguno, B. C. Satishkumar, R. Haggenmueller, K. I. Winey, D. E. Luzzi, J. E. Fischer, G. U. Sumanasekera and P. C. Eklund, Electrical and thermal properties of C-60-filled single-wall carbon nanotubes, in *Molecular Nanostructures*, H. Kuzmany, J. Fink, M. Mehring and S. Roth, Eds., *AIP Conf. Proc.* **633**, 127 (2002).
72. J. E. Fischer, H. Dai, A. Thess, R. Lee, N. M. Hanjani, D. DeHaas and R. E. Smalley, Metallic resistivity in crystalline ropes of single-wall carbon nanotubes, *Phys. Rev. B* **55**, R4921 (1997).
73. M. S. Fuhrer, M. L. Cohen, A. Zettl and V. Crespi, Localization in single-walled carbon nanotubes, *Solid State Commun.* **109**, 105 (1998).
74. R. S. Lee, H. J. Kim, J. E. Fischer, A. Thess and R. E. Smalley, Conductivity enhancement in single-walled carbon nanotube bundles doped with K and Br, *Nature* **388**, 255 (1997).
75. M Radosavljevic, Improving carbon nanotube nanodevices: ambipolar field effect transistors and high current interconnects, PhD thesis, University of Pennsylvania (2001).
76. P. Sheng, Fluctuation-induced tunneling conduction in disordered materials, *Phys. Rev. B* **21**, 2180 (1980).
77. J. Vavro, J. M. Kikkawa and J. E. Fischer, Metal–insulator transition in doped single-wall carbon nanotubes, *Phys. Rev. B* **71**, 155410 (2005).
78. T. Pichler, M. Knupfer, M. S. Golden, J. Fink, A. Rinzler and R. E. Smalley, Localized and delocalized electronic states in single-wall carbon nanotubes, *Phys. Rev. Lett.* **80**, 4729 (1998).
79. X. Liu, T. Pichler, M. Knupfer and J. Fink, Electronic and optical properties of alkali-metal-intercalated single-wall carbon nanotubes, *Phys. Rev. B* **67**, 125403 (2003).
80. J. Hwang, H. H. Gommans, A. Ugawa, H. Tashiro, R. Haggenmueller, K. I. Winey, J. E. Fischer, D. B. Tanner and A. G. Rinzler, Polarized spectroscopy of aligned single-wall carbon nanotubes, *Phys. Rev. B* **62**, R13310 (2000).

81. M. F. Islam, D. E. Milkie, C. L. Kane, A. G. Yodh, and J. M. Kikkawa, Direct measurement of the polarized optical absorption cross section of single-wall carbon nanotubes, *Phys. Rev. Lett.* **93**, 037404 (2004).
82. N. M. Nemes, J. E. Fischer, K. Kamarás, D. B. Tanner and A. G. Rinzler, Synthesis, isolation and characterisation of new alkaline earth endohedral fullerenes, in *Molecular nanostructures*, H. Kuzmany, J. Fink, M. Mehring and S. Roth, Eds., *AIP Conf. Proc.* **633**, 259 (2002).
83. B. Ruzicka, L. Degiorgi, R. Gaal, L. Thien-Nga, R. Bacsa, J.-P. Salvetat and L. Forró, Optical and dc conductivity study of potassium-doped single-walled carbon nanotube films, *Phys. Rev. B* **61**, R2468 (2000).
84. W. Zhou, J. Vavro, N. M. Nemes, J. E. Fischer, F. Borondics, K. Kamaràs and D. B. Tanner, *Phys. Rev. B* **71**, 205423 (2005).
85. J. Vavro, M. C. Llaguno, J. E. Fischer, S. Ramesh, R. K. Saini, L. M. Ericson, V. A. Davis and R. E. Smalley, Thermoelectric power of p-doped single-wall carbon nanotubes and the role of phonon drag, *Phys. Rev. Lett.* **90**, 065503 (2003).
86. C. L. Kane and E. J. Mele, Size, shape, and low-energy electronic structure of carbon nanotubes, *Phys. Rev. Lett.* **78**, 1932 (1997).
87. C. L. Kane and E. J. Mele, Ratio problem in single-carbon nanotube fluorescence spectroscopy, *Phys. Rev. Lett.* **90**, 207401 (2003).
88. A. Thess, R. Lee, P. Nikolaev, H. Dai, P. Petit, J. Robert, C. Xu, H. Lee, S. G. Kim, D. T. Colbert, G. Scuseria, D. Tomanek, J. E. Fischer and R. E. Smalley, Crystalline ropes of metallic carbon nanotubes, *Science* **273**, 483 (1996).
89. P. Petit, E. Jouguelet, J. E. Fischer, A. Thess and R. E. Smalley, Electron spin resonance and microwave resistivity of single-wall carbon nanotubes, *Phys. Rev. B* **56**, 9275 (1997).
90. A. S. Claye, N. M. Nemes, A. Janossy and J. E. Fischer, Structure and electronic properties of potassium-doped single-wall carbon nanotubes, *Phys. Rev. B* **62**, R4845 (2000).
91. A. A. Maarouf, C. L. Kane, and E. J. Mele, Electronic structure of carbon nanotube ropes, *Phys. Rev. B* **61**, 156 (2000).
92. O. Cespedes, M. S. Ferreira, S Sanvito, M. Kociak and J. M. D. Coey, Contact-induced magnetism in carbon nanotubes, *J. Phys.: Condens. Matter* **16**, L155–L161 (2004).
93. R. Saito, G. Dresselhaus and M. S. Dresselhaus, Physical properties of carbon nanotubes, Imperial College Press, London, 1999
94. A. Yu. Kasumov, R. Deblock, M. Kociak, B. Reulet, H. Bouchiat, I. I. Khodos, Yu. B. Gorbatov, V. T. Volkov, C. Journet and M. Burghard, Supercurrents through single-walled carbon nanotubes, *Science* **284**, 1508–1511 (1999).
95. Z. K. Tang, L. Zhang, N. Wang, X. X. Zhang, G. H. Wen, G. D. Li, J. N. Wang, C. T. Chan and P. Sheng, Superconductivity in 4 Å single-walled carbon nanotubes, *Science* **292**, 2462–2465 (2001).

5 Chemistry of Carbon Nanotubes

Eduard G. Rakov
D.I. Mendeleev University of Chemical Technology,
Moscow, Russia

CONTENTS

ABSTRACT

The main trends and recent achievements in carbon nanotube chemistry are reviewed. Apart from "traditional" subjects such as opening, filling, and decoration of nanotubes, some new subjects have also been discussed. A special emphasis has been placed on the functionalization and solubilization of carbon nanotubes, their self-assembly, film and fiber formation, and sensor and biosensor preparation. Some basics on carbon nanotubes are introduced.

5.1 INTRODUCTION

Owing to their electronic, mechanical, optical, and chemical characteristics, carbon nanotubes (NTs) attract a good deal of attention from physicists, chemists, biologists, and scientists from several other fields.[1–5] Possible applications in the fields of molecular electronics, nanomechanic devices, information display, sensoring, energy storage, and composite materials are of interest for industry.[6]

The perspectives of NT application are greatly dependent on NT chemistry. Chemical behavior of NTs is very diverse and the processes of NT synthesis, purification, modification, and solubilization[7,8] all contribute to this diversity.

There are different ways to modify NTs:

- Partial oxidation and decapping (opening) of NTs
- Attachment of functional groups to the open ends of NTs
- Attachment of functional groups to the sidewalls of NTs
- Chemical reactions of functionalities attached to NTs
- Filling of inner cavities of the NTs with different substances (gaseous, liquid, or solid) and carrying out a chemical reaction inside the NTs
- Replacement of the carbon atoms of NTs by atoms of other chemical elements or groups
- Intercalation (insertion) of "guest" atoms or molecules into the intertubular space of single-wall NTs (SWNTs) bundles or in between the walls of multi-wall NTs (MWNTs)
- Decoration of outer walls of NTs and using NTs as templates
- Adsorption of gases

NTs having very large molecular weights cannot form true solutions. Therefore, solubilization of NT means the formation of their colloid solutions (dispersions). The solubilization can be subdivided into the formation of aqueous, organic, or polymeric dispersions.

The geometry and size of NTs allows them to take part in self-assembly and aligning processes. The directional deposition on certain surfaces, structuring by Langmuir–Blodgett films and by liquid crystals, and formation of colloidal systems are mentioned here.

In its chemical behavior, NTs partially resemble graphite and fullerenes; however, there are also noticeable differences from both graphite and fullerenes.[8,9] Graphite represents a typical layered polymeric crystal and each fullerene can be considered as a molecule which can form molecular crystals (fullerites). However, a great many NTs cannot be classified as either usual molecules or crystals. SWNTs are similar to polymeric molecules of simple substances and MWNTs resemble structured nanoparticles. The individual NT can be also assumed as 1-D crystal and well-ordered NT bundles as 2-D crystals.

Graphite has planar structure corresponding to sp^2 for σ bonds and p for π bond. Fullerenes and NTs have hybrid bonding orbitals between sp^2 and sp^3. NTs having low percentage of sp^3 bonds are in this regard nearer to graphite. All these bonds in straight NTs are concentrated in half-spherical or conical caps, and in curved NT they are concentrated in the bends. The difference in chemical activity between NT caps and sidewalls as well as between straight and curved NTs is determined by the sp^2:sp^3 bonds ratio.

Specific chemical properties of graphite, fullerenes, and NTs as well as of fullerenes or NTs of different diameters are also different owing to dissimilar surface curvatures.[10]

The chemistry of new carbon allotropes has been described with a pyramidalization angle θ_p formalism.[11] For graphite, $\theta_p = 0°$. All carbon atoms in C_{60} have $\theta_p = 11.6°$. Pyramidalization angle of SWNTs (n, n) of various n (n = 2 to 10) is calculated to vary between 14–17° and 2°.[12] Pyramidalization changes the hybridization of atomic orbitals at the C atom so that the π orbital contains different portions of s and p orbitals, leading to different chemical reactivity. Because of this hybridization, fullerenes and NTs are known to be more reactive than graphite. The deformation energy of sp^2 bond is inversely proportional to the diameter of NT, and therefore tubes with smaller diameter have greater reactivity. The enthalpy of the reaction decreases with increase in the diameter. The enthalpy of homolytic reactions of H atoms and methyl radicals with atoms of curved carbon plane is linearly dependent on the pyramidalization angle and can differ by 1 eV.[13]

The cups of NT, which are often similar to fullerene molecule halves, contain more reactive C atoms, than the sidewalls. Experimental evidence of the higher chemical reactivity of conformationally strained carbon sites in MWNTs has been reported.[14]

NTs exhibit more differences owing to various structure and morphology (kinked, branched, conical NTs, etc.).[15] The NTs differ from fullerenes by the larger size of internal cavity, and from graphite by the greater share of accessible surface sites.

Fullerites, graphite, and NTs contain van der Waals gaps, which on being filled can form intercalates, or "guest–host" compounds. The dimensionality of such compounds is different: 0-D for fullerites, 2-D for graphite, and 1-D for NTs. NTs can form "guest–host" compounds of different types: for instance, the "guests" can exist in the inner cavity of SWNT or MWNT, in the intertube space of the bundled NTs, or in between the walls of MWNTs having scroll structure.

The development of the chemistry of NTs will determine the fields of their practical application. Primarily, NT chemistry is involved with the rational routes of NT purification and sorting. Chemical modification of NTs can open the way to modify the properties of these materials.

Unlike physical investigation of the solid-state properties of NTs, the study of their chemical reactivity is still in its infancy. At the same time, there have been very impressive achievements in the study of the chemistry of NTs in recent years. There are a large number of original publications and some reviews on the subject.[8,10,16–21] The present review pertains mainly to works in the last five years.

5.2 CARBON NANOTUBE MORPHOLOGY AND STRUCTURE

Dozens of different morphological varieties of filamentous carbon nanoparticles were revealed in a remarkably short period of time after the discovery of "classical" NTs. As was mentioned by Hilding et al.,[10] NTs can differ by "aspect ratio, NT diameters, surface structures, defect densities, and physical entanglements."

The NT of the "classical" type represents a cylindrical particle formed from graphene — a flat carbon net with the atoms located in the corners of joined hexagons. They may be single-walled with a diameter between ~0.3 and ~5.0 nm (typical SWNTs have diameters of 1.0 to 1.4 nm, and length up to 50 to 100 μm) or multi-walled. SWNTs as a rule contain less topological defects and possess better mechanical and electrophysical properties. The specific surface area of SWNTs is independent of their diameter and is equal to 1315 m^2/g (for outer surface).

MWNTs consist of several (from two to tens) coaxial tubes, with outer diameter of ~1.4 to 100 nm. Their specific surface area depends on the number of walls, and to a lesser extent on the diameter of the inner tube. The theoretical surface area of double-wall NTs is between 700 and 800 m^2/g, and of ten-wall NTs is about 200 m^2/g. Nanofibers (NFs) have a diameter from tens to hundreds of nanometers.

Some MWNTs and NFs have internal cross connections formed by curved graphenes. A moderate relative number (density) of cross connections correspond to a "bamboo-like" structure of

MWNT, while a high relative number of connections may be attributed to conical structures such as "herringbone-like" or "cup-stacked" types. The angle of conicity in the conical structures varies from 15 to 85°. Grafene layers in NFs may also be located perpendicular to the fiber axis. Nanofibers having regularly changing diameter ("nanobeads") have been synthesized.[22] And finally, there are amorphous NTs or NFs.

SWNTs, MWNTs, and NFs can spontaneously form "secondary" structures. A classification of carbon nanotubular particles into primary, secondary, and tertiary forms was first introduced by De Jong and Geus.[23] The most popular secondary form of the SWNT is a bundle ("rope"), which consists of tubes in a 2-D triangular lattice, with a lattice constant of 1.7 nm. The bundles usually have greater lengths as compared to individual NTs. For example, 1-m-long bundles of NTs have been produced. They can combine to form a structure of higher order. Tangled SWNTs or MWNTs can form "bucky paper" ("nanopaper" and "nanomats").

Single-walled nanohorns (nanocones) quite often combine to produce flower- or bud-like structures.

"Secondary" structures formed by MWNTs are more diverse. The formation of bundles of MWNT is less typical. More often, kinked (L-shaped) and branched (Y-, T-, H-like, "octopus," tree-like) forms were synthesized. Tangled MWNTs form aggregates up to 3 mm in diameter ("worms" and "boiled spaghetti"). The aggregates alongwith conical "ceder forest," and "bucky pearl" some others are the members of "tertiary" structure.

A pyrolytic synthesis sometimes yields coiled NTs, helixes, double helixes, helixes inside NTs, and even more complex structures, such as brushes, entangled worm-like features, and foil-like structures at the nanometer scale. Transitional forms, such as nanopeas (fullerenes inside SWNTs), are also among the structures formed.

The chemistry of different structures must be notably diverse. This diversity has not been studied yet, and the overwhelming majority of published results pertain to SWNTs, SWNT bundles, and MWNTs.

5.3 SYNTHESIS OF CARBON NANOTUBES

There are two main methods or groups of processes of NT synthesis: sublimation of graphite with subsequent desublimation, and decomposition of carbon-containing compounds.[5,7,24] The first group of processes is associated with high temperatures (up to 4000°C), which can be obtained in electric arcs (see, for example, Refs. 25–29), by the process of laser ablation,[29–34] by focused solar radiation,[34,35] or by resistive heating of graphite.

The arc process is remarkable for the larger number of versions, among which some versions allow the realization of a semicontinuous process in automated facilities. Arching process in liquid nitrogen,[36,37] in water,[36] and in aqueous solutions[38,39] have also been developed.

Arching processes in gaseous[40] or liquid[41,42] hydrocarbons are classified as combined methods, where the pyrolysis of hydrocarbons takes place along with the sublimation–desublimation of graphite.

The arc-discharge technique is a popular method. The main disadvantages of the method lies in the difficulty of organizing a continuous process, the concurrent formation of amorphous carbon, metal clusters coated with carbon and in some cases fullerenes along with NTs. The total yield of SWNT, as a rule, does not exceed 20 to 40%.

The second group of methods has its own variations: pyrolysis of gases (chemical vapor deposition, CVD process), solids (e.g., pyrolysis of polymers), aqueous solutions (hydrothermal synthesis),[43,44] or organic solutions (supercritical toluene).[45]

The CVD method can produce NTs in large quantities and can be realized at temperatures of 500 to 1300°C. In accordance with the chemical composition of the carbon source, the method can be subdivided on the disproportionation of CO,[29,33,46] the pyrolysis of hydrocarbons (CH_4, C_2H_2, C_6H_6, etc., including polymers),[23,47–49] pyrolysis of CH_xO_y compounds (for example, alcohols[50]), and pyrolysis of heteroatomic $CH_xA_yB_z$ compounds (A, B = N, O, S, Cl, …, e.g., amines).

It is also possible to synthesize NTs via a template method, applying, for example, porous anodic alumina membrane. CVD using hydrocarbons as NT precursors over patterned catalyst arrays leads to the formation of different complex structures and opens up exciting opportunities in nanotechnology.[48]

The thermal disproportionation of CO is realized in two main variants: HiPco[2,5,46] and CoMoCAT.[5,51] These methods are considered by American researchers as the most promising for the commercial production of SWNTs.

High-value NTs, viz. SWNTs, are produced at temperatures of 900 to 1200°C, mainly using CO or CH_4 as a precursor. The availability of precursors, such as C_2H_2, methanol, and ethanol, for SWNT synthesis is also shown. SWNTs in all instances are produced only by catalytic reactions.

Methods other than the ones mentioned above, for example, thermal decomposition of metal carbides[7,52,53] or carbonitrides,[54] chlorination of carbides,[7] electrolysis of molten salts,[7] interaction of cesium metal with microporous carbon,[7] defoliation of graphite by forming and subsequent transformation of "guest-host" intercalated compound, transformation of fullerenes C_{60} and C_{70},[55] "rapid thermal processing" of amorphous carbon film containing iron,[56] sonochemical production,[57] AC plasma processing,[58] etc., are not widely used.

5.4 OPENING OF CARBON NANOTUBES

Independent of their synthesis method, pristine SWNTs have large aspect ratio (10^3 to 10^4) and closed ends. Open-ended NTs offer unique possibilities as conduits for flow of low-surface-tension fluids through their cylindrical pores. Applications of NTs in molecule separation devices, in biocatalysis, in molecule detection, and as encapsulation media have been proposed. The end cups on NTs must be destroyed to make the inner cavity available for filling. The simplest method to open NTs is their oxidative treatment. The oxidation tends to initiate on the end cups, thus providing a mechanism for opening the NT. The treatment is accompanied by functionalization of NTs with oxygen-containing groups (see below).

Liquid or gaseous chemical agents are used as oxidants. Refluxing, sonication, or microwave (MW) digestion in concentrated acids, such as HNO_3, H_2SO_4 and their mixtures, are the most popular methods of oxidation. Refluxing of MWNTs in concentrated HNO_3 leads not only to oxidative opening, but also in the reduction of the NT length and diameter as well as the breaking of entangled MWNTs.[59] Treatment of SWNTs results in tube cutting and narrowing of diameter distribution.[60,61] The bundles of SWNTs become disordered and partly exfoliated, when they are immersed in 70% HNO_3 for a long period of time.[62] Nitric acid can be intercalated into SWNT bundles, in that way disintegrate the tube walls into graphitic flakes and then reforms them into various multi-shell phases such as MWNTs, cone-shaped phases, and onion-like phases.[63] A prolonged treatment of SWNTs leads to amorphization and complete destruction of the tubes.

Bundles in raw SWNT material are significantly thinner (<10 NTs) than those found in sonicated and HNO_3-oxidized samples (>30 NTs).[64,65] It has been suggested that this thickening is promoted by the H-bonding between –COOH sidegroups formed during oxidation.

The concentrated H_2SO_4/HNO_3 mixture (3:1) is a better agent for cutting SWNTs[60,66] and for enrichment of large-diameter SWNTs.[67,68]

Oxidation of SWNTs with H_2O_2 is a common tube-opening procedure.[69–71] SWNTs react exothermically with the H_2SO_4/H_2O_2 mixture.[60] Oxidation in solution ($HNO_3/H_2O_2/H_2SO_4$) has been found to be effective for opening SWNTs. Aqueous solutions of OsO_4, $OsO_4/NaIO_3$,[72] RuO_4, $KMnO_4$, $H_2SO_4/KMnO_4$, $H_2SO_4/(NH_4)_2S_2O_8$[73] have also been successively used to open NTs. Superacids such as HF–BF_3, have been shown to act as an etchant of NTs at room temperature.

The opening of MWNTs can be realized at room temperature electrochemically in H_2SO_4[74] or in dilute aqueous KCl solutions.[75] Supercritical water acts on MWNT as an opening and thinning agent.[76]

Gaseous thermal oxidation is more effective than acid treatment. Thinner SWNTs burn more quickly than thicker SWNTs during oxidation by oxygen gas.[77,78] Fixed ambient air,[79,80] fixed air activated by microwave irradiation,[81] air flow,[82–84] 5% O_2/Ar mixture,[85,86] reduced O_2 atmosphere,[61] O_2/H_2S mixture,[87,88] O_2, and H_2O plasma[89] used for oxidation. It has been shown that the oxidative stability of SWNT is higher than that of amorphous carbon but lower than the oxidative stability of graphitic carbon.

The pore structure and specific surface area of SWNT aggregates are changed by air oxidation.[82] However, unlike oxidation with H_2SO_4/HNO_3 (3:1) solution, the air oxidation process preferentially oxidizes SWNTs without introducing sidewall defects.[90] The air oxidation rate of SWNTs is clearly correlated to the amount of metal impurity. Ultrafine gold particles catalyze the oxidation.[91]

A mechanism for oxidative etching by O_2 includes adsorption of O_2 molecules on the tube cup or wall, successive transformation of adsorbed molecules, and tube cup being etched away.[92] Defective sites on the ends and the walls of MWNTs facilitate the thermal oxidative destruction of the tubes.[93] The kinetics of oxidation in an air flow has been studied at 400 to 450°C.[94] The apparent activation energy of oxidation has been found to be equal to 150 kJ/mol and corresponds to the data for oxidation of carbon soot.[95] A kinetic model of the process has been proposed.[84]

Ozone at reduced or room temperature[96–101] and CO_2/Ar (2:1) mixture at 600°C[102] are suitable for the oxidation of NTs.

As a rule, the oxidation procedure is used for the purification of crude SWNTs and MWNTs containing amorphous carbon, catalyst, and graphitic nanoparticles. Acid reflux followed by thermal oxidation or reciprocal manner of treatment are common.[5,9,10,79,83,85,86,103–105] Acid treatment of SWNTs in combination with tangential filtration[106] or centrifugation[104] have been tested. Microwave acid digestion allows a reduction in the operational time.[107] In some cases, HCl[71,108] or HF[109,110] is used for the dissolution of metal impurities. Multi-step purification procedures including acid treatment[80,111] or air oxidation[112,113] have been developed. Hydrogen peroxide has been shown to be an effective agent in the process of carbon nanostructure purification from amorphous carbon impurities.[114] The methods that are usually used to remove impurities from the as-prepared SWNT material lead to hole-doped purified SWNTs.[115]

5.5 FUNCTIONALIZATION OF CARBON NANOTUBES

Functionalization allows the segregation of entangled or bundled NTs for their subsequent alignment. It is widely used for solubilization of NTs and for purification and classification of NTs in solutions. The surface modification of NTs plays an important role in their use in composites, providing strong fiber–matrix bonding and thus improving the mechanical properties of the material. The integration of NTs into integrated circuits and working devices, such as sensors and actuators requires robust, well-defined connections, for which few processes are better than covalent functionalization.

All the existing methods of chemical derivatization of NTs are divided into two groups, depending on whether attached moieties are introduced onto the NT tips or sidewalls. The use of the latter offers wider opportunities to change the original NT properties, since it allows high coverage with attached groups. The attachment can be realized either by covalent bond formation, or by simple adsorption via noncovalent interactions (hydrophobic, π stacking, etc.).

The covalent bonding can be realized via chemical or electrochemical reactions. The chemical functionalization involves oxidation, fluorination, amidation, and other reactions. Two main paths are usually followed for the functionalization of NTs: attachment of organic moieties either to carboxylic groups that are formed by oxidation of NTs with strong acid, or by direct bonding to the surface double bonds.[116]

Using NTs as either anode or cathode in an electrochemical cell enables oxidation or reduction of small molecules on the surface of the NT, leading to the formation of radical species which can be covalently bonded.

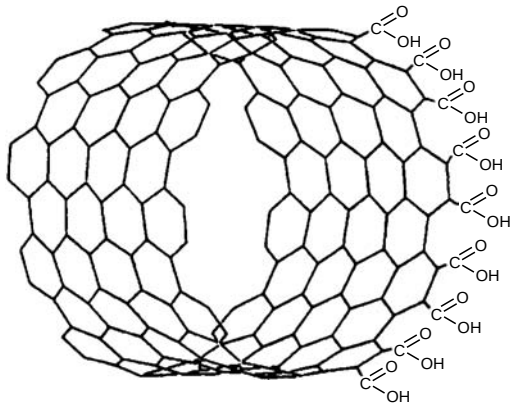

FIGURE 5.1 Structure of (10,10) SWNT–COOH.

5.5.1 Attachment of Oxidic Groups

By analogy with other carbonaceous materials, concentrated HNO_3 and mixtures of H_2SO_4 with HNO_3, H_2O_2, or $KMnO_4$ have been widely used for attaching acidic functionalities to NTs. First, acidic groups are attached to the open ends of SWNTs (Figure 5.1).

Refluxing NTs in a H_2SO_4/HNO_3 mixture results in a clear, colorless solution, which on evaporation of the solvent and removal of excess acid, gives a white solid containing functionalized NTs.[72] Neutralization of the acidic solution by alkali results in precipitation of a brown solid containing nanotubes.

The main acidic functionalities comprise –COOH, –C=O, and –OH groups[117] approximately in the proportion of 4:2:1.[118] The concentration of surface acid groups in the NTs treated by different oxidants varies in the range of 2×10^{20} to 10×10^{20} sites/g.[72] On a molar basis, the concentration of acid groups is equal to 5.5 to 6.7%,[119] ~6%,[120] ~5%[121] for shortened SWNTs or ~4% for full-length SWNTs.[122] Simple acid–base titration method shows that three different samples of purified SWNTs had about 1 to 3% of acidic sites and about 1 to 2% of –COOH functionalities.[123] The functional group concentration is time-dependent.

Treatment of SWNTs with concentrated H_2SO_4 containing $(NH_4)_2S_2O_7$ and P_2O_5, followed by treatment with H_2SO_4 and $KMnO_4$, results in the formation of material containing C/O/H in the atomic ratio of 2.7:1.0:1.2.[73]

A "one-pot" oxidative method via ozonolysis of the NT sidewall has been developed.[99] The ozonized NTs can react with several types of reagents, thus providing control over functional groups (Table 5.1).

Along with functionalization with carboxylic, alcoholic, aldehydic, and ketonic groups, acidic treatment leads to sizeable attaching of protons. The MWNTs after acidic purification contain 76.6% CH_x, 13.0% C–O, 4.2% C=O, and 6.2% N–C=O and O–C=O groups[124] $–CSO_3H$ groups are also attached using sulfuric acid.

Acid-functionalized, purified, and shortened SWNTs can be dispersed in water by sonication.[125] No tube precipitation was observed with solutions containing 0.03 to 0.15 g/L after a month. The solubility and stability of the solution are pH-dependent.

5.5.2 Reactions of Carboxylic Groups Attached to Nanotubes

The carboxylic groups at the SWNT tips can chemically react in organic solutions to form closed rings (Figure 5.2).[126] The average diameter of the rings is 540 nm with a narrow size distribution.

The most important aspect for further covalent or ionic functionalization is the possibility of exploiting carboxylic groups at the tube ends or walls. Amines are among the reagents that have drawn

TABLE 5.1
Relative Amounts of Different Surface Oxygenated Groups (%) on HiPco SWNTs Subjected to Ozonolysis at –78°C in Methanol Followed by Selective Chemical Treatment

Sample	C–OH	C=O	COOH, O–C=O
Ozonated	13.3	50.8	35.9
Treated with H_2O_2	37.0	9.4	53.6
Treated with DMS	28.7	41.1	30.2
Treated with $NaBH_4$	29.1	36.3	34.6

Source: From Banerjee, S. and Wong, S.S., *J. Chem. Phys.*, **B 106**, 12144–12151, 2002. With permission.

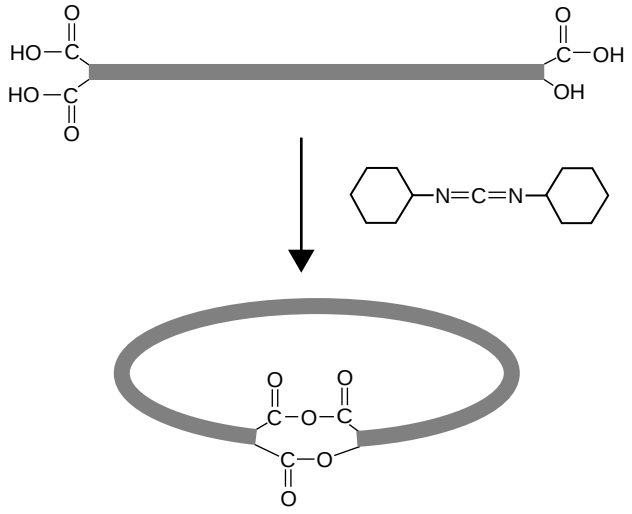

FIGURE 5.2 A possible scheme for the ring-closure reaction with 1,3- dicyclohexylcarbodiimide. (Reprinted with permission from Sano, M. et al., *Science*, **293**, 1299–1301, 2001.)

the greatest attention. There are three types of carboxylic group reactions with amines: (1) amidation, (2) acid–base interaction, and (3) condensation. Besides, amines can be physisorbed on NT walls.

Haddon and coworkers[118,120,127,128] pioneered the approach of functionalizing the carboxylic groups of shortened oxidized SWNTs through amidation with amines bearing long alkyl chains. To modify SWNTs with the amide functionality, the reactions shown in Figure 5.3 were used.

Shortened SWNTs were stirred in $SOCl_2$ containing dimethylformamide (DMF) at 70°C for 24 h, and after centrifugation, decantation, washing, and drying, the residual solid was mixed with octadecylamine (ODA) and heated at 90 to 100°C for 96 h. During this process, the volume of the SWNTs expanded several times.

The second and the third routes to attach amines are the direct reactions of carboxylic groups with amine (see Section 5.5.4).

The concentration of functional groups bound in SWNTs functionalized with $SOCl_2$ seems to be sensitive to gamma irradiation.[129] SWNTs and MWNTs containing acyl chloride groups are solubilized via poly(propionylethylenimine-*co*-ethylenimine) attachment.[130–132] Reaction with polyethyleneimine caused the formation of a product, which is soluble in chloroform.[133] MWNTs functionalized with –COCl groups can covalently attach polythiophene.[134]

The refluxing of functionalized NTs with an excess of $NaBH_4$ in absolute ethanol leads to the reduction of the carboxylic acid groups into hydroxyl groups.

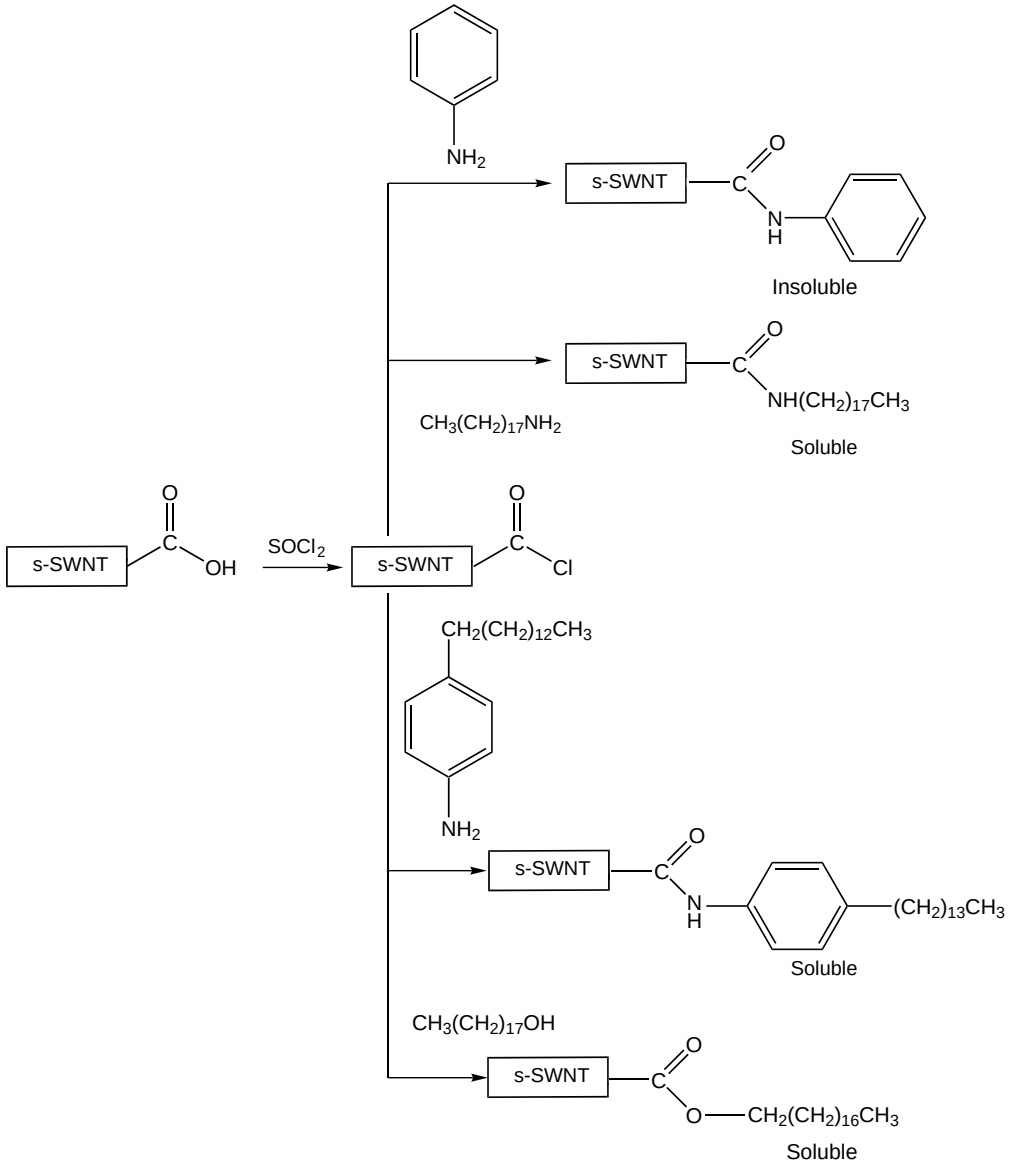

FIGURE 5.3 Covalent chemistry at the open ends of SWNTs. (Reprinted with permission from Niyogi, S. et al., *Acc. Chem. Res*., **35**, 1105–1113, 2002. Copyright 2002. American Chemical Society.)

Esterification of the NT ends or sidewalls after their carboxylation[130,135–141] differs from many other methods of functionalization in the simplicity of defunctionalization.[136] The attached groups can be easily removed by a hydrolysis reaction, catalyzed by acids or bases. The NTs evolve from the solution after hydrolysis.

Oxidized carbon atoms can act as specific sites for adsorption of metal ions.[142,143] The simplest reaction may be expressed by the equation

$$\text{NT–COOH} + \text{M}^{+}\text{X}^{-} \rightarrow \text{NT–COOM} + \text{HX}$$

Individual Pb^{2+}, Cu^{2+}, and Cd^{2+} ion-adsorption capacities are equal to 97, 28, and 11 mg/g, respectively.[143] Hg(II) ions form groups of two types: $(–COO)_2Hg$ and $(–O)_2Hg$, in the ratio (%) of

30:70.[142] Ultrasonication of a dispersion of MWNTs in water–isopropanol solution containing $RuCl_3 \cdot 3H_2O$ leads to Ru attachment.[144] The surface carboxylic groups are used to attach the relatively bulky metal complexes such as Vaska's complex (*trans*-$IrCl(CO)(PPh_3)_2$),[145] Wilkinson's complex ($RhCl(PPh_3)_3$),[146] and also TiO_2 or CdSe nanoparticles.[147,148] It has been shown that Ir coordinates to the NTs by two distinctive pathways. With raw tubes, the metal attaches as if the tubes were electron-deficient alkenes. With oxidized tubes, oxygen atoms form a hexacoordinate around the Ir atom. The Rh atom similarly coordinates to these NTs through the increased number of oxygenated species. The functionalization reaction, in general, appears to increase significantly oxidized NT solubility in DMF in the case of Vasca's and in dimethyl sulfoxide (DMSO) in the case of Wilkinson's.

Among the range of reagents tested, the most effective for MWNTs silylation were *N*-(*tert*-butyldimethylsilyl)-*N*-methyltrifluoroacetamide and 1-(*tert*-butyldimethylsilyl)imidazole.[149]

The oxidized groups present on SWNTs allow the formation of polymer/NT films by the alternate adsorption of the polyelectrolyte and SWNTs onto substrates.[150] Such groups on MWNT walls can react with 3-mercaptopropyl trimethoxysilane.[151] Alkoxysilane-terminated amide acid oligomers are used to disperse NTs.[152] Alkoxysilane functional ends on the oligomer, once hydrolyzed, react with functionalities on the ends of the purified SWNTs, thus leading to polymer formation.

The formation of NT arrays by self-assembling COOH-terminated NTs onto certain metal oxide substrates (e.g., Ag, Cu, Al) has been demonstrated.[153] In such reactions, the ability of carboxylic groups to deprotonate in contact with metal oxides is utilized.[20] An assembling acid-functionalized SWNTs on patterned gold surface has been developed.[154,155] The reaction mechanism is presumed to include an ester intermediate formation.

The carboxylated tips of NWNT are used to force titrations by atomic force microscope (AFM.[156]) The ability of carboxylic groups at the tips of NT to be readily derivatized by a variety of reactions allows the preparation of a wide range of molecular probes for AFM.[157,158]

Air heating of derivatized NTs at controlled temperatures and for controlled periods leads to the decomposition of carboxylic groups and to the formation of hydroxyl groups.[159] The carboxylic groups could be removed by thermal vacuum decarboxylation without damaging the electron system of the NTs, but defects remain on the tube walls.[65] It is generally accepted that carboxylic groups decomposed on heating to CO_2 gas and carbonyl groups, desorbed in the form of CO (Figure 5.4).[160,161] The CH_x groups decompos giving CH_4 and H_2.[161]

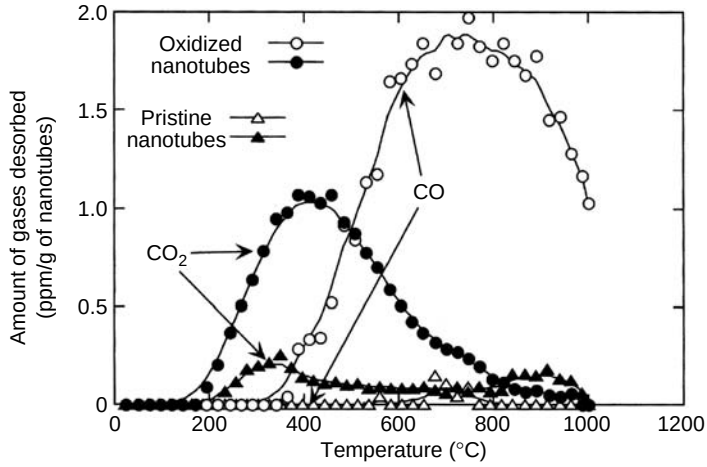

FIGURE 5.4 CO_2 and CO temperature programmed desorption patterns of oxidized and pristine NTs. (Reprinted from Kyotani, S. et al., *Carbon*, **39**, 771–785, 2001. With permision from Elsevier.)

5.5.3 FLUORINATION

Fluorination plays an important role in the chemistry of NTs because of the simplicity in acheiving a high degree of functionalization, the very high stability of fluorinated NTs, and the possibility to change the attached fluorine atoms to other functional groups. The fluorination reaction can easily be scaled-up.

The first work devoted to fluorination of fibrous carbon material was published by Nakajima et al.[162] before NTs were discovered. This work showed that the reaction starts at room temperature. The composition of the products prepared at fluorine pressure of 1 atm corresponds to $C_{8–12}F$.

After a decade, MWNTs were fluorinated at different temperatures and the formation of $(CF)_n$ at 500°C was documented.[163] A year later, French specialists, using a mixture of F_2–HF–IF_5 for fluorination of MWNTs, observed a modification of NT structure after reaction at high temperatures, and studied the electrochemical behavior of the fluorinated NT ("fluorotubes") as electrode material in a lithium cell.[164,165] The fluorination of MWNTs by vapor over a solution of BrF_3 in liquid Br_2 at room temperature revealed a decrease of cage nanoparticles in the fluorinated material relative to the pristine sample, which was connected with unrolling the NTs during fluorination.[166] Insufficient purity of the samples used in these works makes the full interpretation of the results difficult.

The amount of doped fluorine increases with increasing doping temperature. Doping at lower temperatures resembles the intercalation of graphite with fluorine and leads to the buckling of the outer MWNT walls.[167]

The fluorination of the internal surfaces of NTs, prepared by a template carbonization technique and which are less crystalline than those synthesized by arc discharge or laser methods, by elemental fluorine at 200°C shows that the resulting compound corresponds to $CF_{1.42}$.[168]

Fluorination of purified SWNTs in the form of "bucky paper," by flow of fluorine gas diluted by helium at a reaction time of 5 h demonstrated that the composition of fluorinated NTs varied from $CF_{0.1}$ at 150°C to $CF_{1.0}$ at 600°C.[169] It appeared that fluorination at 400°C and higher temperatures leads to destruction (e.g., "unzipping") of SWNTs, to the formation of structures resembling MWNTs, and to the evolution of gaseous products such as CF_4, C_2F_4, C_2F_6. Once fluorinated at temperatures up to 325°C, which corresponds to the formation of C_2F, SWNTs were defluorinated with anhydrous hydrazine and were rejuvenated. Partial or complete elimination of fluorine can be done by $LiBH_4/LiAlH_4$ treatment.[170]

In their subsequent works, Peng et al.[171] realized the fluorination of purified SWNTs with F_2/HF mixture at 250°C (HF acts as a catalyst).

Heat annealing of fluorinated SWNTs having C/F ratios between 2.0 and 2.3, in a flow of noble gas, indicates that NTs could be recovered at 100°C.[172] Tubes fluorinated at 250°C to a $CF_{0.43}$ stoichiometry lose fluorine on annealing under flowing helium gradually with increasing temperature.[173] Upon heating, the largest fluorine loss occurred between 200 and 300°C.

The fluorination of purified HiPco tubes to a stoichiometry CF_x ($x \leq 0.2$) followed by pyrolysis of partially fluorinated material up to 1000°C was found to have "cut" the NTs.[174] In an argon atmosphere, the fluorine was driven off the NT structure in the form of gaseous CF_4 and COF_2. Short bundles comprising strongly interacting individual NTs were found in the cut nanotube sample.

As a result of band-gap enlargement, the resistivity of fluorinated SWNT mat increases with increasing fluorination temperature, i.e., fluorine content.[175] The electronic properties are also altered by fluorination. As they are fluorinated, NTs reduce their tendency to self-agglomerate.

The most important property of fluorotubes is their ability to form soluble derivatives (Figure 5.5).[176–179]

Sidewall-alkylated NTs are obtained by interaction of fluorinated NTs with alkyl magnesium bromides in a Grignard synthesis or by reaction with alkyllithium precursors. The alkylated NTs are soluble in various organic solvents, including chloroform, methylene chloride, and tetrahydrofuran. For example, the solubility of hexyl-solubilized SWNTs in chloroform is up to ~0.6 g/L,

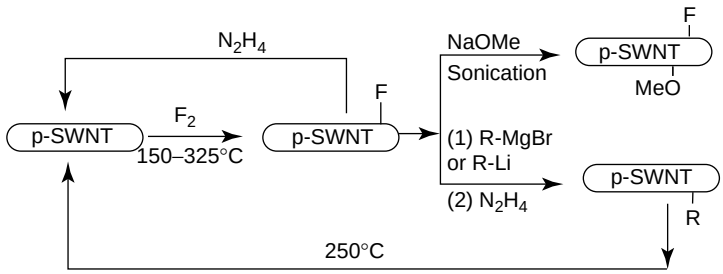

FIGURE 5.5 Sidewall fluorination of SWNTs and fluorine substitution reactions. (Reprinted with permission from Niyogi, S. et al., *Acc. Chem. Res.*, **35**, 1105–1113, 2002. Copyright 2002. American Chemical Society.)

in tetrahydrofuran to ~0.4 g/L, in methylene chloride to ~0.3 g/L, as compared with maximum concentration of 0.1 g/L of pristine NTs in DMF.

Sonication of SWNTs in some solvents for ~5 min also results in the selective solubilization of highly fluorinated (isopropanol) or sparcely fluorinated (DMF) samples. Fluorotubes can be solvated in alcohols yielding metastable solutions. Of the solvent used, 2-propanol and 2-butanol seemed to be the best, reaching SWNT concentration of 1 g/L. A probable mechanism of such solvation would be hydrogen bonding between the hydroxyl hydrogen atom in alcohol and NT-bound fluorine. Water, diethylamine, perfluorinated solvents, or acetic acid do not solvate NTs.

Fluorotubes dissolved in alcohols can react with alkoxides or terminal diamines such as $H_2N(CH_2)_nNH_2$ (n = 2, 3, 4, 6). They are capable of reacting with hydrogen peroxide, organic peroxides (e.g., lauroyl, benzoyl, *tert*-butyl), and with a number of solid inorganic compounds, such as alkali halides, Li_2S, ZnS, Li_2O_2, and AlP.

The atomic and electronic structures of fluorinated SWNTs have been examined in a few experimental and theoretical works.[175,180–188] As a result of fluorination, a significant charge transfer occurs from the NT wall to the fluorine atoms, resulting in partially ionic bonds. This transforms the non-polar SWNT to the polar one.

X-ray photoelectron spectroscopy can identify the type of bonding within CF_x compounds. The spectra of fluorinated samples give peaks appearing at 287 eV (semi-ionic C–F), at 288 to 299 eV (nearly covalent C–F), and at 292.0 to 294.05 eV (covalent CF_2 and CF_3).[175]

Fluorinated SWNTs are used to form composites with poly(ethylene oxide).[189]

5.5.4 AMIDATION

Amines, particularly ODA, have attracted special attention in the studies of functionalization of CNs. The SWNT–COOH product treated with oxalyl chloride at 0°C and then heated with ODA at 100°C, after purification contains 4 mol% of amine.[190] Shortened MWNTs attach considerably larger amounts of ODA, up to 41.7 wt%, after 96-h functionalization.[191]

Acid-chloride-functionalized SWNTs are used to attach glucosamine,[192] didecylamine,[193,194] 4-dodecyl-aniline, and 4-$CH_3(CH_2)_{13}C_6H_4NH_2$.[118] NTs functionalized with aniline prove to be soluble only in aniline, whereas NTs derivatized with tetradecylaniline are soluble in CS_2 and aromatic solvents. The anilination reaction solubilizes SWNTs and allows their purification chromatographically using excess of adsorbed aniline. A product with the ratio of NT carbons to aniline sites of 360:1 has been prepared by refluxing oxidatively end-cut SWNTs.[195] The functionalized group of MWNTs modified with aniline was determined to be $C_6H_6N^-$.[196] The terminal chlorinated carboxylic groups were used to append pyrenyl subunits[197] and *n*-pentyl ethers.[141]

SWNTs absorb MW radiation, and thus tubes can be rapidly heated by radiated. A procedure based on MW heating, which allow the attachment of monoamine-terminated poly(ethylene glycol) molecules to shortened SWNTs–COCl, has been developed.[198]

The acid-chloride-functionalized SWNTs were attached in pyridine suspension to chemically functionalized Si surfaces.[199]

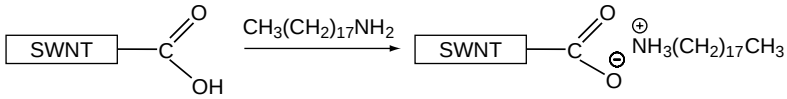

FIGURE 5.6 Zwitter-ionic functionalization of SWNTs. (Reprinted with permission from Niyogi, S. et al., *Acc. Chem. Res*., **35**, 1105–1113, 2002. Copyright 2002. American Chemical Society.)

It is supposed that SWNT in DMF can form covalent bonds with tenth generation poly(amidoamine) starburst dendrimer.[200] A "grafting-from" method has been developed for production of hyperbranched poly(amidoamine)-modified NTs.[201]

Solution of SWNTs in DMF derivatized with ODA is used for chromatographic purification procedure.[202] The NT end-to-side or end-to-end junctions are created by the reaction between modified NTs and diamines.[203,204]

The CdSe quantum dots were coupled to individual acid-chloride-modified SWNTs via amide-bond formation.[205]

Oxygen-containing groups that are present on NT tips can condense with alkoxysilane groups-terminated amide acid polymers and facilitate the formation of NT/polymer films for electrostatic charge mitigation.[152,206]

The simplest possible route to the solubilization of SWNTs is direct reaction of the molten amine with the shortened SWNT–COOH. Thus a simple acid–base reaction is realized and zwitterions are formed (Figure 5.6).[118] The products of the reaction are found to be soluble in tetrahydrofuran (THF) and CH_2Cl_2. Zwitterion-functionalized shortened SWNTs are used for length separation via gel permeation chromatography[207] and for selective precipitation of metallic SWNTs upon solvent evaporation.[208] The method is used to solubilize full-length SWNTs.[122] The derivatization of the oxidized MWNTs with triethylenetetramine leads to subsequent covalent bonding with the epoxy resin used as a matrix for MWNTs.[209] $^+NH_3(CH_2)_{17}CH_3$ ions, as has been stated, can readily exchange with other ions, e.g., metal ions.[11] Cysteamin allows the realization of thiolization reaction of carboxyl-terminated SWNTs and deposition of the NTs onto a gold surface.[210] A version of region-specific NT deposition onto prepatterned surface via amidation of acid-functionalized NTs is described.[211,212]

Sun et al.[213] studied the reaction and dispersal of noncarboxylated SWNTs by refluxing in aniline. Dark-red complexes are formed in the process. The solubility of SWNTs in aniline is up to 8 g/L. This aniline–NT solution can be readily diluted with other organic solvents such as acetone, THF, and DMF. As evidenced by their relatively high solubility in aniline, NTs may form donor–acceptor interactions with aniline.[213] Complexing with aromatic amines makes both single- and multi-wall tubes dispersable in organic solvents.

The condensation reaction of acid-functionalized SWNTs with 2-aminoethanesulfonic acid allows to supply the end of SWNT with sulfonic groups and enhance its solubility in water.[214] This technique has been used for attachment of aminopolymers.[132] The amidation of NT-bound carboxylic acids can be accomplished in diimide-activated reactions. Functionalization with poly(propionylethylenimine-*co*-ethylenimine) in the presence of 1-ethyl-3-(3-dimethylaminopropyl)carbodiimide has been found to be significantly improved in both efficiency and yield by sonication under ambient conditions.[215]

The attachment of poly(styrene-*co*-aminomethylstyrene) is possible under amidation reaction.[139] The ball-milling process in ammonia atmosphere allows the introduction of amine and amide groups onto MWNTs.[216]

Basiuk et al.[217] attempted to simplify convenient solution method, and to apply gas-phase derivatization of oxidized NTs containing carboxylic groups on their tips according to the equation

$$SWNT–COOH + HNR^1R^2 \rightarrow SWNT–CO–NR^1R^2 + H_2O$$

Nonylamine, dipentilamine, ethylenediamine, and propylenediamine[217] have been used as test compounds. This procedure consists of treating SWNTs with amine vapors under reduced pressure and at a temperature of 160 to 170°C. Amine molecules not only formed derivatives with SWNT tips but physisorbed inside SWNTs. The content of physisorbed nonylamine is about one order of magnitude higher than the amide content.

Theoretical consideration of the amidation reaction with methylamine shows that the formation of amide derivatives on carboxylated armchair SWNT tips is more energetically preferable than that on the zigzag NTs.[218]

The physisorption on metallic SWNTs causes no significant change in the electrical conductance, whereas adsorption of amines (such as butylamine and propylamine) on partial length of semiconducting NTs causes modulated chemical gating.[219]

Other works on amidation have been published; among them is the amidation of HiPco SWNTs,[220] and the functionalization of SWNTs with phthalocyanine molecules through amide bonds.[221]

5.5.5 Other Types of Covalent Bonding

Direct covalent functionalization of NT can be realized via addition of carbenes,[127,222–226] nitrenes,[223,227–229] 1,3-dipoles,[230–232] aryl cations,[19,233,234] and radicals (Figure 5.7).[19,233,235–241]

For direct functionalization, one can use processes such as ultrasonication in organic media,[10] plasma treatment, UV irradiation, or irradiation with energetic particles.

Carbenes have the general formula CRR′, where R, R′ = H, halogen, organic residuum, etc., and represent unstable compounds of bivalent carbon. Dichlorocarbene is an electrophilic reagent that adds to deactivated double bonds, but not to benzene. It is capable of attacking C=C bonds, replacing them by CCl_2 bridges. The addition of dichlorocarbene took place at the sidewall of both insoluble SWNT[222] and shortened SWNTs (s-SWNTs).[127] It was reacted with NTs in a refluxing chloroform/water suspension. Around 5% of chlorine was incorporated into or onto the SWNTs.[222]

Hu et al.[225] used dichlorobenzene solution of $PhCCl_2HgBr$ and showed that the addition of dichlorocarbene converts metallic SWNTs to semiconducting SWNTs. Thermal treatment of (s-SWNT)CCl_2 above 300°C results in the breakage of C–Cl bonds, but the electronic structure of the SWNTs was not recovered. Monthioux[224] published a method for dichlorocarbene formation and attachment to the SWNT by the decomposition of chloroform under UV irradiation. The $C{=}Cl_2$ bridges are assumed to be removed under UV treatment.

The two-level Our owN n-layered Integrated molecular Orbital + molecular mechanics Method (ONIOM) technique has been employed to study the [2+1] cycloadditions of dichlorocarbene, silylene, germilene, and oxycarbonitrene onto the sidewall of SWNT.[226] Results showed that the reactions are site-selective and yield three-membered ring species. The thermal stability of the SWNT derivatives follows the order oxycarbonitrene >> dichlorocarbene > silylene > germilene. The derivatives can be good starting points for further functionalization.

Nitrenes are analogs of carbenes; they represent unstable compounds of monovalent nitrogen and have general formula RN, where R = alkyl, aryl, getaryl, NR'_2, CN, etc. Among the methods of nitrene generation, thermal and photochemical decomposition of azides and other compounds should be mentioned. The addition of (R-)-oxycarbonyl nitrenes allows the bonding of a variety of different groups such as alkyl chains, aromatic groups, dendrimers, crown ethers, and oligoethylene glycol units.[227]

For functionalization based on the 1,3-dipolar cycloaddition of azomethine ylides,[230–232] the heterogeneous reaction mixture of SWNTs suspended in DMF together with excess aldehyde and modified glycine was heated at 130°C for 5 days. The modified NTs are remarkably soluble in most organic solvents ($CHCl_3$, CH_2Cl_2, acetone, methanol and ethanol) and even in water. The solubility of SWNTs in $CHCl_3$ is close to 50 g/L without sonication. The reactions were successful with the use of either short-oxidized or long-nonoxidized SWNTs, without notable differences in their solubility. The functionalized NTs are less soluble in toluene and THF, and practically insoluble in less polar solvents including diethyl ether and hexane.

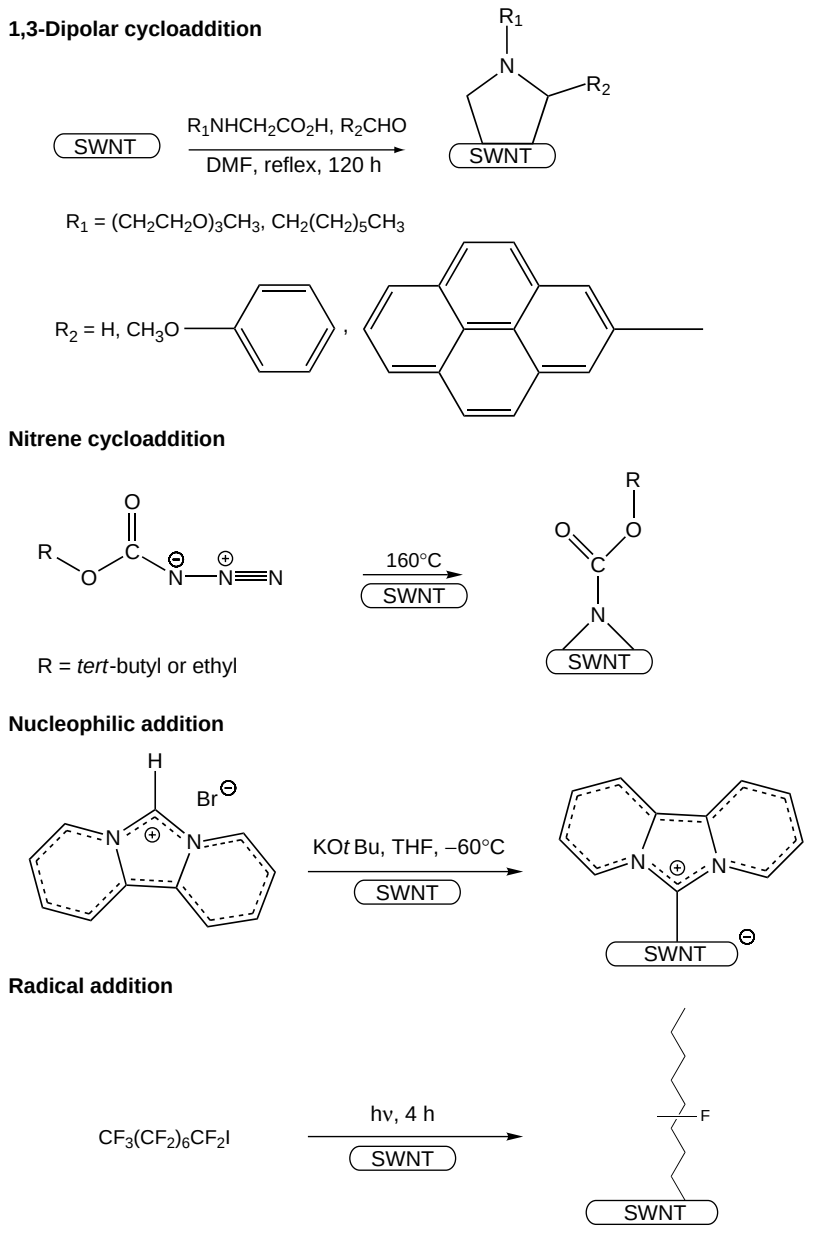

FIGURE 5.7 Sidewall covalent chemistry on SWNTs. (Reprinted with permission from Niyogi, S. et al., *Acc. Chem. Res.*, **35**, 1105–1113, 2002. Copyright 2002. American Chemical Society.)

It was reported that sonication and homogenization of a mixture of SWNTs and a monochlorobenzene solution of poly(methylmetacrylate) increased the ratio of shorter and thinner SWNTs[242–244] and led to the chemical modification of SWNTs.[245] Organic molecules decompose at the hot spots, and reactive species react with damaged SWNT sidewalls. FT-IR spectra show the formation of C–H and C=O groups. The sonication of purified SWNTs in monochlorobenzene solution leads to the formation of two kinds of modified SWNTs.[243,244] Sonochemical decomposition of *o*-dichlorobenzene[246] and 1,2-dichrorobenzene[247] also leads to the attachment of decomposition products to SWNTs and to the stabilization of SWNT dispersions. Other organic solvents

formed NT dispersions under sonication (see the next section) most likely by an analogous mechanism.

For the purpose of SWNT sidewalls functionalization using organic radicals, Ying et al.[239] decomposed benzoyl peroxide in the presence of alkyl iodides and obtained phenyl radicals. These radicals reacted with alkyliodides, which generated iodobenzene and alkyl radicals. The procedure allowed them to attach long-chain alkanes, alkyl halides, amides, nitriles, and ethers to the sidewalls of the NTs. Methyl radicals can also bond to the sidewalls, but the resulting NTs are generally insoluble in organic solvents.

Water-soluble diazonium salts can react with NTs.[233,235,237] A reactive radical can be produced by electrochemical reduction of different aryl diazonium salts using a bucky-paper electrode.[235] The estimated degree of functionalization is up to 5% of carbon atoms. Along with reductive coupling, it is possible to provide oxidative coupling (Figure 5.8).[238,248] The derivatization with aryl diazonium salts is not limited to the electrochemically induced reaction.[237]

NTs derivatized with a 4-*tert*-butylbenzene moiety exhibit the highest solubility in organic solvents. Solvent-free functionalization has short reaction times.[233]

Addition of diazonium salts to NTs suspended in aqueous solution opens a way to select chemically and separate NTs based on their electronic structure. Metallic NTs under certain controlled conditions give up electrons more readily than semiconducting NTs, a factor that the diazonium reagent can respond to.[240] The chemistry is reversible. Heating of the functionalized NTs in inert media at 300 to 400°C stimulates pyrolysis of arene groups and leads to restoration of the pristine electronic structure of NTs. This work also proves that the assumption that NT chemistry is controlled solely by their diameter (with smaller-diameter NTs being less stable) is in fact not always true.

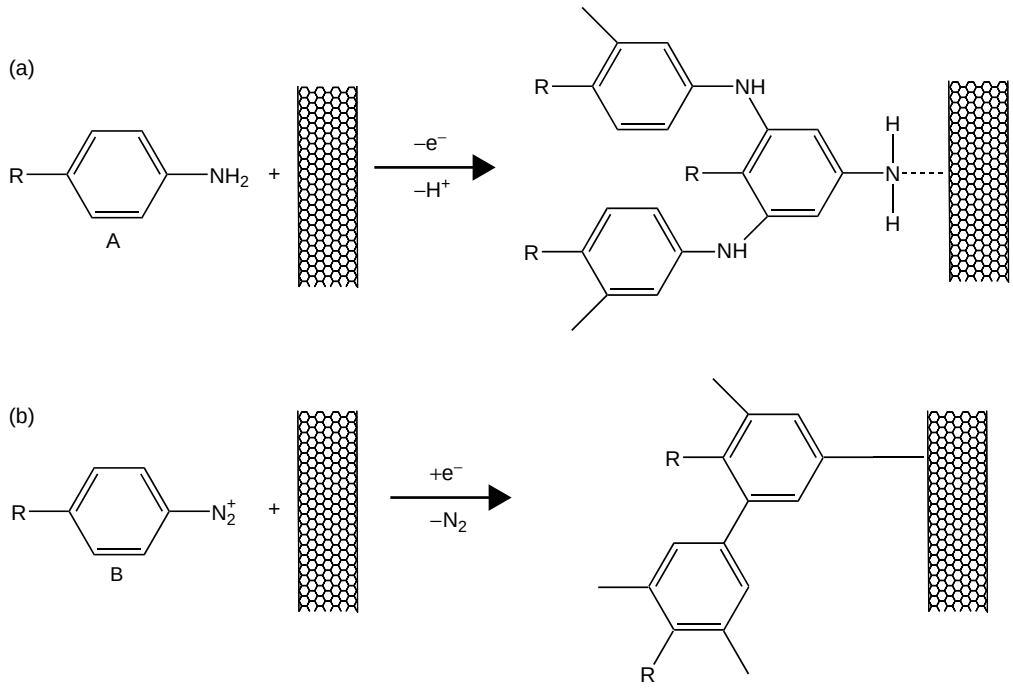

FIGURE 5.8 Oxidative (a) and reductive (b) electrochemical modification of SWNTs. The broken line in (a) indicates the formation of electro-polymerized layers of A on the SWNT, without the creation of chemical bonds. (Reprinted with permission from K. Balasubramanian, et al., *Adv. Mater*., **15**, 1517–1518 (2003).

Since organic thiol derivatives are generally well known to interact strongly with noble metal surfaces, therefore, the selective thiolation may be used to make a good electrical junction between a NT and a metal electrode, or to position the NT relative to a metal surface. The first thiolated NTs, NT–$(CH_2)_{11}$–SH, with long alkyl chains, were synthesized by Smalley and coworkers.[66] Because of the long and flexible alkyl chain, the latter compounds do not anchor on a metal surface in a specific orientation and give rise to a large contact resistivity. To overcome these problems, another type of compound, NT–CONH–$(CH_2)_2$SH, with a shorter alkyl chain, was synthesized.[210] The compound, however, contains an amide bond that tends to react easily in an acid or basic environment.

The new form of thiolated NT, which contains thiol groups almost directly linked to the body of NT, was synthesized by Lim et al.[249] The formation of NT–CH_2–SH is achieved via successive carboxylation, reduction, chlorination, and thiolation of the open ends of NTs.

Time-dependent plasma etching and irradiation with energetic particles can provide controlled introduction of defects and functionalities into NTs. Irradiation creates links between NTs, and leads to coalescence and welding of NTs (see, e.g., Refs. 250 and 251). Argon ion irradiation enhances the field emission of NTs.[252]

It has been shown that H_2O plasma can be used to open end-caps selectively of perpendicularly aligned NTs without any structural change.[253] The treatment of NTs with oxygen plasma at a low pressure for some minutes results in an oxygen concentration up to 14% and formation of outer layers consisting of hydroxide, carbonyl, and carboxyl groups.[254]

Interaction of SWNTs with high-energy protons at low irradiation doses causes the formation of wall defects.[255] The NTs curve at higher doses (>0.1 mC) and degrade into amorphous material at even higher doses (approaching 1 mC). The hydrogenation of NTs can be achieved in a cold MW plasma at low pressure.[256] A 30 sec exposure to a plasma of H_2 generated by glow-discharge results in near-saturation coverage of SWNT with atomic hydrogen.[257]

Calculations using molecular dynamics show that CH_3 radicals with energies of higher than 19 eV can attach to NT sidewalls.[258,259] The heat of the attachment reaction changes from ~0.8 eV for graphite to ~1.6 eV for fullerene C_{60}, and has intermediate, close to figures for graphite, values for NTs.[13]

The experiments show evidence of chemical functionalization of MWNTs by attachment of CF_3^+ ions at incident energies of 10 and 45 eV.[259] The exposure of SWNTs to CF_4 gaseous plasma leads to the formation of semi-ionic and covalent C–F bonds.[260,261] The ion bombardment does not result in loss of NT structure.[261]

Ion beams of certain energies can be used to create nanotube-based composites with improved adhesion between the filler and polymer matrixes as well as to create covalent cross-links between NTs and the C_{60} molecules.[262]

The modification of NTs is possible with acetaldehyde plasma activation.[212] Plasma-modified NTs improve the properties of nanotube-epoxy composites.[263] The hydrogen plasma treatment enhances field emission of NTs.[264] By using hydrothermal synthesis it is possible to produce hydrophilic SWNTs or MWNTs that are wetted by water and water solutions, because their outer and inner surfaces are terminated with OH groups.

An electrochemical derivatization method can also be used to attach carboxylate groups to NT walls (see Ref. 265 and references therein).

5.5.6 Noncovalent Bonding

Carbon NTs have been solubilized in water with the aid of surfactants, which can deposit on the NT surface and help to form stable colloidal dispersion. The repulsive force introduced by the surfactant overcomes the van der Waals attractive force between the carbon surfaces. However, there is a problem when the surfactant is removed from the NT surface.

Sodium dodecyl sulfate (NaDDS, $CH_3(CH_2)_{11}OSO_3Na$),[266–276] lithium dodecyl sulfate (LiDDS, $CH_3(CH_2)_{11}OSO_3Li$),[277–279] and sodium dodecylbenzene sulfonate (NaDDBS, $C_{12}H_{25}C_6H_4SO_3Na$)[280–284] are among the simplest and most popular surfactants used for NT solubilization.

At low NaDDS concentration, large and dense clusters of the initial NTs were still found after sonication. At higher surfactant concentrations, black and apparently homogeneous solutions, stable over several weeks, were obtained.[269] The phase diagram of the NaDDS–SWNT–water system is not a simple one.[271] The domain of homogeneously dispersed NTs is limited and has an optimum (good NT solubility and system stability) at ~0.35 wt% in NTs and 1.0 wt% in NaDDS.

Suspensions of MWNTs or SWNTs in water stabilized by 0.25% NaDDS solution have been used for purification and size separation of tubes.[266–268] An individual SWNT encased in close-packed columnar NaDDS micelle has a specific gravity of ~1.0, whereas that of an NaDDS-coated bundle has a specific gravity of ~1.2 or more.[270] Therefore, NaDDS suspensions (2 g/L) prepared by sonication of raw, solid SWNTs in 0.5% NaDDS solution are capable of separating bundled SWNTs from isolated individuals.[272] The MWNT dispersion stabilized by NaDDS allows the production of MWNTs/hydroxyapatite composites.[276]

Non-specific physical adsorption of NaDDBS allows the solubilization of lightweight fraction SWNTs in water.[280,282] The NT stabilization depends on the structure of surfactant molecules that lie on the tube, parallel to the cylindrical axis (Figure 5.9). It was possible to achieve relatively high SWNT concentration (up to 10 g/L as a mixture of isolated and small bundles of SWNTs) without nematic ordering in suspension. The optimum NT/surfactant ratio was found to be 1:10 (by weight). The properties of a dispersion depend on the sonication technique used (high-power or mild mode of operation, tip or bath sonicator). The mechanism of NT solubilization determines the hydrophobic forces between the surfactant tail and the NT surface. Each NT is covered by a monolayer of NaDDBS molecules, in which the heads form a compact outer surface of a cylindrical micelle.[283] The aqueous (D_2O) suspension in the presence of NaDDBS surfactant exhibits the presence of SWNT aggregates, but not rigid rods.[284]

The dispersing power of Triton X-100 (TX-100, $C_8H_{17}C_6H_4(OCH_2CH_2)_nOH$; $n \sim 9.5$),[60,66,131,280,285–288] sodium octylbenzene sulfonate ($C_8H_{17}C_6H_4SO_3Na$),[280] sodium butylbenzene sulfonate ($C_4H_9C_6H_4SO_3Na$),[280] sodium benzoate ($C_6H_5CO_2Na$),[280] dodecyltrimethylammonium bromide (DTAB, $CH_3(CH_2)_{11}N(CH_3)_3Br$),[280,289,290] cetyltrimethylammonium bromide (C_{16}TMAB, $CH_3(CH_2)_{14}CH_2N(CH_3)_3Br$),[291] cetyltrimethylammonium chloride ($CH_3(CH_2)_{14}CH_2N(CH_3)_3Cl$),[289] cetyl alcohol derivative ($CH_3(CH_2)_{14}CH_2(OC_2H_5)_{10}OH$),[291] pentaoxoethylenedodecyl ether ($C_{12}E_5$),[289] and hexadecyltrimethylammonium bromide ($CH_3(CH_2)_{16}N(CH_3)_3Br$)[292] have been studied. Both NaDDBS and TX-100 dispersed the NTs better than NaDDS, because of their benzene rings; NaDDBS dispersed better than TX-100 because of its headgroups and slightly longer alkyl chain.[280] DTAB and $C_{12}E_5$ solutions, at concentrations ranging from 0.05% to a few percent, do not stabilize the NTs.[289]

Ultrasonication of a mixture of distilled water and MWNTs in the presence of 5 vol% TX-100, followed by centrifugation to remove unsuspended material allows the production of a suspension of

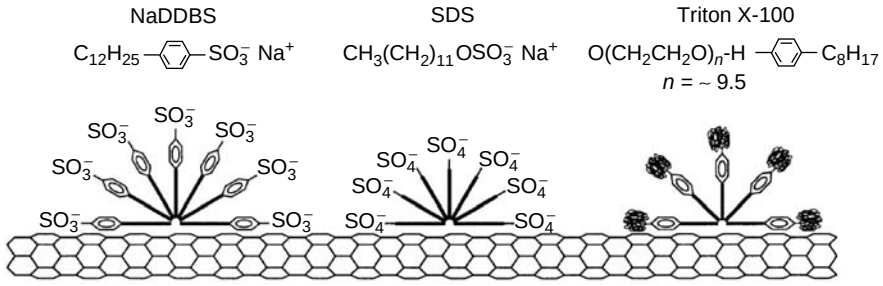

FIGURE 5.9 A representation of surfactant molecules adsorbed onto NT surface. (Reprinted with permission from Islam, M.F. et al., *Nano Lett.*, **3**, 269–273, 2003. Copyright 2003. American Chemical Society.)

concentration of 0.1 g/L.[287] An aqueous (or alcoholic) solution of TX-100 has been used to prepare SWNT dispersion, followed by alignment under AC electric field.[286] Such dispersions are suitable to prepare thin film coatings on flexible plastic substrates.[288,291]

Spectral study reveals that the most essential spectral shift of lines compared with the spectrum of SWNT in KBr pellet is observed for NT aqueous solutions with the surfactants containing charged groups.[293]

Acidification of a solution of surfactant-dispersed SWNTs in water in the pH region of 6.0 to 2.5 results in the reversible and selective reaction of protons at the sidewall of SWNTs.[290] The equilibrium constants are dependent on the NT band gap, and metallic NTs appear more sensitive to acidity of the solution. A crucial role is played by adsorbed O_2, which controls both the rate and equilibrium extent of the reaction. The results of this investigation hold promise for chemical separation and sorting of NTs having different electronic structures.

C_{16}TMAB or other surfactants are used to prepare a SiO_2/NT composite.[291,294]

SWNTs can be solubilized in water at g/L concentrations by non-covalent wrapping them with water-soluble linear polymers, most successfully with polyvinyl pyrrolidone[295,296] and sodium polystyrene sulfonate.[295,297,298] Polymetacrylic acid,[298] polypyrrole,[299] poly(phenylacetylene),[300] poly(diallyldimethylammonium chloride)[301,302] have also been tested. The solubilization of SWNTs by polymer wrapping might provide a series of useful techniques, such as purification, fractionation, and manipulation of the SWNTs.

For many applications, bio-compatible water-soluble derivatives of NTs are desirable. For this reason. the solubilization of NTs in cyclodextrins,[303–305] polysaccharides and natural mixtures of polysaccharides such as gelatine,[306,307] Gum Arabic,[275,289] and starch[308] has been studied.

Nanotubes are not soluble in aqueous solutions of starch but they are soluble in a starch–iodine complex. The starch, wrapped helically around small molecules, will transport NTs into aqueous solutions.[308] The process is reversible at high temperatures which permits the separation of NTs in their starch-wrapped form. The addition of glucosidases to these starched NTs results in the precipitation of the NTs from the solution. Readily available starch complexes can be used to purify NTs. An effective process to produce colloidal solution of SWNT–amylose complexes is elaborated.[309] The solubility of sonicated NTs improves by dilution of water with DMSO (10 to 25 vol%). Some natural polysaccharides wrap SWNTs, forming helical suprastructures.[310]

An amphiphilic α-helical peptide specifically designed not only to coat and solubilize NTs, but also to control the assembly of the peptide-coated NTs into macromolecular structures, is described.[311] The NTs can be recovered from their polymeric wrapping by changing their solvent system.

As for the solubility of pure SWNTs in organic solvents, these solvents are divided into three groups.[285] The "best" solvents are *N*-methylpirrolidone (NMP), DMF, hexamethylphosphoramide, cyclopentanone, tetramethylene sulfoxide, and ε-caprolactone, which readily disperse SWNTs, forming light-gray, slightly scattering liquid phases. All of these solvents are nonhydrogen-bonding Lewis bases. Group 2 includes DMSO, acrylonitrile, 4-chloroanisole, and ethylisothyocyanate. The third group includes 1,2-dichlorobenzene, 1,2-dimethylbenzene, bromobenzene, iodobenzene, and toluene.

Using solvochromic and thermochemical parameters of different solvents Torrens also categorized them into three groups.[312] The first group include the "best" solvents mentioned earlier. In the group of "good" solvents, he includes toluene, 1,2-dimethylbenzene, CS_2, 1-methylnaphthalene, iodobenzene, chloroform, bromobenzene, and *o*-dichlorobenzene. Group 3 are the "bad" solvents, *n*-hexane, ethyl isothyocyanate, acrylonitrile, DMSO, water, and 4-chloroanisole.

As reported earlier, the best solvents for generating SWNT dispersions in organic solvents are amides, particularly DMF and NMP.[176] The solubilities of SWNTs in 1,2-dichlorobenzene, chloroform, 1-methylnaphthalene, and 1-bromo-2-methylnaphthalene are equal to 95, 31, 25, and 23 mg/L,[247] respectively. Solubilities of purified and functionalized SWNTs in ethanol, acetone, and DMF is 0.5, 1.06, and 2.0 mg/L,[313] respectively. According to Ref. 247, the solubilities are <1, <1, and 7.2 mg/L.

MWNTs cannot be dispersed in toluene into the level of single tubes even when diluted to a concentration of ~10^{-3} g/L.[314] It has been found that the aggregation decreases with increasing temperature.

A procedure for the quantitative evaluation of the purity of bulk quantities of SWNT soot on the basis of near infrared (NIR) spectroscopy of a sample dispersed in DMF is described.[315]

Organic solutions of NTs in poly(*p*-phenylenevinylene-*co*-2,5-dioctoxy-*m*-phenylenevinylene),[316] poly(*m*-phenylenevinylene-*co*-2,5-dioctoxy-*p*-phenylenevinylene),[317] poly(2,6-pyridinylenevinilene-*co*-2,5-doictyloxy-*p*-phenylenevinylene),[317] a family of poly(*m*-phenylenevinylene-*co*-*p*-phenylenevinylene)s,[318] can be formed due to the physical adsorption of polymers. Certain polymers such as polyphenylenevinylene derivatives, and vinyl-based polymers such as polyvinylalcohol and polyvinylpyrrolidone tend to disperse NTs, while rejecting other carbon-based impurities (see Ref. 319).

The solubilization of small-diameter NTs is possible using rigid side-chain poly(aryleneethylene).[320] The method includes the dissolution of SWNTs in methylene chloride and polymer under vigorous stirring or sonication, and yields a solubility as high as 2.2 g/L. Researchers believe that the most probable mechanism is a π stacking which stabilizes the polymer–NT interaction.

Noncovalent solubilization of NTs can be realized by encapsulation of SWNTs by metallomacrocyclic rings.[216,321] A DMF solution of poly(vinylidene fluoride) can be used for size fractionation of MWNTs.[322]

5.5.7 Dispersions in Oleum

Successive dispersion of SWNTs in oleum at concentrations up to 4 wt% was first achieved at Rice University.[323] It was shown that at very low concentrations of SWNTs (<0.25 wt%), a single phase with uniformly dispersed tubes was formed. The SWNTs in the dilute system behave as Brownian (noninteracting) rods. The SWNT concentration in the dispersion can be increased up to 10 wt%; the dispersion process is promoted by the protonation of the SWNT sidewall, and the tubes are stabilized against aggregation due to the formation of electrostatic double layer of protons and negatively charged counterions.[324] Increasing the concentration of SWNTs in the acid leads to the formation of a highly unusual nematic phase of spaghetti-like, self-assembled supra-molecular strands of SWNTs. As concentration increases (to 4 vol% in 102% H_2SO_4), the strands self-assemble into a single-phase nematic liquid crystal. If a small amount of water is added, the liquid crystal separates into ~20 μm long, needle-like strands of highly aligned SWNTs, termed "alewives." This phase can be processed, under anhydrous conditions, into highly aligned fibers of pure SWNTs with a typical alignment ratio of 20:1 to 30:1. A syringe pump was used to extrude the mixture through a 0.15-mm internal diameter needle, followed by spinning the neat SWNT fibers up to 1 m long. The detailed structure and properties of the fiber have been studied.[325] High-temperature annealing of the fibers does not affect the SWNT alignment.

A solution of purified SWNTs in oleum (H_2SO_4/30% SO_3) was used to cast optically isotropic film exhibiting fibrillar morphology.[326] The electrical conductivity of this film (1×10^5 S/m) is about an order of magnitude higher than that for the SWNT bucky paper.

Chlorosulfonic acid, triflic acid, and anhydrous HF–BF_3 solution can also be used for the solubilization of NTs.

5.5.8 Self-Assembly, Film, and Fiber Formation

A promising feature of NTs in nanotechnology is that they are potentially amenable to a "bottom-up," self-assembly-based manufacturing approach. It is essential to fabricate well-aligned structures of NTs for various electric and optical applications. The necessity for aligned and micropatterned NTs has been elaborated in many articles (see, e.g., review 20).

There are two general strategies to align NTs: (1) *in situ* synthesis and (2) postsynthesis ordering. The first approach includes CVD processes on a prepatterned (with catalyst) surfaces or a template-based synthesis.[20,48,327] This approach is not considered here.

The second approach includes a variety of chemical or electrochemical processes[9] such as different functionality reactions and noncovalent (e.g., electrostatic) interactions between the NTs and surface-bound moieties.

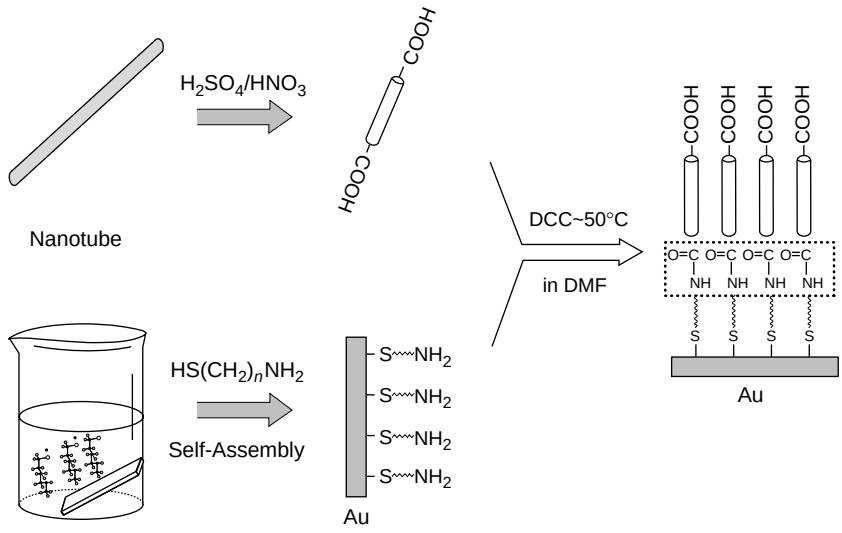

FIGURE 5.10 Schematic illustration of the formation of highly aligned SWNTs on gold surface. (Reprinted from Nan, X. et al., *J. Colloid Interf. Sci.*, **245**, 311–318, 2002. Copyright 2002. With permission from Elsevier.)

To organize NTs on gold or silver substrates, the carboxylic groups at the end of NTs were thiol-functionalized to form Au–S or Ag–S chemical bonds (Figure 5.10).[153–155,210–212] Flexible SWNTs with many thiol groups at their ends are more likely to bend on metal surface to form the "bow-type" structure, while a more rigid form of SWNT or MWNT with less thiol groups, will stand upright on the surface, forming a rod-like structure.[249] The monolayer of randomly tangled SWNTs is attached to a gold surface containing HS–$(CH_2)_{10}$–COOH.[328]

It is possible to use a patterned self-assembled monolayer which can either enhance or deter NT adherence.[329–330] Silicon wafers can be coated with either nonpolar methyl groups or with polar carboxyl and amino groups.[199,331] When the substrate is placed in a suspension of SWNTs, the tubes are attracted toward the polar regions and self-assemble to organize pre-designed structures. To form self-assembled monolayers with amino-terminated surface, silicon wafers were silanized using 3-aminopropyltriethoxysilane.[332] The octadecyltrichlorosilane is used to attach methyl-terminated groups.

Polyelectrolyte layers on a silicon substrate have been used to align MWNTs.[333] The carboxylate anion groups of MWNTs bind on the oppositely charged polycationic poly(diallyldimethylammonium chloride) (PDSC). The possibility of forming multi-layer assemblies such as Si/PDSC/PSS/PDSC/MNT (where PSS stands for poly(sodium 4-styrenesulfonate)) using coulombic interaction has been demonstrated.

An original method to produce a hollow spherical cage of nested SWNTs using self-assembly technique consists of attaching of NTs to amidated silica gel spheres and subsequent drying and dissolution of the template.[334]

The aligning of NTs can be realized under the influence of the capillary force and the tensile force that appear in the process of solvent evaporation.[335–339] The vacuum evaporation of concentrated (20 to 50 g/L) aqueous dispersion of purified MWNTs at 100°C yields long ribbons of aligned NTs, self-assembled on the wall of the container.[337] The ribbons form in one of the two orthogonal orientations to the bottom of the container (glass beaker): perpendicular when vacuum is applied, and parallel when no vacuum is applied. The ribbons are 50 to 100 μm wide, 4 to 12 μm thick, and 100 mm long. Presumably, the key factor is the rate of evaporation.

Using a dispersion of shortened purified SWNTs in de-ionized water, Shimoda et al.[338,339] formed a thin film on the surface of a soaked glass substrate with natural vaporization of water. The

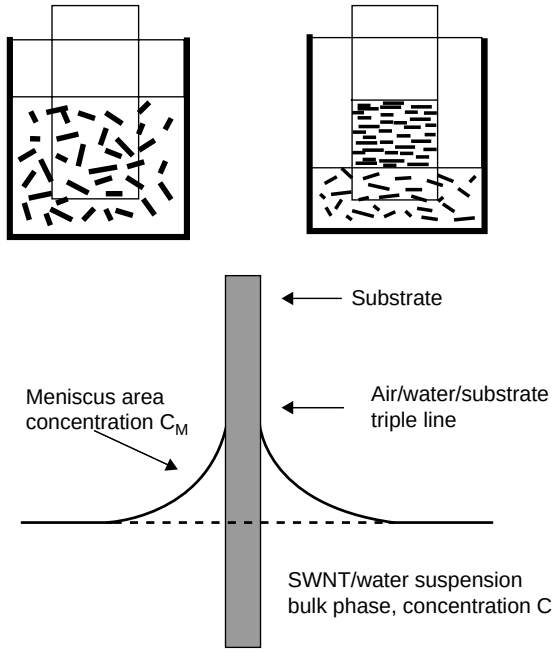

FIGURE 5.11 Self-assembly process of shortened SWNTs onto a hydrophilic glass slide.

SWNT bundles were uniaxially aligned parallel to the bottom of the container (Figure 5.11). In this process, SWNT bundles are first dispersed at a concentration of 0.5 to 1.0 g/L. Then a clean hydrophilic glass sheet is immersed vertically into the suspension. As the water evaporates, the NTs deposit near the triple borderline air/water/NTs and the deposit progresses downward. By means of patterned hydrophilic regions, patterned deposits were produced in the form of squares and strips, 100 μm in width.

Capillary forces arising during the evaporation of liquids from dense NT arrays were used to re-assemble the NTs into 2-D contiguous cellular foams.[340]

Natural self-assembly and cooperative mechanisms of liquid crystals can be employed to manipulate the alignment of NTs.[341] Thermotropic liquid crystals used as a solvent provide a tool for aligning SWNTs and MWNTs.[342] The broad range of possibilities of liquid crystals has been demonstrated.

An alignment of NTs can be realized under the electric field with both DC and AC voltage between the electrodes.[343] This method allows the orientation and spatial positioning of the SWNTs[344] to be controlled. The room-temperature method, called "minimal-lithography" technique, has been used to prepare crossbars of SWNT ropes and deterministic wiring networks from SWNTs. Electrophoretic deposition of NT films[345] and dielectrophoretic formation of fibrils[346] has been demonstrated.

Multi-layer polymer/SWNT films can be formed by electrostatic assembly.[150] The Langmuir–Blodgett method is used to deposit thin uniform films of SWNTs onto substrates.[277,347,348] Thin films have been made with NTs embedded in a surfactant matrix suspended on top of an aqueous subphase and then pulling the substrate through the surface. The Langmuir–Blodgett method has been used to prepare a monolayer of crown ether-modified full-length MWNTs and SWNTs.[349] A method of laying down thin uniform films of NTs on substrates of arbitrary composition resembling the Langmuir–Blodgett deposition technique has been developed.[350] The composite Langmuir–Schaefer conducting organic/MWNT films with useful optical and electrochemical properties have been studied.[351]

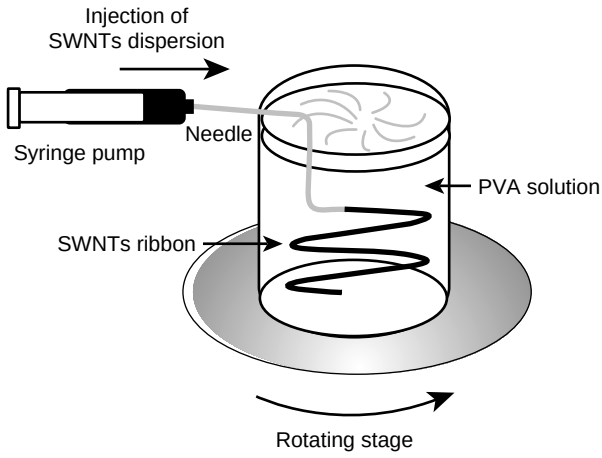

FIGURE 5.12 Simplified drawing of the experimental setup used to make NT ribbons. (From Poulin, P. et al., *Carbon*, **40**, 1741–1749, 2002. With permission.)

Fukushima et al.[352] have found a way to distribute NTs evenly through a gel, to form an electrically versatile material. The "bucky gel" materials were produced by grinding suspensions of SWNTs in imidasolium cation-based ionic liquids in an agate mortar. The gel can be printed using inkjet printer or polymerized. Lowering the temperature of the gels results in long-range ordering of the ionic liquid molecules and formation of crystal-like materials.

Yodh and his colleagues embedded isolated SWNTs coated with NaDDBS into a cross-linked polymer matrix, an *N*-isopropyl acrylamide gel.[281] The volume of the gel is highly temperature-dependent, and a change in temperature results in volume-compression transition. The condensed gel thus creates concentrations of isolated, aligned NTs that cannot be achieved when they are suspended in water.

Re-condensing of surfactant-stabilized NT solutions is used for the formation of aligned NT fibers.[269,353] In this method, NTs are sonicated in an aqueous solution of NaDDS. The dispersion is injected into a co-flowing stream of poly(vinyl alcohol) (PVA) via capillary tube. This principle was modified to produce long aligned fibers of NTs.[278] The process consists of introducing SWNT dispersion into a co-flowing stream of PVA in a cylindrical pipe, thereby causing the agglomeration of the SWNTs into a ribbon. The fibers are then unwound and passed through a series of washing stages to remove the excess PVA.

The extrusion of aqueous dispersions of NTs into rotating viscous solution of PVA leads to aggregation of NTs into narrow strips (Figure 5.12).[269] These strips, a few micrometers thick and a few millimeters wide, contract when dried in air forming dense fibers.

Electro-spinning allows the fabrication of an oriented poly(ethylene oxide) NFs in which MWNTs are embedded mostly aligned along the fiber axis (Figure 5.13).[275] The feasibility of this electrostatically induced self-assembly process for incorporation of NTs into NFs, production of membranes, and nanofiber yarn have been demonstrated.[354,355]

Macroscopic fibers have been produced from NT dispersions in oleum by spinning technique.[324,325]

5.6 FILLING THE INNER CAVITY OF CARBON NANOTUBES

Numerous attempts to fill the nanoscale cavities of NTs have been made following the discovery of these materials. The filling was attempted to achieve one of the two goals. First, being a kind of template synthesis, filling allows the preparation of nanostructured materials with controlled size, shape, and purity. Secondly, doping can modify the electronic properties of NTs. The thus prepared

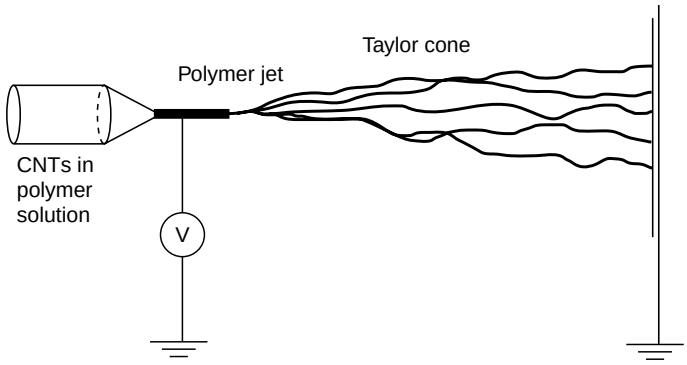

FIGURE 5.13 Schematic of the electrospinning process used to form SWNT-filled composites.

compounds are also interesting as nanosized objects to investigate size–crystal structure relations and size effects.

The filling of SWNTs attracts more attention than filling of MWNTs due to the smaller diameter of SWNT inner cavities, better stability, and more perfect structure of SWNTs. The afterward removal of SWNT used as nanomolds is a more easy procedure than removing the MWNT shield.

The filler can exist either in solid, liquid, or gaseous state. As far as solid materials are concerened, the inner cavity of NTs can be filled with single crystalline nanorods, polycrystalline nanorods, amorphous nanorods, or discrete nanoparticles.

Many solid substances can fill the inner cavities of NTs. The list of fillers includes metals (Cs, Cu, Ag, Au, Sn, Fe, Co, Ni, Pd, Rh, etc.), alloys (Fe–Ni, Fe–Pt, Pt–Ru, $Nd_2Fe_{14}B$), nonmetals (Ge, S, Se, Te, I_2, etc.), oxides (SnO, Sb_2O_3, NiO, UO_{2-x}), hydroxides ($Ni(OH)_2$), halides (KI, $LaCl_3$, $ZrCl_4$), salts ($AgNO_3$), carbides (B_4C, LaC_x, NbC_x, FeC_x), sulfides (AuS_x, CdS, CoS_x), nitrides (BN, GaN), organic substances ($CHCl_3$), acids (HNO_3), polymers (polystyrene), complex inorganic compounds and eutectic mixtures ($FeBiO_3$, $CoFe_2O_4$, AgCl–AgBr, KCl–UCl_4), fullerene and endofullerene molecules (C_{60}, Gd@C_{82}), complex hybrid materials ($FeCl_3$–C_{60}, K–C_{60}, Pt–WO_3).[7,8,224,356–358] Quantum chemical simulations predicted the stability of alkali metal compounds (Na@SWNT) and metallocarbohedrene derivatives (Ti_8C_{12}@SWNT).

Water, inorganic acids, aqueous solutions, $CHCl_3$ solutions, and molten salts are among liquid substances suitable to fill NTs.

The solid and liquid substances can fill the cavity entirely or partially. Materials produced by filling of NT inner cavities can be used as magnetic media, catalysts, sorbents, quantum wires, field emitters, electromagnetic shielding, etc.

The results of theoretical calculations show that the radius as well as the helicity of the most stably doped SWNT are different for different kinds of impurity atoms.[359]

There are two basic strategies of filling: *in situ* synthesis of filled NTs or post-production methods that require an opening of the tubes.

5.6.1 *IN SITU* FILLING

All synthesis strategies may be accompanied by filling of NTs produced. In an arching process, the filler precursor can be introduced either by graphite anode doping (the most commonly used technique) or by dissolution in a liquid medium (if the process takes place in liquid environment). In the first stage of NT study, most information was obtained by using arc-discharge method in an inert gas flow. For filling of arc-produced NTs, a variety of metals, oxides, or salts have been used to dope the anode. With a few exclusions (Co, Cu, Pd), the encapsulated materials were always carbides.

Close-capped NTs can be filled *in situ* with metallic Co, S, and CoS_x from aqueous solution of $CoSO_4$ by arching.[38] A simplified arc-discharge in aqueous solution of $PdCl_2$ yields Pd-nanoparticles-filled NTs.[360]

All types of pyrolytic synthesis of NTs (using supported, dissolved, or floating catalysts, different physical activation methods) are inevitably accompanied by capture of some part of the catalyst and encapsulation of catalyst particles. Consequent purification with boiling HNO_3 or other oxidants cannot eliminate the metals completely.[361] The filling can be controlled to some extent by varying the process parameters, but sometimes, relative amount of incorporated material reach substantial values.

For example, the HiPco technique results in SWNTs partially filled with Fe (total Fe content in crude product is about 20 to 30%). The oxidation treatment of $LaNi_2$ alloy followed by CVD process using a CH_4/Ar mixture at 550°C leads to the formation of MWNTs filled with single-crystal Ni nanowires.[362] The synthesis of NTs filled with Ni by CVD over the Raney-Ni catalyst gives straight and two types of bamboo-shaped NTs.[363] The synthesis of Fe-, Ni-, and Co-filled NTs by using the pyrolysis of metallocenes (cyclopentadienyles) has been performed at 900 to 1150°C.[364,365] Invar ($Fe_{65}Ni_{35}$) has been introduced into NTs by pyrolyzing an atomized solution of $NiCp_2/FeCp_2$ in C_6H_6 at 800°C (Cp stands for cyclopentadiene).[366] The pyrolysis of methane over Fe_2O_3/Al_2O_3 binary aerogel at 880°C yields multi-wall nanohorns filled with Fe nanoparticles.[367] The decomposition of gaseous $Fe(CO)_5$ in a mixture with CO or C_6H_6 yields NTs partially filled with Fe.[368] MWNT-encapsulated Co particles have been produced by the catalytic method using water-soluble NaCl/NaF mixture as a support for the metal.[369]

Plasma-enhanced CVD on Si wafers allows the production of NTs-containing magnetic Fe, $Nd_2Fe_{14}B$, or Fe–Pt nanoparticles.[358] The formation of simple and branched Cu-filled NTs has been observed in the plasma-activated CVD process.[370] The Cu electrodes serve as a metal source in this process. Microwave-plasma-enhanced CVD process yields almost 100% GaN-filled NTs.[371]

"Double template" synthesis demands exploration of a material with aligned micropores. For example, NTs filled with Co have been synthesized using the CVD method and molecular sieve AlPO-5 and AlPO-31 as a primary template to formate NTs.[372]

A high-temperature process interaction of pulverized $Fe(NO_3)_3$ solution with carbon black and boron precursor results in the formation of Fe nanowire encapsulated in the inner cavity of carbon NT having an inner layer of BN.[373] The mechanism of the phase separation between C and BN is not clear.

An original, but complicated, method to produce relatively long cobalt nanowires filling the NT consists of a reaction of $Co(CO)_3NO$ with magnesium in closed vessel cell.[374,375]

During a hydrothermal synthesis of MWNTs, some gases, particularly CO_2, H_2O, and CH_4 can be trapped in the inner cavity of the tube.[376] Theoretical analysis of phase equilibria in such systems reveals an enhanced layering effect in the liquid phase.[377]

5.6.2 Post-Processing Filling

Nanotubes of two types are used in the filling process: NT synthesized by an usual method and NTs prepared by a template method in pores of Al_2O_3, AlPO-5, AlPO-31, or other suitable membranes. The usual methods lead to the formation of NTs of different diameters, whereas membrane synthesis ("double template" or "second-order" template synthesis) allows for the preparation of NTs of similar diameter and therefore in the production of encapsulated materials of uniform size. The second method is more complex and less productive.

5.6.2.1 Filling from Liquid Media

Filling by capillarity is possible only if the NTs are opened. The classification of liquid fillers or precursors includes:

- water and aqueous solutions
- liquid organic compounds

- hydrothermal solutions
- supercritical solutions
- molten metals, salts, and molten eutectic mixtures

The wetting properties of different carbons have been found to depend on the surface tension of the fluid, with a threshold value of 100 to 200 mN/m. Therefore, water having surface tension of 72 mN/m should wet NTs.[378,379] The boundary value is dependent on the inner diameter of NT.

The study of the filling of NT with water is of considerable importance in many biological systems and for the development of molecular devices. The behavior of water in the inner channel of NT has been discussed in a set of works.[380–387] Hummer et al.[380] showed, by molecular dynamics simulations that water molecules enter NTs of diameter greater than 0.81 nm even though carbon is hydrophobic. The possibility of transport of an electrolytic solution (KCl) through a carbon NT by a molecular dynamics simulation has also been explored.[388]

Certain metal oxides (V, Bi, Mo, Mn, Fe) can be doped by refluxing closed NTs with HNO_3 in the presence of metal nitrate and by subsequent calcination of metal nitrates inside NTs.[389,390] Filling with Ag (presumably silver oxide) has been achieved using concentrated aqueous solution of $AgNO_3$.[391] Aligned, open MWNTs can also be filled with Ag nanorods of up to 9 μm in length, using aqueous nitrate solution.[89] The reduction to metal Ag was achieved with CH_3COOH at 300°C. Interaction of the opened MWNTs with inner channel diameter of 60 nm with aqueous nitrate solution and subsequent heat treatment under inert atmosphere at 100°C, leads to the formation of spinel $CoFe_2O_4$ in the form of nanowire several micrometers long.[392–394] Immersion of a sample of pretreated SWNT in a saturated aqueous solution of $RuCl_3$ leads to filling with this salt.[395]

Platinum–ruthenium nanoparticle (1.6 nm) filled NTs have been prepared by immersing the carbon/alumina template composite in an aqueous solution of H_2PtCl_2 and $RuCl_3$ for 5 h, and subsequently drying at room temperature, reducing in H_2 at 550°C, and dissolution of the membrane.[396,397] This method was used to load Pt, Pt–Ru, and Pt–WO_3 nanoparticles inside NTs.[398,399] A second-order template method was used for electrochemical Ni deposition inside NTs.[400] Highly crystalline nanorods of α-Fe_2O_3 were synthesized in the cavity of carbon NTs by hydrothermal treatment with NaOH aqueous solution.[401]

A solution of chromium(III) oxide in hydrochloric acid is used to fill NTs with the oxide at room temperature.[391,402] Wet chemical techniques to produce CuO nanoparticles, 20 to 90 nm in diameter and 250 to 700 nm in length, using MWNTs as templates has been developed.[403]

Gold nanoparticles can be introduced into the inner cavity of MWNT after its heat treatment in NH_3.[404]

The rapid filling of metals (Pd, Ni, and Cu) into MWNTs can be achieved using super-critical CO_2 as the reaction medium.[405] Britz et al.[406] used a metal-β-diketone complex $M(hfa)_2$ (hfa stands for hexafluoroacetylacetonate), which was reduced by H_2 dissolved in super-critical CO_2. Super-critical CO_2 solutions were used to fill SWNTs with C_{60} and $C_{61}(COOEt)_2$ molecules.

The solvent method of peapod preparation based on the refluxing of *n*-hexane suspension makes it possible to get a high yield of C_{60}@SWNT, C_{70}@SWNT and to synthesize N@C_{60}:C_{60}@SWNT.[407] Two others methods of nanopeapod formation consist of establishing a contact of SWNT and fullerene ethanol or toluol solutions/suspensions (Figure 5.14).[408]

A synthetic method of integrating organic molecules, such as *tetrakis*(dimethyl-amino)ethylene and tetracyanoquinodimethane into SWNTs[409] has strong potential for molecular electronics. Molecular dynamic simulations have indicated that even DNA could be encapsulated inside NTs in a water solute environment via an extremely rapid dynamic interaction process, provided that the tube size exceeds a certain critical value.[410]

Capillary filling with molten oxides,[411,412] molten metal salts, such as chlorides,[395,413–415] and some molten metals[416,417] is also widely used. Metal nanowires encapsulated in NTs have been obtained by treating SWNTs with metal salts at melting temperatures in vacuum-sealed quartz tubes, followed by reduction with hydrogen.

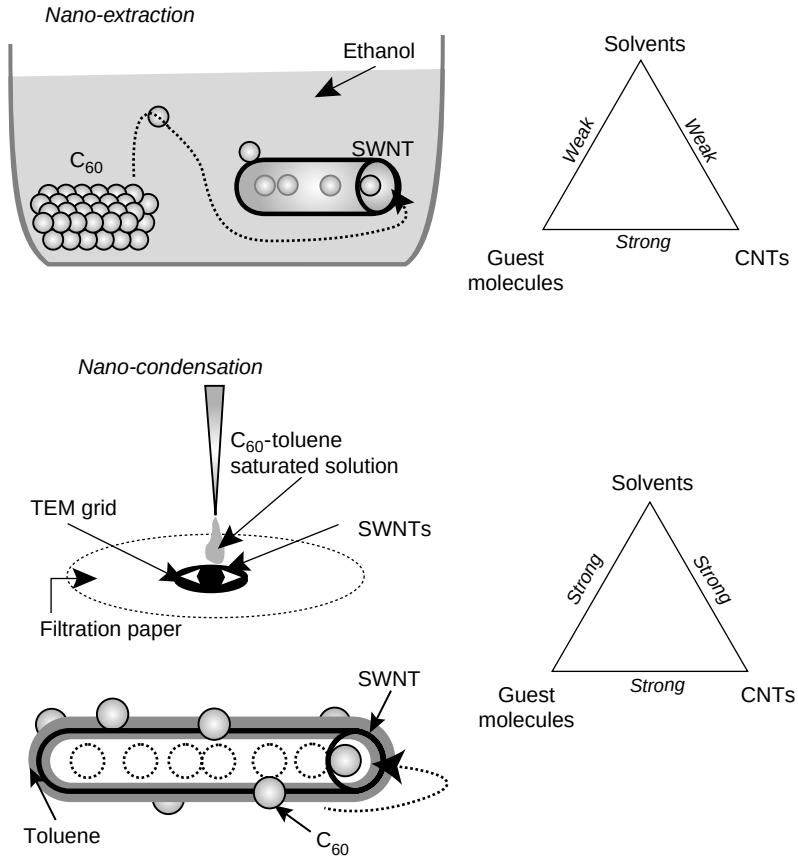

FIGURE 5.14 Schemes of nanoextraction and nanocondensation methods. The difference in relative affinities among the three components are shown in the triangles. (From Yudasaka, M. et al., *Chem. Phys. Lett.*, **380**, 42–46, 2003. With permission.)

The doping of SWNT bundles by immersion in molten iodine gives quite different results compared to using iodine vapors. This is due to the dissociative character of the melt.[418] Iodine atoms form charged polyiodide chains inside MWNTs of different inner diameter.[419]

A carbon nanotube 75 nm in diameter and 10 μm long, filled with liquid Ga, acts as a thermometer as claimed by Gao and Bando.[420] The height of the continuous, unidirectional column of Ga inside the nanotube varies linearly with temperatures ranging from 50 to 500°C.

5.6.2.2 Filling from Gas Phase

In SWNTs with open ends, nitrogen and oxygen are adsorbed first in the inside of the tubes, and next in the interstitial channels of bundles (see Section 5.7).[421] In each site, gases can be adsorbed with the stoichiometry of $C_{20}N_2$ or $C_{20}O_2$, as a monolayer.

Theoretical analysis of the behavior of some of the simplest molecules (methane, ethane, ethylene) in the NT cavity predicts normal-mode molecular diffusion for methane, and intermediate between molecular diffusion and single-file diffusion for ethane and ethylene at room temperature.[422,423]

The filling of NT with vapors of halcogenes (Se),[390] hydrides (SiH_4),[424] metal halogenides ($ZrCl_4$),[425] fullerenes (C_{60}, $Sc_2@C_{84}$, $La@C_{82}$),[426–429] and metallocenes ($Fe(Cp)_2$, and $Ni(Cp)_2$)[429–432] has been studied. Volatile metal carbonyls, metal diketonates, and metal phthalocyanines can also be used.

Reaction with Se in vapor phase using the two-bulb method allows to reach a filling of 50 to 80% of NTs.[390] The thermal decomposition of SiH_4 inside NTs by double-template technique leads to the formation of NTs/Si core-sheath composite.[424] Filling of SWNTs by $ZrCl_4$ is possible by heating of the mixture of components with mass ratio of 1:1, in a sealed ampoule at 623 K.[425] It is possible that under the experimental conditions (under pressure), $ZrCl_4$ formed melt and the NT filling is induced by capillary effect. Filling of opened NTs with fullerene molecules is possible by heating the mixture of components at 400 to 650°C in a sealed quartz or glass tube.[426,428] Mechanochemical activation under nitrogen atmosphere of solid-phase mixture of SWNTs and C_{60} fullerene leading to fullerene-modified NTs[433] presumably involved evaporation of fullerene.

An unusual process of Cs encapsulation inside SWNT via plasma-ion irradiation has also been demonstrated.[434]

5.6.3 Reactions inside Nanotube

Many interesting chemical reactions can be performed inside NT cavities. Among these are:

- thermal decomposition of salts (e.g., metal nitrates)
- thermal decomposition and pyrolysis of volatile compounds (e.g., silane, metallocenes)
- chemical reduction of salts (e.g., metal halides or nitrates)
- air oxidation (e.g., metal halides)
- hydrolysis and pyrohydrolysis (metal halogenides, trimethylaluminum)
- polymerization (styrene, C_{60})
- formation of complex salts ($CoFe_2O_4$)
- alloy formation ($Nd_2Fe_{14}B$)
- sorption of vapors
- photolytic reduction

Some processes are complex and involve reactions of different type, e.g., thermal decomposition, reduction, and alloying. It is also possible to modify the inserted solid materials by *in situ* electron irradiation at intermediate accelerating voltages (100 to 400 kV). Electron[435] or carbon-ion[436] beam irradiation can form a connection between NTs. The structural change observed in NTs with encapsulated Ni particles is quite different as compared to empty samples, and leads to the formation of short-range fibrous or amorphous structures instead of a layered structure.[437] The crystalline–amorphous phase transformation has been observed under irradiation of encapsulated Fe.[438]

The first example of a chemical reaction inside SWNT is the H_2 reduction of $RuCl_3$ yielding Ru metal.[395] Some other examples of reactions (thermal decomposition of $AgNO_3$ to produce Ag nanowire, reduction of the salts, and CVD processes) have been mentioned earlier. One-dimensional crystals may be reduced to form metallic wires or templated 0-D nanocrystals of regulated sizes.

The reaction of trimethylaluminum and water vapor at 300°C using atomic-layer deposition technique yields Al_2O_3 nanorods inside MWNTs.[439]

Bando and coworkers[440] revealed that MWNT filled with Ga at 800°C can effectively absorb copper vapor, forming Ga–Cu alloy. The absorption rate for sealed tubes was equal to or even greater than the rate for open-ended tubes. This is presumably due to the fact that the Ga vapor pressure within a closed NT is much higher than that in an open one. and the Cu penetrates inside via defects.

Polymerization of C_{60} and generation of double-wall NTs takes place under heat treatment (the temperature must be above ~800°C) or irradiation.[116,441–443] Photopolymerization of C_{60} or C_{70} inside NT under blue-laser irradiation has also been detected.[444] A Raman investigation revealed that inner SWNTs produced by polymerization are remarkably defect-free.[443] It is interesting that in the polymerization of C_{60}, short inner NTs with diameters of ~0.7 nm are preferentially formed first. Such short NTs merge together and lengthen with diameter increasing in the course of polymerization.[445,446]

The polymerization of C_{60} fullerenes takes place also after heavy doping of the peapod system with an alkali metal.[116] A polymeric phase of K_6C_{60} has not been observed so far outside the NTs. The coalescence of $Sm@C_{82}$ has been observed under electron irradiation.[447]

In contrast to fullerenes, in the case of $LnCl_3$ and $ZrCl_4$, the formation of clusters has been observed.[414,425]

MWNTs can be hydrothermally synthesized from different precursors in the presence of metal powder catalyst. One of the important features of some MWNTs produced in hydrothermal conditions is their large inner diameter, well suited for inner-tubular chemical reactions.[43] Since a part of these MWNTs have closed tips and contain encapsulated water and gases (supercritical mixtures of CO, CO_2, H_2O, H_2, and CH_4),[43,44,448] it was important to investigate interaction between the fluid and inner carbon walls.[376] It has been shown that strong interaction between the tube wall and aqueous mixture results in penetration of liquid between the graphitic layers, swelling of the inner wall layers, bending of graphite layers toward the tube center, and inter-calation of several inner layers with O–H species, and interlayer spacing increasing to 0.61 nm. The chemical interaction leads to dissolution of the tube wall and increase in the internal diameter of the tube in the vicinity of the liquid inclusions.

Recently, NTs with an outer diameter of ~90 nm and tube walls inclined with respect to the tube axis were found to form at 770°C and 50 to 90 MPa.[449] The conical-scroll structure of these tubes, with a high density of graphene edges at both inner and outer surfaces, enables functionalization of both surfaces. The outer wall of these NTs is shown to be covered by a hair-like layer of functional groups containing oxygen and carbon, thus making the hydrothermal NTs hydrophilic.

It is expected that nanopeapods could be used as chemical nanoreactors.[445,447]

Selectively opened NTs with 2.0 nm opening would allow many organic molecules to enter and leave. As pointed by Green,[450] rather than having a "ship-in-the-bottle" situation, one would have what could be described as a "fleet-in-the-harbor," and the idea of NT catalysis is very attractive. Encapsulation of polystyrene within MWNTs can be realized using solutions of monomer styrene and benzoyl peroxide (initiator) in super-critical CO_2.[451]

Some inner-tubular chemical and physical processes of NTs have been reviewed by Yang et al.[452]

5.6.4 The Structure of Crystals inside Nanotubes

The restricted diameter range of NT confines the crystals formed inside the NT cavity. As nanocrystal size decreases, surface energy becomes an increasing factor in structural stability. For a given size, surface energy also influences the structural phase diagram in the temperature–pressure plane. Simple thermodynamic models, which predict a lowering of the melting point if the surface energy of the solid is higher than that of the liquid, describe the data semi-quantitatively.

The size of an NT inner cavity is usually small enough to show the dimension effect on embedded particles. The effect consists, for example, of size dependency of melting temperature of encapsulated nanocrystals.[453] But, besides enhanced surface energy, there are other factors affecting the crystal structure of material inside NT; e.g., van der Waals interaction and interaction with the NT wall.

The structure of the encapsulated materials significantly deviates from the structure of bulk materials, with lower surface coordination and substantial lattice distortion. The most noticeable studies in these fields were carried out at Oxford University and Cambridge University (see Refs. 414, 454, 455 and references therein).

The "Feynman crystal's" growth inside SWNTs is atomically regulated. One-dimensional KI having nine atoms in cross section (inside an NT of 1.6 nm diameter) and four atoms (inside NT of 1.4 nm diameter) were among the first such crystals studied.[453,456] In both cases, the crystal structure peculiar to the bulk crystal is distorted due to interaction with NT walls and change in the coordination number (CN). Especially, noticeable contraction was observed in 4×4 crystals, in which crystal parameters were about 4/9 of the standard ones for the bulk crystal. A novel, low-dimensional, crystal structures such as "twisted" crystal, was found.[457,458]

TABLE 5.2
Packing Behavior Observed in SWNTs as a Function of Bulk Structure Type

Halide Filling	Common Bulk Structure Type	CN in Bulk	Structure Inside SWNTs	CNs Observed or Predicted within SWNTs[a]
KI	3-D rock salt	6	Rock salt	**4, 5, 6**
AgX[b]	3-D rock salt	6	Rock salt	4, 5, 6
	Wurzite	4	Wurzite	**3, 4**
SrI_2	3-D network	7	1-D PHC[c]	**4, 6**
BaI_2	3-D network	7 + 2	1-D PHC	**5, 6**
PbI_2	2-D layered	6	1-D PHC	**5, 6**
$LnCl_3$[d]	2-D layered	6	1-D PHC	**5, 6**

[a] CNs in bold have been observed experimentally. Bulk coordination is predicted for polyhedra in the center of wide capillary SWNTs.

[b] X includes Cl or Br and I.

[c] 1-D PHC, 1-D polyhedral chain.

[d] Ln = La to Tb (UCI_3-type) only, Ln = Tb to Lu ($PuBr_3$-type) only.

Source: From Sloan, J. et al., *Chem. Commun*., 1319–1332, 2002. With permission.

It was stated later that the form of the structures varies depending on whether the bulk material is a single packed structure (e.g., rocksalt or wurzite) or represents 1-D chain structure of simple coordination polyhedra (Table 5.2).

The chains of lanthanoide halides[415] and zirconium tetrachloride[425] consist of edge-shared MCl_6 polyhedra. "Twisted" $CdCl_2$ structure closely resembles helical iodine chains.[418] Double-helix iodine chains with the period of ~5 nm correspond to a composition of IC_{20}.

In the case of Sb_2O_3 filling, the material is identified as a single crystal in the valentinite form (i.e., the high-pressure modification as opposed to its senarmontite form). In comparison to the bulk structure of valentinite, the encapsulated crystal shows a longitudinal contraction of ~13% and significant lattice distortions.

The fullerenes inside NTs of appropriate diameter (close to that of (10,10) NT for C_{60}) form 1-D molecular chains. Two different domains, where the dominant alignment of C_{70} molecular long axis is standing or lying with respect to the NT axis, have been observed.[459] The ratio of the standing to the lying C_{70} domains is roughly 7:3.

Molecular dynamic simulations show that water molecules inside NTs at 300 K and 1 atm tend to organize themselves into a solid-like wrapped-around ice sheets.[384] A variety of new ice phases that are not seen in bulk ice, and a solid–liquid critical point where the distinction between solid and liquid phases disappears, are observed.[383] The water has been observed to exhibit first-order freezing transition to hexagonal and heptagonal ice nanotubes, as also a continuous phase transformation into solid-like square or pentagonal ice nanotubes.

5.7 ADSORPTION AND STORAGE OF GASES

Owing to the specific structure and morphology of NTs, there are a variety of possible sites available for adsorption. In ideal, defect-free, and bundled SWNTs, the sites having different energy of gas adsorption include (1) the internal cavity of opened SWNTs, (2) the interstitial channels between NTs in bundles, and (3) the grooves at the periphery of the bundles (Figure 5.15). Adsorptive capacity of single-wall nanohorns (nanocones) differs from the capacity of SWNTs. The surface structure of MWNTs may be more complex due to different topological defects, such as

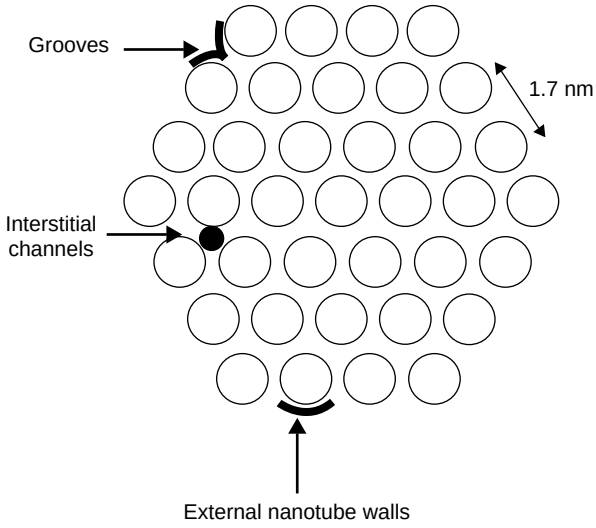

FIGURE 5.15 The three possible adsorption sites on a bundle of SWNTs with closed ends. (From Babaa, M.R. et al., *Carbon*, **42**, 1549–1554, 2004. With permission.)

pentagons and heptagons, holes and dislocations in sidewalls, etc. The structure of MWNT can be scroll-like, branched, or coiled. The tubes can form second- and third-order structures (see Section 5.2) and aligned arrays. Therefore the adsorption behavior of MWNTs is more complicated than that of SWNTs. Admixtures such as amorphous carbon, graphitic nanoparticles, or catalyst residues, attached to tube walls functionalities, exert influence upon the adsorption characteristics.

5.7.1 Hydrogen Problem

Hydrogen is an ideal fuel for the future. If hydrogen fuel cells were used to power automobiles and other vehicles, air pollution would be reduced. But the problem is not only to develop effective fuel cells or cost-effective method of hydrogen production. It is necessary to supply every vehicle with a safe, cheap, compact on-board hydrogen accumulator. The nearest goal is to achieve an adsorption capacity of 6.5 wt% or 62 kg H_2 m^{-3} at room temperature.

There are two methods to store hydrogen in NTs: one is to store it under high gas pressure, and the other is to employ an electrochemical charge–discharge cycling method.[5]

The first article on the possibility of hydrogen storage in NTs was published in 1997.[460] Dillon et al.[460] estimated that SWNTs can adsorb from 5 to 10 wt% of hydrogen under ambient conditions. In 1998, Rodriguez and coworkers[461] claimed that certain graphite NFs can store more than 50 wt% at room temperature. In 1999, Chen et al.[462] reported hydrogen uptake at 300 K and a pressure of 0.1 MPa up to 20 wt% by alkali metal-doped MWNTs. Aligned MWNTs with diameters of 50 to 100 nm show a reversible hydrogen storage capacity of 5 to 7 wt% at room temperature under 1 MPa pressure.[463] Pre-treatments of MWNTs increase the storage capacity up to 13 wt%.

Subsequent studies could not confirm these results. Other experimental data are given in Table 5.3.

Most of the work given in Table 5.3 have been done with minor quantities of highly impure and badly characterized samples of NT materials, and only some of the latest publications seemed to be accurate. Therefore the measurements using samples up to 85 g show low adsorptive capacities of MWNTs.[486] The thermal desorption spectra show that hydrogen desorbs below 300 K and at 656 K.[495] The D_2 sorption at 77 K has been found to be 0.45 wt% in raw SWNTs and 0.67 wt% in potassium-doped SWNTs.[496]

Results indicate that hydrogen uptake by metal-containing NT bundles is substantially enhanced compared with uptake by pure tubes. MWNTs seems to be more promising materials than SWNTs.

TABLE 5.3
Hydrogen Adsorption Levels in NTs

NT Type	Adsorption Conditions	Adsorption Capacity (wt%)	Year	Reference
SWNTs	300 K, 0.1 MPa, E[a]	0.35	1999	464
SWNTs	300 K, 0.1 MPa, E[a]	2.9	2000	465
SWNTs	300 K, 0.1 MPa	0.04–1.5	2001	466
SWNTs	300 K, 0.1 MPa, E[a]	1.84	2002	467
SWNTs	300 K, 0.1 MPa, E[a]	6	2002	468
SWNTs	300 K, 0.1 MPa	1.8	2004	469
SWNTs	300 K, 0.1 MPa	0.01	2004	470
SWNTs	295 K, 0.1 MPa	0.93	2002	471
SWNTs	300 K, 9 MPa	0.3	2003	472
SWNTs	300 K, 9 MPa	0.3–0.4	2004	473
SWNTs	300 K, 10 MPa	3.5	2001	474
SWNTs	300 K, 10 MPa	<0.2	2002	475
SWNTs	300 K, 12 MPa	4.2	1999	476
SWNTs	253 K, 6 MPa	1	2004	477
SWNTs	77 K, 0.04 MPa	3	2004	478
SWNTs	77 K, 0.1 MPa	1	2004	470
SWNTs	77 K, 0.1 MPa	2.37	2002	471
SWNTs	77 K, 0.2 MPa	6	2002	479
SWNTs	77 K, 1 MPa	0.7	2002	475
SWNTs	77 K, 2 MPa	0.6	2003	480
SWNTs	77 K, 2.5 MPa	2.4	2003	474
SWNTs	77 K, 10 MPa	8.2	1999	481
MWNTs	300 K, 0.1 MPa	0.25	2000	482
MWNTs	300 K, 0.1 MPa, E[a]	0.7	2000	483
MWNTs	300 K, 0.1 MPa, E[a]	0.1–1.6	2001	484
MWNTs	300 K, 0.1 MPa, E[a]	1.6	2003	74
MWNTs	300 K, 0.1 MPa, E[a], Li	0.6–2.3	2001	484
MWNTs	300 K, 0.1 MPa, Li, K	1.8–2.5	2000	485
MWNTs	300 K, 0.1 MPa	0.30	2004	486
MWNTs	300 K, 3 MPa	<0.2	2002	475
MWNTs	300 K, 10 MPa	0.7–2.4	2001	487
MWNTs	300 K, 10 MPa	0.5–2	2001	488
MWNTs	300 K, 10 MPa	1.16–2.67	2000	489
MWNTs	290 K, 10 MPa	3.4	2001	490
MWNTs	300 K, 12 MPa, KNO_3	3.2	2002	491
MWNTs	300 K, 13.5 MPa	2.5–4.6	2003	492
MWNTs	77 K, 0.1 MPa	2.27	2004	486
MWNTs	77 K, 3 MPa	~0.3	2002	475
NFs	300 K, 0.1 MPa, KNO_3	5.1	2003	493
NFs	300 K, 12 MPa	6.5	2002	494

[a] E = electrochemical storage.

The results of theoretical calculations on hydrogen sorption in NTs[5,497–515] are also controversial. It is clear that purified SWNTs store hydrogen in the molecular form. The hydrogen uptake is due to physisorption, therefore the relative amount of adsorbed hydrogen is proportional to the specific surface area of the sorbent material (1.5 wt% per 1000 m^2/g at 77 K). It has been shown that different

forms of carbon are essentially the same for hydrogen molecules.[516] Close-ended SWNTs and open SWNTs have a relatively low accessible surface areas due to bundling of the tubes.

MWNTs can be used as additives to metal adsorbents.[517] Mg–5 wt% MWNTs composite absorbed 4.86 wt% (80% maximum hydrogen storage capacity) within 1 min at 553 K, under 2.0 MPa.

The problem has been discussed in the reviews.[518–527] One can trace the change from rather optimistic estimations of the prospects to use NTs as effective storage media in early publications, to more cautious conclusions and even to a pessimistic point of view in the latest ones. Today, it is still unclear whether NTs will have real practical applications in the hydrogen storage area. Addition of some metals and salts to the NTs, chemical activation, and aligning of NTs leads to an increase in adsorption capacity. However, some other problems which need to be solved include achievement of fast kinetics of discharge, high stability during cycling, low self-discharge level, etc.

5.7.2 Carbon Nanotube Gas Sensors

The adsorption of different gases and vapors in NT materials as reported in publications up to year 2000 has been briefly reviewed earlier.[8] Apart from hydrogen, adsorption of noble gases,[528–532] nitrogen,[531–534] oxygen,[531,532,534–536] carbon monoxide,[534] carbon dioxide,[531,533,537–539] nitrogen dioxide,[531,540] ammonia,[531,540] water vapor,[531,534] methane,[528,531,533,541–544] acetylene,[545] acetone,[546] carbon tetrachloride,[547] carbon tetrafluoride,[530] sulfur hexafluoride,[530] methanol,[548] ethanol,[548,549] linear-chain alkanes, and fatty acids[550] has been characterized in the last 5 years. The gas transport properties of NTs has been measured.[551,552]

NTs have been found to be an effective separation media for removing some admixtures from flue gases; they can store gases having relatively high molecular mass (e.g., methane). However, the most promising field of their application is the development of new sensing devices. Sensing gaseous molecules is important in environmental monitoring, control of chemical processes and agriculture, and biological and medical applications. NT-based sensors have huge prospects in outer planetary exploration and for incorporation into yarns and fabrics.

Chemical doping of NTs, particularly of SWNTs, changes their electronic properties and can induce strong changes in conductance[48,553,554] and in thermoelectric power.[555–557] Chemical sensors are measurement devices that convert a chemical or physical property of a specific analyte into a measurable signal whose magnitude is usually proportional to the concentration of the analyte. For sensing applications, NTs have advantages, such as small size with larger surface, high sensitivity, fast response, and good reversibility.

The first sensor based on SWNTs was reported by Dai and coworkers,[558] who demonstrated that small concentrations of NO_2 produced large changes in sensor conduction. To clarify the reason for the discrepancy of recovery time between theoretical results and experimental data, the formation of adsorbed NO_3 has been postulated.[559] Recent works[560,561] show the possibility of using MWNT thin films for measuring sub-ppm NO_2 concentrations (10 to 100 ppb) in dry air, with the maximum response at 165°C. The gas-sensing properties of NT thin films depend on the nature of the defect and concentration.[562]

Gas-sensing characteristics of MWNTs as applied to humidity, NH_3, CO, and CO_2 partial pressure have been studied.[563] A practical gas sensor for ammonia and water vapor, based on measuring the variation of the electrical conductivity of MWNT ropes, has been proposed.[564] In particular, the absorption of different gases in the MWNT/SiO_2 layer changes the permittivity and conductivity of the material, consequently altering the resonant frequency of the sensor, which is tracked remotely, using a loop antenna.[564] Detecting properties of MWNTs for NH_3 allow the exploitation of the sensor at room temperature.[565]

The construction of gas sensors based on MWNT thin films to measure NO_2, CO, NH_3, H_2O, and C_2H_5OH concentrations has been described.[561]

The thermoelectric response due to the interaction of adsorbed molecules with NT walls can be used to detect gases such as He, N_2, and H_2.[566]

The viability of using boron- or nitrogen-doped NT films as sensors has been suggested[567] and verified.[568] It was shown that sensors fabricated using individual films of CN_x NTs have a fast response for NH_3 and reach saturation within 2 to 3 sec. The experiments also indicate a great potential in the manufacture of solvent vapor sensors, and especially for ethanol, acetone, and chloroform detection. The simple casting of SWNTs on an inter-digitated electrode allows to the fabrication of a gas sensor for detection of NO_2 and nitrotoluene.[569]

Rational chemical modification of NTs leads to the fabrication of a sensor having good molecular selectivity. A selective molecular hydrogen sensor has been formed using SWNTs decorated with Pd nanoparticles.[570] Sensing properties of NTs can be amplified using conjugated polymer composites (see Ref. 571 and references therein).

5.8 ATTACHMENT OF BIOMOLECULES

NTs are considered to be biocompatible[572–576] and attract great interest as a material for biological applications. The main fields of such applications include: (1) fabrication of bioprobes and biosensors, (2) synthesis of molecular structures for the transport of vaccines and drugs, especially water-insoluble substances into the body or to a certain body organ, (3) formation of anti-fouling surfaces (enzyme-containing composites), (4) use of NTs as a template to grow cells, and (5) creation of implantable bioelectronic devices.

5.8.1 BIOSENSORS

The development of biosensors has taken greater importance in the past years of heightened security. Biosensors are defined as analytical devices incorporating biological material (e.g., DNA, enzymes, antibodies, microorganisms, etc.) associated with or integrated within a physico-chemical transducer. In contrast to gas sensors, biosensors act in the aqueous phase, particularly in physiological solutions. NTs have definite advantages in sensing applications: small size, large specific surface, high sensitivity, fast response, and good reversibility.[577]

Amperometric sensors are based on the reaction between a biomolecule immobilized on the sensor electrode with the analyte. The reaction produces an electric current, which is proportional to the analyte concentration and can be measured.

The NT film can be easily fabricated on a glassy carbon or edge-plane carbon surfaces to form an electrode.[576] Nonfunctionalized NT electrodes have been used in electrochemical oxidation of dopamine and norepinephrine[578,579] and to determine thyroxine.[580] The NT sidewalls can be functionalized for biocompatibility and to display selective binding sites for specific biological analytes.[573] Different bio-molecules, such as proteins, enzymes, and DNAs, can be attached to the NTs. The attachment can be covalent or noncovalent. The noncovalent linking of DNA is a usual way to modify NTs.[573,581–584] The method elaborated by Chen et al.[583] involves a bi-functional molecule, 1-pyrenebutanoic acid, and succinimidyl ester, irreversibly adsorbed onto the inherently hydrophobic surfaces of SWNTs in an organic solvent. Succinimidyl ester groups are highly reactive to nucleophilic substitution by primary and secondary amines that exist in abundance on the surface of most proteins.

The covalent binding of DNA with NTs has been described.[585–587] A major area of interest for biosensor developers is the study of human DNA. The NT array electrode functionalized with DNA/PNA can detect the hybridization of targeted DNA/RNA from the sample. A nanoelectrode array based on vertically aligned MWNTs embedded in SiO_2 has been reported by Li et al.[588] and Koehne et al.[589] Oligonucleotide probes were selectively attached to the ends of the MWNTs. The hybridization of subattomole DNA targets was detected by combining the electrode array with ruthenium bipyridine-mediated guanine oxidation.

Such electro-chemical assay provides enhanced daunomycin signals.[590] A MWNTs–COOH-modified glassy carbon electrode was fabricated and oligonucleotides with 5′-amino groups were covalently bonded to the carboxyl group of NTs.

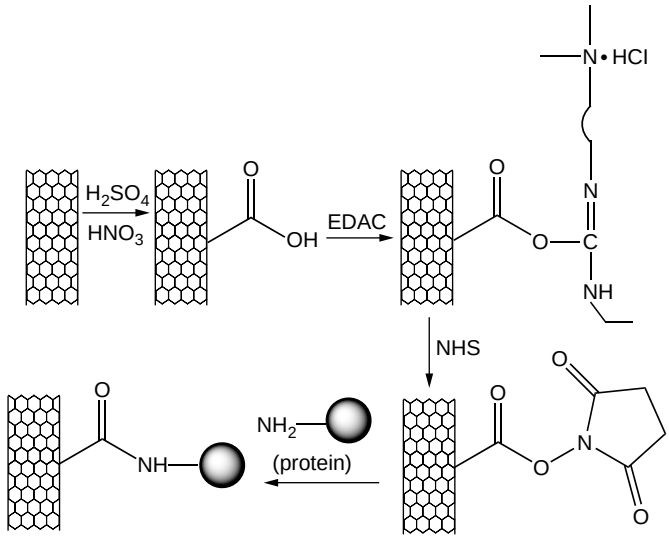

FIGURE 5.16 The attachment of proteins to NTs via a two-step process of diimide-activated amidation. (From Jiang, K. et al., *J. Mater. Chem.*, **14**, 37–39, 2004. With permission.)

Trace levels of oligonucleotides and polynucleotides can be readily detected following short accumulation periods with detection limits of 25, 60, 126, and 219 µg/L for oligo(dG)(21), oligo(dG)(11), ss, and da calf thymus DNA, respectively.[591]

A novel glucose biosensor based on NT-modified electrode is also of great practical interest. Glucose oxidase (GOx) is a flavine enzyme used commercially on a massive scale to monitor blood glucose levels in diabetics. The GOx adsorbs spontaneously on NT sheets and can be reversibly oxidized without complete loss of enzymatic activity.[592] A vertical array of MWNTs with GOx molecules is adsorbed non-specifically on the exposed ends.[593] The electrode exhibits an amperometric response in the presence of varying glucose concentrations. Different methods of GOx immobilization onto NTs have been described.[594–596]

SWNTs fabricated into field effect transistors have several advantages over conventional sensor systems, providing high sensitivity and allowing real-time detection.[597] This approach has been used to fabricate biosensors for streptavidin recognition.[598] NT coated with a polymer functional layer was functionalized with protein biotin, thus providing specific molecular detection.

The immobilization of different proteins and enzymes onto NTs for the development of new biosensors has been described.[599–606] Two different methods were employed for NTs functionalization with bioactive peptides:[607] (1) fragment condensation of fully protected peptides and (2) selective chemical ligation. The latter is shown in Figure 5.16.

Biosensors can be applied for detecting of diseases, particularly in cancer diagnostics.[608,609]

Detection of organophosphorus pesticides and nerve gases by biosensors is possible.[610] Detection of pathogens and toxins, and direct determination of total cholesterol in blood, has been studied. Bacterial binding has been used to create biosensors.[611] The capture of specific bacteria by particular antibodies can be detected by different sensor platforms, e.g., by acoustic wave sensors, using piezoelectric resonator. NTs can also be potentially used as ion channel biosensors.[388]

The study of the kinetics and thermodynamics of biological redox processes by biosensors is an important part of biochemistry.[576,612] As per theory, NIR-radiation-excited NT ropes could control the activity of proteins *in vivo*.[613]

5.8.2 Others Fields of Application

Enzyme-containing polymer/SWNT composites have been explored as unique biocatalytic materials.[614] NTs functionalized with bioactive peptides act as a medium to transfer peptides across the cell membranes.[615]

MWNTs functionalized with hemin are able to detect oxygen in solution.[616,617] Bucky paper can be used for transplanting cells into the retina. In experiments, the substrate worked as a scaffold for the growth of the retinal cells taken from white rabbits, for implanting in other rabbits. The NTs served as substrates for neuronal growth.[618,619]

Some biomolecules solubilize NTs. Lipid rings[620] and DNA[621] have been studied as solubilizers to dissolve NTs in aqueous solutions. The solubility of β-galactoside-modified SWNTs in water was shown to be increased by adsorption of lectin molecules.[622] NTs in the presence of galactose-specific lectins form micrometer-sized nanostructures.

Solubilization using single-stranded DNA allows the purification and separation of NTs.[623,624] By screening a library of oligonucleotides, scientists found that a certain sequence of single-stranded DNA self-assembles into a helical structure around individual NTs. Since NT/DNA hybrids have different electrostatic properties that depend on the NT diameter and electronic structure, they can be separated and sorted using anion-exchange chromatography. DNA-stabilized dispersions of NTs prepared by Barisci et al.[625] are concentrated (up to 1%, by mass) and are better suited for fiber spinning than conventional surfactants.

Selective localization of SWNTs on aligned DNA molecules on surfaces is an important tool in bottom-up bio-templated nanofabrication.[626] Self-assembly based on molecular recognition could be the best approach for constructing complex architectures (e.g., field-effect transistor[627]) for miniature biological electronics and optical devices. The attachment of DNA to oxidatively opened ends of MWNT arrays[587] and the DNA-guided assembly of NTs[628] have been studied.

5.9 NANOTUBES AS TEMPLATES

5.9.1 Substitution of the Carbon Atoms of Nanotubes

The incorporation of some chemical elements in carbon NTs leads to a new nanomaterial without a significant modification of the NT structure, but with possible improvement of their properties. Substitution of carbon atoms with nitrogen or boron atoms is most interesting from a practical standpoint. It allows the formation of hetero-junctions within a single NT, and opens a way to use such a tube in electronic devices. Besides, substitution with silicon has also been studied.

Tight-binding calculations show that the presence of nitrogen atoms is responsible for introducing donor states near Fermi level.[629,630] Nitrogen-doped carbon NTs have been found to be metals[630,631] (earlier it was stated that the modified tubes were metals or semiconductors depending on the relative position of nitrogen and carbon atoms[632]).

Arc-discharge process[633,634] and pyrolysis[629,635–646] are the main methods of nitrogen-substituted carbon NT synthesis. The third method is carbon-resistive heating under high isostatic nitrogen pressure.[647]

The incorporation of nitrogen into carbon NTs grown by arc-discharge method takes place in an helium–nitrogen atmosphere[633] or by introducing nitrogen-rich organic or inorganic precursors into the anode rods.[634] Metal phthalocyanines,[636,641] methane and nitrogen mixtures,[637–639,646] ferrocene and melamine mixtures,[629,640] acetylene/ammonia/iron carbonyl mixtures,[642] acetylene/ammonia/hydrogen mixtures,[643] and acetonitrile or acetonitrile/hydrogen mixtures[644,645] have been used in CVD processes.

The amount of incorporated nitrogen varies from some tenths of a percent to 9%[641] and even 13%.[647] The nitrogen incorporation enhances the growth of NTs by the CVD process and induces visible changes in the NT structure and morphology. Overall, the presence of nitrogen suppresses the formation of bundles, changes the tube conformation, and leads to the NT texturing.

All boron-doped carbon NTs exhibit highly metallic electronic character. Boron has been shown to play a key role at the open end of a growing carbon NT, thus increasing its overall length.

Boron-substituted NTs are formed by arc-discharge[634,648,649] or CVD[650,651] methods. Moreover, solid-state[652–655] and gas–solid[656,657] reactions are also employed to prepare the material.

It is possible to reach boron-substitutional level up to 20%[653,654] and synthesize carbon-free BN nanotubes.[656,658] The methods described allow the preparation of B–C–N NTs[635] and NFs.[634,658–661]

The determined properties of silicon-doped carbon NTs and a suggestion how such tubes can be synthesized have been published.[662,663] The interaction of carbon NTs with SiO_2 or Si yields SiC nanorods (see the next section). Some substitution reactions have been developed to produce hetero-structures of SWNTs and metal-carbide nanorods.[664]

5.9.2 Decoration of Carbon Nanotubes

Surface-modified carbon NTs, inorganic NTs, and nanorods are of great significance in various practical applications, such as catalysis, electrocatalysis, photocatalysis, ion-exchange and gas sorption, electron emitter and nanodevice fabrication, and production of composites. "Decoration" is often referred to as a process of covering NTs with a substance that does not form strong chemical bonds with carbon atoms. At the same time, several decoration processes yield a covering substance linked by weak chemical or electrostatic forces to the NTs.

NTs can be decorated with metals (Cu, Ag, Au, Al, Ti, Ni, Pt, Pd), alloys (Co–B, Ni–P, Mo–Ge), nonmetals (Se), metal oxides (ZnO, CdO, Al_2O_3, CeO_2, SnO_2, SiO_2, TiO_2, V_2O_5, Sb_2O_5, MoO_2, MoO_3, WO_3, RuO_2, IrO_2), metal chalcogenides (ZnS, CdS, CdSe, CdTe), metal carbides (SiC), metal nitrides (SiN_x, AlN), and polymers (polyaniline, polypyrrole). The list of such substances can go on. It is possible to prepare the covering of NTs in the form of quantum dots and nanoparticles, to isolate nanotubules or nanorods and nanowires. The surface structure of NTs, and the strategy and extent of deposition greatly influence the morphology of a coating.

The approaches to decoration of NTs include physical evaporation, electroless deposition, electroplating, CVD, sol–gel process, chemical attachment of metal ions or complexes with subsequent reduction or thermal decomposition, solid-state reactions, solid–gas reactions, self-assembling, polymerization, and others chemical processes.

The decoration of NTs with nickel is achieved by electroless plating method,[665–668] by electrochemical deposition process,[669,670] by chemical reduction of $NiCl_2$ with hydrogen,[671] or by electron-beam evaporation of the metal.[672,673] Copper has been deposited onto NTs by electroless plating[667] or by reduction of $CuCl_2$ with hydrogen.[674] Cobalt has been plated onto NTs via electroless plating[675] or by reduction of $Na_2Co(OH)_4$ using KBH_4 solution.[676] Electroless plating usually demands preliminary chemical activation of a substrate.

Several procedures have been used to decorate acid-treated NTs with nanoscale clusters of Ag, Au, Pt, and Pd. For instance, Satishkumar et al.[677] carried out the refluxing with $HAuCl_4$ and HNO_3 or *tetrakis* hydroxymethyl phosphonium chloride, with H_2PtCl_6 and HNO_3 or ethylene glycol, and with $AgNO_3$ and HNO_3; Li et al.[678] refluxed NTs for 6 h with H_2PtCl_6 dissolved in ethylene glycol. The activity of Pt cathode catalyst for direct methanol fuel cells has been shown to be dependent on the ratio of water/ethylene glycol.[679] Pt/NTs composite prepared by reduction of H_2PtCl_6 with $Na_2S_2O_6$ in water/alcohol solution exhibited good catalytic properties.[69] It is possible to use sorption of Pd^{2+} ions from solution with subsequent hydrogen reduction.[680,681] Contact of an acetone solution of H_2PtCl_6 with NTs allows production of NTs decorated with platinum clusters without any surface functionalization.[682] Decomposition and reduction of H_2PtCl_6, $HPdCl_3$, $HAuCl_4$, or $AgNO_3$ dispersed on NTs at temperatures from 300 to 700°C gives metal nanoparticles with average size of 7 to 17 nm.[683] Nanoparticle/NT hybrid structures have been prepared by forming Au and Pd nanoparticles on the sidewalls of SWNTs using reducing reagents or catalyst-free electroless deposition, as a result of direct redox reaction between metal ions and NTs.[684] Because Au^{3+} and Pt^{2+} have much higher reduction potential than NTs, they are reduced spontaneously. Hydrogen reduction of a Pd(II)-β-diketone precursor in super-critical carbon dioxide produces Pd nanoparticles on MWNTs.[405,685]

As for gold and silver nanoparticles, the usual thiol-linking procedure can be used to anchor them to NTs.[686–688] Silver clusters on SWNT surface have been grown by the decomposition of (cycloocta-1,5-diene)(hexafluoroacetylacetonate)silver(I).[686] A highly selective electroless deposition of gold nanoparticles on SWNTs has been reported.[684] Sonication allows the deposition of gold onto MWNTs directly from gold colloid solution.[689] A method to fabricate gold nanowires using NTs as positive templates has been demonstrated.[690] The first step was to self-assemble gold nanocrystals along NTs. After thermal treatment, the nanocrystal assemblies were transformed into continuous polycrystalline gold nanowires. Monolayer-protected Au clusters strongly adsorb onto both end-opened and solubilized when refluxed in aniline SWNTs.[195]

Formation of different metal nanowires using NTs as positively charged template has been described.[691]

To form a SiO_2 or SiO_x coating on NTs as well as to prepare silica nanotubes, silica nanorods and silica/NT composites, sol–gel technique has been employed by many researchers.[692–696] Tetraethoxysilane (tetraethyl-*o*-silicate) was the usual precursor in this process. Silica-coated SWNTs have also been produced by adding silica/H_2SiF_6 solution to a surfactant-stabilized dispersion of SWNTs[697] or by hydrolysis of 3-aminopropyltriethoxysilane.[698]

NTs have been coated with titania by using titanium *bis*-ammonium lactato dihydroxide,[699] tetraethyl-*o*-titanate,[696,700] titanium tetraisopropoxide,[147,700] titanium oxysulfate,[700] and titanium tetrachloride[701] as precursors. Sol–gel method has been used to sheathe NT tips for field emission electron emitters (Figure 5.17).[702] The coating morphology depends on the precursor composition and method of deposition.[700] Covalent linking of TiO_2 nanocrystals to SWNTs by short-chain organic molecule linker is demonstrated.[147]

Coating of NTs with alumina[692,696,703] or $Al(OH)_3$[704] is possible by either thermal or chemical decomposition of aluminum sources, such as aluminum isopropoxide, aluminum trichloride, or aluminum nitrate. Oxidation of a powdered aluminum metal/MWNT mixture with O_2 or air leads to the formation of Al_2O_3 nanotubes or nanowires.[705] Treating the same mixture in NH_3 atmosphere at 300 to 500°C yields AlN nanowires or particles.[705]

SWNTs and MWNTs can be coated with a thin or thick film of SnO_2.[706–708] Heat treatment of MWNTs with zinc at various temperatures gives ultra-thin films of ZnO on the tubes, ZnO quantum dots, or nanowires.[709] Deposition of CeO_2 nanoparticles on the surface of MWNTs by hydrolysis of $CeCl_3$ in aqueous solution has been described.[710] Covering of NTs with oxides of different metals (V, Sb, Mo, Ir, Ru) has been characterized.[711,712]

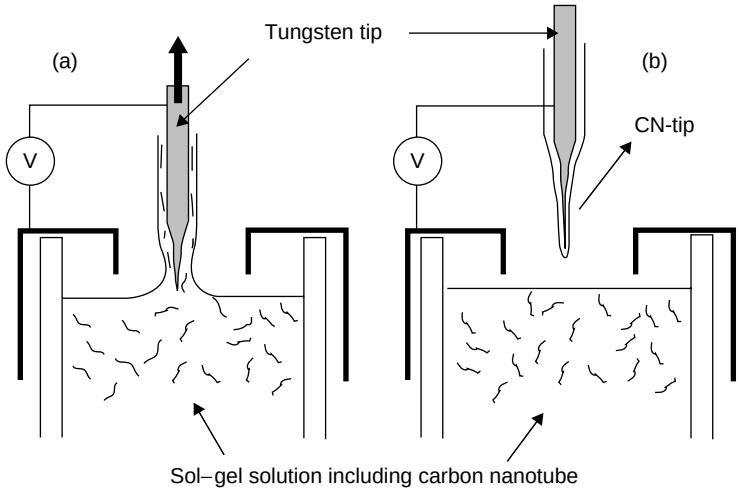

FIGURE 5.17 Schematic illustration of the sol–gel coating process under DC voltage. (From Brioude, A. et al., *Appl. Surf. Sci.*, **221**, 4–9, 2004. With permission.)

Semiconductor metal chalcogenide nanoparticles such as CdS,[713] CdSe,[147,205,714,205] CdTe,[148] and ZnS[715,714] have been bound to the surfaces of NTs. The example of an attachment process is presented in Figure 5.18.

Reaction of carbon NTs and carbon NFs with silicon[716,717] as well as with silica[718] allows the production of SiC coatings, NFs or nanorods. The plasma enhanced CVD (PECVD) method using mixtures of SiH_4 with C_2H_2 or with NH_3 introduced into the reaction chamber at 250°C has been used to coat MWNTs with amorphous films of SiC or SiN_x.[719] A process of simultaneous growth of carbon NTs and SiC nanorods has been realized by means of CVD.[720]

The aligned NTs can be used to make conducting polymer/NT coaxial nanowires by electrochemical deposition of a concentric layer of conducting polypyrrole.[721] Ultra-thin films of pyrrole were deposited on the surfaces of MWNTs using a plasma polymerization technique.[722] Polymer nanoshells on NTs can be formed via layer-by-layer deposition on NT template.[723]

Interesting and unusual nanowires of rare-earth phthalocyanine have been produced via the templated assembly method.[724] When the solvent is evaporated gradually, $RErPc_2$ nanoparticles and nanowires are found to self-assemble on the exterior walls of NTs.

5.10 INTERCALATION OF "GUEST" MOIETIES

Similar to graphite, NTs can form guest–host compounds with electron acceptors (e.g., bromine, iodine, interhalogens, $FeCl_3$, HNO_3) and electron donors (alkali metals).[8,16,18] The guest species can be inserted between the graphene shells of MWNTs or in the open inter-tubular spaces inside the bundles of SWNTs. Reversible inter-calation proceeds by both direct vapor/liquid contacting and electrochemical insertion of ions. The doping is accompanied by charge transfer and enhancement of NT conductivity.

The inter-calation of bromine into MWNTs at 50°C shows an unusual ordered accumulation along the direction perpendicular to the NT surface.[725] Iodine reversibly forms charged polyiodide chains into SWNT bundles,[726] which is similar to the chains in iodine-doped SWNTs[418] and MWNTs.[419]

The behavior of MWNTs depends on their structure. In addition to $FeCl_3$, other metal chlorides ($ZnCl_2$, $CdCl_2$, $AlCl_3$, and YCl_3) formed inter-calation compounds with MWNTs having scroll structure.[18]

The HNO_3 molecules intercalate into the bundles of SWNT,[727] and HNO_3, H_2SO_4, and HCl intercalate into the SWNT film ("bucky paper").[728] In all cases, an acceptor-type doping of the SWNTs has been observed.

Fluorine, as was mentioned earlier (see Section 5.5.3), forms strong semi-ionic or covalent bonds with carbon atoms of NTs and cannot be deintercalated in diatomic molecular form.

Much more information has been obtained on NT doping with alkali metals. Some theoretical models of inter-calation products have been offered.[16,18] Potassium and other heavy-weight alkali metals at saturation state form MC_8 compounds corresponding to the first-stage graphite inter-calation compounds (GIC).[16,18] The doping of SWNTs is diameter-selective.[729,730] The dopant atoms initially deposited on the tips of aligned MWNTs diffuse toward their roots at extremely small rates.[731]

The rapid development of lithium-ion batteries, which use graphite or carbonaceous materials as one of the electrodes, gives rise to a great interest in NT material inter-calation with lithium.[5,522] A significant reversible capacity has been found.[732] SWNTs can be reversibly inter-calated with lithium up to $Li_{1.7}C_6$ composition.[733] The reversible lithium storage capacity after etching of SWNTs increases to Li_2C_6.[734,735] Moreover, this saturation composition increases to $Li_{2.7}C_6$ by applying a suitable ball-milling treatment to the purified SWNTs.[736] It means that SWNTs can contain roughly twice the energy density of graphite. To explain the results of Refs. 732 and 736, a non-GIC mechanism of storage has been proposed.[737] In this mechanism, except for the lithium intercalated between graphene layers to form GIC, the higher charge capacity should be related to lithium doped into disordered graphitic structures, defects, microcavities, and edge of graphitic layers.

The reversible capacity increases as compared to that of raw NTs after treatment with lithium compounds such as $LiNO_2$.[738] The lithium diffusion coefficient decreases with an increase of the

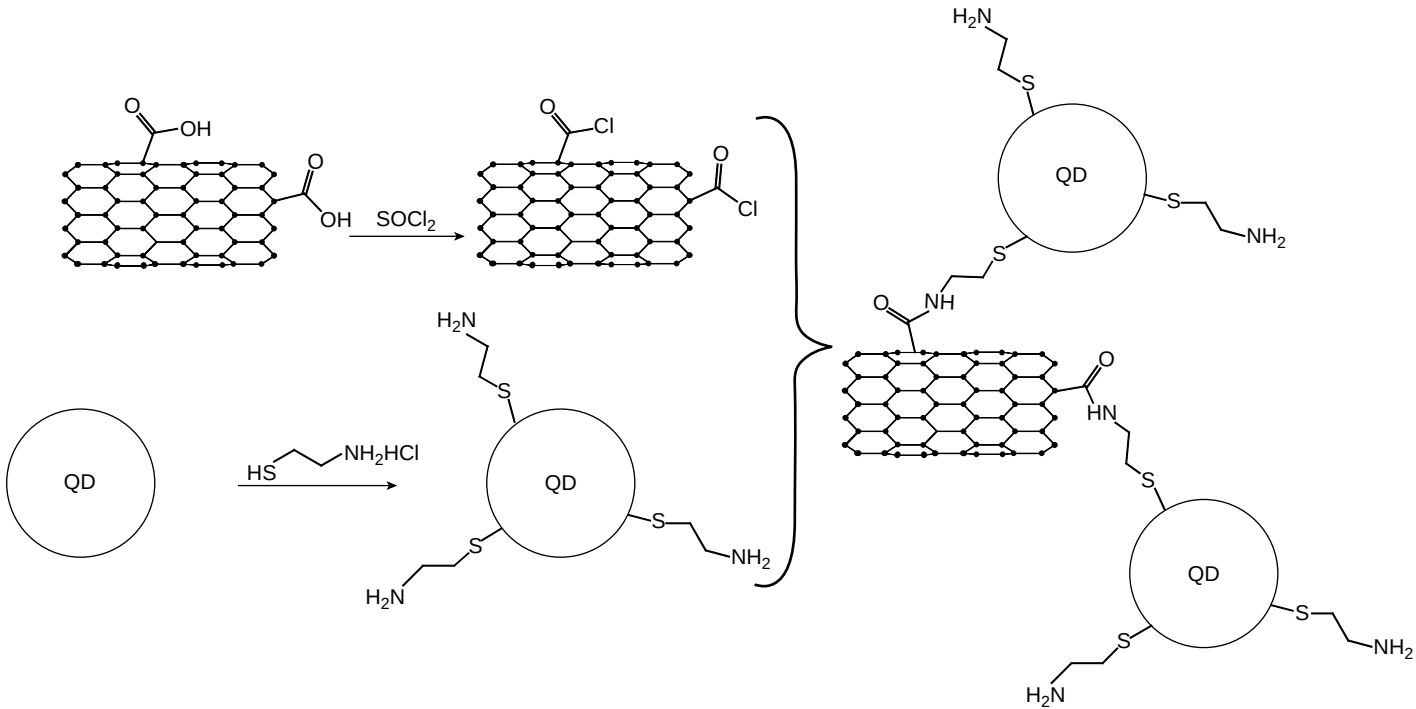

FIGURE 5.18 Quantum dots (QD) attachment at cut ends or at defects along NT sidewall. (From Haremza, J.M. et al., *Nano Lett.*, **2**, 1253–1258, 2002. With permission.)

open-circuit voltage. This phenomenon is presumably connected with a change of composition and properties of thin inorganic film covering the NTs.

5.11 SUMMARY AND CONCLUSIONS

Carbon NTs represent a set of materials including numerous variants with different structure, morphology, and properties. Some of these materials are now coming to the industrial arena as new attractive resources with many remarkable properties and dozens of promising applications. Several scaleable continuous chemical methods of NT production have been elaborated and scaled.

The practical significance of carbon NT chemistry and its achievements is sharply increased. Today, this branch of NT "general chemistry" subdivides into carbon NT inorganic, organic, bioorganic, colloidal, and polymeric chemistry. NT chemistry now occurs in solution, in such a way that it opens many new possibilities to purify, sort, and modify the material and to integrate it in electronic devices.

Carbon NTs are among the most important materials of modern nanoscience and nanotechnology, including molecular electronics, and the chemistry of NTs play a remarkable role in the development of this interdisciplinary area.

ACKNOWLEDGMENTS

The author is grateful to Mr. I. Anoshkin and Mr. Nguyen Tran Hung for their helpful assistance.

REFERENCES

1. J.-M. Bonard, H. Kind, T. Stöckli, and L.-O. Nilsson, Field emission from carbon nanotubes: the first five years, *Solid-State Electron.* **45**, 893–914 (2001).
2. R.H. Baughman, A.A. Zakhidov, and W.A. de Heer, Carbon nanotubes — the route toward applications, *Science* **297**, 787–792 (2002).
3. Ph. Avouris, Carbon nanotube electronics, *Chem. Phys.* **281**, 429–445 (2002).
4. T.W. Odom, J.-L. Huang, and C.M. Lieber, Single-walled carbon nanotubes: from fundamental studies to new device concepts, *Ann. N.Y. Acad. Sci.* **960**, 203–215 (2002).
5. M. Daenen, R.D. de Fouw, B. Hamers, P.G.A. Janssen, K. Schouteden, and M.A.J. Veld, *The Wondrous World of Carbon Nanotubes. A Review of Current Carbon Nanotube Technologies.* Eindhoven University of Technology, 2003, p. 93.
6. *Nanotubes: Technology and Directions*. Business Communication Co., Inc., 2003, p. 280 [http://www.marketresearch. com/map/prod/967076.html].
7. E.G. Rakov, Methods for preparation of carbon nanotubes, *Russ. Chem. Rev*. **69**, 35–52 (2000).
8. E.G. Rakov, The chemistry and application of carbon nanotubes, *Russ. Chem. Rev*. **70**, 827–863 (2001).
9. O. Zhou, H. Shimoda, B. Gao, S. Oh, L. Fleming, and G. Yue, Materials science of carbon nanotubes: fabrication, integration, and properties of macroscopic structures of carbon nanotubes, *Acc. Chem. Res.* **35**, 1045–1053 (2002).
10. J. Hilding, E.A. Grulke, Z.G. Zhang, and F. Lockwood, Dispersion of carbon nanotubes in liquids, *J. Disp. Sci. Technol.* **24**, 1–41 (2003).
11. S. Niyogi, M.A. Hamon, H. Hu, B. Zhao, P. Bhowmik, R. Sen, M.E. Itkis, and R.C. Haddon, Chemistry of single-walled carbon nanotubes, *Acc. Chem. Res.* **35**, 1105–1113 (2002).
12. Z. Chen, W. Thiel, and A. Hirsch, Reactivity of the convex and concave surfaces of single-walled carbon nanotubes (SWNTs) toward addition reactions: dependence on the carbon-atom piramidalization, *Chem. Phys. Chem*. **4**, 93–97 (2003).
13. T. Yu. Astakhova, G.A. Vinogradov, O.D. Gurin, and M. Menon, Effect of local strain on the reactivity of carbon nanotubes, *Russ. Chem. Bull.* **51**, 704–708 (2002).
14. K.D. Ausman, H.W. Rohrs, M. Yu, and R.S. Ruoff, Nanostressing and mechanochemistry, *Nanotechnology* **10**, 258–262 (1999).

15. D. Srivastava, D.W. Brenner, J.D. Schall, K.D. Ausman, M.F. Yu, and R.S. Ruoff, Predictions of enhanced chemical reactivity at regions of local conformational strain on carbon nanotubes: kinky chemistry, *J. Phys. Chem.* **B 103**, 4330–4337 (1999).
16. J.E. Fischer, Chemical doping of single-wall carbon nanotubes, *Acc. Chem. Res*. **35**, 1079–1086 (2002).
17. Y.-P. Sun, K. Fu, Y. Lin, and W. Huang, Functionalized carbon nanotubes: properties and applications, *Acc. Chem. Res*. **35**, 1096–1104 (2002).
18. L. Duclaux, Review of the doping of carbon nanotubes (multiwalled and single-walled), *Carbon* **40**, 1751–1764 (2002).
19. A. Hirsch, Functionalization of single-walled carbon nanotubes, *Angew. Chem. Int. Edit*. **41**, 1853–1859 (2002).
20. L. Dai, A. Patil, X. Gong, Z. Guo, L. Liu, Y. Liu, and D. Zhu, Aligned nanotubes, *Chem. Phys. Chem.* **4**, 1150–1169 (2003).
21. T. Lin, V. Bajpai, T. Ji, and L. Dai, Chemistry of carbon nanotube, *Aust. J. Chem*. **56**, 635–651 (2003).
22. J.-M. Ting and J.B.C. Lan, Beaded carbon tubes, *Appl. Phys. Lett.* **75**, 3309–3311 (1999).
23. K.De Jong and J.W. Geus, Carbon nanofibers: catalytic synthesis and applications, *Catal. Rev. Sci. Eng*. **42**, 481–510 (2000).
24. C.T. Kingston and B. Simard, Fabrication of carbon nanotubes, *Anal. Lett.* **36**, 3119–3145 (2003).
25. C. Journet, W.K. Maser, P. Bernier, A. Loiseau, M. Lamy de la Chapelle, S. Lefrant, P. Deniard, R. Lee, and J.E. Fischer, Large-scale production of single-walled carbon nanotubes by the electric-arc technique, *Nature* **388**, 756–758 (1997).
26. Z. Shi, Y. Lian, X. Zhou, Z. Gu, Y. Zhang, S. Iijima, L. Zhou, K.T. Yue, and S. Zhang, Mass-production of single wall carbon nanotubes by arc discharge method, *Carbon* **37**, 1449–1453 (1999).
27. M. Takizawa, S. Bandow, M. Yudasaka, Y. Ando, H. Shimoyama, and S. Iijima, Change of tube diameter distribution of single-wall carbon nanotubes induced by changing the bimetallic ratio of Ni and Y catalysts, *Chem. Phys. Lett*. **326**, 351–357 (2000).
28. M. Cadek, R. Murphy, B. McCarthy, A. Drury, B. Lahr, R.C. Barklie, M. in het Panhuis, J.N. Coleman, and W.J. Blau, Optimization of the arc-discharge production of multi-wall carbon nanotubes, *Carbon* **40**, 923–928 (2002).
29. A.V. Krestinin, N.A. Kiselev, A.V. Raevskii, A.G. Ryabenko, D.N. Zakharov, and G.I. Zvereva, Perspectives of single-wall carbon nanotube production in the arc discharge process, *Euras. Chem. Tech. J*. **5**, 7–18 (2003).
30. T. Guo, P. Nikolaev, A. Thess, D.T. Colbert, and R.E. Smalley, Catalytic growth of single-walled nanotubes by laser vaporization, *Chem. Phys. Lett*. **243**, 49–54 (1995).
31. M. Yudasaka, T. Komatsu, T. Ichihashi, and S. Iijima, Single-wall carbon nanotube formation by laser ablation using double-targets of carbon and metal, *Chem. Phys. Lett*. **278**, 102–106 (1997).
32. O. Jost, A.A. Gorbunov, J. Möller, W. Pompe, A. Graff, R. Friedlein, X. Liu, M.S. Golden, and J. Fink, Impact of catalyst coarsening on the formation of single-wall carbon nanotubes, *Chem. Phys. Lett*. **339**, 297–304 (2001).
33. D.T. Colbert and R.E. Smalley, Past, present and future of fullerene nanotubes: buckytubes. *Perspectives of Fullerene Nanotechnology*. Ed. E. Osawa. Kluwer Academic Publishers, 2002, pp. 3–10.
34. W.K. Maser, A.M. Benito, and M.T. Martínez, Production of carbon nanotubes: the light approach, *Carbon* **40**, 1685–1695 (2002).
35. D. Laplaze, P. Bernier, W.K. Maser, G. Flamant, T. Guillard, and A. Loiseau, Carbon nanotubes: the solar approach, *Carbon* **36**, 685–688 (1998).
36. M.V. Antisari, R. Marazzi, and R. Krsmanovic, Synthesis of multiwall carbon nanotubes by electric arc discharge in liquid environments, *Carbon* **41**, 2393–2401 (2003).
37. N. Sano, J. Nakano, and T. Kanki, Synthesis of single-walled carbon nanotubes with nanohorns by arc in liquid nitrogen, *Carbon* **42**, 686–688 (2004).
38. Y.L. Hsin, K.C. Hwang, F.-R. Chen, and J.-J. Kai, Production and in-situ metal filling of carbon nanotubes in water, *Adv. Mater*. **13**, 830–833 (2001).
39. H.W. Zhu, X.S. Li, B. Jiang, C.L. Xu, Y.F. Zhu, D.H. Wu, and X.H. Chen, Formation of carbon nanotubes in water by the electric-arc technique, *Chem. Phys. Lett.* **366**, 664–669 (2002).
40. K. Shimotani, K. Anazawa, H. Watanabe, and M. Shimizu, New synthesis of multi-walled carbon nanotubes using an arc discharge technique under organic molecular atmospheres, *Appl. Phys*. **73 A**, 451–454 (2001).

41. V.A. Ryzhkov, On producing carbon nanotubes by a self-regulated electric contact arc discharge in hydrocarbon liquids. *NANOTUBE'02 Workshop*, Abstr. P-103 [http://dielc.kaist.ac.kr/nt02/abstracts/P103.shtml].
42. V.A. Ryzhkov, Use of self-regulated arc discharge in hydrocarbon liquids for bulk production of carbon nanotubes, *Int. Conf. Sci. Applic. Nanotubes 2003*, July 7–11, 2003, Seoul, Korea [http://nt03.skku.ac.kr/abstract/view.html?idx= NTqRCh4KAnABY].
43. Y. Gogotsi, J.A. Libera, and M. Yoshimura, Hydrothermal synthesis of multiwall carbon nanotubes, *J. Mater. Res.* **15**, 2591–2594 (2000).
44. J.A. Libera and Y. Gogotsi, Hydrothermal syntyesis of graphite tubes using Ni catalyst, *Carbon* **39**, 1307–1318 (2001).
45. D.C. Lee, F.V. Mikulec, and B.A. Korgel, Carbon nanotube synthesis in supercritical toluene, *J. Am. Chem. Soc.* **126**, 4951–4957 (2004).
46. P. Nikolaev, M.J. Bronikowski, R.K. Bradley, F. Rohmumd, D.T. Colbert, K.A. Smith, and R.E. Smalley, Gas-phase catalytic growth of single-walled carbon nanotubes from carbon monoxide, *Chem. Phys. Lett.* **313**, 91–97 (1999).
47. R. Andrews, D. Jacques, D. Qian, and T. Rantell, Multiwall carbon nanotubes: synthesis and application, *Acc. Chem. Res.* **35**, 1008–1017 (2002).
48. H. Dai, Carbon nanotubes: synthesis, integration, and properties, *Acc. Chem. Res.* **35**, 1035–1044 (2002).
49. K.B.K. Teo, C. Singh, M. Chhowalla, and W.I. Milne, Catalytic synthesis of carbon nanofibers. *Encyclopedia of Nanoscience and Nanotechnology.* Ed. H.S. Nalwa. Vol. 10, American Sci. Pub. 2003, pp. 1–22.
50. S. Maruyama, R. Kojima, Y. Miyauchi, S. Chiashi, and M. Kohno, Low-temperature synthesis of high-purity single-walled carbon nanotubes from alcohol, *Chem. Phys. Lett.* **360**, 229–234 (2002).
51. CoMoCat Process (University of Oklahoma, School Chem. Eng. Mater. Sci.) [http://www.ou.edu/engineering/nanotube/comocat.html].
52. M. Kusunoki, T. Suzuki, C. Honjo, T. Hirayama, and N. Shibata, Selective synthesis of zigzag-type aligned carbon nanotubes on SiC (000-1) wafers, *Chem. Phys. Lett.* **366**, 458–462 (2002).
53. T. Nagano, Y. Ishikawa, and N. Shibata, Preparation of silicon-on-insulator substrate on large free-standing carbon nanotube film formation by surface decomposition of SiC film, *Jpn. J. Appl. Phys.* **42**, 1717–1721 (2003).
54. Y.L. Li, Y.D. Yu, and Y. Liang, A novel method for synthesis of carbon nanotubes: low temperature solid pyrolysis, *J. Mater. Res.* **12**, 1678–1680 (1997).
55. S. Maruyama, Y. Miyauchi, T. Edamura, Y. Igarashi, S. Chiashi, and Y. Murakami, Synthesis of single-walled carbon nanotubes with narrow diameter-distribution from fullerene, *Chem. Phys. Lett.* **375**, 553–559 (2003).
56. T.S. Wong, C.T. Wang, K.H. Chen, L.C. Chen, and K.J. Ma, Carbon nanotube growth by rapid thermal processing, *Diamond Rel. Mater.* **10**, 1810–1813 (2001).
57. R. Katoh, Y. Tasaka, E. Sekreta, M. Yumura, F. Ikazaki, Y. Kakudate, and S. Fujiwara, Sonochemical production of a carbon nanotube. *Ultrason. Sonochem.* **6**, 185–187 (1999).
58. F. Fabry, T.M. Gruenberger, J. Gonzalez-Aguilar, H. Okuno, E. Grivei, N. Probst, L. Fulcheri, G. Flamant, and J.-C. Charlier, Continuous mass production of carbon nanotubes by 3-phase AC plasma processing, *Nanotech 2004, Vol. 3, Techn. Proc. of the 2004 NSTI Nanotechnology Conf. and Trade Show*, 228–231 (2004). March 7–11, Boston Sheraton Hotel & Copley Convention Center, Boston, MA.
59. Z. Jia, Z. Wang, J. Liang, B. Wei, and D. Wu, Production of short multi-walled carbon nanotubes, *Carbon* **37**, 903–906 (1999).
60. E. Farkas, M.E. Anderson, Z. Chen, and A.G. Rinzler, Length sorting *cut* single wall carbon nanotubes by high performance liquid chromatography, *Chem. Phys. Lett.* **363**, 111–116 (2002).
61. E. Borowiak-Palen, T. Pichler, X. Liu, M. Knupfer, A. Graff, O. Jost, W. Pompe, R.J. Kalenczuk, and J. Fink, Reduced diameter distribution of single-wall carbon nanotubes by selective oxidation, *Chem. Phys. Lett.* **363**, 567–572 (2002).
62. C. Bower, A. Kleinhammes, Y. Wu, and O. Zhou, Intercalation and partial exfoliation of single-walled carbon nanotubes by nitric acid, *Chem. Phys. Lett.* **288**, 481–486 (1998).
63. K.H. An, K.K. Jeon, J.-M. Moon, S.J. Eum, C.W. Yang, G.-S. Park, C.Y. Park, and Y.H. Lee, Transformation of singlewalled carbon nanotubes to Multiwalled carbon nanotubes and onion-like structures by nitric acid treatment, *Synt. Met.* **140**, 1–8 (2004).
64. K.B. Shelimov, R.O. Esenaliev, A.G. Rinzler, C.B. Huffman, and R.E. Smalley, Purification of single-wall carbon nanotubes by ultrasonically assisted filtration, *Chem. Phys. Lett.* **282**, 429–434 (1998).

65. A. Kukovecz, Ch. Kramberger, M. Holzinger, H. Kuzmany, J. Schalko, M. Mannsberger, and A. Hirsch, On the stacking behavior of functionalized single-wall carbon nanotubes, *J. Phys. Chem.* **B 106**, 6374–6380 (2002).
66. J. Liu, A.G. Rinzler, H. Dai, J.H. Hafner, R.K. Bradley, P.J. Boul, A. Lu, T. Iverson, K. Shelimov, C.B. Huffman, F. Rodriguez-Macias, Y.-S. Shon, T.R. Lee, D.T. Colbert, and R.E. Smalley, Fullerene pipes, *Science* **280**, 1253–1255 (1998).
67. Y. Yang, J. Zhang, X. Nan, and Z. Liu, Toward the chemistry of carboxylic single-walled carbon nanotubes by chemical force microscopy, *J. Phys. Chem*. **B 106**, 4139–4144 (2002).
68. Y. Yang, H. Zou, B. Wu, Q. Li, J. Zhang, Z. Liu. X. Guo, and Z. Du, Enrichment of large-diameter single-walled carbon nanotubes by oxidative acid treatment, *J. Phys. Chem*. **B 106**, 7160–7162 (2002).
69. J. Chen, C. Xu, Z. Mao, G. Chen, B. Wei, J. Liang, and D. Wu, Fabrication of Pt deposited on carbon nanotubes and performance of its polymer electrolyte membrane fuel cells, *Sci. China* **45**, 82–86 (2002).
70. F. Simon, Á. Kukovecz, and H. Kuzmany, Controlled oxidation of single-wall carbon nanotubes: a Raman study, *AIP Conf. Proc*. **685**, No. 1, 185–188 (2003).
71. Y. Feng, G. Zhou, G. Wang, M. Qu, and Z. Yu, Removal of some impurities from carbon nanotubes, *Chem. Phys. Lett.* **375**, 645–648 (2003).
72. B.C. Satishkumar, A. Govindaraj, J. Mofokeng, G.N. Subbanna, and C.N.R. Rao. Novel experiments with carbon nanotubes: opening, filling, closing and functionalizing, *J. Phys.* **B 29**, 4925–4934 (1996).
73. N.I. Kovtyukhova, T.E. Mallouk, L. Pan, and E.C. Dickey, Individual single-walled nanotubes and hydrogels made by oxidative exfoliation of carbon nanotube ropes, *J. Am. Chem. Soc.* **125**, 9761–9769 (2003).
74. J.M. Skowroński, P. Scharff, N. Pfänder, and S. Cui, Room temperature electrochemical opening of carbon nanotubes followed by hydrogen storage, *Adv. Mater.* **15**, 55–57 (2003).
75. T. Ito, L. Sun, and R.M. Crooks, Electrochemical etching of individual multiwall carbon nanotubes, *Electrochem. Solid-State Lett.* **6**, C4–C7 (2003).
76. J.-Y. Chang, A. Ghule, J.-J. Chang, S.-H. Tzing, and Y.-C. Ling, Opening and thinning of multiwall carbon nanotubes in supercritical water, *Chem. Phys. Lett.* **363**, 583–590 (2002).
77. S. Nagasawa, M. Yudasaka, K. Hirahara, T. Ichihashi, and S. Iijima, Effect of oxidation on single-wall carbon nanotubes, *Chem. Phys. Lett.* **328**, 374–380 (2000).
78. E. Borowiak-Palen, X. Liu, T. Pichler, M. Knupfer, J. Fink, and O. Jost, Diameter control of single-walled carbon nanotubes by selective oxidation, *NANOTUBE'02 Workshop*, Sa-RS2-Sy46, Log Number: P-53 [http://dielc.kaist.ac.kr/nt02/abstracts/P53.shtml].
79. J.-M. Moon, K.H. An, Y.H. Lee, Y.S. Park, D.J. Bae, and G.-S. Park, High-yield purification process of singlewalled carbon nanotubes, *J. Phys. Chem*. **B 105**, 5677–5681 (2001).
80. P.X. Hou, S. Bai, Q.H. Yang, C. Liu, and H.M. Cheng, Multi-step purification of carbon nanotubes, *Carbon* **40**, 81–85 (2002).
81. E. Vázques, V. Georgakilas, and M. Prato, Microwave-assisted purification of HIPCO carbon nanotubes, *Chem. Commun.* 2308–2309 (2002).
82. C.-M. Yang, K. Kaneko, M. Yudasaka, and S. Iijima, Effect of purification on pore structure of HiPco single-walled carbon nanotube aggregates, *Nano Lett.* **2**, 385–388 (2002).
83. C. Xu, E. Flahaut, S.R. Bailey, G. Brown, J. Sloan, K.S. Coleman, V.C. Williams, and M.L.H. Green, Purification of single-walled carbon nanotubes grown by a chemical vapour deposition (CVD) method, *Chem. Res. Chinese Univ.* **18**, 130–132 (2002).
84. S. Gajewski, H.-E. Maneck, U. Knoll, D. Neubert, I. Dörfel, R. Mach, B. Strauβ, and J.F. Friedrich, Purification of single walled carbon nanotubes by thermal gas phase oxidation, *Diamond Rel. Mater.* **12**, 816–820 (2003).
85. I.W. Chiang, B.E. Brinson, R.E. Smalley, J.L. Margrave, and R.H. Hauge, Purification and characterization of single-wall carbon nanotubes, *J. Phys. Chem*. **B 105**, 1157–1161 (2001).
86. I.W. Chiang, B.E. Brinson, A.Y. Huang, P.A. Willis, M.J. Bronikowski, J.L. Margrave, R.E. Smalley, and R.H. Hauge, Purification and characterization of single-wall carbon nanotubes (SWNTs) obtained from gas-phase decomposition of CO (HiPco process), *J. Phys. Chem*. **B 105**, 8297–8301 (2001).
87. T. Jeong, W.-Y. Kim, and Y.-B. Hahn, A new purification method of single-wall carbon nanotubes using H_2S and O_2 mixture gas, *Chem. Phys. Lett*. **344**, 18–22 (2001).
88. T. Jeong, T.H. Kim, W.-Y. Kim, K.-H. Lee, and Y.-B. Hahn, High yield purification of carbon nanotubes with H_2S–O_2 mixture, *Korean J. Chem. Eng*. **19**, 519–523 (2002).
89. S. Huang and L. Dai, Plasma etching for purification and controlled opening of aligned carbon nanotubes, *J. Phys. Chem*. **B 106**, 3543–3545 (2002).

90. J.G. Wiltshire, A.N. Khlobystov, L.J. Li, S.G. Lyapin, G.A.D. Briggs, and R.J. Nicholas, Comparative studies on acid and thermal based selective purification of HiPCO produced single-walled carbon nanotubes, *Chem. Phys. Lett.* **386**, 239–243 (2004).
91. E. Mizoguti, F. Nihey, M. Yudasaka, S. Iijima, T. Ichihashi, and K. Nakamura, Purification of single-wall carbon nanotubes by using ultrafine gold particles, *Chem. Phys. Lett*. **321**, 297–301 (2000).
92. C.-Y. Moon, Y.-S. Kim, E.-C. Lee, Y.-G. Jin, and K.J. Chang, Mechanism for oxidative etching in carbon nanotubes, *Phys. Rev.* **B 65**, 155401.1–4 (2002).
93. D. Bom, R. Andrews, D. Jacques, J. Anthony, B. Chen, M.S. Meier, and J.P. Selegue, Thermogravimetric analysis of the oxidation of multiwalled carbon nanotubes: evidence for the role of defect sites in carbon nanotube chemistry, *Nano Lett.* **2**, 615–619 (2002).
94. E.G. Rakov, I.G. Ivanov, S.N. Blinov, N.V. Kazakov, V.V. Skudin, N.G. Digurov, and A.K. Bogdanovich, Kinetics of carbon multi-wall nanotube synthesis by catalytic pyrolysis of methane, *Fullerenes Nanotubes Carbon Nanostruct.* **12**, 29–32 (2004).
95. Summary of oxidation studies pertinent to soot and carbon solids [http://me.lsu,edu/~mechar/current/sootoxid.html].
96. D.B. Mawhinney, V. Naumenko, A. Kuznetsova, J.T. Yates, Jr., J. Liu, and R.E. Smalley, Infrared spectral evidence for the etching of carbon nanotubes: ozone oxidation at 298 K, *J. Am. Chem. Soc.* **122**, 2383–2384 (2000).
97. X. Lu, L. Zhang, X. Xu, N. Wang, and Q. Zhang, Can the sidewalls of single-wall carbon nanotubes be ozonized? *J. Phys. Chem.* **B 106**, 2136–2139 (2002).
98. K. Hernadi, A. Siska, L. Thiên-Nga, L. Forró, and I. Kiricsi, Reactivity of different kinds of carbon during oxidative purification of catalytically prepared carbon nanotubes, *Solid State Ionics* **141–142**, 203–209 (2001).
99. S. Banerjee and S.S. Wong, Rational sidewall functionalization and purification of single-walled carbon nanotubes by solution-phase ozonolysis, *J. Chem. Phys.* **B 106**, 12144–12151 (2002).
100. S. Banerjee, M.G.C. Kahn, and S.S. Wong, Rational chemical strategies for carbon nanotube functionalization, *Chem. Eur. J.* **9**, 1898–1908 (2003).
101. O. Byl, P. Kondratyuk, S.T. Forth, S.A. FitzGerald, L. Chen, J.K. Johnson, and J.T. Yates, Jr., Adsorption of CF_4 on the internal and external surfaces of opened single-walled carbon nanotubes: a vibrational spectroscopy study, *J. Am. Chem. Soc.* **125**, 5889–5896 (2003).
102. M.R. Smith, S.W. Hedges, R. LaCount, D. Kern, N. Shah, G.P. Huffman, and B. Bockrath, Selective oxidation of single-walled carbon nanotubes using carbon dioxide, *Carbon* **41**, 1221–1230 (2003).
103. O.P. Gorelik, P. Nikolaev, and S. Arepalli, Purification procedures for single-wall carbon nanotubes, *Report NASA/CR-2000-208926*, 2001, p. 64 [http://mmptdpublic.jsc.nasa.gov/hscnano/CR-2000-208926.pdf].
104. H. Huang, H. Kajiura, A. Yamada, and M. Ata, Purification and alignment of arc-synthesis single-walled carbon nanotube bundles, *Chem. Phys. Lett.* **356**, 567–572 (2002).
105. K.L. Strong, D.P. Anderson, K. Lafdi, and J.N. Kuhn, Purification process for single-wall carbon nanotubes, *Carbon* **41**, 1477–1488 (2003).
106. L. Vaccarini, C. Goze, R. Aznar, V. Micholet, C. Journet, and P. Bernier, Purification procedure of carbon nanotubes, *Synt. Met.* **103**, 2492–2493 (1999).
107. M.T. Martinez, M.A. Callejas, A.M. Benito, W.K. Maser, M. Cochet, J.M. Andrés, J. Schreiber, O. Chauvet, and J.L.G. Fierro, Microwave single walled carbon nanotubes purification, *Chem. Commun.* 1000–1001 (2002).
108. F. Li, H.M. Cheng, Y.T. Xing, P.H. Tan, and G. Su, Purification of single-walled carbon nanotubes synthesized by the catalytic decomposition of hydrocarbons, *Carbon* **38**, 2041–2045 (2000).
109. J.-F. Colomer, P. Piedigrosso, I. Willems, C. Journet, P. Bernier, G. Van Tendeloo, A. Fonseca, and J.B. Nagy, Purification of catalytically produced multi-wall carbon nanotubes, *J. Chem. Soc. Faraday Trans.* **94**, 3753–3758 (1998).
110. J.-F. Colomer, P. Piedigrosso, A. Fonseca, and J.B. Nagy, Different purification methods of carbon nanotubes produced by catalytic synthesis, *Synth. Met.* **103**, 2482–2483 (1999).
111. S.R.C. Vivekchand and A. Govindaraj, A new method of preparing single-walled carbon nanotubes, *Proc. Indian Acad. Sci.* **115**, 509–518 (2003).
112. Y. Sato, T. Ogawa, K. Motomiya, K. Shinoda, B. Jeyadevan, K. Tohji, A. Kasuya, and Y. Nishina, Purification of MWNTs combining wet grinding, hydrothermal treatment, and oxidation, *J. Phys. Chem.* **B 105**, 3387–3392 (2001).

113. H. Kajiura, S. Tsutsui, H. Huang, and Y. Murakami, High-quality single-walled carbon nanotubes from arc-produced soot, *Chem. Phys. Lett.* **364**, 586–592 (2002).
114. W.-K. Choi, S.-G. Park, H. Takahashi, and T.-H. Cho, Purification of carbon nanofibers with hydrogen peroxide, *Synth. Met.* **139**, 39–42 (2003).
115. M.E. Itkis, S. Niyogi, M.E. Meng, M.A. Hamon, H. Hu, and R.C. Haddon, Spectroscopic study of the Fermi level electronic structure of single-walled carbon nanotubes, *Nano Lett.* **2**, 155–159 (2002).
116. H. Kuzmany, A. Kukovecz, F. Simon, M. Holzweber, Ch. Kramberger, and T. Pichler, Functionalization of carbon nanotubes, *Synth. Met.* **141**, 113–122 (2004).
117. K. Esumi, M. Ishigami, A. Nakajima, K. Sawada, and H. Honda, Chemical treatment of carbon nanotubes, *Carbon* **34**, 279–281 (1996).
118. M.A. Hamon, J. Chen, H. Hu, Y. Chen, M.E. Itkis, A.M. Rao, P.C. Eklund, and R.C. Haddon, Dissolution of single-walled carbon nanotubes, *Adv. Mater*. **11**, 834–840 (1999).
119. A. Kuznetsova, I. Popova, J.T. Yates Jr., M.J. Bronikowski, C.B. Huffman, J. Liu, R.E. Smalley, H.H. Hwu, and J.G. Chen, Oxygen-containing functional groups on single-wall carbon nanotubes: NEXAFS and vibrational spectroscopic studies, *J. Am. Chem. Soc*. **123**, 10699–10704 (2001).
120. M.A. Hamon, H. Hu, P. Bhowmik, S. Niyogi, B. Zhao, M.E. Itkis, and R.C. Haddon, End-group and defect analysis of soluble single-walled carbon nanotubes, *Chem. Phys. Lett.* **347**, 8–12 (2001).
121. D.B. Mawhiney, V. Naumenko, A. Kuznetsova, J.T. Yates Jr., J. Liu, and R.E. Smalley, Surface defect site density on single walled carbon nanotubes by titration, *Chem. Phys. Lett*. **324**, 213–216 (2000).
122. J. Chen, A.M. Rao, S. Lyuksyutov, M.E. Itkis, M.A. Hamon, H. Hu, R.W. Cohn, P.C. Eklund, D.T. Colbert, R.E. Smalley, and R.C. Haddon, Dissolution of full-length single-walled carbon nanotubes, *J. Phys. Chem*. **B 105**, 2525–2528 (2001).
123. H. Hu, P. Bhowmik, B. Zhao, M.A. Hamon, M.E. Itkis, and R.C. Haddon, Determination of the acidic sites of purified single-walled carbon nanotubes by acid-base titration, *Chem. Phys. Lett*. **345**, 25–28 (2001).
124. L. Liu, Y. Qin, Z.-X. Guo, and D. Zhu, Reduction of solubilized multi-walled carbon nanotubes, *Carbon* **41**, 331–335 (2003).
125. W. Zhao, C. Song, and P.E. Pehrsson, Water-soluble and optically pH-sensitive single-walled carbon nanotubes from surface modification, *J. Am. Chem. Soc.* **124**, 12418–12419 (2002).
126. M. Sano, A. Kamino, J. Okamura, and S. Shinkai, Ring closure of carbon nanotubes, *Science* **293**, 1299–1301 (2001).
127. J. Chen, M.A. Hamon, H. Hu, Y. Chen, A.M. Rao, P.C. Eklund, and R.C. Haddon, Solution properties of single-walled carbon nanotubes, *Science* **282**, 95–98 (1998).
128. B. Zhao, H. Hu, S. Niyogi, M.E. Itkis, M.A. Hamon, P. Bhowmik, M.S. Meier, and R.C. Haddon, Chromatographic purification and properties of soluble single-walled carbon nanotubes, *J. Am. Chem. Soc.* **123**, 11673–11677 (2001).
129. V. Skakalova, U. Dettlaff-Weglikowska, and S. Roth, Gamma-irradiated and functionalized single wall nanotubes, *Diamond Rel. Mater.* **13**, 296–298 (2004).
130. J.E. Riggs, Z. Guo, D.L. Carroll, and Y.-P. Sun, Strong luminescence of solubilized carbon nanotubes. *J. Am. Chem. Soc*. **122**, 5879–5880 (2000).
131. J.E. Riggs, D.B. Walker, D.L. Carroll, and Y.-P. Sun, Optical limiting properties of suspended and solubilized carbon nanotubes, *J. Phys. Chem.* **B 104**, 7071–7076 (2000).
132. Y. Lin, A.M. Rao, B. Sadanadan, E.A. Kenik, and Y.-P. Sun, Functionalizing multiple-walled carbon nanotubes with aminopolymers, *J. Phys. Chem.* **B 106**, 1294–1298 (2002).
133. I. Yamaguchi and T. Yamamoto, Soluble self-doped single-walled carbon nanotube, *Mater. Lett.* **58**, 598–603 (2004).
134. B. Philip, J. Xie, A. Chandrasekhar, J. Abraham, and V.K. Varadan, A novel nanocomposite from multiwalled carbon nanotubes functionalized with a conducting polymer, *Smart Mater. Struct.* **13**, 295–298 (2004).
135. Y.-P. Sun, W. Huang, Y. Lin, K. Fu, A. Kitaygorodsky, L.A. Riddle, Y.J. Yu, and D.L. Caroll, Soluble dendron-functionalized carbon nanotubes: preparation, characterization and properties, *Chem. Mater*. **13**, 2864–2869 (2001).
136. K. Fu, W. Huang, Y. Lin, L.A. Riddle, D.L. Carroll, and Y.-P. Sun, Defunctionalization of functionalized carbon nanotubes, *Nano Lett.* **1**, 439–441 (2001).
137. Y.-P. Sun, B. Zhou, K. Henbest, K. Fu, W. Huang, Y. Lin, S. Taylor, and D.L. Carroll, Luminescence anisotropy of functionalized carbon nanotubes in solution, *Chem. Phys. Lett.* **351**, 349–353 (2002).

138. M.A. Hamon, H. Hui, P. Bhowmik, M.E. Itkis, and R.C. Haddon, Ester-functionalized soluble single-walled carbon nanotubes, *Appl. Phys.* **A 74**, 333–338 (2002).
139. D.E. Hill, Y. Lin, L.F. Allard, and Y.-P. Sun, Solubilization of carbon nanotubes via polymer attachment, *Int. J. Nanosci.* **1**, 213–221 (2002).
140. S. Qin, D. Qin, W.T. Ford, D.E. Resasco, and J.E. Herrera, Polymer brushes on single-walled carbon nanotubes by atom transfer radical polymerization of *n*-butyl methacrylate, *J. Am. Chem. Soc.* **126**, 170–176 (2004).
141. M. Alvaro, P. Atienzar, P. de la Cruz, J.L. Delgado, H. Garcia, and F. Langa, Synthesis and photochemistry of soluble, pentyl ester-modified single wall carbon nanotube, *Chem. Phys. Lett.* **386**, 342–345 (2004).
142. A.M. Bond, W. Miao, and C.L. Raston, Mercury(II) immobilized on carbon nanotubes: synthesis, characterization, and redox properties, *Langmuir* **16**, 6004–6012 (2000).
143. Y.-H. Li, J. Ding, Z. Luan, Z. Di, Y. Zhu, C. Xu, D. Wu, and B. Wei, Competitive adsorption of Pb^{2+}, Cu^{2+} and Cd^{2+} ions from aqueous solutions by multiwalled carbon nanotubes, *Carbon* **41**, 2787–2792 (2003).
144. G. Arabale, D. Wagh, M. Kulkarni, I.S. Mulla, S.P. Vernekar, K. Vijayamohanan, and A.M. Rao, Enhanced supercapacitance of multiwalled carbon nanotubes functionalized with ruthenium oxide, *Chem. Phys. Lett.* **376**, 207–213 (2003).
145. S. Banerjee and S.S. Wong, Functionalization of carbon nanotube with a metal-containing molecular complex, *Nano Lett.* **2**, 49–53 (2002).
146. S. Banerjee and S.S. Wong, Structural characterization, optical properties, and improved solubility of carbon nanotubes functionalized with Wilkinson's catalyst, *J. Am. Chem. Soc.* **124**, 8940–8948 (2002).
147. S. Banerjee and S.S. Wong, Synthesis and characterization of carbon nanotube-nanocrystal heterostructures, *Nano Lett.* **2**, 195–200 (2002).
148. S. Banerjee and S.S. Wong, In situ quantum dot growth on multiwalled carbon nanotubes, *J. Am. Chem. Soc.* **125**, 10342–10350 (2003).
149. M. Aizawa and M.S.P. Shaffer, Silylation of multi-walled carbon nanotubes, *Chem. Phys. Lett.* **368**, 121–124 (2003).
150. J.H. Rouse and P.T. Lillehei, Electrostatic assembly of polymer/single walled carbon nanotube multilayer films, *Nano Lett.* **3**, 59–62 (2003).
151. C. Velasco-Santos, A.L. Martínez-Hernández, M. Lozada-Cassou, A. Alvarez-Castillo, and V.M. Castaño, Chemical functionalization of carbon nanotubes through an organosilane, *Nanotechnology* **13**, 495–498 (2002).
152. J.G. Smith Jr., K.A. Watson, C.M. Thompson, and J.W. Connell, Carbon nanotube/space durable polymer nanocomposite films for electrostatic charge dissipation, p. 12, 2002 [http://techreport.larc.nasa.gov/ltrs/PDF/2002/mtg/NASA-2002-34sampe-jgs.pdf].
153. B. Wu, J. Zhang, Z. Wei, S. Cai, and Z. Liu, Chemical alignment of oxidatively shortened single-walled carbon nanotubes on silver surface, *J. Phys. Chem.* **B 105**, 5075–5078 (2002).
154. X.-L. Nan, J. Zhang, Z.-F. Liu, Z.-J. Shi, and Z.-N. Gu, Patterned assembly of shortened single-walled carbon nanotubes on gold surface, *Acta Phys. Chim. Sin.* **17** (5), 393–396 (2001).
155. X. Nan, Z. Gu, and Z. Liu, Immobilizing shortened single-walled carbon nanotubes (SWNTs) on gold using a surface condensation method, *J. Colloid Interf. Sci.* **245**, 311–318 (2002).
156. S.S. Wong, A.T. Woolley, E. Joselevich, and C.M. Lieber, Functionalization of carbon nanotube AFM probes using tip-activated gases, *Chem. Phys. Lett.* **306**, 219–225 (1999).
157. S.S. Wong, E. Joselevich, A.T. Woolley, C.L. Cheung, and C.M. Lieber, Covalently functionalized nanotubes as nanometre-sized probes in chemistry and biology, *Nature* **394**, 52–55 (1998).
158. S.S. Wong, A.T. Woolley, E. Joselevich, C.L. Cheung, and C.M. Lieber, Covalently-functionalized single-walled carbon nanotube probe tips for chemical force microscopy, *J. Am. Chem. Soc.* **120**, 8557–8558 (1998).
159. M. Sano, A. Kamino, and S. Shinkai, Activation of hydroxyl groups on carbon nanotubes by thermal theatment in air, *NANOTUBE'02 Workshops* Sa–P71–Sy17. Log Number: P160 [http://dielc.kaist.ac.kr/nt02/abstracts/P160.shtml].
160. T. Kyotani, S. Nakazaki, W.-H. Xu, and A. Tomita, Chemical modification of the inner walls of carbon nanotubes by HNO_3 oxidation, *Carbon* **39**, 771–785 (2001).
161. A. Kuznetsova, D.B. Mawhinney, V. Naumenko, J.T. Yates Jr., J. Liu, and R.E. Smalley. Enhancement of adsorption inside of single-walled nanotubes: opening the entry ports, *Chem. Phys. Lett.* **321**, 292–296 (2000).

162. T. Nakajima, N. Watanabe, I. Kameda, and M. Endo, Preparation and electrical conductivity of fluorine-graphite fiber intercalation compound, *Carbon* **24**, 343–351 (1986).
163. T. Nakajima, S. Kasamatsu, and Y. Matsuo, Synthesis and characterization of fluorinated carbon nanotubes, *Eur. J. Solid State Inorg. Chem*. **33**, 831–840 (1996).
164. A. Hamwi, H. Alvergnat, S. Bonnamy, and F. Béguin, Fluorination of carbon nanotubes, *Carbon* **35**, 723–728 (1997).
165. A. Hamwi, P. Gendrand, H. Gaucher, S. Bonnamy, and F. Beguin, Electrochemical properties of carbon nanotube fluorides in a lithium cell system, *Mol. Cryst. Liq. Cryst.* **310**, 185–190 (1998).
166. A.V. Okotrub, N.F. Yudanov, A.L. Chuvilin, I.P. Asanov, Yu.V. Shubin, L.G. Bulusheva, A.V. Gusel'nikov, and I.S. Fyodorov, Fluorinated cage multiwall carbon nanoparticles, *Chem. Phys. Lett.* **322**, 231–236 (2000).
167. H. Touhara and F. Okino, Property control of carbon material by fluorination, *Carbon* **38**, 241–267 (2000).
168. Y. Hattori, Y. Watanabe, S. Kawasaki, F. Okino, B.K. Pradhan, T. Kyotani, A. Tomita, and H. Touhara, Carbon-alloying of the rear surfaces of nanotubes by direct fluorination, *Carbon* **37**, 1033–1038 (1999).
169. E.T. Mickelson, C.B. Huffman, A.G. Rinzler, R.E. Smalley, R.H. Hauge, and J.L. Margrave, Fluorination of single-wall carbon nanotubes, *Chem. Phys. Lett*. **296**, 188–194 (1998).
170. I.W. Chiang, E.T. Mickelson, P.J. Boul, R.H. Hauge, R.E. Smalley, and J.L. Margrave, Fluorination, defluorination, and derivatization of single-wall carbon nanotubes, *Abstr. Pap. — Am. Chem. Soc. 2000, 220th*, IEC-153. Washington, DC, Aug. 20–24, 2000.
171. H. Peng, Z. Gu, J. Yang, J.L. Zimmerman, P.A. Willis, M.J. Bronikowski, R.E. Smalley, R.H. Hauge, and J.L. Margrave, Fluorotubes as cathodes in lithium electrochemical cells, *Nano Lett*. **1**, 625–629 (2001).
172. W. Zhao, C. Song, B. Zheng, J. Liu, and T. Viswanathan, Thermal recovery behavior of fluorinated single-walled carbon nanotubes, *J. Phys. Chem.* **B 106**, 293–296 (2002).
173. P.E. Pehrsson, W. Zhao, J.W. Baldwin, C. Song, J. Liu, S. Kooi, and B. Zheng, Thermal fluorination and ahhealing of single-wall carbon nanotubes, *J. Phys. Chem.* **B 107**, 5690–5695 (2003).
174. Z. Gu, H. Peng, R.H. Hauge, R.E. Smalley, and J.L. Margrave, Cutting single-wall carbon nanotubes through fluorination, *Nano Lett.* **2**, 1009–1013 (2002).
175. Y.S. Lee, T.H. Cho, B.K. Lee, J.S. Rho, K.H. An, and Y.H. Lee, Surface properties of fluorinated single-walled carbon nanotubes, *J. Fluor. Chem*. **120**, 99–104 (2003).
176. P.J. Boul, J. Liu, E.T. Mickelson, C.B. Huffman, L.M. Ericson, I.W. Chiang, K.A. Smith, D.T. Colbert, R.H. Hauge, J.L. Margrave, and R.E. Smalley, Reversible sidewall functionalization of buckytubes, *Chem. Phys. Lett*. **310**, 367–372 (1999).
177. K.F. Kelly, I.W. Chiang, E.T. Mickelson, R.H. Hauge, J.L. Margrave, X. Wang, G.E. Scuseria, C. Radloff, and N.J. Halas, Insight into the mechanism of sidewall functionalization of single-walled nanotubes: an STM study, *Chem. Phys. Lett.* **313**, 445–450 (1999).
178. E.T. Mickelson, I.W. Chiang, J.L. Zimmerman, P.J. Boul, J. Lozano, J. Liu, R.E. Smalley, R.H. Hauge, and J.L. Margrave, Solvation of fluorinated single-wall carbon nanotubes in alcohol solvents, *J. Phys. Chem*. **B 103**, 4318–4322 (1999).
179. V.N. Khabashesku, W.E. Billups, and J.L. Margrave, Fluorination of single-wall carbon nanotubes and subsequent derivatization reactions, *Acc. Chem. Res*. **35**, 1087–1095 (2002).
180. D.V. Kirin, N.N. Breslavskaya, and P.N. D'yachkov, Heterojunktions based on chemically modified carbon nanotubes, *Doklady Phys. Chem.* **374**, 161–166 (2000).
181. H.F. Bettinger, K.N. Kudin, and G.E. Scuseria, Thermochemistry of fluorinated single wall carbon nanotubes, *J. Am. Chem. Soc.* **123**, 12849–12856 (2001).
182. K.N. Kudin, H.F. Bettinger, and G.E. Scuseria, Fluorinated single-wall carbon nanotubes, *Phys. Rev*. **B 63**, 045413.1–8 (2001).
183. T. Hayashi, M. Terrones, C. Scheu, Y.A. Kim, M. Rűhle, T. Nakajima, and M. Endo, NanoTeflons: structure and EELS characterization of fluorinated nanotubes and nanofibers, *Nano Lett*. **2**, 491–496 (2002).
184. P.R. Marcoux, J. Schreiber, P. Batail, S. Lefrant, J. Renouard, G. Jacob, D. Albertini, and J.-Y. Mevellec, A spectroscopic study of the fluorination and defluorination reactions on single-walled carbon nanotubes, *Phys. Chem. Phys.* **4**, 2278–2285 (2002).
185. H.F. Bettinger, Experimental and computational investigation of the properties of fluorinated single-walled carbon nanotubes, *Chem. Phys. Chem.* **4**, 1283–1289 (2003).
186. K.H. An, K.A. Park, J.G. Heo, J.Y. Lee, K.K. Jeon, S.C. Lim, C.W. Yang, Y.S. Lee, and Y.H. Lee, Structural transformation of fluorinated carbon nanotubes induced by in situ electron-beam irradiation, *J. Am. Chem. Soc.* **125**, 3057–3061 (2003).

187. K.A. Park, Y.S. Choi, and Y.H. Lee, Atomic and electronic structures of fluorinated single-walled carbon nanotubes, *Phys. Rev*. **B 68**, 045429.1–8 (2003).
188. R.L. Jaffe, Quantum chemistry study of fullerene and carbon nanotube fluorination, *J. Phys. Chem*. **B 107**, 10378–10388 (2003).
189. H. Geng, R. Rosen, B. Zheng, H. Shimoda, L. Fleming, J. Liu, and O. Zhou, Fabrication and properties of composites of poly(ethylene oxide) and functionalized carbon nanotubes, *Adv. Mater.* **14**, 1387–1390 (2002).
190. R.L. Jaffe, Quantum chemistry study of chemical functionalization reactions of fullerenes and carbon nanotubes, *Proc. Electrochem. Soc*. **12**, 153–162 (1999). Fullerenes Vol. 7: Recent Advances in the Chemistry and Physics of Fullerenes and Related Mater. (12th Int. Symp.), K.M. Kadish, P.V. Kamat, and D.M.Guldi, PV 99–12, Seattle, Washington, Spring 1999.
191. M. Xu, Q. Huang, Q. Chen, P. Guo, and Z. Sun, Synthesis and characterization of octadecylamine grafted multi-walled carbon nanotubes, *Chem. Phys. Lett.* **375**, 598–604 (2003).
192. F. Pompeo and D.E. Resasco, Water solubilization of single-walled carbon nanotubes by functionalization with glucosamine, *Nano Lett*. **2**, 369–373 (2002).
193. L. Liu, S. Zhang, T. Hu, Z.-X. Guo, C. Ye, L. Dai, and D. Zhu, Solubilized multi-walled carbon nanotubes with broadband optical limiting effect, *Chem. Phys. Lett.* **359**, 191–195 (2002).
194. W. Wu, J. Li, L. Liu, L. Yanga, Z.-X. Guo, L. Dai, and D. Zhu, The photoconductivity of PVK-carbon nanotube blends, *Chem. Phys. Lett.* **364**, 196–199 (2002).
195. J. Zhang, G. Wang, Y.-S. Shon, O. Zhou, R. Superfine, and R.W. Murray, Interactions of small molecules and Au nanoparticles with solubilized single-wall carbon nanotubes, *J. Phys. Chem*. **B 107**, 3726–3732 (2003).
196. W.-Y. Chen, C.-Y. Chen, K.-Y. Hsu, C.-C. Wang, and Y.-C. Ling, Reaction monitoring of polyaniline film formation on carbon nanotubes with TOF-SIMS, *Appl. Surf. Sci.* **231–232**, 845–849 (2004).
197. M. Álvaro, P. Atienzar, J.L. Bourdelande, and H. García, An organically modified single wall carbon nanotube containing a pyrene chromophore: fluorescence and diffuse reflectance laser flash photolysis study, *Chem. Phys. Lett.* **384**, 119–123 (2004).
198. F. Della Negra, M. Meneghetti, and E. Menna, Microwave-assisted synthesis of a soluble single wall carbon nanotube derivative, *Fullerenes Nanotubes Carbon Nanostruct.* **11**, 25–34 (2003).
199. H.-J. Lee, H. Park, S. Koo, and H. Lee, Vertical alignments of single-walled carbon nanotubes on chemically functionalized silicon substrates [http://otlf.hanyang.ac.kr/publications/pdf/2003/Vertical%20alignments%20of%20SWNTs%20on%20chemicall%20functionalized%20silicon%20substrates.pdf].
200. M. Sano, A. Kamino, and S. Shinkai, Construction of carbon nanotube "stars" with dendrimers, *Angew. Chem. Int. Edit.* **40**, 4661–4663 (2001).
201. L. Cao, W. Yang, J. Yang, C. Wang, and S. Fu, Hyperbranched poly(amidoamine)-modified multiwalled carbon nanotubes via grafting-from method, *Chem. Lett.* **33**, 490–491 (2004).
202. S. Niyogi, H. Hu, M.A. Hamon, P. Bhowmik, B. Zhao, S.M. Rozenzhak, J. Chen, M.E. Itkis, M.S. Meier, and R.C. Haddon, Chromatographic purification of soluble SWNTs, *J. Am. Chem. Soc*. **123**, 733–734 (2001).
203. P.W. Chiu, G.S. Duesberg, U. Dettlaff-Weglikowska, and S. Roth, Interconnection of carbon nanotubes by chemical functionalization, *Appl. Phys. Lett*. **80**, 3811–3813 (2002).
204. K. Niesz, Z. Kónya, A.A. Koós, L.P. Biró, Á. Kukovecz, and I. Kiricsi, Synthesis procedures for production of carbon nanotube junctions, *AIP Conf. Proc.* **685**, No. 1, 253–256 (2003).
205. J.M. Haremza, M.A. Hahn, T.D. Krauss, S. Chen, and J. Calcines, Attachment of single CdSe nanocrystals to individual single-walled carbon nanotubes, *Nano Lett.* **2**, 1253–1258 (2002).
206. J.G. Smith Jr., J.W. Connell, D.M. Delozier, P.T. Lillehei, K.A. Watson, Y. Lin, B. Zhou, and Y.-P. Sun, Space durable polymer/carbon nanotube films for electrostatic charge mitigation, *Polymer* **45**, 825–836 (2004).
207. D. Chattopadhyay, S. Lastella, S. Kim, and F. Papadimitrakopoulos, Length separation of zwitterion-functionalized single wall carbon nanotubes by GPC, *J. Am. Chem. Soc.* **124**, 728–729 (2002).
208. D. Chattopadhyay, I. Galeska, and F. Papadimitrakopoulos, A route to bulk separation of semiconducting from metallic single-wall carbon nanotubes, *J. Am. Chem. Soc*. **125**, 3370–3375 (2003).
209. F. Gojny, J. Nastalczyk, Z. Roslaniec, and K. Schulte, Surface modified multi-walled carbon nanotubes in CNT/epoxy composites, *Chem. Phys. Lett.* **370**, 820–824 (2003).

210. Z. Liu, Z. Shen, T. Zhu, S. Hou, L. Ying, Z. Shi, and Z. Gu, Organizing single-walled carbon nanotubes on gold using a wet chemical self-assembling technique, *Langmuir* **16**, 3569–3573 (2000).
211. Q. Chen and L. Dai, Plasma patterning of carbon nanotubes *Appl. Phys. Lett.* **76**, 2719–2721 (2000).
212. Q. Chen, L. Dai, M. Gao, S. Huang, and A. Mau, Plasma activation of carbon anotubes for chemical modification, *J. Phys. Chem.* **B 105**, 618–622 (2001).
213. Y. Sun, S.R. Wilson, and D.I. Schuster, High dissolution and strong light emission of carbon nanotubes in aromatic amine solvents, *J. Am. Chem. Soc*. **123**, 5348–5349 (2001).
214. B. Li, Z. Shi, Y. Lian, and Z. Gu, Aqueous soluble single-wall carbon nanotube, *Chem. Lett.* 2001, 598–599.
215. W. Huang, Y. Lin, S. Taylor, J. Gaillard, A.M. Rao, and Y.-P. Sun, Sonication-assisted functionalization and solubilization of carbon nanotubes, *Nano Lett*. **2**, 231–234 (2002).
216. Z. Kónya, I. Vesselenyi, K. Niesz, A. Kukovecz, A. Demortier, A. Fonseca, J. Delhalle, Z. Mekhalif, J.B. Nagy, A.A. Koós, Z. Osváth, A. Kocsonya, L.P. Biró, and I. Kiricsi, Large scale production of short functionalized carbon nanotubes, *Chem. Pgys. Lett.* **360**, 429–435 (2002).
217. E.V. Basiuk, V.A. Basiuk, J.-G. Bañuelos, J.-M. Saniger-Blesa, V.A. Pokrovskiy, T.Yu. Gromovoy, A.V. Mischanchuk, and B.G. Mischanchuk. Interaction of oxidized single-walled carbon nanotubes with vaporous aliphatic amines, *J. Phys. Chem*. **B 106**, 1588–1597 (2002).
218. V.A. Basiuk, ONIOM studies of chemical reactions on carbon nanotube tips: effects of the lower theoretical level and mutual orientation of the reactants, *J. Phys. Chem.* **B 107**, 8890–8897 (2003).
219. J. Kong and H. Dai, Full and modulated chemical gating of individual carbon nanotubes by organic amine compounds, *J. Phys. Chem.* **B 105**, 2890–2893 (2001).
220. F. Hennrich, M.M. Kappes, M.S. Strano, R.H. Hauge, and R.E. Smalley, Infrared analysis of amine treated single-walled carbon nanotubes produced by decomposition of CO, *AIP Conf. Proc*. **685**, No. 1, 197–201 (2003).
221. G. de la Torre, W. Blau, and T. Torres, A survey on the functionalization of single-walled nanotubes. The chemical attachment of phtalocyanine moieties, *Nanotechnology* **14**, 765–771 (2003).
222. Y. Chen, R.C. Haddon, S. Fang, A.M. Rao, P.C. Eklund, W.H. Lee, E.C. Dickey, E.A. Grulke, J.C. Pendergrass, A. Chavan, B.E. Haley, and R.E. Smalley, Chemical attachment of organic functional groups to single-walled carbon nanotube material, *J. Mater. Res.* **13**, 2423–2431 (1998).
223. M. Holzinger, O. Vostrowsky, A. Hirsch, F. Hennrich, M. Kappes, R. Weiss, and F. Jellen, Sidewall functionalization of carbon nanotubes, *Angew. Chem. Int. Edit*. **40**, 4002–4005 (2001).
224. M. Monthioux, Filling single-wall carbon nanotubes, *Carbon* **40**, 1809–1823 (2002).
225. H. Hu, B. Zhao, M.A. Hamon, K. Kamaras, M.E. Itkis, and R.C. Haddon, Sidewall functionalization of single-walled carbon nanotubes by addition of dichlorocarbene, *J. Am. Chem. Soc.* **125**, 14893–14900 (2003).
226. X. Lu, F. Tian, and Q. Zhang, The [2+1] cycloadditions of dichlorocarbene, silylene, germylene, and oxycarbonylnitrene onto the sidewall of armchair (5,5) single-wall carbon nanotube, *J. Phys. Chem.* **B 107**, 8388–8391 (2003).
227. M. Holzinger, J. Abraham, P. Whelan, R. Graupner, L. Ley, F. Hennrich, M. Kappes, and A. Hirsch, Functionalization of single-walled carbon nanotubes with (R-)oxycarbonyl nitrenes, *J. Am. Chem. Soc.* **125**, 8566–8580 (2003).
228. J. Abraham, P. Whelan, A. Hirsch, F. Hennrich, M. Kappes, D. Samaille, P. Bernier, A. Vencelová, R. Graupner, and L. Ley, Covalent functionalization of arc discharge, laser ablation and HiPCO single-walled carbon nanotubes, *AIP Conf. Proc.* **685**, No. 1, 291–296 (2003).
229. S. Qin, D. Qin, W.T. Ford, D.E. Resasco, and J.E. Herrera, Functionalization of single-walled carbon nanotubes with polystyrene via grafting to and grafting from methods, *Macromolecules* **37**, 752–757 (2004).
230. V. Georgakilas, K. Kordatos, M. Prato, D.M. Guldi, M. Holzinger, and A. Hirsch, Organic functionalization of carbon nanotubes, *J. Am. Chem. Soc*. **124**, 760–761 (2002).
231. V. Georgakilas, D. Voulgaris, E. Vázquez, M. Prato, D.M. Guldi, Kukovecz, and H. Kuzmany, Purification of HiPCO carbon nanotubes via organic functionalization. *J. Am. Chem. Soc.* **124**, 14318–14319 (2002).
232. N. Tagmatarchis and M. Prato, Functionalization of carbon nanotubes via 1,3-dipolar cycloadditions, *J. Mater. Chem*. **14**, 437–439 (2004).
233. C.A. Dyke and J.M. Tour, Solvent-free functionalization of carbon nanotubes, *J. Am. Chem. Soc*. **125**, 1156–1157 (2003).
234. C.A. Dyke and J.M. Tour, Overcoming the insolubility of carbon nanotubes through high degrees of sidewall functionalization, *Chem. Eur. J.* **10**, 812–817 (2004).

235. J.L. Bahr, J. Yang, D.V. Kosynkin, M.J. Bronikowski, R.E. Smalley, and J.M. Tour, Functionalization of carbon nanotubes by electrochemical reduction of aryl diazonium salts: a bucky paper electrode, *J. Am. Chem. Soc*. **123**, 6536–6542 (2001).
236. J.L. Bahr and J.L. Tour, Highly functionalized carbon nanotubes using in situ generated diazonium compounds, *Chem. Mater*. **13**, 3823–3824 (2001).
237. J.L. Bahr and J.M. Tour, Covalent chemistry of single-wall carbon nanotubes, *J. Mater. Chem*. **12**, 1952–1958 (2002).
238. S.E. Kooi, U. Schlecht, M. Burghard, and K. Kern, Electrochemical modification of single carbon nanotubes, *Angew. Chem. Int. Ed.* **41**, 1353–1355 (2002).
239. Y. Ying, R.K. Saini, F. Liang, A.K. Sadana, and W.E. Billups, Functionalization of carbon nanotubes by free radicals, *Org. Lett.* **5**, 1471–1473 (2003).
240. M.S. Strano, C.A. Dyke, M.L. Usrey, P.W. Barone, M.J. Allen, H. Shan, C. Kittrell, R.H. Hauge, J.M. Tour, and R.E. Smalley, Electronic structure control of single-walled carbon nanotube functionalization, *Science* **301**, 1519–1522 (2003).
241. P. Umek, J.W. Seo, K. Hernadi, A. Mrzel, P. Pechy, D.D. Mihailovic, and L. Forro, Addition of carbon radicals generated from organic peroxides to single wall carbon nanotubes, *Chem. Mater.* **15**, 4751–4755 (2003).
242. M. Yudasaka, M. Zhang, C. Jabs, and S. Iijima, Effect of an organic polymer in purification and cutting of single-wall carbon nanotubes, *Appl. Phys.* **A 71**, 449–451 (2000).
243. M. Zhang, M. Yudasaka, A. Koshio, and S. Iijima, Effect of polymer and solvent on purification and cutting of single-wall carbon nanotubes, *Chem. Phys. Lett.* **349**, 25–30 (2001).
244. M. Zhang, M. Yudasaka, A. Koshio, and S. Iijima, Thermogravimetric analysis of single-wall carbon nanotubes ultrasonicated in monochlorobenzene, *Chem. Phys. Lett.* **364**, 420–426 (2002).
245. A. Koshio, M. Yudasaka, M. Zhang, and S. Iijima, A simple way to chemically react single-wall carbon nanotubes with organic materials using ultrasonication, *Nano Lett.* **1**, 361–363 (2001).
246. S. Niyogi, M.A. Hamon, D.E. Perea, C.B. Kang, B. Zhao, S.K. Pal, A.E. Wyant, M.E. Itkis, and R.C. Haddon, Ultrasonic dispersions of single-walled carbon nanotubes, *J. Phys. Chem.* **B 107**, 8799–8804 (2003).
247. J.L. Bahr, E.T. Mickelson, M.J. Bronikowski, R.E. Smalley, and J.M. Tour, Dissolution of small diameter SWNTs in organic solvents? *Chem. Commun*. 193–194 (2001).
248. K. Balasubramanian, M. Friedrich, C. Jiang, Y. Fan, A. Mews, M. Burghard, and K. Kern, Electrical transport and confocal Raman studies of electrochemically modified individual carbon nanotubes, *Adv. Mater.* **15**, 1515–1518 (2003).
249. J.K. Lim, W.S. Yun, M.-h. Yoon, S.K. Lee, C.H. Kim, K. Kim, and S.K. Kim, Selective thiolation of single-walled carbon nanotubes, *Synt. Met*. **139**, 521–527 (2003).
250. A.V. Krasheninnikov and K. Nordlund, Irradiation effects in carbon nanotubes, *Nucl. Instr. Meth. Phys. Res.* **B 216**, 355–366 (2004).
251. A.V. Krasheninnikov and K. Nordlund, Signatures of irradiation-induced defects in scanning-tunneling microscopy images of carbon nanotubes, *Phys. Solid State* **44**, 470–472 (2002).
252. D.-H. Kim, H.-S. Jang, C.-D. Kim, D.-S. Cho, H.-D. Kang, and H.-R. Lee, Enhancement of the field emission of carbon nanotubes straightened by application of argon ion irradiation, *Chem. Phys. Lett.* **378**, 232–237 (2003).
253. L. Dai, H.J. Griesser, and A.W.H. Mau, Surface modification by plasma etching and plasma patterning, *J. Phys. Chem.* **B 101**, 9548–9554 (1997).
254. H. Bubert, S. Haiber, W. Brandl, G. Marginean, M. Heintze, and V. Brüser, Characterization of the uppermost layer of plasma-treated carbon nanotubes, *Diamond Rel. Mater.* **12**, 811–815 (2003).
255. V.A. Basiuk, K. Kobayashi, T. Kaneko, Y. Negishi, E.V. Basiuk, and J.-M. Saniger-Blesa, Irradiation of single-walled carbon nanotubes with high-energy protons, *Nano Lett*. **2**, 789–791 (2002).
256. B.N. Khare, M. Meyyappan, A.M. Cassell, C.V. Nguyen, and J. Han, Functionalization of carbon nanotubes using atomic hydrogen from a glow discharge, *Nano Lett.* 2, 73–77 (2002).
257. B.N. Khare, M. Meyyappan, J. Kralj, P. Wilhite, M. Sisay, H. Imanaka, J. Koehne, and C.W. Baushchlicher Jr., A glow-discharge approach for functionalization of carbon nanotubes, *Appl. Phys. Lett.* **81**, 5237–5239 (2002).
258. B. Ni and S.B. Sinnott, Chemical functionalization of carbon nanotubes through energetic radical collisions, *Phys. Rev*. **B 61**, R16343–R16346 (2000).

259. B. Ni, R. Andrews, D. Jacques, D. Qian, M.B.J. Wijesundara, Y. Choi, L. Hanley, and S.B. Sinnott, A combined computational and experimental study of ion-beam modification of carbon nanotube bundles, *J. Phys. Chem.* **B 105**, 12719–12725 (2001).
260. N.O.V. Plank, L. Jiang, and R. Cheung, Fluorination of carbon nanotubes in CF_4 plasma, *Appl. Phys. Lett.* **83**, 2426–2428 (2003).
261. N.O.V. Plank and R. Cheung, Functionalization of carbon nanotubes for molecular electronics, *Microelectronic Eng.* **73–74**, 578–582 (2004).
262. Y. Hu and S. Sinnott, Nanometer-scale engineering of composites, *11th Foresight Conf. Molec. Nanotech.* [http://www.foresight.org/Conferences/MNT11/Abstracts/Hu/].
263. Y. Breton, S. Delpeux, R. Benoit, J.P. Salvetat, C. Sinturel, F. Beguin, S. Bonnamy, G. Desarmot, and L. Boufendi, Functionalization of multiwall carbon nanotubes: properties of nanotubes-epoxy composites, *Mol. Cryst. Liq. Cryst.* **387**, 135–140 (2002).
264. C.Y. Zhi, X.D. Bai, and E.G. Wang, Enhanced field emission from carbon nanotubes by hydrogen plasma treatment, *Appl. Phys. Lett.* **81**, 1690–1692 (2002).
265. S.A. Miller, V.Y. Young, and C.R. Martin, Electroosmotic flow in template-prepared carbon nanotube membranes, *J. Am. Chem. Soc.* **123**, 12335–12342 (2001).
266. G.S. Duesberg, J. Muster, V. Krstic, M. Burghard, and S. Roth, Chromatographic size separation of single-wall carbon nanotubes, *Appl. Phys.* **A 67**, 117–119 (1998).
267. G.S. Duesberg, M. Burghard, J. Muster, G. Philipp, and S. Roth, Separation of carbon nanotubes by size exclusion chromatography, *Chem. Commun.* 435–436 (1998).
268. G.S. Duesberg, W. Blau, H.J. Byrne, J. Muster, M. Burghard, and S. Roth, Chromatography of carbon nanotubes, *Synth. Met.* **103**, 2484–2485 (1999).
269. B. Vigolo, A. Pénicaud, C. Coulon, C. Sauder, R. Pailler, C. Journet, P. Bernier, and P. Poulin, Macroscopic fibers and ribbons of oriented carbon nanotubes, *Science* **290**, 1331–1334 (2000).
270. M.J. O'Connell, S.M. Bachilo, C.B. Huffman, V.C. Moore, M.S. Strano, E.H. Haroz, K.L. Rialon, P.J. Boul, W.H. Noon, C. Kittrell, J. Ma, R.H. Hauge, R.B. Weisman, and R.E. Smalley, Band gap fluorescence from individual single-walled carbon nanotubes, *Science* **297**, 593–596 (2002).
271. P. Poulin, B. Vigolo, and P. Lannois, Films and fibers of oriented single wall nanotubes, *Carbon* **40**, 1741–1749 (2002).
272. S.K. Doorn, M.S. Strano, M.J. O'Connell, E.H. Haroz, K.L. Rialon, R.H. Hauge, and R.E. Smalley, Capillary electrophoresis separation of bundled and individual carbon nanotubes, *J. Phys. Chem.* **B 107**, 6063–6069 (2003).
273. A.V. Neimark, S. Ruetsch, K.G. Kornev, P.I. Ravikovitch, P. Poulin, S. Badaire, and M. Maugey, Hierarchical pore structure and wetting properties of single-wall carbon nanotube fibers. *Nano Lett.* **3**, 419–423 (2003).
274. J. Wang, R.P. Deo, P. Poulin, and M. Mangey, Carbon nanotube fiber microelectrodes, *J. Am. Chem. Soc.* **125**, 14706–14707 (2003).
275. Y. Dror, W. Salalha, R.L. Khalfin, Y. Cohen, A.L. Yarin, and E. Zussman, Carbon nanotubes embedded in oriented polymer nanofibers by electrospinning, *Langmuir* **19**, 7012–7020 (2003).
276. L. Zhao and L. Gao, Novel in situ synthesis of MWNTs-hydroxyapatite composites, *Carbon* **42**, 423–426 (2004).
277. V. Krstic, G.S. Duesberg, J. Muster, M. Burghard, and S. Roth, Langmuir-Blodgett films of matrix-diluted single-walled carbon nanotubes, *Chem. Mater.* **10**, 2338–2340 (1998).
278. A.B. Dalton, S. Collins, E. Muñoz, J.M. Razal, Von H. Ebron, J.P. Ferraris, J.N. Coleman, B.G. Kim, and R. Baughman, Super tough carbon nanotube fibers, *Nature* **423**, 703 (2003).
279. A.B. Dalton, S. Collins, J. Razal, E. Munoz, Von H. Ebron, B.G. Kim, J.N. Coleman, J.P. Ferraris, and R. Baughman, Continuous carbon nanotube composite fibers: properties, potential applications, and problems, *J. Mater. Chem.* **14**, 1–3 (2004).
280. M.F. Islam, E. Rojas, D.M. Bergey, A.T. Johnson, and A.G. Yodh, High weight-fraction surfactant solubilization of single-wall carbon nanotubes in water, *Nano Lett.* **3**, 269–273 (2003).
281. M.F. Islam, A.M. Alsayed, Z. Dogic, J. Zhang, T.C. Lubensky, and A.G. Yodh, Nematic nanotube gels, *Phys. Rev. Lett.* **92**, 1–4 (2004).
282. J.I. Paredes and M. Burghard, Dispersions of individual single-walled carbon nanotubes of high length, *Langmuir*, **20**, 5149–5152 (2004).
283. O. Matarredona, H. Rhoads, Z. Li, J.H. Harwell, L. Balzano, and D.E. Resasco, Dispersion of single-walled carbon nanotubes in aqueous solutions of the anionic surfactant NaDDBS, *J. Phys. Chem.* **B 107**, 13357–13367 (2003).

284. W. Zhou, M.F. Islam, H. Wang, D.L. Ho, A.G. Yodh, K.I. Winey, and J.E. Fischer, Small angle neutron scattering from single-wall carbon nanotube suspensions: evidence for isolated rigid rods and rod networks, *Chem. Phys. Lett.* **384**, 185–189 (2004).
285. K.D. Ausman, R. Piner, O. Lourie, R.S. Ruoff, and M. Korobov, Organic solvent dispersions of SWNTs: toward solutions of pristine nanotubes, *J. Phys. Chem*. **B 104**, 8911–8915 (2000).
286. X. Liu, J.L. Spencer, A.B. Kaiser, and W.M. Arnold, Electric-field oriented carbon nanotubes in different dielectric solvents, *Curr. Appl. Phys.* **4**, 125–128 (2004).
287. Z. Hongbing, C. Wenzhe, W. Minquan, Zhengchan, and Z. Chunlin, Optical limiting effects of multi-walled carbon nanotubes suspension and silica xerogel composite, *Chem. Phys. Lett.* **382**, 313–317 (2003).
288. N. Saran, K. Parikh, D.-S. Suh, E. Muñoz, H. Kolla, and S.K. Manohar, Fabrication and characterization of thin films of single-walled carbon nanotube bundles on flexible plastic substrates, *J. Am. Chem. Soc.* **126**, 4462−4463 (2004).
289. R. Bandyopadhyaya, E. Nativ-Roth, O. Regev, and R. Yerushalmi-Rosen, Stabilization of individual carbon nanotubes in aqueous solutions, *Nano Lett*. **2**, 25–28 (2002).
290. M.S. Strano, C.B. Huffman, V.C. Moore, M.J. O'Connell, E.H. Haroz, J. Hubbard, M. Miller, K. Rialon, C. Kittrell, S. Ramesh, R.H. Hauge, and R.E. Smalley, Reversible, band-gap-selective protonation of single-walled carbon nanotubes in solution, *J. Phys. Chem.* **B 107**, 6979–6985 (2003).
291. J. Ning, J. Zhang, Y. Pan, and J. Guo, Surfactants assisted processing of carbon nanotube-reinforced SiO_2 matrix composites, *Ceramics Int.* **30**, 63–67 (2004).
292. Z. Jin, L. Huang, S.H. Goh, G. Xu, and W. Ji, Characterization and nonlinear optical properties of a poly(acrylic acid)–surfactant–multi-walled carbon nanotube complex, *Chem. Phys. Lett*. **332**, 461–466 (2000).
293. V.A. Karachevtsev, A.Yu. Glamazda, U. Dettlauff-Weglikowska, V.S. Leontiev, A.M. Plokhotnichenko, and S. Roth, Spectroscopy study of SWNT in aqueous solution with different surfactants, *AIP Conf. Proc.* **685**, No. 1, 202–206 (2003).
294. G.L. Hwang and K.C. Hwang, Carbon nanotube reinforced ceramics, *J. Mater. Chem.* **11**, 1722–1725 (2001).
295. K.D. Ausman, M.J. O'Connell, P. Boul, L.M. Ericson, M.J. Casavant, D.A. Walters, C. Huffman, R. Saini, Y. Wang, E. Haroz, E.W. Billups, and R.E. Smalley, Roping and wrapping carbon nanotubes [http://smalley.rice.edu/rick's%20publications/ausman.pdf].
296. M.J. O'Connell, P. Boul, L.M. Ericson, C. Huffman, Y. Wang, E. Haroz, C. Kuper, J. Tour, K.D. Ausman, and R.E. Smalley, Reversible water-solubilization of single-walled carbon nanotubes by polymer wrapping *Chem. Phys. Lett*. **342**, 265–271 (2001).
297. D.W. Schaefer, J.M. Brown, D.P. Anderson, J. Zhao, K. Chokalingam, D. Tomlin, and J. Ilavsky, Structure and dispersion of carbon nanotubes, *J. Appl. Cryst.* **36**, 553–557 (2003).
298. D.W. Schaefer, J. Zhao, J.M. Brown, D.P. Anderson, and D.W. Tomlin, Morphology of dispersed carbon single-walled nanotubes, *Chem. Phys. Lett.* **375**, 369–375 (2003).
299. G.Z. Chen, M.S.P. Shaffer, D. Coleby, G. Dixon, W. Zhou, D.J. Fray, and A.H. Windle, Carbon nanotube and polypyrrole composites: coating and doping, *Adv. Mater.* **12**, 522–526 (2000).
300. B.Z. Tang and H. Xu, Preparation, alignment, and optical properties of soluble poly(phenylacetylene)-wrapped carbon nanotubes, *Macromolecules* **32**, 2569–2576 (1999).
301. D. Li, H. Wang, J. Zhu, X. Wang, L. Lu, and X. Yang, Dispersion of carbon nanotubes in aqueous solutions containing poly(diallyldimethylammonium chloride), *J. Mater. Sci. Lett.* **22**, 253–255 (2003).
302. B. Kim, H. Park, and W.M. Sigmund, Electrostatic interactions between shortened multiwall carbon nanotubes and polyelectrolytes, *Langmuir* **19**, 2525–2527 (2003).
303. J. Chen, M.J. Dyer, and M.-F. Yu, Cyclodextrin-mediated soft cutting of single-walled carbon nanotubes, *J. Am. Chem. Soc.* **123**, 6201–6202 (2001).
304. H. Dodziuk, A. Ejchart, W. Anczewski, H. Ueda, E. Krinichnaya, G. Dolgonos, and W. Kutner, Determination of the number of different types of SWNTs by complexation with η-cyclodextrin, *Chem. Commun.* 986 (2003).
305. Z.H. Wang, G.A. Luo, and S.F. Xiao, Functionalization of cyclodextrins-incorporated carbon nanotube electrodes for neutral nitrophenol recognition, *Sensors, 2003. Proceedings of IEEE*. Vol. 2, 941–945 (2003).
306. T. Takahashi, K. Tsunoda, H. Yajima, and T. Ishii, Isolation of single-wall carbon nanotube bundles through gelatin wrapping and unwrapping processes, *Chem. Lett.* **31**, 690–691 (2002).
307. H. Li, D.Q. Wang, H.L. Chen, B.L. Liu, and L.Z. Gao, A novel gelatin-carbon nanotubes hybrid hydrogel, *Macromol. Biosci.* **3**, 720–724 (2003).

308. A. Star, D.W. Steuerman, J.R. Heath, and J.F. Stoddart, Starched carbon nanotubes, *Angew. Chem. Int. Edit.* **41**, 2508–2512 (2003).
309. O.-K. Kim, J. Je, J.W. Baldwin, S. Kooi, P.E. Pehrsson, and L.J. Buckley, Solubilization of single-wall carbon nanotubes by supramolecular encapsulation of helical amylose, *J. Am. Chem. Soc.* **125**, 4426–4427 (2003).
310. M. Numata, M. Asai, K. Kaneko, T. Hasegawa, N. Fujita, Y. Kitada, K. Sakurai, and S. Shinkai, Curdlan and schizophylan (β-1,3-glucans) can entrap single-wall carbon nanotubes in their helical superstructure, *Chem. Lett.* **33**, 232–233 (2004).
311. G.R. Dieckmann, A.B. Dalton, P.A. Johnson, J. Razal, J. Chen, G.M. Giordano, E. Muñoz, I.H. Musselman, R.H. Baughman, and R.K. Draper, Controlled assembly of carbon nanotubes by designed amphiphilic peptide helices, *J. Am. Chem. Soc.* **125**, 1770–1777 (2003).
312. F. Torrens, Calculation on solvent dispersions of carbon nanotubes, *The Electrochem. Soc. 205th Meet.*, Abs. 457 (2004).
313. Z. Shi, Y. Lian, X. Zhou, Z. Gu, Y. Zhang, S.Iijima, Q. Gong, H. Li, and S.-L. Zhang, Single-wall carbon nanotube colloids in polar solvents, *Chem. Commun*. 461–462 (2000).
314. X. Gao, T. Hu, L. Liu, and Z. Guo, Self-assembly of modified carbon nanotubes in toluene, *Chem. Phys. Lett.* **370**, 661–664 (2003).
315. M.E. Itkis, D.E. Perea, S. Niyogi, S.M. Rickard, M. Hamon, H. Hu, B. Zhao, and R.C. Haddon, Purity evaluation of as-prepared single-walled carbon nanotube soot by use of solution-phase near-IR spectroscopy, *Nano Lett.* **3**, 309–314 (2003).
316. A.B. Dalton, W.J. Blau, G. Chambers, J.N. Coleman, K. Henderson, S. Lefrant, B. McCarthy, C. Stephan, and H.J. Byrne, A functional conjugated polymer to process, purify and selectively interact with single wall carbon nanotubes, *Synth. Met.* **121**, 1217–1218 (2001).
317. D.W. Steuerman, A. Star, R. Narizzano, H. Choi, R.S. Ries, C. Nicolini, J.F. Stoddart, and J.R. Heath, Interactions between conjugated polymers and single-walled carbon nanotubes, *J. Phys. Chem.* **B 106**, 3124–3130 (2002).
318. A. Star, Y. Liu, K. Grant, L. Ridvan, J.F. Stoddart, D.W. Steuerman, M.R. Diehl, A. Boukai, and J.R. Heath, Noncovalent side-wall functionalization of single-walled carbon nanotubes, *Macromolecules* **36**, 553–560 (2003).
319. J.N. Coleman, D.F. O'Brien, M. in het Panhius, A.B. Dalton, B. McCarthy, R.C. Barklie, and W.J. Blau, Solubility and purity of nanotubes in arc discharge carbon powder, *Synth. Met.* **121**, 1229–1230 (2001).
320. J. Chen, H. Liu, W.A. Weimer, M.D. Halls, D.H. Waldeck, and G.C. Walker, Noncovalent engineering of carbon nanotube surface by rigid functional conjugated polymers, *J. Am. Chem. Soc.* **124**, 9034–9035 (2002).
321. J.-M. Nam, M.A. Ratner, X. Liu, and C.A. Mirkin, Single-walled carbon nanotubes and C_{60} encapsulated by a molecular macrocycles, *J. Phys. Chem*. **B 107**, 4705–4710 (2003).
322. Z. Jin, L. Huang, S.H. Goh, G. Xu, and W. Ji, Size-dependent optical limiting behavior of multi-walled carbon nanotubes, *Chem. Phys. Lett.* **352**, 328–333 (2002).
323. V.A. Davis, L.M. Ericson, R. Saini, R. Sivarajan, R.H. Hauge, R.E. Smalley, and M. Pasquali, Rheology, phase behavior, and fiber spinning of carbon nanotube dispersion, *Paper prepared for presentation at the 2001 AIChE annual meeting, 9 November, 2001, T7019 session.*
324. V.A. Davis, L.M. Ericson, A.N.G. Parra-Vasquez, H. Fan, Y. Wang, V. Prieto, J.A. Longoria, S. Ramesh, R.K. Saini, C. Kittrell, W.E. Billups, W.W. Adams, R.H. Hauge, R.E. Smalley, and M. Pasquali, Phase behavior and rheology of SWNTs in superacids, *Macromolecules* **37**, 154–160 (2004).
325. W. Zhou, J. Vavro, C. Guthy, K.I. Winey, J.E. Fisher, L.M. Ericson, S. Ramesh, R. Saini, V.A. Davis, C. Kittrell, M. Pasquali, R.H. Hauge, and R.E. Smalley, Single wall carbon nanotube fibers extruded from super-acid suspensions: preferred orientation, electrical, and thermal transport, *J. Appl. Phys.* **95**, 649–655 (2004).
326. T.V. Sreekumar, T. Liu, S. Kumar, L.M. Ericson, R.H. Hauge, and R.E. Smalley, Single-wall carbon nanotube films, *Chem. Mater.* **15**, 175–178 (2003).
327. H. Dai, J. Kong, C. Zhou, N. Franklin, T. Tombler, A. Cassell, S. Fan, and M. Chapline, Controlled chemical routes to nanotube architectures, physics, and devices, *J. Phys. Chem.* **B 103**, 11246–11255 (1999).
328. X. Yu, T. Mu, H. Huang, Z. Liu, and N. Wu, The study of the attachment of a single-walled carbon nanotube to a self-assembled monolayer using X-ray photoelectron spectroscopy, *Surf. Sci.* **461**, 199–207 (2000).

329. J. Liu, M.J. Casavant, M. Cox, D.A. Walters, P. Boul, W. Lu, A.J. Rimberg, K.A. Smith, D.T. Colbert, and R.E. Smalley, Controlled deposition of individual single-walled carbon nanotubes on chemically functionalized templates, *Chem. Phys. Lett*. **303**, 125–129 (1999).
330. K.H. Choi, J.P. Bourgoin, S. Auvray, D. Esteve, G.S. Duesberg, S. Roth, and M. Burghard, Controlled deposition of carbon nanotubes on a patterned substrate, *Surf. Sci*. **462**, 195–202 (1999).
331. S.G. Rao, L. Huang, W. Setyawan, and S. Hong, Large-scale assembly of carbon nanotubes, *Nature* **425**, 36 (2003).
332. B. Wincheski, J. Smits, M. Namkung, J. Ingram, N. Watkins, J.D. Jordan, and R. Louie, Nanomanipulation and lithography for carbon nanotube based nondestructive evaluation sensor development [http://techreports.larc.nasa.gov/ltrs/PDF/2002/mtg/NASA-2002-sem-bw.pdf].
333. B. Kim and W.M. Sigmund, Self-alignment of shortened multiwall carbon nanotubes on polyelectrolyte layers, *Langmuir* **19**, 4848–4851 (2003).
334. M. Sano, A. Kamino, J. Okamura, and S. Shinkai, Non-covalent self- assembly of carbon nanotubes for construction of 'cages', *Nano Lett.* **2**, 531–533 (2002).
335. J. Chen and W.A. Weimer, Room-temperature assembly of directional carbon nanotube strings, *J. Am. Chem. Soc.* **124**, 758–759 (2002).
336. Y. Yang, H. Zou, B. Wu, J. Zhang, Z. Liu, X. Guo, and Z. Du, Directional carbon nanotube assembly via solvent evaporation induced mechanical stretching, *Advanced Nanomaterials Nanodevices (IUMRS-ICEM 2002, Xian, China, 10–14 June 2002)*. 12–22 (2002).
337. Y.-H. Li, C. Xu, B. Wei, X. Zhang, M. Zheng, D. Wu, and P.M. Ajayan, Self-organized ribbons of aligned carbon nanotubes, *Chem. Mater.* **14**, 483–485 (2002).
338. H. Shimoda, S.J. Oh, H.Z. Geng, R.J. Walker, X.B. Zhang, L.E. McNeil, and O. Zhou, Self-assembly of carbon nanotubes, *Adv. Mater.* **14**, 899–901 (2002).
339. H. Shimoda, L. Fleming, K. Horton, and O. Zhou, Formation of macroscopically ordered carbon nanotube membranes by self-assembly, *Physica* **B 323**, 135–136 (2002).
340. N. Chakrapani, B. Wei, A. Carrillo, P.M. Ajayan, and R.S. Kane, Capillary-driven assembly of two-dimensional cellular carbon nanotube foams, *Proc. Nat. Acad. Sci.* **101**, 4009–4012 (2004).
341. I. Dierking, G. Scalia, P. Morales, and D. LeClere, Aligning and re-orienting carbon nanotubes by nematic liquid crystals [http://www.mat.casaccia.enea.it/link6.pdf].
342. M.D. Lynch and D.L. Patrick, Organizing carbon nanotubes with liquid crystals, *Nano Lett*. **2**, 1197–1201 (2002).
343. M. Senthil Kumar, T.H. Kim, S.H. Lee, S.M. Song, J.W. Yang, K.S. Nahm, and E.-K. Suh, Influence of electric field type on the assembly of single walled carbon nanotubes, *Chem. Phys. Lett.* **383**, 235–239 (2004).
344. M.R. Diehl, S.N. Yaliraki, R.A. Beckman, M. Barahona, and J.R. Heath, Self-assembled, deterministic carbon nanotube wiring networks, *Angew. Chem. Int. Ed.* **41**, 353–356 (2002).
345. B. Gao, G.Z. Yue, Q. Qiu, Y. Cheng, H. Shimoda, L. Fleming, and O. Zhou, Fabrication and electron field emission properties of carbon nanotube films by electrophoretic deposition, *Adv. Mater.* **13**, 1770–1774 (2001).
346. J. Tang, B. Gao, H. Geng, O.D. Velev, L.-C. Qin, and O. Zhou, Assembly of 1D nanostructures into sub-micrometer diameter fibrils with controlled and variable length by electrophoresis, *Adv. Mater.* **15**, 1352–1355 (2003).
347. M. Burghard, G. Duesberg, G. Philipp, J. Muster, and S. Roth, Controlled adsorption of carbon nanotubes on chemically modified electrode arrays, *Adv. Mater.* **10**, 584–588 (1998).
348. Y. Guo, J. Wu, and Y. Zhang, Manipulation of single-wall carbon nanotubes into aligned molecular layers, *Chem. Phys. Lett.* **362**, 314–318 (2002).
349. L. Feng, H. Li, F. Li, Z. Shi, and Z. Gu, Functionalization of carbon nanotubes with amphiphilic molecules and their Langmuir-Blodgett films, *Carbon* **41**, 2385–2391 (2003).
350. N.P. Armitage, J.-C.P. Gabriel, and G. Grüner, Quasi-Langmuir-Blodgett thin film deposition of carbon nanotubes, *J. Appl. Phys.* **95**, 3328–3330 (2004).
351. V. Bavastrello, S. Carrara, M.K. Ram, and C. Nicolini, Optical and electrochemical properties of poly(*o*-toluidine) multiwalled carbon nanotubes composite Langmuir-Schaefer films, *Langmuir* **20**, 969–973 (2004).
352. T. Fukushima, A. Kosaka, Y. Ishimura, T. Yamamoto, T. Takigawa, N. Ishii, and T. Aida, Molecular ordering of organic molten salts triggered by single-walled carbon nanotubes, *Science* **300**, 2972–2974 (2003).

353. B. Vigolo, P. Poulin, M. Lukas, P. Launois, and P. Bernier, Improved structure and properties of single wall carbon nanotube spun fibers, *Appl. Phys. Lett.* **81**, 1210–1212 (2002).
354. F. Ko, Y. Gogotsi, A. Ali, N. Naguib, H. Ye, G. Yang, C. Li, and P. Willis, Electrospinning of continuous carbon nanotube filled nanofiber yarns, *Adv. Mater.* **15**, 1164–1165 (2003).
355. R. Sen, B. Zhao, D. Perea, M.E. Itkis, H. Hu, J. Love, E. Bekyarova, and R.C. Haddon, Preparation of single-walled carbon nanotube reinforced polystyrene and polyurethane nanofibers and membranes, *Nano Lett.* **4**, 459–464 (2004).
356. T.E. Műller, D.G. Reid, W.K. Hsu, J.P. Hare, H.W. Kroto, and D.R.M. Walton, Synthesis of nanotubes via catalytic pyrolysis of acetylene: a SEM study, *Carbon* **35**, 951–966 (1997).
357. Y.K. Chen, A. Chu, J. Cook, M.L.H. Green, P.J.F. Harris, R. Heesom, M. Humphries, J. Sloan, S.C. Tsang, and J.F.C. Turner, Synthesis of carbon nanotubes containing metal oxides and metals of the d-block and f-block transition metals and related studies, *J. Mater. Sci.* **7**, 545–549 (1997).
358. C.T. Kuo, C.H. Lin, and A.Y. Lo, Feasibility studies of magnetic particle-embedded carbon nanotubes for perpendicular recording media, *Diamond Rel. Mater.* **12**, 799–805 (2003).
359. H. Liu, J.-M. Dong, M.-C. Qian, and X.-G. Wan, Dependence of in-tube doping on the radius and helicity of single-wall carbon nanotubes, *Chinese Phys.* **12**, 542–547 (2003).
360. D. Bera, S.C. Kuiry, M. McCutchen, A. Kruize, H. Heinrich, M. Meyyappan, and S. Seal, In-situ synthesis of palladium nanoparticles-filled carbon nanotubes using arc-discharge in solution, *Chem. Phys. Lett.* **386**, 364–368 (2004).
361. E. Dujardin, C. Meny, P. Panissod, J.-P. Kintzinger, N. Yao, and T.W. Ebbesen, Interstitial metallic residues in purified single shell carbon nanotubes, *Solid State Commun*. **114**, 543–546 (2000).
362. X.P. Gao, Y. Zhang, X. Chen, G.L. Pan, J. Yan, F. Wu, H.T. Yuan, and D.Y. Song, Carbon nanotubes filled with metallic nanowires, *Carbon* **42**, 47–52 (2004).
363. C.H. Liang, G.W. Meng, L.D. Zhang, N.F. Shen, and X.Y. Zhang, Carbon nanotubes filled partially or completely with nickel, *J. Cryst. Growth* **218**, 136–139 (2000).
364. B.C. Satishkumar, A. Govindaraj, P.V. Vanitha, A.K. Raychaudhuri, and C.N.R. Rao, Barkhausen jumps and related magnetic properties of iron nanowires encapsulated in aligned carbon nanotube bundles, *Chem. Phys. Lett.* **362**, 301–306 (2002).
365. A. Leonhardt, M. Ritschel, R. Kozhuharova, A. Graff, T. Mühl, R. Huhle, I. Mönch, D. Elefant, and C.M. Schneider, Synthesis and properties of filled carbon nanotubes, *Diamond Rel. Mater.* **12**, 790–793 (2003).
366. N. Grobert, M. Mayne, M. Terrones, J. Sloan, R.E. Dunin-Borkowski, R. Kamalakaran, T. Seeger, H. Terrones, M. Rűhle, D.R.M. Walton, H.W. Kroto, and J.L. Hutchison, Alloy nanowires: invar inside carbon nanotubes, *Chem. Commun.* 471–472 (2001).
367. X. Li, Z. Lei, R. Ren, J. Liu, X. Zuo, Z. Dong, H. Wang, and J. Wang, Characterization of carbon nanohorn encapsulated Fe particles, *Carbon* **41**, 3068–3072 (2003).
368. R. Sen, A. Govindaraj, and C.N.R. Rao, Metal-filled and hollow carbon nanotubes obtained by the decomposition of metal-containing free precursor molecules, *Chem. Mater.* **9**, 2078–2081 (1997).
369. B.H. Liu, J. Ding, Z.Y. Zhong, Z.L. Dong, T. White, and J.Y. Lin, Large-scale preparation of carbon-encapsulated cobalt nanoparticles by the catalytic method, *Chem. Phys. Lett.* **358**, 96–102 (2002).
370. G.Y. Zhang and E.G. Wang, Cu-filled carbon nanotubes by simultaneous plasma-assisted copper incorporation, *Appl. Phys. Lett.* **82**, 1926–1928 (2003).
371. C.Y. Zhi, D.Y. Zhong, and E.G. Wang, GaN-filled carbon nanotubes: synthesis and photoluminescence, *Chem. Phys. Lett.* **381**, 715–719 (2003).
372. A.K. Sinha, D.W. Hwang, and L.-P. Hwang, A novel approach to bulk synthesis of carbon nanotubes filled with metal by a catalytic chemical vapor deposition method, *Chem. Phys. Lett.* **332**, 455–460 (2000).
373. R. Ma, Y. Bando, and T. Sato, Coaxial nanocables: Fe nanowires encapsulated in BN nanotubes with intermediate C layers, *Chem. Phys. Lett.* **350**, 1–5 (2001).
374. S. Liu and J. Zhu, Carbon nanotubes filled with long continuous cobalt nanowires, *Appl. Phys*. **A 70**, 673–675 (2000).
375. S. Liu, S. Zhu, Y. Mastai, I. Felner, and A. Gedanken, Preparation and characteristics of carbon nanotubes filled with cobalt, *Chem. Mater.* **12**, 2205–2211 (2000).
376. Y. Gogotsi, N. Naguib, and J.A. Libera, In situ chemical experiments in carbon nanotubes, *Chem. Phys. Lett.* **356**, 354–360 (2002).
377. J.L. Rivera, C. McCabe, and P.T. Cummings, Layering behavior and axial phase equilibria of pure water and water + carbon dioxide inside single wall carbon nanotubes, *Nano Lett*. **2**, 1427–1431 (2002).

378. E. Dujardin, T.W. Ebbesen, H. Hiura, and K. Tanigaki, Capillarity and wetting of carbon nanotubes, *Science* **265**, 1850–1852 (1994).
379. E. Dujardin, T.W. Ebbesen, A. Krishnan, and M.M. Treacy, Wetting of single shell carbon nanotubes, *Adv. Mater*. **10**, 1472–1475 (1998).
380. G. Hummer, J.C. Rasaiah, and J.P. Noworyta, Water conduction through the hydrophobic channel of a carbon nanotube, *Nature* **414**, 188–190 (2001).
381. M.S.P. Sansom and P.C. Biggin, Biophysics: water at the nanoscale, *Nature* **414**, 156 (2001).
382. J. Martí and M.C. Gordillo, Temperature effects on the static and dynamic properties of liquid water inside nanotubes. *Phys. Rev.* **E 64**, 21504.1–6 (2001).
383. K. Koga, G.T. Gao, H. Tanaka, and X.C. Zeng, Formation of ordered ice nanotubes inside carbon nanotubes, *Nature* **412**, 802–805 (2001).
384. W.H. Noon, K.D. Ausman, R.E. Smalley, and J. Ma, Helical ice-sheets inside carbon nanotubes in the physiological condition, *Chem. Phys. Lett*. **355**, 445–448 (2002).
385. A. Waghe, J.C. Rasaiah, and G. Hummer, Filling and emptying kinetics of carbon nanotubes in water, *J. Chem. Phys.* **117**, 10789–10795 (2002).
386. A. Kalra, S. Garde, and G. Hummer, Osmotic water transport through carbon nanotube membranes, *Proc. Nat. Acad. Sci. USA* **100**, 10175–10180 (2003).
387. M.P. Rossi, H. Ye, Y. Gogotsi, S. Babu, P. Ndungu, and J.-C. Bradley, Environmental scanning electron microscopy study of water in carbon nanopipes, *Nano Lett.* **4**, 989–993 (2004).
388. S. Joseph, R.J. Mashl, E. Jacobsson, and N.R. Aluru, Ion channel based biosensors: ionic transport in carbon nanotubes, *Nanotech 2003*, **1**, 158–161 (2003) [http://www.nsti.org/procs/Nanotech2003v1/8/T23.05].
389. S.C. Tsang, Y.K. Chen, P.J.F. Harris, and M.L. Green, A simple chemical method of opening and filling carbon nanotubes, *Nature* **372**, 159–162 (1994).
390. J. Chancolon, F. Archaimbault, S. Delpeux, A. Pineau, M.L. Saboungi, and S. Bonnamy, Filling of multiwalled carbon nanotubes with oxides and metals, *AIP Conf. Proc.* **633**, No. 1, 131–134 (2002).
391. P. Corio, A.P. Santos, P.S. Santos, M.L.A. Temperini, V.W. Brar, M.A. Pimenta, and M.S. Dresselhaus, Characterization of single wall carbon nanotubes filled with silver and with chromium compounds, *Chem. Phys. Lett.* **383**, 475–480 (2004).
392. C. Pham-Huu, N. Keller, C. Estournès, G. Ehret, and M.J. Ledoux, Synthesis of $CoFe_2O_4$ nanowire in carbon nanotubes. A new use of confinement effect, *Chem. Commun*. 1882–1883 (2002).
393. C. Pham-Huu, N. Keller, C. Estournès, G. Ehret, J.M. Grenèche, and M.J. Ledoux, Microstructural investigation and magnetic properties of $CoFe_2O_4$ nanowires synthesized inside carbon nanotubes, *Phys. Chem. Chem. Phys*. **5**, 3716–3723 (2003).
394. N. Keller, C. Pham-Huu, C. Estournès, J.-M. Grenèche, G. Ehret, and M.J. Ledoux, Carbon nanotubes as a template for mild synthesis of magnetic $CoFe_2O_4$ nanowires, *Carbon* **42**, 1395–1399 (2004).
395. J. Sloan, J. Hammer, M. Zwiefka-Sibley, and M.L.H. Green, The opening and filling of single walled carbon nanotubes (SWTs), *Chem. Commun.* 347–348 (1998).
396. B. Rajesh, K.R. Thampi, J.-M. Bonard, and B. Viswanathan, Preparation of a Pt–Ru bimetallic system supported on carbon nanotubes, *J. Mater. Chem.* **10**, 1757–1759 (2000).
397. B. Rajesh, K.R. Thampi, J.-M. Bonard, and B. Visvanathan, Preparation of Pt-Ru bimetallic catalyst supported on carbon nanotubes, *Bull. Mater. Sci.* **23**, 341–344 (2000).
398. B. Rajesh, V. Karthik, S. Karthikeyan, K.R. Thampi, J.-M. Bonard, and B. Viswanathan, Pt–WO_3 supported on carbon nanotubes as possible anodes for direct methanol fuel cells, *Fuel* **81**, 2177–2190 (2002).
399. B. Rajesh, K.R. Thampi, J.-M. Bonard, N. Xanthopoulos, H.J. Mathieu, and B. Viswanathan, Carbon nanotubes generated from template carbonization of polyphenyl acetylene as the support for electrooxidation of methanol, *J. Phys. Chem.* **B 107**, 2701–2708 (2003).
400. J. Bao, Q. Zhou, J. Hong, and Z. Xu, Synthesis and magnetic behavior of an array of nickel-filled carbon nanotubes, *Appl. Phys. Lett.* **81**, 4592–4594 (2002).
401. K. Matsui, T. Kyotani, and A. Tomita, Hydrothermal synthesis of nano-sized iron oxide crystals in the cavity of carbon nanotubes, *Mol. Cryst. Liq. Cryst.* **387**, 1–5 (2002).
402. J. Mittal, M. Monthioux, H. Allouche, and O. Stephan, Room temperature filling of single-wall carbon nanotubes with chromium oxide in open air, *Chem. Phys. Lett*. **339**, 311–318 (2001).
403. H.-Q. Wu, X.-W. Wei, M.-W. Shao, J.-S. Gu, and M.-Z. Qu, Synthesis of copper oxide nanoparticles using carbon nanotubes as templates, *Chem. Phys. Lett*. **364**, 152–156 (2002).

404. L. Jiang and L. Gao, Modified carbon nanotubes: an effective way to selective attachment of gold nanoparticles, *Carbon* **41**, 2923–2929 (2003).
405. X.-R. Ye, Y. Lin, C. Wang, and C.M. Wai, Supercritical fluid fabrication of metal nanowires and nanorods templated by multiwalled carbon nanotubes, *Adv. Mater.* **15**, 316–319 (2003).
406. D.A. Britz, A.N. Khlobystov, J. Wang, A.S. O'Neil, M. Poliakoff, A. Ardavan, and G.A.D. Briggs, Selective host-guest interaction of single-walled carbon nanotubes with functionalized fullerenes, *Chem. Commun.* 176–177 (2004).
407. F. Simon, H. Kuzmany, H. Rauf, T. Pichler, J. Bernardi, H. Peterlik, L. Korecz, F. Fülöp, and A. Jánossy, Low temperature fullerene encapsulation in single wall carbon nanotubes: synthesis of N@C_{60}@SWCNT, *Chem. Phys. Lett.* **383**, 362–367 (2004).
408. M. Yudasaka, K. Ajima, K. Suenaga, T. Ichihashi, A. Hashimoto, and S. Iijima, Nano-extraction and nano-condensation for C_{60} incorporation into a single-wall carbon nanotubes in liquid phases, *Chem. Phys. Lett.* **380**, 42–46 (2003).
409. T. Takenobu, T. Takano, M. Shiraishi, Y. Murakami, M. Ata, H. Kataura, Y. Achiba, and Y. Iwasa, Stable and controlled amphoteric doping by encapsulation of organic molecules inside carbon nanotubes, *Nat. Mater.* **2**, 683–688 (2003).
410. H. Gao, Y. Kong, D. Cui, and C.S. Ozkan, Spontaneous insertion of DNA oligonucleotides into carbon nanotubes, *Nano Lett.* **3**, 471–473 (2003).
411. S. Friedrichs, R.R. Meyer, J. Sloan, A.I. Kirkland, J.L. Hutchison, and M.L.H. Green, Complete characterization of a Sb_2O_3/(21,–8)SWNT inclusion composite, *Chem. Commun.* 929–930 (2001).
412. S. Friedrichs, J. Sloan, M.L.H. Green, J.L. Hutchison, R.R. Meyer, and A.I. Kirkland, Simultaneous determination of inclusion crystallography and nanotube conformation for a Sb_2O_3/single-walled nanotube composite, *Phys. Rev.* **B 64**, 045406.1–8 (2001).
413. J. Sloan, D.M. Wright, H.-G. Woo, S. Bailey, G. Brown, A.P.E. York, K.S. Coleman, J.L. Hutchison, and M.L.H. Green, Capillarity and silver nanowire formation observed in single walled carbon nanotubes, *Chem. Commun.* 699–700 (1999).
414. J. Sloan, A.I. Kirkland, J.L. Hutchison, and M.L.H. Green, Integral atomic layer architectures of 1D crystals inserted into single walled carbon nanotubes, *Chem. Commun.* 1319–1332 (2002).
415. C. Xu, J. Sloan, G. Brown, S. Bailey, V.C. Williams, S. Friedrichs, K.S. Coleman, E. Flahaut, J.L. Hutchison, R.E. Dunin-Borkowski, and M.L.H. Green, 1D lanthanide halide crystals inserted into single-walled carbon nanotubes, *Chem. Commun*. 2427–2428 (2000).
416. C.-H. Kiang, J.-S. Choi, T.T. Tran, and A.D. Bacher, Molecular nanowires of 1 nm diameter from capillary filling of single-walled nanotubes, *J. Phys. Chem.* **B 103**, 7449–7451 (1999).
417. C.-H. Kiang, Electron irradiation induced dimensional change in bismuth filled carbon nanotubes, *Carbon* **38**, 1699–1701 (2000).
418. X. Fan, E.C. Dickey, P.C. Eklund, K.A. Williams, L. Grigorian, R. Buczko, S.T. Pantelides, and S.J. Pennycook, Atomic arrangement of iodine atoms inside single-walled carbon nanotubes, *Phys. Rev. Lett.* **84**, 4621–4624 (2000).
419. W. Zhou, S. Xie, L. Sun, D. Tang, Y. Li, Z. Liu, L. Ci, X. Zou, G. Wang, P. Tan, X. Dong, B. Xu, and B. Zhao, Raman scattering and thermogravimetric analysis of iodine-doped multiwall carbon nanotubes, *Appl. Phys. Lett.* **80**, 2553–2555 (2002).
420. Y. Gao and Y. Bando, Carbon nanothermometer containing gallium, *Nature* **415**, 599 (2002).
421. A. Fujiwara, K. Ishii, H. Suematsu, H. Kataura, Y. Maniwa, S. Suzuki, and Y. Achiba, Gas adsorption in the inside and outside of single-walled carbon nanotubes, *Chem. Phys. Lett.* **336**, 205–211 (2001).
422. Z. Mao, A. Garg, and S.B. Sinnott, Molecular dynamics simulations of the filling and decorating of carbon nanotubules, *Nanotechnology* **10**, 273–277 (1999).
423. Z. Mao and S.B. Sinnott, A computational study of molecular diffusion and dynamic flow through carbon nanotubes, *J. Phys. Chem.* **B 104**, 4618–4624 (2000).
424. M. Li, M. Lu, C. Wang, and H. Li, Preparation of well-aligned carbon nanotubes/silicon nanowires core-sheath composite structure arrays in porous anodic aluminium oxide templates, *Sci. China* **45 B**, No. 4, 435–444 (2002).
425. G. Brown, S.R. Bailey, J. Sloan, C. Xu, S. Friedrichs, E. Flahaut, K.S. Coleman, J.L. Hutchison, R.E. Dunin-Borkowski, and M.L.H. Green, Electron beam induced *in situ* characterization of 1D $ZrCl_4$ chains within single-walled carbon nanotubes, *Chem. Commun.* 845–846 (2001).
426. H. Kataura, Y. Maniwa, T. Kodama, K. Kikuchi, K. Hirahara, K. Suenaga, S. Iijima, S. Suzuki, Y. Achiba, and W. Krätschmer, High-yield fullerene encapsulation in single-wall carbon nanotubes, *Synth. Met.* **121**, 1195–1196 (2001).

427. K. Hirahara, K. Suenaga, S. Bandow, H. Kato, T. Okazaki, H. Shinohara, and S. Iijima, One-dimensional metallofullerene crystal generated inside single-walled carbon nanotubes, *Phys. Rev. Lett.* **85**, 5384–5387 (2000).
428. K. Hirahara, S. Bandow, K. Suenaga, H. Kato, T. Okazaki, H. Shinohara, and S. Iijima, Electron diffraction study of one-dimensional crystals of fullerenes, *Phys. Rev.* **B 64**, 115420.1–5 (2001).
429. A.R. Harutyunyan, B.K. Pradhan, G.U. Sumanasekera, E.Yu. Korobko, A.A. Kuznetsov, Carbon nanotubes for medical applications, *Eur. Cells Mater.* **3**, Suppl. 2, 84–87 (2002).
430. B.K. Pradhan, T. Toba, T. Kyotani, and A. Tomita. Inclusion of crystalline iron oxide nanoparticle in uniform carbon nanotubes prepared by a template carbonization method, *Chem. Mater*. **10**, 2510–2515 (1998).
431. B.K. Pradhan, T. Kyotani, and A. Tomita, Nickel nanowires of 4 nm diameter in the cavity of carbon nanotubes, *Chem. Commun*. 1317–1318 (1999).
432. K. Matsui, B.K. Pradhan, T. Kyotani, and A. Tomita, Formation of nickel oxide nanoribbons in the cavity of carbon nanotubes, *J. Phys. Chem.* **B 105**, 5682–5688 (2001).
433. X. Li, L. Liu, Y. Qin, W. Wu, Z.-X. Guo, L. Dai, and D. Zhu, C_{60} modified single-walled carbon nanotubes, *Chem. Phys. Lett.* **377**, 32–36 (2003).
434. G.-H. Jeong, A.A. Farajian, T. Hirata, R. Hatakeyama, K. Tohji, T.M. Briere, H. Mizuseki, and Y. Kawazoe, Encapsulation of cesium inside single-walled carbon nanotubes by plasma-ion irradiation method, *Thin Solid Films* **435**, 307–311 (2003).
435. F. Banhart, The formation of a connection between carbon nanotubes in an electron beam, *Nano Lett.* **1**, 329–332 (2001).
436. Z. Wang, L. Yu, W. Zhang, Y. Ding, Y. Li, Z. Zhu, J. Han, H. Xu, G. He, Y. Chen, and G. Hu, Amorphous molecular junctions by ion irradiation on carbon nanotubes, *Phys. Lett.* **A 324**, 321–325 (2004).
437. D. Ding and J. Wang, Electron irradiation of multi-walled carbon nanotubes with encapsulated Ni particles, *Carbon* **40**, 787–803 (2002).
438. R. Che, L.-M. Peng, Q. Chen, X.F. Duan, B.S. Zou, and Z.N. Gu, Controlled synthesis and phase transformation of ferrous nanowires inside carbon nanotubes, *Chem. Phys. Lett.* **375**, 59–64 (2003).
439. J.S. Lee, B. Min, K. Cho, S. Kim, J. Park, Y.T. Lee, N.S. Kim, M.S. Lee, S.O. Park, and J.T. Moon, Al_2O_3 nanotubes and nanorods fabricated by coating and filling of carbon nanotubes with atomic-layer deposition, *J. Cryst. Growth* **254**, 443–448 (2003).
440. Z. Liu, Y. Gao, and Y. Bando, Highly effective metal vapor absorbents based on carbon nanotubes, *Appl. Phys. Lett.* **81**, 4844–4846 (2002).
441. B.W. Smith, M. Monthioux, and D.E. Luzzi, Encapsulated C_{60} in carbon nanotubes, *Nature* **396**, 323–324 (1998).
442. J. Sloan, R.E. Dunin-Borkowski, J.L. Hutchison, K.S. Coleman, V.C. Williams, J.B. Claridge, A.P.E. York, C. Xu, S.R. Bailey, G. Brown, S. Friedrichs, and M.L.H. Green, The size distribution, imaging and obstructing properties of C_{60} and higher fullerenes formed within arc-grown single walled carbon nanotubes, *Chem. Phys. Lett.* **316**, 191–198 (2000).
443. R. Pfeiffer, Ch. Kramberger, Ch. Schaman, A. Sen, M. Holzweber, H. Kuzmany, T. Pichler, H. Kataura, and Y. Achiba, Defect free inner tubes in DWCNTs, *AIP Conf. Proc.* **685**, No. 1, 297–301 (2003).
444. H. Kataura, Y. Maniwa, M. Abe, A. Fujiwara, T. Kodama, K. Kikuchi, M. Imahori, Y. Misaki, S. Suzuki, and Y. Achiba, Optical properties of fullerene and non-fullerene peapods, *Appl. Phys.* **A 74**, 349–354 (2002).
445. S. Bandow, M. Takizawa, K. Hirahata, M. Yudasaka, and S. Iijima, Raman scattering study of double-wall carbon nanotubes derived from the chains of fullerenes in single-wall carbon nanotubes, *Chem. Phys. Lett.* **337**, 48–54 (2001).
446. S. Bandow, T. Hiraoka, T. Yumura, K. Hirahara, H. Shinohara, and S. Iijima, Raman scattering study on fullerene derived intermediates formed within single-wall carbon nanotube: from peapod to double-wall carbon nanotube, *Chem. Phys. Lett.* **384**, 320–325 (2004).
447. T. Okazaki, K. Suenaga, K. Hirahara, S. Bandow, S. Iijima, and H. Shinohara, Real time reaction dynamics in carbon nanotubes, *J. Am. Chem. Soc.* **123,** 9673–9674 (2001).
448. C.M. Megaridis, A. Güvenç Yazicirogly, J.A. Libera, and Y. Gogotsi, Attoliter fluid experiments in individual closed-end carbon nanotubes: liquid film interface dynamics, *Phys. Fluids* **14**, L5–8 (2002).
449. H. Ye, N. Naguib, Y. Gogotsi, A.G. Yazicirogly, and C.M. Megaridis, Wall structure and surface chemistry of hydrothermal carbon nanofibres, *Nanotechnology* **15**, 232–236 (2004).

450. M. Green, *Carbon nanotubes. Chemistry in a carbon cage*. The Institute of Applied Catalysis, 2000. [http://www.iac.org.uk/pages/vis3.html].
451. Z. Liu, X. Dai, J. Xu, B. Han, J. Zhang, Y. Wang, Y. Huang, and G. Yang, Encapsulation of polystyrene within carbon nanotubes with the aid of supercritical CO_2, *Carbon* **42**, 423–460 (2004).
452. Q. Yang, L. Li, H. Cheng, M. Wang, and J. Bai, Inner-tubular physicochemical processes of carbon nanotubes, *Chin. Sci. Bull.* **48**, 2395–2403 (2003).
453. Q. Jiang, N. Aya, and F.G. Shi, Nanotube size-dependent melting of single crystals in carbon nanotubes, *Appl. Phys.* **A 64**, 627–629 (1997).
454. J. Sloan, S. Friedrichs, R.R. Meyer, A.I. Kirkland, J.L. Hutchison, and M.L.H. Green, Structural changes induced in nanocrystals of binary compounds confined within single wall carbon nanotubes: a brief review, *Inorg. Chim. Acta* **330**, 1–12 (2002).
455. J. Sloan, A.I. Kirkland, J.L. Hutchison, and M.L.H. Green, Structural characterization of atomically regulated nanocrystals formed within single-walled carbon nanotubes using electron microscopy, *Acc. Chem. Res.* **35**, 1054–1062 (2002).
456. J. Sloan, M.C. Novotny, S.R. Bailey, G. Brown, C. Xu, V.C. Williams, S. Friedrichs, E. Flahaut, R.R. Callender, A.P.E. York, K.S. Coleman, M.L.H. Green, R.E. Dunin-Borkowski, and J.L. Hutchison, Two layer 4:4 co-ordinated KI crystals grown within single walled carbon nanotubes, *Chem. Phys. Lett.* **329**, 61–65 (2000).
457. M. Wilson, Structure and phase stability of novel 'twisted' crystal structures in carbon nanotubes, *Chem. Phys. Lett.* **366**, 504–509 (2002).
458. M. Wilson, The formation of low-dimensional ionic crystallites in carbon nanotubes, *J. Chem. Phys.* **116**, 3027–3041 (2002).
459. Y. Maniwa, H. Kataura, M. Abe, A. Fujiwara, R. Fujiwara, H. Kira, H. Tou, S. Suzuki, Y. Achiba, E. Nishibori, M. Takata, M. Sakata, and H. Suematsu, C_{70} molecular stumbling inside single-walled carbon nanotubes, *J. Phys. Soc. Jpn.* **72**, 45–48 (2002).
460. A.C. Dillon, K.M. Jones, T.A. Bekkedahl, C.H. Kiang, D.S. Bethune, and M.J. Heben, Storage of hydrogen in single-walled carbon nanotubes, *Nature* **386**, 377–379 (1997).
461. A. Chambers, C. Park, R.T.K. Baker, and N.M. Rodriguez, Hydrogen storage in graphite nanofibers, *J. Phys. Chem.* **B 102**, 4253–4256 (1998).
462. P. Chen, X. Wu, J. Lin, and K.L. Tan, High H_2 uptake by alkali-doped carbon nanotubes under ambient pressure and moderate temperatures, *Science* **285**, 91–93 (1999).
463. Y. Chen, D.T. Shaw, X.D. Bai, E.G. Wang, C. Lund, W.M. Lu, and D.D.L. Chung, Hydrogen storage in aligned carbon nanotubes, *Appl. Phys. Lett.* **78**, 2128–2130 (2001).
464. C. Nűtzenadel, A. Zűttel, D. Chartouni, and L. Schlapbach, Electrochemical storage of hydrogen in nanotube materials, *Electrochem. Solid-State Lett.* **2**, 30–32 (1999).
465. N. Rajalakshmi, K.S. Dhathathreyan, A. Govindaraj, and B.C. Satishkumar, Electrochemical investigation of single-walled carbon nanotubes for hydrogen storage, *Electrochim. Acta* **45**, 4511–4515 (2000).
466. M. Hirscher, M. Becher, M. Haluska, U. Dettlaff-Weglikowska, A. Quintel, G.S. Duesberg, Y.-M. Choi, P. Downes, M. Hulman, S. Roth, I. Stepanek, and P. Bernier, Hydrogen storage in sonicated carbon materials, *Appl. Phys.* **A 72**, 129–132 (2001).
467. G.-P. Dai, C. Liu, M. Liu, M.-Z. Wang, and H.-M. Cheng, Electrochemical hydrogen storage behavior of ropes of aligned single-walled carbon nanotubes, *Nano Lett.* **2**, 503–506 (2002).
468. F.J. Owens and Z. Iqbal, Electrochemical functionalization of carbon nanotubes with hydrogen [www.asc2002.com/summaries/1/LP-11.pdf].
469. H. Takagi, H. Hatori, Y. Soneda, N. Yoshizawa, and Y. Yamada, Adsorptive hydrogen storage in carbon and porous materials, *Mater. Sci. Eng.* **B 108**, 143–147 (2004).
470. A. Ansón, M.A. Callejas, A.M. Benito, W.K. Maser, M.T. Izquierdo, B. Rubio, J. Jagiello, M. Thommes, J.B. Parra, and M.T. Martínez, Hydrogen adsorption studies on single wall carbon nanotubes, *Carbon* **42**, 1243–1248 (2004).
471. N. Nishimiya, K. Ishigaki, H. Takikawa, M. Ikeda, Y. Hibi, T. Sakakibara, A. Matsumoto, and K. Tsutsumi, Hydrogen sorption by single-walled carbon nanotubes prepared by a torch arc method, *J. Alloys Comp.* **339**, 275–282 (2002).
472. M. Shiraishi, T. Takenobu, and M. Ata, Gas-solid interactions in the hydrogen/single-walled carbon nanotube system, *Chem. Phys. Lett.* **367**, 633–636 (2003).
473. M. Shiraishi, T. Takenobu, H. Kataura, and M. Ata, Hydrogen adsorption and desorption in carbon nanotube systems and its mechanisms, *Appl. Phys.* **A 78**, 947–953 (2004).

474. B.P. Tarasov, J.P. Maehlen, M.V. Lototsky, V.E. Muradyan, and V.A. Yartys, Hydrogen sorption properties of arc generated single-wall carbon nanotubes, *J. Alloys Comp.* **356–357**, 510–514 (2003).
475. P. David, T. Piquero, K. Metenier, Y. Pierre, J. Demoment, and A. Lecas-Hardit, Hydrogen adsorption in carbon materials [http://www.waterstof.org/2003072EHECP2-200.pdf].
476. C. Liu, Y.Y. Fan, M. Liu, H.T. Cong, H.M. Cheng, and M.S. Dresselhaus, Hydrogen storage in single-walled carbon nanotubes at room temperature, *Science* **286,** 1127–1129 (1999).
477. D. Luxembourg, G. Flamant, A. Guillot, and D. Laplaze, Hydrogen storage in solar produced single-walled carbon nanotubes, *Mater. Sci. Eng.* **B 108**, 114–119 (2004).
478. M.A. Callejas, A. Ansón, A.M. Benito, W. Maser, J.L.G. Fierro, M.L. Sanjuán, and M.T. Martínez, Enhanced hydrogen adsorption on single-wall carbon nanotubes by sample reduction, *Mater. Sci. Eng.* **B 108**, 120–123 (2004).
479. B.K. Pradhan, A.R. Harutyunyan, D. Stojkovic, J.C. Grossman, P. Zhang, M.W. Cole, V. Crespi, H. Goto, J. Fujiwara, and P.C. Eklund, Large cryogenic storage of hydrogen in carbon nanotubes at low pressures, *J. Mater. Res.* **17**, 2209–2216 (2002).
480. P. Sudan, A. Züttel, Ph. Mauron, Ch. Emmenegger, P. Wenger, and L. Schlapbach, Physisorption of hydrogen in single-walled carbon nanotubes, *Carbon* **41**, 2377–2383 (2003).
481. Y. Ye, C.C. Ahn, C. Witham, B. Fultz, J. Liu, A.G. Rinzler, D. Colbert, K.A. Smith, and R.E. Smalley, Hydrogen absorption and cohesive energy of single-walled carbon nanotubes, *Appl. Phys. Lett.* **74**, 2307–2309 (1999).
482. X.B. Wu, P. Chen, J. Lin, and K.L. Tan, Hydrogen uptake by carbon nanotubes, *Int. J. Hydrogen Energy* **25**, 261–265 (2000).
483. X. Qin, X.P. Gao, H. Liu, H.T. Yuan, D.Y. Yan, W.L. Gong, and D.Y. Song, Electrochemical hydrogen storage of multiwalled carbon nanotubes, *Electrochem. Solid-State Lett.* **3**, 532–535 (2000).
484. A.K.M. Fazle Kibria, Y.H. Mo, K.S. Park, K.S. Nahm, and M.H. Yun, Electrochemical hydrogen storage behaviors of CVD, AD and LA grown carbon nanotubes in KOH medium, *Int. J. Hydrogen Energy*, **26**, 823–829 (2001).
485. R.T. Yang, Hydrogen storage by alkali-doped carbon nanotubes — revisited, *Carbon* **38**, 623–641 (2000).
486. G.Q. Ning, F. Wei, G.H. Luo, Q.X. Wang, Y.L. Wu, and H. Yu, Hydrogen storage in multi-wall carbon nanotubes using samples up to 85 g, *Appl. Phys.* **A 78**, 955–959 (2004).
487. A. Cao, H. Zhu, X. Zhang, X. Li, D. Ruan, C. Xu, B. Wei, J. Liang, and D. Wu, Hydrogen storage of dense-aligned carbon nanotubes, *Chem. Phys. Lett.* **342**, 510–514 (2001).
488. X. Li, H. Zhu, L. Ci, C. Xu, Z. Mao, B. Wei, J. Liang, and D. Wu, Hydrogen uptake by graphitized multi-walled carbon nanotubes under moderate pressure and at room temperature, *Carbon* **39**, 2077–2079 (2001).
489. H.W. Zhu, A. Chen, Z.Q. Mao, C.L. Xu, X. Xiao, B.Q. Wei, J. Liang, and D.H. Wu, The effect of surface treatments on hydrogen storage of carbon nanotubes, *J. Mater. Sci. Lett.* **19**, 1237–1239 (2000).
490. H. Zhu, A. Cao, X. Li, C. Xu, Z. Mao, D. Ruan, J. Liang, and D. Wu, Hydrogen adsorption in bundles of well-aligned carbon nanotubes at room temperature, *Appl. Surf. Sci.* **178**, 50–55 (2001).
491. W.Z. Huang, X.B. Zhang, J.P. Tu, F.Z. Kong, J.X. Ma, F. Liu, H.M. Lu, and C.P. Chen, The effect of pretreatments on hydrogen adsorption of multi-walled carbon nanotubes, *Mater. Chem. Phys.* **78**, 144–148 (2002).
492. P.-X. Hou, S.-T. Xu, Z. Ying, Q.-H. Yang, C. Liu, and H.-M. Cheng, Hydrogen adsorption/desorption behavior of multi-walled carbon nanotubes with different diameters, *Carbon* **41**, 2471–2476 (2003).
493. K. Hanada, H. Shiono, and K. Matsuzaki, Hydrogen uptake of carbon nanofiber under moderate temperature and low pressure, *Diamond Rel. Mater.* **12**, 874–877 (2003).
494. D.J. Browning, M.L. Gerrard, J.B. Lakeman, I.M. Mellor, R.J. Mortimer, and M.C. Turpin, Studies into the storage of hydrogen in carbon nanofibers: proposal of a possible reaction mechanism, *Nano Lett.* **2**, 201–205 (2002).
495. K. Ichimura, K. Imaeda, and H. Inokuchi, Characteristic bonding of rare gases in solid carbon nanotubes, *Synth. Met.* **121**, 1191–1192 (2001).
496. S. Challet, P. Azaïs, R.J.-M. Pellenq, L. Duclaux, D_2 adsorption in potassium-doped single-wall carbon nanotubes: a neutron diffraction and isotherms study, *Chem. Phys. Lett.* **377**, 544–550 (2003).
497. M. Rzepka, P. Lamp, and M.A. de la Casa-Lillo, Physisorption of hydrogen on microporous carbon and carbon nanotubes, *J. Phys. Chem.* **B 102**, 10894–10898 (1998).

498. M.K. Kostov, M.W. Cole, J.C. Lewis, P. Diep, and J.K. Johnson, Many-body interactions among adsorbed atoms and molecules within carbon nanotubes and in free space, *Chem. Phys. Lett.* **332**, 26–34 (2000).
499. C.W. Bauschlicher Jr., Hydrogen and fluorine binding to the sidewalls of a (10,0) carbon nanotube, *Chem. Phys. Lett.* **322**, 237–241 (2000).
500. K.A. Williams and P.C. Eklund, Monte Carlo simulations on H_2 physisorption in finite-diameter carbon nanotube ropes, *Chem. Phys. Lett.* **320**, 352–358 (2000).
501. S.M. Lee, K.S. Park, Y.C. Choi, Y.S. Park, J.M. Bok, D.J. Bae, K.S. Nahm, Y.G. Choi, S.C. Yu, N.-G. Kim, T.Frauenheim, and Y.H. Lee, Hydrogen adsorption and storage in carbon nanotubes, *Synth. Met.* **113**, 209–216 (2000).
502. S.M. Lee and Y.H. Lee, Hydrogen storage in single-walled carbon nanotubes, *Appl. Phys. Lett.* **76**, 2877–2879 (2000).
503. S.-P. Chan, G. Chen, X.G. Gong, and Z.-F. Liu, Chemisorption of hydrogen molecules on carbon nanotubes under high pressure, *Phys. Rev. Lett.* **87**, 205502 (2001).
504. C. Gu, G.-H. Gao, Y.-X. Yu, and Z.-Q. Mao, Simulation study of hydrogen storage in single walled carbon nanotubes, *Int. J. Hydrogen Energy* **26**, 691–696 (2001).
505. S.M. Lee, K.H. An, Y.H. Lee, G. Seifert, and T. Frauenheim, A hydrogen storage mechanism in single-walled carbon nanotubes, *J. Am. Chem. Soc.* **123**, 5059–5063 (2001).
506. S.M. Lee, K.H. An, W.S. Kim, Y.H. Lee, Y.S. Park, G. Seifert, and T. Frauenheim, Hydrogen storage in carbon nanotubes, *Synt. Met.* **121**, 1189–1190 (2001).
507. Y. Ren and D.L. Price, Neutron scattering study of H_2 adsorption in single-walled carbon nanotubes, *Appl. Phys. Lett.* **79**, 3684–3686 (2001).
508. H. Cheng, G.P. Pez, and A.C. Cooper, Mechanism of hydrogen sorption on single-walled carbon nanotubes, *J. Am. Chem. Soc.* **123**, 5845–5846 (2001).
509. C.W. Bauschlicher Jr., High coverages of hydrogen on (10,0) carbon nanotube, *Nano Lett.* **1**, 223–226 (2001).
510. M.K. Kostov, H. Cheng, A.C. Cooper, and G.P. Pez, Influence of carbon curvature in carbon-based materials: a force field approach, *Phys. Rev. Lett.* **89**, 146105 (2002).
511. M.K. Kostov, H. Cheng, R.M. Herman, M.W. Cole, and J.C. Lewis, Hindered rotation of H_2 adsorbed interstitially in nanotube bundles, *J. Chem. Phys.* **116**, 1720–1724 (2002).
512. Y. Ma, Y. Xia, M. Zhao, and M. Ying, Hydrogen storage capacity in single-walled carbon nanotubes, *Phys. Rev.* **B 65**, 155430.1–6 (2002).
513. R.A. Trasca, M.K. Kostov, and M.W. Cole, Isotopic and spin selectivity of H_2 adsorbed in bundles of carbon nanotubes, *Phys. Rev.* **B 67**, 035410.1–8 (2003).
514. J. Li, T. Furuta, H. Goto, T. Ohashi, Y. Fujiwara, and S. Yip, Theoretical evaluation of hydrogen storage capacity in pure carbon nanostructures, *J. Chem. Phys.* **119**, 2376–2385 (2003).
515. M. Haluska, M. Hirscher, M. Becher, U. Dettlaff-Weglikowska, X. Chen, and S. Roth, Interaction of hydrogen isotopes with carbon nanostructures, *Mater. Sci. Eng.* **B 108**, 130–133 (2004).
516. H.G. Schimmel, G. Nijkamp, G.J. Kearley, A. Rivera, K.P. de Jong, and F.M. Mulder, Hydrogen adsorption in carbon nanostructures compared, *Mater. Sci. Eng.* **B 108**, 124–129 (2004).
517. D. Chen, L. Chen, S. Liu, C.X. Ma, D.M. Chen, and L.B. Wang, Microstructure and hydrogen storage property of Mg/MWNTs composites, *J. Alloys Comp.* **372**, 231–237 (2004).
518. B.P. Tarasov, N.G. Goldshleger, and A.P. Moravsky, Hydrogen-containing carbon nanostructures: synthesis and properties, *Russ. Chem. Rev.* **70**, 131–146 (2001).
519. H.-M. Cheng, Q.-H. Yang, and C. Liu, Hydrogen storage in carbon nanotubes, *Carbon* **39**, 1447–1454 (2001).
520. F.L. Darkrim, P. Malbrunot, and G.P. Tartaglia, Review of hydrogen storage by adsorption in carbon nanotubes, *Int. J. Hydrogen Energy* **27**, 193–202 (2002).
521. V.V. Simonyan and J.K. Johnson, Hydrogen storage in carbon nanotubes and graphitic nanofibers, *J. Alloys Comp.* **330–332**, 659–665 (2002).
522. E. Frackowiak and F. Béguin, Electrochemical storage of energy in carbon nanotubes and nanostructured carbons, *Carbon* **40**, 1775–1787 (2002).
523. A. Zűttel, P. Sudan, Ph. Mauron, T. Kiyobayashi, Ch. Emmenegger, and L. Schlapbach, Hydrogen storage in carbon nanostructures, *Int. J. Hydrogen Energy* **27**, 203–212 (2002).
524. M. Becher, M. Haluska, M. Hirscher, A. Quintel, V. Skakalova, U. Dettlaff-Weglikovska, X. Chen, M. Hulman, Y. Choi, S. Roth, V. Meregalli, M. Parrinello, R. Ströbel, L. Jörissen, M.M. Kappes, J. Fink, A. Zűttel, I. Stepanek, and P. Bernier, Hydrogen storage in carbon nanotubes, *C. R. Physique* **4**, 1055–1062 (2003).

525. B. Viswanathan, M. Sankaran, and M.A. Scibioh, Carbon nanomaterials – are they appropriate candidates for hydrogen storage? *Bull. Catal. Soc. India* **2**, 12–32 (2003).
526. A. Zűttel, P. Wenger, P. Sudan, P. Mauron, and S.-I. Orimo, Hydrogen density in nanostructured carbon, metals and complex materials, *Mater. Sci. Eng.* **B 108**, 9–18 (2004).
527. M. Conte, P.P. Prosini, and S. Passerini, Overview of energy/hydrogen storage: state-of-the-art of the technologies and prospects for nonomaterials, *Mater. Sci. Eng.* **B 108**, 2–8 (2004).
528. S. Talapatra, A.Z. Zambano, S.E. Weber, and A.D. Migone, Gases do not adsorb on the interstitial channels of closed-ended single-walled carbon nanotube bundles, *Phys. Rev. Lett.* **85**, 138–141 (2000).
529. M.M. Calbi, S.M. Gatica, M.J. Bojan, and M.W. Cole, Phases of neon, xenon, and methane adsorbed on nanotube bundles, *J. Chem. Phys.* **115**, 9975–9981 (2001).
530. M. Muris, N. Dupont-Pavlovsky, M. Bienfait, and P. Zeppenfeld, Where are the molecules adsorbed on single-walled nanotubes? *Surf. Sci.* **492**, 67–74 (2001).
531. J. Zhao, A. Buldum, J. Han, and J.P. Lu, Gas molecule adsorption in carbon nanotubes and nanotube bundles, *Nanotechnology* **13**, 195–200 (2002).
532. B.-Y. Wei, M.-C. Hsu, Y.-S. Yang, S.-H. Chien, and H.-M. Lin, Gases adsorption on single-walled carbon nanotubes measured by piezoelectric quartz crystal microbalance, *Mater. Chem. Phys.* **81**, 126–133 (2003).
533. A. Kleinhammes, S.-H. Mao, X.-J. Yang, X.-P. Tang, H. Shimoda, J.P. Lu, O. Zhou, and Y. Wu. Gas adsorption in single-walled carbon nanotubes studied by NMR, *Phys. Rev.* **B 68**, 075418.1–6 (2003).
534. A. Goldoni, R. Larciprete, L. Petaccia, and S. Lizzit, Single-wall carbon nanotube interaction with gases: sample contaminants and environmental monitoring, *J. Am. Chem. Soc.* **125**, 11329–11333 (2003).
535. S.-H. Jhi, S.G. Loui, and M.L. Cohen, Electronic properties of oxidized carbon nanotubes, *Phys. Rev. Lett.* **85**, 1710–1713 (2000).
536. S. Dag, O. Gülseren, and S. Ciraci, A comparative study of O_2 adsorbed carbon nanotubes, *Chem. Phys. Lett.* **380**, 1–5 (2003).
537. M. Cinke, J. Li, C.W. Bauschlicher Jr., A. Ricca, and M. Meyyappan, CO_2 adsorption in single-walled carbon nanotubes, *Chem. Phys. Lett.* **276**, 761–766 (2003).
538. C. Matranga, L. Chen, M. Smith, E. Bittner, J.K. Johnson, and B. Bockrath, Trapped CO_2 in carbon nanotube bundles, *J. Phys. Chem.* **B 107**, 12930–12941 (2003).
539. W.-L. Yim, O. Byl, J.T. Yates Jr., and J.K. Johnson, Vibrational behavior of adsorbed CO_2 on single-walled carbon nanotubes, *J. Chem. Phys.* **120**, 5377–5386 (2004).
540. H. Chang, J.D. Lee, S.M. Lee, Y.H. Lee, Adsorption of NH_3 and NO_2 molecules on carbon nanotubes, *Appl. Phys. Lett.* **79**, 3863–3865 (2001).
541. S.E. Weber, S. Talapatra, C. Journet, A. Zambano, and A.D. Migone, Determination of the binding energy of methane on single-walled carbon nanotube bundles, *Phys. Rev.* **B 61**, 13150–13154 (2000).
542. H. Tanaka, M. El-Merraoui, W.A. Steele, and K. Kaneko, Methane adsorption on single-walled carbon nanotube: a density functional theory model, *Chem. Phys. Lett.* **352**, 334–341 (2002).
543. S. Talapatra and A.D. Migone, Adsorption of methane on bundles of closed-ended single-wall carbon nanotubes, *Phys. Rev.* **B 65**, 454161–454166 (2002).
544. L. Valentini, I. Armentano, L. Lozzi, S. Santucci, and J.M. Kenny, Interaction of methane with carbon nanotube thin films: role of defects and oxygen adsorption, *Mater. Sci. Eng.* **C 24**, 527–533 (2004).
545. Gy. Onyestyák, J. Valyon, K. Hernádi, I. Kiricsi, and L.V.C. Rees, Equilibrium and dynamics of acetylene sorption in multiwalled carbon nanotubes, *Carbon* **41**, 1241–1248 (2003).
546. N. Chakrapani, Y.M. Zhang, S.K. Nayak, J.A. Moore, D.L. Carroll, Y.Y. Choi, and P.M. Ajayan, Chemisorption of acetone on carbon nanotubes, *J. Phys. Chem.* **B 107**, 9308–9311 (2003).
547. M.R. Babaa, N. Dupont-Pavlovsky, E. McRae, and K. Masenelli-Varlot, Physical adsorption of carbon tetrachloride on as-produced and on mechanically opened single walled carbon nanotubes, *Carbon* **42**, 1549–1554 (2004).
548. C.-M. Yang, H. Kanoh, K. Kaneko, M. Yudasaka, and S. Iijima, Adsorption behaviors of HiPco single-walled carbon nanotube aggregates for alcohol vapors, *J. Phys. Chem.* **B 106**, 8994–8999 (2002).
549. J.A. Nisha, M. Yudasaka, S. Bandow, F. Kokai, K. Takahashi, and S. Iijima, Adsorption and catalytic properties of single-wall carbon nanohorns, *Chem. Phys. Lett.* **328**, 381–386 (2000).
550. H. Ago, R. Azumi, S. Ohshima, Y. Zhang, H. Kataura, and M. Yumura, STM study of molecular adsorption on single-wall carbon nanotube surface, *Chem. Phys. Lett.* **383**, 469–474 (2004).
551. M. Bienfait, B. Asmussen, M. Johnson, and P. Zeppenfeld, Methane mobility in carbon nanotubes, *Surf. Sci.* **460**, 243–248 (2000).

552. S.M. Cooper, B.A. Cruden, and M. Meyyappan, Gas transport characteristics through a carbon nanotubule, *Nano Lett.* **4**, 377–381 (2004).
553. P.G. Collins, K. Bradley, M. Ishigami, and A. Zettl, Extreme oxygen sensitivity of electronic properties of carbon nanotubes, *Science* **287**, 1801–1804 (2000).
554. R. Pati, Y. Zhang, S.K. Nayak, and P.M. Ajayan, Effect of H_2O adsorption on electron transport in a carbon nanotube, *Appl. Phys. Lett.* **81**, 2638–2640 (2002).
555. G.U. Sumanasekera, C.K.W. Adu, S. Fang, and P.C. Eklund, Effect of gas adsorption and collisions on electrical transport in single-walled carbon nanotubes, *Phys. Rev. Lett.* **85**, 1096–1099 (2000).
556. K. Bradley, S.-H. Jhi, P.G. Collins, J. Hone, M.L. Cohen, S.G. Louie, and A. Zettl, Is the intrinsic thermoelectric power of carbon nanotubes positive? *Phys. Rev. Lett.* **85**, 4361–4364 (2000).
557. G.U. Sumanasekera, B.K. Pradhan, H.E. Romero, K.W. Adu, and P.C. Eklund, Giant thermopower effects from molecular physisorption on carbon nanotubes, *Phys. Rev. Lett.* **89**, 166801 (2002).
558. J. Kong, N.R. Franklin, C. Zhou, M.C. Chapline, S. Peng, K. Cho, and H. Dai, Nanotube molecular wires as chemical sensors, *Science* **287**, 622–625 (2000).
559. S. Peng, K. Cho, P. Qi, and H. Dai, Ab initio study of CNT NO_2 gas sensor, *Chem. Phys. Lett.* **387**, 271–276 (2004).
560. C. Cantalini, L. Valentini, I. Armentano, J.M. Kenny, L. Lozzi, and S. Santucci, Carbon nanotubes as new materials for gas sensing applications, *J. Eur. Ceram. Soc.* **24**, 1405–1408 (2004).
561. L. Valentini, C. Cantalini, I. Armentano, J.M. Kenny, L. Lozzio, and S. Santucci, Highly sensitive and selective sensors based on carbon nanotubes thin films for molecular detection, *Diamond Rel. Mater.* **13**, 1301–1305 (2004).
562. L. Valentini, F. Mercuri, I. Armentano, C. Cantalini, S. Picozzi, L. Lozzi, S. Santucci, A. Sgamellotti, and J.M. Kenny, Role of the defects on the gas sensing properties of carbon nanotubes thin films: experiment and theory, *Chem. Phys. Lett.* **387**, 356–361 (2004).
563. O.K. Varghese, P.D. Kichambre, D. Gong, K.G. Ong, E.C. Dickey, and C.A. Grimes, Gas sensing characteristics of multi-wall carbon nanotubes, *Sensors Actuators* **B 81**, 32–41 (2001).
564. K.G. Ong, K. Zeng, and C.A. Grimes, A wireless, passive carbon nanotube-based gas sensor, *IEEE Sensor J.* **2**, 82–88 (2002).
565. S.G. Wang, Q. Zhang, D.J. Yang, P.J. Sellin, and G.F. Zhong, Multi-walled carbon nanotube-based gas sensors for NH_3 detection, *Diamond Rel. Mater.* **13**, 1327–1332 (2004).
566. C.K.W. Adu, G.U. Sumanasekera, B.K. Pradhan, H.E. Romero, and P.C. Eklund, Carbon nanotubes: a thermoelectric nano-nose, *Chem. Phys. Lett.* **337**, 31–35 (2001).
567. S. Peng and K. Cho, Ab initio study of doped carbon nanotube sensors, *Nano Lett.* **3**, 513–517 (2003).
568. F. Villalpando-Páez, A.H. Romero, E. Muñoz-Sandoval, L.M. Martínez, H. Terrones, and M. Terrones, Fabrication of vapor and gas sensors using films of aligned CN_x nanotubes, *Chem. Phys. Lett.* **386**, 137–143 (2004).
569. J. Li, Y. Lu, Q. Ye, M. Cinke, J. Han, and M. Meyyappan, Carbon nanotube sensors for gas and organic vapor detection, *Nano Lett.* **3**, 929–933 (2003).
570. J. Kong, M.G. Chapline, and H. Dai. Functionalized carbon nanotubes for molecular hydrogen sensors, *Adv. Mater*. **13**, 1384–1386 (2001).
571. L. Dai, P. Soundarrajan, and T. Kim, Sensors and sensor arrays based on conjugated polymers and carbon nanotubes, *Pure Appl. Chem*. **74**, 1753–1772 (2002).
572. A. Huczko, H. Lange, E. Caiko, H. Grubek-Jaworska, and P. Droszcz, Physiological testing of carbon nanotubes: are they asbestos-like? *Fullerene Sci. Technol. (Fullerenes Nanotubes Carbon Nanostruct.)* **9**, 251–254 (2001).
573. M. Shim, N.W.S. Kam, R.J. Chen, Y. Li, and H. Dai, Functionalization of carbon nanotubes for biocompatibility and biomolecular recognition, *Nano Lett*. **2**, 285–288 (2002).
574. K. Besteman, J.-O. Lee, F.G.M. Wiertz, H.A. Heering, and C. Dekker, Enzyme-coated carbon nanotubes as single-molecule biosensors, *Nano Lett.* **3**, 727–730 (2003).
575. A. Bianco and M. Prato, Can carbon nanotubes be considered useful tools for biological applications? *Adv. Mater.* **15**, 1765–1768 (2003).
576. J.J. Davis, K.S. Coleman, B.R. Azamian, C.B. Bagshaw, and M.L.H. Green, Chemical and biochemical sensing with modified single walled carbon nanotubes, *Chem. Eur. J.* **9**, 3733–3739 (2003).
577. Q. Zhao, Z. Gan, and Q. Zhuang, Electrochemical sensors based on carbon nanotubes, *Electroanalysis* **14**, 1609–1613 (2002).

578. P.J. Britto, K.S.V. Santhanam, and P.M. Ajayan, Carbon nanotube electrode for oxidation of dopamine, *Bioelectrochem. Bioenergetics* **41**, 121–125 (1996).
579. J. Wang, M. Li, Z. Shi, N. Li, and Z. Gu, Electrocatalytic oxidation of norepinephrine at a glassy carbon electrode modified with single wall carbon nanotubes, *Electroanalysis* **14**, 225–230 (2002).
580. K. Wu, X. Ji, J. Fei, and S. Hu, The fabrication of a carbon nanotube film on a glassy carbon electrode and its application to determining thyroxine, *Nanotechnology* **15**, 287–291 (2004).
581. S.C. Tsang, Z. Guo, Y.K. Chen, M.L.H. Green, H.A.O. Hill, T.W. Hambley, and P.J. Sadler, Immobilization of platinated and iodinated oligonucleotides on carbon nanotubes, *Angew. Chem. Int. Edit.* **36**, 2200–2220 (1997).
582. Z. Guo, P.J. Sadler, and S.C. Tsang, Immobilization and vizualization of DNA and proteins on carbon nanotubes, *Adv. Mater.* **10**, 701–703 (1998).
583. R.J. Chen, Y. Zhang, D. Wang, and H. Dai, Noncovalent sidewall functionalization of single-walled carbon nanotubes for protein immobilization, *J. Am. Chem. Soc*. **123**, 3838–3839 (2001).
584. R.J. Chen, S. Bangsaruntip, K.A. Drouvalakis, N.W.S. Kam, M. Shim, Y. Li, W. Kim, P.J. Utz, and H. Dai, Noncovalent functionalization of carbon nanotubes for highly specific electronic biosensors, *Proc. Nat. Acad. Sci. USA* **100**, 4984–4989 (2003).
585. S.E. Baker, W. Cai, T.L. Lasseter, K.P. Weidkamp, and R.J. Hamers, Covalently bonded adducts of deoxyribonucleic acid (DNA) oligonucleotides with single-wall carbon nanotubes: synthesis and hybridization, *Nano Lett.* **2**, 1413–1417 (2002).
586. K.A. Williams, P.T.M. Veenhuizen, B.G. de la Torre, R. Eritja, and C. Dekker, Nanotechnology: carbon nanotube with DNA recognition, *Nature*, **420**, 761 (2002).
587. C.V. Nguyen, L. Delzeit, A.M. Cassell, J. Li, J. Han, and M. Meyyappan, Preparation of nucleic acid functionalized carbon nanotube arrays, *Nano Lett.* **2**, 1079–1081 (2002).
588. J. Li, H.T. Ng, A.M. Cassell, W. Fan, H. Chen, Q. Ye, J. Koehne, J. Han, and M. Meyappan, Carbon nanotube nanoelectrode array for ultrasensitive DNA detection, *Nano Lett.* **3**, 597–602 (2003).
589. J. Koehne, H. Chen, J. Li, A.M. Cassell, Q. Ye, H.T. Ng, J. Han, and M. Meyyappan, Ultrasensitive label-free DNA analysis using an electronic chip based on carbon nanotube nanoelectrode arrays, *Nanotechnology* **14**, 1239–1245 (2003).
590. H. Cai, X. Cao, Y. Jiang, P. He, and Y. Fang, Carbon nanotube-enhanced electrochemical DNA biosensor for DNA hybridization detection, *Anal. Bioanal. Chem.* **375**, 287–293 (2003).
591. M.L. Pedano and G.A. Rivas, Immobilization of DNA on glassy carbon electrodes for the development of affinity biosensors, *Biosens. Bioelectron.* **18**, 269–277 (2003).
592. A. Guiseppi-Elie, C. Lei, and R.H. Baughman, Direct electron transfer of glucose oxidase on carbon nanotubes, *Nanotechnology* **13**, 559–564 (2002).
593. S. Sotiropoulou and N.A. Chaniotakis, Carbon nanotube array-based biosensor, *Anal. Bioanal. Chem.* **375**, 103–105 (2003).
594. L. Wang and Z. Yuan, Direct electrochemistry of glucose oxidase at a gold electrode modified with single-wall carbon nanotubes, *Sensors* **3**, 544–554 (2003).
595. J.H.T. Luong, S. Hrapovic, D. Wang, F. Bensebaa, and B. Simard, Solubilization of multiwall carbon nanotubes by 3-aminopropyltriethoxysilane towards the fabrication of electrochemical biosensors with promoted electron transfer, *Electroanalysis* **16**, 132–139 (2004).
596. K.P. Loh, S.L. Zhao, and W.D. Zhang, Diamond and carbon nanotube glucose sensors based on electropolymerization, *Diamond Rel. Mater.* **13**, 1075–1079 (2004).
597. R.J. Chen, H.C. Choi, S. Bangsaruntip, E. Yenilmez, X. Tang, Q. Wang, Y.-L. Chang, and H. Dai, An investigation of the mechanisms of electronic sensing of protein adsorption on carbon nanotube devices, *J. Am. Chem. Soc.* **126**, 1563–1568 (2004).
598. A. Star, J.-C.P. Gabriel, K. Bradley, and G. Grüner, Electronic detection of specific protein binding using nanotube FET devices, *Nano Lett.* **3**, 459–463 (2003).
599. S.C. Tsang, J.J. Davis, M.L.H. Green, H.A.O. Hill, Y.C. Leung, and P.J. Sadler, Immobilization of small proteins in carbon nanotubes: high-resolution transmission electron microscopy study and catalytic activity, *Chem. Commun.* 1803–1804 (1995).
600. J.J. Davis, M.L.H. Green, H.A.O. Hill, Y.C. Leung, P.J. Sadler, J. Sloan, A.V. Xavier, and S.C. Tsang, The immobilization of proteins in carbon nanotubes, *Inorg. Chim. Acta* **272**, 261–266 (1998).
601. F. Balavoine, P. Schultz, C. Richard, V. Mallouh, T.W. Ebbesen, and C. Mioskowski, Helical crystallization of proteins on carbon nanotubes: a first step towards development of new biosensors, *Angew. Chem. Int. Ed*. **38**, 1912–1915 (1999).

602. B.R. Azamian, J.J. Davis, K.S. Coleman, C.B. Bagshow, and M.L.H. Green, Bioelectrochemical single-walled carbon nanotubes, *J. Am. Chem. Soc.* **124**, 12664–12665 (2002).
603. W. Huang, S. Taylor, K. Fu, Y. Lin, D. Zhang, T.W. Hanks, A.M. Rao, and Y.-P. Sun, Attaching proteins to carbon nanotubes via diimide-activated amidation, *Nano Lett.* **2**, 311–314 (2002).
604. X. Yu, D. Chattopadhyay, I. Galeska, F. Papadimitrakopoulos, and J.F. Rusling, Peroxidase activity of enzymes bound to the ends of single-wall nanotube forest electrodes, *Electrochem. Commun.* **5**, 408–411 (2003).
605. M. in het Panhuis, C. Salvador-Morales, E. Franklin, G. Chambers, A. Fonseca, J.B. Nagy, W.J. Blau, and A.I. Minetta, Characterization of an interaction between functionalized carbon nanotubes and an enzyme, *J. Nanosci. Nanotech.* **3**, 209–213 (2003).
606. K. Jiang, L.S. Schadler, R.W. Siegel, X. Zhang, H. Zhang, and M. Terrones, Protein immobilization on carbon nanotubes *via* a two-step process of diimide-activated amidation, *J. Mater. Chem.* **14**, 37–39 (2004).
607. D. Pantarotto, C.D. Partidos, R. Graff, J. Hoebeke, J.-P. Briand, M. Prato, and A. Bianco, Synthesis, structural characterization, and immunological properties of carbon nanotubes functionalized with peptides, *J. Am. Chem. Soc.* **125**, 6160–6164 (2003).
608. R.D. Klausner, Challenges and vision for nanoscience and nanotechnology in medicine: cancer as a model, *BECON Nanoscience and Nanotechnology Symp. Report*, June 2000, 8–9.
609. M. Meyyappan, D.J. Loftus, J. Han, A.M. Cassell, J. Kaysen, C.V. Nguyen, S. Liang, R.M.D. Stevens, R. Jaffe, A. Hermone, and S. Verma, Applications of nanotube nanotechnology to biosensors and cancer research, *Principal Investigators Meeting Unconventional Innovations Program*, June 28–29, 2000, Hyatt Dulles Hotel, Herdnon, Virginia, US [http://otir.nci.nih.gov/cgi-bin/uip_search.cgi?ABSTRACTID=UIP-00-015].
610. Y. Lin, F. Lu, and J. Wang, Disposable carbon nanotube modified screen-printed biosensor for amperometric detection of organophosphorus pesticides and nerve agents, *Electroanalysis* **16**, 145–149 (2004).
611. T.S. Huang, Y. Tzeng, Y.K. Liu, Y.C. Chen, K.R. Walker, R. Guntupalli, and C. Liu, Immobilization of antibodies and bacterial binding on nanodiamond and carbon nanotubes for biosensor applications, *Diamond Rel. Mater.* **13**, 1098–1102 (2004).
612. Y.Z. Guo and A.R. Guadalupe, Direct electrochemistry of horseradish peroxidase adsorbed on glassy carbon electrode from organic solutions, *Chem. Commun.* 1437–1438 (1997).
613. P. Král, Control of catalytic activity of proteins in vivo by nanotube ropes excited with infrared light, *Chem. Phys. Lett.* **382**, 399–403 (2003).
614. K. Rege, N.R. Raravikar, D.-Y. Kim, L.S. Schadler, P.M. Ajayan, and J.S. Dordick, Enzyme–polymer–single walled carbon nanotube composites as biocatalytic films, *Nano Lett.* **3**, 829–832 (2003).
615. D. Pantarotto, J.-P. Briand, M. Prato, and A. Bianco, Translocation of bioactive peptides across cell membranes by carbon nanotubes, *Chem. Commun.* 16–17 (2004).
616. L. Zhang, G.-C. Zhao, X.-W. Wei, and Z.-S. Yang, Electroreduction of oxygen by myoglobin on multiwalled carbon nanotube-modified glassy carbon electrode, *Chem. Lett.* **33**, 86–87 (2004).
617. J.-S. Ye, Y. Wen, W.D. Zhang, H.-F. Cui, L.M. Gan, G.Q. Xu, and F.-S. Sheu, Application of multiwalled carbon nanotubes functionalized with hemin for oxygen detection in neutral solution, *J. Electroanal. Chem.* **562**, 241–246 (2004).
618. M.P. Mattson, R.C. Haddon, and A.M. Rao, Molecular functionalization of carbon nanotubes and use as substrates for neuronal growth, *J. Mol. Neurosci.* **14**, 175–182 (2000).
619. H. Hu, Y. Ni, V. Montana, R.C. Haddon, and V. Parpura, Chemically functionalized carbon nanotubes as substrates for neuronal growth, *Nano Lett.* **4**, 507–511 (2004).
620. C. Richard, F. Balavoine, P. Schultz, T.W. Ebbesen, and C. Mioskowski, Supramolecular self-assembly of lipid derivatives on carbon nanotubes, *Science* **300**, 775–778 (2003).
621. N. Nakashima, S. Okuzono, H. Marukami, T. Nakai, and K. Yoshikawa, DNA dissolves single-walled carbon nanotubes in water, *Chem. Lett.* **32**, 456–457 (2003).
622. K. Matsuura, K. Hayashi, and N. Kimizuka, Lectin-mediated supramolecular junctions of galactose-derivatized single-walled carbon nanotubes, *Chem. Lett.* **32**, 212–213 (2003).
623. M. Zheng, A. Jagota, M.S. Strano, A.P. Santos, P. Barone, S.G. Chou, B.A. Diner, M.S. Dresselhaus, R.S. Mclean, G.B. Onoa, G.G. Samsonidze, E.D. Semke, M. Ursey, and D.J. Walls, Structure-based carbon nanotube sorting by sequence-dependent DNA assembly, *Science* **302**, 1545–1548 (2003).

624. M. Zheng, A. Jagota, E.D. Semke, B.A. Diner, R.S. McLean, S.R. Lustig, R.E. Richardson, and N.G. Tassi, DNA-assisted dispersion and separation of carbon nanotubes, *Nat. Mater.* **2**, 338–342 (2003).
625. J.N. Barisci, M. Tahhan, G.G. Wallace, S. Badaire, T. Vaugien, M. Maugey, and P. Poulin, Properties of carbon nanotube fibers spun from DNA-stabilized dispersions, *Adv. Funct. Mater.* **14**, 133–138 (2004).
626. H. Xin and A.T. Woolley, DNA-templated nanotube localization, *J. Am. Chem. Soc.* **125**, 8710–8711 (2003).
627. K. Keren, R.S. Berman, E. Buchstab, U. Sivan, and E. Braun, DNA-templated carbon nanotube field-effect transistor, *Science* **302**, 1380–1382 (2003).
628. C. Dwyer, M. Guthold, M. Falvo, S. Washburn, R. Superfine, and D. Erie, DNA-functionalized single-walled carbon nanotubes, *Nanotechnology* **13**, 601–604 (2002).
629. R. Czerw, M. Terrones, J.-C. Charlier, X. Blase, B. Foley, R. Kamalakaran, N. Grobert, H. Terrones, D. Tekleab, P.M. Ajayan, W. Blau, M. Rühle, and D.L. Carroll, Identification of electron donor states in N-doped carbon nanotubes, *Nano Lett.* **1**, 457–460 (2001).
630. M. Terrones, N. Grobert, M. Terrones, H. Terrones, P.M. Ajayan, F. Banhart, X. Blase, D.L. Carroll, R. Czerw, B. Foley, J.C. Charlier, B. Foley, R. Kamalakaran, P.H. Kohler-Redlich, M. Rühle, and T. Seeger, Doping and connecting carbon nanotubes, *Mol. Cryst. Liq. Cryst.* **387**, 51–62 (2002).
631. A.H. Nevidomskyy, G. Csányi, and M.C. Payne, Chemically active substitutional nitrogen impurity in carbon nanotubes, *Phys. Rev. Lett.* **91**, 105502-1–4 (2003).
632. Y. Huang, J. Gao, and R. Liu, Structure and electronic properties of nitrogen-containing carbon nanotubes, *Synth. Met.* **113**, 251–255 (2000).
633. R. Droppa Jr., P. Hammer, A.C.M. Carvalho, M.C. dos Santos, and F. Alvarez, Incorporation of nitrogen in carbon nanotubes, *J. Non-Cryst. Solids* **299–302**, 874–879 (2002).
634. M. Glerup, J. Steinmetz, D. Samaille, O. Stéphan, S. Enouz, A. Loiseau, S. Roth, and P. Bernier, Synthesis of N-doped SWNT using the arc-discharge procedure, *Chem. Phys. Lett.* **387**, 193–197 (2004).
635. R. Sen, B.C. Satishkumar, A. Govindaraj, K.R. Harikumar, G. Raina, J.-P. Zhang, A.K. Cheetham, and C.N.R. Rao, B–C–N, C–N and B–N nanotubes produced by the pyrolysis of precursor molecules over Co catalysts, *Chem. Phys. Lett.* **287**, 671–676 (1998).
636. K. Suenaga, M. Yudasaka, C. Colliex, and S. Iijima, Radially modulated nitrogen distribution in CN_x nanotubular structures prepared by CVD using Ni phtalocyanine, *Chem. Phys. Lett.* **316**, 365–372 (2000).
637. R. Kurt and A. Karimi, Influence of nitrogen on the growth mechanism of decorated C:N nanotubes, *Chem. Phys. Chem.* **2**, 388–392 (2001).
638. R. Kurt, J.-M. Bonard, and A. Karimi, Structure and field emission properties of decorated C/N nanotubes tuned by diameter variations, *Thin Solid Films* **398–399**, 193–198 (2001).
639. R. Kurt, C. Klinke, J.-M. Bonard, K. Kern, and A. Karimi, Tailoring the diameter of decorated C–N nanotubes by temperature variations using HF-CVD, *Carbon* **39**, 2163–2172 (2001).
640. M. Terrones, P.M. Ajayan, F. Banhart, X. Blase, D.L. Carroll, J.C. Charlier, R. Czerw, B. Foley, N. Grot, R. Kamalakaran, P. Kohler-Redlich, M. Rühle, T. Seeger, and H. Terrones, N-doping and coalescence of carbon nanotubes: synthesis and electronic properties, *Appl. Phys.* **A 74**, 355–361 (2002).
641. X. Wang, Y. Liu, D. Zhu, L. Zhang, H. Ma, N. Yao, and B. Zhang, Controllable growth, structure, and low field emission of well-aligned CN_x nanotubes, *J. Phys. Chem.* **B 106**, 2186–2190 (2002).
642. C.J. Lee, S.C. Lyu, H.-W. Kim, J.H. Lee, and K.I. Cho, Synthesis of bamboo-shaped carbon-nitrogen nanotubes using C_2H_2–NH_3–$Fe(CO)_5$ system, *Chem. Phys. Lett.* **359**, 115–120 (2002).
643. T.-Y. Kim, K.-R. Lee, K.Y. Eun, and K.-H. Oh, Carbon nanotube growth enhanced by nitrogen incorporation, *Appl. Phys. Lett.* **372**, 603–607 (2003).
644. H. Yan, Q. Li, J. Zhang, and Z. Liu, The effect of hydrogen on the formation of nitrogen-doped carbon nanotubes via catalytic pyrolysis of acetonitrile, *Adv. Nanomat. Nanodevices* (*8th International Conference on Electronic Materials*, IUMRS-ICEM 2002, Xi'an, China, 10–14 June 2002), preprint [http://nanotechweb.org/dl/nanomaterials/Xian_article_01_was153468.pdf].
645. H. Yan, Q. Li, J. Zhang, and Z. Liu, The effect of hydrogen on the formation of nitrogen-doped carbon nanotubes via catalytic pyrolysis of acetonitrile, *Chem. Phys. Lett.* **380**, 347–351 (2003).
646. C.H. Lin, H.L. Chang, C.M. Hsu, A.Y. Lo, and C.T. Kuo, The role of nitrogen in carbon nanotube formation, *Diamond Rel. Mater.* **12**, 1851–1857 (2003).
647. V.D. Blank, E.V. Polyakov, D.V. Batov, B.A. Kulnitskiy, U. Bangert, A. Gutiérrez-Sosa, A.J. Harvey, and A. Seepujak, Formation of N-containing C-nanotubes and nanofibres by carbon resistive heating under high nitrogen pressure, *Diamond Rel. Mater.* **12**, 864–869 (2003).

648. J. Maultzsch, S. Reich, C. Thomsen, S. Webster, R. Czerw, D.L. Carroll, S.M.C. Vieira, P.R. Birkett, and C.A. Rego, Raman characterization of boron-doped multiwalled carbon nanotubes, *Appl. Phys. Lett.* **81**, 2647–2649 (2002).
649. J. Xu, M. Xiao, R. Czerw, and D.L. Carroll, Optical limiting and enhanced optical nonlinearity in boron-doped carbon nanotubes, *Chem. Phys. Lett.* **389**, 247–250 (2004).
650. B.C. Satishkumar and C.N.R. Rao, Boron-carbon nanotubes from the pyrolysis of C_2H_2–B_2H_6 mixtures, *Chem. Phys. Lett.* **300**, 473–477 (1999).
651. C.F. Chen, C.L. Tsai, and C.L. Lin, The characterization of boron-doped carbon nanotube arrays, *Diamond Rel. Mater.* **12**, 1500–1504 (2003).
652. J.Y. Lao, W.Z. Li, J.G. Wen, and Z.F. Ren, Boron carbide nanolumps on carbon nanotubes, *Appl. Phys. Lett.* **80**, 500–502 (2002).
653. E. Borowiak-Palen, T. Pichler, G.G. Fuentes, A. Graff, R.J. Kalenczuk, M. Knupfer, and J. Fink, Efficient production of B-substituted single-wall carbon nanotubes, *Chem. Phys. Lett.* **378**, 516–520 (2003).
654. E. Borowiak-Palen, T. Pichler, A. Graff, R.J. Kalenczuk, M. Knupfer, and J. Fink, Synthesis and electronic properties of B-doped single wall carbon nanotubes, *Carbon* **42**, 1123–1126 (2004).
655. Y.-J. Lee, H.-H. Kim, and H. Hatori, Effects of substitutional B on oxidation of carbon nanotubes in air and oxygen plasma, *Carbon* **42**, 1053–1056 (2004).
656. W. Han, Y. Bando, K. Kurashima, and T. Sato, Synthesis of boron nitride nanotubes from carbon nanotubes by a substitution reaction, *Appl. Phys. Lett.* **73**, 3085–3087 (1998).
657. W. Han, Y. Bando, K. Kurashima, and T. Sato, Boron-doped carbon nanotubes prepared through a substitution reaction, *Chem. Phys. Lett.* **299**, 368–373 (1999).
658. D. Golberg, Y. Bando, K. Kurashima, and T. Sato, Synthesis, HRTEM and electron diffraction studies of B/N-doped C and BN nanotubes, *Diamond Rel. Mater.* **10**, 63–67 (2001).
659. X.D. Bai, J.D. Guo, J. Yu, E.G. Wang, J. Yuan, and W. Zhou, Synthesis and field-emission behavior of highly oriented boron carbonitride nanofibers, *Appl. Phys. Lett.* **76**, 2624–2626 (2000).
660. D. Golberg, Y. Bando, L. Bourgeois, K. Kurashima, and T. Sato, Large-scale synthesis and HRTEM analysis of single-walled B- and N-doped carbon nanotube bundles, *Carbon* **38**, 2017–2027 (2000).
661. D. Golberg, P. Dorozhkin, Y. Bando, M. Hasegawa, and Z.-C. Dong, Semiconducting B–C–N nanotubes with few layers, *Chem. Phys. Lett.* **359**, 220–228 (2002).
662. R.J. Baierle, S.B. Fagan, R. Mota, A.J.R. da Silva, and A. Fazzio, Electronic and structural properties of silicon-doped carbon nanotubes, *Phys. Rev.* **B 64**, 085413.1–4 (2001).
663. S.B. Fagan, R. Mota, A.J.R. da Silva, and A. Fazzio, Substitutional Si doping in deformed carbon nanotubes, *Nano Lett.* **4**, 975–977 (2004).
664. Y. Zhang, T. Ichihashi, E. Landree, F. Nihey, and S. Iijima, Heterostructures of single-walled carbon nanotubes and carbide nanorods, *Science* **285**, 1719–1722 (1999).
665. Q. Li, S. Fan, W. Han, C. Sun, and W. Liang, Coating of carbon nanotube with nickel by electroless plating method, *Jpn. J. Appl. Phys.* **36 B**, L501–L503 (1997).
666. Z. Shi, X. Wang, and Z. Ding, The study of electroless deposition of nickel on graphite fibers, *Appl. Surf. Sci.* **140**, 106–110 (1999).
667. L.M. Ang, T.S.A. Hor, G.Q. Xu, C.H. Tung, S.P. Zhao, and J.L.S. Wang, Decoration of activated carbon nanotubes with copper and nickel, *Carbon* **38**, 363–372 (2000).
668. F.Z. Kong, X.B. Zhang, W.Q. Xiong, F. Liu, W.Z. Huang, Y.P. Sun, J.P. Tu, and X.W. Chen, Continuous Ni-layer on multiwall carbon nanotubes by an electroless plating method, *Surf. Coat. Technol.* **155**, 33–36 (2002).
669. Q. Xu, L. Zhang, J. Zhu, Controlled growth of composite nanowires based on coating Ni on carbon nanotubes by electrochemical deposition method, *J. Phys. Chem.* **B 107**, 8294–8296 (2003).
670. S. Arai, M. Endo, and N. Kaneko, Ni-deposited multi-walled carbon nanotubes by electrodeposition, *Carbon* **42**, 641–644 (2004).
671. T.V. Reshetenko, L.B. Avdeeva, Z.R. Ismagilov, and A.L. Chuvilin, Catalytic filamentous carbon as supports for nickel catalysts, *Carbon* **42**, 143–148 (2004).
672. Y. Zhang, W. Franklin, R.J. Chen, and H. Dai, Metal coating on suspended carbon nanotubes and its implication to metal-tube interaction, *Chem. Phys. Lett.* **331**, 35–41 (2000).
673. Y. Zhang and H.J. Dai, Formation of metal nanowires on suspended single-walled carbon nanotubes, *Appl. Phys. Lett.* **77**, 3015–3017 (2000).
674. P. Chen, X. Wu, J. Lin, and K.L. Tan, Synthesis of Cu nanoparticles and microsized fibers by using carbon nanotubes as a template, *J. Phys. Chem.* **B 103**, 4559–4561 (1999).

675. X. Chen, J. Xia, J. Peng, W. Li, and S. Xie, Carbon-nanotube metal-matrix composites prepared by electroless plating, *Composites Sci. Technol*. **60**, 301–306 (2000).
676. Z.-J. Liu, Z. Xu, Z.-Y. Yuan, W. Chen, W. Zhou, and L.-M. Peng, A simple method for coating carbon nanotubes with Co–B amorphous alloy, *Mater. Lett.* **57**, 1339–1344 (2003).
677. B.C. Satishkumar, E.M. Vogl, A. Govindaraj, and C.N.R. Rao, The decoration of carbon nanotubes by metal nanoparticles, *J. Phys.* **D 29**, 3173–3176 (1996).
678. W. Li, C. Liang, J. Qiu, W. Zhou, H. Han, Z. Wei, G. Sun, and Q. Xin, Carbon nanotubes as support for cathode catalyst of a direct methanol fuel cell, *Carbon* **40**, 791–794 (2002).
679. W. Li, C. Liang, W. Zhou, J. Qiu, H. Li, G. Sun, and Q. Xin, Homogeneous and controllable Pt particles deposited on multi-wall carbon nanotubes as cathode catalyst for direct methanol fuel cells, *Carbon* **42**, 436–439 (2004).
680. R. Yu, L. Chen, Q. Liu, J. Lin, K.-L. Tan, S.C. Ng, H.S.O. Chan, G.-Q. Xu, and T.S.A. Hor, Platinum deposition on carbon nanotubes via chemical modification, *Chem. Mater.* **10**, 718–722 (1998).
681. V. Lordi, N. Yao, and J. Wei, Method for supporting platinum on single-walled carbon nanotubes for a selective hydrogenation catalyst, *Chem. Mater.* **13**, 733–737 (2001).
682. S.H. Joo, S.J. Choi, I. Oh, J. Kwak, Z. Liu, O. Terasaki, and R. Ryoo, Ordered nanoporous arrays of carbon supporting high dispersions of platinum nanoparticles, *Nature* **412**, 169–172 (2001).
683. B. Xue, P. Chen, Q. Hong, J. Lin, and K. Tan. Growth of Pd, Pt, Ag and Au nanoparticles on carbon nanotubes, *J. Mater. Chem*. **11**, 2378–2381 (2001).
684. H.C. Choi, M. Shim, S. Bangsaruntip, and H. Dai, Spontaneous reduction of metal ions on the sidewalls of carbon nanotubes, *J. Am. Chem. Soc*. **124**, 9058–9059 (2002).
685. X.R. Ye, Y. Lin, and C.M. Wai, Decorating catalytic palladium nanoparticles on carbon nanotubes in supercritical carbon dioxide, *Chem. Commun.* 642–643 (2003).
686. B.R. Azamian, K.S. Coleman, J.J. Davis, N. Hanson, and M.L.H. Green, Directly observed covalent coupling of quantum dots to single-wall carbon nanotubes, *Chem. Commun*. 366–367 (2002).
687. A.V. Ellis, K. Vijayamohanan, R. Goswami, N. Chakrapani, L.S. Ramanathan, P.M. Ajayan, and G. Ramanath, Hydrophobic anchoring of monolayer-protected gold nanoclusters to carbon nanotubes, *Nano Lett.* **3**, 279–282 (2003).
688. L. Liu, T. Wang, J. Li, Z.-X. Guo, L. Dai, D. Zhang, and D. Zhu, Self-assembly of gold nanoparticles to carbon nanotubes using a thiol-terminated pyrene as interlinker, *Chem. Phys. Lett.* **367**, 747–752 (2003).
689. A. Fási, I. Pálinkó, J.W. Seo, Z. Kónya, K. Hernadi, and I. Kiricsi, Sonication assisted gold deposition on multiwall carbon nanotubes, *Chem. Phys. Lett.* **372**, 848–852 (2003).
690. S. Fullam, D. Cottell, H. Rensmo, and D. Fitzmaurice, Carbon nanotube templated self-assembly and thermal processing on gold nanowires, *Adv. Mater.* **12**, 1430–1432 (2000).
691. W.S. Yun, J. Kim, K.H. Park, J.S. Ha, Y.-J. Ko, K. Park, S.K. Kim, Y.-J. Doh, H.-J. Lee, J.P. Salvetat, and L. Forró, Fabrication of metal nanowire using carbon nanotubes as a mask, *J. Vac. Sci. Technol.* **A 18**, 1329 (2000).
692. B.C. Satishkumar, A. Govindaraj, E.M. Vogl, L. Basumallick, and C.N.R. Rao, Oxide nanotubes prepared using carbon nanotubes as templates, *J. Mater. Res.* **12**, 604–606 (1997).
693. T. Seeger, Ph. Redlich, N. Grobert, M. Terrones, D.R.M. Walton, H.W. Kroto, and M. Rühle, SiO_x-coating of carbon nanotubes at room temperature, *Chem. Phys. Lett*. **339**, 41–46 (2001).
694. M. Rűhle, T. Seeger, Ph. Redlich, N. Grobert, M. Terrones, D.R.M. Walton, and H.W. Kroto, Novel SiO_x-coated carbon nanotubes, *J. Ceram. Process. Res*. **3**, 1–5 (2002).
695. T. Seeger, Th. Kűhler, Th. Frauenheim, N. Grobert, M. Rühle, M. Terrones, and G. Seifert, Nanotube composites: novel SiO_2 coated nanotubes, *Chem. Commun.* 34–35 (2002).
696. K. Hernadi, E. Ljubović, J.W. Seo, and L. Forró, Synthesis of MWNT-based composite materials with inorganic coating, *Acta Mater.* **51**, 1447–1452 (2003).
697. E.A. Whitsitt and A.R. Barron, Silica coated single walled carbon nanotubes, *Nano Lett.* **3**, 775–778 (2003).
698. Q. Fu, C. Lu, and J. Han, Selective coating of single wall carbon nanotubes with thin SiO_2 layer, *Nano Lett.* **2**, 329–332 (2002).
699. S.W. Lee and W.M. Sigmund, Formation of anatase TiO_2 nanoparticles on carbon nanotubes, *Chem. Commun.* 780–781 (2003).
700. A. Jitianu, T. Cacciaguerra, R. Benoit, S. Delpeux, F. Béguin, and S. Bonnamy, Synthesis and characterization of carbon nanotubes — TiO_2 nanocomposites, *Carbon* **42**, 1147–1151 (2004).
701. J. Sun, M. Iwasa, L. Gao, and Q. Zhang, Single-walled carbon nanotubes coated with titania nanoparticles, *Carbon* **42**, 895–899 (2004).

702. A. Brioude, P. Vincent, C. Journet, J.C. Plenet, and S.T. Purcell, Synthesis of sheated carbon nanotube tips by the sol-gel technique, *Appl. Surf. Sci.* **221**, 4–9 (2004).
703. Y.-H. Li, S. Wang, A. Cao, D. Zhao, X. Zhang, C. Xu, Z. Luan, D. Ruan, J. Liang, D. Wu, and B. Wei, Adsorption of fluoride from water by amorphous alumina supported on carbon nanotubes, *Chem. Phys. Lett.* **350**, 412–416 (2001).
704. K. Hernadi, E. Couteau, J.W. Seo, and L. Forró, $Al(OH)_3$/multiwalled carbon nanotubes composite: homogeneous coverage of $Al(OH)_3$ on carbon nanotube surfaces, *Langmuir* **19**, 7026–7029 (2003).
705. Y. Zhang, J. Liu, R. He, Q. Zhang, X. Zhang, and J. Zhu, Synthesis of alumina nanotubes using carbon nanotubes as template, *Chem. Phys. Lett*. **360**, 579–584 (2002).
706. M.H. Chen, Z.C. Huang, G.T. Wu, G.M. Zhu, J.K. You, and Z.G. Lin, Synthesis and characterization of SnO-carbon nanotube composite as anode material for lithium-ion batteries, *Mater. Res. Bull.* **38**, 831–836 (2003).
707. W.-Q. Han and A. Zettl, Coating single-walled carbon nanotubes with tin oxide, *Nano Lett.* **3**, 681–683 (2003).
708. L. Zhao and L. Gao, Coating of multi-walled carbon nanotubes with thick layers of tin(IV) oxide, *Carbon* **42**, 1858–1861 (2004).
709. H. Kim and W. Sigmund, Zinc oxide nanowires on carbon nanotubes, *Appl. Phys. Lett.* **81**, 2085–2087 (2002).
710. J. Ding, Y. Li, C. Xu, and D. Wu, Depositing CeO_2 nano-particles on surface of carbon nanotubes, *J. Chin. Rare Earth Soc.* **21**, 441–444 (2003) (in Chinese).
711. B.C. Satishkumar, A. Govindaraj, M. Nath, and C.N.R. Rao, Synthesis of metal oxide nanorods using carbon nanotubes as templates, *J. Mater. Chem*. **10**, 2115–2119 (2000).
712. C.N.R. Rao and A. Govindaraj, Nanotubes and nanowires, *Proc. Indian Acad. Sci.* **113**, 375–392 (2001).
713. J. Shi, Y. Qin, W. Wu, X. Li, Z.-X. Guo, and D. Zhu, In situ synthesis of CdS nanoparticles on multi-walled carbon nanotubes, *Carbon* **42**, 455–458 (2004).
714. S. Ravindran, S. Chaudhary, B. Colburn, M. Ozkan, and C.S. Ozkan, Covalent coupling of quantum dots to multi-walled carbon nanotubes for electronic device applications, *Nano Lett*. **3**, 447–453 (2003).
715. H. Kim and W. Sigmund, Zinc sulfide nanocrystals on carbon nanotubes, *J. Cryst. Growth* **255**, 114–118 (2003).
716. J.W. Liu, D.Y. Zhong, F.Q. Xie, M. Sun, E.G. Wang, and W.X. Liu, Synthesis of SiC nanofibers by annealing carbon nanotubes covered with SiC, *Chem. Phys. Lett*. **348**, 357–360 (2001).
717. E. Muñoz, A.B. Dalton, S. Collins, A.A. Zakhidov, R.H. Baughman, W.L. Zhou, J. He, C.J. O'Connor, B. McCarthy, and W.J. Blau, Synthesis of SiC nanorods from sheets of single-walled carbon nanotubes, *Chem. Phys. Lett*. **359**, 397–402 (2002).
718. Y-J. Lee, Formation of silicon carbide on carbon fibers by carbothermal reduction of silica, *Diamond Rel. Mater.* **13**, 383–388 (2004).
719. K.C. Chin, A. Gohel, H.I. Elim, W. Ji, G.L. Chong, K.Y. Lim, C.H. Sow, and A.T.S. Wee, Optical limiting properties of amorphous Si_xN_y and SiC coated carbon nanotubes, *Chem. Phys. Lett.* **383**, 72–75 (2004).
720. B.Q. Wei, J.W. Ward, R. Vajtai, P.M. Ajayan, R. Ma, and G. Ramanath, Simultaneous growth of silicon carbide nanorods and carbon nanotubes by chemical vapor deposition, *Chem. Phys. Lett.* **354**, 264–268 (2002).
721. M. Gao, S. Huang, L. Dai, G. Wallace, R. Gao, and Z. Wang, Aligned coaxial nanowires of carbon nanotubes sheathed with conducting polymers, *Angew. Chem. Int. Ed.* **39**, 3664–3667 (2000).
722. D. Shi, J. Lian, P. He, L.M. Wang, W.J. van Ooij, M. Schulz, Y. Liu, and D.B. Mast, Plasma deposition of ultrathin polymer films on carbon nanotubes, *Appl. Phys. Lett.* **81**, 5216–5218 (2002).
723. A.B. Artyukhin, O. Bakajin, P. Stroeve, and A. Noy, Layer-by-layer electrostatic self-assembly of polyelectrolyte nanoshells on individual carbon nanotube templates, *Langmuir* **20**, 1442–1448 (2004).
724. L. Cao, H.-Z. Chen, H.-B. Zhou, L. Zhu, J.-Z. Sun, X.-B. Zhang, J.-M. Xu, and M. Wang, Carbon-nanotube-templated assembly of rare-earth phthalocyanine nanowires, *Adv. Mater.* **15**, 909–913 (2003).
725. Z.-X. Jin, G.Q. Xu, and S.H. Goh, A preferentially ordered accumulation of bromine on multi-wall carbon nanotubes, *Carbon* **38**, 1135–1139 (2000).
726. L. Grigorian, K.A. Williams, S. Fang, G.U. Sumanasekera, A.L. Loper, E.C. Dickey, S.J. Pennycook, and P.C. Eklund, Reversible intercalation of charged iodine chains into carbon nanotube ropes, *Phys. Rev. Lett.* **80**, 5560–5563 (1998).

727. M.T. Martínez, M.A. Callejas, A.M. Benito, M. Cochet, T. Seeger, A. Ansón, J. Schreiber, C. Gordon, C. Marhic, O. Chauvet, J.L.G. Fierro, and W.K. Maser, Sensitivity of single wall carbon nanotubes to oxidative processing: structural modification, intercalation and functionalisation, *Carbon* **41**, 2247–2256 (2003).
728. R. Graupner, J. Abraham, A. Vencelová, T. Seyller, F. Hennrich, M.M. Kappes, A. Hirsch, and L. Ley, Doping of single-walled carbon nanotube bundles by Brønsted acids, *Phys. Chem. Chem. Phys.* **5**, 5472–5476 (2003).
729. A. Kukovecz, T. Pichler, R. Pfeiffer, C. Kramberger, and H. Kuzmany, Diameter selective doping of single wall carbon nanotubes, *Phys. Chem. Chem. Phys.* **5**, 582–587 (2003).
730. Y. Liu, H. Yukawa, and M. Morinaga, First-principles study on lithium absorption in carbon nanotubes, *Computat. Mater. Sci.* **30**, 50–56 (2004).
731. S. Suzuki, Y. Watanabe, T. Ogino, S. Heun, L. Gregoratti, A. Barinov, B. Kaulich, M. Kiskinova, W. Zhu, C. Bower, and O. Zhou, Extremely small diffusion constant of Cs in multiwalled carbon nanotubes, *J. Appl. Phys.* **92**, 7527–7531 (2002).
732. A.S. Claye, J.E. Fischer, C.B. Huffman, A.G. Rinzler, and R.E. Smalley, Solid-state electrochemistry of the Li-single wall carbon nanotube system, *J. Electrochem. Soc.* **147**, 2845–2852 (2000).
733. B. Gao, A. Kleinhammes, X.P. Tang, C. Bower, L. Fleming, Y. Wu, and O. Zhou, Electrochemical intercalation of single-walled carbon nanotubes with lithium, *Chem. Phys. Lett.* **307**, 153–157 (1999).
734. H. Shimoda, B. Gao, X.P. Tang, A. Kleinhammes, L. Fleming, Y. Wu, and O. Zhou, Lithium intercalation into etched single-wall carbon nanotubes, *Physica* **B 323**, 133–134 (2002).
735. H. Shimoda, B. Gao, X.P. Tang, A. Kleinhammes, L. Fleming, Y. Wu, and O. Zhou, Lithium intercalation into opened single-wall carbon nanotubes: storage capacity and electronic properties, *Phys. Rev. Lett.* **88**, 015502.1–4 (2002).
736. B. Gao, C. Bower, J.D. Lorentzen, L. Fleming, A. Kleinhammes, X.P. Tang, L.E. McNeil, Y. Wu, and O. Zhou, Enhanced saturation lithium composition in ball-milled single-walled carbon nanotubes, *Chem. Phys. Lett.* **327**, 69–75 (2000).
737. C.H. Mi, G.S. Cao, and X.B. Zhao, A non-GIC mechanism of lithium storage in chemical etched MWNTs, *J. Electroanal. Chem.* **526**, 217–221 (2004).
738. Z. Yang, S. Sang, K. Huang, and H.-Q. Wu, Lithium insertion into the raw multi-walled carbon nanotubes pre-doped with lithium — an electrochemical impedance study, *Diamond Rel. Mater.* **13**, 99–105 (2004).

6 Graphite Whiskers, Cones, and Polyhedral Crystals

Svetlana Dimovski and Yury Gogotsi
Department of Materials Science and Engineering,
Drexel University, Philadelphia, Pennsylvania

CONTENTS

ABSTRACT

Carbon nanotubes and fullerenes have been extensively studied and are described in separate chapters in this book. However, the world of carbon nanostructures is not limited to these two groups of materials. Carbon nanocones, whiskers, and larger polygonized nanotubes, called graphite polyhedral crystals, are a whole new class of carbon nanomaterials; which, along with vapor-grown carbon fibers, can be placed between graphite and fullerene families of carbon. They are elongated and, typically, axially symmetric structures. This chapter provides a comparative study of several such graphitic nanomaterials. The discussion covers the gamut of such materials — from the first

graphite cones and whiskers discovered long before the beginning of "nano" age, to the latest additions to this family of nano- and micromaterials. Some of these particles are as large as several micrometers, and they provide a bridge between carbon nanomaterials such as nanotubes, and conventional materials such as carbon fibers or planar graphite. Their structure, properties, Raman spectra, and potential applications are discussed in detail in this chapter.

6.1 PREFACE

Both planar graphite[1] and carbon nanotubes[2] have been extensively studied, and their structure and properties are well documented in the literature. This section is a review of the current understanding of some less common nonplanar graphitic materials, such as graphite whiskers, cones, and polygonized carbon nanotubes (graphite polyhedral crystals). Although nonplanar graphitic microstructures in the shape of cones were reported as early as 1957,[3,4] it is only recently[5–8] that attention has been paid to these exotic classes of graphitic materials. There is no doubt that this growing interest has been triggered by the discovery of fullerenes[9] and nanotubes,[2,10] which has stimulated very intensive research on carbonaceous nanomaterials over the past 20 years. While fullerenes and nanotubes have been discussed in several books during the past decade, carbon cones, whiskers, and other similar structures have received much less attention. Our intention here is to give an overview of the current understanding of their structure, synthesis methods, properties, and potential applications.

Some of the engineering disciplines that could benefit from the emergence of these forms of carbon are:

- *Materials engineering*: graphitic cones and polyhedral crystals will enable the development of new functional nanomaterials and fillers for nanocomposites.
- *Chemistry and biomedicine*: in the development of new chemical sensors, cellular probes, and micro-/nanoelectrodes.
- *Analytical tools and instrumentation development*: cones and polyhedral crystals can act as probes for atomic force and scanning tunneling microscopes.
- *Energy, transportation, and electronic devices*: as materials for energy storage, field emitters, and components for nanoelectromechanical systems.

The common features of carbon whiskers, cones, scrolls, and graphite polyhedral crystals, besides their chemistry and the graphitic nature of their bonds, are their morphology and the high length-to-diameter aspect ratio, which places them between graphite and carbon nanotube materials. In the following sections, we will examine various types of these materials, and we will show the effect of structural conformation as well as describe their properties and potential applications.

6.2 GRAPHITE WHISKERS AND CONES

Graphite whiskers, cones, and polyhedral crystals are all needle-like structures — meaning that their length is considerably larger than their width or diameter. The major difference between the graphitic cones and polyhedral crystals, besides their shape, is in their texture, i.e., in the orientation of the atomic planes within the structure. While graphite polyhedral crystals (GPCs) comprise of (0 0 0 1) planes parallel to their main axis, carbon cones and whiskers may have various textures. Therefore, we will consider GPCs separately from cones and whiskers. The orientation and the stacking arrangement of the planes is closely related to the nucleation mechanism and the growth conditions of the cones. The following section explains currently available methods for synthesis of carbon whiskers and cones. Also, two different types of cones have also been observed in natural deposits of carbon. These are described briefly in a separate section. A detailed explanation of their structure and properties in relation to their potential applications follows.

6.2.1 Synthetic Whiskers and Cones

6.2.1.1 Whiskers

Graphite whiskers are the first known nonplanar graphitic structures that were obtained through a controlled preparation. Bacon[11] succeeded in growing high-strength graphite whiskers on carbon electrodes using a DC arc under an argon pressure of 92 atm. The temperatures developed in the arc were sufficiently close to the sublimation point of graphite (above 3600°C), which enabled carbon to vaporize from the tip of the positively charged electrode, and form cylindrical deposits embedded with whiskers of up to 3 cm in length and a few microns in diameter.[12] Carbon deposition under extreme conditions, such as a "flash CVD" process, also resulted in the growth of very peculiar micron-sized tree-like carbon structures.[13]

Whiskers and filaments of graphite have also been observed to form during pyrolytic deposition of various hydrocarbon materials. Hillert and Lange[14] studied the thermal decomposition of n-heptane and reported the formation of filamentous graphite on iron surfaces at elevated temperatures. Pyrolysis of methane,[15] and carbon monoxide[16] on iron surfaces or heated carbon filaments[17] also resulted in the formation of similar structures as well as the thermal decomposition of acetylene on Nichrome wires below 700°C.[18]

Whisker growth during pyrolytic deposition process is generally considered as being catalyzed by metals.[19,20] Haanstra et al.[21] however, observed noncatalytic columnar growth of carbon on β-SiC crystals by pyrolysis of carbon monoxide at 1 atm pressure above 1800°C (Figure 6.1). The experiments showed that the growth of carbon whiskers in that case was defined by rotation twinning and stacking faults on {1 1 1} habit plane of the β-SiC substrate. The cylindrical carbon columns formed by this mechanism were observed to consist of parallel conical graphitic layers stacked along the column axis. Most specimens of a run had the diameter between 3 and 6 μm, and they were several tens of microns long. The apex angle of the conical mantle was measured to be about 141°. The conical nuclei of these columns were produced on defects in twinned β-SiC, such as the dislocation with a screw component perpendicular to the surface.

Very similar "needle"- or "spine"-like graphitic materials were also reported by Knox et al.[22] In an attempt to synthesize porous graphitic carbon material that would be capable of withstanding considerable shear forces, such as those seen in high-performance liquid chromatography, they produced porous glassy carbon spheres, which in most cases contained graphitic needles. Knox et al. impregnated the high-porosity silica gel spheres with a melt of phenol and hexamethylenetetramine (hexamine) in a 6:1 weight ratio. Impregnated material was first heated gradually to 150°C to form

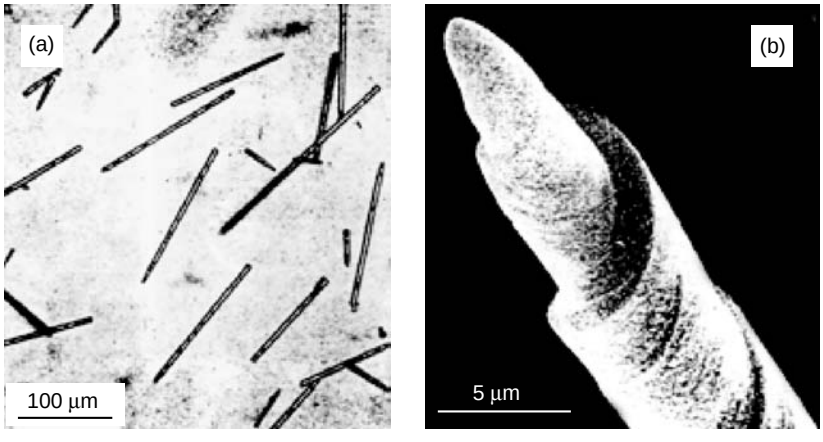

FIGURE 6.1 Electron micrographs of (a) pencil-like carbon columns; (b) columnar carbon specimen with screw-like markings on side.[21]

phenol-formaldehyde resin within the pores of the silica gel, and then carbonized slowly at 900°C in a stream of oxygen-free nitrogen. The silica was then dissolved with hot aqueous potassium hydroxide (at least 99% complete), and the remaining porous glassy carbon was consequently heated up to 2500°C in oxygen-free argon.

Besides the expected glassy carbon structure, the resulting product often contained considerable amounts of needle-like material that was determined to have a three-dimensional graphitic structure. The graphitic whiskers resulting from the experiments were usually a few microns long and about 1 μm thick. Electron diffraction and transmission electron microscopy (TEM) revealed the twinned structure of the whiskers. The angle between the layers was measured to be about 135°.

Since this material was a side product of their experiment, Knox et al. neither provided any further details of its structure nor explained the nucleation mechanism. It is, however, highly probable that their graphitic needles were nucleated and grown in a pretty much the same way as were Haanstra's whiskers shown in Figure 6.1. Incomplete dissolution of the silica matrix could have caused formation of twinned β-SiC phase during the glassy carbon pyrolysis between 1000 and 2500°C, which further induced growth of columnar graphite from disproportionated CO within the porous glassy carbon spheres. The 135° whiskers have also been synthesized recently at 2100°C from gaseous CO and ball-milled natural graphite[23,24] contaminated with zirconia particles during milling. When heated above 1900°C, the zirconia particles react with the carbon to form ZrC.[25] The growth of the graphitic whiskers was probably initiated by screw dislocations on the surfaces of ZrC particles.

Similarly, Gillot et al.[26] studied the heat treatment of products of martensite electrolytic dissolution, and observed the formation of "cigar"-shaped crystals of graphite at 2800°C. The model of the texture they obtained is shown in Figure 6.2a. The length of the crystals ranged from a few microns to 250 μm with a length-to-diameter ratio of about 10. It was suggested that the growth mechanism of the "cigars" involved mass transfer through the gas phase. The graphite layers in the whisker had the shape of an obtuse cone, the axis of which was coincident with the axis of the whisker, and had basically the same structure noted but not fully described by Knox et al. Such whiskers were assumed to be formed by a single graphene sheet coiled around the axis in a helix, each turn of the helix having the shape of a cone (Figure 6.2b). The angular shift θ of the (h k 0) crystallographic directions from one whorl to the next one in the helix was measured to be $\theta \approx 60°$. All graphitic layers were found to have the same stacking arrangement as of a perfect graphite crystal. Later, Double and Hellawell[27] proposed the cone-helix growth mechanism of such

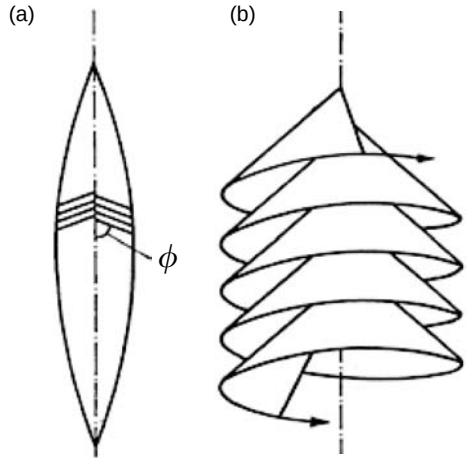

FIGURE 6.2 Model illustrating the formation of cigar-like graphite: (a) longitudinal cross section of the cigars showing their texture; (b) cone-helix structure of graphitic filaments.[26]

structures, which relies on the formation of a negative wedge disclination within a graphene sheet. This model will be explained in detail in the following section.

6.2.1.2 Cones

Ge and Sattler,[6] Sattler,[7] and Krishnan et al.[8] were among the first to observe and study fullerene nanocones, i.e., seamless conical structures formed when one or more pentagonal rings are incorporated into a graphene network. Incorporation of pentagonal and heptagonal defects into graphene sheets and nanotubes had at that time been already discussed by Iijima et al.,[28] Ajayan,[29,30] Ebbesen,[31] Ebbesen and Takada,[32] and others,[33–35] to explain conical morphologies of carbon nanotube tips observed by high-resolution transmission electron microscopy (HRTEM). The importance of the pentagonal defects in the formation of three-dimensional conical graphitic structures, however, was not fully recognized till the thorough investigation of their electron diffraction patterns by Amelinckx et al.,[5,36,37] who studied helically wound conical graphite whiskers (Figure 6.3a) by electron microscopy and electron diffraction. Whiskers gave rise to unusual diffraction effects consisting of periodically interrupted circular ring patterns (Figure 6.3b). Very similar diffraction patterns had been previously obtained from whiskers described in Ref. 21. Amelinckx et al. proposed a growth mechanism whereby the initial graphite layer adopts a slitted dome-shaped configuration (Figures 6.4a and b) by removing a sector β and introducing a five-fold carbon ring in the sixfold carbon network (Figure 6.4c). Successive graphene sheets were then rotated with respect to the previous one over a constant angle, thus realizing a helical cone around a "disclination," with a five-fold carbon ring core. The model explains the morphological features and the particular diffraction effects observed on these reproducibly prepared columnar graphite crystals and it also builds on the other cone models.[21,27]

The first true multishell fullerene graphitic cones consisting of seamless axially stacked conical surfaces (Figure 6.5) were observed in the products of chlorination of silicon carbide at temperatures above 1000°C in 1972[38] and then reported by Millward and Jefferson[39] in 1978. Since these structures were rather singular observations in the products of the reaction, they were not recognized as a new material until much later.[38] Similar structures in large quantities were for the first time successfully produced by Ge and Sattler.[6] Up to 24 nm in length and 8 nm in base diameter, these nanometer-sized structures were generated by vapor condensation of carbon atoms on a highly oriented pyrolytic graphite substrate. All of the cones had the same apex angle ~19°, which is the smallest among five possible opening angles for perfect graphitic cones (Figure 6.6a). The growth of these nanostructures is thought to be initiated exclusively by fullerene-type nucleation seeds with

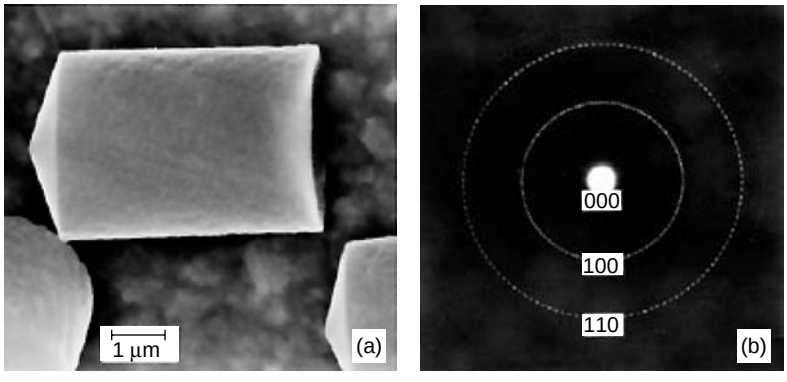

FIGURE 6.3 Conical graphite whiskers. (a) SEM micrograph of a cleavage fragment of conically wound graphite whisker. Note the 140° apex angle of the conical cleavage plane. (b) Electron diffraction pattern with the incident electron beam along the normal to the cleavage 'plane' of the conically wound whiskers. Note the 126-fold rotation symmetry of the pattern.[36]

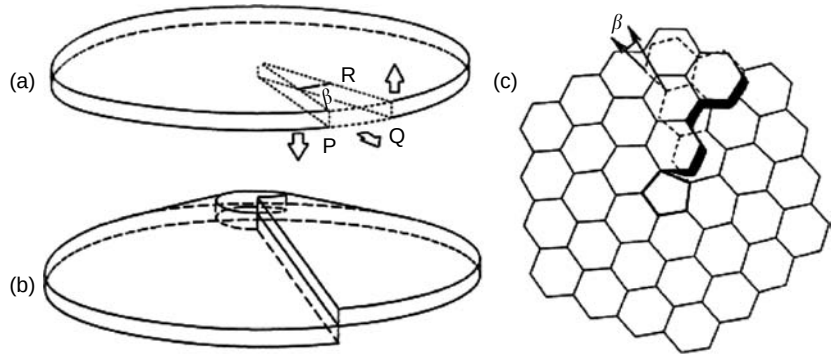

FIGURE 6.4 Model illustrating the formation of a conical helix. (a) Sector β is removed from a disc. (b) The angular gap is closed and a cone is formed. (c) Twisted nucleus of the conical helix containing one pentagonal ring in the graphene network. Conical helix is formed through rotation of successive graphene sheets over a constant angle.[36]

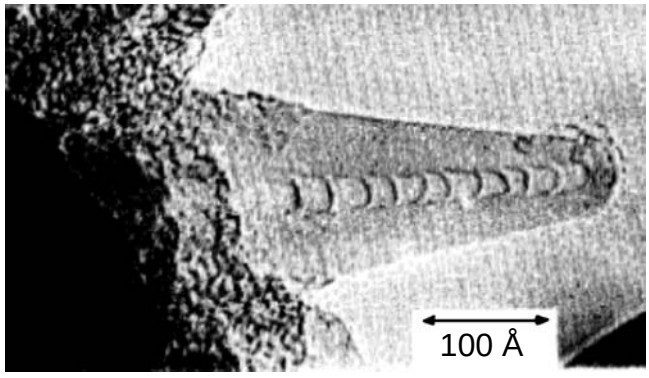

FIGURE 6.5 Carbon cone showing separation of layers in fullerenic end cups.[38]

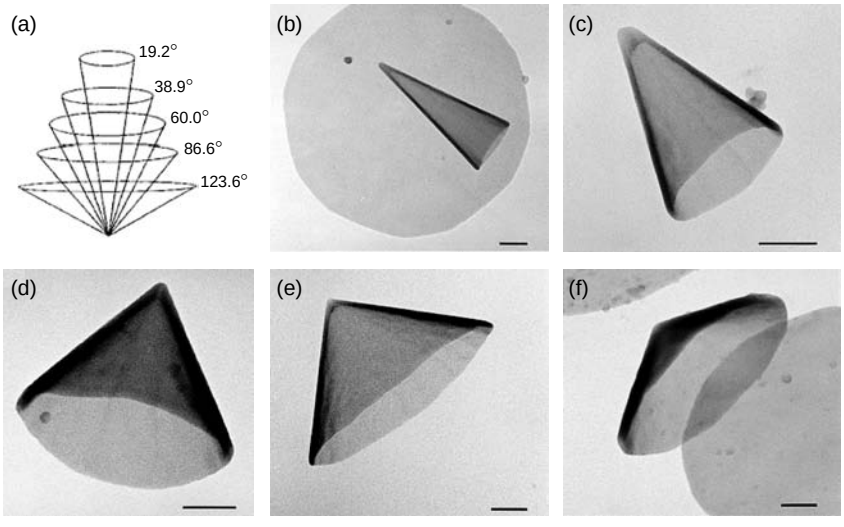

FIGURE 6.6 Fullerene cones. (a) The five possible seamless graphitic cones, with cone angles of 19.2, 38.9, 60, 86.6, and 123.6°.[6,7] Electron micrographs of the corresponding five types of cones (scale bars in b–f, 200 nm). Apex angles: (b) 19.2°, (c) 38.9°, (d) 60.0°, (e) 84.6°, and (f) 112.9°.[8]

different number of pentagons. Fullerene cones of other apex angles corresponding to 1 to 4 pentagons were produced and reported 3 years later by Krishnan et al.[8] (Figures 6.6c–f). They also reproduced the ~19° cone (Figure 6.6b).

Graphite conical crystals of very small apex angles (from ~3 to ~20°) and perfectly smooth surfaces (Figure 6.7) have been reported to form in the pores of glassy carbon at high temperatures,[40,41] in addition to other various axial graphitic nano- and microcrystals.[42] Graphitic structures from the glassy carbon pores were produced from carbon-containing gas formed during decomposition of phenol formaldehyde. The size of these graphite conical crystals ranged from about 100 to 300 nm in the cone base diameter, and their lengths ranged from about 500 nm to several micrometers. Similarly, a few other conical structures of graphite were produced by thermal decomposition of hydrocarbons[43] with or without the aid of a catalyst, or by employing various thermochemical routes.[44] The structure of the majority of catalyst-free cones observed is consistent with the cone-helix growth model; however, some of the small apex angle cones (~2.7°), as seen in Figure 6.7c,[40,41] do not conform to this rule. These are most likely carbon scroll structures.[45,46] Orientation of layers in catalytically produced cones is closely related to and resembles the shape of the catalyst particle.[47–49] Catalytically produced cones can adopt open,[49–51] helical,[49,51] or close-shell structures.[49]

Several other types of cones have been reported that are actually composed of cylindrical graphite sheets.[52,53] So-called tubular graphite cones (TGCs) (Figure 6.8) have been synthesized on an iron needle using a microwave-plasma-assisted chemical vapor deposition (MWCVD) method[52] in a CH_4/N_2 gaseous environment. Corn-shape carbon nanofibers with metal-free tips have also been synthesized by a MWCVD method using CH_4 and H_2 gases.[53] Graphitic coils wound around a tapered carbon nanotube core have also been produced by the same technique using different substrate material.[54] What

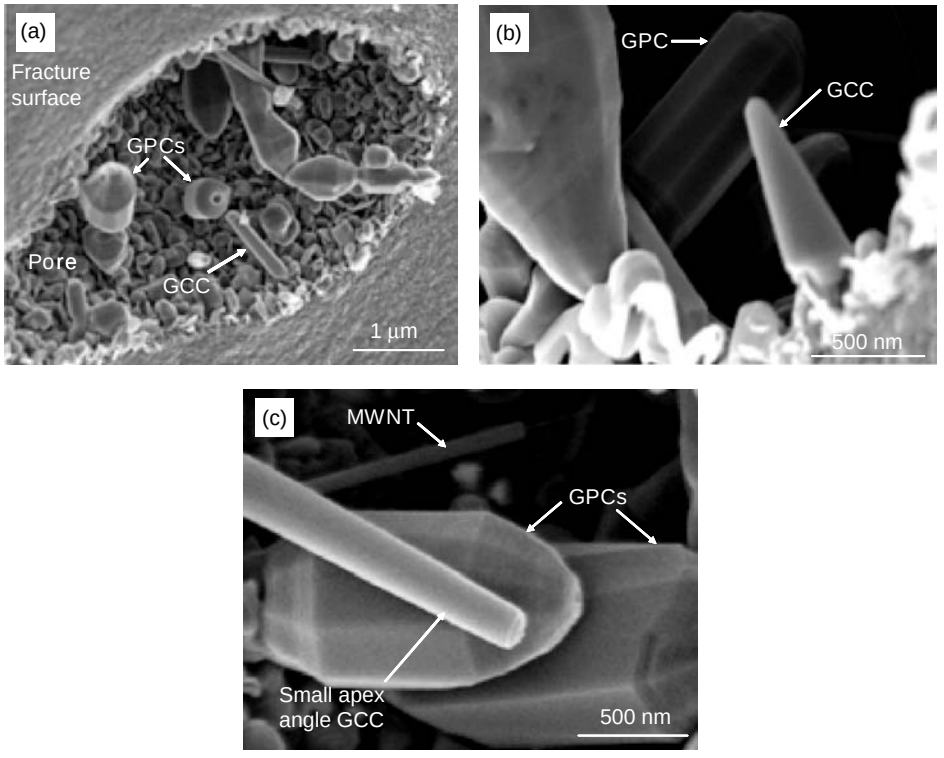

FIGURE 6.7 SEM micrographs of carbon nano- and microcrystals found in pores of glassy carbon. (a) Fracture surface, showing crystals in a pore. (b) Graphite polyhedral crystals (GPCs) and graphite conical crystals (GCCs). (c) A small apex angle GCC growing along with GPCs, and a stylus-like multiwall carbon nanotube (MWNT).[41]

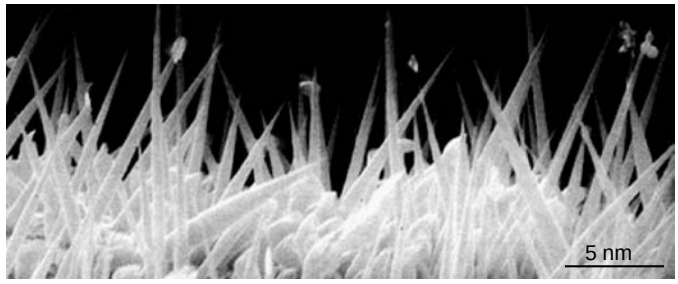

(a)

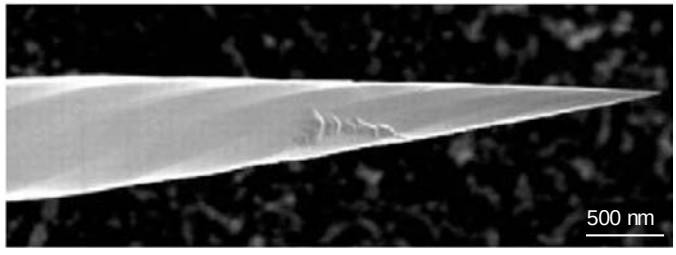

(b)

FIGURE 6.8 Tubular graphite cones. (a) Aligned TGCs grown on an iron needle surface. (b) A high-resolution view of one TGC shows the faceted and helical appearance.[52]

makes these and similar structures cone-shaped is not purely an inclination of their graphitic layers with respect to the cone axis, but rather the continuous shortening of graphitic wall layers from the interior to the exterior of the structure,[55] or a combination of both mechanisms, as in the case of carbon nanopipettes.[54] Although their morphology resembles a cone, intrinsically their microstructure is that of the multiwall carbon nanotubes. This implies different mechanical and electronic properties. Tailoring carbon nanotubes to cone shapes can now be done routinely.[56–59]

6.2.2 Occurrence of Graphite Whiskers and Cones in Nature

Graphite whiskers and cones have also been observed growing on natural Ticonderoga graphite crystals,[60] Gooderham carbon aggregates,[61] and friable, radially aligned fibers of Kola graphite.[62] In their brief communication, Patel and Deshapande[60] reported the growth of 65 to 125-μm-thick graphite whiskers in ⟨0 0 0 1⟩ direction, the (0 0 0 1) planes of graphite being perpendicular to the whisker axis. The growth of the whiskers was presumed to be a result of a screw dislocation mechanism during the growth of graphite, but no details indicating the relationship of the structure and the geological origin of the sample were given. Several other exotic forms of graphite have been observed recently from two different geological environments: arrays of graphite cones in calcite from highly sheared metamorphic rocks in eastern Ontario (Gooderham graphite, Figure 6.9a),[61] cones, and scrolls of tubular graphite in syenitic igneous rock from the Kola Peninsula of Russia (Figures 6.9b–d).[62]

In a few geological occurrences, graphite forms compact spherical aggregates with radial internal textures,[62–66] similar to those observed in graphite spheres in cast iron.[27] One prominent natural occurrence is in metasedimentary rocks exposed at a roadcut, south of Gooderham, Ontario, Canada.[67,68] In this region, graphite crystallizes in calcite in various forms of tabular flakes, spherical, spheroidal, and triskelial polycrystalline aggregates,[62,69] some of which were found to contain large arrays of graphitic cones dominating the surfaces of the samples.[61] Cone heights ranged from less than a micron to 40 μm, and unlike most laboratory-produced cones, they showed a wide distribution of apex angles. The apex angles were found to vary from 38 to ~140°, with 60° being the most common. The cone structure can be well described by the Double and Hellawell[27] disclination

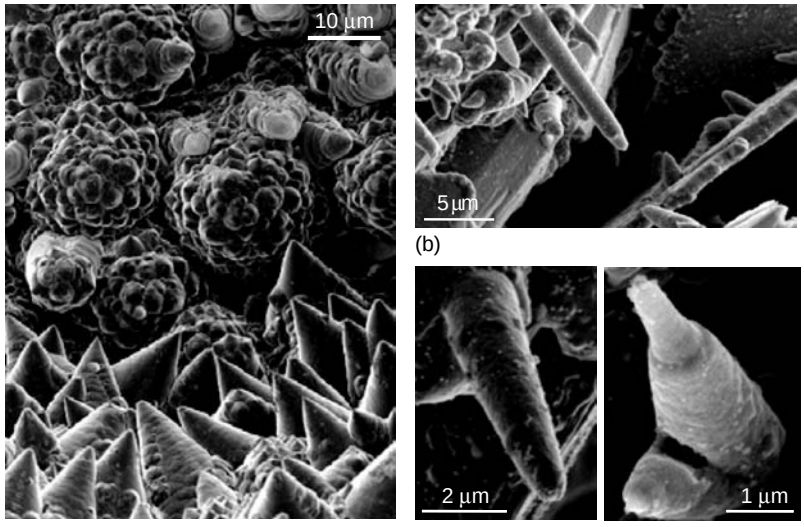

FIGURE 6.9 FESEM images of graphite cones from (a) Gooderham, Ontario, Canada. [61] (b–d) Graphite cones, scrolls, and tubes from Hackman Valley, Kola Peninsula, Russia. A scroll-type structure is suggested in (b). Some of the Kola cones appear to be hollow, as indicated by a fractured structure (d).[62]

model. Other than full and solid cones, some Gooderham samples also revealed partly conical hollow structures composed of curved graphite shells ("protocones").[62] These indicate a possible earlier growth stage for the cones reported in Ref. 61. Unlike large solid cones, many of these graphitic structures have partly faceted surfaces (Figure 6.10). The tips of the polygonal cones typically have six facets, and these facets only extend part way down the surfaces of the cones, which maintain a circular base.[62] The faceted cones are reminiscent of the polyhedral graphite crystals from glassy carbon pores.[42] The morphology and the surface topography of the cones and petrologic relations of the samples suggest that the cones formed from metamorphic fluids.

Numerous scroll-type graphite whiskers, up to 15 µm in length and up to 1 µm in diameter (Figures 6.9b–d), were discovered to cover inner and outer surfaces of channels comprised of tabular graphite crystals. They have been found in samples of alkaline syenitic pegmatite of Kola Peninsula, Russia.[70] The surfaces of cavities in the host rock were coated with fine-grained graphite layer comprised solely of such whiskers. Some of the Kola natural graphite whiskers are cigar-like (Figure 6.9b), while others exhibit true conical (Figure 6.9c) morphologies with dome-shaped tips. The conical whiskers appear to be significantly larger and more abundant than the tube-like whiskers. Many Kola cones show distinct spiral growth steps at the surfaces of their tips, suggesting that they have a scroll-type structure, as seen previously in other synthetic whiskers.[11,17,21,26] SEM images of some broken cones reveal that they are hollow (Figure 6.9d).

6.2.3 Structure: Geometrical Considerations

We have seen in the previous section that, on the basis of their structure, a distinction can be made between the two major classes of graphitic cones. One type has a "scroll-helix" structure, while the second type comprises seamless conical graphene layers stacked over each other along their axis (therefore called "fullerene cones"). This classification may be considered as an equivalent to differentiating between "scroll" and "Russian-doll" type of multiwall carbon nanotubes.[71]

Pure "scroll-helix" cones are made up of a single graphene sheet that coils around an axis, each layer having a cone shape. The nucleation of this kind of structure is generally controlled by a line defect (dislocation), although we will see later that in addition, it always involves a screw dislocation

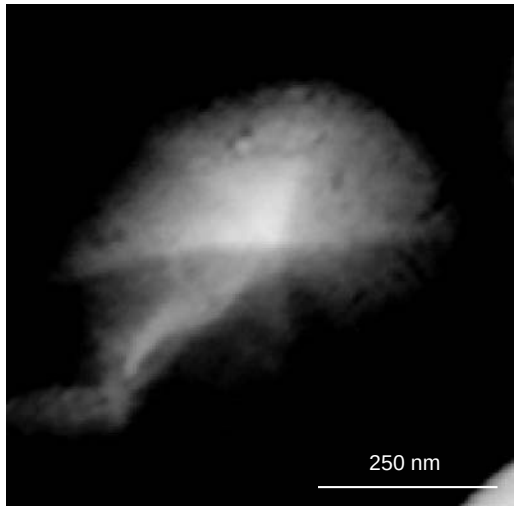

FIGURE 6.10 FESEM micrograph of a graphite "protocone" having a faceted tip.[62]

and some kind of point defect at the terminated side of the dislocation line, as indicated in Figure 6.4. On the other hand, an ideal "fullerene" cone contains only point defects in the form of pentagonal, heptagonal, or lower/higher order carbon rings and their various combinations. It is also possible that some of the actual graphitic cones are neither purely helical nor purely fullerene structures, but rather a combination of the two.

Euler's theorem[72] has been found particularly useful in explaining geometrical aspects and generation of fullerenes and fullerene cones. Suppose that a polyhedral object is formed by enclosing a space with polygons. The number of polygons is therefore equal to the number of faces (F) of such object. If V is the number of vertexes, E the number of edges, and g a genus of the structure, then the four parameters correlate as follows:

$$V - E + F = 2(1 - g) \tag{6.1}$$

For bulk three-dimensional solids, g is equivalent to the number of cuts required to transform a solid structure into a structure topologically equivalent to a sphere (for instance, $g = 0$ for a polygonal sphere such as C_{60} or C_{70}, and $g = 1$ for a torus). Suppose, further, that the object is formed of polygons having different (i) number of sides. The total number of faces (F) is then

$$F = \sum N_i \tag{6.2}$$

where N_i is the number of polygons with i sides. Each edge, by definition, is shared between two adjacent faces, and each vertex between three adjacent faces, which is represented as

$$E = (1/2) \sum iN_i \tag{6.3}$$

and

$$V = (2/3)E \tag{6.4}$$

By substituting Equations (6.2) to (6.4) into (6.1), Euler's postulate for $i \geq 3$ is represented as

$$3N_3 + 2N_4 + N_5 - N_7 - 2N_8 - 3N_9 - \cdots - = 12(1 - g) \tag{6.5}$$

$$\sum (6 - i)N_i = 12(1 - g) \tag{6.6}$$

It can be observed from Equation (6.5) that the number of hexagons does not play a role, and a balance between the number of pentagons and higher order polygons ($i \geq 7$) is required in order to form an enclosed structure. If each vertex is considered an atomic site containing an sp^2-hybridized C atom, and each edge is assigned to one C–C bond, then according to Equations (6.5) and (6.6), only 12 pentagons are needed to form a fullerene or a nanotube. If one heptagon is present, then 13 pentagons will close the structure.

The total disclination in a completely closed structure, such as a sphere, is 720° (i.e., 4π). Each out of 12 pentagons contributes a positive disclination of 720°/12 = 60°, and a heptagon, similarly, creates a negative 60° disclination. Incorporation of a heptagon in a graphene sheet will, therefore, produce a saddle-like deformation,[73] while adding pentagons will result in conical structures. Exactly five different cones (Figure 6.6) are generated by having respectively 1 to 5 pentagonal rings in their structure, as experimentally observed[6,7] and mentioned in a previous section. Careful examination of such cones suggests that pentagons are isolated from each other by hexagonal rings, as in fullerene molecules and fullerene nanotube caps. The apex angles for these cones can be calculated from the following relation:[74]

$$\sin(\theta/2) = 1 - (N_5/6) \tag{6.7}$$

where N_5 is the number of pentagons in the cone structure.

Topo-combinatoric conformations of i-polygonal carbon rings (where i = 1, 2, 3, 4, 5, 7, 9, …) within a hexagonal carbon network had been studied in detail even before the discovery of fullerenes, carbon nanotubes, and graphitic cones.[75,76] Growing interest in this topic resulted in the number of publications[73,77–80] that revealed the fine structure of the cone tip, such as the reconfiguration of carbon atoms and distribution of defects in the near vicinity of the tip. It had also been shown that the pentagons separated by hexagons (Figure 6.11)[74] make the most stable conformation of the cone tip structure, as observed experimentally. Establishing valid theoretical models of structure later helped in calculating the electronic properties of cones and curved carbon surfaces.[81–84]

Apart from seamless cones, there are conical structures that are formed by introducing a wedge disclination (Figure 6.12a) and a screw dislocation (Figure 6.12b) in a graphite sheet, as observed experimentally by various groups.[4,5,21,22,26,36] The cone-helix model[27] is based on growth around a positive disclination with a screw dislocation component (Figure 6.12c). As a graphene sheet wraps around the disclination, adjacent overlapping layers are rotated with respect to one another by an angle equal to the disclination angle. Among practically unlimited number of disclination angles, some of them should be energetically more favorable (Figure 6.12c and inset table in Figure 6.13). Their value can be calculated from the following equation:

$$\alpha = n \times 60°, \quad \text{or} \quad \alpha = n \times 60° \pm \omega \tag{6.8}$$

where n = 0, 1, 2, … , 6, and ω = 13.2, 21.8, 27.8°, … are expected low-energy (0 0 1) twist grain-boundary angles based on lattice coincides, which are a measure of "goodness of fit," but do not

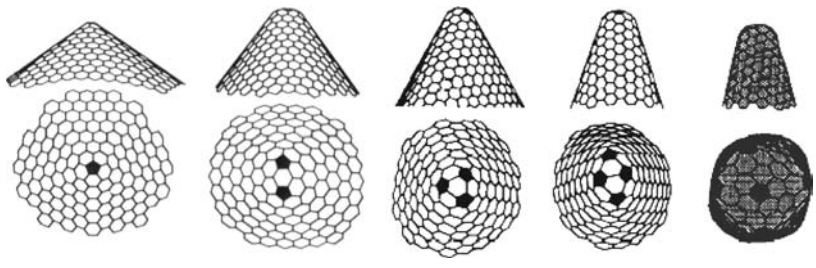

FIGURE 6.11 Distribution of pentagonal defects within the cone tip. The apex angle changes with the number of pentagons.[74]

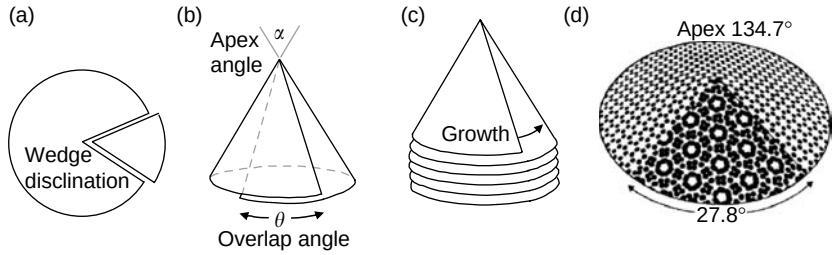

FIGURE 6.12 Formation of helical cones. (a) Positive wedge disclination is created after a sector is removed from a graphene sheet and (b) the cone is formed by an overlap through a screw dislocation. (c) Model illustrating growth of columnar carbon, and (d) one of several energetically preferred stacking arrangements.[27]

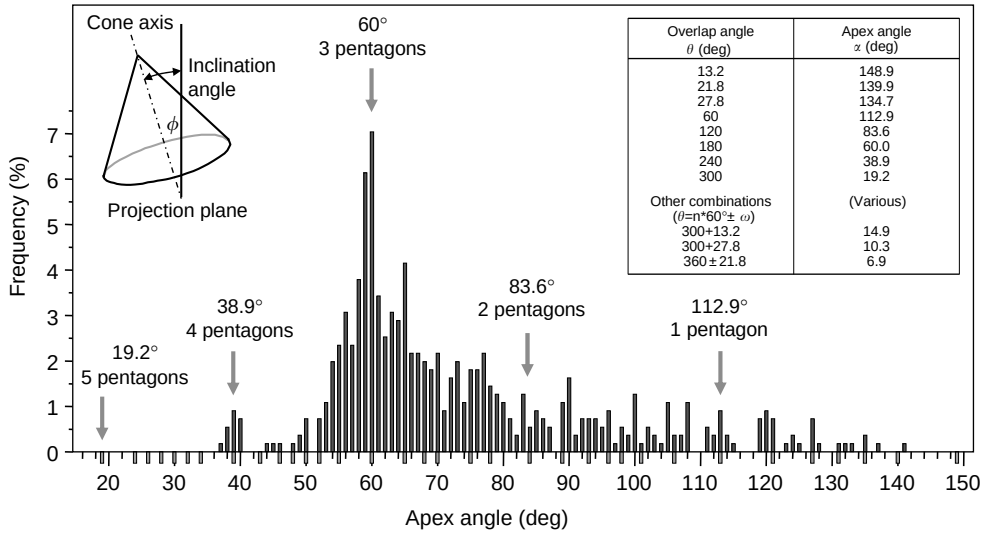

Overlap angle θ (deg)	Apex angle α (deg)
13.2	148.9
21.8	139.9
27.8	134.7
60	112.9
120	83.6
180	60.0
240	38.9
300	19.2
Other combinations (θ=n*60°± ω)	(Various)
300+13.2	14.9
300+27.8	10.3
360±21.8	6.9

FIGURE 6.13 Frequency of occurrence of various apex angles for natural graphite cones. The maximum is observed at 60°. Apex angels that correspond to "goodness" of fit are listed in the table. When measuring apex angles of cones, the inclination of cones to the projection plane of the microscope has been taken into account (inset, left).[61]

account for atomistic interactions and the curvature of the sheets. Disclinations with overlap angles equal to integer multiples of 60° should be energetically the most favorable, because they preserve the graphite crystal structure without stacking faults, provided the screw component of the disclination has a Burgers vector corresponding to an even multiple of the graphite's *c*-axis interplanar spacing. Values of corresponding apex angles are calculated from the following relation:

$$\theta = 2\sin^{-1}(1 - \alpha/360°) \tag{6.9}$$

and they range from 6 to 149°. Graphitic cones having such apex angles should predominate over others.[61] The apex-angle distribution in a sample of natural cones is shown in Figure 6.13. Among all possible apex angles, the 60° angle is found to be the most frequent. Cones with smaller apex angles may be disfavored because of the higher elastic energy due to bending required to form the corresponding disclinations.

The dislocation line usually terminates with a point defect that includes bond recombination within the hexagonal network to form a pentagon or some other kind of polygon, as shown in Figure 6.4c.

6.2.4 Properties and Applications

6.2.4.1 Electronic Properties of Synthetic Whiskers and Cones

Carbon nanotubes are known to be either metallic or semiconducting, depending on their diameter and chirality.[85–89] The role of pentagon, heptagon, or pentagon–heptagon pair topological defects in structural and electronic properties of nanotubes has also been studied theoretically,[81,84,90] and experimentally by means of scanning tunneling microscopy (STM) and scanning tunneling spectroscopy (STS).[84] Special attention has been paid to curved surfaces of capped carbon nanotube tips, since these can be considered as regions of high density of defects. As the density of defect states increases at the tube ends, it can be expected that the electronic band structure of the end differs significantly from that elsewhere on the tube.[81–84] This has been successfully demonstrated by means of spatially resolved STM/STS carried out on a conically shaped tube end (Figures 6.14a and b),[84] which in fact is a fullerene-type carbon nanocone structure.

An STM image of one such conical tip is shown in Figure 6.14a. The apex of the cone has a diameter of 2.0 nm. The tunneling spectra were acquired at four different positions along the tube (marked with white letters in Figure 6.14a). Local densities of states (LDOS), derived from the scanning tunneling spectra, are represented in Figure 6.14b. In addition, the tight-binding calculations performed on two different tip morphologies are given in Figures 6.14c and d.

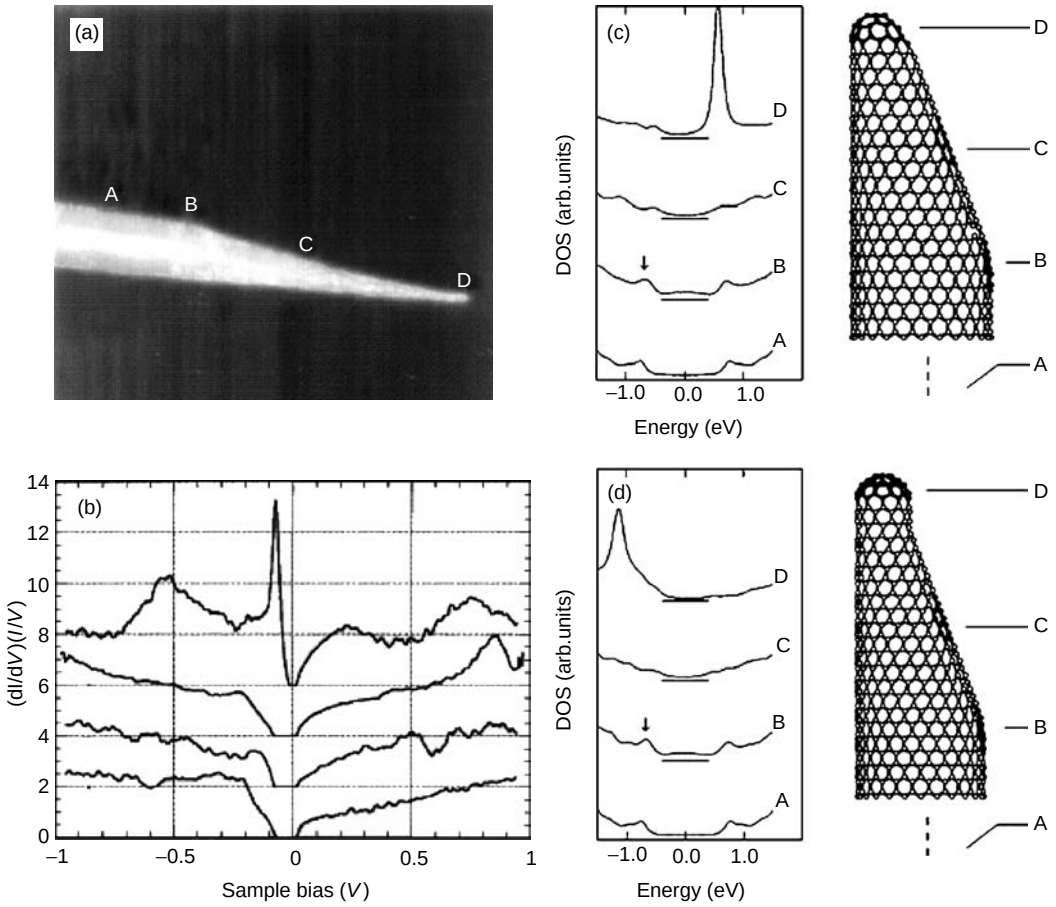

FIGURE 6.14 Electronic structure and localized states at carbon nanotube tips: (a) STM image of a fullerene carbon cone; (b) local densities of states for a cone tip derived from scanning tunneling spectra at four (A–D) points along the tip; and (c–d) tight-binding calculations for two different configurations of cone tips.[84]

As we move along the tube from position A to position D, the density of topological defects increases, since the topological defects are concentrated in a smaller volume. As a result, the effect of confinement on electronic structure becomes more and more pronounced. This does not seem to be very striking in the case of the conduction band, where only a slight and broad enhancement has been noted in the LDOS at the cone apex. The valence band, however, is found to alter considerably, exhibiting sharp resonant states at the cone tip (Figure 6.14b, curve D). The strength and position of these resonant states with respect to the Fermi level is, in addition, very sensitive to the distribution and position of defects within the cone. This is illustrated with two models of cones having different morphologies obtained by altering the position of pentagons within the tip structure (Figures 6.14c and d). In the two examples, the (A), (B), and (C) LDOS calculated by the tight-binding method are very similar. Strong and sharp peaks in (D) LDOS have different shape and position in the case of models I and II. The values calculated for model II show better fit to the experimental values given in Figure 6.14b. The distribution of the defects and their effect on electronic properties of the cones have been studied in detail elsewhere.[91] LDOS of helix-type carbon cones are obtained by establishing the tight-binding model of a screw dislocation in graphite.[81]

Localized resonant states are very important in predicting the electronic behavior of carbon cones. They can also strongly influence the field emission properties of cones (For more details on field emission properties of carbon nanotubes see Chapter 24).

6.2.4.2 Raman Spectra

Owing to its sensitivity to changes in the atomic structure of carbons, Raman spectroscopy has proven a useful tool in understanding the vibrational properties and the microstructure of graphitic crystals and various disordered carbon materials.[92–97] The relationship between the spectra and the structure has been extensively discussed in the literature, and the studies cover a wide range of carbon materials, such as pyrolytic graphite (PG)[94,95] and highly oriented pyrolytic graphite (HOPG),[95,98,99] microcrystalline graphite, amorphous carbon and glassy carbon, fullerenes, carbon onions, nanotubes, etc. Little work is carried out on the Raman scattering from graphite whiskers,[100–102] which usually consist of carbon layers oriented parallel to the growth axes. For such structures, it is expected that their Raman spectra will be similar to those of disordered graphite crystals and carbon fibers.

Figure 6.15 shows the Raman spectra of an individual graphite whisker and turbostratically stacked particles, using 632.8 nm excitation wavelength. Whiskers were synthesized in a graphitization furnace using a high-temperature heat-treatment method.[23] Carbon layers in these whiskers are almost perpendicular to their growth axes. Most of the first- and second-order Raman modes in whiskers, such as the D, G, and D′ modes at ~1333, 1582, and 1618 cm^{-1}, respectively, can be assigned to the corresponding modes in HOPG and PG.

In contrast to other carbon materials, the Raman spectra of whiskers exhibit several distinct characteristics. For example, the intensity of the 2D overtone is found to be 13 times stronger than that of the first-order G mode in whiskers. The strong enhancement of the D and 2D modes is also found in the Raman spectra of whiskers with 488.0 and 514.5 nm laser excitations.[100] Second, there are two additional low-frequency sharp peaks located around 228 and 355 cm^{-1}, and two additional strong modes (around 1833 and 1951 cm^{-1}) observed in the second-order frequency region. The line widths of the D, G, D′, 2D, and 2D′ modes in whiskers are 17, 18, 10, 20, and 14 cm^{-1}, respectively. Because the frequencies of the L_1 and L_2 modes are in the frequency region of acoustic modes, these two modes are supposed to be the resonantly excited acoustic modes in the transverse-acoustic and longitudinal-acoustic phonon branches. The two high-frequency modes at 1833 and 1951 cm^{-1} are designated as $L_1 + D'$ and $L_2 + D'$ modes, respectively. The observed excitation-energy dependence (140 cm^{-1} eV^{-1}) of the 1833 cm^{-1} mode is in excellent agreement with the theoretical value of 139 cm^{-1} eV^{-1} of the $L_1 + D'$ mode.[100]

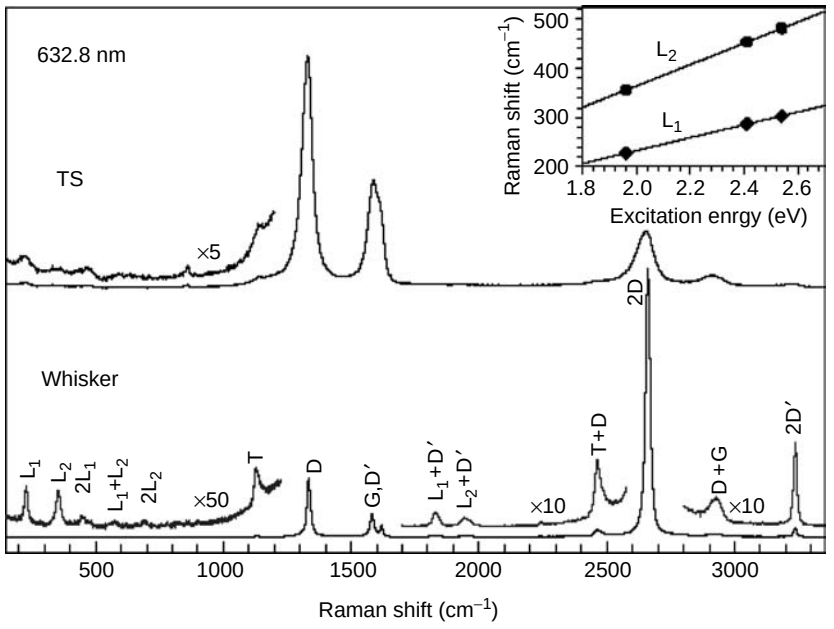

FIGURE 6.15 Raman spectra of turbostratically stacked (TS) particles and an individual graphite whisker excited with 632.8 nm laser excitation. The inset gives the energy dependence of the frequencies of the L_1 and L_2 modes.[102]

The intensity enhancement of the dispersive modes indicates that double-resonance Raman scattering may be responsible for this phenomenon.[103] Such enhancement of the 2D mode is also observed in GPCs (Figure 6.17) that have a similar loop-edge structure in brim regions.[42]

Raman spectra from tubular, helix-type, and naturally occurring carbon cones are available elsewhere in the literature.[61,102]

6.3 GRAPHITE POLYHEDRAL CRYSTALS — POLYGONAL MULTIWALL TUBES

6.3.1 SYNTHESIS

The structure of single- and multiwall carbon nanotubes, and single-wall carbon nanotube ropes have been widely studied over the last 10 years[2,31,71,104–108] and are described separately in Sections 4 and 5.

While the ability of carbon to form multiwall tubular nanostructures is well known and these tubes have been studied extensively, very little information is available about carbon nanotube structures having polygonal cross sections. Although an occurrence of polygonal vapor-grown carbon fibers with a core carbon nanotube protrusion was noted by Speck et al.[109] as early as 1989, no details were given about core fiber structure and its polygonization.

Zhang et al.[110] have studied the structure of an arc-discharge-produced carbon soot by the HRTEM, and they were the first to indicate the possibility of polygonal multiwall carbon nanotubes, assuming that the tubes consisted of closed coaxial concentric layers. The first evidence for occurrence of polygonized carbon nanotubes came from Liu and Cowley,[104,105,108] who used nanodiffraction in conjunction with HRTEM and selected area electron diffraction to investigate the structures of carbon nanotubes having diameters of a few nanometers. Nanodiffraction is a form of convergent beam electron diffraction, which allows one to obtain a diffraction pattern from regions of the specimen about 1 nm or less in diameter. The tubes used in this study were produced by a variant of Kratschmer–Huffman arc-discharge method[111] in helium gas at a pressure of 550 Torr. The DC

voltage applied to electrodes was 26–28 V and the corresponding current was 70 A. The carbon nanotubes obtained at the given experimental conditions consisted of 3 to 30 carbon sheets and had a length of up to 1 μm. The inner diameters of these tubes ranged from 2.2 to 6 nm, and the outer diameters ranged from 5 to 26 nm. In addition to nanotubes of circular cylindrical cross section, with zero, one or several helix angles, there were many tubes having polygonal cross sections, made up of flat regions joined by regions of high and uniform curvature.[105] An HRTEM image of one such structure is given in Figure 6.16a. Polygonization of the cross section is observed indirectly through formation of uneven patterns of lattice fringes on the two sides of the tube, with spacings varying from 0.34 nm from the circular cylinder tubes, to 0.45 nm from the regions of high curvature (Figure 6.16b).

In their study of the intershell spacing of multiwall carbon nanotubes prepared by the same Kratschmer–Huffman arc-discharge method, Kiang et al.,[112] similarly, found that the intershell spacing in carbon nanotubes ranged from 0.34 to 0.39 nm among different nanotubes, decreasing with the increase in the tube diameter (Figure 6.16c). Some other reports have also shown variation of the values from 0.344 nm (obtained by the electron and powder x-ray diffraction measurements)[113] to 0.375 nm (based on the HRTEM images).[114]

Faceted multiwall carbon nanotubes with larger diameters, called graphite polyhedral crystals (GPCs), have been reported to grow at high temperatures in the pores of a glassy carbon material (Figures 17a and b).[42] The glassy carbon containing polyhedral tubes was made from a thermoset phenolic resin by carbonization at 2000°C in N_2 atmosphere at ~10 Torr. The density of glassy carbon was 1.48 g/cm^3 with an open porosity of ~1%; its microstructure and properties are typical of other glassy carbons. After the structure of the matrix was set and some closed pores were formed, polyhedral nanotubes grew from C–H–O (N_2) gas trapped within these pores during the resin carbonization phase.

Graphite polyhedral crystals have a very complex morphology. Their size ranges from 100 to 1000 nm in diameter and up to few micrometers in length. The number of facets can vary from 5 to 14 and more, and they may possess a helical habit or be axially true. Many of the crystals terminate with a thin protruding needle that appears to be a multiwall nanotube (Figure 6.17b), typically with

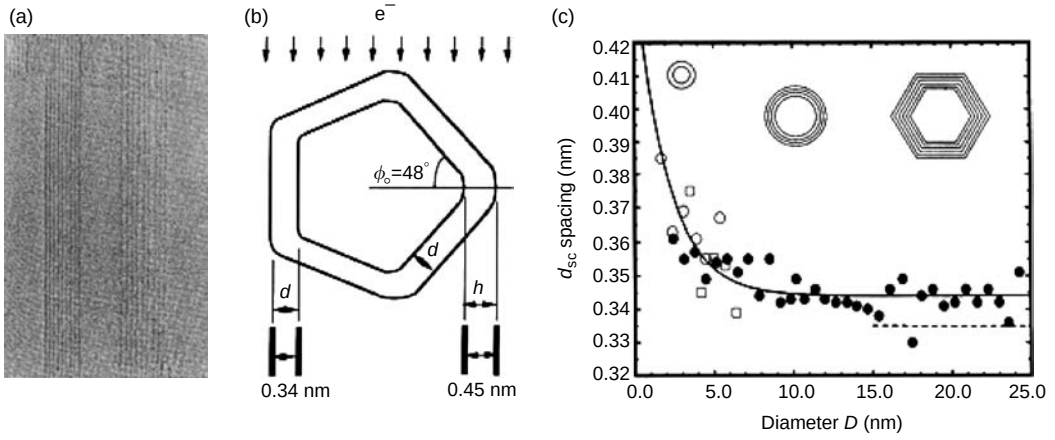

FIGURE 6.16 (a) HRTEM image of a nine-sheet nonsymmetric tube. A *d* spacing of 0.34 nm is found on the left side and a *d* spacing of 0.45 nm is seen on the right side.[108] (b) Model illustrating the formation of the nonsymmetric fringes from a tube (a) with polygonal cross section.[108] (c) The graphitic interplanar spacing decreases as the tube diameter increases, and approaches 0.344 nm at roughly $D = 10$ nm. The data were measured from three different nanotubes indicated by different symbols. Hollow circles: from a seven-shell tube with innermost diameter $D_{min} = 1.7$ nm. For large *D*, graphitization may occur resulting in a polygonal cross section. The broken line indicates the expected decrease in interplanar spacing owing to local graphitic stacking.[112]

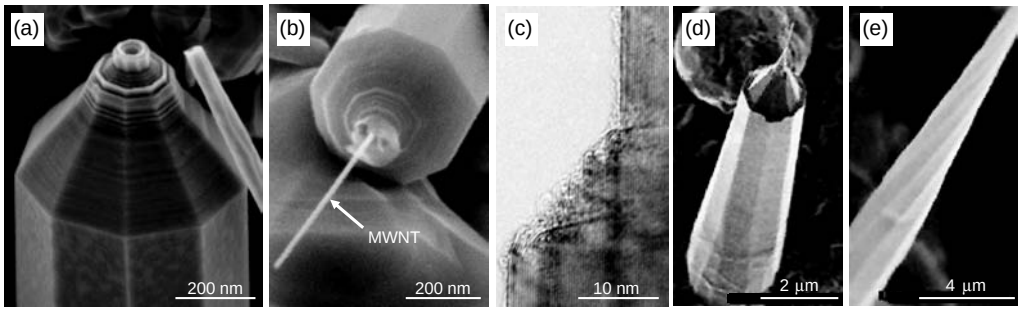

FIGURE 6.17 Graphite polyhedral crystals (GPCs). (a) SEM micrograph of a faceted GPC.[102] (b) A carbon nanotube stylus is connected to a microsize body. (c) TEM image of a GPC's lattice fringes indicates that GPCs are highly graphitic and that the basal planes are terminated by a closed-loop structure.[102] (d–e) GPCs produced by using the flame combustion method.[115]

a core diameter of about 5 to 20 nm and a conical, dome-capped, or semitoroidal tip. There is no evidence about catalytic nucleation of the graphite polyhedral crystals. Formation of highly ordered structures is promoted with the high temperature of treatment, the supersaturation of the environment with carbon atoms, slow reaction kinetics, and the presence of active species such as hydrogen and oxygen atoms that balance the crystal growth rate with the surface etching rate. This explains the surprisingly large number of ordered carbon layers (up to 1500) growing on the core nanotube, resulting in complex axis-symmetric structures. GPCs of somewhat less perfect structures (Figures 6.17c and d) have been successfully produced recently by using the flame combustion method.[115]

Annealing of carbon nanotubes with a circular cross section at high temperatures causes polygonization of their walls. An HRTEM image of a CVD carbon nanotube sample before and after annealing is shown in Figure 6.18. The tubes were annealed for 3 h in a 10^{-6} Torr vacuum at 2000°C. High-temperature annealing of carbon nanotubes in a vacuum or an inert environment allows for the transformation of circular tubes into polygonal ones. However, polygonization will not be uniform along the tube, nor will the cross section take the shape of a regular polygon.

To the best of our knowledge, natural counterparts of polygonal carbon multiwall nanotubes have not been observed so far, but it would not come as a surprise if they are discovered in the near future. Very short needle-like polygonal multiwall carbon nanotubes have also been synthesized from a supercritical C–H–O fluid by hydrothermal treatment of various carbon precursor materials[116,117] with and without the aid of a metal catalyst. Hollow carbon nanotubes, with multiwall structures, comprising of well-ordered concentric graphitic layers, have been produced by treating amorphous carbon in pure water at 800°C and 100 MPa.[117] HRTEM analysis of the reaction products indicates the presence of carbon nanotubes with polygonal cross sections (varying contrast and lattice spacing along the tube diameter) within these samples. The experimental conditions for hydrothermal synthesis of nanotubes resemble to a great extent the conditions of geological metamorphic fluids, and it is possible that some polygonal tubes are present in the Earth's crust along with the natural graphitic cones and tubules but have not been found yet.

6.3.2 Structure of Polygonal Tubes

One of the earliest works dealing with the polygonization of the cross section of carbon nanotube, is a report by Zhang et al.[110] Based on experimental observations, it was suggested that the fine structure of carbon nanotubes is determined by two competing accommodation mechanisms (Figure 6.19a). As a result of one of the mechanisms, the successive tube can adopt different helical shapes to accommodate the change in circumference, therefore keeping an orientationally disordered (turbostratic) stacking. As a result of the second mechanism, the rows of hexagons in successive tubes

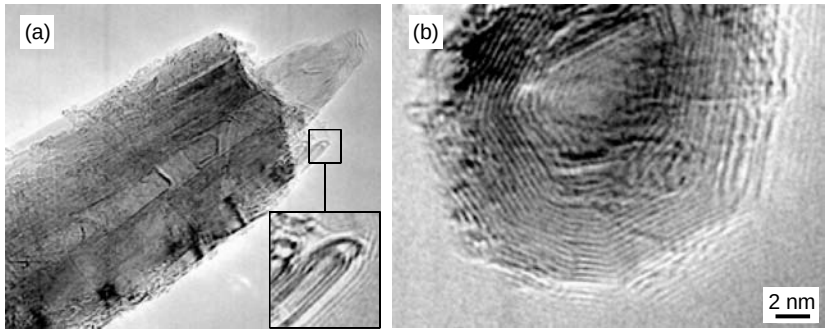

FIGURE 6.18 Transformation of multiwall carbon nanotubes into polygonal GPC-like structures by annealing in vacuum at 2000°C. (a) TEM image of a tube with a core nanotube in the form of stylus extension. Arched semitoroidal structures, similar to that of GPCs, have been also formed (inset) through elimination of dangling bonds at high temperature. (b) Polygonized cross section and graphitic walls of an annealed hollow tube. TEM micrographs courtesy of H. Ye.

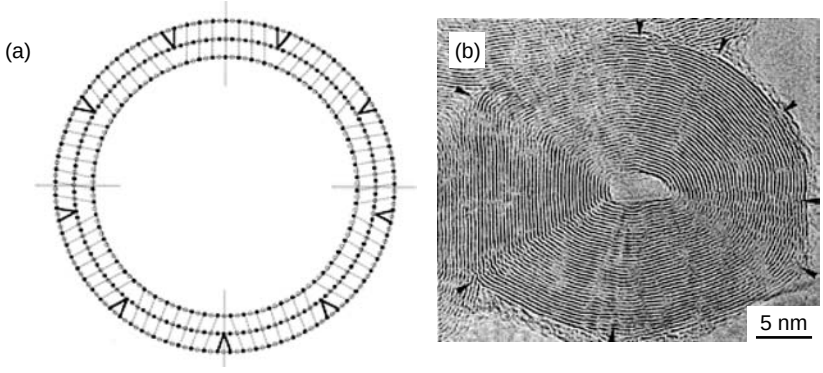

FIGURE 6.19 (a) Schematic model of a nanotube cross section. "Interfacial dislocations" (bold lines) are introduced to accommodate the strains on the tube surfaces. The graphite stacking is maintained in the tube walls (as indicated by lines). The full circles represent the atoms in the paper plane and the open circles are projected positions of the atoms of the paper plane. (b) Defect regions in the HRTEM image of a carbon "onion." The defect regions are characterized by their abnormal image contrast.[110]

remain parallel and adopt a graphitic stacking, thus inducing some regions of stacking faults due to the deformation of hexagons. The regions of stacking fault are assumed to be evenly distributed along the tube circumference,[110] and are separated from the graphitic structure by interfacial dislocations (bold lines in Figure 6.19a). Polygonization of carbon nanotubes therefore may appear as a result of the necessity to allow graphitic stacking of the layers, as often seen in carbon onions (Figure 6.19b).[110,118,119] It is easy to envision a trade-off between the energy associated with turbostratic stacking vs. the strain energy associated with shape changes and stacking faults. The mechanism prevailing depends strongly on the tube size. The relative strain required to maintain graphitic order is smaller with increasing tube size; therefore thicker tubes are expected to have graphitic ordering and polygonal cross sections with discrete regions of stacking faults, while thinner tubes are more likely to retain turbostratic concentric structures with cylindrical cross section and varying helicity between the individual shells.

In the near-planar regions of the polygonized tubes, an ordering of the stacking sequence of the carbon layers gives rise to hexagonal and possibly rhombohedral graphite structure.[108] The near-planar regions are connected into seamless shells through the regions of high curvature (Figure 6.16b).

A small value for the radius of curvature is preferred in regions of bending of the carbon sheets between the extended near-planar regions because of the nature of local perturbations of the carbon bonding arrangement.[104,105,108]

A tube structure model has been proposed to explain the variation of intershell spacing as a function of tube diameter (Figure 6.20a). Individual intershell spacings as a function of tube diameters were measured in real space from HRTEM images of various nanotubes.[112] The empirical equation for the best fit to these data is given as

$$\hat{d}_{0\,0\,2} = 0.344 + 0.1e^{-D/2} \tag{6.10}$$

The function is plotted in Figure 6.20b. The large full circles show experimental values.

The increase in the intershell spacing with decreased nanotube diameter is attributed to the high shell curvature of small diameter tubes and it has also been suggested that polygonization of the tube cross section will occur for inner tube diameters larger than ~12 nm (see Figure 6.16c). This observation is in agreement with the model suggested by Zhang et al.[110]

Furthermore, it has also been proposed that multiwall nanotubes most likely consist of circular core shells and polygonal outer layers.[120] In their pioneering work on nanodiffraction from carbon nanotubes, Liu[104] and Cowley[105] noted a possibility that there might be some nanotubes with neither entirely polygonal nor fully cylindrical cross sections. Such tubes could be considered as a mixture of the two possible morphologies, with structure varying along the tube length and the shell diameter. A schematic illustrating this model, taking into account variations of intershell spacing, is given in Figure 6.20.

In order to obtain direct evidence of tube microstructure, there have been several cross-sectional TEM studies[121–124]. These studies were conducted on both carbon nanotubes produced by arc-discharge method and the tubes produced by a chemical vapor deposition. A large number of defects in CVD tubes is very common, and it is an intrinsic property of the CVD process and, therefore, will not be discussed further here. HRTEM images of the cross sections of tubes reveal their nested structure, but they do not confirm models proposed by Liu,[105] Zhang,[110] and others.[112,120] Instead, rather random dislocation lines extending radially have been recorded.[121]

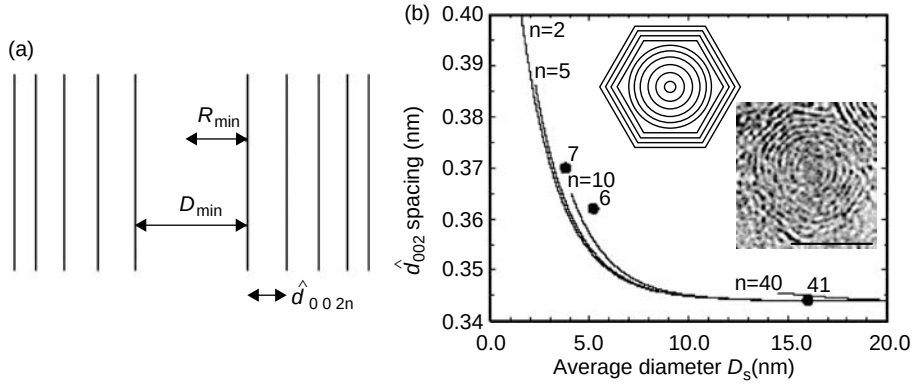

FIGURE 6.20 Effect of tube diameter on interplanar spacing. (a) Model for a nanotube crystal with a varying intershell spacing. (b) The *d* spacing is given an exponential function of tube diameter (Equation [6.10]). The intershell spacing *d* is plotted as a function of the average tube diameter (D_a), where *n* is the number of shells in a nanotube. The curves are calculated for $n = 2$, 5, 10, and 40, using the above model and Equation (6.10). The three data points shown by the large full circles were obtained based on experimental observations.[112] Insets: Model illustrating change of interplanar spacing *d* and polygonization of tube cross section with increase of tube diameter, as observed in some TEM micrographs. (TEM image: courtesy of S. Welz; scale bar, 5 nm).

Aside from their polygonal cross section, GPCs[42,115] possess another important feature that may affect their electrical, chemical, and mechanical properties to a great extent. This is the several nanometer thick loop-like layer (Figure 6.17c and inset in Figure 6.18a) formed by zipping of the adjacent graphitic shells at their terminations.[125,126] This phenomenon is also observed in edge planes of some high-temperature planar graphites,[125,127] and on the surfaces of cup-like multiwalled carbon nanotubes annealed in argon atmosphere above 900°C.[128] In the case of planar graphite, zipping of graphitic layers (also known as "lip–lip" interactions) forms nanotube-like sleeves, while in the case of multiwall nanotubes, the resulting structure resembles concentric polygonal hemitoroidal structures.[126] "Lip–lip" interactions are especially pronounced when samples are annealed at temperatures above 1600°C.[42,51,125,128–130] The reactive edge sites transform into stable multiloops through the elimination of dangling bonds due to enhanced carbon mobility at higher temperatures. Multiloops are typically built by 2 to 6 adjacent graphitic layers. Typically, single-loop structures are formed between 900 and 1200°C, while 1500°C is considered as the threshold for the formation of multilayer loops.[128] The radius of curvature of the outer layer is similar to the average radius of double-walled nanotubes.[131]

6.3.3 Properties and Applications

6.3.3.1 Electronic Band Structure

Electronic properties of cylindrical single- and multiwall carbon nanotubes have been widely studied both theoretically and experimentally over the past 15 years, and findings have been summarized in several books about carbon nanotubes,[71,132] as well as in Chapter 4 of the present Handbook.

Electronic structure of polygonal single-wall carbon nanotubes has been investigated theoretically within a tight-binding and *ab initio* frameworks,[133,134] and it has been found that polygonization changes the electronic band structure qualitatively and quantitatively. An example of a zigzag nanotube is given. Considered is the (10, 0) tube with: a circular (a) and pentagonal (b) cross section (Figure 6.21). The (10, 0) carbon nanotube with a circular cross section is a semiconductor, with a band gap of 0.82 eV. In calculating the band structure of a polygonal tube, it is reasonable to assume that the zones of strong curvatures near the edges of the polygonal tube will introduce a σ^*–π^* hybridization of carbon bonds. This local variation of bonding with strong sp^3 character in the folds creates a sort of defect line in the sp^2 carbon network.[135] In addition to the effect of bond hybridization, polygonization of the cross section lowers the symmetry from a ten- to a fivefold

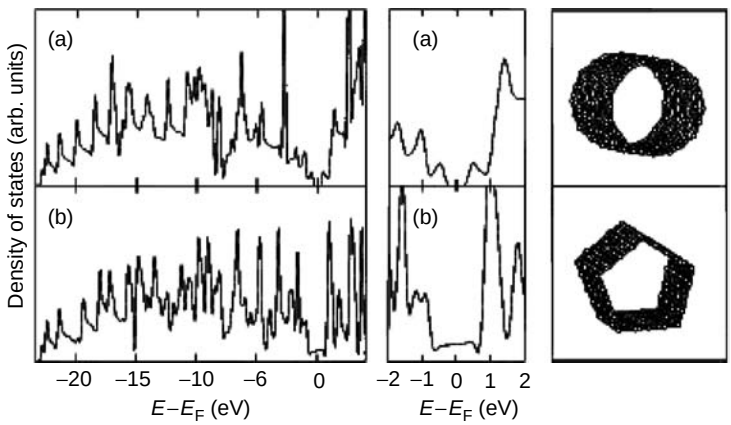

FIGURE 6.21 Tight-binding densities of states (states/eV/cell) for the (10, 0) cylindrical (a), and the (10, 0)[5] pentagonal (b) cross-section nanotubes. The Fermi level is positioned at zero energy. Both nanotubes are also represented in inset on the right of their respective DOS.[134]

axis. Furthermore, out-of-plane bending of the hexagonal carbon rings along the polygonal edges brings new pair of atoms closer than the second-neighbor distance in graphite. All this leads to the modification of the electronic band structure, and as a consequence, the semiconducting band gap of the (10, 0) polygonal tube is almost completely closed (Figure 6.21b). The *ab initio* calculations[134] confirm these tight-binding results and predict a gap of 0.08 eV for the pentagonal cross section. Electronic behavior of metallic armchair nanotubes is not so strongly altered with polygonization because the σ^*–π^* hybridization is not possible in the case of armchair configurations.

Theoretical studies also suggest that the perturbation of electronic properties of carbon nanotubes will be different for various degrees of polygonization (i.e., various numbers of facets).[134] An example is given for a (12, 0) nanotube. Zigzag (12, 0) nanotube of circular cross section is metallic. When different polygonal cross sections (triangle, square, and hexagon) are considered, the results indicate that all kinds of electronic properties arise (Figure 6.22). The first two cases are metallic, while the third is a 0.5 eV band gap semiconductor. It is important to remember here that these calculations are given for a carbon nanotube comprised of a single shell.

6.3.3.2 Raman Spectra

Vibrational properties of GPCs have been studied by means of Raman spectroscopy,[42,102,115] and it has been confirmed that they are highly graphitized structures with the extinct disorder-induced (D) band and the strong graphitic (G) band of about the same full-width at half-maximum (FWHM = 14 cm^{-1}) as in crystals of natural graphite.[136] The selective micro-Raman spectra from the crystal's side face and tip are shown in Figure 6.23. Spectra from the crystal faces correspond to perfect graphite with a narrow G band at 1580 cm^{-1}. In addition to 1580 cm^{-1} peak, the spectra from the tips feature a weak D band at 1352 cm^{-1}, and an unusually strong 2-D (2706 cm^{-1}) overtone that exceeds the intensity of the G band. A similar effect was observed on graphite scrolls (Figure 6.15). Raman spectra of GPCs contain two additional bands in the second-order frequency range at ca. 1895 and 2045 cm^{-1} (Figure 6.23). A number of weak low-frequency bands including a doublet at 184/192 cm^{-1} has been observed in some samples.[42] These low-frequency bands, typical for single-wall nanotubes,[137] may come from the innermost carbon nanotube shells protruding

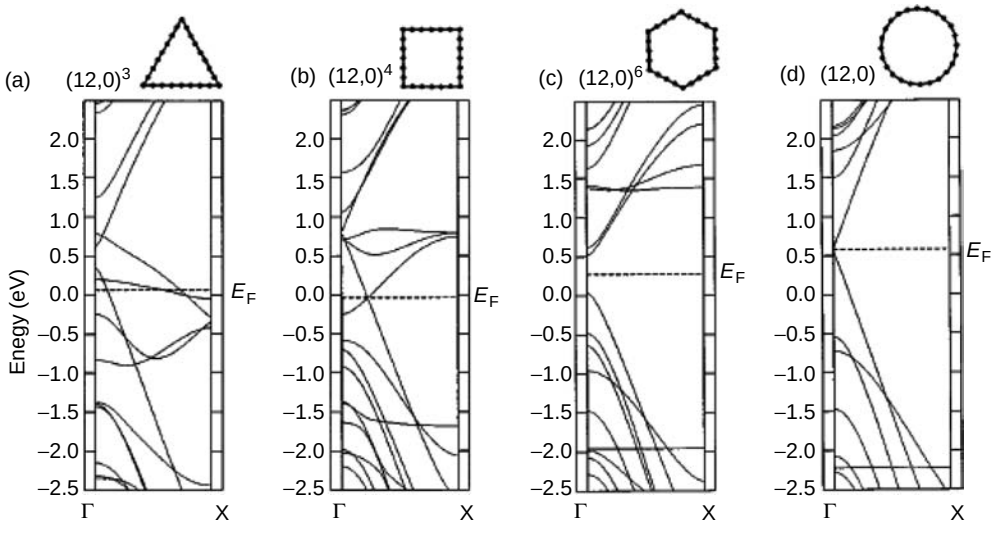

FIGURE 6.22 Tight-binding band structures of the metallic (12, 0) nanotube, illustrating the effect of the degree of polygonization of the cross section on electronic behavior. Given here are examples of (a) the triangle $(12, 0)^3$, (b) square $(12, 0)^4$, and (c) hexagonal $(12, 0)^6$ geometries that are compared to the pure cylinder case tube (d).[134]

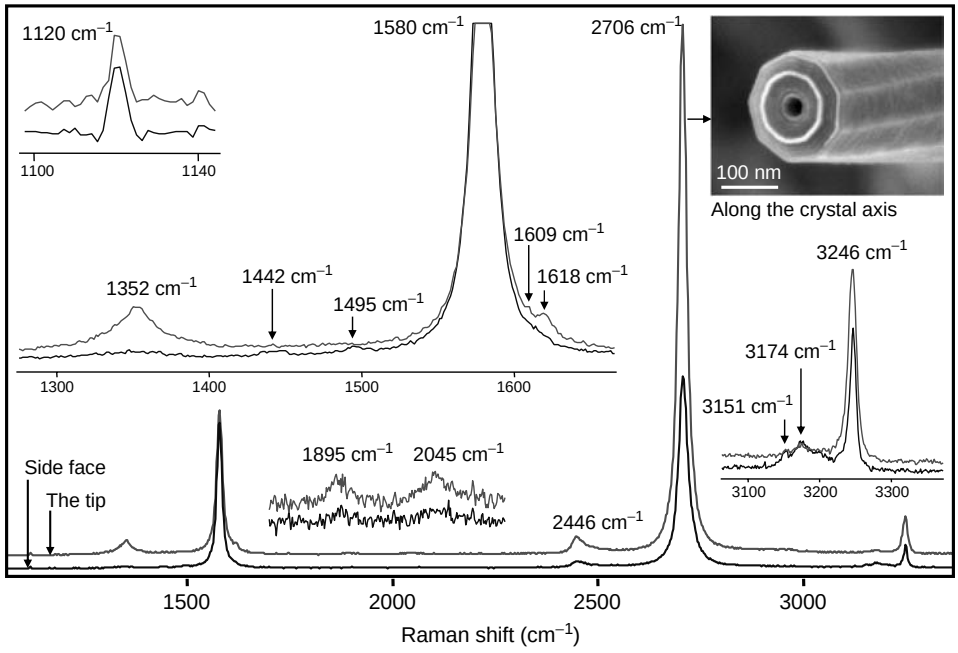

FIGURE 6.23 Fundamental modes, combination modes, and overtones in Raman spectra taken from the side face and the tip of an individual graphite polyhedral crystal (514.5 nm excitation). Inset: an SEM micrograph of a different crystal having structure similar to the one used to record Raman spectra.[102]

sometimes from the GPCs (see Figure 6.17b). Low-intensity bands are also present in the range 1440 to 1500 cm^{-1} (Figure 6.24), the origin of which has not been unambiguously determined yet.

6.3.3.3 Chemical, Thermal, and Mechanical Stability

Functionalization and chemical activity of carbon nanotubes is the subject of intensive study, and many breakthroughs have been made in this field over the past 5 years. Side walls of single-wall carbon nanotubes have been successfully functionalized with fluorine,[138] carboxylic acid groups,[139] isocyanate groups,[140] dichlorocarbene,[141] poly-methyl methacrylate,[142] and polystyrene.[143] Various functional groups have been attached to tube edge sites. This has made it possible to utilize carbon nanotubes and other tubular carbon materials in the fabrication of sorbents,[144] catalyst supports,[145,146] gas storage materials,[147] and polymer matrix composites.[148,149] The effect of polygonization on chemical behavior of carbon nanotubes has not been thoroughly investigated yet; however it is expected that polygonal tubes have chemical properties similar to those of circular multiwall carbon nanotubes and graphite, and that they may be more reactive (less stable) along the polygonal edges than in the extended near-planar regions.[120] Another interesting property of GPCs is polygonized hemitoroidal edge plane terminations.[150] Transformation of active sites into loops promotes the GPC into a more stable (or chemically inert) structure. Moreover, due to their specific spatial conformation, they allow for easier intercalation with foreign atoms such as lithium and others.[127,151]

Several methods have been utilized to probe the chemical activity of polygonal tubes. In one of them, GPCs were intercalated with 50:50 H_2SO_4/HNO_3 for 1 h, washed in deionized water, dried for 24 h and then exfoliated by rapid heating at about 980°C for about 15 sec or until maximum volume expansion is reached. GPCs survived very severe intercalation and exfoliation conditions, most of them retaining their original shape of faceted axial whiskers, although damage in the form of cracks along the axis and striations on the hemitoroidal surfaces was observed on most of the crystals.

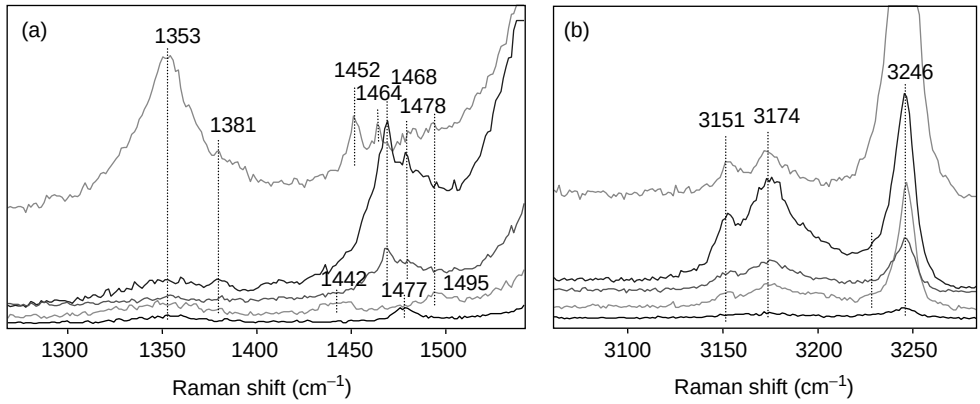

FIGURE 6.24 Raman spectra of graphite polyhedral crystals showing additional weak bands in the range: (a) 1400 to 1500 cm^{-1} and (b) 3100 to 3200 cm^{-1} (for 514.5 nm excitation).[102]

Corrosion studies of graphitic polyhedral crystals showed that exposure of GPCs to overheated steam at normal pressure for 1 h will cause their complete oxidation at temperatures between 600 and 700°C. Similarly, 700°C was determined as an onset temperature for oxidation in air. However, they were more stable than disordered glassy carbon in supercritical water.[42]

Polygonization of the cross section of a tube is not expected to significantlyaffect its tensile strength, nor should it drastically affect the bending modulus of the tube. However, for a helical polygonal multiwall nanotube, the pull-out strength is expected to be higher than in the case of its cylindrical counterpart, because of the more favorable stress distribution upon loading.

6.4 CONCLUSIONS

Extended growth of nanotubes or fullerene cones leads to formation of a myriad of nano- and microstructures, which are larger relatives of carbon nanotubes. Graphite cones and whiskers have much in common with carbon nanotubes and nanofibers. They inherit the conical structure of scrolled tubes (also known as "herring-bone" structure in carbon nanotubes). Seamless graphite nano- and microcones can have five different apex angles with "magic" numbers of 19.2, 38.9, 60.0, 83.6, and 112.9°, which correspond to 60, 120, 180, 240, and 300° disclinations in graphite. Scrolled conical structures may have virtually any apex angle, and very small (2 to 3°) angles have been observed. A few other specific values also occur more frequently as they are energetically preferred because they allow the registry between graphene sheets in the cone.

Polygonization of nanotubes accompanied by growth in the radial direction leads to the formation of GPCs. They have nanotube cores and graphite crystal faces. Unusual symmetries have been observed in GPCs. Most of them are built of co-axial graphite shells.

Cones and large nanotubes have been produced synthetically in the laboratory, and several methods for their synthesis are known. GPCs have only been discovered in synthetic carbon materials and can be grown by CVD or hydrothermally. However, since many natural graphites have been formed from hydrothermal deposits in nature, it would not be surprising to learn that GPCs exist in nature as well. Large carbon nanotubes have already been observed in natural deposits along with carbon cones.

Cones, whiskers, and GPC can bridge the nano- and microworlds and may have numerous applications, where sizes between nanotubes and carbon fibers are required. They may also have interesting electronic and mechanical properties determined by their geometry. However, while their structure has been well understood, very little is known about their properties. Properties need to be studied before their wide-scale applications can be explored.

ACKNOWLEDGMENT

This work was supported by the US Department of Energy grant DE-FJ02-01ER45932.

REFERENCES

1. B. T. Kelly, *Physics of Graphite*, Applied Science Publishers, London, 1981.
2. S. Iijima, *Nature*, 354, 56, 1991.
3. T. Tsuzuku, *Proceedings of the 3rd Conferene on Carbon*, Pergamon Press, University of Buffalo, New York, 1957, p. 433.
4. T. Tsuzuku, *J. Phys. Soc. Jpn.*, 12, 778, 1957.
5. S. Amelinckx, W. Luyten, T. Krekels, et al., *J. Cryst. Growth*, 121, 543, 1992.
6. M. Ge and K. Sattler, *Chem. Phys. Lett.*, 220, 192, 1994.
7. K. Sattler, *Carbon*, 33, 915, 1995.
8. A. Krishnan, E. Dujardin, M. M. J. Treacy, et al., *Nature*, 388, 451, 1997.
9. H. W. Kroto, J.R.Heath, S.C.O'Brien, et al., *Nature*, 318, 162, 1985.
10. S. Iijima, *MRS Bull.*, 19, 43, 1994.
11. R. Bacon, *J. Appl. Phys.*, 31, 283, 1960.
12. D. W. McKee, *Annu. Rev. Mater. Sci.*, 03, 195, 1973.
13. P. M. Ajayan, J. M. Nugent, R. W. Siegel, et al., *Nature*, 404, 243, 2000.
14. M. Hillert and N. Lange, *Z. Kristallogr. Kristallgeometrie Krystallphys. Kristallchem.*, 111, 24, 1958.
15. S. D. Robertson, *Carbon*, 8, 365, 1970.
16. P. L. J. Walker, J. F. Rakszawski, and G. R. Imperial, *J. Phys. Chem.* 63, 133, 1959.
17. M. L. Lieberman, C. R. Hills, and C. J. Miglionico, *Carbon*, 9, 633, 1971.
18. P. A. Tesner, E. Y. Robinovich, I. S. Rafalkes, et al., *Carbon*, 8, 435, 1970.
19. W. R. Davis, R. J. Slawson, and G. R. Rigby, *Trans. Br. Ceram. Soc.*, 56, 67, 1957.
20. A. Fonseca, K. Hernadi, P. Piedigrosso, et al., *Appl. Phys. A: Mater. Sci. Process.*, 67, 11, 1998.
21. H. B. Haanstra, W. F. Knippenberg, and G. Verspui, *J. Cryst. Growth*, 16, 71, 1972.
22. J. H. Knox, B. Kaur, and G. R. Millward, *J. Chromatogr.*, 352, 3, 1986.
23. J. Dong, W. Shen, B. Zhang, et al., *Carbon*, 39, 2325, 2001.
24. J. Dong, W. Shen, F. Kang, et al., *J. Cryst. Growth*, 245, 77, 2002.
25. P. T. B. Shaffer, *Plenum Press Handbooks of High-Temperature Materials No. 1 Materials Index*, Plenum Press, New York, 1964.
26. J. Gillot, W. Bollman, and B. Lux, *Carbon*, 6, 381, 1968.
27. D. D. Double and A. Hellawell, *Acta Metall.*, 22, 481, 1974.
28. S. Iijima, T. Ichihashi, and Y. Ando, *Nature*, 356, 776, 1992.
29. P. M. Ajayan, T. Ichihashi, and S. Iijima, *Chem. Phys. Lett.*, 202, 384, 1993.
30. P. M. Ajayan and S. Iijima, *Nature*, 358, 23, 1992.
31. T. W. Ebbesen, *Annu. Rev. Mater. Sci.*, 24, 235, 1994.
32. T. W. Ebbesen and T. Takada, *Carbon*, 33, 973, 1995.
33. A. L. Mackay and H. Terrones, *Nature*, 352, 762, 1991.
34. H. Terrones and A. L. Mackay, *Carbon*, 30, 1251, 1992.
35. B. I. Dunlap, *Phys. Rev. B.*, 46, 1933, 1992.
36. W. Luyten, T. Krekels, S. Amelinckx, et al., *Ultramicroscopy*, 49, 123, 1993.
37. S. Amelinckx, A. Lucas, and P. Lambin, *Rep. Prog. Phys.*, 62, 1471, 1999.
38. H. P. Boehm, *Carbon*, 35, 581, 1997.
39. G. R. Millward and D. A. Jefferson, in *Chemistry and Physics of Carbon*, Vol. 14, P. L. J. Walker and P. A. Thrower, Eds., Dekker, New York, 1978, p. 1.
40. S. Dimovski, J. Libera, and Y. Gogotsi, *Mat. Res. Soc. Symp. Proc.*, 706, Z6.27.1, 2002.
41. Y. Gogotsi, S. Dimovski, and J. A. Libera, *Carbon*, 40, 2263, 2002.
42. Y. Gogotsi, J. A. Libera, N. Kalashinkov, et al., *Science*, 290, 2000.
43. N. Muradov and A. Schwitter, *Nano Lett.*, 2, 673, 2002.
44. J. Liu, W. Lin, X. Chen, et al., *Carbon*, 42, 669, 2004.
45. S. F. Braga, V. R. Coluci, S. B. Legoas, et al., *Nano Lett.*, 4, 881, 2004.
46. L. M. Viculis, J. J. Mack, and R. B. Kaner, *Science*, 299, 1361, 2003.

47. N. M. Rodriguez, A. Chambers, and R. T. K. Baker, *Langmuir*, 11, 3862, 1995.
48. V. I. Merkulov, A. V. Melechko, M. A. Guillorn, et al., *Chem. Phys. Lett.*, 350, 381, 2001.
49. V. I. Merkulov, M. A. Guillorn, D. H. Lowndes, et al., *Appl., Phys., Lett*., 79, 1178, 2001.
50. H. Terrones, T. Hayashi, M. Muños-Navia, et al., *Chem. Phys. Lett.*, 343, 241, 2001.
51. M. Endo, Y. A. Kim, T. Hayashi, et al., *Appl. Phys. Lett.*, 80, 1267, 2002.
52. G. Y. Zhang, X. Jiang, and E. G. Wang, *Science*, 300, 472, 2003.
53. Y. Hayashi, T. Tokunaga, T. Soga, et al., *Appl. Phys. Lett*., 84, 2886, 2004.
54. R. C. Mani, X. Li, M. K. Sunkara, et al., *Nano Lett.*, 3, 671, 2003.
55. P. Liu, Y. W. Zhang, and C. Lu, *Appl. Phys. Lett.*, 85, 1778, 2004.
56. Z. F. Ren, Z. P. Huang, D. Z. Wang, et al., *Appl. Phys. Lett.*, 75, 1086, 1999.
57. Q. Yang, C. Xiao, W. Chen, et al., *Diamond Relat. Mater.*, 13, 433, 2004.
58. H. Lim, H. Jung, and S.-K. Joo, *Microelectron. Eng.*, 69, 81, 2003.
59. Y. K. Yap, J. Menda, L. K. Vanga, et al., *Mat. Res. Soc. Symp. Proc.*, 821, P3.7.1, 2004.
60. A. R. Patel and S. V. Deshapande, *Carbon*, 8, 242, 1970.
61. J. A. Jaszczak, G. W. Robinson, S. Dimovski, et al., *Carbon*, 41, 2085, 2003.
62. S. Dimovski, J. A. Jaszczak, G. W. Robinson, et al. Extended Abstracts of Carbon 2004, Biennial Conference on Carbon, American Carbon Society, RI, 2004.
63. J. A. Jaszczak, in *Mesomolecules: From Molecules to Materials*, G. D. Mendenhall, A. Greenberg, and J. F. Liebman, Eds., Chapman & Hall, New York, 1995, p. 161.
64. V. N. Kvasnitsa and V. G. Yatsenko, *Mineralogicheskii Zh.*, 13, 95, 1991.
65. V. G. Kvasnitsa, V. N. Yatsenko, and V. M. Zagnitko, *Mineralogicheskii Zh.*, 20, 34, 1998.
66. C. Lemanski, *Picking Table*, 32, 1, 1991.
67. B. A. Van der Pluijm and K. A. Carlson, *Geology*, 17, 161, 1989.
68. Carlson, B. A. Van der Pluijm, and S. Hanmer, *Geol. Soc. Am. Bull.*, 102, 174, 1990.
69. J. A. Jaszczak and G. W. Robinson, *Rocks Miner.*, 75, 172, 2000.
70. S. N. Britvin, G. U. Ivanyuk, and V. N. Yakovenchuk, *World of Stones*, 5/6, 26, 1995.
71. P. J. F. Harris, *Carbon Nanotubes and Related Structures*, Cambridge University Press, Cambridge, 1999.
72. E. A. Lord and C. B. Wilson, *The Mathematical Description of Shape and Form*, Halsted Press, New York, 1984.
73. S. Ihara, S. Itoh, K. Akagi, et al., *Phys. Rev. B*, 54, 14713, 1996.
74. M. Endo, K. Takeuchi, K. Kobori, et al., *Carbon*, 33, 873, 1995.
75. J. R. Dias, *Carbon*, 22, 107, 1984.
76. A. T. Balaban, D. J. Klein, and X. Liu, *Carbon*, 32, 357, 1994.
77. D. J. Klein, *Phys. Chem. Chem. Phys.*, 4, 2099, 2002.
78. D. J. Klein, *Intl. J. Quantum Chem.*, 95, 600, 2003.
79. K. Kobayashi, *Phys. Rev. B*, 61, 8496, 2000.
80. Mizes and J. S. Foster, *Science*, 244, 559, 1989.
81. R. Tamura, K. Akagi, M. Tsukada, et al., *Phys. Rev. B*, 56, 1404, 1997.
82. R. Tamura and M. Tsukada, *Phys. Rev. B*, 52, 6015, 1995.
83. R. Tamura and M. Tsukada, *Phys. Rev. B*, 49, 7697, 1994.
84. D. L. Carroll, P. Redlich, P. M. Ajayan, et al., *Phys. Rev. Lett.*, 78, 2811, 1997.
85. B. I. Dunlap, *Phys. Rev. B*, 49, 5643, 1994.
86. J. W. Mintmire, B. I. Dunlap, and C. T. White, *Phys. Rev. Lett.*, 68, 631, 1992.
87. R. Saito, M. Fujita, G. Dresselhaus, et al., *Phys. Rev. B*, 46, 1804, 1992.
88. J.-C. Charlier and J.-P. Issi, *Appl. Phys. A: Mater. Sci. Process*, 67, 79, 1998.
89. J. W. G. Wilder, L. C. Venema, A. G. Rinzler, et al., *Nature*, 391, 1998.
90. J. C. Charlier, T. W. Ebbesen, and P. Lambin, *Phys. Rev. B*, 53, 11108, 1996.
91. S. Berber, Y.-K. Kwon, and D. Tománek, *Phys. Rev. B*, 62, 2291, 2000.
92. R. Vidano and D. B. Fischbach, *J. Am. Cer. Soc.*, 61, 13, 1978.
93. P. Lespade, R. Al-Jishi, and M. S. Dresselhaus, *Carbon*, 20, 427, 1982.
94. G. Katagiri, H. Ishida, and A. Ishitani, *Carbon*, 26, 565, 1988.
95. Y. Kawashima and G. Katagiri, *Phys. Rev. B*, 52, 10053, 1995.
96. G. G. Samsonidze, R. Saito, A. Jorio, et al., *Phys. Rev. Lett.*, 90, 027403, 2003.
97. F. Tuinstra and J. L. Koenig, *J. Chem. Phys.*, 53, 1126, 1970.
98. R. J. Nemanich and S. A. Solin, *Phys. Rev. B*, 20, 392, 1979.
99. P. H. Tan, Y. M. Deng, and Q. Zhao, *Phys. Rev. B*, 58, 5435, 1998.

100. P. H. Tan, C. Y. Hu, J. Dong, et al., *Phys. Rev. B*, 6421, 214301, 2001.
101. J. Dong, W. C. Shen, and B. Tatarchuk, *Appl. Phys. Lett.*, 80, 3733, 2002.
102. P. H. Tan, S. Dimovski, and Y. Gogotsi, *Phil. Trans. Royal Soc. Lond. A*, 362, 2289, 2004.
103. Thomsen, C. and Reich, S. *Phys. Rev. Lett.*, 85, 5214, 2000.
104. M. Q. Liu and J. M. Cowley, *Mater. Sci. Eng. A*, 185, 131, 1994.
105. M. Liu and J. M. Cowley, *Ultramicroscopy*, 53, 333, 1994.
106. S. Amelinckx, D. Bernaerts, X. B. Zhang, et al., *Science*, 267, 1334, 1995.
107. N. G. Chopra, L. X. Benedict, V. H. Crespi, et al., *Nature*, 377, 135, 1995.
108. M. Liu and J. M. Cowley, *Carbon*, 32, 393, 1994.
109. J. S. Speck, M. Endo, and M. S. Dresselhaus, *J. Cryst. Growth*, 94, 834, 1989.
110. X. F. Zhang, X. B. Zhang, G. Van Tendeloo, et al., *J. Cryst. Growth*, 130, 368, 1993.
111. W. Kratschmer, L. D. Lamb, K. Fostriopoulos, et al., *Nature*, 347, 354, 1990.
112. C.-H. Kiang, M. Endo, P. M. Ajayan, et al., *Phys. Rev. Lett.*, 81, 1869, 1998.
113. Y. Saito, T. Yoshikawa, S. Bandow, et al., *Phys. Rev. B*, 48, 1907, 1993.
114. M. Bretz, B. G. Demczyk, and L. Zhang, *J. Cryst. Growth*, 141, 304, 1994.
115. H. Okuno, A. Palnichenko, J.-F. Despres, et al., *Carbon*, 43, 692, 2005.
116. J. M. Calderon-Moreno and M. Yoshimura, *Mater. Trans.*, 42, 1681, 2001.
117. J. M. Calderon Moreno and M. Yoshimura, *J. Am. Chem. Soc.*, 123, 741, 2001.
118. S. Iijima, *J. Cryst. Growth*, 50, 675, 1980.
119. D. Ugarte, *Nature*, 359, 707, 1992.
120. Y. Maniwa, R. Fujiwara, H. Kira, et al., *Phys. Rev. B*, 64, 073105, 2001.
121. L. A. Bursill, P. Ju-Lin, and F. Xu-Dong, *Philos. Mag. A* (*Phys. Condens. Matter, Defects Mech. Prop.*), 71, 1161, 1995.
122. S. Q. Feng, D. P. Yu, G. Hub, et al., *J. Phys. Chem. Solids*, 58, 1887, 1997.
123. G. Hu, X. F. Zhang, D. P. Yu, et al., *Solid State Commun.*, 98, 547, 1996.
124. J.-B. Park, Y.-S. Cho, S.-Y. Hong, et al., *Thin Solid Films*, 415, 78, 2002.
125. S. V. Rotkin and Y. Gogotsi, *Mater. Res. Innovations*, 5, 191, 2002.
126. A. Sarkar, H. W. Kroto, and M. Endo, *Carbon*, 33, 51, 1995.
127. K. Moriguchi, Y. Itoh, S. Munetoh, et al., *Phys. B: Condens. Matter*, 323, 127, 2002.
128. M. Endo, B. J. Lee, Y. A. Kim, et al., *New J. Phys.*, 5, 121.1, 2003.
129. H. Murayama and T. Maeda, *Nature*, 345, 791, 1990.
130. M. Endo, Y. A. Kim, T. Hayashi, et al., *Carbon*, 41, 1941, 2003.
131. Z. Zhou, L. Ci, X. Chen, et al., *Carbon*, 41, 337, 2003.
132. M. S. Dresselhaus, G. Dresselhaus, and P. C. Eklund, *Science of Fullerenes and Carbon Nanotubes*, Academic Press, New York, 1996.
133. P. Lambin, A. A. Lucas, and J.-C. Charlier, *J. Phys. Chem. Solids*, 58, 1833, 1997.
134. J.-C. Charlier, P. Lambin, and T. W. Ebbesen, *Phys. Rev. B*, 54, R8377, 1996.
135. H. Hiura, T. W. Ebbesen, J. Fujita, et al., *Nature*, 367, 148, 1994.
136. K. Ray and R. L. McCreery, *Analyt. Chem.*, 69, 4680, 1997.
137. A. M. Rao, E. Richter, S. Bandow, et al., *Science*, 275, 187, 1997.
138. E. T. Mickelson, I. W. Chiang, J. L. Zimmerman, et al., *J. Phys. Chem. B*, 103, 4318, 1999.
139. J. Chen, M. A. Hamon, H. Hu, et al., *Science*, 282, 95, 1998.
140. C. Zhao, L. Ji, H. Liu, et al., *J. Solid State Chem.*, 177, 4394, 2004.
141. H. Hu, B. Zhao, M. A. Hamon, et al., *J. Am. Chem. Soc.*, 125, 14893, 2003.
142. H. Kong, C. Gao, and D. Yan, *J. Am. Chem. Soc.*, 126, 412, 2004.
143. G. Viswanathan, N. Chakrapani, H. Yang, et al., *J. Am. Chem. Soc.*, 125, 9258, 2003.
144. Y. Xu, J. W. Zondlo, H. O. Finklea, et al., *Fuel Process Technol.*, 68, 189, 2000.
145. J. Ma, C. Park, N. M. Rodriguez, et al., *J. Phys. Chem B*, 105, 11994, 2001.
146. M. Endo, Y. A. Kim, M. Ezaka, et al., *Nano Lett.*, 3, 723, 2003.
147. A. Chambers, C. Park, R. T. K. Baker, et al., *J. Phys. Chem. B*, 102, 4253, 1998.
148. R. Andrews and M. C. Weisenberger, *Curr. Opinion Solid State Mater. Sci.*, 8, 31, 2004.
149. V. Datsyuk, C. Guerret-Piecourt, S. Dagreou, et al., *Carbon*, 43, 873, 2005.
150. J. Han, *Chem. Phys. Lett.*, 282, 187, 1998.
151. K. Moriguchi, S. Munetoh, M. Abe, et al., *J. Appl. Phys.*, 88, 6369, 2000.

7 Nanocrystalline Diamond

Olga Shenderova and Gary McGuire
International Technology Center, Research Triangle Park,
North Carolina

CONTENTS

7.1 INTRODUCTION

The term "nanodiamond" is broadly used for a variety of diamond-based materials at the nanoscale (lengths in the scale of ~1 to 100 nm), including pure-phase diamond films, diamond particles, and their structural assemblies, such as loosely bound particle agglomerates or particles incorporated into other material matrices. The recently fabricated one-dimensional (1-D) diamond nanorods (DNR) and 2-D diamond nanoplates complete the set of possible dimensionalities of these structures. There is a special class of nanodiamond material called "ultrananocrystalline" diamonds (UNCD), the basic diamond constituents whose length is of the order of a few nanometers. They are called "ultra-nanocrystalline," to distinguish them from other diamond-based nanostructures with characteristic sizes above ~10 nm. Among UNCD materials, the most promising for nanotechnological applications in the immediate future are *UNCD particles* produced by detonation of carbon explosive materials (characteristic size of primary particles ~5 nm) developed in the former USSR in the 1960s, and pure-phase *UNCD films* produced by chemical vapor deposition (CVD) (characteristic size of grains 2 to 5 nm) recently developed in the Argon National Laboratory [1]. UNCD particles and films possess unique properties, and have different niche applications. These two technologically important materials have been the focus of several recent reviews [1–4], monographs [5–7], as well as recent nanodiamond conferences [8–10], and will be major topics of this chapter.

Methods for synthesizing diamond powder in the form of single particles with micro- and nanometer sizes were developed in the beginning of the 1960s by DuPont de Nemours (USA) and the product has been commercially available since the 1970s (Mypolex™). DuPont produced polycrystalline diamond particles up to 50 μm in size, using shock wave compression of carbon materials (graphite, carbon black) mixed with catalyst. The size of the primary grains in the polycrystalline particles is about 20 nm. Recently, the Mypolex polycrystalline diamond business has been acquired from DuPont by Microdiamant AG, Switzerland, a company specializing in the micron and submicron diamond market. The finest diamond fraction produced by milling followed by grading, encompasses the range of 0 to 50 nm with an average particle size of about 25 nm. In addition to Mypolex polycrystalline diamond, Microdiamant AG also provides the finest fractions of particles of size down to 0 to 50 nm processed from high-pressure high-temperature (HPHT) synthetic diamond (both mono- and polycrystalline) as well as from natural diamond powders. The commercialization of this nanodiamond material has matured and it has been in use for high-precision polishing applications for a long time. An approach for producing UNCD powder with a characteristic size of primary particles of ~5 nm is the conversion of carbon-containing explosive compounds into diamond during firing of explosives in hermetic tanks. Details on the fascinating history of the discovery of the UNCD particulate can be found in [3,5,11]. This method was initiated in Russia in the early 1960s, soon after DuPont's work on shock wave synthesis. A large-scale production foundry, "ALTAI," was founded in Russia in 1983 to commercialize the process of detonation diamond production in bulk quantities (of the order of tons of the product per year) [5]. According to a USSR government report (1989) on UNCD particulate production, the plan was to increase UNCD production by up to 250 million carats per year [5]. Presently, however, the production of detonation diamond by ALTAI is limited. Currently, there are several commercial centers in Russia, Ukraine, Byelorussia, Germany, Japan, and China, producing UNCD particulates by explosives detonation. Although discovered several decades ago, UNCD particles have become an object of keen interest outside of Russia only within the last few years [8,10] as the field of nanotechnology has developed.

While developed relatively recently [1] as compared to UNCD particles, UNCD films are close to successful commercialization. Their ultrananocrystallinity is the result of a new growth and nucleation mechanism, which uses argon-rich plasmas instead of the hydrogen-rich plasmas normally used to deposit microcrystalline diamond films. Ultrananocrystalline diamond films are superior in many ways to traditional microcrystalline diamond films: they are smooth, dense, pinhole-free, phase-pure, and can be deposited conformally on a wide variety of materials and high-aspect-ratio structures [1].

Diamonds with characteristic sizes encompassing several nanometers have also been synthesized by other methods, particularly by chlorination of carbides [12], ion irradiation of graphite [13], electron irradiation of carbon onions [14], and in the vapor phase in a substrate-free, low-pressure, microwave-plasma CVD reactor [15]. Astronomical observations suggest that as much as 10 to 20% of the interstellar carbon is in the form of nanodiamonds[16]. The questions of when and how a nanodiamond originates in the Cosmos remain open.

This chapter is organized as follows: After a short section on the carbon phase diagram at the nanoscale and theoretical predictions of nanodiamond stability, nanodiamond structures of different dimensionalities synthesized to date will be summarized. Next, the synthesis, properties, and applications of UNCD particles of detonation origin, which have been on the market in FSU countries for decades, UNCD films that possess very unique properties, and carbide-derived UNCD films that are distinct by the simplicity of their production, will be discussed in more detail. These UNCD materials are synthesized by completely different techniques and have rather different properties, providing each of them specific application niches.

7.2 STABILITY OF NANODIAMOND

It is well known that the most stable carbon phase on the macroscale is graphite and that diamond is metastable. The energy difference between the two phases is only 0.02 eV/atom. However, because

of the high activation barrier for a phase transition (~0.4 eV/atom), very high temperatures and pressures and the use of a catalyst are required to realize the phase transformation. At the nanoscale, however, the carbon phase diagram has to be re-considered by introducing in addition to pressure and temperature a third parameter — cluster size [17,18]. In the expressions for the Gibbs free energy per atom of a cluster of *n* atoms in a given phase, the surface energy contribution has to be added to the bulk free energy. Estimates of the displacement of phase equilibrium lines for small carbon particles containing several hundred to several tens of thousands of atoms have been made recently [17,18] (Figure 7.1a). The authors report better agreement with calculations for experimental shock

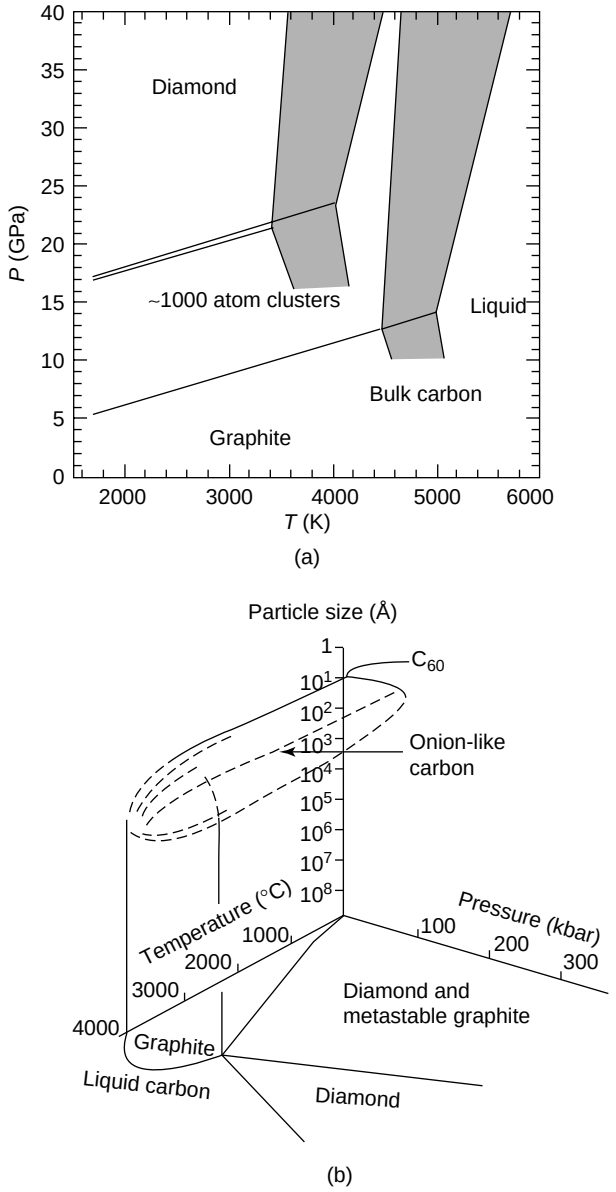

FIGURE 7.1 Approximate phase diagram for 1000 atom carbon cluster. Shadowed region corresponds to estimated uncertainties in location of equilibrium lines derived from available experimental data. Schematic three-dimensional phase diagram including fullerenes. (a: From Viecelli, J.A. and Ree, F.H., *J. Appl. Phys*., 88, 683–690, 2000; b: from Kuznetsov, V.L. et al., *Mater. Res. Soc. Proc*., 359, Pittsburgh, PA, 1995, 105. With permission.)

pressure–volume and temperature data using "nanocarbon phase diagram" than for those obtained with a bulk carbon equation of state. The results also suggest that carbon particles of the order of 10^3 to 10^4 atoms can exist in the liquid state at lower temperatures than bulk carbon. As a further extension of the carbon phase diagram, according to the fact that at sizes below 1.8 nm other carbon forms such as fullerenes and onions are abundant, it has been suggested to assign the corresponding region of the state diagram to fullerenes and onions [19], as shown schematically in Figure 7.1b.

However, analysis of the optimized geometries of the bare nanodiamond surfaces showed that the stability of nanocarbon species is quite complicated. Recent *ab initio* simulations demonstrate that within the size range of 1 [20–22] to 3 nm for spherical clusters [23]), the crystal morphology plays a very important role in cluster stability. While surfaces of cubic crystals exhibit structures similar to bulk diamonds, surfaces of octahedral, cuboctahedral, and spherical clusters show a transition from sp^3 to sp^2 bonding. The preferential exfoliation of the (1 1 1) surfaces begins for clusters in the subnanometer size range and promotes cluster transition to endo-fullerence for small clusters (~tens of atoms) and onion-like shells with diamond cores (buckydiamond) for larger clusters [20] (Figure 7.2b and Figure 7.3a). Recently, Barnard and colleagues included fullerenes, onions, and buckydiamonds in the "traditional" analysis of the relative stability of diamond and graphite at the nanoscale, and defined size regions of the stability of these structures [24]. According to the results in [24], as the system size for all-carbon structures is increased, the most stable carbon form at the nanoscale changes from fullerene — to onions — to buckydiamond — to nanodiamond — to graphite. The crossover from fullerenes to closed nanotubes has also been analyzed recently [25]. Regarding small carbon clusters, three regions of stability can be outlined [26]: below 20 atoms, the most stable geometries are one-dimensional ring clusters; between 20 and 28 atoms, clusters with quite different types of geometry have similar energetics; for larger clusters, fullerenes should be more stable. The hierarchy of the stabilities of carbon forms at the nanoscale is summarized in Figure 7.4. In general, for all-carbon nanostructures, it has been demonstrated by the highest level of sophistication computational approaches that nanodiamonds are more stable thermodynamically than graphite when the particle size is less than 5 to 10 nm in contrast to the macroscale where diamond is metastable. At the same time, computational methods indicate that nanodiamond stability is restricted by the smallest sizes of ~1.9 nm, below which fullerene-related structures are more stable.

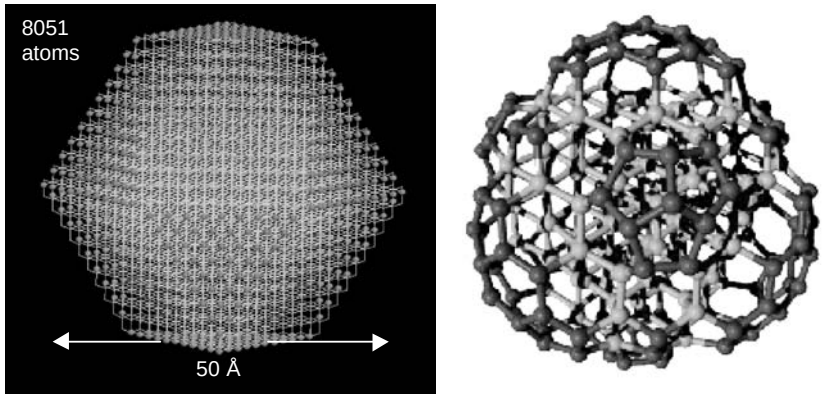

FIGURE 7.2 Structural models of nanodiamond clusters. Polyhedral (a) (cuboctahedron) shape with all four-coordinated carbon atoms can be preserved if cluster surface is terminated by hydrogen. Three- and two-coordinated atoms on the surface of the cuboctahedral cluster are orange and white colored, respectively. (b) Bare surface of nonhydrogenated diamond clusters experience surface reconstruction, resulting in a cluster with a diamond core and a fullerene-like shell. Red colored atoms are sp^2 carbon atoms. (b: Courtesy of Guilia Galli, Lawrence Livermore National Laboratory.)

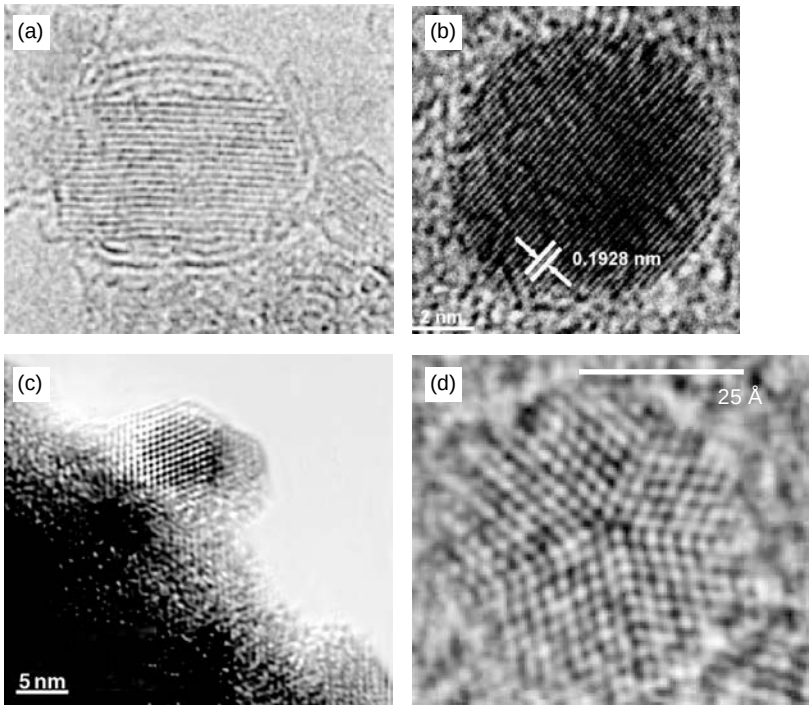

FIGURE 7.3 HRTEM images of a bucky-diamond formed from a UNCD particle of detonation origin (a), spherical diamond in a carbide matrix synthesized by carbide chlorination process (b), polyhedral particle of detonation UNCD (c), and a multiple twin particles of a presolar diamond (d). (Courtesy of T.L. Daulton, Naval Research Laboratory.) (a: From Kuznetsov, V.L. et al., *J. Appl. Phys*., 86, 863, 1999; b: from Welz, S. et al., *J. Appl. Phys.*, 93, 4207, 2003; c: from Tyler, T. et al., *Appl. Phys. Lett.*, 82, 2904, 2003. With permission.)

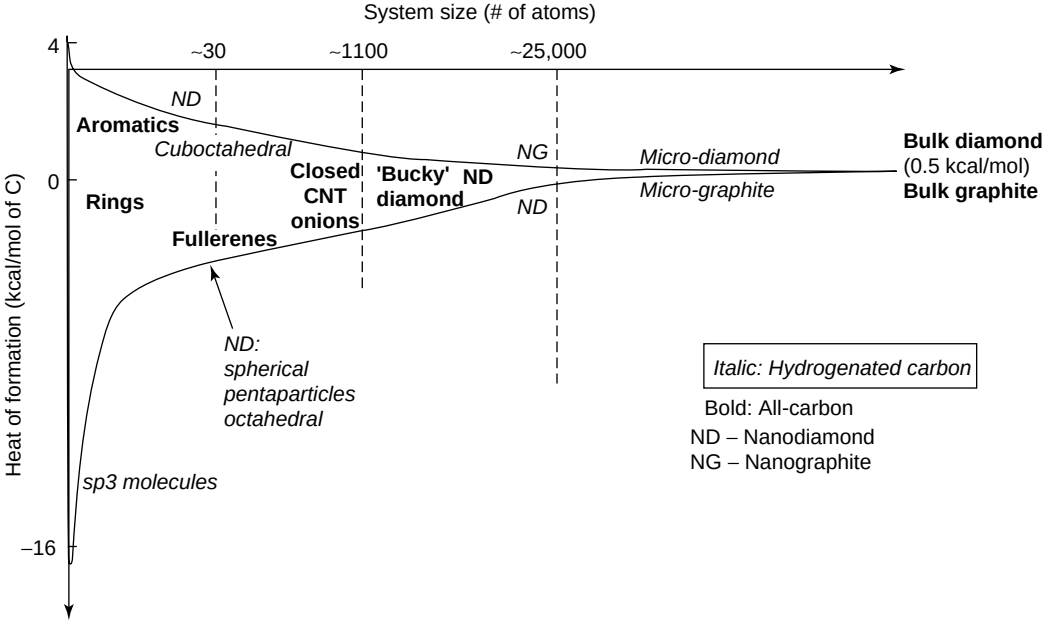

FIGURE 7.4 Schematic representation of the most stable carbon phase (all-carbon and hydrogenated species) depending on the size of the carbon structure.

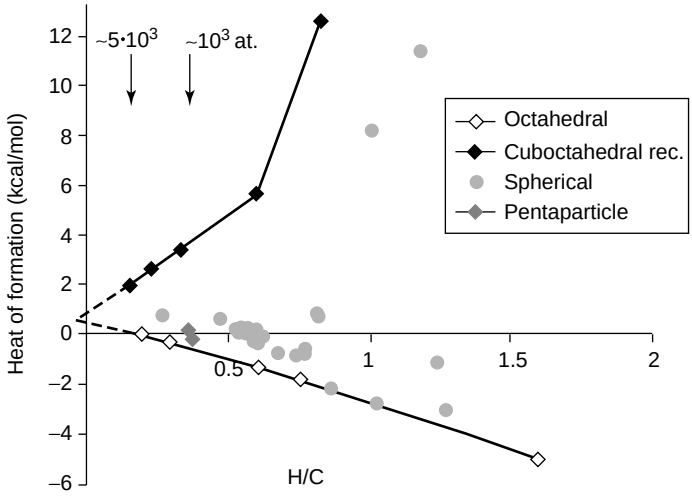

FIGURE 7.5 Heats of formation for hydrogenated octahedra, (0 0 1) 2 × 1 reconstructed cuboctahedra, spherical clusters, and two clusters with pentagonal shape.

The relative stability of different nanodiamond morphologies changes if one considers saturation of the dangling bonds on a particle surface by specific functional groups on an isolated particle surface, or on the interface between a UNCD particle and the surrounding matrix if a particle is incorporated into a matrix (as, for example, UNCD grains in CVD films, nanodiamond in agglomerates, etc.). Until recently, most of the experimental work dealing with nanodiamonds produced by means of detonation described the shape of clusters as being spherical. Figure 7.3b illustrates the perfect spherical shape of nanodiamond particles; in this case, a particle surrounded by carbide material during synthesis by a carbide chlorination process. However, high-resolution transmission electron microscopy (HRTEM) images of a single nanodiamond cluster on the surface of a Mo tip clearly indicate the presence of facets on the particle surface, with the cluster resembling a polyhedral shape (Figure 7.3c) [29]. In order to address the most stable shapes of the hydrogenated nanodiamond particles, heats of formation have been calculated for several nanodiamond series for particles relaxed with bond order potential [30]. Results of calculations for cuboctahedral, octahedral, spherical particles, and pentaparticles are illustrated in Figure 7.5. All of the series are bounded by curves corresponding to hydrogenated octahedra and (0 0 1) 2 × 1 reconstructed cuboctahedra. Extrapolated curves intersect the ordinate axis at a point corresponding to the heat of formation of bulk diamond (~0.5 kcal/mol). It can be concluded that the most stable morphologies for hydrogenated nanodiamond are octahedra, pentaparticles, and groups of spherical particles. Obviously, there are many more series of different nanodiamond morphologies that can be constructed, which, however, will probably be bound by the octahedra/(0 0 1) 2 × 1 reconstructed cuboctahedra curves. In combination with the above analysis on all-carbon clusters, the hierarchy of the stabilities of H-containing carbon forms at the nanoscale is summarized in Figure 7.4. The region of the relative stability of different forms of hydrogenated carbon is highlighted in order to emphasize the plurality of possible morphologies for nanodiamond particles that comprise this region as demonstrated above. To make the overall scheme more quantitative, all related simulations need to be done using the same computational approach (of *ab initio*) level.

7.3 TYPES OF NANODIAMOND AND METHODS OF THEIR SYNTHESIS

There are numerous reports on experimental observations of nanosized diamond, summarized in [3]. Reported methods of nanodiamond synthesis are very diverse, involving methods such as a

gas-phase nucleation at ambient pressure [15], chlorination of carbide material at moderate temperatures [12], HPHT graphite/nanocarbon transformation within a shock wave [31,32], and carbon condensation during explosive detonation [2].

The information on types of nanodiamonds is arranged below according to the dimensionality of the diamond constituents. We discuss systems of increasing complexity, beginning with the zero-dimensional structures in the form of isolated particles, going on to particles embedded within a matrix of another material, followed by recently synthesized exotic forms of 1-D and 2-D nanodiamond structures. Finally, three-dimensional assemblies of diamond nanocrystals grown as thin films or compacted from UNCD powder to preformed bulk shapes are reviewed.

7.3.1 Zero-Dimensional Nanodiamond Structures

We discuss below methods of synthesis of nanodiamond particles according to the characteristic sizes of the primary particles. We start with a discussion of nanocrystalline particles, followed by a discussion of UNCD, and then diamond molecules. Information on the characteristic sizes of commercially available isolated diamond particles is summarized in Figure 7.6.

Isolated nanodiamond particles with sizes of several tens of nanometers may be monocrystalline or polycrystalline (Figure 7.6). These are obtained by processing micron-sized diamond particles, which are, in turn, a by-product of natural diamond or HPHT diamond synthesis. Synthetic diamond with sizes below 50 μm represent the raw material for making micron and submicron diamond sizes. The processing of micron-sized diamond particles to smaller fractions includes the processes of milling, purification, and grading of the powder. Monocrystalline nanodiamond particles have rather sharp edges (Figure 7.6).

Polycrystalline nanodiamond powder (Figure 7.6) can be processed from micron-sized polycrystalline diamond particles obtained by shock synthesis [32] (Figure 7.6). Under suitable conditions, explosively produced shock waves can create high-pressure (~140 GPa) high-temperature conditions in confined volumes for a sufficient duration to achieve partial conversion of graphite into nanometer-sized diamond grains (~20 nm), which compact into micron-sized, polycrystalline particles (Figure 7.6). In order to avoid transformation of the diamond back to graphite, copper is mixed with graphite used in shock wave synthesis. This enables faster heat dissipation at the high temperatures that are reached during the explosion [5]. Polycrystalline diamond particles of micron size are more friable than monocrystalline diamond microparticles (natural or produced by HPHT), and are widely used in fine polishing applications. It is important to note that agglomerate-free suspensions of nanocrystalline diamond particles (for both mono- and polycrystalline forms) in water and oil have been developed [33]. Some recent studies have reported that low dynamic pressures up to 15 GPa are sufficient to produce diamond from ordered pyrolytic graphite (with voids between particles), using planar shock waves parallel to the basal plane of the graphite [34]. Diamond particles consisting of crystallites with grain sizes of several tens of nanometers have been observed by high-resolution electron microscopy (HREM) in postshock samples. There are several modifications of the shock wave process for diamond synthesis. Particularly, graphite (or other carbonaceous materials such as carbon black, and coal, etc.) can be loaded into explosives [35] vs. loading in a fixture, external to the explosives.

Primary particles of UNCD with characteristic sizes of about 5 nm (Figure 7.3 and Figure 7.6) are obtained by the detonation of solid explosives in an inert atmosphere. This class of nanodiamond material is technologically important since detonation UNCD can be produced in bulk quantities. The product obtained in detonation synthesis, called detonation soot, contains the diamond phase, which is separated from soot by chemical treatment. More details on synthesis of UNCD particles will be provided in Section 7.4.1. While it is possible to isolate the smallest UNCD particles, ~2 to 5 nm in size (Figure 7.3 and Figure 7.6), under laboratory conditions, in general, agglomeration of the particles remains one of the most serious problems in “true” nanotechnological applications. At the same time there are several very recent reports that suspensions of

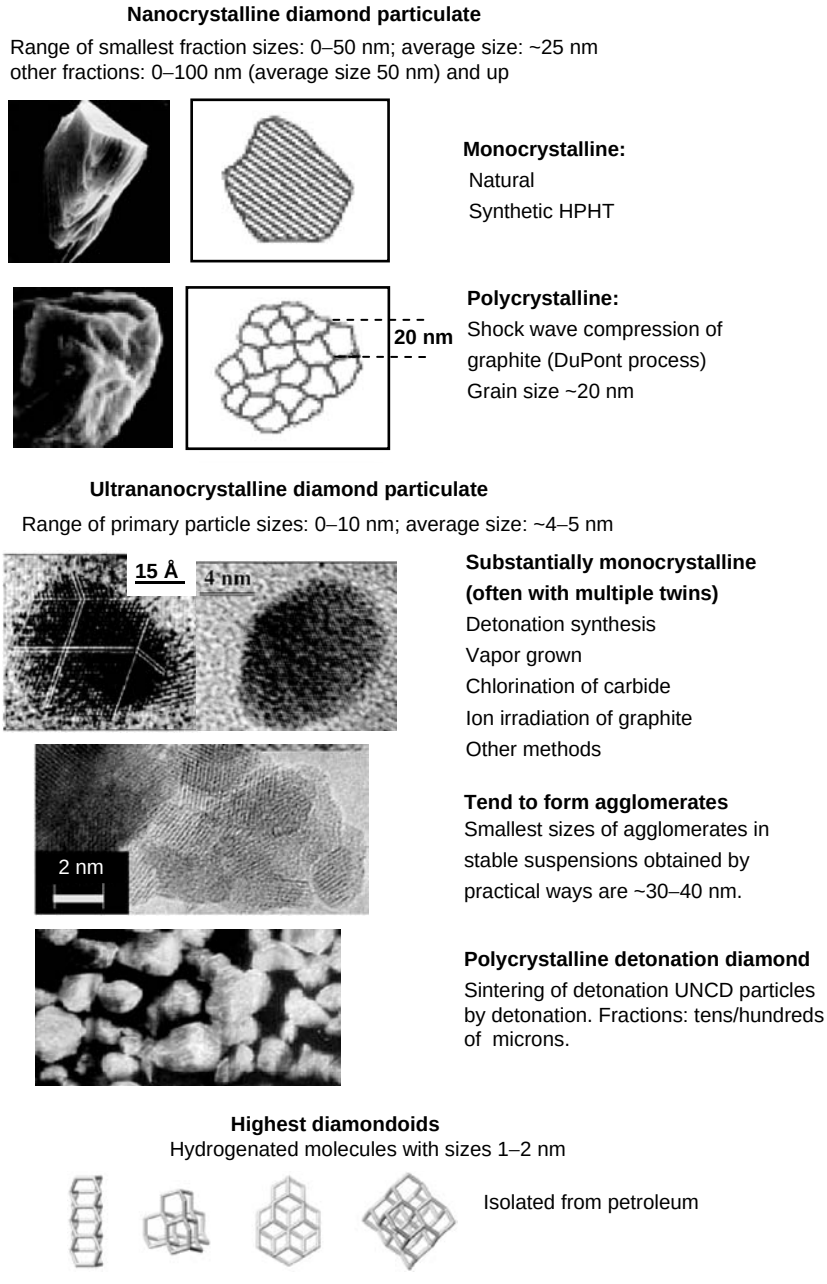

FIGURE 7.6 Summary of nanodiamond particles sizes and structures. (Pictures on nanocrystalline diamond are courtesy of Microdiamant AG, Switzerland. Pictures on UNCD single particles are courtesy of T.L. Daulton, Naval Research Laboratory. Picture of polycrystalline detonation diamond is courtesy of Alit, Kiev. Examples of higher diamondoids from petroleum, 1 to 2 nm hydrogen-terminated diamond molecules (left to right): rod-shaped [1 2 1 2] pentamantane $C_{26}H_{32}$, pyramid-shaped [1 (2, 3) 4] pentamantane $C_{26}H_{32}$, irregular disc-shaped [1 2 1 3 2 1] heptamantane $C_{30}H_{34}$, octahedral [1 2 3 1 2 4 1 (2) 3] decamantane $C_{35}H_{36}$. (Graphics courtesy of Chevron Texaco Molecular Diamond Technologies, Richmond, CA.)

detonation UNCD particles of sizes ranging from ten to several tens of nanometers have been developed [10]. Another interesting particulate material obtained from UNCD of detonation origin is micron-sized polycrystalline particles. This is obtained by detonation sintering using the initial UNCD powder (Figure 7.6) [7]. Owing to its more rounded form than Mypolex and monocrystalline diamond particles, this new type of diamond particulate is expected to have different niche applications [7].

Recently, a whole family of hydrogen-terminated diamond species, ~1 to ~2 nm size, has been discovered, literally filling the gap between adamantane molecules that are the smallest crystals of H-terminated cubic diamond containing only ten carbon atoms, and the wide plethora of UNCD particles with sizes more than 2 nm described above. These so-called higher diamondoids (number of crystal diamond cages more than 3) extracted from petroleum, are diamond molecules that are nanometer-sized rods, helices, discs, pyramids, etc. [36,37] (Figure 7.6). Their highly rigid, well-defined, and readily derivatizable structures make them valuable molecular building blocks for na otechnology. Certain higher diamondoids can now be produced in gram quantities and are available through Molecular Diamond Technologies, Inc., Richmond, CA. The exact mechanisms of the formation of these higher diamondoids in petroleum is still a mystery [37]. So far it has not been possible to synthesize higher diamondoids. Higher diamondoid molecules crystallize into a variety of crystal systems [36]. For example, depending on the isomer type, crystals of pentamantane can be orthorhombic, triclinic, or monoclinic. Rod-shaped [1 2 1 2] pentamantane molecules form orthorhombic crystals (Figure 7.7), in which they are aligned parallel to their long axis, perpendicular to their diamond (1 1 0) lattice faces [37].

In the above section different classes of commercially available nanodiamond particles were discussed. In the following section we will provide a brief overview of nanodiamond particles synthesized at the laboratory scale. In order to systemize the currently known methods of nanodiamond synthesis, a tentative scheme is suggested in Figure 7.8.

While a particular class of commercial nanodiamonds is obtained as a by-product of HPHT synthesis, there are laboratory studies of HPHT conversion of exotic carbon forms to nanodiamond. The HPHT process requires approximately 6 GPa pressure and 1500°C to convert graphite powder into diamond in the presence of a catalyst. Synthesis of diamonds starting from exotic precursor materials such as fullerenes [38] as well as carbon nanotubes [39] takes place at much

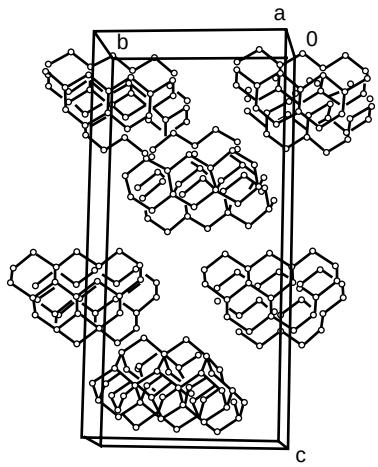

FIGURE 7.7 Higher diamondoids are diamond molecules that can be isolated in high purity and crystallized. Illustrated is the unit cell of [1 2 1 2] pentamantane determined by x-ray crystallography on a single orthorhombic crystal (space group $P2_12_12_1$). (Graphics courtesy of Chevron Texaco Molecular Diamond Technologies, Richmond, CA.)

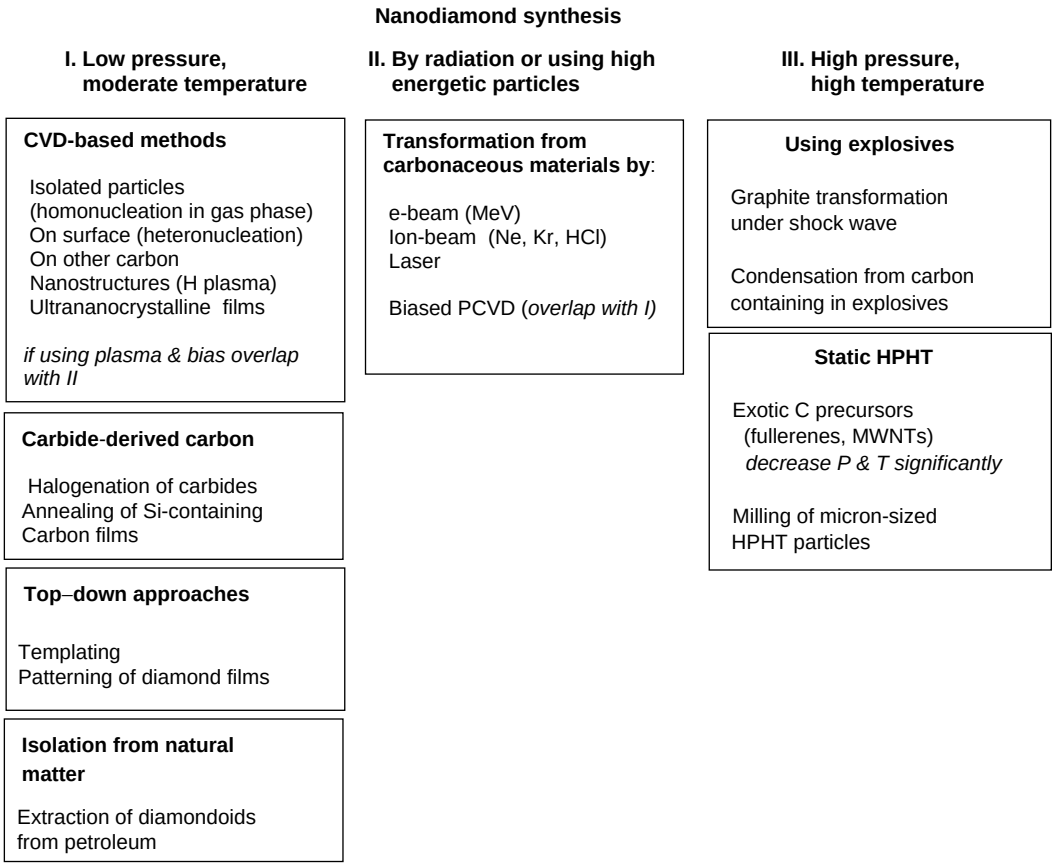

FIGURE 7.8 Tentative scheme summarizing methods of synthesis of diamond nanostructures.

lower temperatures and externally applied pressures as compared to graphite. For example, the transformation of buckyballs to diamond at high static pressure can be performed at room temperature and does not require a catalyst [38]. Another group of authors reported conversion of fullerenes into diamond under "moderate" conditions of 5.0 to 5.5 GPa and 1400°C [40]. Carbon nanotubes have been converted to diamond at 4.5 GPa and 1300°C using NiMnCo catalyst [39]. On the basis of HRTEM observations, the authors suggest that under HPHT conditions the tubular structures collapse and broken graphitic shells curl up and close into spheroidal networks to eliminate the dangling bonds at the edges. The high curvature of the nested graphitic shells formed, and cross-links between the layers in the onion-like structures that are formed, lead to an increased fraction of sp^3 bonds, which facilitates the formation of diamond.

We discuss below methods of nanodiamond synthesis based upon the CVD technique as well as methods using radiation and high energetic particles.Frenklach and coworkers [42] studied nucleation and growth of nanodiamond powder directly from the vapor phase in a substrate-free, low-pressure, microwave-plasma CVD reactor. The particles were collected downstream of the reaction zone on a filter within the tubular flow reactor, and subjected to wet oxidation to remove nondiamond carbon. Homogeneous diamond nucleation took place when dichloromethane–oxygen and trichloroethylene–oxygen mixture were used as source material. The particles formed had crystalline shapes with an average particle size around 50 nm. A mixture of diamond polytypes was observed in the powder.

Frenklach et al. [15] also studied the effects of heteroatom addition on the nucleation of solid carbon in a low-pressure plasma reactor. The addition of diborane (B_2H_6) resulted in substantial production of diamond particles, 5 to 450 nm in diameter, under the same conditions that show no diamond formation without the presence of diborane. The yield of oxidation-resistant powder produced in boron-containing mixtures was observed to be as high as 1.3 mg/h. It was found that nanodiamonds in the CVD residue have an abundance of linear twins and star-twin microstructures consistent with radial (isotropic) gas-phase growth conditions. Studies of diamond nucleation directly from an activated gas phase have important implications in revealing mechanisms of interstellar dust formation.

Another example of homogeneous diamond nucleation in the gas phase is laser-induced decomposition of C_2H_4 at low pressures and temperatures [43], which results in diamond powder formation with grain diameters of 6 nm to 18 μm. According to Buerki and Leutwyler [43], high-purity, homogeneously nucleated diamond nanoparticles had spherical and faceted morphology.

Another group of methods of nanodiamond formation include direct transformation of carbon solids to nanodiamond. Recent experiments have shown that heavy ion or electron irradiation induces nucleation of diamond crystallites inside concentric nested carbon fullerenes [14,44]. High-energy electron irradiation (1.2 MeV, $>10^{24}$ e/cm^2; ~100 dPa) was successfully used to convert the cores of concentric-shell graphitic onions into nanometer-size diamonds at irradiation temperatures above 900 K [14]. These experiments were performed *in situ* in an electron microscope, which allowed continuous observation of the formation process. A strong compression in the interior of the onion was inferred by the reduction observed in the spacing between adjacent concentric shells during irradiation. Ion beam irradiation of carbon solids also resulted in the formation of nanodiamond [44]. Irradiation with Ne^+ (3 MeV, 4×10^{19} cm^{-2}; ~600 dPa) at temperatures between 700 and 1100°C converted graphitic carbon soot into nanometer-size diamonds [44]. Again the diamonds were found to nucleate in the cores of graphitic onions that developed under irradiation. The increased diamond yield through this process as compared to e-beam irradiation is explained by the higher displacement cross section, the higher energy transfer, and the higher total beam current on the specimen. Other carbon materials can also be transformed to nanodiamond by using laser pulses, MeV electron, or ion beams. Nanodiamond particles have been synthesized from fine particles of carbon black exposed to intense laser irradiation [45]. Similarly, the transformation from carbon nanotubes to carbon onions and then to nanodiamond as a result of laser irradiation has been reported in [46]. Nanodiamond nucleation inside graphite occurs under ion irradiation at ambient temperature, when implanted with Kr^+ ions (350 MeV, 6×10^{12} cm^{-2}) [13]. The residue of the ion-irradiated graphite was found to contain nanodiamonds with an average diameter of 7.5 nm. Another example of nanodiamond formation includes irradiation of highly oriented pyrolytic graphite surfaces using a highly charged ion (HCI) [47]. In [41], multiwalled carbon nanotubes (MWCNT) were heated in a diamond anvil cell by a laser, above 17 GPa and 2500 K. The recovered product comprised of nanosized octahedral crystals (diamond) of less than 50 nm. The tubular structure completely changed to granular, and grain sizes corresponded to the diameter of nanotubes. The grain size of the diamond suggests that the transformation took place by direct conversion of nanotubes. This might provide a means to control diamond size by the choice of the multiwall (carbon) nanotubes (MWNT) size.

In contrast to the above works, transformation of spherical carbon onions to diamond by low-temperature heat treatment at 500°C in air without electron and ion irradiation has also been reported [48]. High-resolution transmission electron microscopy images showed that diamond particles, several tens of nanometers in diameter, co-exist with carbon onions after the heat treatment in air. From detailed HRTEM and electron energy-loss spectroscopy studies, the authors [48] suggest that sp^3 sites in the onions and the presence of oxygen during the heat treatment play important roles in transformation in the absence of irradiation.

Structural phase transformation from MWCNT to nanocrystalline diamond has been recently achieved by posttreatment of 20 to 40-nm-diameter MWCNT samples in hydrogen plasma. Nanocrystalline diamond particles with diameters ranging from 5 to 30 nm were embedded in an

amorphous matrix (Figure 7.9a). It was proposed that the diamond formation and growth mechanism were a consequence of the formation of sp^3-bonded amorphous carbon clusters. As discussed by Sun et al. [49], hydrogen chemisorption on the curved graphite network and energy deposition on carbon nanotubes by continuous impingement of activated molecular or atomic hydrogen are responsible for the formation of an amorphous carbon matrix. Similar to the role of hydrogen in conventional CVD diamond growth, hydrogen plasma etching prevents graphite formation in the thermally activated processes.

Nanodiamond nucleation in amorphous carbon films also takes place via the bias-enhanced CVD method, in which the substrate is negatively biased and exposed to CVD plasma. Diamond nuclei of 5 to 10 nm in diameter have been recently observed in amorphous carbon films grown using bias-enhanced CVD [50]. The authors suggested a general model for diamond nucleation by energetic species (for example, using bias-enhanced CVD or with direct ion beam bombardment). This processs involves spontaneous bulk nucleation of a diamond embryo cluster in a dense, amorphous carbon hydrogenated matrix; stabilization of the cluster by favorable boundary conditions of nucleation sites and hydrogen termination; and ion bombardment-induced growth through a preferential displacement mechanism. Formation of a dense amorphous hydrogenated carbon phase occurs via a subimplantation process, wherein energetic carbon, hydrocarbon, and hydrogen species bombard the surface and get incorporated into subsurface layers.

Finally, a new class of nanostructured carbon has been recently synthesized, in which nanodiamond particles form hybrid structures with singlewall (carbon) nanotubes (SWNTs) [51]. The deposition experiments have been carried out in a hot-filament CVD reactor equipped with an apparatus to allow the introduction of powder. The reactants were carbon powder (40 nm in diameter) and atomic H. The Si substrate was coated by submicron catalytic Fe particles that promoted initial growth of SWNTs. In the first stage of the growth sequence, aligned bundles of SWNT up to 15 μm long were formed, followed by synthesis at the outer parts of the SWNTs, of well-shaped diamond crystallites with diameters in the 20 to 100 nm range (Figure 7.9b). Terranova et al. [51] attribute the nanodiamond nucleation and growth to the presence of an unusually high concentration of atomic H.

7.3.2 One-Dimensional Nanodiamond Structures

First, aligned diamond whiskers were formed by a "top-down" approach by air plasma etching of polycrystalline diamond films, particularly of as-grown diamond films and films with molybdenum

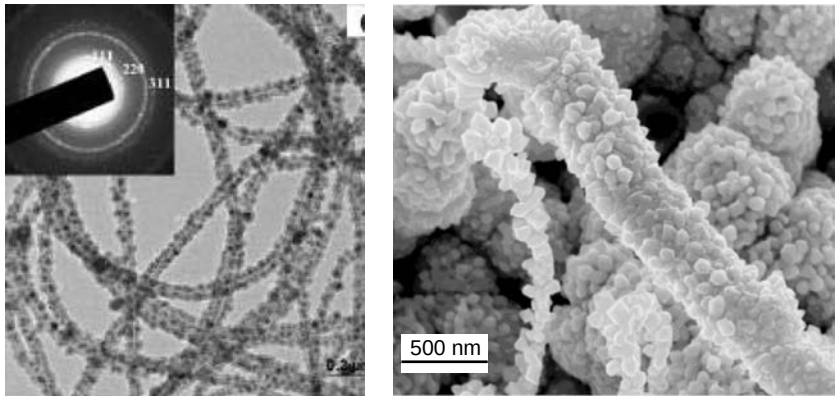

(a) (b)

FIGURE 7.9 (a) TEM image shows diamond crystallites embedded in amorphous carbon clusters and partial reservation of CNT hollow structure after hydrogen plasma-treated MWCNTs. (b) Nanodiamond–carbon nanotubes composites grown by CVD method. (a: From Sun, L.T. et al., *Appl. Phys. Lett.*, 84, 2901, 2004; b: from Terranova, M.L. et al., *Chem. Mater.*, 17, 3214, 2005. With permission.)

deposited as an etch-resistant mask [52] (Figure 7.10). In the case of the as-grown diamond films, nanowhiskers were found to form preferentially at the grain boundaries of diamond crystals. On dry etching of diamond films with preformed Mo deposits, well-aligned whiskers of 60 nm diameter were formed uniformly over the entire film surface with a density of 50 μm^{-2}.

Micron-diameter filaments formed by colloidal assemblies of UNCD particles have been observed in [53]. After extracting and drying, the filaments were similar to glass fibers, but no measurements of mechanical properties has been performed. Koscheev et al. [53] also succeeded in the synthesis of submicron-diameter filaments consisting of UNCD particles, obtained by laser ablation of pressed nanodiamond pellets. In contrast to dense filaments in colloids, every laser-ablated fiber is a network of nanoparticle chains (Figure 7.11). Studies of the elemental composition as well as the infrared (IR) and Raman spectra of filaments confirmed that they consist of the original nanoparticles, which still retained diamond structure. After extraction from the vacuum chamber, the whole assembly behaved like an aerogel. In both examples of UNCD-based filaments, the filament networks are rather tangled.

Polycrystalline diamond nanocylinders have been grown on anodic aluminum oxide templates using microwave plasma-assisted CVD and 50 nm nanodiamond particles as seeds [54]. Ordered 300 nm diamond nanocylinder arrays with cylinder lengths of about 5 mm are illustrated in Figure 7.12.

Most recently, monocrystalline diamond nanorods have been fabricated by Ando et al. [55] using reactive ion etching. The HPHT synthetic single-crystal diamond substrates with (1 0 0) and (1 1 0)-oriented surfaces were etched with oxide impurities acting as micro-masks; another mask set consisted of arrays of Al dots. Fabricated arrays of DNR were 50 to 200 nm in diameter and several microns in height (Figure 7.13).

Theoretical aspects of thermodynamic stability of DNR and preferable morphologies have been investigated by Barnard [56] and are summarized in a recent review. By first principle modeling of

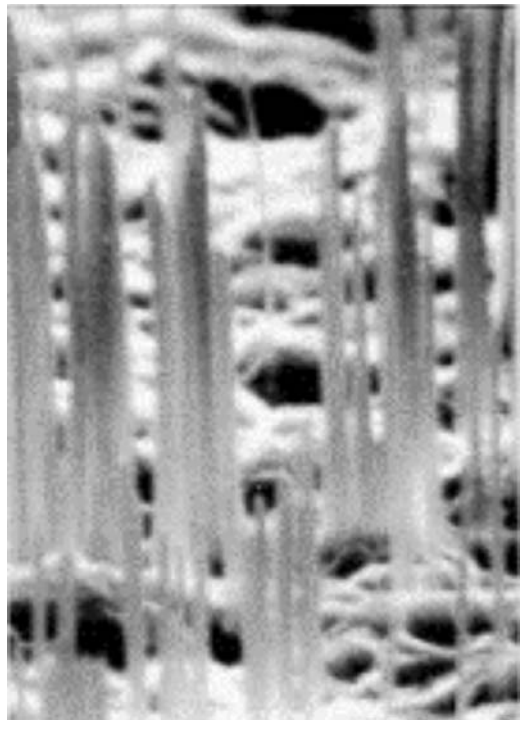

FIGURE 7.10 Magnified SEM micrograph of diamond nanowhiskers 60 nm in diameter (2.5 μm across the picture). (From Baik, E.S., *Thin Solid Films*, 377, 295, 2000. With permission.)

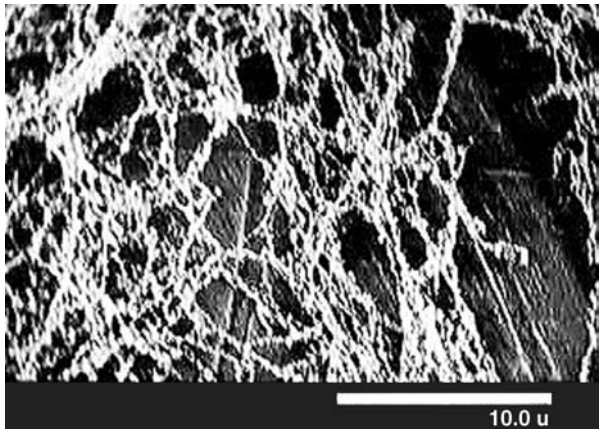

FIGURE 7.11 Diamond filaments obtained by laser ablation of pressed UNCD particle pellets. (Image courtesy of A. Koscheev.)

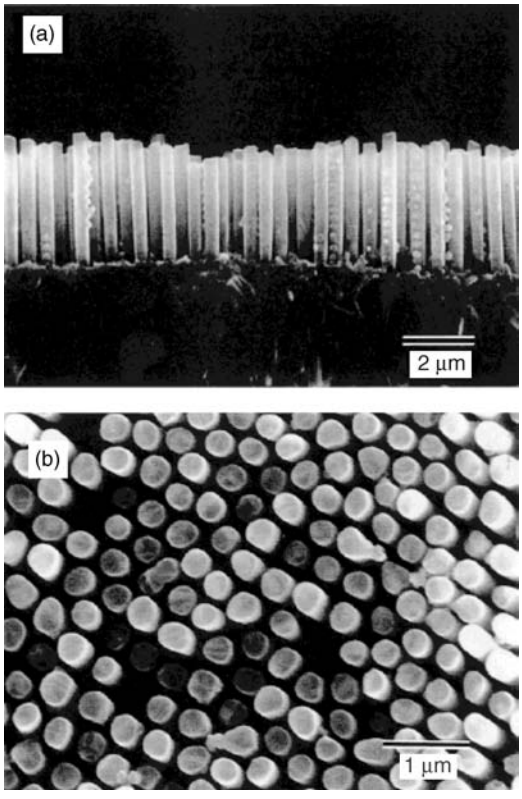

FIGURE 7.12 SEM micrographs of nanodiamond cylindrical structure. (a) Cross-sectional view of the diamond cylinder membrane after dissolving the alumina template. (b) Top view of the cylinder membrane. (From Masuda, H. et al., *Adv. Mater*., 13, 247, 2001. With permission.)

different DNR morphologies, the role of surface hydrogenation was emphasized for reliably obtaining DNR with structural properties analogous to bulk diamond. It was also theoretically predicted that the band gaps of DNR with diameters less than ~1.8 nm are significantly smaller than bulk diamond [57]. According to [57], DNR may be semimetallic or semiconducting depending on the

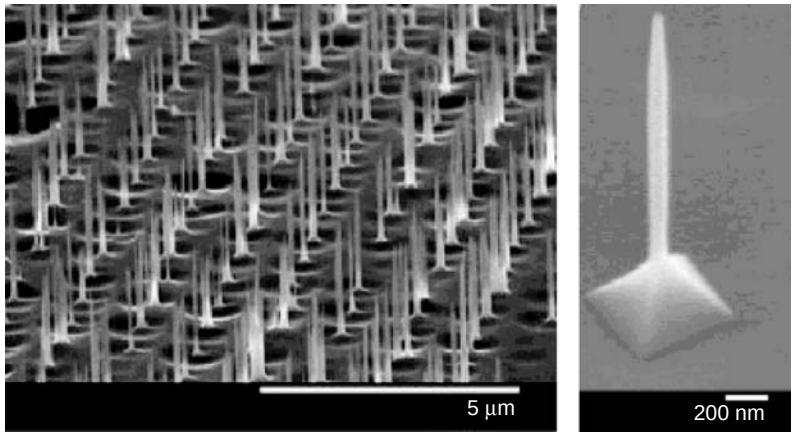

FIGURE 7.13 SEM micrographs of (a) array of diamond rods fabricated by reactive ion etching and (b) single nanorod. (From Ando, Y. et al., *Diam. Rel. Mater*., 13, 633, 2004. With permission.)

nanowire diameter, surface morphology, and degree of surface hydrogenation. Another theoretical prediction based on literature *ab initio* data [58] suggests that DNR would have a brittle fracture force and stiffness that exceeds that of carbon nanotubes for radii greater than ~1 to 3 nm, depending on the orientation of DNR. In general, it becomes evident that DNR represent an important and viable target structure for synthesis.

7.3.3 Two-Dimensional Nanodiamond Structures

Single-crystalline diamond nanoplatelets have recently been grown on polycrystalline diamond substrates [59] coated with a 100-nm-thick film of nickel before deposition. Deposition was carried out at a temperature above 1000°C in a microwave plasma CVD reactor using a 3% CH_4/H_2 gas mixture. Scanning electron microscope and transmission electron microscope (TEM) micrographs revealed that these nanoplatelets had regular shapes of triangles and parallelograms with well-faceted surfaces, their thickness ranging from 30 to 70 nm, and length from several hundred nanometers to a few micrometers (Figure 7.14). The edges of the platelets are along <1 1 0> directions, with top and bottom surfaces parallel to {1 1 1} planes. The platelet morphology suggests that they are formed by lateral growth, although the influence of Ni on the formation of diamond nanoplatelets is unknown [59]. This result, in combination with the results on growth of DNR discussed above, proves that the synthesis of single-crystalline nanodiamond of desired dimensionality has become a reality.

7.3.4 Three-Dimensional Nanodiamond Structures

Three types of three-dimensional UNCD structures that are currently being commercialized are UNCD films, carbide-derived diamond-structured carbon, and bulk sintered UNCD particles of detonation origin. The synthesis and applications of the former two materials will be discussed in more detail in Sections 7.5 and 7.6, respectively.

UNCD films with 2 to 5 nm grains has been synthesized in Argon National Laboratory by Gruen and colleagues [1,60,61], using a new plasma deposition process which utilizes a high content of noble gas. Ultrananocrystalline diamond films are superior in many ways to traditional microcrystalline diamond films: they are smooth, dense, pinhole-free, and phase-pure, and can be conformally coated on a wide variety of materials and high-aspect-ratio structures.

Recently, a method for the synthesis of diamond-structured carbon has been developed by Gogotsi et al. [12]. The method is based on extracting silicon from silicon carbide or metal carbide

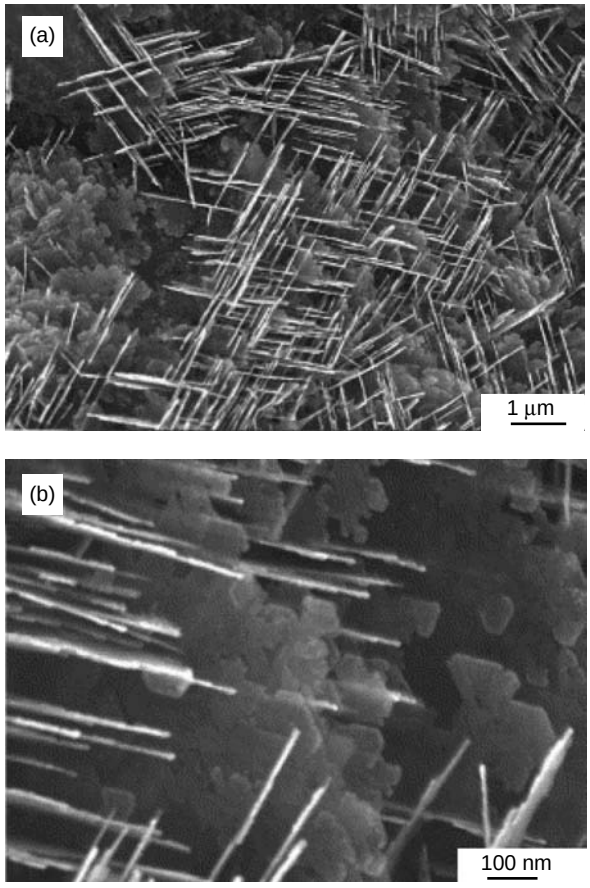

FIGURE 7.14 SEM micrographs of diamond nanoplatelets with different magnifications. (b) demonstrates that the thickness of platelets is approximately 30 nm. (From Chen, H. and Chang, L., *Diam. Rel. Mat.*, 13, 545, 2004. With permission.)

in chlorine-containing gases at ambient pressure and temperatures not exceeding 1000°C. Nanocrystalline diamonds with an average crystallite size of 5 nm are formed after extraction of silicon or metal from the carbide. Figure 7.3b demonstrates a diamond particle with an average size of 5 nm, embedded in an amorphous matrix formed during chlorination of TiC [28]; the absolutely round particle shape is worth noting. An amorphous carbon/nanodiamond structure has been recently produced in a similar way by annealing Si-containing carbon films [62]. Carbon and silicon were simultaneously evaporated on amorphous carbon substrates at room temperature in a vacuum of 10^{-4} Pa. Nanodiamond grains of 1.2 nm size were detected in the as-deposited Si-containing carbon film. Then the as-deposited films were heated at 400 to 800°C in a vacuum. At this stage, diamond grains of 5 to 30 nm size were grown depending on the annealing temperature. The growth of diamond and β-SiC were controllable by adjusting the heating temperature and the proportion of Si. The role of Si as a catalyst in this process was revealed; when Ge was substituted for Si, nanodiamond formation was not observed.

Another interesting bulk form of nanodiamond particles is the so-called nanodiamond composite [63], which consists of UNCD particles connected by a pyrocarbon matrix. The UNCD powder is placed in a container of a predetermined shape, and bonded together by pyrocarbon formed by means of methane decomposition through the entire volume of the diamond powder [63]. This material is characterized by a high porosity (50 to 70%) and demonstrates a relatively high Young's

modulus of 30 GPa. The reported pore size is not greater than 20 to 30 nm, with an average radius of 4.5 nm. Owing to the high density of nanopores, the material possesses a high sorption activity, particularly for large biomolecules (e.g., trypsin) [63]. The production of the material has been realized at Skeleton Technologies, Inc., Baar, Switzerland.

In summary, a rich plethora of new methods of nanodiamond synthesis have appeared within the last few years.

7.4 ULTRANANOCRYSTALLINE DIAMOND PARTICULATE PRODUCED BY EXPLOSIVE DETONATION

7.4.1 Synthesis and Properties

In the method of using energy from an explosion for diamond production, diamond clusters are formed from carbon atoms contained within explosive molecules themselves, so only the explosive material is used as a precursor material. A wide variety of explosive materials can be used. A typical explosive is a mixture of TNT (2-methyl-1,3,5-trinitrobenzene) and hexogen (in the proportion 60:40) composed of C, N, O, and H with a negative oxygen balance (i.e., with the oxygen content lower than the stoichiometric value), so that "excess" carbon is present in the system. A negative oxygen balance in the system is an important condition for UNCD formation. The explosion takes place in a nonoxidizing medium (Figure 7.15) of either gas (N_2, CO_2, Ar, or other medium that can be under pressure) or water (ice), called "dry" or "wet" synthesis respectively. The medium acts as a coolant. In order to prevent the UNCD formed in the detonation wave from transforming into graphite at the high temperature generated by the detonation, the cooling rate of the reaction products should be no less than 3000 K/min [5]. The initial shock from a detonator compresses the high-explosive material, heating it and causing chemical decomposition, thereby releasing enormous amounts of energy in a fraction of a microsecond (Figure 7.15). As the detonation wave propagates through the material it generates high temperatures (3000 to 4000 K) and high pressures (20 to 30 GPa) which correspond to the region of thermodynamic stability for diamond (Figure 7.16). During detonation, the free carbon coagulates into small clusters, which grow larger by diffusion [17,18]. The product of detonation synthesis,

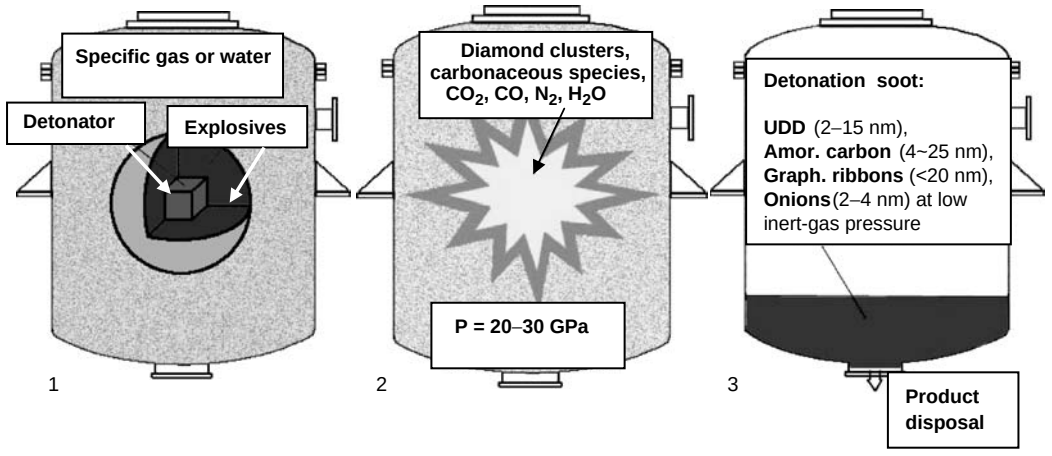

FIGURE 7.15 Schematic illustration of steps of controlled detonation synthesis of nanodiamond from carbon-containing explosives (1). During explosion, (2) the highly dispersed carbon medium condenses from free explosive carbon in a fraction of a microsecond. After disposal, the product has to undergo several stages of purification. Big industrial detonation reactors are able to deliver tons of detonation diamond per month. (Pictures are based on pictures of the detonation process. Courtesy of PlasmaChem GmbH, Mainz, Germany.)

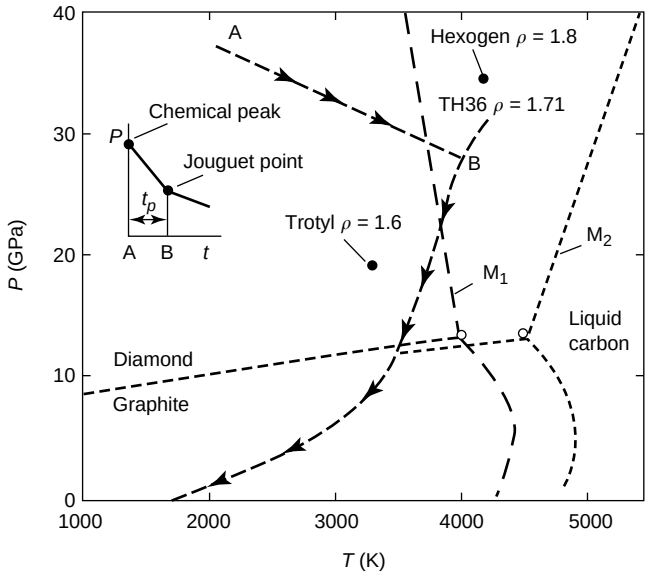

FIGURE 7.16 Phase diagram of carbon and explosives detonation process path. The inset illustrates the pressure profile in a detonation wave: A corresponds to the shock compression of the explosives (chemical peak), AB corresponds to decomposition of explosive molecules and condensation of free carbon to UNCD at pressures higher than 20 GPa; B represents termination of decomposition (the Jouguet point), and t_p the duration of decomposition. In the diagram, M_1 and M_2 are possible melting lines of carbon according to Danilenko [11], and ρ is density (in g/cm^3). (From Danilenko, V.V., *Phys. Solid State*, 46, 595, 2004. With permission.)

called detonation soot or diamond blend, contains 40 to 80 wt% of the diamond phase depending on the detonation conditions. The carbon yield is 4 to 10% of the explosive weight.

In general, there are two major technical requirements for UNCD synthesis using explosives: the composition of the explosives must provide the thermodynamic conditions for diamond formation, and the composition of gas atmosphere must provide the necessary quenching rate (by appropriate thermal capacity) to prevent diamond oxidation. The diamond yield depends to a large extent on the explosive mixture [17]. The shape of the explosive also influences the yield: the ideal shape is spherical but, for convenience, a cylindrical one is regularly used [5]. The relationship between the mass of the explosives and the mass of the surrounding media also influences the yield (for example, 5 kg of explosive requires a detonation chamber of ~11 m^3 with gas media at ambient pressure to provide the necessary quenching rate) [5].

In addition to UNCD, the diamond blend contains graphite-like structures (35 to 45 wt%), and incombustible impurities (metals and their oxides — 1 to 5 wt%) [2]. Using x-ray diffraction and small-angle x-ray scattering, it was shown that an UNCD cluster in detonation soot has a complex structure consisting of a diamond core of about 4.3 nm in size and a shell made up of sp^2-coordinated carbon atoms [64].

UNCD purification is performed by mechanical and chemical methods. After mechanical removal of process admixtures, the diamond-carbon powder is subjected, for example, to thermal oxidation with nitric acid under pressure to separate the diamond phase [2]. In this method, metals are dissolved and nondiamond carbon is oxidized simultaneously. The diamond needs to be flushed with water after separation from the acidic media. After purification typically, powders of UNCD can be considered as a composite consisting of different forms of carbon (80 to 89%), nitrogen (2 to 3%), hydrogen (0.5 to 1.5%), oxygen (up to 10%) and an incombustible residue (0.5 to 8%) [2]. The carbon phase consists of a mix of diamond (90 to 99%) and nondiamond carbon (1 to 10%). In general, methods of UNCD purification as well as UNCD purity vary from vendor to vendor.

The impurity content of nanodiamonds produced by detonation synthesis is higher when compared with other artificial diamonds (for instance, HPHT diamonds contain no less than 96% carbon). Commercial products of purification have the following grades: a water suspension of diamond and powder obtained from suspensions by drying and grinding of UNCD. To remove non-carbon impurities, the chemically purified product is subjected in some cases to additional purification using ion-exchange and membrane technologies.

In general, UNCD production consists of detonation synthesis, chemical purification and acid washing of UNCD, product conditioning, and modification of the diamond.

The properties of UNCD particles are mainly defined by their nanometer-scale sizes (4 to 6 nm in diameter), which are in the transitional size range between macromolecules and crystalline solids. Half of all atoms in such particles are on the surface, and therefore are unavoidably bound to adsorbed atoms, molecules, and functional groups. These adsorbed atoms, which may exceed the number of atoms in the diamond particle, can strongly affect the physical and chemical properties of the particles. Different functional groups, which in principle can be attached to the diamond surface or have been detected on UNCD particles surface, are schematically illustrated in Figure 7.17. To minimize surface energy, the primary UNCD particles with diameters of ~4 nm form larger clusters, 20 to 30 nm in size that, in their turn, form larger weakly bound aggregates (of an order of magnitude of hundreds of nanometers).

Reviews [2–4] summarize a wide variety of experimental data on UNCD powder characterization including x-ray, electronic, electron paramagnetic resonance (EPR), nuclear magnetic resonance (NMR), IR, Raman, Auger, photoluminescent spectra, results of HRTEM as well as results of other measurements. Table 7.1 shows selected properties of UNCD particulates. Note that these are collective properties of UNCD powders. Below in this section, we provide results related to the fundamental studies of electrical and electronic properties of UNCD particulates. Properties of detonation nanodiamonds related to practical aspects (e.g., purity of UNCD produced by different vendors, dispersivity, stability in suspensions, maximum concentration in stable suspensions, and controlled surface functionalization) can be found in [2,6,10,65].

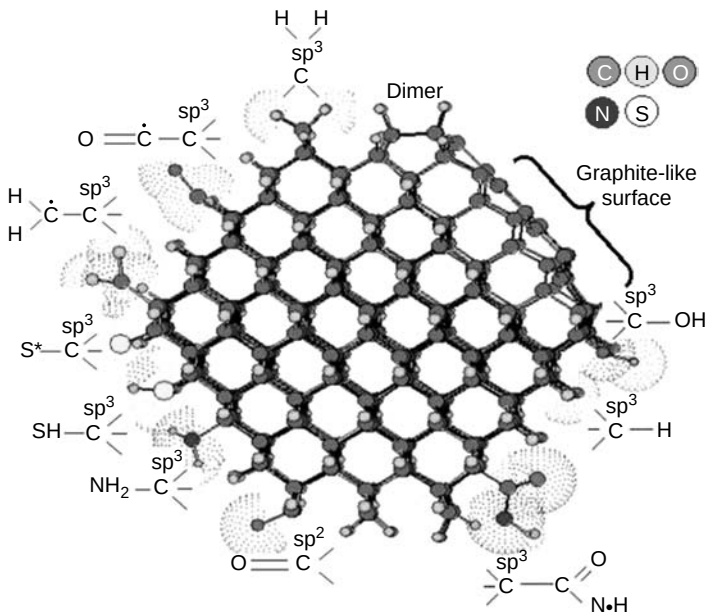

FIGURE 7.17 Schematic illustration of different functional groups on surface of UNCD particle detected after different purification/surface modification treatments. One of the facets corresponds to a buckydiamond structure. (Courtesy of O. Shenderova, I.V. Shugalei, and Y.V. Dolmatov.)

TABLE 7.1
Selected Properties of Ultradispersed Diamond Based on Refs. [2,10,63]

Structure	Cubic ($a = 0.3573 \pm 0.0005$ nm)
Density	3.30 g/cm^3
Crystal lattice parameter	0.3562 ± 0.0004 nm
Size of crystallites	2–10 nm
Average monocrystal size	4.3 nm
Size of smallest aggregates	20–50 nm
Specific surface area	300–400 m^2/g
Pore volume in powder	0.3–1 sm^3/g
Density of dislocations	1.8×10^{17}
Composition (at%)	C (90–100); O, N, H (0–10)
Incombustible impurities (wt%)	0.2–1.4 (Fe, Cr, Si, Al, Na, Cu, Ca, Mg, Mn, Ti)
Raman frequencies	1321–1322 cm^{-1}
Initial air oxidation temperature (depends on purity)	430°C
Initial vacuum graphitization temperature	1100–1200°C
Resistivity	$7.7 \times 10^9\ \Omega$ m
Electrophoretic surface charge	−78.44 mV
Refractive index	~2.55 (at $\lambda = 580$ nm)

The surface and electronic properties of nanometer-sized diamond particles have been studied by x-ray photoelectron spectroscopy (XPS) and UV photoelectron spectroscopy (UPS) [66]. In these experiments, nanodiamonds (NdO from Table 7.2) were deposited on Si(100) substrates by electrophoresis. According to XPS analysis, the UNCD powder did not contain any detectable impurities except nitrogen. The N content was estimated to be 1 to 2 at%. The as-deposited UNCD powder films showed a strong oxygen peak. After treatment in a hydrogen microwave plasma and transfer in air to the XPS system, the nanodiamond films were found to be almost free from oxygen contamination. HeI ($h\nu = 21.2$ eV) and HeII ($h\nu = 40.8$ eV) UPS measurements have been performed on as-deposited and hydrogen plasma-treated nanodiamond films. The emission width of the as-deposited sample was 15.0 eV with a low-energy cutoff at 3.1 eV, which results in a positive value of electron affinity of +0.7 eV, assuming the band gap is $E_g = 5.5$ eV. After H_2 plasma treatment, the samples showed an emission width of 15.9 eV with a very sharp, low-energy cutoff at 2.1 eV, indicating a negative electron affinity of –0.2 eV.

Some measurements of collective electrical characteristics of powders and suspensions are given in Table 7.1. Gordeev et al. [67] reported a resistivity for bulk nanodiamond composites obtained by pressing UNCD powders. The room-temperature resistivity of such UNCD composites was 1.2×10^9 W m, consistent with the resistivity reported by Dolmatov [2] (Table 7.1).

Belobrov et al. [68] reported results of studies on UNCD powders of different surface modifications by electron paramagnetic resonance and NMR [68]. They found that the nanodiamond EPR signal is independent of the chemical modification of the nanodiamond surface. The *g*-factor for UNCD was found to be 2.0027(5) [68]. Hence they concluded that the paramagnetic properties of nanodiamonds are determined only by the sp^3 core of the diamond particle. Analyzing ^{13}C-NMR spectrum for nanodiamonds, the authors [68] concluded that the resonance line is asymmetric and well decomposed into two Gaussian components. The authors interpreted the narrow line with $\delta = 35.1$ ppm as relating to diamond carbon, and the wide line with $\delta = 34.2$ ppm as being caused by distortion of the tetrahedral coordination. The authors [68] concluded that only 30% of bonds in nanodiamonds are nondistorted sp^3 bonds; 70% of carbon bonds are distorted and these distorted bonds also have sp^3 hybridization. For comparison, natural jewel-quality diamonds have a characteristic chemical shift $\delta = 50$ ppm.

TABLE 7.2
Properties of Three Types of Detonation Nanodiamond Particles Produced at Russian Federal Research Center-All-Union Research Institute of Technical Physics, Snezhinsk, Russia and Field Electron Emission Parameters of Corresponding Nanodiamond Coatings

Nanodiamond Type	Nd	NdP1	NdO
Description	Standard (chromic acid purification)	Nd with additional acid and high-temperature treatment; "bottom" fraction	NdP1 with additional ozone treatment
Impurities	O, N, H ~8–10%	O, N, H ~2–4%	N, O ~6%
pH of 10% water suspension	5.6–6.2	3.5–4.5	1.6–2.0
Field electron emission parameters			
Change in field emission threshold, compared to bare Si field emitter (%)	−15	−25	−15
Change in normalized integral transconductance compared to bare Si field emitter (%)	−37	−30	+33

Zhirnov et al. [69,70] characterized UNCD particles using field electron emission measurements by depositing small amounts (0.2 μm in thickness) of UNCD on metal or silicon tips by electrophoresis. In these experiments, the field emission characteristics of tips with UNCD coatings were compared with characteristics of bare tips. The emission experiments showed that the emission characteristics differ significantly for different UNCD coating conditions. The different UNCD coating conditions were obtained from one original UNCD powder (marked as Nd in Table 7.2) using different physical and chemical treatments. The modifications differed in concentration of impurities, pH of water suspension, and density as shown in Table 7.2. Table 7.2 also contains a summary of emission characteristics for different UNCD coatings. It can be seen from Table 7.2 that all three types of nanodiamond coatings showed improvement in field emission threshold. Additional hydrogen plasma treatment was used to modify the surface properties of emitters with NdO and NdP1. Figures 7.18a and b show emission characteristics before and after the plasma treatment. As can be seen, the effect of hydrogen plasma treatment is very different for the two types of nanodiamond particles. The in-depth discussion of the possible influence of different surface groups on field emission properties of nanodiamond particles is given in [71]. In general, it is concluded that nanodiamonds purified by ozone treatment followed by hydrogen plasma modification are most promising for field emission applications.

The smallest amount of diamond matter, which can be prepared and studied in isolation, are primary particles of UNCD. Recently Tyler et al. [29] reported a new technique for isolating individual nanodiamond particles by depositing them on sharp (radius of 10 to 50 nm) metal tips by pulsed electrophoresis of alcohol suspensions of UNCD. Apparently, a very high electric field near the sharp tip breaks the agglomerates, and thus it is possible to manipulate individual nanodiamond particles. The typical size of diamond nanoparticles as measured in TEM was about 3 nm (Figure 7.3c). It should be noted that in all cases, only particles with faceted shape were observed.

Results of field emission characterization of UNCD reveal a considerable difference in emission behavior of single isolated diamond nanoparticles and multiparticle nanodiamond thin films [29]. A substantial increase (~30%) in threshold voltage was observed for a tip capped with a single isolated diamond nanoparticle, in comparison with the bare Mo tip (Figure 7.18c). The *I–V* curves also exhibited non-Fowler–Nordheim behavior. However, after the additional deposition of nanodiamond and the formation of a thicker nanodiamond film (~20 nm), a drastic decrease in

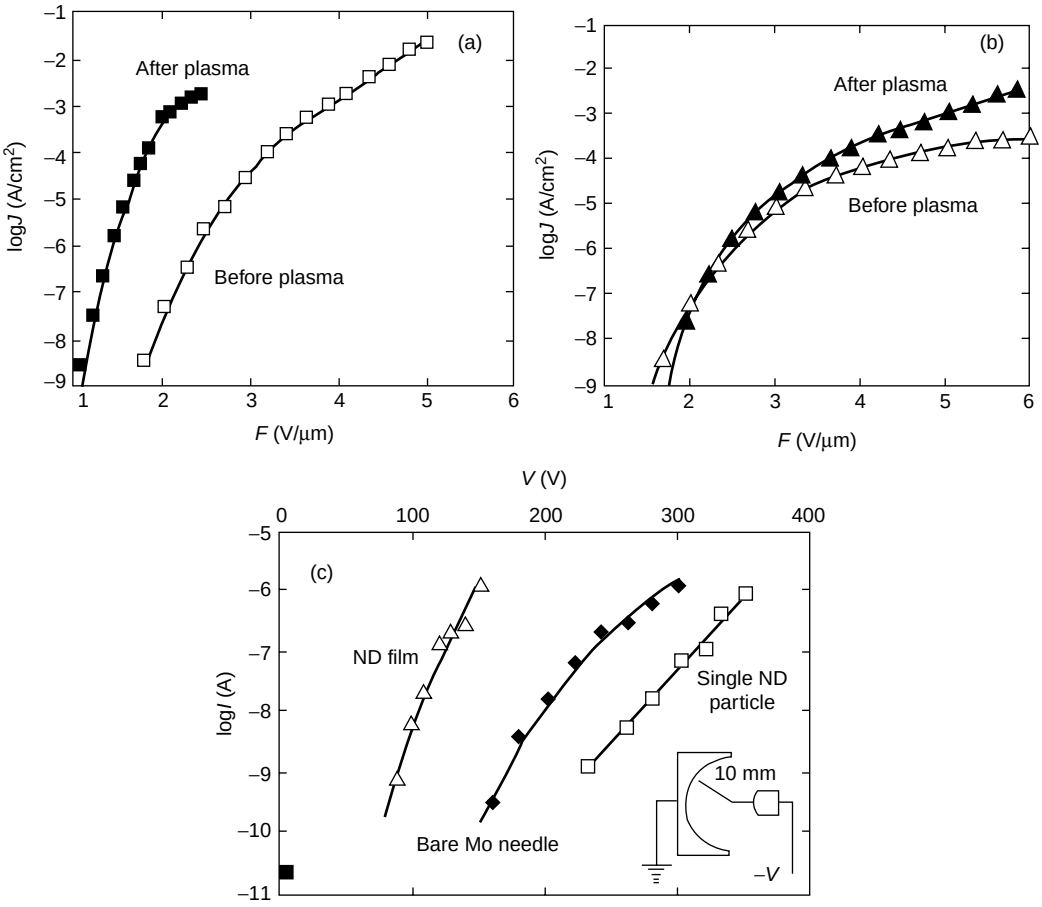

FIGURE 7.18 Field emission characteristics of detonation nanodiamond: hydrogen plasma effect on coatings of NdO (a) and NdP1 (b); for an isolated nanodiamond particle and a nanodiamond film, compared to a bare tip (c). Inset in (c): schematic of experimental set-up. (From Zhirnov V.V. et al., *Phys. Solid State*, 46, 641, 2004. With permission.)

threshold voltage (~48%) and an increase in transconductance (~115%) were observed – characteristics typical of nanodiamond coated tips. The emission suppression in a structure with a single UNCD particle can be explained on the basis of triple junction effect [72], due to the local suppression of electric field at the metal–dielectric–vacuum boundary. Obviously, there are no triple junction interfaces in coatings containing more than one monolayer of particles.

Very interesting transformations between carbon forms at the nanoscale were discovered in the mid-1990s. Upon annealing at temperatures between 1300 and 1800 K, nanodiamond particles transform to carbon onions with a transformation temperature that depends upon the particle size [73]. X-ray diffraction data show graphitic phase formation at $T > 1200$ K [74]. The diamond–graphite phase transition temperature observed in UNCD ($T_{pt} > 1200$ K) is considerably lower than the phase transition temperature of bulk single-crystal diamonds ($T_{pt} > 1900$ K).

In summary, detonation nanodiamond particles have been investigated in great detail after their invention 40 years ago. In most cases, it was collective properties of UNCD powders that have been investigated; only very recently have nanodiamond particles been isolated and their structural, compositional, and electronic properties begun to be studied. Among the current active areas of research, the most important one from the practical point of view is developing an understanding of the relationships

between the surface chemistry of the particles, and conditions needed to maintain stable colloidal suspensions of nanodiamonds of ultrahigh dispersivity (particle sizes of 5 to 30 nm).

7.4.2 Applications of Ultrananocrystalline Diamond Particulate

Applications of UNCD particles of detonation origin can be categorized as *traditional* — those on which work has been going on for the last couple of decades; and *novel* — those on which work has started only recently owing to advances in nanotechnology throughout the world. Within the novel applications, *biological* applications should be considered separately due to their high specificity. Biological applications of detonation UNCD will be discussed in Section 7.7. Technological applications of UNCD particles have been summarized in [2–7,65]; review [4] particularly provides an extensive discussion of biological applications of UNCD particulates. The bibliographic index [9] contains references on categorized nanodiamond applications.

Traditional UNCD particulate applications include metal–diamond galvanic coatings, polishing pastes and suspensions, polymer composities, lubricating oils, greases, and lubricant coolants.

Electrochemical deposition of UNCD together with metals, using standard galvanic equipment, has been demonstrated to be useful in a variety of applications for coatings of components of transportation units, tools for electronics, electrical engineering, medicine, watch, and jewelry industry [2,6]. The advantages of adding UNCD to galvanic coatings include increase in wear resistance (2 to 13 times depending on metal); microhardness (may be up to 2 times depending on the metal); an increase in corrosion resistance (2 to 6 times depending on the metal); decrease in porosity (pores can be completely eliminated depending on the metal); significant decrease of friction coefficient; considerable improvement of adhesion and cohesion; and high throwing power of the electrolyte. According to [2,6], the service life of products is increased 2 to 10 times, even when coating thicknesses are decreased by a factor of 2 to 3. The strengthening effect is observed in coatings of many metals, including silver, gold, and platinum, which are employed in electronic applications. Particularly, UNCD is most widely used in strengthening chromium coatings deposited using an electrolytic process. In this process, UNCD-containing additives are added to the chrome-plating electrolyte without any modification of the standard production line. Such coatings increase the operating life of molds, high-precision bearing surfaces and other similar components by a few times [6]. The UNCD content in a metal coating averages 0.3 to 0.5 wt%. The amount of UNCD consumed for a metal layer of 1 mm thickness is 0.2 g (1 carat)/m^2.

UNCD particles are being used for finishing precision polished materials for electronics, radio engineering, optics, medical, and jewelry industries [2]. The compositions with UNCD allow one to obtain a surface of complex geometrical form, with a relief height roughness of 2 to 8 nm. Recently, 4 Å roughness has been achieved for polished Al_2O_3, and SiC surfaces using UNCD suspensions (according to the Alit, Inc., Kiev, Ukraine). UNCD is employed in polishing compositions used for the final treatment of silicon wafers in the microelectronics industry. UNCD has been also used in the electronics industry as a component of heat-removal pastes, and compounds for chip packaging, replacing the highly toxic beryllium oxide that has been traditionally used. The amount of UNCD consumed for this application is 1 to 10 g/m^2.

The addition of UNCD to polymers provides an increase in their mechanical strength, wear-resistance, and heat-aging resistance [2,6]. According to [2], highly effective coatings based on the incorporation of UNCD into fluoroelastomers and polysiloxanes have been developed; the elastic strength of rubbers based on polyisoprene, butadiene–styrene, butadiene–nitrile, and natural rubbers has been considerably improved. For example, for fluoroelastomers filled with UNCD particles, the tensile modulus at 100% elongation and the conditional rupture strength increased more than tenfold (from 8.5 to 92 MPa and from 15.7 to 173 MPa, respectively). In this case, the elongation increased by a factor of 1.6 (from 280 to 480%). An increase in cross-linking is one of the mechanisms to which the influence of UNCD particles on the strength properties of polymer composites has been attributed [2]. According to [2], addition of UNCD into rubbers decreases attrition wear

by an average of 3 to 5 times, increases rupture strength by 30%, and breaking temperature by 15%. Epoxy adhesives, which incorporate UNCD, have high adhesion and cohesion properties. The specific consumption of UNCD or diamond blend (mix containing UNCD and significant percent of other carbon-based products of detonation explosion) is 1 to 5 kg/1000 kg of rubber (polymer) and 1 to 5 kg/1000 m^2 of polymer coating or film.

The addition of UNCD and diamond blend to oils allows one to obtain sedimentation-stable and environmentally safe systems with particle sizes of less than 0.5 μm [2]. According to [2], the use of nanodiamonds in oils increases the service life of motors and transmissions, reduces friction torque by 20 to 40%, and decreases wear of rubbed surfaces by 30 to 40%. Recently, UNCD particulates have been examined for thermal conductivity enhancement of dielectric oils [75]. It was demonstrated that dispersion of nanodiamonds (1 wt%) in oil (XO-class) can increase the overall thermal conductivity of cooling oils those, e.g., for use in power transformers by over 25% [75]. The specific consumption of UNCD or diamond blend in oils is 0.01 to 0.2 kg/1000 kg of oil [2].

Novel UNCD niche applications developed recently [10,65] include UNCD for systems of magnetic recording, as adsorbents of a new type, as components in the production of diamond ceramics and molds made of diamond-containing materials, as coatings in field emission devices, in heterogeneous and electrochemical catalysis, and in proton-conducting nanocomposite membranes in fuel cells applications. UNCDs have also been employed for seeding substrates used in the CVD growth of diamond films. Dry UNCD is known to absorb and retain water in amounts that are four times the weight of the UNCD. This allows its use as an inert solid water absorber in materials like magnetic carriers, whose quality is determined by the residual water content.

In systems of magnetic recording, UNCD is used as an antifriction additive and as a physical modifier for ferro-lacquer coating of magnetic tapes and disks, and also as an additive to solutions for electrochemical deposition of composite magneto-recording tapes to improve the properties of magnetic recording devices [76]. The addition of UNCD decreases ferro-magnetic grain size, thus allowing an increase in recording density while reducing abrasive wear and friction coefficient.

Carbon-containing adsorbents are widely used in various industries such as medicine and pharmacology. The most abundant of them are activated coals and graphitized thermal carbon black. Synthetic diamonds, particularly submicron diamond composites as well as sintered UNCDs represent a new class of carbon-containing adsorbents [77], characterized by chemical inertness and high strength. Another beneficial effect is the possibility of using the adsorbent repeatedly, by modifying and recovering the diamond surface.

A very interesting application of nanodiamonds for advanced information processing is the generation of light sources that are able to emit individual photons on demand. While nanodiamond particles of nondetonation origin have been reported by Beveratos et al. [78,79], nothing prevents the use of nanodiamond of different origins in this application. Beveratos et al. investigated the quantum properties of the light emitted by diamond nanocrystals containing a single nitrogen-vacancy color center [78]. The typical size of diamond particles used in these experiments was 40 nm. According to the authors, there are several very important optical properties of diamond nanocrystals, which contribute to their usefulness as individual photon light sources. First, the subwavelength size of these nanocrystals renders refraction irrelevant. A nanocrystal can be regarded as a point light source. Second, the very small volume of diamond excited by the pump light yields very small background light. This is very important for single-photon sources. By exciting nanodiamond crystals using a YAG laser ($\lambda = 532$ nm), the authors were able to observe fluorescence with almost background-free photon antibunching from single nitrogen-vacancy centers in diamond nanocrystals at room temperature. The excited state lifetime in the bulk is $t_b = 11.6$ ns. The measured lifetime in the nanocrystals was 25 ns. The authors argue that this lifetime modification is a quantum electrodynamic effect. In a later paper by Beveratos et al. [78], a full implementation of a quantum cryptography protocol using a stream of single photon pulses generated by a stable and efficient source operating at room temperature has been reported. The quantum bit error rate was less than 4.6% and the secure bit rate was 7700 bits/sec. The overall performances of the system

were reported to be at a stage where single photons have a measurable advantage over an equivalent system based on attenuated light pulses.

In summary, there is striking evidence that niche applications for nanodiamonds, particularly nanodiamonds of detonation origin which are a commercial product, are expanding significantly. A big advantage of nanodiamonds of detonation origin is their affordability due to low cost, and the well-developed infrastructure for the scale-up production.

7.5 ULTRANANOCRYSTALLINE DIAMOND FILMS PRODUCED BY CHEMICAL VAPOR DEPOSITION

Ultrananocrystalline diamond films with 2 to 5 nm grains (both H-containing and H-free) have been recently synthesized in the Argonne National Laboratory, Illinois, USA, by Gruen and colleagues [1,60,69,79], using a microwave plasma-assisted chemical vapor deposition process. The UNCD thin films were synthesized using argon-rich plasmas instead of the hydrogen-rich plasmas normally used to deposit microcrystalline diamond. By adjusting the noble gas:hydrogen ratio in the gas mixture, a continuous transition from micro- to nanocrystallinity was achieved. The controlled, continuous transition from the micro- to nanoscale is a unique feature of the method [1].

The use of small amounts of carbon-containing source gases (C_{60}, CH_4, C_2H_2) along with argon leads to the formation of C_2-dimers, which is the growth species for all UNCD thin films. The nanocrystallinity is the result of a new growth and nucleation mechanism, which involves the insertion of C_2 into the π bonds of the nonhydrogenated reconstructed (1 0 0) surface of diamond. Then, unattached carbon atoms react with other C_2 molecules from the gas phase to nucleate new diamond crystallites [1,80]. This results in an extremely high, heterogeneous nucleation rate (10^{10} $cm^{-2}sec^{-1}$, which is 10^6 times higher than from conventional CH_4/H_2 plasmas). The UNCD grown from C_2 precursors consists of ultrasmall (2 to 5 nm) grains and atomically sharp grain boundaries. Up to 10% of the total carbon in the nanocrystalline films is located within the 2 to 4 atom-wide grain boundaries. Because the grain boundary carbon is π bonded, the mechanical, electrical, and optical properties of nanocrystalline diamond particles are profoundly altered. More subtle control of the properties of UNCD films can be accomplished via the addition of supplementary gases to the plasma (N_2, H_2, B_2H_6, PH_3) and changes in the growth conditions (biasing, power). For instance, the addition of hydrogen leads to highly insulating films with large columnar grains. Adding nitrogen leads to the formation of CN in addition to C_2 in the plasma. The presence of CN results in decreased renucleation rates during growth, which leads to larger grains and grain boundary widths.

Ultrananocrystalline diamond films are superior in many ways to traditional microcrystalline diamond films: they are smooth, dense, pinhole free, and phase-pure, and can be conformally coated on a wide variety of materials and high-aspect-ratio structures [1]. The set of unique properties include mechanical (high hardness ~100 GPa, and Young's modulus ~960 GPa), tribological (extremely low friction ~0.01), transport (tunable electrical conductivity, high thermal conductivity), electrochemical (wide working potential window), and electron emission (low, stable threshold voltage).

In studies of UNCD-coated flat substrates and microtip arrays for cold cathodes applications [1,81], consistently low threshold fields (1 to 2 V/μm) and current densities of 4×10^{-4} A/cm^2 at 4 V/mm has been achieved using thin films of UNCD grown from C60 – 80% Ar – 20% H2 microwave plasmas [1].

Ultrananocrystalline diamond is slightly p-type as it grows [82]. As nitrogen is added, this material becomes n-type, with a very shallow activation energy. The origin of this conductivity is related to disorders and π bonding at the grain boundaries, which introduce states within the gap and band tails, resulting in high carrier concentrations and low mobilites. Ultrananocrystalline diamond particles have been grown with the incorporation of nitrogen up to 8×10^{20} atoms/cm^3 by the addition of nitrogen to plasmas during the CVD growth of diamond films [81]. This is the highest carrier concentration seen for any n-type diamond material to date, resulting in several orders of magnitude

increase in UNCD conductivity. This has promising applications in heterojunction electronic devices. The maximum conductivity measured was 400 $\Omega^{-1}cm^{-1}$ for 20% N_2 in the gas phase [82]. Recently, high-temperature operation of a heterostructure diode utilizing n-type UNCD as an electrode has been demonstrated [82].

UNCD electrodes exhibit a wide working potential window, a low background current, and a high degree of electrochemical activity for redox systems. These results, in combination with the biocompatibility properties of UNCD, could lead to the application of UNCD electrodes for nerve stimulation [1].

UNCDs have been considered for a variety of applications including micro-electro-mechanical systems (MEMS) and moving mechanical assembly (MMA) devices, surface acoustic wave devices, biosensors and electrochemical sensors, coatings for field emission arrays, photonic and radio frequency (RF) switching, and neural prostheses. Particularly, in the future, MEMS applications that involve significant rolling or sliding contact (MEMS MMAs) will require the use of new materials with significantly improved mechanical and tribological properties, and the ability to perform in harsh environments. Since the feature resolution in polycrystalline MEMS is limited by grain size, the use of MEMS made by conventional CVD diamond methods is limited. In addition, the conventional CVD diamond films have large grain size (~1 μm), high internal stress, poor inter-granular adhesion, and rough surfaces (rms ~1 mm). Diamond-like coatings, generally grown by physical vapor deposition, cannot cover high-aspect-ratio features conformally for applications such as MEMS, and require high-temperature postdeposition processing to relieve stress, which compromises their mechanical properties. UNCD coatings possess morphological and mechanical properties that are ideally suited for MEMS applications in general, and MMA use in particular [1,82]. The roughness of the film is about 20 to 40 nm and the friction coefficient can be as low as 0.01. The surfaces are very smooth (rms ~30 to 40 nm) and the hardness is as high as ~100 GPa. As compared to Si-based MEMS, the brittle fracture strength is 23 times that of Si, and the projected wear life of MEMS MMAs from diamond is 10,000 times greater than that of Si MMAs. The group from the Argonne National Laboratory have demonstrated three dimensional MEMS structures fabricated from UNCD material, including cantilevers and multilevel devices, acting as precursors to microbearings and gears.

Although discovered very recently, UNCD films have found a surprisingly wide range of niche applications. In many cases, prototype devices have been demonstrated.

7.6 CARBIDE-DERIVED DIAMOND-STRUCTURED CARBON

Recently, a completely different method, distinct by its simplicity, from what has been discussed in the previous two sections, has been developed for the synthesis of diamond-structured carbon in bulk quantities [12,28]. The method developed by Gogotsi et al is based on extracting silicon from silicon carbide or metal carbide, using chlorine-containing gases at ambient pressure and temperatures not exceeding 1000°C. Nanocrystalline diamond particles with an average crystallite size of 5 nm are formed, as is illustrated in Figure 7.3b for a diamond nanocrystal embedded in amorphous carbon in carbide-derived carbon produced by chlorination of TiC [28].

Following continued heat treatment at low hydrogen content, a typical film microstructure obtained by chlorination of SiC consists of a nanocrystalline diamond layer several microns thick near the SiC–carbon interface, followed by a region of diamond nanocrystals surrounded by carbon onions and disordered carbon. The third, closest to the surface layer, consists of carbon onions, as well as curved graphite sheets, some planar graphite, and porous and disordered amorphous carbon [12]. Initially, for stable conversion of silicon carbide into the diamond phase, the presence of hydrogen in the gas mixture was considered essential to saturate dangling bonds on the surface of the diamond particles [12]. Nanocrystalline diamond films grown up to 50 μm thick at high hydrogen content has been demonstrated [84]. However, later, large nanocrystalline diamond areas were found in some regions of SiC samples treated in pure chlorine with no hydrogen [28]. The fact that hydrogen is not essential for the growth of diamonds using the carbide chlorination process outside

its range of thermodynamic stability is consistent with the conditions necessary for diamond synthesis from fullerene [1] or during codeposition of carbon and Si [62].

The specific feature of diamond-structured carbon is multiple diamond structures including cubic, hexagonal (londsdalite) structures, as well as a variety of other diamond polytypes [12,28]. It is also possible to vary the pore size from angstroms to a few nanometers, depending on the carbide precursor type leading to the growth of nanoporous carbon or nanoporous diamond [12,83].

In principle, chlorination of carbides for the production of carbon-based materials and particularly, nanoporous carbon, is a relatively mature technology that has been commercialized (see, for example, http://www.skeleton-technologies.com). However, the synthesis of nanocrystalline diamonds by this technique [12] is a recent achievement. Coatings of diamond-structured carbon produced by this route show hardness values in excess of 50 GPa and Young's moduli up to 800 GPa.

Carbide-derived carbon and diamond coatings show excellent tribological behavior in both room air and dry nitrogen, and are at the stage of commercialization for tribological applications, particularly as nanodiamond coatings for SiC dynamic seals for water pumps [84]. The coatings are self-lubricating with remarkably low friction coefficients which can be tailored by altering the reaction parameters, and show no measurable wear. Favorable tribological properties of carbide-derived nanodiamond make it a potential candidate for applications in the manufacture of different types of prosthesis [84].

Conformal coatings produced by selective etching can be useful in MEMS applications where very thin and uniform coatings are required. In addition, permeability of films produced by chlorination of SiC and an extremely narrow pore size distribution in carbide-derived carbon provide effective molecular sieves, high-surface area electrodes and other applications, where vapor-deposited diamond films cannot be applied. The large-scale, solid-state synthesis of technical diamonds at ambient pressure and moderate temperatures with no plasma activation can provide diamond materials at low cost for a variety of high-volume applications such as brake pads, where diamond could not be used previously because of its cost.

7.7 MEDICAL AND BIOLOGICAL APPLICATIONS OF NANODIAMOND

All major forms of carbon at the nanoscale (fullerenes, nanotubes, and nanodiamond — both particulate and films) appear to be valuable resources for biomedical applications [85]. In the mid-1990s it was demonstrated that fullerene compounds have biological activity, and their potential as therapeutic products for the treatment of several diseases has been reported. As a result, a private biopharmaceutical company, C Sixty Inc., Houston, TX, was created, with a primary focus on the discovery and the development of a new class of therapeutics based on the fullerene molecule. At 7.2 Å in diameter, C60 is similar in size to steroid hormones or peptide α-helices, and thus fullerene compounds are ideal molecules to serve as ligands for enzymes and receptors [86]. In the last few years, a number of useful fullerene-based applications have been reported, including therapeutics such as antiviral agents and anticancer drugs, as biosensors for diagnostic applications [87,88], as a protective agent against iron-induced oxidative stress [89], and as an *in vitro* antibacterial agent [90]. Fullerenes have also been demonstrated to be useful in DNA-templated assemblies of inorganic–organic building blocks [91].

The exploration of buckytubes in biomedical applications is also underway. Multiwall carbon nanotubes have been used for the immobilization of proteins, enzymes, and oligonucleotides [92–94]. Significant progress has been made in the last few years in the effort to overcome some of the fundamental and technical barriers toward bioapplications, especially with regard to issues concerning the aqueous solubility, and biocompatibility of carbon nanotubes, modifications of carbon nanotubes with various biological and bioactive species, and on the design and fabrication of prototype biosensors. A comprehensive review of the advances in this fast-moving research field has been recently published by Lin et al. [95].

CVD diamond films (both conventional and UNCD) have been suggested as an ideal platform for future biochips and biosensors because of their superior mechanical, thermal, and chemical

properties as compared to glass, silicon, and gold surfaces [96]. Outstanding biocompatibility of diamond films and micron-sized particles with living cells has been demonstrated, and related research is summarized in [85]. The immobilization of biomolecules on diamond for the fabrication of integrated biochips and sensors requires surface activation processing such as sequential plasma treatment, amination, and carboxylation steps [98,99] in order to form covalent linkages to amino- or phosphate-modified DNA. The electrochemical deposition of polyaniline (PANI)/polyimide (PAA) conducting polymer layer on boron-doped diamond film has also been reported [97]. The PANI/PAA thin film provides freely accessible carboxylic groups that have high chemical specificity in the covalent immobilization of oligonucleotides. Recently, Yang et al. [96] used photochemical methods to create a homogeneous layer of amine groups on nanocrystalline and UNCD films, which served as binding sites for DNA attachment. By comparing DNA-modified ultra- and nanocrystalline diamond films with other commonly used surfaces for biological modification, such as gold, silicon, glass and glassy carbon, Yang et al. [96] concluded that diamond is unique in many ways: its ability to achieve very high stability while, gold–thiol bonds for example, are very susceptible to oxidation, leading to solubilization of the attached layers; chemically modified surfaces involving Si–O linkages degrade under basic conditions; both crystalline silicon and SiO_2 surfaces are susceptible to amine-induced degradation because oxidation of silicon is catalyzed by amines. It was also emphasized [97] that nanodiamond surfaces possess superior sensitivity while also being compatible with microelectronics processing technologies.

Nanocrystalline diamond coatings on suitable substrates are promising materials for medical implants, cardiovascular surgery, and for coating of certain components of artificial heart valves, due to their extremely high chemical inertness, smoothness of the surface, and good adhesion of the coatings to the substrate [100]. Nanocrystalline diamond coating (reported grain size ~10 nm) deposited by radio-frequency plasma chemical vapor deposition (RF-PCVD) of methane with nitrogen on millimeter-sized steel implants demonstrated excellent biocompatibility and biostability in situations where the implant had been inserted to tissue and bones for up to 52 weeks [100].

The first biomedical applications of UNCD particulate was reported by Kossovsky et al. [101], where nanodiamond was used for immobilization of antigens. Nanodiamond was chosen because of requirements of high surface area, high surface energy, and nontoxicity, as compared, for example, with toxic tin oxide particles. General Electric, Inc. (GE) powder of blocky 5 to 10 nm particles was treated with cellobiose (4 to 6 nm layer) following adsorption of antigen mussel adhesive protein (MAP) by dialysis. The resulting colloidal system of nanodiamond/cellobiose/MAP aggregates of 300 nm in size was used as antigen delivery vehicles for prolonged production of antibody.

An extensive set of experiments on biological activity of UNCD particles and their potential applications has been carried out by Puzyr et al. [102–107]. Reference [102] demonstrates the possibility of preparation of materials composed of particles with significantly different chemical structure and physical properties, using protein molecules as a cross-linking agent. Particularly promising for design of new composites biomaterials is the nanodiamond–protein–Al_2O_3 complex, where UNCD particles and δ-Al_2O_3 were used as building blocks and protein as cross-linking agents.. In the first stage, a recombinant apoobelin (a light-emitting protein) was adsorbed on nanodiamond particles, and in the second stage, the nanodiamond–protein complex was adsorbed onto the δ-Al_2O_3 particles. As an extension of that work, obelin–nanodiamond particle complexes were immobilized on a plane aluminum oxide structure [103], which allowed them to devise a bioluminescent test system to record calcium ions, as an alternative to the well-known methods of calcium measurement performed within the volume of the reaction mixture. Importantly, biological activity of apoobelin in the composites was retained even for a dry plate, so that the analyzed solution can be placed on a dry plate. It is claimed that the designed plane luminescent sensors (biochips) are capable of operating under “extraordinary” conditions [103]. For example, prolonged space missions are known to promote decalcination of human bone tissue. The express method of analysis that does not require any solution other than the one under analysis, eliminates the problem of working with a variety of liquids under microgravity and makes it much easier to obtain information on

the dynamics of calcium ions in physiological liquids (saliva, urine, blood, or tears). Recently, a luminescent biochip prototype for use in bioluminescent analysis has been designed, whose main element consists of detonation UNCD particles functionalized with light-emitting proteins such as bacterial luciferase and obelin [107]. It was demonstrated that, in these structures, the enzyme retains the catalytic activity.

Detonation nanodiamond has also been used for the separation and purification of recombinant apoobelin and recombinant luciferase from bacterial cells of *Escherichia coli* [105] in bulk. It has been demonstrated that the application of nanodiamonds simplifies the procedures for purifying the proteins, decreases the time of their separation to 30 to 40 min (as compared to conventional methods which take several days), eliminates the necessity of using special chromatographic equipment, and makes it possible to prepare high-purity apoobelin and luciferase materials with protein yields of 35 to 45% and 45 to 60%, respectively. As possible mechanisms of interaction of proteins with particles surfaces formation of S–S bridges, coordination bonds, or multiple points interaction of a protein molecule with different functional groups on a particle surface was considered [105].

Puzyr et al. [104] performed a study of the effects of UNCDs on human white and red blood cells *in vitro*. Experiments were carried out using seven different samples of detonation UNCD purified from by-products of explosion-induced synthesis by different methods and obtained from different vendors. Two parameters were used to understand the effects of nanodiamond particles on white blood cells: (1) the kinetics of generation of active oxygen species (AOS) and (2) the cell viability. The kinetics of AOS generation was measured using the chemiluminescence luminol reaction (CLR), and cell viability was tested by staining with a trypan blue solution. It was observed that the detonation UNCD had a damaging effect on both white cells and erythrocytes [104]. The results of the study suggest that nanodiamond particles in whole blood interact with white blood cells and activate AOS generation in these cells. On the other hand, there was almost no correlation between the physicochemical characteristics of the nanodiamond samples used in the study and their effects on the whole blood CLR kinetics. It was concluded [104] that the active functional groups that are exposed on the surface of nanoparticles, rather than their diamond core, are the decisive factor of the UNCDinduced effect on cells. On the other hand, experiments performed by a group from Poland [108] demonstrated that detonation UNCD increases blood cells survivability in systems with high concentration of free radicals as compared to nanodiamond particles synthesized by other means. Definitely, this important area requires more work to be done to reveal the mechanisms of interaction of UNCD with blood cells as well as other types of cells. Figure 7.19 is a TEM micrograph of an ultrathin section of a mammalian cell, demonstrating results of incubation of modified UNCD with a cell. White arrows highlight places where presumably UNCD particles penetrated the cell membrane. This is an important fact demonstrating that, in principle, UNCD particles (at least modified UNCD [106]) can serve as delivery vehicles for different substances into cells. Also, UNCD particulates have been specifically modified with the ultimate goal of adapting them to biological investigations [106]. Powders of modified nanodiamonds are characterized by a high colloidal stability of the particles, virtually independent of particle concentration. They form stable hydrosols on simple addition of water, and do not need ultrasonic dispersion. After repeated removal of the dispersive medium and subsequent addition of water to the dry, modified nanodiamond powder, again a stable hydrosol can be obtained. The use of highly stable colloidal solutions of modified UNCD in biological investigations (buffer solutions, culture media, physiological liquids), and for achieving a uniform distribution of nanoparticles in an agar gel, has been demonstrated. It was also reported [106] that organosols with modified UNCD possess high colloidal stability over a wide range of temperatures, namely, from the boiling point to the freezing point of the dispersive medium. After freezing and melting, the organosol retains the colloidal stability.

Another group active in the development of biological and medical applications of UNCDs is the team led by Dolmatov [2]. In preliminary experiments on animals with Erlich carcinoma, and several clinical tests on terminally ill cancer patients, the research team [109] found that treatment with aqueous suspensions of nanodiamonds resulted in improvement of the overall condition of the

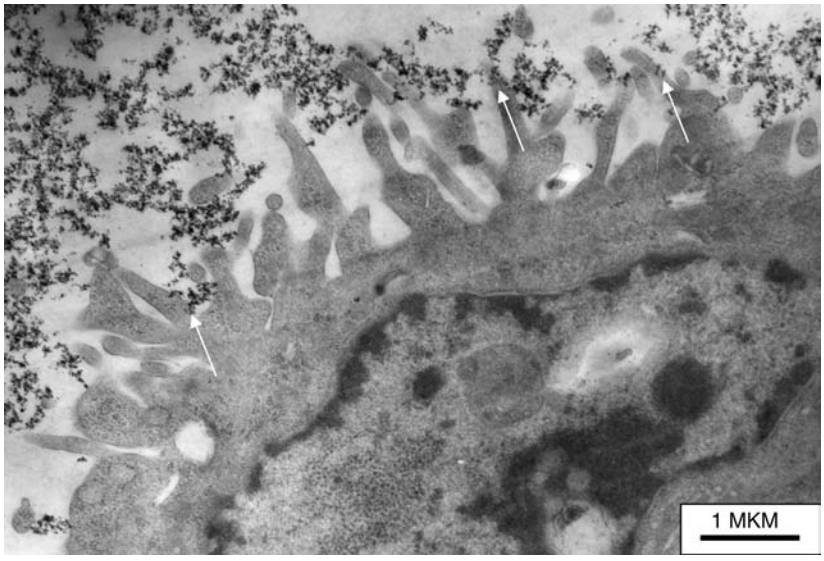

FIGURE 7.19 TEM micrograph of an ultrathin section of a mammalian cell, demonstrating results of incubation of modified UNCD with a cell. (Courtesy of A.P. Puzyr, O.A. Mogilnaya, and V.S. Bondar.)

patients, normalization of gastrointestinal function, decrease in the intoxication and, in some cases, reduction of the tumor size [2,109]. However, no detailed mechanism-of-action studies have been conducted so far. According to Dolmatov et al. [2,109], UNCD can be considered as a potential medical agent (not just drug-delivery agent) in oncology, gastroenterology, and vascular disease, and an efficient remedy for the after-effects of burns, in skin diseases, and intoxication. The characteristics of UNCDs which make them suitable for medical applications are the anomalously high adsorption capacity, high specific surface areas, abundance of free electrons on the surface (a multiple radical donor), nanoscale size, significant amount of oxygen-containing functional groups on the surface, chemically inert cores, and hydrophobicity of the surface [2]. According to Dolmatov [2], owing to their high adsorption capacities, UNCDs exhibit extremely high absorbing/bonding activities with respect to pathogenic viruses, microbes, and bacteria. The absorbing/bonding may be selective to particular drugs that can enhance the drugs' activity. According to [2,109], UNCDs exhibit no carcinogenic or mutagenic properties and are not toxic.

While the preliminary results, particularly in oncology, are encouraging [109], a very limited amount of research has been conducted so far on the pharmacological effects of UNCD, and extensive fundamental studies will be required before a clear understanding of the benefits can be developed.

7.8 CONCLUSION

Nanodiamond particles have very diverse structures at the nanoscale, ranging from individual clusters to high-purity films, can be produced by very diverse techniques such as the detonation explosives method, low-pressure CVD, and the chlorination of carbides. Different types of nanodiamond are at varying stages of commercialization. Production of nanodiamond particulates for polishing applications, obtained by fractioning and grinding of micron-sized monocrystalline and polycrystalline particles is a very mature technology. The purity of nanodiamond for polishing applications is not as critical as it is for other applications, so the specifications for nanodiamond quality in this application is more relaxed. The recently developed process of depositing UNCD films with very unique properties is at the very early stage of commercialization. The process of producing UNCD films by the carbide-derivation process is distinct due to its simplicity and is being rapidly implemented in some market niches because of the existing infrastructure for producing carbide films.

It is interesting that before nanotechnology became widely popular, there is a long history of application of detonation UCND in traditional areas such as in polymer composites and polishing compounds, as additions to lubricants and in solutions for galvanic coatings, in the countries of the former Soviet Union.

UNCDs can be easily produced in tons quantities however, it is very hard to produce UNCD completely free of contamination due to the incombustible impurities (metals, nonmetals, and their oxides), which are located in inter-particle areas within agglomerates of UNCD particles. High purity of UNCD is not required, however, for the traditional applications mentioned above. Depending on the application, technologies developed earlier for UNCD purification, surface modification as well as generation of aggregate-free UNCD suspensions, are now being scaled up for industrial use. Application-specific modification of UNCDs is underway. It should be emphasized that developing an understanding of the relationship between the complex structure of the surface of UNCDs and their physical properties is an area of very active research. Especially important, although very challenging, is developing an understanding of the properties of individual nanodiamond particles. Regarding novel applications of UNCD, we have pointed out that biomedical applications is an area of research that is just beginning to emerge.

In conclusion, nanocrystalline diamond with wide diversity of forms, is a rapidly developing area from both the point of view of fundamental research as well as the current perspective of application in many areas of nanotechnology.

REFERENCES

1. Gruen, D.M., Nanocrystalline diamond films, *Annu. Rev. Mater. Sci*., 29, 211, 1999.
2. Dolmatov, V.Y., Detonation synthesis ultradispersed diamonds: properties and applications, *Russian Chem. Rev.*, 70, 607, 2001.
3. Shenderova, O.A., Zhirnov, V.V., and Brenner, D.W., Carbon nanostructures, *Crit. Rev. Solid State Mater. Sci.*, 27, 227, 2002.
4. Belobrov, P.I., Nature of nanodiamond state and new applications of diamond nanotechnology, Proceedings of the IX International Conference on "High-tech for Russian Industry", Russia, Moscow, 11–13 September, vol. 1, 2003, pp. 235–269 (in Russian).
5. Vereschagin, A.L., *Detonation Nanodiamonds*, Altai State Technical University, Barnaul, Russian Federation, 2001 (in Russian).
6. Dolmatov, V.Y., *Ultradisperse Diamonds of Detonation Synthesis: Production, Properties and Applications*, St. Petersburg, State Polytechnical University, 2003.
7. Danilenko, V.V., *Synthesis and Sintering of Diamond by Detonation*, Energoatomizdat, 2003 (in Russian).
8. Benedek, G., Milani, P., and Ralchenko, V.G., Eds., *Nanostructured Carbon for Advanced Applications*, NATO Science Series, Vol. 24, Kluwer Academic, Dordrecht, 2001.
9. Vul, A., Dolmatov, V., and Shenderova, O., *Detonation Nanodiamonds and Related Materials*, Bibliography Index, First Issue, "FIZINTEL", St. Petersburg, Russia, 2003.
10. Gruen, D., Vul, A., and Shenderova, O., Eds., *Ultrananocrystalline Diamond: Synthesis, Properties and Applications*, NATO Science Series, Springer, 2005.
11. Danilenko, V.V., On the history of the discovery of nanodiamond synthesis, *Phys. Solid State*, 46, 595, 2004.
12. Gogotsi, Y., Welz, S., Ersoy, D.A., and McNallan, M.J., Conversion of silicon carbide to crystalline diamond-structured carbon at ambient pressure. *Nature*, 411, 283, 2001.
13. Daulton, T.L., Kirk, M.A., Lewis, R.S., and Rehn, L.E., Production of nanodiamonds by high-energy ion irradiation of graphite at room temperature, *Nucl. Instrum. Methods B*, 175, 12, 2001.
14. Banhart, F. and Ajayan, P.M., Carbon onion as nanoscopic pressure cell for diamond formation, *Nature*, 382, 433, 1996.
15. Frenklach, M., Howard, W., Huang, D., Yuan, J., Spear K.E., and Koba, R., Induced nucleation of diamond powder. *Appl. Phys. Lett.*, 59, 546, 1991.
16. Tielens A., Seab C., Hollenbach, D.J., and Mckee, C.F., Shock processing of interstellar dust — diamonds in the sky, *Astrophys. J*., 319, L109, 1987.

17. Vicelli, J.A. and Ree, F.H., Carbon particle phase transformation kinetics in detonation waves, *J. Appl. Phys*., 88, 683–690, 2000.
18. Vicelli, J.A., Bastea, S., Glosli, J.N., and Ree, F.H., Phase transformations of nanometer size carbon particles in shocked hydrocarbons and explosives, *J. Chem. Phys*., 115, 2730, 2001.
19. Kuznetsov, V.L., Chuvilin, A.L., Butenko, Yu.V., and Usoltseva, A., Carbon phase diagram at the nanoscale, in *Science and Technology of Fullerence Materials*, Bernier, P., Ebbesen, T.W., Bethune, D.S., Metzger, R.M., Chiang, L.Y., and Mintmire J.W., Eds., Mater. Res. Soc. Proc., vol. 359, Pittsburgh, PA, p. 105, 1995.
20. Barnard, A.S, Russo, S.P., and Snook, I.K., Structural relaxation and relative stability of nanodiamond morphologies, *Diam. Rel. Mater*., 12, 1867, 2003.
21. Barnard, A.S., Russo, S.P., and Snook, I.K., Size dependent phase stability of carbon nanoparticles: nanodiamond versus fullerenes, *J. Chem. Phys*., 118, 5094, 2003.
22. Barnard, A.S, Russo, S.P., and Snook, I.K., Ab initio modelling of the stability of nanocrystalline diamond morphologies, *Phil. Mag. Lett.*, 83, 39, 2003.
23. Raty, J.Y., Galli, G., Bostedt, C., van Buuren, T.W., and Terminello, L.J., Quantum confinement and fullerene-like surface reconstructions in nanodiamonds, *Phys. Rev. Lett*., 90, 037401, 2003.
24. Barnard A., Russo, S., and Snook, I.K., Coexistence of bucky diamond with nanodiamond and fullerene carbon phases, *Phys. Rev. B*, 68, 073406, 2003.
25. Park, N., Lee, K., Han, S.W., Yu, J.J., and Ihm, J., Energetics of large carbon clusters: crossover from fullerenes to nanotubes, *Phys. Rev. B*, 65, 121405, 2002.
26. Tomanek, D. and Schluter, M.A., Growth regimes of carbon clusters, *Phys. Rev. Lett*., 67, 2331–2335, 1991.
27. Kuznetsov, V.L., Zilberberg, I.L., Butenko, Y.V., Chuvilin, A.L., and Segall, B., Theoretical study of the formation of closed curved graphite-like structures during annealing of diamond surface, *J. Appl. Phys*., 86, 863, 1999.
28. Welz, S., Gogotsi, Y., and McNallan, M.J., Nucleation, growth, and graphitization of diamond nanocrystals during chlorination of carbides, *J. Appl. Phys.*, 93, 4207, 2003.
29. Tyler, T., Zhirnov, V., Kvit, A., Kang, D., and Hren, J., Electron emission from diamond nanoparticles on metal tips, *Appl. Phys. Lett.*, 82, 2904, 2003.
30. Brenner, D.W., Shenderova, O.A., Harrison, J.A., and Sinnott, S., Second generation reactive empirical bond order (REBO) potential energy expression for hydrocarbons, *J. Phys.: Condens. Matter*, 14, 783, 2002.
31. Zhu, Y.Q., Sekine, T., Kobayashi, T., Takazawa, E., Terrones, M., and Terrones, H., Collapsing carbon nanotubes and diamond formation under shock waves, *Chem. Phys. Lett*., 287, 689, 1998.
32. DeCarli, P. and Jamieson, J., Formation of diamond by explosive shock, *Science*, 133, 1821, 1961.
33. Website of Microdiamant, AG Lengwil, Switzerland, www.microdiamant.com.
34. Yamada, K. and Tanabe, Y., Shock-induced phase transition of oriented pyrolytic graphite to diamond at pressures up to 15 GPa, *Carbon*, 40, 261–269, 2002.
35. Adadurov, G.A., Bavina, T.V., Breusov, O.N., Drobyshev, V.N., Messinev, M.J., Rogacheva, A.I., Ananiin, A.V., Apollonov, V.N., Dremin, A.N., Doronin, V.N., Dubovitsky, F.I., Zemlyakova, L.G., Pershin, S.V., and Tatsy, V.F., Method of producing diamond and/or diamond-like modifications of boron nitride, U.S. Patent 4,483,836, 1984.
36. Dahl, J.E., Liu, S.G., and Carlson, R.M.K., Isolation and structure of higher diamondoids, nanometer-sized diamond molecules, *Science*, 299, 96, 2003.
37. Carlson, R.M.K., Dahl, J.E.P., and Liu, S.G., in *Diamond Molecules Found in Petroleum*, in *Ultrananocrystalline Diamond*: *Synthesis, Properties and Applications*, Gruen, D., Vul, A., and Shenderova, O., Eds., NATO Science Series, Springer, 2005, p. 63.
38. Núñez-Regueiro, M., Monceau, P., and Hodeau, J.-L., Crushing C60 to diamond at room temperature, *Nature*, 355, 237–239, 1992.
39. Cao, L.M., Gao, C.X., Sun, H.P., Zou, G.T., Zhang, Z., Zhang, X.Y., He, M., Zhang, M., Li, Y.C., Zhang, J., Dai, D.Y., Sun, L.L., and Wang, W.K., Synthesis of diamond from carbon nanotubes under high pressure and high temperature, *Carbon*, 39, 311, 2001.
40. Ma, Y.Z., Zou, G.T., Yang, H.B., and Meng, J.F. Conversion of fullerenes to diamond under high pressure and high temperature, *Appl. Phys. Lett*., 65, 822, 1994.
41. Yusa, H., Nanocrystalline diamond directly transformed from carbon nanotubes under high pressure, *Diam. Relat. Mater.*, 11, 87, 2002.

42. Frenklach, M., Kematick, R., Huang, D., Howard, W., Spear, K.E., Phelps, A.W., and Koba, R., Homogeneous nucleation of diamond powder in the gas phase, *J. Appl. Phys*., 66, 395–399, 1989.
43. Buerki, P.R. and Leutwyler, S., Homogeneous nucleation of diamond powder by CO_2 laser-driven reactions, *J. Appl. Phys*., 69, 3739, 1991.
44. Wesolowski, P., Lyutovich, Y., Banhart, F., Carstanjen, H.D., and Kronmuller, H., Formation of diamond in carbon onions under MeV ion irradiation, *Appl. Phys. Lett*., 71, 1948, 1997.
45. Fedoseev, D.V., Bukhovets, V.L., Varshavskaya, I.G., Lavrentev, A.V., and Derjaguin, B.V., Transition of graphite into diamond in a solid state under the atmospheric pressure, *Carbon*, 21, 237, 1983.
46. Wei. B., Zhang, J., Liang, J., and Wu, D., The mechanism of phase transformation from carbon nanotube to diamond, *Carbon*, 36, 997, 1998.
47. Meguro, T., Hida, A., Suzuki, M., Koguchi, Y., Takai, H., Yamamoto, Y., Maeda, K., and Aoyagi, Y., Creation of nanodiamonds by single impacts of highly charged ions upon graphite, *Appl. Phys. Lett*. 79, 3866, 2001.
48. Tomita, S., Fujii, M., Hayashi, S., and Yamamoto, K., Transformation of carbon onions to diamond by low-temperature heat treatment in air, *Diam. Rel. Mater*., 9, 856, 2000.
49. Sun, L.T., Gong, J.L., Zhu, Z.Y., Zhu, D.Z., He, S.X., Wang, Z.X., Chen, Y., and Hu, G., Nanocrystalline diamond from carbon nanotubes, *Appl. Phys. Lett*., 84, 2901, 2004.
50. Lifshitz, Y., Kohler, T., Frauenheim, T., Guzmann, I., Hoffman, A., Zhang, R.Q., Zhou, X.T., and Lee, S.T., The mechanism of diamond nucleation from energetic species, *Science*, 297, 1531, 2002.
51. Terranova, M.L., Orlanducci, S., Fiori, A., Tamburri, E., Sessa, V., Rossi, M., and Barnard, A.S., Controlled evolution of carbon nanotubes coated by nanodiamond: the realization of a new class of hybrid nanomaterials, *Chem. Mater.*, 17, 3214, 2005.
52. Baik, E.S., Fabrication of diamond nanowhiskers, *Thin Solid Films*, 377, 295, 2000.
53. *Ximia i zizn* (*Chemistry and Life*), 1, 14–16, 1999 (in Russian; about work of Koscheev A.)
54. Masuda, H., Yanagishita, T., Yasui, K., Nishio, K., Yagi, I., Rao, T.N., and Fujishima, A., Synthesis of well aligned diamond nanocylinders, *Adv. Mater*., 13, 247, 2001.
55. Ando, Y., Nishibayashi, Y., and Sawabe, A., Nano-rods of single crystalline diamond, *Diam. Rel. Mater*., 13, 633, 2004.
56. Barnard, A.S., Structural properties of diamond nanowires: theoretical predictions and experimental progress, *Rev. Adv. Mater. Sci.*, 6, 94, 2004.
57. Barnard, A., From nanodiamond to nanowires, in *Ultrananocrystalline Diamond: Synthesis, Properties and Applications*, Gruen, D., Vul, A., and Shenderova, O., Eds., NATO Science Series, Springer, 2005, p. 25.
58. Shenderova, O., Brenner, D., and Ruoff, R.S., Would diamond nanorods be stronger than fullerene nanotubes? *Nano Lett*., 3, 805, 2003.
59. Chen, H. and Chang, L., Characterization of diamond nanoplatelets, *Diam. Rel. Mater*., 13, 545, 2004.
60. Gruen, D.M., Liu, S.Z., Krauss, A.R., and Pan, X.Z., Buckyball microwave plasmas: fragmentation and diamond-film growth, *J. Appl. Phys*., 75, 1758, 1994; *Appl. Phys. Lett*., 64, 1502, 1994.
61. Gruen, D.M., 356350 Ultracrystalline diamond in the laboratory and the cosmos, *MRS Bull*., 26, 771–776, 2001.
62. Kimura, Y. and Kaito, C., Production of nanodiamond from carbon film containing silicon, *J. Cryst. Growth*, 255, 282, 2003.
63. Gordeev, S.K., in *Nanostructured Carbon for Advanced Applications*, Benedek, G., Milani, P., and Ralchenko, V.G., Eds., NATO Science Series, Vol. 24, Kluwer Academic, Dordrecht, 2001, pp. 71–88.
64. Aleksenskii, A.E., Baidakova, M.V., Vul', A.Y., and Siklitskii, V.I., The structure of diamond nanoclusters, *Phys. Solid State*, 41, 668–671, 1999.
65. *Proceedings of the 1st International Symposium, Detonation Nanodiamond: Synthesis, Properties, and Applications*, St Petersburg, 7–9 July 2003, *Phys. Solid State*, 46, 2004.
66. Maillard-Schaller, E., Kuettel, O.M., Diederich, L., and Zhirnov, V., Surface properties of nanodiamond films deposited by electrophoresis on Si(100), *Diam. Rel. Mater*., 8, 805, 1999.
67. Gordeev, S.K., Belobrov, P.I., Kiselev, N.I., Petrakovskaya, E.A., and Ekstrom, T.C., Novel solid nano diamond/pyrocarbon semiconductor materials, *Mater. Res. Soc. Symp. Proc*., 63, F14.16.1, 2001.
68. Belobrov, P.I., Gordeev, S.K., Petrakovskaya, E.A., and Falaleev, O.V., Paramagnetic properties of nanodiamond, *Doklady Phys*., 46, 459, 2001.

69. Zhirnov, V.V., Kuttel, O.M., Groning, O., Alimova, A.N., Detkov, P.Y., Belobrov, P.I., Maillard-Schaller, E., and Schlapbach, L., Characterization of field emission cathodes with different forms of diamond coatings, *J. Vac. Sci. Technol*., 17, 666, 1999.
70. Alimova, A.N., Chubun, N.N., Belobrov, P.I., Detkov, P.Y., and Zhirnov, V.V., Electrophoresis of nanodiamond powder for cold cathode fabrication, *J. Vac. Sci. Technol. B*, 17, 715, 1999.
71. Zhirnov, V.V., Shenderova, O.A., Jaeger, D.L., and Brenner, D., Electron emission properties of detonation nanodiamonds, *Phys. Solid State*, 46, 641, 2004.
72. Jaeger, D.L., Tyler, T., Kvit, A.K., Zhirnov, V.V., and Hren, J.J., Electrostatic factors affecting emission from discrete isolated diamond nanodots, *Proceedings of Cold Cathodes II*, Electrochemical Society, Philadelphia, PA, 2002, p. 291.
73. Kuznetsov, V.L., Chuvilin, A.L., Butenko, Yu.V., Malkov, I.Yu., and Titov, V.M., Onion-like carbon from ultra-disperse diamond, *Chem. Phys. Lett*., 222, 343, 1994.
74. Aleksenskii, A.E., Baidakova, M.V., Vul, A.Y., Davydov, V.Y., and Pevtsova, Y.A., Diamond-graphite phase transition in ultradisperse-diamond clusters, *Phys. Solid State*, 39, 1007, 1997.
75. Davidson, W.P. and Kang, J.L., *Applying CVD Diamond and Particulate Nanodiamond*, in *Ultrananocrystalline Diamond: Synthesis, properties and Applications*, Gruen, D., Vul A., and Shenderova, O., NATO Science Series, Springer, 2005, p. 357.
76. Timoshkov, Y.V., Danilyuk, A.L., Molchan, I.S., *Galvanotekhnika and Obrabotka Poverkhnosti*, 7, 20–26, 1999 (in Russian).
77. Bogatyreva, G.P., Marinich, M.A., and Gvyazdovskaya, V.L., Diamond — an adsorbent of a new type *Dia. Rel. Mater*., 9, 2002–2005, 2000.
78. Beveratos, A., Brouri, R., Gacoin, T., Poizat, J.P., and Grangier, P., Nonclassical radiation from diamond nanocrystals, *Phys. Rev. A*, 64, 1802, 2001.
79. Curtiss, L.A., Zapol, P., Sternberg, M., and Gruen, D., *Quantum Chemical Studies of Growth Mechanisms of Ultrananocrystalline Diamond*, in *Ultrananocrystalline Diamond: Synthesis, Properties and Applications*, Gruen, D., Vul, A., and Shenderova, O., Eds., NATO Science Series, Springer, 2005, p. 39.
80. Corrigan, T.D., Gruen, D.M., Krauss, A.R., Zapol, P., and Chang, R.P.H., The effect of nitrogen addition to Ar/CH4 plasmas on the growth, morphology and field emission of ultrananocrystalline diamond, *Diam. Rel. Mater*., 11, 43–48, 2002.
81. Williams, O., Zimmermann, T., Kubovic, M., and Gruen, D., *Electronic Properties and Applications of Ultrananocrystalline Diamond*, in *Ultrananocrystalline Diamond: Synthesis, properties and Applications*, Gruen, D., Vul, A., and Shenderova, O., Eds., NATO Science Series, Springer, 2005, p. 373.
82. Krauss, A.R., Auciello, O., Gruen, D.M., Jayatissa, A., Sumant, A., Tucek, J., Mancini, D.C., Moldovan, N., Erdemir, A., Ersoy, D., Gardos, M.N., Busmann, H.G., Meyer, E.M., and Ding, M.Q., Ultrananocrystalline diamond thin films for MEMS and moving mechanical assembly devices, *Diam. Rel. Mater*., 10, 1952–1961, 2001.
83. Gordeev, S.K., in *Nanostructured Carbon for Advanced Applications*, Benedek, G., Milani, P., and Ralchenko, V.G., Eds., NATO Science Series, Vol. 24, Kluwer Academic, Dordrecht, 2001, pp. 71–88.
84. Gogotsi, Yu., personal communication, 2003.
85. Frietas, R.A., *Nanomedicine*, Volume 1: *Basic Capabilities*, Landes Bioscience, 1999; Nanomedicine, Volume IIA: Biocompatibility, Landes Bioscience, 2003.
86. Wilson, S.R., Biological aspects of fullerenes, in *Fullerenes: Chemistry, Physics, and Technology*, Kadish, K.M., and Ruoff, R.S., Eds., Wiley, New York, 2000.
87. Nanotechnology in Biology: The Good of Small Things, *The Economist*, December 22, 2001.
88. http://www.csixty.com
89. Lin, A.M.Y., Chyi, B.Y., Wang, S.D., Yu, H.H., Kanakamma, P.P., Luh, T.Y., Chou, C.K., and Ho, L.T., Carboxyfullerene prevents iron-induced oxidative stress in rat brain, *J. Neurochem*., 72, 1634–1640, 1999.
90. DaRos, T., Prato, M., Novello, F., Maggini, M., and Banfi, E., Easy access to water-soluble fullerene derivatives via 1,3-dipolar cycloadditions of azomethine ylides to C60, *J. Org. Chem*., 61, 9070, 1996.
91. Niemeyer, C.M., Nanoparticles, proteins, and nucleic acids: biotechnology meets materials science, *Angew. Chem. Int. Ed*., 40, 4128–4158, 2001.

92. Tsang, S.C., Davis, J.J., Chen, Y.K., Green, M.L.H., Hill, H.A.O., Hambley, T.W., and Sadler, P.J., Immobilization of small proteins in carbon nanotubes — high-resolution transmission electron-microscopy study and catalytic activity, *J. Chem. Soc. Chem. Commun.*, 12, 1803–1805, 1995.
93. Tsang, S.C., Guo, Z.J., Chen, Y.K., Green, M.M.H., Hill, H.A.O., Hambley, T.W., and Sadler, P.J., Immobilization of platinated and iodinated oligonucleotides on carbon nanotubes, *Angew. Chem. Int. Ed.*, 36, 2198–2200, 1997.
94. Davis, J.J., Green, M.L., Hill, H.A., Leung, Y.C., Sadler, P.J., Sloan, J., Xavier, A.V., and Tsang, S.C., The immobilization of proteins in carbon nanotubes, *Inorg. Chim. Acta*, 272, 261–266, 1998.
95. Lin, Y., Taylor, S., Li, H.P., Fernando, K.A.S., Qu, L.W., Wang, W., Gu, L.R., Zhou, B., and Sun, Y.P., Advances toward bioapplications of carbon nanotubes, *J. Mater. Chem*., 14, 527, 2004.
96. Yang, W.S., Auciello, O., Butler, J.E., Cai, W., Carlisle, J.A., Gerbi, J., Gruen, D.M., Knickerbocker, T., Lasseter, T.L., Russell, J.N., Smith, L.M., and Hamers, R.J., DNA-modified nanocrystalline diamond thin-films as stable, biologically active substrates, *Nat. Mater*., 1, 253, 2002.
97. Gu, H., Su, X., and Loh, K.P., Conductive polymer-modified boron-doped diamond for DNA hybridization analysis, *Chem. Phys. Lett*., 388, 483, 2004.
98. Takahashi, K., Tanga, M., Takai, O., and Okamura, H., DNA preservation using diamond chips *Diam. Rel. Mater*., 12, 572, 2003.
99. Ushizawa, K., Sato, Y., Mitsumori, T., Machinami, T., Ueda, T., and Ando, T., Covalent immobilization of DNA on diamond and its verification by diffuse reflectance infrared spectroscopy, *Chem. Phys. Lett*., 351, 105, 2002.
100. Mitura, S., Mitura, A., Niedzielski, P., and Couvrat, P., Nanocrystalline diamond coatings, *Chaos Solitons Fractals*, 10, 2165, 1999.
101. Kossovsky, N., Gelman, A., Hnatyszyn, H.J., Rajguru, S., Garrell, R.L., Torbati, S., Freitas, S.S.F., and Chow, G.M., Surface modified diamond nanoparticles as antigen delivery vehicles, *Bioconjugate Chem*., 6, 507, 1995.
102. Puzyr, A.P., Bondar, V.S., Belobrov, P.I., and Bukaemskii, A.A., Preparation of nanodiamond-protein-δ-aluminum oxide complex, *Dokl. Acad. Sci. USSR*, 373, 408, 2000.
103. Purtov, K.V., Bondar', V.S., and Puzyr', A.P., Supramolecular structure of nanodiamond particles and obelin built up on a two-dimensional plate, *Dokl. Akad. Nauk*., 380, 339, 2001.
104. Puzyr, A.P., Neshumayev, D.A., Tarskikh, S.V., Makarskaya, G.V., Dolmatov, V.Y., and Bondar, V.S., Damaging effect of detonation diamonds on human white and red blood cells in vitro, *Dokl. Biochem. Biophys*., 385, 201, 2002.
105. Bondar', V.S., Pozdnyakova, I.O., and Puzyr', A.P., Applications of nanodiamonds for separation and purification of proteins *Phys. Solid State*, 46, 758–760, 2004.
106. Bondar', V.S. and Puzyr', A.P., Nanodiamonds for biological investigations *Phys. Solid State*, 46, 716–719, 2004.
107. Puzyr', A.P., Pozdnyakova, I.O., and Bondar', V.S., Design of a luminescent biochip with nanodiamonds and bacterial luciferase, *Phys. Solid State*, 46, 761–763, 2004.
108. Bakowicz, K. and Mitura, S., Influence of bioactive diamond powder particles on human red blood cells in conditions of oxidative free radical damage. Abstract for IVC-16/ICSS-12/NANO-8/AIV-17, June 28–July 2, Venice, Italy, 2004.
109. Dolmatov, V.Yu. and Kostrova, L.N., Detonation-synthesized nanodiamonds and the possibility to develop a new generation of medicines, *J. Superhard Mater*., 3, 79, 2000.

8 Carbide-Derived Carbon

G. Yushin, A. Nikitin, and Y. Gogotsi
Department of Materials Science and Engineering,
Drexel University, Philadelphia, Pennsylvania

CONTENTS

ABSTRACT

This chapter gives a comprehensive overview of various nanostructured carbon materials produced from carbides by selective etching in halogens, molten salts, and supercritical water, as well as by vacuum decomposition. Both experimental results and thermodynamic modeling of carbon formation are provided. Amorphous and nanocrystalline graphitic carbon, nanotubes, fullerene-like structures, carbon onions, nanocrystalline diamond, and ordered graphite can be produced by selective etching or decomposition of metal carbides. The discussed method of carbon synthesis offers unique control over carbon microstructure and porosity at the nanoscale, thus allowing optimization of material properties for improved performance in advanced applications. These applications include hydrogen and methane storage media, electrodes in electrochemical energy-storage systems, tribological coatings, sorbents, and catalyst supports, among others.

8.1 INTRODUCTION

Carbon is a very special element. It plays a dominant role in the chemistry of all living organisms and is considered to be the only truly biocompatible material in all its forms. Carbon is the backbone of all organic substances and a whole class of materials — polymers — is based on carbon compounds. Being the sixth most common element in the universe, it is present in most of the things that surround us. In addition, carbon is the only element that has a major monthly scientific journal named after it — *Carbon*, published by Elsevier Science. This journal publishes papers dealing with carbon materials only: mainly amorphous carbons, graphite, diamond, fullerene-like structures, and nanotubes, which have numerous practical applications. Moreover, some of the carbon allotropes, diamond and fullerene, have journals dedicated to them as well (*Diamond and Related Materials*, *Fullerene Science and Technology*, and others).

There has been a new wave of interest in carbon materials caused by the recent "nano-" revolution, which has affected all science and engineering fields. Many nanotechnology papers are devoted to carbon-based nanostructures. Not only nanotubes and fullerenes but also nanodiamond, nanographite, carbon onions, and nanoporous carbons are steadily attracting increasing attention [1–7]. Biocompatibility of carbons may provide them a unique place in medical applications of nanotechnology [3,8–11].

The range of mechanical, optical, and electrical properties that carbon materials can provide is amazing. For example, diamond is one of the hardest materials known (microhardness of $>$100 GPa) and is used to make cutting tools and abrasives, while graphite is one of the softest materials (microhardness is about 1 GPa) and is used as a solid lubricant. While diamond is an optically transparent material, being a wide-band-gap semiconductor, graphite is not transparent, being a good electric conductor. The recently discovered carbon nanotubes (CNTs) are considered to be the strongest fibers known. Depending on their crystallographic structure, CNTs may have the conductivity of copper (metallic single-wall nanotubes) or silicon (semiconducting single-wall nanotubes). In addition to the known carbon allotropes, amorphous or disordered carbons form a whole new class of materials for which all properties, such as electrical conductivity, hardness, wear resistance, gas permeability, optical transparency, and many others can be finely tuned by controlling the sp^2/sp^3 carbon ratio, porosity/density, size, and ordering of nanocrystals, and inclusions of various allotropic forms of carbon and other elements.

There are many ways to produce carbon materials. Very high temperatures are typically required for the synthesis of ordered graphite because of a very low mobility of carbon atoms in its

covalently bonded layers. Diamond is produced either at high pressures or by using plasma and other high-energy activation techniques. Many carbon nanostructures such as fullerenes, carbon onions, and nanotubes can be produced by vaporization of graphite (e.g., by electric current, laser heating, explosion, plasma, etc.) in the presence of an inert quenching gas. Chemical vapor deposition (CVD) is currently a common method for the synthesis of thin and thick films of disordered graphitic carbon, diamond, and nanotubes. Many porous and disordered carbons, including carbon fibers and activated carbons, are made by thermal decomposition of organic compounds.

The age of nanotechnology requires new methods that enable engineers to control the growth of carbon materials at the atomic level, provide a better control over the structure of carbon materials as well as capability to produce selectively novel carbon structures such as nanotubes, onions, nanocrystalline diamond, or nanoporous carbon with a narrow pore-size distribution for gas storage, batteries, supercapacitors, and other applications.

Selective etching of carbides is considered to be a promising technique for the synthesis of various carbon structures [12]. Carbon produced by extraction of metals from metal carbides (MeCs) is called carbide-derived carbon (CDC). Leaching in supercritical water, high-temperature treatment in halogens, vacuum decomposition, and other methods can be used to remove metals from carbides, producing carbon coatings or bulk and powdered carbon. The linear reaction kinetics, which were demonstrated for chlorination of both bulk-sintered polycrystalline SiC [13] and single-crystalline SiC nanowhiskers [14], allow transformation to any depth, until the complete particle or component is converted into carbon. Carbide-derived carbon demonstrates a variety of carbon phases depending on experimental conditions. Amorphous and nanocrystalline graphitic carbon [15], nanotubes [16], fullerene-like structures [17], carbon onions [17,18], nanocrystalline diamond [19,20], and ordered graphite [21] have been reported. Thus, this method allows the synthesis of almost all carbon allotropes. Since the metal carbide lattice is used as a template and metal is extracted layer-by-layer, atomic-level control can be achieved in the synthesis process and the structure of the carbon can be templated by the carbide structure, with an opportunity for further structure modification by controlling the temperature, composition of the environment, and other process variables. An important advantage of the CDC process over the CVD or the PVD process for coating synthesis is that the transformation is conformal and does not lead to a change in the carbide sample size and shape. This may be of particular importance in nanotechnology when nanometer-range accuracy must be achieved.

Significant progress in CDC synthesis has been achieved over the past decade and a review of the synthesis has been published [22]. However, during the last few years, a significantly better understanding of the mechanisms involved in CDC formation has been achieved and better control over CDC properties has been developed. This chapter presents an up-to-date summary of the work done in this exciting area, which shows various approaches to CDC synthesis (leaching by supercritical water, halogens, salts, and decomposition in vacuum), analyzes similarities and differences between different techniques, and describes the variety of structures produced, their applications as well as the potential of the method for producing new carbon structures with required properties.

8.2 SELECTIVE ETCHING OF CARBIDES BY HALOGENS

8.2.1 Chlorination of Carbides for Production of Chlorides

A manufacturing process based on the reaction of silicon carbide with chlorine gas was reported in 1918 for the first time [23]. Hutchins patented a method for the production of silicon tetrachloride using the reaction

$$SiC + 2Cl_2 = SiCl_4 + C \tag{8.1}$$

The reaction was conducted by passing dry chlorine over silicon carbide heated to a temperature of 1000°C or above. The main product of the reaction, silicon tetrachloride vapor, passed through the

outlet pipe into a condenser. Residual carbon was disposed of. A development of this method was patented in 1956 [24]. In order to remove carbon without cooling off the reactor, air was periodically blown through it to burn the carbon waste. This method was widely used until the 1960s, when the availability of large quantities of inexpensive Si manufactured for the semiconductor industry led to the replacement of SiC with Si in $SiCl_4$ production.

Treatment of other MeCs in chlorine gas has been used to produce corresponding chlorides. Therefore, kinetics of chlorination of titanium and niobium carbides [25] and zirconium carbide [26] were studied. The reactions

$$MeC + x/2Cl_2 = MeCl_x + C \tag{8.2}$$

(where $x = 4$ when Me = Ti, Zr; and $x = 5$ when Me = Nb) were conducted in a quartz-tube flow reactor in the temperature range 600 to 800°C in the case of TiC and NbC, and 450 to 950°C in the case of ZrC. Samples were produced by hot-pressing the carbide powders. The rates of the reactions were controlled by measuring the weight loss and the amount of chlorides. Carbon that formed on the surface of the samples in the course of the reaction was considered to be porous graphite or carbonaceous "cinder." This layer did not affect the reaction rate at 400°C but at higher temperatures the diffusion resistance was considerable. In the case of niobium carbide, the chlorination rate at 600°C was higher than at 800°C. This phenomenon was attributed to the increased adhesion of the carbon layer to the carbide surface, but our recent work shows that it should primarily be attributed to changes in the CDC structure. For some carbides, the mechanism of the interaction with chlorine and the composition of reaction products may change with temperature. Therefore, it is important to consider the thermodynamics of the reactions of carbides with halogens.

8.2.2 Thermodynamic Simulations

Thermodynamic simulations can be utilized to estimate the effect of various process parameters on CDC formation and help in choosing the optimum synthesis conditions [27]. Such simulations were performed on a number of carbides [28–32]. The Gibbs free energy minimization program (such as FactSage or ChemSage from GTT Technologies, Germany) was employed to estimate the equilibrium amounts of reaction species as a function of the chlorination temperature for different amounts of chlorine. The calculations were always done for a closed system with a constant total pressure of 1 atm. The gas phase was considered to be a mixture of ideal gases, and the solid phase was treated as a mechanical mixture of compounds with unit activities. It was found that carbon formation is possible by the halogenation of SiC, TiC, ZrC, V_2C, NbC, Nb_2C, TaC, Ta_2C, Cr_3C_2, Mo_2C, MoC, W_2C, WC, BaC_2, CaC_2, SrC_2, Al_4C_3, B_4C, Fe_3C, Ti_3SiC_2, and Ti_2AlC. We will use the designation "MeC CDC" for carbon produced from a metal carbide (MeC) by selective removal of the metal.

Figure 8.1 shows an example of the thermodynamic calculations discussed with regard to the formation of carbon from ZrC for different amounts of initial Cl_2 content. Low content of Cl_2 in the reaction mixture limits the CDC conversion efficiency and the reaction products contain a considerable amount of untransformed carbide (Figure 8.1a). Adding more Cl_2 into the system results in the complete conversion of ZrC into $ZrCl_4$, CCl_4, and C. Different temperature ranges can be distinguished. In the low-temperature range (range I), no CDC synthesis is thermodynamically possible under equilibrium conditions due to the preferential formation of CCl_4 over solid C. The medium-temperature range (range II) corresponds to the formation of both CDC and CCl_4. As can be seen from Figure 8.1, increasing the temperature leads to a higher CDC yield. In the high-temperature region (range III), no loss of carbon as CCl_4 is observed. Each range depends on the amount of Cl_2 used in the calculation. Range II, for example, changed from ~50–700°C to ~350–800°C and to ~450–870°C when the amount of Cl_2 changed from 3 to 5 and to 10 mol, respectively, while the amount of ZrC was kept constant (1 mol). The thermodynamic simulations suggest an optimum Cl_2/ZrC ratio, where maximum carbon yield is achieved over a large temperature range. Adding too much or too little Cl_2 will affect the temperature range yielding maximum

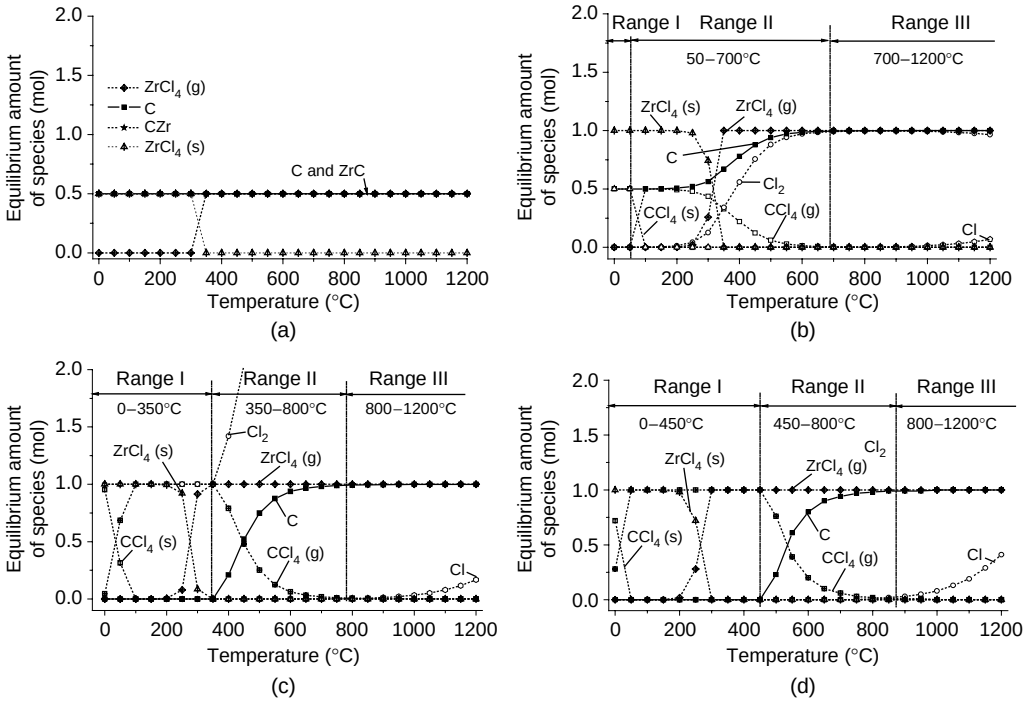

FIGURE 8.1 Example of thermodynamic analysis for zirconium carbide chlorination: equilibrium amount of species vs. chlorination temperature for 1 mol (a), 3 mol (b), 5 mol (c), and 10 mol (d) of Cl_2 (From Dash, R.K. et al., Synthesis, structure and porosity analysis of microporous and mesoporous carbon derived from zirconium carbide, *Microporous and Mesoporous Mater*., **86**, 50–57, 2005. Generally, three temperature ranges can be distinguished: range-I with no CDC formation predicted due to high stability of CCl_4 at low temperatures, range-II corresponding to the increase of CDC amount with temperature, and range-III is where CDC efficiently forms due to the higher stabilities of gaseous $ZrCl_4$ and solid C compared to CCl_4. Each range clearly depends on the amount of Cl_2 in the system. Formation of solid $ZrCl_4$ is expected at temperatures below 300°C. Incomplete reaction takes place in case of insufficient Cl_2 amount.

carbon. Undesirable formation of solid zirconium chloride is expected at temperatures below 300 to 350°C, depending on the initial Cl_2 amount.

Figure 8.2 shows equilibrium compositions for TiC/Cl_2 and SiC/Cl_2 systems (1:5 molar ratio) at ambient pressure. In both cases, no formation of solid chlorides is predicted and CDC forms in high yield at above 600°C. We have also conducted thermodynamic simulations for interactions of a variety of carbides with other halogens such as F and I and halogen-containing gases such as HCl and HF (data not shown), and confirmed the possibility of CDC formation in nonchlorine environments.

The thermodynamic calculations provide information about a closed system in equilibrium. The experimental set-up used for CDC synthesis is in most cases an open system, where gaseous reaction products are continuously removed with a gas flow, and the actual product composition may be determined by the kinetics of the process. However, the results obtained provide general guidelines for the experimental design. They show that selective removal of metals is possible by using small amounts of Cl_2, as well as suggesting that a moderate amount of Cl_2 is the key to efficient CDC synthesis. Excess Cl_2 can be used at high temperatures, when CCl_4 is unstable to accelerate the process.

8.2.3 Historic Overview of Carbide-Derived Carbon Studies

Carbide-derived carbon did not attract major attention from researchers until 1959, when Mohun [15] introduced "a fourth class of amorphous carbons" along with the three known ones (hard carbons,

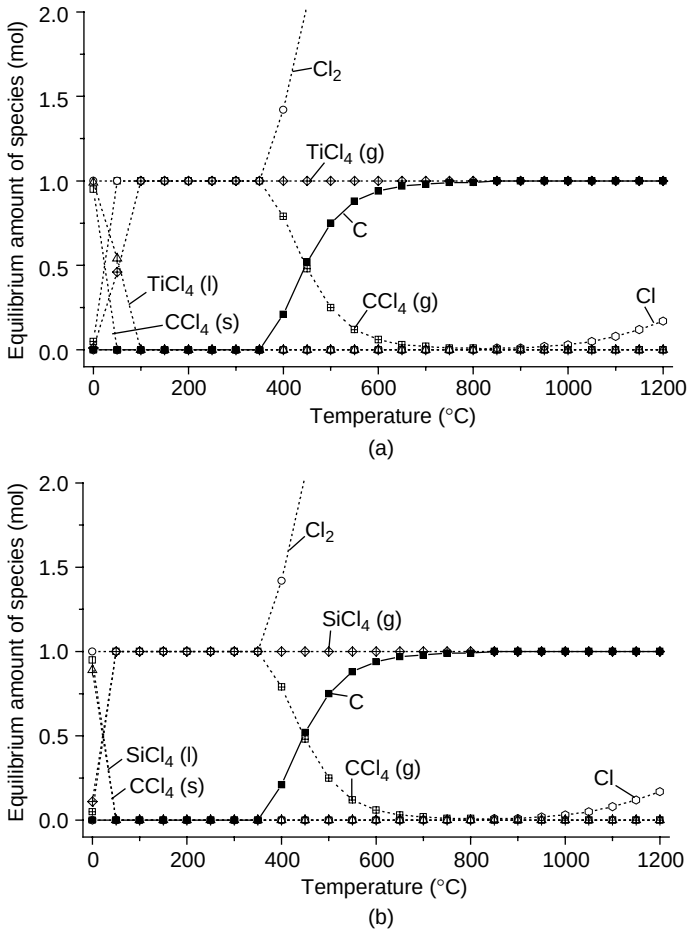

FIGURE 8.2 Examples of thermodynamic analysis for chlorination of TiC (a) and SiC (b) in 5 mol of Cl_2, demonstrating efficient formation of CDC at above 600°C.

soft carbons, and carbon black). The term "mineral carbons" was proposed for carbons formed by the chlorination of inorganic carbides to distinguish them from carbons of organic origin. Unlike organic carbon, which also includes substantial quantities of hydrogen and other elements, CDC was claimed to be real elemental amorphous carbon. Chlorination of silicon, aluminum, boron, titanium, zirconium carbides, and zirconium carbonitride was carried out in the temperature range from 150 for ZrC · ZrN to 1650°C for SiC in chlorine flow. Reactor tubes were made of quartz or mullite and were provided with an external electric heater. Owing to the strong exothermic effect of the reaction and the substantial size of the samples (20 to 250 g), temperature of the sample was rather difficult to control. After the chlorination process was completed, carbon samples were cooled in an atmosphere of chlorine or dry nitrogen and treated to remove the residual chlorine.

Mohun extended his study and eventually patented the new materials and the processes of their production [33,34]. Figure 8.3 shows some sorption properties of SiC CDC reported in these patents as a function of chlorination temperature and the cooling environment. Vapor adsorption capacity of the CDC generally peaked at some intermediate chlorinated temperatures and decreased when the processing temperature increased to 1650°C, possibly due to the graphitization of the CDC and the corresponding decrease of the specific surface area (SSA, surface area of material per unit weight) as we know from our experiments. Vapor adsorption also noticeably increased when samples were

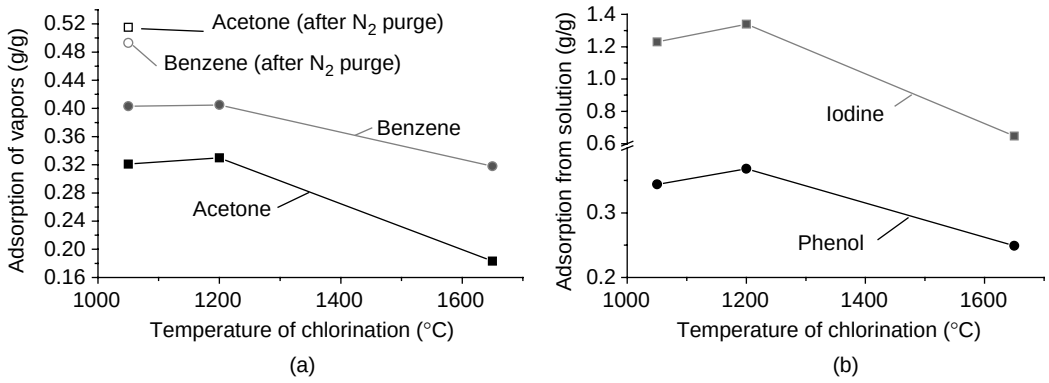

FIGURE 8.3 Adsorption capacity of SiC CDC cooled in Cl_2 as a function of chlorination temperature: vapor adsorption (a) and adsorption from solution (b). A maximum adsorption at intermediate temperature was observed. Dechlorination of SiC CDC prepared at 1050°C by purging N_2 through it resulted in a noticeable increase of the vapor adsorption capacity.

cooled in N_2 rather than in Cl_2, demonstrating the importance of the dechlorination procedure. The patents also give a detailed description of all the methods employed for the dechlorination of the CDC samples. The techniques described include heating in static air, heating in gas stream (air, nitrogen, water vapor, and carbon dioxide), vacuum dechlorination, and wet dechlorination with the use of various washing solutions. Chlorine content in the samples was controlled by weight loss during dechlorination, and measuring the pH of the aqueous suspension. It was found that the flow of nitrogen or other gases over the sample heated at 150°C at atmospheric pressure provided rapid and complete dechlorination. Of considerable importance are the chlorides, which remain trapped in the carbon when reaction is complete. It was shown that they are readily removed by any cyclic fluctuation in temperature or pressure carried out at the same time as dechlorination. Another interesting property of CDCs discovered in the studies was the absence of measurable paramagnetic electron spin absorption. This distinguishes CDCs from organic chars in which free radicals are trapped during carbonization of organic matter.

The chlorination set-up used in most of the CDC experiments is a common set-up for treatment of the solid samples in the gas flow at elevated temperatures. Figure 8.4 shows a version of the experimental apparatus.

8.2.4 Kinetics of Halogenation of Carbides

The kinetics of CDC formation has been studied for various carbides. In 1960, Kirillova et al. [25] investigated the chlorination of bulk TiC and NbC and observed a linear increase in the CDC layer thickness with time, suggesting that the transformation rate is not controlled by the diffusion of gases. The chlorination rates were determined, and activation energies of CDC synthesis in the 400 to 800°C range were found to be 50 and 38 kJ/mol for TiC CDC and NbC CDC, respectively. The chlorination kinetics of a lower zirconium carbide was discussed in the Ph.D. dissertation of Vasilenko [35] in 1956. Experiments were carried out in the 400 to 800°C range on bulk and powder samples. It was shown that CDC synthesis follows linear reaction kinetics and that the chlorination temperature has only a small influence on the CDC synthesis rate.

In 1964, Kuriakose and Murgrave published the results of their studies on the fluorination of bulk ZrC and HfC in the 300 to 900°C range [36,37]. They determined the activation energies of the fluorination to be 92 kJ/mol and observed a constant fluorination rate with time. In 1966 Orekhov et al. [26] performed in-depth studies of chlorination kinetics of bulk ZrC in the 450 to 950°C range. The activation energy of the chlorination was found to increase from ~67 to

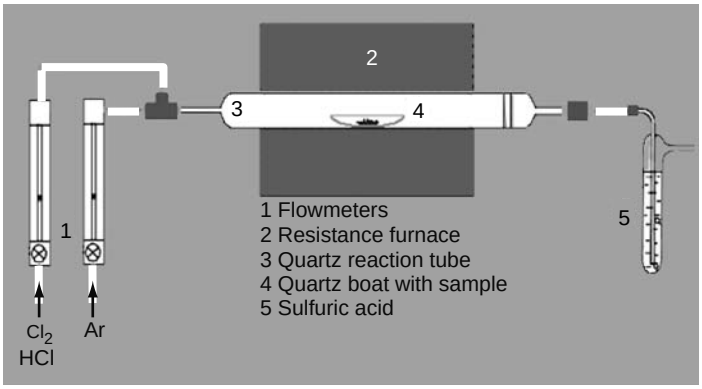

FIGURE 8.4 Typical experimental set-ups used for the chlorination of carbides.

~121 kJ/mol with an increase in the chlorination temperature. Chlorination rates were determined for various temperatures and Cl_2 gas velocities. The increase of CDC thickness was linear with time for relatively thin coatings (<500 μm). However, for thicker CDC layers, the diffusion became the limiting factor of the transformation rate, resulting in a parabolic dependence of the CDC thickness over time. More recent studies of the halogenation of various carbides (see, e.g., [38]) generally confirmed the linear transformation kinetics of bulk polycrystalline carbides to CDC, which allows easy and precise control over the coating thickness, desirable for most of the applications. Recent transmission electron microscopy (TEM) studies on the chlorination of SiC nanowhiskers [14] revealed linear kinetics for CDC transformation of single-crystalline carbides starting from the initial stage, when a nanometer-thick coating is formed.

8.2.5 Conservation of Shape

As mentioned in the introduction, halogenation of carbides results in a conformal transformation. Conservation of shape during the CDC synthesis had been observed in macro and microscopic objects [38,39] for a long time. However, most studies were conducted on powders, fibers, and bulk samples, and until very recently [14], it was not known how precisely the carbon formed could follow the original shape of the carbide crystal. In addition, it was not known if the stresses existing at the interface between CDC and the substrate might destroy nanoscale objects having a high aspect ratio (e.g., components of SiC-based microelectromechanical systems [MEMS], during the transformation). Our recent TEM studies [14] provided direct nanoscale observations of all stages of the CDC transformation (Figure 8.5). They revealed that no matter what the final structure of the transformed carbon or what metal extraction method was employed, a complex shape of a carbide nano-object could be preserved.

8.2.6 Nanoporous Structure and Adsorption Properties

8.2.6.1 Pore Formation

Selective removal of metals from MeCs generally results in the formation of porous carbon with a density lower than that of graphite. The size of pores in the CDC is influenced by the distribution of carbon atoms in the initial carbide, the CDC's atomic structure, the amounts of chlorides and chlorine trapped in the CDC, the size of the chloride molecule, the presence of catalytic particles, and the effect of optional post-treatments, such as activation, or mild oxidation.

Porous structure and molecular sieve properties of CDC were first investigated by Boehm and Warnecke [40] in 1975. Carbon samples were prepared by treating tantalum and silicon carbides in

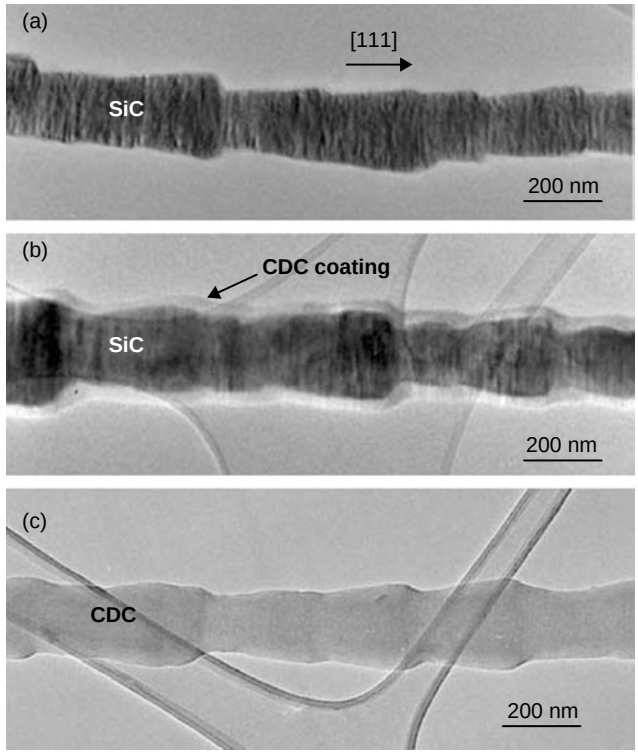

FIGURE 8.5 Transmission electron microscopy micrographs of SiC whiskers at different stages of the transformation to carbon: (a) initial: as-received SiC whisker, (b) intermediate: carbon coating on a SiC whisker, and (c) final: completely transformed to amorphous carbon. (From Cambaz, Z.G. et al., Conservation of shape during formation of carbide-derived carbon on silicon carbide nano-whiskers, *J. Am. Ceram. Soc*., 2005, in press.) The whiskers were treated in Cl_2 at 700°C (b) and 1200°C (c).

chlorine flow at 500 and 900°C, respectively. The completeness of the reaction was confirmed by the disappearance of the x-ray diffraction (XRD) peaks of the original carbides. The CDC samples produced from TaC were additionally heat-treated at various temperatures. Sorption isotherms (the quantity of the gas adsorbed onto or desorbed from the solid adsorbent surface at a constant temperature in the range of equilibrium vapor pressures) of CDCs were measured for N_2 at −196°C, for CO_2 at 0°C, and for a variety of organic adsorptives at 25°C. All isotherms were of Type I in the Brunauer classification, which indicated the nanoporous structure of the CDC samples. There was a peak in N_2 uptake for CDC from TaC after heat treatment at 1450°C. The low sorption capacity of the CDC prepared at 500°C was explained by the presence of tantalum pentachloride, which blocked a considerable part of the pore volume. However, our experience shows that a very small pore size can also limit the applicability of sorption techniques for the analysis of CDC produced from transition MeCs at ~500°C. The maximum pore volume accessible to N_2 in CDC after heat treatment at 1450°C was 0.644 cm^3/g, which is in excellent agreement with the theoretically calculated pore volume value of 0.645 cm^3/g. Evaluation of the CO_2 isotherms of the CDCs heat-treated in the range 500 to 1100°C gave a maximum pore volume of 0.273 cm^3/g, indicating that not all the pores were accessible to larger CO_2 molecules. Adsorption of organic vapors (benzene, tetrachloromethane, toluene, and α-pinene) demonstrated strong molecular sieve effects for CDC from TaC heat-treated above 1500°C. CDC from SiC post-treated in hydrogen at 800°C was proven to be suitable for gas chromatography. It was possible to separate low-molecular weight gases with its use. For example, O_2, N_2, CO, and CO_2 could be separated with a 1 m column at 30°C and CH_4, C_2H_2, C_2H_4, and C_2H_6 at 100°C.

The porous structure and adsorption properties of CDC from silicon carbide and carbides of transition metals of IV to VI groups were studied by Fedorov et al. [41–44] in the early 1980s. Three forms of SiC (green and black α-SiC and β-SiC, temperature is not indicated) [41]; TiC in the temperature range 500 to 1100°C [42]; ZrC, HfC, VC, NbC, WC, Cr_3C_2, Mo_2C, B_4C, and UC at 700°C [43] were treated in chlorine gas flow in the quartz-tube reactor. Vapors of bromine and iodine, besides chlorine gas, were used for etching zirconium carbide [44]. Completeness of the reaction was controlled by the weight loss during the process and by the carbide contents in the sample. The porous structure of the CDCs obtained was studied by a combination of pycnometric, mercury-porosimetric, and sorption methods. Theoretical values of the apparent density δ were calculated assuming that no shrinkage of the samples occurred during the chlorination process (confirmed by electron microscopy), using the following formula:

$$\delta = dA \tag{8.3}$$

where d is carbide density and A is the mass fraction of carbon in the carbide. Theoretical total pore volume V_Σ was calculated on the basis of pycnometric density of carbon ($d_C = 2.00$ g/cm^3) by the formula

$$V_\Sigma = \frac{1}{\delta} - \frac{1}{d_C} \tag{8.4}$$

It was found that the theoretical δ and V_Σ values are generally in satisfactory agreement with experimental data taking into account the porosity of the initial carbide granules.

According to the IUPAC definition, porosity in solids is classified by pore size [45]:

1. pores with widths exceeding about 50 nm are called *macropores*;
2. pores of widths between 2 and 50 nm are called *mesopores*;
3. pores with widths not exceeding about 2 nm are called *micropores*.

As currently accepted, we use the term *nanopores* for the pores of $\leq$2 nm, which reflects their actual size more appropriately.

Sorption analysis was carried out with the use of benzene vapor as an adsorptive agent. Isotherms were generally of Type I in the Brunauer classification that characterizes these carbons as nanoporous adsorbents. The sole exception was Mo_2C CDC, which developed mesopore volume. This was explained by the larger distances between the carbon atoms in Mo_2C compared to the other transition MeCs, and the correspondingly smaller density of Mo_2C CDC. Our experience shows that the pore-size distribution may also be affected by many other parameters, including the CDC microstructure, which, in turn, depends on the carbide and the temperature of its chlorination. The isotherms were evaluated using Dubinin's theory of volume filling of nanopores [46,47]. The characteristic energy of adsorption, which is the principal parameter of nanoporous structure of CDCs was at the level of the values for the best activated carbons.

A mechanism of nanopore formation in carbon materials produced by the interaction of carbides with chlorine was proposed in [48]. In essence, this theory is as follows: a series of nonlinear chemical reactions proceed in the course of a chemical interaction between chlorine and carbide. If the external parameters, the component fluxes, and the diffusion rates satisfy certain relations, the self-organization process can occur. This process results in the creation of a periodic nanoporous structure in the carbon material formed. A mathematical model was proposed, the main characteristics of the process were calculated, and the restrictions on the parameters at which the formation of the porous structure becomes possible were found.

8.2.6.2 Effect of the Chlorination Temperature

Temperature dependence of the pore-size distribution, BET specific surface area (S_{BET}) [216], and microstructure of Ti_3SiC_2, Ti_2AlC, B_4C, ZrC, and SiC CDCs were studied in the range of 200 to 1200°C

[30,31,49–52]. Samples were prepared in a horizontal tube furnace (Figure 8.4). After chlorination, the samples were purged with Ar for ~15 min at the chlorination temperature and then cooled down in an Ar atmosphere. A combination of TEM, Raman spectroscopy, and XRD was employed for the analysis of carbon microstructure. Pore structure was studied using Ar or CH_3Cl sorption, or small-angle x-ray scattering (SAXS). It was discovered that chlorination temperature might control the pore structure and the pore size with sub-angstrom accuracy. Figure 8.6 shows the differential pore-size distributions for Ti_3SiC_2 CDC and the dependence of the pore size on the processing temperature. Low-temperature chlorination resulted in very uniform pores [49]. Pore-size distribution for these CDCs was narrower than that of single-walled carbon nanotubes (SWCNT) and activated carbons, and comparable to that of zeolites. Increasing CDC synthesis temperature generally leads to pore enlargement and eventually (above 1100°C in case of Ti_3SiC_2 CDC) to a broader distribution of pore sizes. Similar dependences were demonstrated for CDCs produced from other carbides. Figure 8.7 and Figure 8.8 show the differential pore-size distribution of Ti_2AlC CDC and ZrC CDC in the temperature range 400 to 1200°C.

The observed changes in the pore structure are inherently connected to the changes in the microstructure of the CDCs. Uniform, relatively small pores formed during chlorination at lower temperatures were found to be associated with the amorphous structure of the CDCs, while less uniform and generally larger pores formed at higher synthesis temperatures were linked to graphitic ribbon network structure (see Figure 8.7 and Figure 8.8).

S_{BET} as a function of synthesis temperature of the as-prepared CDCs generally follows a "bell-shape" curve (Figure 8.9). Samples prepared at low temperature are of amorphous structure, have pores filled with considerable amounts of trapped chlorine and chlorides, and thus show a small effective S_{BET}. It is also possible that some of the pores are too small to be fully accessible to N_2 or Ar molecules used for S_{BET} measurement. As CDC processing temperature increases, the size of pores in the CDC increases as well. This allows chloride molecules to be removed from the pores more efficiently, and the effective S_{BET} to be increased. In addition, high processing temperatures increase the diffusion rates of gases (chlorides, chlorine, Ar, etc.) into and out of pores, thus contributing to the CDC cleaning efficiency and the corresponding increase in an accessible CDC surface area. However, above a certain temperature, multiwalled graphitic structures start forming in

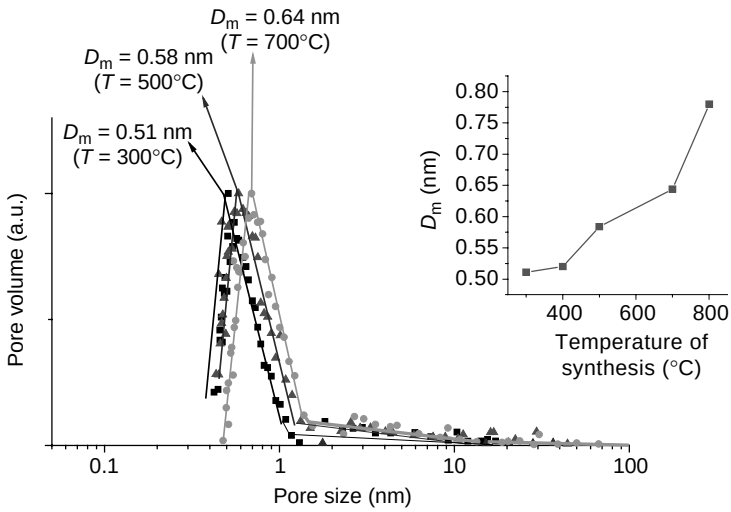

FIGURE 8.6 Pore-size distributions of Ti_3SiC_2 CDC showing uniform pore size when produced at low temperatures (From Gogotsi, Y. et al., Nanoporous carbide-derived carbon with tunable pore size, *Nature Mater.*, **2**, 591–594, 2003.). The calculations were performed using the Horvath–Kawazoe method and assuming a slit pore model. Inset (top right): demonstrates fine tunability of the pores by varying the synthesis temperature. D_m represents the maximum pore-size distribution.

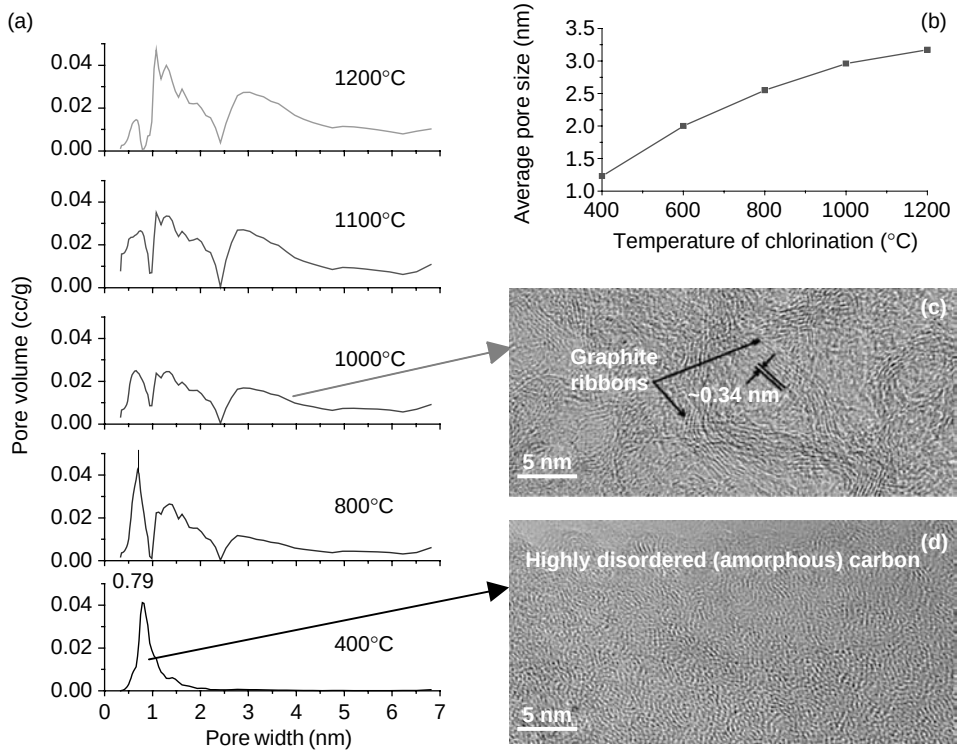

FIGURE 8.7 Pore-size distribution (a) and the weighted average pore size (b) of Ti_2AlC CDC as a function of chlorination temperature, showing drastic changes in the pore structure (From Hoffman, E.N. et al., Synthesis of carbide-derived carbon by chlorination of Ti_2AlC, *Chem. Mater*., **17**, 2317–2322, 2005.). The distributions were calculated using DFT, assuming slit pores. The pore volume was used as a weighting factor for the calculation of the average pore size in the 1–7 nm range. The TEM micrographs show the structure of the Ti_2AlC CDC produced at 1000°C (c) and 400°C (d), revealing the correlation between the microstructure and the porosity.

CDC. The area between the walls in such structures is generally not accessible to N_2 and Ar, as the interwall spacing is generally close to interplanar spacing in graphite (0.335 nm), which is too small for N_2 or Ar to fit in between. As such, formation of a substantial amount of well-organized multiwalled graphite ribbons in CDC may lower its S_{BET} value. The optimum synthesis temperature for large S_{BET} CDC would correspond to the conditions when all of the pores formed in the CDC are open; large enough to be accessible to inert gases and free from contaminants, while the amount of multiwalled graphite ribbons in the CDC is limited.

The temperature of graphite formation in CDC seems to depend strongly on the initial carbide, its purity, presence of catalyst particles, and halogen chosen. SiC CDC, for example, shows very limited formation of graphite ribbons even at 1200°C synthesis temperature and its S_{BET} does not decrease substantially at temperatures below 1200°C (Figure 8.9). In contrast, Dimovski et al. [21] observed the formation of planar microcrystalline graphite during the CDC synthesis from Fe_3C at 1200°C. It was suggested that above the eutectic temperature in the Fe–Fe_3C system (1130°C) a liquid phase formed, which was further supersaturated with carbon due to the removal of Fe upon interaction with Cl_2, and that graphite crystals nucleated and grew from this melt. It should also be mentioned that significant graphitization was observed even at lower temperatures (above 600°C). The catalytic effect of iron played a significant role in the phenomena observed.

Temperature dependence of Al_4C_3 CDC structure was reported in [53,54]. The nitrogen sorption isotherm of a low-temperature Al_4C_3 CDC (300°C) was of a type I in the Brunauer classification,

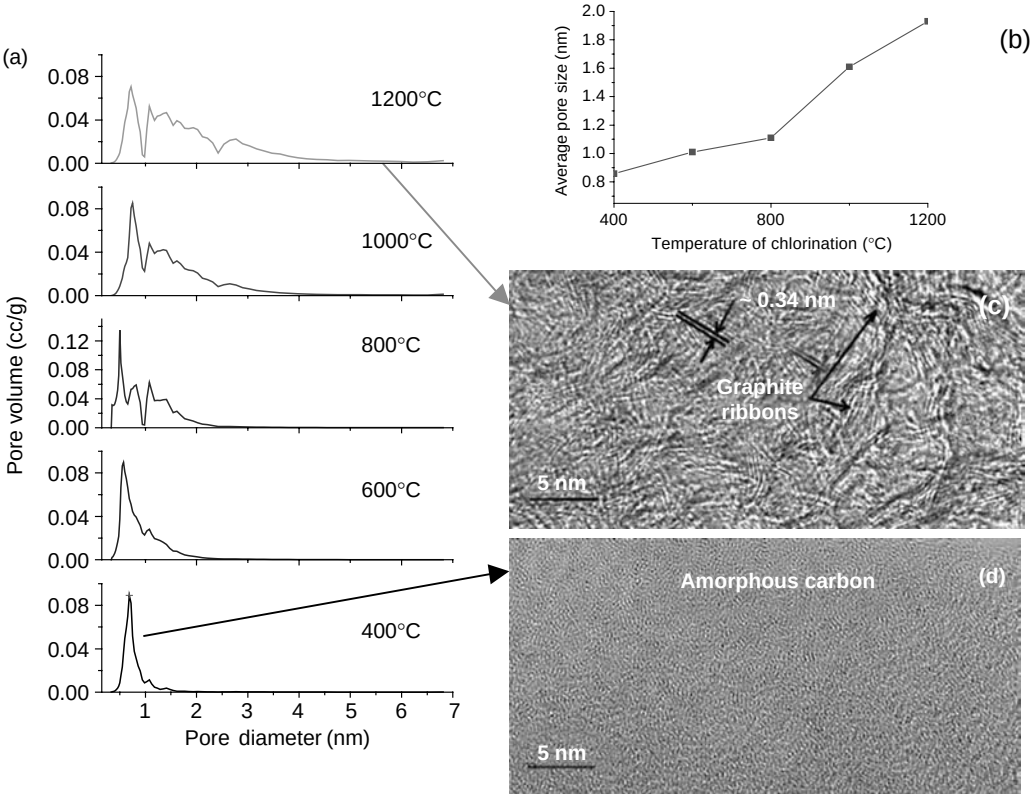

FIGURE 8.8 The DFT pore-size distribution (a) and the weighted average pore size (b) of the ZrC CDC as a function of chlorination temperature. (From Dash, R.K. et al., Synthesis, structure and porosity analysis of microporous and mesoporous carbon derived from zirconium carbide, *Microporous and Mesoporous Mater*., **86**, 50–57, 2005.), showing similar dependence to that observed for Ti_2AlC CDC. Slit pores were assumed for DFT calculations and the pore volume was used as a weighting factor for the calculation of the average pore size. The TEM micrographs show the structure of the ZrC CDC produced at 1000°C (c) and 300°C (d).

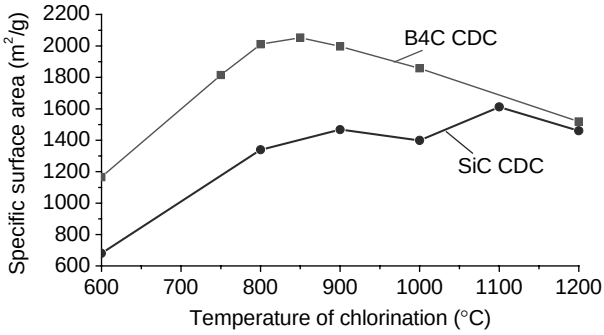

FIGURE 8.9 The BET specific surface area of the B_4C CDC and SiC CDC as a function of chlorination temperature, showing the maximum value at intermediate temperatures (From Dash, R.K. et al., Microporous carbon derived from boron carbide. *Microporous Mesoporous Mater*., **72**, 203–208, 2004; Gogotsi, Y. et al., Effect of synthesis temperature on structure and properties of nanoporous carbon derived from silicon carbide, *Carbon*, 2005, in press.). Clogging of the CDC pores when synthesis is performed at low temperature and graphitization observed at higher temperatures limit the surface area achieved. The decrease in the surface area in SiC CDC is not pronounced even at 1200°C as in this material noticeable graphitization starts at higher temperatures.

indicating that this sample had a nanoporous structure. High-resolution transmission electron microscopy (HRTEM) revealed the amorphous structure of the material. However, CDCs produced at 500 to 900°C demonstrated considerable graphitization, as confirmed by both HRTEM and XRD, and their sorption isotherms were of a type IV, which indicates the presence of mesopores [45]. The average pore size was calculated according to the Barrett Joyner Halenda (BJH) theory [55] and the S_{BET} values of Al_4C_3 CDC were plotted as a function of chlorination temperature in Figure 8.10. The large S_{BET} of Al_4C_3 CDC synthesized at 300°C is probably related to the efficient removal of the chlorides and the relatively large pores fully accessible to N_2. Upon increasing the processing temperature, S_{BET} steadily decreased as a result of CDC graphitization. It is necessary to note that the presence of condensed $AlCl_3$, which has a melting point of 192°C, can affect the pore structure of this CDC.

Temperature dependence of the pore structure of TiC CDC was investigated in [56]. As in some of the previous studies, TiC CDC sample chlorinated at a lower temperature demonstrated an apparent density higher than the theoretical value. The presence of $TiCl_4$ in a significant part of the pore volume provided a possible explanation. Samples produced in the 700 to 1100°C range showed virtually equal values of total pore volume, while their pore-size distributions were different. Volume occupied by mesopores increased with increasing chlorination temperature as a result of the ordering of turbostratic carbon structures. Figure 8.11 shows the mesopore volume measured by means of benzene adsorption and mercury porosimetry as a function of the synthesis temperature. The differences in the mesopore volume obtained by these two techniques are explained by the failure of mercury porosimetry to detect pores of equivalent radius below 3 nm. CDC produced at 1100°C evidently had some mesopores of less than 3 nm in equivalent size.

8.2.6.3 Effect of the Carbide Structure

The distribution of carbon atoms within carbides may differ substantially even when densities of the corresponding CDCs are similar. The carbide microstructure discussed may have a strong influence on the microstructure of the CDC produced and thus on its pore shape and pore size. Figure 8.12 shows a layered C structure in a hexagonal Ti_3SiC_2 and a uniform distribution of C in a cubic SiC (3C polytype), while Figure 8.13 compares the microstructure of the CDCs obtained at 1200°C. It is clearly seen that under the same processing conditions, CDC obtained from Ti_3SiC_2 consists of a disordered network of graphite ribbons (Figure 8.13a), whereas CDC from SiC shows an amorphous structure (Figure 8.13b).

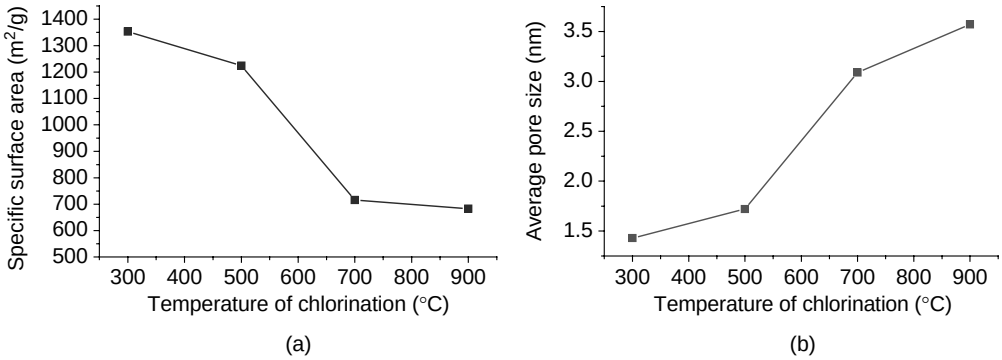

FIGURE 8.10 The BET-specific surface area (a) and the calculated average pore size using the BJH theory (b) of Al_4C_3 CDC as a function of chlorination temperature. (From Leis, J. et al., Carbon nanostructures produced by chlorinating aluminium carbide, *Carbon*, **39**, 2043–2048, 2001.) A sharp decrease in the surface area and increase of the pore size value occur at −500°C as a result of low-temperature formation of graphitic structures in such material. It is believed that formation of these structures was facilitated by the presence of transition metal impurities in the Al_4C_3.

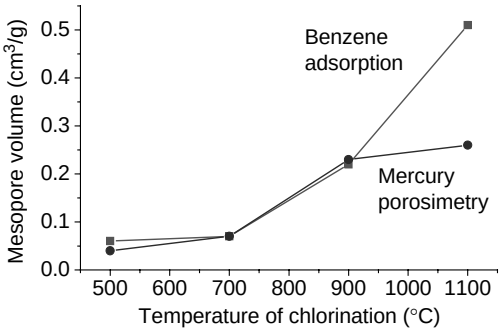

FIGURE 8.11 The mesopore volume of TiC CDC measured using benzene adsorption and mercury porosimetry as a function of chlorination temperature (From Fedorov, N.F. et al., Porous structure of carbon adsorbents from titanium carbide, *Z. Prikladnoi Khimii*, **55**, 46–50, 1982 [in Russian].). Inability of mercury porosimetry to detect pores smaller than 3 nm resulted in considerable difference in the mesopore volume measured in the material processed at 1100°C.

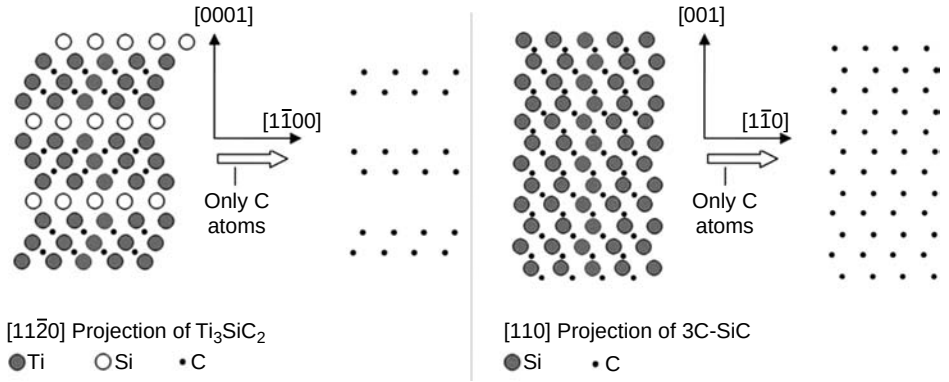

FIGURE 8.12 Schematic of the lattice structure of Ti_3SiC_2 with and without Ti and Si atoms shown (a), and schematic of the lattice structure of SiC with and without Si atoms shown (b).

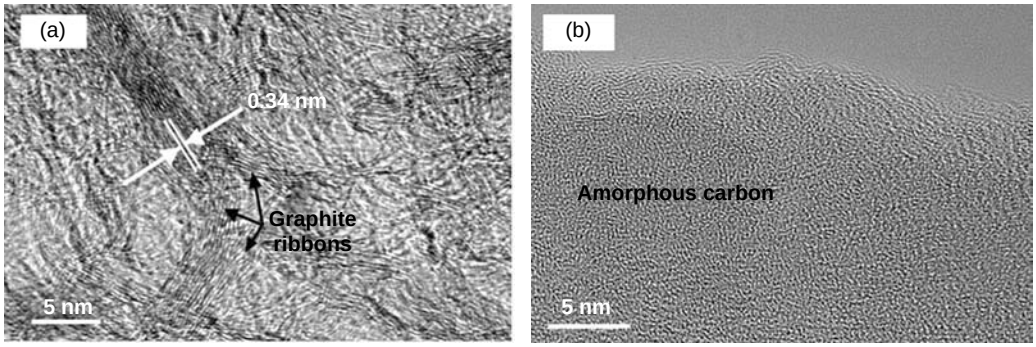

FIGURE 8.13 High-resolution TEM of CDC produced at 1200°C from Ti_3SiC_2 (a) and SiC (b) at 1200°C. (From Yushin, G. et al., Synthesis of nanoporous carbide-derived carbon by chlorination of titanium silicon carbide, *Carbon*, **43**, 2075–2082, 2005; Gogotsi, Y. et al., Effect of synthesis temperature on structure and properties of nanoporous carbon derived from silicon carbide, *Carbon*, 2006, in press.)

8.2.6.4 Effect of Catalysts on the Surface Area and Microstructure of CDC

The influence of 3d-transition metal catalysts on the temperature dependence of the microstructure and S_{BET} of TiC CDC was studied in [57]. Titanium carbide powder samples were chlorinated for 1 h in the temperature range 400 to 1200°C. Pure TiC samples as well as TiC with an added mixture of Co, Ni, and Fe chlorides (~73 mg of each chloride per gram of TiC) were converted into CDC. S_{BET} was calculated from the data of N_2 sorption at −196°C (Figure 8.14a); micropore volume was determined by measuring dynamic benzene adsorption at room temperature (Figure 8.14b). The S_{BET} temperature dependence followed the expected bell-like curve, where the trapped chlorides lowered the accessible surface area in samples processed at low temperatures, and graphitization of carbon with the formation of multiwalled graphite structures limited the surface area of the material formed at higher temperatures. The slow increase in the micropore volume with an increase in chlorination temperature could be explained by mild oxidation or structural change during the CDC synthesis. The effect of metal catalysts was not significant at temperatures below 700°C. But at higher temperatures, the catalysts strongly increased the graphitization degree and correspondingly lowered the S_{BET} value. Judging from the S_{BET} values and XRD spectra, TiC sample chlorinated at 900°C in the presence of catalysts showed a higher degree of graphitization (thickness of graphitic structures in the 0 0 2 direction) than the pure TiC sample chlorinated at 1200°C.

8.2.6.5 Effect of a Halogen

The influence of the nature of reacting halogens on the porous structure of CDC was demonstrated in [44]. In that study, ZrC CDC was synthesized by treatment in chlorine, bromine, and iodine at 800°C. Equal values of the total pore volume were found by measuring benzene adsorption in all the samples. At the same time, their sorption capacities for halogens differed significantly. The highest capacities for bromine vapor and iodine adsorption were observed in the case of the CDC sample prepared by bromination and iodination, respectively. This was considered evidence that the porous structure of CDC was affected by the size of the halogen and evolving zirconium tetrahalogenide molecules as well as by surface termination of CDC produced using different halogens.

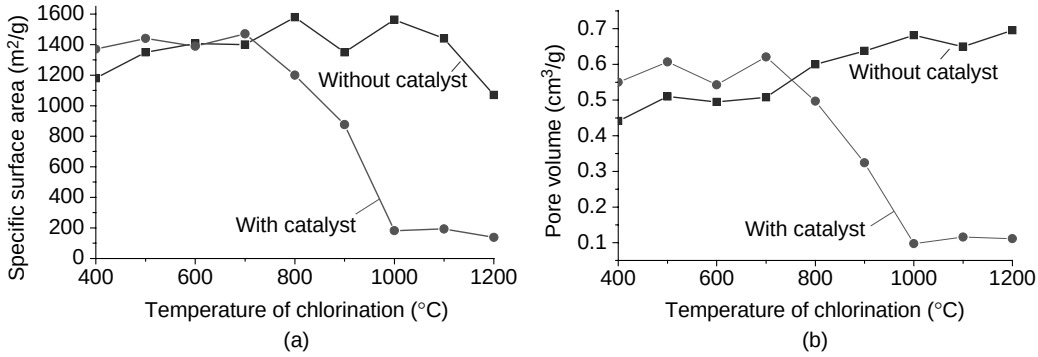

FIGURE 8.14 The BET-specific surface area (a) and the pore volume (b) of TiC CDC as a function of processing temperature, showing the effect of the metal chloride catalysts present in TiC before the synthesis (From Leis, J. et al., Catalytic effect of metals of the iron subgroup on the chlorination of titanium carbide to form nanostructural carbon, *Carbon*, **40**, 1559–1564, 2002.). Graphitization at lower temperature caused by the catalysts resulted in the decrease of the surface area and pore volume at temperatures above 700°C. The catalyst mixture consisted of $CoCl_2$, $NiCl_2$, and $FeCl_3$ solutions in ethanol with a final content of 73 mg of each chloride per gram of carbide.

8.2.6.6 Effect of the Initial Carbide Porosity

Carbide-derived carbons from carbide single crystals do not possess macroporosity, unlike carbons produced from porous sintered samples of carbides having initial porosity of 6 to 16% (by vol.). This means that the original macropore volume of sintered carbides does not change during the chlorination process and can be controlled by controlling the porosity of carbides. Kukushkina et al. [58,59] studied the influence of the initial porosity in polycrystalline carbides on the porosity of the corresponding CDC. The chlorine treatment of the dense polycrystalline carbides (SiC, TiC, HfC, and ZrC) at 600 to 1100°C resulted in completely nanoporous CDCs, similar to the CDCs produced from single crystals, with the experimental values of apparent density and total pore volume in good agreement with the theoretically expected ones. The chlorination of polycrystalline SiC with various initial porosities revealed a linear relationship between the total pore volume of the synthesized CDC and the initial pore volume.

Total volume and characteristic dimensions of meso- and nanopores can be predicted and achieved by the selection of proper binary or ternary carbides or carbide mixtures, and variation of the chlorination process parameters. This statement is illustrated with an example of the CDC produced from TiC and HfC solid solutions of variable composition. Linear dependence of the total pore volume measured by benzene adsorption on the composition is shown in Figure 8.15.

The above considerations allow simple calculations to be used for the evaluation of the total pore volume in CDC [60]:

$$V_V = d(1 - \varepsilon_0)\left(\frac{1}{d}\frac{\varepsilon_0}{1 - \varepsilon_0} + \frac{\alpha}{d} - \frac{\alpha}{d_C}\frac{M_C}{M}\right) \tag{8.5}$$

where V_V is the total volume of pores per total material volume (cm^3/cm^3), ε_0 is the relative pore volume of the initial carbide, α is the fractional conversion of the chlorination reaction, M_C and M are the molecular masses of carbon and the carbide, respectively, and d and d_C are the densities of carbon and the carbide, respectively.

8.2.6.7 CDC Composites

Fedorov et al. [61] and later Gordeev et al. [62–64] offered a method for production of nanoporous carbon bodies of any shape having sufficient mechanical strength and open pores. The method consists of forming an intermediate blank of MeC having porosity in the range of 30 to 50% (by vol.) in the desired shape (e.g., by sintering). The blank is then impregnated with carbon as a binder by exposure to a gaseous hydrocarbon mixture at a temperature exceeding the decomposition temperature of hydrocarbons (700 to 1000°C) until the mass of the blank increases by 10 to 25% due to formation of pyrocarbon. The blank is then treated in chlorine at 900 to 1100°C. A nanoporous

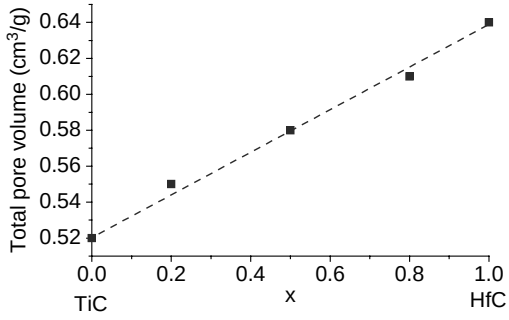

FIGURE 8.15 Pore volume of CDC produced from solid solution of $Ti_{1-x}Hf_xC$ as a function of composition showing a linear dependence (From Kukushkina, et al., Parameters of the porous structure of carbon produced by thermochemical treatment of nanoporous carbides, *Russ. J. Appl. Chem.*, **69**, 620–622, 1996).

structure is formed after the removal of volatile chlorides of carbide-forming elements according to Equation (8.2). As a version of the method, the blank made of silicon carbide may be impregnated with liquid silicon. Then the hydrocarbon mixture interacts with the liquid silicon to form a secondary silicon carbide. It was shown that macroporosity that developed in the course of formation of the carbide–pyrocarbon composite remained unchanged after thermochemical treatment in chlorine [61]. The influence of pyrocarbon content on the porous structure and physical properties, including resistivity, heat conductivity, and compression strength, were systematically studied for the SiC CDC–pyrocarbon composites [65].

8.2.7 Analysis of CDC Structure

As discussed to some extent in the previous subsections, CDCs of different hybridization, microstructure, density, and porosity can be produced by chlorination. Since the structure of CDC has a strong effect on its mechanical, electrical, and sorption properties, it is important to review the studies on the structure of CDCs obtained from various carbides under various experimental conditions.

8.2.7.1 Graphitization and Detection of Nanocrystals

By using the Scherrer equation and the FWHM of the carbon peaks, the average thickness of the graphite crystals in [0 0 2] (L_c) and [1 0 0] (L_a) directions could be estimated. Although the use of the Scherrer equation for the estimation of the crystallite size in carbons with a low degree of ordering has been demonstrated to provide adequate results [66], one should realize that the values obtained might be affected by the short-range order in the amorphous material, as well as by the irregularity and distortion of the crystalline structure. Nevertheless, qualitatively, XRD is clearly capable of providing valuable information on the CDC structure even when the CDC is produced at low temperatures and is disordered.

Mohun [15,33,34] used XRD to determine the degree of graphitization and the average size of graphite crystallites in CDC produced from a variety of carbides. As in most other studies, significant graphitization was observed only in samples obtained at higher temperatures. Unfortunately, he did not publish systematic results on the changes of XRD patterns of CDC produced from different carbides as a function of the chlorination temperature. However, he reported the general dependencies and some random data for CDC. For instance, he determined the thickness of graphite crystallites (L_c) in SiC CDC at the highest investigated temperature of 1650°C (2.5 h) to be ~4 nm. Mohun was the first to point out that graphitization degree also depends on the duration of the chlorination process: CDC samples produced at 1050°C (24 h) and 825°C (630 h) demonstrated the same graphitization degree. As such, graphitization was clearly determined to be a kinetically controlled process. CDC samples produced at low temperatures were completely amorphous and showed absolutely no diffraction pattern when chlorinated for 24 h.

The structure of SiC CDC was investigated by XRD in another early work [67]. CDC for that study was produced in the course of neutron activation analysis of silicon carbide [68]. β-SiC was treated in the chlorine gas flow in the quartz tube reactor at 1200 to 1250°C. Some samples were slowly cooled after the chlorination and stored for several months prior to the XRD measurement. Debye–Scherrer films of these samples showed only the diffuse rings typical for amorphous substances. Another sample of CDC, which was subjected to XRD was fresh (2 days old) and had been rapidly cooled after chlorination in a stream of cold nitrogen. In this case, Debye–Scherrer films showed in addition to the diffuse rings, a number of spotty lines, most of which were identified as β-SiC. In the first case, the samples were easy to break with the touch of fingertips, while the quenched samples were hard and brittle. It was noted that the size and shape of the bodies did not change during the reaction.

L_a and L_c values for the heat-treated TaC CDC and SiC CDC were calculated from the corresponding XRD patterns in [40]. The L_a values were larger than for conventional activated carbons treated to the same temperatures. In contrast, the L_c dimensions were very low as presented in

Figure 8.16, indicating the formation of thin and wide graphitic structure. In the case of TaC CDC, distinct graphite reflexes became apparent after heat treatment at 1700°C (see Figure 8.16), while temperatures above 2000°C were needed for pronounced graphite peaks to appear in diffraction patterns of SiC CDC samples. The authors suggested that as-prepared CDC from SiC and TaC consisted of disordered bent graphene layers with very little parallel stacking. We performed the analysis of similar samples by TEM in our laboratory and confirmed a low degree of ordering in as-prepared SiC CDC. After heat treatment, the diameter of the coherently scattering segments of the layers clearly increased and, in consequence, the mesopore volume increased as well. The open structure began to collapse at 1500°C for TaC CDC; the stacks of carbon layers grew in height and the distance between these stacks decreased to that of the ordered graphite. In the case of TaC CDC, the pore volume decreased to nearly zero at 1900°C, and the layers aligned to the perfect graphite structure at 2800°C.

Formation of carbon films and carbon-rich surface layers was repeatedly observed in the course of investigating high-temperature corrosion of SiC-based ceramics in mixed oxygen–chlorine environments [69–75] and during etching of SiC surfaces with chlorine and fluorine-containing gases for electronic device fabrication [76–79]. Study of the properties and the structure of carbon was not the object of the cited studies; moreover its formation was frequently considered to be undesirable.

Further investigations of CDC structure were reported in a number of papers by Gordeev et al. [48,80–84]. X-ray scattering studies of the structure of CDC prepared at 700 to 1000°C from 6H-SiC single crystals, polycrystalline α-SiC and polycrystalline SiC, TiC, and Mo_2C were conducted. The angular dependences of the scattering intensity obtained were treated as a result of scattering from nanoparticles of different size. By unfolding the experimental curves into components corresponding to particles with different gyration radii R_g, scattering distribution functions with respect to gyration radius were calculated. Samples prepared from different carbides differed in the degree of nanoparticle uniformity. The most uniform in size were the nanoparticles in the samples prepared from SiC. The size of the particles was found to depend on the carbide source (and possibly purity) as well as on its crystallinity. In CDC produced from polycrystalline SiC, the average R_g was <0.6 nm, while in CDC from α-SiC and 6H-SiC single crystals, most of the particles had $R_g \approx 1.0$ to 1.2 nm [80]. A possible cause of the larger particle formation in the case of single crystals is their lower chlorination rate and consequently longer time of treatment. In the report [81], irrespective of the type of the starting carbide, particles with $R_g \approx 0.5$ nm made up the largest fraction in porous carbon. In other studies [82], nanoparticles in CDC produced from different carbides varied in size. A study of the temperature dependences of the electrical resistivity, Hall coefficient, and thermoelectromotive force in the temperature range 1.5 to 300 K for the materials characterized by SAXS in [82] showed that the structural units responsible for the character of charge transport in

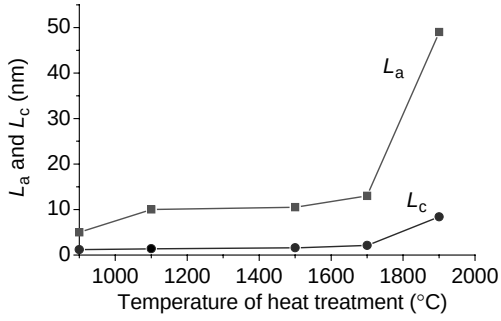

FIGURE 8.16 Dimensions of graphite crystallites in heat-treated TaC-CDC produced at 500°C as a function of the annealing temperature, showing pronounced graphitization at temperatures above 1700°C (From Boehm, H.P. et al., Structural parameters and molecular sieve properties of carbons prepared from metal carbides, *Proceedings of the 12th Biennial Conference on Carbon*, Pergamon, Oxford, 1975, pp. 149–150).

these materials were carbon nanoclusters of 1 to 3 nm in size [84]. SiC CDC produced from powders with various particle sizes (8 to 10, 180 to 200, and 800 to 1000 μm) was analyzed by XRD and SAXS [83], and it was shown that the mean size and number of nanoparticles (presumably graphite nanostructures) increases with increasing particle size. Possibly longer times required for carbonization of coarser grains were responsible for the higher graphitization degree observed. The XRD and SAXS data on the CDC structure from [80–82] were revised and later summarized with confirmation from the HRTEM images in [85]. It is noticeable that besides amorphous and partially graphitized carbon, some diamond nanocrystallites were detected in the CDC from SiC [85].

Carbon coatings on silicon carbide powders and monolithic specimens produced by treatment in diluted chlorine and chlorine–hydrogen mixtures were examined by Gogotsi and McNallan in a series of works [12,13,19,28,86–89]. The β-SiC powder was treated in the Cl_2 (2 to 3.5%)–H_2 (0 to 2%)–balance Ar gas mixtures in the temperature range 500 to 1000°C at ambient pressure [28,86,87]. Experiments were continued for 5 to 72 h depending on the material. The progress of the reactions conducted at 800°C was monitored by thermogravimetric analysis. The mass decreases approximately linearly with time, approaching a minimum value, which is dependent on the ratio of chlorine to hydrogen. Gas mixtures that were low in hydrogen produced the highest reaction rates. Uniform amorphous carbon or nanocrystalline graphite films were produced by treatment in Cl_2–Ar media as shown by XRD, Raman spectroscopy, and TEM. In the Raman spectra, D and G bands of disordered graphite were observed. From the relative intensities of these bands, the size (L_a) of the graphite crystallites was evaluated to be 2 to 4 nm. As the temperature of the treatment increases, the size of these crystallites and the thickness of the film formed after a fixed period of exposure increase. BET SSAs of carbon layers were calculated using the results of N_2 or Ar sorption measurements and taking into account the presence of unreacted silicon carbide. High values of surface area (Figure 8.9) provide the evidence that nanoporous CDC was produced.

Raman spectra of CDC prepared from polycrystalline α-SiC and TiC [90] support a cluster structure of nanoporous carbon and size quantization of the electronic and vibrational spectra in carbon nanoclusters. The presence of fragments of strained cubic or hexagonal diamond was observed in a number of cases.

Chlorination of SiC fibers was also studied [91,92]. Fibers from polymer precursors are nanoscale mixtures of SiC, carbon, and SiC_xO_y. Their chlorination can be conducted at 400°C and above, thus well below the temperatures necessary to produce CDC on SiC crystals or micropowders.

8.2.7.2 Carbon Nanostructures

It has been previously discussed that the major part of the CDC structure generally consists either of amorphous (highly disordered) nanoporous carbon or a porous network of graphite ribbons. However, recent TEM studies revealed the formation of various carbon nanostructures, including nanodiamond, carbon onions, nanotubes, barrel-like particles, and fullerene-like structures during the chlorination of carbides (Figure 8.17).

Studies performed by Gogotsi et al. [12,13,19,88] revealed that addition of hydrogen into the reaction mixture of Cl_2–Ar used for chlorination of carbides not only reduced the reaction rate but also influenced the composition and properties of the products. The sharp diamond band at ~1330 cm^{-1} was observed in the Raman spectra of the powder treated in 2.6% Cl_2–1.3% H_2–Ar at 950°C, and diamond regions were clearly visible under an optical microscope. Other bands, which may correspond to crystallized and amorphous diamond, were present in the Raman spectra as well. Thus, hydrogen plays a significant role in the formation of diamond by stabilizing dangling bonds of cubic diamond formed from β-SiC upon extraction of silicon. Chlorination of monolithic sintered and CVD samples of α- and β-SiC under the conditions described above [28] resulted in the formation of gray and translucent areas in thin section films in cases of low Cl_2/H_2 ratios in the reaction mixture [12,13,19,88]. These films probably acted as a diffusion barrier and prevented further

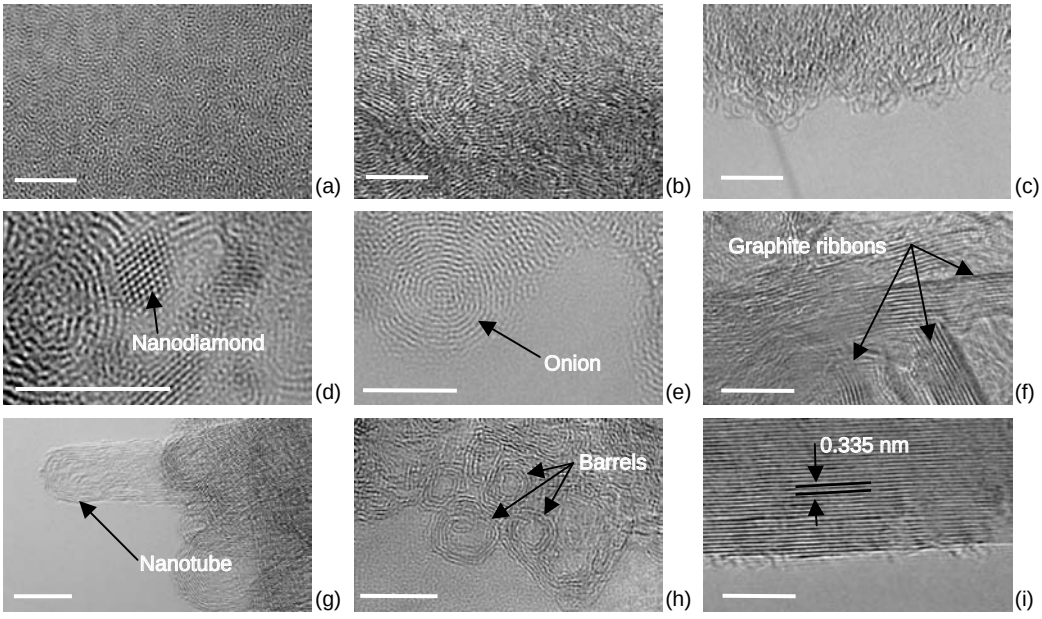

FIGURE 8.17 High-resolution TEM images of various carbon structures produced by chlorination of carbides: amorphous carbon (a), turbostratic graphite (b), fullerene-like carbon (c), nanodiamond (d), carbon onion (e), graphite ribbons (f), CNTs (g), barrel-like particles (h), and ordered graphite. Scale bar, 5 nm.

reaction. Lattice fringing (Figure 8.17d), electron diffraction patterns, and electron energy-loss spectroscopy (EELS) confirmed the formation of nanocrystalline diamond-structured carbon. The analysis of Raman spectra supported the presence of sp^3 bonding, which is also confirmed by a very high hardness (up to 50 GPa) and Young's modulus (up to 600 GPa) of these coatings. CDC coatings produced by treatment in chlorine or chlorine–hydrogen mixtures at $Cl_2/H_2 \geqslant 2{:}1$ consisted of a loosely attached, powdery top carbon layer with a dense, highly disordered, adherent amorphous or nanocrystalline layer below it. The adherent layers were shown to be composed of a mixture of graphitic and diamond-structured carbon [19] or highly disordered sp^2 carbon [13]. The thickness of the carbon layer increased linearly during the process. Because the kinetics is linear, the controlling factor of the reaction is not the diffusion of reactant species through the growing carbon layer.

Detailed HRTEM study of diamond crystals, produced by treatment of SiC in the gas mixtures of 1 to 3.5% Cl_2 and 0 to 2% H_2–Ar at 1000°C, showed local epitaxial growth of diamond on the SiC surface [93]. It has been shown that the presence of hydrogen in the environment is not required for diamond synthesis. However, hydrogen can stabilize the nanocrystals and lead to an increased diamond content in CDC. If no hydrogen is added, diamond nanocrystals transform to graphitic carbon, forming carbon onions and other curved graphitic structures. Diamond formation is also favored by low temperature of synthesis providing moderate carbon mobility. This result is in accordance with the x-ray photoelectron spectra of CDC from SiC, TiC, and ZrC produced at various temperatures [94]. It was shown that the degree of sp^3 hybridization increases as the temperature of the process is reduced from 1100 to 350°C.

When Danishevskii et al. [95] studied the effects of preparation conditions on nanodiamond formation during chlorination of SiC they observed that smaller SiC grains generally lead to smaller sized diamond. When SiC precursor contained pyrocarbon, the formation of diamond was hindered. The researchers suggested that the fast propagation velocity of the reaction front and the correspondingly strong nonequilibrium conditions favor diamond nucleation.

Theoretical studies of graphite and diamond growth on the (1 0 0 0) Si-surface of 6H-SiC were carried out using molecular dynamics simulation [12,96]. It was shown that very high lattice strains do not allow continuous growth of diamond on SiC, and fragmentation occurs leading to nanocrystalline material. Small diamond clusters on SiC are predicted to have a good adhesion to the substrate and maintain sp^3 coordination of carbon atoms in the cluster. Transmission electron microscopy studies [19] proved that SiC was converted to sp^3 carbon, and formation of crystalline diamond-structured carbon occurred from disordered Si-depleted SiC within nanometers of the SiC/C interface. Growth of larger crystals of diamond-structured carbon was probably the result of coalescence of continuous nanocrystalline regions. The presence of hydrogen helps to maintain sp^3 hybridization of carbon, stabilizing the dangling bonds.

Carbon onions in CDC were first observed during the chlorination of titanium carbide [97] near particle edges. These structures with concentric spherical graphitic shells were observed to have outer diameters in the range 15 to 35 nm. The distance between graphitic planes in the shells was 0.34 nm, slightly larger than the interplanar distance in graphite. As a comparison, HRTEM images of CDC from SiC produced at 1000°C did not indicate onion-like shells. However, our work showed the formation of carbon onions in CDC produced from SiC [19]. The mechanism of their formation via diamond nanoparticles is described in [98]. High-resolution TEM images of carbon onions and other carbon shells found in CDC are presented in Figures 8.17d, e, and h.

It is interesting to note that according to Boehm [99], CNTs were first observed in 1972, during the TEM analysis of SiC CDC. Boehm observed multiwall CNTs and carbon onions only occasionally in CDCs, and concluded that these structures were present in SiC before the chlorination. However, we believe that nanotube synthesis may have occurred during the CDC production (Figure 8.17g). Gogotsi et al. [19,100] reported the formation of carbon onions and CNT in SiC CDC formed at 1000–1200°C. Weltz [98] observed CNT and carbon onions in CDC produced from SiC and TiC at similar temperatures. Hoffman et al. [50] observed the formation of short CNT on the surface of Ti_2AlC CDC particles formed at ~800°C. Higher temperatures resulted in the formation of graphite ribbon networks and amorphous carbon. No tubular graphitic structures were found in these samples. The CDC produced at 600°C consisted only of porous amorphous carbon. Similar curved graphitic structures with characteristics similar to short CNT or elongated carbon onions were observed in the CDC produced from Ti_3SiC_2 at 800°C [31]. A considerable amount of amorphous and turbostratic carbon was also present in this sample.

Similar multiwall nanostructures, called “nano-barrels” were also observed in CDCs produced from Al_4C_3 [101–103]. The CDC from Al_4C_3 produced at 700°C consisted, to a large part (~80%), of barrel-like multiwall nanoparticles and nanotubes. The sample chlorinated at 900°C was primarily turbostratic carbon forming randomly oriented band-like graphitic lamellae and large sheets. The observed nanobarrels were considered to be intermediates between empty onion-like particles and multiwall nanotubes and patented as a “nanotubular carbon material” [101]. We observed nanobarrels in CDC produced from other carbides, including TiC and SiC (Figure 8.17h), however, the yield was noticeably smaller than that observed in Al_4C_3 CDC.

The mechanisms governing the growth of various nanostructures during chlorination of carbides are not yet clear. A catalytic effect of impurities present in carbides [102], metals, or metal chlorides might play a significant role in nanostructure formation. Carbide structure and optimum temperature regime also seem to be important parameters for the selective synthesis of various nanostructures. Further investigation is needed to clarify the phenomena observed.

8.3 SELECTIVE ETCHING OF CARBIDES BY MELTS AND SUPERCRITICAL WATER

8.3.1 Reaction of Calcium Carbide with Inorganic Salts

Salt-like carbides react at elevated temperatures with a number of reagents, resulting in the formation of carbon formation along with other reaction products [104]. The few reports there are on this

carbide-thermal process and the resulting carbon material have all been devoted to calcium carbide reactions with metal salts [105–111]. Generally, the process can be considered as the high-temperature exchange reaction of calcium carbide and metal salt producing a calcium salt and a new unstable salt-like carbide, decomposing to give free metal and carbon [110].

This method was first applied for the production of macrocrystalline graphite with the use of magnesium chloride [105]. The process included the following exchange and decomposition reactions:

$$CaC_2 + MgCl_2 = MgC_2 + CaCl_2 \tag{8.6}$$

$$2MgC_2 = Mg_2C_3 + C \tag{8.7}$$

$$Mg_2C_3 = 2Mg + 3C \tag{8.8}$$

The reaction mixture was heated to 600 to 1275°C for 1 to 5 h. The best yield and quality of graphite were achieved in the range 950 to 1200°C. After removal of the unreacted carbides and salts and amorphous carbon the yield was up to 85%. X-ray diffraction showed that both graphitic and turbostratic carbon were present in the product. It is important to note that since $CaCl_2$ has a high melting point of 772°C and low vapor pressure, pure CDC cannot be produced by chlorination of CaC_2.

The porous structure and adsorption properties of the CDC material prepared by the carbide-thermal process were first studied by Fedorov et al. [106]. Reaction of calcium carbide with sodium chloride according to the overall equation

$$CaC_2 + 2NaCl = 2C + 2Na + CaCl_2 \tag{8.9}$$

was conducted in the temperature range 400 to 900°C and resulted in a sorption-active carbon material. Parameters of the porous structure were determined by measuring benzene sorption isotherms. Carbonaceous materials from CaC_2 had an extensive and variable mesopore volume of up to 0.63 cm^3/g, but a relatively low specific surface area (below 330 m^2/g) compared to the CDC produced by chlorination of carbides.

Measurements of the yield of free carbon for various CaC_2/NaCl ratios in the initial mixture showed that two routes of reaction are possible at 900°C [109]. Decomposition of CaC_2 catalyzed by chloride takes place at low CaC_2/NaCl ratios (1:0.03–1.2 eq.). Reaction (8.9) proceeds at higher CaC_2/NaCl ratios.

The technique of producing CDC adsorbents from CaC_2 includes the following steps: mixing of the initial components with the particle size of 100 to 300 μm in the ratio 1:(1–3); compaction at 5 to 40 MPa; and thermal treatment at 600 to 1000°C in the inert gas medium, followed by cleansing in water or acid, drying, and crushing. These sorbents can be used as soil detoxicants, gas drying agents, chemical adsorbents, and catalysts [111].

8.3.2 Hydrothermal Leaching of Carbides

8.3.2.1 Thermodynamic Analysis

Thermodynamic stability of a number of MeCs under hydrothermal conditions has been analyzed [27]. The possible reaction routes and products were predicted using Gibbs energy minimization. Thermodynamic calculations were conducted in the temperature range from 300 to 1000°C and pressures in the range between 2 and 200 MPa for the M_xC–nH_2O(g) system, where $n = 2$ and 10, and x = Si, Ti, Ta, Nb, W, and B. The following idealization was used to carry out these calculations: hydrothermal fluid is treated as steam, solid phase is a mechanical mixture of compounds with unit activities, and gas phase is a mixture of ideal gases. Also kinetic factors and effects such as pH were not taken into consideration.

The analysis indicated that carbon, MeO_x, CH_4, CO_2, CO, and H_2 are the main products of hydrothermal reactions in the temperature range of the study and principal reactions in the M_xC–nH_2O(g) system can be written as follows:

$$x/2\ \mathrm{MeC} + x\mathrm{H_2O} = \mathrm{Me_{x/2}O_x} + x/2\ \mathrm{CH_4} \tag{8.10}$$

$$\mathrm{MeC} + (x+1)\mathrm{H_2O} = \mathrm{MeO_x} + \mathrm{CO} + (x+1)\mathrm{H_2} \tag{8.11}$$

$$\mathrm{MeC} + (x+2)\mathrm{H_2O} = \mathrm{MeO_x} + \mathrm{CO_2} + (x+2)\mathrm{H_2} \tag{8.12}$$

$$\mathrm{MeC} + x\mathrm{H_2O} = \mathrm{MeO_x} + \mathrm{C} + x\mathrm{H_2} \tag{8.13}$$

$$\mathrm{MeO_x} + n\mathrm{H_2O} = \mathrm{MeO_x \cdot} n\mathrm{H_2O} \tag{8.14}$$

Thermodynamic calculations show that the formation of carbon on the surface of SiC depends crucially on the H_2O/SiC ratio and three regimes can be identified. At low H_2O/SiC ratios (regime 1), both carbon and silica are deposited on the surface. At intermediate H_2O/SiC ratios (regime 2), carbon and silica are formed. Silica is dissolved in water according to Equation (8.14). Thus, reaction (8.13) tends to move further to the right. At higher H_2O/SiC ratios (regime 3), since they dissolve in the excess water, neither carbon nor silica precipitates.

It was shown that the yield of methane, which is unstable at high temperatures, decreases with temperature and thus the yield of elemental carbon, which is produced due to instability of CH_4 increases. Higher pressures led to a slight increase in stability of methane and, accordingly to a lower yield of carbon.

The behavior of TaC, TiC, and NbC is very similar to that of SiC. Tantalum carbide seems to be more stable at low water contents. Carbon formation was calculated for TaC at temperatures >700°C and only at relatively low pressures. However, it is important to remember that most metal oxides, unlike silica, cannot be easily dissolved in supercritical water. Thus, a mixture of carbon and metal oxide (or hydroxide) is produced. The behavior calculated for WC is somewhat different as compared with previously discussed carbides. A lower carbide W_2C and a number of stable oxides exist. Free carbon is predicted to form only at the lower temperatures. Boron carbide is the only carbide from the group studied that is not predicted to convert to free carbon under hydrothermal conditions. The present calculations provide some general guidelines and, as will be shown, are generally in good agreement with experimental results.

The formation of carbon-rich layers on the surface of carbides was repeatedly detected in the course of investigations on controlled oxidation of HfC [112–117], ZrC [116–121], and TiC [115,117] at low pressures of oxygen (0.02 to 16 kPa). These layers contained up to 25 at% of carbon in addition to metal oxides and oxicarbides. As characterized by Raman spectroscopy, this carbon was mainly amorphous. In some cases, formation of carbon in the form of hexagonal diamonds was reported [118].

8.3.2.2 Experimental Results

Formation of carbon from carbides after hydrothermal treatment was first reported by Gogotsi and Yoshimura in 1994 [87,122–125]. This phenomenon was observed in the course of corrosion studies of amorphous SiC (Tyranno) fibers at 300 to 800°C and about 100 MPa. Tyranno is a type of silicon carbide fiber containing titanium and oxygen, made by pyrolysis of an organometallic polymer precursor. It consists of SiC nanocrystals, which are connected by Si–O–C and Ti–O (Ti–C–O) interlayers and can be considered as an amorphous SiO_xC_y matrix with nanometer-size β-SiC inclusions. The outer surface of the fibers treated at temperatures up to 450°C remained smooth and almost featureless. Auger electron spectroscopy depth analysis of the surface layer showed that a

carbon layer containing traces of silicon was formed [123]. The thickness of this layer varied from 10 to 20 nm to 1 to 2 μm. Raman spectra of the fibers showed a band of graphite (G) and a disorder-induced band (D), thus confirming the formation of amorphous or nanocrystalline carbon [122]. The crystallites were of very small grain size and sp^2 C–C bonds dominated.

Formation of amorphous carbon has been reported on the surface of Tyranno fibers after hydrothermal treatment at 300 to 400°C and 100 MPa [87,91,126,127]; CVD-SiC fibers after treatment at 400 to 700°C and 200 MPa [128]; α- and β-SiC platelets, whiskers, and powders at 600 to 800°C [27,87,126,127,129]. Some amounts of disordered diamond as well as graphite and amorphous carbon were found on the surface of α- and β-SiC powder and single crystals after treatment at 300 to 800°C and 100 to 500 MPa [130–134]. The hydrothermal method was also found to be suitable for preparation of CDC from other carbides including WC, TaC, NbC, and TiC at 500 to 750°C and 100 to 170 MPa [27].

8.4 THERMAL DECOMPOSITION OF CARBIDES

It is known that silicon carbide and many other carbides decompose at high temperatures [104]. This thermal decomposition in vacuum or inert environment is accompanied by the formation of carbon and preferential evaporation of the carbide-forming element due to the low vapor pressure of graphite at elevated temperatures compared to that of most metals.

A consideration of transport processes leading to the formation of carbon during the thermal decomposition of SiC was attempted by Motzfeldt and Steinmo [135]. Vapor pressure over the SiC(s)–C(s) was studied by means of Knudsen effusion method for three different orifice sizes. It was found that surface diffusion is of great importance in the process. The overall process was visualized in the following way: The outermost layer of the SiC crystal loses silicon by evaporation from the surface, and a layer of microporous carbon is left. A gradient in silicon is established through this layer and silicon from the interior moves through it by surface diffusion and then evaporates from the surface. One can find indirect evidence of silicon surface migration during the silicon carbide decomposition in the report [136] published in 1970.

8.4.1 Carbon Structure and Conservation of Shape

The first documented observation of carbon formation after heat treatment of SiC in vacuum at temperatures up to 2000°C was published in 1960 [67]. As in the case of CDC prepared by chlorination of silicon carbide, the size and shape of the large particles did not change noticeably after the treatment. The same phenomenon was observed in 1963 in the course of the study of SiC dissociation [137].

Several attempts to investigate the structure of carbon obtained by decomposition of silicon carbide have been reported. An X-ray diffraction study was conducted by Badami [138,139]. Single crystals of α-SiC (6H) were heated in a vacuum (10^{-5} Torr) at 2050–2280°C for 1 h. The sample produced by heating to 2050°C had undergone only partial decomposition as demonstrated by its diffraction pattern. On the basis of an examination of various parts of the samples produced at 2050°C, the author concluded that the carbon produced consisted of a matrix of turbostratic carbon with strong preferred orientation of the carbon layers parallel and perpendicular to the layers of silicon carbide and graphite nanocrystals having a common *c* axis and axial symmetry about it. Samples produced at 2280°C exhibited a gradually changing structure. The outer layers of carbon consisted mainly of crystalline graphite with small amount of turbostratic graphite. Deeper inside the sample, there was turbostratic graphite and, finally, completely disordered carbon. Higher levels of graphite ordering at the particle surface could be explained by surface diffusion and effectively longer time of carbon annealing. Silicon atoms migrating from inside the particles to the surface may also provide an additional transport mechanism for the reorganization of carbon atoms.

Selected area electron diffraction was used to investigate the decomposition of single-crystal β-SiC whiskers [140]. Whiskers, averaging about 300 nm in diameter, were heated to about 2400°C at 10^{-6} Torr for 2 to 3 min. In spite of such a high temperature, whiskers were found at various stages of decomposition. Graphite crystallites about 10 nm or less in diameter, were observed at the outer surface of the partially decomposed whiskers. It was concluded on the basis of selected area diffraction patterns that the crystallites were grown with their basal planes tangential to the whisker surface.

It should be mentioned that, in our experience, the level of decomposition depends not only on temperature but also on the position of a microcrystal (SiC particle or whisker) in a sample holder. Particles from the outer layer transform at a higher rate, possibly due to the gradient in pressure and composition of the residual gas across the sample holder inside the vacuum chamber. As a result, a thicker layer of particles may lead to the retarded decomposition.

In recent electron microscopy studies of β-SiC whiskers annealed in vacuum (10^{-5} Torr) at 1700–2000°C, conservation of shape during carbide decomposition has been shown [14]. We observed that at lower temperatures the shape of the whiskers does not change considerably. However, we found some distortion of the sharp features at the surface of nanoobjects at higher temperatures. Figure 8.18 shows graphitic CDC structures obtained by annealing of SiC whiskers in vacuum. Similar to the CDC processes described previously, the whiskers annealed at 1700°C retained their original shape as shown in both SEM (Figure 8.18a) and TEM (Figure 8.18c) micrographs. When we increased the vacuum treatment temperature to 2000°C, all SiC transformed to well-ordered graphitic carbon. The same cross-sectional shape was found by TEM studies (Figure 8.18d). SEM investigations (Figure 8.18b) revealed that the general hexagonal cross-section was preserved; however, the edges of the hexagonal platelets were not straight any more, and a wrinkled graphitic structure was formed.

Later research on SiC surfaces at elevated temperatures was triggered by the demand of the electronics industry for the development of good metal-semiconductor contacts and thus the need to perfect a procedure for producing atomically clean SiC crystal surface [141]. These studies were mainly conducted on (0 0 0 1) (Si) and (0 0 0 $\bar{1}$) (C) faces of 6H and (1 1 1) (Si-) and ($\bar{1}$ $\bar{1}$ $\bar{1}$) (C-) faces of 3C SiC.

Bommen et al. [142] studied thermal decomposition of Si and C faces of 6H SiC crystals in vacuum (10^{-10} Torr) by low-energy electron diffraction (LEED) and Auger electron spectroscopy (AES). They observed the formation of a graphite monolayer at temperatures as low as 800°C. On

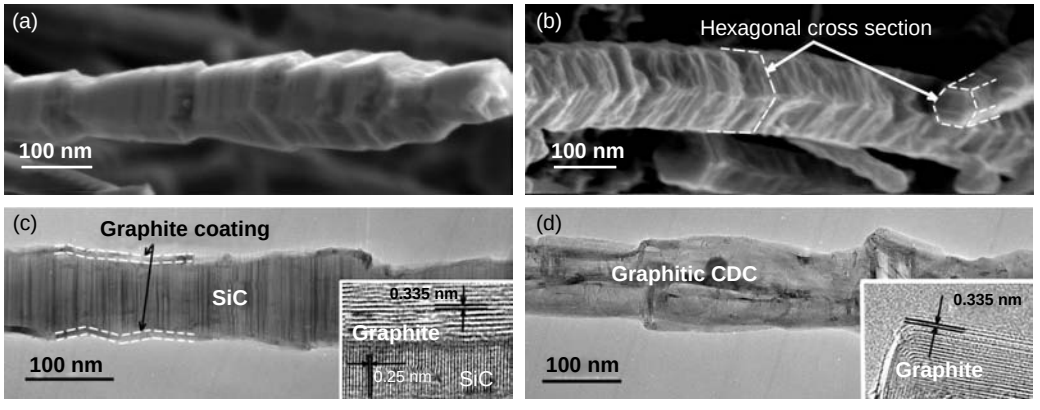

FIGURE 8.18 Scanning electron microscopy (a, b) and TEM (c, d) images of the whiskers obtained by annealing of SiC whiskers in vacuum at 1700°C (a, c) and 2000°C (b, d) for 30 min. (From Cambaz, Z.G. et al., Conservation of shape during formation of carbide-derived carbon on silicon carbide nano-whiskers, *J. Am. Ceram. Soc.*, 2005, in press.) The insets in (c) and (d) show HRTEM of the surface of the whiskers annealed at 1700°C and 2000°C, respectively, revealing highly ordered graphite structures.

the Si face, this monolayer is monocrystalline with the unit cell rotated 30° with respect to the SiC unit cell. On the C face, this layer was polycrystalline with no preferred orientation. These results agree well with the ellipsometry [143], scanning probe microscopy (SPM) [144–146], angle-resolved inverse photoemission spectroscopy (KRIPS) [147], and EELS [148,149] studies as well as with further LEED [144,147,150–155] investigations performed by other research groups, who studied surface reconstruction on the (0 0 0 1) and (0 0 0 $\bar{1}$) surfaces of SiC crystals at high temperatures. It was also shown that the rate of carbon layer growth on the carbon face is higher than that on the Si face. Bonzo et al. [156] and Muehlhoff et al. [148] performed a detailed study of the surface graphitization of SiC in vacuum (10^{-9} Torr) as a function of temperature by using X-ray photoelectron spectroscopy (XPS) and AES techniques. A short annealing time of 5 min at 300 to 1400 K was chosen for their studies. Four temperature ranges were distinguished. At temperatures below 900 K (range I), no evidence for carbon segregation was found on either SiC face. At temperatures between 900 and 1100 K (range II), carbon segregation occurred on the C face of SiC and the amount of carbon formed in the surface layer increased slightly with temperature from 1 to 1.3 C/Si ratio. At temperatures between 1100 and 1300 K (range III), carbon also formed only on the C face of SiC but the C/Si ratio did not vary with temperature. Above 1300 K (range IV), strong graphitization took place on both SiC faces with the C face showing a higher rate of carbon growth. However, due to a short annealing time and moderate experimental temperatures (<1400 K), the thickness of the graphite layer was limited to below 1 nm.

Iijima [157] studied the decomposition of silicon carbide under electron beam irradiation in 1982. Small flakes of 6H SiC were irradiated with the electron beam at a pressure of 10^{-6} Torr. The decomposition was controlled to some extent by halting the irradiation after a short exposure to the beam. Electron diffraction patterns showed a gradual disappearance of the SiC reflections and graphitzation of the sample at the same time. The preferred orientation of graphite was similar to the data of the XRD by Badami [138]. However, the decomposition did not completely preserve the particle shape, as shown by electron micrographs. Many ordered graphite bands and no regions of amorphous or turbostratic carbon were recognized in these micrographs. Images of the interface between SiC and graphite clearly showed the topotaxial mechanism of the reaction.

The only published source on the thermal decomposition of carbides other than SiC is the report by Foster et al. [158]. Decomposition of aluminum carbide at 2400°C and atmospheric pressure for 2 h in argon resulted in the formation of graphite crystals with a low *c*-spacing (0.33545 nm), chemical purity, large size, and the general absence of cleavage and twinning.

8.4.2 Synthesis of Carbon Nanotubes and Carbon Onions

A new interest in the thermal decomposition of SiC arose in 1997 when Kusunoki et al. [16,159–164] discovered growth of self-organized carbon nanotube (CNT) films during the decomposition of SiC. In contrast to the more conventional CVD growth technique, this technique allows the formation of highly aligned nanotubes and no catalyst is required for the CNT development. Moreover, selective preparation of CNTs of the zigzag type is possible [163]. To the best of our knowledge, this is currently the only method that permits preparation of CNTs of the same chirality. Other methods, such as arc-discharge, laser evaporation, and CVD, usually result in zigzag, armchair, and chiral tubes coexisting in the products.

Initial studies were conducted on β-SiC particles heated to 1700°C at 10^{-9} Torr for a few minutes in a TEM equipped with a YAG laser-heating holder [16]. Overlapped CNT with caps of 2 to 5 nm oriented along the [1 1 1] direction on [$\bar{1}\,\bar{1}\,\bar{1}$] surface plane of β-SiC single crystal were observed on the heated samples. Further research of this group was focused on the production of large-area continuous films or membranes of aligned and interconnected CNT [159,162,165] (Figure 8.19) and on understanding the mechanisms governing the CNT growth [160,161,164].

It was found that resistive heating of SiC in vacuum also results in CNT formation and thus laser heating is not essential for successful growth. More important conditions for the growth seem to be

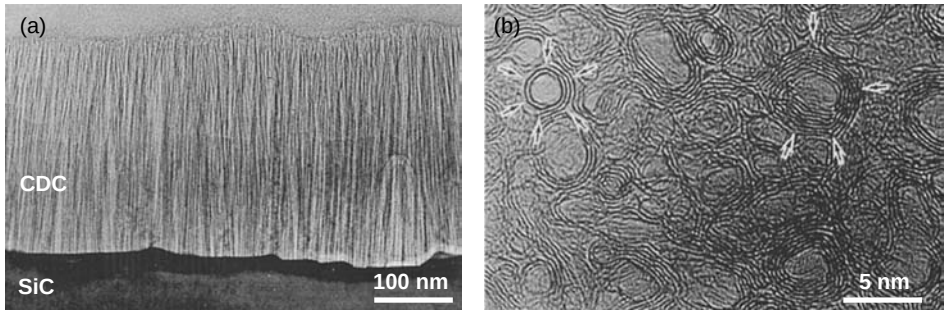

FIGURE 8.19 Transmission electron microscopy images of a CNT film grown by thermal decomposition of the C-face of 6H-SiC. Cross-sectional TEM micrograph (a) and plain-view HRTEM image (b). (From Kusunoki, M. et al., Formation of self-aligned carbon nanotube films by surface decomposition of silicon carbide, *Phil. Mag. Lett.*, **79**, 153–161, 1999. Courtesy of Dr. M. Kusunoki of Japan Fine Ceramic Center.)

the orientation and face of SiC crystals, level of vacuum, crystal morphology, and heating rate. A remarkable difference between the carbon structures formed on (0 0 0 1) (Si) and (0 0 0 $\bar{1}$) (C) faces of a 6H-SiC single crystal was found [161,162]. While CNT growth was observed under various experimental conditions on the C-face, only flat graphite sheets parallel to the surface were found on the Si-face. Similar face dependence was observed in β-SiC (1 1 1) films [165]. When the structure of the uppermost layers of SiC was changed by using laser irradiation, the structure of the carbon formed changed dramatically [164]. Porous amorphous carbon layer formed on both the C- and Si-faces during the vacuum annealing of the irradiated areas of the sample, while CNT and thin ordered graphite formed on the nonmodified areas of the C- and Si-terminated faces, respectively. Clearly, atomic structure of the very top SiC surface is a key factor that governs the structure of the CDC formed. The observed segregation of oxygen at the interface between the CNT film and SiC plane led Kusunoki [160] to suggest that residual oxygen in the vacuum chamber may play an important role in the formation of CNTs. Lower CNT growth rate in higher vacuum [160] supported this hypothesis. Further HRTEM analyses of various stages of CNT formation allowed the authors to propose a model, which consisted of three stages. At temperatures above 1000°C (stage I), several graphite sheets are formed parallel to the $(0\ 0\ 0\ 1)_{SiC}$ plane. At a temperature of ~1300°C (stage II), carbon nanocaps are formed by generation of bubbles of SiO gas. At stage III, the graphite sheets stand up and CNTs grow toward the interior of the SiC crystal. Possibly, stronger bonding of graphite layer to the Si-face of SiC prohibits formation of nanocaps, and thus further CNT growth.

Interestingly, in a later study by Derycke et al. [166] using scanning tunneling microscopy (STM) and atomic force microscopy (AFM), CNTs were found on an Si face of partially decomposed 6H SiC wafers. Samples were rapidly heated in ultra-high vacuum ($<10^{-9}$ Torr) to 1650°C by passing a DC current through them, and maintained at this temperature for 15 min. Scanning tunneling microscopy and AFM images clearly showed highly ordered SWNT networks on and below the surface with their axes parallel to it. The nanotubes had a very narrow size distribution in the 1.2–1.6 nm range.

The initial growth process of CNT from SiC was also investigated *in situ* by time-resolved HRTEM [167]. The sample of 3C SiC single crystal was slowly heated to 1360°C at ~10^{-9} Torr. Dynamic observation was conducted at a time resolution of 1/60 sec. Two types of CNTs were observed with diameters 0.8 and 1.5 nm. It was shown that first amorphous carbon was formed and then it crystallized to graphene sheets parallel to the (1 1 1) plane. Carbon nanotubes were formed by the lift of a part of the graphene sheet along the [1 1 1] direction.

The influence of SiC morphology on the CDC structure is worth a separate discussion. Kusunoki et al. [160] investigated the interface between the CNT film and C-face SiC (Figure 8.20). As previously discussed, all graphite (0 0 0 2) planes are perpendicular to the (0 0 0 1) plane of SiC (CNTs grow perpendicular to the basal planes of SiC). However, on a step of SiC, graphite sheets

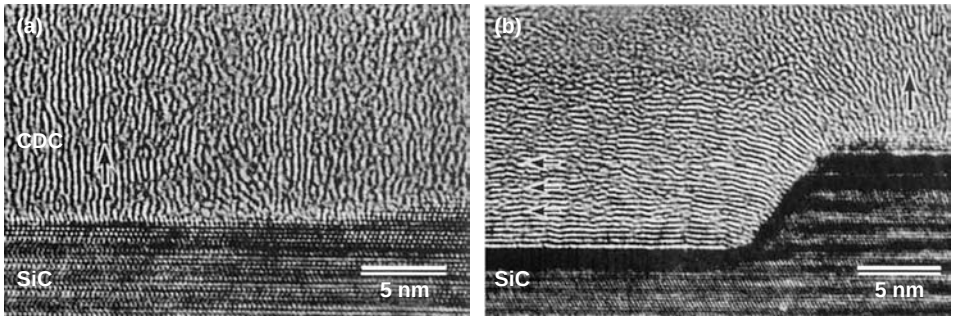

FIGURE 8.20 Cross-sectional HRTEM images of the interface between CDC film and C-face SiC annealed for 30 min at 1700–2000°C in vacuum, showing the effect of morphology on the orientation of graphite (0 0 0 2) planes relative to the (0 0 0 1) planes of SiC (From Kusunoki, M. et al., Formation of self-aligned carbon nanotube films by surface decomposition of silicon carbide, *Phil. Mag. Lett.*, **79**, 153–161, 1999.). In case of a flat SiC surface, all graphite (0 0 0 2) planes grow perpendicular to the SiC basal plane (a) while at an SiC step, graphite sheets lie down gradually, and on a large area, graphite sheets are oriented parallel to the SiC basal plane (b). (Courtesy of Dr. M. Kusunoki of Japan Fine Ceramic Center.)

lie down and become oriented parallel to the SiC basal planes, which suppresses CNT formation. During our investigation of β-SiC whiskers grown along the [1 1 1] direction and annealed in a vacuum using a resistive heater, we generally did not observe CNT formation on the tip of the whiskers as we initially expected. Only occasionally when the tip of the whisker was broken and a sufficiently large flat area of the C-face SiC basal plane was exposed to the vacuum during the annealing, some large multiwall CNT-like structures were produced (Figure 8.21). As one may notice, due to the irregular shape of the whisker, its relatively small diameter and thus strong effect of the edges, the shape of the nanotubes is highly distorted and the average wall thickness of the formed structures noticeably exceeds that of CNTs obtained by Kusunoki et al. (Figure 8.19). Possibly, CNT formation from the irregularly shaped SiC particles reported earlier [16] could be explained by the rapid heating of the particles by laser as compared to regular heating at a rate of 1–15°C/min by using a graphite-resistive heater. Since planar graphite structures are more thermodynamically stable than CNTs, nonequilibrium processes may favor CNT growth. The relatively large size of the SiC particles as compared to the whiskers may also play a role in CNT formation.

The possibility of the transformation of SiC to nanotubes on larger SiC particles by means of rapid heating of the particles in a vacuum resistance furnace was also investigated [168]. Silicon carbide powder was heated to 1600 to 1700°C within 5 min, kept for another 10 to 15 min at high temperatures and then cooled to room temperature. Dense layers of elongated carbon structures (possibly MWCNTs), typically 20 to 50 nm in diameter and up to 1 μm in length, were observed on the surface of 40% of the SiC powder. Unfortunately, no TEM analysis was performed on the CDC produced to reveal its microstructure.

Botti et al. [169] reported catalyst-free formation of SWCNT by rapid laser annealing of cold-pressed pellets of silicon carbide nanoparticles. The size of the nanoparticles varied from 30 to 70 nm, while the pellets were 13 mm in diameter and 3 mm in thickness. A defocused (10 mm) beam of the CO_2 laser with a power of 80 W irradiated SiC samples for 5 min in low vacuum (10^{-3} Torr), was used, achieving temperatures of 1050°C. CDC was produced in the form of CNT bundles 60 to 80 nm in diameter. Raman spectroscopy suggested the presence of SWCNT in the bundles. However, it is important to note that double- or triple-walled CNT, similar to the ones reported by Kusunoki, can also produce radial breathing modes (RBM) in Raman spectra.

The same research group reported the formation of CNT by laser heating of amorphous SiC film in vacuum (10^{-4} Torr) [170]. The 300-nm-thin SiC films were grown on HF-etched Si wafer

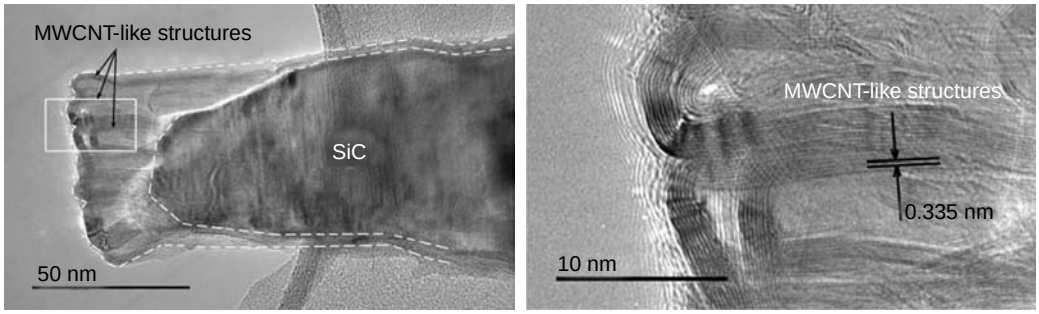

FIGURE 8.21 Tip of a broken SiC whisker annealed in vacuum at 1700°C for 30 min: TEM (a) and HRTEM of the framed section of the whisker (b), demonstrating growing MWCNT-like structures.

by CVD from disilane and acetylene. By using a CO_2 laser, the amorphous films were heated to 950 or 1050°C and maintained at these temperatures for 90 and 30 min, respectively. The resultant CDC in the form of nanofilaments consisted of SWCNT and MWCNT. The diameter of the nanotube bundles increased from 14 to 20 to 30 to 50 nm when the synthesis temperature increased from 950 to 1050°C. Samples processed at higher temperature were more ordered, but distribution of tube diameters was similar at both temperatures, as observed by Raman spectroscopy.

Gorelik et al. [171] produced carbon onions from amorphous silicon carbide using a single shot of a KrF laser (pulse duration 25 nm, energy density 800 mJ/cm^2, wavelength 248 nm). The temperature of the surface layer during the laser shot was estimated from numerical calculations to reach ~4000 K. Amorphous SiC films were produced either by laser ablation from a sintered SiC target or by ion implantation (Ge ions) into 6H-SiC. No difference of the CDC/SiC structure formed after laser irradiation of either type of substrate was detected. In each case, the irradiation resulted in the material crystallizing into the nanocrystalline cubic (β) structure of SiC in the near-surface region down to 50 to 100 nm and formation of ~10 nm carbonaceous (CDC) layer at the very surface due to the preferential evaporation of Si from the surface. The size of SiC crystals ranged from 5 to 50 nm with larger crystals situated at the surface and smaller crystals at the interface between the crystallized and unaffected material. Carbon onions were observed both inside the polycrystalline SiC region and inside the carbonaceous surface layer. However, onions formed inside the SiC region were larger and less defective, suggesting different formation mechanisms.

Lower temperatures of crystalline silicon carbide decomposition may be required to form CNTs in the presence of metal catalysts [172]. The metal-coated substrates of polycrystalline SiC were heated to 1000 to 1200°C at 10^{-2} Torr in a vacuum electric furnace. As a result, in the case of Pt, Ni, Co, Rh, and PtPd, carbon tubular nanostructures (tubes and fibers) grew at 1200°C. The SEM observation revealed that the synthesized structures range from 100 nm to 10 μm in length. According to TEM images, the synthesized CNTs are multiwalled, ranging from 2 to 10 nm in diameter. Most of the tubular structures included a metal particle at the tip. The growth mechanism is thought to be similar to a CVD process.

We have shown previously that SiC whiskers generally decompose during high-temperature vacuum annealing into irregular porous graphitic structures (Figure 8.18). However, when SiC whiskers were synthesized using a $Fe(CO)_5$ catalyst with a considerable amount of Fe left in the whisker tip, we observed transformation of an SiC whisker into a single multiwalled carbon nanotube (MWCNT) (Figure 8.22). At the tip of the CNT, one may see a hollow onion-like structure, where a catalyst particle was presumably located prior to evaporation. The presence of metal has been reported to enhance SiC graphitization [173]. We assume that decomposition of the whisker started from the tip and continued along the whisker growth axis, leading to the CNT formation.

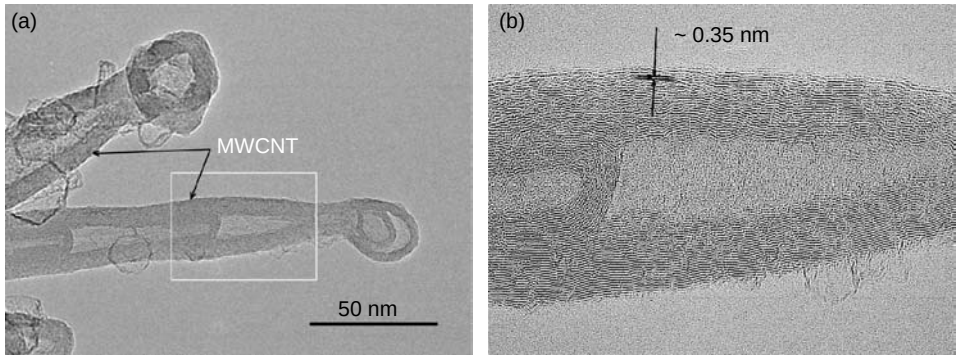

FIGURE 8.22 Two SiC whiskers transformed into two MWCNTs during 1700°C annealing for 30 min in vacuum: TEM (a) and HRTEM of the framed section of the CNT (b). SiC whiskers were synthesized using $Fe(CO)_5$ catalyst and had a considerable amount of Fe impurities left in the tips.

8.5 APPLICATIONS

It has already been mentioned that CDC has a variety of applications including molecular sieves, sorbents for gas chromatography, soil detoxification, dehumidification, and catalysis. This section describes other potential applications of CDC in more detail.

8.5.1 SUPERCAPACITORS

Supercapacitors, which are also called ultracapacitors or electrical double-layer capacitors, are rechargeable devices for electrical energy storage. They are poised to begin displacing batteries in applications where high power and low weight are essential. As batteries rely on slow rate-determining chemical reactions, they lack the ability to supply quick power bursts. In addition, chemical reactions in batteries contribute to 20 to 25% of the charging energy being lost. Most high-power batteries offer limited lifetime, require narrow temperature window for efficient operation, and are not environmentally friendly. Supercapacitors offering long-cycle life (>100,000 cycles), high efficiency (>90%), and fast charging/discharging are competitive alternatives to batteries for such applications as personal electronic devices, mobile telecommunications, back-up power storage, peak power sources for hybrid electric, electric and traditional vehicles, among others [174–178].

A supercapacitor consists of two porous electrodes with high surface area separated by an ion-conducting membrane. Energy is stored as a charge separation in a thin double layer at the interface between the electrode and the electrolyte. To increase energy storage, the electrodes in a supercapacitor should have as high a surface area accessible to the electrolyte as possible. Till date, various carbon materials have been used as electrodes in double-layer capacitors, including activated carbons, carbon fiber composites, and CNT. The main disadvantage of high surface area activated carbons used in supercapacitors is their wide pore-size distribution. A large fraction of the pores is too small to permit the electrolyte ions to freely diffuse in and out of pores, so that only a fraction of the total surface area is utilized to form a double layer (Figure 8.23). The presence of very small pores also increases the electrode resistance. Very large pores that are present in activated carbons are not so efficient for energy storage. Electrodes made from carbon fibers and CNT also suffer from a wide pore-size distribution. In the ideal case, the electrode material should have a narrow pore-size distribution with an average pore size tailored to suit the electrolyte used.

CDC produced by halogenation of carbides is an attractive material for supercapacitor electrodes. Among the advantages of CDC, high specific surface area and controlled pore size distribution (Figure 8.7 and Figure 8.8) are the most important. By choosing an appropriate precursor, synthesis conditions, and by using various post-treatments (e.g., activation), one can design CDCs

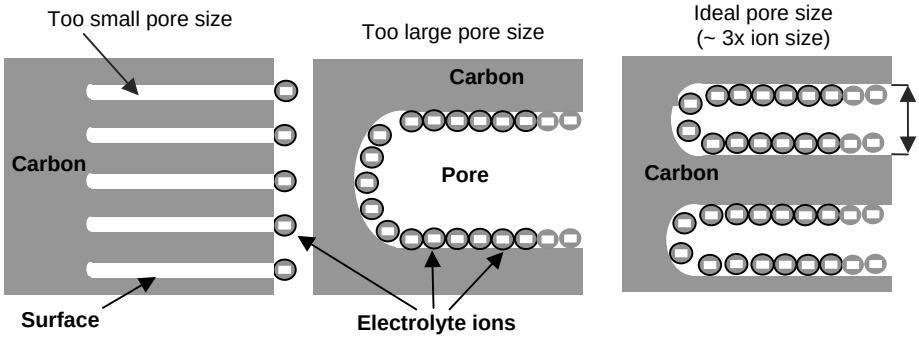

FIGURE 8.23 Schematic explanation of the optimum pore size for the highest surface area accessible by the electrolyte ions.

with pore size tuned for the most efficient electrode performance. Two approaches to the design of CDC electrode bodies have been proposed. The first one suggests production of CDC–pyrocarbon composites that offer an increased mechanical strength [63,64,179]. This method was employed for preparation of supercapacitor electrodes with specific capacitance of up to 39 F/cm^3 in aqueous electrolyte [180–182]. The second approach is conventional: CDC powder is mixed with an appropriate binder and then formed into a 100 to 400-μm-thick film [183–190]. Specific capacitance values above 140 F/g (in case of organic electrolyte) and above 250 F/g (in the case of aqueous electrolyte) have been demonstrated. These values are considerably higher than those achieved with most activated carbons and CNT-based electrodes (20–100 F/g) [191]. Additional optimization of the CDC structure should further improve its electrochemical performance.

8.5.2 Hydrogen Storage

The success of any future hydrogen economy depends, in large part, on our ability to develop inexpensive high-tech materials with sufficiently high hydrogen-storage capacity. Many types of materials have been tried or suggested for use as hydrogen-storage media. These include nano-materials, high-surface-area materials, synthetic metals, and chemical and metal hydrides. There are presently three generic routes known for the storage of hydrogen in materials; namely (1) *physisorption* as in the case of many porous carbon and zeolite materials, (2) *chemisorption* as in hydrogen storage in metal hydrides, and finally (3) *chemical reaction* such as complex metal hydrides and chemical hydrides. The sorption process typically requires highly porous materials to maximize the surface area available for hydrogen sorption to occur and to allow for easy uptake and release of hydrogen from the material. Among different types of hydrogen-storage materials discussed above, the carbon-based materials have received considerable attention. This is mainly due to carbon's lightweight and low cost, its large abundance in nature, its nontoxic behavior (compared to metal hydrides), and high S_{BET} [192]. It is intuitive to suggest that hydrogen adsorption on porous carbon materials with similar structure should depend linearly on its specific surface area. This concept has been further generalized to include even dissimilar carbons [193]. However, in our experience, other parameters of nanoporous carbons, including their pore size, surface chemistry, and structure, may play a vital role in improved hydrogen (or any other gas) adsorption. We observed that CDC with S_{BET} under 1400 m^2/g adsorbed twice as much hydrogen as other porous carbons with S_{BET} of over 2000 m^2/g.

Compared to other carbons, CDCs offer independent control over pore shape, pore size, surface area, surface termination, and microstructure of carbon. As such, CDCs can be tuned for maximum sorption of a given gas (e.g., hydrogen).

Gordeev et al. [194,195] evaluated hydrogen sorption by some CDC at high temperatures of 300 to 700°C and both high (above 90 atm) and low (below 0.1 atm) pressures using the method of thermodesorption spectrometry. Hydrogenation at elevated temperatures leads to chemisorption of

hydrogen. Thermodesorption spectra registered in the temperature range up to 1500°C consisted of several phases. The desorption peaks observed at 500 to 550°C and 800 to 850°C were attributed to the hydrogen adsorbed on dangling carbon bonds and graphite-like carbon surfaces, respectively. The apparent activation energy and heat of sorption were estimated. It was also shown that doping the CDC samples with 0.5 wt% of palladium increased hydrogen uptake about 2.5 times.

Johansson et al. [196] were the first to study the low-temperature hydrogen uptake by CDC. Nanoporous CDC was prepared from Al_4C_3 and SiC by chlorination and hydrogen sorption was measured at −196, −78, and 27°C. At liquid nitrogen temperatures and pressure of ~100 atm, the CDC demonstrated hydrogen uptake of up to 4.1 wt%.

Our preliminary testing has shown that at −196°C and 1 atm, CDC samples exhibit H_2 storage capacity up to 3 wt%, which is one of the highest reported for carbon materials. Interestingly, the SSA of these samples was only 1400 m^2/g. Further optimization of CDC structure and an increase in the SSA to 3000 m^2/g may allow the H_2 uptake of above 6 wt%.

8.5.3 Methane Storage

The use of natural gas (methane) as an automotive fuel offers considerable advantages, including reduced emission, lower maintenance, and most importantly lower fuel cost relative to gasoline. Moreover, the worldwide reserves of natural gas considerably exceed the oil reserves and thus natural gas may offer a solution when oil wells run dry. However, in order to compete with gasoline now (and offer comparable driving distance for vehicles before refueling) advanced methane storage units with large volumetric and gravimetric methane storage capacity need to be developed. Storing natural gas in a compressed form has the disadvantage of high cost of high-pressure cylinders needed to provide adequate methane storage capacity in a reasonably small volume. The use of inexpensive carbon adsorbent materials may allow the storage of considerable amounts of natural gas at relatively low pressure (<40 bar), making it more attractive for practical use.

Similar to hydrogen–storage applications, CDC can be optimized to adsorb a large quantity of methane. We performed preliminary experiments on a selected CDC prepared from SiC and having SSA of 1200 m^2/g and pore size of 0.82 nm [52], which is close to the theoretically calculated ideal pore size of 0.74 nm for high methane uptake [197]. This CDC outperforms commercially available activated carbons, offering 2.8 wt% methane storage at room temperature and atmospheric (≈1 bar) pressure. Pressurizing methane to 40 atm generally increases the porous carbon sorption capacity 10 to 20 times [198–200].

8.5.4 Lithium-Ion Batteries

The lithium battery industry is rapidly expanding. Presently, it represents the largest segment of the portable battery business, dominating the cell phone, camera, and laptop and notebook computer power source market sections. The first lithium batteries had metallic lithium as negative electrodes (anode, the source of lithium). However, it was found to produce dendrites, growing during the battery operation and inducing short circuits. Thus, metallic lithium anodes are not used any longer. Graphite is considered a good material for anodes in lithium-ion batteries as it may intercalate a considerable amount of lithium at low potential. One Li ion per six C atoms (LiC_6) can be reached, which corresponds to a theoretical reversible specific capacity of 372 Ah/kg. Higher capacity values have been obtained for less ordered carbons [201–203], where two types of Li ions contribute to the charge transfer: intercalated Li and quasimetallic Li. Quasimetallic Li, occupying the nanopores, is responsible for very good reversible capacity at very low voltages [202]. Disorganized carbons may offer a longer life cycle and faster charging/discharging rates as compared to graphite, where Li ions have to diffuse a long distance between the closed-spaced graphene layers, leading to fast material degradation. It should be noted, however, that some issues, including relatively large irreversible capacity, still need to be resolved. Additionally, further increase in the reversible Li insertion amount by electrochemistry is highly desirable.

CDC can be prepared at a controlled level of ordering and porosity and thus may be an ideal material for systematic studies of the influence of these parameters on reversible Li insertion degree, ionic conductivity, lifetime, etc. These studies should allow fabrication of advanced Li-ion batteries with high specific power and energy density, longer lifetime, and higher efficiency.

A preliminary study has been performed on CDCs prepared from SiC, TiC, and Mo_2C [204, 205]. Bulk CDC samples were lithiated over the temperature range 30–200°C. Concentration profiles of Li in CDCs were measured using the nuclear reaction $^7Li(p,a)^4He$. Diffusion coefficients obtained were in the range 10^{-9}–10^{-7} cm^2/sec and dependent on the pore size and the diffusion process duration. A mechanism for the process proposed on this basis is mainly Li diffusion along pore walls and Li accumulation in pores followed by the formation of metal clusters [204].

8.5.5 Pt Catalyst on CDC Support

Platinum supported on carbon (Pt/C) is widely used as a catalyst for hydrogenation and oxidation reactions. The porous structure of the carbon support is of primary importance in the catalyst performance. CDC provides an advantage of a narrow pore-size distribution and variable pore diameters. Pt/C catalysts are usually prepared by adsorption of platinum-containing species from the solution on the selected carbon material followed by the reduction of the platinum compound to metal state (see, e.g., [206]). This method is applicable to CDC. A novel one-stage method for preparation of Pt/C catalysts from SiC was proposed by McNallan and Gogotsi [207,208]. Silicon carbide ceramics were treated in Cl_2–H_2–Ar gas mixtures according to the technique described in the reports [28,86,87]. Additionally, metallic platinum was present in the reaction zone in the form of foil or wire. In this case, Pt particles were dispersed in the produced material forming interlayers in the carbon layer. The proposed mechanism of the process begins with platinum transport to the SiC/C interface via the gas phase in the form of triplatinum trichloride. Then Pt_3Cl_3 reacts with Si from the SiC resulting in Pt and $SiCl_4$.

8.5.6 Tribological Coatings

Metal carbides are widely used in a variety of machining and sliding contact applications. Despite their high corrosion and wear resistance, these materials are not lubricious. A novel process for the formation of a low-friction carbon layer on the SiC surface was recently introduced [13,88]. Tribological characterization of the CDC-coated silicon carbide ceramics was carried out in [209]. Sintered α-SiC and CVD β-SiC specimens were treated in Cl_2–H_2–Ar mixtures of various compositions at temperatures from 700 to 1000°C and ambient pressure. Tribological tests consisting of measuring the friction coefficients and wear rates by means of standard ball-on-disk method were performed. It was observed that the produced articles had friction coefficients seven times lower than the untreated SiC. The friction coefficients of ~0.1 were almost independent of the type of initial material and parameters of the ball-on-disk test including contact load and sliding speed. As evidenced by the wear track features, the primary deformation process appears to be plastic flow of the carbon layer, resulting in smooth surface as the wear process progresses.

Further work [210–212] confirmed good tribological properties of CDC coatings in humid environment (air or water) but it also revealed that CDC shows a remarkably low friction coefficient (<0.03) with minimal wear in dry (nitrogen or vacuum) ambient. This behavior is unlike that of graphite and other sp^2 modifications of carbon, where the presence of water vapors is required for lubricity and long-time stability of the coatings. The presence of carbon onions and termination of dangling carbon bonds with hydrogen can explain the excellent performance of CDC in dry atmospheres. Potential applications of CDC coatings (with or without lubricants) include bearings, SiC-based MEMS, and dynamic seals of water pumps, to name a few.

CDC coatings on SiC fibers could be used to improve pull-out behavior and damage tolerance in composite materials [92,213]. Moreover, CDC can be used as a sacrificial layer for the formation of BN and Al–O–N coatings, which offer better oxidation resistance than carbon [214,215]. These

novel methods of coating synthesis by carbothermal nitridation consist of several steps. First CDC layer is produced on SiC fibers, then CDC is infiltrated with either boric acid (for BN formation) or aluminum chloride solution (for Al–O–N formation), and finally samples are treated in ammonia at atmospheric pressure and elevated temperatures to produce BN (or Al–O–N) coatings. The intermediate CDC layer helps to build a strong bonding between the fiber and coating. Formation of BN coatings did not result in any degradation in tensile strength of the SiC fibers. Synthesis of Al–O–N coatings led to more than 65% improvement in the tensile strength and a threefold increase in the Weibull modulus for the fiber with 200 nm coating compared to those for the as-received fibers. The coated fiber exceeds the strength of all other small-diameter SiC fibers reported in literature.

8.6 CONCLUSIONS

The synthesis of almost all known carbon structures including amorphous and nanocrystalline graphitic carbon, graphite ribbons, CNTs, carbon onions, nanodiamond, and ordered graphite is possible by the extraction of metals from carbides. In addition, CDC synthesis allows formation of highly porous carbon materials with good mechanical properties. Microstructure, pore size, pore shape, and surface termination of nanoporous CDC can be precisely controlled by the process parameters and the composition and structure of the initial carbide precursor. As such, the process allows optimization of nanoporous CDC for various applications.

Thermodynamic analysis shows the possibility of carbon synthesis from almost any carbide under appropriate process conditions (temperature, pressure, and etchant). While more experimental data have been obtained on SiC, about 20 other carbides have been successfully used to produce CDC.

Along with conventional applications for porous carbon as sorbents, new applications are enabled by tailorable structure and porosity of CDC. Tests performed to investigate the hydrogen and methane storage capabilities of CDC revealed that CDC could outperform the entire spectrum of commercial porous carbons and most of the other novel carbon materials. As such, CDC is a very promising material for numerous energy-related applications. CDC as a storage medium of active chlorine may be used for various sanitization purposes. Tribological testing of CDC coatings in humid and dry (nitrogen or vacuum) ambient showed the low friction coefficient and high mechanical stability of this material. Carbothermal nitridation of CDC coatings allows formation of well-adhered oxidation-resistant nitride coatings on SiC. Preliminary results on the performance of CDC as electrodes in supercapacitors or Li-ion batteries are also very promising. However, for most of the applications discussed, more research needs to be done in order to understand the mechanisms behind the interaction of CDC with gases, liquids, and organic molecules and to improve further the performance of CDC.

ACKNOWLEDGMENTS

This work was supported by DARPA via ONR contract. Y. Gogotsi acknowledges the productive collaboration with Professor M.J. McNallan (UIC) and help from his students and postdoctoral associates H. Ye, B. Carroll, L. Chen, R. Dash, J. Chmiola, E. Hoffman, and Z.G. Cambaz at Drexel University and S. Welz at University of Illinois at Chicago, who worked with him on the development of new CDC materials.

REFERENCES

1. O.A. Shenderova, V.V. Zhirnov, and D.W. Brenner, Carbon nanostructures, *Critical Rev. Solid State Mat. Sci*., **27**, 227–356, 2004.
2. A.L. Vereshchagin, *Detonation Nanodiamonds*, Altai State Technical University, Barnaul, Russia, 2001.
3. V.Y. Dolmatov, Detonation synthesis of ultradispersed diamonds: properties and applications, *Russ. Chem. Rev*., **70**, 607–626, 2001.

4. M. Inagaki, *New Carbons*. Elsevier, Amsterdam, 2000.
5. S. Subramoney, Novel nanocarbons — structure, properties, and potential applications. *Adv. Mater*., **10**, 1157, 1998.
6. R.W. Baker, Future directions of membrane gas separation technology. *Ind. Eng. Chem. Res*., **41**, 1393–1411, 2002.
7. T. Duren, L. Sarkisov, O.M. Yaghi, and R.Q. Snurr, Design of new materials for methane storage, *Langmuir*, **20**, 2683–2689, 2004.
8. V.Y. Dolmatov and L.N. Kostrova, Detonation synthesis of nanodiamonds and the feasibility of developing a new generation of drugs, *J. Superhard Mater*., **3**, 79–82, 2000.
9. G.P. Bogatyreva and M.A. Marinich, *NATO Advanced Research Workshop on Nanostructured Materials and Coatings for Biomedical and Sensor Applications*, Y. Gogotsi and I. Uvarova, Eds., Kiev, Ukrain, 2002.
10. S.V. Mikhalovsky, Emerging technologies in extracorporeal treatment: focus on adsorption, *Perfusion-UK*, **18**, 47–54, 2003.
11. R.A. Freitas, *Nanomedicine*, Landes Bioscience, TX, USA, 2003.
12. Y. Gogotsi, V. Kamyshenko, V. Shevchenko, S. Welz, D.A. Ersoy, and M.J. McNallan, Nanostructured carbon coatings *on* silicon carbide: experimental *and* theoretical study, in *NATO ASI on Functional Gradient Materials and Surface Layers Prepared by Fine Particles Technology*, M.-I. Baraton and I. Uvarova, Eds., Kluwer Academic, Dordrecht, 2001, pp. 239–255.
13. D.A. Ersoy, M.J. McNallan, and Y. Gogotsi, Carbon coatings produced by high temperature chlorination of silicon carbide ceramics, *Mat. Res. Innovat*., **5**, 55–62, 2001.
14. Z.G. Cambaz, G.N. Yushin, K.L. Vyshnyakova, L.N. Pereselentseva, and Y.G. Gogotsi, Conservation of shape during formation of carbide-derived carbon on silicon carbide nano-whiskers, *J. Am. Ceram. Soc*., 2005, in press.
15. W.A. Mohun, A novel amorphous carbon, *Proceedings of the 4th Biennial Conference on Carbon*, Pergamon, Oxford, 1959, pp. 443–453.
16. M. Kusunoki, M. Rokkaku, and T. Suzuki, Epitaxial carbon nanotube film self-organized by decomposition of silicon carbide, *Appl. Phys. Lett*., **71**, 2620–2622, 1997.
17. S. Welz, Identification of carbon structures synthesized by chlorination of SiC and TiC. Ph.D. dissertation, University of Illinois at Chicago, Chicago, 2003.
18. J. Zhang, T.C. Ekstrom, S.K. Gordeev, and M. Jacob, Carbon with an onion-like structure obtained by chlorinating titanium carbide, *J. Mater. Chem*., **10**, 1039–1041, 2000.
19. Y. Gogotsi, S. Weltz, D.A. Ersoy, and M.J. McNallan, Conversion of silicon carbide to crystalline diamond-structured carbon at ambient pressure, *Nature*, **411**, 283–287, 2001.
20. A.M. Danishevski, G.N. Mosina, E.A. Smorgonskaya, S.K. Gordeev, A.V. Grechinskaya, C. Jardin, R. Meaudre, and O. Marty, Effect of preparation conditions on diamond *c*luster formation in bulk nanoporous carbon, *Diam. Relat. Mater*., **12**, 378–382, 2003.
21. S. Dimovski, A. Nikitin, H. Ye, and Y. Gogotsi, Synthesis of graphite by chlorination of *i*ron carbide at moderate temperatures, *J. Mater. Chem*., **14**, 238–243, 2004.
22. A. Nikitin and Y. Gogotsi, Nanostructured carbide-derived carbon, in *Encyclopedia of Nanoscience and Nanotechnology*, Vol. 7, H.S. Nalwa, Ed., American Scientific Publishers, Stevenson Ranch, CA, USA, 2003, pp. 553–574.
23. O. Hutchins, Method for the Production of Silicon Tetrachloride, US Patent 1271713, 1918.
24. J.N. Andersen, Silicon Tetrachloride Manufacture, US Patent 2739041, 1956.
25. G.F. Kirillova, G.A. Meerson, and A.N. Zelikman, Kinetics of chlorination of titanium and niobium carbides, *Izvestiya vuzov, Tsvetnaya. Metallurgiya*., **3**, 90–96, 1960.
26. V.P. Orekhov, G.V. Seryakov, A.N. Zelikman, T.M. Starobina, T.I. Kahzanova, K.V. Petrova, and P.M. Sverchkov, Kinetics of chlorination of zirconium carbide briquets. *J. Appl. Chem. USSR*, **42**, 230–237, 1969.
27. N.S. Jacobson, Y.G. Gogotsi, and M. Yoshimura, Thermodynamic and Experimental Study of Carbon Formation on Carbides under Hydrothermal Conditions. *J. Mater. Chem*., **5**, 595–601, 1995.
28. Y.G. Gogotsi, I.-D. Jeon, and M.J. McNallan, Carbon coatings on silicon carbide by reaction with chlorine-containing gases, *J. Mater. Chem*., **7**, 1841–1848, 1997.
29. M.J. McNallan, Y.G. Gogotsi, and I. Jeon, Preparation of carbon films by high temperature chlorination of metal carbides, *Proceedings of the 9th International Conference on High Temperature Materials Chemistry*, Vol. 97–39, K.E. Spear, Ed., The Electrochemical Society, Inc., Pennington, NJ, 1997.

30. R.K. Dash, G. Yushin, and Y. Gogotsi, Synthesis, structure and porosity analysis of microporous and mesoporous carbon derived from zirconium carbide, *Microporous and Mesoporous Mater*., **86**, 50–57, 2005.
31. G. Yushin, E. Hoffman, A. Nikitin, H. Ye, M.W. Barsoum, and Y. Gogotsi, Synthesis of nanoporous carbide-derived carbon by chlorination of titanium silicon carbide. *Carbon*, **43**, 2075–2082, 2005.
32. R.K. Dash, A. Nikitin, and Y.Gogotsi, Nanoporous carbon derived from boron carbide. *Microporous Mesoporous Mater*., **72**, 203–208, 2004.
33. Nillok Chemicals, Improvements in and Relating to Mineral Active Carbons and to a Process for Their Preparation. Great Britain Patent 971943, 1964.
34. W.A. Mohun, Mineral Active Carbon and Process for Producing Same, US Patent 3066099, 1962.
35. B.D. Vasilenko, Ph.D. Dissertation, Studies of carbide chlorination, Mintsvetmetzoloto, Moscow, USSR, 1956.
36. A.K. Kuriakose and J.L. Murgrave, Kinetics of reactions of elemental fluorine — 1, *J. Phys. Chem.*, **68**, 290–295, 1964.
37. A.K. Kuriakose and J.L. Murgrave, Kinetics of reactions of elemental fluorine — 2, *J. Phys. Chem*., **68**, 2343–2345, 1964.
38. D. Ersoy, M.J. McNallan, and Y.G. Gogotsi, Carbon coatings produced by high temperature chlorination of silicon carbide ceramics, *Mater. Res. Innov*., **5**, 55–62, 2001.
39. L. Chen, H. Ye, Y. Gogotsi, and M. McNallan, Carbothermal synthesis of boron nitride coatings on silicon carbide. *J. Am. Ceram. Soc*., **86**, 1830–1837, 2003.
40. H.P. Boehm and H.H. Warnecke, Structural parameters and molecular sieve properties of carbons prepared from metal carbides, *Proceedings of the 12th Biennial Conference on Carbon*, Pergamon, Oxford, 1975, pp. 149–150.
41. N.F. Fedorov, G.K. Ivakhnyuk, V.V. Tetenov, and G.V. Matyukhin, Carbon adsorbents based on silicon carbide, *J. Appl. Chem. USSR*, **54**, 1239–1242, 1981.
42. N.F. Fedorov, G.K. Ivakhnyuk, and D.N. Gavrilov, Porous structure of carbon adsorbents from titanium carbide, *Z. Prikladnoi Khimii*, **55**, 46–50, 1982.
43. N.F. Fedorov, G.K. Ivakhnyuk, and D.N. Gavrilov, Carbon adsorbents from carbides of the IV–VI groups transition metals, *Z. Prikladnoi Khimii*, **55**, 272–275, 1982.
44. O.E. Babkin, G.K. Ivakhnyuk, and N.F. Fedorov, Porous structure of carbon adsorbents from zirconium carbide, *Z. Prikladnoi Khimii*, **57**, 504–508, 1984.
45. K.S.W. Sing, D.H. Everett, R.A.V. Haul, L. Moscou, R.A. Pierotti, J. Rouquerol, and T. Siemieniewska, Reporting physisorption data for gas/solid systems, *Pure Appl. Chem*., **57**, 603–619, 1985.
46. M.M. Dubinin, Microporous structures and absorption properties of carbonaceous adsorbents, *Carbon*, **21**, 359–366, 1983.
47. M.M. Dubinin, Generalization of the theory of volume filling of micropores to nonhomogeneous microporous structures, *Carbon*, **23**, 373–380, 1985.
48. S.K. Gordeev, S.A. Kukushkin, A.V. Osipov, and Y.V. Pavlov, Self-organization in the formation of a nanoporous carbon material, *Phys. Solid State*, **42**, 2314–2317, 2000.
49. Y. Gogotsi, A. Nikitin, H. Ye, W. Zhou, J.E. Fischer, B. Yi, H.C. Foley, and M.W. Barsoum, Nanoporous carbide-derived carbon with tunable pore size, *Nature Mater.*, **2**, 591–594, 2003.
50. E.N. Hoffman, G. Yushin, M.W. Barsoum, and Y. Gogotsi, Synthesis of carbide-derived carbon by chlorination of Ti_2AlC, *Chem. Mater*., **17**, 2317–2322, 2005.
51. R.K. Dash, A. Nikitin, and Y. Gogotsi, Microporous carbon derived from boron carbide. *Microporous Mesoporous Mater*., **72**, 203–208, 2004.
52. Y. Gogotsi, V.L. Kuznetsov, G.N. Yushin, A. Nikitin, A.V. Okotrub, A.I. Romanenko, A.I. Boronin, and E. Pozhetnov, Effect of synthesis temperature on structure and properties of nanoporous carbon derived from silicon carbide, *Carbon*, 2006, in press.
53. J. Leis, A. Perkson, M. Arulepp, M. Kaarik, and G. Svensson, Carbon nanostructures produced by chlorinating aluminium carbide, *Carbon*, **39**, 2043–2048, 2001.
54. M. Jacob, U. Palmqvist, P. Alberius-Henning, and T. Ekstrom, Bulk synthesis of nanotube-like carbon material. *Mat. Res. Soc. Symp. Proc*., **593**, 87–92, 2000.
55. E.P. Barrett, L.G. Joyner, and P.P. Halenda, The determination of the pore volume and area distributions in porous substances: computations from nitrogen isotherms, *J. Am. Ceram. Soc*., **73**, 373–380, 1951.
56. N.F. Fedorov, G.K. Ivakhnyuk, and D.N. Gavrilov, Porous structure of carbon adsorbents from titanium carbide, *Z. Prikladnoi Khimii*, **55**, 46–50, 1982 [in Russian].

57. J. Leis, A. Perkson, M. Arulepp, P. Nigu, and G. Svensson, Catalytic effect of metals of the iron subgroup on the chlorination of titanium carbide to form nanostructural carbon, *Carbon*, **40**, 1559–1564, 2002.
58. Y.A. Kukushkina, R.G. Avarbe, and V.V. Sokolov, Parameters of the porous structure of carbon produced by thermochemical treatment of nonporous carbides, *Russ. J. Appl. Chem.*, **69**, 620–622, 1996.
59. Y.A. Kukushkina, R.G. Avarbe, V.V. Sokolov, and T.V. Mazaeva, Properties of tubular carbon articles prepared by chlorination of silicon carbide with various initial porosities, *Russ. J. Appl. Chem.*, **69**, 623–625, 1996.
60. S.K. Gordeev and A.V. Vartanova, Porosity of materials produced by chlorination of covalent and metal-like carbides, *Z. Prikladnoi Khimii*, **64**, 1178–1182, 1991 [in Russian].
61. G.K. Ivakhnyuk, O.E. Babkin, and N.F. Fedorov, Technological principles of the synthesis of model adsorbent for chromatography, *Russ. J. Phys. Chem.*, **67**, 1849–1852, 1993.
62. S.K. Gordeev and A.V. Vartanova, Porosity variation in the process of forming of carbide materials and making compact carbon adsorbents on their basis, *Z. Prikladnoi Khimii*, **67**, 1080–1084, 1994 [in Russian].
63. S.K. Gordeev, R.G. Avarbz, A.E. Kravtjik, J.A. Kukusjkina, V.V. Sokolov, T.V. Mazaeva, and A. Grechinskaya, A method for Producing a Porous Article and an Article Produced Thereby, PCT Patent WO 98/54111, 1998.
64. S.K. Gordeev and A.V. Vartanova, Novel approach for obtaining of bulk microporous materials, *Z. Prikladnoi Khimii*, **67**, 1375–1377, 1994 [in Russian].
65. Y.A. Kukushkina, R.G. Avarbe, V.V. Sokolov, and A.E. Kravchik, Influence of pyrocarbon content on properties of carbon–carbon sorption-active composites, *Russ. J. Appl. Chem.*, **72**, 2144–2145, 1999.
66. A. Manivannan, M. Chirila, N.C. Giles, and M.S. Seehra, Microstructure, dangling bonds and impurities in activated carbons, *Carbon*, **37**, 1741–1747, 1999.
67. F. Euler and E.R. Czerlinsky, X-ray studies of amorphous carbon from silicon carbide, *Proceedings of the Conference on Silicon Carbide. A High Temperature Semiconductor*, J. Smiltens, Ed., Pergamon Press, Oxford, 1960, pp. 155–161.
68. L.F. Lowe, H.D. Thompson, and J.P. Cali, Neutron activation analysis of silicon carbide, *Proceedings of the Conference on Silicon Carbide. A High Temperature Semiconductor*, J. Smiltens, Ed., Pergamon Press, Oxford, 1960, pp. 221–226.
69. M.J. McNallan, S.Y. Ip, S. Saam, and W.W. Liang, High Temperature corrosion of SiC based ceramics in chlorine containing environments, in *High Temperature Materials Chemistry — III*, D. Cubiciotti, Ed., The Electrochemical Society, Pennington, NJ, 1986, pp. 328–338.
70. S.Y. Ip, M.J. McNallan, and M.E. Schreiner, Oxidation of SiC ceramic heat exchanger materials in the presence of chlorine at 1300°C, in *Silicon Carbide '87 Ceramic Transactions*, Vol. 2, C.E. Semler, Ed., The American Ceramic Society: Columbus, OH, 1989, pp. 289–299.
71. M.J. McNallan, S.Y. Ip, S.Y. Lee, and C. Park, Corrosion of silicon-based ceramics in mixed oxygen–chlorine environments, in *Corrosion and Corrosive Degradation of Ceramics, Ceramic Transactions.*,Vol. 10, M.J. McNallan, Ed., The American Ceramic Society: Columbus, OH, 1990, pp. 309–332.
72. D.S. Park, M.J. McNallan, C. Park, and W.W. Liang, Active corrosion of alpha-silicon carbide in oxygen–chlorine gases at elevated temperatures, *J. Am. Ceram. Soc.*, **73**, 1323–1329, 1990.
73. J.E. Marra, E.R. Kreidler, N.S. Jacobson, and D.S. Fox, Reactions of silicon-based ceramics in mixed oxidation chlorination environments, *J. Am. Ceram. Soc.*, **71**, 1067–1073, 1988.
74. J.E. Marra, E.R. Kreidler, N.S. Jacobson, and D.S. Fox, The behavior of SiC and Si_3N_4 ceramics in mixed oxidation/chlorination environments, in *Silicon Carbide '87. Ceramic Transactions.*,Vol. 2, C.E. Semler, Ed., The American Ceramic Society, Columbus, OH, 1989, pp. 275–286.
75. J.E. Marra, E.R. Kreidler, N.S. Jacobson, and D.S. Fox, Direct mass spectromic identification of silicon oxychloride compounds, *J. Electrochem. Soc.*, **135**, 1571–1574, 1988.
76. M. Balooch and D.R. Olander, Etching of silicon carbide by chlorine, *Surf. Sci.*, **261**, 321–324, 1992.
77. W.-S. Pan and A.J. Steckl, Reactive ion etching of SiC thin films by mixtures of fluorinated gases and oxygen, *J. Electrochem. Soc.*, **137**, 212–220, 1990.
78. P.H. Yih and A.J. Steckl, Effects of hydrogen additive on obtaining residue-free reactive ion etching beta-SiC in fluorinated plasmas, *J. Electrochem. Soc.*, **140**, 1813–1824, 1993.
79. P.H. Yih and A.J. Steckl, Residue-free reactive ion etching of 3C-SiC and 6H-SiC in fluorinated mixture plasmas, *J. Electrochem. Soc.*, **142**, 2853–2860, 1995.

80. R.N. Kyutt, É.A. Smorgonskaya, A.M. Danishevskii, S.K. Gordeev, and A.V. Grechinskaya, Structural studies of nanoporous carbon produced from silicon carbide, *Phys. Solid State*, **41**, 808–810, 1999.
81. R.N. Kyutt, É.A. Smorgonskaya, A.M. Danishevski, S.K. Gordeev, and A.V. Grechinskaya, Structural study of nanoporous carbon produced from polycrystalline carbide Materials: small-angle x-ray scattering, *Phys. Solid State*, **41**, 1359–1363, 1999.
82. É.A. Smorgonskaya, R.N. Kyutt, S.K. Gordeev, A.V. Grechinskaya, Y.A. Kukushkina, and A.M. Danishevskii, On fractal nature of the structure of nanoporous carbon obtained from carbides, *Phys. Solid State*, **42**, 1176–1181, 2000.
83. É.A. Smorgonskaya, R.N. Kyutt, A.V. Shchukarev, S.K. Gordeev, and A.V. Grechinskaya, X-ray studies of nanoporous carbon powders produced from silicon carbide, *Semiconductors*, **35**, 661–665, 2001.
84. V.V. Popov, S.K. Gordeev, A.V. Grechinskaya, and A.M. Danishevskii, Electrical and thermoelectric properties of nanoporous carbon, *Phys. Solid State*, **44**, 789–792, 2002.
85. E. Smorgonskaya, R. Kyutt, A. Danishevskii, C. Jardin, R. Meaudre, O. Marty, S. Gordeev, and A. Grechinskaya, X-ray and HRTEM structural studies of bulk nanoporous carbon materials produced from carbides, *J. Non-Crystalline Solids*, **299–302**, 810–814, 2002.
86. I.D. Jeon, M.J. McNallan, and Y.G. Gogotsi, Formation of carbon coatings on silicon carbide by reactions in halogen containing media, in *Proceedings of the Symposium on Fundamental Aspects of High Temperature Corrosion*, Vol. 96–26, P.Y. Hou, Ed., The Electrochemical Society: Pennington, NJ, 1996, pp. 256–268.
87. Y.G. Gogotsi, Formation of carbon coatings on carbide fibers and particles by disproportionation reactions, in *Advanced Multilayered and Fibre-Reinforced Composites*, Y.M. Haddad, Ed., Kluwer Academic Publishers: Dordrecht, 1998, pp. 217–230.
88. D.A. Ersoy, M.J. McNallan, and Y. Gogotsi, High temperature chlorination of SiC for preparation of tribological carbon films, *Proceedings of the Symposium on High Temperature Corrosion and Materials Chemistry*, Vol. 98–99, P.Y. Hou, M.J. McNallan, R. Oltra, E.J. Opila, and D.A. Shores, Eds., The Electrochemical Society, Inc.: Pennington, NJ, 1998, pp. 324–333.
89. Y. Gogotsi, V.L. Kuznetsov, G.N. Yushin, A. Nikitin, A.V. Okotrub, A.I. Romanenko, A.I. Boronin, and E. Pozhetnov, Effect of synthesis temperature on structure and properties of nanoporous carbon derived from silicon carbide, *Carbon*, 2006, in press.
90. A.M. Danishevskii, É.A. Smorgonskaya, S.K. Gordeev, and A.V. Grechinskaya, Raman light scattering in nanoporous carbon obtained from silicon and titanium carbides, *Phys. Solid State*, **43**, 137–144, 2001.
91. Y.G. Gogotsi, S. Welz, J. Daghfal, M.J. McNallan, I.-D. Jeon, K.G. Nickel, and T. Kraft, Formation of carbon coatings on SiC fibers by selective etching in halogens and supercritical water, *The 22th Annual Conference on Composites, Advanced Ceramics, Materials and Structures: A*, D. Bray, Ed., Am. Ceram. Soc., Westerville, OH, 1998, pp. 87–94.
92. M.J. McNallan, Y. Gogotsi, and D.A. Ersoy, Reaction formed coatings for SiC fibers in ceramic matrix composites, in *Elevated Temperature Coatings*: *Science and Technology III*, J.M. Hampikian and N.B. Dahotre, Eds., The Minerals, Metals & Materials Society, Warrendale, PA, USA, 1999, pp. 351–359.
93. S. Welz, Y. Gogotsi, and M. McNallan, Nucleation, growth, and graphitization of diamond nanocrystals during chlorination of carbides, *J. Appl. Phys.*, **93**, 4207–4214, 2003.
94. O.E. Babkin, G.K. Ivakhnyuk, Y.N. Lukin, and N.F. Fedorov, Study of structure of carbide derived carbon by XPS, *Z. Prikladnoi Khimii*, **57**, 1719–1721, 1984.
95. A.M. Danishevskii, G.N. Mosina, E.A. Smorgonskaya, S.K. Gordeev, A.V. Grechinskaya, C. Jardin, R. Meaudre, and O. Marty, Effect of preparation conditions on diamond cluster formation in bulk nanoporous carbon, *Diam. Relat. Mater.*, **12**, 378–382, 2003.
96. V.V. Kamyshenko, V.I. Shevchenko, Y.G. Gogotsi, and V.V. Kartuzov, Theoretical studies of diamond film growth on (1 1 1) SiC surface, in *Mathematical Models and Computing Experiment in Materials Science*, Vol. 5, B.A. Galanov, Ed., Frantsevich Institute for Problems of Materials Science, Kiev, 2001, pp. 65–71.
97. J. Zheng, T.C. Eckström, S.K. Gordeev, and M. Jacob, Carbon with an onion-like structure obtained by chlorinating titanium carbide, *J. Mater. Chem.*, **10**, 1039–1041, 2000.
98. S. Weltz, Identification of Carbon Structures Synthesized by Chlorination of SiC and TiC, Ph.D. dissertation, University of Illinois at Chicago, Chicago, 2003.
99. H.P. Boehm, The first observation of carbon nanotubes, *Carbon*, **35**, 581–584, 1997.

100. Y. Gogotsi, A. Nikitin, H. Ye, W. Zhou, J.E. Fischer, B. Yi, H.C. Foley, and M.W. Barsoum, Nanoporous carbide-derived carbon with tunable pore size, *Nature Mater*., **2**, 591–594, 2003.
101. T. Ekstrom, M. Jacob, J. Zheng, P. Berius-Henning, U. Palmqvist, J. Leis, and A. Perkson, Method for Producing a Nanotubular Carbon Material and the Material Produced Thereby, PCT Patent WO 01/16023, 2001.
102. A. Perkson, J. Leis, M. Arulepp, M. Kaarik, S. Urbonaite, and G. Svensson, Barrel-like carbon nanoparticles from carbide by catalyst assisted chlorination, *Carbon*, **41**, 1729–1735, 2003.
103. J. Leis, A. Perkson, M. Arulepp, M. Kaarik, and G. Svensson, Carbon nanostructures produced by chlorinating aluminium carbide, *Carbon*, **39**, 2043–2048, 2001.
104. T.Y. Kosolapova, *Carbides. Properties, Production, and Applications*, Plenum Press, New York, 1971.
105. D. Osetzky, Macrocrystalline graphite from magnesium carbide, *Carbon*, **12**, 517–523, 1974.
106. N.F. Fedorov, G.K. Ivakhnyuk, and V.V. Samonin, Mesoporous carbon adsorbents from calcium carbide, *J. Appl. Chem. USSR*, **54**, 2253–2255, 1981.
107. G.K. Ivakhnyuk, V.V. Samonin, N.F. Fedorov, V.A. Vladimirov, L.V. Stepanova, and O.M. Kas'yanova, Carbon enriched calcium carbide and possibility of its application, *Z. Prikladnoi Khimii*, **60**, 852–856, 1987.
108. G.K. Ivakhnyuk, V.V. Samonin, and N.F. Fedorov, Study of properties of carbon derived from calcium carbide in the presence of nitrogen, *Z. Prikladnoi Khimii*, **60**, 1413–1415, 1987.
109. V.V. Samonin, G.K. Ivakhnyuk, and N.F. Fedorov, On mechanism of interaction between calcium carbide and metal chlorides, *Z. Prikladnoi Khimii*, **60**, 2357–2358, 1987.
110. N.F. Fedorov and V.V. Samonin, Theoretical foundations of carbide-thermal technology for production of activated carbon and sorption-active materials, *Russ. J. Appl. Chem*., **71**, 584–588, 1998.
111. N.F. Fedorov and V.V. Samonin, Production, pore structure, adsorption properties, and fields of application of composite sorbents from calcium carbide, *Russ. J. Appl. Chem*., **71**, 795–798, 1998.
112. S. Shimada, M. Inagaki, and K. Matsui, Oxidation kinetics of hafnium carbide in the temperature range of 480–600°C, *J. Am. Ceram. Soc*., **75**, 2671–2678, 1992.
113. C.B. Bargeron and R.C. Benson, Oxidation of hafnium carbide in the temperature range 1400–2060°C, *J. Am. Ceram. Soc*., **76**, 1040–1046, 1993.
114. S. Shimada, K. Nakajima, and M. Inagaki, Oxidation of single crystals of hafnium carbide in a temperature range of 600–900°C, *J. Am. Ceram. Soc*., **80**, 1749–1756, 1997.
115. S. Shimada, F. Yunazar, and S. Otani, Oxidation of hafnium carbide and titanium carbide single crystals with the formation of carbon at high temperatures and low oxygen pressures, *J. Am. Ceram. Soc*., **83**, 721–728, 2000.
116. S. Shimada, Formation and mechanism of carbon-containing oxide scales by oxidation of carbides (ZrC, HfC, TiC), *Mater. Sci. Forum*, **369–372**, 377–384, 2001.
117. S. Shimada, A thermoanalytical study on the oxidation of ZrC and HfC powders with formation of carbon, *Solid State Ionics*, **149**, 319–326, 2002.
118. S. Shimada and T. Ishii, Oxidation kinetics of zirconium carbide at relatively low temperatures, *J. Am. Ceram. Soc*., **73**, 2804–2808, 1990.
119. S. Shimada, M. Nishisako, M. Inagaki, and K. Yamamoto, Formation and microstructure of carbon-containing oxide scales by oxidation of single crystals of zirconium carbide, *J. Am. Ceram. Soc*., **78**, 41–48, 1995.
120. S. Shimada, Microstructural observations of ZrO_2 scales formed by oxidation of ZrC single crystals with formation of carbon, *Solid State Ionics*, **101–103**, 749–753, 1997.
121. S. Shimada, M. Yoshimatsu, M. Inagaki, and S. Otani, Formation and characterization of carbon at the ZrC/ZrO_2 interface by oxidation of ZrC single crystals, *Carbon*, **36**, 1125–1131, 1998.
122. Y.G. Gogotsi and M. Yoshimura, Formation of carbon films on carbides under hydrothermal Conditions, *Nature*, **367**, 628–630, 1994.
123. Y.G. Gogotsi and M. Yoshimura, Low-temperature oxidaton, hydrothermal corrosion, and their effects on properties of SiC (Tyranno) fibers, *J. Am. Ceram. Soc*., **78**, 1439–1450, 1995.
124. Y. Gogotsi and M. Yoshimura, Degradation of SiC (Tyranno) fibers in high-temperature, high-pressure water, *J. Mater. Sci. Lett*., **14**, 755–759, 1995.
125. Y.G. Gogotsi, Y. Tanabe, E. Yasuda, and M. Yoshimura, Effect of oxidation and hydrothermal corrosion on strength of SiC fibres, in *Advanced Materials '93, I/A: Ceramics, Powders, Corrosion and Advanced Processing*, N. Mizutani, Ed., Elsevier, Amsterdam, Netherlands, 1994.

126. Y. Gogotsi, *Hydrothermale Korrosion von SiC — Betrachtung der schädlichen und nützlichen Aspekte*, in *Korrosion und Verschleiß von keramischen Werkstoffen*, R. Telle and P. Quirmbach, Eds., Deutsche Keramische Gesellschaft, Aachen, 1994, pp. 114–122.
127. Y.G. Gogotsi, M. Yoshimura, M. Kakihana, Y. Kanno, and M. Shibuya, Hydrothermal synthesis of carbon films on SiC fibers and particles, in *Ceramic Processing Science and Technology*, H. Hausner, G.L. Messing, and S.-I. Hirano, Eds., American Ceramic Society, Westerville, OH, 1995, pp. 243–247.
128. T. Kraft, K.G. Nickel, and Y.G. Gogotsi, Hydrothermal degradation of chemical vapour deposited SiC fibres, *J. Mater. Sci.*, **33**, 4357–4364, 1998.
129. T. Kraft and K.G. Nickel, Carbon formed by hydrothermal treatment of alpha-SiC crystals, *J. Mater. Chem.*, **10**, 671–680, 2000.
130. Y.G. Gogotsi, K.G. Nickel, and P. Kofstad, Hydrothermal synthesis of diamond from diamond-seeded β-SiC powder, *J. Mater. Chem.*, **5**, 2313–2314, 1995.
131. Y.G. Gogotsi, P. Kofstad, M. Yoshimura, and K.G. Nickel, Formation of sp^3-bonded carbon upon hydrothermal treatment of SiC, *Diamond Relat. Mater.*, **5**, 151–162, 1996.
132. Y.G. Gogotsi and K.G. Nickel, Hydrothermal synthesis of diamond: challenges and opportunities, *The 21st Annual Conference on Composites, Advanced Ceramics, Materials and Structures — B*, American Ceramic Society, Westerville, OH, 1997, pp. 747–754.
133. R. Roy, D. Ravichandran, A. Badzian, and E. Breval, Attempted hydrothermal synthesis of diamond by hydrolysis of β-SiC powder, *Diamond Relat. Mater.*, **5**, 973–976, 1996.
134. K.G. Nickel, T. Kraft, and Y.G. Gogotsi, Hydrothermal synthesis of diamond, in *Handbook of Ceramic Hard Materials*, R. Riedel, Ed., Wiley-VCH, Weinheim, 2000, pp. 374–389.
135. K. Motzfeldt and M. Steinmo, Transport processes in the thermal decomposition of silicon carbide, *Proceedings of the Ninth International Conference on High Temperature Materials Chemistry*, Vol. 97–39, K.E. Spear, Ed., The Electrochemical Society, Inc., Pennington, NJ, 1997, pp. 523–528.
136. N.I. Voronin, V.L. Kuznetsova, and R.I. Bresker, Durability of silicon carbide heaters in various gaseous media, in *Silicon Carbide*, I.N. Frantsevich, Ed., Consultants Bureau, New York, 1970, pp. 81–87.
137. W.F. Knippenberg, Growth phenomena in silicon carbide, *Philips Res. Reports*, **18**, 161–274, 1963.
138. D.V. Badami, Graphitisation of alpha-silicon carbide, *Nature* (*London*), **193**, 569–570, 1962.
139. D.V. Badami, X-ray studies of graphite formed by decomposing silicon carbide carbon, *Carbon*, **3**, 53–57, 1965.
140. J.J. Comer, Electron microscopy and diffraction data of thermally decomposed β-silicon carbide whiskers, *J. Appl. Cryst.*, **4**, 12–15, 1971.
141. M.J. Bozack, Surface studies on SiC as related to contacts, *Phys. Stat. Sol* (*b*), **202**, 549–580, 1997.
142. A.J. van Bommel, J.E. Crombeen, and A. van Tooren, LEED and Auger electron observations of the SiC(0 0 0 1) surface, *Surf. Sci.*, **48**, 463–472, 1975.
143. F. Meyer and G.J. Loyen, Ellipsometry applied to surface problems, *Acta Electron.*, **18**, 33–38, 1975.
144. C.S. Chang, I.S.T. Tsong, Y.C. Wang, and R.F. Davis, Scanning tunneling microscopy and spectroscopy of cubic -SiC(1 1 1) surfaces, *Surf. Sci.*, **256**, 354–360, 1991.
145. M.A. Kulakov, P. Heuell, V.F. Tsvetkov, and B. Bullemer, Scanning tunnelling microscopy on the 6H SiC(0 0 0 1) surface, *Surf. Sci.*, **315**, 248–254, 1994.
146. F. Owman and P. Martensson, Scanning tunneling microscopy study of SiC(0 0 0 1) surface reconstructions, *J. Vac. Sci. Technol. B*, **14**, 933–937, 1996.
147. I. Forbeaux, J.-M. Themlin, and J.-M. Debever, High-temperature graphitization of the 6H-SiC (0 0 0−1) face, **442**, 1999.
148. L. Muehlhoff, W.J. Choyke, M.J. Bozack, and J.T. Yates, Comparative electron spectroscopic studies of surface segregation on SiC(0 0 0 1) and SiC(0 0 0−1), *J. Appl. Phys.*, **60**, 2842–2853, 1986.
149. T. Angot, M. Portail, I. Forbeaux, and J.M. Layet, Graphitization of the 6H-SiC(0 0 0 1) surface studied by HREELS, *Surf. Sci.*, **502–503**, 81–85, 2002.
150. S. Nakanishi, H. Tokutaka, K. Nishimori, S. Kishida, and N. Ishihara, The difference between 6H-SiC (0 0 0 1) and (0 0 0) faces observed by AES, LEED and ESCA, *Appl. Surf. Sci.*, **41/42**, 44, 1989.
151. R. Kaplan, Surface structure and composition of 6H-SiC, *Surf. Sci.*, **215**, 111–134, 1989.
152. U. Starke, C. Bram, P.-R. Steiner, W. Hartner, L. Hammer, K. Heinz, and K. Müller, The (0 0 0 1) — surface of 6H-SiC: morphology, composition and structure, *Appl. Surf. Sci.*, **89**, 175–185, 1995.
153. J. Schardt, C. Bram, S. Müller, U. Starke, K. Heinz, and K. Müller, LEED structure determination of hexagonal SiC surfaces, *Surf. Sci.*, **337**, 232–242, 1995.

154. K. Heinz, U. Starke, J. Bernhardt, and J. Schardt, Surface structure of hexagonal SiC surfaces: key to crystal growth and interface formation? *Appl. Surf. Sci.*, **162–163**, 9–18, 2000.
155. I. Forbeaux, J.M. Themlin, A. Charrier, F. Thibaudau, and J.M. Debever, Solid-state graphitization mechanisms of silicon carbide 6H-SiC polar faces, *Appl. Surf. Sci.*, **162**, 406–412, 2000.
156. F. Bonzo, L. Muehlhoff, M. Trenary, W.J. Choyke, and J.T. Yates, Electron spectroscopy study of SiC, *J. Vac. Sci. Technol. A*, **2**, 1271–1274, 1984.
157. S. Iijima, Graphitization of silicon carbide due to electron beam irradiation, *J. Solid State Chem.*, **42**, 101–105, 1982.
158. L.M. Foster, G. Long, and H.C. Stumpf, Production of graphite single crystals by the thermal decomposition of aluminum carbide, *Am. Mineral.*, **43**, 285–296, 1958.
159. M. Kusunoki, J. Shibata, M. Rokkaku, and T. Hirayama, Aligned carbon nanotube film self-organized on a SiC wafer, *Jpn. J. Appl. Phys.*, **37**(5B), L605–L606, 1998.
160. M. Kusunoki, T. Suzuki, K. Kaneko, and M. Ito, Formation of self-Aligned carbon nanotube films by surface decomposition of silicon carbide, *Phil. Mag. Lett.*, **79**, 153–161, 1999.
161. M. Kusunoki, T. Suzuki, T. Hirayama, J. Shibata, and K. Kaneko, A formation mechanism of carbon nanotube films on SiC(0 0 0 1), *Appl. Phys. Lett.*, **77**, 531–533, 2000.
162. M. Kusunoki, T. Suzuki, T. Hirayama, and N. Shibata, Aligned carbon nanotube films on SiC(0 0 0 1) wafers, *Physica B*, **323**, 296–298, 2002.
163. M. Kusunoki, T. Suzuki, C. Honjo, T. Hirayama, and N. Shibata, Selective synthesis of zigzag-type aligned carbon nanotubes on SiC (0 0 0 1) wafers, *Chem. Phys. Lett.*, **366**, 458–462, 2002.
164. H. Konishi, H. Matsuoka, N. Toyama, M. Naitoh, S. Nishigaki, and M. Kusunoki, Growth control of carbon nanotubes on silicon carbide surfaces using the laser irradiation effect, *Thin Solid Films*, **464–465**, 295–298, 2004.
165. T. Shimizu, Y. Ishikawa, M. Kusunoki, T. Nagano, and N. Shibata, Creation of highly oriented free-standing carbon nanotube film by sublimating decomposition of silicon carbide film, *Jpn. J. Appl. Phys.*, **39**, L1057–L1059, 2000.
166. V. Derycke, R. Martel, M. Radosavljevic, F.M. Ross, and P. Avouris, Catalyst-free growth of ordered single-walled carbon nanotube networks, *Nano Lett.*, **2**, 1043–1046, 2002.
167. H. Watanabe, Y. Hisada, S. Mukainakano, and N. Tanaka, *In situ* observation of the initial growth process of carbon nanotubes by time resolved high-resolution transmission electron microscopy. *J. Microscop.*, **203**, 40–46, 2001.
168. H. Takikawa, R. Miyano, M. Yatsuki, and T. Sakakibara, Carbon nanotubes on SiC powder surface grown by a vacuum heating process, *Jpn. J. Appl. Phys.*, **37**, L187–L189, 1998.
169. S. Botti, R. Ciardi, L. Asilyan, L. De Dominicis, F. Fabbri, S. Orlanducci, and A. Fiori, Carbon nanotubes grown by laser-annealing of SiC nanoparticles, *Chem. Phys. Lett.*, **400**, 264–267, 2004.
170. S. Botti, L.S. Asilyan, R. Ciardi, F. Fabbri, S. Lorety, A. Santoni, and S. Orlanducci, Catalyst-free growth of carbon nanotubes by laser annealing of amorphous SiC films, *Chem. Phys. Lett.*, **396**, 1–5, 2004.
171. T. Gorelik, S. Urban, F. Falk, U. Kaiser, and U. Glatzel, Carbon onions produced by laser irradiation of amorphous silicon carbide, *Chem. Phys. Lett.*, **373**, 642–645, 2003.
172. K. Tsugawa, A. Goto, and Y. Koga, Carbon nanotubes and carbon nanofibers synthesized by sublimating decomposition of silicon carbide with catalysts, *Proceedings of the 6th ADC/FCT Conference*, 2001, pp. 800–804.
173. A. Hahnel and J. Woltersdorf, Platinum-enhanced graphitization in sandwich structures of silicon carbide and borosilicate glass, *Mat. Chem. Phys.*, **83**, 380–388, 2004.
174. A. Burke, Ultracapacitors: why, how, and where is the technology? *J. Power Sources*, **91**, 37–50, 2000.
175. B.E. Conway, W.G. Pell, Double-layer and pseudocapacitance types of electrochemical capacitors and their applications to the development of hybrid devices, *J. Solid State Electrochem.*, **7**, 637–644, 2003.
176. Q. Jiang, M.Z. Qu, B.L. Zhang, Z.L. Yu, Progress of research on electrode materials for electrochemical supercapacitors, *J. Inorganic Mater.*, **17**, 649–656, 2002.
177. R.A. Huggins, Supercapacitors and electrochemical pulse sources, *Solid State Ionics*, **134**, 179–195, 2000.
178. B.E. Conway, *Electrochemical Supercapacitors*, Vol. 1, Kluwer Academic/Plenum Publishers, New York, 1999, p. 698.
179. S.K. Gordeev and A.V. Vartanova, Porosity variation in the process of forming of carbide materials and making compact carbon adsorbents on their basis, *Z. Prikladnoi Khimii*, **67**, 1080–1084, 1994.

180. R.G. Avarbz, A.V. Vartanova, S.K. Gordeev, S.G. Zjukov, B.A. Zelenov, A.E. Kravtjik, V.P. Kuznetsov, J.A. Kukusjkina, T.V. Mazaeva, O.S. Pankina, and V.V. Sokolov, Double Layer Capacitor with Porous Carbon Electrodes and Method for Manufacturing These Electrodes, PCT Patent WO 97/20333, 1997.
181. R.G. Avarbz, A.V. Vartanova, S.K. Gordeev, S.G. Zjukov, B.A. Zelenov, A.E. Kravtjik, V.P. Kuznetsov, J.A. Kukusjkina, T.V. Mazaeva, O.S. Pankina, and V.V. Sokolov, Process of Manufacturing a Porous Carbon Material and a Capacitor Having the Same, US Patent 5876787, 1999.
182. R.G. Avarbz, A.V. Vartanova, S.K. Gordeev, S.G. Zjukov, B.A. Zelenov, A.E. Kravtjik, V.P. Kuznetsov, J.A. Kukusjkina, T.V. Mazaeva, O.S. Pankina, and V.V. Sokolov, Electrode Having a Carbon Material with a Carbon Skeleton Network and a Capacitor Having the Same, US Patent 6110335, 2000.
183. Y.A. Maletin, N.G. Strizhakova, V.G. Izotov, A.A. Mironova, S.G. Kozachkov, V.G. Danilin, S.N. Podmogilny, M. Arulepp, J.A. Kukusjkina, A.E. Kravtjik, V.V. Sokolov, A. Perkson, J. Leis, J. Zheng, S.K. Gordeev, J.Y. Kolotilova, J. Cederstrom, and C.L. Wallace, A Supercapacitor and a Method of Manufacturing Such a Supercapacitor, PCT Patent WO 02/39468, 2002.
184. J. Chmiola, G. Yushin, R.K. Dash, and Y. Gogotsi, Effect of pore size and surface area of carbide derived carbons on specific capacitance, *J. Power Sources*, 2005, accepted.
185. A. Arulepp, L. Permann, J. Leis, A. Perkson, K. Rumma, A. Janes, and E. Lust, Influence of the solvent properties on the characteristics of a double layer capacitor, *J. Power Sources*, **133**, 320–328, 2004.
186. E. Lust, A. Janes, and M. Arulepp, Influence of electrolyte characteristics on the electrochemical parameters of electrical double layer capacitors, *J. Solid State Chem.*, **8**, 488–496, 2004.
187. E. Lust, G. Nurk, A. Janes, M. Arulepp, P. Nigu, P. Moller, S. Kallip, and V. Sammelselg, Electrochemical properties of nanoporous carbon electrodes in various nonaqueous electrolytes, *J. Solid State Electrochem.*, **7**, 91–105, 2003.
188. A. Janes, L. Permann, M. Arulepp, and E. Lust, Electrochemical characteristics of nanoporous carbide-derived carbon materials in non-aqueous electrolyte solutions, *Electrochem. Commun.*, **6**, 313–318, 2004.
189. E. Lust, A. Janes, T. Parn, and P. Nigu, Influence of nanoporous carbon electrode thickness on the electrochemical characteristics of a nanoporous carbon/tetraethylammonium tetrafluoroborate in acetonitrile solution interface, *J. Solid State Electrochem.*, **8**, 224–237, 2004.
190. A. Janes, L. Permann, M. Arulepp, and E. Lust, Voltammetric and electrochemical impedance spectroscopy studies of the nanoporous carbon vertical bar 1 M $(C_2H_5)_3CH_3NBF_4$ electrolyte solution interface, *J. Electroanalyt. Chem.*, **569**, 257–269, 2004.
191. J. Chmiola, G. Yushin, R.K. Dash, E.N. Hoffman, J.E. Fischer, M.W. Barsoum, and Y. Gogotsi, Double-layer capacitance of selected carbide-derived carbons in sulfuric acid, *Electrochem. Solid State Commun.*, **8**, A357–A360, 2005.
192. L. Schlapbach and A. Zuttel, Hydrogen-storage materials for mobile applications, *Nature*, **414**, 353–358, 2001.
193. M.G. Nijkamp, J.E.M.J. Raaymakers, A.J. van Dillen, and K.P. de Jong, Hydrogen storage using physisorption — materials demands, *Appl. Phys.* A, **72**, 619–623, 2001.
194. E.A. Evard, A.P. Voit, S.K. Gordeev, and I.E. Gabis, Kinetics of sorption and release of hydrogen by nanoporous carbon, *Mater. Sci.*, **36**, 499–505, 2000.
195. I.E. Gabis, E.A. Evard, S.K. Gordeev, and T. Ekstrom, Carbon nanomaterial for hydrogen uptake and storage, in *Hydrogen Materials Science and Chemistry of Metal Hydrides*, M.D. Hampton, Ed., Kluwer Academic, Dordrecht, 2002, pp. 383–390.
196. E. Johansson, B. Hjorvarsson, T. Ekström, and M. Jacob, Hydrogen in carbon nanostructures, *J. Alloys Compounds*, **330–332**, 670–675, 2002.
197. X.S. Chena, B. Mcenaneya, T.J. Maysa, J. Alcaniz-Mongeb, D. Cazorla-Amorosb, and A. Linares-Solanob, Theoretical and experimental tudies of methane adsorption on microporous carbons, *Carbon*, **35**, 1251–1258, 1997.
198. K.R. Matranga, A.L. Myers, and E.D. Glandt, Storage of natural gas by adsorption on activated carbon, *Chem. Eng. Sci.*, **47**, 1569–1579, 1992.
199. D. Lozano-Castello, D. Cazorla-Amoros, A. Linares-Solano, and D.F. Quinn, Influence of pore-size distribution on methane storage at relatively low pressure preparation of activated carbon with optimum pore size, *Carbon*, **40**, 989–1002, 2002.
200. D. Lozano-Castello, D. Cazorla-Amoros, and A. Linares-Solano, Powered activated carbons and activated carbon fibers for methane storage: a comparative study, *Energy Fuels*, **16**, 1321–1328, 2002.

201. S. Gautier, F. Leroux, E. Frackowiak, A.M. Faugere, J.-N. Rouzaud, and F. Beguin, Influence of the pyrolysis conditions on the nature of lithium inserted in hard carbons, *J. Phys. Chem. A*, **105**, 5794–5800, 2001.
202. M. Letellier, F. Chevallier, F. Beguin, E. Frackowiak, and J.-N. Rouzaud, The first *in situ* Li NMR study of reversible lithium insertion mechanism in disordered carbons, *J. Phys. Chem. Solids*, **65**, 245–251, 2004.
203. S. Flandrois and B. Simon, Carbon materials for lithium-ion rechargeable batteries, *Carbon*, **37**, 165–180, 1999.
204. I.M. Kotina, V.M. Lebedev, A.G. Ilves, G.V. Patsekina, L.M. Tuhkonen, S.K. Gordeev, M.A. Yagovkina, and T. Ekström, Study of the lithium diffusion in nanoporous carbon materials produced from carbides, *J. Non-Cryst. Solids*, **299–302**, 815–819, 2002.
205. I.M. Kotina, V.M. Lebedev, A.G. Ilves, G.V. Patsekina, L.M. Tuhkonen, S.K. Gordeev, M.A. Yagovkina, and T. Ekström, The Phase Composition of the Lithiated Samples of Nanoporous Carbon Materials Produced from Carbides, *J. Non-Cryst. Solids*, **299–302**, 820–823, 2002.
206. E. Antolini, F. Gardellini, E. Giacometti, and G. Squadrito, Study of the formation of Pt/C catalysts by non-oxidized active carbon support and a sulfur-based reducing agent, *J. Mater. Sci*., **37**, 133–139, 2002.
207. D.A. Ersoy, M.J. McNallan, and Y. Gogotsi, *Platinum Reactions with Carbon Coatings Produced by High-Temperature Chlorination of Silicon Carbide*, Vol. 99–38, The Electrochemical Society, Inc., Pennington, NJ, 1999, pp. 456–467.
208. D.A. Ersoy, M.J. McNallan, and Y. Gogotsi, Platinum reactions with carbon coatings produced by high-temperature chlorination of silicon carbide, *J. Electrochem. Soc*., **148**, C774–C779, 2001.
209. D.A. Ersoy, M.J. McNallan, Y. Gogotsi, and A. Erdemir, Tribological properties of carbon coatings produced by high-temperature chlorination of silicon carbide STLE, *Tribol. Trans*., **43**, 809–815, 2000.
210. B. Carroll, Y. Gogotsi, A.M. Koval'chenko, A. Erdemir, and M. McNallan, in *NATO Advanced Research Workshop on Nanostructured Materials and Coatings for Biomedical and Sensor Applications*, Y. Gogotsi, Ed., Kluwer Academic Publishers, Dordrecht, 2002.
211. B. Carroll, Y. Gogotsi, A. Kovalchenko, A. Erdemir, and M.J. McNallan, Effect of humidity on the tribological properties of carbide-derived carbon (CDC) films on silicon carbide, *Tribology Lett*., **15**, 51–55, 2003.
212. B. Carroll, Y. Gogotsi, A. Kovalchenko, A. Erdemir, and M. McNallan, Tribological characterization of carbide-derived carbon layers on silicon carbide for dry friction applications. Euro Ceramics VIII, PTS 1-3 *Key Eng.*, **264–268**, 465–468, 2004.
213. L. Chen, G. Behlau, Y. Gogotsi, and M.J. McNallan, Carbide-derived carbon (CDC) coatings for Tyranno ZMI SiC fibers, *Ceram. Eng. Sci. Proc*., **24**, 57–62, 2003.
214. L. Chen, H. Ye, Y. Gogotsi, and M.J. McNallan, Carbothermal synthesis of boron nitride coatings on silicon carbide, *J. Am. Ceram. Soc*., **86**, 1830–1837, 2003.
215. L. Chen, H. Ye, and Y. Gogotsi, Carbothermal synthesis of Al–O–N coatings increasing strength of SiC fibers, *Int. J. Appl. Ceramic Technol.*, **1**, 68–75, 2004.
216. S. Brunauer, P. Emmett, and E. Teller, Adsorption of gases in multimolecular layers, *J. Am. Chem. Soc.*, **60**, 309–319, 1938.

9 One-Dimensional Semiconductor and Oxide Nanostructures

Jonathan E. Spanier
Department of Materials Science and Engineering,
Drexel University, Philadelphia, Pennsylvania

CONTENTS

ABSTRACT

Within the last 10 years, inorganic single-crystalline semiconducting nanowires (NWs), functional-oxide NWs have emerged as one of the most important nanostructured-material platforms. These

nanomaterials have enabled fundamental investigations of the size and shape dependence on physical, optical, electronic, magnetic, mechanical, and functional properties. Moreover, these hierarchal nanostructures are the building blocks for the development of a range of new devices and materials applications in several fields including electronics, photonics, sensing, photovoltaics, and thermoelectric power. In this chapter, we review methods of producing these inorganic nanostructures, and highlight some of the widening array of nanowire (NW) and other one-dimensional (1-D) materials. We also discuss some of the recent progress in the chara-cterization of some of the more unique structural, mechanical, thermal, electronic, optical, and other functional properties of semiconducting and oxide NWs and related nanostructures. Finally, we highlight important application areas, and we discuss current levels of understanding with respect to modeling of the size- and shape-dependent properties of these single-component and hierarchal 1-D nanostructures.

9.1 INTRODUCTION

Fundamental understanding, control, and application of the rich variation in the properties of nanoscaled crystalline solids with size and shape remain central themes at the frontier of nanomaterials research. For example, insights into the size-induced depression of melting temperature [1], and on solid–solid phase transitions, temperatures, and pressures [2,3] gained from studies of low-dimensional materials have important implications for the development of new process routes for material synthesis and of new nanostructural topologies. The altered and often unusual behavior of electronic carriers confined to within one dimension in materials with altered or unique electronic-band structures [4] has enabled new classes of electronic logic, memory, and sensing devices. Twelve years following their introduction, the technological and commercial impact of chemically synthesized semiconducting quantum dots (QDs) [5] as “artificial atoms” continues to grow.

The technology sectors in which advances in nanomaterials research are expected to contribute significantly are diverse: drug delivery, medical therapies, medical testing and diagnostics, imaging and sensing, electronics, computing logic and architecture, telecommunications, transportation, information storage, thermal management, energy conversion and storage, and manufacturing. The transfer of nanoscience from the research laboratory to practical applications will be aided in part by (1) progress in bridging length scales between micro- or mesoscopic materials and molecular systems, and an improved understanding of the origin of size evolution of properties, (2) engineering functional and adaptable surfaces for the interfacing of inorganic-functional materials and biological systems at the nanoscale, (3) providing a high level of connectivity within nanostructured systems, and (4) providing addressability of nanoscaled components — whether by mechanical, electrical, optical, or other means. *Inorganic nanowires* and related nanostructures produced by so-called “bottom-up” synthesis methods have emerged as important building blocks within nanotechnology for addressing these challenges. With nanowires (NWs) and segmented NWs, finite-size effects can be realized in the radial and axial dimensions without the loss of connectivity. Considerable progress has been achieved in the development of (1) a large and growing library of nanowire (NW) materials systems, (2) methods that yield structures with control of diameter, length, shape, composition, and hierarchal complexity, (3) improved techniques for probing their properties, (4) effective methods of controlling their assembly, and (5) application of computational methods for predicting properties in nanostructures.

This chapter is organized into five sections. In Section 9.2, we review the methods and likely mechanisms for growth of 1-D single-crystalline inorganic nanostructures, and highlight some members of the array of 1-D nanomaterials that have been produced. In Section 9.3, we discuss recent progress in realizing more advanced nanostructures, including ongoing efforts in controlling the diameter, shape, topology, and spatial modulation of composition in axial and radial directions. We also briefly discuss branched and hierarchal nanostructures, nanobelts, nanosprings, and other nanostructures. In Section 9.4, we survey experimental work to date in characterizing selected properties that are unique to these

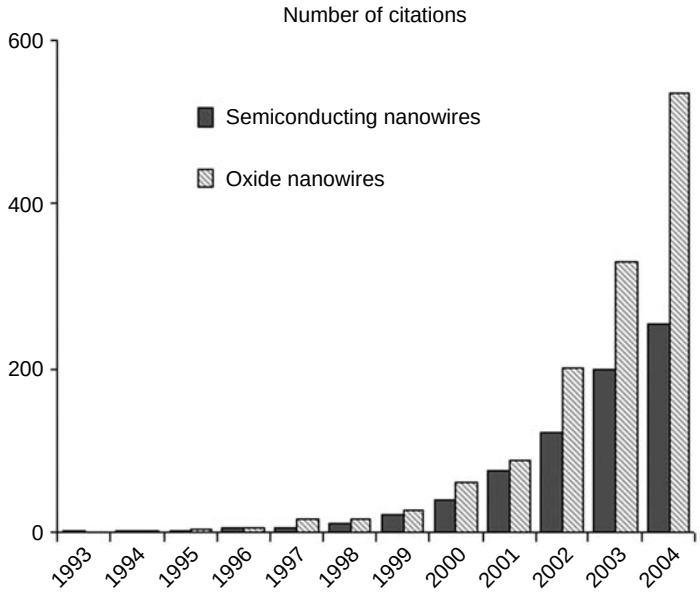

FIGURE 9.1 Annual growth in numbers of 1-D nanostructure-related publications.

1-D nanomaterials. We also identify selected applications. Finally, in Section 9.5, we conclude with a brief outlook for 1-D semiconductor and oxide-nanostructure material technology.

An important clarification is warranted: the phrase "one-dimensional" nanostructure is ambiguous; structures may be regarded as 1-D with respect to the behavior of one or more elementary excitations — e.g., electronic carriers, phonons, or photons — as distinguished from two- or zero-dimensional (0-D) structures. Specifically, this would involve the comparison of a relevant length scale, e.g., the Fermi wavelength, excitonic radius, coherence length, or scattering length, with the NW diameter. Alternatively, an even more stringent use of 1-D is reserved for cases in which fluctuations in an order parameter prevent the long-range order necessary to support the existence of a phase transition. In this chapter, the term 1-D is used to indicate that the diameters of the structures are all $<$100 nm, and that the length-to-diameter aspect ratio is significantly greater than unity. Given the importance of crystalline quality, for example, on electronic carrier mobility, and its effect on overall electronic device characteristics and performance, and that grain boundaries typically have a deleterious effect on many electronic, photonic, and other functional properties, we focus our discussion here primarily on *single-crystalline* NWs.

The NW research and development landscape is vast: a search of the keywords "nanowires" and "semiconductor" and "nanowires" and "oxide" produced well over 2400 publications over the last 12 years. (Included were synonyms for nanowire, e.g., nanowhiskers, nanofibers, and nanorods.) Figure 9.1 shows the rapid growth in annual number of publications for each. In early 2004, one estimate [6] placed the number of groups actively engaged in research and development of NW materials and devices at ~100. Recently, comprehensive reviews of inorganic NWs have been presented [7,8].

9.2 STRATEGIES FOR THE SYNTHESIS OF 1-D NANOSTRUCTURES

Common to the synthesis or deposition of bulk and nanocrystalline solids — whether from the liquid or vapor phase — are the concepts of nucleation and growth. Nucleation of the solid phase on a surface or in solution, by definition involves the initial formation of clusters of atoms due to supersaturation and subsequent precipitation of a selected elemental species or compound. Viewing

synthesis of nanostructures as the early stage of bulk crystal growth, it should be emphasized that in contrast to 0-D (sphere-like) and 2-D growth, the formation of 1-D structures is far less likely to occur in the absence of a symmetry-breaking event, of interfacial strain between the substrate and the nuclei, or of differences among crystallographic surfaces that can lead to strongly anisotropic growth rates.

Some 1-D nanostructured materials may be grown using methods in which there is inherent growth rate anisotropy to the crystalline structure. However, for other technologically important materials (e.g., Si, GaAs) crystalline structure alone often does not typically provide the necessary driving force to overcome more energetically favorable growth modes. Thus, a central challenge in the rational synthesis of 1-D nanostructured materials is to employ growth conditions, which employ a symmetry-breaking feature. Additionally, for some applications and fundamental studies, methods that permit dislocation and twin-free structures or precise control of diameter and length, and size dispersion may be important. In some situations, methods that produce periodic or nonperiodic arrays of aligned nanostructures may be desired. Finally, the need to adapt a process for other material systems or compositions to carry out growths at lower temperatures, to have compatibility with existing processes, and adaptability for multi-component architectures, may also be important considerations.

The methods of synthesizing single-crystalline 1-D nanostructured materials from the bottom-up may be classified into those that employ inherent crystalline anisotropy, those that exploit a metal nanocluster catalyst to facilitate 1-D growth, those that rely on templates, and those that rely on kinetic control and capping agents. Specifically, kinetic control is gained by monomer concentration or by multiple surfactants, bringing about conditions that strongly favor anisotropic growth. Though not discussed here, self- or directed-assembly of 0-D nanostructures into 1-D nanostructures, and size reduction of 1-D structures are additional process routes. Alternatively, one can classify the strategies into chemical solution-based syntheses, and those via vapor condensation routes (e.g., by solid source evaporation), by metallorganic-vapor phase, by thermal means (e.g., sublimation), or by laser ablation.

9.2.1 Metal Nanoclusters: Facilitating 1-D Growth

Vapor–liquid–solid (VLS) growth refers to a deposition route involving the condensation of species from the vapor phase onto a miscible liquid, followed by supersaturation of a species and its subsequent precipitation, forming the solid phase. Though VLS growth is commonly used for the synthesis of NWs, an understanding of the conditions for whisker growth via VLS methods was developed several decades ago by Wagner [9]. For more than two decades, 1-D semiconductor nanostructures were realized by subtractive or top-down methods: narrow mesas were etched from thin films, or structures produced by vicinal growth on selected steps were used in device configurations in which electrostatic potential applied to electrodes was used to provide adjustable degrees of confinement of electronic carriers to narrow channels within a planar 2-D electron or hole gas. Though the top-down approaches are technologically significant and robust, the lower limits of diameter or width are often restricted by the limits imposed by lithographic patterning techniques (e.g., electron-beam lithography, typically ~20 nm), by film removal, or by direct writing techniques (e.g., focused-ion beam). Following the early work of Wagner and Ellis [9], Hiruma et al. [10] produced free-standing, single-crystalline GaAs NWs with diameters as small as 10 nm via metallorganic vapor-phase epitaxy (MOVPE) on SiO_2-patterned substrates. In 1992, the same group showed that metal nanocluster droplets selectively catalyze NW growth, demonstrating the synthesis of InAs NWs [11]. A brief review of early GaAs and InAs nanowhisker growth was also presented by these authors [12]. We note that the first synthesis of silicon nanowires (Si NWs) was reported by Yu et al. [13]; the authors used thermal evaporation, specifically the sublimation of hot-pressed targets containing Si and Fe in flowing Ar at 1200°C at ~100 torr. This relatively simple method produced NWs with diameters of ~15 nm, with lengths reaching tens of microns. However,

it was the 1998 publication by Morales and Lieber [14], of a generalizable strategy for synthesizing high-quality single-crystalline NWs via laser ablation-produced nanocluster catalyst and reactant that stimulated enormous interest in the synthesis, characterization and application of semiconductor and oxide NW and other 1-D nanostructures.

Today, two of the most common methods of producing high-quality elemental and binary semiconductor NWs are condensation of laser-ablation-produced reactant and flowing of gaseous precursors (or a combination thereof), with a carrier gas in vacuum and at elevated temperature, such that selective adsorption onto substrate-bound metal nanocluster catalyst particles is promoted. In practice, metal nanoclusters can be in the form of colloidal nanocrystals (NCs) dispersed on the substrate or by deposition of an ultrathin film followed by an elevated thermal treatment in an inert atmosphere, to promote the formation of nanoscale islands. In the case of growth via laser ablation [14], nanocluster catalysts can also be formed by ablating target material that includes the catalyst metal. The requirement for the needed symmetry-breaking at the nanoscale for a given gas-phase species may be satisfied by a combination of appropriately chosen metal nanocluster species, temperature, and partial pressures. Following condensation and supersaturation of the adsorbate in the metal droplets, a nucleation event occurs, producing an interface between the precursor component and the catalyst alloy, and excess atoms from the precursor precipitate from the melt and crystallize as NW material. Under conditions that suppress the thermal decomposition of the precursor and the resulting uncatalyzed deposition, subsequent growth is strongly favored at the interface of the nanodroplet and crystal, forming the basis for the desired shape-anisotropic growth mode. In practice, the NW synthesis via metal-nanocluster catalyst routes can be achieved using some of the same methods that are used to deposit thin films: i.e., via laser ablation of a source target, via decomposition of flowing gaseous precursors (or both), by metallorganic chemical vapor deposition (MOCVD), or thermal decomposition and evaporation of a source material. In general, the selection of metal catalyst is guided by the requirement that it forms a miscible liquid phase with the NW components, and that the metal in the solid phase cannot be more thermodynamically stable than the NW material.

Specifically, the conditions that permit growth of NWs can be understood in terms of the Gibbs–Thomson effect. If the chemical potentials of the relevant bulk-solid phase, NW-solid phase, and vapor-phase precursor component are denoted by μ_{bulk}, μ_{wire}, and μ_{vapor}, the differences in chemical potential $\Delta\mu_{\text{wire}} \equiv \mu_{\text{wire}} - \mu_{\text{vapor}}$ and $\Delta\mu_{\text{bulk}} \equiv \mu_{\text{bulk}} - \mu_{\text{vapor}}$ will determine whether NW growth can ($\Delta\mu_{\text{wire}} < 0$) or cannot ($\Delta\mu_{\text{wire}} > 0$) occur. In addition, $\Delta\mu_{\text{wire}} = \Delta\mu_{\text{bulk}} + 4\Omega\alpha/d$, where Ω, α, and d denote the atomic volume, specific surface energy, and the nanocluster diameter, respectively. Two effects should be noted: (1) for a fixed negative value of $\Delta\mu_{\text{bulk}}$, there exists a minimum for d in order to satisfy the condition for growth ($\Delta\mu_{\text{wire}} < 0$), and (2) this minimum for d can be altered by increasing the partial pressure of the vapor phase during growth, resulting in a larger negative value for $\Delta\mu_{\text{bulk}}$. However, an increase in the partial pressure of the precursor gas can lead to defects in the NW product. In addition, heating of nanocluster-catalyst particles can lead to agglomeration, effectively increasing d and lowering the required minimum vapor pressure at which growth can occur.

9.2.2 Laser-Assisted Metal-Catalyzed Nanowire Growth

In laser-assisted metal-catalyzed nanowire growth (LCG) [14], laser ablation of a target containing the desired NW material(s) provides the source; the process is based, in part, on pulsed laser deposition (PLD), a common route for producing a wide variety of different classes of inorganic thin-film materials. The LCG method involves the flowing of an inert or carrier gas through a furnace, and the use of a laser-ablation target and of a growth substrate with metal nanocluster-catalyst particles. Alternatively, the catalyst material may be contained within the target, and may be prepared by sintering appropriate components. In general, laser wavelengths λ_e for LCG are chosen so that the optical absorption depth is shallow in order to maximize the effect of heating over a relatively small volume. Often, for growth of semiconductor NWs, an Nd:YAG ($\lambda_e = 1064$ nm, or frequency doubled or tripled) or an excimer laser (e.g., ArF, KrF, or XeF) is used. Ablation targets are typically

placed at the upstream end, and in cases where heating of the target is needed, within the hot zone. Alternatively, if the required selected NW growth and furnace temperature is higher than the melting point of the target, targets are placed just outside the furnace.

The LCG method is a highly versatile route for obtaining a wide range of NW materials — many materials can be prepared via laser ablation. It is also attractive in that the laser ablation route eliminates the need for gaseous precursors, many of which are toxic and, in some cases, also pyrophoric. Many of the target materials are widely available or can be prepared, for example, by sintering of particle components. Moreover, the method can be used in conjunction with a vapor deposition process to yield NWs having solid solutions and periodic segments of different composition [15,16]. Finally, as suggested by Duan and Lieber [17], LCG methods can be pursued as a synthesis route even in the absence of detailed phase diagrams. Despite its versatility, a shortcoming of the LCG method for the growth of semiconducting NWs (when used alone) is that the targets themselves typically must contain all of the components required for the NW. This limits the ability to control the introduction of dopants or other dilute impurities during growth, or the ability to adjust the composition. Moreover, to date, precise control of diameter, diameter dispersion, and synthesis of ultranarrow (below ~10 nm) NWs has not been demonstrated with LCG.

9.2.3 Metal-Catalyzed Vapor–Liquid–Solid Growth

Chemical precursors may also be supplied in the gaseous phase for the growth of NWs via chemical vapor deposition (CVD), or VLS growth with metal nanocluster catalyst particles. Growth systems vary in their degree of complexity, but in their simplest forms consist a vacuum furnace or growth chamber at controlled and elevated temperature, into which gaseous precursors or bubbled-liquid-phase precursors and carrier gases are flowed at controlled mass flow rates.

Access to temperature–composition and temperature–pseudobinary phase diagrams can be extremely helpful (if not indispensable) in the design of a metal-catalyzed NW growth process. The conditions which favor NW growth over noncatalyzed deposition are determined from temperature–composition phase diagrams, and judicious tuning of the temperature and partial pressures through mass-flow rate(s), and background pressure is essential in achieving diameter selectivity and narrow diameter dispersion. In Figure 9.2, a representative schematic phase diagram for Ge–Au is shown; at the eutectoid temperature, the metal NC forms a miscible liquid alloy with the precursor. A basic schematic of the stages of the VLS mechanism is also shown in Figure 9.2. With sufficient partial pressure of the precursor, selection of temperatures just above the eutectoid enables precipitation from the alloy melt and thus nucleation of the NW. Wu and Yang [18] reported on *in situ* TEM studies of Ge and Si NW syntheses. The authors observed distinct nucleation and growth phases, and provided the direct evidence that for elemental NWs, the synthesis proceeds by the VLS mechanism. Though Wu and Yang observed secondary nucleation events during the earliest stages of NW growth for some of the alloy droplets, they report that sustained NW growth from a droplet generally proceeds along one direction.

The state of the art in small NW-diameter metal-catalyzed vapor-liquid-solid growth (MCG) growth is perhaps best represented in Si NWs approaching molecular scale as reported by Wu and coworkers [19] (Figure 9.3). The authors also report that large-diameter (20 to 30 nm) NWs grow principally along ⟨111⟩, whereas smallest diameter NWs (<10 nm) grow along ⟨110⟩, with an intermediate range of diameters (10 to 20 nm) exhibiting ⟨112⟩, reflecting important size-dependent differences in the surface energetics. The presence of these planes is explained by the following: during nucleation of NWs from eutectic droplets, the lowest energy growth plane is expected to be the ⟨111⟩ solid–liquid interface, leading to the initial formation of crystal planes. While ⟨111⟩ planes form initially, a ⟨110⟩ NW forms during axial elongation during unidirectional growth. When additional ⟨111⟩ nucleation sites form on the droplet, they drive growth towards a new plane with lower energy, the ⟨110⟩. The final direction ⟨112⟩ occurs as a so-called "transitional" plane between the ⟨111⟩ and ⟨110⟩ NWs, because the ⟨112⟩ plane is a step plane between ⟨111⟩ and ⟨110⟩.

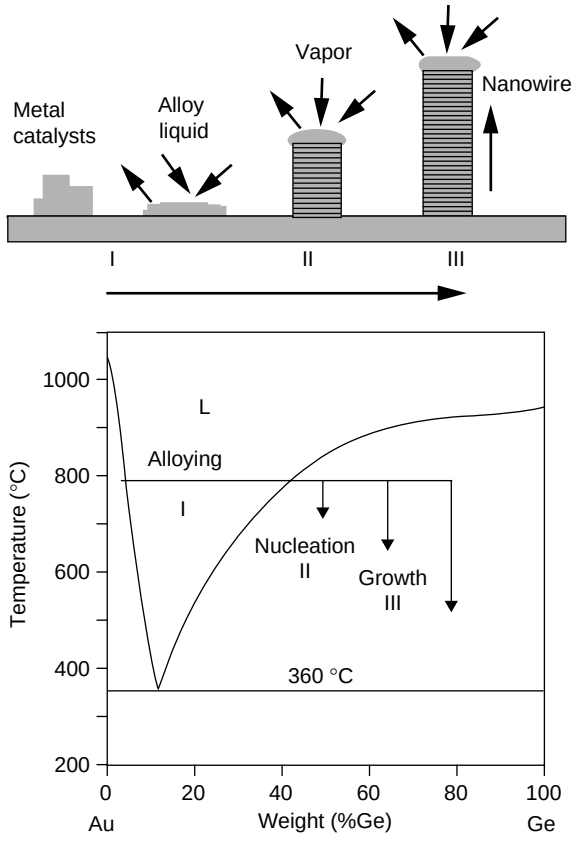

FIGURE 9.2 Upper panel: schematic of VLS growth; lower panel: binary Ge–Au composition phase diagram illustrating that control of temperature and partial pressure of Ge gaseous precursor can control different phases of NW growth. (Reproduced from Xia, Y. et al., *Adv. Mater.*, **15**, 353–389 (2003). With permission.)

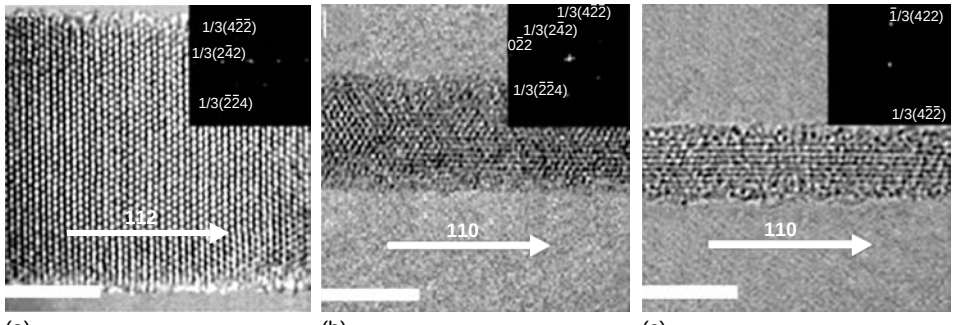

FIGURE 9.3 High-resolution transmission electron microscopy images of SiNWs with diameters of (a) 13.2, (b) 5.7, and (c) 3.5 nm. SiNWs were grown from 10-, 5-, and 2-nm gold nanoclusters catalysts, respectively. The scale bar is 5 nm in each panel. The NW growth axes are indicated by white arrows. (From Wu, Y. et al., *Nano Lett.*, **4**, 433–436 (2004). With permission.)

Some NW materials, such as those of Group III–V materials, can be prepared via MOVPE [12,20,21], in which deposition is carried out via the vapor phase, produced from bubbling of liquid-phase precursors. Like LCG, MOVPE enables access to a broader range of inorganic binary and ternary semiconductor materials and oxides than would be possible with gaseous sources alone.

Using MOVPE and chemical beam epitaxy (CBE), researchers from Lund University have demonstrated precise control of composition in the growth of III–V NWs, approaching monolayer sharpness in axial modulation [21–24]. A representative TEM image of an axially modulated InP–InA interface is shown in Figure 9.4. We also note that molecular beam epitaxy (MBE) has been used to synthesize high-quality semiconducting NWs [25]. Finally, NW synthesis by sublimation of solid sources has been used to produce Si NWs having diameters of ~15 nm [13], and, for example, nitrogen-doped GaN [26], AlN [27], and GaP [28] NWs. In what follows, we briefly review recent evidence for a different growth mechanism for the synthesis of metal nanocluster-catalyzed binary and other compound semiconductor NWs.

9.2.4 Vapor–Solid–Solid Growth

As discussed above, the prevailing view of the mechanism of metal nanocluster-catalyzed NW growth for both elemental and binary semiconductor NWs has been the VLS route. Though this mechanism has been shown to be operative for metal-catalyzed elemental NW synthesis, such as Si and Ge, there have been a number of reports for the formation of NWs on metal nanocluster-catalyst particles at temperatures well below the eutectoid, and on nanoparticles having diameters much larger than those for which the melting temperature is expected to be significantly depressed [12,29,30]. Persson et al. [23] examined recently the question of the validity of the application of the VLS mechanism to describing binary compound NW synthesis. Using *in situ* TEM of GaAs NWs as a representative system Persson et al. demonstrated that a different mechanism is likely to be operative. The authors showed that NW nucleation and growth may proceed by a VSS route in which the NW elemental species are transported by solid-state diffusion. This work is particularly significant because an improved understanding of the growth mechanism should enable the synthesis of a broader range of combinations of NW material components. The Lund group has confirmed that this mechanism may also be operative in the InAs NW vapor-phase-assisted synthesis [31]. This mechanism may help explain the reported

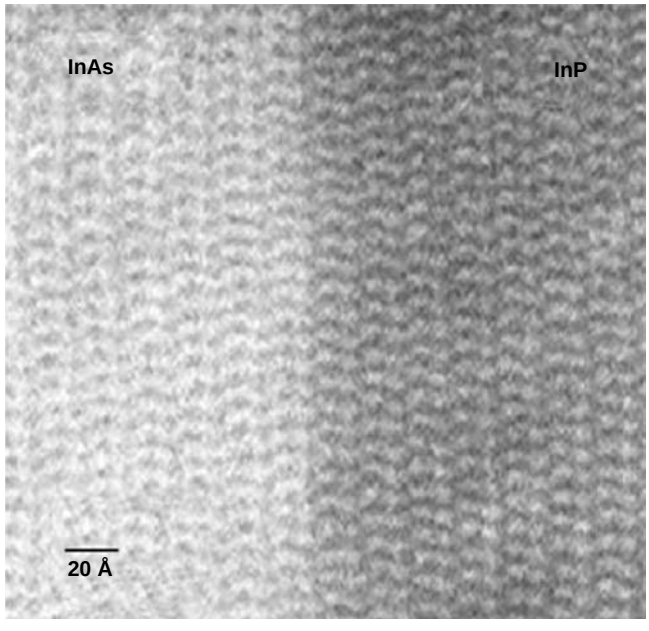

FIGURE 9.4 Scanning transmission electron microscopy (STEM) image of interface within atomically sharp axially modulated InAs-InP NW grown by CBE. The slow growth rate (~1 monolayer/sec) enables the formation of sharp interfaces. (From Samuelson, L. et al., *Physica E*, **25**, 313–318, 2004. With permission.)

growth of Si–Ge alloy NWs at moderate temperatures via MCG from the vapor phase, without laser ablation as reported by Lew et al. [32] and Redwing et al. [33].

9.2.5 Catalyst-Free Vapor-Phase Growth

Metal-catalyzed NW growth process offers a significant degree of control in terms of diameter selectivity and diameter dispersion. However, many semiconductor and oxide NWs can also be grown from the vapor or solid phase in the absence of metal-nanocluster catalysts via a vapor–solid (VS) route. These methods include oxide-assisted (OA) growth, carbothermal growth, sublimation, PLD, and MOCVD. As the name implies, VS growth [9] involves a flowing vapor-phase precursor produced by thermal evaporation, laser ablation, MOCVD, sublimation, or other means. Nanowires of a number of binary-metal oxides have been grown epitaxially without metal nanocluster catalyst, based on the VS growth mechanism.

With respect to binary-semiconductor NWs, Stach and coworkers [34] observed directly that self-catalyzed NW growth can occur. The authors showed that by sublimation of a GaN film, liquid droplets of Ga form, providing nucleation sites for the condensation of the concurrently produced GaN vapor phase. Johnson et al. [35] have reported the synthesis of pure hexagonal wurtzite InN using indium and ammonia. In addition to syntheses of GaN [36,37] and CdS [38], Yang et al. [39] employed vapor–solid growth to produce 20 to 100-nm-diameter single-crystalline NWs of β-SiC on SiC substrates. Yang and Zhang [40] reported the synthesis of 20 to 100-nm-diameter ZnS NWs. Catalyst-free MOCVD has also been employed to produce aligned GaAs and InGaAs NWs on partially masked GaAs and InAs substrates [41]. Pan et al. [42] reported a generalizable synthesis for binary oxides, including ZnO, SnO_2, In_2O_3, and CdO. Among the other binary oxides produced by VS methods are CuO [43], WO_x [44], Ga_2O_3 [45], Al_2O_3 [46], and SiO_2 [47]. In addition, Lee et al. [48] demonstrated growth of ZnO NWs on Si(100). Zhao et al. [49] reported VS synthesis of SeO_2 NWs with diameters of 20 to 70 nm.

Using OA growth, Lee et al. [50] have shown that decomposition of an Si_xO ($x > 1$) vapor produced by either thermal evaporation or laser ablation of SiO_x targets results in a high yield of Si NWs. The authors reported that the Si nanoparticles, which precipitate as a result of this process, serve as nucleation sites for subsequent growth. A combination of the catalytic effect of the Si_xO ($x > 1$) on the NW tips, with the reduction of lateral growth by SiO_2 (formed by decomposition of SiO) on the sides of the Si NWs, produces sustained NW growth. Stacking faults along the growth direction of $\langle 112 \rangle$ and the availability of low-energy [51] surfaces promote the fast growth of NWs along $\langle 112 \rangle$, and chains of nanoparticles in the case of nuclei having nonpreferred orientations. Zhang et al. [52] have reported on a similar process developed for the synthesis of Ge NWs, producing Ge NWs sheathed by a germanium-oxide layer. The growth of GaAs [53] and the high-temperature superconductor yttrium–barium–copper oxide (YBCO) in nanorod form via laser ablation of a YBCO target [54] are also attributed to OA growth.

Carbothermal processes represent a method for producing a large variety of metal oxide, semiconducting metal nitride as well as metal carbide NWs. Carbothermal methods involve the heating of a metal oxide in the presence of activated or nanostructured carbon (e.g., carbon nanotubes [CNTs]), producing a metal suboxide and CO. The suboxide is subsequently reacted, for example, in O_2, N_2, or NH_3 to produce metal oxide or semiconducting-metal nitride NWs. This method has been utilized to produce a wide range of NW materials, including materials such as In_2O_3 [55], GeO_2 [56], and GaN [57] NWs.

9.2.6 Chemical Solution-Based Growth

Chemical solution-based methods are attractive alternatives to vapor-phase methods: the preparations are often carried out at lower temperatures. Chemical-solution methods of promoting anisotropic crystal growth leading to 1D nanostructures are distinguished by either kinetic control

via supersaturation or by the use of coordinating ligands as capping agents. Precise control of size and shape can often be obtained. These strategies include solution–liquid–solid (SLS), solvothermal, and hydrothermal methods.

The SLS method of NW growth is similar to VLS growth. Here, low melting-point metal nanoclusters (e.g., Sn, In, Bi) are used, and metallorganic liquid-phase precursors are decomposed instead of vapor-phase precursors. Nanocluster-catalyst particles composed of metals with low melting temperatures are used, and the decomposition products form an alloy with the miscible NC-liquid droplet. Using this strategy, Buhro et al. [58–60] have synthesized single-crystalline III–V NWs (GaAs, InAs, and GaP) at low (~200°C) temperatures. A variation of this method using the so-called supercritical fluid-liquid solid (SFLS) method was employed by Holmes et al. [61] to produce high-quality, defect-free, single-crystalline Si NWs. The SFLS-produced Si NWs were seeded with 2.5-nm-diameter Au NCs and are nearly monodisperse (~4 to 5 nm in diameter).

Since the seminal work of Murray et al. [5] in synthesizing monodisperse, single-crystalline semiconducting II–VI NCs, significant progress has been made in extending chemical solution-based synthesis methods to produce other binary and ternary semiconducting and oxide-NC materials, and to develop rational methods for producing these NCs as shape-anisotropic 1-D nanostructures in a wide range of material systems. Here we briefly outline the general progress in the area of chemical synthesis of NWs and nanorods. Briefly, NC synthesis from solution involves injection of organic precursors at elevated temperatures into a coordinating solvent. Nucleation occurs from precipitation of the desired stable compound, and adsorption and desorption of the surfactant — typically one monolayer — enables deposition (and removal) of atoms on the nuclei. Kinetic control and focusing of size is regulated by monomer concentration: for monomer concentration above a solubility limit threshold, rapid growth of smaller NCs take place, and less rapid growth of larger NCs occurs. Once the monomer concentration falls below this threshold, Ostwald ripening takes place: NCs below a critical diameter become smaller and larger NCs grow. Capping by the coordinating ligands also prevents agglomeration. The capping also passivates the surface of NCs against oxidation, and improves the photoluminescence characteristics (intensity and monochromic emission) by reducing or eliminating unterminated-surface bonds which lead to nonradiative recombination of electron–hole pairs. Another key feature in attaining high-quality NCs — and highly relevant for nanorod and NW synthesis using this method — is homogeneous nucleation and its separation from the growth phase. In addition, maintaining a concentration of monomer above a given threshold ensures rapid growth of smaller NCs and less rapid growth of larger NCs, i.e., size focusing occurs.

Peng et al. [62] synthesized anisotropic NCs — quantum rods of CdSe — by taking advantage of the anisotropic growth of this wurtzite-structured material when driven by an extremely high monomer concentration. This anisotropy in growth is enhanced by the inherently anisotropic–wurtzite structure, with preferred growth along the *c*-axis. The authors reported the purposeful introduction of impurities to the coordinating ligand, trioctylphosphene oxide (TOPO). Numerous other syntheses of binary semiconductors and oxide materials have been reported, including ZnSe, Bi_2S_3, γ-Fe_2O_3, PZT, PbSe, PbS, ZnO, $BaCrO_4$, Fe_3O_4, BiS, Bi_2O_3, Bi_2Se_3, $MnFe_2O_4$, SnO_2, cerium phosphate ($CePO_4$), InAs, TiO_2, CdTe, CoTe, NiTe, $BaWO_4$, GaP, and europium oxide [7]. A comprehensive review of oxide NW and nanorod materials and their process routes is presented by Patzke et al. [63].

The synthesis of ternary oxide NWs, e.g., perovskite oxide NWs, has been particularly challenging. Urban et al. [64–66] demonstrated the synthesis of single-crystalline perovskite ternary oxide ($BaTiO_3$ and $SrTiO_3$) NWs by decomposition of metal-alkoxide precursors in oleic acid, based on a synthetic strategy for producing monodisperse perovskite NCs developed by O'Brien et al. [67]. The $BaTiO_3$ NWs possess diameters as small as 5 nm and lengths exceeding 10 μm. High resolution TEM and converging-beam electron diffraction confirmed that the NWs are essentially defect-free, single-crystalline, and the *c*-axis is oriented along the long axis of the NW (Figure 9.5). Xu et al. [68] employed a hydrothermal synthesis in the presence of polyvinyl alcohol and polyacrylic acid, to

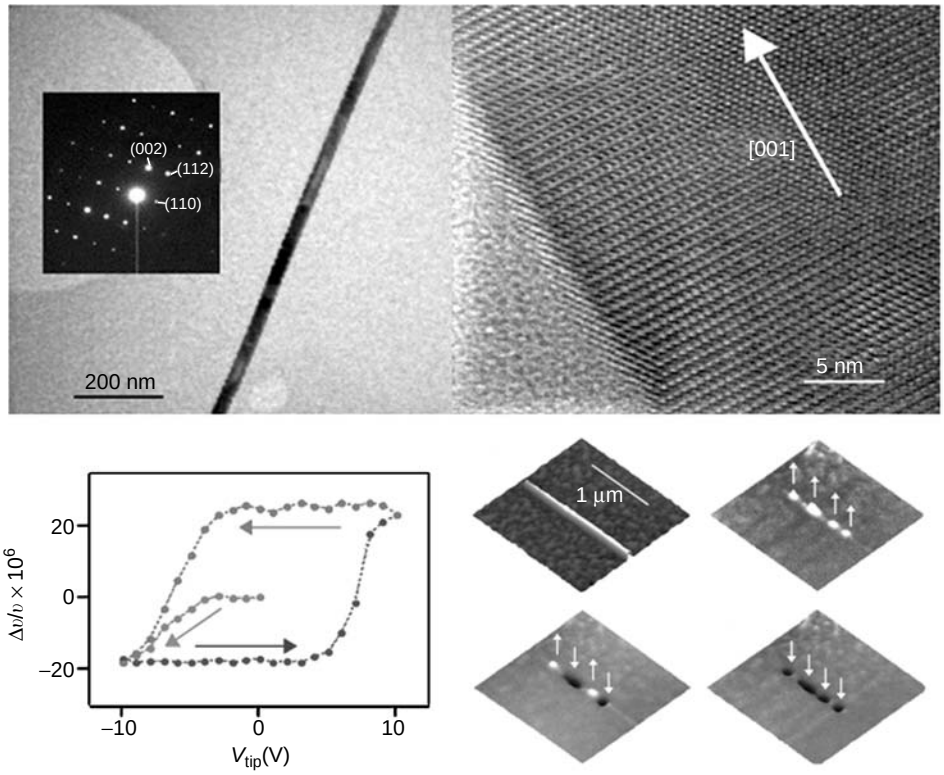

FIGURE 9.5 *Upper panel*: electron microscopy images of a representative single-crystalline $BaTiO_3$ NW. Results from high-resolution transmission electron microscopy, and converging beam electron diffraction (inset),collected at a number of locations along more than 50 NWs confirm that each NW is an essentially defect-free single-crystalline perovskite NW. Lower panel: FE hysteresis of individual FE domain oriented perpendicular to the axis of an 11-nm-diameter NW (left), and independent manipulation of FE polarization within an individual $BaTiO_3$ NW (right), measured by scanning probe microscopy. (From Urban, J.J. et al., *Adv. Mater*., 423–426 (2002); Spanier, J.E. et al., in *Nanowire Materials*, Vol. 1, Wong, Z.L., Ed., Kluwer, Boston, MA, 2002; Yun, W.S. et al., *Nano Lett*., **2**, 447–450 (2002). With permission.)

produce single-crystalline $PbZr_{0.52}Ti_{0.48}O_3$ NWs. Of particular significance is that the $BaTiO_3$ NWs produced by Urban et al. enabled more detailed investigations into ferroelectricity in nanostructured materials [65,66,69]. Electrostatic force microscopy of these NWs reveals that the NWs possess stable ferroelectric (FE) polarizations, which can be reproducibly reoriented perpendicular to the NW axes. As shown in Figure 9.5, these NWs exhibit FE hysteresis, and polarizations in these NWs can be independently induced and manipulated. The FE domains in these NWs represent the smallest volumes of stable FE reported to date. Subsequent studies have revealed distinct scaling behavior of the evolution of FE phase transition temperature, and further fundamental insights into the origins of FE stability in nanostructured and ultrathin-FE films. Our findings and the results of our investigations, combining density-functional theoretical simulations with experiments, will be reported in a forthcoming publication [70].

9.2.7 Template-Assisted Growth

Another route for obtaining 1-D nanostructures involves the use of nanostructured templates, which act as a host material into or onto which NWs (or alternatively NTs) of a wide range of materials can be grown. For example, Ge NWs have been formed via deposition onto periodic corrugations

(V-grooves produced by anisotropic etching in Si[100]) [71]. Salamo and coworkers [72] have used MBE on high-index GaAs surfaces to promote the assembly of (In, Ga)As NWs and other nanostructures during deposition. Following the growth or deposition into templates, selective etchants can be used to isolate NWs. Among the advantages for this method is straightforward alignment of NWs using template material having columnar pores, and the wide flexibility in deposition methods, including metal-catalyzed growth, catalyst-free growth from the vapor or liquid phases, electrochemical methods, and solution-gelation (sol-gel). In addition, NW diameter is controlled by the template-pore diameter. A principal disadvantage, however, is that the NWs produced using template-assisted growth (TAG) are frequently not single crystalline. Moreover, the lower limit of diameter of NWs is governed by the template-pore diameter, and some of the hierarchal structures that can be produced via MCG may not be as easily prepared using TAG. In addition, aspect ratios of TAG may be limited by mass transport. Among templates, two types of nanoporous-membrane templates are frequently used: anodic aluminum oxide, (AAO) [73–76] and porous-polymer films [77]. Pathways for the production of inorganic NWs include CNTs [78] and zeolites [79]. To produce AAO templates, aluminum films are electrochemically oxidized, and local etching takes place producing pores that have local hexagonally close-packed ordering. Subsequent anodization of the film leads to columnar pores with relatively monodisperse diameters ranging from 5 nm to >100 nm, depending upon preparation conditions, e.g., electrolyte composition and concentration, and anodization voltage. Such template materials (e.g., Anodisc™) can be obtained commercially via Whatman™ or prepared. Shingubara [80] has presented a review of the use of AAO templates for the preparation of nanomaterials. Polymer films having track-etched channels are formed by irradiation of heavy ions from nuclear fissions [81]. In many cases, following deposition, the NWs can be isolated by selective etching of the template; often an appropriately selected acidic solution provides the necessary selective etching. A diverse number of materials, including metals, semiconductors, and binary oxides have been deposited in templates via vapor phase, electrochemical means, or sol-gel methods.

Lew et al. [82], Lew and Redwing [83], and Redwing et al. [33] demonstrated that high-quality, single-crystalline Si and SiGe NWs can be produced using AAO templates with a metal catalyst. In contrast to template-free MCG, in this case, the NW diameter is controlled by the template diameter. This process has several notworthy features: it provides one possible route for growth-aligned NWs; it enables investigation of growth mechanisms and kinetics in the absence of catalyst-particle size-driven considerations. The demonstration of SiGe NW growth suggests the possibility of producing more complex NW materials and compositions, such as Si_xGe_{1-x} NWs, whose composition is controlled. Template-based methods have not been limited to AAO and polymer-based templates: for example, Han et al. [78] used CNTs as templates to facilitate the syntheses of single-crystalline GaN and Si_3N_4 NWs.

Al-Mawlawi and coworkers [84] demonstrated synthesis of CdS NW arrays via electrodeposition using AAO. Electrochemical methods typically yield NWs, which are polycrystalline and not single crystalline; for many applications, however template-assisted electrochemical deposition offers a rather easy route for synthesizing 1-D structures. Often limitations due to mass transport — well understood from the electrodeposition through or in vias in top-down semiconductor device processing — can be ameliorated by use of pulsed or alternating current (AC) electrodeposition techniques. In selected cases, high-quality and even single-crystalline NWs have been produced using this technique. Another attractive (though not exclusive) feature of electrodeposition is that multiple species can be reduced and deposited at selected over potentials, enabling the formation of compositionally segmented NWs within a single electrochemical bath.

For several decades, sol-gel methods [85] have represented an attractive, low-cost method for producing both planar and nonplanar-thin films of a diverse number of materials, including binary, ternary, and quaternary oxides, and binary semiconductors. For more than a decade, sol-gel methods have been used with nanoporous templates to produce 1-D nanostructures, both NWs and NTs. In nearly all cases, these nanostructures are polycrystalline in nature with varying degrees of control of

orientation or texture, though there have been some exceptions. For example, Miao et al. [86] reported the synthesis of single-crystal anataste TiO_2 NWs via an electrochemically enhanced sol-gel route. Frequently, the instability of polymeric precursors in air requires sol-gel methods to be carried out in an anhydrous environment. Here, the commercially available, air-stable polymeric precursors for sol-gel processing routes have been helpful in furthering the research in the synthesis and characterization of nanomaterials.

9.2.8 Selected Other Methods

One particularly novel template-like method for producing a wide range of single-crystalline NW materials, developed by Belcher and coworkers [87], is through the use of a virus-based scaffold. Selected peptides that were shown to exhibit control of composition, size, and phase during nanoparticle nucleation were expressed on a highly ordered capsid of a bacteriophage, providing a template for directed synthesis of NWs. Variation of the synthetic route via substrate-specific peptides through the virus offers a new material tunability not previously available. Other routes are possible as well. For example, an additional route particularly suited for the preparation of metal oxide NWs is the thermal oxidation of metal NWs produced by template-assisted or chemical solution-based methods, and Tang et al. [88] have shown that dipole-dipole interactions can be used to facilitate the assembly of monodisperse CdTe NCs into highly crystalline NWs with uniform sizes.

9.3 HIERARCHAL COMPLEXITY IN 1-D NANOSTRUCTURES

Control of NW diameters, diameter dispersion, and crystallographic and physical orientation are important features for fundamental investigations of size-scaling effects and for enabling the use of NWs as building blocks for nanotechnology. Moreover, synthesis routes for preparing other quasi-1-D topologies may provide new insights into mechanisms of nanostructure growth and new material platforms for a range of technologies. In addition to the well-known effects of finite size on electronic-band structure, the effects of finite size on nonlinear-optical properties, electrical and thermal conductivity, ferroelectricity, ferromagnetism, superconductivity, phonons, and on the evolution of phase-transition temperatures and pressures, and susceptibility behavior, are all areas of intense investigation.

9.3.1 Control of Diameter and Diameter Dispersion

While several methods permit synthesis of NWs with lengths of many microns or even tens of microns, and with diameters of the order of 10 nm and higher, controlled and reproducible growth of NWs with smaller diameters (<5 nm) and with narrow diameter dispersion has been more challenging. Control of the relative growth rates in axial and radial directions is an important feature in enabling access to a range of NW architectures. As pointed out by Wagner [9] for the VLS mechanism, it is hypothesized that several factors are significant in determining the diameter of the NWs. The size(s) of the catalyst nanoclusters is important, since the eutectic-droplet size for nucleation is defined by these. Secondly, the temperature will profoundly affect the diameter (and in some cases also the shape), since the solubility of the precursor reactant in the nanocluster will alter the eutectic droplet size, which in turn will alter the NW diameter. Finally, a vapor pressure of the precursor reactant in excess of the critical value at which deposition of the precursor reactant onto the NW surface (as opposed to the eutectic droplet) takes place, will also have the effect of producing radial as well as axial NW growth.

Gudiksen and Lieber [89] and Gudiksen et al. [90] demonstrated that Si NWs with control of mean diameter and with relatively narrow size dispersions can be synthesized: 5 (4.9 ± 1.0), 10 (9.7 ± 1.5), 20 (19.8 ± 2.0), and 30 (30.0 ± 3.0) nm-diameter Au colloid was used to produce Si NWs with diameters of 6.4 ± 1.2, 12.3 ± 2.5, 20 ± 2.3, and 31.1 ± 2.7 nm, respectively. The authors

point out that the dispersion in diameters for each size group is comparable to that of the catalyst particles, providing further evidence of the distinct role of nanocluster size in determining NW diameter.

Single-walled CNTs have attracted significant interest because they behave as 1-D metallic conductors or semiconductors with respect to electronic carriers. With regard to NWs, one challenge has been to produce "molecular wires" in which the diameter of the NWs is as small as possible — approaching a single chain of atoms. Such wires would find application, for instance, to the probing of size scaling and dimensionality effects in electronic transport, for extreme carrier or phonon confinement, or, for example, unique signatures in metal-insulating transitions associated with Peierls distortions in 1-D. In principle, the minimum NW radius is governed by equilibrium thermodynamics, namely that $r_{min} = 2\sigma_{LV}V_L/RT \ln \sigma$, where σ_{LV} is the liquid–vapor surface-free energy, V_L the molar volume of liquid, and σ the vapor-phase supersaturation. This suggests that nucleation and growth of ultranarrow-diameter NWs may be achieved using a higher partial pressure of precursor for the nucleation phase, followed by lower partial pressure for the growth phase. This has recently been applied by Wu et al. [19] in the VLS synthesis of molecular-scale Si NWs as shown in Figure 9.3.

In chemical solution-based NW synthesis, however, the control of diameter can be superior to those produced through VLS. For example, as of now, several investigators have applied size-selective precipitation methods originally developed by Murray et al. [5], to produce a growing number of nanostructured materials with size dispersion of the order of one monolayer. Peng et al. [62] have shown that the CdSe nanorods possess narrowsize dispersions, as demonstrated by the periodic ordering of these structures. Control of diameter and diameter dispersion has been shown in binary-oxide NW systems. For example, O'Brien and coworkers [91,92] reported on an aqueous solution-based chemical synthesis producing ZnO NWs with monodisperse-diameter NW yields, with diameters as narrow as 2 nm; the authors also reported on the measurement of strong excitonic confinement in these structures.

9.3.2 Control of Shape: Novel Topologies

One of the significant features of inorganic-nanomaterial synthesis by surfactant-mediated chemical routes is the possibility of controlling the size and shape of nanostructures, thereby effectively manipulating their properties. Manna et al. [93] demonstrated the growth of a range of nanostructures by varying the relative concentrations of two types of surfactants–TOPO and hexylphosphonic acid (HPA) — and systematically varying the monomer concentration with time. The HPA serves to accentuate the difference between growth rates on different crystal faces. Different systematic variations yield long rods, arrow-shaped NCs, teardrop-shaped NCs, tetrapods, and dendritic tetrapods. Manna et al. have also reported [93] that differences between wurtzite and rocksalt free energies and surface energetics govern the evolution of some of these structures — particularly stacking faults in the tetrapods. They have explained the topology in terms of abrupt changes in the crystal structure, from wurtzite in the rod segments to rock salt in the sphere-like vertices. Very recent investigations by Manna and coworkers, however, have indicated that this multiphase description of the tetrapod, and the corresponding model of their formation may not be valid: rather, it seems that the tetrapod nanostructures may consist of single phase, and that it is likely that the formation of twins plays a significant role in the unique evolution of their topologies [94].

The control of the relative axial and radial growth rates is the basis for the synthesis of coaxial, or core–shell nanostructures as discussed above. In our laboratory at Drexel, we have demonstrated the growth of apex-angle-controlled crystalline Si nanocones (Si NCs) and Ge nanocones (Ge NCs) of diamond-hexagonal phase through simultaneous control of axial and radial growth rates using metal-catalyzed CVD; we have also synthesized single-crystalline Ge nanosprings and characterized its composition and crystallinity with electron microscopy and Raman scattering. As shown in Figure 9.6, the Si NCs are tapered polyhedra, possessing hexagonal cross-sections. They are typically several

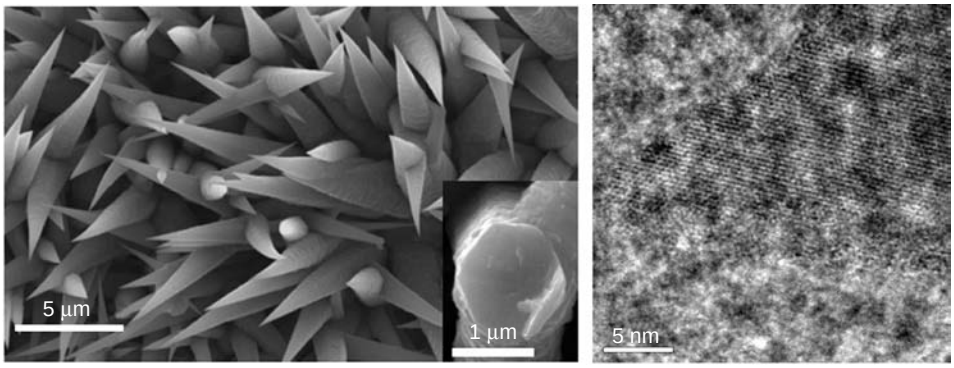

FIGURE 9.6 Silicon nanocones (Si NCs) formed by metal nanocluster-catalyzed CVD. The left panel shows an array of nanocones, which are tapered polyhedra, possessing hexagonal cross-sections. These Si NCs are typically several microns in base diameter. As shown in the panel on the right, the radius of curvature at the tip is as small as 1 to 2 nm. Though not shown, control of conical angle and its dispersion has also been achieved. (From Cao, L. et al., *J. Am. Chem. Soc*. in press (2005). With permission.)

microns in base diameter, and the radius of curvature at the tip is as small as 1 to 2 nm. Significantly, these nanocones are of the diamond-hexagonal polymorph, and the taper angles can be tuned during growth. These Si NCs may offer new opportunities as scanning probes and as central components in single-molecule sensing. Details on the synthesis and characterization of the unique structural, optical, and other properties will be presented in several forthcoming publications [95,96].

9.3.3 Other Binary Oxide 1-D Nanostructures

An incredibly diverse range of 1-D nanostructure topologies composed of binary oxides has been developed by Z. L.Wong and coworkers at Georgia Tech, using solid-state thermal sublimation and other techniques. A representative group of these 1-D nanostructures is shown in Figure 9.7. Briefly, oxide powder is placed in the hot zone of a furnace, and ions from the vapor-phase condense onto a nearby substrate in a lower temperature zone of the furnace. The control of growth kinetics of the polar surface-dominated nanostructures as well as the use of templates and metal nanoclusters leads to the synthesis of a wide range of nanostructured topologies, including nano-belts, nano-ribbons, nano-rings and nano-bows [97], nano-saws [98,99], and nano-helixes [100] — comprehensive reviews are presented in [101–104]. While this diverse class of nanostructures possess a common feature in that each is composed of a binary oxide with polar surfaces, we have recently identified CVD-based synthesis methods in our own laboratory to produce similar crystalline-elemental nanostructures, including Ge nano-helices and tree-branched Ge nanostructures possessing sixfold branching symmetry [105]. Our findings of synthesis conditions producing crystalline nanosprings in a material without polar surfaces (e.g., Ge as shown in Figure 9.8) suggests that mechanisms other than polar surface-specific energies and piezoelectricity may also be operative in the formation of one or more of the binary-oxide nanostructures, this is an area of ongoing investigation by our group [105].

9.3.4 Hierarchal 1-D Nanostructures

The integration of two or more semiconductor or other materials and the controlled incorporation of dopants within individual components of nanostructures are essential characteristics of the advancing development of NWs as building blocks for nanotechnology. Homo- and heterojunctions within individual NWs enable fabrication of bipolar devices within individual NWs, opening up possibilities for light-emitting diodes, photodetectors, and band gap-engineered devices within individual NWs, and even NW-based superlattices.

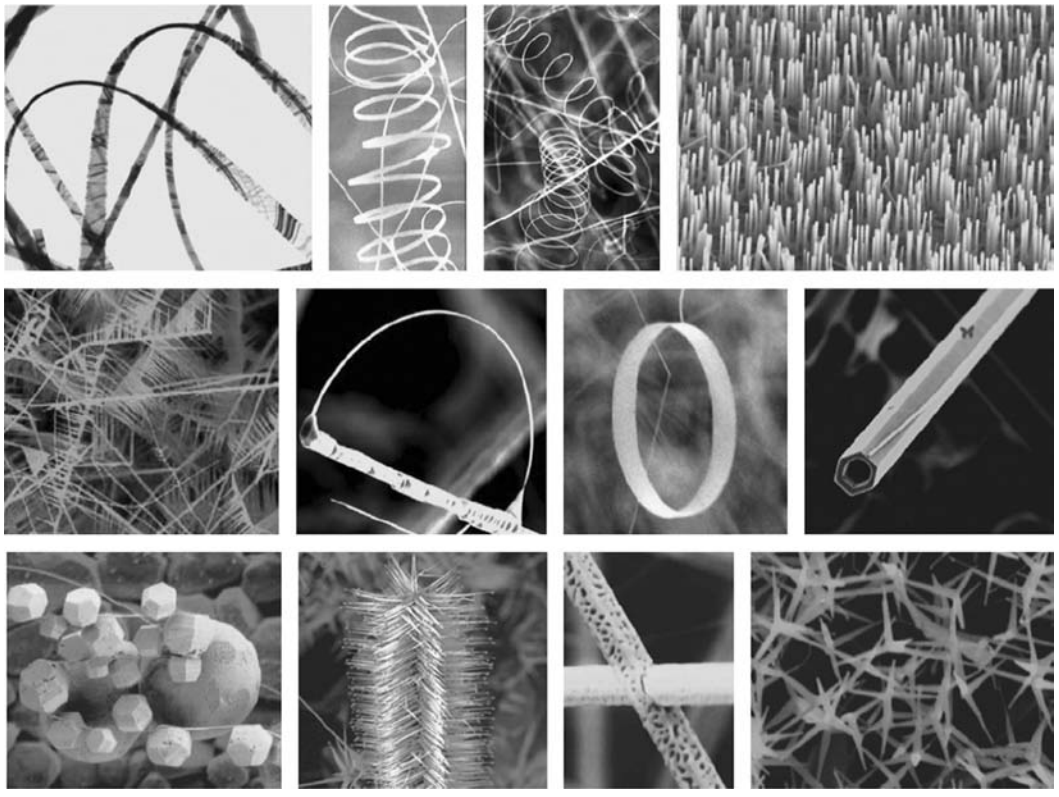

FIGURE 9.7 Representative polar surface-dominated, single-crystalline, zinc oxide 1-D nanostructures. (From Wang, Z.L., *Mater. Today*, 26–33 (2004). With permission.)

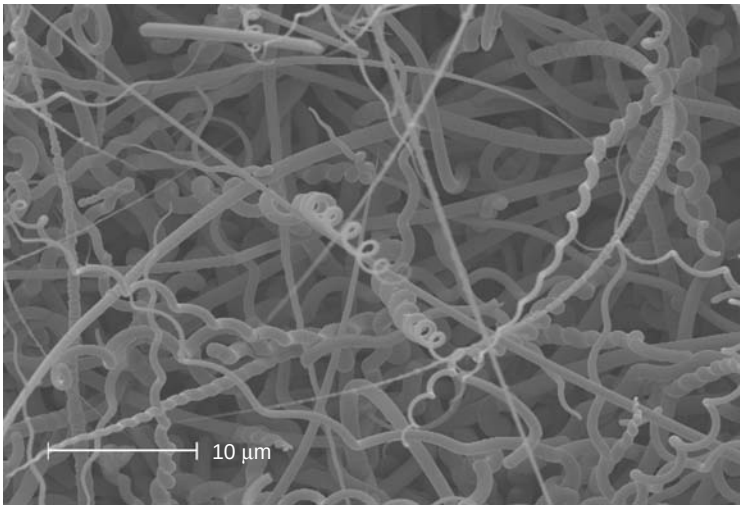

FIGURE 9.8 Scanning electron micrograph of crystalline germanium nanosprings. The formation of nanosprings having inversion symmetry may generate further debate on the formation mechanisms of these and similar structures, in both polar and nonpolar crystalline materials. (From Martin, R.R. et al., submitted. With permission.)

Some synthesis methods permit formation of hierarchal nanostructures, including NWs with segments composed of different materials. For most electronic or photonic device applications, synthesis of single-crystalline components with some degree of control of composition at interfaces is desired. To this end, synthesis of hierarchal nanostructures via metal-catalyzed and catalyst-free VLS and solid–liquid–solid methods has been demonstrated successfully in several semiconducting and functional-oxide material systems. Specifically, modulation of composition and doping in axial and radial directions in a number of material systems has been achieved.

9.3.5 Axial and Radial Modulation of Composition and Doping

Groups at Harvard and Lund University independently reported the synthesis of semiconductor NWs with compositionally modulated segments. The Harvard group employed the LCG method in low vacuum to demonstrate the formation of GaAs/GaP heterojunctions as well as *p–n* junctions within Si and InP NWs [106]. The group at Lund University reported the synthesis of axially modulated III–V NWs via CBE and MOVPE [107,108]. The Lund University group also demonstrated synthesis of NW heterostructure interfaces with near-atomic sharpness.

Using a combination of MCG and LCG, Wu et al. [16] demonstrated the growth of segments of SiGe alloy within Si NWs. The SiGe segments were produced by periodic additional use of laser ablation of a Ge target at elevated furnace. As detailed by Dresselhaus et al. elsewhere in this monograph, the Seebeck coefficient, a measure of the figure of merit for thermoelectric materials, can be raised above bulk values in NWs through careful selection of diameters, compositions, carrier concentrations. Alternatively, engineered nanostructures, which combine some degree of carrier confinement, phonon scattering, and high electrical conductivity via such superlattices in nanostructures, may yet offer new routes for advanced high-performance thermoelectrics [109,110]. Advances in the science and technology of such systems would support further miniaturization of electronic devices through improved thermal management.

The formation of metal–semiconductor heterostructures within single-crystalline NWs can add to the array of device capabilities. Wu et al. [111] reported the synthesis of single-crystalline metal–semiconductor heterostructure NWs composed of segments of Si and nickel silicide. The synthesis relies on the VLS-growth method via metal-catalyzed CVD. Following the Si NW synthesis, NWs placed transverse to the Si NWs acted as a mask for evaporation of Ni. Following the segmented Ni deposition on the surface of the Si NWs, an annealing step was used to form the single-crystalline silicide segments.

Within 1 year of the first reports of axial modulation, Lauhon et al. [112] reported the synthesis of radially modulated semiconductor NWs. Such nanostructures are synthesized by adjustment of process conditions to strongly favor either selective decomposition on the metal alloy droplet or thermal decomposition and noncatalyzed deposition. In this experiment, following the synthesis of NW cores, the conditions were altered to favor noncatalyzed deposition. As reported in [112], this usually involves raising the process temperature and lowering the substrate temperature by adjusting its position in the furnace. In addition, deposited amorphous shell layers were also recrystallized with subsequent heating, producing high-quality epitaxial interfaces. Lauhon et al. [112] reported the synthesis of core–shell structures consisting of intrinsic (i) Si/p-type doped Si and of Si/Ge. They also extended the methods to produce core-multishell structures composed of i-Si/SiO_x/p-Si, of i-Ge/SiO_x/p-Ge and of Si/Ge/Si. As shown in Figures 9.9 and 9.10, the synthesis of radially modulated structures composed of p-type Si core with successive shell layers of i-Ge, SiO_x and p-Ge was used to demonstrate coaxially gated NW transistors. Other researchers have demonstrated field-effect devices in other coaxial nanostructures, including the use of Ga_2O_3 as a gate oxide shell material on GaP NW cores [113].

Following the initial demonstration of coaxial semiconductor NW heterostructures, syntheses of a number of other radially modulated semiconductor and oxide heterostructures have been demonstrated, including preparations involving GaN, GaP [114,115], and CNT sheaths on InP cores

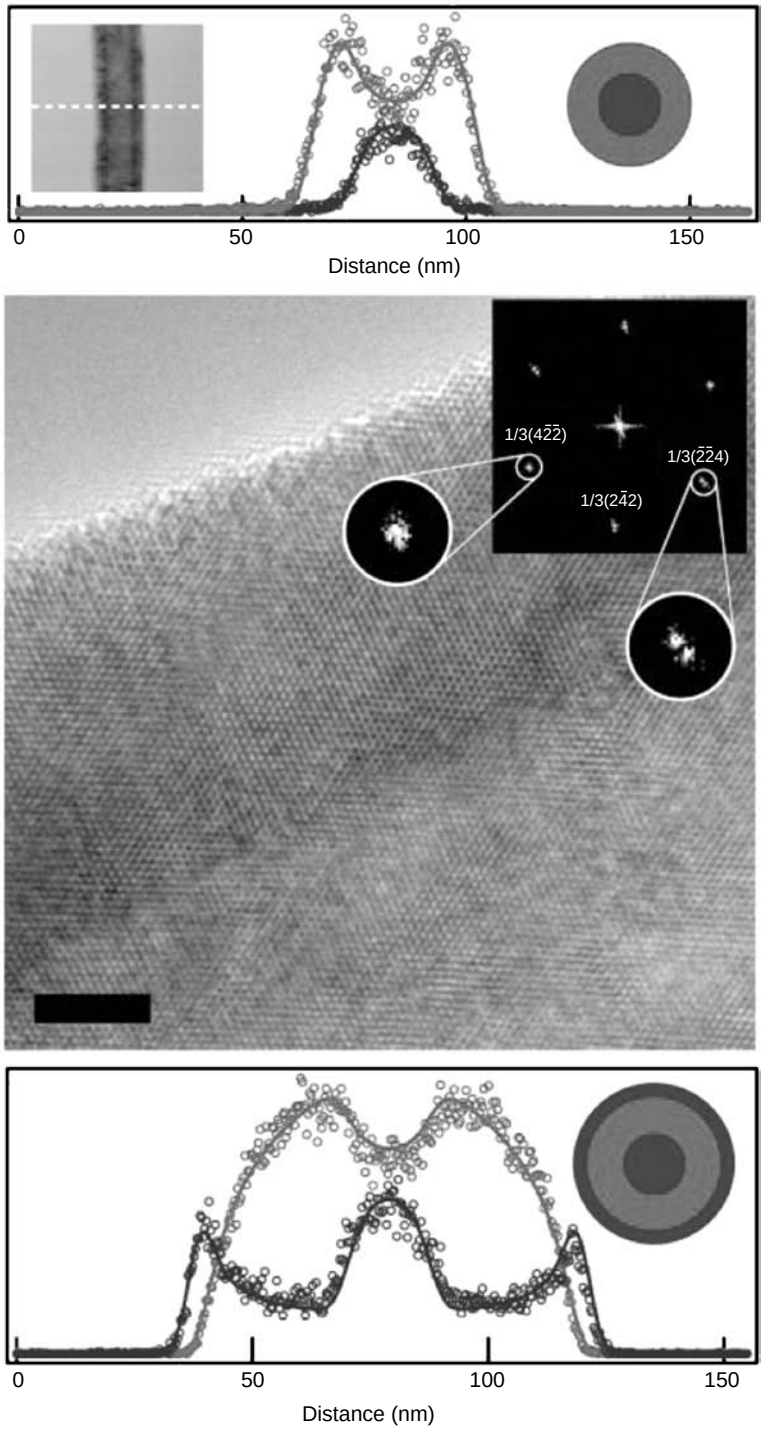

FIGURE 9.9 Radially modulated Si–Ge and Si–Ge–Si core–shell and core–multishell NWs. Upper panel: elemental mapping of the cross-section, revealing a 21-nm-diameter Si core, a 10-nm-thick Ge shell and an interface of ~1 nm. Below this is shown a high-resolution TEM image of a representative NW from the same synthesis; the scale bar, 5 nm. The inset shows a 2-D Fourier transform of the real-space image showing the [111] zone axis. Bottom panel: cross-sectional elemental mapping of a double shell structure. (From Lauhon, L.J. et al., *Nature*, **420**, 57 (2002). With permission.)

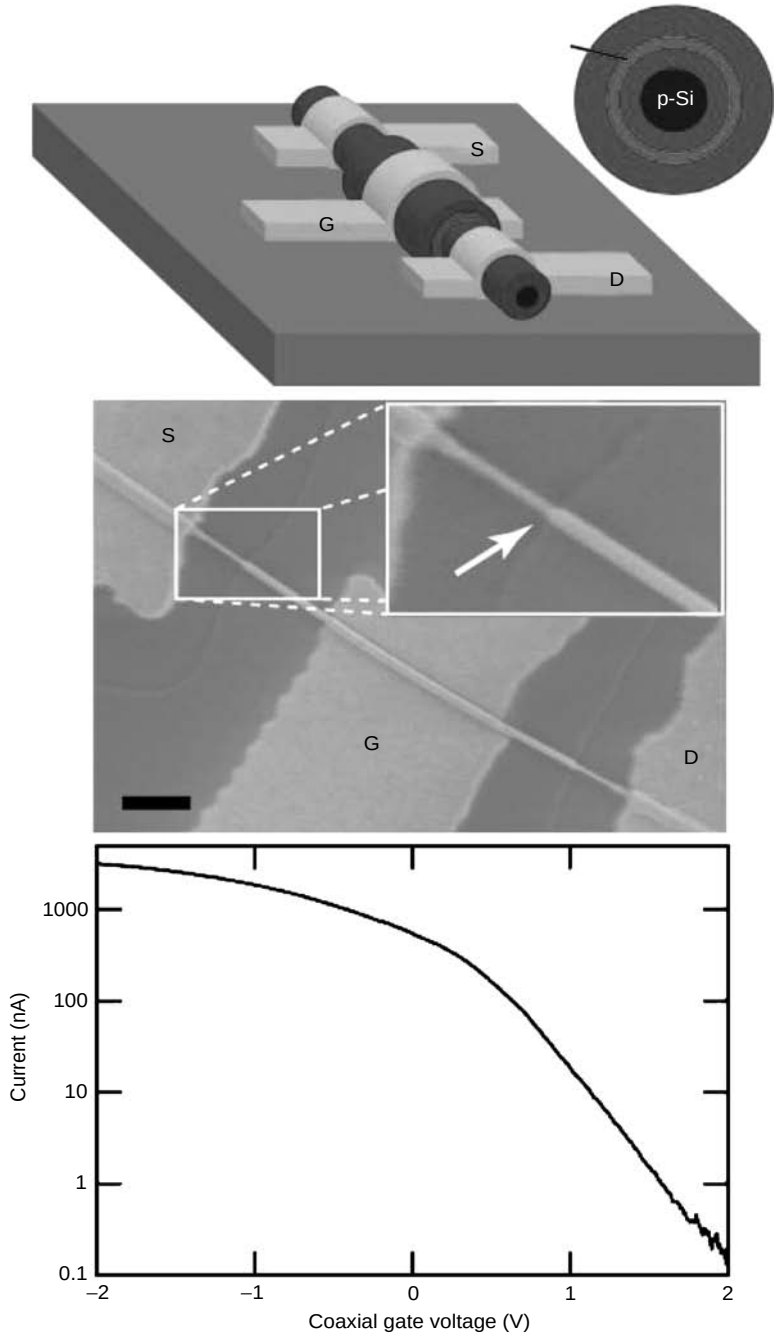

FIGURE 9.10 Coaxially gated NW transistors. At the top is the device schematic showing the transistor structure. The inset shows the cross-section of the as-grown NW, starting with a p-doped Si core with subsequent layers of i-Ge (10 nm), SiO_x (4 nm), and p-Ge (5 nm). The source (S) and drain (D) electrodes are contacted to the inner i-Ge core, while the gate electrode (G) is in contact with the outer p-Ge shell, and electrically isolated from the core by the SiO_x layer. Scanning electron micrograph (SEM) of a coaxial transistor. Scale bar, 500 nm. Gate response of the coaxial transistor at $V_{SD} = 0.1$ V, showing a maximum transconductance of 1500 nA V21. Charge transfer from the p-Si core to the i-Ge shell produces a highly conductive and gateable channel. (From Lauhon, L.J. et al., *Nature*, **420**, 57 (2002). With permission.)

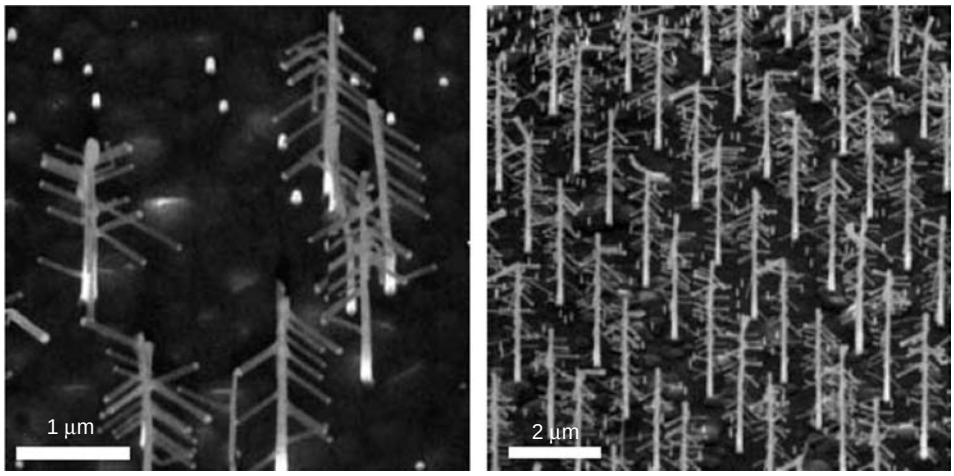

FIGURE 9.11 Branched and hyper-branched NWs composed of III–V NWs produced by sequential seeding of nanostructures with catalyst particles. Such nanostructures may find a number of applications, including the guiding of neuron growth. (From Dick, K.A. et al., *Nat. Mater*., **3**, 380–384 (2004). With permission.)

[116]. One particularly important area of development has been efforts by the group of Chongwu Zhou at the University of Southern California in integrating functional oxides, including perovskites, and superconducting oxides, as epitaxial shells on binary-oxide (MgO and ZnO) NW cores. Han et al. [117] reported synthesis and characterization of such core–shell NWs with shells of FE piezoelectric single-crystalline lead zirconate titanate (PZT), and alternatively, superconducting YBCO, the colossal magnetoresistive material $La_{0.67}Ca_{0.33}MnO_3$ (LCMO) and of maghemite (Fe_3O_4). The authors also performed electronic transport characterizations of LCMO shells of various thicknesses, and demonstrated the persistence of metal–insulator transition and magnetoresistance, down to the nanoscale.

A number of other hierarchal 1-D nanostructures have been produced. For example, Zhang et al. [118] reported the synthesis of SiC/SiO_x core–shell nano-helices [118], and Li et al. [79] reported on the synthesis of Mg_2Zn_{11}-MnO belt-like core–shell nano-cables via CVD. Li et al. [119] reported on Zn/ZnS nano-cabled coaxial structures. We also note that chemical solution methods have also been employed to produce core–shell nanorods. Manna et al. [120] and Mokari and Banin [121] reported the synthesis of core–shell CdSe/CdS/ZnS and CdSe/ZnS nanorods respectively, demonstrating increased quantum efficiencies in the photoluminescence associated with the passivation of the nanorod core surfaces.

Shape anisotropy and hierarchal complexity can enhance the array of interesting and technologically exciting optical properties of nanostructures. For example, the photoluminescence characteristics of GaP semiconducting NWs are observed to strong optical polarization parallel to the axis of the NWsnanowires as well as strong polarization sensitivity to the photoconductive and absorption response [122,123]. Significantly, NWs can be used as optical-resonance cavities. As reported by Yang and coworkers [124], ZnO and GaN NWs can be made to produce lasing emission despite the cross-section of the NW cavity being well below the wavelength of light. The availability of core–shell architecture (e.g., GaN/Al GaN) with the shell material having a larger band gap than the core provides simultaneous confinement of the exciton and photon, providing the necessary wave-guiding function to the nanostructure. Nanowire-based lasers are key components in the development of highly adaptable and flexible nanostrucured solutions for the formation of optical networks and other device components [125].

Dick et al. [185] and others have used secondary seeding of Au nanoclusters on III–V NWs in order to produce branched and hyperbranched structures as shown in Figure 9.11. The authors

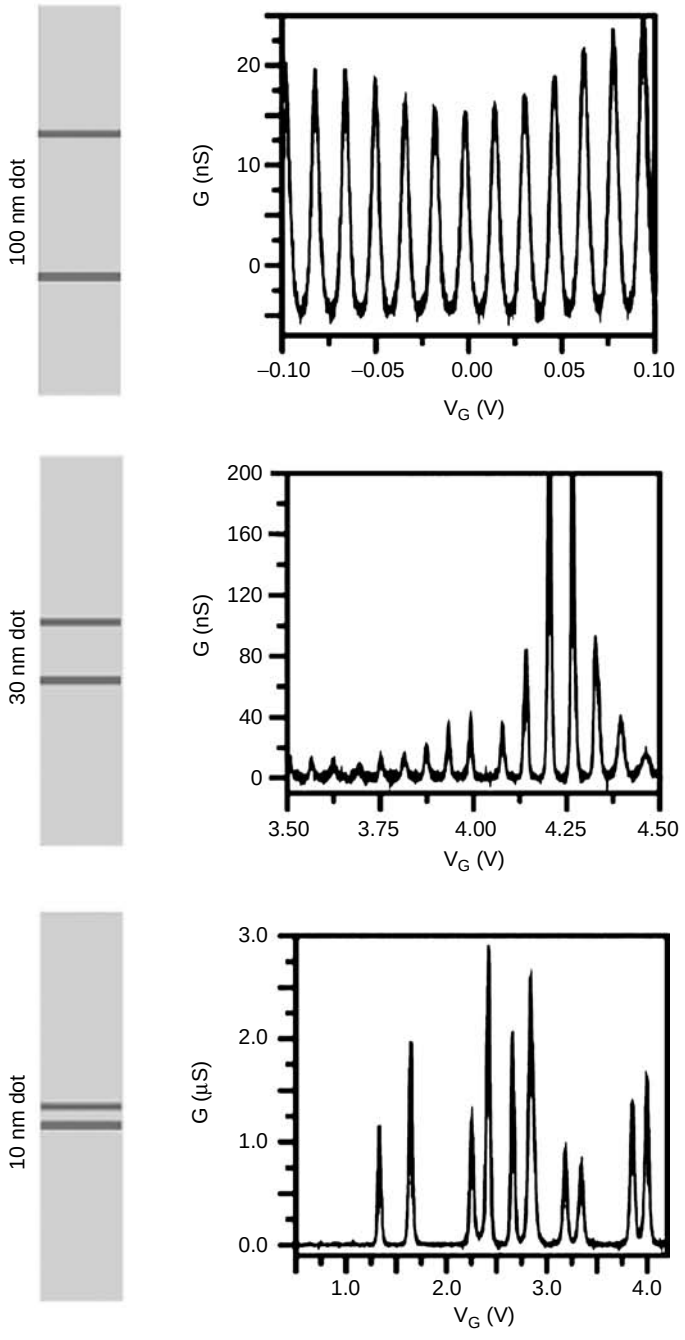

FIGURE 9.12 Effect if reduced quantum dot length. Top: gate characteristics of a single electron transistor with a 100 nm long dot. The oscillations are perfectly periodic and are visible up to 12 K. Middle: when the dot length is 30 nm, the energy level spacing at the Fermi energy is comparable to the charging energy and the Coulomb oscillations are no longer completely periodic. Bottom: a 10 nm dot results in a device depleted of electrons at zero gate voltage. By increasing the electrostatic potential electrons are added one by one. For some electron configurations the addition energy is larger, corresponding to filled electron shells. All data in this figure were recorded at 4.2 K. (From Bjork, M.T. et al., *Nano Lett.*, **4**, 1621–1625 (2002). With permission.)

demonstrated that the diameter, length, number, and chemical composition of each branch can be controlled. Such three-dimensional networked structures have the potential for a diverse number of applications, including the guiding of neuron growth.

9.4 SELECTED PROPERTIES AND APPLICATIONS

9.4.1 MECHANICAL AND THERMAL PROPERTIES AND PHONON TRANSPORT

It has long been known that the mechanical properties of materials are not scale-invariant. For example, for materials that undergo plastic deformation, the so-called Hall [127] and Petch [128] behavior — the increase in the hardness and yield strength of a polycrystalline material with reduction in grain size — involves the relative increase in the area of grain boundaries and the associated piling up of dislocations. The reduction in grain size leads to more impediments to dislocation motion and results in a scale-dependent toughness, though there exists a finite nanoscale size for which the toughness reaches a maximum. With respect to ceramic nanomaterials, relatively little has been reported on the scaling of mechanical properties (stiffness, modulus, toughness, hardness) in the semiconducting and oxide NW or nanobelt materials. Moreover, the synthesis of essentially defect-free 1-D *single-crystalline* nanostructured materials has created opportunities for investigating the theoretical strength of materials in the absence of defects. Lieber and coworkers [129] have measured the elasticity, strength, and toughness of individual SiC nanorods in fixed-free configurations via atomic force microscopy (AFM). The authors reported values in good agreement with theoretically predicted modulus for [110]-oriented SiC. Wang and coworkers [130,131] have developed a method of evaluating Young's modulus in individual NTs, NWs, nanobelts and other nanostructures. The authors relate electric-field-induced mechanical resonances in these nanostructures produced by electron beam in a TEM to values of elastic moduli. Despite this and other progress, a systematic experimental study of the scaling of modulus and other mechanical properties of single-crystalline semiconducting or oxide 1-D nanostructures has not been reported to date.

Thermal conduction via phonons is expected to be significantly reduced in narrow NWs. When the dimensions of a NW approach the mean free path of phonons, the thermal conductivity is reduced relative to bulk values by scattering of phonons by surfaces and interfaces. The miniaturization of electronic and photonic devices, e.g., the higher number density of transistors, is accompanied by new challenges in effective thermal management. A figure of merit for thermoelectric materials, however, involves the unusual combination of poor thermal conductivity with high electrical conductivity. Yang and his group at Berkeley have demonstrated that axial periodicity in Si/SiGe axial superlattice NWs may be highly effective in tuning NW thermal conductivities for thermoelectric applications; they reported the reduction in the thermoconductivity of Si/SiGe superlattice NWs by five times, compared with elemental undoped Si NWs of the same diameter [109,110].

Raman scattering is one of the most powerful experimental tools for characterizing lattice dynamics and corresponding thermodynamic properties in solids [132]. A number of investigations have been performed to characterize the effects of finite size and wire-like geometry on the confinement of phonons. Theoretical predictions indicate that for Si NWs of diameters $<\sim$20 nm, phonon dispersions become altered and group velocities are lowered relative to bulk values [133,134]. Reduction in NW diameter is accompanied by a downshifting and asymmetric broadening of the Raman line shape, and has been attributed to the confinement of optical phonon(s). In perfect bulk single crystals with no loss of translational symmetry, first-order Raman scattering is restricted to $q = 0$ phonons in accordance with momentum selection rules. The reduction of size, however, leads to the relaxation of these selection rules and necessitates an inclusion of a larger fraction of the dispersion curves away from the Γ point. A model for including and averaging $q \rightarrow 0$

phonons was developed and applied by Richter et al. [135] and by Herman and coworkers [136]. This Gaussian-correlation model has been used to describe the sampling of the phonon dispersion, and is widely used to model phonon confinement in nanostructures, including NWs. Enhancements of the model are included to incorporate known-size dispersion and the effects of strain via a Grüneisen parameter [137]. In addition, the effects of lattice strain at and near the NW surface defects, and coupling of free carriers to longitudinal optical phonons in degenerately doped semiconductors may also affect the Raman line shapes and zone-center phonon energies. In all cases reported to date, the measurements have been carried out on ensembles of NWs with varying degrees of diameter dispersion. One of the most systematic studies of the effects of finite size on Raman spectra in NWs was recently presented by Eklund and coworkers [138]. Though a number of papers have been published on Raman scattering from Si and other semiconducting and oxide NWs, a recent theoretical study of Si NWs [139] predicts the presence of Raman-active low-frequency breathing modes. This prediction and an experimental confirmation of these modes may be helpful in providing another means of characterizing the diameters of NWs. In future, as the use of hierarchal nanostructures becomes more prevalent in nanoelectronics and nanophotonics, Raman scattering will continue to play a unique role in the evaluation of 1-D nanostructure materials and devices, including, for example, crystal structure and quality, interfacial strain, thermal management, and strongly correlated electron behavior.

9.4.2 Electronic Properties of Nanowires

Since the invention of modulation doping and the higher electron mobility transistors by Stormer et al. [140], precise control of the composition in semiconductors remains a critical component to 2-D electronic and photonic devices. In a seminal 1980 publication, Sasaki [141] pointed out that the restriction of electronic carriers to 1-D from 2-D or 3-D would result in significantly reduced carrier-scattering rates, owing to the reduction in the possible *k*-space points accessible to carriers. In general, electronic-carrier mobility in real systems can be affected by the scattering of carriers in a number of ways: scattering by other carriers, by surfaces, by interfacial roughness, by acoustic phonons, optical phonons, impurities, and by plasmons. Significant theoretical and experimental work involving electronic transport in CNTs has helped in distinguishing ballistic and diffusive modes of transport. However, for free-standing semiconductor NWs, experimental and theoretical consensus of carrier-scattering mechanisms that are most significant in single- and multicomponent coaxial semiconductor NWs is less clear. In some cases, carrier mobilities in Si NW-field effect transistors and transconductance values have been reported to exceed those associated with conventional Si planar technology devices [142].

Even if the mobility of carriers in semiconductor NWs in a given device is lower than that in the corrsponding bulk material, there are a number of other possible advantages to 1-D transistor devices over their 2-D counterparts. With respect to electronic properties, NWs represent an important link between bulk and molecular materials. The electronic properties of many bulk semiconductors, including oxide semiconductors, are well known, and the electronic-band structures have, in many cases, been modeled in great detail. Systematic control of NW diameter enables systematic investigation of the effects of dimensionality on electronic transport. In general, the diameter below which electronic transport is significantly altered is related to the degree of confinement of carriers and excitons, the Fermi wavelength and Coulomb interactions, although NWs with larger diameters still possess significant surface-to-volume ratios that can affect electronic transport via surface scattering. Semiconductor NWs, like CNTs, are currently being investigated for elements in nanoscale spintronic devices by introducing dilute concentrations of magnetic dopants. Several groups have reported successful doping of semiconductor NWs with manganese [143–146], using different methods. There are numerous reports on the field emission properties of transition metal oxide nanowires and semiconductor nanocones.

There have been a number of simulations reported of the electronic transport and properties of semiconductor NWs. The strategies can be classified into effective mass and $k \cdot p$ methods [147–150], tight-binding theory [151–153], and pseudopotential approaches [154–157]. In the past, the sizes of unit cells required to describe NWs, using first-principles density functional theoretical (DFT) methods, were too computationally expensive to pursue; this has changed of late. Musin et al. [158] have contributed a (DFT) study of the structural and electronic properties of [111]-oriented Si-Ge core–shell interface in very small-diameter (1 to 2 nm) NWs. Significantly, the authors found positive and negative deviations from Vegard's law for compressively strained Ge and tensile-strained Si cores respectively. They also found that the direct-to-indirect transition for the fundamental band gap is found in Ge-core/Si-shell NWs, while Si-core/Ge-shell NWs preserve a direct energy gap almost over the whole compositional range. We note an earlier study by Zhao et al. [159] in which the authors reported density-functional theoretical simulations of electronic-band structure and optical properties of Si NWs, predicting that NWs having a principal axis along $\langle 110 \rangle$ possess a direct gap at the Γ point for wires modeled up to 4.2 nm in diameter. These findings hold significant promise for the potential application of such Group IV single component and coaxial NW heterostructures for a broader range of photonic applications.

The formation of addressable 0-D semiconductor structures is important for fundamental studies of electronic transport phenomenon, and for future applications in single-electron transistors, quantum computing, and metrology. Axial modulation of the composition of NWs may be used to produce precisely located 0-D and 1-D segments within NWs (Figure 9.12) as shown by Samuelson and coworkers [108,160,161]. The authors reported the fabrication of single-electron transistors and resonant-tunneling diodes by producing heterostructural interfaces separated by as few as several monolayers or as many as large as hundreds of nanometers. In addition, the authors have recently used these so-called 1-D/0-D/1-D structures to fabricate nanowire-based, single-electron memory devices [162]. Superlattices in NWs based on these structures may enable extension of the quantum cascade laser as pioneered by Capasso [163]. Addressability of individual NWs for electronic and optical devices is an important consideration for practical applications: among the developments in this area, Zhong et al. [164] reported on the use of NW-crossbar arrays as address decoders.

Electronic transport in semiconductor-NW devices has been shown to be a highly sensitive means of selective binding and detection of molecules on NW surfaces functionalized with receptors. Nanowire-based detection of a number of analytes, including the prostate-specific antigen (pSA) [165], label-free [166], single virus detection [167] has been demonstrated. NW arrays with selectively functionalized NW surfaces represent one of the frontiers in high-sensitivity detection of a broad range of chemical and biological molecules and other species. An overview of this work has been presented in a recent review [168].

Among the most significant recent achievements pertaining to electronic transport are reports of coherent transport in molecular scale semiconductor NWs [169] and the report of formation of a 1-D hole gas in a Ge/Si NW heterostructure [170]. The authors reported room-temperature ballistic hole transport in semiconductor NWs with electrically transparent contacts, opening important further possibilities for new fundamental studies in low-dimensional, strongly correlated carrier gases and high-speed, high-performance nanoelectronic devices based on semiconductor NWs [171]. Recently, proximal superconductivity was reported in semiconductor NWs, in which the electronic transport characteristics of InAs NWs with closely spaced aluminum electrodes were measured at temperatures below the superconducting transition temperature of Al. The NW-electrode interfaces act as mesoscopic Josephson junctions with electrically tunable coupling [172].

9.4.3 Optical Properties of Nanowires

In NWs, like their 0-D nanostructure and 2-D ultrathin film counterparts, confinement of electronic carriers leads to altered electronic-band structures that are manifested as changes in band-to-band transition emission and absorption energies, and changes in other optical properties according to the

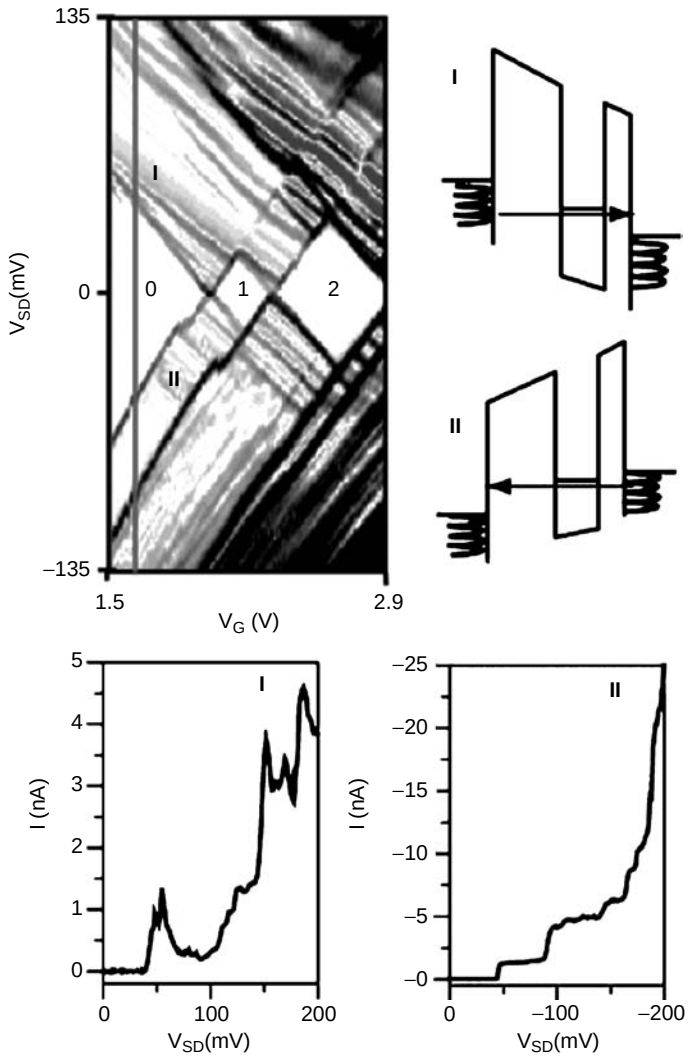

FIGURE 9.13 Resonant tunneling and Coulomb blockade. Upper left: differential conductance as a function of bias and gate voltage for zero, one, and two electrons on the dot for large bias voltages at 300 mK. The vertical line indicates the (italic: I–V) curves shown in (lower left panel) and (lower right panel). Lower left: for positive bias voltage (insert I) tunneling occurs to the dot via the thicker barrier and electrons then escape quickly to the collector. Hence, charging effects are weak. Resonances in the transport characteristics (dark diagonal lines) appear when emitter states are aligned with discrete states in the dot. Lower right: for negative bias voltages (insert II) electrons tunnel quickly to the dot through the thin barrier, whereas the tunneling rate out of the dot is lower, resulting in charging effects, i.e. a Coulomb staircase. (From Bjork, M.T. et al., *Nano Lett.*, **4**, 1621–1624 (2002). With permission.)

degree of confinement. In order to provide a basic description of the effect of the confinement of electronic carriers to within a NW, the electronic wave functions and bound-state energies are obtained by solving the Schrödinger equation under the effective mass model and with the assumption that the NW has a circular cross-section. The ground-state solution to the particle-in-a-cylinder [173] is given by the wave function

$$\Psi(r_{e,h}, z_{e,h}) = N_R N_L \cdot J_0\left(\alpha_{01}\frac{r_{e,h}}{R}\right)\sin\left(\frac{\pi z_{e,h}}{L}\right)$$

where $J_0(\alpha_{01}\cdot r/R)$ is the zero-order Bessel function, α_{01} the first zero of the zero-order Bessel function, L the length of the cylinder, and

$$N_R = \left(2\pi\int_0^R rJ_0^2\left(\alpha\frac{r_{e,h}}{R}\right)dr\right)^{-1/2}$$

and $N_L = (2/L)^{1/2}$ are normalization factors for the radial and axial portions of the wave function. The confinement energy increase in the band gap is then given by

$$\Delta E_{QC} = \frac{h^2}{2m^*}\left[\left(\frac{\alpha_{01}}{R}\right)^2 + \left(\frac{\pi}{L}\right)^2\right]$$

where m^* is the reduced effective excitonic mass, $m^* = m_e m_h/(m_e+m_h)$, and Q is the Planck's constant.

In cases involving electronic excitations (e.g., those involving optical transitions), an additional contribution to the energy from the excitonic Coulomb interaction must also be considered. This is typically a small correction relative to the confinement energy, except for small (~10 nm) diameters. The contribution for QDs is exactly solvable, and results in the additional term $\sim 1.8e^2/\varepsilon R$ [174,175]. However, an analytical solution for the cylindrical geometry is not possible. Gudiksen [176] has compared the results of a numerical evaluation of the required matrix element to experimental data of size-dependent excitonic photoluminescence from III–V NWs. Wang and Gudiksen [122] also reported that the shape anisotropy of NWs produces strong effects in the optical properties, namely that the luminescence emission is strongly polarized, and that the photoconductivity of NW-based photodetectors is highly polarization sensitive. Though these features are explained on the basis of classical electromagnetic theory for an anisotripic dielectric material, these findings were the first to suggest possibilities for single-photon polarized emission and detection based on NW arrays.

One of the most exciting developments involving the optical properties of NWs is the demonstration of room-temperature lasing emission in the ultraviolet from individual NWs. As reported by Yang and coworkers, well-faceted ZnO and GaN [124] NWs produced using VLS growth methods and having diameters from 100 to 500 nm support predominantly axial Fabry–Perot waveguide modes, which are separated by $\Delta\lambda = \lambda^2/[2Ln(\lambda)]$, where L is the cavity length and $n(\lambda)$ the group index of refraction. Structures with smaller diameters are prevented from lasing due to diffraction, and photoluminescence emission is lost in the form of surrounding radiation. Lieber and coworkers [177] have reported on lasing in CdS NW optical cavities. The flexibility of the hierarchal structure of NWs has also been applied to NW lasers.Using the core–shell $GaN/Al_{0.75}Ga_{0.25}N$ configuration, Yang and coworkers [178] were able to provide simultaneous exciton and photon confinement in NW cores having diameters as small as 5 nm — much smaller than the normal minimum to avoid the diffraction effects that prevent lasing. The Berkeley group has extended these concepts to a family of NW photonic components, and taken advantage of the ability of these NWs to sustain significant deformation without fracture in order to develop NW-based optical networks and devices [125]. In fact, the large nonlinear optical response of ZnO NWs, as reported by the Yang group [179], may enable these to be used in optical frequency conversion for nanoscale optical circuitry.

Semiconductor nanostructures with wide band gaps (e.g., TiO_x) have emerged as important components in a new class of photovoltaic devices. Highly conductive wide band gap transition metal oxide nanostructures have been used in dye-sensitized solar cells to provide a conductive path for the collection of photoexcited carriers. As shown recently by Law et al. [180], and Baxter and Aydil [181], dye-sensitized solar cells based on aligned ZnO NWs offer features of a large specific surface area, connectivity for carriers, and the desired optical response.

9.5 CONCLUDING REMARKS

Presently, significant new results involving the development of novel 1-D semiconductor and oxide nanostructure materials and devices, experimental characterizations, and theoretical predictions and simulations are being reported every few weeks. The wider dissemination and use of methods for controllably producing materials of selected composition and hierarchal topologies in 1-D nanostructured form as introduced here undoubtedly will enable the advancement of material technologies, and facilitate wider adoption of 1-D-based semiconductor and oxide NW technologies in commercial, consumer, and defense sectors. Significant challenges involving the controlled growth, processing, and assembly of 1-D nanostructures remain to be addressed before these materials displace the prevalence of top-down fabricated devices. However, this situation may change rather soon: for example, the recent demonstration of monolithic integration of III–V NWs with standard Si technology [182,183] represents a significant achievement in advancing the next generation of optoelectronics devices and technologies. Nevertheless, issues regarding biocompatibility of these nanomaterials, unknown environmental and health hazards pertaining to their production, handling, use and disposal, and intellectual property considerations have not been addressed in a systematic way. These and other challenges and opportunities for applying controlled growth, the flexibility of working with nontraditional substrates and platforms, and advantages in the electronic, thermal, and optical response and sensing capability of many 1-D nanostructured materials over their bulk counterparts will continue to attract researchers and technologists across many disciplines, as well as investors from the public and private sectors worldwide. It seems increasingly likely that the prospects for NWs and related nanostructures to impact the quality of our everyday lives will continue its steady rise.

ACKNOWLEDGMENTS

I am grateful to the students in my group for their dedication and hard work, and to my colleagues Bahram Nabet and Yury Gogotsi of Drexel, and Jon Lai and Brian Lim of Atomate Corporation for supportive and stimulating discussions. I would also like to acknowledge the U.S. Army Research Office under Young Investigator Award (W911NF-04-100308), the NSF under DMR-0216343, and Drexel University for support during the preparation of this manuscript.

REFERENCES

1. A.N. Goldstein, C.M. Echer, and A.P. Alivisatos, Melting in semiconductor nanocrystals, *Science*, **256**, 1425–1427 (1992).
2. S.H. Tolbert, A.B. Herhold, L.E. Brus, and A.P. Alivisatos, Pressure-induced structural transformations in Si nanocrystals: surface and shape effects, *Phys. Rev. Lett*., **76**, 4384–4387 (1996).
3. C.-C. Chen, A.B. Herhold, C.S. Johnson, and A.P. Alivisatos, Size dependence of structural metastability in semiconductor nanocrystals, *Science*, **276**, 398–401 (1997).
4. P.L. McEuen, Nanotechnology — carbon-based electronics, *Nature*, **393**, 15 (1998).
5. C.B. Murray, D.J. Norris, and M.G. Bawendi, Synthesis and characterization of nearly monodisperse CdE (E=S, Se, Te) semiconductor nanocrystallites, *J. Am. Chem. Soc*., **115**, 8706–8715 (1993).
6. Ivan Amato, 10 Emerging Technologies that Will Change Your World, *MIT Technology Review*, **107**, 38–40 (2004).
7. C.N.R. Rao, F.L. Deepak, G. Gundiah, and A. Govindaraj, Inorganic nanowires, *Prog. Solid State Chem*., **31**, 5–147 (2003).
8. Y. Xia, P. Yang, Y. Sun, Y. Wu, B. Mayers, B. Gates, Y. Yin, F. Kim, and H. Yan, One-dimensional nanostructures: synthesis, characterization, and applications, *Adv. Mater*., **15**, 353–389 (2003).
9. R.S. Wagner and W.C. Ellis, Vapor liquid solid mechanism of single-crystal growth, *App. Phys. Lett*., **4**, 89 (1964).

10. K. Hiruma, T. Katsuyama, K. Ogawa, M. Koguchi, H. Kakibayashi, and G.P. Morgan, Quantum size microcrystals grown using organometallic vapor phase epitaxy, *Appl. Phys. Lett*., **59**, 431 (1991).
11. M. Yazawa, M. Koguchi, A. Muto, M. Ozawa, and K. Hiruma, Effect of one monolayer of surface gold atoms on the epitaxial growth of InAs nanowhiskers, *Appl. Phys. Lett*., **61**, 2051–2053 (1992).
12. K. Hiruma, M. Yazawa, T. Katsuyama, K. Ogawa, K. Haraguchi, M. Koguchi, and H. Kakibayashi, Growth and optical properties of nanometer-scale GaAs and InAs whiskers, *J. Appl. Phys*., **77**, 447–462 (1995).
13. D.P. Yu, Z.G. Bai, Y. Ding, Q.L. Hang, H.Z. Zhang, J.J. Wang, Y.H. Zou, W. Qian, G.C. Xiong, H.T. Zhou, and S.Q. Feng, Nanoscale silicon wires synthesized using simple physical evaporation, *Appl. Phys. Lett*., **72**, 3458–3460 (1998).
14. A.M. Morales and C.M. Lieber, A laser ablation method for the synthesis of crystalline semiconductor nanowires, *Science*, **279**, 208–211 (1998).
15. M.S. Gudiksen, L.J. Lauhon, J. Wang, D. Smith, and C.M. Lieber, Growth of nanowire superlattice structures for nanoscale photonics and electronics, *Nature*, **415**, 617–620 (2002).
16. Y. Wu, R. Fan, and P. Yang, Block-by-block growth of single-crystalline Si/SiGe superlattice nanowires, *Nano Lett*., **2**, 83–86 (2002).
17. X. Duan and C.M. Lieber, *Adv. Mater*., **12**, 298 (2001).
18. Y. Wu and P. Yang, Direct observation of vapor-liquid-solid nanowire growth, *J. Am. Chem. Soc*., **123**, 3165–3166 (2001).
19. Y. Wu, Y. Cui, L. Huynh, C.J. Barrelet, D.C. Bell, and C.M. Lieber, Controlled growth and structures of molecular-scale silicon nanowires, *Nano Lett*., **4**, 433–436 (2004).
20. K. Hiruma, M. Yazawa, K. Haraguchi, K. Ogawa, T. Katsuyama, M. Koguchi, and H. Kakibayashi, *J. Appl. Phys*., **74**, 3162 (1993).
21. M. Borgstrom, K. Deppert, L. Samuelson, and W. Seifert, *J. Cryst. Growth*, **260**, 18 (2004).
22. B.J. Ohlsson, M.T. Bjork, M.H. Magnusson, K. Deppert, L. Samuelson, and L.R. Wallenberg, *Appl. Phys. Lett*., **79**, 3335 (2001).
23. A.I. Persson, M.W. Larsson, S. Stenstrom, B.J. Ohlsson, L. Samuelson, and L.R. Wallenberg, Solid-phase diffusion mechanism for GaAs nanowire growth, *Nature Mater*., **3**, 677–681 (2004).
24. P.J. Poole, J. Lefebvre, and J. Fraser, Spatially controlled, nanoparticle-free growth of InP nanowires, *Appl. Phys. Lett*., **83**, 2055–2057 (2003).
25. Z.H. Wu, M. Sun, X.Y. Mei, and H.E. Ruda, Growth and photoluminescence characteristics of AlGaAs nanowires, *Appl. Phys. Lett*., **85**, 657–659 (2004).
26. J.Y. Li, Z.Y. Qiao, X.L. Chen, Y.G. Cao, Y.C. Lan, and C.Y. Wang, Morphologies of GaN one-dimensional materials, *Appl. Phys. A (Mater. Sci. Proc.)* **A71**, 587–588 (2000).
27. H. Chen, X.K. Lu, S.Q. Zhou, X.H. Hao, and Z.X. Wang, Fabrication and characteristics of AlN nanowires, *Modern Phys. Lett. B*, **15**, 1455–1458 (2001).
28. H.W. Seo, S.Y. Bae, J. Park, M.-I. Kang, and S. Kim, Nitrogen-doped gallium phosphide nanowires, *Chem. Phys. Lett*., **378**, 420–424 (2003).
29. T.I. Kamins, R.S. Williams, D.P. Basile, T. Hesjedal, and J.S. Harris, Ti-catalyzed Si nanowires by chemical vapor deposition: microscopy and growth mechanisms, *J. Appl. Phys*., **89**, 1008–1016 (2001).
30. B.J. Ohlsson, M.T. Bjork, A.I. Persson, C. Thelander, R.L. Wallenberg, M.H. Magnusson, K. Deppert, and L. Samuelson, Growth and characterization of GaAs and InAs nano-whiskers and InAs/GaAs heterostructures, *Physica E*, **13**, 1126–1130 (2002).
31. K.A. Dick, K. Deppert, T. Mårtensson, B. Mandl, L. Samuelson, and W. Seifert, Failure of the vapor-liquid-solid mechanism in Au-assisted MOVPE growth of InAs nanowires, *Nano Lett*., **5**, 761–674 (2005).
32. K.-K. Lew, L. Pan, E. Dickey, and J.M. Redwing, Vapor-liquid-solid growth of silicon-germanium nanowires, *Adv. Mater*., **15**, 2073–2076 (2003).
33. J.M. Redwing, K.-K. Lew, T.E. Bogard, L. Pan, E.C. Dickey, A.H. Carim, Y. Wang, M.A. Cabassi, and T.S. Mayer, Synthesis and properties of Si and SiGe/Si nanowires, *Proc. SPIE — Int. Soc. Opt. Eng*., **5361**, 52–59 (2004).
34. E.A. Stach, P.J. Pauzauskie, T. Kuykendall, J. Goldenberger, R. He, and P. Yang, Watching GaN nanowires grow, *Nano Lett*., **3**, 867–869 (2003).
35. M.C. Johnson, C.J. Lee, E.D. Bourret-Courchesne, S.L. Konsek, S. Aloni, W.Q. Han, and A. Zettl, Growth and morphology of 0.80 eV photoemitting indium nitride nanowires, *Appl. Phys. Lett*., **85**, 5670–5672 (2004).

36. S.M. Zhou, Y.S. Feng, and L.D. Zhang, A physical evaporation synthetic route to large-scale GaN nanowires and their dielectric properties, *Chem. Phys. Lett*., **369**, 610–614 (2003).
37. H.Y. Peng, N. Wang, X.T. Zhou, Y.F. Zheng, C.S. Lee, and S.T. Lee, Control of growth orientation of GaN nanowires, *Chem. Phys. Lett*., **359**, 241–245 (2002).
38. C. Ye, G. Meng, Y. Wang, Z. Jiang, and L. Zhang, On the growth of CdS nanowires by the evaporation of CdS nanopowders, *J. Phys. Chem. B*, **106**, 10338–10341 (2002).
39. W. Yang, H. Araki, Q. Hu, N. Ishikawa, H. Suzuki, and T. Noda, In situ growth of SiC nanowires on RS-SiC substrate(s), *J. Cryst. Growth*, **264**, 278–283 (2004).
40. Y. Yang and W. Zhang, Preparation and photoluminescence of zinc sulfide nanowires, *Mater. Lett*., **58**, 3836–3838 (2004).
41. J. Motohisa, J. Noborisaka, J. Takeda, M. Inari, and T. Fukui, Catalyst-free selective-area MOVPE of semiconductor nanowires on (111) B oriented substrates, *J. Crystl. Growth*, **272**, 180–185 (2004).
42. Z.W. Pan, Z.R. Dai, and Z.L. Wang, *Science*, **291**, 1947 (2001).
43. L.S. Huang, S.G. Yang, T. Li, B.X. Gu, Y.W. Du, Y.N. Lu, and S.Z. Shi, Preparation of large-scale cupric oxide nanowires by thermal evaporation method, *J. Cryst. Growth*, **260**, 130–135 (2004).
44. G. Gu, B. Zheng, W.Q. Han, S. Roth, and J. Liu, Tungsten oxide nanowires on tungsten substrates, *Nano Lett*., **2**, 849–851 (2002).
45. H.Z. Zhang, Y.C. Kong, Y.Z. Wang, X. Du, Z.G. Bai, J.J. Wang, D.P. Yu, Y. Ding, Q.L. Hang, and S.Q. Feng, Ga_2O_3 nanowires prepared by physical evaporation, *Solid State Commn*., **109**, 677–682 (1999).
46. X.S. Peng, L.D. Zhang, G.W. Meng, X.F. Wang, Y.W. Wang, C.Z. Wang, and G.S. Wu, Photoluminescence and infrared properties of α-Al_2O_3 nanowires and nanobelts, *J. Phys. Chem. B*, **106**, 11163–11167 (2002).
47. Y. Zhang, N. Wang, S. Gao, T. He, S. Miao, J. Liu, J. Zhu, and X. Zhang, A simple method to synthesize Si_3N_4 and SiO_2 nanowires from Si or Si/SiO_2 mixture, *J. Cryst. Growth*, **233**, 803–808 (2001).
48. J.-S. Lee, M.-I. Kang, S. Kim, M.-S. Lee, and Y.-K. Lee, Growth of zinc oxide nanowires by thermal evaporation on vicinal Si(100) substrate, *J. Cryst. Growth*, **249**, 201–207 (2003).
49. Q. Zhao, H.Z. Zhang, B. Xiang, X.H. Luo, X.C. Sun, and D.P. Yu, Fabrication and microstructure analysis of SeO_2 nanowires, *Appl. Phys. A (Mater. Sci. Proc.)*, **A79**, 2033–2036 (2004).
50. S.T. Lee, Y.F. Zhang, N. Wang, Y.H. Tang, I. Bello, C.S. Lee, and Y.W. Chung, Semiconductor nanowires from oxides, *J. Mater. Res*., **14**, 4503–4507 (1999).
51. H. Alouach and G.J. Mankey, Epitaxial growth of copper nanowire arrays grown on H-terminated Si(110) using glancing-angle deposition, *J. Mater. Res*., **19**, 3620–3625 (2004).
52. Y.F. Zhang, Y.H. Tang, N. Want, C.S. Lee, I. Bello, and S.T. Lee, Germanium nanowires sheathed with an oxide layer, *Phys. Rev. B*, **61**, 4518–4521 (2000).
53. W.S. Shi, Y.F. Zheng, N. Wang, C.S. Lee, and S.T. Lee, Oxide-assisted growth and optical characterization of gallium-arsenide nanowires, *Appl. Phys. Lett*., **78**, 3304–3306 (2001).
54. Y.F. Zhang, Y.H. Tang, X.F. Duan, Y. Zhang, C.S. Lee, N. Wang, I. Bello, and S.T. Lee, Yttrium-barium-copper-oxygen nanorods synthesized by laser ablation, *Chem. Phys. Lett.* **323**, 180–184 (2000).
55. X.C. Wu, J.M. Hong, Z.J. Han, and Y.R. Tao, Fabrication and photoluminescence characteristics of single crystalline In_2O_3 nanowires, *Chem. Phys. Lett*., **373**, 28–32 (2003).
56. X.C. Wu, W.H. Song, B. Zhao, Y.P. Sun, and J.J. Du, Preparation and photoluminescence properties of crystalline GeO_2 nanowires, *Chem. Phys. Lett*., **349**, 210–214 (2001).
57. L.D. Zhang, G.W. Meng, and F. Phillipp, Synthesis and characterization of nanowires and nanocables, *Mater. Sci. Eng. A (Struct. Mater.: Prop., Microstruct. Proc.)*, **A286**, 34–38 (2000).
58. T.J. Trentler, K.M. Hickman, S.C. Goel, A.M. Viano, P.C. Gibbons, and W.E. Buhro, Solution-liquid-solid growth of crystalline III–V semiconductors: an analogy to vapor-liquid-solid growth, *Science*, **270**, 1791–1794 (1995).
59. W.E. Buhro, K.M. Hickman, and T.J. Trentler, Turning down the heat on semiconductor growth: solution-chemical synthesis and the solution-liquid-solid mechanism, *Adv. Mater*., **8**, 685–688 (1996).
60. T.J. Trentler, S.C. Goel, K.M. Hickman, A.M. Viano, M.Y. Chiang, A.M. Beatty, P.C. Gibbons, and W.E. Buhro, Solution-liquid-solid growth of indium phosphide fibers from organometallic precursors: elucidation of molecular and nonmolecular components of the pathway, *J. Am. Chem. Soc*. **119**, 2172–2181 (1997).
61. J.D. Holmes, K.P. Johnston, R.C. Doty, and B.A. Korgel, Control of thickness and orientation of solution-grown silicon nanowires, *Science*, **287**, 1471–1473 (2000).

62. X. Peng, L. Manna, W. Yang, J. Wickham, E. Scher, A. Kadavanich, and A.P. Alivisatos, Shape control of CdSe nanocrystals, *Nature*, **404**, 59–61 (2000).
63. G.R. Patzke, F. Krumeich, and R. Nesper, Oxide nanotubes and nanorods — anisotropic modules for a future nanotechnology, *Angew. Chem. Ind. Ed*., **41**, 2446–2461 (2002).
64. J.J. Urban, W.S. Yun, Q. Gu, and H. Park, Synthesis of single-crystalline perovskite nanorods composed of barium titanate and strontium titanate, *J. Am. Chem. Soc*., **124**, 1186–1187 (2002).
65. J.J. Urban, J.E. Spanier, L. Ouyang, W.S. Yun, and H. Park, Single-crystalline barium titanate nanowires, *Adv. Mater*., 423–426 (2002).
66. J.E. Spanier, J.J. Urban, L. Ouyang, W.S. Yun, and H. Park, in *Nanowire Materials*, Vol. 1, Z.L. Wong, Ed., Kluwer, Boston, MA, 2002.
67. S. O'Brien, L. Brus, and C.B. Murray, Synthesis of monodisperse nanoparticles of barium titanate: toward a generalized strategy of oxide nanoparticle synthesis, *J. Am. Chem. Soc*., **123**, 12085–12086 (2001).
68. G. Xu, Z. Ren, P. Du, W. Weng, G. Shen, and G. Han, Polymer-assisted hydrothermal synthesis of single-crystalline tetragonal perovskite $PbZr_{0.52}Ti_{0.48}O_3$ nanowires, *Adv. Mater*., **17**, 907–910 (2005).
69. W.S. Yun, J.J. Urban, Q. Gu, and H. Park, Ferroelectric properties of individual barium titanate nanowires investigated by scanned probe microscopy, *Nano Lett*., **2**, 447–450 (2002).
70. J.E. Spanier, A. Kolpak, I. Grinberg, J. Urban, L. Ouyang, W.S. Yun, A.M. Rappe, and H. Park, Adsorbate-induced stabilization of ferroelectricity in perovskite nanowires, submitted (2005).
71. T. Muller, K.-H. Heinig, and B. Schmidt, Formation of Ge nanowires in oxidized silicon V-grooves by ion beam synthesis, *Nucl. Instr. Methods Phys. Res., B*, **175–177**, 468–473 (2001).
72. S. Seydmohamadi, Z.M. Wang, and G.J. Salamo, Self assembled (In,Ga) as quantum structures on GaAs (411) A, *J. Cryst. Growth*, **269**, 257–261 (2004).
73. C.R. Martin, Nanomaterials: a membrane-based synthetic approach, *Science*, **266**, 1961–1966 (1994).
74. D. Routkevitch, A.A. Tager, J. Haruyama, D. Almawlawi, M. Moskovits, and J.M. Xu, Nonlithographic nano-wire arrays: fabrication, physics, and device applications, *IEEE Trans. Electron Devices*, **43**, 1646–1658 (1996).
75. J.P. O'Sullivan and G.C. Wood, The morphology and mechanism of porous anodic films on aluminum, *Proc. Roy. Soc. Lond. A*., **317**, 511–543 (1970).
76. H. Masuda and K. Fukuda, Ordered metal nanohole arrays made by a two-step replication of honeycomb structures of anodic alumina, *Science*, **268**, 1466–1468 (1995).
77. V.M. Cepak, J.C. Hulteen, G. Che, K.B. Jirage, B.B. Lakshmi, E.R. Fisher, and C.R. Martin, Fabrication and characterization of concentric-tubular composite micro- and nanostructures using the template-synthesis method, *J. Mater. Res*., **13**, 3070–3080 (1998).
78. W. Han, S. Fan, Q. Li, and Y. Hu, Synthesis of gallium nitride nanorods through a carbon nanotube-confined reaction, *Science*, **277**, 1287–1289 (1997).
79. C.P. Lee, X.H. Sun, N.B. Wong, C.S. Lee, S.T. Lee, and B.K. Teo, Ultrafine and uniform silicon nanowires grown with zeolites, *Chem. Phys. Lett*., **365**, 22–26 (2002).
80. S. Shingubara, Fabrication of nanomaterials using porous alumina templates, *J. Nanopart. Res*., **5**, 17–30 (2003).
81. R.L. Fleicher, P.B. Price, and R.M. Walker, *Nuclear Tracks in Solids*, University of California Press, Berkeley, CA (1975).
82. K.-K. Lew, C. Reuther, A.H. Carim, J.M. Redwing, and B.R. Martin, Template-directed vapor-liquid-solid growth of silicon nanowires, *J. Vac. Sci. Technol. B*, **20**, 389–392 (2002).
83. K.-K. Lew and J.M. Redwing, Growth characteristics of silicon nanowires synthesised by vapor-liquid-solid growth in nanoporous alumina templates, *J. Cryst. Growth*, **254**, 14–22 (2003).
84. D. Al-Mawlawi, C.Z. Liu, and M. Moskovits, Nanowires formed in anodic oxide nanotemplates, *J. Mater. Res*., **9**, 1014–1018 (1994).
85. J.D. MacKenzie, Sol-gel research-achievements since 1981 and prospects for the future, *J. Sol-Gel Sci. Technol*., **26**, 23–27 (2003).
86. Z. Miao, D. Xu, J. Ouyang, G. Guo, X. Zhao, and Y. Tang, Electrochemically induced sol-gel preparation of single-crystalline TiO_2 nanowires, *Nano Lett*., **2**, 717–720 (2002).
87. C. Mao, D.J. Solis, B.D. Reiss, S.T. Kottmann, R.Y. Sweeney, A. Hayhurst, G. Gerogiou, B. Iverson, and A.M. Belcher, Virus-based toolkit for the directed synthesis of magnetic and semiconducting nanowires, *Science*, **303**, 213–217 (2004).
88. Z. Tang, N.A. Kotov, and M. Giersig, Spontaneous organization of single CdTe nanoparticles into luminescent nanowires, *Science*, **279**, 237–240 (2002).

89. M.S. Gudiksen and C.M. Lieber, Diameter-selective synthesis of semiconductor nanowires, *J. Am. Chem. Soc*., **122**, 8801–8802 (2000).
90. M.S. Gudiksen, J. Wang, and C.M. Lieber, Synthetic control of the diameter and length of single crystal semiconductor nanowires, *J. Phys. Chem. B*, **105**, 4062–4064 (2001).
91. M. Yin, Y. Gu, I.L. Kuskovsky, T. Andelman, Y. Zhu, G.F. Neumark, and S. O'Brien, Zinc oxide quantum rods, *J. Am. Chem. Soc*., **126**, 6206–6207 (2004).
92. Y. Gu, I.L. Kuskovsky, M. Yin, S. O'Brien, and G.F. Neumark, Quantum confinement in ZnO nanorods, *Appl. Phys. Lett*., **85**, 3833–3835 (2004).
93. L. Manna, E.C. Sher, and A.P. Alivisatos, Synthesis of soluble and processable rod-, arrow-, teardrop- and tetrapod-shaped CdSe nanocrystals, *J. Am. Chem. Soc*., **122**, 12700–12706 (2000).
94. L. Manna, private communication (2005).
95. L. Cao, L. Laim, C. Ni, B. Nabet, and J.E. Spanier, Diamond-hexagonal semiconductor nanocones with controllable apex angle, *J. Am. Chem. Soc.*, in press (2005).
96. L. Cao and J.E. Spanier, submitted (2005).
97. W.L. Hughes and Z.L. Wang, Formation of piezoelectric single-crystal nanorings and nanobows, *J. Am. Ceram. Soc*., **126**, 6703–6709 (2004).
98. C. Ma, Y. Ding, D. Moore, X.D. Wang, and Z.L. Wang, Single-crystal CdSe nanosaws, *J. Am. Ceram. Soc*., **126**, 708–709 (2004).
99. Y. Ding, C. Ma, and Z.L. Wong, Self-catalysis and phase transformation in the formation of CdSe nanosaws, *Adv. Mater*., **16**, 1740–1743 (2004).
100. R. Yang, Y. Ding, and Z.L. Wang, Deformation free single crystal nanohelixes of polar nanowires, *Nano Lett*., **4**, 1309–1312 (2004).
101. Z.L. Wang, X.Y. Kong, Y. Ding, P. Gao, W.L. Hughes, R. Yang, and Y. Zhang, Semiconducting and piezoelectric oxide nanostructures induced by polar surfaces, *Adv. Funct. Mater*., **14**, 943–956 (2004).
102. Z.L. Wang, *Mater. Today*, **7**, 26–33 (2004).
103. Z.L. Wang, Functional oxide nanobelts — materials, properties and potential applications in nanosystems and biotechnology, *Ann. Rev. Phys. Chem*., **55**, 159–196 (2004).
104. G.-C. Yi, C. Wang, and W.I. Park, ZnO nanorods: synthesis, characterization and applications, *Semicond. Sci. Technol*., **20**, 22–34 (2005).
105. R.R. Martin, L. Cao, S. Nonnenmann, and J.E. Spanier, submitted (2005).
106. M.S. Gudiksen, L.J. Lauhon, J. Wang, D.C. Smith, and C.M. Lieber, Growth of nanowire superlattice structures for nanoscale photonics and electronics, *Nature*, **415**, 617–620 (2002).
107. M.T. Bjork, B.J. Ohlsson, T. Sass, A.I. Persson, C. Thelander, M.H. Magnusson, K. Deppert, L. Wallenberg, and L. Samuelson, One-dimensional heterostructures in semiconductor nanowhiskers, *Appl. Phys. Lett*., **80**, 1058–1060 (2002).
108. M.T. Bjork, B.J. Ohlsson, T. Sass, A.I. Persson, C. Thelander, M.H. Magnusson, K. Deppert, L.R. Wallenberg, and L. Samuelson, One-dimensional steeplechase for electrons realized, *Nano Lett*., **2**, 87–89 (2002).
109. D. Li, Y. Wu, P. Kim, L. Shi, P. Yang, and A. Majumdar, Thermal conductivity of individual silicon nanowires, *Appl. Phys. Lett*., **83**, 2934–2936 (2003).
110. D. Li, Y. Wu, R. Fan, P. Yang, and A. Majumdar, Thermal conductivity of Si/SiGe superlattice nanowires, *Appl. Phys. Lett*., **83**, 3186–3188 (2003).
111. Y. Wu, J. Uang, C. Yang, W. Lu, and M.L. Charles, Single-crystal metallic nanowires and metal/semiconductor nanowire heterostructures, *Nature*, **430**, 61–65 (2004).
112. L.J. Lauhon, M.S. Gudiksen, D. Wang, and C.M. Lieber, Epitaxial core-shell and core-multishell nanowire heterostructures, *Nature*, **420**, 57 (2002).
113. B.-K. Jim, J.-J. Kim, J.-O. Lee, K.-J. Kong, H.J. Seo, and C.J. Lee, Top-gated field-effect transistor and rectifying diode operation of core-shell structured GaP nanowire devices, *Phys. Rev. B Condens. Matter Mater. Phys.*, **71**, 153313–1 (2005).
114. F. Qian, Y. Li, S. Gradecak, D. Wang, C.J. Barrelet, and C.M. Lieber, Gallium nitride-based nanowire radial heterostructures for nanophotonics, *Nano Lett*., **4**, 1975–1979 (2004).
115. H.-M. Lin, Y.-L. Chen, J. Yang, Y.-C. Liu, K.-M. Yin, J.-J. Kai, F.-R. Chen, L.-C. Chen, Y.-F. Chen, C.-C. Chen, Synthesis and characterization of core-shell GaP@GaN and GaN@GaP nanowires, *Nano Lett*., **3**, 537–541 (2003).
116. L.W. Yin, Y. Bando, Y.C. Zhu, and M.S. Li, Controlled carbon nanotube sheathing on ultrafine InP nanowires, *Appl. Phys. Lett*., **84**, 5314–5316 (2004).

117. S. Han, C. Li, Z. Liu, D. Zhang, W. Jin, X. Liu, T. Tang, and C. Zhou, Transition metal oxide core-shell nanowires: generic synthesis and transport studies, *Nano Lett*., **4**, 1241–1246 (2004).
118. H.-F. Zhang, C.-M. Wang, and L.-S. Wang, Helical crystalline SiC/SiO_2 core-shell nanowires, *Nano Lett*., **2**, 941–944 (2002).
119. Y.B. Li, Y. Bando, and D. Golberg, Mg_2Zn_{11}-MgO belt-like nanocables, *Chem. Phys. Lett*., **375**, 102–105 (2003).
120. L. Manna, E.C. Scher, L.-S. Li, and A.P. Alivisatos, Epitaxial growth and photochemical annealing of graded CdS/ZnS shells on colloidal CdSe nanorods, *J. Am. Chem. Soc*., **124**, 7136–7145 (2002).
121. T. Mokari and U. Banin, Synthesis and properties of CdSe/ZnS core/shell nanorods, *Chem. Mater*., **15**, 3955–3960 (2003).
122. J. Wang, M.S. Gudiksen, X. Duan, Y. Cui, and C.M. Lieber, Highly polarised photoluminescence and photodetection from single indium phosphide nanowires, *Science*, **293**, 1455–1457 (2001).
123. J. Wang, M. Gudiksen, X.F. Duan, Y. Cui, and C.M. Lieber, Highly polarized photoluminescence and polarization-sensitive photodetectors from single indium phosphide nanowires, *Science*, **293**, 1455 (2001).
124. J.C. Johnson, H.-J. Choi, K.P. Knutsen, R.D. Schaller, P. Yang, and R.J. Saykally, Single gallium nitride nanowire lasers, *Nat. Mater*., **1**, 106–110 (2002).
125. M. Law, D.J. Sirbuly, J.C. Johnson, J. Goldberger, R.J. Saykally, and P. Yang, Nanoribbon waveguides for subwavelength photonics integration, *Science*, **305**, 1269 (2004).
126. J. Wang, E. Polizzi, and M. Lundstrom, paper presented at the *IEEE International Electron Devices Meeting*, Washington DC, 2003.
127. E.O. Hall, *Proc. Phys. Soc. London B*, **64**, 747 (1951).
128. N.J. Petch, *J. Iron Steel Inst*., **174**, 25 (1953).
129. E.W. Wong, P.E. Sheehan, and C.M. Lieber, Nanobeam mechanics: elasticity, strength and toughness of nanorods and nanotubes, *Science*, **277**, 1971–1975 (1997).
130. Z.L. Wang, Z.R. Dai, R.P. Gao, Z.G. Bai, and J.L. Gole, Side-by-side silicon carbide-silica biaxial nanowires: synthesis, structure, and mechanical properties, *Appl. Phys. Lett*., **77**, 3349–3351 (2000).
131. Z.L. Wang, R.P. Gao, Z.W. Pan, and Z.R. Dai, Nano-scale mechanics of nanotubes, nanowires, and nanobelts, *Adv. Eng. Mater*., **3**, 657–661 (2001).
132. I. Herman, *Optical Diagnostics for thin Film Processing*, Elsevier/Academic Press, San Diego, 1996.
133. A. Buldum, S. Ciraci, and C.Y. Fong, Quantum heat transfer through an atomic wire, *J. Phys. Condens. Mater*., **12**, 3349 (2000).
134. K. Schwab, E.A. Henriksen, J.M. Worlock, and M.L. Roukes, Measurement of the quantum of thermal conductance, *Nature*, **404**, 974 (2000).
135. H. Richter, Z.P. Wang, and L. Ley, The one phonon Raman scattering in microcrystalline silicon, *Solid State Commun.* **39**, 625–629 (1981).
136. Z. Sui, P.P. Leong, I.P. Herman, G.S. Higashi, and H. Tempkin, Raman analysis of light-emitting porous silicon, *Appl. Phys. Lett*., **60**, 2086 (1992).
137. J.E. Spanier, R.D. Robinson, F. Zheng, S.W. Chan, and I.P. Herman, Size-dependent properties of CeO2-y nanoparticles as studied by Raman scattering, *Phys. Rev. B*, **64**, 245407/1–8 (2001).
138. K.W. Adu, H.R. Gutierrez, U.J. Kim, G.U. Sumanasekera, and P.C. Eklund, Confined phonons in Si nanowires, *Nano Lett*., **5**, 409–414 (2005).
139. T. Thonhauser and G.D. Mahan, Predicted Raman spectra of Si[111] nanowires, *Phys. Rev. B: Condens. Matter*, **71**, 81307 (2005).
140. H.L. Stormer, K. Baldwin, A.C. Gossard, and W. Wiegmann, Modulation-doped field-effect transistor based on a two dimensional hole gas, *Appl. Phys. Lett*., **44**, 1062 (1984).
141. H. Sasaki, Scattering suppression and high-mobility effect of size-quantized electrons in ultrafine semiconductor wire structures, *Jpn. J. Appl. Phys*., **19**, L735 (1980).
142. Y. Cui, Z. Zhong, D. Wang, W.U. Wang, and C.M. Lieber, High performance silicon nanowire field effect transistors, *Nano Lett*., **3**, 149–152 (2003).
143. F.L. Deepak, P.V. Vanitha, A. Govindaraj, and C.N.R. Rao, Photoluminescene spectra and ferromagnetic properties of GaMnN nanowires, *Chem. Phys. Lett*., **374**, 314 (2003).
144. C. Ronning, P.X. Gao, Y. Ding, and Z.L. Wang, Manganese-doped ZnO nanobelts for spintronics, *Appl. Phys. Lett*., **84**, 783 (2004).
145. D.S. Han, J. Park, K.W. Rhie, S. Kim, and J. Chang, Ferromagnetic Mn-doped GaN nanowires, *Appl. Phys. Lett*., **86** (2005).

146. P.V. Radovanociv, C.J. Barrelet, S. Gradecak, F. Qian, and C.M. Lieber, General synthesis of manganese-doped II-VI and III-V semiconductor nanowires, *Nano Lett.*, **5**, 1407–1411 (2005).
147. G. Bastard, J.A. Brum, R. Ferreria, Eds., *Solid State Physics*, **44**, 1991.
148. C.R. Proetto, Self-consistent electronic structure of a cylindrical quantum wire, *Phys. Rev. B: Condens. Matter*, **45**, 11911 (1992).
149. A. Gold and A. Ghazali, Analytical results for semiconductor quantum-well wire: plasmons, shallow impurity states, and mobility, *Phys. Rev. B: Condens. Matter*, **41**, 7626–7640 (1990).
150. T. Ogawa and T. Takagahara, Optical absorption and Sommerfeld factors of one-dimensional semiconductors: an exact treatment of excitonic effects, *Phys. Rev. B (Condens. Matter)*, **44**, 8138 (1991).
151. Y. Arakawa, T. Yamauchi, and J.N. Schulman, Tight binding analysis of energy band structures in quantum wires, *Phys. Rev. B (Condens. Matter)*, **43**, 4732 (1991).
152. Y.M. Niquet, C. Delerue, G. Allan, and M. Lanoo, Method for tight-binding parametrization: application to silicon nanostructures, *Phys. Rev. B (Condens. Matter)*, **62**, 5109 (2000).
153. M.P. Persson and H.Q. Xu, Electronic structure of nanometer-scale GaAs whiskers, *Appl. Phys. Lett.*, **81**, 1309 (2002).
154. A. Franceschetti and A. Zunger, Comparison between direct pseudopotential and single-band truncated-crystal calculations, *J. Chem. Phys*., **104**, 5572 (1996).
155. A. Franceschetti and A. Zunger, Free-standing versus AlAs-embedded GaAs quantum dots, wires and films: the emergence of a zero-confinement state, *Appl. Phys. Lett*., **68**, 3455 (1996).
156. D.W. Wood and A. Zunger, Successes and failures of the k–p method: a direct assessment for GaAs/AlAs quantum structures, *Phys. Rev. B (Condens. Matter)*, **53**, 7949 (1996).
157. J.-B. Xia and K.W. Cheah, Quantum confinement effect in thin quantum wires, *Phys. Rev. B (Condens. Matter)*, **55**, 15688 (1997).
158. R.N. Musin and X.-Q. Wang, Structural and electronic properties of epitaxial core-shell nanowire heterostructures, *Phys. Rev. B (Condens. Matter Mater. Phys.)*, **71**, 155318/1–4 (2005).
159. X. Zhao, C.M. Wei, L. Yang, and M.Y. Chou, Quantum confinement and electronic properties of silicon nanowires, *Phys. Rev. Lett*., **92**, 236805 (2004).
160. C. Thelander, B.J. Ohlsson, M.T. Bjork, T. Martensson, A.I. Persson, K. Deppert, M.W. Larsson, L.R. Wallenberg, and L. Samuelson, Paper presented at the *IEEE International Symposium on Compound Semiconductors*, San Diego, CA, 25–27 August 2003.
161. C. Thelander T. Martensson, M.T. Bjork, B.J. Ohlsson, M.W. Larsson, L.R. Wallenberg, and L. Samuelson, Single-electron transistors in heterostructure nanowires, *Appl. Phys. Lett*., **83**, 2052–2054 (2003).
162. C. Thelander, H.A. Nilsson, L.E. Jensen, and L. Samuelson, Nanowire single-electron memory, *Nano. Lett*., **5**, 635–638 (2005).
163. F. Capasso, C. Gmachl, D.L. Silvo, and A.Y. Cho, *Phys. Today*, **55**, 34 (2002).
164. Z. Zhong, D. Wang, Y. Cui, M.W. Bockrath, and C.M. Lieber, Nanowire crossbar arrays as address decoders for integrated nanosystems, *Science*, **302**, 1377–1379 (2003).
165. Y. Cui, Q. Wei, H. Park, and C.M. Lieber, Nanowire nanosensors for highly-sensitive, selective and integrated detection of biological and chemical species, *Science*, **293**, 1289 (2001).
166. W.U. Wang, C. Chen, K. Lin, Y. Fang, and C.M. Lieber, Label-free detection of small molecule-protein interactions by using nanowire nanosensors, *Proc. Natl. Acad. Sci*., **102**, 3208–3212 (2005).
167. F. Patolsky, G. Zheng, O. Hayden, M. Lakadamyali, X. Zhuang, and C.M. Lieber, Electrical detection of single viruses, *Proc. Natl. Acad. Sci*., **101**, 14017–14022 (2004).
168. F. Patolsky and C.M. Lieber, *Mater. Today*, **8**, 20–28 (2005).
169. Z. Zhong, Y. Fang, W. Lu, and C.M. Lieber, Coherent single charge transport in molecular scale silicon nanowires, *Nano Lett*., **5**, 1143–1146 (2005).
170. W. Lu, J. Xiang, B.P. Timko, Y. Wu, and C.M. Lieber, One-dimensional hole gas in germanium silicon nanowire heterostructures, *PNAS*, **102**, 10046–10051 (2005).
171. R.S. Friedman, M.C. McAlpine, D.S. Ricketts, D. Ham, and C.M. Lieber, High speed integrated nanowire circuits, *Nature*, **434**, 1085 (2005).
172. Y.-J. Doh, J.A.V. Dam, A.L. Roest, E.P.A.M. Bakkers, L.P. Kouwenhoven, and S. De Franceschi, Tunable supercurrent through semiconductor nanowires, *Science*, **309**, 272–275 (2005).
173. G.B. Arfken and H.J. Weber, *Mathematical Methods for Physicists*, Academic Press, San Diego, 1995.

174. L.E. Brus, Electron–electron and electron–hole interactions in small semiconductor crystallites: the size dependence of the lowest excited electronic state, *J. Chem. Phys*., **80**, 4403 (1984).
175. M.L. Steigerwald and L.E. Brus, Semiconductor crystallites — a class of large molecules, *Acc. Chem. Res*., **23**, 183–188 (1990).
176. M.S. Gudiksen, Semiconductor nanowires and nanowire heterostructures: development of complex building blocks for nanotechnology, Ph.D. thesis, Harvard University, Harvard, 2003.
177. R. Agarwal, C.J. Barrelet, and C.M. Lieber, Lasing in single cadmium sulfide optical cavities, *Nano Lett*., **5**, 917–920 (2005).
178. H.-J. Choi, J.C. Johnson, R. He, S.-K. Lee, F. Kim, P. Pauzauskie, J. Goldberger, R.J. Saykally, and P. Yang, *J. Phys. Chem. B*, **107**, 8721 (2003).
179. J.C. Johnson, H. Yan, R.D. Schaller, P.B. Petersen, P. Yang, and R.J. Saykally, Near-field imaging of nonlinear optical mixing in single zinc oxide nanowires, *Nano Lett*., **2**, 279–283 (2002).
180. M. Law, L.E. Greene, J.C. Johnson, R. Saykally, and P.D. Yang, Nanowire dye-sensitized solar cells, *Nat. Mater*., **4**, 455–459 (2005).
181. J.B. Baxter and E.S. Aydil, Nanowire-based dye-sensitized solar cells, *Appl. Phys. Lett*., **86** (2005).
182. E.P.A.M. Bakkers, *Nat. Mater*., **3**, 769 (2004).
183. T. Martensson, *Nano Lett*. **4**, 1987 (2004).
184. L. Samuelson, C. Thelander, M.T. Bjork, M. Borgstrom, K. Deppert, K.A. Dick, A.E. Hansen, T. Martensson, N. Panev, A.I. Persson, W. Siefert, N. Skold, M.W. Larsson, and L.R. Wallenberg, Semiconductor nanowires for 0D and 1D physics and applications, *Physica E*, **25**, 313–318 (2004).
185. K.A. Dick, K. Deppert, M.W. Larsson, T. Martensson, W. Siefert, L.R. Wallenberg, and L. Samuelson, Synthesis of branched 'nanotrees' by controlled seeding of multiple branching events, *Nat. Mater*., **3**, 380–384 (2004).
186. M.T. Bjork, C. Thelander, A.E. Hansen, L.E. Jensen, M.W. Larsson, L.R. Wallenberg, and L. Samuelson, Few-electron quantum dots in nanowires, *Nano Lett*., **4**, 1621–1625 (2002).

10 Inorganic Nanotubes and Fullerene-Like Materials of Metal Dichalcogenide and Related Layered Compounds

R. Tenne
Department of Materials and Interfaces,
Weizmann Institute, Rehovat, Israel

CONTENTS

10.1 PREFACE

The discovery of carbon fullerenes [1] and later carbon nanotubes [2] stimulated research on carbonaceous nanomaterials and also the search for nanotubes and fullerene-like structures from other layered compounds. Numerous inorganic compounds possess layer (2-D) structure, including metal dichalcogenides (sulfides, selenides, and tellurides), metal dihalides (chlorides, bromides, and iodides), metal oxides, and numerous ternary or quaternary compounds, resembling thereby graphite. The metal dichalcogenides, MX_2 (M = Mo, W, Nb, Ta, Hf, Ti, Zr, Re; X = S, Se) contain a metal layer sandwiched between two chalcogen layers with the metal in a trigonal pyramidal or octahedral coordination mode [3,4]. Analogous to graphite (Figure 10.1a), weak van der Waals forces are responsible for the stacking of the MX_2 layers along the *c*-axis (Figure 10.1b). The molecular sheets of inorganic layered compounds consist of multiple layers of different atoms chemically bonded together.

The stimulus for the formation of fullerenes and nanotubes can be understood on the basis of the structure of the parent bulk compound, graphite, which consists of atomically flat carbon (graphene) sheets. Here, each carbon atom is bonded to its three nearest-neighboring carbon atoms via sp^2

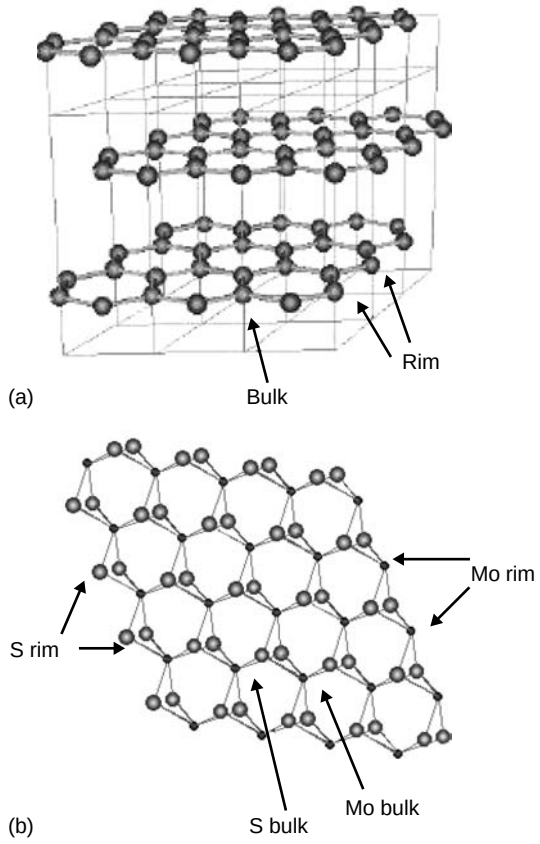

FIGURE 10.1 (a) Schematic structure of graphite. (b) Schematic presentation of MoS_2 layer with both bulk and rim atoms delineated.

hybridization, forming a hexagonal (honeycomb) network. The layers are stacked together via weak van der Waals forces. Carbon atoms that are disposed on the rim of the sheet are only twofold-bonded, each one thus having dangling bond. When the graphene sheet size shrinks, the ratio of rim/bulk atoms increases as 2^n, where n is the number of cutting cycles of the sheet into smaller pieces. The large increase in the ratio of rim/bulk atoms with shrinking size of the graphene sheet makes the planar nanostructure unstable. This instability results in folding of the graphite layers and the formation of carbon fullerenes and nanotubes, which are seamless structures. While the nanotubes involve winding of the graphene nanosheet in one axis, the fullerenes are obtained by folding the nanosheet along two axes. Since the latter process requires much higher elastic energy, the folding is realized by disposing 12 pentagons into the hexagonal carbon network. It is important to realize that folding of the graphene nanosheet involves overcoming an elastic energy activation barrier, which is provided by heating or irradiation. The invested energy is more than compensated once the fullerene is closed and the dangling bonds at the periphery of the nanosheet disappear.

In analogy to that, one notes that the chalcogen atoms of MX_2 compounds on the basal (0 0 0 1) plane are fully bonded and therefore nonreactive. In contrast the metal and chalcogen atoms on the rim of the nanosheet are not fully bonded. While the metal atom within the MX_2 layer is six- fold-coordinated to the nearest chalcogen atoms, it is only fourfold-coordinated at the edge of the MS_2 nanocluster. Similarly, the chalcogen atom in the rim is only twofold-bonded to the metal atoms instead of being threefold-coordinated as in the bulk (Figure 10.1b). Therefore, planar nanosheets of the dichalcogenide compounds become unstable, forming structures reminiscent of nested carbon fullerenes and nanotubes (Figure 10.2), referred hereafter as inorganic fullerene like (IF) structures

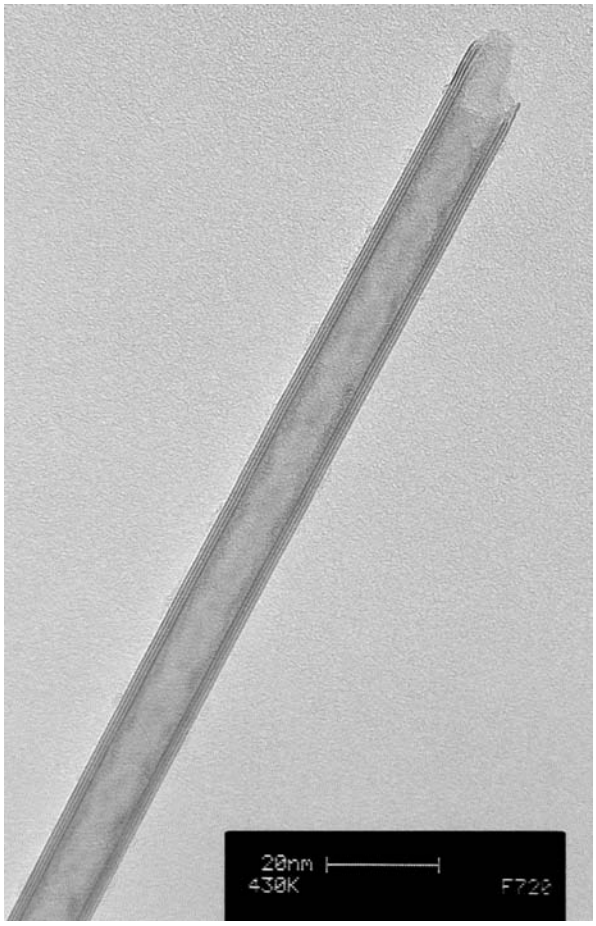

FIGURE 10.2 TEM image of a WS_2 nanotube.

[5,6]. Generally, the fullerene-like structures are less regular in their shape than the respective nanotubes and contain many defects (however see below). Other related structures are nanoscrolls, which are obtained by winding molecular sheets several times around their axial direction. In the energy landscape, nanoscrolls can be considered to be an intermediate stage between a perfectly crystalline the stable nanotubular structure and the unstable flat nanosheets. Nanoscrolls are preferably produced by "chemie douce" (low temperature) processes, like sol–gel, intercalation–exfoliation, hydrothermal synthesis, etc., in which the thermal energy is not sufficiently large to induce growth of the ultimately more stable nanotubular structure.

Over the past few years, considerable progress has been achieved in the synthesis of nanotubes from layered metal dichalcogenides and several other layered compounds. Nanotubes of various layered transition metal compounds, including halides like $NiCl_2$ [7], and various layered-type oxides like V_2O_5 [8,9] and $H_2Ti_3O_7$ [10], have been synthesized using different methodologies. The advent of the synthesis, structural characterization, properties, and applications of inorganic nanotubes have been covered by a number of recent review articles, see, e.g., [11,12].

Perhaps, the most well-known example of an early tube-like structure with diameters in the submicrometer range is formed by the asbestos minerals, like chrysotile, kaolinite, etc. The folding of kaolinite sheet was studied by Pauling [13], and was attributed to an asymmetry of the layered structure, which consists of fused silica tetrahedra and alumina octahedra (Figure 10.3). The larger alumina octahedra occupy the outer face of the scrolling sheet, whereas the smaller silica tetrahdra are found

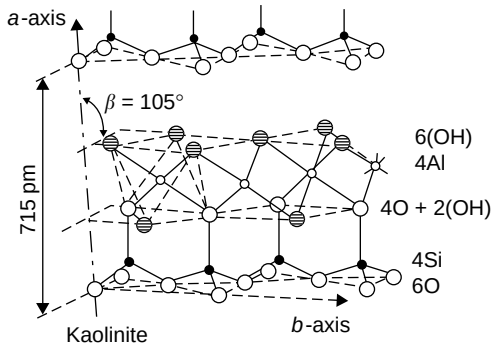

FIGURE 10.3 Schematic representation of the mineral kaolinite.

at the inner face of the asbestos sheet. More recently, a systematic effort to synthesize "misfit" compounds, in which cubic crystals like PbS are intercalated between layers of, e.g., NbS_2, forming thereby an artificial superlattice, is well documented [14]. Owing to lattice mismatch between the two compounds, an asymmetry arises in the "misfit" lattice, which induces folding of the layers and the formation of tubular structures [15]. The synthesis of mesoporous silica with well-defined nanopores in the range 2 to 20 nm was reported by Beck and Kresge and their coworkers [16]. The syntheses strategy involved the self-assembly of liquid crystalline templates. The pore size in zeolitic and other inorganic porous solids is varied by a suitable choice of the template. In contrast with the IF phases, which consist of isolated nanoparticles, mesoporous materials form an interconnected and extended lattice.

Using various templates, recent efforts have resulted in the synthesis of nanotubes from isotropic 3-D (nonlayered) compounds also, further widening the scope of inorganic nanotubes. Even folding of sheets of 3-D compounds, like silica or AlN into nanotues with below 100 nm diameter requires very large amounts of elastic energy and is therefore prohibitive. Even higher elastic energy is required for the formation of quasi-spherical polyhedral (fullerene-like) nanostructures from 3-D compounds. One way for a 3-D compound to overcome this energy barrier is to introduce grain boundaries and dislocations, leading thereby to polycrystalline nanotubes. Nanotubes of 3-D compounds can be obtained through a templated growth using an artificial scaffold. Earlier, amorphous silica nanotubes were obtained by hydrolysis of tetraethylorthosilicate (TEOS) in a mixture of water, ammonia, ethanol, and tartaric acid [17,18]. Later on, polycrystalline silica, alumina, and vanadia nanotubes were obtained by using carbon nanotubes as a template and subsequent calcination of the product at elevated temperatures [19]. Recently, however, highly faceted and crystalline nanotubes of isotropic (3-D) compounds were obtained by growth along an easy axis, as demonstrated for AlN [20] (Figure 10.4) and for microtubules of Ga_2O_3 (Figure 10.5) [21]. Here, the *c*-axis $\langle 0\ 0\ 0\ 1 \rangle$ serves as the fast growth axis for this wurzite-type lattice, with $(1\ 0\ \bar{1}\ 0)$ and $(1\ 1\ \bar{2}\ 0)$ faces making the facets of the tubes. The atomic structure of the edges between two such facets has not been studied in detail so far. Nanotubes of 3-D compounds are inherently unstable and their surface is generally very reactive, a property which can be very useful for catalyzing chemical reactions.

10.2 SYNTHESIS OF INORGANIC NANOTUBES

Even before IF materials were recognized as a universal phenomenon, tubular and fullerene-like forms of layered compounds were reported. Perhaps the earliest among them were nanoscrolls of MoS_2 obtained by reacting $MoCl_4$ with Li_2S in tetrahydrofurane (THF) solution, and subsequent annealing at 400°C [22]. In another study, NiS–MoS_2 core–shell structures, in which closed MoS_2 layers enfold NiS nanoparticles, were reported [23]. Over the past few years, a number of synthetic strategies have been successfully used for the production of nanotubes from layered (2-D) as well

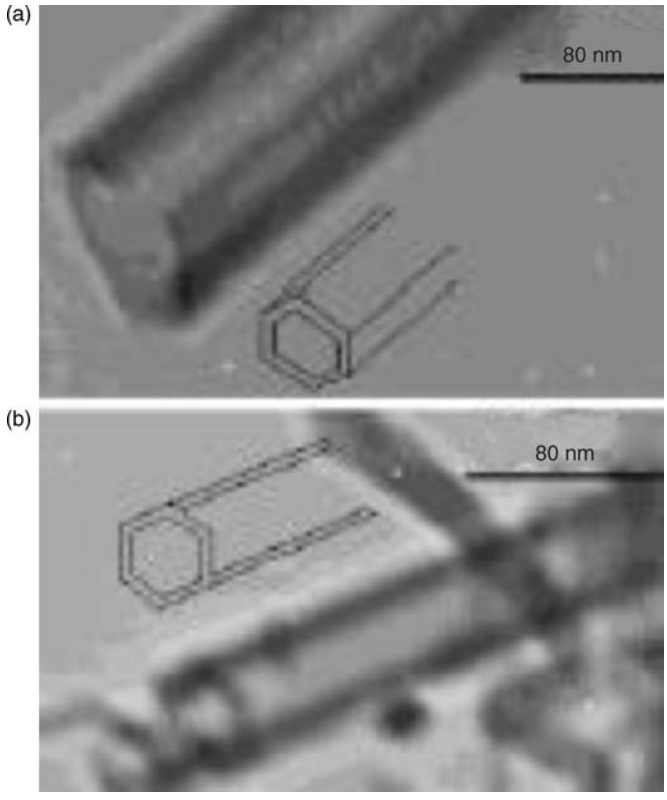

FIGURE 10.4 SEM image of faceted AIN nanotubes. (Adapted from Wu, Q. et al., *J. Am. Chem. Soc*., 125, 10176, 2003.)

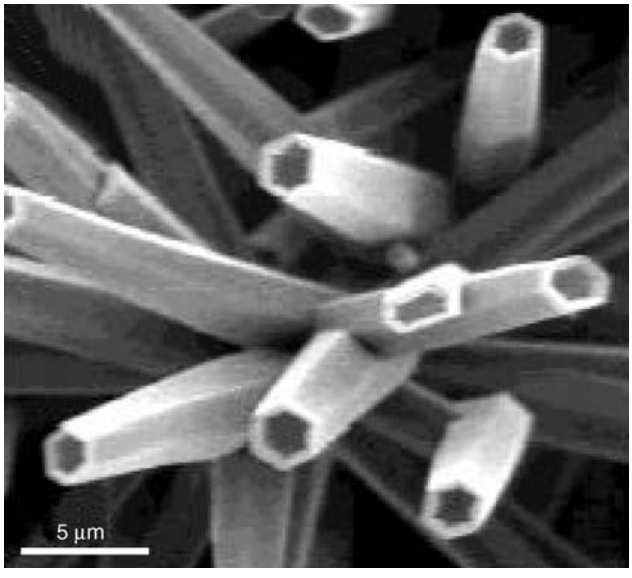

FIGURE 10.5 Faceted microtubules of Ga_2O_3. (Adapted from Sharma, S. and Sunkara, M.K., *J. Am. Chem. Soc*., 124, 12288, 2002.) Note the clear hexagonal cross section of the tubes in both cases.

TABLE 10.1
Summary of the Inorganic Nanotubes Reported in the Literature and the Synthetic Procedures Used for Their Production

Compound	Synthetic Approach	References	Comments
MS_2 (M=W, Mo) ReS_2	Reaction with the respective oxide at elevated temperature	[5,24–26]	ReS_2 is a 2-D compound with Re-Re bonds
MS_2 (M=W, Mo)	Chemical vapor transport (CVT)	[27,28]	
Single wall MoS_2 nanotubes	CVT(I_2)+C_{60} catalyst	[29]	
MoS_2	Ammonium thiometallate (ATM) solution in porous alumina template, reaction with H_2S	[30,31]	Not perfectly crystalline
MS_2 (M=Nb, Ta, Ti, Zr, Hf)	Decomposition of MS_3 at elevated temperature	[32,33]	
MoS_2	Heating MoS_2 powder in a closed Mo crucible	[34]	
NbS_2, ReS_2	Depositing $NbCl_2$ ($ReCl_3$) from solution onto carbon nanotubes; firing in H_2S at elevated temperature	[35,36]	
$NbSe_2$	Direct reaction of the elements at 800°C	[37]	
MoS_2	Hydrothermal reaction of ATM; crystallization from acetone; firing in H_2S at 600°C	[38]	Non-perfect crystallinity
WS_2	Firing of ATM in thiophene/hydrogen at 360–450°C	[39]	
TiS_2	CVT(I_2)	[40]	
MoS_2	Firing of ATM in H_2	[41]	
MoS_2	Firing of MoO_3 nanobelts in the presence of sulfur	[42]	
WS_2	Hydrothermal synthesis with organic amines and a cationic surfactant and firing at 850°C	[43]	
WS_2	Growth of WO_{3-x} nanowhiskers; annealing in H_2S/H_2 atmosphere at elevated temperature	[44,45]	
NbS_2/C	Deposition of $NbCl_4$ on carbon nanotubes template/firing in H_2S	[46]	
MX_2 (M=Mo, Nb; X=S, Se, Te)	Electron beam irradiation of MX_2 powder	[47–50]	
MS_2	Arc discharge of submerged electrodes	[51]	
MoS_2, WS_2	Microwave plasma	[52]	
SnS_2/SnS (misfit)	Laser ablation of SnS_2	[54]	
InS	Reacting t-Bu_3In with H_2S in aprotic solvent at 203°C in the presence of benzenethiol present	[88]	Metastable phase

as nonlayered (3-D) compounds. Table 10.1 brings a concise summary of the various metal dichalcogenide nanotubes that have been reported over the last few years, and the synthetic procedures which have been used for their production. This summary shows the large versatility of the chemical apparatus that has been developed for the synthesis of these nanotubes. It further suggests that these nanostructures are thermodynamically stable, with the sole constraint that their diameter is smaller than approximately 100 nm. Most commonly, the synthesis of metal dichalcogenide nanotubes is done at elevated temperatures. "Chemie douce" (low-temperature) processes like hydrothermal synthesis, which are very useful for the synthesis of metal-oxide nanotubes, have not been developed so far for chalcogenide nanotubes. Heating is not only important for accelerating

the reaction kinetics, but also to endow sufficient thermal energy to the nanoclusters. This thermal energy induces structural fluctuations in the lamella, leading to folding of the planar nanosheet into a crystalline nanotubular structure. Obviously, ionizing or nonionizing irradiation can serve as a source of energy to elicit the chemical reaction and the structural transformation [47–49]. This effect was first recognized in the electron beam synthesis of fullerene-like MoS_2 nanoparticles [50]. However, such a procedure is not likely to become a useful way to grow macroscopic amounts of inorganic nanotubes. Arc-discharge of MoS_2 electrode submerged in water led to the synthesis of fullerene-like nanoparticles of this compound [51]. Microwave plasma has also been used to synthesize fullerene-like nanoparticles of WS_2 and MoS_2 [52]. Sonochemical reaction has been used to synthesize nanoscrolls of the layered compound GaO(OH) [53].

Laser ablation has been successfully used for the growth of carbon nanotubes and nanowires of Si, GaAs, and the similar compounds (see Chapter 2, of this handbook). Recently, very short nanotubes and nested fullerne-like nanoparticles of "misfit" compound SnS_2/SnS have been obtained by laser ablation of an SnS_2 pellet [54]. Here an ordered superstructure with one or a pair of SnS layers sheathed between two SnS_2 layers was observed. The formation of these unusual nanostructures can be attributed to the volatility of sulfur during the laser ablation process. Unfortunately, the "misfit" nanotubes are rather short (<1 μm) and cannot be produced in large amounts. Laser ablation of MoS_2 and WS_2 targets yielded nanoparticles with fullerene-like structure [55,56]. Growth of $NiCl_2$ nanotubes by a laser ablation process was demonstrated [57]. The nanotubes were shown to grow in a vapor–liquid–solid (VLS) mechanism. However, little control over the growth mode could be established, and the yield of the nanotubes was extremely low.

Hexagonal boron nitride (BN) crystallizes in a graphite-like structure. Here, the iso-electronic B–N pair replaces a C–C pair in the graphene sheet. Partial or entire replacement of the C–C pairs by the B–N pairs in the hexagonal network of graphite leads to the formation of a wide array of two-dimensional phases, like BC_2N. BN tubes with turbostratic structure were reported by Hamilton et al. [58]. The first synthesis of crytalline BN nanotubes was reported shortly afterwards [59]. BN nanotube phases have been produced by several synthetic approaches [60–62]. Double-wall BN nanotubes were obtained by plasma arc reaction using boron anodes impregnated with nickel and cobalt catalysts [63]. Likewise, BC_xN nanotubes were synthesized by reacting aligned CN_x nanotubes with B_2O_3 in the presence of CuO in N_2 atmosphere and at 1800°C [64]. Sheated carbon/BN nanotubes were synthesized as well [65]. Here a graphite cathode was arced with an HfB_2 anode in a nitrogen atmosphere. In this configuration, the three constituents have different sources: the anode for boron, the cathode for carbon, and the chamber atmosphere for nitrogen. In addition, hafnium present in the plasma may be acting as a catalyst. Reactive magnetron sputtering of graphite target in the presence of nitrogen atmosphere led to the synthesis of carbon fullerenes with 20% N content. The aza-fullerene $C_{48}N_{12}$ (Figure 10.6) is considered to be the most stable cluster belonging to the CN_x family of compounds [66]. Each of the 12 pentagons is decorated by a single nitrogen atom.

In summary, the plurality of methods used to synthesize $B_xC_yN_z$ nanotubes suggests that these nanostructures, which are derived from macroscopically stable 2-D compounds are themselves thermodynamically stable phasses, given the sole constraint that their diameter is smaller than approximately 0.1 μm.

Systematic attempts to grow nanotubular structures from quasi-isotropic (3-D) oxide and chalcogenide compounds have been undertaken [19,67]. By coating carbon nanotubes (CNTs) with the respective metal-oxide gels and subsequently burning the carbon, polycrystalline nanotubes and nanowires of a variety of metal oxides, including ZrO_2, SiO_2, and MoO_3 have been obtained [19]. Using a surfactant (Triton 100-X) as scaffold at low temperatures, polycrystalline CdSe and CdS nanotubes were obtained after firing at 300 to 400°C [67].

The synthesis of numerous kinds of oxide nanotubes through "chemie douce" processes have been recently documented. Sol–gel synthesis of oxide nanotubes is also possible in the pores of alumina membranes [68]. An interesting case is that of the titania nanotubes, which are hypothesized to exhibit excellent photocatalytic and photoelectrochemical properties for self-cleaning surfaces or

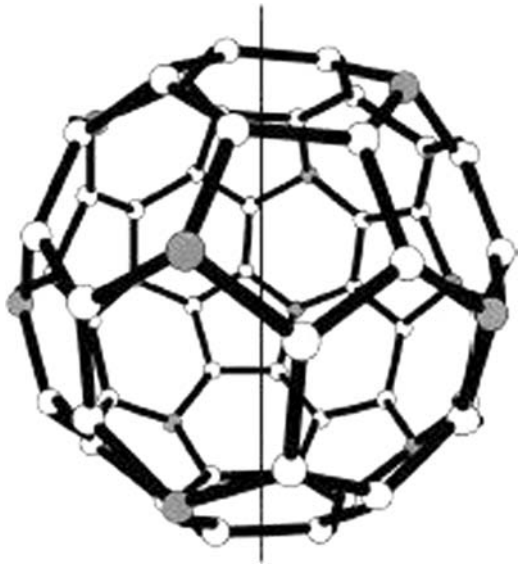

FIGURE 10.6 Schematic representation of $C_{48}N_{12}$ aza-fullerene. (Adapted from Hultman, L., et al., *Phys. Rev. Lett*., 87, 225503, 2001.)

dye-sensitized solar cells. Titania nanotubes have been obtained by treating anatase or rutile structure TiO_2 with NaOH at 120°C, and subsequent washing with HCl solution [69,70]. The resulting titania nanotubes (nanoscrolls) are 50 to 200 nm long and their diameter is about 10 nm. TEM images of such nanotubes reveal lattice fringes with 0.78 nm spacing. Frequently, the number of molecular layers is not the same on both sides of the nanotube, indicating that the nanotube is made of a continuous molecular sheet which is wound like a folded carpet or a scroll, and hence is termed nanoscroll (Figure 10.7). Indeed, a recent series of works [16,71] concluded that the NaOH treatment leads to recrystallization of the anatase and exfoliation of individual $Na_xH_{2-x}Ti_3O_7$ molecular sheets, which fold into an open-ended nanoscroll. The driving force for the exfoliation of the titanate sheets was attributed to the NaOH, which extracts protons from the exposed surface. This process produces a charge imbalance between the two sides of the solution-exposed $H_2Ti_3O_7$ nanosheet. Consequently, detachment of the nanosheet from the crystal surface and subsequent folding leads to the formation of the nanoscroll [72]. Similarly, nanotubes (nanocrolls) of the lamellar compound $K_4Nb_6O_{17}$ were obtained by exfoliation of the parent crystallites with tetra (n-butyl) ammonium hydroxide [73]. The radius of the nanoscrolls is determined by a very delicate balance between the van der Waals interactions and the elastic energy, which explains the size uniformity of these self-assembled structures.

Nanotubes from various layered metal-silicates were recently prepared via hydrothermal synthesis, i.e., under moderate temperatures (generally < 200°C) and pressure of a few MPa [74]. These nanotubes were shown to exhibit high surface area, appreciable hydrogen storage capacity, and when loaded with Pd metal, high catalytic reactivity toward CO and C_2H_6 oxidation. Nanotubes of δ-MnO_2 were synthesized by hydrothermal conversion of the layered α-$NaMnO_2$ compound [75]. The importance of this advance is in the possibility of using such nanotubular phases as cathodes in high performance Li intercalation batteries.

Nanotubular and fullerene-like structures of various rare-earth hydroxides have been prepared by hydrothermal synthesis [76]. Furthermore, dehydration and subsequent reactions led to the formation of nanotubular structures of rare earth oxides, oxisulfides and oxifluorides. Nanotubes of the ferroelectric materials $BaTiO_3$ and $SrTiO_3$ with perovskite structure were obtained by a two-step hydrothermal synthesis [77]. In the preliminary step, TiO_2 (or titanate) nanotubes were prepared by hydrothermal synthesis with NaOH and subsequent wash with HCl solution. In the following step, the $BaTiO_3$ and $SrTiO_3$ were synthesized by hydrothermal reaction between the titanate nanotubes

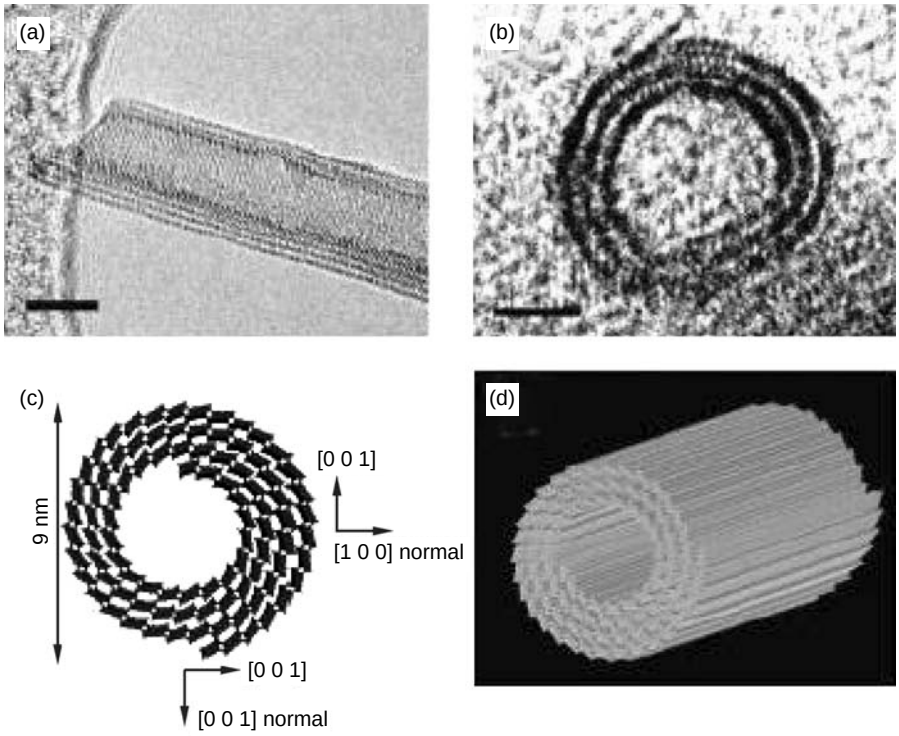

FIGURE 10.7 TEM image and schematic representation of $H_2Ti_3O_7$ nanotubes: (a) axial direction; (b) cross section showing clearly the winding of the sheets into nanoscroll structure; (c) schematic rendering of the cross section; and (d) schematic rendering of the winding of the nanosheet into a nanoscroll. (Adapted from Chen, Q. et al., *Adv. Mater*., 14, 1208, 2002.)

and $Ba(OH)_2$ and $SrCl_2$, respectively. Although the XRD and TEM analyses suggest that the nanotubes are crystalline, a more thorough analysis is needed in order to understand the morphology of the nanotubes. Nested fullerene-like nanoparticles of the layered compound Tl_2O were synthesized from $TlCl_3$ solutions using a sonochemical method [78]. Tl_2O possesses the relatively rare anti-$CdCl_2$ structure. Here, each molecular sheet consists of an oxygen layer in the center, sandwiched between two outer thalium layers. Numerous metal hydroxides afford a layered structure and can therefore be transformed into nanoscrolls. Thus, $Cu(OH)_2$ nanoscrolls were obtained by simply dipping the metal foil in a basic ammonical solution [79].

Various oxide nanotubes have also been obtained via high-temperature syntheses. Nanotubes of the cubic compound In_2O_3 were synthesized by heating In and In_2O_3 powders under vacuum in an induction furnace at 1300°C [80]. The nanotubes were crystalline, with one of their tips closed and much of their hollow core filled with indium. $Mg_3B_2O_6$ nanotubes with polyhedral cross sections were synthesized by heating Si wafer coated with thin film of boron in the presence of magnesium vapor under mixed oxygen–argon atmosphere [81]. Magnesium borate is a thermoluminescing material, which also possesses excellent tribological properties as an additive to lubricants.

Microtubes and nanotubes of pure elements like Te [82,83] and Se [84], have been synthesized as well. A variety of techniques, including wet [82,84] and simple thermal evaporation [83], were successfully used for this purpose. Bi nanotubes were synthesized by solvothermal reduction of Bi_2O_3 with ethylene glycol [85], or alternatively by reduction of $BiCl_3$ with Zn at room temperature [86]. Similar processes have been used by the same group for the synthesis of Sb nanotubes [87].

An interesting case is that of InS nanotubes [88], which have been synthesized by a "chemie douce" process. While the stable crystalline structure of InSe and GaS is lamellar, the more ionic InS compound crystallizes in an orthorhombic lattice structure. Using a low-temperature solution-based

synthesis with benzenethiol (C_6H_5SH) as a catalyst, InS nanotubes were obtained. This work shows that kinetic control could lead to the preferential growth of an otherwise metastable layered structure, which does not exist in the bulk InS material.

Nanotubes of various III–V compounds with zincblende structure, like GaN and AlN nanotubes, were recently reported [20,89]. Clearly, simple folding of a molecular sheet is not possible in this case. Here uniaxial growth along an easy axis is promoted resulting in a highly faceted nanotube morphology. The faceted faces of the nanotube are chemically very reactive. Therefore, protection of the facets' surfaces with respect to the ambient atmosphere remains a great challenge for various applications like field emission, etc.

In summary, over the past few years, a large chemical apparatus has been conceived in order to synthesize new nanotubular and fullerene-like structures; part of this effort has been summarized in this rather noncomprehensive listing.

10.3 INORGANIC NANOTUBES AND FULLERENE-LIKE STRUCTURES STUDIED BY COMPUTATIONAL METHODS

Computational methods play a major role in the progress of materials science in general, and nanomaterials in particular. Pioneering efforts in this direction were undertaken by the Cohen–Louie group, who studied various $B_xC_yN_z$ nanotubes [90–92] (see also Table 10.2). Following this preliminary work, Seifert and coworkers [94–96,101] undertook a systematic approach to elucidate the structural aspects and the physical behavior of metal-dichalcogenide nanotubes [102]. These studies indicated that the strain in the nanotube increases like $1/R^2$, where R is the radius of the nanoubes. Furthermore, due to the bulky structure of the multiple atom S–M–S layer, the strain energy of an MS_2 nanotube was found to be about an order of magnitude larger than that of carbon nanotubes with the same diameter. These calculations clearly indicated that in agreement with the experiment, multiwall WS_2 (MoS_2) nanotubes consisting of 4 to 7 layers, with an inner radius of 6 to 12 nm, are the most stable moities [101].

Generally, the formation of a polyhedral nanoparticle by folding the molecular sheet in two directions is more demanding in terms of elastic energy than folding the lamella in one direction to obtain a nanotube. One manifestation of this conjecture is the fact that the number of defects and irregularities in nested fullerene-like nanoaprticles of WS_2 is appreciably higher than those observed in WS_2 nanotubes. Furthermore, while the cross section of WS_2 nanotubes is in general circular, fullerene-like nanoparticles of WS_2 have been shown to exhibit a phase transformation from an evenly curved surface into polyhedral (faceted) configuration, when the number of molecular layers (i.e., the thickness) exceeds a critical number (3 to 4 layers) [125]. This principle has been confirmed also in the case of black phosphorous, where a stable configuration could be calculated for the nanotubes, while fullerene-like nanoparticles of similar dimensions have been found to be unstable [117–119].

The electronic structure of MS_2 nanotubes have been studied in considerable detail. It was found that semiconducting materials, like MoS_2 and WS_2 [94,95], form nanotubes with forbidden gaps, which shrink with decreasing diameter of the nanotubes. It is clear then that in contrast to the ubiquitous semiconducting quantum dots and nanowires, the quantum size effect in MS_2 nanotubes is not particularly large. The diminutive nature of the quantum size effect in IF nanoparticles can be attributed to the confinement of their electronic states within the molecular sheet. On the other hand, the lattice distortion induced by the bending of the molecular layer, which increases with the shrinkage of the nanoparticle radius, leads to an opposite effect, i.e., reduction of the bandgap. Many of the semiconducting layered compounds possess an indirect transition and therefore exhibit a weak luminescence, if any. While (n,n) armchair nanotubes also possess an indirect gap, (n,0) zigzag nanotubes were shown to be direct bandgap semiconductors, suggesting a variety of optical effects in such nanotubes. Nanotubes of materials with metallic character, like NbS_2, remain metallic in nature, irrespective of their diameter and chirality [96,98]. The high density of states near the Fermi level suggests that such nanotubes may become superconductors at low temperatures.

TABLE 10.2
Summary of First-Principle Calculations for Inorganic Nanotubes

Compound	Method Used	References	Comment
BN	DFT–LDA	[90]	Insulator
BC_2N	DFT–LDA	[91]	Chiral; metals or semiconductors
BC_3	DFT–LDA	[92]	
GaSe	DFT–LDA	[93]	Semiconductor
WS_2	DFT–TB	[94]	Semiconductor — Z Z, direct; AC indirect; bandgap shrinks with decreasing diameter
MoS_2	DFT–TB	[95]	Like WS_2
NbS_2	DFT–TB	[96]	Metal, possibly superconductor
TiS_2	DFT–TB	[97]	
$NbSe_2$	TB	[98]	Metal, possibly superconductor
ZrS_2	TB	[99]	Semiconductor—Z Z, direct; AC, indirect; bandgap shrinks with decreasing diameter stability: ZZ>AC
$MoS_2I_{1/3}$ bundles	DFT	[100]	Stable mostly as bundles; metallic
WS_2, MoS_2	DFT–TB	[101]	Stability of the nanotubes was confirmed
WS_2, MoS_2	DFT–TB	[102]	Bandgap of the nanotubes as a function of diameter was determined
$(MS_2)_{64}$ (M=Mo, Nb, Zr, S) nanooctahedra	TB	[103]	Stable nanooctahedra; metallic
$Ca(AlSi)_2$ and $Sr(GaSi)_2$	TB	[104]	Metallic, possibly superconducting;
$CaSi_2$	LDA–DFT	[105]	metallic
V_2O_5	TB	[106]	Semiconductors; bandgap shrinks with decreasing diameter
ZrNCl	TB	[107]	ZZ — metal; AC — semiconductor (becomes metal upon removal of 30% chlorine)
B	HF–SCF	[108–110]	Nanotubes are stable nanostructures, metallic character
AlB_2	HF–SCF	[111]	Metallic
Bi	DFT	[112]	Semiconductors
MB_2 (M=Mg,Be,Sc,Ca, Al,Ti,,Cr,Mo,Ta,Zr)	TB	[113–115]	Metallic, possibly superconducting
V_2O_5	TB	[116]	Semiconductors; bandgap shrinks with decreasing diameter — effect is stronger with ZZ as compared with AC nanotubes
Black-P, As	DFT–TB	[117–119]	Nanotubes — stable; fullerenes — unstable
GaN	DFT	[120]	Folded graphite-like GaN; bandgap decreases with shrinking diameter; ZZ — direct gap; AC — indirect gap
AlN	DFT	[121–123]	Folded graphite-like AlN; bandgap decreases with shrinking diameter; ZZ — direct gap; AC — indirect gap. Fullerene-like structures — stable
InP	SCF–MO	[124]	

TB, tight binding; DFT, density functional theory; HF-SCF, Hartree-Fock self-consistent field; LDA, local density approximation; SCF-MO, Self-consistent–field-molecular orbital; ZZ, zigzag; AC, armchair.

The structure of the stable polyhedral clusters of metal dichalcogenide and other layered compounds was first discussed in [6]. It was hypothesized that instead of pentagons, which occur in carbon fullerenes and carbon nanotubes, rhombi and triangles would be the stable elements among IF nanoparticles. Later work provided the first evidence for the existence of nanooctahedra (six rhombi) and nanotetrahedra (four triangles) in MoS_2 [126]. More decisive evidence in support of the existence and stability of MoS_2 nanooctahedra was obtained by laser ablation of an MoS_2 target [55]. Figure 10.8 shows an HRTEM image of one such MoS_2 nanooctahedron (left) and its Fourier transform filtered image (right). These images clearly reveal the precise arrangement of the Mo atoms in the cluster. Recently, the IF nanooctahedra of metal dichalcogenide compounds have been theoretically analyzed and their atomic and electronic structure evaluated [103,127]. Figure 10.9 shows the structure of an $(MoS_2)_{64}$ nanooctahedron calculated by tight binding (TB) theory. The structures of similar nanooctahedra of Nb, Zr, and Sn disulfides were also investigated. Most interestingly, all the nanooctahedra studied were found to be metallic, irrespective of the electronic structure of the parent compound. This conclusion, which remains to be verified experimentally, shows the importance of elucidating the structure of IF nanoparticles and their properties. Also, more accurate first-principle calculations have to be carried out in order to verify the proposed stable structure of such nanooctahedra.

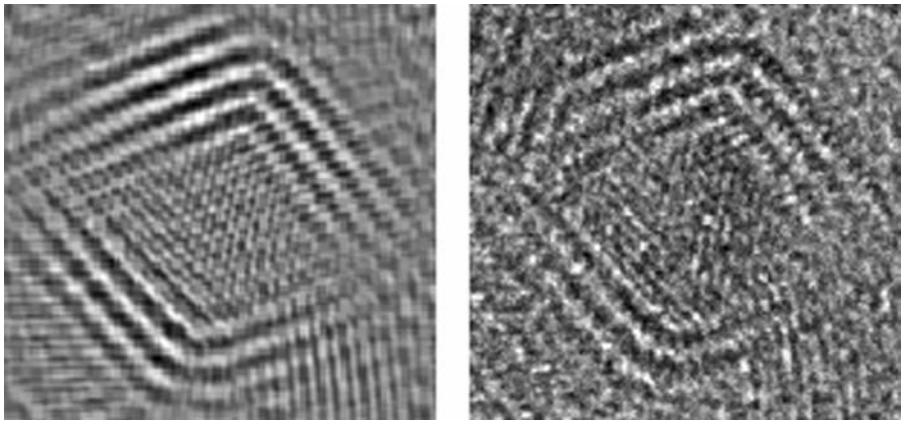

FIGURE 10.8 HRTEM image (right) and its Fourier filtered image (left) of an MoS_2 nanooctahedron prepared by laser ablation of an MoS_2 target (Courtesy of M. Bar-Sadan and S.Y. Hong).

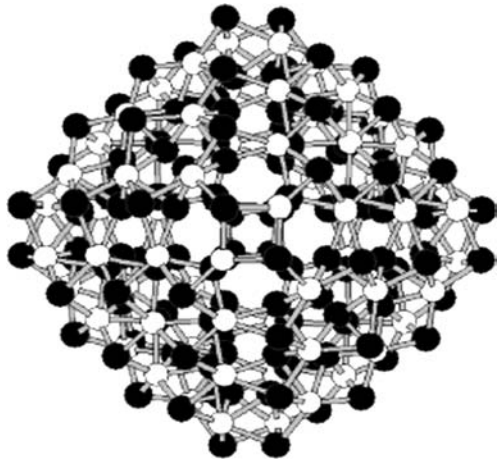

FIGURE 10.9 Schematic representation of the structure of $(MoS_2)_{64}$. (Adapted from Enyashin, A.N. et al., *Inorg. Mater*., 40, 395, 2004.)

The structure, stability, and properties of GaN and AlN nanotubes were studied as well [120–122]. In analogy to the semiconducting MS_2 nanotubes, and in sharp contrast to carbon nanotubes, the bandgap shrinks with a decreasing diameter of the nanotubes. Furthermore, while (*n*,*n*) armchair nanotubes were found to exhibit an indirect transition, direct transition was seen for (*n*,0) zigzag nanotubes.

An interesting case is presented by nanotubes of the layered compound β-ZrNCl (see Figure 10.10a). This compound is a semiconductor with a bandgap of 2 eV in the bulk. It was converted into a superconductor (T_c = 13 to 15 K) by intercalating such electron donors as alkali atoms, or by deintercalation of some of the lattice chlorine atoms. The structure and electronic properties of β-ZrNCl nanotubes were investigated in detail in [107] (Figure 10.10b). The (*n*,*n*) armchair nanotubes were shown to be semiconductors, but (*n*,0) zigzag nanotubes with diameter larger than 2.8 nm are found to be all metallic. Furthermore, while the (29,0) nanotube is metallic, its unfolded stripe is a semiconductor with a bandgap of 1.2 eV. As in semiconducting MS_2 nanotubes [93,94], the

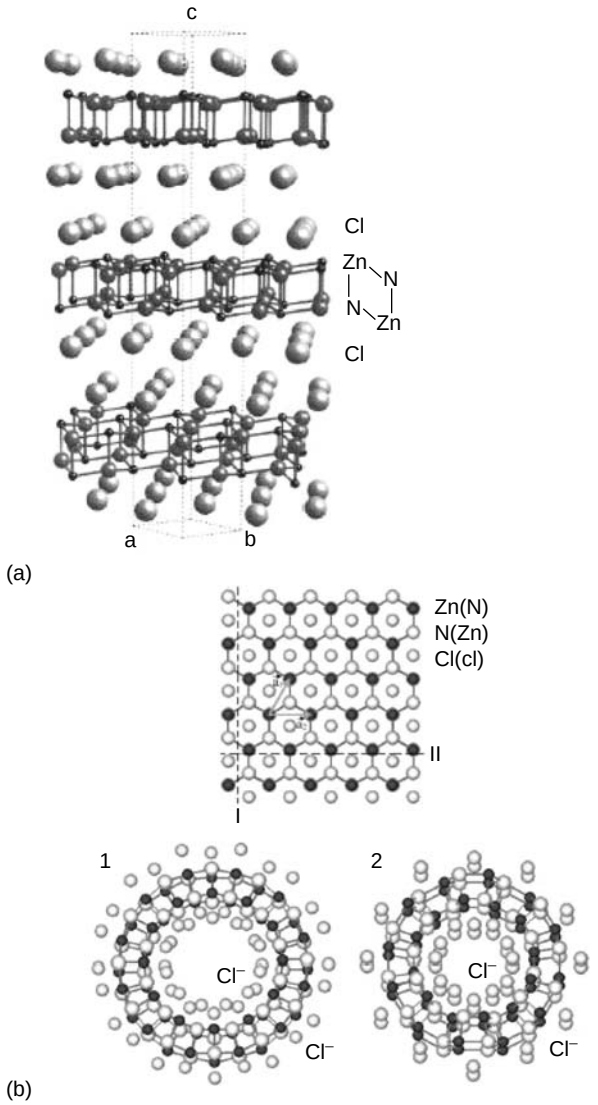

FIGURE 10.10 (a) Crystal structure of a β-ZrNCI lattice; 1, Zigzag (12,0); 2, armchair (12,12) ZrNCI nanotube. (Adapted from Enyashin, A.N. et al., *Chem. Phys. Lett.*, 387, 85, 2004.)

bandgap of the armchair nanotubes shrinks with decreasing nanotube diameter. Moreover, intrinsic or extrinsic doping may lead to significant variation of the electronic properties of nanotubes. Thus, deintercalation of 30% of chlorine atoms endows metallic character to the ZrNCl nanotubes [107], suggesting that they may become superconductors at sufficiently low temperatures.

In conclusion, the structure and electronic properties of various inorganic nanotubes have been investigated in some detail. While some of the properties could be confirmed by experiment, much more work is needed to elucidate the electronic and optical properties of these novel nanomaterials.

10.4 STUDY OF THE PROPERTIES OF INORGANIC NANOTUBES IN RELATION TO THEIR APPLICATIONS

The properties of inorganic nanotubes and IF nanoparticles have been studied only recently (see Table 10.3). In spite of that, a major application area for the IF nanoparticles in solid lubrication has emerged from these studies. It was initially hypothesized that the quasi-spherical nanoparticles

TABLE 10.3
Summary of Potential Applications of Inorganic Nanotubes and Fullerene-Like Nanoparticles

Compound	Properties and Proposed Applications	References	Comment
MoS_2,WS_2	Tribology: additives to lubricating fluids	[51,128,129]	Oils, greases, machining fluids, etc.
MoS_2,WS_2	Tribological coatings (metallic, polymers)	[129–131]	Medical applications
MoS_2,WS_2	Tribology: self-lubricating porous structures	[132]	Sliding bearings
MoS_2, WS_2	Impact resistance	[133]	
MS_2 (M=W, Mo)	Mechanical properties (nanocomposites, etc.)	[134–136]	
MS_2 (M=Mo,Ti)	Rechargeable batteries	[40,137–139]	
MS_2 (M=Mo, Ti)	Hydrogen storage	[40,41]	
MoS_2	Catalysis	[140]	$CO+3H_2 \rightarrow CH_4+H_2O$
MoS_2I_y	Field emission	[141]	
BN	Mechanical properties	[142,143]	Young's modulus of 700–1200 GPa
BN	H_2 storage	[144]	Up to 4.2 wt%
BCN	Field emission	[145]	Comparable to multiwall carbon nanotubes
VO_x	Cathodes for rechargeable Li batteries	[146–148]	100 cycles; >200 mAh/g
VO_x	Optical limiting	[149]	
$Mg_3Si_2O_5(OH)_4$ $CuSiO_3{\cdot}2H_2O$	H_2 storage; catalyst support for CO oxidation	[150]	
Rare earth oxisulfides	Non-linear optics	[76]	
Titanates (e.g., $H_2Ti_3O_7$)	Dye sensitized solar cells	[151]	Solar to electrical efficiency of 5%
GaN	Optical nanodevices	[89]	
Y_2O_3:Eu	Optical nanodevices	[152]	
Silicate	Catalysis, H_2 stoarge	[74]	Catalytic CO and C_2H_6 oxidation

would exhibit facile rolling and sliding. Coupled with its mechanical stability and chemical inertness it was thought that IF-WS_2 (MoS_2) nanoparticles could become very efficient nanoball bearings, especially under high loads, where lubricating fluids tend to be squeezed out of the contact region between the two moving pieces. This hypothesis was invariably confirmed [51,128]. Apparently, the favorable role played by IF nanoparticles in alleviating friction and wear is a much more complex phenomenon than initially believed. A number of studies have indicated that during friction tests under load, the IF nanoparticles gradually deform and exfoliate, depositing molecular WS_2 (MoS_2) nanosheets on the underlying surfaces. These transferred molecular sheets (third body) provide easy shear for the mating metal pieces, further alleviating friction [129]. Recent technical tests of IF-WS_2 in various industrial environments demonstrated the large potential of such nanoparticles for numerous tribological applications in the automotive, aerospace, electronics, and many other industries. Figure 10.11 shows the detrimental effect of addition of a minute amount of IF-WS_2 nanoparticles on the friction coefficient between a ceramic pair, i.e., a Si_3N_4 ball and alumina flat. The effect of the IF-WS_2 nanoparticles on the wear rate of the ball was similar. The large-scale application of IF-WS_2 (MoS_2) would not be possible, should scaling of the production and its cost effectiveness would not be proved. Indeed, a fluidized-bed reactor with a capacity of more than 100 g/day of a pure IF-WS_2 phase was realized sometime ago [153], and the construction of a mock-up system for full-scale production is in progress. The feedstocks for the present process are quite cheap and notwithstanding the small amount of the nanomaterials needed to alleviate both friction and wear, the cost effectiveness of the IF-WS_2 nanolubricant seems to have been realized.

Many of the proposed applications of inorganic nanotubes are in their infancy stage and thus they are not expected to reach the marketplace before a decade or so. Recent work has indicated the large impact resistance of WS_2 nanotubes to shockwaves, suggesting numerous applications for nanocomposites formulated with such nanoparticles [133].

One of the most appealing applications of inorganic nanotubes is in the field of cathode material for rechargeable lithium batteries. Two of the most demanding requirements for host material are a large capacity to accommodate significant amounts of the foreign lithium atoms and the reversibility with respect to charge/discharge cycles. Intercalation of the lithium and hydrogen atoms have been accomplished within the van der Waals gap between two layers of the nanotube [138,139]. An extra capacity of the alkali atoms may exist also in the cylindrical hollow core of the nanotube, but the mechanism of charge transfer in this case may be quite different from that of the alkali atoms intercalated between each two layers. The metal atoms in the core may not be in direct contact with the

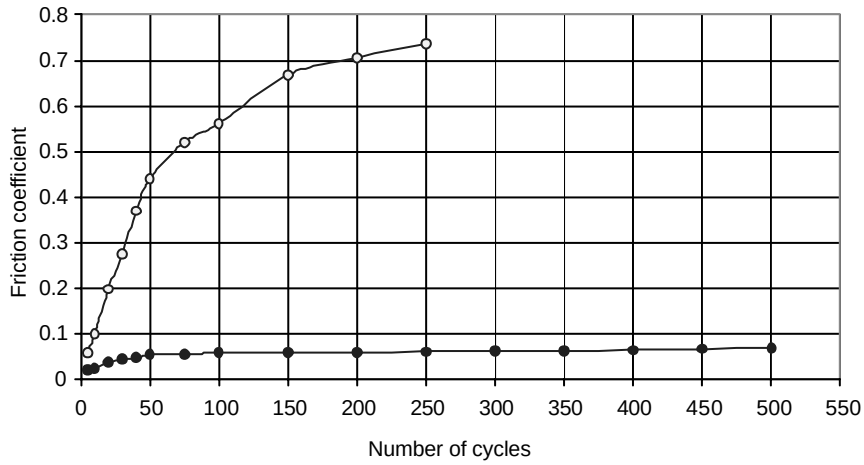

FIGURE 10.11 Friction coefficient vs. number of cycles for alumina Al_2O_3 plat — Si_3N_4 ball pair. Load P = 0.75 N. Open circles — non-lubricated part; full circles — IF lubricated pair.

wall of the nanotube to permit a fast charge transfer from the alkali atoms to the host, and take part in the electrochemical reaction effectively. The other property which makes inorganic nanotubes an intriguing cathode material for rechargeable batteries is their inherent stability, which in general is not common to nanostructured materials. The inherent stability of inorganic nanotubes coupled with their large internal surfaces accessible to small molecules, also suggests that inorganic nanotubes can serve as efficient and selective catalysts, which so far was realized in a few cases only [74,140].

10.5 CONCLUSIONS

Building upon the analogy between the structure of graphite and inorganic layered compounds, nanotubes and fullerene-like nanoparticles of various compounds have been synthesized and investigated in some detail. The versatility in choosing the starting material coupled with the structural complexity of inorganic layered compounds led to numerous intriguing observations, and some important potential applications. Many fundamental issues remain to be addressed; most fundamental among them is the elucidation of the detailed structure of inorganic nanotubes and fullerene-like particles. In order to study the physical properties and chemically modify these nanotubes, macroscopic amounts of the nanotubes must first be synthesized, which in some cases has proved to be an illusive goal. Finally, by careful characterization of these nanophases, new applications may emerge with time.

ACKNOWLEDGMENTS

R.T. is supported by the Helen and Martin Kimmel Center for Nanoscale Science and holds the Drake Family Chair in Nanotechnology. The support of the Israel Science Foundation and "Nanomaterials Ltd." is acknowledged.

REFERENCES

1. Kroto, H.W., Heath, J.R., O'Brien, S.C., Curl, R.F., and Smalley, R.E., C_{60}: Buckminsterfullerene, *Nature*, 318, 162, 1985.
2. Iijima, S., Helical microtubules of graphitic carbon, *Nature*, 354, 56, 1991.
3. Wilson, J.A. and Yoffe A.D., Transition metal dichalcogenides discussion and interpretation of observed optical, electrical and structural properties, *Adv. Phys.* 269, 193–335, 1969.
4. Lévy, F., *Structural Chemistry of Layer-Type Phases*, Vol. 5, D. Reidel, Dordrecht, 1976.
5. Tenne, R., Margulis, L., Genut, M., and Hodes, G., Polyhedral and cylindrical structures of tungsten disulphide, *Nature*, 360, 444, 1992.
6. Margulis, L., Salitra, G., Tenne, R., and Talianker, M., Nested fullerene-like structures, *Nature*, 365, 113, 1993.
7. Rosenfeld, H.Y. et al., Cage structures and nanotubes of $NiCl_2$, *Nature*, 395, 336, 1998.
8. Ajayan, P.M. et al., Carbon nanotubes as removable templates for metal oxide nanocomposites and nanostructures, *Nature*, 375, 564, 1995.
9. Patzke, G.R., Krumeich, F., and Nesper, R., Oxidic nanotubes and nanorods — anisotropic modules for a future nanotechnology, *Angew. Chem. Int. Ed.* 41, 2446, 2002.
10. Chen, Q. et al., Tritanate nanotubes made via a single alkali treatment, *Adv. Mater*., 14, 1208, 2002.
11. Tenne, R., Advances in the synthesis of inorganic nanotubes and fullerene-like nanoparticles, *Angew. Chem. Int. Ed*., 42, 5124, 2003.
12. Nath, M. and Rao, C.N.R., Inorganic nanotubes, *Dalton Trans.*, 1, 1, 2003.
13. Pauling, L., The structure of the chlorites, *Proc. Natl. Acad. Sci*., 16, 578, 1930.
14. Wiegers, G.A. and Meerschut, A., Structures of misfit layer compounds $(MS)_nTS_2$ (MSn, Pb, Bi, rare earth metals; TNb, Ta, Ti, V, Cr; $1.08 < n < 1.23$), *J. Alloys Comp*., 178, 351, 1992.

15. Suzuki, K., Enoki,T., and Imaeda, K., Synthesis, characterization and physical properties of incommensurate layered compounds/$(RES)_xTaS_2$ (RE=Rare earth metal), *Solid State Commun.* 78, 73, 1991.
16. Kresge, C.T. et al., Control of metal radial profiles in alumina supports by carbon-dioxide, *Nature*, 259, 710, 1992.
17. Stöber, W., Fink, A., and Bohn, E., Controlled growth of monodisperse silica spheres in micron size range, *J. Colloid Interf. Sci*., 26, 62, 1968.
18. Nakamura, M. and Matsui, Y., Silica gel nanotubes obtained by the sol–gel method, *J. Am. Chem. Soc*., 117, 2651, 1995.
19. Satishkumar, B.C. et al., Oxide nanotubes prepared using carbon nanotubes as templates, *J. Mater. Res*., 12, 604, 1997.
20. Wu, Q. et al., Synthesis and characterization of faceted hexagonal aluminum nitride nanotubes, *J. Am. Chem. Soc*., 125, 10176, 2003.
21. Sharma, S. and Sunkara, M.K., Direct synthesis of gallium oxide tubes, nanowires, and nanopaintbrushes, *J. Am. Chem. Soc*., 124, 12288, 2002.
22. Chianelli, R.R. et al., Molybdenum disuflide in the poorly crystalline "Rag" structure, *Science*, 203, 1105, 1979.
23. Sanders, J.V., Structure of catalytic particles, *Ultramicroscopy*, 20, 33, 1986; Sanders, J.V., Transmission electron-microscopy of catalysts, *J. Electron Microsc. Tech*., 3, 67, 1986.
24. Feldman, Y. et al., High rate gas phase growth of MoS_2 nested inorganic fullerene-like and nanotubes, *Science*, 267, 222, 1995.
25. Rosentsveig, R., et al., WS_2 nanotube bundles and foils, *Chem. Mater.*, 14, 471, 2002.
26. Coleman, K.S., The formation of ReS_2 inorganic fullerene-like structures containing Re_4 parallelogram units and metal–metal bonds, *J. Am. Chem. Soc*., 124, 11580, 2002.
27. Remskar, M. et al., MoS_2 as micro tubes, *Appl. Phys. Lett*., 69, 351, 1996.
28. Remskar, M. et al., New crystal structures of WS_2: microtubes, ribbons, and ropes, *Adv. Mater*., 10, 246, 1998.
29. Remskar, M. et al., Self-assembly of subnanometer-diameter single-wall MoS_2 nanotubes, *Science*, 292, 479, 2001.
30. Zelenski, C.M. and Dorhout, P.K., Template synthesis of near-monodisperse microscale nanofibers and nanotubules of MoS_2, *J. Am. Chem. Soc*., 120, 734, 1998.
31. Santiago, P., et al., Synthesis and structural determination of twisted MoS_2 nanotubes, *Appl. Phys. A*., 78, 513, 2004.
32. Nath, M. and Rao, C.N.R., New metal disulfide naotubes, *J. Am. Chem. Soc*., 123, 4841, 2001.
33. Nath, M. and Rao, C.N.R., Nanotubes of group 4 metal disulfides, *Angew. Chem. Int. Ed*., 41, 3451, 2002.
34. Hsu, W.K. et al., An alternative route to molybdenum disulfide nanotubes, *J. Am. Chem. Soc*., 122, 10155, 2000.
35. Zhu, Y.Q. et al., Carbon nanotube template promoted growth of NbS_2 nanotubes/nanorods, *Chem. Commun*., 2184, 2001.
36. Brorson, M., Hansen, T.W., Jacobsen, C.J.H., Rhenium(IV) sulfide nanotubes, *J. Am. Chem. Soc*., 124, 11582, 2002.
37. Tsuneta, T. et al., Formation of metallic $NbSe_2$ nanotubes and nanofibers, *Curr. Appl. Phys*., 3, 473, 2003.
38. Afansiev, P. et al., Molybdenum polysulfide hollow microtubules grown at room temperature from solution, *Chem. Comm*., 1001, 2000.
39. Chen, J. et al., Synthesis and characterization of WS_2 nanotubes, *Chem. Mater*., 15, 1012, 2003.
40. Chen, J. et al., Titanium disulfide nanotubes as hydrogen-storage materials, *J. Am. Chem. Soc*., 125, 5284, 2003.
41. Chen J. et al., Electrochemical hydrogen storage in MoS_2 nanotubes, *J. Am. Chem. Soc.*, 123, 11813, 2001.
42. Li, X.L. and Li, Y.D., Formation of MoS_2 inorganic fullerenes (IFs) by the reaction of MoO_3 nanobelts and S, *Chem. Eur. J*., 9, 2726, 2003.
43. Li., Y.D. et al., Artificial lamellar mesostructures to WS_2 nanotubes, *J. Am. Chem. Soc*., 124, 1411, 2002.

44. Zhu, Y.Q. et. al., Production of WS_2 nanotubes, *Chem. Mater*., 12, 1190, 2000.
45. Rothschild, A., Sloan, J., and Tenne, R., The growth of WS_2 nanotubes phases, *J. Am. Chem. Soc*., 122, 5169, 2000.
46. Zhu, Y.Q. et al., An alternative route to NbS_2 nanotubes, *J. Phys. Chem. B*, 106, 7623, 2002.
47. Galvan D.H., Rangel, R. and Adem, E., *Fullerenes Nanotubes Carbon Nanostruct*, 10, 127, 2002.
48. Flores, E. et al., Optimization of the electron irradiation in the production of MoS_2 nanotubes, *Fullerene Sci. Tech*., 9, 9, 2001.
49. Galvan, D.H. et al., Effect of electronic irradiation in the production of $NbSe_2$ nanotubes, *Fullerene Sci. Tech*., 9, 225, 2001.
50. Yacaman, M.J. et al., Studies of MoS_2 structures produced by electron irradiation, *Appl. Phys. Lett*., 69, 1065, 1996.
51. Chhowalla, M. and Amaratunga, G.A.J., Thin films of fullerene-like MoS_2 nanoparticles with ultra-low friction and wear, *Nature*, 407, 164, 2000.
52. Vollath, D. and Szabo, D.V., Nanoparticles from compounds with layered structures, *Acta Mater*., 48, 953, 2000.
53. Avivi, S. et al., Sonochemical hydrolysis of Ga^{3+} ions: synthesis of scroll-like cylindrical nanoparticles of gallium oxide hydroxide, *J. Am. Chem. Soc*., 121, 4196, 1999.
54. Hong, S.Y. et al., Synthesis of SnS_2/SnS fullerene-like nanoparticles: a superlattice with polyhedral shape, *J. Am. Chem. Soc*., 125, 10470, 2003.
55. Parilla, P.A. et al., The first inorganic fullerenes, *Nature*, 397, 114, 1999.
56. Sen, R. et al., Encapsulated and hollow closed-cage structures of WS_2 and MoS_2 prepared by laser ablation at 450–1050°C, *Chem. Phys. Lett*., 340, 242, 2001.
57. Rosenfeld, H.Y. et al., Synthesis of $NiCl_2$ nanotubes and fullerene-like structures by laser ablation *Phys. Chem. Phys*., 5, 1644, 2003.
58. Hamilton, E.J.M. et al., Preparation of amorphous boron-nitride and its conversion to a turbostratic, tubular form, *Science*, 260, 659, 1993.
59. Chopra, N.G. et al., Boron-nitride nanotubes, *Science*, 269, 966, 1995.
60. Gleize, P. et al., Growth of tubular boron-nitride filaments, *J. Mater. Sci*., 29, 1575, 1994.
61. Lourie, O.R. et al., CVD growth of boron nitride nanotubes, *Chem. Mater*., 12, 1808, 2000.
62. Ma, R., Bando, Y., and Sato, T., CVD synthesis of boron nitride nanotubes without metal catalysts, *Chem. Phys. Lett*., 337, 61, 2001.
63. Cumings, J. and Zettl, A., Mass-production of boron nitride double-wall nanotubes and nanococoons, *Chem. Phys. Lett*., 316, 211, 2000.
64. Terrones, M. et al., Production and state-of-the-art characterization of aligned nanotubes with homogeneous BC_xN ($1 <= x <= 5$) compositions, *Adv. Mater*., 15, 1899, 2003.
65. Suenaga, K. et al., Synthesis of nanoparticles and nanotubes with well-separated layers of boron nitride and carbon, *Science*, 278, 653, 1997.
66. Hultman, L. et al., Cross-linked nano-onions of carbon nitride in the solid phase: existence of a novel $C_{48}N_{12}$ aza-fullerene, *Phys. Rev. Lett*., 87, 225503, 2001.
67. Rao, C.N.R. et al., Surfactant-assisted synthesis of semiconductor nanotubes and nanowires, *Appl. Phys Lett*., 78, 1853, 2001.
68. Imai, H. et al., Direct preparation of anatase TiO_2 nanotubes in porous alumina membranes, *J. Mater. Chem*., 9, 2971, 1999.
69. Kasuga, T. et al., Formation of titanium oxide nanotube, *Langmuir*, 14, 3160, 1998.
70. Kasuga, T. et al., Titania nanotubes prepared by chemical processing, *Adv. Mater*., 11, 1307, 1999.
71. Sun, X. and Li, Y.D., Synthesis and characterization of ion-exchangeable titanate nanotubes, *Chem. Eur. J*., 9, 2229, 2003.
72. Zhang, S. et al., Formation mechanism of $H_2Ti_3O_7$ nanotubes, *Phys. Rev. Lett*., 91, 256103, 2003.
73. Saupe, G.B. et al., Nanoscale tubules formed by exfoliation of potassium hexaniobate, *Chem. Mater.*, 12, 1556, 2000.
74. Wang, X. et al., Thermally stable silicate nanotubes, *Angew. Chem. Int. Ed*., 43, 2017, 2004.
75. Wang, X., and Li, Y.D., Rational synthetic strategy. From layered structure to MnO_2 nanotubes, *Chem. Lett*., 33, 48, 2004.

76. Wang, X. and Li, Y.D., Rare-earth-compound nanowires, nanotubes, and fullerene-like nanoparticles: synthesis, characterization, and properties, *Chem. Eur. J.*, 9, 5627, 2003.
77. Mao, Y., Banerjee, S. and Wong, S.S., Hydrothermal synthesis of perovskite nanotubes, *Chem. Commun.*, 408, 2003.
78. Avivi, S., Mastai, Y. and Gednaken, A., A new fullerene-like inorganic compound fabricated by the sonolysis of an aqueous solution of $TlCl_3$, *J. Am. Chem. Soc.*, 2000, 122, 4331.
79. Zhang, W., Single-crystalline scroll-type nanotube arrays of copper hydroxide synthesized at room temperature, *Adv. Mater.*, 15, 822, 2003.
80. Li, Y., Bando, Y. and Golberg, D., Single-crystalline In_2O_3 nanotubes filled with In, *Adv. Mater.*, 15, 581, 2003.
81. Ma, R. et al., Magnesium borate nanotubes, *Angew. Chem. Int. Ed.*, 42, 1836, 2003.
82. Mayers, B. and Xia, Y., Formation of tellurium nanotubes through concentration depletion at the surfaces of seeds, *Adv. Mater.*, 14, 279, 2002.
83. Li, X.-Y. et al., Synthesis and magnetoresistance measurement of tellurium microtubes, *J. Mater. Chem.*, 14, 244, 2004.
84. Zhang, H. et al., Selenium nanotubes synthesized by a novel solution phase approach, *J. Phys. Chem. B*, 108, 1179, 2004.
85. Liu, X. et al., Novel bismuth nanotube arrays synthesized by solvothermal method, *Chem. Phys. Lett.*, 374, 348, 2003; Li, Y.D. et al., Bismuth nanotubes: a rational low-temperature synthetic route, *J. Am. Chem. Soc.*, 123, 9904, 2001.
86. Yang, B. et al., A room-temperature route to bismuth nanotube arrays, *Eur. J. Inorg. Chem.*, 3699, 2003.
87. Hu, H. et al., A rational complexing-reduction route to antimony nanotubes, *New J. Chem.*, 27, 1161, 2003.
88. Hollingsworth, J.A. et al., Catalyzed growth of a metastable InS crystal structure as colloidal crystals, *J. Am. Chem. Soc.*, 122, 3562, 2000.
89. Goldberger, J. et al., Single-crystal gallium nitride nanotubes, *Nature*, 422, 529, 2003.
90. Blasé, X. et al., Stability and band-gap constancy of boron-nitride nanotubes, *Europhys. Lett.*, 28, 335, 1994.
91. Miyamoto, Y. et al., Chiral tubules of hexagonal BC_2N, *Phys. Rev. B*, 50, 4976, 1994.
92. Miyamoto, Y. et al., Electronic-properties of tubule forms of hexagonal BC_3, *Phys. Rev. B*, 50, 18630, 1994.
93. Cote, M., Cohen., M.L., and Chadi, D.J., Theoretical study of the structural and electronic properties of GaSe nanotubes, *Phys. Rev. B*, 58, R4277, 1998.
94. Seifert, G. et al., On the electronic structure of WS_2 nanotubes, *Solid State Commun.*, 114, 245, 2000.
95. Seifert, G. et al., structure and electronic properties of MoS_2 nanotubes, *Phys. Rev. Lett.*, 85, 146, 2000.
96. Seifert, G. et al., Novel NbS_2 metallic nanotubes, *Solid State Commun.*, 115, 635, 2000.
97. Ivanovskaya, V.V. and Seifert, G., Tubular structures of titanium disulfide TiS_2, *Solid State Commun.*, 130, 175, 2004.
98. Ivanovskaya, V.V. et al., Electronic properties of superconducting $NbSe_2$ nanotubes, *Phys. Stat. Sol.*, 238, R1, 2003a.
99. Ivanovskya, V.V. et al., Computational studies of electronic properties of ZrS_2 nanotubes, *Internet Electron J. Mol. Des.*, 2, 499, 2003b.
100. Verstraete, M. and Charlier, J.-C., *Ab initio* study of MoS_2 nanotube bundles, *Phys. Rev. B*, 68, 045423, 2003.
101. Seifert, G., Köhller and Tenne, R, Stability of metal chalcogenide nanotubes, *J. Phys. Chem. B*, 106, 2497, 2002.
102. Scheffer, L. et al., Scanning tunneling microscopy study of WS_2 nanotubes, *Phys. Chem. Chem. Phys.*, 4, 2095, 2002.
103. Enyashin, A.N. et al., Structure and electronic spectrum of fullerene-like nanoclusters based on Mo, Nb, Zr, and Sn disulfides, *Inorg. Mater.*, 40, 395, 2004.
104. Shein, I.R., et al., Electronic properties of new $Ca(Al_xSi_{1-x})_2$ and $Sr(Ga_xSi_{1-x})_2$ superconductors in crystalline and nanotubular states, *JETP Lett.*, 76, 189, 2002.

105. Gemming, S. and Seifert, G., Nanotube bundles from calcium disilicide: a density functional theory study, *Phys. Rev. B*, 68, 75416, 2003.
106. Ivanovskya, V.V. et al., Electronic properties of single-walled V_2O_5 nanotubes, *Solid State Commun*., 126, 489, 2003.
107. Enyashin, A.N., Makurin, Yu.N. and Ivanovskii, A.L., Electronic band structure of β-ZrNCl-based nanotubes, *Chem. Phys. Lett*., 387, 85, 2004.
108. Boustani, I. and Quandt, A., Nanotubules of bare boron clusters: *Ab initio* and density functional study *Europhys. Lett*., 39, 527, 1997.
109. Boustani, I. et al., New boron based nanostructured materials, *J. Chem. Phys*., 110, 3176, 1999.
110. Gindulyte, A., Lipscomb, W.N., and Massa, L., Proposed boron nanotubes, *Inorg. Chem*., 37, 6544, 1998.
111. Quandt, A., Liu, A.Y., and Boustani, I., Density-functional calculations for prototype metal-boron nanotubes, *Phys. Rev. B*, 64, 125422, 2001.
112. Su, C., Liu, H.T. and Li, J.M., Bismuth nanotubes: potential semiconducting nanomaterials, *Nanotechnology*, 13, 746, 2002.
113. Ivanovskii, A.L., Band structure and properties of superconducting MgB_2 and related compounds (a Review), *Phys. Solid State*, 45, 1829, 2003.
114. Chernozatonskii, L.A., Diboridebifullerenes and binano tubes, *JETP Lett*., 74, 335, 2001.
115. Guerini, S. and Piquini, P., Theoretical investigation of TiB_2 nanotubes, *Microelectron. J*., 34, 495, 2003.
116. Ivanovskaya, V.V. et al., Electronic properties of single-walled V_2O_5 nanotubes, *Solid State Commun*., 126, 489, 2003.
117. Seifert, G. and Hernandez, E., Theoretical prediction of phosphorus nanotubes, *Chem. Phys. Lett*., 318, 355, 2000.
118. Seifert, G., Heine, T. and Fowler, P.W., Inorganic nanotubes and fullerenes. Structure and properties of hypothetical phosphorus fullerenes, *Eur. Phys. J. D*, 16, 341, 2001.
119. Cabria, I. and Mintmire, J.W., Stability and electronic structure of phosphorus nanotubes, *Euro Phys. Lett*., 65, 82, 2004.
120. Lee, S.M. et al., Stability and electronic structure of GaN nanotubes from density-functional calculations, *Phys. Rev. B*, 60, 7788, 1999.
121. Zhao, M., et al., Stability and electronic structure of AlN nanotubes, *Phys. Rev*., *B*, 68, 235415, 2003.
122. Chang, Ch. et al., Computational evidence for stable fullerene-like structures of ceramic and semiconductor materials, *Chem. Phys. Lett*., 350, 399, 2001.
123. Zhang, D. and Zhang, R.Q., Theoretical predictions on inorganic nanotubes, *Chem. Phys. Lett*., 371, 426, 2003.
124. Erkoc, S., Semi-empirical SCF-MO calculations for the structural and electronic properties of single-wall InP nanotubes, *J. Mol. Struct.* (*Thermochem*.), 676, 109, 2004.
125. Srolovitz, D.J. et al., Relaxed curvature elasticity and morphology of nested fullerenes, *Phys. Rev. Lett*., 74, 1779, 1995.
126. Tenne, R., Doped and heteroatom fullerene-like structures and nanotubes, *Adv. Mater*., 7, 965, 1995.
127. Parilla, P.A., et al., Formation of nanooctahedra in molybdenum disulfide and molybdenum diselenide using pulsed laser vaporization, *J. Phys. Chem*., *B*, 108, 6197, 2004.
128. Rapoport, L. et al., Hollow nanoparticles of WS_2 as potential solid-state lubricants, *Nature*, 387, 791, 1997.
129. Rapoprt, L., Fleishcer, N., and Tenne, R., Fullerene-like WS_2 nanoparticles: superior lubricants for harsh conditions, *Adv. Mater*., 15, 651, 2003.
130. Chen, W.X. et al., Wear and friction of NiP electroless composite coating including inorganic fullerene-like WS_2 nanoparticles, *Adv. Eng. Mater*., 4, 686, 2002.
131. Rapoport, L. et al., Polymer nanocomposites with fullerene-like solid lubricant, *Adv. Eng. Mater*., 6, 44, 2004.
132. Rapoport, L. et al., Slow release of fullerene-like WS_2 nanoparticles from Fe–Ni–graphite matrix: a self-lubricating nanocomposite, *Nanoletters*, 1, 137, 2001.
133. Zhu, Y.Q. et al., WS_2 nanotubes: shockwave resistance, *J. Am. Chem. Soc*., 125, 1329, 2003.
134. Zhang, W. et al., Use of functionalized WS_2 nanotubes to produce new polystyrene/polymethylmethacrylate nanocomposites, *Polymer*., 44, 2109, 2003.

135. Kaplan-Ashiri, I. et al., Mechanical behavior of WS_2 nanotubes, *J. Mater. Res*., 19, 454, 2004.
136. Kis, A. et al., Shear and Young's moduli of MoS_2 nanotube ropes, *Adv. Mater*., 15, 733, 2003.
137. Dominko, R. et al., Electrochemical preparation and characterisation of Li_2MoS_{2-x} nanotubes, *Electrochim. Acta*, 48, 3079, 2003.
138. Chen, J., Tao, Z.L., and Li, S.L., Lithium intercalation in open-ended TiS_2 nanotubes, *Angew. Chim. Int. Ed*., 42, 2147, 2003.
139. Chen, J., Li, S.L., and Tao, Z.L., Novel hydrogen storage properties of MoS_2 nanotubes, *J. Alloys Comp*., 356, 413, 2003.
140. Chen, J. et al., Synthesis of open-ended MoS_2 nanotubes and the application as the catalyst of methanation, *Chem. Commun*., 1722, 2002.
141. Nemanic, V. et al., Field-emission properties of molybdenum disulfide nanotubes, *Appl. Phys. Lett*., 82, 4573, 2003.
142. Chopra, N.G. and Zettl, A., Measurement of the elastic modulus of a multi-wall boron nitride nanotube, *Solid State Commun*., 105, 297, 1998.
143. Suryavanshi, A.P., et al., Elastic modulus and resonance behavior of boron nitride nanotubes, *Appl. Phys. Lett*., 84, 2527, 2004.
144. Tang, C., et al., Catalyzed collapse and enhanced hydrogen storage of BN nanotubes, *J. Am. Chem. Soc*., 124, 14550, 2002.
145. Dorozhkin, P., et al., Field emission from individual B–C–N nanotube rope, *Appl. Phys. Lett*., 81, 1083, 2002.
146. Spahr, M.E. et al., Vanadium oxide nanotubes a new nanostructured redox-active material for the electrochemical insertion of lithium, *J. Electrochem. Soc*., 146, 2780, 1999.
147. Nordlinder, S., Edström, K., and Gustafsson, T., The performance of vanadium oxide nanorolls as cathode material in a rechargeable lithium battery, *Electrochem. Solid-State Lett*., 4, A129, 2001.
148. Manganese vanadium oxide nanotubes: synthesis, characterization, and electrochemistry, *Chem. Mater*., 13, 4382, 2001.
149. Xu, J.F. et al., Nonlinear optical transmission in VO_x nanotubes and VO_x nanotube composites, *Appl. Phys. Lett*., 81, 1711, 2002.
150. Wang, X. et al., Thermally stable silicate nanotubes, *Angew. Chem. Int. Ed*., 43, 2017, 2004.
151. Adachi, M. et al., Formation of titania nanotubes and applications for dye-sensitized solar cells, *J. Electrochem. Soc*., 150, G488, 2003.
152. Wu, C. et al., Photoluminescence from surfactant-assembled Y_2O_3: Eu nanotubes, *Appl. Phys. Lett*., 82, 520, 2003.
153. Feldman, Y. et al., New reactor for production of tungsten disulfide onion-like (inorganic fullerene-like) nanoparticles, *Solid State Sci*., 2, 663, 2000.

11 Boron Nitride Nanotubes: Synthesis and Structure

Hongzhou Zhang and Ying Chen
Department of Electronic Materials Engineering,
Research School of Physical Sciences and Engineering,
The Australian National University, Canberra, Australia

CONTENTS

ABSTRACT

This chapter discusses the structure and major synthesis methods of boron nitride nanotubes (BNNTs). Structure and chiralities of BNNTs are introduced from the standpoint of curling up hexagonal boron nitride (h-BN) sheets into nanosized cylinders, and are compared with carbon nanotubes (CNTs). Major synthesis methods including arc-discharge, laser, ball milling-annealing, carbon substitutions and chemical vapor deposition (CVD) have been reviewed. The recent successful synthesis of high yield and large quantities of BNNTs will lead to significant application progresses.

11.1 INTRODUCTION

After the discovery of carbon nanotubes (CNTs) in 1991 [1], researchers immediately started to seek other materials that have the same tubular structure. Boron nitride (BN) is one of them, and NTs in BN were first theoretically predicted in 1994 [2], and subsequently synthesized successfully

in 1995 by Zettl's group at University of California, Berkeley [3]. Like CNTs, BNNTs too have superstrong mechanical properties, because of their tubular structure and the strong sp^2 bonding within a tube layer. The upper range of theoretical estimates of the elastic modulus of BNNTs is ~850 GPa, about 80% that of CNTs [4,5]. Experimental results demonstrate a distinct mechanical property with the measured modulus in the range of ~722 GPa to 1.22 Tpa [6,7], which is comparable with that of CNTs. In addition to these useful properties, which are similar to those of CNTs, BNNTs have several other useful properties, and in some parameters, are even better than CNTs. For example, theoretical studies suggest that BNNTs are insulating materials with a uniform electronic band gap of about 5.5 eV [2,8], which is independent of either the diameter or chirality of an NT. Therefore, all BNNTs show insulating or semiconducting behavior in electrical conductance measurements [9,10]. On the other hand, most CNT samples synthesized currently consist of both conducting and semiconducting NTs, and it is quite difficult to separate them. Boron nitride nanotubes also exhibit more stable chemical properties — for instance, they have a much stronger resistance to oxidation at elevated temperatures [11,12]. Boron nitride nanotubes synthesized using a ball-milling annealing method can be oxidized only at over 800°C. Some BNNTs with perfect nanocrystalline structures can withstand temperatures of up to 900°C, while CNTs are readily oxidized in air at a temperature of 400°C, and burned completely at 700°C when sufficient oxygen is supplied [12]. Owing to the high resistance to oxidation, BNNTs are ideal for composite material applications.

Though BNNTs have such promising properties when compared with CNTs, several of their properties, such as energy storage [13–15], optical [16], piezoelectricity and electrical-polarization effects [5,16,17], field emission [10], and so on, have not yet been adequately studied. To explore BNNTs' properties and applications, a sufficient amount of high yield BNNT samples is essential. This was not possible until recently because the synthesis methods known till recently did not give the requisite yields. A large number of methods for BNNT synthesis have been documented hitherto, and in recent years, a significant progress has been achieved. This chapter first provides a brief introduction of BNNT structures, which will help in understanding the process of the formation of BNNTs. Following this, it presents a literature review on major synthesis methods reported from 1995 to 2004.

11.2 STRUCTURES OF BORON NITRIDE NANOTUBES

Boron nitride nanotubes can be regarded as wrapped hexagonal BN (h-BN) sheets from the standpoint of their structure — the simplest way to construct a NT. It is thus helpful to start from the discussion of the structures of bulk BN. Bulk BN exhibits polymorphism in its crystalline structures and has at least four different crystallographic forms: hexagonal (h-BN), rhombohedra (r-BN), cubic (c-BN), and wurtzite (w-BN) structures. Interestingly, bulk C also has four similar corresponding structures — this stems from the fact that BN and C are isoelectronic substances, with the same average number of valence electrons per atom. However, in this section, only h-BN will be discussed, because the layered structure of h-BN is the key to understanding BNNT structures. The similar and different aspects of h-BN and carbon graphite structures will also be presented. Some geometric quantities of BNNTs such as chirality will be defined in this section. Finally, typical transmission electron microscopy (TEM) experimental results of BNNT structures will be discussed briefly.

11.2.1 Hexagonal Boron Nitride

The ball-stick model of h-BN structure is illustrated in Figure 11.1. The model shows four coordinated layers (or sheets) of threefold hexagonal networks stacked together and forming the h-BN structure. The hexagonal layers are generally referred to as basal planes. The flat basal planes consist only of hexagon rings, built with strong sp^2 bonds between B and N atoms. Between basal

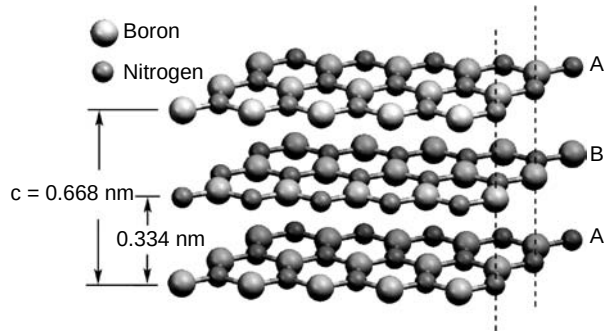

FIGURE 11.1 Crystal structure of h-BN. Large and small balls represent boron and nitrogen atoms, respectively. The lattice constant of c_0 is 0.668 nm. Along the *c*-direction, B and N atoms alternate in adjacent basal planes, thus forming a stacking sequence of ABAB…

planes, much weaker Van der Waals interactions operate to keep them together in certain coordination to form a three-dimensional structure. As shown in Figure 11.1, a boron atom in one layer is directly over an nitrogen atom in the adjacent layers, i.e., along the *c*-axis, B and N atoms alternate. The adjacent layers are thus distinguished from each other and exhibit an ABAB… stacking sequence. h-BN hence has a $P6_3mmc$ symmetry. The distance between adjacent basal planes of h-BN is $d = 3.34$ Å, while the lattice constant along the *c*-direction should be $2d = 6.68$ Å.

11.2.2 Boron Nitride Nanotube Structure

Single-walled nanotubes (SWNTs) can be regarded as a seamlessly wrapped mono-atomic sheet of hexagonal networks. Multiwalled nanotubes (MWNTs) are several such tubulars concentrically organized and nested into each other. As with CNTs, there are many different ways to wrap BN basal planes and, consequently, the NTs exhibit different diameters and chiralities, which will be discussed in this section.

To construct an SWNT, a sheet of hexagonal network can be curled up so that a selected lattice point in the network is superposed on a predefined origin. For example, the predefined origin (0, 0) is labeled "O" and the other lattice point A (12,6) is selected as shown in Figure 11.2(a). As to the indices of the lattice points, i.e., (*n*, *m*), a crystallographic convention is adopted. The inter-angle between basis vectors is 120° as shown in Figure 11.2(a). The NT formed by bringing point O to A is shown in Figure 11.2(b). The NT can be named after the indices of lattice point A; thus a (12, 6) BNNT is shown in Figure 11.2(b). The following geometric relation of the tubular structure is obvious but it is still worth pointing out: the length of OA equals the perimeter of the NT, and the axis of the NT is along the direction of OA′.

We do not distinguish h-BN and carbon graphite in the above discussion. This is because the graphite and h-BN have the same symmetry, and the wrapping operation depends solely on the symmetry of the hexagonal network. In the case of graphite, two kinds of carbon atoms exist in a single graphite sheet, with their adjacent atoms in different geometric relationships; for example, the atoms at points O and O′ (see Figure 11.2[a], disregarding the difference of species between B and N atoms, the schematic picture of a BN sheet shown in Figure 11.2[a] is similar to a carbon graphitic sheet). Two adjacent carbon atoms (O and O′) form a pair, and these pairs are fixed on the hexagonal Bravais lattice, which exhibits the required symmetry for the curling-up operation, i.e., these two kinds of carbon atoms can never be superimposed to form a tube. In the case of h-BN, geometrically, two atoms (B and N) play the same roles as the two types of carbon atoms play in a graphite sheet. Therefore, we cannot superimpose a boron atom with a nitrogen atom, which also means that, theoretically, by curling up an h-BN sheet to construct a perfect tubular structure, a homo-atomic bonding (B–B or N–N) is impossible. There are infinite ways to roll up a sheet into

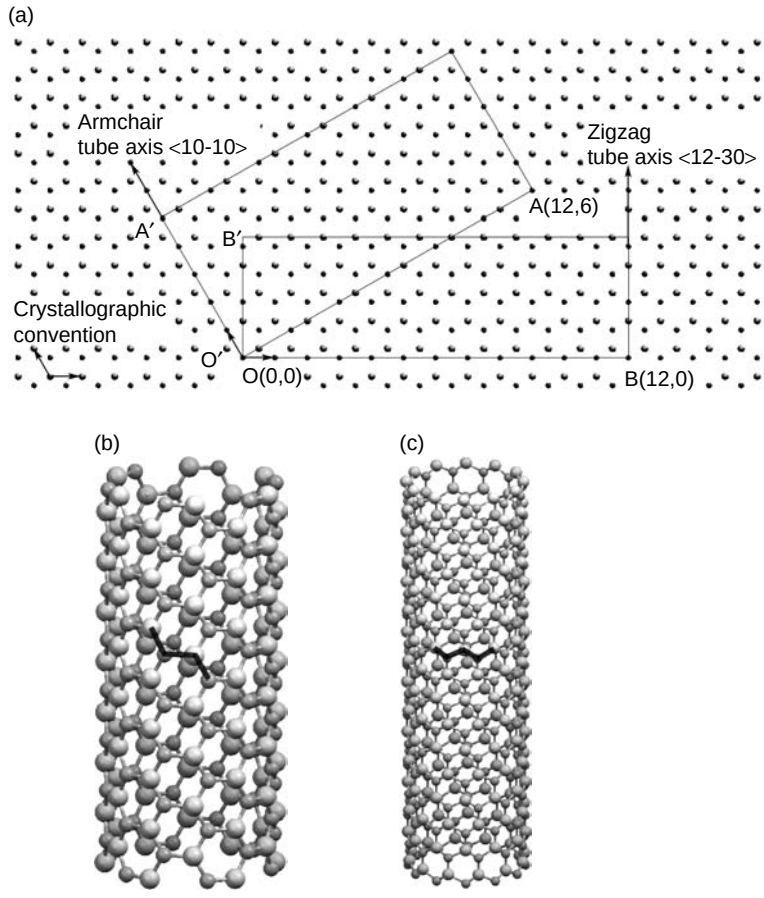

FIGURE 11.2 (a) Atom configuration of h-BN basal plane. The lattice constant of a_0 is 0.252 nm. For crystallographic convention, the inter-angle between the basis vectors is 120°. By wrapping the basal plane and superimposing lattice point A(12,6) with origin O, an armchair tube, as shown in (b), can be constructed. Point B(12,0) hence corresponds to a zigzag tube shown in (c). The black lines in (b) and (c) indicate the armchair and zigzag shapes, respectively.

an NT with different atomic configurations, though some duplicate cases and mirror-symmetric equivalents can be ruled out by symmetry considerations. By defining the chirality angle of an NT as the angle between the zigzag edge (shown in Figure 11.2[a]) and the tube perimeter (OA in Figure 11.2[a]), different ways of rolling result in NTs with different chirality angles. Two configurations of NTs are special: the NT shown in Figure 11.2(b) is the so-called armchair NT, since we can liken the configuration of the atoms (see bold lines) to an armchair. All (2*n*, *n*) NTs, where *n* is a positive integer, are armchair-type NTs. Similarly, NTs with (*n*, 0) indices are zigzag. A (12,0) zigzag NT is shown in Figure 11.2(c), which corresponds to the lattice point B in Figure 11.2(a) in the sense of curling up the basal plane.

There is no essential difference between BNNTs and CNTs as far as wall structures or configuration are concerned. However, there are differences in their tip morphologies. An SW CNT is generally considered to be capped by a half-fullerene molecule (C60) consisting of six-membered hexagons and five-membered pentagons, and thus CNTs have typical cone-shape tips [18]. Most BNNTs have flat tips as shown in Figure 11.3, which are formed with four-membered squares instead of five-membered pentagons [19]. Theoretical investigations reveal that five-membered pentagons in BN would require energetically unfavorable B–B or N–N bonds that destabilize the structure [20].

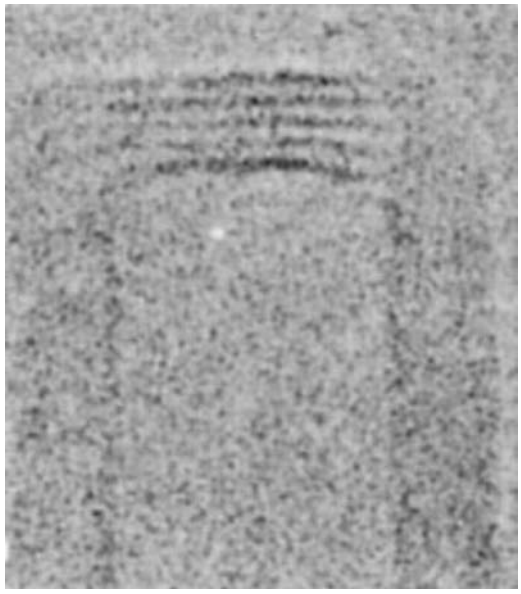

FIGURE 11.3 A typical flat tip of BNNTs. (From Loiseau, A. et al., *Carbon*, 36, 743–752, 1998. Reproduced with permission from *Elsevier Science*.)

In addition to typical straight parallel-walled cylindrical tubes, bamboo and cone-like BNNTs can also be produced [21]. Moreover, BNNTs can also be filled with metals (Fe, Ni, W, …) and buckyballs [22]; BN sheath can also be coated on the surface of CNTs [23].

In the following section, chirality of straight and hollow BNNT will be introduced.

11.2.3 Transmission Electron Microscopy Studies of Boron Nitride Nanotube Chirality

From the above discussion, we know that by determining the chirality and diameter of an SWNT, its atomic configuration is determined completely. Transmission electron microscopy is an indispensable tool for measuring the diameter and chirality of NTs. While diameter measurement is straightforward, the determination of BNNT chirality is not a trivial job. Electron diffraction (ED) has been used to elucidate the helical structures of both CNTs and BNNTs [19,24–28]. The other complementary method within TEM for measuring NT chirality is high-resolution TEM [29–31]. In addition to TEM, any measurement that can reach atomic resolution with the scales of NTs can discern the chirality of CNTs — for example, scanning tunneling microscopy or atomic force microscopy [32,33]. In this section, basic knowledge of ED of NTs is first illustrated briefly. Then we will introduce some of the experimental work on BNNT chirality.

The theory of ED, and thorough reviews can be found in some distinguished review articles [22,24,25]. Instead of trying to go through the diffraction theories strictly and systematically, here we have tried to give a simple picture of the ED of thin NTs. For an MWNT, with its tube axis perpendicular to the incidence beam as shown in Figure 11.4(a), the top and bottom walls of the NT are perpendicular to the incidence beam, i.e., the electron beam is along the 0002 direction of these parts of the NT (in the *z*-axis direction). Hence, the top and bottom basal planes of the NT will result in a diffraction pattern like the two-dimensional reciprocal lattice shown in Figure 11.4(b). If the walls of the NT are aligned to each other, a simple diffraction pattern is expected; otherwise the 10−10 diffraction spots of each wall (even the top and bottom layers of a single wall) may split, which is the case of helical NTs or the walls of MWNTs with different chiralities. On the other hand, the sidewalls of the NT shown in Figure 11.4(a) are parallel to the incidence beam, i.e., the

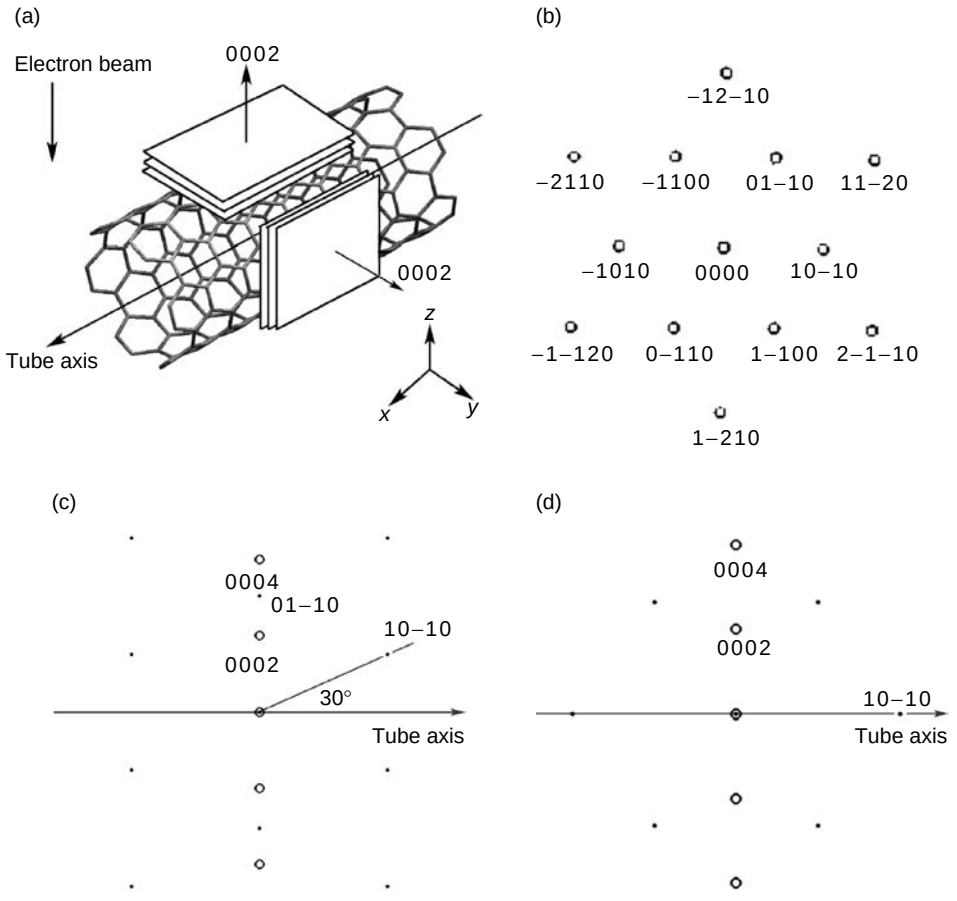

FIGURE 11.4 (a) Electron diffraction of MWNTs. The innermost layer is shown as a hexagonal network, and the outer layers are represented by the flat sheets. Tube walls normal to the incident electron beam generate diffraction patterns as shown in (b), which are also shown as solid dots in (c) and (d). Tube walls oriented edge-on to the incident electron beam display a row of (000*l*) spots, shown as open circles in (c) and (d). (c) and (d) are diffraction patterns of armchair and zigzag tubes, respectively.

0002 direction of these parts of the NT is along the *y*-axis direction. The electron beam incidences along some direction in the basal planes. The significant diffraction spots of such a configuration are 0002 spots, which are perpendicular to the tube axis — this is because the stacking of the walls is perpendicular to the tube axis. We can now draw a schematic picture of the diffraction patterns of an armchair and zigzag NTs — shown in Figures 11.4(c) and (d), respectively. The open circles in these pictures are the diffraction spots from the sidewalls, and the small dots are from the top and bottom walls. In detail, the schematic picture of the diffraction patterns is constructed as follows: (1) we draw the 0002 diffraction spots, which can determine the tube axis; (2) along the tube axis, in real space, the crystallographic direction is 10 −10 for an armchair NT. In reciprocal space, the corresponding direction of 10 −10 is along a direction with a 30° inter-angle between its real space counterparts. The angle between 10 −10 diffraction spot and the tube axis is thus 30°, which is an indicator for the identification of an armchair NT. The same analysis applies to zigzag tubes and results in the pattern shown in Figure 11.4(d). The characteristic of a zigzag diffraction pattern is that the 10 −10 diffraction spot is along the tube axis, i.e., perpendicular to the direction of the 0002 diffraction spots. It is worth clarifying that if one claims that the tube axis of a zigzag tube is along

10 –10, it means that the indices are in the reciprocal space; correspondingly, the very same direction in the real space is 12 –30.

In practice, nanobeam diffraction (NBD) technique is usually conducted to investigate the chirality of NTs [34]. The chiralities of BNNTs have been investigated by several research groups. It seems that different chiralities were obtained from BNNTs prepared through different growth methods. For the BNNTs produced by arc-discharge method using HfB_2 as the electrode [19], diffraction patterns from two as-grown NTs suggest either chiral or nonchiral, however, a preference toward nonchiral is suggested. Compared with Figures 11.4(c) and (d), Figure 11.5(A) is an armchair and Figure 11.5(B) is a zigzag [19]. For a given NT, the distribution peak of helicities of its walls is always close to either 0, i.e., armchair, or 30, i.e., zigzag, with a rather small dispersion of ~10.

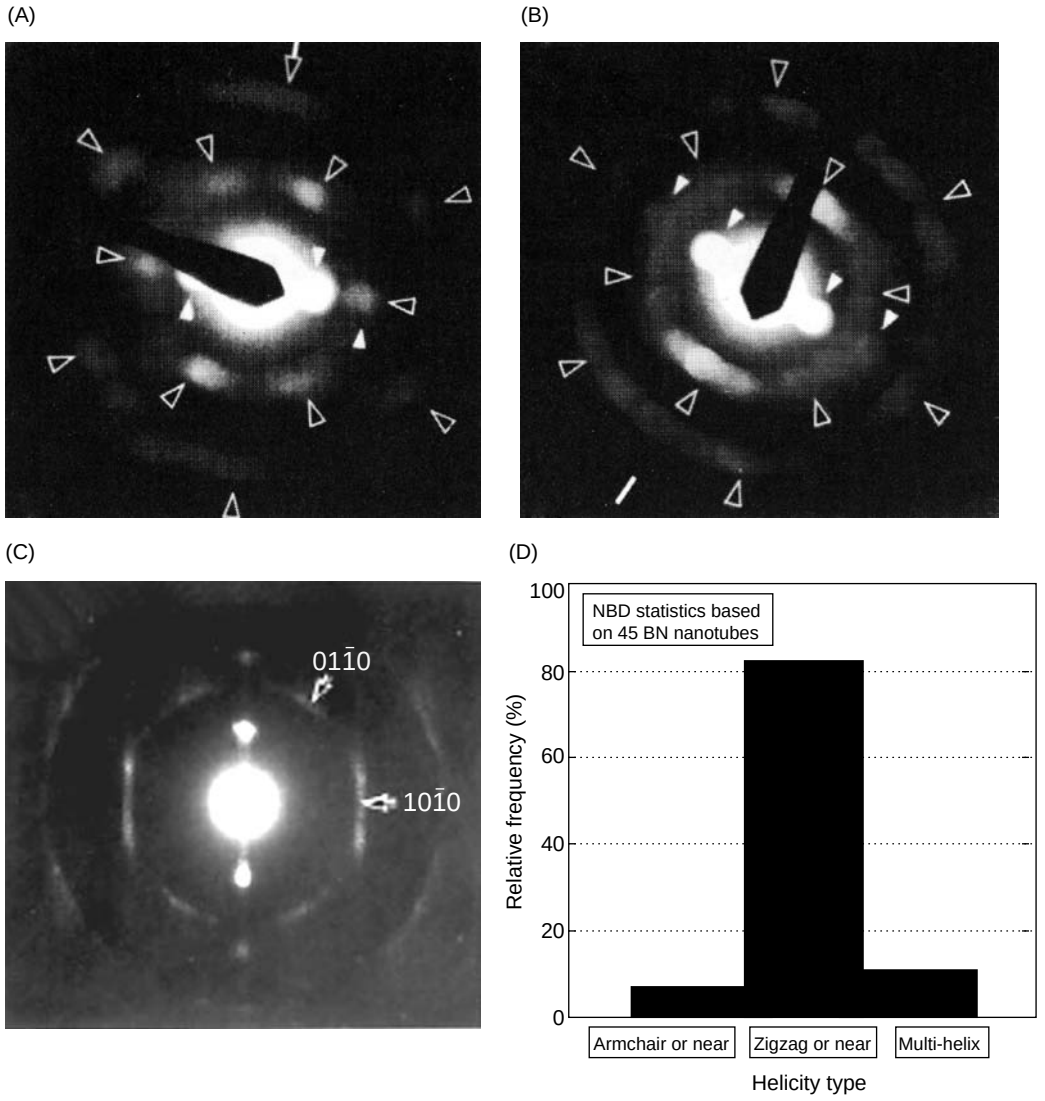

FIGURE 11.5 Electron diffraction patterns from individual BNNTs exhibiting armchair (A) and zigzag (B) configurations (From Loiseau, A. et al., *Carbon*, 36, 743–752, 1998.) (C) A characteristic NBD pattern taken from a rope of zigzag BNNTs, and the histogram (D) shows the preference of zigzag orientation. (From Golberg, D. et al., *Solid State Commn.*, 116, 1–6, 2000. Reproduced with permission from *Elsevier Science.*)

In Golberg's [27,31] work, the zigzag type of BNNTs is overwhelming. An NBD pattern of the sample is shown in Figure 11.5(C), and the distribution of the NT chirality is shown in Figure 11.5(D). Besides different tip morphologies, it is believed that the second major difference between the structures of BNNTs and CNTs is that dominant BNNT structures are zigzag tubes. Armchair and chiral tubes are fewer, possibly due to the special tip configurations [35], while CNTs with zigzag, armchair, and chiral structures are all particularly abundant.

To conclude the discussion on BNNT structure, the preferences of both their flat tips and the achiral configurations should be stressed, which could be a characteristic of BNNTs. However, the tips of BNNTs could also be cone-like [36], open [37], and flag-like [38]. Although pentagons or heptagons can result in homogeneous bonding (B–B or N–N), which is energy unfavorable [2], these multimorphology tips and the bending of BNNTs indicate the existence of these rings [31]. Different chiralities of BNNTs have been observed, and the preference of specific chirality may depend on the growth technique employed. As pointed by Golberg [26], BNNTs grown directly from the vapor phase frequently have armchair configuration, while those grown from laser-heating and carbon substituted methods, are zigzag-dominant type [26,39]. The formation of achiral BNNTs, either armchair or zigzag, is probably a consequence of the so-called lip–lip interaction during the NT growth, which induces a correlation between the chiralities of adjacent layers and selects the growth of particular pairs of tubes [20]. It is definite that the growth method affects the morphologies of BNNTs. In the following section, we will review the major synthesis methods developed since the discovery of BNNTs.

11.3 SYNTHESIS METHODS OF BORON NITRIDE NANOTUBES

The growth of BNNTs involves the formation of boron and nitrogen hexagon networks curled up to seamless tubular forms as discussed in the previous section. This is directly related to the rearrangement of boron and nitrogen atoms via nitriding chemical reactions. To make the rearrangement possible and efficient, atomic scale boron and nitrogen clusters need to be first generated, which requires a significant amount of energy to be supplied. Different forms of energy can be exploited to fulfill this task, and the growth methods can then be coarsely classified according to the types of energy supplied. In this section, we will discuss most successful growth methods reported so far.

11.3.1 Arc Discharge and Arc Melting

Pure BNNTs, like their carbon counterparts [1], were first fabricated by using arc-discharge method [3]. Conventional arc discharge is a method in which the reactants are used as electrodes and vaporized between the two electrodes by electric energy. So far, several variations of the growth technique for BNNTs have been proposed. Figure 11.6(A) is a schematic diagram of an arc-discharge set-up. The basic configuration of the set-up consists of a vacuum chamber, gas-flow controls, and two electrodes with a DC power supply. Depending on the requirements of specific experiments, the ambient condition inside the chamber can be either inert gas (e.g., helium, argon) or some reactive gas, for instance, nitrogen gas in the case of growing BNNTs. During the growth, the pressure inside the chamber is usually a few hundred torr [3,19,36–38,40–42]. The reactant materials are compressed or shaped into rods, which are used as the electrodes. To synthesize CNTs, the electrodes used are graphite rods, while for the growth of BNNTs, the situation is more complicated and is discussed below. The voltage exerted between the electrodes is ~20 to 40 V, and a high current up to 150 A is applied to generate the arc [3,19,36–38,40–42]. For given values of the voltage and current, we can adjust the gap between the electrodes (i.e., cathode and anode) to sustain a stable arc. The duration of the discharge is normally several minutes. During the discharge, the high current can easily increase the temperature of the electrodes to ~4000 K and evaporate the electrodes into clusters at atomic scale. The anode is normally the consumed electrode because a large

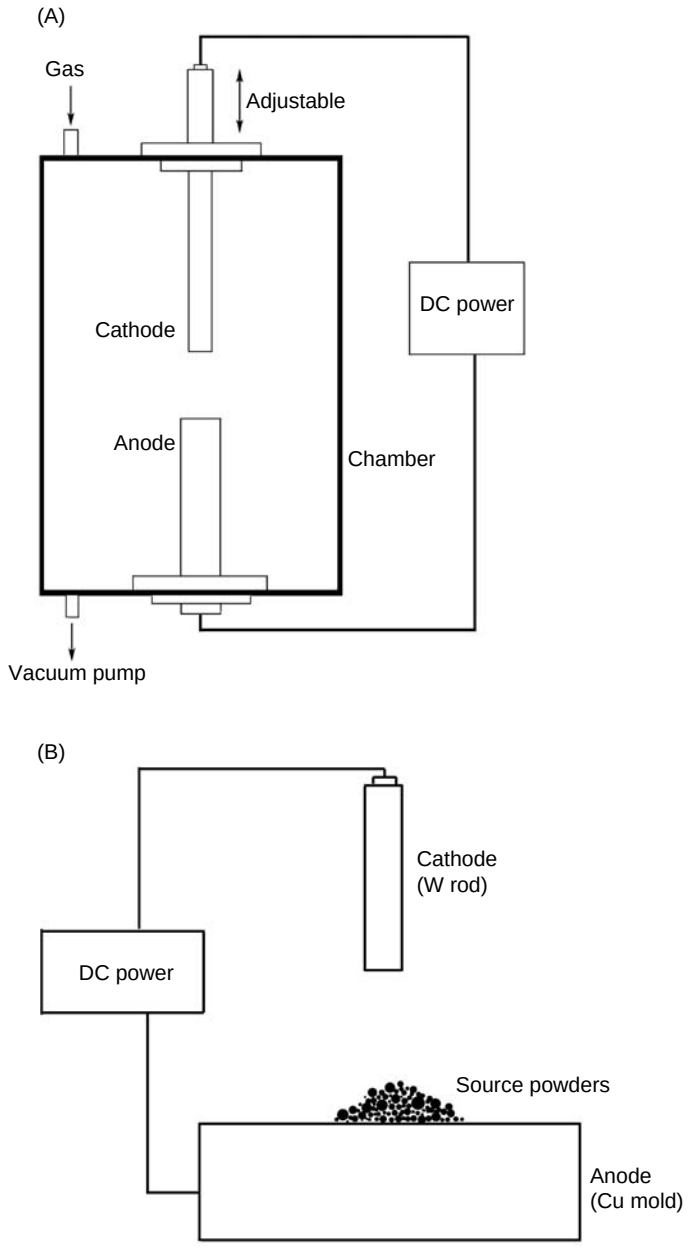

FIGURE 11.6 Schematic diagrams of (A) arc-discharging and (B) arc-melting apparatus.

quantity of electrons from the arc-discharge is accelerated toward the anode and collides with the anodic rod. Deposits can be found on the cathode as well as on the inner wall of the chamber. The deposits consist of many nanosized structures including NTs.

The rod-like electrodes, i.e., the reactants, should exhibit reasonable electrical conductance — otherwise a high current, and thus a stable arc, are not possible. Unfortunately, this criterion was the difficulty encountered when scientists first tried to make BNNTs using the arc-discharge method. Practically, bulk h-BN is an electrical insulator because of its wide band gap of 5.8 eV. Therefore, pure BN electrodes cannot carry such a high current as required in the normal discharge process.

Alternative conductive electrodes need to be considered. To circumvent this problem, Chopra et al. [3] used a hollow tungsten tube stuffed with BN powders as the anode, and water-cooled copper as the cathode. This modification in the preparation of new electrodes made arc discharge the first successful method for pure BNNT synthesis. Multiwalled BNNTs were found in the dark-gray cathode soot. The typical length of these MW BNNTs was about 200 nm, with diameters in the range of 6 to 8 nm. It is worth noting that metal particles were found at the ends of all the investigated BNNTs. The composition ratio of B over N was about 1.14, as determined by electron energy loss spectroscopy (EELS). One year later, Terrones et al. [36] tried tantalum tubes filled with BN powders. Stoichiometric BN MWNTs have been fabricated, and the as-grown BN MWNTs can be several micrometers in length. In the two cases above, the starting materials are BN compounds, no chemical reactions are needed to bind B and N together, although the break and reconnection of B–N bonds may happen. The formation process is very similar to the case of CNTs. In both cases, metal particles from the anodes were found in the BNNT samples and they accidentally played the role of catalysts.

Some groups have used conducting metal borides as both the cathode and anode. Hot-pressed HfB_2 [19,37] or ZrB_2 [38,40] electrodes have been demonstrated to be successful so far. In the case of boride electrodes, nitriding reactions definitely occur during the arcing process. An nitrogen or ammonia ambient is thus usually established as the nitrogen source for the nitriding reaction. As well as MW BNNTs, some SW BNNTs have been observed, which was first reported by Loiseau et al. [19,37]. The image of an SW BNNT is reproduced as Figure 11.7(A). The aforementioned modifications have resulted in the successful synthesis of BNNTs, and verified the theoretical prediction proposed several years ago [2]. However, unlike the case of CNTs, in which the arc-discharge is already a routine method for high yield synthesis, the yield of BNNTs is very low through the use of these methods. To improve the yield and, also to overcome the conductance problem of electrodes, Cumings [41] and Altoe [42] have developed another technique within the framework of arc discharge. Metal addictives (e.g., Ni and Co) and boron powders were mixed, melted and then cooled to form an ingot. The ingot was shaped into electrodes. This method can improve the NT yield. Mass quantity production of the order of a milligram has also been realized. An interesting feature of the as-grown BNNTs is that double-walled BNNTs (see Figure 11.7[B]) are the dominant morphology of the products, as can be seen from the histogram of the wall numbers as shown in the inset of Figure 11.7(C).

Arc melting is similar to the conventional arc-discharge method but with a simpler set-up configuration and experimental procedure. Instead of shaping the reactants into rod-like electrodes, the reactant powders are put on a Cu mold (anode), as shown in Figure 11.6(B). The cathode is a tungsten gun. When the voltage and current (e.g., 200 V, 125 A) are applied between the electrodes, an arc is generated and the powders on the mold are melted [45,46]. Together with the contribution from the ambient gas, which may be one of the reactants, the evaporated clusters from the melted sources form an ion gas. The growth of nanostructures can then occur in the ion gas by forming quasi-liquid particles first. The presence of a catalyst, especially transition metal borides exemplified by LaB_6 [43], are necessary in this method. The as-grown BNNTs are MW, with an appropriate stoichiometry. The effects of different catalysts have been examined as well [44]. This method is also called plasma-jet evaporation [45,46]. Only MW BNNTs were synthesized using arc-discharge method, and SW BNNTs were not reported. This is different from CNTs, and might suggest different growth conditions between BNNTs and CNTs. Arc-discharge method was the first technique in successful synthesis of CNTs and BNNTs, but complications in the scale-up process keep it as a laboratory technique.

11.3.2 Laser-Assisted Method

In addition to electrical energy, photonic energy can also be converted into heat, which evaporates the starting materials into ion gas instantly. Nowadays, the outputs of some advanced lasers have a very high-energy density in either a continuous wave mode or at kHz-repetition rates. For example,

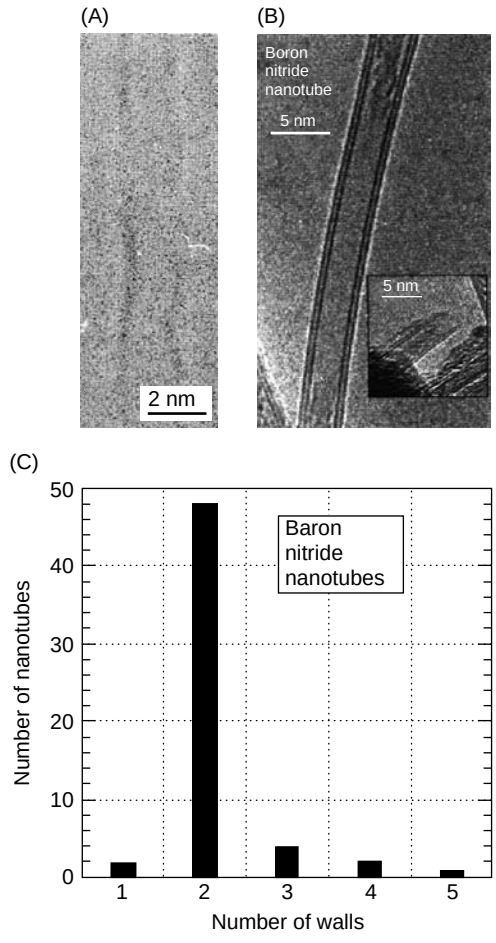

FIGURE 11.7 Boron nitride nanotube produced by arc-discharge method (A) SW BNNT. (From Loiseau, A. et al., *Carbon*, 36, 743–752, 1998.) (B) Double-walled BNNT (C) Histogram of BNNT walls. (From Cumings, J. and Zettl, A., *Chem. Phys. Lett.*, 316, 211–216, 2000. Reproduced with permission from *Elsevier Science*.)

at 10.6 μm, the output power of a CO_2 laser-emitting infrared radiation can reach as high as 1 kW, and can be further focused to a spot of several millimeters. When the light, either continuous beam or discrete pulses, is focused on the target of the source materials with such small spot size, the energy provided by the incident light elevates the temperature of the irradiated zone to several thousand Kelvin within a very short period of time. If the temperature is above the sublimation temperature of the target material, local explosions may occur and the source materials may effuse from the surface. The ion gas of atomic scale reactants is thus generated. This process is called laser ablation [47–49]. On the other hand, if the target temperature is below the sublimation point under the laser radiation, the radiation then only increases the temperature of the target without obvious ejection of materials from it. This process is referred to as laser heating [50,51]. Both these processes have been attempted for the fabrication of BNNTs in recent years.

A schematic diagram of the laser-ablation set-up is shown in Figure 11.8. Air-cooled metallic trap and filer are used to collect the ablation products, while the products of laser heating are obviously located on the surface and around the irradiated zone of the target. As shown in Figure 11.8, a tube furnace can be used as an additional energy supply to maintain the temperature of the target [47]. A diamond anvil cell under high N_2 pressure (~GPa) was also used for this purpose by Golberg et al. [50] in laser-heating process. Targets of laser-assisted processes are usually pure BN or B, and

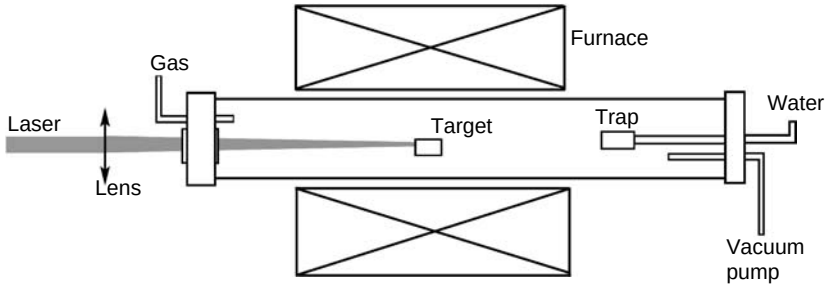

FIGURE 11.8 Schematic set-up of Laser-assisted method for the growth of BNNTs.

therefore the products are metal catalyst free. It is worth mentioning that both laser-heating [51] and laser-ablation [48] methods produce BNNTs in macroscopic quantity (up to 1 g) with stoichiometric ratio of B over N.

By ablating a rotating BN target in a flowing N_2 ambient (100 ml/s) under pressure of 1 bar, Lee et al. [48] have synthesized SW- dominant BNNTs in gram quantities (0.6 g/h). The SWNTs are self-organized into bundles as shown in Figure 11.9(A). When Ni/Co are used as catalyst, SWNTs can also be found in the products (see Figure 11.9(B)) of laser ablation [47]. Similar to the arc-discharge method, the laser method involves a significant amount of energy and very high temperatures (several thousands Kelvin). The formation processes of BNNTs are probably very similar. Both methods produce BNNTs with almost the same small size range and perfect cylindrical structures with minimum defects. Scaling-up of the process is required to produce much larger quantity and high yield of SWNTs, which is very important for property and application studies.

11.3.3 Ball Milling and Annealing

This is a two-step method involving first a ball-milling process at room temperature, and a subsequent annealing at relatively low temperatures. These two processes, actually, correspond to separate nucleation and growth processes, respectively. As mentioned in the preceding section, atomic scaled B and N clusters are expected for the growth of BNNTs. The starting materials used in the previous methods are usually powders or rods that have bulk properties. Generally, the surface to volume ratio of bulk materials is low. To increase the effectiveness of the effusion, a large surface to volume ratio of the starting material is helpful. Regarding the chemical reaction involved in the formation of BN, when one of the reactants is bulk boron, high temperature is required to achieve a practical rate of the reaction. They are the reasons for exploiting high-temperature routines such as with the assistance of an electric arc or a high-energy laser for the growth of BNNTs. A different type of energy is used to achieve this reaction at lower temperatures. Chen et al. [52–54], in 1999, were the first to fabricate BNNTs using high-energy ball milling (HEBM) to pretreat boron or boron nitride powders

Repeated high-energetic milling impacts provide mechanical energy to material powders during ball-milling process [55]. The grinding energy of HEBM is at least a thousand times higher than that from conventional ones. Therefore, HEBM can create structural defects and induce structural changes as well as chemical reactions at room temperature. There are several types of high-energy ball mills, such as Spex vibrating mill, planetary ball mill, rotating ball mill, attritors [56]. As an example, a photo and a schematic diagram of a room-temperature vertical-planetary ball mill are shown in Figures 11.10(A) and (B), respectively. For the synthesis of BNNTs, boron (or BN) powders were loaded into a stainless-steel cell with several hardened steel balls. The milling chamber was then filled with NH_3 or N_2 up to a pressure of 300 kPa. An external magnet applies pulling forces on the balls and thus increases milling energy. When the milling chamber rotates, the balls drop to the bottom of the chamber due to both gravity and magnetic force, as they reach the top of

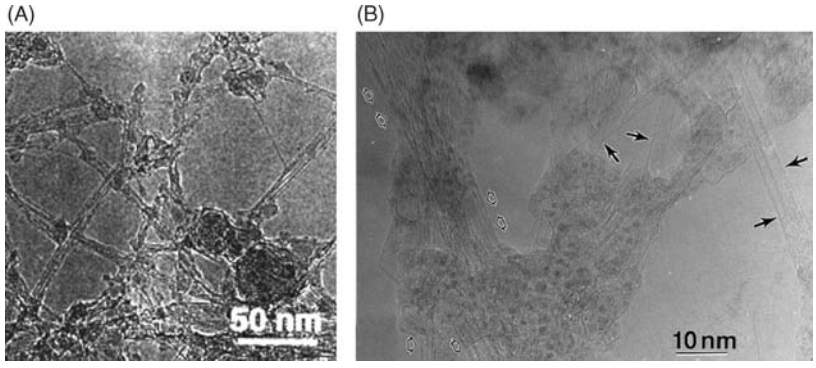

FIGURE 11.9 (A) BNNTs produced by laser-assisted method organized in bundles. (Lee, R.S. et al., *Phys. Rev. B*, 64, 121405, 2001. Reproduced with permission from *American Physical Society*.) (B) SW BNNTs produced by laser-assisted method. (From Yu, D.P. et al., *Appl. Phys. Lett.*, 72, 1966–1968, 1998. Reproduced with permission from *American Institute of Physics*.)

the chamber. This impact movement of the balls generates a strong energetic collision toward the boron/BN powders on the bottom of the chamber. The impact energy can be controlled by adjusting the position of the magnet and the rotation frequency of the chamber. The milling process usually lasts over 100 h to ensure complete structural changes.

The milling process embraces a complex mixture of fracturing, grinding, high-speed plastic deformation, cold welding, thermal shock, intimate mixing, etc. of the materials. Because the structural changes and chemical reactions are induced by mechanical energy rather than thermal energy, reactions are possible at low temperatures (room temperature). In the case of growth of BNNTs, a nitriding reaction between boron and atomic nitrogen inside the milling chamber was realized at room temperature. Boron nitride was evidenced in the as-milled powders by X-ray diffraction (XRD) as shown in Figure 11.11. XRD results also indicate that the as-milled boron powders are either amorphous or consist of extremely small, highly disordered crystallites. The ball-milling treatment creates a precursor.

The as-milled boron powders were then put into a tube furnace and annealed in nitrogen or ammonia at a temperature of 1000°C or higher for several hours. Large quantities of BN MWNTs have been found in the products. The high yield can be observed in the scanning electron microscope (SEM) image shown is Figure 11.12. The yield of the growth is up to 85%, and due to the capability of the ball milling, a kg-quantity production is possible. Therefore, this method provides an opportunity to synthesize BNNTs in an industrial-compatible quantity. This method is very different from the other methods, and special formation mechanisms have been observed. In the case where BN compounds are used as the starting materials, because the growth temperature during thermal annealing (1200°C) is far below the melting point of BN phase, no vapor could possibly be generated as in arc-discharge and laser-ablation cases. The BNNT formation is a solid-state process. Transmission electron microscopy investigation has revealed that crystal growth driven by surface diffusion is a possible mechanism under such low-temperature growth conditions [53,54,57,58]. By varying growth conditions, morphologies such as hollow tubes, and bamboo-like structures, (see Figure 11.13) can be produced separately [21,52,59]. This method has been used by several groups and demonstrated to be a very efficient method for production of BNNTs in large quantities [60,61]. Actually, the first commercial source for BNNTs was established based on this synthesis method.

11.3.4 Carbon Nanotube Substitution

Several one-dimensional structures have been prepared by using CNTs as templates. The functionalities of CNTs in these syntheses might be (1) their open hollow structures being filled by other materials through capillary effects, (2) their fine cylinders being coated by some materials,

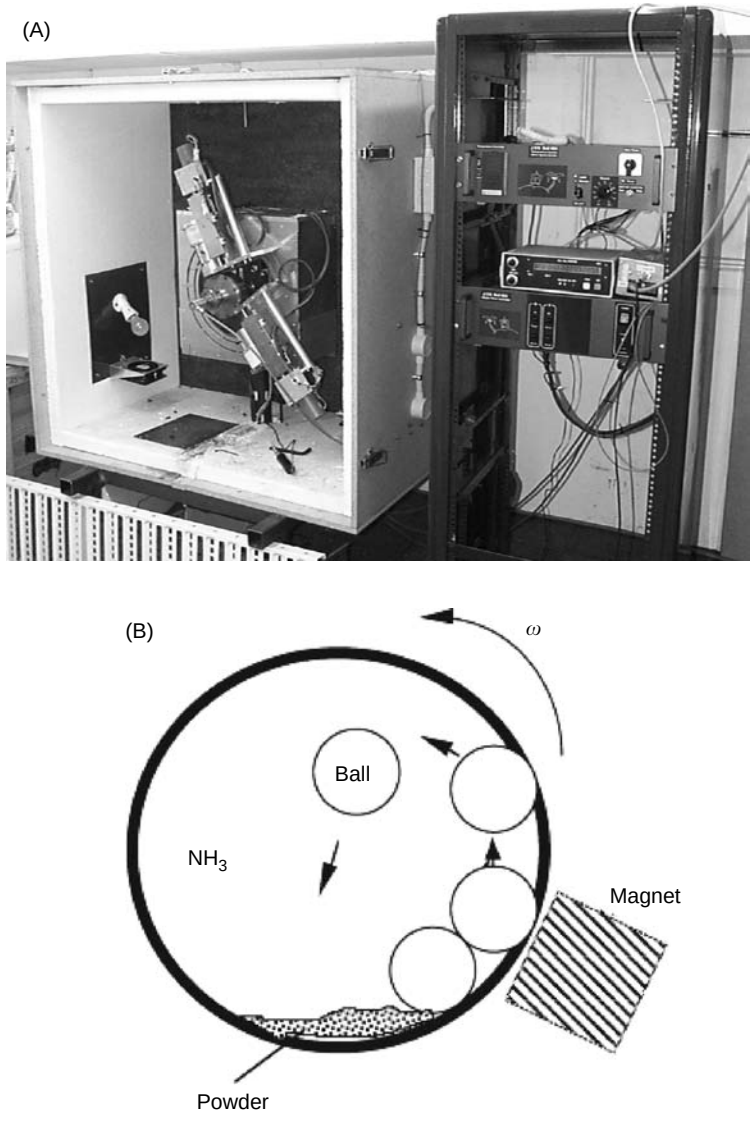

FIGURE 11.10 Photo (A) and schematic diagram (B) of an HEBM set-up.

and (3) the hexagonal-carbon network in the tubular network reacting with other materials. The last functionality may result in either solid nanowire structures or hollow NTs. If the product structure reserves the framework of CNTs, the reaction is named CNT-substituted reaction and has been used for the synthesis of BNNTs. Bando's group in Japan covered B_2O_3 powders with carbon MWNTs and annealed them at 1773 K in flowing nitrogen for half an hour [26,62]. The substitution reaction is

$$B_2O_3 + 3C(NTs) + N_2(g) \rightarrow 2BN(NTs) + 3CO(g)$$

B_2O_3 exhibits a much lower melting point of 450°C compared with B (2076°C) and BN (~3000°C). Therefore, reasonable amount of B_2O_3 vapor can flow up and react with CNTs.

The general morphologies of BNNTs and CNTs are much alike. However, on an average, as-grown BNNTs have a smaller number of walls than those of the CNT templates. The EELS

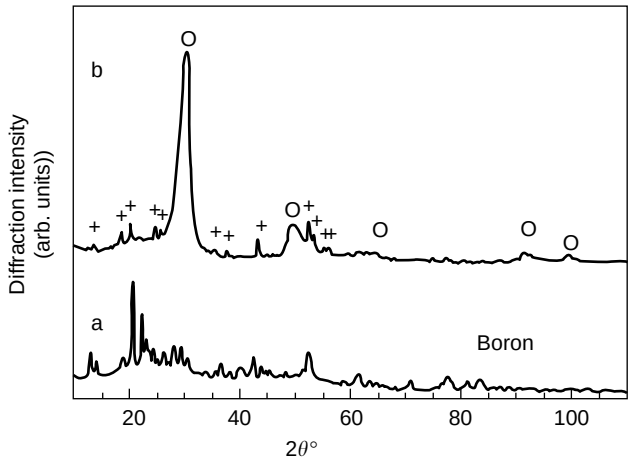

FIGURE 11.11 XRD patterns of ball-milled and annealed samples. (Chen, Y. et al., *Chem. Phys. Lett.*, 299, 260–264, 1999. Reproduced with permission from *Elsevier Science*.)

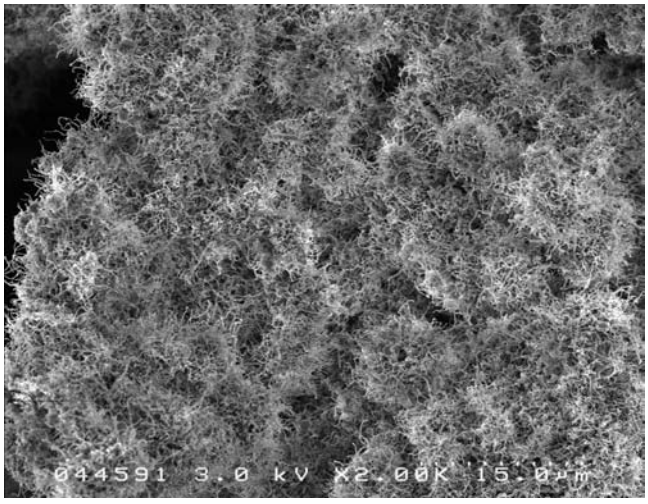

FIGURE 11.12 Scanning electron microscope image of ball-milling and annealing products showing large quantity and high yield of BNNTs.

shows that the composition of the products can be pure BN without obvious trace of carbon. A striking increase in BN MWNT yield and self-assemblage of tubes into ropes have also been seen when MoO_3 or V_2O_5 is introduced as an oxidizing-promoting agent during the substituted reaction [27,63–65]. In addition to the improved yield, this method takes advantage of the alignment of carbon nitride nanotube (CNNT) arrays, i.e., by starting from aligned CNNTs, the as-grown BNNTs are also aligned [66]. Pure BNNTs can be fabricated by this method, but it has been noted that these attempts frequently resulted in C traces in the products and there were insurmountable difficulties in preparing 100% pure BN nanomaterials. In fact, similar growth techniques, but with a lower temperature (1373 K) and a longer anneal time (4 h), are used to fabricate boron doped CNTs [67,68]. The boron carbon nitride nanotubes (BCN NTs) are easier to get than pure BNNTs, but it is difficult to control the B level. To purify the BCN NTs from carbon contaminations so as to transform BCN NTs into pure BNNTs, Han et al. [69] burned BCN NTs in air at about 700°C for 30 min,

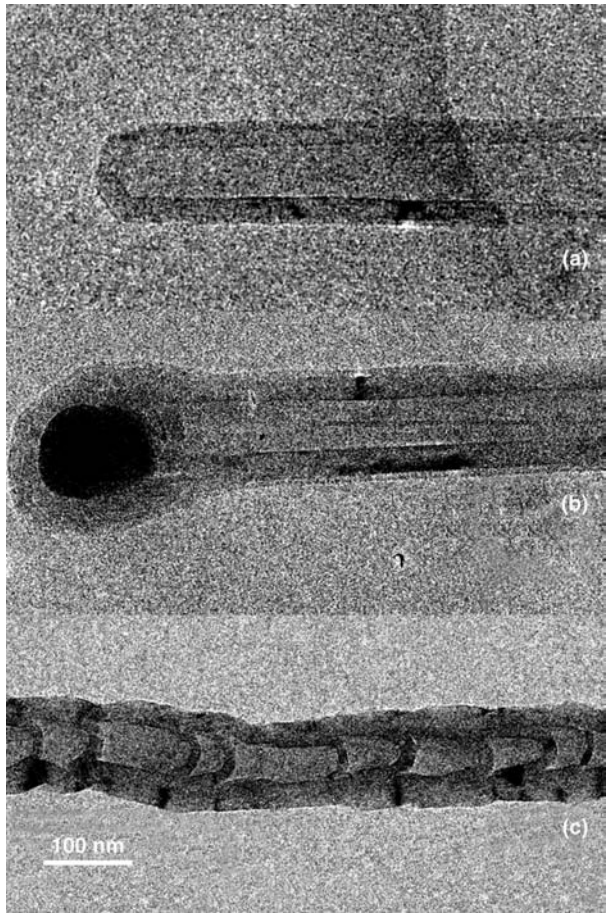

FIGURE 11.13 Different morphologies of BNNTs fabricated from the ball-milling and annealing method. (From Chen, L. et al., *J. Mater. Res.*, 17, 1896–1899, 2002. Reproduced with permission from *Material Research Society.*)

and found that up to 60% of the BCN NTs could be transformed. The quantity of BNNTs produced using this method depends on that of CNTs.

11.3.5 Chemical Vapor Deposition and Other Thermal Methods

In this section, we review several methods that, from the standpoint of energy provided, use thermal energy only. During heat treatment, the formation of BNNTs may be through different kinds of chemical reactions, depending on the starting materials that are used in the process. This has resulted in several terminologies concerning these processes.

When amorphous boron (or mixed with h-BN) was heated in ammonia gas with the presence of Li vapor for 10 to 20 h [70,71], boron nitride MWNTs with a typical diameter of 10 nm were formed. In addition to Li vapor, oxides such as Fe_2O_3, MgO, Ga_2O_3, and SiO_2 have also been co-heated with amorphous B, and NH_3 was usually exploited for the nitriding reaction as well. Using various oxides, Tang [72] reported that straight concentric pure BNNTs with a large diameter distribution from several nm to 70 nm were fabricated in large scale. The conversion rate was ~40%. The oxides may act as media, reacting with boron and generating an intermediate product of

B_2O_2, which is in vapor phase at the reaction temperature. B_2O_2 vapor and ammonia react and thus facilitate the formation of BNNTs. Taking MgO as an example, the possible reactions are

$$2B(s)+2MgO(s) \rightarrow B_2O_2(g)+2Mg(g)$$

$$B_2O_2(g)+2NH_3(g) \rightarrow 2BN(s)+2H_2O(g)+H_2(g)$$

Heating temperature and B/oxides ratio have noticeable effects on the NT formation [73,74]. Boron oxides (B_2O_3) can also be heated directly either as discussed in the carbon-substituted reaction [26,62], or as described in Bartnitskaya et al.'s work [75]. Boron nitride powders have also been heated at high temperature (1750 to 2000°C) in nitrogen ambient to fabricate BNNTs [76]. Local three-dimensional order was first observed in the as-grown products.

Chemical vapor deposition (CVD) has also been attempted for fabrication of BNNTs. A CVD process is a process of chemically reacting a volatile compound of a material to be deposited, with other gases, to produce a non-volatile solid that deposits atomistically on a suitably placed substrate. The volatile compound of the first CVD routine for BNNTs was $B_3N_3H_6$ [77], and it was carried by N_2 to the substrate of Si covered with catalysts (Co, Ni, and NiB). The temperature of the substrate was 1000 to 1100°C. $B_3N_3H_6$ vapor was decomposed and BNNTs were deposited on the Si wafer. Changing the volatile materials, Ma et al. [78–81] have developed several CVD routines for the fabrication of BNNTs. Other compounds such as NH_4BF_4 and KBH_4 are also used as precursor materials, and heated in a nitrogen-containing atmosphere to synthesize BNNTs [82]. The yield of the CVD synthesis for BNNTs is not clear, though the CVD process itself is believed to be a low-cost and high-yield method. Integrated into the CVD method, nanoporus templates have become widely used to confined grow 1-D nanostructures. Anodic alumina membranes (AAMs) are one of the most popular templates. The pores of AAM with adjustable diameters in the range of 5 to 200 nm are perpendicular to the surface of the AAM and are organized into arrays. The density of the pores may be up to $10^{11}/cm^2$. The nanopores are filled with desired materials (e.g., BN) via CVD process. After the filling, the template itself can be removed by proper chemical solutions. Shelimov has used this technique to grow aligned BNNTs. Compared with other growth methods, the temperature of the deposition is very low (750°C) [83]. However, because of the low temperature, the as-grown BNNTs are polycrystalline in nature.

11.4 SUMMARY

BNNTs have a similar tubular structure as CNTs with different capes and possibly different chiralities. More detailed research on a large number of BNNT samples is needed to fully clarify the structure. BNNT synthesis is, however, much more complicated than that of CNTs, even using the same processing techniques. This is probably because two different elements, B and N, are involved rather than the single C, and consequently B–N pairs have to be created via a chemical reaction prior to (or simultaneous to) the growth of tubular nanostructure. According to supplied energy classification of various synthesis methods, most successful synthesis methods reviewed previously do not rely on traditional thermal energy as general chemical reactions and crystal growths normally require. Electric (arc discharge), photonic (laser), mechanical (ball milling), and chemical (CNT substitution) energies are more successful than thermal energy (pure-furnace heating). This implies that the nitriding-reaction and NT-formation processes are thermo-dynamical nonequilibrium processes. Compared with bulk h-BN, the curved BN basal planes in NTs at nanometer scale are metastable structures, which are difficult to be produced with pure thermal energy under equilibrium conditions. Similar to the CNT, the formation process needs to be detailed fully. Nevertheless, the growth techniques of BNNTs still require significant improvement, and new synthesis methods with better control over the growth directions and locations are needed. There is only one paper [48] describing the BN SWNT dominant fabrication, while, to the best of our knowledge, study on the

alignment growth and selective growth of BNNTs is still absent. We believe that the research and application of BNNTs will be extensively developed, and a fundamental breakthrough of the growth technique can be achieved.

ACKNOWLEDGMENTS

We wish to acknowledge the permission given by Dr. Dmitri Golberg, Dr. Francois Willaime, Dr. John Cumings, and Dr. Dapeng Yu for using their published images of BNNTs. This research has been supported by the Australian Research Council under the Centre of Excellent program (ARC Centre of Nanofunctional Materials).

REFERENCES

1. Iijima, S., Helical microtubules of graphitic carbon, *Nature*, 354, 56–58, 1991.
2. Rubio, A., Corkill, J.L., and Cohen, M.L., Theory of graphitic boron-nitride nanotubes, *Phys. Rev., B* 49, 5081–5084, 1994.
3. Chopra, N.G., Luyken, R.J., Cherrey, K., Crespi, V.H., Cohen, M.L., Louie, S.G., and Zettl, A., Boron-nitride nanotubes, *Science*, 269, 966–967, 1995.
4. Kudin, K.N., Scuseria, G.E., and Yakobson, B.I., C2F, BN, and C nanoshell elasticity from ab initio computations, *Phys. Rev.*, B 64, 235406, 2001.
5. Mele, E.J. and Kral, P., Electric polarization of heteropolar nanotubes as a geometric phase, *Phys. Rev. Lett.*, 88, 56803, 2002.
6. Chopra, N.G. and Zettl, A., Measurement of the elastic modulus of a multi-wall boron nitride nanotube, *Solid State Commn.*, 105, 297–300, 1998.
7. Suryavanshi, A.P., Yu, M.F., Wen, J.G., Tang, C.C., and Bando, Y., Elastic modulus and resonance behavior of boron nitride nanotubes, *Appl. Phys. Lett.*, 84, 2527–2529, 2004.
8. Blase, X., Rubio, A., Louie, S.G., and Cohen, M.L., Stability and band-gap constancy of boron-nitride nanotubes, *Europhys. Lett.*, 28, 335–340, 1994.
9. Radosavljevic, M., Appenzeller, J., Derycke, V., Martel, R., Avouris, P., Loiseau, A., Cochon, J.L., and Pigache, D., Electrical properties and transport in boron nitride nanotubes, *Appl. Phys. Lett.*, 82, 4131–4133, 2003.
10. Cumings, J. and Zettl, A., Field emission and current-voltage properties of boron nitride nanotubes, *Solid State Commn.*, 129, 661–664, 2004.
11. Golberg, D., Bando, Y., Kurashima, K., and Sato, T., Synthesis and characterization of ropes made of BN multiwalled nanotubes, *Scr. Mater.*, 44, 1561–1565, 2001.
12. Chen, Y., Zou, J., Campbell, S.J., and Le Caer, G., Boron nitride nanotubes: pronounced resistance to oxidation, *Appl. Phys. Lett.*, 84, 2430–2432, 2004.
13. Oku, T. and Kuno, M., Synthesis, argon/hydrogen storage and magnetic properties of boron nitride nanotubes and nanocapsules, *Diamond Relat. Mater.*, 12, 840–845, 2003.
14. Seayad, A.M. and Antonelli, D.M., Recent advances in hydrogen storage in metal-containing inorganic nanostructures and related materials, *Adv. Mater.*, 16, 765–777, 2004.
15. Ma, R.Z., Bando, Y., Zhu, H.W., Sato, T., Xu, C.L., and Wu, D.H., Hydrogen uptake in boron nitride nanotubes at room temperature, *J. Am. Chem. Soc.*, 124, 7672–7673, 2002.
16. Wu, J., Han, W.Q., Walukiewicz, W., Ager, J.W., Shan, W., Haller, E.E., and Zettl, A., Raman spectroscopy and time-resolved photoluminescence of BN and BxCyNz nanotubes, *Nano Lett.*, 4, 647–650, 2004.
17. Kral, P., Mele, E.J., and Tomanek, D., Photogalvanic effects in heteropolar nanotubes, *Phys. Rev. Lett.*, 85, 1512–1515, 2000.
18. Iijima, S., Ichihashi, T., and Ando, Y., Pentagons, heptagons and negative curvature in graphite microtubule growth, *Nature*, 356, 776–778, 1992.
19. Loiseau, A., Willaime, F., Demoncy, N., Schramchenko, N., Hug, G., Colliex, C., and Pascard, H., Boron nitride nanotubes, *Carbon*, 36, 743–752, 1998.
20. Charlier, J.C., Blase, X., De Vita, A., and Car, R., Microscopic growth mechanisms for carbon and boron-nitride nanotubes, *Appl. Phys. a—Mater. Sci. Process.*, 68, 267–273, 1999.

21. Chen, Y., Conway, M., Williams, J.S., and Zou, J., Large-quantity production of high-yield boron nitride nanotubes, *J. Mater. Res*., 17, 1896–1899, 2002.
22. Golberg, D. and Bando, Y., Electron microscopy of boron nitride nanotubes, in *Electron Microscopy of Nanotubes*, 1st ed., Wang, Z.L. and Hui, C., Eds., Tsinghus University Press, Beijing, 2004, pp. 221–250.
23. Chen, L., Ye, H., and Gogotsi, Y., Synthesis of boron nitride coating on carbon nanotubes, *J. Am. Ceram. Soc*., 87, 147–151, 2004.
24. Qin, L.C., Ichihashi, T., and Iijima, S., On the measurement of helicity of carbon nanotubes, *Ultramicroscopy*, 67, 181–189, 1997.
25. Lucas, A.A., Bruyninckx, V., Lambin, P., Bernaerts, D., Amelinckx, S., Landuyt, J.V., and Tendeloo, G.V., Electron diffraction by carbon nanotubes, *Scanning Microsc*., 12, 415–436, 1998.
26. Golberg, D., Han, W., Bando, Y., Bourgeois, L., Kurashima, K., and Sato, T., Fine structure of boron nitride nanotubes produced from carbon nanotubes by a substitution reaction, *J. Appl. Phys*., 86, 2364–2366, 1999.
27. Golberg, D., Bando, Y., Kurashima, K., and Sato, T., Ropes of BN multi-walled nanotubes, *Solid State Commn*., 116, 1–6, 2000.
28. Saito, Y., Maida, M., and Matsumoto, T., Structures of boron nitride nanotubes with single-layer and multilayers produced by arc discharge, *Japanese J. Appl. Phys. Part 1-Regular Pap. Short Notes Rev. Pap*., 38, 159–163, 1999.
29. Demczyk, B.G., Cumings, J., Zettl, A., and Ritchie, R.O., Structure of boron nitride nanotubules, *Appl. Phys. Lett*., 78, 2772–2774, 2001.
30. Narita, I. and Oku, T., Atomic structure of boron nitride nanotubes with an armchair-type structure studied by HREM, *Solid State Commn*., 129, 415–419, 2004.
31. Golberg, D., Bando, Y., Bourgeois, L., Kurashima, K., and Sato, T., Insights into the structure of BN nanotubes, *Appl. Phys. Lett*., 77, 1979–1981, 2000.
32. Wildoer, J.W.G., Venema, L.C., Rinzler, A.G., Smalley, R.E., and Dekker, C., Electronic structure of atomically resolved carbon nanotubes, *Nature*, 391, 59–62, 1998.
33. Odom, T.W., Huang, J.L., Kim, P., and Lieber, C.M., Atomic structure and electronic properties of single-walled carbon nanotubes, *Nature*, 391, 62–64, 1998.
34. Cowley, J.M., *Nanodiffraction of Carbon Nanotubes*, 1st ed., Tsinghua University Press, Beijing, 2004.
35. Menon, M. and Srivastava, D., Structure of boron nitride nanotubes: tube closing versus chirality, *Chem. Phys. Lett*., 307, 407–412, 1999.
36. Terrones, M., Hsu, W.K., Terrones, H., Zhang, J.P., Ramos, S., Hare, J.P., Castillo, R., Prassides, K., Cheetham, A.K., Kroto, H.W., and Walton, D.R.M., Metal particle catalysed production of nanoscale BN structures, *Chem. Phys. Lett*., 259, 568–573, 1996.
37. Loiseau, A., Willaime, F., Demoncy, N., Hug, G., and Pascard, H., Boron nitride nanotubes with reduced numbers of layers synthesized by arc discharge, *Phys. Rev. Lett*., 76, 4737–4740, 1996.
38. Saito, K., Maida, M., and Matsumoto, T., Structures of boron nitride nanotubes with single-layer and multilayers produced by arc discharge, *Japanese J. Appl. Phys. Part 1-Regular Pap. Short Notes Rev. Pap*., 38, 159–163, 1999.
39. Golberg, D., Bando, Y., Eremets, M., Takemura, K., Kurashima, K., Tamiya, K., and Yusa, H., Boron nitride nanotube growth defects and their annealing-out under electron irradiation, *Chem. Phys. Lett*., 279, 191–196, 1997.
40. Saito, Y. and Maida, M., Square, pentagon, and heptagon rings at BN nanotube tips, *J. Phys. Chem. A*, 103, 1291–1293, 1999.
41. Cumings, J. and Zettl, A., Mass-production of boron nitride double-wall nanotubes and nanococoons, *Chem. Phys. Lett*., 316, 211–216, 2000.
42. Altoe, M.V.P., Sprunck, J.P., Gabriel, J.C.P., and Bradley, K., Nanococoon seeds for BN nanotube growth, *J. Mater. Sci*., 38, 4805–4810, 2003.
43. Kuno, M., Oku, T., and Suganuma, K., Synthesis of boron nitride nanotubes and nanocapsules with LaB6, *Diamond Relat. Mater*., 10, 1231–1234, 2001.
44. Narita, I. and Oku, T., Synthesis of boron nitride nanotubes by using NbB2, YB6 and YB6/Ni powders, *Diamond Relat. Mater*., 12, 1912–1917, 2003.
45. Shimizu, Y., Moriyoshi, Y., Komatsu, S., Ikegami, T., Ishigaki, T., Sato, T., and Bando, Y., Concurrent preparation of carbon, boron nitride and composite nanotubes of carbon with boron nitride by a plasma evaporation method, *Thin Solid Films*, 316, 178–184, 1998.

46. Shimizu, Y., Moriyoshi, Y., Tanaka, H., and Komatsu, S., Boron nitride nanotubes, webs, and coexisting amorphous phase formed by the plasma jet method, *Appl. Phys. Lett*., 75, 929–931, 1999.
47. Yu, D.P., Sun, X.S., Lee, C.S., Bello, I., Lee, S.T., Gu, H.D., Leung, K.M., Zhou, G.W., Dong, Z.F., and Zhang, Z., Synthesis of boron nitride nanotubes by means of excimer laser ablation at high temperature, *Appl. Phys. Lett*., 72, 1966–1968, 1998.
48. Lee, R.S., Gavillet, J., de la Chapelle, M.L., Loiseau, A., Cochon, J.L., Pigache, D., Thibault, J., and Willaime, F., Catalyst-free synthesis of boron nitride single-wall nanotubes with a preferred zig-zag configuration, *Phys. Rev. B*, 64, 121405, 2001.
49. Golberg, D., Rode, A., Bando, Y., Mitome, M., Gamaly, E., and Luther-Davies, B., Boron nitride nanostructures formed by ultra-high-repetition rate laser ablation, *Diamond Relat. Mater*., 12, 1269–1274, 2003.
50. Golberg, D., Bando, Y., Eremets, M., Takemura, K., Kurashima, K., and Yusa, H., Nanotubes in boron nitride laser heated at high pressure, *Appl. Phys. Lett*., 69, 2045–2047, 1996.
51. Laude, T., Matsui, Y., Marraud, A., and Jouffrey, B., Long ropes of boron nitride nanotubes grown by a continuous laser heating, *Appl. Phys. Lett*., 76, 3239–3241, 2000.
52. Chen, Y., Fitz Gerald, J.D., Williams, J.S., and Bulcock, S., Synthesis of boron nitride nanotubes at low temperatures using reactive ball milling, *Chem. Phys. Lett*., 299, 260–264, 1999.
53. Chen, Y., Chadderton, L.T., FitzGerald, J., and Williams, J.S., A solid-state process for formation of boron nitride nanotubes, *Appl. Phys. Lett*., 74, 2960–2962, 1999.
54. Chen, Y., Chadderton, L.T., Williams, J.S., and Fitz Gerald, J.D., Solid-state formation of carbon and boron nitride nanotubes, *Metastable, Mech. Alloyed Nanocryst. Mater., Parts 1 and 2*, 343, 63–67, 2000.
55. Benjamin, J.S., Dispersion strengthened superalloys by mechanical alloying, *Metall. Trans*., 1, 2943, 1970.
56. Suryanarayana, C., Nanocrystalline materials, *Int. Mater. Rev*., 40, 41, 1995.
57. Chadderton, L.T. and Chen, Y., A model for the growth of bamboo and skeletal nanotubes: catalytic capillarity, *J. Cryst. Growth*, 240, 164–169, 2002.
58. Chadderton, L.T. and Chen, Y., Nanotube growth by surface diffusion, *Phys. Lett. A*, 263, 401–405, 1999.
59. Chen, Y., Halstead, T., and Williams, J.S., Influence of milling temperature and atmosphere on the synthesis of iron nitrides by ball milling, *Mater. Sci. Eng. A*, 206, 24–29, 1996.
60. Tang, C.C., Bando, Y., and Sato, T., Synthesis and morphology of boron nitride nanotubes and nanohorns, *Appl. Phys. a—Mater. Sci. Process*., 75, 681–685, 2002.
61. Bae, S.Y., Seo, H.W., Park, J., Choi, Y.S., Park, J.C., and Lee, S.Y., Boron nitride nanotubes synthesized in the temperature range 1000–1200°C, *Chem. Phys. Lett*., 374, 534–541, 2003.
62. Han, W.Q., Bando, Y., Kurashima, K., and Sato, T., Synthesis of boron nitride nanotubes from carbon nanotubes by a substitution reaction, *Appl. Phys. Lett*., 73, 3085–3087, 1998.
63. Golberg, D., Bando, Y., Kurashima, K., and Sato, T., Synthesis, HRTEM and electron diffraction studies of B/N-doped C and BN nanotubes, *Diamond Relat. Mater*., 10, 63–67, 2001.
64. Golberg, D. and Bando, Y., Unique morphologies of boron nitride nanotubes, *Appl. Phys. Lett*., 79, 415–417, 2001.
65. Golberg, D., Bando, Y., Mitome, M., Kurashima, K., Sato, T., Grobert, N., Reyes-Reyes, M., Terrones, H., and Terrones, M., Preparation of aligned multi-walled BN and B/C/N nanotubular arrays and their characterization using HRTEM, EELS and energy-filtered TEM, *Physica B-Condens. Matter*, 323, 60–66, 2002.
66. Deepak, F.L., Vinod, C.P., Mukhopadhyay, K., Govindaraj, A., and Rao, C.N.R., Boron nitride nanotubes and nanowires, *Chem. Phys. Lett*., 353, 345–352, 2002.
67. Han, W.Q., Bando, Y., Kurashima, K., and Sato, T., Boron-doped carbon nanotubes prepared through a substitution reaction, *Chem. Phys. Lett*., 299, 368–373, 1999.
68. Golberg, D., Bando, Y., Bourgeois, L., Kurashima, K., and Sato, T., Large-scale synthesis and HRTEM analysis of single-walled B- and N-doped carbon nanotube bundles, *Carbon*, 38, 2017–2027, 2000.
69. Han, W.Q., Mickelson, W., Cumings, J., and Zettl, A., Transformation of BxCyNz nanotubes to pure BN nanotubes, *Appl. Phys. Lett*., 81, 1110–1112, 2002.
70. Terauchi, M., Tanaka, M., Matsuda, H., Takeda, M., and Kimura, K., Helical nanotubes of hexagonal boron nitride, *J. Electron Microsc*., 46, 75–78, 1997.

71. Terauchi, M., Tanaka, M., Suzuki, K., Ogino, A., and Kimura, K., Production of zigzag-type BN nanotubes and BN cones by thermal annealing, *Chem. Phy. Lett*., 324, 359–364, 2000.
72. Tang, C., Bando, Y., Sato, T., and Kurashima, K., A novel precursor for synthesis of pure boron nitride nanotubes, *Chem. Commn*., (12), 1290–1291, 2002.
73. Tang, C.C., de la Chapelle, M.L., Li, P., Liu, Y.M., Dang, H.Y., and Fan, S.S., Catalytic growth of nanotube and nanobamboo structures of boron nitride, *Chem. Phys. Lett*., 342, 492–496, 2001.
74. Tang, C.C., Fan, S.S., Li, P., Liu, Y.M., and Dang, H.Y., Synthesis of boron nitride in tubular form, *Mater. Lett*., 51, 315–319, 2001.
75. Bartnitskaya, T.S., Oleinik, G.S., Pokropivnyi, A.V., and Pokropivnyi, V.V., Synthesis, structure, and formation mechanism of boron nitride nanotubes, *JETP Lett*., 69, 163–168, 1999.
76. Bourgeois, L., Bando, Y., and Sato, T., Tubes of rhombohedral boron nitride, *J. Phys. D-Appl. Phys*., 33, 1902–1908, 2000.
77. Lourie, O.R., Jones, C.R., Bartlett, B.M., Gibbons, P.C., Ruoff, R.S., and Buhro, W.E., CVD growth of boron nitride nanotubes, *Chem. Mater*., 12, 1808, 2000.
78. Ma, R., Bando, Y., and Sato, T., CVD synthesis of boron nitride nanotubes without metal catalysts, *Chem. Phys. Lett*., 337, 61–64, 2001.
79. Ma, R.Z., Bando, Y., Sato, T., and Kurashima, K., Growth, morphology, and structure of boron nitride nanotubes, *Chem. Mater*., 13, 2965–2971, 2001.
80. Ma, R.Z., Bando, Y., Sato, T., and Kurashima, K., Thin boron nitride nanotubes with unusual large inner diameters, *Chem. Phys. Lett*., 350, 434–440, 2001.
81. Ma, R.Z., Bando, Y., and Sato, T., Controlled synthesis of BN nanotubes, nanobamboos, and nanocables, *Adv. Mater*., 14, 366–368, 2002.
82. Xu, L.Q., Peng, Y.Y., Meng, Z.Y., Yu, W.C., Zhang, S.Y., Liu, X.M., and Qian, Y.T., A co-pyrolysis method to boron nitride nanotubes at relative low temperature, *Chem. Mater*., 15, 2675–2680, 2003.
83. Shelimov, K.B. and Moskovits, M., Composite nanostructures based on template-crown boron nitride nanotubules, *Chem. Mater*., 12, 250–254, 2000.

12 Sintering of Nanoceramics

Xiao-Hui Wang
Tsinghua University, Beijing, China

I-Wei Chen
University of Pennsylvania, Philadelphia, Pennsylvania

CONTENTS

ABSTRACT

With the ongoing trend of miniaturization and integration in the electronic device industry, the quest for nanoceramics, especially nano electroceramics, has naturally focused on the processing methods that can produce fully dense nanoscale ceramics at relatively low temperatures. This chapter

surveys the common methods to acquire green bodies and fire ceramics, emphasizing the need to avoid both agglomeration in powder compact and coarsening during sintering. The recent development of an unconventional two-step sintering strategy featuring densification without grain growth is deemed particularly exciting, since it promises to deliver nanoceramics by pressureless sintering and has already been demonstrated for several distinctly different ceramics. The principle of this method, which exploits the different kinetics between densification diffusion and grain boundary mobility, is also reviewed in terms of solid-state and liquid-phase sintering mechanisms.

12.1 INTRODUCTION

Nanocrystalline ceramics have attracted considerable interest in recent years because of the promise of new and interesting properties that are crystallite-size sensitive. These properties include mechanical, optical, electrical, and magnetic, many of them only manifest in dense ceramics. These new properties are linked to the high density of grain boundaries and interfaces that result from their nanoscale structure (characteristic length scale below 100 nm) [1]. Over the past 20 years, nanocrystalline oxide and nonoxide powders of high purity have also become available from a variety of synthetic routes, such as precipitation, sol–gel, inert gas condensation, chemical vapor deposition, high-energy milling, and hydrothermal reactions. As a result, considerable progress has been made in fabricating nanocrystalline ceramics. In the field of electroceramics, this progress is additionally driven by the technological imperative to miniaturize, because of the small device sizes and the increasing desire to impart multifunctionality into a single component. This trend is expected to continue into the foreseeable future; hence, the increasing importance of the fabrication processes, such as sintering, that may enable nanotechnology [2].

While fabrication of nanoceramics logically starts from nanosized powders, the passage from nanosized powders to dense ceramics maintaining the nanometric microstructure ($<$100 nm) has proved challenging for the following reasons. First, agglomeration of powders increases with decreasing particle size, and the size of the agglomerates rather than the size of the nanopowders defines the characteristic length scales in sintering and final microstructure. Second, final-stage sintering is always accompanied by rapid grain growth, which has increasing driving force with decreasing grain size, making it difficult to maintain the microstructure while improving density. Third, while there are conventional ceramic methods to enhance densification kinetics and suppress grain growth; they either depend on additives, which might adversely alter the physical properties, or resort to “bruit force” such as large applied pressure, which increases the cost and limits the process flexibility. Therefore, innovation is required to overcome or circumvent these problems in order to achieve efficient fabrication of nanoceramics.

The aim of this chapter is to provide an outline of major techniques that are available for fabricating dense nanocrystalline ceramics starting with powders. Key aspects of powder processing that are especially important for nanocrystalline ceramics are first emphasized. A review of the various densification methods for fabricating such ceramics follows. The main body of the chapter is devoted to a novel two-step sintering approach, which we developed some time ago [3], using low-temperature holding to exploit the different kinetics of grain boundary diffusion and grain boundary migration, achieving densification without grain growth. The kinetics of constant structure sintering in yttria and the successful application of this approach to several oxide and nonoxide ceramics will be described.

12.2 POWDER COMPACT

The first problem encountered in fabricating nanograined ceramics is powder compaction before sintering. The ideal green body should be a uniformly dense arrangement of powders without flaws or

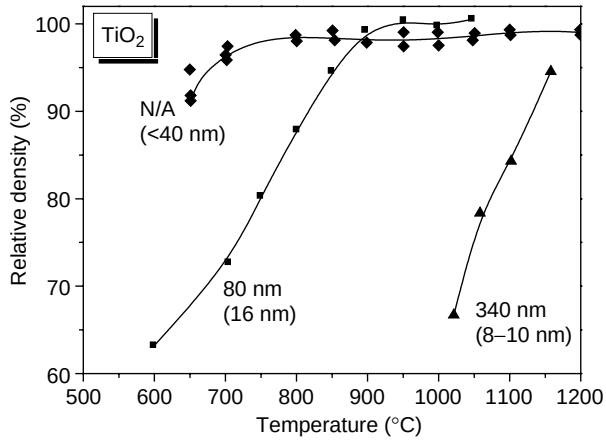

FIGURE 12.1 Sintering behavior of nanocrystalline TiO_2 powders with different agglomerate sizes. The bold-face types indicate the agglomerate sizes (N/A = no-agglomerate); the crystallite sizes are shown in parentheses.

defects. In reality, the quality of powder compact is as much related to the powder characteristics as to the method of compaction. Powder agglomerates formed during the synthesis process or during compaction have a decisively negative effect on subsequent sintering.

Gleiter [4] has used the gas-phase condensation technique to produce nanocrystalline material since the 1980s. Originally developed for preparing nanocrystalline metallic powders [5], it has since been modified to synthesize nanoceramic powders, such as TiO_2, ZnO, and MgO [6,7] by oxidation of the metal precursors. The powders obtained, however, are highly agglomerated. Since the largest pore spacing in the compact obtained from these powders is of the order of the agglomerate size, relatively long holding time and high temperature are needed to eliminate large inter-agglomerate pores during sintering, which usually lead to grain growth [8–11]. Figure 12.1 shows the densification behavior for three kinds of nanocrystalline TiO_2 powders with different agglomerate sizes. It is clear that the larger the agglomerate size, the higher the sintering temperature required. Typically, the grain size obtained is at least as large as the agglomerate size. For this reason, all early attempts of fabricating nanocrystalline ceramics using conventional sintering methods failed.

Pressureless-sintered nanocrystalline ceramics with grain sizes of 60 to 90 nm and of various densities have been reported starting from nanopowders that are free of agglomerates [12–15]. To avoid agglomeration, one strategy is to modify the surface properties of powders by adjusting synthesis conditions or using dispersants. For example, alcohol washing is a well-known method to prevent the formation of hydroxyl bridges between powders [16,17]. For TiO_2 powders prepared by the gas-phase condensation method, slower oxidation and lower temperature were found to reduce the heat of exothermic reaction, thus lessening powder agglomeration to a large extent [18,19]. Compacting under a high pressure to gain a highly dense green body is another technique that is used to break down the agglomerates. High pressure can make particles slide, pores deform, and pore size shrink. Therefore agglomeration is eliminated indirectly.

Besides powder agglomeration, packing homogeneity is also essential for obtaining dense ceramics. In the absence of agglomeration, particles still tend to interact with each other via van der Waals forces during powder handling (e.g., drying, storage, and compacting). The very high surface-to-volume ratio of nanopowders elevates the importance of this force, making it rather difficult to obtain green bodies of high packing density. Studies on nano powders have shown that, in many cases, the low density of sintered nanoceramics is due to this kind of agglomeration [20].

Several methods have been used to compact nanocrystalline powders into green bodies:

1. *Uniaxial pressing* [21]. The drawback of this simple method is that it often results in density and stress gradients throughout the green body. This problem tends to become worse with higher pressure. However, some researchers do prefer large pressure (reaching several GPa), because it can crush agglomerates, decrease pore size, and even eliminate pores, resulting in a high green density.
2. *Cold isostatic pressing*. No density or stress gradients should result from isostatic pressing because of the absence of die-wall friction. However, the applied pressure is usually limited to several hundred MPa in most commercial equipment.
3. *Colloidal processing.* Dispersion and deagglomeration of powders can be readily achieved for powders in the liquid, forming colloids. If subsequent drying is avoided and direct shape forming is undertaken using colloidal processing schemes, such as slip casting, then the green compact is free of agglomerates, which is advantageous for nanoceramics [22–24].
4. *Osmotic consolidation* [25]. Osmotic consolidation has often been used by biologists to consolidate protein solutions. Recently, this technique has also been found effective in forming compacts of nanopowders. The chemical potential difference across the membrane drives the solvent away from the particle suspension through diffusion across the enclosure membrane, leaving behind particles to consolidate at the "drain" side of the membrane forming a "cake" similar to the one in slip casting.

12.3 SINTERING

Sintering is the process whereby interparticle pores in a granular material are eliminated by atomic diffusion driven by capillary forces. It is the preferred manufacturing method for industrial ceramics. However, during the final stage of sintering rapid grain growth occurs because the intergrain pore channels that provide effective grain boundary pinning have already disappeared. Meanwhile, the capillary driving forces for sintering (involving surfaces) and grain growth (involving grain boundaries) are comparable in magnitude, both being proportional to the reciprocal grain size. Many efforts have been made to control grain growth in order to produce dense materials with nanometer-scale structure (grain size less than 100 nm). These are outlined below.

12.3.1 Sintering Additives

It is a well-known practice in ceramics to add solutes or second phase to a ceramic in order to reduce grain boundary mobilities or to pin grain boundaries, thus aiding sintering. For example, in the work of Rahaman [26], CaO was added to nanocrystalline Cs_2O to cause grain boundary segregation and to obtain fully dense nanoceramics of a grain size of 30 nm after sintering at 1350°C. Hahn et al. [27] found that when Y_2O_3 was added to nanocrystalline TiO_2, both partially dissolved in the grain boundary regions and formed a second phase thus limiting grain growth. Consequently, nanoceramic TiO_2 better than 99% dense was achieved with a grain size of less than 30 nm, compared to undoped but similarly sintered TiO_2 ceramics of only 90% dense with a grain size of 50 nm. Sintering additives may also result in liquid-phase formation. For example, Kleinlogel et al. [28] reported sintering of nanocrystalline CeO_2 ceramics with transition metal oxide additives, which led to size-dependent melting to allow dense ceramics at 900°C with a grain size of 100 nm. This final grain size was about 2 to 3 times the size of the starting powders. However, the use of sintering aids has its limitation, because the additives may also adversely affect the physical and chemical properties of the ceramics.

12.3.2 Hot Pressing and Sinter Forging

Hot pressing is the most common method that utilizes a mechanical driving force to supplement the sintering driving force in order to achieve rapid densification. It has often been used

for fabricating nanometer-scaled ceramics. By decreasing the densification time, grain growth is usually reduced, resulting in finer grained ceramics. Especially effective is to hot press at very high pressure and low temperature, so that grain deformation by dislocation plasticity, which aids densification but not grain growth, becomes dominant. Using pressures from 0.5 to 1.3 GPa and temperatures between 500 and 650°C, nano-TiO_2 ceramic discs with high densities (>95% of TD) and fine grain size (15 nm) can be prepared by this method [29,30]. Another mechanically assisted method of densification is sinter forging, which does not involve any die that provides the transverse pressure. Here the stress state is uniaxial, which facilitates shear deformation that helps in eliminating large pores [31]. As a result, lower applied pressure and temperature may suffice in sinter forging compared to hotpressing. Ceramics of TiO_2 [32,33] and 3% Y_2O_3-doped ZnO [34] have been successfully prepared by this method. However, both hotpressing and sinter forging require expensive mechanical presses and ancillary equipment, and the shapes of parts that can be produced by these methods are rather limited. Therefore, they have less appeal for applications at an industrial level.

12.3.3 Spark Plasma Sintering

Spark plasma sintering is a newly developed sintering process that combines the use of mechanical pressure and microscopic electric discharge between the particles. The enhanced densification in this process has been attributed to localized self-heat generation by the discharge, activation of the particle surfaces, and the high speed of mass and heat transfer during the sintering process. As a result, samples can rapidly reach full density at relatively low temperature. This process has been used to prepare a large variety of submicron and nanograined ceramics, including Al_2O_3 [35] and $BaTiO_3$ [36].

12.3.4 Transformation Sintering

There have been many reports in materials science literature on the enhanced shape deformation kinetics during a concomitant phase transformation. This is a kind of transformation plasticity, which has been shown to assist sintering-forming nanoceramics, e.g., by P. Morgan in 1960s. More recently, Kumar et al. [37] utilized the anatase–rutile transformation to sinter TiO_2 sol–gel powders at about 600°C (around the transformation temperature), obtaining >99% dense nanostructured titania with an average grain size of less than 60 nm. The authors suggested that the increased atomic mobility during the phase transformation was responsible for the enhanced sintering rate.

12.3.5 Two-Step Sintering

We have developed an entirely unconventional pressureless sintering method using a two-step sintering schedule with a prolonged, low-temperature hold following the initial sintering at a higher temperature. The most remarkable feature of this method is that there is continued densification in the second step but the final-stage grain growth is completely suppressed. Nanocrystalline ceramics can be obtained using this method. This was first demonstrated [3] for cubic Y_2O_3 (melting point, 2439°C), which was fully densified at the second-step temperature of 1000°C with a final grain size of 60 nm. The suppression of final-stage grain growth is achieved by exploiting the difference in the kinetics between grain-boundary diffusion and grain-boundary migration. Because there is no need for applied pressure and the sintering temperature is relatively low, this two-step sintering method, when optimized, is believed to be quite cost-effective. In the following sections, first the details of this method as applied to yttria, barium titanate, and NiCuZn ferrite based on the work in our laboratories, are described. This is followed by a review of the further application of the same approach to liquid-phase sintering of two nanostructured ceramics, zinc oxide and silicon carbide.

12.4 TWO-STEP SINTERING OF Y_2O_3 NANOCERAMICS

12.4.1 INTRODUCTION

Yttria (Y_2O_3) has a cubic defective fluorite structure with a very high melting point 2439°C. Fully dense Y_2O_3, typically sintered at above 1700°C, has superior thermal stability and is used as an optical material, having transmission at longer IR wavelengths than most other oxides (9.5 μm cutoff). Various processing techniques have been utilized to produce yttria powders that can be sintered at lower temperatures. These include urea method [38], hydroxide method [39], and ammonia-precipitation method [40]. For example, Chen and Chen [41,42] and Chen [43] synthesized several fine Y_2O_3 powders that were brought to full density at 45% of their melting points using normal sintering method. More recently, we have used a simple pressureless two-step sintering method to obtain fully dense Y_2O_3 with a grain size of 60 nm at temperatures of about 1000°C [3]. The suppression of final-stage grain growth is achieved in this process by exploiting the difference in the kinetics between grain-boundary diffusion and grain-boundary migration. These aspects are described below to illustrate the salient features of the method.

12.4.2 SINTERING OF Y_2O_3

Pure Y_2O_3 powders were synthesized by solution–polymerization route using yttrium nitrate and polyethylene glycol. Nanopowders with a grain size from 10 to 60 nm were obtained. We have also investigated Mg- and Nb-doped (1 at%) powders, since Mg is known to enhance kinetics in Y_2O_3, while the opposite holds for Nb. These dopants were introduced by coating the above powders using $Mg(NO_3)_2$ and niobium isopropoxide as cation sources, followed by low-temperature calcination. To avoid SiO_2 contamination, powder processing was conducted using plastic ware, and sintering was performed in a dedicated "clean" furnace. Cylindrical pellets (diameter = 10 mm, thickness = 10 mm) were prepared by die-pressing followed by cold isostatic pressing. Pressure up to 310 MPa was applied to obtain green bodies with different densities. Typically, a green body with density of 45% of the theoretical density (5.013 g/cm^3 for Y_2O_3 [40]) was used.

12.4.2.1 Normal Sintering

Normal sintering was conducted in air using a heating rate of 10°C/min up to 1500°C, holding it there until the maximum density was reached. The density was continuously monitored during heating and some runs were interrupted to measure grain size. Figure 12.2 shows the results of normal sintering for undoped Y_2O_3, Y_2O_3 doped with 1 at% Mg as well as Nb, all having an initial powder

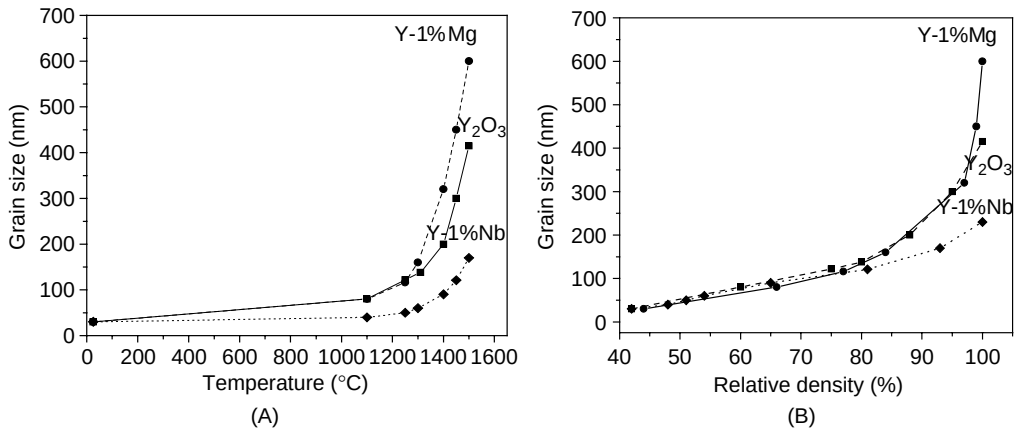

FIGURE 12.2 Grain size of Y_2O_3 in normal sintering vs. (A) sintering temperature; (B) relative density.

size of 30 nm. Depending on the composition, the final grain size varies between 200 and 600 nm, with most of the increase and variation occurring when the density exceeds 80%. This is in accord with the common experience of accelerated grain growth during final-stage sintering, where the effect of sintering additives is the alteration of the competition between densification and grain growth. Clearly, fully dense ceramics with a grain size below 100 nm cannot be obtained even with 30 nm powders and sintering additives.

12.4.2.2 Two-Step Sintering

In two-step sintering, the heating schedule shown in Figure 12.3 was followed. In the first step, the samples were heated from room temperature to a high temperature (T_1) at a rate of 10°C/min. Then the temperature was lowered at a rate of 50°C/min to a lower temperature (T_2) and held there until maximum density was reached, which required 10 to 40 h. We have shown that in the second step, densification can proceed without grain growth. It turns out that there is a minimum density, to be referred to as critical density, which needs to be exceeded in the first step in order to achieve full densification without grain growth, in the second step. This density is independent of the temperature (T_2) and time taken in the second step. There is also a temperature window for T_2 within which full densification without grain growth becomes possible. The lower limit of this window is typically much below the temperature required for normal sintering to reach full density [42,44].

Table 12.1 gives some of the two-step sintering results for both undoped and doped Y_2O_3 using powders with an initial size of 30 nm. After two-step sintering, all samples approached full density (above 99% theoretical density). The contrast of microstructure development in normal vs. two-step sintering can be seen in Figure 12.4, which shows rapid grain growth at high density in normal sintering, but no grain growth in two-step sintering. These results are in complete contradiction to the generally accepted theory of sintering. On the other hand, it has been shown that at densities above 70%, all pores in Y_2O_3 are subcritical and unstable against shrinkage (which occurs by capillary action) [41,42,45]. Such pores can be filled as long as grain-boundary diffusion allows it, even if the particle network is frozen as it clearly is in the second-step sintering. Therefore, the densification in the second step is thermodynamically feasible. The data in Table 12.1 indicate a lower limit for the density after the first step at about 75%, which may be regarded as the critical density and rationalized by the above reasoning.

12.4.2.3 Nanograined Y_2O_3

The grain size in Figure 12.2B typically increases by a factor of 4 to 5 when the density increases from 40 to 80%. This ratio is not sensitive to the dopant, sintering temperature, or the initial powder

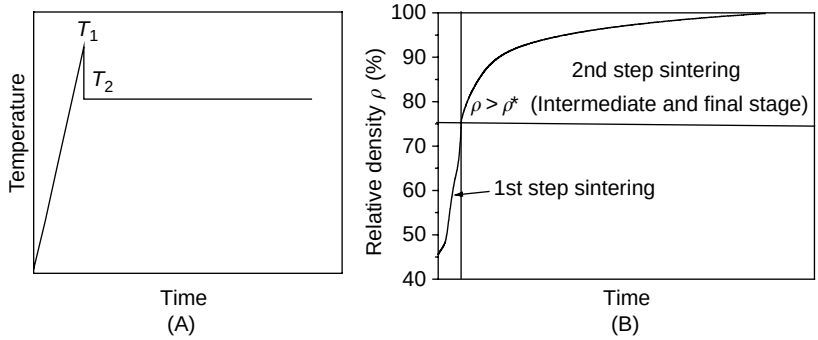

FIGURE 12.3 Temperature schedule for two-step sintering and the corresponding density variation.

TABLE 12.1
Results of Two-Step Sintering of Undoped and Doped Y_2O_3 Powder Compacts (Initial Grain Size of 30 nm)

Sample	After First-Step Sintering					After Second-Step Sintering			
	ρ_0 (%)	T_1 (°C)	t_1 (h)	ρ_1 (%)	G_1 (nm)	T_2 (°C)	t_2 (h)	ρ_2 (%)	G_2 (nm)
Y_2O_3-1	44	1250	0	75	122	1150	20	99.5	125
Y_2O_3-2	44	1250	0	75	122	1100	30	99.0	123
Y_2O_3-3	44	1310	0	80	138	1150	20	99.6	140
Y_2O_3-4	44	1310	0	80	138	1100	30	99.6	140
Y_2O_3-5	44	1350	0	85	160	1150	20	99.5	165
Y_2O_3-6	44	1350	0	85	160	1100	30	99.0	162
Y_2O_3-7	44	1400	0	88	200	1150	20	99.5	202
Y_2O_3-8	44	1400	0	88	200	1050	40	99.0	196
Y-1%Mg-1	44	1250	0	78	116	1100	20	100	120
Y-1%Mg-2	44	1250	0	78	116	1050	30	100	118
Y-1%Mg-3	44	1300	0	84	155	1050	20	100	157
Y-1%Mg-4	44	1300	0	84	155	1000	20	100	160
Y-1%Nb-1	44	1450	0	82	115	1250	20	99.2	120
Y-1%Nb-2	44	1450	0	82	115	1200	40	99.0	118

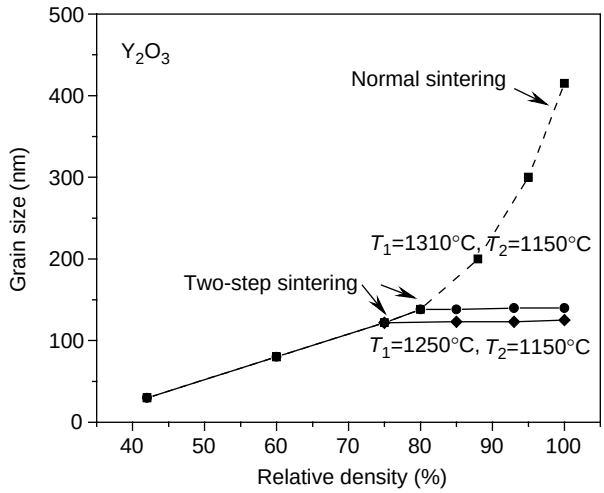

FIGURE 12.4 Different gain size trajectories followed by normal sintering and two-step sintering. In normal sintering, grain size continues to increase at high density. In contrast, in two-step sintering, with a lower temperature (T_2) during the second step, grain growth is completely suppressed while sintering continues.

size. Since two-step sintering can allow full densification from 75% without increasing the grain size, the final grain size is about 4 to 5 times the initial powder size. Therefore, to obtain a dense ceramic with a grain size of less than 100 nm, powders of 10 to 20 nm are needed. Indeed, using 10 nm powders and two-step sintering, we obtained several dense, doped Y_2O_3 nanoceramics. Examples of these experiments are shown in Table 12.2. The microstructure of a dense ceramic with a grain size of 60 nm is also shown in Figure 12.5. The same powder, with Mg addition, sinters to full density at twice the grain size if normal sintering is used (see Figure 12.6).

TABLE 12.2
Results of Two-Step Sintering of Y_2O_3 Doped with 1% Mg (Initial Grain Size of 10 nm)

Sintering Condition		Relative Density (%)	Grain Size (nm)
First step	**Second step**		
1080°C–0 min	N/A	76	55
1080°C–0 min	1000°C–10 h	99.5	56
1080°C–0 min	1000°C–20 h	100	60
1120°C–0 min	N/A	85	80
1120°C–0 min	1000°C–10 h	100	84
1120°C–0 min	1000°C–20 h	100	90

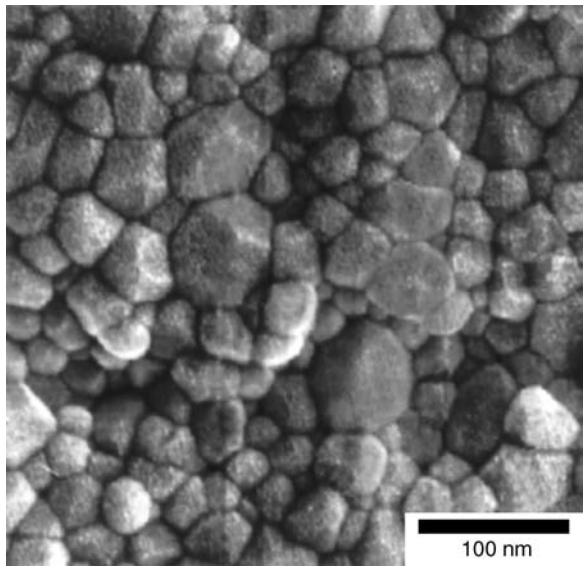

FIGURE 12.5 Microstructure of fully dense Y_2O_3 doped with 1% Mg. This specimen was sintered at 1000°C for 20 h, after reaching 76% relative density in an initial firing at 1080°C.

12.4.3 Kinetics of Constant Structure Sintering

An interesting observation in the second-step sintering is illustrated in Figure 12.7, which shows that the normalized densification rates from five representative runs are self-similar. This observation can be understood from the scaling argument of Herring [46], which states that the normalized densification rate can be expressed as

$$\frac{\mathrm{d}\rho}{\rho \mathrm{d}t} = F(\rho)\,\frac{3\gamma\Omega}{kT}\,\frac{\delta D}{G^4} \tag{12.1}$$

Here t is the time, γ the surface energy, Ω the atomic volume, k the Boltzmann constant, T the absolute temperature, G the mean grain diameter, δ the width of the grain boundary, D the grain boundary diffusivity, and $F(\rho)$ an unspecified function of density ρ. This argument applies if grain boundary diffusion is the dominant mechanism and if self-similarity in the microstructure is preserved during sintering. Note that the data shown here include the same composition sintered at different temperatures, with different starting grain sizes (governed by the choice of the first-step

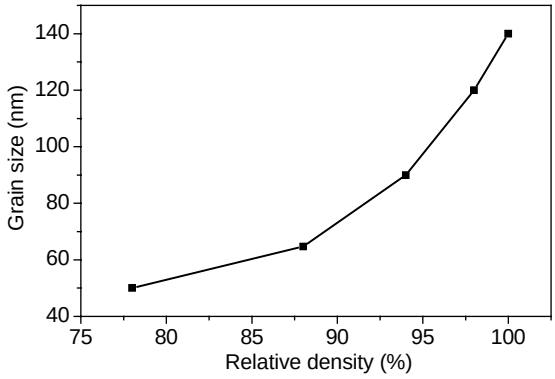

FIGURE 12.6 The grain size of Y_2O_3, doped with 1% Mg and with an initial particle size of 10 nm, increases with relative density during 10 h normal sintering at 1080°C.

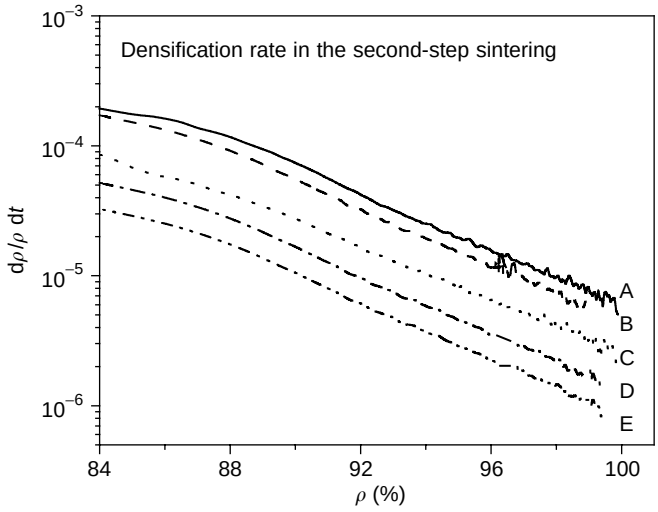

FIGURE 12.7 Normalized densification rate vs. relative density during second-step sintering (heating schedule is same as in Figure 12.3). Trace A, Y_2O_3; 1250°C, then 1150°C for 20 h (final grain size, 122 nm); B, Y_2O_3; 1210°C, then 1150°C for 20 h (final grain size, 140 nm); C, Y_2O_3 (1% Nb); 1450°C, then 1200°C for 40 h (final grain size, 118 nm); D, Y_2O_3; 1310°C, then 1100°C for 30 h (final grain size, 140 nm); E, Y_2O_3 (1% Mg); 1250°C, then 1050°C for 30 h (final grain size, 116 nm). All curves are parallel to each other.

sintering parameters) and different dopants. Despite these variations, the curves are parallel to each other supporting the notion that $F(\rho)$ is a universal function.

The magnitude of the normalized densification rate can be used to determine the grain size exponent in Equation (12.1). By plotting normalized densification rate against grain size in the log–log form, we obtained the exponent 3.7, for undoped Y_2O_3, which is consistent with Equation (12.1). The normalized densification rate can also be used to determine the activation energy of grain boundary diffusivity. This can be seen by rewriting Equation (12.1) as

$$\delta D = \frac{d\rho}{\rho\, dt}\ \frac{1}{F(\rho)}\ \frac{kT}{3\gamma\Omega}\, G^4 \tag{12.2}$$

and obtaining the activation energy from its Arrhenius plot. The activation energies — 410 kJ/mol for Y_2O_3, 550 kJ/mol for Mg-doped Y_2O_3, and 310 kJ/mol for Nb-doped Y_2O_3 — are comparable in

TABLE 12.3
Activation Energy for Grain Boundary Diffusion of Undoped and Doped Yttria Calculated

Sample	Present Results (kJ/mol)	Reference Result (kJ/mol)
Y_2O_3	410	340[47], 398[48]
Y-1% Mg	553	636[48]
Y-1% Nb	310	272[48]

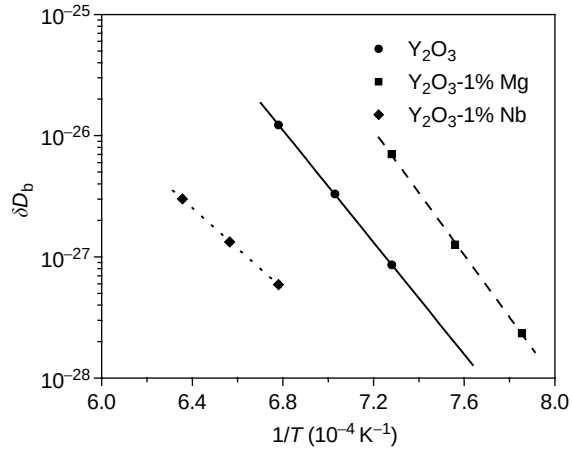

FIGURE 12.8 Grain boundary diffusivity, multiplied by grain boundary thickness, vs. temperature for undoped and doped Y_2O_3. From sintering data obtained at density of 86% with same grain size.

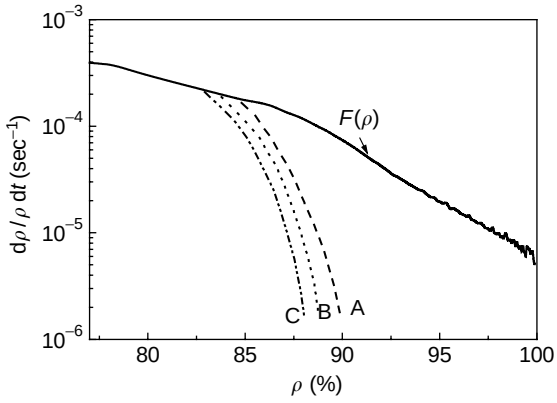

FIGURE 12.9 Densification rate is exhausted during second-step sintering if T_2 is too low, as in the three cases A–C.

magnitude to the activation energies for grain boundary mobilities previously determined for these materials at higher temperatures (see Table 12.3 and Figure 12.8). This is consistent with the notion that the densification kinetics in the constant grain size regime is controlled by a grain boundary process.

The above analysis applies if second-step sintering results in full densification and no grain growth. However, if second-step sintering is conducted at too low a temperature, sintering may proceed for a while but then is exhausted. The normalized sintering rates of such runs, shown in Figure 12.9, deviate

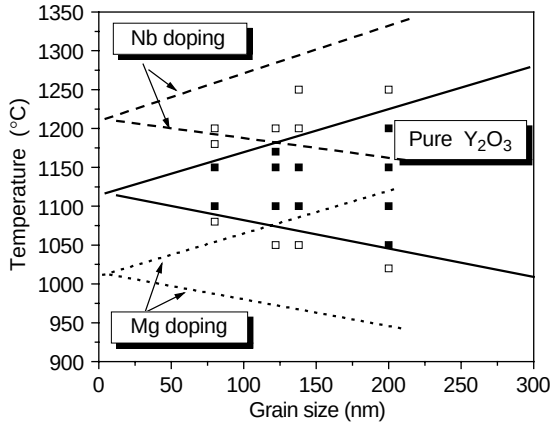

FIGURE 12.10 Kinetic window for reaching full density without grain growth. Solid symbols are temperature and grain-size conditions of successful second-step sintering runs for Y_2O_3. Open symbols above the upper boundary are conditions that showed grain growth in second-step sintering. Open symbols below the lower boundary are ones that did not reach full density in second-step sintering. Similar boundaries are shown for Y_2O_3 doped with 1% Nb (broken lines) and with 1% Mg (dotted lines).

from the universal shape described above. The rather abrupt termination of densification is probably caused by the exhaustion of diffusion itself. The temperature and the grain size regime where this occurs is shown in Figure 12.10, in which the solid symbols represent conditions when second-step sintering can be completed without grain growth, while the data points below the lower boundary line are ones, where densification is exhausted without grain growth. On the other side of the upper boundary line are conditions where grain growth is observed. Therefore, the two boundary lines define the kinetic window for the second-step sintering within which densification without grain growth may be achieved. This general behavior was observed in both undoped and doped Y_2O_3.

Exhaustion of diffusion could arise because of the exhaustion of kinks, ledges, sources and sinks, which are required to provide and accommodate diffusing atoms and point defects. Some of these, such as kinks and ledges, may be eliminated when they are filled by atoms/point defects during diffusion proceeds. Nucleation of new sources and sinks may be difficult, especially in small grains, because of poor nucleation statistics in small volume as well as the increased threshold energy required. For example, if a screw dislocation loop is envisioned for the source and sink, then the threshold energy is inversely proportional to the grain size. In this regard, we note that in Figure 12.10 the lower boundary has a slightly negative slope indicating that the exhaustion of sintering is more obvious at smaller grain size. On the other hand, it is noted that the upper boundary line has a positive slope. This could be because the driving force for grain growth decreases with grain size, and so a higher temperature is needed.

Finally, we will speculate on the mechanism that allows densification without grain growth, which requires grain boundary diffusion while suppressing grain boundary migration. Since successful two-step sintering can be achieved in both undoped and doped (with Nb suppressing kinetics as well as with Mg enhancing kinetics) samples, we do not think solute drag is a central element in the mechanism. It is clear, however, that grain boundary migration must involve additional kinetic processes beyond grain boundary diffusion. Furthermore, if such processes have a higher activation energy, then grain boundary migration can be suppressed at lower temperature despite active grain boundary diffusion. Czubayko et al. [48] reported that in high-purity zinc tricrystals, grain boundary migration was severely retarded at lower temperatures by the drag of the triple point. (At high temperatures, the drag is negligible.) This observation lends support to the above speculation and leads us to propose the schematic in Figure 12.11, in which we plot the grain boundary diffusivity, the intrinsic grain boundary mobility

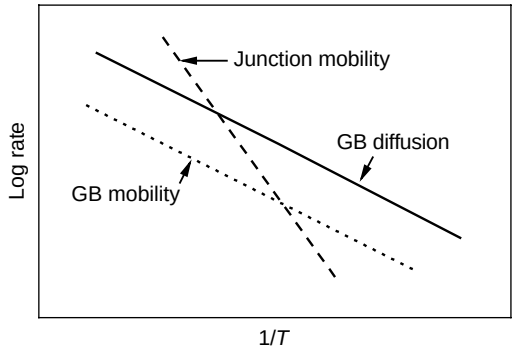

FIGURE 12.11 Schematic Arrhenius plot for grain diffusion, mobility of pore/grain-boundary junction or four-grain junction, and intrinsic mobility of grain boundary (without extrinsic drag due to nodal points/lines).

(e.g., of a bicrystal grain boundary, which has the same activation energy as grain boundary diffusivity), and the mobility of junctions (triple point and/or pore-boundary junction), which has a higher activation energy. For a polycrystal, the apparent grain boundary mobility is controlled by the slower of two — the intrinsic grain boundary mobility or the junction mobility. At low temperature, it is then possible for grain boundary diffusion to have an activation energy smaller than that of the apparent polycrystal grain boundary mobility, resulting in the suppression of grain growth without quenching densification. The design of two-step sintering seeks to take advantage of this disparity.

12.5 TWO-STEP SINTERING OF OTHER FUNCTIONAL AND STRUCTURAL CERAMICS

In this section, we review the successful applications of the two-step sintering approach to other ceramics in the pursuit of fine grain and nanograin ceramics. Specifically, $BaTiO_3$, NiCuZn spinel ferrite, ZnO varistor, and SiC will be described. For the latter two systems, liquid-phase sintering additives are commonly used in conventional sintering; this practice has also been adopted in two-step sintering.

12.5.1 $BaTiO_3$ Ceramics

Barium titanate has perovskite structure and is one of the most important electroceramics. It is extensively used as high dielectric constant capacitors, PTC resistors, transducers, and ferroelectric memories [49]. The electrical properties such as permittivity, Curie temperature, and phase assemblage are known to be sensitive to the grain size and the characteristics of grain boundaries [50–53]. Therefore, the development of fine grain and nanostructured $BaTiO_3$ is of current scientific interest. In addition, since the dimensions of $BaTiO_3$-containing components, such as multilayer chip ceramic capacitors, continue to shrink, there is also a technological need to develop fine grain $BaTiO_3$. (Currently, the thickness of the dielectric layer is 2 μm and, therefore, the grain size should be 200 nm or less in a polycrystalline layer to assure property uniformity.) To date, most studies on the size effect on $BaTiO_3$ have focused on powders and films of a much smaller thickness than for practical applications. Recently, Park and Cho [54] hot-pressed bulk $BaTiO_3$ ceramic with a grain size of 40 to 50 nm, but the density reached was only 3.56 g/cm^3, which is much lower than the theoretical density of 6.03 g/cm^3. As will be shown below, we have used two-step sintering to fabricate fully dense $BaTiO_3$ with a grain size of about 60 to 70 nm, which is the first presureless-sintered dense nanograined $BaTiO_3$ ceramic ever reported.

$BaTiO_3$ nanopowders used here were prepared by an oxalate precipitation method [55]. The mean particle size was determined to be 10 to 30 nm. After isopressing at 200 MPa (relative density = 46% of theoretical), the green compacts were sintered using two-step sintering. The first step used

TABLE 12.4
Conditions for Two-Step Sintering of $BaTiO_3$ (30 nm Powders) Reaching High Density without Grain Growth

Sintering Condition		Relative Density (%)		Final Grain Size (nm)
First step	Second step	ρ_1	ρ_2	
1100°C–0 min	900°C–20 h	73	96	150
1100°C–0 min	950°C–20 h	73	97	150
1150°C–0 min	900°C–20 h	78	96	200
1150°C–0 min	950°C–20 h	78	97	200
1150°C–0 min	1000°C–20 h	78	97	200
1200°C–0 min	900°C–20 h	87	96	500
1200°C–0 min	1000°C–20 h	87	96	500
1200°C–0 min	1100°C–10 h	87	97	500

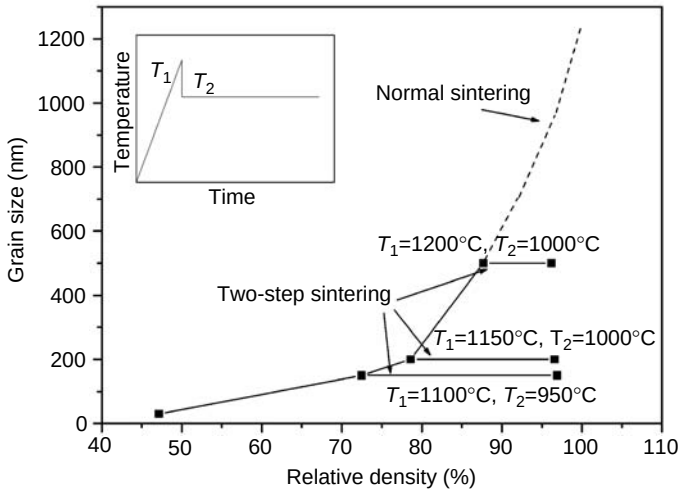

FIGURE 12.12 Grain size vs. density for $BaTiO_3$ specimens sintered by two-step and by normal sintering.

a higher temperature T_1 ranging from 1100 to 1250°C. After reaching T_1, immediate cooling to a lower temperature T_2 ranging from 1150 to 850°C was used for 10 to 20 h for isothermal sintering. The initial heating rate was 10°C/min, and the intermediate cooling rate (from T_1 to T_2) was 30°C/min. During the second-step sintering, density improved from a lower value (73 to 87%) to better than 96% without any grain growth. These results are summarized in Table 12.4 and Figure 12.12.

For $BaTiO_3$ at T_1 the critical density , which is required for producing dense ceramics during the second-step sintering, is about 73%. This is essentially the same value as for Y_2O_3 (about 75%). The kinetic "window" for reaching full density without grain growth is shown in Figure 12.13. As in the case of Y_2O_3 (Figure 12.10), closed symbols have been used to indicate the conditions to obtain full densification without grain growth. Above this window grain growth was observed; below this window sintering was exhausted before achieving full density. Clearly, the phenomenology and the shape of the kinetic window are very similar in both sets of ceramics despite their very different chemistry and crystal structure.

The finest grain size of dense, undoped $BaTiO_3$ ceramics (98.5% of theoretical density) obtained so far is around 60 to 70 nm, using starting powders with an initial size of 10 nm (see Figure 12.14). This nanograined $BaTiO_3$ ceramic shows only cubic phase according to x-ray

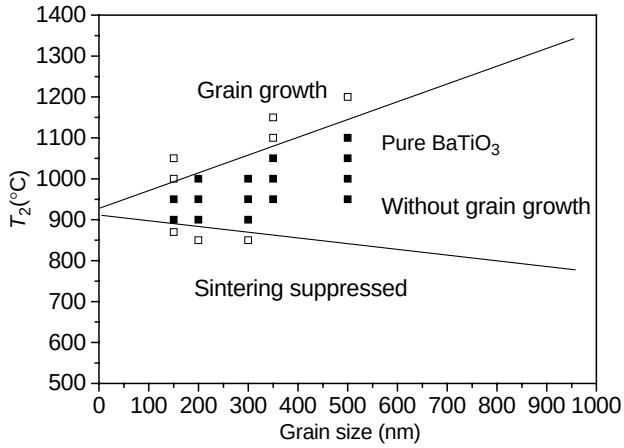

FIGURE 12.13 Kinetic window for second-step sintering without grain growth for $BaTiO_3$. Closed symbols: successful runs; open symbols: unsuccessful ones with either grain growth (upper) or poor density (lower).

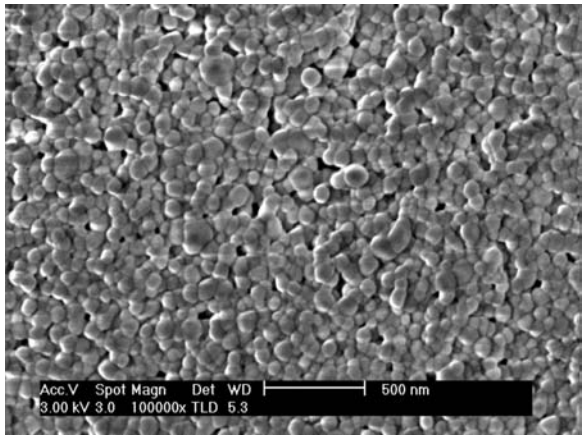

FIGURE 12.14 SEM image of nanograined $BaTiO_3$ ceramics prepared by two-step sintering.

diffraction. Further investigation of the size effect on the microstructure and physical properties of these $BaTiO_3$ ceramics is currently in progress.

12.5.2 NiCuZn Ferrite

Ferrites have the spinel structure A_2BO_4 in which Fe may occupy either A or B site, or both. They are ferrimagnetic and widely used as soft magnets. In the past 10 years, with the development of surface-mounting technology, considerable progress has been made in the miniaturization of electromagnetic components. NiCuZn ferrite is commonly used in various electronic devices such as multilayer chip inductor in the high-frequency region [56–59]. In order to be co-fired with the electrode (usually Ag, with a melting point of 961°C), NiCuZn ferrite is sintered at $<$900°C. For this purpose, sintering aids such as Bi_2O_3 and V_2O_5 are commonly used to lower the sintering temperature. However, these additives tend to harm the magnetic property of the ceramics acquired. Therefore, ultrafine grained NiCuZn ferrite with a uniform composition and microstructure, densifiable at low temperature without sintering aids, is of considerable interest [60]. Using two-step sintering and nanosized ferrite powders, we have obtained submicro grain-sized NiCuZn ferrites with excellent

properties, including high initial permeability of up to 1000 and high resistivity above $10^{10}\ \Omega$ cm, which are two orders of magnitude higher than those obtained in conventional ferrite ceramics.

In this research, starting ferrite powders with a composition of $(Ni_{0.2}Cu_{0.2}Zn_{0.6}O)(Fe_2O_3)$ were prepared via a citrate precursor method [61]. The mean grain size of powders varies from 10 to 60 nm, depending on the heat-treatment condition. These powders have excellent sinterability and can be densified at <900°C without any addition of sintering aids. During two-step sintering, the powder compacts were first heated to a high temperature T_1 ranging from 850 to 930°C, then immediately cooled to lower temperature T_2 ranging from 750 to 870°C, with a dwell time from 4 to 8 h to reach high density. Some results of two-step sintering using a heating rate of 10°C/min and a cooling (from T_1 to T_2) rate of 30°C/min, are listed in Table 12.5.

In the NiCuZn ferrite system, the critical density obtained at T_1 that is required to produce dense ceramics during subsequent T_2 sintering is about 76%. Once again, this value is essentially the same as for Y_2O_3 and $BaTiO_3$. Figure 12.15 shows the kinetic window for reaching full density without grain growth. Solid symbols are temperature and grain-size conditions of successful second-step sintering runs for NiCuZn ferrite. Open symbols above the upper boundary indicate conditions that showed grain growth in the second step, whereas open symbols below the lower boundary indicate

TABLE 12.5
Conditions for NiCuZn Ferrite (Initial Particle Size of 10 nm) Fabricated Using Two-Step Sintering That Shows No Grain Growth during the Second Step

Sintering Condition		Relative Density (%)		Final Grain Size (nm)
First step	Second step	ρ_1	ρ_2	
850°C–0 min	760°C–8 h	76	96	200
850°C–0 min	800°C–6 h	76	97	200
890°C–0 min	750°C–6 h	81	97	400
890°C–0 min	825°C–6 h	81	98	400
910°C–0 min	750°C–8 h	87	97	500
910°C–0 min	800°C–6 h	87	98	500
910°C–0 min	850°C–4 h	87	99	500
930°C–0 min	800°C–4 h	91	99	800
930°C–0 min	850°C–4 h	91	99	800
930°C–0 min	870°C–4 h	91	99	800

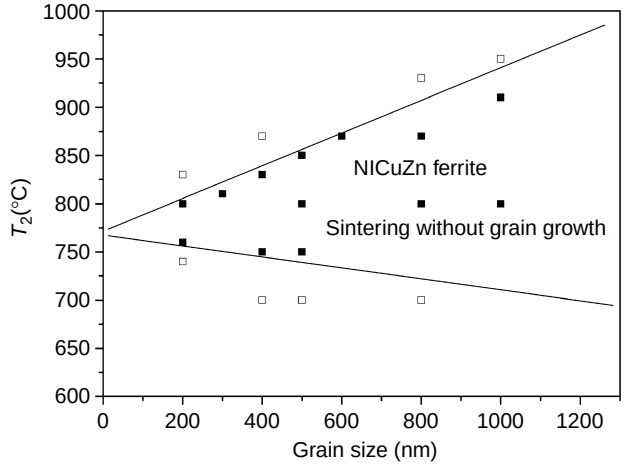

FIGURE 12.15 Kinetic window for reaching full density without grain growth for NiCuZn ferrite.

grain growth that did not reach full density in the second-step sintering. The general behavior is quite similar to that of Y_2O_3 and $BaTiO_3$. Therefore, the feasibility of two-step sintering to achieve high density without grain growth has again been established for another complex oxide system using pressureless means without sintering aids.

The finest NiCuZn sample obtained in this study has a grain size of 200 nm and a density of over 97%. It was initially heated to 850°C (T_1), then cooled to 800°C (T_2), and sintered there for 6 h without grain growth. In another case, the sample was heated to a higher temperature of 930°C (T_1), and high density of 99% was attained with grain size of 700 to 800 nm after holding for 4 h at 850°C (T_2), during which time there was no grain growth. Figure 12.16 shows the SEM micrographs of two such samples (Figures 12.16A and B), and of one sample obtained from conventional processing (Figure 12.16C) (using normal sintering and powders from solid-state reactions). The contrast in microstructure is rather dramatic, with the two-step-sintered samples showing much finer, uniform microstructure.

The frequency-dependent permeability curves of the ceramic samples prepared by two-step sintering and normal sintering method are compared in Figure 12.17. The sample prepared by two-step sintering has an initial permeability of up to 1000, more than three times that of the sample prepared by the conventional ceramic method. This extremely high magnetic permeability value has not been reported for NiCuZn ferrite before, suggesting the benefit of a very fine and uniform microstructure, high density, and chemical purity (in the absence of sintering aid).

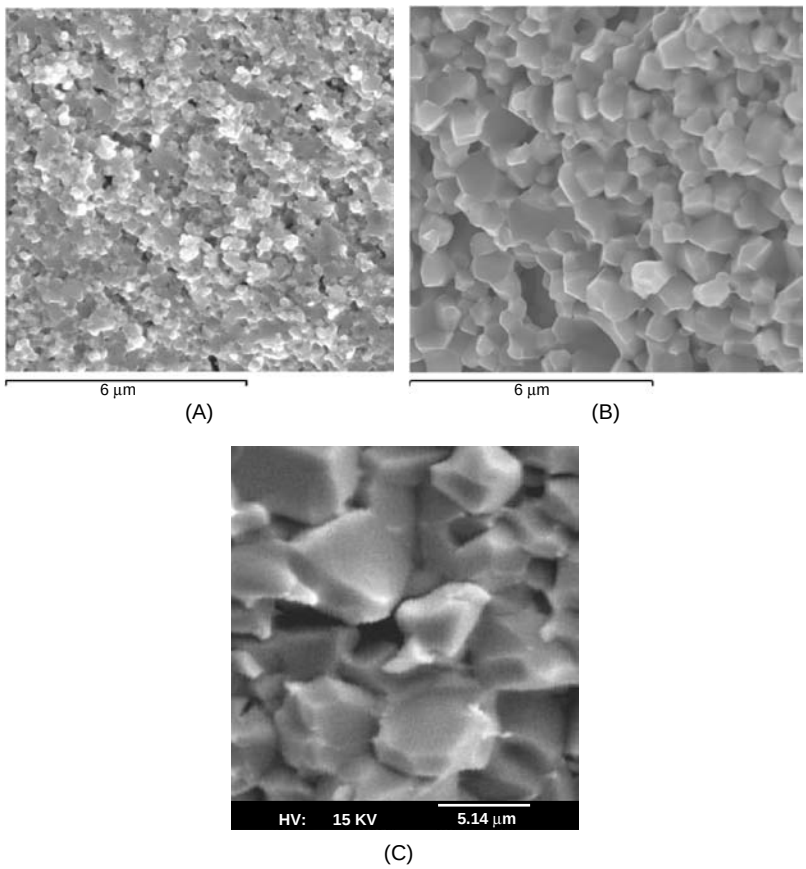

FIGURE 12.16 SEM images of fracture surface microstructures for NiCuZn ferrite made from (A) nanocrystalline powder densified by two-step sintering (T_1 = 850°C/0 min, T_2 = 800°C/6 h), (B) nanocrystalline powder densified by two-step sintering (T_1 = 930°C/0 min, T_2 = 850°C/4 h), and (C) solid-state reaction powder densified by normal sintering.

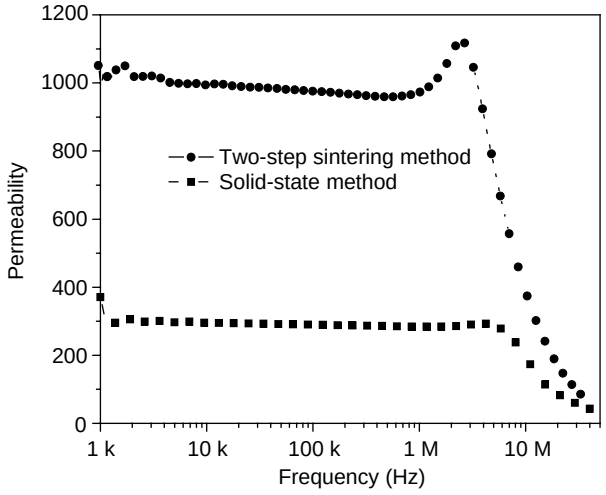

FIGURE 12.17 Frequency-dependent permeability curves of ceramic specimens made from (A) nanocrystalline powder densified by two-step sintering (T_1 = 930°C/0 min, T_2 = 850°C/4 h) and (B) solid-state reaction powders fired via normal sintering route.

An adequate DC resistivity is also required for ferrite to avoid "creeping" during electroplating, which may adversely affect the quality of the components. Usually, by conventional ceramic processing methods, ceramics with DC resistivity of 10^7 to 10^8 Ω cm can be achieved, which hardly satisfies the requirement. The ultrafine grain ferrites obtained by two-step sintering show high DC resistivity, over 10^{10} Ω cm, which is much more suitable for practical applications and has much enhanced reliability. As is well known, one important factor that affects the resistivity of a ceramic is the fraction of grain boundaries in a polycrystal. This fraction increases with decreasing grain size and may account for the superior resistivity observed here.

12.5.3 ZnO Varistor

Zinc oxide has wurtzite structure and is semiconducting. Sintered with the addition of Bi_2O_3 as a liquid-forming sintering aid, ZnO ceramics are widely used as varistors. Commercial varistors prepared by the conventional ceramic method contain compositional and microstructural heterogeneities, along with a large grain size of more than 5 μm. As a result, they have a relatively low breakdown strength, which has limited their use in higher voltage (>10 kV/cm) applications. Using two-step sintering, Duran et al. [62] fabricated fully dense Bi_2O_3-doped ZnO varistors with submicron grain size. The ceramics exhibited a nonlinear current coefficient as high as 270 and a breakdown field V_b (at 1 mA/cm^2) of about 20 kV/cm. These values are more than one order of magnitude higher than those found in commercial ZnO varistors.

In this work, nanopowders of Bi_2O_3-doped ZnO (total additives of 2 mol% including Bi_2O_3, Sb_2O_3, CoO, and MnO) were prepared by thermal decomposition of a metal–citrate polymeric complex precursor. The powders have a Brunauer-Emmett-Teller (BET) surface area of 40 m^2/g with a particle size of 28 nm. After isopressing at 200 MPa (relative density = 46%), the green compact was densified using two-step sintering. Following initial heating to 900°C (T_1) and sintering for 5 min, the temperature was lowered to 825°C (T_2) and held there for 10 h. Grain growth was suppressed during second-step sintering while densification proceeded, reaching full density with a grain size of 500 nm. In another case, after the first step of 940°C (T_1), sintering was continued at 825°C (T_2) for 6 h to reach full density without grain growth, with a grain size of 700 nm. In contrast, in normal sintering, the grain size achieved for the dense ceramic body was about 5 μm. The critical density required for the first step was between 80 to 90% in order to obtain fully dense bodies during the second step.

TABLE 12.6
Sintering Schedule Adopted for SiC [64]

Sintering Method	Specimens	Sintering Conditions	
Conventional sintering	C1		1500°C–8 h
	C2		1550°C–8 h
	C3		1750°C–5 min
	C4		1750°C–30 min
Zero-time sintering	Z1		1700°C–0 min
	Z2		1750°C–0 min
	Z3		1800°C–0 min
	Z4		1850°C–0 min
Two-step sintering		First step	Second step
	T1	1650°C–0 min	1500°C–8 h
	T2	1700°C–0 min	1500°C–8 h
	T3	1700°C–0 min	1550°C–2 h
	T4	1700°C–0 min	1550°C–8 h
	T5	1750°C–0 min	1550°C–8 h

In the ZnO–Bi_2O_3 system, a liquid phase forms at above 825°C. Therefore, the relatively high densification level attained in the first step (T_1>825°C) is achieved by liquid-phase sintering, involving a rapid rearrangement of the solid ZnO nanoparticles. From SEM observations, it was found that the intergranular liquid phase is continuous at T_1 but discontinuous at T_2 (dihedral angle much higher than zero), indicating a strong temperature dependence of the dihedral angle [63]. During cooling from T_1 to T_2, the wetting liquid rapidly recedes from the two-grain boundaries to the multigrain junctions. Thereafter, most ZnO grains will be in direct contact with each other without a liquid phase in between. For this reason, grain boundary mobility is suppressed in second-step sintering.

The electrical properties of a varistor strongly depend on the density and the microstructure uniformity. The small grain size is apparently an added advantage. As a result, two-step sintering has yielded varistors that have excellent electrical performance.

12.5.4 SiC Ceramics

Silicon carbide has either a zinc blende structure (β-SiC) or a wurtzite structure (α-SiC), but other structures that are related to these two by way of different stacking sequence are also common. In all cases, bonding of SiC is highly covalent, which distinguishes it from all the oxides described so far. Sintering of SiC typically requires the addition of liquid-forming sintering aids. Even so, very high sintering temperature, in excess of 1800°C, is usually needed. Since grains grow more readily during liquid-phase sintering than during solid-state sintering, it is difficult to obtain nanostructured ceramics by conventional means. Recently, Lee et al. [64] reported fully dense nanostructured liquid-phase-sintered SiC with agrain size of 40 nm, using two-step sintering under hot-pressing conditions (20 MPa). Therefore, the feasibility of densification without grain growth by two-step sintering has also been demonstrated for covalent ceramics, albeit with pressure assistance.

In this work, SiC powders (particle size of 20 nm and mostly β phase) were mixed with sintering aids, 7 wt% Al_2O_3, 2 wt% Y_2O_3, and 1 wt% CaO, then hot-pressed in Ar atmosphere under an applied pressure of 20 MPa. The additives are expected to form a liquid phase at about 1400°C. Three different heating schedules as shown in Table 12.6 were used. In two-step sintering, the powder compacts were first heated to a temperature (T_1) ranging from 1650 to 1750°C, then immediately cooled to (T_2) 1500 or 1550°C. The specimens were further treated at this temperature for up

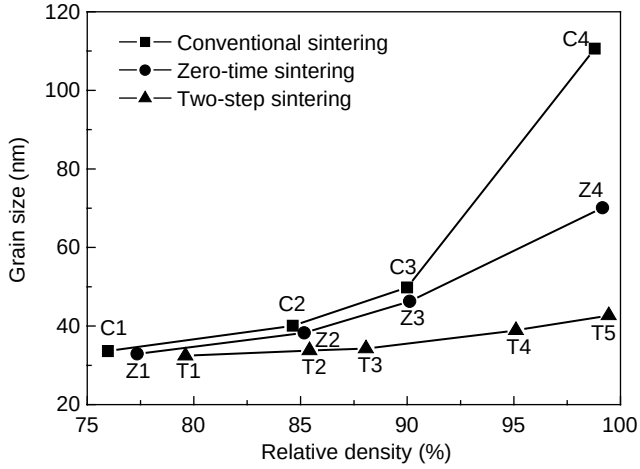

FIGURE 12.18 Grain size vs. density for SiC specimens sintered by various methods.

to 8 h. The heating rate to T_1 was 20°C/min, and the cooling rate from T_1 to T_2 was 40°C/min. For comparison, normal sintering was also carried out.

As shown in Figure 12.18, significant grain growth occurs during the final stage of densification, but this was absent in two-step sintering (Samples T4 and T5). An examination of the data in Figure 12.18 also indicates that the critical density, which needs to be achieved in the first-step sintering in order to assure full densification in the second-step sintering, is about 85% of theoretical density. This value is similar to the one found in Bi_2O_3-doped ZnO, another liquid-phase sintering system. It is, however, significantly higher than the critical density (75%) for Y_2O_3, $BaTiO_3$, and NiCuZn ferrite, all sintered by solid-state mechanisms.

During liquid-phase sintering, the final-stage densification mainly involves the elimination of isolated pores through liquid flow into them. Thermodynamically, this requires the pores to be relatively small compared to grains, so that it "drains" the liquid from the surrounding meniscus. For this reason, grain growth that eventually renders pores unstable to be filled by the liquid is an essential mechanism. Conversely, without grain growth, pore-filling-controlled liquid-phase sintering cannot proceed. Although the slower grain-flattening mechanism for liquid-phase sintering could contribute to densification, we believe pore elimination in the present case is more likely due to the applied pressure, which affects deformation and local grain rearrangement, bringing pores to transient configurations that are temporarily unstable. Unlike the case of ZnO, however, there is no clear evidence of liquid redistribution observed in the present case in view of the large amount of liquid, typically 10 to 15% in volume fraction, used [65]. Therefore, the suppression of grain growth cannot be attributed to liquid recession and the actual mechanism is yet to be determined.

12.6 CONCLUSIONS

Dense, nanograin ceramics are of current scientific and technological interest, especially for applications in electromagnetic devices in which miniaturization and integration are essential. The processing challenge is to fabricate fully dense ceramics at low temperature, preferably without additives and pressure, and with the least amount of coarsening of the initial microstructure. In this review, we have emphasized the importance of agglomeration-free green-body fabrication and two-step sintering, the latter being a unique, unconventional, yet industrially viable process capable of densification without grain growth. Two-step sintering exploits the difference in the kinetics between grain boundary diffusion and grain boundary migration at low temperature, and it has been demonstrated for simple oxides (Y_2O_3, with and without dopants), complex oxides ($BaTiO_3$ and NiCuZn spinel ferrite), and

liquid-phase-sintered ZnO and SiC. As nanocrystalline powders in the size range 5 to 10 nm are becoming increasingly available, we believe it should be possible to achieve dense, nanostructured industrial materials of a grain size 25 to 50 nm using two-step sintering. The simplicity of this sintering approach should also make it a useful tool for preparing model systems to study grain size-dependent properties in nanostructured materials and grain boundary kinetics at low temperatures.

ACKNOWLEDGMENTS

XHW is supported by the Ministry of Sciences and Technology of China through 973-project under grant 2002CB613301. IWC is supported by the National Science Foundation, Grant Nos. DMR03-03458 and DMR05-20020.

REFERENCES

1. Gleiter, H., Nanostructured materials: basic concepts and microstructure, *Acta Mater*., 48, 1, 2000.
2. Setter, N., Electroceramics: looking ahead, *J. Eur. Ceram. Soc.*, 21, 1279, 2001.
3. Chen, I.W. and Wang, X.H., Sintering dense nano-crystalline ceramics without final stage grain growth, *Nature*, 404, 168, 2000.
4. Birringer, R. et al., Nano-crystalline materials an approach to a novel solid structure with gas-like disorder, *Phys. Lett.*, 102A, 365, 1984.
5. Siegel, R.W. et al., Characterization, properties of nano-phase TiO_2, *J. Mater. Res.*, 3, 1367, 1988.
6. Eastman, J.A. et al., Processing of advanced ceramics, in *Materials Research Society Symposium Proceedings*, Vol. 155, Aksay, I.A., Ed., Materials Research Society, Pittsburgh, PA, 1989, p. 255.
7. Mayo, M.J. et al., Nanoidentation of nanocrystalline ZnO, *J. Mater. Res.*, 7, 973, 1992.
8. Pampuch, R. and Haberko, K., in *Ceramic Powders*, Vincenzini, P., Ed., Agglomerates in Ceramic Micropowder and Their Behavior on Cold Pressing and Sintering, Elsevier, Amsterdam, 1983, p. 623.
9. Mayo, M.J., Processing of nanocrystalline ceramics from ultrafine particles, *Int. Mater. Rev.*, 41, 85, 1996.
10. Boschi, A.O. and Gilbart, E., in *Advanced Ceramic Processing and Technology*, Pinner, I.J.G., Ed., Wet Forming Process as a Potential Solution to Agglomeration Problems, Noyes, Park Ridge, NJ, 1990, p. 73.
11. Rhodes, W.H., Agglomerate and particle size effects on sintering yttria-stabilized zirconia, *J. Am. Ceram. Soc*., 64, 19, 1981.
12. Winnubst, A.J.A. et al., in *Structure Ceramics: Processing, Microstructure and Properties*, Bentzen, J.J. et al., Eds., Microstructure Development during Sintering of Nanocrystalline Tetragonal Zirconia, Riso National Laboratory, Roskilde, Denmark, 1990, p. 523.
13. Mayo, M.J., Synthesis and application of nano-crystalline ceramics, *Mater. Des.*, 14, 323, 1993.
14. Chen, D.J. and Mayo, M.J., Densification and grain growth of ultra-fine 3 mol% Y_2O_3–ZrO_2 ceramics, *Nanostruct. Mater.*, 2, 469, 1993.
15. Skandan, G. et al., Ultrafine grained dense monoclinic and tetragonal zirconia, *J. Am. Ceram. Soc.*, 77, 1706, 1994.
16. Readey, M.J. et al., Processing and sintering of ultra-fine MgO–ZrO_2 and (MgO,Y_2O_3)–ZrO_2 powders, *J. Am. Ceram. Soc*., 73, 1499, 1990.
17. Jones, S.L. and Norman, C.J., Dehydration of hydrous zirconia with methanol, *J. Am. Ceram. Soc.*, 71, 190, 1988.
18. Skandan, G., Hahn, H., and Parker, J.C., Nano-structured Y_2O_3: synthesis and relation to microstructure and properties, *Scr. Metall. Mater*., 25, 2389, 1991.
19. Skandan, G. et al., Molecularly designed ultra-fine/nano-structured materials, in *Materials Research Society Symposium Proceedings*, Vol. 351, Gonsalves, K.E. et al., Eds., Materials Research Society, Pittsburgh, PA, 1994, p. 207.
20. Patton, T.C., *Paint Flow and Pigment Dispersion*, Wiley, New York, 1979, p. 266.
21. Reed, J.S. and Runk, R.B., in *Treatise on Materials Science and Technology*, Vol. 9, Wang, F.F.Y., Ed., Dry Pressing, Academic Press, New York, 1976, p. 71.
22. Lange, F.F., Powder processing science and technology for increased reliability, *J. Am. Ceram. Soc*., 72, 3, 1989.

23. Ferkel, H. and Hellming, R.J., Effect of nanopowder deagglomeration on the densities of nanocrystalline ceramic green bodies and their sintering behaviour, *Nanostruct. Mater.*, 11, 617, 1999.
24. Liu, D.M., Adsorption, rheology, packing, and sintering of nanosize ceramic powders, *Ceram. Int.*, 25, 107, 1999.
25. Miller, K.T. and Ukoski, C.F., Osmotic consolidation of suspensions and gels, *J. Am. Ceram. Soc.*, 77, 2473, 1994.
26. Rahaman, M.N., in *Sintering Technology*, Messing, G.L. and Cornwall, R.G., Eds., Sintering and Grain Growth of Ultrafine Ceramic Powders, Marcel Dekker, New York, 1996, p. 93.
27. Hahn, H. et al., Cluster and cluster–assembled materials, in *Materials Research Society Symposium Proceedings*, Vol. 206, Averback, S. et al., Eds., Materials Research Society, Pittsburgh, PA., 1991, p. 569.
28. Kleinlogel, C. and Gauckler, L.J., Sintering of nanocrystalline CeO_2 ceramics, *Adv. Mater.*, 13, 1081, 2001.
29. Terwilliger, C.D. and Chiang, Y.M., Characterization of chemically- and physically-derived nanophase titanium dioxide, *Nanostruct. Mater.*, 2, 37, 1993.
30. Terwilliger, C.D. and Chiang, Y.M., *Nanophase and nano-structured materials*, in *Materials Research Society Symposium Proceedings*, Vol. 286, Komarneni, S. et al., Eds., Materials Research Society, Pittsburgh, PA., 1993, p. 15.
31. Averback, R.S. et al., Sintering and grain growth in nano-crystalline ceramics, *Nanostruct. Mater.*, 1, 173, 1992.
32. Mayo, M.J., Hague, D.C., and Chen, D.J., Processing nanocrystalline ceramics for applications in surperplasticity, *Mater. Sci. Eng.* A, 166, 145, 1993.
33. Hague, D.C. and Mayo, M.J., in *Mechanical Properties and Deformation Behavior of Materials Having Ultrafine Microstructures*, Nastasi, M. et al., Eds., Sintering-Forging of Chemically Precipated Nanocrystalline TiO_2, Kluwer, Dordrecht, The Netherlands, 1993, p. 539.
34. Owen, D.M. and Chokshi, A.H., Evaluation of the densification characteristics of nano-crystalline materials, *Nanostruct. Mater.*, 2, 181, 1993.
35. Wang, S.W., Chen, L.D., and Hirai, T., Densification of powder using spark plasma sintering, *J. Mater. Res.*, 15, 982, 2000.
36. Li, B.R., Wang, X.H., and Li, L.T., Densification of uniformly small-grained $BaTiO_3$ using spark-plasma-sintering, *Mater. Chem. Phys.*, 82, 173, 2003.
37. Kumar, K.N. P. et al., Densification of nano-structured titania assisted by a phase transformation, *Nature*, 358, 48, 1992.
38. Sordelet, J. and Akinc, M., Preparation of spherical, monosized Y_2O_3 precursor particles, *J. Colloid Interface Sci.*, 122, 47, 1988.
39. Rasmussen, D., Akinc, M., and Hunter, O., Jr., Processing of yttria powders derived from hydroxide precursors, *Ceram. Int.*, 11, 51, 1985.
40. Chen, P.L. and Chen, I.W., Preparation and sintering characteristics of Y_2O_3 powders, Presented at the 97th Annual Meeting of the American Ceramic Society, Cincinnatic, OH, May 1, 1995 (Science, Technology and Commercialization of Powder Synthesis and Shape Forming Processes Symposium, paper no. SXIX-4-95).
41. Chen, P.L. and Chen, I.W., Sintering of fine oxide powder: I, Microstructural evolution, *J. Am. Ceram. Soc.*, 79, 3129, 1996.
42. Chen, P.L. and Chen, I.W., Sintering of fine oxide powders. II, Sintering Mechanisms, *J. Am. Ceram. Soc.*, 80, 637, 1997.
43. Chen, P.L., CeO_2 and Y_2O_3 Systems: Powder Synthesis, Sintering Characteristics and Dopant Effects, Ph.D. dissertation, University of Michigan, 1995.
44. Dogan, F., Roosen, A., and Hausner, H., Influence of hydroxide-precursor processing on the densification of yttrium oxide powders, in *Advances in Ceramics, Vol. 21, Ceramic Powder Science.*, Messing, G.L., McCauley, J.W., Mazdiyasni, K.S., and Haber., R. A., Eds., American Ceramic Society, Westerville, OH, 1987, p. 681.
45. Kingery, W.D. and Francois, B., in *Sintering and Related Phenomena*, Kuczynski, G.C., Hooton, N.S., and Gibbon, C.F., Eds., The Sintering of Crystalline Oxides, I. Interactions between Grain Boundaries and Pores, Gordon and Breach, New York, 1967, p. 471.
46. Herring, C., Effect of change of scale on sintering phenomena, *J. Appl. Phys.*, 21, 301, 1950.
47. Sordelet, D.J. and Akinc, M., Sintering of monosized spherical yttria powder, *J. Am. Ceram. Soc.*, 7, 1148, 1988.

48. Czubayko, L. et al., Influence of triple junctions on grain boundary motion, *Acta Mater.*, 46, 5863, 1998.
49. Hertling, G.H., Ferroelectric ceramics: history and technology, *J. Am. Ceram. Soc*., 82, 797, 1999.
50. Alrt, G., Hennings, D., and De With, G., Dielectric properties of fine-grained barium titanate ceramics, *J. Appl. Phys*, 58, 1619, 1985.
51. Frey, M.H. and Payne, D.A., Grain size effect on structure and phase transformations for barium titanate, *Phys. Rev. B*, 54, 3158, 1996.
52. Frey, M.H. et al., The role of interfaces on an apparent grain size effect on the dielectric properties for ferroelectric barium titanate ceramics, *Ferroelectrics*, 206, 337, 1998.
53. Waser, R. and Hoffmann, S., Microstructure property relationships of (Ba,Sr)TiO_3 films, *J. Korea Phys. Soc.*, 32, 1340, 1998.
54. Park, M.B. and Cho, N.H., Phase transition and physical characteristics of nanograined $BaTiO_3$ ceramics synthesized from surface-coated nanopowders, *J. Am. Ceram. Soc.*, 87, 510, 2004.
55. Wang, X.H. et al., Synthesis and properties of barium titanate based X7R ceramics by chemical method, *Ferroelectrics*, 262, 1225, 2001.
56. Yamaguchi, T. and Shinagawa, M., Effect of glass addition and quenching on the relation between inductance and external compressive stress in Ni-Cu-Zn ferrite glass composites, *J. Mater. Sci.*, 30, 504, 1995.
57. Jean, J.H. and Lee, C.H., Effects of lead (II) oxide on processing and properties of low-temperature-cofirable, *J. Am. Ceram. Soc*., 82, 343, 1999.
58. Hsu, J.Y., Ko, W.S., and Chen, C.J., The effect of V_2O_5 on the sintering of NiCuZn ferrite, *IEEE Trans. Magn.*, 31, 3994, 1995.
59. He, X.H. et al., Low-temperature sintering of NiCuZn ferrite for multilayer-chip Inductor, *J. Inorg. Mater.*, 14, 71, 1999.
60. Date, S.K. and Deshpande, C.E., Magnetism in materials — processing and microstructure, *Met. Mater. Process.*, 7, 15, 1995.
61. Wang, X.H., Qu, W.G., and Li, L.T., Investigation of NiCuZn ferrite with high performance derived from nano ferrite powders, *Ceram. Trans.*, 129, 211, 2002.
62. Duran, P. et al., A strategic two-stage low-temperature thermal processing leading to fully dense and fine-grained doped-ZnO varistors, *Adv. Mater.*, 14, 137, 2002.
63. Gambino, J.P. et al., Effect of heat treatments on the wetting behavior of bismuth rich intergranular phases in ZnO:Bi:Co varistors, *J. Am. Ceram. Soc*., 72, 642, 1989.
64. Lee, Y.-II et al., Fabrication of dense nanostructures silicon carbide ceramics though two-step sintering, *J. Am. Ceram. Soc*., 86, 1803, 2003.
65. Chen, I.W., personal communication with Kim, Y.W.

13 Nanolayered or Kinking Nonlinear Elastic Solids

Michel W. Barsoum
Department of Materials Science and Engineering,
Drexel University, Philadelphia, Pennsylvania

CONTENTS

ABSTRACT

Recently we postulated that most solids with a high *c*/*a* ratio belong to the same class, which we designated as kinking nonlinear elastic (KNE).[1] The high *c*/*a* ratio renders slip, other than basal and non-basal slip and twinning, prohibitively expensive. Thus only basal slip, that leads to kinking is activated during deformation. The signature of KNE solids is the formation of fully reversible, hysteretic, stress–strain loops, on repeat loadings. This full reversibility, in turn, is due to the formation of incipient kink bands (IKB), comprised of two nearly parallel dislocation walls of opposite polarity that are attracted to each other; when the load is removed that they annihilate. The energy dissipated per cycle is usually substantial and increases with increasing stress. Recently, we have also shown that repeated spherical nanoindentations, on the same location, is a technique that is ideally suited to identify and characterize KNE solids. Examples on Ti_3SiC_2, mica, hexagonal boron nitride, graphite, and sapphire are presented. KNE solids tend to be nanolayered, but as shown herein, sapphire, which is not, also behaves like a KNE solid.

13.1 INTRODUCTION

Graphite, ice, sapphire single crystals, layered semiconductors, high-T_c superconductors, hexagonal boron nitride (h-BN), Mg, Bi, Zn, the ternary carbides and nitrides (the so-called MAX phases, see below) mica, and other layered silicates, among others, are not thought to be related. In this chapter we not only show them to be related, but we also demonstrate why they are all members of a huge new class of solids, best described as kinking nonlinear elastic (KNE) solids.[1] In doing so, we demonstrate how repeated loadings onto the same location with a hemispherical nanoindenter tip is a powerful technique for characterizing these solids.[1–4] The considerable information gleaned from this technique is outlined herein.

Kinking is a ubiquitous and well-known phenomenon in nature that can be seen easily at many scales. At the largest scale, kinking and kink bands (KBs) are quite common in geologic formations. This mechanism has been invoked to explain deformation in single-crystal hexagonal metals, such as Cd and Zn,[5,6] highly constrained rocks, organic crystals, card decks, rubber laminates, oriented polymer fibers, wood, graphite fibers, laminated C–C and C-epoxy composites, among others.[7]

Before proceeding further it is important to emphasize that this chapter deals with kinking in crystalline solids exclusively; kinking in amorphous solids or polymers is not discussed.

Orowan was the first to report on kinking in a metal.[5] Later, Hess, and Barrett[6] suggested that the formation of KBs entailed the formation of pairs of dislocations of opposite signs that move in opposite directions in response to a shear stress. It is the coalescence of these mobile dislocation walls (MDWs) into a narrow region that gives rise to kink boundaries.[6,7] A few years later, Frank and Stroh (F&S)[8] derived an analytic expression, based on energy arguments, that predicted the remote stress at which a KB nucleus became unstable. Recently, we adapted the F&S theory and introduced the concept of IKBs discussed in more detail below.[9,10]

In our previous work we suggested that a sufficient, but not necessary, condition for a solid to be a KNE solid is a high c/a ratio.[1] This condition ensures that *only* basal plane dislocations are energetically favorable and eliminates twinning as a possible deformation mechanism. Under those constraints a solid can either deform by kinking or fracture.

This chapter is structured as follows: the next section describes kinking and its characteristics at all levels — atomic, microscopic and macroscopic. Section 13.3 deals with the kinking in bulk samples. The theoretical aspects of kinking — with special emphasis on the F&S model — and spherical nanoindentations are discussed in Section 13.4. Section 13.5 deals with specific examples, including mica, sapphire, graphite, Ti_3SiC_2, and Ti_2AlC, as representatives of the MAX phases. The latter are a novel class of layered, machinable, hexagonal ternary carbides and nitrides that number over 50, with the chemical formula $M_{n+1}AX_n$, where M is an early transition metal, A is an A-group element (mostly IIIA and IVA), and X is C or N.[11–13] The last section links the results obtained from nanoindentations and bulk compression specimens and provides an overview of KNE solids.

13.2 KINKING IN CRYSTALLINE SOLIDS

As noted above, at the macroscopic level, kinking is manifested in many systems ranging from geologic formations to card decks (Figure 13.1a). In general, kinking will occur whenever a plastic, anisotropic system is loaded parallel to the deformation or slip plane.

At the microscopic level kinking is observed as bucking in individual grains.[14] For the most part, because kinking is essentially a buckling phenomenon, it is associated with delaminations and lack of constraints. This is why, for example, when samples with highly oriented grains are loaded parallel to the easy or basal slip planes they kink at the unconstrained corners rather than in the bulk[7] (Figure 13.1b). It is also the reason that, as discussed below, kinking under an indenter is much more difficult than in simple compression experiments.

Atomically, the so-called stove-pipe configuration, where two kink boundaries are separated from each other by a dislocation free region is identified as a KB (Figure 13.1c).[15] Kink boundaries are essentially thin regions into which numerous MDWs have collapsed. In other words, MDWs — which

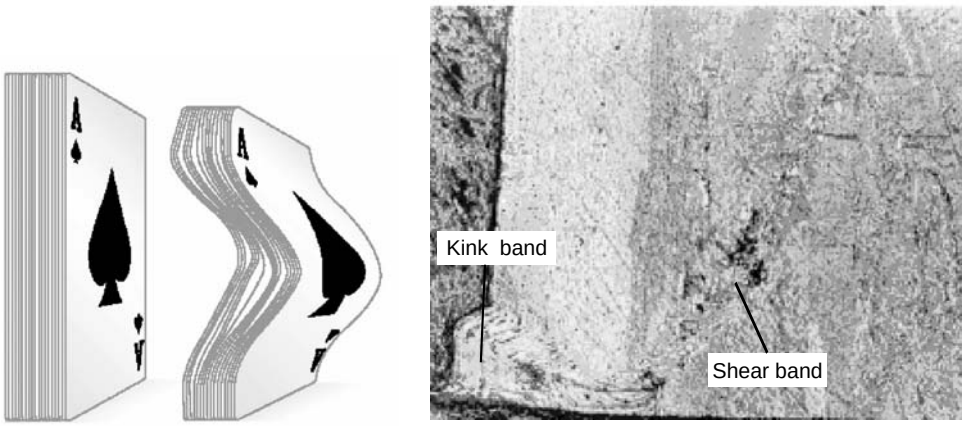

(a) (b)

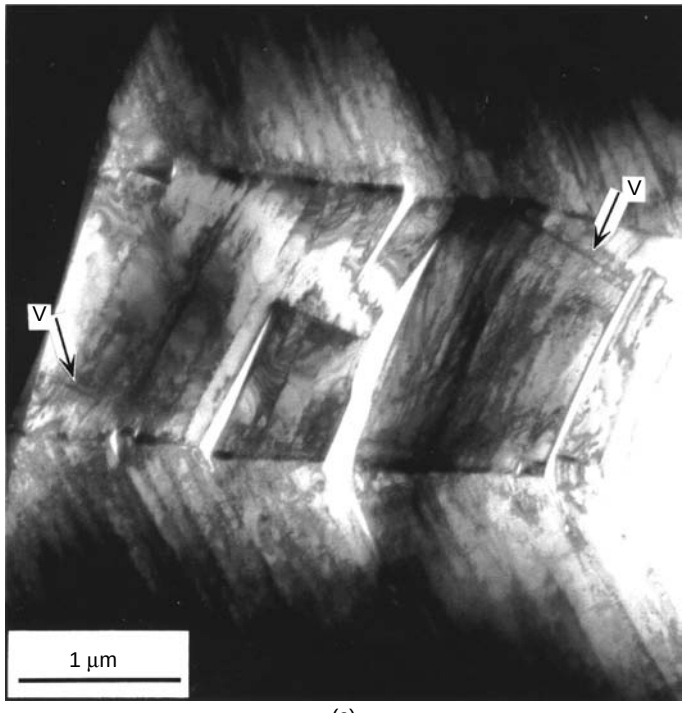

(c)

FIGURE 13.1 Kink bands in (a) a deck of cards loaded parallel to the cards,[11] (b) Ti_3SiC_2,[7] and (c) TEM of a KB comprised of two kink boundaries.[15] Note similarity to twinning.

are but low-angle grain boundaries — are the precursors of kink boundaries. It is important not to confuse kink boundaries with twins. The latter are crystallographically determined, while the former, also symmetrical across the kink boundary, can take any angle. The kink boundary angle depends on the number of MDWs that ultimately end up in it.

13.3 KINKING NONLINEAR ELASTIC SOLIDS

Before reviewing the nanoindentation results of typical KNE solids — most of which have been single crystals — it is instructive to review briefly the response of their polycrystalline counterparts

under cyclic loading. There are two typical responses. Type I, where all the loops are closed, including the first loop (Figure 13.2a) and type II, where the first loop is open, but all subsequent loops are closed or fully reversible (Figure 13.2b). The response of some of the MAX phases tested to date, such as Ti_3SiC_2 and Ti_2AlC, is of type I;[9] and that of graphite, sapphire, and h-BN are of type II.[2] The reasons for the differences are not entirely clear but could reflect differences in grain boundary strengths and ease of delaminations; the latter favored by a low c_{44}. What is occurring, however, is better understood; in type I, only fully reversible IKBs are nucleated. In type II, during the first cycle, MDWs result in KBs, which in turn lead to a reduction in domain size resulting in hardening. In all subsequent cycles, only fully reversible IKBs form.

In recent chapters, we developed atomistic[10] and constitutive models[16] for describing KNE solids. Only the atomistic model, based on the F&S paper,[8] is described here. F&S considered the

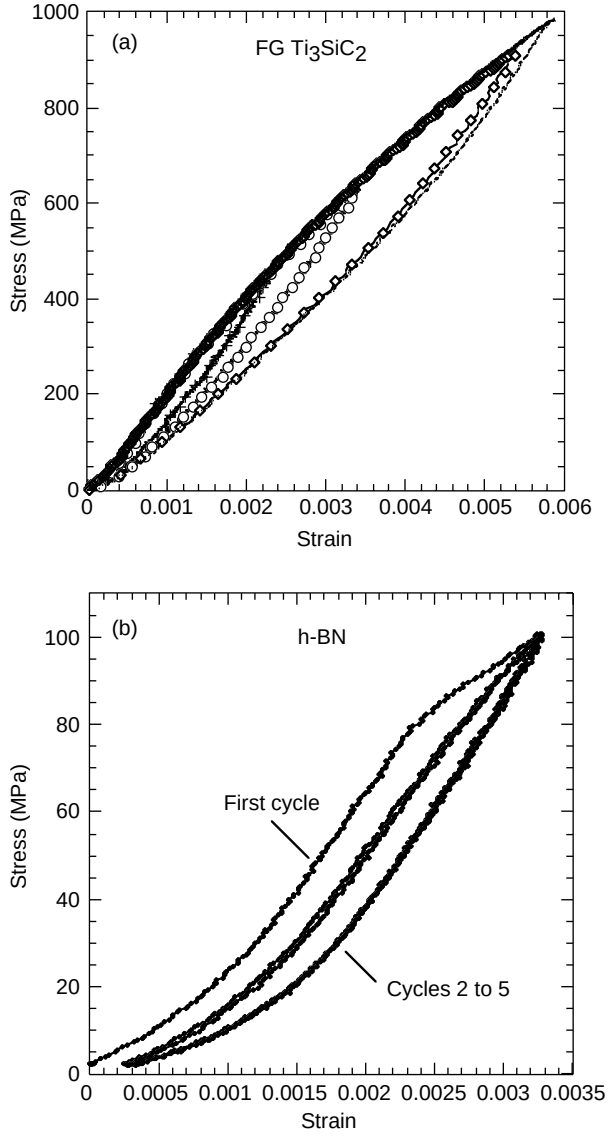

FIGURE 13.2 Compressive stress–strain curves for (a) Ti_3SiC_2,[9] which exhibits type I behavior, and (b) BN,[34] which exhibits type II behavior. Note fully reversible nature of loops.

problem of the growth of a thin elliptical subcritical kink — with dimensions α and β, such that $\alpha >> \beta$ — comprised of opposite sign dislocations (Figure 13.3a). Initially, the thin elliptical kink is subcritical because it increases the free energy of the system. Using an energy approach, reminiscent of Griffith's, F&S showed that the remote shear stress τ needed to render a subcritical KB unstable depends on α and is given by[8]

$$\tau > \tau_c = \sqrt{\frac{G^2 b \gamma c}{2\alpha}} \tag{13.1}$$

where b is the Burger's vector, G the shear modulus (for single crystals G is replaced by c_{44}), and γ_c the critical kinking angle given by

$$\gamma_c = \frac{b}{D} \approx \frac{3\sqrt{3}(1-\nu)\tau_{loc}}{2G} \tag{13.2}$$

with ν being Poisson's ratio and D the distance between dislocations in the walls (Figure 13.3a).

F&S modeled a two-dimensional single crystal and thus assumed, correctly, that once the inequality in Equation 13.1 was satisfied, a subcritical KB would rapidly and autocatalytically grow to the edge of the sample and dissociate into two parallel MDWs (Figure 13.3b). Continued loading would then result in the formation of other IKBs and MDWs within the first one. It is the repetition of this process that ultimately leads to the formation of the KBs.[6,7]

However, in order to explain our recent results, many of which are discussed in this chapter, we had to invoke the idea of an IKB.[9,10,17] An IKB is one in which the ends *remain attached* and is therefore fully reversible (Figure 13.3a).

In a polycrystal, 2α is determined by the thickness of the grains.[10] The situation under a nanoindenter indented into a single crystal is different. To model this situation we make the plausible assumption that[4]

$$a = \alpha \tag{13.3}$$

where a is the contact radius of the indenter (see below). Once α is known, β, can be determined from[8,17]

$$2\beta = \frac{2\alpha(1-\nu)}{2G}(\sigma - \sigma_t) \tag{13.4}$$

where σ_t is a threshold stress, below which the response is purely elastic.

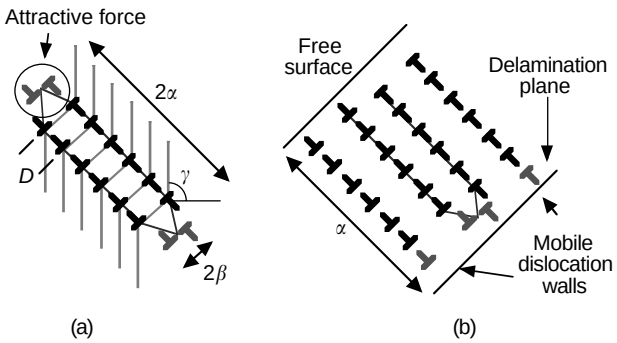

FIGURE 13.3 Schematic of (a) an IKB with length 2α and width 2β. As long as the ends remain attached, the force is attractive. (b) IKB under an indenter showing MDWs bracketing an IKB; upon removal of the load only the latter disappears. Note the delamination plane, which must accompany the IKB to MDW transformation.

Recently, we have shown that the number of IKBs per unit volume, N_k, is given by[10,17]

$$N_k \approx \frac{2G^2\gamma_c}{\pi\alpha^3(1-\nu)^2[\sigma-\sigma_t]^2}\varepsilon_{1KB} \tag{13.5}$$

where ε_{IKB} is the nonlinear strain under the indenter due to the formation of the IKBs. In other words, $\varepsilon_{IKB} = \varepsilon_{tot} - \varepsilon_{el}$, where ε_{tot} is the total strain and ε_{el} the elastic strain. In this model and in the following discussion, the formation of dislocation pileups is ignored, because their contributions to the inelastic strain is small compared to those from kinking.[10,17]

Once N_k, α and β are determined, a near complete picture of the dislocation configuration under the indenter comes into focus. The results are shown schematically in Figure 13.4 and can be summarized as follows: below σ_t the response is linear elastic; at $\sigma > \sigma_t$ a large number of short IKBs are introduced in the material (Figure 13.4a). With increasing load the number of IKBs actually *decrease* at the same time that their lengths increase (Figure 13.4b). This somewhat counterintuitive result comes about because with increasing stress, the IKBs get longer and wider, merge and thus decrease N_k. Without a merging mechanism, the IKBs could not penetrate deeper into the crystal while maintaining the shape dictated by Equation 13.4. How that is accomplished is unclear at this time, but most probably occurs by the annihilation of adjacent IKB walls that have opposite polarities.

As the loads are increased further, the IKBs penetrate deeper into the sample and when the tensile stresses that develop at their tip exceed the delamination stresses of the material, delaminations occur below the indenter (Figure 13.4c). With delaminations, the walls making up the IKBs immediately become mobile and are swept away from under the indenter and end up as pileups or mounds on either side of the indenter (Figure 13.4c).

As clearly demonstrated in this chapter, the formation of fully reversible, reproducible hysteretic stress–strain loops upon load cycling is one of the signatures of IKBs (e.g., Figure 13.2a). The area within each loop, W_d, represents the energy dissipated per unit volume per cycle as a result of the to and fro motion of the dislocations comprising the IKBs. W_d is related to the energy dissipated by a dislocation line of unit length sweeping a unit area, Ω, by[10,17]

$$\frac{\Omega}{b} = \frac{G^2\gamma_c}{\pi N_k\alpha^3(\sigma-\sigma_t)^2}W_d \tag{13.6}$$

In deriving Equation 13.6, W_d is assumed to be solely due to the movement of IKB related dislocations; the motion of pileup dislocations is again neglected. With that caveat, we believe Ω/b is a material property that is proportional to, if not equal to, the critical resolved shear stress (CRSS) of basal plane dislocations involved in the IKBs. This comment notwithstanding, more work is needed to establish the relationship between Ω/b and the CRSS.

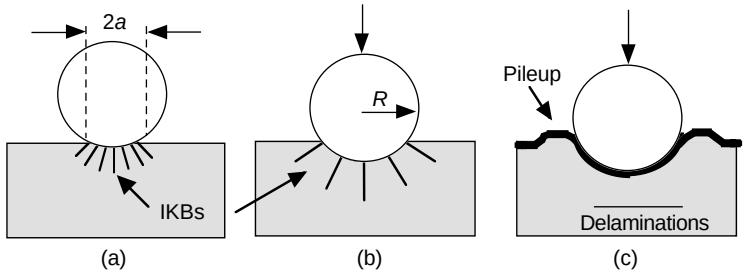

FIGURE 13.4 Schematic of microstructure under a spherical nanoindenter with (a) low loads; (b) higher load, but before IKB to KB transformation. Note that size and density of IKBs is less at higher loads. (c) Loads corresponding to stresses greater than delamination stresses. Note plastic deformation and pileups around the indentation marks.

13.4 THEORETICAL ASPECTS OF SPHERICAL NANOINDENTATIONS

According to Hertz, applying a load of P using a spherical indenter of radius R (Figure 13.5a) results in an elastic penetration depth, h_e, relative to the original surface given by

$$h_e = \left(\frac{3P}{4E^*}\right)^{2/3}\left(\frac{1}{R}\right)^{2/3} \tag{13.7}$$

E^* is a reduced modulus given by

$$\frac{1}{E^*} = \frac{1-\nu_s^2}{E_s} + \frac{1-\nu_i^2}{E_i} \tag{13.8}$$

The subscripts s and i refer to the specimen and the indenter, respectively.

Geometrically, as long as $h_c << R$, the actual contact diameter $2a$ is related to h_c by

$$a = \sqrt{2Rh_c} \tag{13.9}$$

where h_c is the depth at which the indenter and surface are no longer conformal (see Figure 13.5a).[3] If one further assumes that[18]

$$h_c = h_{tot} - h_e/2 \tag{13.10}$$

a can be readily calculated from Equation 13.9 once h_e is calculated from Equation 13.7. This assumption, shown schematically in Figure 13.5b, is a very good approximation as long as the system remains in the elastic regime.

Furthermore, in the purely elastic regime,[18,19]

$$h_c \approx h_{tot}/2 \tag{13.11}$$

combining Equations 13.7 to 13.12 it can be shown that

$$\frac{P}{\pi a^2} = \frac{4E^*}{3\pi}\left(\frac{a}{R}\right) \tag{13.12}$$

The left-hand side is the indentation stress and a/R can be considered to be an indentation strain. Hence a plot of $P/\pi a^2$ vs. a/R should, in the elastic regime, yield straight lines with slopes that are proportional to the E^*.

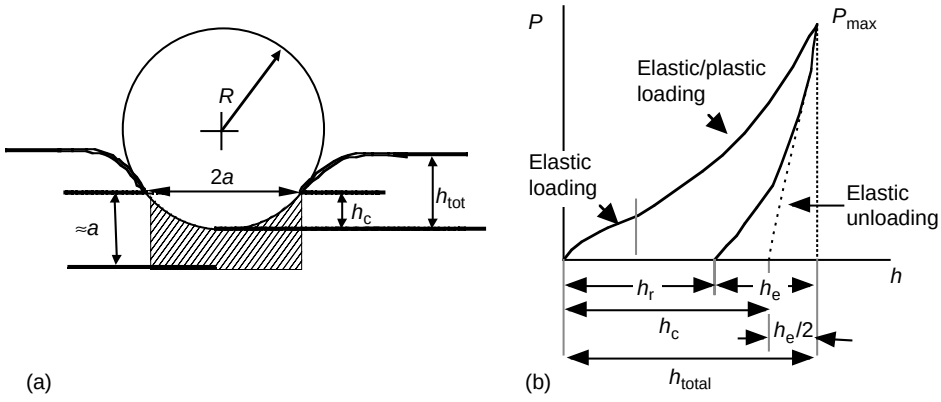

FIGURE 13.5 Schematic of (a) indentation at maximum load, and (b) of corresponding load–displacement-nanoindentation curve. In order to convert these results to stress–strain the approximation that $h_c \approx h_t - h_e/2$ is made.

As discussed below the response under the repeated loadings of a spherical nanoindenter depends on applied stress; at stresses below the stress needed to initiate the IKBs, the response is linear-elastic. At stresses high enough to initiate IKBs but not sunder them, i.e., not to cause delaminations, the response is of type I. At even higher stresses the response is of type II. It is crucial to note that the IKB to KB transition must be accompanied by delaminations that, as discussed below, more often than not, result in massive pop-ins.

13.5 NANOINDENTATION RESULTS ON KNE SOLIDS

In the following sections, our recent nanoindentation results on sapphire, graphite, Ti_3SiC_2, h-BN, and mica are reviewed.

13.5.1 SAPPHIRE

Typical load–displacement results of a sapphire single crystal loaded normal to its basal planes by with a spherical diamond indenter of 1 μm radius are shown in Figure 13.6a.[20] Unless otherwise noted, the indenter is typically pushed into the same location five consecutive times. This cycling is crucial because it is only when the third and subsequent cycles fully reproduce the second cycle that a solid can be unambiguously characterized as KNE (see below). The results shown in Figure 13.6a clearly show that at around 30 mN, a pop-in of the order of 100 nm is observed. When the load–displacement curves were converted into stress–strain curves (not shown) the stresses at which the pop-ins occurred were ≈ 40 GPa. Figure 13.6b plots the load–displacement results for a region indented 24 times, zooming on the middle section of the loops. The reproducibility of these hysteretic loops is noteworthy, especially that the maximum normal stresses in every cycle were of the order 40 GPa.[20] This reproducibility is consistent with the formation of fully reversible IKBs.

In metals, the theoretical shear stress needed to create a dislocation in a perfect crystal is assumed to be $\approx G/2\pi$.[21] Recent nanoindentation results and theoretical models have verified this assumption; in some cases the measured strengths were actually higher than $G/2\pi$.[22–24] If one assumes the maximum shear stress, τ_m, under the indenter to be $\approx \sigma_n/2$ (20 GPa in this case) and noting that c_{44} for sapphire is 148 GPa,[25] it follows that τ_m for sapphire is at least equal to $c_{44}/7.5$, which, gratifyingly, is $\approx G/2\pi$. The very high stresses needed to initiate the IKBs are compelling evidence that the small volume probed by the indenter must have been perfect, or near perfect.

In general, and despite pop-ins of the order 2–3 μm, it was not easy to find the locations of the indentations in the SEM or with an AFM. In a few cases, we were able to trace the indentation and confirmed that material pileup was seen around the indenter.[20] In agreement with previous work on the nanoindentation of sapphire single crystals,[26–29] there was no evidence for surface linear features associated with slip lines or twins, when the loading was parallel to the *c*-axis. When the loading was parallel to the *a*-axis, linear features were observed, again in agreement with the previous work.[26,28,29]

In order to find the indentations, a square array was introduced into the surface. When the distance between the indentations was ≈ 6 μm, in some areas, the surface was damaged exposing the locations of the nanoindentations marks, and as important it provided direct evidence for the formation of kink bands.[20]

The implications of the results shown herein are not inconsequential. They unambiguously show that dislocations, most probably in the form of IKBs, are mobile even at room temperature. Furthermore, if the factors by which IKBs in sapphire nucleate can be understood, and lowered significantly, it may be possible to impart some limited ductility to an otherwise very brittle solid.

13.5.2 THE MAX PHASES

Like other KNE solids, the response of the MAX phases to indentations, depends on the applied load. For example, for a fine-grained (3–5 μm) Ti_3SiC_2 polycrystalline samples in the low load regime (Figure 13.7a), the response, while slightly noisy, was fully reversible.[30] When these results are converted into stress–strain (Figure 13.7b), the response on initial loading and initial unloading

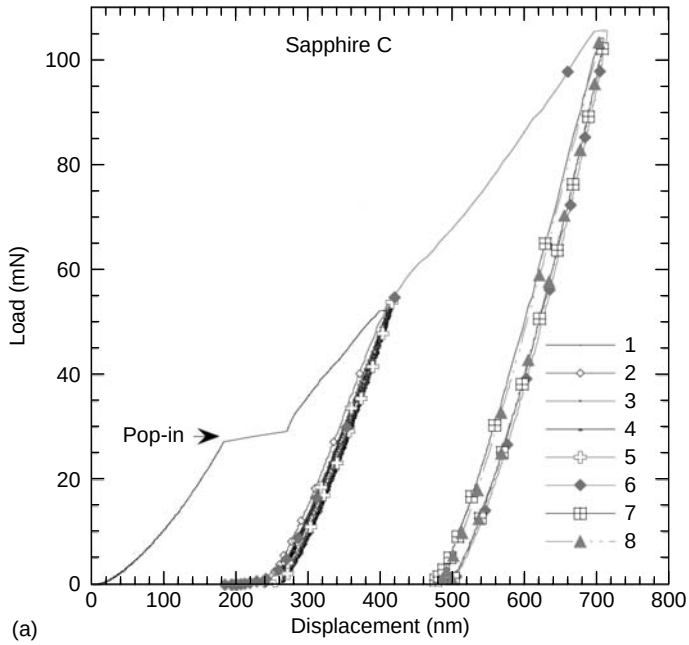

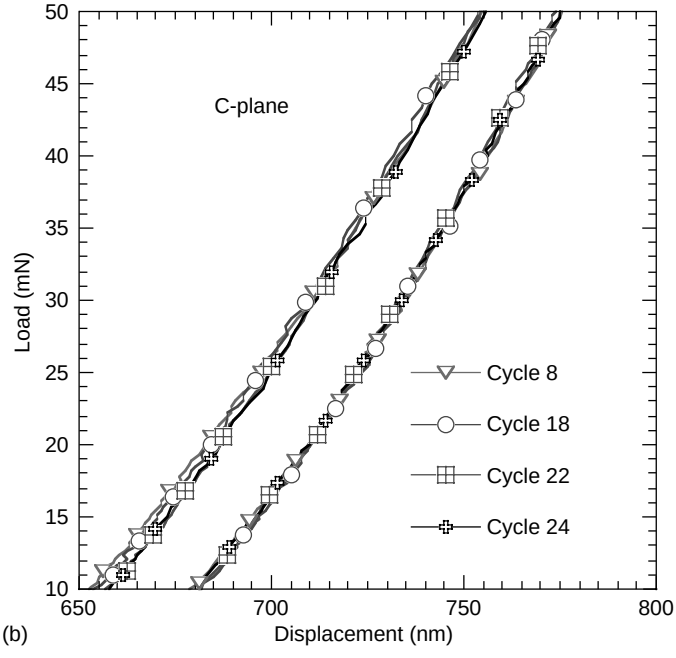

FIGURE 13.6 Typical load–displacement curves obtained when sapphire single crystals repeatedly loaded — parallel to the *c*-axis — with a 1 μm diameter hemisphere,[20] (a) first to 50 mN and then to 100 mN. Note pop-in at ≈10 mN. Also note lack of hysteretic loops when loaded to 50 mN. (b) Same as (a), but focused on the middle of the hysteretic loops showing reproducibility despite maximum stresses of ≈40 GPa. This indentation was repeated 24 times in the same location. Reproducibility of loops is noteworthy.[20]

is linear-elastic. Note that the loops, even the first, are fully reversible indicating that the response is of type I.

At higher loads the response is of type II (Figure 13.8a). When these results, obtained on coarse-grained (100 μm diameter and ≈15 μm thick) Ti_2AlC polycrystalline samples, are converted into

stress–strain curves (Figure 13.8b), the response is one where an elastic region is followed by a plastic region at ≈ 3 GPa.[17] The response is clearly of type II. The slope of the lines upon initial loading and unloading correspond to the Young's moduli values of Ti_2AlC.[30]

The results shown in Figure 13.7 and Figure 13.8 were obtained on polycrystalline samples and the response on the first loading in the different locations was quite stochastic.[31] However, the response of the second and subsequent cycles, was much more reproducible from location to location and harder than during the first cycle. As noted above, reproducibility and hardening after the first indent is a characteristic of KNE solids, and results when the indenter essentially creates its own "equilibrium" microstructure.[3] The hardening is due to the formation of smaller domains under the indenter as a result of the deformation. Despite being layered solids, the MAX phases in general, and Ti_3SiC_2 and Ti_2AlC in particular, are reasonably tough and we were thus not able directly to observe this domain reduction.

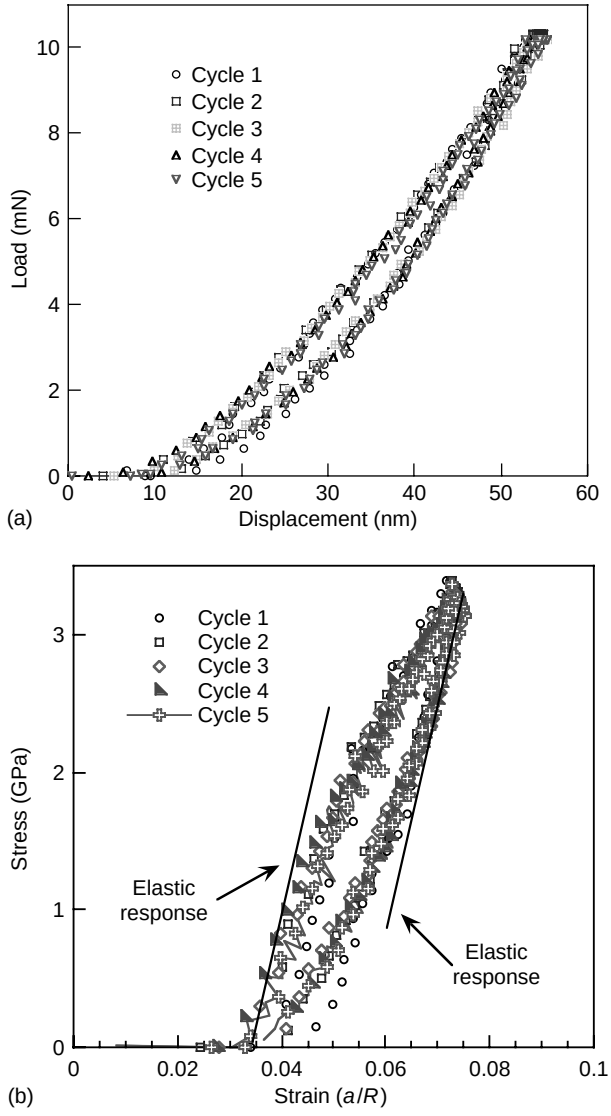

FIGURE 13.7 (a) Typical load–displacement curves of fine-grained Ti_3SiC_2 loaded to 10 mN.[31] (b) Stress–strain curves of results shown in (a). The solid inclined lines shown in (b) represent the elastic response, assuming a c_{33} of ≈ 325 GPa.[35] Note response is of type I.

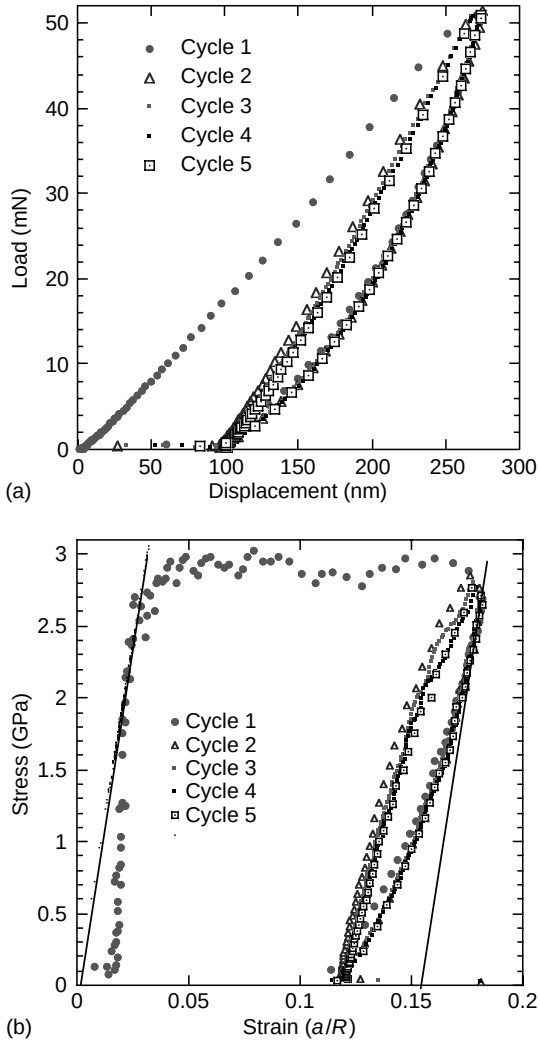

FIGURE 13.8 (a) Typical load–displacement curves of a coarse-grained Ti_2AlC_2 polycrystalline sample loaded to 50 mN.[17] (b) Stress–strain curves of results shown in (a). Note yield point at ≈ 3 GPa. Solid inclined lines represent the elastic response, assuming a modulus of ≈ 278 GPa.[30]

Graphite and mica are more brittle and direct evidence for domain reduction is shown below (see Figure 13.11). As important, direct TEM evidence for the formation of KBs and delaminations under a Berkovich indenter in epitaxial thin films of Ti_3SiC_2 — loaded parallel to the *c*-axis — exists.[32]

It is important to note that despite loads corresponding to stresses of the order of 6–8 GPa, SEM observations of areas indented showed little trace of the indentations (Figure 13.9a). At the highest stresses, however, a clear crater is observed (Figure 13.9b). The slip lines along the basal planes of some grains are clearly visible.

Every MAX phase tested to date — Cr_2AlC, Ti_3GeC_2, Ti_3AlC_2, and Zr_2InC, among others — has been shown to be a KNE solid. These results will be published in the near future.

13.5.3 GRAPHITE

Similar to sapphire and the MAX phases, the response of graphite single crystals loaded normal to their basal planes with a 13.5 μm radius hemispherical diamond indenter depends on load.[2] At low

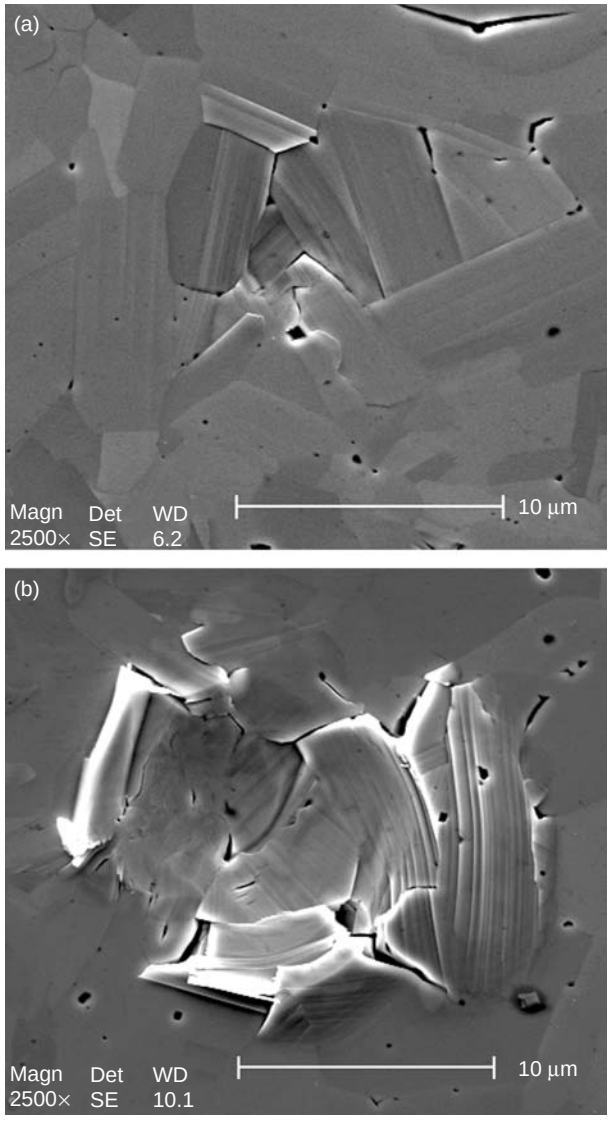

FIGURE 13.9 Typical SEM micrographs of a fine-grained polycrystalline Ti_3SiC_2 sample loaded to (a) 200 mN, and (b) 500 mN.[31] Deformation in (b) is significant. In contradistinction, and in full accord with the notion that IKBs are fully reversible, the crater formed at 200 mN is much more shallow and almost imperceptible.

loads (not shown) the response is of type I.[2] At ≈10 mN or ≈0.5 GPa, the response changes from type I to type II. At higher loads, the response is clearly of type II (Figure 13.10a). In Figure 13.10b, the slope of the solid inclined line corresponds to an elastic modulus of 36.5 GPa, which is the value of c_{33} reported in the literature for graphite.[33] Note clear evidence for a yield point around 0.4 GPa.

Postindentation SEM micrographs of most surfaces loaded to 200 mN showed no trace of indentation. In a few instances, a faint circumferential crack pattern was observed (see inset in Figure 13.10a).

In one experiment a massive, 60 µm, pop-in was registered.[2] When the specimen surface was examined in the SEM a graphitic "rose" with sixfold symmetry was clearly visible[2] (Figure 13.11a). Higher magnification SEM micrographs of the center of the crater provide unambiguous evidence

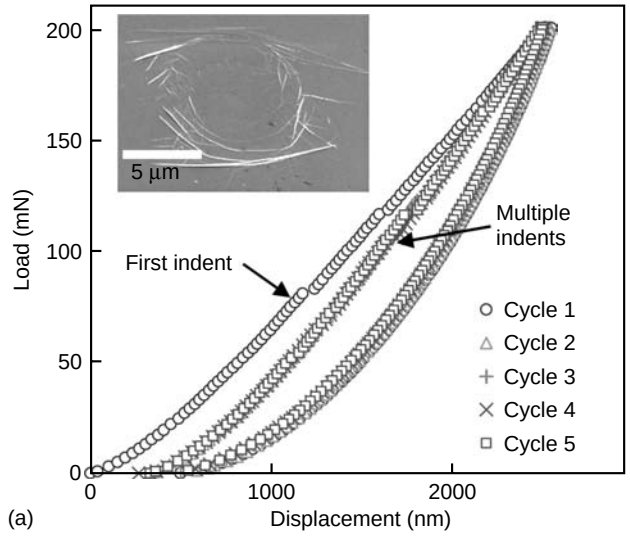

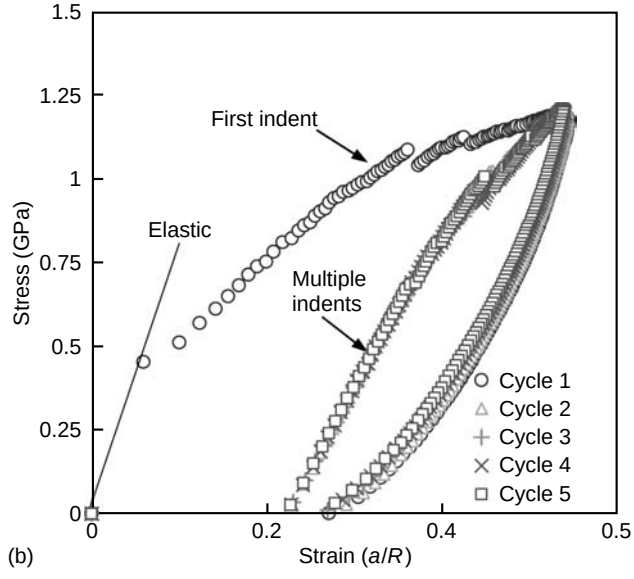

FIGURE 13.10 (a) Typical load–displacement curves for a single-crystal graphite sample loaded parallel to its *c*-axis with a 13.5 µm indenter. Inset is an SEM micrograph of sample after loading to 200 mN, where only a faint network of circumferential cracks is visible. (b) Stress–strain curves for results shown in (a). Note yield at ≈ 0.4 GPa. Response is of type 1.

for the break up of the single crystal into smaller domains alluded to above.[2] The nanolaminate nature of graphite and direct evidence for the formation of KBs is shown in Figure 13.11b. That graphite forms KBs had been known for a long time.[33] The fundamental role IKBs play in the deformation process was not appreciated until quite recently. The deformation of polycrystalline graphite was finally understood only by understanding that role.[2]

13.5.4 MICA

The response of mica single crystals, loaded normal to their basal planes, with a 13.5 µm spherical diamond indenter was found to be a strong function of the quality of mica sheets used.[1] The response of

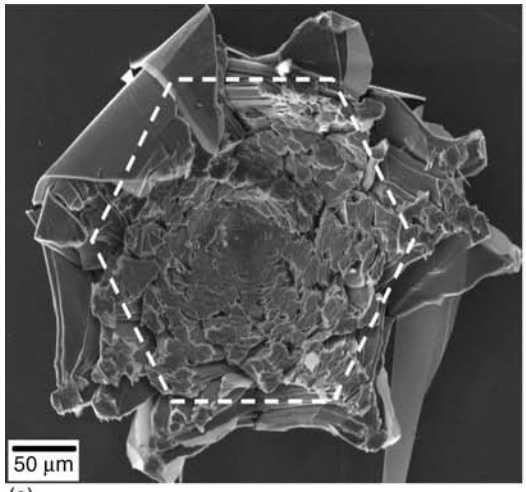

(a)

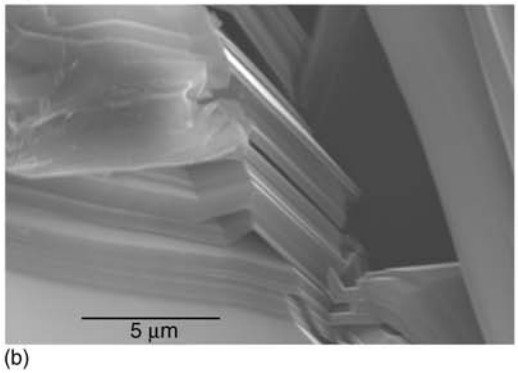

(b)

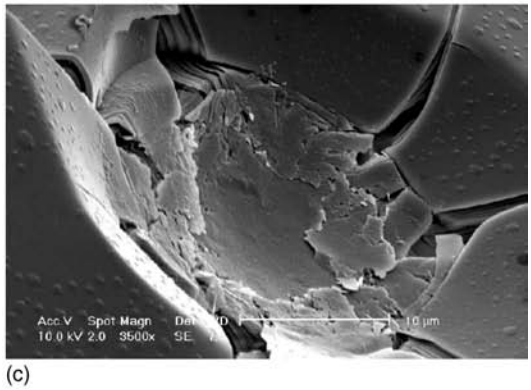

(c)

FIGURE 13.11 SEM micrograph of a (a) graphite single crystal that experienced a 60 µm pop-in.[2] (b) Same as (a), but at a higher magnification and with emphasis on the center of the crater. (c) Mica single crystal, after a ≈ 2 µm pop-in.[1]

the best quality mica (Grade A) was linear-elastic up to, in some cases, 8 GPa (cycles 1 and 2 in Figure 13.12a). In other cases, the linear elastic regime was interrupted by massive pop-ins[4] (cycle 3 in Figure 13.12a). Surprisingly, and despite these massive pop-ins, in some cases, the response upon reloading was again linear-elastic (cycles 4 and 5 in Figure 13.12a). The pop-ins, however, create a crater that reduces the stress under the indenter (Figure 13.12b). The fact that the response after a pop-in of ≈ 1 µm, is elastic is intriguing and not well understood. Clearly dislocations must have nucleated and

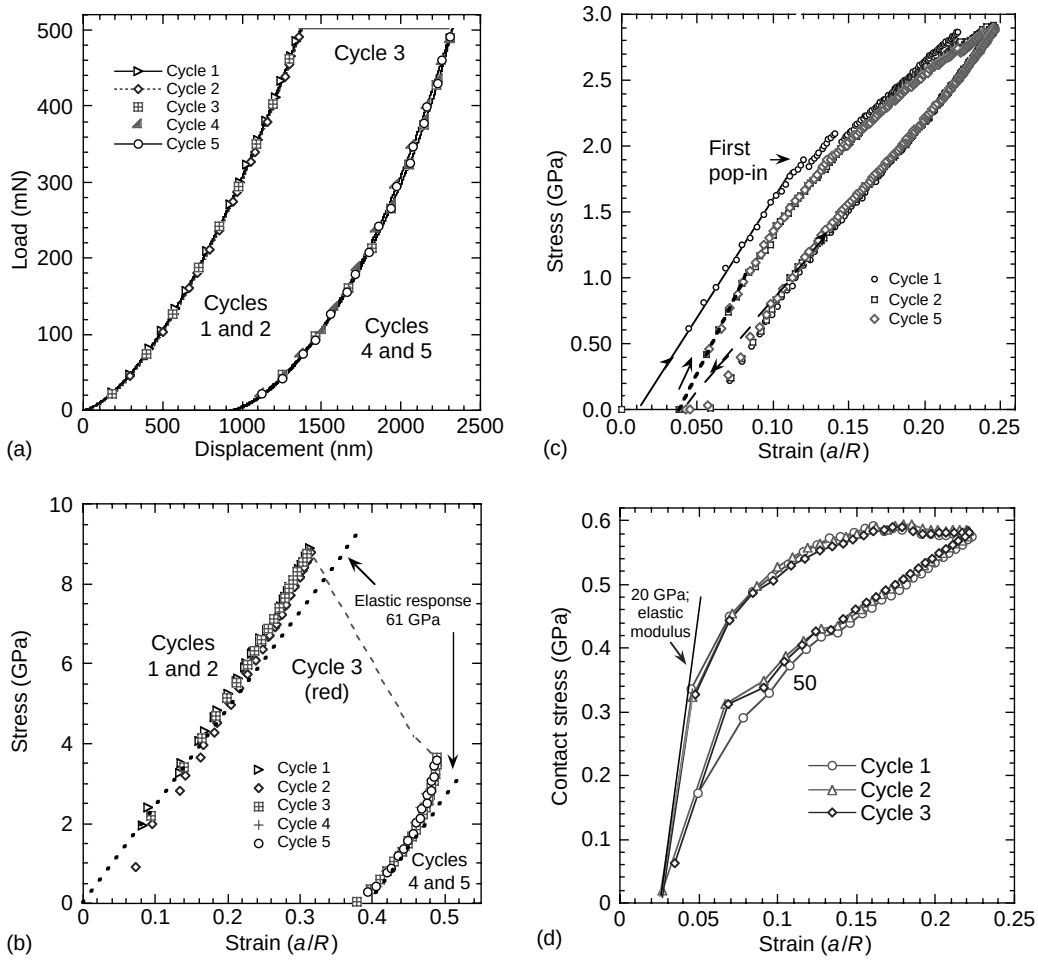

FIGURE 13.12 Load–displacement curves obtained when single-crystal mica samples — loaded parallel to the *c*-axis with a 13.5 μm radius spherical nanoindenter — were indented. (a) Grade A. (b) Stress–strain curves of results shown in (a). (c) Grade B. Here the response is fully reversible, but the difference between the first and subsequent cycles is small. Small gap on unloading is an artifact of the experiment,[1] (d) Stress–strain curves for Grade C mica. Here the note slope on initial loading is roughly half than that in (c).[4]

moved, which in turn implies delaminations. The pop-in also most probably resulted in a penny-shaped delaminated volume under the indenter. Why no evidence for IKB formation — i.e., fully reversible hysteretic loops — is observed is not clear. One possibility is that the domains formed after the massive pop-ins are too small for an IKB to nucleate in them. For the latter to occur, a higher stress is probably needed; a situation not unlike the one shown in Figure 13.6a. These comments notwithstanding, more work is needed, some of which is ongoing, to understand better this intriguing behavior.

When a lesser grade mica (Grade B) was used, the response was of type II[1] (Figure 13.12c). It is important to note that the small openings at the end of the repeat cycles shown in this figure are artifacts of the experiment; the actual load–displacement response (not shown) is fully reversible. This was confirmed several times by sometimes indenting the same location repeatedly — in one case up to 100 cycles — and then examining the indentation location in the SEM. In all cases, no trace of the indentation was found, which would not have been the case had the response not been fully reversible. Another important clue is the area encompassed within the load–displacement curves: for a KNE solid this areas asymptote to a constant value, after a few cycles.

When an even more defective mica (Grade C) was indented, the response was unique (Figure 13.12d).[4] The modulus upon loading was significantly lower than the one measured in Figure 13.12c, i.e., < c_{33}. The reason for this state of affairs is not entirely clear at this time, but suggests that the nucleation of IKBs in this mica is significantly easier than in either Grade A or B.

As noted above, in some cases, massive pop-ins — of the order of 2 μm (Figure 13.12a) — were observed. SEM micrographs of the indented regions (Figure 13.11c) showed large craters

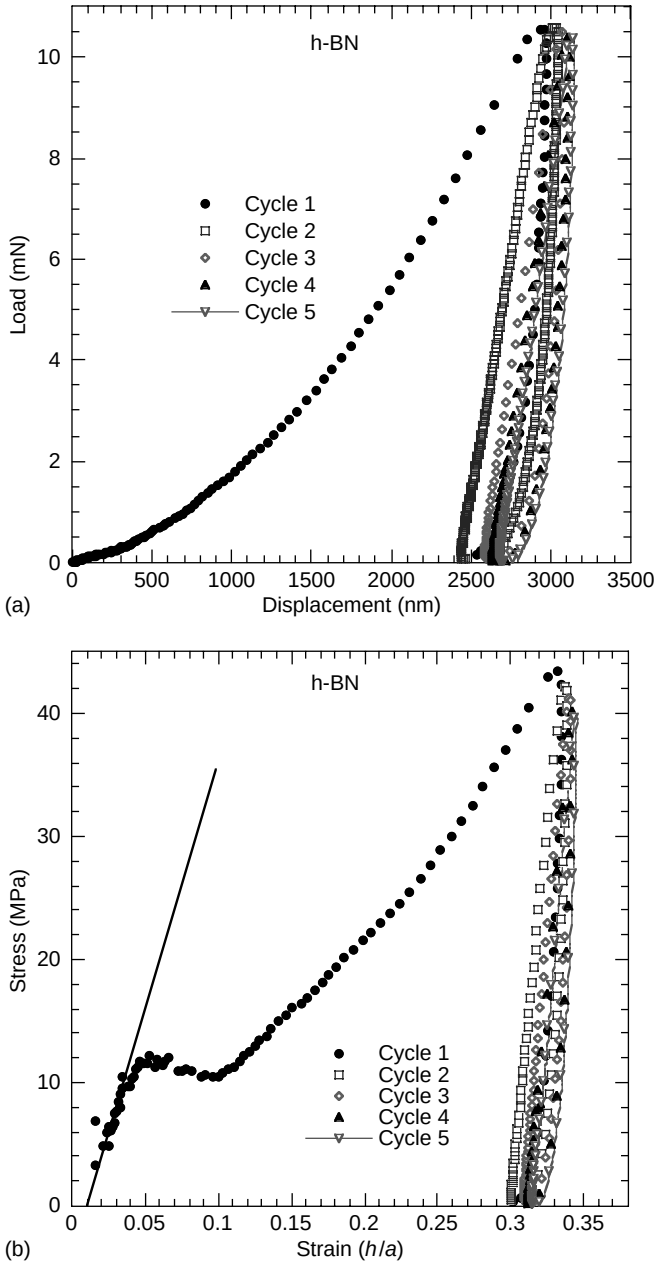

FIGURE 13.13 (a) Load–displacement curves of polycrystalline h-BN samples loaded to 10 mN with a 13.5 μm radius spherical nanoindenter.[34] (b) Stress–strain curves of results shown in (a). Note that here the penetration depth is so large as to make Equation 13.12 invalid, as evidenced by the negative slopes upon initial unloading.

reminiscent of those formed in graphite (Figure 13.11a). Here again, the nanolaminate nature of mica, direct evidence for kinks and, as important, the break up of the single crystal into smaller ones is unambiguous.

13.5.5 Hexagonal Boron Nitride

Typical stress–strain curves derived from nanoindentation load–displacement (Figure 13.13a) curves in polycrystalline h-BN are shown in Figure 13.13b. The response here is unlike any other material explored to date. The response is initially elastic (solid line) is followed by yield and considerable hardening. Upon reloading, fully reversible loops are observed. In this case, however, the penetration is so deep that Equation 13.12 breaks down. This is manifested by slopes that, upon initial unloading, are too steep to be physically meaningful. Note the same problem is encountered in Figure 13.12b and may explain the positive curvature of the curves.

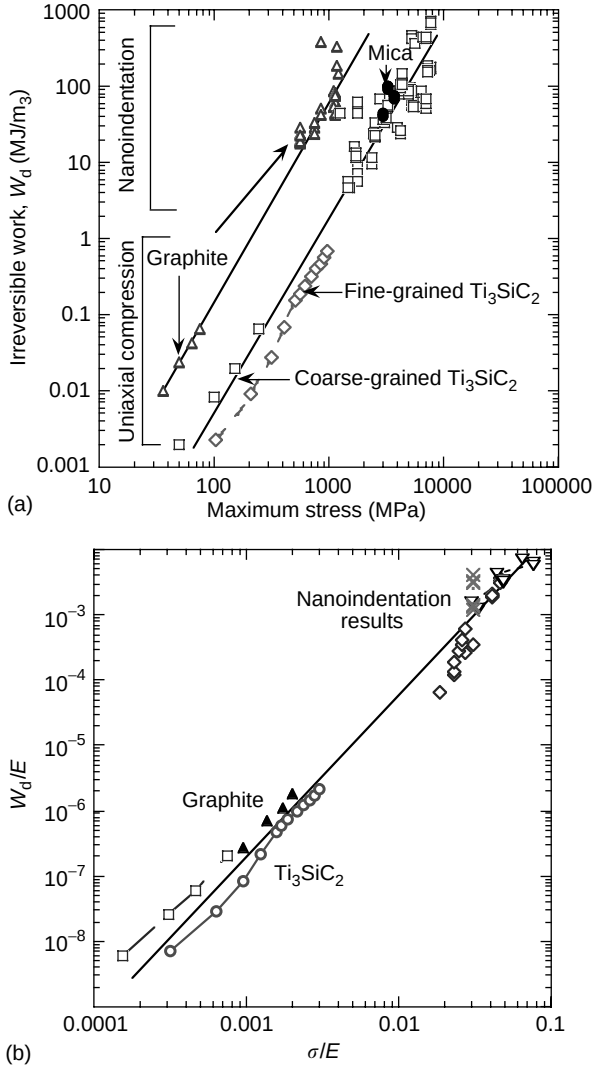

FIGURE 13.14 Log–log plot of (a) W_d vs. σ_{max} for select KNE solids. (b) Same plot as in (a) but with axes normalized by appropriate Young's modulus (bulk) or c_{33} for single-crystal nanoindentation work.

13.6 BULK VS. NANOINDENTATION RESULTS

Figure 13.14 is a log–log plot of W_d vs. σ for a number of solids obtained from nanoindentation experiments and compression of polycrystalline bulk samples such as those shown in Figure 13.2. The agreement between the two sets of results for Ti_3SiC_2 and graphite over five orders of magnitude is gratifying and confirms that our procedure to converting load–displacement curves to stress–strain is reasonably valid. When the results shown in Figure 13.14a are normalized by the appropriate elastic constants the different curves collapse on one universal curve (Figure 13.14b) strongly suggesting that the same underlying mechanism — kinking — is operative in all cases.[1]

13.7 SUMMARY AND CONCLUSIONS

Kinking nonlinear elastic solids are an important newly identified and fairly ubiquitous class of solids. Repeated spherical nanoindentations, into the same location, on single and polycrystalline samples is a powerful technique to identify KNE solids and obtain important information about what is occurring under the indenter. The technique also clearly delineates the important and crucial role that IKBs and KBs play in the deformation of these solids.

ACKNOWLEDGMENTS

This work was funded by the NSF (DMR-0503711) and ARO (DAAD19-03-1-0213). The help of my current (S. Basu, A. Zhou) and former (A. Murugaiah) graduate students in preparing this manuscript is greatly appreciated. Many fruitful discussions with my colleague Prof. S. Kalidindi were also critical is shaping this manuscript.

REFERENCES

1. Barsoum, M.W., Murugaiah, A., Kalidindi, S.R., and Zhen, T., *Phys. Rev. Lett.*, 92, 255508, 2004.
2. Barsoum, M.W., Murugaiah, A., Kalidindi, S.R., and Gogotsi, Y., *Carbon*, 42, 1435–1445, 2004.
3. Murugaiah, A., Barsoum, M.W., Kalidindi, S.R., and Zhen, T., *J. Mater. Res.*, 19, 1139–1148, 2004.
4. Murugaiah, A., Basu, S., Kalidindi, S.R., and Barsoum, M.W., submitted, 2005, unpublished results.
5. Orowan, E., *Nature*, 149, 463–464, 1942.
6. Hess J.B., and Barrett, C.S., *Trans. AIME*, 185, 599–606, 1949.
7. Barsoum M.W. and El-Raghy, T., *Metall. Mater. Trans.*, 30A, 363–369, 1999.
8. Frank, F.C. and Stroh, A.N., *Proc. Phys. Soc.*, 65, 811–821, 1952.
9. Barsoum, M.W., Zhen, T., Kalidindi, S.R., Radovic, M., and Murugahiah, A., *Nature Mater.*, 2, 107–111, 2003.
10. Barsoum, M.W., Zhen, T., Zhou, A., Basu, S., and Kalidindi, S.R., *Phys. Rev. B.*, 71, 134101, 2005.
11. Barsoum, M.W. and El-Raghy, T., *Am. Sci.*, 89, 336–345, 2000.
12. Barsoum, M.W. and Radovic, M., in *Encyclopedia of Materials Science and Technology*, Buschow, R.W.C.K.H.J., Flemings, M.C., Kramer, E.J., Mahajan, S., and Veyssiere, P., Eds., Elsevier, Amsterdam, 2004.
13. Barsoum, M.W., *Prog. Solid State Chem*, 28, 201–281, 2000.
14. El-Raghy, T., Zavaliangos, A., Barsoum, M.W., and Kalidindi, S.R., *J. Amer. Cer. Soc.*, 80, 513–516, 1997.
15. Barsoum, M.W., Farber, L., El-Raghy, T., and Levin, I., *Met. Mater. Trans.*, 30A, 1727–1738, 1999.
16. Kalidindi, S.R., Zhen, T., and Barsoum, M.W., submitted.
17. Zhou, A.G., Barsoum, M.W., Basu, S., Kalidindi, S.R., and El-Raghy, T., *Acta Mater.*, in print.
18. Iwashita, N., Swain, M.V., Field, J.S., Ohta, N., and Bitoh, S., *Carbon*, 39, 1525–1532, 2001.
19. Johnson, K.L., *Indentation Contact Mechanics*, Cambridge, Cambridge University Press, 1985.
20. Basu, S., Barsoum, M.W., and Kalidindi, S.R., *J. Appl. Phys.*, in print.
21. Courtney, T.H., *Mechanical Behavior of Materials*, McGraw-Hill, New York, 1990.

22. Li, J., Van Vliet, K.J., Zhu, T., Yip, S., and Suresh, S., *Nature*, 418, 307, 2002.
23. Van Vliet, K.J., Li, J., Zhu, T., Yip, S., and Suresh, S., *Phys. Rev. B*, 67, 104105, 2003.
24. Kelchner, C.L., Plimpton, S.J., and Hamilton, J.C., *Phys. Rev. B*, 58, 11085–11088, 1998.
25. Wachtman, J.B.J., Tefft, W.E., Lam, D.C.J., and Stenchfield, R.P., *J. Res. NBS*, 64A, 213, 1960.
26. Nowak R., and Sakai, M., *Acta Mater.*, 47, 2879–2891, 1994.
27. Nowak, R., Sekino, T., Maruno, S., and Niihara, K., *Appl. Phys. Lett.*, 68, 1063–1065, 1996.
28. Nowak, R., Manninen, T., Heiskanen, K., Sekino, T., Hikasa, A., Niihara, K., and Takagi, T., *Appl. Phys. Lett.*, 83, 5214–5216, 2003.
29. Tymiak, N.I., Daugela, A., Wyrobek, T.J., and Warren, O.L., *Acta Mater.*, 52, 553–563, 2004.
30. Radovic, M., Ganguly, A., Barsoum, M.W., Zhen, T., Finkel, P., Kalidindi, S.R., and Lara-Curzio, E., submitted.
31. Murugaiah, A., Ph.D. thesis, Drexel University, 2004, p. 56.
32. Molina-Aldareguia, J.M., Emmerlich, J., Palmquist, J., Jansson, U., and Hultman, L., *Scripta Mater.*, 49, 2003.
33. Kelly, B.T., *Physics of Graphite*, Applied Science Publishers, London, 1981.
34. Zhen, T., Ph.D. thesis, Drexel University, 2004.
35. Holm, B., Ahuja, R., and Johansson, B., *Appl. Phys. Lett.*, 79, 1450, 2001.

14 Nanocrystalline High-Melting Point Carbides, Borides, and Nitrides

Rostislav A. Andrievski
Institute of Problems of Chemical Physics,
Russian Academy of Sciences, Chernogolovka, Russia

CONTENTS

ABSTRACT

In this chapter, nanocrystalline bulks and films based on high-melting point carbides, borides, and nitrides are described and discussed in the context of preparation, structure, and properties. Special attention is given to the widespread compounds, such as silicon carbide, silicon nitride, aluminum nitride, boron nitride, boron carbide, titanium boride, titanium carbide, titanium nitride, tungsten carbides, and composites on their base. The poorly known and complex data are discussed and pointed.

14.1 INTRODUCTION

High-melting-point compounds (HMPCs) are carbides, borides, nitrides, oxides, intermetallics, and other compounds with melting temperatures (T_m) above 2000°C (or even 2500°C). The above given T_m limits are the conventional limits choosen for considerations of convenience, with no physical reasons for their selection. At present, the number of known two-component HMPCs with T_m>2500°C is at least 130, and with T_m > 2000°C about 240.[1] However, the number of the well-studied and practically used HMPCs is considerably less. This survey concerns HMPCs such as TiC, TiB_2, TiN, ZrC, NbC, WC, SiC, AlN, Si_3N_4, B_4C, BN, and some others that have been most extensively studied, as well as triple compounds and composites on their base. Nanocrystalline oxide HMPCs are discussed in other chapters.

The first comprehensive reviews on nanocrystalline HMPC-based materials have been published by the present author about 10 years ago.[2–4] This topic appeared very popular, and during the following 10 years more than 30 reviews (see, for example, Refs.[5–37] including our 10 reviews[6,7,10–12,18,21,25,26,29]) were published. The great attention enjoyed everywhere by nanomaterials in general and by nanocrystalline HMPCs in particular for the past 10–15 years is due to at least three reasons.

First, there is the hope of realzing unique mechanical, physical, chemical, and biological properties (and therefore performance) in the nanocrystalline state. It is common knowledge that HMPCs are the base of many advanced materials that are important in many modern technological fields, such as tool industry, mechanical engineering, electronics, nuclear technology, engine industry, and chemical engineering. Keeping in mind that transition in nanocrystalline state results in many new properties and correspondingly in the broadening of the applications, the information generalization on synthesis, structure, and properties of nanocrystalline HMPCs is very timely and topical. Second, the topic of nanoscience and nanotechnology is interdisciplinary, and many specialists in physics, chemistry, materials science, and biology are involved in this field. Third, this topic revealed many gaps not only in our understanding of fundamental features of nanocrystalline state, but in technological aspects too. In general, information on nanomaterials accumulated in an avalanche mode, which also is the reason for making this present review.

As before,[2–4,6,7,10–12,18,21,25,26,29] attention is focused on ultrafine powder (UFP), nanostructured bulks, and films/coatings. As usual the upper limit of UFP size and of crystallite one in bulks and films/coatings will be about 100 nm. Information on nanotubes and nanowires based on HMPCs is also analyzed.

14.2 ULTRAFINE POWDER, AMORPHOUS PRECURSORS, NANOTUBES, AND NANOWIRES

14.2.1 General Characteristics

As for any common powder, UFP preparation methods may be classified into physical and chemical groups with some variants (see Table 14.1).[2] This classification is very conventional because, in many cases, the preparation method is based on more than one basic principle (e.g., gas-condensation technique in reactive atmosphere, mechanical alloying that is called mechanosynthesis, etc.). It is generally supposed that the boundary between different powder preparation methods is often diffuse and poorly defined. Table 14.1 presents information from review 2 along with some additional information. The references on results before 1994 can be found in Ref. 2 and most of the attention with regard to the synthesis routes is focussed on recent works.

As can be seen from Table 14.1, there are several methods for the production of nearly all UFPs, which not only enlarges the technical possibilities but also creates competition. Under these conditions, the ability to generate UFPs of required specifications and economical considerations are the basis for the choice of the route.

TABLE 14.1
Methods of Carbide, Nitride, Boride UFP Preparation

Group	Method	Variation	Compound
Physical	Gas condensation	In inert gas or vacuum	SiC
		In reactive gas	TiN, ZrN, NbN, AlN, VN, HfN
	High-energy destruction	Milling	ZrC, Si_3N_4, AlN, α-SiC
		Mechanical alloying	TiC, ZrC, TaC, WC, SiC, TiB_2, TiN, BN, Si_3N_4, AlN, (Ti,Al)N, (W,Al)C
		Detonative treatment	BN, SiC, TiC
Chemical	Synthesis	Thermal	BN, SiC, Si(C,N), WC-Co, AlN, $(Mo,W)_2C$, TiB_2, TiN+TiB_2
		Laser	TiB_2, SiC, Si_3N_4
		Plasma	TiN, ZrN, HfN, NbN, Ti(C,N), AlN, BN, Si_3N_4, TiC, SiC, WC, Si_3N_4+SiC, TiN+TiB_2
		Self-propagated	AlN, SiC, $MoSi_2$, TaC
		Electrolysis	WC, WB_4
		Electro-spark	TiC, TiN
		In solutions or liquids	Mo_2C, W_2C, TiB_2, SiC
	Thermal decomposition	Condensive precursors	SiC, Si_3N_4, Si (N,C), BN, AlN, NbN
		Gaseous precursors	ZrB_2, BN, TiB_2, HfB_2

Source: Modified from Andrievski, R.A., *J. Mater. Sci.*, 29, 614, 1994. With permission.

It is well known that bulk nanomaterials can be obtained not only by powder technology methods but also by controlled crystallization from amorphous state. In this connection, attention will be focussed on amorphous precursors. New subjects such as nanotubes and nanowires will also be described.

14.2.2 Silicon Carbide and Silicon Nitride

Several strategies such as conventional, direct, and carbothermal syntheses, laser synthesis, thermal decomposition, mechanical alloying by high-energy ball milling (HEBM), and others can be used for SiC, Si_3N_4, and Si(N,C) powder preparation. In many cases, some additional demands such as sinter additives (e.g., about 1 wt% boron to SiC or several wt% oxides to Si_3N_4) as well as spherical uniform shape, high purity, and no agglomeration are made to technology.

The high cost of elemental Si and silane (SH_4) sources leads to a relatively expensive product, although in these cases, high-quality UFP can be produced. The reaction between carbon and silica in inert atmosphere or in nitrogen stream (for S_3N_4 or Si(N,C) synthesis) provides an inexpensive route, but the precise control of narrow particle size distribution and high purity is very difficult if not impossible, in general. For example, β-SiC powders have been prepared by a carbothermal reacting of silica gel with hydrocarbon gas (propylene, C_3H_6) at 1650°C.[38] This process results in nonagglomerated and low-cost powders, but their particle size was only 0.1 to 0.3 μm and oxygen content was 0.8 wt%. Syntheses of SiC powder via carbothermal reduction of SiO_2 in the presence of Mg and direct reaction of Si and C revealed that, in the first case, the decrease in particle size was very significant (up to mean size of ~0.02 μm).[39] Nonstoichiometric high-purity β-SiC powder was obtained by reacting silicon and natural graphite particles in the regime of self-propagating high-temperature synthesis (SHS), but the average size of particles was also only 0.15 to 0.30 μm.[40]

SHS followed by milling was also used for the preparation of nanocomposite SiC–AlN submicron particles smaller than 200 nm.[41]

More effective methods in the synthesis of nanophase SiC, Si_3N_4, and Si(C,N) powders are sol-gel and carbothermal syntheses (with the use of special precursors) as well as laser and plasma technologies. β-SiC nanopowders were synthesized under the carbothermal reduction of precursors prepared by liquid mixing methods (polymerized mix of ethylsilicate/phenolic resin).[42] The particle size was in a range of 40 to 100 nm. Boron-doped powders had two types of particle agglomerates with an average particle size of ~25 and ~70 nm.

The Institute for Laser- and Plasmaphysics (University of Dusseldorf, Germany) produced β-SiC nanopowders by a CO_2 laser-assisted synthesis using a mixture of silane and acetylane.[24,43] The boron additives are introduced by adding diborane to the reactant gases. The mean particle sizes measured by transmission electron microscopy (TEM) were 15 nm for SiC and 13 nm for SiC(B) powder, with narrow particle size distribution. Oxygen content was 1 to 2 wt%. The production rate was about 50 g/h. For comparison, SiC nanopowders (Pieper-SiC), produced commercially by laser synthesis had a mean particle size of 50 $\pm$ 25 nm and an oxygen content of 1.4 wt%.

Three different strategies for the preparation of SiC–Si_3N_4 composites from organosilicon preceramic polymers were investigated.[44] Composites were synthesized from blends containing polymeric precursor for SiC and Si_3N_4, mixes of polysilane precursors for SiC and silicon powder, and co-polycycloclodisilazane-silane single polymeric precursor. X-ray diffraction (XRD) studies confirmed that in all cases SiC–Si_3N_4 composites were obtained successfully after pyrolysis and crystallization by heat treatment. A monodispersed spherical Si_3N_4/SiC nanocomposite powder was prepared by heat treatment under argon at 1450°C of a spherical Si_3N_4/C powder, which in its turn had been synthesized by heating organosilica powder in a nitrogen atmosphere.[45]

Nanocomposite powder of 20 vol% TiN–Si_3N_4 systems can be prepared by *in situ* direct nitridation of TiO_2–Si_3N_4 nanocomposite powders, which in turn are obtained from TiO_2 nanoparticles with a particle size of ~20 nm and commercial Si_3N_4 powder (grade SN-110, UBE, Japan).[46]

Plasma-chemical processes such as direct-current arc jet, radio-frequency (r.f.) plasma, and hybrid plasma as well as sol–gel synthesis were also used for SiC, Si_3N_4 a Si(C,N) UFP preparation,[2,47–51] but the precise narrow size distribution regulation and phase control are not so easy. In many cases, synthesis of Si_3N_4 UFP results in the preparation of amorphous phase. The phase composition of Si_3N_4 nanopowder synthesized by vapor-phase reaction of $SiCl_4$ and NH_3 in r.f. plasma and crystallized at 1250 to 1500°C is shown in Table 14.2.[50] It can be seen that, after synthesis, the major phase is amorphous and only after heat treatment at $T > 1450$°C the crystalline content became very high (more than 75%). Gubicza et al.[50] have used different methods to elucidate the mean particle size of UFP (d) and estimated firstly their dislocations density (ϕ).

Amorphous polymer-derived ceramics in Si–N–C and Si–N–C–B systems are used for consolidation by controlled crystallization from amorphous state at temperature lower than conventional

TABLE 14.2
The Phase Composition, Average Particle Size Calculated from XRD and Specific Surface Area d, and Dislocation Density ϕ of the As-Synthesized and Heat-Treated Si_3N_4 Powders

Phase	As-Synthesized			$T = 1350$°C			$T = 1500$°C		
	vol%	d (nm)	ϕ (m^{-2})	vol%	d (nm)	ϕ (m^{-2})	vol%	d (nm)	ϕ (m^{-2})
Amorphous	80	—	—	65	—	—	20	—	—
α	17	35–75	5×10^{14}	32	50–60	2×10^{14}	67	N/A	N/A
β	3	N/A	N/A	3	N/A	N/A	13	95	7×10^{15}

Source: Modified from Gubicza, J. et al., *J. Mater. Sci.*, 35, 3711, 2000. With permission.

sintering techniques without incorporation of oxide sintering additives. A flow diagram for the preparation of precursor-derived ceramics includes various stages such as synthesis, cross-linking, thermolysis, and crystallization.[52] For example, suitable monomers are polymerized into macromolecular compounds by following cross-linking of the polymers at moderate temperatures and a transformation into a preceramic network. Its thermolysis at high temperatures (1000 to 1400°C) resulted in an amorphous ceramics, which in turn were crystallized under specific conditions to a nanoceramics. Copolymerized alkyl/aryl-substituted polysilane, polysilazanes, polysilycarbodiimides, polydimethylsiloxane, polyborosilazanes, borazine-based oligosilazanes and so on that are cross-linked via C–B–C bridges or N–B–N units were used for precursor synthesis.[52–56] For example, as precursors, the commercial polysilazane $[Si(CH)_3R\text{-}NH]_n$-[CO-NH] and boron oligovinylsilazane $\{B(C_2H_4\text{-}Si(H)\text{-}NH]_3\}_n$, respectively, were used for the systems Si–C–N and Si–B–C–N. After cross-linking, bulk samples were milled, sieved, and compacted in a graphite die at pressure of 48 MPa and temperatures of 150 to 400°C, followed by thermolysis in an argon atmosphere at 1050 to 1400°C.

Silicon carbide bulks and films can be used for the synthesis of nano- and microcrystalline diamond-structured carbon by extracting silicon from SiC in chlorine-containing gases (Ar-[1–3.5% $]Cl_2$ – [0–2%]H_2) at ambient pressure and temperatures not exceeding 1000°C.[57]

The synthesis of silicon carbide nanotubes by decomposing SiO on multiwalled carbon nanotubes has been reported.[58] Beside SiC nanotubes the reaction products also included β-SiC nanowires and biaxial SiC-SiO_x nanowires. Structural and electronic properties of two distinct types of stable SiC nanotubes with a Si/C ratio of 1:1 were predicted and published.[59] β-Si_3N_4 nanofibers with diameter of about 60 to 400 nm were prepared through a combustion synthetic route (the heating of $Si/Si_3N_4/NH_4F/Al$ mixture in a nitrogen pressure of 100 atm. with the highest combustion temperature in the center of the sample of about 1900°C).[60]

14.2.3 Aluminium Nitride, Boron Nitride, and Boron Carbide

As it has been described in Ref. 2, AlN nanopowder can be synthesized by several methods such as plasma technology, calcination of aluminium chloride and glucose mix, electrochemical synthesis, and cryomilling. In special carbothermal synthesis, a precursor[61] that contains an intimate mixture of Al_2O_3 nanopowder and carbon has been prepared by a chemical pyrophoric reaction followed by heating in a flowing nitrogen-gas atmosphere up to 1723 K. The synthesized AlN particles have a diameter lower than 100 nm. Direct nitridation of aluminium vapor in a microwave plasma forced-flow reactor resulted in synthesis of fully nitrided powder with particle sizes of 10 to 100 nm and surface areas of 45 to 370 m^2/g.[62] Gas–reduction–nitridation method was used for treatment of alumina nanopowder by NH_3–C_3H_8 gas mixture.[63] The AlN nanopowder synthesized had a mean particle size of about 50 nm. Electric explosion of aluminum wire (pulsed wire discharge) in an atmosphere nitrogen-containing gas (NH_3/N_2) can be used for the preparation of nanometer-sized AlN powder with an average particle size of 30 nm and AlN content of 95 to 97 wt%.[64,65] Polymer pyrolysis has also been described for AlN UFP synthesis.[2] A method for the preparation of AlN–BN nanocomposite powder has been developed.[66] This method involves the pyrolysis of precomposite gels $(AlN)_x$–$(BN)_y$ from aqueous solutions of $AlCl_3\,6H_2O + H_3BO_3 + (NH_2)CO$ at 800 to 1100°C for 10 h in a flow of ultrahigh-purity anhydrous ammonia followed by N_2 annealing of composite powder between 1100 and 1600°C. Particle sizes of AlN and BN were found to be of 18 to 47 and 4 nm respectively.

Different methods of BN UFP synthesis have been analyzed in Ref. 67. The most effective way to obtain BN nanopowder is to use B_2O_3 reduction–nitridation in N_2 with magnesium as the reducing agent. There are many polymeric precursors such as polyborazine, polyvinylborazine, and polyvinylpentaborane for the preparation of BN and B_4C nanopowders.[68] As in the case of Si_3N_4 UFP, BN and B_4C nanopowders are also mainly in the amorphous state. Quasi-spherical BN nanocrystals in the range of 30 to 80 nm have been prepared by pulsed-laser-induced liquid/solid interfacial reaction at normal temperatures and pressures.[69]

In recent times, there have been many publications describing the synthesis of BN nanotubes by several methods, such as laser ablation,[70] mechanothermal treatment,[71] extended vapour–liquid–solid method.[72] (See also Chapter 11.) A continuous CO_2 laser ablation reactor can produce BN single-wall nanotubes with a prefered zig-zag configuration in gram quantities.[70] Mechanothermal method involving extensive milling treatment of boron powders and their heating in N_2 gas at 1200°C results in large quantity production of multiwalled BN nanotubes with cylindrical or bamboolike structure in amounts of the order of a kilogram.[71] BN nanotubes of diameter about 20 nm have been synthesized by reacting a mixture of NH_3/N_2 over nanoscale Fe-B "catalyst" particles at 1100°C.[72] Some examples of BN nanotube filling by ZrO_2 rods and Co have also been described.[73,74]

AlN nanowires (approximately 10 to 50 nm in diameter) have been synthesized at 1100°C by reacting $Al+Al_2O_3$ mix in a flowing NH_3 atmosphere, using carbon nanotubes as templates.[75] The reaction of a mixture of N_2 and NH_3 gases and nanoscale α-FeB particles at 1100°C results in the formation of BN nanowire with diameter about 20 nm and length up to several tens of microns.[76]

14.2.4 Tungsten Carbide, Titanium Carbide (Nitride, Boride), and Related Compounds

Tungsten carbide nanopowder as a base for high-application hard metal attracts considerable attention because there is a strong tendency toward production of fine and ultrafine grained WC–Co and related materials (see, for example, Refs. 77–82). Thermochemical synthesis of WC–Co nanopowder includes the use of a precursor compound, tris (ethylenediamine) cobalt tungstate — $Co(en)_3WO_4$, in which tungsten and cobalt are intimately mixed at the molecular level; subsequent reduction and controlled carburization yield desired composite product with a high surface area and extremely good mixing.[77] Nanophase WC–Co powder was doped with vanadium carbide (VC) and VC/TaC by solution process to overcome coarsening and abnormal grain growth of the WC particles during sintering.[78–82]

There are many other examples of WC-based nanopowder synthesis, such as WC mechanochemical synthesis in different versions, including Mg and Al additions,[83–86] WC synthesis from carbon-coated precursors,[87] WC–Co synthesis from precursors obtained by co-precipitation,[88] WC–TiC–Co, and Ti(C,N)–WC–Ni nanocomposite powder synthesis.[89,90] There are many difficulties with the various approaches for obtaining high-performance hard metals, such as the developing of thermal stable homogeneous nanostructure, the strong requirements on the carbon content in hard metal, and economical considerations. For example, the integrated mechanical and thermal activation process is proposed, including the HEBM of $WO_3+CoO+C$ starting with not expensive materials and subsequent heating at 650° and 1000°C.[85] The resulting powder has a narrow particle size distribution (0.3 to 0.5 μm) and the crystallite size of the WC phase is about 30 nm. However, these and many other results have been obtained only on the laboratory scale. Companies such as H.C. Starck (Germany), Wolfram BHG (Austria), Dow Chemical Company (USA) and others produce ultrafine WC powder with a particle size in the range less than 0.2 to 0.3 μm.[79–81] USA Inframat Corporation ("IMC") produces WC and WC/(5 to 15%Co) nanopowders with carbide grain size of 40 to 80 nm.[91] These nanograined WC nanoparticles are agglomerated in agglomerates with average size of 0.2 to 0.4 μm. The WC/Co granules with size 5 to 45 μm are also produced for thermal spray application. IMC has developed WC/Co bulk consolidated materials with high Vickers microhardness (H_V) of 23 GPa and fracture toughness (K_{IC}) of about 7 MPa $m^{1/2}$.

A wide variety of the synthesis versions for TiN (TiC, TiB_2) and related nanocompounds are also widely described in the literature (see, for example, Refs. 2, 92–112). In addition to the widely used methods mentioned earlier, such as plasma and laser synthesis, milling, and reduction synthesis, in recent times, HEBM, SHS, and thermal decomposition reactions are gaining acceptance. Special attention is being given to the preparation of multicomponent composite UFPs. TiN/TiB_2 composite nanopowders have been synthesized from a mixture of $Ti+TiB_2$ powders under N_2 atmosphere or a mixture of Ti+BN powders under Ar-atmosphere by HEBM.[92–94] Formation of

$TiB_2/TiN/Ti(C_xN_{1-x})$ nanocomposite powder via HEBM and subsequent heating has been also analyzed.[95] The evolution of different reactions in the case of using two initial mixtures (Ti/B_4C one and Ti/BN one) during milling under Ar-atmosphere and following heat treatment in vacuum at 400, 700, and 1300°C (the heating rate was 10°C/h) have been examined by XRD and TEM. The ball-to-powder weight ratio was 10:1 and it was found that within 10 h of milling, the following reactions occured:

$$Ti + B_4C \rightarrow TiC + 4B \quad \text{(amorphous)} \tag{14.1}$$

$$Ti + BN \rightarrow TiN + B \quad \text{(amorphous)} \tag{14.2}$$

During ball milling for 10 to 30 h, the following reaction occured:

$$5Ti + B_4C \rightarrow BN + B \quad \text{(amorphous)} \rightarrow TiC + TiN + 3TiB2 \tag{14.3}$$

Formation of Ti(C,N) has been detected only after heat treatment at 1300°C. The grains in $TiB_2/TiN/Ti(C_xN_{1-x})$ nanocomposite powder were found to be 30 to 60 nm in size.

Titanium nitride nanocomposites with alumina can be prepared by mechanochemical reduction of rutile with aluminum in N_2 atmosphere.[96] The following reaction occured after milling for 100 h:

$$3TiO_2 + 4Al + 3/2N_2 \rightarrow 3TiN + 2\,Al_2O_3 \tag{14.4}$$

The as-milled powders were <1 μm in size, although XRD measuments revealed that the crystallite sizes were <20 nm for all phases.

Regarding the synthesis of TiN, TiC, TiB_2, HfB_2, ZrB_2, $MoSi_2$, and ZrC, some new results have been published (see, for example, Refs. 37, 97–112), including SHS, electric field-activated combustion, reduction–nitridation synthesis, plasma nitridation synthesis, gas-phase reactions, and electro-spark synthesis. A special aging heat treatment has been proposed for the formation of nanostructure in nonstoichiometric vanadium carbide ($VC_{0.875}$).[113]

14.2.5 Properties of UFP and Nanotubes

Because of its small size, the main properties of UFP are connected with their high surface area value. For the UFP spherical form, the following equation can readily be obtained.

$$S = 6/\gamma_{th} d_s \tag{14.5}$$

where S is the specific surface area, γ_{th} the theoretical density, and d_s the mean particle diameter defined from the S measurements. d_s is obtained from gas low-adsorption experiments. The particle sizes have also been studied by XRD analysis and TEM method. In some cases, measured values of d show considerable variation between TEM method and S or XRD-analysis determinations. This is probably due to the influence of particle morphology, particle-size distribution, agglomeration degree and crystallinity. The morphology of UFP can be very different: spherical particles, polyhedral and needle-shaped forms, irregular powders and aggregates.[2] The particle-size distributions have mainly log-normal (Gaussian) forms but some deviations from the theoretical log-normal distribution, such as a normal one, a bimodal one (presence of two peaks), are observed. The best way to obtain precise information on nanoparticle-size distribution is the use of several different methods followed by a comparison of the results.

Table 14.3 gives the S values for some UFPs. It is clear from these data that the variations in S for different UFPs with identical d_s vary by about six times because of the difference in γ_{th} values.[2]

TABLE 14.3
Specific Area Values for Some UFPs (γ_{th} in Parentheses)

d_s (nm)	S ($m^2\ g^{-1}$)			
	B_4C, BN (2.3–2.5 g/cm³)	Si_3N_4, SiC, AlN (~3.2 g/cm³)	TiB_2, TiC, TiN (4.5–5.4 g/cm³)	WC (15.8 g/cm³)
100	24–26	~19	11–13	4
50	48–52	~38	22–26	8
10	240–260	~190	110–130	40

Source: Modified from Andrievski, R.A., *J. Mater. Sci.*, 29, 614, 1994. With permission.

Different properties of UFPs such as interparticle friction and particle packing, chemical and phase composition, gas evolution characteristics, compressibility, and behavior at pressureless sintering, as applied mainly to TiN and Si_3N_4, have been analyzed elsewhere.[2–4,6,114–119] The most interesting features of these results are a great enrichment of the nanoparticle surface by carbon monoxide, hydrogen, and other gases as well as the poor compressibility of UFP. Figure 14.1 shows the effect of high-vacuum heat treatment on the rate of gas evolution for TiN UFP (d_s~70 nm).[6,116] It is obvious that there are two gas evolution peaks at ~250°C (for H_2O and N_2) and at ~650°C (for CO, CO_2, and H_2). Carbon monoxide dominates appreciably in the evolving gases. The total volume, V, of escaped gases for different TiN powders is shown in Table 14.4.[2,116]

A roughly similar situation has also been observed in the case of Si_3N_4 UFP. The content of evolved gases for as-prepared and annealed Si_3N_4 nanopowders (d_s~20 nm) is given in Table 14.5.[6,117] During high-vacuum heat treatment, the main peaks of gas evolution have been fixed at 300 to 400°C (for H_2O and CO_2) and at 500 to 900°C (for CO, H_2, and N_2). Vacuum annealing results in significant decrease of desorbed gas quantity.

The data on gas escape are very important for the development of consolidation regimes by hot pressing and other methods because the presence of adsorbed gases in closed pores hinders the full densification. UFP before consolidation need vacuum heat treatment for removal of adsorbing gases.

It is well known that the compressibility of powders decreases markedly with decreasing particle size, and so UFP compressibility is very poor. This may be due to severe interparticle friction of nanoparticles for the high value of specific surface area. In connection with the interparticle friction, the UFP apparent density is also very low, e.g., for Si_3N_4 powders with a particle size of about 10^3, 50, and 17 nm, the apparent densities are 0.5, 0.1, and 0.03 g/cm³, respectively.[3] Table 14.6 demonstrates the comparison of the compressibility of Si_3N_4 and TiN nanopowders with different particle size.[3,6] From these data it is evident that the behavior of these powders during compaction depends critically on particle size and, therefore, it is impossible to obtain near-dense compacts from UFP under cold compaction conditions even at high compaction pressures of up to 8 GPa.

Information on properties of nanotubes, nanowires, and nanofibers, based on BN, SiC, AlN, and Si_3N_4, is not very comprehensive. To our knowledge, information is limited to some data on structure, band gap, and Young's modulus (see, e.g., Refs. 58–60, 70–76, 120–123). BN nanotubes are now better understood and it is known that their band gap is of ~5.5 eV, independent of nanotube diameter. With regard to the measured elastic properties, there are at least two different results, such as $E = 1.22 \pm 0.24$ TPa, which greatly exceeds the elastic modulus of any known fibres,[72] and the average value of E obtained from measurements of 18 cantilevered nanotubes was 722 GPa (theoretical value of E is ~850 GPa).[120] The peculiarities of structure, electron, and other physical properties of noncarbon nanotubes are reviewed in Refs. 121 and 122. The comprehensive review on synthetic strategies and properties of inorganic nanowires, including BN, BCN, SiC, Si_3N_4, AlN, TiC, and BC_x, has also been published.[123] (See also Chapters 10 and 11.)

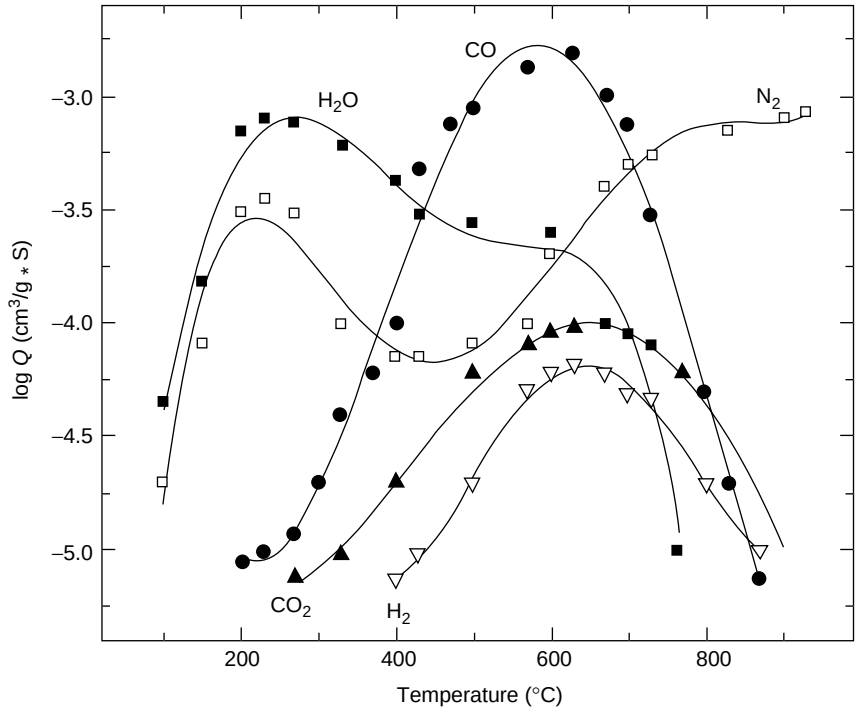

FIGURE 14.1 Temperature dependence of the gas evolution rate (Q) for TiN UFP. (From Andrievski, R.A., in *Nanotechnology. Molecularly Designed Materials*, Chow, G.-M. and Gonsalves, K.E., Eds., ACS, Washington, DC, 1996, chap. 20. With permission.)

TABLE 14.4
Volume of Escaped Gases for TiN Powder

Characteristics	S (m^2/g)		
	0.15	**16**	**62**
d_s (nm)	8×10^3	70	18
V (cm^3/g)	1	7	33

Source: Andrievski, R.A., *J. Mater. Sci.*, 29, 614, 1994. With permission.

TABLE 14.5
Some Characteristics of Gas Evolution for Si_3N_4 UFP before (1) and after High-Vacuum Annealing for 1 h at 1200°C (2)

Powder Type	Total Gas Volume (cm^3/g)	Predominant Gas Content (mass %)			
		CO	H_2	N_2	H_2O
As-prepared (1)	625	59	11	21	9
Annealed (2)	89	79	7	10	4

Source: Andrievski, R.A., *Nanotechnology. Molecularly Designed Materials*, Chow, G.-M. and Gonsalves, K.E., Eds., ACS, Washington, DC, 1996, chap. 20. With permission.

TABLE 14.6
Effect of Particle Size d_s and Compaction Pressure P on Relative Density τ_p, (%) of Si_3N_4 and TiN Powders (the Compact Diameter, ~10 mm)

Powder	d_s (nm)	τ_p at P (GPa)			
		1	4	6	8
Si_3N_4	1000	64	74	79	82
	50	54	65	70	72
	17	52	60	63.5	68
TiN	80	64	80	84	85
	70	60	75	80	81

Source: Modified from Andrievski, R.A., in *Nanotechnology. Molecularly Designed Materials*, Chow, G.-M. and Gonsalves, K.E., Eds., ACS, Washington, DC, 1996, p. 297. With permission.

14.3 NANOCRYSTALLINE BULKS

14.3.1 General Characteristic of Consolidation

As indicated above, UFP cold compaction at high pressure does not result in their dense consolidation. The dynamic high-pressure methods, such as shock compaction and magneto-impulse technique, are also not very effective in UFP dense consolidation at room temperatures.[2] All known high-temperature consolidation methods of powder technology such as sintering and various versions of hot pressing may be used in UFP processing. One of the main problems in nanomaterial (NM) fabrication is consolidation with full densification but without sacrificing the nanocrystalline structure. In this connection, conventional regimes of sintering and hot pressing (which are assisted by intensive recrystallization and disappearance of nanostructure) are mainly invalid with regard to nanomaterial preparation. It is mainly special regimes of sintering and hot pressing such as rate-controlled sintering (RCS),[35] reactive hot pressing (RHP),[124,125] spark plasma sintering or plasma-activated sintering (PAS — combination of high alternating current with unaxial pressure),[103,104,126,127] rapid liquid-state sintering,[77] and transformation-assisted consolidation (TAC),[127,128] which are suitable for near-full densification with nanostructure preservation. It is also important to use nanopowders with very low grain size such as those obtained by HEBM or in amorphous state.

Table 14.7 summarizes information on some results of consolidation by different methods including data on initial powder size, regimes, related density τ, and grain size L of consolidated bulks. It is probable that these data are the most representative. It is worth noting that in most cases the characteristics of nanostructures were on the upper side, i.e., the grain size L was more than 30 to 50 nm. Conventional hot isostatic pressing (HIP) of nanophase nonoxide powders (SiC, TiN, TiC, etc.) led to densities of only about 92 to 98% of theoretical value (the grain size after HIP was 70 to 200 nm).[24] High pressure sintering (HPS) and PAS with UFP obtained by HEBM seem to be more effective both in values of density and grain size but demands special equipment. Shock compaction or sintering in shock waves also result in the preparation of high dense compacts with nanostructure, but in many cases the general macrostructure is not so uniform.[131,132]

Regimes of UFP consolidation have a great effect on the density and nanostructure of bulks. Figure 14.2 show the effect of HPS temperature on relative density and properties of TiN and ZrC bulks, respectively.[6,103,133] From Figure 14.2 it is obvious that using compaction pressure of 4 GPa results in a decrease in the active densification temperature of 600 to 800°C, as compared with pressureless sintering; it is also evident that the further increase in pressure up to 7.7 GPa is not very effective. As it is clear from Figure 14.2 the values of E and H_V are practically changed monotonously with the density. Some

decrease in the hardness change in the interval 1130 to 1400°C may be related to the progress in recrystallization. Intensive recrystallization can be seen in the case of ZrC high-temperature consolidation at compacting pressure of 1.5 GPa (Figure 14.3).[103]

There are interesting scientific problems in the mechanism of nanopowder consolidation with the constraint of nanostructure sacrificing. Thus, in the RCS method, it is necessary to separate the proper sintering and recrystallization processes, providing the full densification and minimum grain growth. The effectivness of nonisothermal sintering of special regimes helping to obtain a dense nanostructure in sintered solids can be estimated on the basis of some experiments.[35] Very intriguing effect of TAC is observed in the case of SiC and Si_3N_4. In the former, the disorder–order transformation between 1600 and 1700°C is expected to increase the densification at high level. Figure 14.4 demonstrates clearly the role of ordering in the densification of nanostructured SiC prepared by mechanical alloying under HEBM conditions.[127] XRD study revealed that this powder in the as-received state has disorder hexagonal structure that on heating between 1600 and 1700°C transforms to ordered cubic structure. The rapid densification observed at sintering seems to be related to an enhanced mass transport by structural ordering. At the same time, a commercial SiC nanopowder (30 nm SiC*) with initial cubic structure is densified at sintering conventionally.

In the latter, the pressure-induced phase transformation from amorphous state to crystalline β/α-Si_3N_4 is expected to nucleate many new grains without their coarsening significantly.[128]

Amorphous Si–C–N and Si–B–C–N ceramics were fabricated from polymer powders by multistep thermal conversation but the total porosities of the samples obtained ranged from 11 to 15%.[56] Controlled crystallization from amorphous state combines with amorphous powder consolidation and leads to nanostructure formation. However, as it has been demonstrated with silicon carbonitride and silicon nitride samples, some residual closed pores have been revealed.[54]

As regards nanocomposites, in Table 14.7, there are only some examples on TiN/TiB_2, TiB_2/TiC, and TiN/Si_3N_4 composites. Information on microcomposites and micro-/nanocomposites is much wider (see, e.g., Refs. 124, 125, 141–146) but in the most cases these materials have a grain size of about 1 μm and higher or contain small volumes of nanoparticles (some of their properties will be described later).

There are many results on sintering of submicron and ultrafine grained (nanophase) hard metal based on tungsten carbide (see, e.g., Refs. 77–82, 86–91, 147). Keeping in mind the industrial application of these data, it seems important to point out that using grain growth inhibitors such as VC, Cr_3C_2, TaC, etc. results in the production of a new ultrafine WC hard metal.The comparative dilatometric study of sintering of conventional micron size WC+7.8% Co+0.7% VC powder and nanopowder of the same composition (the average WC grain size of about 30 nm) revealed that the major part of sintering of nanopowder was completed in the solid state while most of the densification of micropowder was done by liquid-state sintering.[147] However, in spite of carbide doping effect, the real size of WC phase is not less than 50 to 100 nm but normally about 100 to 200 nm because of intensive recrystallization and difficulties in obtaining a dense nanostructure. In this connection, it must be noted that in many cases there is a competition between advantages of nanomaterials and the economics of the new complex technology.

14.3.2 Structure and Properties

14.3.2.1 Structure

Scanning electron microscopy (SEM), TEM, and XRD are the main methods for nanomaterials structure study. Figure 14.5 shows SEM and TEM micrographs of TiN, ZrC, and TiN/Si_3N_4 bulks consolidated by HPS, PAS, and hot pressing, respectively.[12,46,103] Using the SEM method gives the possibility to study fracture surfaces; as is evident from Figure 14.5a, the fracture of TiN nanobulks is intercrystalline. The increase in grain size results in the transition from intercrystalline fracture to transcrystalline one.[12] TEM study provides information both on structure, by microdiffraction study, and chemical composition of different regions by energy dispersive spectroscopy (EDS) analysis, as shown in Figure 14.6

TABLE 14.7
Some Results of Non-Oxide Bulk Consolidation by Different Methods

HMPC	Method; Initial Powder Size (nm)	Regime (Temperature, Pressure, Time)	τ (%)	L (nm)	Reference
SiC	HIP; 15–20	1650°C, 350 MPa, 1 h	98.6	70	24
	HPS; 10–200; 3–50	1700°C, 4–6 GPa	98 (assumed)	~50	129
	PAS+TAC; 5–10/100–150 (agglomerates)	1700°C, 40 MPa, 10 min	98	30–50	127
Si3N4	HPS+TAC; amorphous nanopowder	1100–1300°C, 6–8 GPa	85–96	25–40	128
	HPS; 18	1000–1100°C, 5 GPa, 30 min	93–95	160–200	130
		1300–1420°C, 5 GPa, 30 min	95–96	240–450	
	Shock compaction; 70/400–500 (agglomerates)	40 GPa, 1200°C	99	40–60	131
BN	Sintering in shock waves		96	25	132
SiC/Si3N4 nano/nanocomposite	Thermolysis of compacted polymer powders	~1650°C, 2 h	Near dense(without open pores)	~30	54
Si-B-C-N and Si-C-N ceramics	Thermolysis of compacted polymer powders	1050–1400°C, 2–5 h	85–89	Amorphous	56
TiN	HPS	1200°C, 4–7 GPa, 5 min			
	~70		98–99	40–80	6, 131–136
	~40		95–96	30–60	93
	~16–18		95	30–40	134
	PAS; ~5	1690°C, 20–38 MPa, 30 min	>96	~65	126
	RCS	Sintering in non-isothermal regimes up to 1200–1600°C			35, 137
	~80		99 (1600°C)	150–200	

	~45		96 (1460°C)	250	
	~15		98 (1200°C)	50	
TiC	PAS; <5	1690°C	Near dense	~60	138
ZrC	PAS; HPS; ~5	1330°C; 38 MPa	98.5	65	103
		1300°C; 1.5 GPa	99.5	95	
MoSi2	PAS+RHP; HEBM reactants	*I*=1600 A, 106 MPa, 3–6 min	82–93	58–75	104
WC	PAS; ~7	1690°C, 20–38 MPa,	~99	25	83
WC/MgO				<50	
TiN/TiB2	HPS; 80 (TiN)/400 (TiB2)	1200–1400°C, 4 GPa, 5 min	96	250–300	93, 135
	270 (HEBM)		97	N/A	
TiB2/TiC	PAS+RHP; HEBM reactants	800°C (5 min for gas evolution)+ 1400°C (~3 min), 30 MPa	Up to 98.6	60–70	139
WC/Co	Hot mechanical working; liquid-phase sintering (VC doping)	N/A	~100	100–300	140
		N/A	~100	100–300	
20 vol% TiN–Si3N4	Hot pressing; nanopowders with sintering acids up to (Al2O3/Y2O3)	1550–1800°C, 30 MPa, 60 min	98	100–600	46

Source: Modified from Andrievski, R.A., *J. Mater. Sci.*, 29, 614, 1994. With permission.

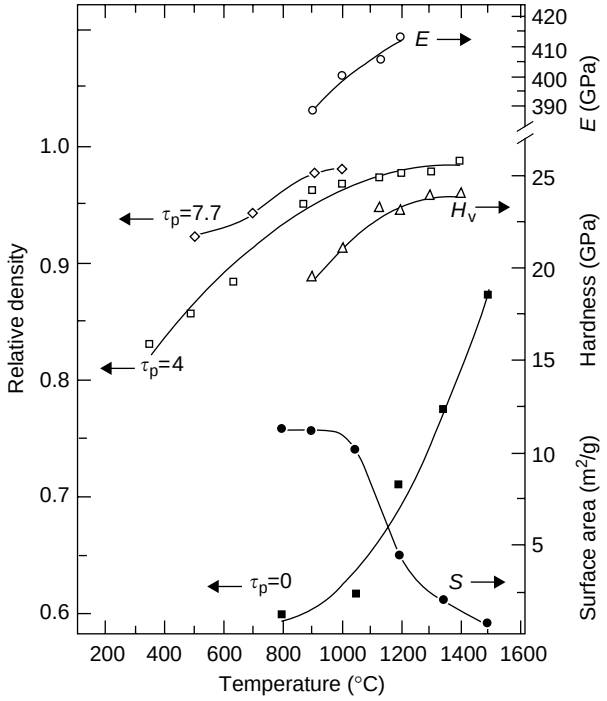

FIGURE 14.2 Effect of temperature on relative density (τ_p), microhardness (H_V), and elastic modulus (E) at $P = 4$ GPa and τ_p at $P = 7.7$ GPa as well as at $P = 0$ and specific surface area (S) during pressureless sintering. (From Andrievski, R.A., in *Nanotechnology. Molecularly Designed Materials*, Chow, G.-M. and Gonsalves, K.E., Eds., ACS, Washington, DC, 1996, chap. 20. With permission.)

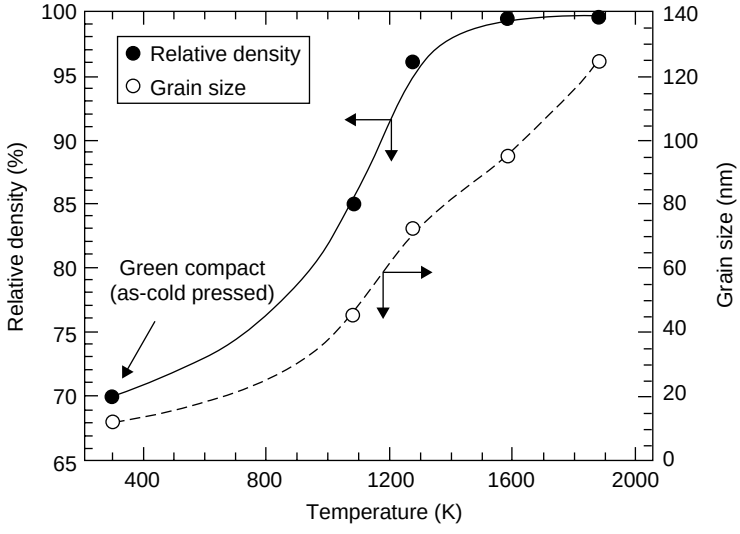

FIGURE 14.3 Change of the relative density and the average grain size as a function of the temperature for ZrC consolidated at 1.5 GPa. (From Mahday, A.A., *J. Alloy Comp.*, 299, 244, 2000. With permission.)

for regions A, B, and C of Figure 14.5c.[46] It is evident from Figure 14.5c and Figure 14.6 that in the structure of the investigated nanocomposite there are not only Si_3N_4 and TiN phases (regions A and B), but also some admixtures such as oxygen, yttrium, and aluminum, in the grain boundary (region C) originating from the surface oxidation layer (SiO_2) in initial powder and the sintering aids.

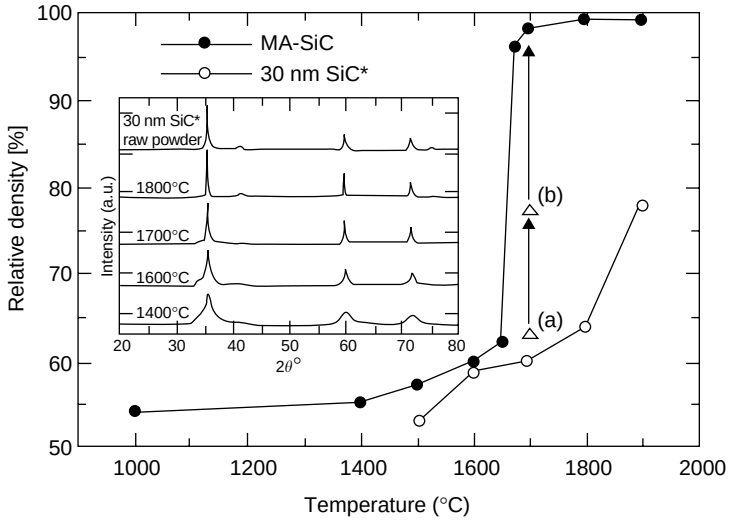

FIGURE 14.4 Dependence of relative density on sintering temperature of mechanical alloying (MA) SiC and commercial nanostructured SiC (30 nm SiC*); sintering time = 10 min unless otherwise indicated. Points (a) and (b) in the figure represent results on MA-SiC sintered at 1700°C for 0.2 min, respectively. The inset shows typical XRD patterns of the sintered materials. An arrow in the inset shows the diffraction peak marking the stacking-ordered SiC. (From Ohyanagi, M. et al., *Scr. Mater.*, 50, 111, 2004. With permission.)

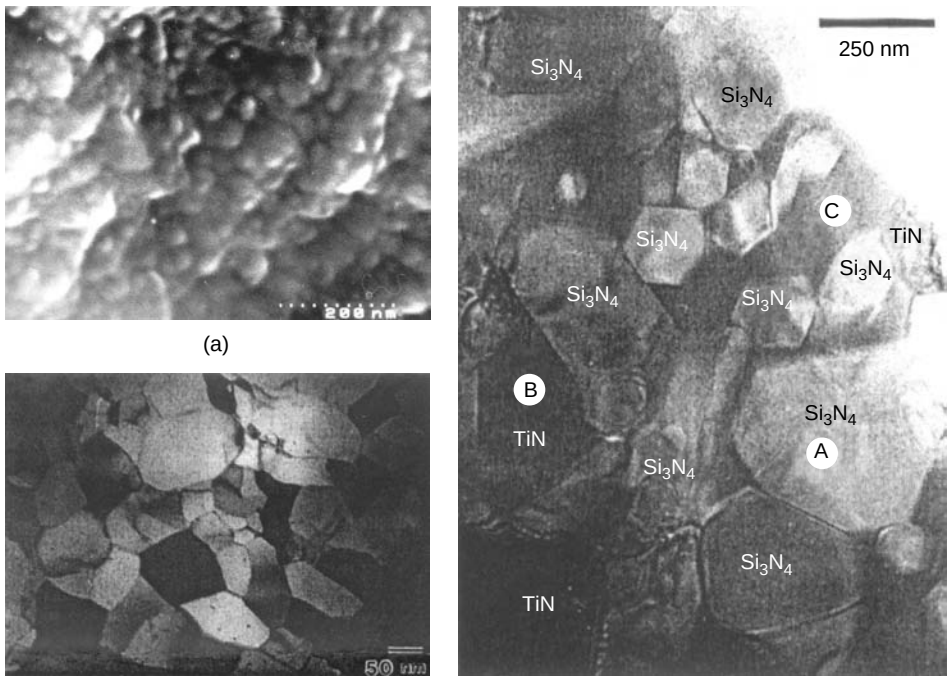

FIGURE 14.5 SEM (a) and bright-field image TEM (b, c) micrographs of consolidated TiN (*a*), ZrC (*b*), and 20 vol% TiN /Si_3N_4 (*c*) nanopowders. (a: From Andrievski, R.A., in *Nanostructured Materials*, Chow, G.-M. and Noscova, N.I., Eds., Kluwer Academic Publishers, Dordrecht, 1998, chap. 13. With permission. b: From Mahday, A.A. et al., *J. Alloy Comp.*, 299, 244, 2000. With permission. c: Gao, L. et al., *J. Eur. Ceram. Soc.*, 24, 381, 2004. With permission.)

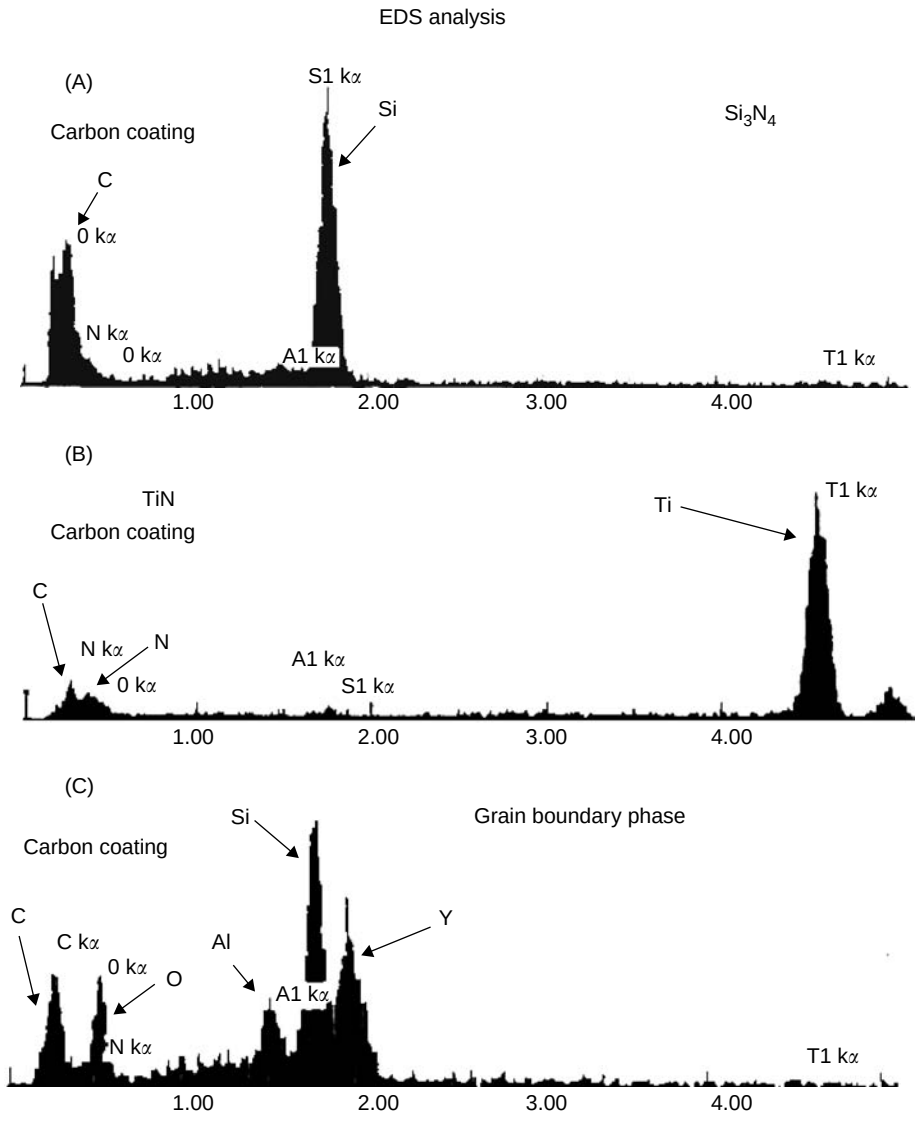

FIGURE 14.6 EDS analysis of 20 vol% TiN/Si_3N_4 composite. (From Gao, L., *J. Eur. Ceram. Soc.*, 24, 381, 2004. With permission.)

In addition, the grain size distribution can be obtained from TEM micrographs (Figure 14.7).[103] In many cases, the grain size distribution information is important for the analysis of size effect in NM, i.e., for an understanding of nanostructure influence on properties.

To obtain the most representative information on nanostructure, it is desirable to use several independent methods including XRD, which gives information from the much biggest place as compared with SEM and TEM examination.

High-resolution TEM study of TiN and TiB_2 nanostructured films revealed the presence of edge dislocations inside the crystallites.[25] Figure 14.8 shows a TEM micrograph with clear dislocation image in the TiN film. The estimation of the characteristic length of the dislocation stability in nano-TiN resulted in a value of about 0.1 nm, implying that the dislocation observations in TiN film with a grain size of about 5 to 10 nm seem to be very realistic.

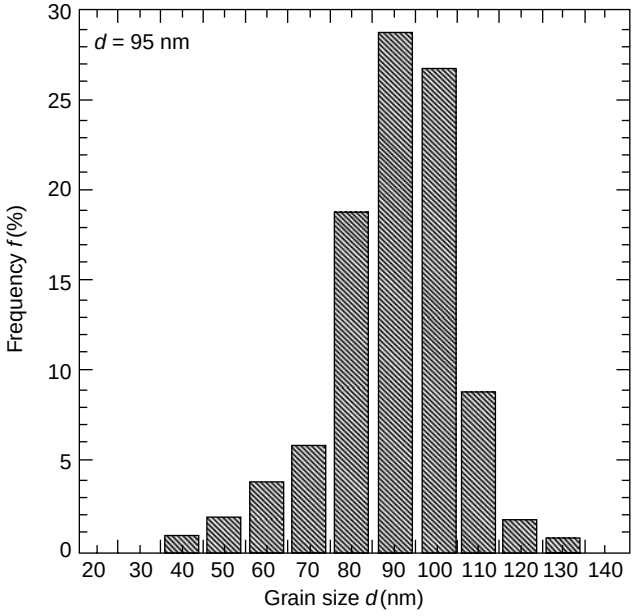

FIGURE 14.7 Grain size distribution of consolidated ZrC as determined from several micrographs (about 150 representative grains). (From Mahday, A.A. et al., *J. Alloy Comp.*, 299, 244, 2000. With permission.)

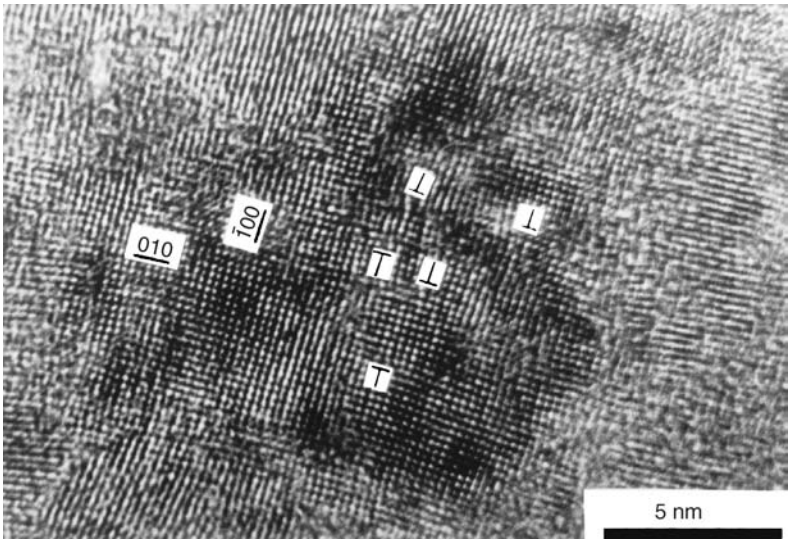

FIGURE 14.8 High-resolution TEM micrograph of TiN film (obtained by D.V. Shtanskiy). (From Andrievski, R.A., in *Functional Gradient Materials and Surface Layers Prepared by Fine Particles Technology*, Baraton, M.-I. and Uvarova, I., Eds., Kluwer Academic Publishers, Dordrecht, 2001, p. 17. With permission.)

14.3.2.2 Properties

14.3.2.2.1 Mechanical Properties

The most investigated properties of HMPC-based materials are the mechanical properties, especially hardness. It is necessary to point that HMPC-based materials are brittle solids and their brittleness is a well-known inherent property associated with the high value of the Peierls–Nabarro stress with a high barrier for dislocation glide and the absence of plastic deformation. The dislocation low mobility in HMPCs is a reason for their high value of hardness.

The brittle-to-ductile transition temperature (BDTT) of most HMPCs is $\geqslant$1000°C and higher.[1] In relation to the above, the study of nanostructured HMPC mechanical properties has at least two very important fundamental and practical aspects.[2,12,25] First is an attempt to increase the HMPC hardness up to the level of that of diamond, i.e., to develop new types of superhard materials. The second is contrary and is the possibility to decrease the BDTT, i.e., to make HMPC materials more ductile. These aspects demand comprehensive information on the material's nanostructure.

Tables 14.8 and 14.9 summarize information on the mechanical properties of consolidated HMPCs, including data on their relative density τ and grain size L. The mechanical properties, such as Vickers hardness H_V, fracture toughness K_{IC}, Young's modulus E, shear modulus G, bulk modulus K, Poisson's ratio ν, and flexural (bend) strength (or transverse rupture stress) σ_f for conventional polycrystalline and single-crystal specimens are also included for comparison.

Before proceeding to Tables 14.8 and 14.9, some observations can be made. Mechanical properties of HMPC-based materials are very structure-sensitive and are not depend only on grain size but are nearly connected with many other factors such as porosity, deviation on stoichiometrical content, the presence of impurities, and residual stresses.[1] Literature data on mechanical and other properties of HMPC-based materials are not complete as compared to the characterization of nanomaterials, and a detailed comparison of their properties is often not a simple task. Figure 14.9 shows the effect of relative density on hardness and Young's modulus of TiN bulks consolidated by HPS of different UFPs.[134] It is evident that there is a significant change in H_V and E values under the effect of τ. Moreover, in the case of hardness, there is an additional effect of grain size; the E values in the investigated size range were independent of L. For a small range of τ, the following relationships can be written in terms of porosity θ in a fraction of unity ($\theta = 1-\tau$)

$$H_v \cong \begin{cases} H_{VO}\,(1 - 4.7\theta) & \text{for } L = 40 - 80 \text{ nm} \quad (14.6) \\ H_{VO}\,(1 - 2.1\theta) & \text{for } L = 30 - 40 \text{ nm} \quad (14.7) \end{cases}$$

$$E \cong E_o\ (1 - 3.9\theta) \quad (14.8)$$

where H_{Vo} and E_o are the values of hardness and Young's modulus for porous-free specimens.

Linear character of relationships (14.6)–(14.8) is typical for a small interval of porosity; in larger intervals there are other dependances, e.g., exponential, etc.[1]

Vickers hardness values are frequently measured by using different loads; so Table 14.8 includes information on load P. For comparison with the literature data, it must be remembered that values obtained at lower loads have proved to be generally higher. For example, the difference in the hardness measurements between $P = 0.5$ and 100 N is expected to be equal up to 500 Vickers units (5 GPa).[82]

Many relationships exist between hardness and grain size for nanomatrials (see, e.g., review 157). In many cases these relationships reflect the increase of hardness with the refinement of grain size and is described by the well-known Hall–Petch equation,

$$H_v(\sigma_y) = H_o\ (\sigma_o) + k_y L^{-1/2} \quad (14.9)$$

where σ_y is the yield strength, H_o the grain-body hardness, σ_o the internal stress hindering the propagation of plastic shear in the grain body, and k_y is the proportionality coefficient. However, there is some abnormal behavior in the nanocrystalline range such as the anti-Hall–Petch relationship and deviations of exponents from 0.5 in Equation (14.9). In general, in brittle solids,

TABLE 14.8
Hardness and Fracture Toughness of Consolidated HMPCs

HMPC	Consolidation Method	τ (%)	L (nm)	Microhardness H_V		Fracture Toughness K_{IC} (MPa $m^{1/2}$)
				GPa	Load (N)	
SiC	HIP[24]	98.6	70	24–25	100	3.0–4.2
	Shock compaction[148]	96–97	60–100	23–27	2	N/A
	Hot pressing with	95–99	200–300	27–29.8	4.9	2.5–3
	Al aids[149]	>99	670	25.6	4.9	5.1
	HPS[150]	~100	330	32–41.5	20	N/A
	Single crystal[1]	—	—	—	1	—
	(0001)	—	—	36.7	—	1–3
	(1010)	—	—	46.9	—	3
	Polycrystal[1,25]	~100	$>10^3$	26±2; 32.5	1–5	3–6
Si_3N_4	HPS[25]	99	~500	32.5	1	N/A
	Shock compaction[131]	99	40–60	23	5	N/A
	HIP[24]	97	300–400	18.4	100	4.5
	Single crystal[117]					
	(0001)	—	—	26–28	2–5	1.5–2
	(1100)	—	—	32–36	2–5	—
	Polycrystalline cubic (<0.5 wt% oxygen)[151]	N/A	N/A	43	0.01	N/A
	β phase[25]	~100	$>10^3$	30±2	1–5	3–5
TiN	HPS[12,93,133,134,152,153]	(~100)	40–80	26.2	0.5	3.8±1.8
		95–96	30–60	30–31	0.5	—
		(~100)	30–40	29	0.5	—
	RCS[137]	96	250	18±1	0.5	N/A
		98.1	50	25±1.5	0.5	N/A
		99.3	150–200	23±1	0.5	N/A
	PAS[126]	>96	~65	19–20	500	N/A
	Single crystal (111)[11]	—	—	22.6	0.03	N/A
	Polycrystal[1,25]	~100	10^3	20±2	1–3	4–5
Ti(N,C)	HIP[24]	96.6	100	16	100	3.5
TiC	HIP[24]	97.6	10^2–10^3	21	100	2.9
	PAS[138]	~100	~60	32	500	N/A
	Single crystal[1]					
	(001)	—	—	29.5	1–5	2
	(110)	—	—	27	1–5	N/A
	(111)	—	—	27.8	1–5	N/A
	Polycrystal[1,25]	~100	$>10^3$	30±2	1–3	2
ZrC	HPS[103]	99.5	95	27	300	N/A
	Single crystal[1]					
	(001)	—	—	25.1	1–5	3
	(110)	—	—	23.4	1–5	N/A
	(111)	—	—	24	1–5	N/A
	Polycrystal[1]	~100	$>10^3$	24–26	1–5	2–3
WC	PAS[83]	~99	25	23	500	4
	Single crystal[1]					
	(0001)	—	—	19–23.5	9.8	N/A
	(1010)	—	—	12–17.5	9.8	N/A
	Polycrystal[1]	~100	$>10^3$	16.7	0.3	7.5

Continued

TABLE 14.8 (*Continued*)

HMPC	Consolidation Method	τ (%)	L (nm)	Microhardness H_V		Fracture Toughness K_{IC} (MPa $m^{1/2}$)
				GPa	Load (N)	
TiN/Si_3N_4	Hot pressing[46]	98	100–600	14	100	5.9
TiN/TiB_2	HPS[12,93,153]	97–99	250–300	33–34	0.5	4.5–5.2
	HIP[143]	95–99	N/A	~20	5	4–5
TiB_2/TiC	RHP[146]	94–97	N/A	N/A	N/A	8.5–12.2
	PAS[139]	98.6	60–70	20.6	4	N/A
TiB_2/B_4C	Sintering with Fe aid[144]	99.9	4×10^3	27	10	5.7
TiB_2/AlN	HIP[143]	99	N/A	30–40	5	6–7
SiC/AlN	Reactive HIP[154]	Near dense	200–500	28–32	4.9	4–4.6
Si_3N_4/TiN	Hot pressing[145]	Near dense	200–500	17.8	100	6.4–7.2
WC/Co	Liquid-phase sintering					
	6 wt% Co					~5[82]
	Grade NY6A[155]	~100	290	24.3	50	N/A
	Grade WC 0.1 L[79]	~100	~100	22.8	300	N/A
	Conventional S6[155]	~100	1300	16.8	50	11–12
	10 wt% Co					~5[82]
	Grade nano[77,78]	~100	100–200	19–20.5	N/A	1–2[156]
	Grade NY10A[155]	~100	290	19	50	N/A
	Grade WC 0.1 L[79]	~100	~100	20.4	300	N/A
	Conventional S10[155]	~100	1320	15.2	50	11–12
WC/MgO	PAS[83]	99	<50	15	500	14
Ti(C,N)/WC/Ni	Liquid-phase sintering[90]	~100	300–600	14	100	8–10

including HMPC-based materials, hardness increases with the refinement of the grain size much less as compared with ductile metals. On the whole, the nature of the H_V–L relationship needs further investigation, also the possible extrapolation procedure in Equations (14.6)–(14.9) demands careful and detailed discussion.

Taking into account the above-mentioned remarks, the data in Tables 14.8 and 14.9 can be analysed in the following way:

1. The obtained hardness values of covalent nanobulks of SiC and Si_3N_4 are close to or lower than those for polycrystals and single crystals. High values[150] are supposed to be related to superstoichiometric carbon content, the presence of planar carbon defects, and the growth of dislocation density. The low values of H_V can be attributed to residual porosity and to not very low values of L.[24,25,131,148,149]
2. The same situation prevails for some metal-like HMPCs (TiC, ZrC, and Ti(N,C)). Only nano-TiN and nano-WC specimens obtained by HPS and PAS, respectively, have hardness values higher by half than those obtained for polycrystals and single crystals. Maximum hardness for binder-free WC nanoceramics is expected to be about 30 GPa with a grain size of about 40 nm.[82] Maximum hardness for TiN nanocrystalline film (see below) is about 35 GPa.
3. Two-phase or multicomponent nanocomposites on a base of TiN, TiB_2, and SiC also have moderate hardness values. Only ultrafine and partly nanocrystalline WC/Co hard materials are characterized by hardness values higher by half as compared with conventional hard ones. Maximum hardness value for WC/Co nanoalloys is estimated to be about 25 GPa.[82]
4. However, nanocrystalline HMPCs are characterized by not very high values of fracture toughness. The situation is the same in the case of many brittle NMs (see, e.g., Refs. 24,

TABLE 14.9
Elastic Properties

HMPC	τ (%)	L (nm)	E (GPa)	G (GPa)	K (GPa)	ν	σ_f (MPa)
SiC[149]	95–99	200–300	N/A	N/A	N/A	N/A	380–410
TiN							
HPS[134,152]	~100	40–80	470	188	—	0.25	N/A
PAS[126]	96	65	440	180	270	0.23	N/A
Polycrystal[1]	~100	$>10^3$	440–600	160–180	290	0.2–0.25	400–600
TiC[138]	~100	~60	450	185	270	0.26	N/A
Polycrystal[1]	~100	$>10^3$	450–485	190–200	240–290	0.2–0.22	400–600
WC[83]	~99	25	813.5	405	273	0.004	N/A
Polycrystal[83]	~100	$>10^3$	N/A	419	300	N/A	350
WC/MgO[83]	N/A	<50	413	171	237	0.21	N/A
TiN/Si_3N_4[46]	98	100–600	N/A	N/A	N/A	N/A	920–1155
TiB_2/TiC[146]	94–97	N/A	N/A	N/A	N/A	N/A	450–680
TiB_2/B_4C[144]	99.9	4×10^3	~500	N/A	N/A	N/A	580–620
TiB_2/AlN[143]	99	N/A	300–500	N/A	N/A	N/A	400–500
TiB_2/TiN[143]	95–99	N/A	300–400	N/A	N/A	N/A	200–450
Si_3N_4/TiN[145]	~100	200–500	N/A	N/A	N/A	N/A	1000
SiC/AlN[154]	~100	200–500	N/A	N/A	N/A	N/A	600–800
WC/Co[155]							
6 wt% Co	~100	290	N/A	N/A	N/A	N/A	910
	~100	1300	N/A	N/A	N/A	N/A	2610
10 wt% Co	~100	290	N/A	N/A	N/A	N/A	1660
	~100	1300	N/A	N/A	N/A	N/A	2740

E, elastic (Young's) modulus; *G*, shear modulus; *K*, bulk modulus; *ν*, Poisson's ratio; and σ_f, flexural (bending) strength.

82, 156, 158, 159). The decrease can be related to intercrystalline fracture of NMs.[12] Unfortunately, the optimistic prognosis on the possibility of ductility increase for nanoceramics[160] is not verified in full measure. In reality, the enhancement of nanoceramics fracture toughness is expected to be for many-phase nanocomposites, where the realization of the crack propagation way increase could be fulfilled.[12] Note also that for hard alloys with similar hardness and different grain size (e.g., conventional micro WC/Co and Inframat nano WC/Co), the K_{IC} value for is about >70%.[91] Improved K_{IC} values have been observed for Al_2O_3 nanocomposites with additions of carbon nanotubes and nanocrystalline niobium.[161] In these experiments, the PAS consolidation for near-dense state was used and K_{IC} values about of 13–14 MPa $m^{1/2}$; for pure nanocrystalline alumina, K_{IC} values more than 300% have been obtained.

5. As indicated earlier, the elastic properties of investigated NMs are comparable to those of conventional materials. It is well known that amorphous solids exhibit lower elastic moduli (about 70%) than their polycrystalline counterparts and so the decrease in elastic properties may be observed in cases when the nanomaterial grain size is lower than several nm, i.e., when the proportion of grain boundary regions in the nanostructure is $\gtrsim$10%.
6. The absolute values of σ_f for investigated materials are not so high and are typical for conventional HMPC-based materials with a wide interval of deviation.

As is evident from the above discussion, the general level of mechanical properties of HMPC-based materials is not very high. This is in contrast with the case of nanometals which are characterized by hardness level 4 to 6 times higher than conventional polycrystal metals.[157]

Such a situation can be explained by the different nature of brittle/plastic deformation and the not-so-small grain size in nanoceramics (L > 30 to 50 nm) with residual porosity (see Table 14.7).

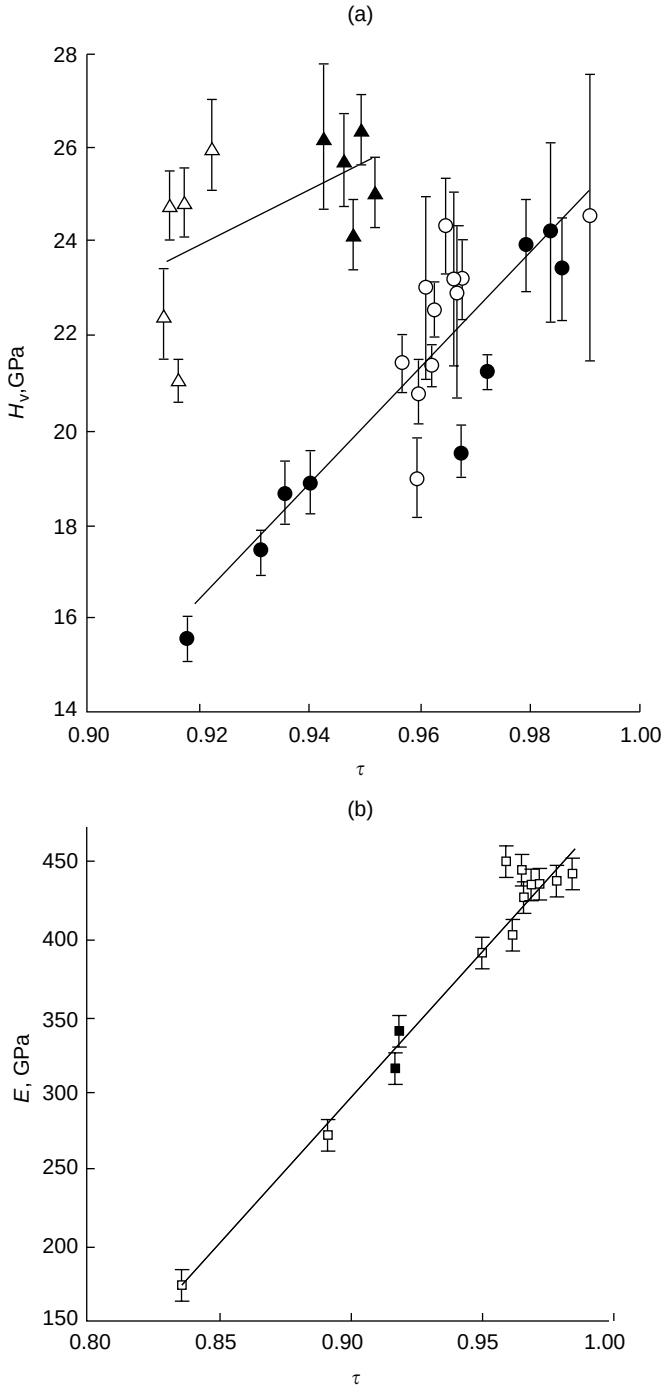

FIGURE 14.9 Effect of relative density τ on (a) microhardness H_V and (b) elastic modulus E of nanocrystalline TiN prepared by HPS: (a) (● and ○) L=40–80 nm; (▲ and △) L=30–40 nm; (b) (■ and □) L=30–80 nm. (From Andrievski, R.A. et al., *Phys. Doklady*, 42, 496, 1997 (English transl.). With permission.)

In addition, it is important to note that almost all types of HMPC consolidation (with the exception of RCS and thermolysis of compacted polymer powders) take place in a very short time and the deformation conditions of PAS and HPS cannot result in equilibrium configuration of grain boundaries.[35] Therefore, the lowering of mechanical properties can be observed because, as it was pointed

out earlier, the fracture of HMPC-based materials is intercrystalline (see Figure 14.5a) and the crack propagation depends on the grain boundary strength. The nature of grain boundaries and triple junctions in HMPC-based materials have been investigated in a limited way and need further study.[25,35,162]

There is little information on the high-temperature deformation of HMPCs.[12,56,155,163–165] To our knowledge, as applied to nanomaterials, the effect of grain size on the BDTT has not been studied in detail. The possibility of superplasticity in TiN/TiB_2 and Si_3N_4/TiB_2 microcomposites was investigated with the use of compacts prepared by HPS from powder mixes, of 80 nm/400 nm and 80 nm/1 μm, respectively.[12,163] Figure 14.10 shows the concentration dependence of the creep rate in the Si_3N_4–TiB_2 system (temperature of 1600°C, load of 20 MPa, and duration of 30 min).[2,163] It is evident that there is a maximum value of creep rate (about 1.7×10^{-4} sec^{-1} that corresponds to the total deformation at compression of about 30%) for the Si_3N_4–75 vol% TiB_2 when using Si_3N_4 UFP. The maximum revealed may be related to the display of superplasticity. It should be noted that analogous creep investigations ($T = 1600$°C) in Si_3N_4–TiN, Si_3N_4–SiC, and TiB_2–BN systems have not revealed anomalies in content dependences as exhibited by Si_3N_4–TiB_2 composite. Hot hardness investigations at 900°C in the TiN/TiB_2 system have also revealed no anomalies.[12] Nevertheless, more than 30 years ago, anomalies in the creep rate/concentration dependences (which were explained as the superplasticity manifestation) have been fixed at 2100 to 2400°C in many two-phase polycrystalline HMPCs, such as VC/ZrC, TiC/TiB_2, ZrN/ZrB_2, and TiC/C.[1,166,167]

Real nanoscale Si_3N_4/SiC composites with grain size of 30 to 50 nm were produced by thermolysis of compacted polymer powders.[56,165] These composites exhibited extremely low creep rates. The dominant creep mechanism might be Coble or Nabarro–Herring diffusion without evidence of a dislocation activity in postdeformed specimens. Low deformation rates have also been fixed in the creep investigation of amorphous Si–C–N and Si–B–C–N ceramics derived from polymers.[56] The compressive flow stress of boron-doped and undoped SiC specimens with grain size of 200 and 30 nm, obtained by HPS, were studied at 1600 to 1800°C.[164]

The study of creep and superplasticity of HMPC-based materials is important both for the development of high-temperature low deformed materials and for commercial superplastic-forming

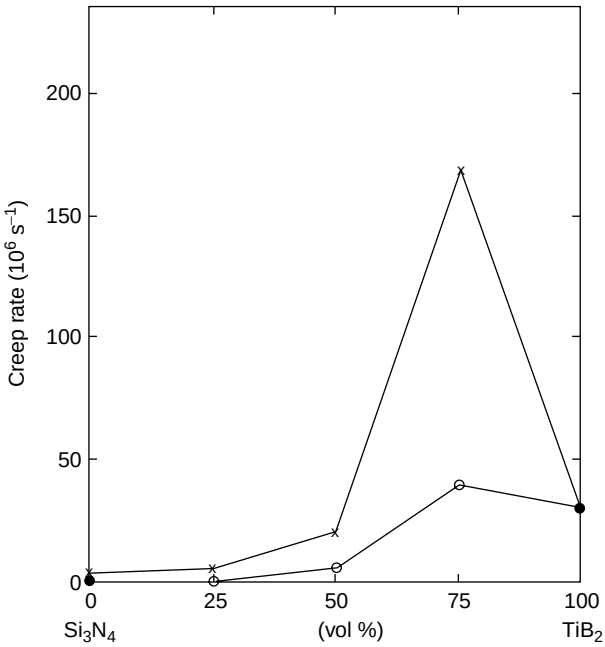

FIGURE 14.10 Creep rate change in Si_3N_4–TiB_2 system ($T = 1600$°C, $\sigma = 20$ MPa, $t = 30$ min.): O — initial powder size 1 μm/1 μm; X — initial powder size 80 nm/1 μm. (From Andrievski, R.A., *J. Mater. Sci.*, 29, 614, 1994. With permission.)

operations, such as sinter-forging. The commercial superplastic-forming operations have also been investigated as applied to oxide nanocomposites, such as ZrO_2/Y_2O_3, $ZrO_2/Y_2O_3/CeO_2$, Al_2O_3/ZrO_2, and TiO_2, intensively and successfully.[13]

14.3.2.2.2 Physical, Physical–Chemical, and Other Properties

Figure 14.11 shows the effect of TiN content on electrical resistivity (ρ) of Si_3N_4–TiN composites with grain size of 100 to 600 nm.[46] In this, the composite silicon nitride is dielectric and TiN is a good metal-like conductor. It is evident that ρ decreases considerably up to ~0.11 Ω cm, i.e., the decrease in ρ of pure Si_3N_4 at about 15 orders and electroconductivity has been observed. In the other case, in one-phase NM, the numerous grain boundaries present result in the enhanced scattering of carriers and photons and lead to a decrease in the thermal diffusivity, thermal, and electrical conductivity. The temperature dependence of thermal diffusivity of conventional and nanophase SiC as well as the ratio of their thermal diffusivity are shown in Figure 14.12.[24] At higher temperatures, the effect of grain boundaries is generally reduced due to the larger proportion of phonon–phonon scattering.

The important result of Ref. 24 is that it highlighted the observation that the high number of grain boundaries led to a fast recovery of irradiation-induced defects, i.e., nanomaterials should be more radiation-resistant than their conventional polycrystalline counterparts.

Detailed study of lattice parameters and superconductivity properties of NbN, Nb(N,C), and (Nb,Ti)(C,N) nanopowders with a mean particle size of 10 to 70 nm prepared by r.f. plasma has been realized in Ref. 168. In all cases, the lattice parameter values of nanoparticles for investigated systems were lower than those for same conventional powders with a particle size of about 100 μm. Figure 14.13 illustrates the size effect on the critical magnetic field. It is evident that the considerable increase in the critical magnetic field with transition to nanocrystalline state is probably connected with the change of phonon spectrum in nanoparticles.

Unfortunately, other physical and especially physical–chemical properties of HMPC-based materials have been investigated only on a limited scale. So far as we know, the important information on the influence of particle size on phase equilibria is exhaustive with the calculations on TiC–TiB_2, TiN–TiB_2, TiN–AlN systems.[2,169,170] These calculations were performed in a very simple regular solution approximation and depend only on rough approximation. Tables 14.10 and 14.11 show the eutectic temperature changes in response of grain size. Although these estimations can present only an approximation, the possibility of decreasing T_E in HMPC-based composites must be taken into account in the development of their processing and application.

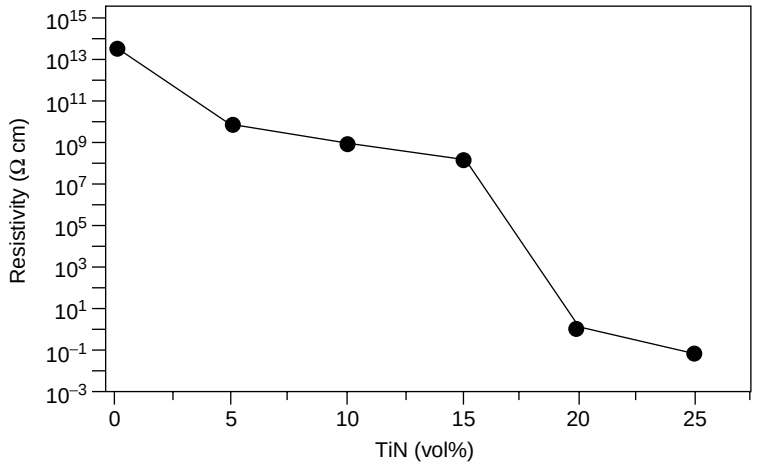

FIGURE 14.11 Resistivity change in Si_3N_4–TiN system. (From Gao, L. et al., *J. Eur. Ceram. Soc.*, 24, 381, 2004. With permission.)

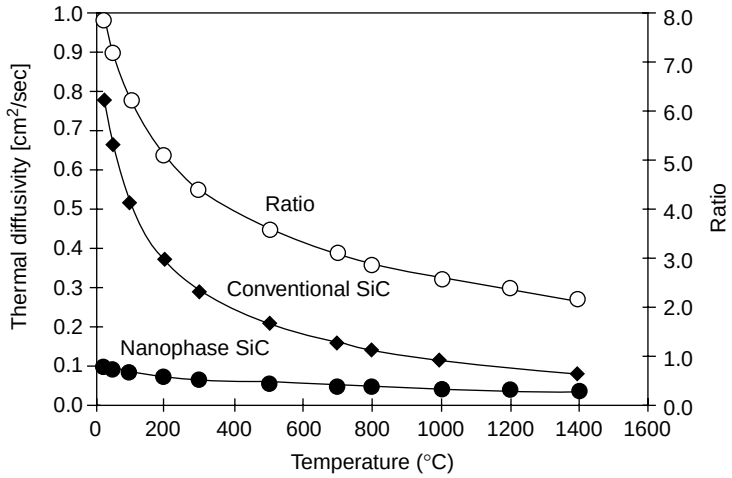

FIGURE 14.12 Temperature dependence of thermal diffusion of conventional HIPed SiC with 3 to 5 μm grain size and nanophase HIPed SiC with about 70 nm grain size, as well as the temperature change of thermal diffusion ratio of these subjects. (From Vassen, R. and Stover, D., *Mater. Sci. Eng. A*, 301, 59, 2001. With permission.)

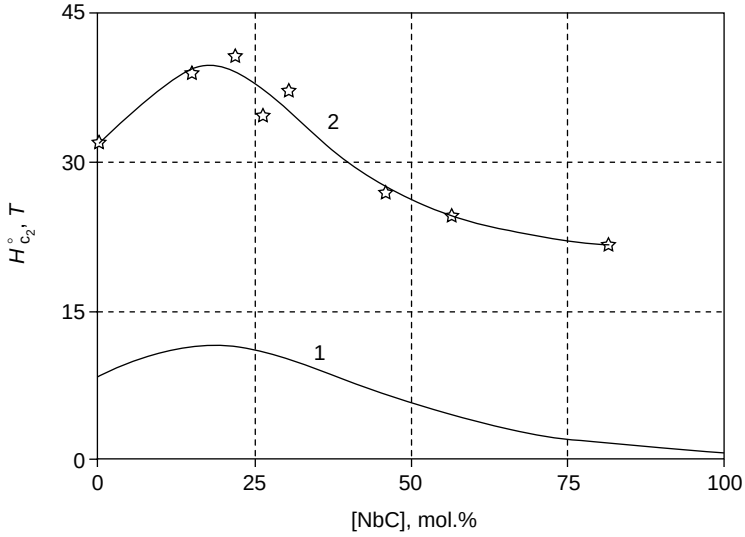

FIGURE 14.13 Dependence of the critical magnetic field on NbC content in NbN–NbC system for conventional coarse-grained powders (1) and UFPs with particle size of 20 to 60 nm (2). (From Troitskiy, V.N. et al., *J. Nanoparticle Res.*, 5, 521, 2003. With permission.)

14.4 NANOCRYSTALLINE FILMS AND COATINGS

14.4.1 General Characteristics of Preparation

There are various methods of preparation of nanocrystalline films and coatings based on HMPCs and are shown in Table 14.12.[11] As in the case of UFP (see Table 14.1), these preparation methods can be generally classified as physical and chemical ones, with some variants. As shown in the classification in Table 14.1, that is also conventional in Table 14.12, because often the preparation methods are based on more than one basic principle and the boundary between them is frequently very diffuse and poorly defined. Chemical reactions have a profound impact on thermal evaporation and

TABLE 14.10
Influence of Grain Size of One Component in TiC (TiN)–TiB_2 Systems, on Change (ΔT_E) in Eutectic Temperature (T_e=2790 K, TiC–TiB_2; T_e=2870 K, TiN–TiB_2)[169]

Grain size (nm)	ΔT_E (K)	
	TiC (TiN)–TiB_2	TiB_2–TiC (TiN)
200	~45	~35
100	~90	~70
20	~450	~350
10	~900	~700

Source: Modified from Andrievski, R.A., *J. Mater. Sci.*, 29, 614, 1994. With permission.

TABLE 14.11
Eutectic Temperature in TiN–AlN System as a Function of Grain Size (L) (for Conventional Polycrystalline Samples the T_E Value is 2715 K)[170]

Dispersed Component	L (nm)	T_E (K)
TiN	200	2660
	100	2610
	20	2160
AlN	200	2710
	100	2690
	20	2565
TiN, AlN	200	2650
	100	2590
	20	2110

Source: Modified from Andrievski, R.A. and Anisimova, I.A., *Inorg. Mater.*, 27, 1450, 1991. With permission.

TABLE 14.12
Main Methods of Films and Coatings Preparation

Group	Method	Main Variations	HMPC
Physical	Thermal evaporation	Electron beam	Borides and carbides
		Laser	Borides, nitrides, and carbides
	Ion plating	Arc deposition	Nitrides and carbides
		Magnetron sputtering	Borides, nitrides, and carbides
		Ion-beam-assisted deposition	Nitrides and borides
		Implantation	Borides, nitrides, and carbides
	Thermal spraying	High velocity oxygen fuel spraying	Carbides
Chemical	Deposition from gas phase	Plasma-assisted and plasma enhanced CVD	Borides, nitrides, and carbides
		Electron cyclotron resonance	Nitrides
	Thermal decomposition	Gaseous and condensed precursors	Nitrides and borides
	Thermochemical treatment	Nitriding	Nitrides

Source: Modified from Andrievski, R.A. *J. Mater. Sci.*, 32, 4463, 1997. With permission.

ion plating, while the physical and laser actions such as plasma or laser are in considerable use for the acceleration of chemical reactions. In the pure state, the existing terms, chemical vapor deposition (CVD) and physical vapor deposition (PVD) are mainly of historical significance. The latter is mainly used for film preparation with thickness up to several micrometers (a value of 1 to 5 μm seems to be the most widely accepted). CVD is used both for film and coating (with thickness >10 μm) deposition. Coatings with thickness up to several tens and even hundreds of micrometers can be produced by thermal spraying and detonation guns.

It is worth noting that the methods enumerated in Table 14.12 result not only in preparation of two-component one-phase films and coating, but in many-component, many-phase and multilayer coating deposition too, such as TiN, (Ti,Al)N, Ti(N,C,B), TiN + Pt, and TiN/NbN. TiN-based films are good examples for modeling experiments and so are often quoted in publications on synthesis/properties. In addition, the application of TiN films is also very wide. The features of different preparation methods of films can be found elsewhere.[5,11,16,17,20,31,32] As compared with nanobulk preparation methods, film/coating preparation methods provide more widespread possibilities in nanocrystalline structure creation although the film/coating thickness is limited.

14.4.2 Film Structure and Content

For film structure and content investigations, many methods such as XRD, SEM, and TEM including high-resolution (HRTEM) versions, EDS, Auger electron spectroscopy (AES), x-ray photoelectron spectroscopy (XPS), Rutherford backscattering spectroscopy (RBS), selected-area electron diffraction (SAED), scanning tunneling microscopy (STM), atomic force microscopy (AFM), electron energy loss spectroscopy (EELS), Fourier transform infrared spectroscopy (FTIRS), Raman spectroscopy, and electron probe microanalysis (EPMA) are being used in different combinations.

In most PVD films, especially produced by magnetron sputtering at low substrate temperatures grain sizes <10 to 20 nm and even <5 to 10 nm are often fixed. The dislocation presence in TiN film produced by magnetron sputtering has been shown in Figure 14.8. The presence of edge misfit dislocations with a Burger vector ½ [110], which is characteristic for the carbides and nitrides (with the NaCl cubic structure) has been detected in multilayer TiN, NbN, VN, and (Ti,V)N films.[11]

Dark-field TEM and HRTEM micrographs are used for grain size determining grain size. Figure 14.14 shows dark-field image and SAED pattern as well as the grain size distribution of Ti(B,N) film deposited by magnetron sputtering from TiB_2+50 TiN target.[171,172] The presence of a very small grain size is evident. An interesting method of film nanostructure change is using additional external magnetic fields (EMF).[172,173] Figure 14.15 shows AFM images of TiN films deposited with and without EMF.[172] In these images, it is possible to observe the typical columnar structure (the dome-rounded shape) as is often occuring in the case of TiN films,[5,11] but the deposition with EMF results in significant topography change and decrease in column height/width. Table 14.13 shows the effect of an additional EMF on the deposited film grain size. It can be seen that in essentially all cases, the L values decrease and a significant change of standard deviation is also observed. An analogous situation of the EMF effect has been resolved in the TiB_2/B_4C films.[172]

HRTEM also provides a good deal of information about multilayer films (superlattices). Figure 14.16 demonstrates an HRTEM micrograph of a TiN/AlN superlattice.[19] The SAED pattern is shown in the upper-right inset and a magnified portion of the pattern is shown at the left inset. The lattice fringes retain a square symmetry throughout the image and the diffraction pattern verifies the cubic symmetry. This HRTEM picture confirms that a hexagonal AlN phase is converted in a metastable cubic AlN phase in the TiN/AlN superlattices.

Examples of XRD spectra and AES analysis of TiB_2/TiN films prepared by magnetron nonreactive sputtering are shown in Figure 14.17, Figure 14.18, and in Table 14.14.[162,171,174,175] As is evident from XRD and SAED information, the mutual solubility of TiB_2 in TiN and TiN in TiB_2 is very high as contrasted to the equilibrium state phase diagram (typical eutectic sytem with very low mutual solubility[1]). From the AES results it is evident that there is satisfactory even distribution of the film

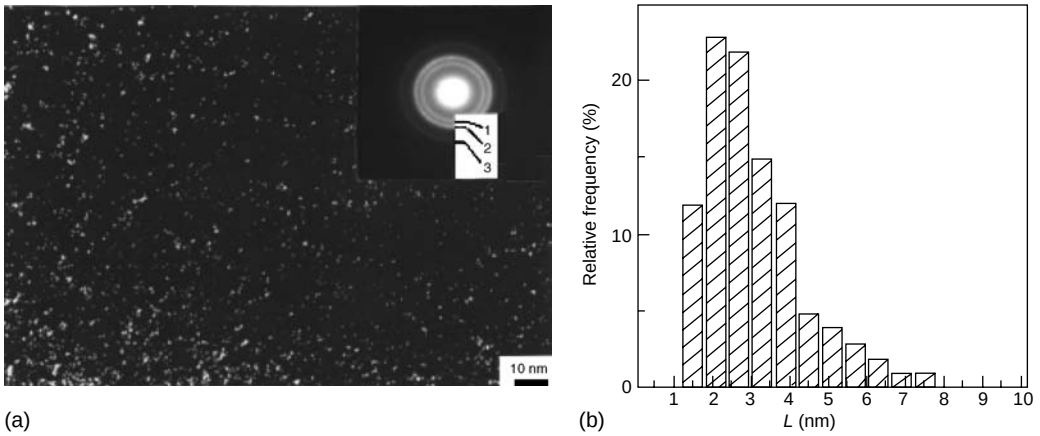

FIGURE 14.14 (a) Dark-field HRTEM micrograph and corresponding SAED pattern [(1) reflection (111), (2) reflection (200), and (3) reflection (220)] of Ti(B,N) film IV (see Table 14.14). (From Andrievski, R.A. and Kalinnikov, G.V., *Surf. Coat. Technol.*, 142–144, 573, 2001. With permission.) (b) Distribution of grain size in Ti (B,N) film IV. (From Andrievski, R.A. and Kalinnikov, G.V., in *Nanostructured Thin Films and Nanodispersion Strengthened Coatings*, Voevodin, A. et al., Eds., Kluwer Academic Publishers, Dordrecht, 2004, p. 175. With permission.)

components with the exception of only some surface layers with a thickness of about 20 to 30 nm. This situation gives the possibility of evaluating the approximate formula composition of films. It is assumed that all nonmetallic and metallic components are substituted separately in nonmetallic and metallic sublattices respectively, and the films have single-phase compositions that have been verified by XRD and SAED analyses. From Table 14.14 it is evident that all films contain some impurities and are nonstoichiometric phases with a high content of nonthermal (structural) vacancies. For example, the homogeneity region in titanium diboride in the equilibrium state is known to be very narrow ($TiB_{1.89–2.00}$).[1] Therefore films I–III based on TiB_2 are significantly substoichiometric compounds; on the other hand, TiN-based films IV–VI are superstoichiometric. All foregoing features such as the high mutual solubility of TiB_2 and TiN as well as the availability of large deviations from stoichiometric content can be related to the low-temperature film deposition (the substrate temperature was about 150°C) and other peculiarities of magnetron sputtering. At the same time, AlN-based films VII–VIII are near stoichiometric and have a low content of structural vacancies. However, as a rule, for many films based on carbides, borides, and nitrides of transition metals, i.e., so-called interstitial phases, their synthesis is frequently accompanied by the formation of nonstoichiometric compounds such as $NbN_{1.35}$, $NbC_{0.75–0.98}$, and $Zr(B_{0.67}C_{0.17}O_{0.16})_{2..25}$.[11] Contamination by noble gases (Ar, Ne, and Xe) was also observed in films obtained by some PVD methods.[11] The presence of some quantity of admixtures and structural vacancies must be taken into account for the understanding of the film properties. The large effect of oxygen and chlorine contamination on the hardness of Ti–Si–N film produced by plasma-activated CVD process was demonstrated in Ref. 176. Only contents of <0.05 at% of oxygen and <0.5 at% of chlorine result in hardness values of more than 50 GPa. It was shown that 1 to 1.5% of oxygen causes a hardness decrease of about 30 GPa.

The possibilities of XPS as applied to the phase analysis of Ti–B–N films are demonstrated in Figure 14.19, which shows XPS B 1s and N 1s spectra for the three compounds as-deposited and annealed films obtained by r.f. magnetron sputtering.[177] From these data the phase compositions of TiB_2N and $TiBN_{0.5}$ have been estimated by assuming only the presence of the phases TiB_2, TiN, and BN in the films.

Additional examples of detailed characterization of the film by FTIRS, EELS, XPS, Raman spectroscopy, RBS, AES, AFM, HRTEM, XRD, and EPMA can be found in many other papers, e.g., on SiCN,[178,179] BCN,[180] CN,[34,181] TiC,[182] WC,[183] (Ti,Si,Al)N,[184] (W,Si)N,[36] Si_3N_4,[185] Ti–Si–N,[186] and Ti_3N_4.[187]

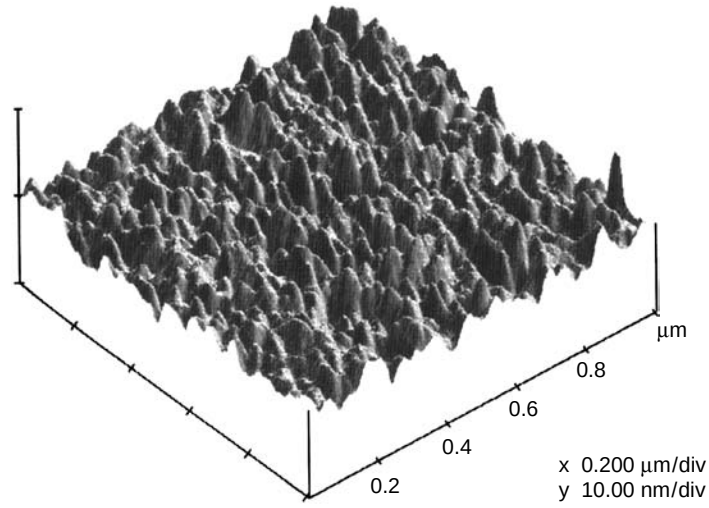

(a)

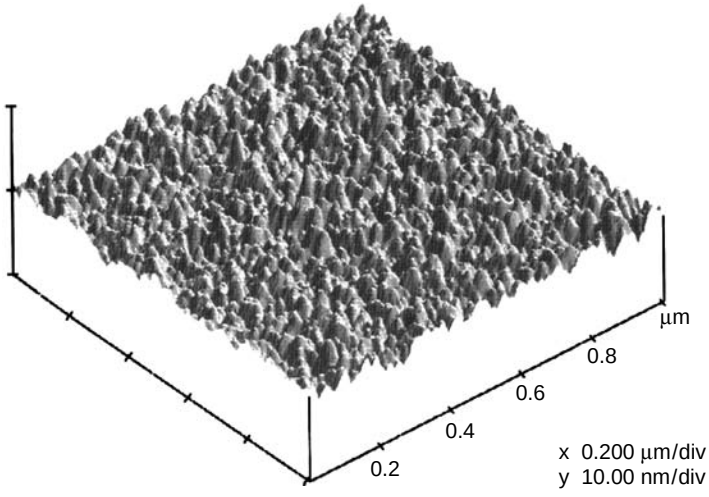

(b)

FIGURE 14.15 Three-dimensional AFM 1 µm × 1 µm images, of TiN films of about 1 µm thickness deposited without external magnetic field (EMF) (a) and with EMF (b). (From Andrievski, R.A. and Kalinnikov, G.V., in *Nanostructured Thin Films and Nanodusper-sion Strengthened Coatings*, Voevodin, A. et al., Eds., Kluwer Academic Publishers, 2004, p. 175. With permission.)

The film lattice parameters are usually greater than those in bulk specimens. This is due to the effect of high compressive stresses, substitutional and interstitial impurities such as oxygen, carbon, hydrogen, noble gases, structural vacancies, etc., and small grain size.[5,11] XRD analysis gives the possibility to determine, side by side with grain size, other important structural characteristics, such as residual stresses, microstrains, and crystallographic orientation (texture coefficients T_c). The residual stresses in films are thought to originate for two reasons: the first is the difference in thermal expansion between the film and the substrate, and the other is a characteristic feature of the film growth. For the majority of PVD films such as TiN, TiB_2, and TiC, the residual stresses are compressive (with a

TABLE 14.13
Average Grain Size *L* of Ti (B,N) Films Prepared by Non-Reactive Magnetron Sputtering without Additional EMF (of about 400 Oe) and with EMF

Target	*L* (nm)	
	Without EMF	With EMF
TiB_2	3.6±1.8	3.3±1.1
$75TiB_2$+25TiN	2.3±1.1	N/D
$50TiB_2$+50TiN	2.9±1.5	1.8±0.3
$25TiB_2$+75TiN	5.9±4.0	6.5±2.5
TiN	29±15	8.8±2.2

Source: Modified from Andrievski, R.A. and Kalinnikov, G.V., in *Nanostructured Thin Films and Nanodispersion Strengthened Coatings*, Voevodin, A. et al., Eds., Kluwer Academic Publishers, Dordrecht, 2004, p. 175. With permission.

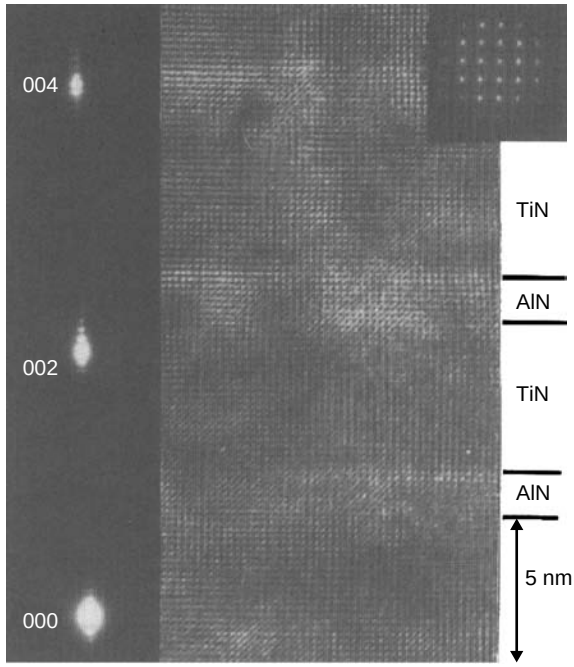

FIGURE 14.16 Cross-sectional high-resolution {002} lattice image of a $[AlN(1.7\ nm)/TiN\ (5.1\ nm)]_{40}$ superlattice. The SAED pattern is shown in the upper-right inset and a magnified portion of the pattern is inset at the left. (From Madan, A. and Barnett, S.A., in *Materials Science of Carbides, Nitrides and Borides*, Gogotsi, Y.G. and Andrievski, R.A., Eds., Kluwer Academic Publishers, Dordrecht, 1999, p. 187. With permission.)

negative sign); however, for TiN CVD films tensile stresses have been noted.[11] In addition, the unmonotonous change of residual stresses was found in the TiN homogeneity range.[188] Table 14.15 shows T_c values, grain sizes, microstrains, residual stresses, and microhardness as functions of the N content in TiN films deposited by cathode arc evaporation on Ti alloy.[188] These results implicitly suggest that all structural and mechanical properties are largely dependent on N content. It is also significant that erosion resistance was found to be superior for the nonstoichiometric films of $TiN_{0.63–0.66}$ that

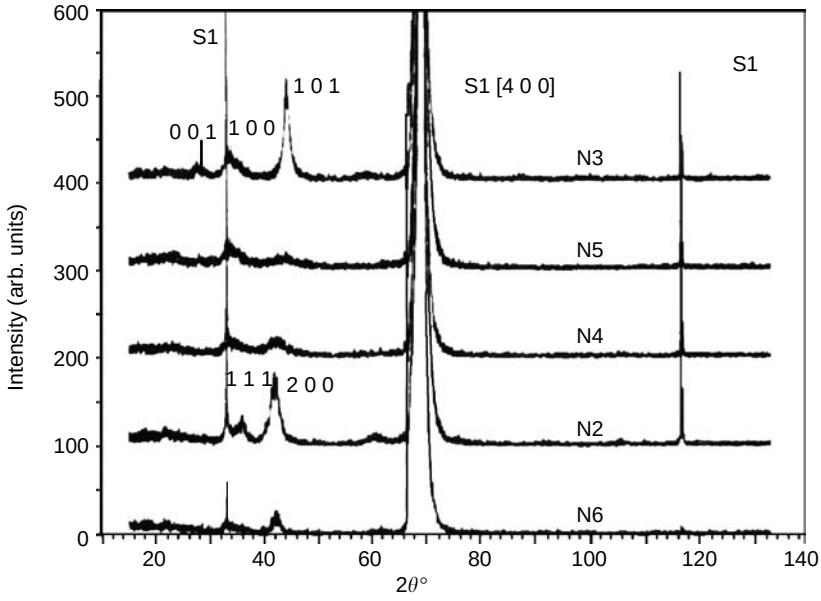

FIGURE 14.17 XRD spectra of films deposited onto Si substrate. Target TiB_2 (No 3) — film II; target $75TiB_2/25TiN$ (No. 5) — film III; target $50TiB_2/50TiN$ (No. 4) — film IV; target $25TiB_2/75TiN$ (No. 2) — film V; target TiN (No6) — film VI (see Table 14.14). (From Andrievski, R.A. and Kalinnikov, G.V., *Surf. Coat. Technol.*, 142–144, 573, 2001. With permission.)

coincides and corresponds with the minimum grain size and residual compressive stress value as well as with the maximum hardness and microstrain.

The film crystallite morphology and their preferred orientation were found to vary with many factors, such as deposition temperature (T_{dep}), plasma gas content, and film thickness, etc. In the case of TiB_2 films, the (001) texture starts to develop at thickness more than >130 nm; for thinner films the crystallites are essentially randomly oriented.[189] The preferred orientation of three kinds of CVD TiN deposition was determined: (100) texture at low T_{dep}, (110) texture at intermediate T_{dep} and low molar ratio of $TiCl_4$ to NH_3, and (111) texture at high T_{dep} and high this ratio.[190]

The film morphology can be represented by columnar and equiaxied grain microstructure with various intermediate cases of the two. Figure 14.20a shows a typical fully dense columnar structure of a TiN film after load indentation.[11,191] The residual plastic deformation of the TiN columnars inspite of the brittle nature of the TiN bulk is also evident. A stone- or cauliflower-like structure with a partly columnar one is observed for TiB_2 and Ti(B,N) films (Figures 14.20b and c).[11]

14.4.3 PROPERTIES

14.4.3.1 Mechanical Properties

Comprehensive tables on hardness and elastic properties with an indication of the preparation method, film thickness, substrate, measuring method, etc. up to 1997, can be found in review 11. Only some recent and very representative results will be described below.

As in the case of nanostructured bulks, undoubtedly, hardness measurements are most popular for film characterization due to the ease of realization and the usefulness of the information obtained. However, in many cases, the interpretation of these results and comparison of results of different authors are not so easy because of the known high structural sensivity of hardness and its dependence on load as well as the test method used. The effect of film thickness and type of substrate, not to mention the influence of residual stresses, content, contamination, and surface topography (see

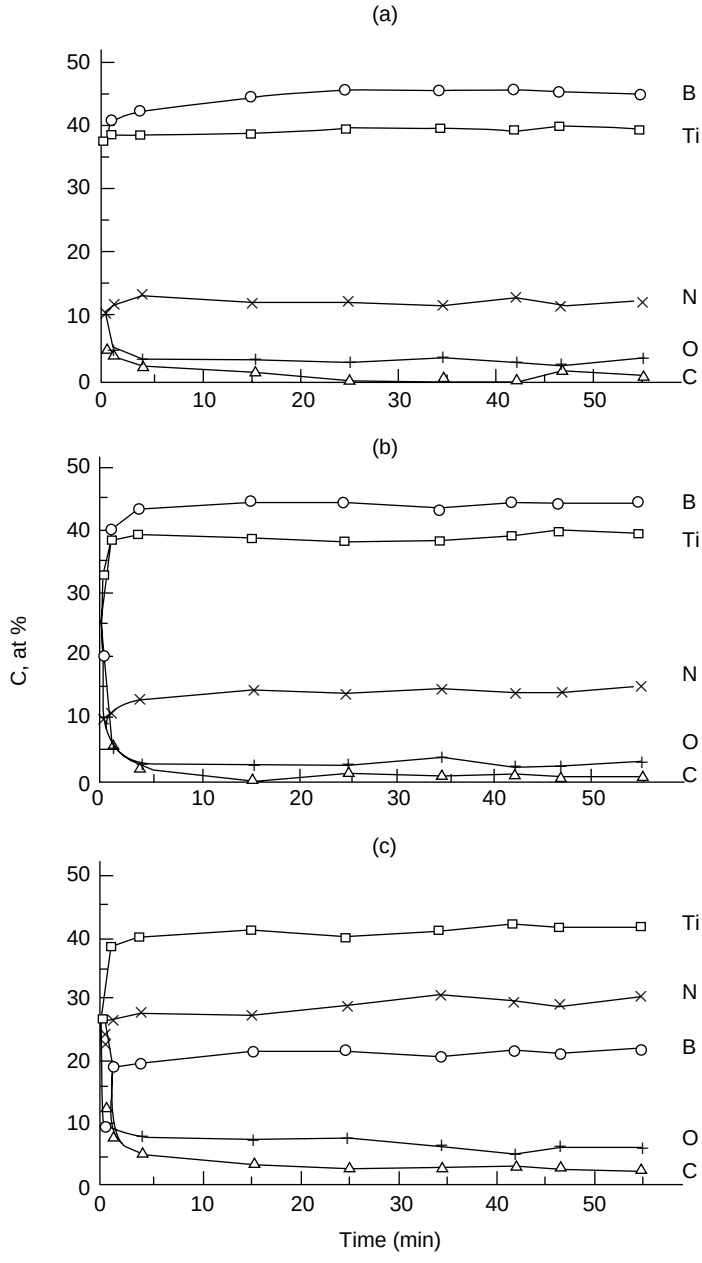

FIGURE 14.18 Depth profiling analyses of films with AES: (a) — film I, (b) — film II, (c) — film IV (See Table 14.14). (From Andrievski, R.A., in *Surface-Controlled Nanoscaled Materials for High-Added-Value Applications*, Vol. 501, Gonsalves, K.E. et al., Eds., MRS, Warrendale, 1998, p. 149. With permission.)

Figures 14.15 and 14.18 as well as Tables 14.13 and 14.15) on the absolute hardness values often demand a detailed consideration.

Tables 14.16 and 14.17 show the hardness values of monolayer and multilayer (superlattice) films respectively. In Table 14.16, the hardness values (see footnote a) relate to estimated values[171,172] using the Jonsson–Yogmark relationship[210] based on an "area law of mixtures." Such modeling of thin film hardness as that of composite (film and substrate) tends to give the hardness of films themselves (or proper hardness) and eliminates appreciably the effect of the film thickness and the substrate material hardness.

TABLE 14.14
Composition and Structure of Films with a Thickness of 1–3 μm Prepared by Using Direct-Current Voltage (I) and Radio-Frequency One (II–VIII)

Sputtering Target (wt%)	Film	Approximate Formula	Crystallite Size (nm)	Structure Type	Parameters (nm)	
					a	*c*
TiB_2	I	$Ti(B_{0.73}N_{0.2}O_{0..05}C_{0..02})_{1.56}$	4–8	AlB_2	0.3060	0.3201
TiB_2	II	$Ti(B_{0.69}N_{0.24}O_{0.04}C_{0.03})_{1.64}$	3.6±1.8	AlB_2	0.3083	0.3246
TiB_2/25TiN	III	$Ti(B_{0.56}N_{0.29}O_{0.05}C_{0.1})_{1.32}$	2.3±1.1	AlB_2	0.3005	0.3263
TiB_2/50TiN	IV	$Ti(B_{0.34}N_{0.49}O_{0.12}C_{0.05})_{1.49}$	2.9±1.5	NaCl	~0.42	—
TiB_2/75TiN	V	N/A	5.9±4.0	NaCl	0.4307	—
TiN	VI	$Ti(N_{0.6}O_{0.2}C_{0.2})_{1.58}$	29 ±15	NaCl	0.4292	—
AlN	VII	Al $(N_{0.78}O_{0.15}C_{0.07})_{0.98}$	5–10	ZnS	N/A	N/A
AlN/50TiN	VIII	$(Ti_{0.55}Al_{0.37}Fe_{0.08})$ $(N_{0.73}O_{0.11}C_{0.16})_{1.075}$	3–10	NaCl	N/A	N/A

Source: Modified from Andrievski, R.A. and Kalinnikov, G.V., *Surf. Coat. Technol.*, 142–144, 573, 2001. With permission.

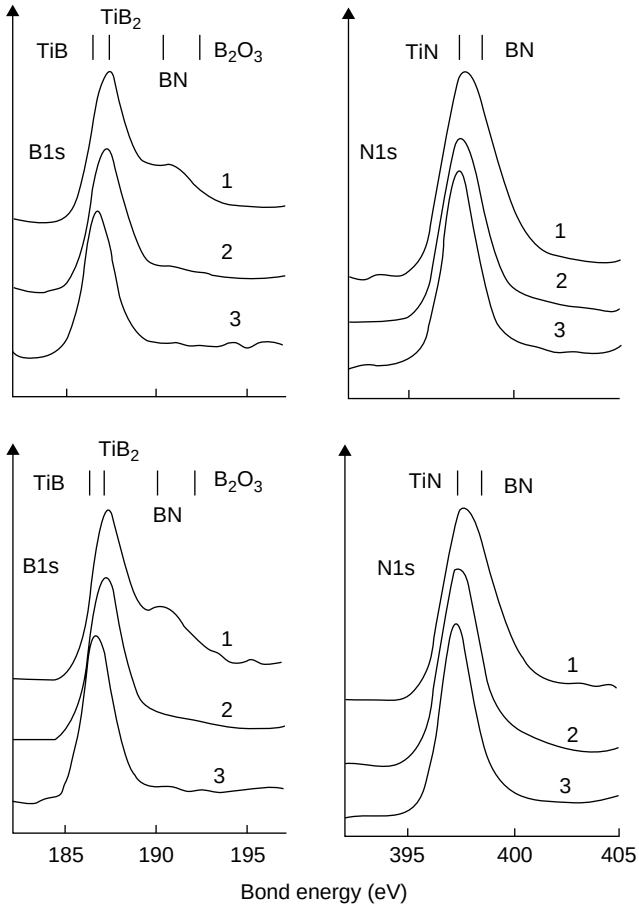

FIGURE 14.19 XPS spectra of B 1s (left) and N 1s (right) of Ti–B–N films of different composition as deposited and annealed at 400°C for 280 min. (From Molart, T.P. et al., *Surf. Coat. Technol.*, 74–75, 491, 1995. With permission.)

TABLE 14.15
Crystallographic Orientation, Grain Size *L*, Microstrain, Residual Stresses, and Microhardness (H_V; Load of 1 N) of Non-Stoichiometric and Stoichiometric TiN Films with a Thickness of 20–25 μm

X Value in TiN_X	Texture Coefficient T_C			*L* (nm)	Micro-Strain (%)	Residual Stresses (GPa)	H_V (GPa)
	TC (111)	*TC* (200)	*TC* (311)				
0.48	0.72	1.57	0.73	18.1	0.100	−2.1±0.15	22.9
0.63	0.37	0.38	2.50	10.9	0.144	−1.8±0.07	26.4
0.66	0.23	0.28	2.96	9.2	0.259	−1.6±0.07	26.1
0.88	3.65	0.03	0.32	16.0	0.127	−2.0±0.15	21.7
0.89	3.82	0	0.18	17.3	0.122	−2.5±0.2	21.2
0.92	3.82	0	0.18	18.6	0.091	−2.7±0.21	21.2
0.97	4.00	0	0	19.2	0.082	−2.9±0.23	20.8
1.00	4.00	0	0	21.2	0.081	−4.1±0.14	18

Source: Modified from Sue, J.A., *Surf.Coat. Technol.*, 61, 115, 1993. With permission.

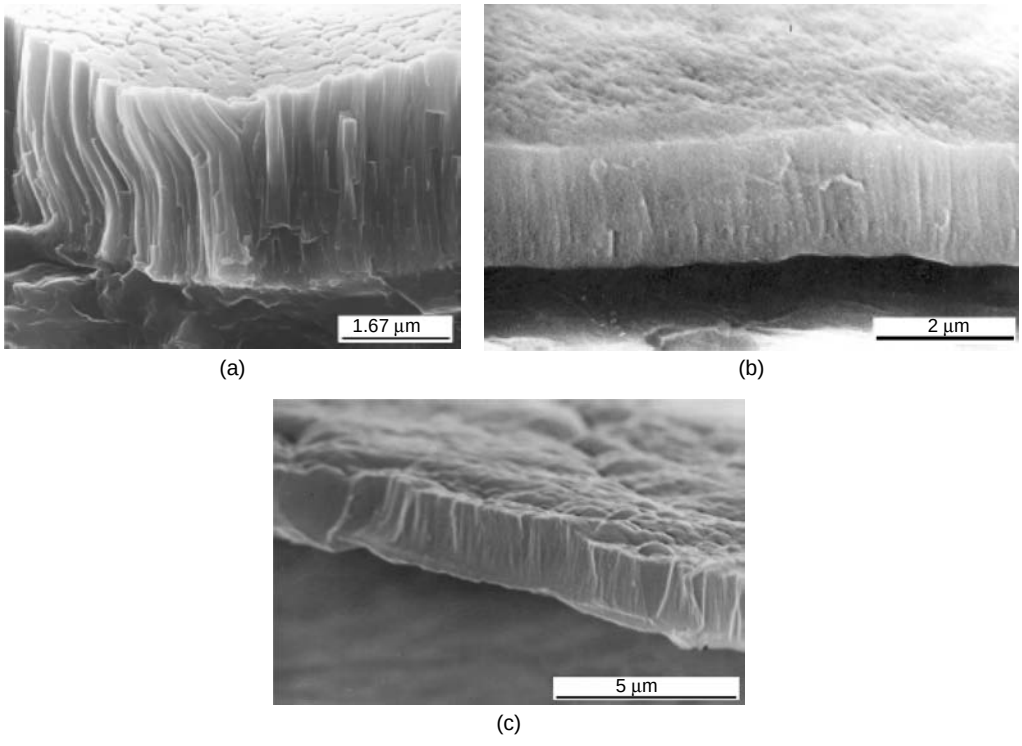

FIGURE 14.20 SEM images of a fracture cross-section of TiN (a), TiB_2 (b) and Ti (B,N) (c) films. (From Andrievski, R.A., *J. Mater. Sci.*, 32, 4463, 1997. With permission.)

The following comments are useful for correct interpretation of the data presented in Tables 14.16 and 14.17:

1. It is evident that inspite of measurements being carried out under different conditions, the values of film hardness are greater than those for nanostructured HMPC bulks and are on

TABLE 14.16
Vickers Microhardness H_V of Monolayer Films and Coatings

HMPC	Preparation Method	Thickness (μm)	Grain Size (nm)	Load (N)	Substrate	H_V (GPa)
1	2	3	4	5	6	7
TiN_x	Different methods[11]	0.3–25	N/A	0.03–1	Different substrates	17–35
TiN	NRMS[173]	4±1	N/A	0.01	Steel	13
	NRMS+EMF[173]	4±1	N/A	0.01	Steel	30
$Ti(N,O,C)_{1.58}$	NRMS[172]	1–2	29±15	0.2–0.5	Si	23–28[a]
	NRMS+EMF[172]	1–2	8.8±2.2	0.2–0.5	Si	36–42[a]
$TiN_{\sim 0.7}$	RMS[192]	7.4±0.2	~20	0.01–0.05	HSS	32±0.7
$TiN_{\sim 1.0}$		1.2±0.2	~90	0.01–0.05	HSS	26.1±0.5
Nano TiN/ amorphous SiN_x	PACVD[17]	3.5	2–10	0.07	Stainless steel	~100
Nano TiN/ amorphous TiSi	RMS[186]	~1	2–15	0.001–0.0035	Si; WC/Co	15–35
$(Ti_{1-x}Al_x)N$	RMS[193]	2.5	10–70	0.015	Cr steel	40–47
(Ti,Al)N	NRMS[171]	2	3–10	0.2–0.5	Si	45–47[a]
Ti(Al,V)N	RMS[194]	3	5–50	N/A	Steel	40–50
NbN_x	CAPD[11]	2	~100	0.5	WC/Co	34±2
$NbN_{\sim 0.2}$	RMS[192]	10.4±0.2	~20	0.01–0.05	HSS	34±0.7
$NbN_{\sim 0.61}$		3.9±0.2	~90	0.01–0.05	HSS	39±1.4
$NbN_{\sim 0.83}$	CAPD[195]	2–3	~30	0.5	WC/Co	42
$NbN_{1.05–1.18}$		2–3	25–30	0.5	WC/Co	35–38
NbN_x	RMS[196]	N/A	30–50	0.015	Steel	36.6
ZrN	NRMS[197]	3–4	10–45	0.03	Steel; Mo	25–41
$CN_{0.13}$	RMS[34]	0.4	~6	0.0005	Si (001)	10
$CN_{0.14}$		0.4	~6	0.0005	Si (001)	7
$CN_{0.18}$		0.4	~6	0.0005	Si (001)	18
$CN_{0.4}$	CAPD + ion beam source[198]	N/A	N/A	N/A	N/A	47
AlN	PLD[199]	0.275	N/A	N/A	Si (100)	15
Al(N,O,C)	NRMS[171]	3.4	5–10	0.2–0.5	Si (100)	21–22[a]
Al(Si,Cu)N	RMS[200]	3	Amorphous	0.02	Si (100)	39–47
(W,Si)N	RMS[36]	0.2–0.3	Amorphous; 60–250 annealed	0.05	N/A	22–31 25–50
$TiB_{2.4}$	NRMS[201]	3–7	80–660	0.05	Steel	61–77
$TiB_{2.8}$	NRMS[197]	3–4	7–25	0.03	Steel; Mo	32–55
$TiB_{1.9–2.5}$	NRMS[173]	4±1	N/A	0.01	N/A	37
	NRMS+EMF[173]	4±1	N/A	0.01	N/A	63
$Ti(B,N,O)_{\sim 1.6}$	NRMS[172]	1–2	3.6±1.8	0.2–0.5	Si	32–39[a]
	NRMS+EMF[172]	1–2	3.3±1.1	0.2–0.5	Si	42–49[a]
TiB_2	NRMS[202]	3–4	N/A	0.98	Steel; Mo	22–69
$Ti(B,N,O)_{\sim 1.6}$	NRMS[171]	1–3	2–10	0.2–0.5	Si	40–80[a]
$ZrB_{2.8}$	NRMS[197]	3–4	7–25	0.03	Steel; Mo	42–55
ZrC	RMS[203]	2	N/A	0.01	Steel	30–32
TiC/a-C	MSPLD[204]	0.5	10	0.001	Steel	32
WC–WS_2/a-C	MSPLD[205]	0.5	1–2 WC; 5–10 WS_2	0.001	Steel	7–16
WC–12%Co	HVOFTS[206]	200–300	35 WC	3	Steel	11.35
SiC	MOCVD[207]	0.15	~100	N/A	Si	32
B_4C	NRMS[208]	0.5	1.7–2.8	N/A	Si	40±4
	NRMS[172]	1–2	Amorphous	0.2–0.5	Si	42–50[a]

Continued

TABLE 14.16 (*Continued*)

HMPC	Preparation Method	Thickness (μm)	Grain Size (nm)	Load (N)	Substrate	H_V (GPa)
1	2	3	4	5	6	7
	NRMS+EMF[172]	1–2	Amorphous	0.2–0.5	Si	48–56[a]
B_4C–TiB_2	NRMS[172]	1–2	Amorphous	0.2–0.5	Si	44–54[a]
	NRMS+EMF[172]	1–2	Amorphous	0.2–0.5	Si	60–71[a]
TiB_2–B_4C	NRMS[172]	1–2	8.5±4	0.2–0.5	Si	40–46[a]
	NRMS+EMF[172]	1–2	2.9±0.3	0.2–0.5	Si	54–58[a]
Si–B–C–N	PACVD[209]	1.2	Amorphous	0.001	Si	2.3±4.4

NRMS, nonreactive magnetron sputtering; EMF, external magnetic field; RMS, reactive magnetron sputtering; PACVD, plasma activated chemical vapor deposition; CAPD, cathodic arc plasma deposition; PLD, pulsed laser deposition; MSPLD, magnetron sputtering assisted by pulsed laser deposition; HVOFTS, high velocity oxygen fuel thermal spaying; MOCVD, metal-organic chemical vapor deposition.

[a]Hardness values estimated using the Jonsson–Yogmark relationship based on an "area law of mixtures."

TABLE 14.17
Vickers Microhardness H_V of Multilayer (Superlattice) Films

Multilayer Film	Preparation Method	Thickness of Individual Layer and Whole Film (nm)	Substrate	Load (N)	Maximum Value of H_V (GPa)
TiN/VN	RMS[211]	2.5 (2.5×10^3)	(100) MgO	0.08	~54
TiN/NbN	RMS[212]	3–4 (2–3×10^3)	(100) MgO	0.1	~48
TiN/NbN	CAPD[213,214]	10 (2×10^3)	WC–Co	0.5	78
TiN/ZrN	CAPD[213,214]	10 (2×10^3)	WC–Co	0.5	70
TiN/CrN	CAPD[213,214]	~45 (2×10^3)	WC–Co	0.5	~50
$TiN/V_{0.3}Nb_{0.7}N$	RMS[19]	~3.5 (N/A)	N/A	N/A	~30
NbN/W(Mo)	RMS[19,30]	~1 (10^3)	N/A	N/A	30–35
TiAlN/VN	RMS[31]	1.75 (3–4×10^3)	Tool steel	N/A	56
TiAlCrN/TiAlYN	RMS[31]	0.85 (3–4×10^3)	Tool steel	N/A	36
TiN/TiB_2; ZrN/ZrB_2	RMS[30]	2.5 (N/A)	Sapphire	N/A	~50 (after annealing)

the hardness level of superhard materials. However, the comparison of the hardness values calculated under different conditions needs thorough discussion with regard to possible effects of different conditions and artifacts. Reviews of possible errors in the hardness and elastic property measurements of superhard films can be found in Refs. 11, 215, and 216.

2. There is no doubt that the high values of H_V in the majority of monolayer and multilayer films are the result of nanocrystalline structure and interfaces. Figure 14.21 shows the effect of a number of layers on the hardness of nitride multilayer films which had a similar total thickness (nearly 2 μm). There are at least four physical reasons for the considerable increase in the hardness observed: (1) the stop crack propagation at interphase boundaries; (2) the low value of crystallite size in monolayers (equal to, lower than the layer thickness); (3) increase in the dislocation density as a result of the layer lattice mismatch; and (4) possibility of a more favorable situation with residual strains in multilayer films. The unmonotonous change in the case of TiN/CrN is connected with the (Ti,Cr)N solution formation and interphase boundary disappearance for layer numbers greater than 100 to 120, as has been shown by XRD analysis. The case of TiN/CrN confirms the effect

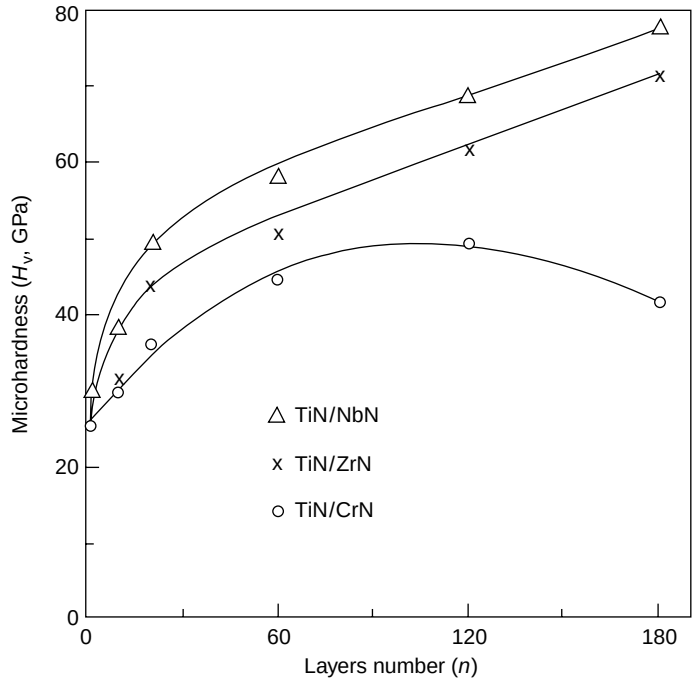

FIGURE 14.21 Influence of the number of layers on the film hardness. Key: Δ —TiN/NbN; × — TiN/ZrN; O — TiN/CrN. (From Andrievski, R.A., *J. Mater. Sci.*, 32, 4463, 1997. With permission.)

of interphase boundaries and lattice mismatch on increasing hardness. The nature of high hardness of the nitride superlattices has also been discussed in reviews 19, and 30.

3. The high hardness values of crystalline films can be explained in addition to nanostructure by a combination of various other effects such as the existence of nonequilibrium phases and supersaturated solutions as well as the availability of compression stresses and so on. The high hardness of some amorphous B_4C and Ti(B,C) films are also noteworthy.
4. The incorporation of some compounds into superlattice layers such as VN, CrN, YN, and AlN introduces components which act as dry lubricants or corrosion decreasing agents. This alloying results in decrease in the friction coefficient and improve temperature, wear, and corrosion characteristics.[31] The effect of hardness on diamond abrason rate measurements for different nitride films is shown in Figure 14.22.[19] However, such clear relationship between wear rate and hardness has not been observed in all cases for TiN/NbN nanostructured polycrystalline multilayer film[192] but their abrasive wear as a whole is lower than that for TiN films.

The deformation and fracture peculiarities of films can be studied by SEM and AFM investigations of fracture surfaces.[12,217–219] There are at least two types of deformation under indentation such as homogeneous deformation (Figure 14.20a and Figure 14.23b) and localized inhomogeneous deformation (Figure 14.23a). The first has been observed mainly in films with clearly defined columnar structure as in the case of TiN film. The homogeneous deformation is probably linked to a slip on the boundary columns. The inhomogeneous deformation mechanism with the formation of shear bands and steps need further clarification. The band width and step height were changed in a wide interval and ranged from 100 nm to a few hundred nanometers in size (films of TiB_2, AlN, (Ti,Al)N, etc.).

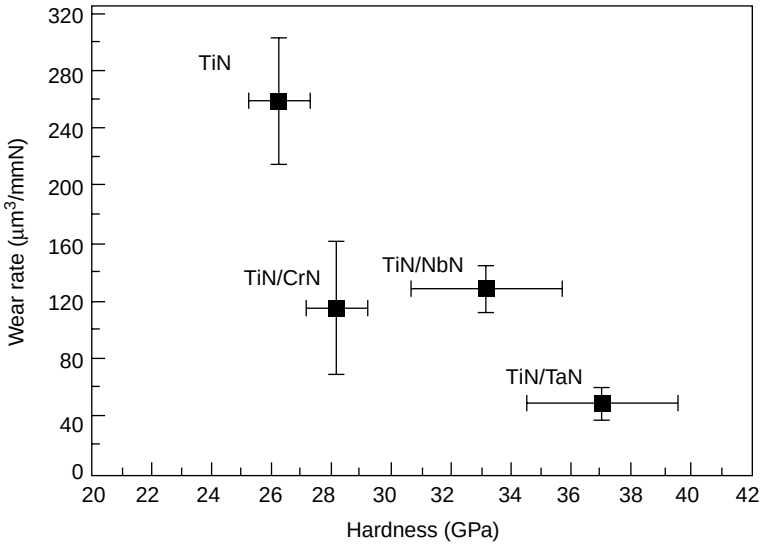

FIGURE 14.22 Abrasive wear rate versus the hardness of TiN/CrN, TiN/NbN, and TiN/TaN superlattices ($\Lambda \sim 10$ nm) as compared to monolithitic TiN. (From Madan, A. and Barnett, S.A., in *Materials Science of Carbides, Nitrides and Borides*, Gogotsi, Y. and Andrievski, R.A., Eds., Kluwer Academic Publishers, Dordrecht, 1999, p. 187. With permission.)

14.4.3.2 Other Properties

Electrical properties (electrical resistance ρ) and corrosion performance of HMPC films have been described in review11. The high-temperature oxidation study of AlN-based film has revealed that AlN/TiN (I), AlN/TiB_2 (II) and AlN/SiC/TiB_2 (III) films have significant thermal stability and considerable oxidation resistance. Figure 14.24 shows differential thermal analysis (DTA) and thermogravimetric analysis (TGA) curves under nonisothermal oxidation (heating rate of 15 K/min) for films I to III deposited on Si substrates from both sides.[171,220] It can be seen that a noticeable mass gain of films I, II, and III starts at ~750, ~950, and 1020°C and the active oxidation temperatures are ~1100°, ~1200°, and 1300°C, respectively. Some exothermic peaks on the DTA curves reflect the formation of TiO_2 and other oxides. Film III appears to be the most oxidation resistant. Comparison of oxidation characteristics with those of similar bulk specimens reveals that under the same conditions, the films, particularly those in an initial amorphous state (films II and III), have a higher oxidation resistance. A fractographic examination by SEM shows that after oxidation the microstructure remained virtually unaltered and was close to a nanocrystalline one, i.e., the size of structural elements was about 100 to 500 nm. The interesting feature in the microstructure after oxidation is the presence of self-reinforced elements and very weak recrystallization, especially in the case of film III.

It is agreed that because of a large contribution from interfaces, nanomaterials are characterized by a higher diffusion permeability and, hence, a lower corrosion resistance as compared to conventional polycrystalline (bulk) materials. The significant thermal stability of film III nanostructure and its considerable scale resistance, which was found to be several times higher than the corresponding characteristics of bulk materials, seem to be rather important. At a first approximation, this may be associated with the self-reinforced structure formation and with the enrichment of the composition in aluminium in the course of film deposition.

Stability of nanomaterials, including thermal and chemical stability as well as stable behavior under deformation and radiation, is a very important parameter which is responsible for the wide and effective application of nanomaterials as a whole and HMPCs films in particular. As applied to

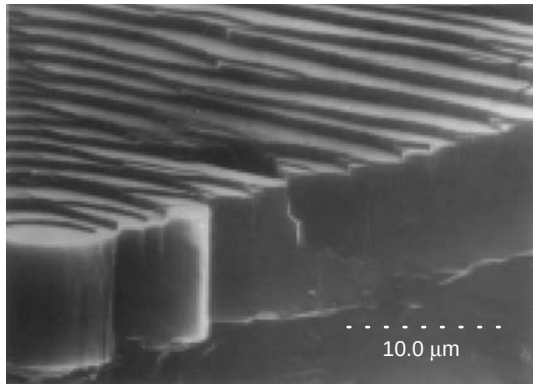

(a)

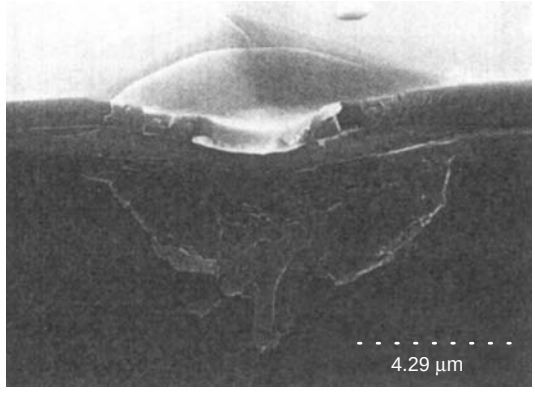

(b)

FIGURE 14.23 Fracture high-resolution field emission SEM images through indentations on TiB_2 (a) and TiN (b). (From Andrievski, R.A., in *Nanostructured Materials. Science & Technology*, Chow, G.-M. and Noskowa, N.I., Eds., Kluwer Academic Publishers, Dordrecht, 1998, p. 263. With permission.)

nanostructured nitride, boride and carbide films, this problem has been analyzed in Refs. 29, 30, 221–224. There are some examples of HMPC film thermal stability up to 1000 to 1100°C, which is related to slow diffusion mobility in HMPCs and spinodal decomposition in some niride solid solutions such as systems of TiN–ZrN, TiC–ZrC and TiN–AlN. Figure 14.25 shows the temperature annealing effect on the hardness value for TiN and ZrN monolayer films, TiN/ZrN multilayer films and alloyed (Ti,Zr)N film. Annealing the latter at 1000 to 1100°C tends to increase the hardness as a result of the TiN–ZrN system spinodal decomposition with formation of a nanocrystalline structure.[11,213] Figure 14.26 demonstrates another interesting example of thermal stability related to the more stable AlN/TiN multilayer film with the lowest value of bilayer period (λ).[225] The possibility to create thermally stable nanomaterials with very fine grain (layer) size was predicted by some theoritical works (see review 29). However, in general, the best way to develop stable HMPC films as soon as information on the deformation and radiation effects need further investigations.

14.5 SUMMARY

As evident from the preceding sections, there are many examples of unique properties of nanocrystalline bulks, films, and coatings based on HMPCs. The recent advances in this area are significant in

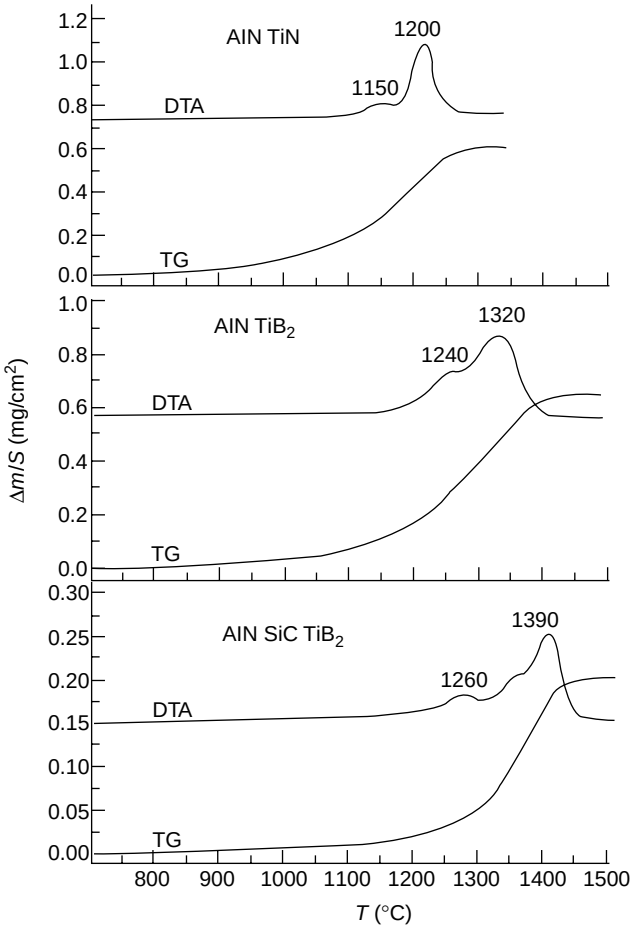

FIGURE 14.24 DTA and TG curves of AlN/TiN (I), AlN/TiB_2 (II),and AlN/SiC/TiB_2 (III) films. (From Andrievski, R.A. and Kalinnikov, G.V., *Surf. Coat. Technol.*, 142–144, 573, 2001. With permission.)

that it is now possible to engineer strong and hard materials that can operate under varied conditions including high temperatures (up to about 1200°C). At the same time, it should be noted that there are still some gaps in the information on preparation, structure, and properties of these nanomaterials, especially as applied to nanobulks. Unfortunately, the progress in the study of some important fundamental problems such as electronic structure and phase diagrams in nanoscale, the nature of thermodynamic and strength properties of nanomaterials, modeling and the prediction possibility seems to be very unsatisfactory.

From the above discussion it is also clear that many of the described results need further refining and understanding. This way of reaching the heart of matter is dictated by not only scientific considerations but also connected with the real application and the potential fields of application of HMPC nanocrystalline bulks and films/coatings, which are continuously broadening. It will suffice to mention several examples such as superhard wear-resistant nanocomposite mono- and multilayer films for advanced machining tools,[31,226] nanocomposite tribological coatings for aerospace application,[20,227] hard coatings for aluminium die casting-soldering,[228] diffusion barriers and other components for electronic and optoelectronic devices,[229,230] wear-resistant coatings for biomedical applications,[231,232] UFP in surface engineering technologies and for improoving properties of conventional powders,[233,234] and gas sensor devices.[235] It is evident that this wide spectrum of applications demands comprehensive scientific investigations for identifying the best strategy for future technology development.

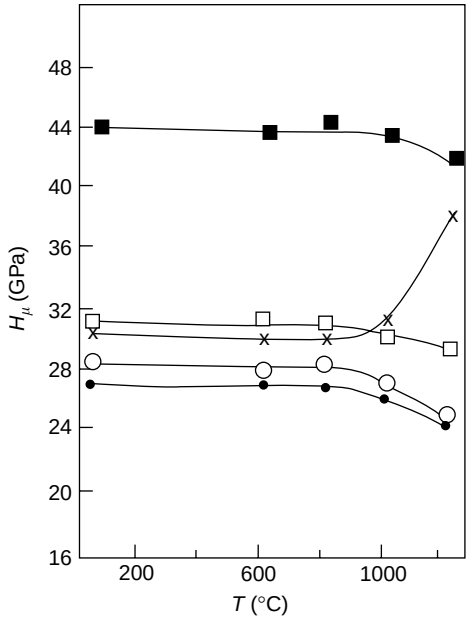

FIGURE 14.25 Effect of annealing temperature on hardness for films with a thickness of 2 μm: ■ — TiN/ZrN (multilayer film λ=100); □ — TiN/ZrN (multilayer film λ=200); × — (Ti,Zr)N (alloyed film); ●—ZrN (monolayer film); ○ — TiN (monolayer film). (From Andrievski, R.A., *J. Mater. Sci.*, 32, 4463, 1997. With permission.)

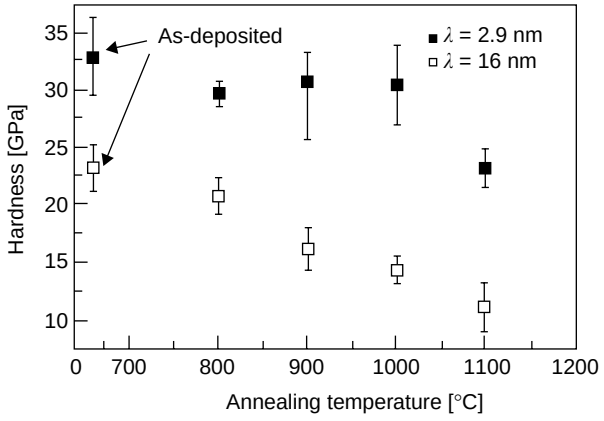

FIGURE 14.26 Hardness of TiN/AlN multilayers with different bilayer periods λ, as a function of annealing temperature. (From Kim, D.-G., Seong, T.-Y., and Baik, Y.-I., *Surf. Coat. Technol.*, 153, 79, 2002. With permission.)

Finally, as before,[18] we emphasize that nano-HMPCs have great importance not only in our earthly problems but also in cosmic ones; silicon carbide, aluminum oxide, and metal carbides are reported to be found as small inclusions in larger presolar grains.[236] This stardust (or UFP!) provides a new thrilling insight into our understanding of many fundamental things such as the dynamics of supernova explosions, the age and chemical evolution of the Galaxy, and processes in the outer envelopes of stars. So nano-HMPCs enjoy a cosmic scale of scientific interests. *Note at proof*. Preparation, properties and applications of plasma-thermal nanopowders see in book 237.

REFERENCES

1. Andrievski, R.A. and Spivak, I.I., *Strength of High-Melting Point Compounds and Materials on their Base*, Metallurgia, Cheliabinsk, 1989, p. 9 (in Russian).
2. Andrievski, R.A., Review — nanocrystalline high-melting point compounds-based materials, *J. Mater. Sci.*, 29, 614, 1994.
3. Andrievski, R.A., Compaction and sintering of ultrafine powders, *Int. J. Powder Metall.*, 30, 59, 1994.
4. Andrievski, R.A., Preparation and properties of nanocrystalline high-melting point compounds, *Russ. Chem. Rev.*, 63, 411, 1994 (English transl.).
5. Sundgren, J.-E. and Hultman, L., Growth, structure and properties of hard nitride based coatings and multilayers, in *Materials and Processes for Surface and Interface Engineering*, Pauleau, Y., Ed., Kluwer Academic Publishers, Dordrecht, 1995, p. 453.
6. Andrievski, R.A., Particulate nanostructured silicon nitride and titanium nitride, in *Nanotechnology. Molecularly Designed Materials*, Chow, G.-M. and Gonsalves, K.E., Eds., American Chemical Society, Washington, DC, 1996, chap. 20.
7. Andrievski, R.A., Processing and properties evolution of nanocrystalline particulate and films materials based on nitrides and borides, in *Processing and Properties of Nano*crystalline *Materials*, Suryanarayana, C., Singh, J., and Froes, F.Y., Eds., A Publication of TMS, Warrendale, 1996, p. 135.
8. Mayo, M.J., Processing of nanocrystalline ceramics from ultrafine particles, *Int. Mater. Rev.*, 41, 85, 1996.
9. Veprek, S., Conventional and new approaches towards the design of novel superhard materials, *Surf. Coat. Technol.*, 97, 15, 1997.
10. Andrievski, R.A., Nanocrystalline borides and related compounds, *J. Solid State Chem.*, 133, 249, 1997.
11. Andrievski, R.A., Review — films of interstitial phases: synthesis and properties, *J. Mater. Sci.*, 32, 4463, 1997.
12. Andrievski, R.A., The-state-of-the-art of nanostructured high-melting point compound base materials, in *Nanostructured Materials. Science & Technology*, Chow, G.-M. and Noskova, N.I., Eds., Kluwer Academic Publishers, Dordrecht, 1998, chap. 13.
13. Mayo, M.J., Nanocrystalline ceramics for structural applications: processing and properties, in *Nanostructured Materials. Science & Technology*, Chow, G.-M. and Noskova, N.I., Eds., Kluwer Academic Publishers, Dordrecht, 1998, chap.18.
14. Skorokhod, V.V. and Ragulya, A.V., Features of nanocrystalline structure formation on sintering of ultrafine powders, in *Nanostructured Materials. Science & Technology*, Chow, G.-M. and Noskova, N.I., Eds., Kluwer Academic Publishers, Dordrecht, 1998, chap. 19.
15. Urbanovich, V.S., Consolidation of nanocrystalline materials by high pressures, in *Nanostructured Materials. Science & Technology*, Chow, G.-M. and Noskova, N.I., Eds., Kluwer Academic Publishers, Dordrecht, 1998, chap. 20.
16. Yashar, P.C. and Sproul, W.D., Nanometer scale multilayered hard coatings, *Vacuum*, 55, 179, 1999.
17. Veprek, S., The search for novel, superhard materials, *J. Vacuum Sci. Technol. A*, 17, 2401, 1999.
18. Andrievski, R.A., The-state-of-the-art of high-melting point compounds, in *Materials Science of Carbides, Nitrides and Borides*, Gogotsi, Y.G. and Andrievski, R.A., Eds., Kluwer Scientific Publishers, Dordrecht, 1999, p. 1.
19. Madan, A. and Barnett, S.A., Fundamentals of nitride-based superlattice thin films, in *Materials Science of Carbides, Nitrides and Borides*, Gogotsi, Y.G. and Andrievski, R.A., Eds., Kluwer Scientific Publishers, Dordrecht, 1999, p. 187.
20. Andrievski, R.A., New superhard materials are becoming a reality, *MRS Bull.*, 23, 3, 1999.
21. Andrievski, R.A., Scientific and technological problems in nanostructured materials science, in *Advanced Science and Technology of Sintering*, Stojanovich, B.D., Skorokhod, V.V., and Nikolic, M.V., Eds., Kluwer Academic/Plenum Publishers, New York, 1999, p. 97.
22. Kroke, E. et al., Silazane derived ceramics and related materials, *Mater. Sci. Eng.* R, 26, 97, 2000.
23. Musil, J., Hard and superhard nanocomposite coatings, *Surf. Coat. Technol.*, 125, 322, 2000.
24. Vassen, R. and Stover, D., Processing and properties of nanophase nonoxide ceramics, *Mater. Sci. Eng. A*, 301, 59, 2001.
25. Andrievski, R.A., New superhard materials based on nanostructured high-melting point compounds: achievements and perspectives, in *Functional Gradient Materials and Surface Layers Prepared by Fine Particles Technology*, Baraton, M.-I. and Uvarova, I., Eds., Kluwer Scientific Publishers, Dordrecht, 2001, p. 17.

26. Andrievski, R.A., Films as nanostructured materials with characteristic mechanical properties, *Mater. Trans.*, 42, 1471, 2001.
27. Voevodin, A.A., Nanocomposite coatings with "chameleon" friction surface adaptation, *J. Vac. Sci. Technol. A*, 20, 1434, 2002.
28. Zhang, S. et al., Recent advances of superhard nanocomposite coatings: a review, *Surf. Coat. Technol.*, 167, 113, 2003.
29. Andrievski, R.A., Review — Stability of nanostructured materials, *J. Mater. Sci.*, 38, 1367, 2003.
30. Barnet, S.A. et al., Stability of nanometer-thick layers in hard coatings, *MRS Bull.*, 28, 169, 2003.
31. Munz, W.-D., Large-scale manufactoring of nanoscale multilayered hard coatings deposited by cathodic arc/unbalanced magnetron sputtering, *MRS Bull.*, 28, 173, 2003.
32. Patscheider, J., Nanocomposite hard coatings for wear protection, *MRS Bull.*, 28, 180, 2003.
33. Zhang, W. et al., Recent advances in cubic boron nitride deposition, *MRS Bull.*, 28, 184, 2003.
34. Hultman, L. et al., Fullerene-like carbon nitride: a resilient coating material, *MRS Bull.*, 28, 194, 2003.
35. Ragulya, A.V. and Skorokhod, V.V., Genesis of nanosized particles, grain and interfaces in the rate-controlled processes of synthesis and sintering of ceramics, in *Nanostructures: Synthesis, Functional Properties and Applications*, Tsakalakos, Th., Ovid'ko, I.A., and Vasudevan, A.K., Eds., Kluwer Academic Publishers, Dordrecht, 2003, p. 139.
36. Cavaleiro, A. and Marques, P., Achievement of nanocrystalline structures after thermal annealing amorphous W–Si–N sputtered films, in *Nanostructures: Synthesis, Functional Properties and Applications*, Tsakalakos, Th., Ovid'ko, I.A., and Vasudevan, A.K., Eds., Kluwer Academic Publishers, Dordrecht, 2003, p. 383.
37. Sytchev, A.E. and Merzhanov, A.G., Self-propagated high-temperature synthesis of nanomaterials, *Russ. Chem. Rev.*, 73, 147, 2004 (English transl.).
38. Koc, R., Glatzmaier, G., and Sibold, J., β-SiC production by reacting silica gel with hydrocarbon gas, *J. Mater. Sci.*, 36, 995, 2001.
39. Rigtrup, K. and Cutler, R.A., Synthesis of submicron SiC, *Int. J. Self-Prop. High-Temp. Synth.*, 1, 96, 1992.
40. Gadzyra, M. et al., Synthesis and structural peculiarities of nonstoichiometric β-SiC, *Diam. Relat. Mater.*, 7, 1466, 1998.
41. Stobierski, L. et al., SHS synthesis of nanocomposite AlN–SiC powders, *Int. J. Self-Prop. High-Temp. Synth.*, 10, 217, 2001.
42. Huang, D. et al., Characterization of β-silicon carbide powders synthesized by the carbothermal reduction of silicon carbide precursors, *J. Am. Ceram. Soc.*, 81, 3173, 1998.
43. Hoesslin, M. et al., CARS diagnostics of a CO_2-laser pyrolytic experiment for the production of nano-sized ceramic powders, *Appl. Phys. B*, 61, 367, 1995.
44. Bao, X. and Edirisinghe, M.J., Different strategies for the synthesis of silicon carbide- silicon nitride composites from preceramic polymers. *Comp. Part A*, 30, 610, 1999.
45. Choi, J.Y., Kim, C.H., and Kim, D.K., Carbothermic synthesis of monodispersed spherical Si_3N_4/SiC nanocomposite powder, *J. Am. Ceram. Soc.*, 82, 2665, 1999.
46. Gao, L. et al., Preparation and properties of TiN–Si_3N_4 composites, *J. Eur. Ceram. Soc.*, 24, 381, 2004.
47. Lee, H.J., Eguchi, K., and Yashida, T., Preparation of ultrafine silicon nitride and silicon nitride and silicon carbide mixed powders in a hybrid plasma, *J. Am. Ceram. Soc.*, 73, 3356, 1990.
48. Allaire, F. and Dallaire, S., Synthesis and characterization of silicon nitride powders produced in a d.c. thermal plasma reactor, *J. Mater. Sci.*, 26, 6736, 1991.
49. Grabis, J., Zalite, I., and Reichel, U., Advantages and characteristics of nanopowders produced using plasma technology, *cfi/Ber. DKG*, 77, E10, 2000.
50. Gubicza, J. et al., The effect of heat-treatment on the grain-size of nanodisperse plasmathermal Si_3N_4 powder, *J. Mater. Sci.*, 35, 3711, 2000.
51. Milonjic, S.K., Cerovich, Lj.S., and Uskokovich, D.P., Sol-gel synthesis of SiC and Si_3N_4 powders and their surface properties, in *Materials Science of Carbides, Nitrides and Borides*, Gogotsi, Y.G. and Andrievski, R.A., Eds., Kluwer Academic Publishers, Dordrecht, 1999, p. 343.
52. Aldinger, F. et al., Nanocrystalline ceramics by solid state thermolysis of organometallic polymers, *Int. J. Self-Prop. High-Temp. Synth.*, 10, 249, 2001.
53. Riedel, R., Strecker, K., and Petzow, G., In situ polysilane-derived silicon carbide particulates dispersed in silicon nitride composite, *J. Am. Ceram. Soc.*, 72, 2071, 1989.
54. Wan, J., Gasch, M.J., and Mukherjee, A.K., Silicon carbonitride ceramics produced by pyrolysis of polymer ceramic precursor, *J. Mater. Res.*, 15, 1657, 2000.

55. Yang, H. et al., Fabrication of high performance ceramic microstructure from a polymeric precursor using soft lithography, *Adv. Mater.*, 13, 54, 2001.
56. Zimmermann, A. et al., High-temperature deformation of amorphous Si-C-N and Si-B-C-N ceramics derived from polymers, *Acta Mater.*, 50, 1187, 2002.
57. Gogotsi, Y. et al., Conversion of silicon carbide to crystalline diamond-structured carbon at ambient pressure, *Nature*, 411, 283, 2001.
58. Sun, X.H. et al., Synthesis of SiC nanotubes, *J. Am. Chem. Soc.*, 124, 14464, 2002.
59. Menon, M. et al., Structure and stability of SiC nanotubes, *Phys. Rev. B*, 69, 115322, 2004.
60. Chen, H. et al., Fabrication of β-Si_3N_4 nano-fibers, *J. Alloy Comp.*, 325, L1, 2001.
61. Pathak, L.C. et al., Carbothermal synthesis of nanocrystalline aluminium nitride powders, *J. Am. Ceram. Soc.*, 82, 257, 1999.
62. Panchula, M.L. and Ying, J.Y., Nanocrystalline aluminium nitride: vapor-phase synthesis in a forced-flow reactor, *J. Am. Ceram. Soc.*, 86, 1114, 2003.
63. Suehiro, T. et al., Synthesis of aluminium nitride nanopowder by gas–reduction–nitridation method, *J. Am. Ceram. Soc.*, 86, 1046, 2003.
64. Kotov, Y.A. and Samatov, O.M., Production of nanometer-sized AlN powders by the exploding wire method, *Nanostruct. Mater.*, 12, 119, 1999.
65. Kinemuchi, Y. et al., Nanosize powders of AlN synthesized by pulsed wire discharge, *J. Am. Ceram. Soc.*, 86, 420, 2003.
66. Chow, G.-M. et al., Compositional and thermal effects on chemically processed AlN-BN nanocomposite powders, *J. Mater. Res.*, 9, 168, 1994.
67. Borovinskaja, I.P. et al., Preparation of BN UFP by self-propagated high-temperature synthesis, *Inorg. Mater.*, 39, 698, 2003 (English transl.).
68. Mirabelli, M.G., Lynch, A.T., and Sneddon, L.G., Molecular and polymeric precursors to boron-based ceramics, *Solid State Ionics*, 32/33, 655, 1989.
69. Wang, J.B. et al., Explosion phase formation of nanocrystalline boron nitride upon pulsed-laser-induced liquid/solid interfacial reaction, *J. Mater. Res.*, 18, 2774, 2003.
70. Lee, R.S. et al., Catalyst-free synthesis of boron nitride single-wall nanotubes with a preffered zig-zag configuration, *Phys. Rev. B*, 64, 121405 (R), 2001.
71. Chen, Y. et al., Large-quantity production of high-yield boron nitride nanotubes, *J. Mater. Res.*, 17, 1896, 2002.
72. Fu, J.J. et al., The synthesis of boron nitride nanotubes by extended vapour–liquid–solid method, *Nanotechnology*, 15, 727, 2004.
73. Shen, Z.Q. et al., Boron nitride nanotubes filled with zirconium oxide nanorods, *J. Mater. Res.*, 17, 2761, 2002.
74 Xu, F.-F. et al., Phases and crystallization of encapsulated cobalt nanorods inside BN nanotubes, *Acta Mater.*, 52, 601, 2004.
75. Liu, J. et al., Novel synthesis of AlN nanowires with controlled diameters, *J. Mater. Res.*, 16, 3133, 2001.
76. Huo, K.F. et al., Synthesis of boron nitride nanowires, *Appl. Phys. Lett.*, 80, 3611, 2002.
77. McCandlish, L.E., Kear, B.H., and Kim, B.K., Processing and properties of nanostructured WC-Co, *Nanostruct. Mater.*, 1, 119, 1992.
78. Kim, B.K. et al., Structure and properties of nanophase WC/Co/VC/TaC hardmetal, *Nanostruct. Mater.*, 9, 233, 1997.
79. Gille, G. et al., Submicron and ultrafine grained hardmetals for microdrills and metal cutting inserts, *Int. J. Refr. Met. Hard Mater.*, 20, 3, 2002.
80. Bock, A. and Zeiler, B., Production and characterization of ultrafine WC powders, *Int. J. Refr. Met. Hard Mater.*, 20, 23, 2002.
81. Carol, D.F., Sintering and microstructural development in WC/Co-based alloys with superfine WC powder, *Int. J. Refr. Met. Hard Mater.*, 17, 123, 1999.
82. Richter, V. and Ruthendorf, M.V., On hardness and toughness of ultrafine and nanocrystalline hard materials, *Int. J. Refr. Met. Hard Mater.*, 17, 141, 1999.
83. Sherif El-Eskandarany, M., Fabrication of nanocrystalline WC and nanocomposite WC-MgO refractory materials at room temperature, *J. Alloy. Comp.*, 296, 175, 2000.
84. Tan, G.-L. et al., Synthesis of nanocrystalline cubic substoichiometric WC_{1-Z} powders by mechanochemical technology, *J. Mater. Sci.*, 35, 3151, 2000.

85. Ban, Z.-G. and Shaw, L.L., Synthesis and processing of nanostructured WC-Co materials, *J. Mater. Sci.*, 37, 3397, 2002.
86. Tang, H.G. et al., Synthesis reactive mechanism and thermal stability of $W_{1-x}Al_xC$ (x=0.33, 0.5, 0.75, 0.86) nanocrystalline, *Mater. Res. Bull.*, 39, 707, 2004.
87. Koc, R. and Kodambaka, S.K., Tungsten carbide (WC) synthesis from novel precursors, *J. Eur. Ceram. Soc.*, 20, 1859, 2000.
88. Zhang, Z. et al., Processing of nanostructured WC-Co powder from precursor obtaned by co-precipitation, *Nanostruct. Mater.*, 12, 163, 1999.
89. Yang, M.C., Xu, J., and Hu, Z.Q., Synthesis of WC-TiC35-Co10 nanocomposite powder by novel method, *Int. J. Refr. Met. Hard Mater.*, 22, 1, 2004.
90. Jung, J. and Kang, S., Effect of ultra-fine powders on the microstructure of Ti(CN)-xWC-Ni cermets, *Acta Mater.*, 52, 1379, 2004.
91. http://www.inframat.com
92. Ogino, Y., Mehanical nitriding and its application to production of nanocrystalline metal-nitride dual phase alloys, in *Processing and Properties of Nanocrystalline Materials*, Suryanarajana, C., Singh, J., and Froes, F.H., Eds., A Publication of TMS, Warrendale, 1996, p. 81.
93. Andrievski, R.A. et al., Consolidation of TiN/TiB_2 ultrafine powder composites under high pressure and properties of obtained ceramics, in *9th Cimtec-World Ceramics Congress*, Part C, Vincenzini, P., Ed., Techna Srl., Faenza, 1999, p. 435.
94. Shim, J.-H., Byun, J.-S., and Cho, Y.W., Mechanochemical synthesis of nanocrystalline TiN/TiB_2 composite powder, *Scr. Mater.*, 47, 493, 2002.
95. Li, J. et al., Formation of TiB_2/TiN/Ti (C_xN_{1-x}) nanocomposite powder via high- energy ball milling and subsequent heat treatment, *J. Alloy. Comp.*, 334, 253, 2002.
96. Welham, N.J., Kerr, T., and Willis, P.E., Ambient-temperature mechanochemical formation of titanium nitride-alumina composites from TiO_2 and $FeTiO_3$, *J. Am. Ceram. Soc.*, 82, 2332, 1999.
97. Andrievski, R.A., Kravchenko, S.E., and Shilkin, S.P., Some properties of ultrafine zirconium boride powders and films, in *Proc. 11th Symp. Boron, Borides and Related Compounds*, Uno, R. and Higashi, J., Eds., Publ. Office JJAP, Tokyo, 1994, p. 198.
98. Andrievski, R.A., Kravchenko, S.E., and Shilkin, S.P., Preparation and some properties of ultrafine zirconium boride and titanium boride powders, *Inorg. Mater.*, 31, 965, 1995 (English transl.).
99. Hsu, M.S., Meyers, M.A., and Berkowitz, A., Synthesis of TiC nanopowder by electro-spark synthesis, *Scr. Metall. Mater.*, 32, 805, 1995.
100. Sato, T. et al., Electro-spark synthesis of TiN in liquid NH_3, *J. Mater. Sci.*, 31, 2495, 1996.
101. Castro, D.T. and Ying, J.Y., Synthesis and sintering of nanocrystalline TiN, *Nanostruct. Mater.*, 9, 67, 1997.
102. Saito, T. et al., Synthesis of ultrafine TiB_2 particles by rapid carbothermal reduction, *J. Mater. Sci.*, 32, 3933, 1997.
103. Mahday, A. et al., Mechanically induced solid state carbothermal synthesis of ZrC UFP, *J. Alloy Comp.*, 299, 244, 2000.
104. Gras, G. et al., Simultaneous synthesis and consolidation of nanostructured $MoSi_2$, *J. Mater. Res.*, 17, 542, 2002.
105. Grave, O.A. and Munir, Z.A., Electric field enhanced synthesis of nanstructured TaC, *J. Mater. Res.*, 17, 609, 2002.
106. Nersisyan, H.H., Lee, J.H., and Won, C.W., Self-propagating high-temperature synthesis of nano-sized TiC powder, *J. Mater. Res.*, 17, 2859, 2002.
107. Yang, X. et al., Reduction–nitridation synthesis of TiN nanocrystals, *J. Am. Ceram. Soc.*, 86, 206, 2003.
108. Fu, B. and Gao, L., Synthesis of nanocrystalline ZrN powders by reduction–nitridation of ZrO_2, *J. Am. Ceram. Soc.*, 87, 656, 2004.
109. Chen, L. et al., A facile one-step route to nanocrystalline TiB_2 powders, *Mater. Res. Bull.*, 39, 609, 2004.
110. Chen, L. et al., Synthesis and oxidation of nanocrystalline HfB_2, *J. Alloy Comp.*, 368, 353, 2004.
111. Bai, Y.-J. et al., Novel synthesis of nanocrystalline TiC hollow polyheedrons, *Chem. Phys. Lett.*, 388, 58, 2004.
112. Axelbaum, R.I. et al., Gas-phase combustion synthesis of TiB_2 nanocrystallites, *J. Mater. Res.*, 11, 948, 1997.

113. Gusev, A.I. and Rempel, A.A., Atomic ordering as a new method of producing a nanostructure, in *Nanostructures: Synthesis, Functional Properties and Applications*, Tsakalakos, Th., Ovid'ko, I.A., and Vasudevan, A.K., Eds., Kluwer Academic Publishers, Dordrecht, 2003, p. 313.
114. Baraton, M.-I., The surface characterization of nanosized powders: relevance of the FTIR surface spectrometry, in *Nanostructured Materialas: Science & Technology,*Chow, G.-M. and Noskova, N.I., Eds., Kluwer Academic Publishers, Dordrecht, 1998, chap. 15.
115. Szepvolgyl, J. et al., Comparative sintering study on non-conventional and commercial silicon nitride powders, *J. Mater. Chem.*, 3, 279, 1993.
116. Andrievski, R.A. et al., Gas evolution and porosity at sintering of TiN YFP, *Inorg. Mater.*, 29, 1474, 1993 (English transl.).
117. Andrievski, R.A., Silicon nitride: synthesis and properties, *Russ. Chem. Rev.*, 64, 291, 1995 (English transl.).
118. Goncharova, N.V. et al., Computational chemistry of Si_3N_4 surface: water, ammonia, and water-ammonia complex, *J. Struct. Chem.*, 36, 58, 1995 (English transl.).
119. Cerovic, L.S. et al., Surface properties of silicon nitride powders, *Colloids and Surf A: Physicochem. Eng. Asp.*, 197, 147, 2002.
120. Suryavanshi, A.P. et al., Elastic modulus and resonance behavior of BN nanotubes, *Appl. Phys. Lett.*, 84, 2527, 2004.
121. Ivanovskiy, A.L., *Nanotubular Forms of Matter*, Ural Branch of Russian Academy of Sciences, Ekaterinburg, 1999, p. 174 (in Russian).
122. Pokropivniy, V.V., Non-carbon nanotubes (Review), *Powder Metall. Metal Ceram.*, No. 11/12, 51, 2001; No. 3/4, 13, 2002 (English transl.).
123. Rao, C.N.R. et al., Inorganic nanowires, *Progr. Solid State Chem.*, 31, 5, 2003.
124. Pampuch, R., Advanced HT ceramic materials via solid combustion, *J. Eur. Ceram. Soc.*, 19, 2395, 1999.
125. Zhang, G.-J., Reactive hot pressing of alumina-silicon carbide nanocomposites, *J. Am. Ceram. Soc.*, 87, 299, 2004.
126. Sherif El-Eskandarany, M. et al., Synthesis of full-density nanocrystalline TiN compacts, *Metal. Mater. Trans. A*, 29, 1973, 1998.
127. Ohyanagi, M. et al., Consolidation of nanostructured SiC with disorder–order transformation, *Scr. Mater.*, 50, 111, 2004.
128. Callaizi, J., Dense nanoscale single- and multi-phase ceramics sintered by transformation assisted consolidation, *Int. J. Powder Metall.*, 37, 45, 2001.
129. Schmidt, W.R. et al., Microstructure evolution of sintered nanoscale SiC powder prepared by various processing routes, in *Surface-Controlled Nanoscale Materials for High-Added-Value Applications*, Vol. 501, Gonsalves, K.E. et al., Eds., MRS, Warrendale, 1998, p. 21.
130. Li, Y.-L. et al., Sintering of nanopowders of amorphous silicon nitride under ultrahigh pressure, *J. Mater. Res.*, 15, 988, 2000.
131. Hirai, H. and Kondo, K., Shock-compacted Si_3N_4 nanocrystalline ceramics: mechanisms of consolidation and transition from α- to β-form. *J. Am. Ceram. Soc.*, 77, 487, 1994.
132. Kovtun, V.I. et al., Sintering of BN in shock waves, *Powder Metall. Metal Ceram.*, No. 12, 38, 1992 (English transl.).
133. Andrievski, R.A. et al., Structure, density and properties evolution of TiN UFP under high pressures and high temperatures, in *4th Euro Ceramics*, Vol. 4, Bellosi, A., Ed., Gruppo Editoriale Faenza, Printed in Italy, 1995, p. 307.
134. Andrievski, R.A. et al., High-temperature consolidation and physical-mechanical properties of nanocrystalline TiN, *Physics-Doklady*, 42, 496, 1997 (English transl.).
135. Andrievski, R.A., Kalinnikov, G.V., and Urbanovich, V.S., Consolidation and evolution of physical-mechanical properties of nanocomposite materials based on high-melting compounds, in *Nanophase and Nanocomposite Materials II*, Vol. 457, Komarneni, S., Parker, J.C., and Wollenberger, H.J., Eds., MRS, Pittsburgh, 1997, p. 413.
136. Andrievski, R.A., Physical-mechanical properties of nanostructured TiN, *Nanostruct. Mater.*, 9, 607, 1997.
137. Zgalat-Lozynskiy, O.B., Ragulya, A.V., and Hermann, M., Rate-controlled sintering of nanostructured titanium nitride powder, in *Functional Gradient Materials and Surface Layers Prepared by Fine Particles Technology*, Baraton, M.-I. and Uvarova, I.V., Eds., Kluwer Academic Publishers, Dordrecht, 2001, p. 151.

138. Sherif El-Eskandarany, M., Structure and properties of nanocrystalline TiC full-density bulk alloy consolidated from mechanically reacted powders, *J. Alloy Comp.*, 305, 225, 2000.
139. Lee, J.W., Munir, Z.A., and Ohyanagi, M., Dense nanocrystalline TiB_2/TiC composites formed by field activation from high-energy ball milled reactants, *Mater. Sci. Eng. A*, 325, 221, 2002.
140. Mohan, K. and Strutt, P.R,, Observation of Co nanoparticle dispersions in WC nanograins in WC-Co cermets consolidated from chemically synthesised powders, *Nanostruct. Mater.*, 7, 547, 1996.
141. Niihara, K., New concept of structural ceramics — ceramic nanocomposite, *J. Ceram. Soc. Jpn.*, 99, 974, 1991.
142. Gogotsi, Y.G., Particulate Si_3N_4-based composites, *J. Mater. Sci.*, 29, 2541, 1994.
143. Desmaison, J. and Desmaison, M., Boride/nitride composites: synthesis and properties, in *Materials Science of Carbides, Nitrides and Borides*, Gogotsi, Y.G. and Andrievski, R.A., Eds., Kluwer Scientific Publishers, Dordrecht, 1999, p. 267.
144. Tuffe, S. et al., Densification, microstructure and mechanical properties of TiB_2-B_4C based composites, *Int. J. Refr. Metals & Hard. Mater.*, 14, 305, 1996.
145. Fricke, M., Nonninger, R., and Schmidt, H., Production of Si_3N_4/TiN nanocomposites, *Adv. Eng. Mater.*, 2, 647, 2000.
146. Wen, G. et al., Reaction synthesis of TiB_2-TiC composites with enhanced toughness, *Acta Mater.*, 49, 1463, 2001.
147. Porat, R., Berger, S., and Rosen, A., Dilatometric study of the sintering mechanism of nanocrystalline cemented carbide, *Nanostruct. Mater.*, 7, 429, 1996.
148. Kondo, K.-I. et al., Shock compaction of SiC powder, *J. Mater. Sci.*, 20, 1033, 1985.
149. Kodama, H. and Miyoshi, T., Preparation of fine-grained SiC ceramics from pyrolyzed polycarbosilane, *Adv. Ceram. Mater.*, 3, 177, 1988.
150. Mykhaylyk, O.O. and Gadzyra, M.P., Superhard materials based on the solid solution SiC-C, *J. Mater. Chem.*, 11, 217, 2001.
151. Tanaka, I. et al., Hardness of cubic silicon nitride, *J. Mater. Res.*, 17, 731, 2002.
152. Andrievski, R.A. et al., Synthesis, structure and properties of nanocrystalline nitrides and borides, *Nanostruct. Mater.*, 6, 353, 1995.
153. Urbanovich, V.S., Properties of nanocrystalline TiN-based materials prepared by high- pressure sintering, in *Functional Gradient Materials and Surface Layers Prepared by Fine Particles Technology*, Baraton, N.-I. and Uvarova, I., Eds., Kluwer Academic Publishers, Dordrecht, 2001, p. 169.
154. Li, J.-F and Watanabe, R., Preparation and mechanical properties of SiC-AlN ceramic alloy, *J. Mater. Sci.*, 26, 4813, 1991.
155. Milman, Yu.V. et al., Results from bending tests on submicron and micron WC-Co grades at eleveted temperatures, *Int. J. Refr. Met. Hard Mater.*, 20, 71, 2002.
156. Cha, S.I. et al., Mechanical properties of WC-10Co cemented carbides sintered from nanocrystalline spray conversion processed powders, *Int. J. Refr. Met. Hard Mater.*, 19, 397, 2001.
157. Andrievski, R.A. and Glezer, A.M., Size effects in nanocrystalline materials: II. Mechanical and physical properties, *Phys. Met. Metallogr.*, 89, 83, 2000 (English transl.).
158. Gan, Y. and Zhou, B., Effect of grain size on the fracture toughness of nanocrystalline FeMoSiB, *Scr. Mater.*, 45, 625, 2001.
159. Bravo-Leon, A. et al., Fracture toughness of nanocrystalline tetragonal ZrO_2 with low Y_2O_3 content, *Acta Mater.*, 50, 4555, 2002.
160. Gleiter, H., Nanocrystalline materials, *Prog. in Mater. Sci.*, 33, 223, 1989.
161. Kuntz, J.D., Zhan, G.-D., and Mukherjee, A.K., Improved fracture toughness in advanced nanocrystalline ceramic composites, in *Nanoscale Materials and Modelling — Relations Among Proccessing, Microstructure amd Mechanical Properties*, Vol. 821, Anderson, P.M. et al., Eds., MRS, Warrendale, 2004, P7.5.1.
162. Andrievski, R.A., Kalinnikov, G.V., and Shtanskiy, D.V., High-resolution TEM and SEM of nanostructured boride/nitride films, *Solid State Phys.*, 42, 760, 2000 (English transl.).
163. Andrievski, R.A., Ivannikov, V.T., and Urbanovich, V.S., Creep studies in Si_3N_4–TiB_2 materials, *Key Eng. Mater.*, 89–91, 445, 1994.
164. Shinoda, Y., Nagano, T., and Wakai, F., Fabrication of nanograined SiC by ultra-high hot isostatic pressing, *J. Am. Ceram. Soc.*, 82, 771, 1999.

165. Mukherjee, A.K., Creep plasticity in nanocrystalline materials, in *NANO2002 Conference Proceedings. Sixth International Conference on Nanostructured Materials*, Tsakalakoc, Th. et al., Eds., Printed at Rutgers University, New Jersey, 2003.
166. Andrievski, R.A., Spivak, I.I., and Klimenko, V.V., The superplasticity revealing in the high- melting point compounds, *Dok. USSR Acad. Sci.*, 203, 1279, 1972 (in Russian).
167. Andrievski, R.A., Sintering and peculiarities of self-diffusion, thermodynamics, and creep of high-melting point compounds, in *Synthetic Materials for Electronics*, Jakowlew, B., Szymanski, A., and Wlosinskiy, W., Eds., Elsevier, Amsterdam, 1981, p. 57.
168. Troitskiy, V.N. et al., Synthesis and characteristics of utra-fine superconducting powders in the Nb–N, Nb–N–C, and Nb–Ti–N–C systems, *J. Nanoparticle Res.*, 5, 521, 2003.
169. Andrievski, R.A., Powder materials with ultradispersed structure — strength and superplasticity, *Mendeleev Chem. J.*, 26 (2), 11, 1991 (English transl.).
170. Andrievski, R.A. and Anisimova, I.A., Calculation of pseudo-binary nitride TiN–AlN phase diagram, *Inorg. Mater.*, 27, 1450, 1991 (English transl.).
171. Andrievski, R.A. and Kalinnikov, G.V., Physical-mechanical and physical-chemical properties of thin nanostructutred boride/nitride films, *Surf. Coat. Technol.*, 142–144, 573, 2001.
172. Andrievski, R.A. and Kalinnikov, G.V., Synthesis and properties of TiB_2/TiN and TiB_2/B_4C films, in *Nanostructured Thin Films and Nanodispersion Strengthened Coatings*, Voevodin, A. et al., Eds., Kluwer Academic Publishers, Dordrecht, 2004, p. 175.
173. Losbichler, P. and Mitterer, C., Non-reactively sputtered TiN and TiB_2 films: influence of activation energy on film growth, *Surf. Coat. Technol.*, 97, 567, 1997.
174. Andrievski, R.A. et al., Structure and physical-mechanical properties of nanostructured TiB_2/TiN films, *Phys. Solid State*, 39, 1661, 1997 (English transl.).
175. Andrievski, R.A., Surface and bulk properties of boride/nitride nanoscale films, in *Surface-Controlled Nanoscale Materials for Hig-Added-Value Applications*, Vol. 501, Gonsalves, K.E. et al., Eds., MRS, Warrendale, 1998, p. 149.
176. Veprek, S. et al., Degradation of superhard nanocomposites by built-in impurities, *J. Vac. Sci. Technol. B*, 22, L5, 2004.
177. Molart, T.P. et al., Nanostructured boron nitride coatings of very high hardness, *Surf. Coat. Technol.*, 74–75, 491, 1995.
178. Bendeddoche, A. et al., Structural characterization of amorphous SiC_XN_Y chemical vapor deposited coatings, *J. Appl. Phys.*, 81, 6147, 1997.
179. Fainer, N.I., Rumianzev, Y.M., and Kosinova, M.L., Functional nanocrystalline films of silicon carbonitride, *Chem. Intersts Stable Develop.*, 9, 865, 2001 (English transl.).
180. Yuki, T., Umeda, S., and Sugino, T., Electrical and optical characteristics of boron carbon nitride films synthesized by plasma-assisted CVD, *Diam. Relat. Mater.*, 13, 1130, 2004.
181. Li, J.J. et al., Thermal stability of magnetron sputtering amorphous carbon nitride films, *Vacuum*, 72, 233, 2004.
182. Delplancke-Ogletree, M.-P. and Monteiro, O.R., Deposition of TiC films from mixed carbon and titanium plasma streams, *J. Vac. Sci. Technol. A*, 15, 1943, 1997.
183. Monteiro, O.R., Delplancke-Ogletree, M.-P., and Brown, I.G., Tungsten-containing amorphous carbon films deposited by pulsed vacuum arc, *Thin Solid Films*, 342, 100, 1999.
184. Carvalho, S. et al., Microstructure of (Ti,Si,Al)N nanocomposite coatings, *Surf. Coat. Technol.*, 177–178, 369, 2004.
185. Schmidt, H. et al., Thermal stability and crystallization kinetics of sputtered amorphous Si_3N_4 films, *Thin Solid Films*, 450, 346, 2004.
186. Shtansky, D.V. et al., Comparative investigation of Ti–Si–N films magnetron sputtered using Ti_5Si_3+Ti and Ti_5Si_3+TiN targets, *Surf. Coat. Technol.*, 182, 204, 2004.
187. Zerkout, S. et al., On the existence of superstructure in TiN_x thin films, *Thin Solid Films*, 441, 135, 2003.
188. Sue, J.A., Development of arc evaporation of non-stoichiometric TiN coatings, *Surf. Coat. Technol.*, 61, 115, 1993.
189. Chen, J. and Barnard, J.A., Growth, structure and stress of sputtered TiB_2 thin films, *Mat. Sci. Eng. A*, 191, 233, 1995.
190. Jiang, C., Goto, T., Hirai, T., Morphology and preferred orientation of TiN plates prepared by CVD, *J. Mater. Sci.*, 29, 669, 1994.

191. Ma, K.J. and Bloyce, A., Observation of mechanical properties and failure mechanisms in TiN coatings after hardness indentation and scratch testing, *Surf. Eng.*, 11, 71, 1995.
192. Ljungcrantz, H. et al., Nanoindentation hardness, abrasive wear, and microstructure of TiN/NbN polycrystalline nanostructured multilayer films grown by reactive magnetron sputtering, *J. Vac. Sci. Technol. A*, 16, 3104, 1998.
193. Musil, J. and Hruby, H., Superhard nanocomposite $Ti_{1-x}Al_xN$ films prepared by magnetron sputtering, *Thin Solid Films*, 365, 104, 2000.
194. Polakova, H. et al., Structure–hardness relations in sputtered Ti–Al–V–N films, *Thin Solid Films*, 444, 189, 2003.
195. Zhitomirsky, V.N. et al., Structure and mechanical properties of vacuum arc-deposited NbN coatings, *Thin Solid Films*, 326, 134, 1998.
196. Han, Z. et al., Magnetron sputtering NbN films and mechanical properties, *Surf. Coat. Technol.*, 179, 188, 2004.
197. Kelosoglu, E. et al., Microstructure and properties of nitride and boride hard coatings deposited under intense mild-energy ion bombardment, *Surf. Coat. Technol*., 116–119, 133, 1999.
198. Cheng, Y.H. et al., Synthesis of superhard and elastic carbon nitride films by filtered cathodic vacuum arc combined with radio frequency ion beam source, *J. Mater. Res.*, 17, 521, 2002.
199. Waters, C. et al., Synthesis and mechanical properties of TiN–AlN thin film heterostructures, in *Mechanical Properties Derived from Nanostructuring Materials*, Vol. 778, Kung, H. et al., Eds., MRS, Warrendale, 2003, p. U2.2.1.
200. Zeman, H. et al., Thermal annealing of sputtered Al–Si–Cu–N films, *Vacuum*, 72, 21, 2004.
201. Kunc, F. et al., Low-stress superhard Ti–B films prepared by magnetron sputtering, *Surf. Coat. Technol.*, 174–175, 744, 2003.
202. Kelosoglu, E. et al., Structure and properties of TiB_2 based prepared by unbalanced DC magnetron sputtering, *Surf. Coat. Technol.*, 98, 1483, 1998.
203. Lugscheider, E. et al., Investigation of multifunctional graded ZrC PVD-Coatings for the application on machine parts, in *Surface Engineering 2002 — Synthesis, Characterization and applications*, Vol. 750, Kumar, A. et al., Eds., MRS, Warrendale, 2003, p. Y4.3.1.
204. Voevodin, A.A., Prasad, S.V., and Zabinski, J.S., Nanocrystalline carbide/amorphous carbon composites, *J. Appl. Phys.*, 82, 855, 1997.
205. Voevodin, A.A., O'Neill, J.P., and Zabinski, J.S., Nanocomposite tribological coatings for aerospace applications, *Surf. Coat. Technol.*, 116–119, 36, 1999.
206. He, J. et al., Synthesis of nanostructured WC-12 pct Co coating using mechanical milling and high velocity oxygen fuel thermal spaying, *Metall. Mater. Trans. A*, 31, 541, 2000.
207. Lim, D.-C. et al., Deposition of epitaxial SiC films using high vacuum MOCVD method for MEMS applications, *Thin Solid Films*, 459, 7, 2004.
208. Guruz, M.U., Dravid, M.U., and Chung, Y.W., Synthesis and characterization of single and multilayer BN and B_4C thin films grown by magnetron sputtering of B_4C, *Thin Solid Films*, 414, 129, 2002.
209. Hegemann, D., Riedel, R., and Oehr, C., PACVD-derived thin films in the system Si–B–C–N, *Chem. Vap. Deposition*, 5, 61, 1999.
210. Jonsson, B. and Hogmark, S., Hardness measurements of thin films, *Thin Solid Films*, 114, 257, 1984.
211. Helmerson, U. et al., Growth of single-crystal TiN/VN strained-layer superlattices with extremely high mechanical hardness, *J. Appl. Phys.*, 62, 481, 1987.
212. Shinn, M. et al., Growth, structure, and microhardness of epitaxial TiN/NbN superlattices, *J. Mater. Res.*, 7, 901, 1992.
213. Andrievski, R.A., Anisimova, I.P., and Anisimov, V.P., Structure and microhardness of TiN compositional and alloyed films, *Thin Solid Films*, 205, 171, 1991.
214. Andrievski, R.A., Anisimova, I.P., and Anisimov, V.P., Structure and hardness of multilayer TiN, NbN, ZrN, and CrN films, *Physica i Chimiya Obrabotki Materialov*, No. 2, 99, 1992 (in Russian).
215. Andrievski, R.A. et al., Nanoindentation and strain characteristics of nanostructured boride/nitride films, *Phys. Sol. State*, 42, 1671, 2000 (English transl.).
216. Veprek, S. et al., Possible artefacts in measurement of hardness and elastic modulus on superhard coatings and the verification of the correctness of the data, in *Surface Engineering 2002 — Synthesis, Characterization and Applications*, Vol. 750, Kumar, A. et al., Eds., MRS, Warrendale, 2003, p. Y1.3.1.

217. Ma, K.J. et al., Microstructural response of mono- and multilayer hard coatings during indentation microhardness testing, *Surf. Coat. Technol.*, 94–95, 322, 1997.
218. Andrievski, R.A. et al., Some peculiarities of fracture of nanocrystalline nitride and boride films, *J. Mater. Sci.*, 35, 2799, 2000.
219. Shtansky, D.V. et al., Localized deformation of multicomponent thin films, *Thin Solid Films*, 420–421, 330, 2002.
220. Andrievski, R.A. et al., High-temperature oxidation of films based on AlN, *Dokl. Phys. Chem.*, 373, 99, 2000 (English transl.).
221. Hultman, L., Thermal stability of nitride thin films, *Vacuum*, 57, 1, 2000.
222. Mayrhofer, P.H., Thermal stability of self-arrangement of nanocrystalline hard coatings, in *Nanostructured Thin Films and Nanodispersion Strengthened Coatings*, Voevodin, A.A. et al., Eds., Kluwer Academic Publishers, Dordrecht, 2004, p. 57.
223. Veprek, S. et al., Avoiding the high-temperature decomposition and softening of (Al,Ti)N coatings by the formation of stable superhard nc-(Al,Ti)N/a-Si_3N_4 nanocomposite, *Mater. Sci. Eng. A*, 366, 202, 2004.
224. Barnet, S.A. and Madan, A., Hardness and stability of metal-nitride nanoscale multilayers, *Scr. Mater.*, 50, 739, 2004.
225. Kim, D.-G. et al., Effects of annealing on the microstructures and mechanical propertties of TiN/AlN nano-multilayer films prepared by ion-beam assisted deposition, *Surf. Coat. Technol.*, 153, 79, 2002.
226. Jilek, M. et al., Towards the industralization of superhard nanocrystalline composites for high speed and dry maching, in *Surface Engineering 2002 — Synthesis, Characterization and Applications*, Vol. 750, Kumar, A. et al., Eds., MRS, Warrendale, 2003, p. Y4.2.1.
227. Voevodin, A.A. and Zabinski, J.S., Smart nanocomposite coatings with chameleon surface adaptation in tribological applications, in *Nanostructured Thin Films and Nanodispersion Strengthened Coatings*, Voevodin, A.A. et al., Eds., Kluwer Academic Publishers, Dordrecht, 2004, p. 1.
228. Mitterer, C. et al., Application of hard coatings in aluminium die casting — soldering, erosion and thermal fatigue behaviour, *Surf. Coat. Technol.*, 125, 233, 2000.
229. Gallis, S. et al., Thermal CVD of SiC films as protective coatings for microfluidic structures, in *Silicon Carbide 2002 — Materials, Processing and Devices*, Vol. 742, Saddow, S.E. et al., Eds., MRS, Warrendale, 2003, p. K2.4.1.
230. Wang, X. et al., Thermal plasma PVD of nanostructured SiC coatings, in *Silicon Carbide 2002 — Materials, Processing and Devices*, Vol. 742, Saddow, S.E. et al., Eds., MRS, Warrendale, 2003, p. K2.19.1.
231. Shtansky, D.V. et al., Structure and properties of Cao- and ZrO_2 doped YiC_xN_y coatings for biomedical applications, *Surf. Coat. Technol.*, 182, 101, 2004.
232. Piscanec, S. et al., Bioactivity of TiN-coated titanium implants, *Acta Mater.*, 52, 1237, 2004.
233. Herrmann, M., Schultz, I., and Zalite, I., Materials based on nanosized β-Si_3N_4 composite powders, *J. Eur. Ceram. Soc.*, 24, 3327, 2004.
234. Levashov, E.A. et al., The prospects of nanodispersive powders application in surface engineering technologies, *Surf. Coat. Technol.*, 180–181, 347, 2004.
235. Abom, A.E. et al., Properties of combined TiN and Pt thin films applied to gas sensing, *J. Vac. Sci. Technol. A*, 20, 667, 2002.
236. Bernatowicz, Th.J. and Walker, R.M., Ancient stardust in the laboratory, *Phys. Today*, 50, 26, 1997.
237. Vissokov, G., *Plasma Nanotechnologies*, Publ. House of Mining Univ., Sofia, 2005, p. 303.

15 Nanostructured Oxide Superconductors

Pavel E. Kazin and Yuri D. Tretyakov
Moscow State University, Moscow, Russia

CONTENTS

ABSTRACT

Oxide superconductors are considered materials structured on micro- and nanoscale level, a necessary condition for obtaining a superconducting material with high critical current density (J_c) values. The fundamentals of superconductivity in relation to magnetic flux pinning and J_c are briefly discussed. Design of superconductors with high density of flux pinning centers is envisaged. The nanostructured materials are classified by the nature of the pinning centers and the methods of their formation. Superconductor materials with advanced properties are shown to correspond to either single-phase materials with crystalline defects or to nanocomposites consisting of superconductor matrix with ultrafine nonsuperconducting inclusions. Preparation routes and properties of such materials are reviewed.

15.1 INTRODUCTION

Since the discovery of high T_c oxide superconductors (HTSC) in 1986 by Müller and Bednorz,[1] these materials have been attracting considerable attention due to their high superconducting transition temperature, which exceeds the boiling temperature of liquid nitrogen. It determines their high potential for application in electronics, for electric power transmission, storage, and utilization, and for producing strong magnetic fields and magnetic levitation. Till now T_c values up to 135 K have been achieved in Hg-based cuprates of the $HgBa_2Ca_nCu_{n+1}O_z$ homologue series.[2,3] Most promising for application rare earth- and bismuth-based superconductors exhibit T_c in the range 90 to 110 K.[4,5] A very important technical parameter of a superconductor is the critical current density J_c, which determines maximum electric current that can flow in the material without energy dissipation. The J_c value has to be high enough and for most applications spans the range of 10^2 to 10^7 A/cm^2. The first HTSC materials prepared possessed low J_c values that further decreased sharply with increasing temperature and applied magnetic field. The main reasons for this were weak intergrain junctions and low magnetic flux pinning. Elaboration of the preparation technique made it possible to overcome these problems to a certain extent and to get high-performance HTSC in the form of epitaxial films, wires with textured superconductor core, and bulk items.[6–8]

High values of J_c can be achieved in inhomogeneous material only, as the magnetic flux lines pin to small areas in the superconductor matrix with different electromagnetic properties. As we show in the next section, advanced superconductors have the necessity to be nanostructured materials.

15.2 SUPERCONDUCTOR PARAMETERS AND MAGNETIC FLUX PINNING

Superconducting state is characterized by zero resistivity and zero magnetic field induction inside the sample. Below T_c the superconducting state (phase) is stable, and consequently a certain amount of energy is required to transform the superconductor to normal metal. That occurs, for example, when high enough magnetic field is applied. Important parameters of the superconducting state are coherence length ξ, determining the interaction distance of the electron pairs and London penetration depth λ determining the magnetic field spreading in the superconducting volume.[9] For a superconductor with $\lambda/\xi > 1/\sqrt{2}$, the magnetic field starts to penetrate the material above lower critical field H_{c1} forming quantum vortices comprising of thin channels with suppressed superconductivity (core) surrounded by circulating current (Figure 15.1), and the main volume of the material remains superconducting. The vortex core diameter is approximately 2ξ, while the superconducting current (and bound magnetic field) extends to a distance of λ from the vortex center. When a vortex appears, some energy (electron pair condensation energy) is consumed to suppress superconductivity in its core, which is compensated by the energy gain due to the magnetic field penetration in the area surrounding the vortex. Repulsion forces acting between the vortices arrange them in a triangular array. On increasing the field further, the number of vortices increases and at upper critical field H_{c2} the vortices touch their cores so that the volume superconductivity disappears.

Oxide superconductors are characterized by $\xi_{ab} \sim 2$ to 4 nm, $\lambda_{ab} \sim 100$ nm (in *ab* plane), $H_{c1} \sim 10^{-1}$ T, and $H_{c2} \sim 10^2$ T.[10] Between H_{c1} and H_{c2} the electrical current applied through the material induces the flow of the vortices under the Lorenz force. The flow is accompanied by energy dissipation, and hence the material cannot be considered as a superconducting one. Fortunately, a vortex can pin when its core intersects, for example, a nonsuperconducting inclusion (see Figure 15.1). In this case, no energy is required for the field to penetrate the volume of the inclusion, and the vortex energy drops by the value corresponding to the condensation energy in the superconductor volume equal to the volume of the intersection of the vortex core with the inclusion.[8] Thus, the vortex gets into an energy (pinning) well and is trapped by the inclusion. The well is characterized by pinning energy E_p and pinning force $f_p = dE_p/dx$. The former characterizes stability of the pinning center toward thermal excitation. The latter determines minimum Lorenz force which must be applied to move the vortex and hence provides nonzero J_c, which is proportional to volume pinning force

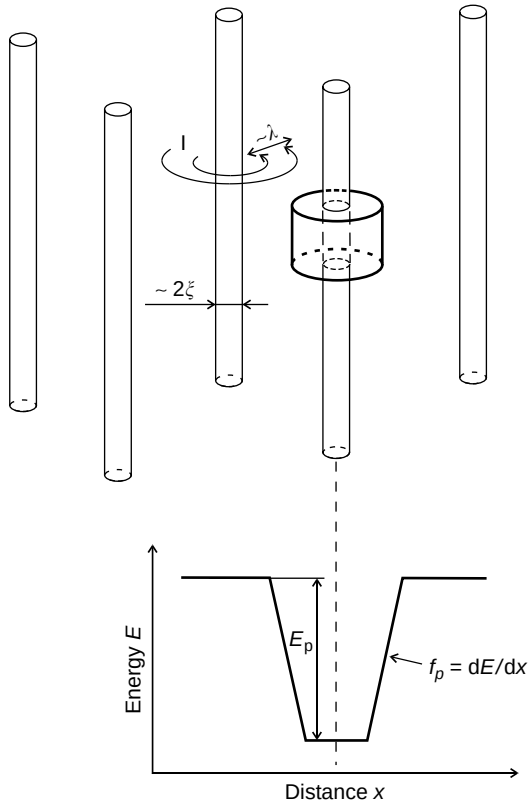

FIGURE 15.1 Magnetic vortices (shown as thin cylinders) in the superconductor. One vortex intersects a nonsuperconducting inclusion (thick cylinder). Such a position of the vortex corresponds to the energy profile depicted below (schematically). The energy drop E_p is equal to the energy required to convert superconductor into metal in the volume of the intersection. The energy well formed causes the vortex to pin to the inclusion.

$F_p = \Sigma f_p/V$. In general, higher concentration of efficient pinning centers provides higher J_c values and weaker suppression of J_c with temperature and magnetic field.

For the best performance, the inclusion diameter should be close to the vortex core diameter, i.e., 4 to 8 nm. Smaller inclusions will give lower E_p and f_p, while bigger ones will have considerable part of their volume not involved in the interaction.

One can imagine that the ideal structure of the material should represent continuous superconductor matrix penetrated by a regular array of nonsuperconducting columns a few nanometers in diameter, the columns being parallel to the magnetic field and perpendicular to the superconducting current flow. It is a challenging task to design such a composite, and the problem is still not fully solved. Less appropriate, but still very efficient is a random distribution of aligned columnar or even equiaxed nanoinclusions or crystalline defects. Calculations show that J_c will grow up to ca. 40 vol% of the included nanophase.[11] As a matter of fact large inclusions also pin the vortices; in fact they can pin several vortices simultaneously, and theoretically J_c can achieve 10^4 to 10^5 A/cm^2 for micron-sized inclusions.[8] However, because of higher concentration at the same volume fraction, nanosized inclusions may provide one to two orders of magnitude higher J_c.

The next important issue is the nature of a pinning center. The steepness in the wall of the pinning well (dE_p/dx) depends on the properties of the inclusion material: a metallic inclusion gives low-gradient dE_p/dx due to the delocalization of the metal electrons, an isolator provides "normal" gradient, while a ferromagnetic particle gives an increased gradient because of fast magnetic suppression

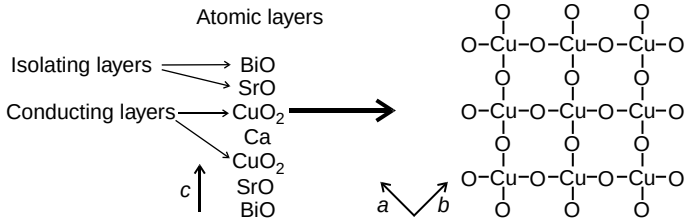

FIGURE 15.2 Crystal structure features of cuprate superconductors exemplified by $Bi_2Sr_2CaCu_2O_{8+x}$. Atomic layer sequence along the *c*-axis (left) and structure of CuO_2 plane running along the *ab* plane (right) are shown.

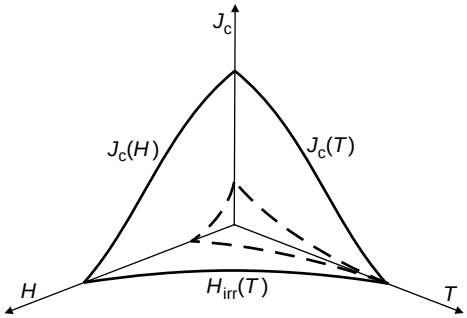

FIGURE 15.3 Schematic diagram of J_c vs. temperature and magnetic field for a superconductor with strong (full curves) and weak (broken curves) magnetic-flux pinning.

of the superconductor order parameter through the interface. An area with weakened (and even strengthened) superconductivity also pins a vortex, but the pinning well has lower energy, proportional to the difference in the condensation energies of the matrix and the inclusion. The wall gradient also depends on the sharpness of the interface matrix or inclusion. Gradual transition from superconducting to nonsuperconducting volume causes smoothing of the wall of the pinning well.

A specific feature of HTSCs is their layered crystal structure (Figure 15.2) representing superconducting CuO_2 planes separated by metal oxide layers with electric isolator character.[12] Thus, a large superconducting current can easily flow in the *ab* plane while along the *c*-axis its value is substantially lower. Therefore, it is important to make textured material and apply the superconducting current flow in the *ab*-direction. Such an electromagnetic anisotropy is also manifested at lower values of ξ_c (of the order of interatomic distance) as compared with ξ_{ab}. As a result, the initial *c*-axis columnar vortex can split into "pancake" vortices localized within the superconducting *ab* planes, which diminishes the effect of pinning. In the case of strong anisotropy, columnar inclusions become less efficient and with regard to the pinning effect, approach the equiaxed ones. The critical current density becomes stronger suppressed by the magnetic field and decreases to zero at a field H_{irr} (irreversibility field) much smaller than H_{c2}.

A schematic diagram showing the J_c dependence on H and T for the cases of weak and strong pinning is presented in Figure 15.3.

15.3 DESIGN OF FLUX PINNING CENTERS

In principle, any inhomogeneity in the superconducting state can be a candidate for flux pinning. The potential pinning sites can be conventionally divided into two groups: crystal structure defects and inclusions. In the first case, one considers the superconductor as single-phase material, and in

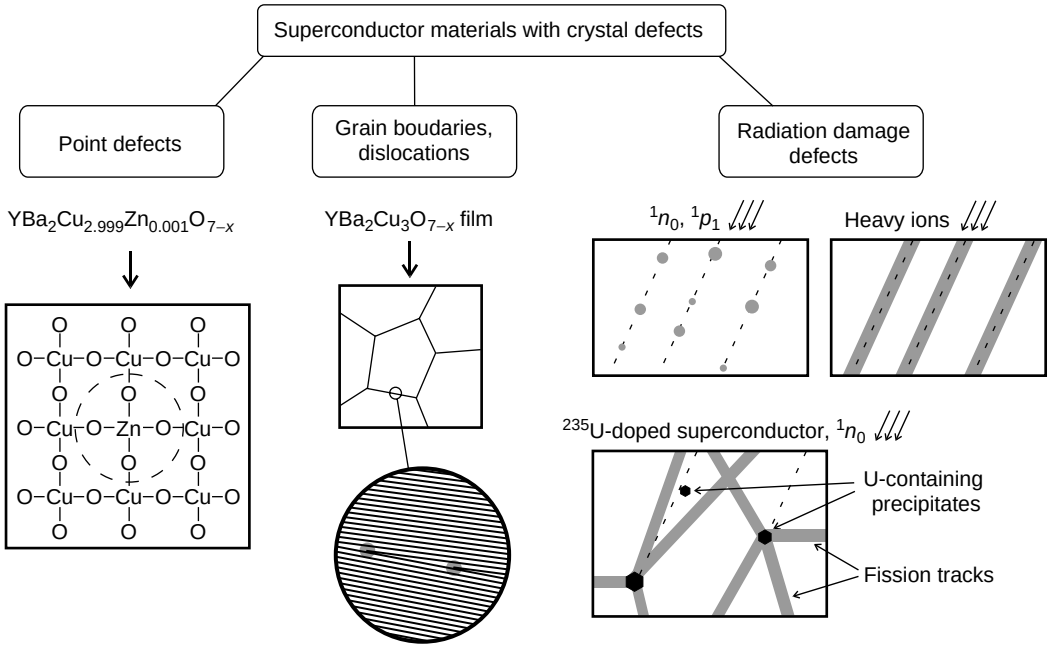

FIGURE 15.4 Crystalline defects in single-phase superconductor, which act as effective pinning centers.

the latter as composite. The defects include point defects such as atomic vacancies, substituted and interstitial atoms (ions), extended defects such as dislocations and grain boundaries, irradiation damage defects representing small areas of amorphized material. Formation of such defects in the superconductor is illustrated in Figure 15.4.

As the included phases the composites may contain secondary phases composed of the same components as the superconductor phase, or foreign phases containing additional chemical elements absent in the superconductor phase. In a special case, the suppression of superconductivity can take place in crystal areas with shifted chemical composition. The nature of the inhomogeneities determines approaches to material formation. We will consider particular materials following that classification in the following section.

15.4 SUPERCONDUCTOR MATERIALS WITH CRYSTALLINE DEFECTS

15.4.1 Point Defects

Often oxide superconductors prepared as homogeneous material (e.g., single crystal) exhibit very high J_c ($>10^5$ A/cm^2) and H_{irr} (>10 T) at 4.2 K, while at higher temperatures, J_c and H_{irr} decrease quickly and at 77 K the material has poor properties. High parameters at low temperature are usually associated with the presence of large number of pinning centers with low energy, presumably oxygen vacancies. With the increase in temperature, the raised thermal energy becomes comparable with the pinning energy so that these defects cannot coerce the vortices. It especially concerns highly anisotropic bismuth-based cuprates $Bi_2Sr_2CaCu_2O_{8+x}$ (Bi-2212) and $(Bi,Pb)_2Sr_2Ca_2Cu_3O_{10}$ (Bi-2223).

To increase pinning these superconductors were doped with many metal oxides (usually in amount of several mol%), and sometimes this led to moderate pinning enhancement, as in the case of Pb and Pr substitution.[13,14] However, the nature of the increase in pinning was not clear, as the dopants could impact the material in various ways: e.g., cation substitution could alter the charge

carrier density and electromagnetic anisotropy, possible secondary-phase impurities formed could act as pinning centers as well.

Later on, stronger evidence was obtained on point defect pinning.[15,16] Melt-textured bulk superconductor $YBa_2Cu_3O_7$ (Y-123) was doped with "homeopathic" amounts of ZnO. T_c of the sample decreased a little (ca. 1 K), while the critical current density increased twice at 77 K in zero field in comparison with the undoped sample. Besides, the increase in J_c became more pronounced in a magnetic field, sometimes showing "peak effect" (a maximum on the $J_c(H)$ curve).

The Zn effect can be illustrated as follows (see Figure 15.4, left). It is well known that Zn replaces Cu in CuO_2 planes and causes a decrease in T_c.[17] Thus, a single Zn ion produces an area with suppressed superconductivity. The diameter of the area in the *ab* plane is expected to be of the order of $2\xi_{ab}$. To allow the superconducting current flow, the areas formed around different Zn ions should not overlap, which gives an estimation of upper doping limit x in $YBa_2(Cu_{1-x}Zn_x)_3O_7$ of the order of 10^{-3}. Indeed, the highest J_c achieved was for $x = 0.0003$, and decreased to the J_c value for undoped Y-123 at $x = 0.001$.[16]

Theoretically, to make an efficient pinning center the dopant ion should completely destroy superconductivity at the distance comparable with ξ_{ab}, i.e., much larger than the interatomic distance. Hence, one can expect that a foreign metal ion such as Zn causes pair breaking also at the many neighboring Cu ions. The real mechanism of the doping effect is not yet clear. It cannot be excluded that the foreign ions could form associates in the lattice, which would be more efficient for the pinning, or induce some extended defects. For example, in single crystals of Bi-2212 doped with Ti ions it was observed that substitution of Cu by Ti led to formation of pairs of antiphase boundaries parallel to *c*-axis so that the CuO_2 planes were broken.[19]

An important feature of point defect pinning is the very small fraction of dopant required. Enhancement in J_c and H_{irr} was observed for Cr-doped $(Bi,Pb)_{2.2}Sr_2Ca_{2.2}Cu_{3-x}Cr_xO_y$ silver-sheathed tapes,[18] with the maximum effect found for $x=0.001$. A local maximum on J_c vs. dopant concentration was reported for Bi-2223 ceramics with contents of TaC, NbC, and HfN additives to be of the order of 0.1 mass%.[20,21] Small amounts of Ti, Zr, and Hf diffused from the silver sheath to Bi-2223 was accounted for the J_c increase observed.[22,23] In all these cases, substantial contribution of point defect pinning to J_c enhancement is quite probable.

15.4.2 Dislocations and Grain Boundaries

It is well known that J_c in Nb_3Sn grows with decrease in the grain size of the polycrystalline material.[24] In that case, grain boundaries play a role of efficient pinning sites, still remaining transparent for superconducting current flow. In nontextured oxide ceramics, grain boundaries usually impede current flow due to low ξ_{ab} value and are responsible for "weak link" behavior (strong suppression of intergrain J_c even in low field). Mechanical treatment of oxide superconductors introduces dislocations, which contribute strongly to the intragrain J_c. At the same time, the intergrain junctions can be destroyed, which leads to poor J_c transport properties. To prevent the latter, hot deformation procedures were applied providing some pinning improvement.[25,26]

The highest J_c is observed in epitaxial thin films. They are usually prepared by vapor deposition (laser ablation, magnetron sputtering, and chemical vapor deposition) on a heated single crystalline substrate ($SrTiO_3$, $NdGaO_3$, MgO, ZrO_2, etc.) having low lattice mismatch with the superconductor. The films have thickness of <1 μm with their *ab* plane parallel to the film surface and exhibit J_c exceeding 10^6 A/cm^2 for R-123 and reaching 10^5 A/cm^2 for Bi-2212 at 77 K.[27] Microstructurally they consist of biaxially oriented submicron grains with low-angle boundaries (see Figure 15.4, center). Each boundary comprises an array of dislocations running perpendicular to the film surface (along the *c*-axis). It was proposed that such dislocations were efficient pinning centers.[28] Direct observations of the vortices supported this.[29,30] The flux lines are captured along the dislocations perpendicular to the current flow in the most advantageous way. The defects exhibit short-range order that leads to a decrease in the inter-vortex repulsion providing stronger pinning.

The boundary (between dislocations), representing only slightly disturbed crystal lattice, remains a good conductor.

Other crystalline defects and nanoinclusions in epitaxial films can also contribute to the pinning to some extent.[31]

15.4.3 Irradiation Defects

Irradiation damage can be produced by exposition of the sample to the beams of particles, or *in situ*, by introducing additives containing atoms subjected to nuclear fission (see Figure 15.4, right). Beam irradiation is extensively used as the defects concentration can be easily controlled by the quantity of radiation. Irradiation with neutrons and protons gives local defects a few nanometers in diameter. Heavy ions with high enough energy (Au, Pb, etc., 1 to 20 GeV) produce long columns of amorphized material with a diameter of the order of 10 nm.[32] Such extended defects impact the flux pinning most strongly, and hence heavy ion irradiation has been studied most extensively. Single crystals of HTSC having initially low J_c at enhanced temperatures exhibit very pronounced increase in J_c (by orders of magnitude) and in H_{irr} after the irradiation. The pinning first grows with the irradiation dose, then decreases when the fraction of the destroyed superconductor becomes substantial. The pinning effect also depends on the direction of the channels. In Y-123 with low anisotropy, substantially stronger effect is observed for the channels running along the *c*-axis (while the current is applied in the *ab* plane). In highly anisotropic Bi-2212, the direction of the channels is not so important which is accounted for by the pancake vortex pinning.[33] Heavy ion irradiation allows to increase J_c considerably even in high-J_c epitaxial films.[34]

It should be noted that irradiation with fast protons causes atomic fission resulting in randomly oriented amorphous tracks in oxide superconductors, especially those containing Hg, Tl, Pb, and Bi.[35] These tracks are similar to columnar defects produced by heavy ion irradiation both in structure and pinning effect.

To employ nuclear fission *in situ* the initial precursors were doped with ^{235}U containing compounds. In the doped Y-123 bulk material after the melt processing, the submicrometer-sized precipitates of $Ba(U_{0.6}Y_{0.4})O_3$ or $Ba_2YU_{0.6}Pt_{0.4}O_6$ (in the presence of platinum) were formed.[36,37] The precipitates themselves acting as pinning centers caused moderate increase in J_c. Then the samples were irradiated by neutrons, which resulted in the appearance of numerous tracks in the superconductor matrix. These new pinning sites provided manifold increase in J_c. This technique allowed the preparation of bulk material with the record J_c value of 3×10^5 A/cm^2 at 77 K.[37]

Silver-sheathed tapes of Bi-2223 were also doped using U_3O_8, which resulted in rather uniform dopant distribution in the material mostly found in fine precipitates of $(Sr,Ca)_3UO_6$.[38] Neutron irradiation led to an increase in J_c in the effective pinning energy and to the shift of the irreversibility line to higher fields.[39]

15.5 SUPERCONDUCTOR MATRIX-BASED COMPOSITES

15.5.1 Formation of Composites

Considering the oxide superconductor material as composite containing two or more phases proved to be a fruitful way to design material with advanced functional properties.[40] Matrix phase of such a composite is a superconducting one that allows smooth current flow without dissipation on grain boundaries. It can be dense highly textured polycrystalline ceramics with clean grain boundaries (directionally solidified ceramics and metal clad wires and tapes) or (quasi) single crystalline materials (epitaxial films and melt-textured bulks). The dispersed phase (pinning additive) should be uniformly distributed in the material to form ultrafine inclusions. The phases have to be chemically inert toward each other both at preparation and application conditions in order to prevent the suppression of superconductivity. Besides, the dispersed phase has to be stable toward its particles coarsening

(Ostvald ripening) and segregation. Chemical stability is best provided if both components of the composite are thermodynamically compatible, i.e., within the range of the material formation conditions (temperature and oxygen partial pressure) they co-exist in chemical and phase equilibrium. The compatibility gains a special importance since the superconductor phase is often obtained either from the melt or solid at temperatures close to the melting. Under such conditions most of the substances regarded as "chemically inert" interact with the superconductor phase or its melt. The interaction has to be much faster for the pinning additive as it represents highly dispersed phase.

Considering the addition of new components to the superconductor system, it should be ensured that superconductive thermodynamic parameters are sustained at high level. As the best chemical compositions for superconductors had mostly been determined in early studies, it is presumable for new components not to be dissolved in the superconductor phase.

There are several pathways to form a composite from precursor materials, which are schematically illustrated in Figure 15.5 with several examples. The most straightforward approach is to choose the components ratio in the precursor, which corresponds to two-phase region on the phase diagram (figurative points 1, 1′): superconductor — dispersed phase, and perform a corresponding thermal treatment. For the preparation of the Bi-2223 core tapes usually a solid-state thermal treatment is applied, though sometimes very short "shock" melting is introduced as an intermediate step. For the R-123 bulk as well as for the Bi-2212 bulk and tapes, the most appropriate is slow solidification from peritectic melt. The process corresponds to the movement from point 1 to point 1′. In order to get very fine inclusions, the precursors have to be homogeneous on a submicron level.

Another approach is to prepare single-phase material with certain composition lying within the superconductor solid solution (figurative points 2 and 3), then change the temperature such as to get in the two-phase region superconductor — secondary phase ($2 \rightarrow 2'$, $2 \rightarrow 2''$). A special type of the decomposition takes place when on cooling an immiscibility gap appears in the superconductor solid solution ($3 \rightarrow 3'$). In this case, the phase separation by spinodal mechanism can occur, leading to nanostructuring of the material. One of the phases formed with weaker superconductivity will play a role of a pinning phase.

Similarly, transition to a certain phase region is possible by changing partial pressure of oxygen.

15.5.2 Composites: Superconductor Matrix — Secondary-Phase Inclusions

The multicomponent chemical systems to which oxide superconductors belong are quite complex and there are many adjacent phases co-existing with the superconductor phase on the phase diagrams.[4,8,40,41] Quite naturally, these phases were first considered as potential pinning additives.

Widely applied is melt processing of $RBa_2Cu_3O_{7-x}$ (R-123)–R_2BaCuO_5 (R-211) bulk composites, where R = Y, Nd, Eu, Sm, Gd, and their mixtures.[8] The R-123 phase melts incongruently around 1000°C according to the reaction

$$\text{R-123} \rightarrow \text{R-211} + \text{liquid}$$

On solidification, the reverse reaction does not proceed completely as the solid particles of R-211 dissolve slowly and are trapped by the growing R-123 grains. An addition of the R-211 surplus (20 to 40 mol%) aids to complete the reaction and leads to the formation of two-phase composite R-123–R-211 (see Figure 15.5). The material is usually prepared by very slow cooling (~1°C/h) of the peritectic melt combined with the initialization of the crystallization with small single crystal seed. The R-123 superconductor forms a matrix composed of quasi-single crystal blocks up to several centimeters in size, while the R-211 phase forms small inclusions. First experiments gave inclusions a few micrometers in diameter.[8] Nevertheless, high J_c exceeding 10^4 A/cm^2 at 77 K was obtained. By tuning the material composition and preparation conditions, the R-211 particles were refined to a submicron size, which allowed to reach J_c above 10^5 A/cm^2 at 77 K.[42–45] It was theoretically estimated that

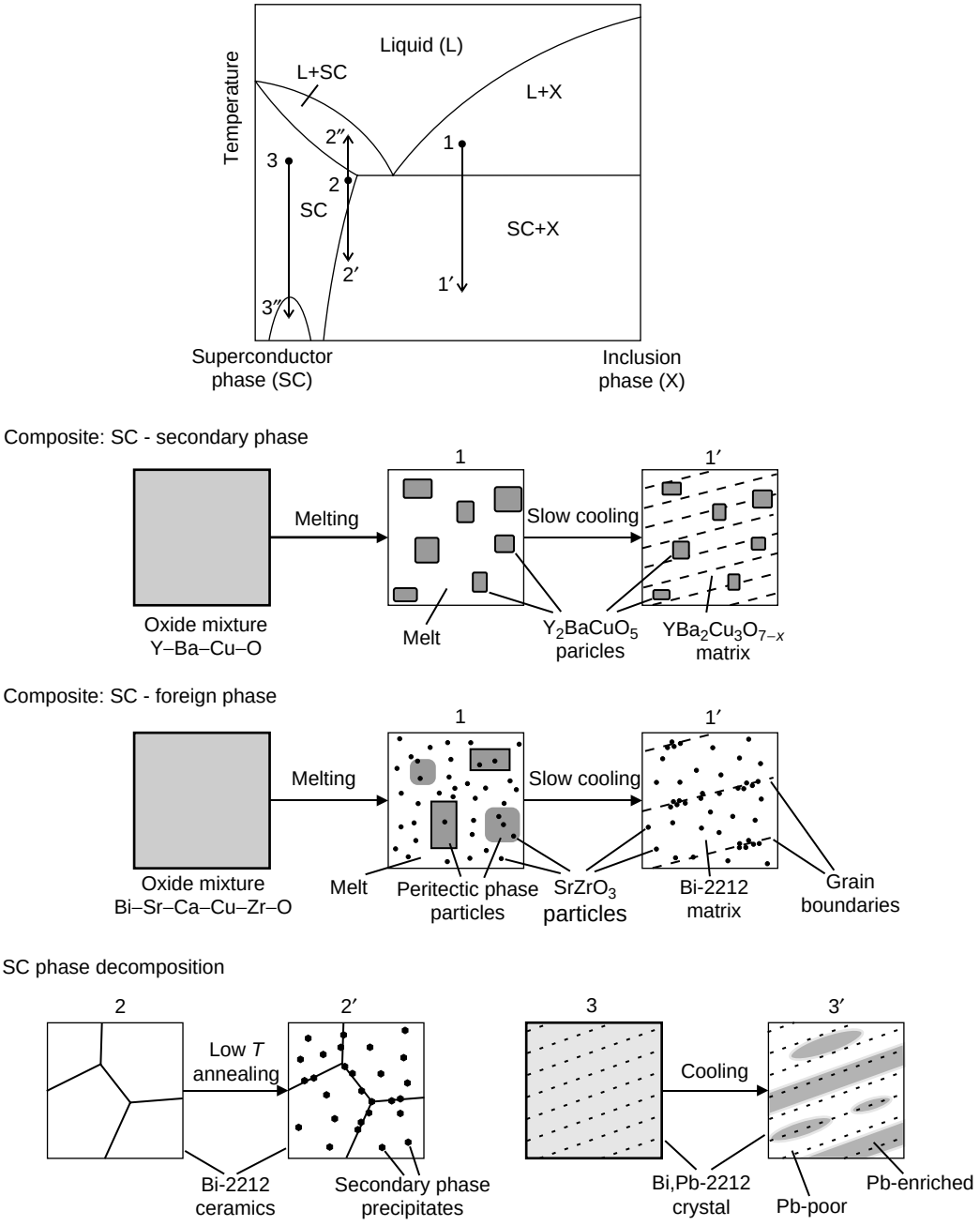

FIGURE 15.5 Pathways of superconductor composite formation. Illustrated by the figurative point movement on the schematic phase diagram and synthesis schemes of particular materials.

flux pinning by the inclusions alone could explain the J_c values observed, though other defects, including those arising from the inclusions (e.g., dislocations), could also contribute.[8] Studies of the bulk pinning force dependence on the magnetic field supported a dominant role of the inclusions (or inclusion–matrix interface).[46,47]

Further refinement of R-211 inclusions is expected to give even higher J_c. The obstacle could be an increasing tendency for the particles to be pushed by the growing R-123 crystal. The theory

of the interaction of a growing crystal with an inclusion introduces critical crystal growth rate v_c below which the trapping rate of the foreign particles dramatically decreases.[48,49]

$$v_c \sim \Delta\sigma/\eta r, \quad \Delta\sigma = \sigma_1 - \sigma_2 - \sigma_3 \tag{15.1}$$

where σ_1, σ_2, and σ_3 are the energies of interfaces particle — crystal, particle — melt and crystal — melt, respectively, η the melt viscosity, and r the particle radius. For very small particles v_c becomes high and it is not possible to incorporate large amounts of ultrafine inclusions in the matrix using the low crystallization rate required for the formation of high-quality superconductor. As was shown in [50], ultrafine Y-211 grains indeed were pushed out of the crystal. Besides, some dopants increased a pushing effect (e.g., Pt) and for Ru doping the Y-211 particles were fully expelled from the Y-123 bulk.[51] The dopant likely changes the interface energies resulting in the increase in $\Delta\sigma$. The right way out seems to be to diminish $\Delta\sigma$ or even make it negative, and probably some other doping will do it.

Similar to R-123 materials the (Bi-2212 — secondary phase) composites can be obtained. By slow solidification of the oxide melt with surplus of CaO and CuO the Bi(Pb)-2212 material was prepared, which contained high concentration of Ca_2CuO_3 inclusions.[52,53] Using a ferromagnetic particles decoration technique, it was shown that vortices pinned to the particle–matrix interface.[54] Single crystals of Bi-2212 with elongated CuO particles were obtained by crystallization from the KCl flux.[55]

In melt-textured Bi-2212, the secondary-phase particles formed are usually several microns in size, and it seems problematic to make them much smaller. This is related to the fact that the peritectic melt contains all the components of the system in comparable quantity and the secondary-phase particle coarsening occurs during the processing.

15.5.3 Composites: Superconductor Matrix — Foreign-Phase Inclusions

Usage of foreign-phase inclusions extends the possibilities to vary microstructure and properties of the composites.

In melt-processed R-123, at first additional components were introduced to impact on the distribution of R-211 phase in the composite. The addition of small amounts of Pt, CeO_2, and ZrO_2 led to the R-211 particles refinement. The additives themselves often formed particles of foreign phases. A range of satellite phases such as phases of Y–Ba–Cu–Pt–O system,[56,57] $BaSnO_3$,[58] $YBa_2SnO_{5.5}$, and its solid solutions were identified in the R-123 matrix.[59] All of them formed submicrometer grains, which were partially pushed from the R-123 crystallites. These phases were often considered as undesired impurities. The situation changed when detailed investigation of the uranium-oxide-doped Y-123 revealed highly dispersed inclusions of $Ba(U_{0.6}Y_{0.4})O_3$, $Ba_2Y(U_{0.6}Pt_{0.4})O_8$.[36,37] Their presence was related to increased J_c observed in the material prior to neutron irradiation. This encouraged the search for other possible pinning additives, as a result of which stable phases containing Mo and W oxides were found.[60,61] In particular, the presence of $Ba_2Y(W_{0.5}Pt_{0.5})O_6$ inclusions of 200 to 300 nm in size provided ca. 60% increase in J_c.[61]

Bi-2212 superconductor looks promising for application as it can be easily melt processed to form highly textured material by that providing uniform superconducting current distribution along conductors such as silver-sheathed tapes, wires, and long rods. Yet, extremely high anisotropy causes low pinning ability at increased temperatures and artificial high-energy pinning centers would help to overcome the problem. As was mentioned above the effect of second phases of the same system was restricted if the melt processing was applied, and therefore the application of foreign-phase additives acquires a special importance.

An extended study on introduction of new components to the Bi–(Pb)–Sr–Ca–Cu–O system showed that a range of metal oxides could be added to the Bi-2212- and Bi-2223-based materials without significant incorporation of their ions into the superconductor crystal lattice thus conserving high T_c values.[41,62,63] The additives form separate phases chemically compatible with Bi-2212 and Bi-2223.

In most cases, the phases represent complex oxides, so if a foreign binary oxide is added it reacts with the superconducting phase consuming certain oxides of the system and thus partially

destroying the material. Hence, it is important that the additive (or surplus to the precursor) should have quite certain elements ratio. The only binary oxide found to be partially compatible with the superconductors is magnesium oxide.[64,65] On annealing in contact with Bi-2212, being in highly dispersed state, pure MgO acquires copper oxide, so that the equilibrium composition is $Mg_{1-x}Cu_xO$, where $x = 0.08–0.15$. As long as the free energy of MgO reaction with CuO is small enough, single-crystalline MgO does not interact with Bi-2212 and its melt and proved to be an excellent substrate for the melt processing of the Bi-2212 material.

Using certain melt processing of a precursor, fine inclusions of the compatible phases can be created in the Bi-2212 superconductor matrix. Different routes of the precursor preparation can be applied (they are further consequently numbered). Route I considers preparation of single highly homogeneous precursor containing all chemical components of the target composite. Co-precipitation and sol–gel methods make it possible to get component mixing on an atomic scale. The same is applicable to the homogeneous oxide glass prepared by rapid quenching of the melt. Route II involves mixing of the final components of the composite: superconductor and nanodispersed foreign phase. In Route III, two precursors are mixed which on subsequent chemical reaction give an equilibrium assemblage: superconductor — foreign phase.

As-obtained precursor is subjected to partial melting followed by slow crystallization of Bi-2212 from the melt (see Figure 15.5). The foreign phase forms small solid particles suspended in the melt which are trapped by the growing Bi-2212 grains. The composite ceramics contain large Bi-2212 plate-like grains (of the order of 100 μm) and foreign-phase particles distributed inside and between the Bi-2212 grains. The particle size, shape, and spatial distribution in the composite strongly depend on the nature of the foreign phase as well as on preparation conditions. In Figure 15.6, electron micrographs of some composites with different inclusion phases are shown.

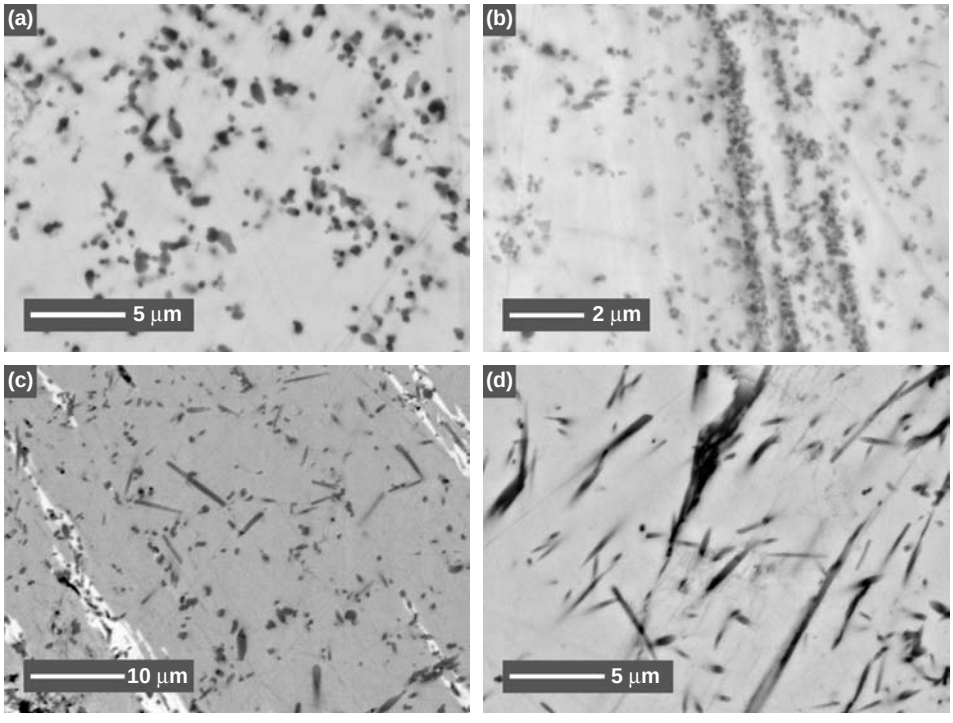

FIGURE 15.6 Scanning electron microscopy images (polished cross-sections, back-scattered electrons) of the melt-processed Bi-2212 superconductor with foreign-phase inclusions. Dark-gray and black rounded and elongated particles, inclusions of foreign phase; light-gray matrix, Bi-2212. Foreign phases: (a) $Mg_{1-x}Cu_xO$, (b) $SrZrO_3$, (c) $(Sr,Ca)In_2O_4$, and (d) $Sr_5(PO_4)_3Cu_xOH_y$.

Particles of the majority of foreign phases tend to segregate partially on the Bi-2212 grain boundaries. The exception is $Mg_{1-x}Cu_xO$, which is always found to be uniformly distributed in the matrix (Figure 15.6a).

By melt processing the mixture of Bi-2212 and 10-nm-sized MgO powder, material with inclusions in the range of 200 to 300 nm is obtained.[65] During the processing, apparently foreign phase grain growth takes place. Application of sol–gel precursor (route II) gives even larger grains of $Mg_{1-x}Cu_xO$. That outlines the problem of keeping the included particle size small enough. The composites exhibit enhanced J_c both at 5 and 77 K, with the increase more pronounced at high temperature.

Finely dispersed magnesium oxide was also used as pinning additive to Bi-2212 tapes, bulk, and single crystals.[66–68]

Doping of Bi-2212 with Al_2O_3 has revealed two thermodynamically compatible foreign phases $BiSr_{1.5}Ca_{0.5}Al_2O_z$ and $(Sr,Ca)_3Al_2O_6$, forming micron-sized grains in the material.[69] The former phase particles are totally pushed from the Bi-2212 crystallites, while the latter phase particles are trapped. Using an oxide glass precursor the $(Sr,Ca)_3Al_2O_6$ particle size was diminished by the order of a magnitude,[70] yet the particles started to aggregate. Considering Equation (15.1) for a fixed Bi-2212 crystal growth rate v_c, the particle size r becomes too small for efficient trapping. In contrast the sub-micron $Mg_{1-x}Cu_xO$ particles are totally trapped, which allows very low or even negative value for $\Delta\sigma$.

Perovskites $SrAO_3$, where A=Zr, Hf, Sn, under similar conditions form in the Bi-2212 matrix finer particles of 100 to 300 nm in size (see Figure 15.6b).[62,71,72] However, even application of nano-sized $SrAO_3$ powders (route II) does not give the resulting particles grain size lower than 100 nm. The particles are partially incorporated into Bi-2212 grains and partially agglomerated, forming thin closed areas between the Bi-2212 lamellas so that many direct junctions between the lamellas are sustained. That allows to obtain high transport J_c in spite of the inhomogeneous foreign-phase distribution. For example, in the silver-sheathed tapes the $SrZrO_3$ inclusions (prepared using route I from co-precipitated oxalates) provided considerably better superconducting parameters.[71] In Particular, in comparison with Bi-2212 undoped tapes at 5 K the difference in J_c was negligible, while at 60 K in zero external field J_c increased twice and in the field 50 mT, the increase exceeded an order of magnitude. By magnetization decay measurements, it was shown that $SrZrO_3$ doping led to appearance of additional number of pinning centers with high energy.[71] It should be mentioned that positive effects of other phase inclusions is also mostly observed at enhanced temperatures.

Unlike foreign phases discussed above, $(Sr,Ca)In_2O_4$ forms anisotropic rod-like particles in the Bi-2212 material (Figure 15.6c).[73] By varying the preparation route, it is possible to get submicron-sized particles with different aspect ratio. Particles with higher aspect ratio are better trapped by the Bi-2212 grains. The most anisotropic particles were prepared by melt processing of the homogeneous oxide glass precursor.[74]

An apatite type $Sr_5(PO_4)_3Cu_xOH_y$ phase[75] yields submicron needles in the Bi-2212 matrix (Figure 15.6d). Elongated inclusions are expected to be more favorable for flux pinning in comparison with equiaxed ones if the magnetic field has a direction parallel to the long dimension of the particle. Therefore, the next step would be to create aligned rods of such foreign phase in the superconductor matrix.

Route III utilizes topochemical reaction of fine grains of the compound containing foreign element with the molten precursor of the Bi–Sr–Ca–Cu–O system. This way complex-shaped inclusions can be formed.[76,77] Thus, micron-sized grains of Sr_2SnO_4 transform into perforated shells of $SrSnO_3$ (Figure 15.7), while $Sr_3Sn_2O_7$ give serrated particles of $SrSnO_3$. Similar reaction with Sr_2TiO_4 results in $SrTiO_3$ shell-like crystals. Ca_2SnO_4 grains with the size of 1 μm are converted into submicron grains of $SrSnO_3$, so that dispersed-phase refinement takes place.

A substantial advance in nanocomposite design was the synthesis of Bi-2212 thick films with aligned uniaxial inclusions.[78] On a single crystal of MgO with specially prepared surface, a “forest” of MgO nanorods was grown using Mg vapor oxidation (Figure 15.8). The nanorods grew perpendicular to the substrate surface, had mean diameter of 25 nm, length of ≥2 μm, and areal density of 3×10^9 cm^{-2}. Then, the amorphous BSCCO layer of 1- to 2-μm thickness was deposited by laser

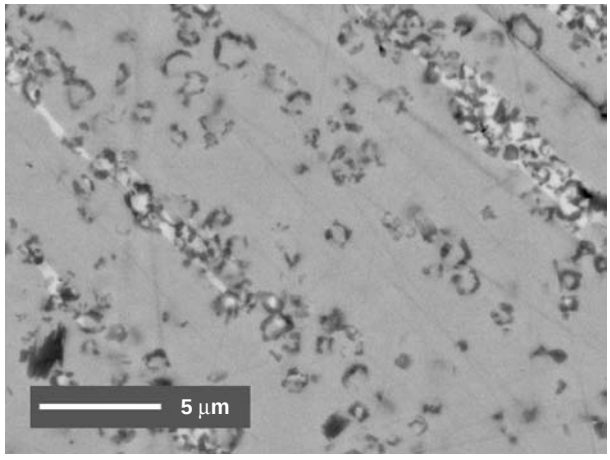

FIGURE 15.7 Scanning electron microscopy image (polished cross-section, back scattered electrons) of the Bi-2212–$SrSnO_3$ composite obtained by melt processing of the mixture of the Bi–Sr–Ca–Cu–O oxide precursor with the Sr_2SnO_4 micron-sized powder. Dark-gray micron-sized broken circles, shell-like inclusions of $SrSnO_3$; light-gray matrix, Bi-2212.

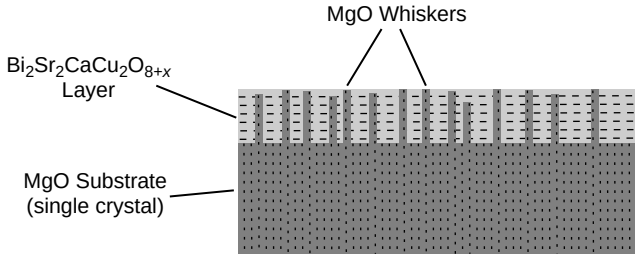

FIGURE 15.8 Thick film of Bi-2212 with MgO nanowhiskers aligned perpendicular to the film surface on the MgO substrate.

sputtering and was subjected to a conventional melt texturing processing. The MgO nanorods penetrated the Bi-2212 matrix perpendicular to the film surface. As mentioned above, such columnar defects had to be most efficient for flux pinning. The introduction of nanorods resulted in the several-fold increase in J_c, which was more pronounced at elevated temperatures. The irreversibility field values increased roughly twice.

The Bi-2223 superconductor was doped also with magnesium oxide.[79–81] It was introduced in the Bi-2223 silver-sheathed tapes in the form of nanoparticles or nanowhiskers and some increase in J_c was observed.

Bi-2223 superconductor is usually obtained by a solid-state reaction. One can expect that the foreign-phase particles coarsening will not be so pronounced as for the melt processing: however the trapping ability of the particles is under question, as the superconductor grains grow much slower. As of now, there is not enough data on composites microstructure to consider these issues.

15.5.4 Composites Obtained by Superconductor Phase Decomposition

The Bi-2212 and Bi-2223 phases exhibit extended ranges of cation solid solutions, with the compositional boundaries depending on temperature and oxygen partial pressure. That makes them convenient to perform partial decomposition of the initially single-phase material by changing the temperature and oxygen partial pressure. This approach was used to synthesize the Bi-2212 ceramics containing sub-micrometer-sized inclusions of Bi-2201, $Sr_3Bi_2O_6$, $Sr_{14}Cu_{24}O_{41}$, and Ca_2CuO_3[82,83]

and Bi-2223 ceramics containing inclusions of Bi-2212, Ca_2CuO_3, and Ca_2CuO_3.[84] For example, at 870°C, pure Bi-2212 was prepared enriched with Sr for account of Ca. Then the sample was heat treated at 700°C for a restricted time, which caused precipitation of secondary-phase inclusions of 100 nm in size, while Bi-2212 adopted composition with lower Sr to Ca ratio (see Figure 15.5). After this procedure, the intra-grain J_c at 30 K increased 3 to 6 times. Longer heat treatment resulted in the secondary-phase particles coarsening and decrease in J_c. Annealing of Bi-2212 at 550°C led to precipitation of smaller secondary-phase particles (20 to 100 nm).[85]

In Refs. 86, 87 the low temperature oxidation of rare earth for alkaline earth substituted Bi-2212 ceramics was investigated. Precipitation of second phases was observed for R = La, Pr, Nd. The fastest precipitation occurred for Pr-substituted samples, which was explained by oxidation of Pr^{3+} to Pr^{4+} followed by its segregation in $SrPrO_3$.

Solid solution separation for composites formation was applied both for Bi-2212 and R-123 superconductors. Phase separation is observed in the lead-doped Bi-2212 with the composition $Bi_{2-x}Pb_xSr_2CaCu_2O_{8+z}$ when x exceeds 0.4.[88,89] In single crystals as well in the large-grained ceramics on cooling, sub-micrometer-sized domains arise, which form layered pattern or appear as nanoscale rounded areas in the matrix (see also Figure 15.5). The crystal structure remains the same, but the chemical composition of the domains is different. The domains are enriched with lead while the matrix is depleted of lead. It is assumed that enriched with lead small areas have lower T_c values and play the role of efficient pinning centers. This explains the fact that the materials exhibit considerably increased J_c and H_{irr} values in comparison with the samples with $x < 0.4$.

The R-123 compound forms an extended solid solution range $R_{1+x}Ba_{2-x}Cu_3O_{7-z}$ when rare earth cation has large radius (La, Nd, Pr). With increasing x, the T_c value decreases quickly. The Nd-containing compound has been studied most extensively.[47,90,91] Samples of $Nd_{1+x}Ba_{2-x}Cu_3O_{7+z}$ with $x \approx 0$ prepared by melt texturing undergo a solid solution separation under particular conditions. The phase with larger x forms nanometer-sized inclusions in the matrix with lower x. The material shows better J_c values at enhanced magnetic field and its $M(H)$ hysteresis curve is often characterized by a peak effect (at an intermediate field J_c first increases with field, reaching a maximum and then decreases back). The effect is associated with the destruction of the superconductivity under the magnetic field in weakly superconducting regions that makes them effective pinning centers. The dependence of a pinning force upon the reduced magnetic field H/H_{irr} passes through a maximum at $H/H_{irr} = 0.4–0.5$, which indicates a pinning of magnetic vortices to small regions with weakened superconductivity.[47,90,91] In contrast to that, pinning to nonsuperconducting inclusions is characterized by the pinning force maximum at a twice lower H/H_{irr}. Similar nanoscale weakly superconducting regions are believed to be responsible for pronounced peak effects in (Nd,Eu,Gd)-123 and (Nd,Sm,Gd)-123.[92,93]

15.6 CONCLUSIONS

Nanostructuring of a superconductor is a key condition to obtain material with higher critical current density values sustained at increased temperatures and magnetic fields. Considerable enhancement in J_c has been achieved by the introduction of high concentration of pinning centers such as crystalline defects or ultrafine nonsuperconducting phase inclusions. General trends in the material development can be defined as moving from micro- to nanoscale pinning centers, constructing the pinning sites with a certain shape (columns), creating a correlated array of the pinning sites. It should be recognized that in a complex material, the advanced parameters obtained can be associated frequently with many factors impacting simultaneously, such as different kinds of pinning centers, quality of inter-grain junctions, and modified matrix superconductor characteristics (lower anisotropy and higher charge carrier density). Further progress in high-performance oxide superconductor design is connected with closer understanding of a particular microstructure and its relation to the superconducting characteristics, with thorough selection of the material chemical composition in multicomponent systems and development of processing to control efficiently the materials structure on a nanoscale level.

ACKNOWLEDGMENTS

The work was partially supported by the Russian Foundation for Basic Research and the Russian Ministry of Education under a Universities of Russia program.

REFERENCES

1. K.A. Müller and J.G. Bednorz, The discovery of a class of high temperature superconductors, *Science* 237, 1133–1139 (1987).
2. S.N. Putilin, E.V. Antipov, O. Chmaissem, and M. Marezio, Superconductivity at 94 K in $HgBa_2CuO_{4+y}$, *Nature* 362, 226–228 (1993).
3. E.V. Antipov, A.M. Abakumov, and S.N. Putilin, Chemistry and structure of Hg-based superconducting Cu mixed oxides, *Supercond. Sci. Technol.* 15, 31–49 (2002).
4. P. Majewski, Phase diagram studies in the system Bi–Pb–Sr–Ca–Cu–O–Ag, *Supercond. Sci. Technol.* 10, 453–467 (1997).
5. R.J. Cava, Oxide superconductors, *J. Am. Ceram. Soc.* 83, 5–28 (2000).
6. J.L. MacManus-Driscoll, Recent developments in conductor processing of high irreversibility field superconductors, *Ann. Rev. Mater. Sci.* 28, 421–462 (1998).
7. P. Vase, R. Flükiger, M. Leghissa, and B. Glowacki, Current status of high-Tc wire, *Supercond. Sci. Technol.* 13, 71–84 (2000).
8. M. Murakami (Ed.), *Melt Processed High-Temperature Superconductors*, World Scientific, Singapore, 1992.
9. E.H. Brandt, Vortices in superconductors, *Physica C* 369, 10–20 (2002).
10. E.Z. Meilikhov and V.G. Shapiro, Critical fields in high-temperature superconductors (review), *Sverkhprovodimost': fizika, khimia, tekhnika* 4, 1437–1492 (1991).
11. L.D. Cooley and L.R. Motowidlo, Advances in high-field superconducting composites by addition of artificial pinning centres to niobium–titanium, *Supercond. Sci. Technol.* 12, R135–R151 (1999).
12. A.P. Malozemoff, L. Krusin-Elbaum, and J.R. Clem, Interlayer coupling in high temperature superconductors, *Physica C* 162–164, 353–354 (1989).
13. M. Wakata, S. Takano, F. Munakata, and H. Yamauchi, Effects of cation substitution on flux pinning in Bi 2212 supercoductors, *Cryogenics* 32, 1046–1051 (1992).
14. P.L. Paulose, S. Patil, H. Franck, and G. Guntherodt, Influence of Pb and Nb substitution on pinning and irreversibility behavior of Bi 2212, *Physica C* 208, 11–17 (1993).
15. G. Krabbes, G. Fuchs, P. Shaetze, S. Gruss, J.W. Park, F. Hardinghaus, G. Stoever, R. Hayn, S.-L. Drechsler, and T. Fahr, Zn doping of $YBa_2Cu_3O_7$ in melt textured materials: peak effect and high trapped fields, *Physica C* 330, 181–190 (2000).
16. M.T. González, N. Hari-Babu, and D.A. Cardwell, Enhancement of J_c under magnetic field by Zn doping in melt-textured Y–Ba–Cu–O superconductors, *Supercond. Sci. Technol.* 15, 1372–1376 (2002).
17. N. Kawaji, K. Muranaka, Y. Oda, and K. Asayama, T_c suppression and hole concentration in Cu substituted $YBa_2[Cu_{1-x}M_x]_3O_{7-\delta}$ with Fe, Co, Ni, Zn, *Physica B* 165–166, 1543–1544 (1990).
18. M.H. Pu, Y. Feng, P.X. Zhang, L. Zhou, J.X. Wang, Y.P. Sun, and J.J. Du, Enhanced the flux pinning in Bi-2223/Ag by induced Cr-ion defects, *Physica C* 386, 41–46 (2003).
19. T.W. Li, R.J. Drost, P.H. Kes, C. Traeholt, H.W. Zandbergen, N.T. Hien, A.A. Menovsky, and J.J.M. France, TEM analysis of planar defects induced by Ti doping in Bi-2212 single crystals, *Physica C* 290, 239–251 (1997).
20. B.P. Mikhailov, P.E. Kazin, V.V. Lennikov, S.V. Shavkin, G.V. Laskova, and A.A. Titov, Influence of finely dispersed additions of niobium carbide on the structure and superconducting properties of $(Bi,Pb)_2Sr_2Ca_2Cu_3O_{10+x}$ ceramics, *Neorg. Mater.* 37, 753–757 (2001).
21. B.P. Mikhailov, G.S. Burkhanov, P.E. Kazin, V.V. Lennikov, M.V. Makarova, I.A. Rudnev, A.E. Khodot, A.V. Eremin, and A.A. Titov, Effect of HfN microadditions on the microstructure and superconducting properties of $(Bi,Pb)_2Sr_2Ca_2Cu_3O_{10+x}$ ceramics, *Neorg. Mater.* 39, 462–468 (2003).
22. M. Ishizuka, Y. Tanaka, and H. Maeda, Superconducting properties and microstructures of Bi-2223 Ag–Cu alloy sheathed tapes doped with Ti, Zr, or Hf, *Physica C* 252, 339–347 (1995).
23. M. Ishizuka, Y. Tanaka, T. Hashimoto, and H. Maeda, Influence of Cu composition and sintering condition in Bi-2223 tapes using Ag–Cu alloy sheath doped with Ti, Zr or Hf, *Physica C* 290, 265–274 (1997).

24. C.S. Pande, Microstructural aspects of high and low T_c superconductors, *Mater. Phys. Mech.* 2, 1–9 (2000).
25. S.X. Dou, H.K. Liu, M.H. Apperley, K.H. Song, C.C. Sorrell, K.E. Easterling, J. Niska, and S.J. Guo, Improvement of critical current density in the Bi–Pb–Sr–Ca–Cu–O system through hot isostatic pressing, *Physica C* 167, 525–528 (1990).
26. R.R. Daminov, M.F. Imayev, M. Reissner, W. Steiner, M.V. Makarova, and P.E. Kazin, Improvement of pinning in Bi2212 ceramics by hot plastic deformation, *Physica C* 408–410, 46–47 (2004).
27. O. Yu Gorbenko, V.N. Fuflygin, Yu.Yu. Erokhin, I.E. Graboy, A.R. Kaul, Yu.D. Tretyakov, G. Wahl, and L. Klippe, YBCO and BSCCO thin films prepared by wet MOCVD, *J. Mater. Chem.* 4, 1585–1589 (1994).
28. V.M. Pan, A.L. Kasatkin, V.L. Svetchnikov, and H.W. Zandbergen, Dislocation model of superconducting transport properties of YBCO thin films and single crystals, *Cryogenics* 33, 21–27 (1993).
29. B. Dam, J.M. Huijbregtse, F.C. Klaassen, R.C.F. Van der Geest, G. Doornbos, J.H. Rector, A.M. Testa, S. Freisem, J.C. Martinez, B. Stäuble-Pümpin, and R. Griessen, Origin of high critical currents in $YBa_2Cu_3O_{7-\delta}$ superconducting thin films, *Nature* 399, 439–442 (1999).
30. A. Volodin, K. Temst, Y. Bruynseraede, C.V. Haesendonck, M.I. Montero, I.K. Schuller, B. Dam, J.M. Huijbregtse, and R. Griessen, Magnetic force microscopy of vortex pinning at grain boundaries in superconducting thin films, *Physica C* 369, 165–170 (2002).
31. H. Yamada, H. Yamasaki, K. Develos-Bagarinao, Y. Nakagawa, Y. Mawatari, J.C. Nie, H. Obara, and S. Kosaka, Flux pinning centres correlated along the *c*-axis in PLD-YBCO films, *Supercond. Sci. Technol.* 17, 58–64 (2004).
32. J. Wiesner, C. Traeholt, J.-G. Wen, H.-W. Zandbergen, G. Wirth, and H. Fuess, High resolution electron microscopy of heavy-ion induced defects in superconducting Bi-2212 thin films in relation to their effect on J_c, *Physica C* 268, 161–172 (1996).
33. W. Gerhauser, G. Ries, H.W. Neumuller, W. Schmidt, O. Eibl, G. Saemann-Ischenko, and S. Klaumunzer, Flux line pinning in $Bi_2Sr_2Ca_1Cu_2O_x$ crystals: interplay of intrinsic 2D behavior and irradiation induced columnar defects, *Phys. Rev. Lett.* 68, 879–882 (1992).
34 B. Roas, L. Schultz, B. Hensel, G. Saemann-Ischenko, and G. Endres, Superconducting properties of irradiation induced effects in epitaxial Y–Ba–Cu–O thin films, *Thin Solid Films* 174, 179–183 (1989).
35. J.R. Thompson, J.G. Ossandon, L. Krusin-Elbaum, H.J. Kim, K.J. Song, D.K. Christen, and J.L. Ullmann, Vortex pinning in high-T_c materials via randomly oriented columnar defects, created by GeV proton-induced fission fragments, *Physica C* 378–381, 409–415 (2002).
36. R. Weinstein, R. Sawh, Y. Ren, M. Eisterer, and H.W. Weber, The role of uranium chemistry and uranium fission in obtaining ultra-high J_c in textured Y123, *Supercond. Sci. Technol.* 11, 959–962 (1998)
37. R. Weinstein, R. Sawh, Y. Ren, and D. Parks, The role of uranium with and without irradiation, in the achievement of $J_c \approx 300000$ A cm^{-1} at 77 K in large grain melt-textured Y123, *Mater. Sci. Eng. B* 53, 38–44 (1998).
38. D. Milliken and S.X. Dou, Chemistry of uranium compound doping in $(Bi,Pb)_2Sr_2Ca_2Cu_3O_x$/silver superconducting tapes, *Physica C* 341–348, 1411–1414 (2000).
39. D. Marinaro, S.X. Dou, J. Horvat, Y.C. Guo, J. Boldeman, A. Gandini, R. Weinstein, R. Sawh, and Y. Ren, The effects of uranium doping and thermal neutron irradiation on the pinning properties of Ag/Bi-2223 Tapes, *Physica C* 341–348, 1119–1120 (2000).
40. P.E. Kazin and Yu.D. Tretyakov, Microcomposites based on superconducting cuprates, *Russian Chem. Rev.* 72, 849–865 (2003).
41. Yu.D. Tretyakov and E.A. Goodilin, Chemical principles of preparation of metal-oxide superconductors, *Russian Chem. Rev.* 69, 1–34 (2000).
42. L. Zhou, S.K. Chen, K.G. Wang, X.Z. Wu, P.X. Zhang, and Y. Feng, Synthesis of ultrafine Y_2BaCuO_5 powder and its incorporation into YBCO bulk by powder melting process, *Physica C* 363, 99–106 (2001).
43. S. Nariki, M. Matsui, N. Sakai, and M. Murakami, Refinement of RE211 particles in melt-textured RE–Ba–Cu–O bulk superconductors, *Supercond. Sci. Technol.* 15, 679–682 (2002).
44. Y. Feng, A.K. Pradhan, Y. Zhao, S.K. Chen, Y. Wu, C.P. Zhang, G. Yan, J.K.F. Yau, L. Zhou, and N. Koshizuka, Improved flux pinning in PMP $YBa_2Cu_3O_y$ superconductors by submicron Y_2BaCuO_5 addition, *Physica C* 385, 363–367 (2003).

45. L. Zhou, S.K. Chen, K.G. Wang, X.Z. Wu, P.X. Zhang, Y. Feng, H.H. Wen, and S.L. Li, Preparation of enhanced J_c YBCO bulks by powder melting process with a combination of submicron 211 precursor and Pt addition, *Physica C* 371, 62–68 (2002).
46. T. Mochida, N. Sakai, S.-I. Yoo, and M. Murakami, Pinning properties in melt-processed $YbBa_2Cu_3O_{7-\delta}$ with finely dispersed Yb_2BaCuO_5 inclusions, *Physica C* 366, 229–237 (2002).
47. T. Mochida, N. Chikumoto, and M. Murakami, Flux pinning by $Nd_4Ba_2Cu_2O_{10}$ inclusions in $NdBa_2Cu_3O_{7-\delta}$ superconductors: a combined effect of point, interface, and pinning at elevated temperatures, *Phys. Rev. B* 62, 1350–1360 (2000).
48. M.P. Delamare, H. Walter, B. Bringmann, A. Leenders, and H.C. Freyhardt, Macrosegregation of Y_2BaCuO_5 particles in top-seeded melt textured monoliths, *Physica C* 323, 107–114 (1999).
49. J. Pötschke and V. Rogge, On the behaviour of foreign particles at an advancing solid–liquid interface, *J. Cryst. Growth* 94, 726–738 (1989).
50. S. Nariki, N. Sakai, M. Murakami, and I. Hirabayashi, High critical current density in Y–Ba–Cu–O bulk superconductors with very fine Y211 particles, *Supercond. Sci. Technol.* 17, 30–35 (2004).
51. P. Diko, L. Shlyk, and G. Krabbes, Ru assisted total 211 particle pushing in melt-grown Y123 superconductor, *Physica C* 390, 143–150 (2003).
52. T. Umemura, K. Egawa, S. Kinouchi, S. Utsunomiya, and M. Nojiri, Synthesis and superconducting properties of BSCCO including precipitates with high density, *Phase Transit.* 42, 47–51 (1993).
53. T. Matsushita, T. Nakatani, E.S. Otabe, B. Ni, T. Umemura, K. Egava, S. Kinouchi, A. Nozaki, and S. Utsunomiya, Irreversibility line superconducting Bi-2212 single grain with fine normal particles, *Cryogenics* 33, 251–255 (1993).
54. M.R. Koblischka, S.G. Huang, K. Fossheim, T.H. Johansen, and H. Bratsberg, Evidence for pinning by $(Sr,Ca)_2CuO_y$ partial-melting processed bulk $Bi_2Sr_2CaCu_2O_{8+\delta}$ ceramics, *Physica C* 300, 207–211 (1998).
55. X.L. Wang, J. Horvat, H.K. Liu, and S.X. Dou, Enhanced flux pinning from CuO inclusions in $Bi_2Sr_2CaCu_2O_y$ crystals, *J. Appl. Phys.* 81, 533–535 (1997).
56. J.C.L. Chow, H.T. Leung, W. Lo, and D.A. Cardwell, Effects of Pt doping on the size distribution and uniformity of Y_2BaCuO_5 particles in large-grain YBCO, *Supercond. Sci. Technol.* 11, 369–374 (1998).
57. M. Yoshida, N. Ogava, I. Hirabayashi, and S. Tanaka, Effects of the platinum group element addition on preparation of Y–Ba–Cu–O superconductor by melt growth method, *Physica C* 185–189, 2409–2410 (1991).
58. K. Osamura, N. Matsukura, Y. Kusumoto, S. Ochiai, B. Ni, and T. Matsushita, Improvement of critical current density in $YBa_2Cu_3O_{6+x}$ superconductor by Sn addition, *Jpn. J. Appl. Phys.* 29, 1621–1623 (1990).
59. K.V. Paulose, P. Murugaraj, J. Koshy, and A.D. Damodaran, $YBa_2SnO_{5.5}$: a new phase in $YBa_2Cu_3O_7$–SnO_2 system, *Jpn. J. Appl. Phys.* 31, 1323–1325 (1992).
60. R. Weinstein and R.-P. Sawh, A class of chemical pinning centers including two elements foreign to HTS, *Physica C* 383, 438–444 (2003).
61. R.-P. Sawh, R. Weinstein, D. Parks, A. Gandini, Y. Ren, and I. Rusakova, Tungsten and molybdenum double perovskites as pinning centers in melt-textured Y123, *Physica C* 383, 411–416 (2003).
62. P.E. Kazin, V.V. Poltavets, V.V. Lennikov, R.A. Shuba, E.A. Eremina, Yu.D. Tretyakov, M. Jansen, B. Freitag, G.F. de la Fuente, and A. Larrea, Formation of stable phase inclusions in Bi-2212 and Bi(Pb)-2223 materials, in *High-Temperature Superconductors and Novel Inorganic Materials*. G. Van Tendeloo, E.V. Antipov and S.N. Putilin, Eds., Kluwer Academic Publishers, Dordrecht, 1999, pp. 69–74.
63. P.E. Kazin, Superconducting phases $Bi_2Sr_2CaCu_2O_{8+\delta}$ and $Bi(Pb)_2Sr_2Ca_2Cu_3O_{10+\delta}$ in multi-component oxide systems, *Zh. Neorg. Khim.* 47, 703–711 (2002).
64. V.V. Lennikov, P.E. Kazin, V.I. Putlyaev, Yu.D. Tretyakov, and M. Jansen, Influence of magnesium oxide on the properties of high temperature superconductor $Bi_2Sr_2CaCu_2O_{8+x}$ obtained by melt techniques, *Zh. Neorg. Khim.* 41, 911–915 (1996).
65. P.E. Kazin, Y.D. Tretyakov, V.V. Lennikov, and M. Jansen, Formation of the $Bi_2Sr_2CaCu_2O_{8+x}$ superconductor with $Mg_{1-x}Cu_xO$ inclusions: the phases compatibility and the effect of the preparation route on the material microstructure and properties, *J. Mater. Chem.* 11, 168–172 (2001).
66. W. Wei, Y. Sun, Y. Schwartz, K. Goretta, U. Balachandran, and A. Bhargava, Preparation and properties of nanosize TiO_2 and MgO-doped $Bi_2Sr_2CaCu_2O_x$ tapes, *IEEE Trans. Appl. Supercond.* 7, 1556–1559 (1997).

67. W. Wei, J. Schwartz, K.C. Goretta, U. Balachandran, and A. Bhargava, Effects of nanosize MgO additions to bulk $Bi_{2.1}Sr_{1.7}CaCu_2O_x$, *Physica C* 298, 279–288 (1998).
68. B. Zhao, W.H. Song, X.C. Wu, W.D. Huang, M.H. Pu, J.J. Du, Y.P. Sun, and H.C. Ku, Enhanced flux pinning in Bi2212 single crystal embedded with MgO particles, *Supercond. Sci. Technol.* 13, 165–168 (2000).
69. P.E. Kazin, V.V. Poltavets, Y.D. Tretyakov, M. Jansen, B. Freitag, and W. Mader, Study on the superconducting composite material formation in the system $Bi_2Sr_2CaCu_2O_{8+x}$/Al-containing phases, *Physica C* 280, 253–266 (1997).
70. P.E. Kazin, V.V. Poltavets, Yu.D. Tretyakov, M. Jansen, B. Freitag, and W. Mader, Phase and microstructure evolution in the process of the composite Bi-2212 — $(Sr,Ca)_3Al_2O_6$ glass-ceramics formation, *Supercond. Sci. Technol.* 12, 475–480 (1999).
71. P.E. Kazin, M. Jansen, A. Larrea, G.F. de la Fuente, and Yu.D. Tretyakov, Flux pinning improvement in Bi-2212 silver sheathed tapes with submicron $SrZrO_3$ inclusions, *Physica C* 253, 391–400 (1995).
72. P.E. Kazin, R.A. Shuba, Yu.D. Tretyakov, A.V. Knotko, M. Jansen, and B. Freitag, Formation of Bi-2212-based composites with submicrometer-grained $(Sr,Ca)SnO_3$, *Supercond. Sci. Technol.* 13, 134–139 (2000).
73. P.E. Kazin, V.V. Poltavets, M.S. Kuznetsov, D.D. Zaytsev, Yu.D. Tretyakov, M. Jansen, and M. Schreyer, Phase compatibility and preparation of Bi-2212-$Sr_{1-x}Ca_xIn_2O_4$ composite, *Supercond. Sci. Technol.* 11, 880–886 (1998).
74. P.E. Kazin, A.A. Kovalevski, V.V. Poltavets, Yu.D. Tretyakov, and M. Jansen, Preparation of the $Bi_2Sr_2CaCu_2O_{8+x}$-matrix composites containing fine strontium calcium indate inclusions via glass crystallization, *Inorg. Mater.* 37, 1183–1187 (2001).
75. P.E. Kazin, A.S. Karpov, M. Jansen, J. Nuss, and Yu.D. Tretyakov, Crystal structure and properties of strontium phosphate apatite with oxocuprate ions in hexagonal channels, *Z. Anorg. Allgem. Chem.* 629, 344–352 (2003).
76. P.E. Kazin, A.S. Karpov, Yu.D. Tretyakov, and M. Jansen, Formation of $SrSnO_3$ shell-like inclusions in the $Bi_2Sr_2CaCu_2O_{8+x}$ superconductor via chemical reaction, *Solid State Sci.* 3, 285–290 (2001).
77. P.E. Kazin, A.S. Karpov, M.V. Makarova, A.A. Kovalevski, Yu.D. Tretyakov, and M. Jansen, Formation of fine precipitates with different shapes in Bi-2212 material. *VI Proceedings of the International Workshop on High Temperature Superconductors and Novel Inorganic Materials Engineering, June 24–30, 2001, Moscow - St.Petersburg, Book of Abstracts*, PII-29.
78. P. Yang and C.M. Lieber, Nanorod-superconductor composites: a pathway to materials with high critical current densities, *Science* 273, 1936–1940 (1996).
79. L. Hua, G. Qiao, J. Yoo, J. Ko, H. Kim, and H. Chung, Microstructure and phase evolution of ultrafine MgO doped Bi-2223/Ag tapes, *Physica C* 291, 149–154 (1997).
80. X. Wan, Y. Sun, W. Song, L. Jiang, K. Wang, and J. Du, Enhancement flux pinning of silver-sheathed $(Bi,Pb)_2Sr_2Ca_2Cu_3O_x$ tapes with nano-MgO particle addition, *Supercond. Sci. Technol.* 11, 1079–1081 (1998).
81. W.D. Huang, W.H. Song, Z. Cui, B. Zhao, M.H. Pu, X.C. Wu, T. Hu, Y.P. Sun, and J.J. Du, Enhancement of flux pinning in (Bi,Pb)-2223/Ag tapes doped with MgO nanorods, *Supercond. Sci. Technol.* 13, 1499–1504 (2000).
82. P. Majewski, The use of phase diagrams for the engineering of flux pinning centres in $Bi_2Sr_2CaCu_2O_8$ ceramics, *Appl. Supercond.* 3, 289–301 (1995).
83. P. Majewski, F. Aldinger, and S. Elschner, Enhanced pinning by second-phase precipitates in Sr rich "$Bi_2Sr_2CaCu_2O_8$" ceramics, *Physica C* 249, 234–240 (1995).
84. P. Majewski, S. Kaesche, F. Aldinger, S. Elschner, B. Hettich, and C. Lang, The increase of pinning in $(Bi,Pb)_2Sr_2Ca_2Cu_3O_{10+d}$ bulk ceramics, *Supercond. Sci. Technol.* 7, 514–517 (1994).
85. V. Putlayev, S. Sokolov, P. Kazin, A. Veresov, and Yu. Tretyakov, On the phase decomposition of $Bi_2Sr_2CaCu_2O_8$, *Solid State Ionics* 101–103, 1075–1078 (1997).
86. A.V. Knotko, A.V. Garshev, M.N. Pulkin, and V.I. Putlyaev, Solid solution homogeneity area on the base of $Bi_2Sr_2CaCu_2O_8$ with alkaline-earth elements by Nd and La substitution, *Zh. Neorg. Khim.* 46, 1364–1367 (2001).
87. A.V. Knotko, A.V. Garshev, M.N. Pulkin, V.I. Putlyaev, and S.I. Morozov, Interconnection between oxygen atoms and the kinetics of solid solutions oxidation on the base of $Bi_2Sr_2CaCu_2O_8$, *Fizika Tverdogo Tela* 46, 414–418 (2004).

88. J. Shimoyama, Y. Nakayama, K. Kitazawa, K. Kishio, Z. Hiroi, I. Chong, and M. Takano, Strong flux pinning up to liquid nitrogen temperature discovered in heavily Pb-doped and oxygen controlled Bi2212 single crystals, *Physica C* 281, 69–75 (1997).
89. I. Chong, Z. Hiroi, M. Izumi, J. Shimoyama, Y. Nakayama, K. Kishio, T. Terashima, Y. Bando, and M. Takano, High critical-current density in the heavily Pb-doped $Bi_2Sr_2CaCu_2O_{8+\delta}$ superconductor: generation of efficient pinning centers, *Science* 276, 770–773 (1997).
90. M.R. Koblischka, A.J.J. van Dalen, T. Higuchi, S.I. Yoo, and M. Murakami, Analysis of pinning in $NdBa_2Cu_3O_{7-\delta}$ superconductors, *Phys. Rev. B* 58, 2863–2867 (1998).
91. T. Higuchi, S.I. Yoo, and M. Murakami, Comparative study of critical current densities and flux pinning among a flux-grown $NdBa_2Cu_3O_y$ single crystal, melt–textured Nd–Ba–Cu–O, and Y–Ba–Cu–O bulks, *Phys. Rev. B* 59, 1514–1527 (1999).
92. M. Muralidhar, M. Jirsa, N. Sakai, and M. Murakami, Matrix chemical ratio and its optimization for highest flux pinning in ternary (Nd–Eu–Gd)$Ba_2Cu_3O_y$, *Supercond. Sci. Technol.* 15, 688–693 (2002).
93. M. Muralidhar, M. Jirsa, N. Sakai, and M. Murakami, Progress in melt-processed (Nd–Sm–Gd)$Ba_2Cu_3O_y$ superconductors, *Supercond. Sci. Technol.* 16, R1–R16 (2003).

16 Electrochemical Deposition of Nanostructured Metals

E. J. Podlaha, Y. Li, J. Zhang, Q. Huang, A. Panda, A. Lozano-Morales, D. Davis, and Z. Guo
Louisiana State University, Baton Rouge, Louisiana

CONTENTS

ABSTRACT

Nanostructured materials fabricated by electrodeposition and electroless processes are presented in this chapter. The fundamental issues that dictate the control of the reaction rate and ensuing thickness and composition of the deposit are discussed in relation to compositionally modulated nanolayers in a variety of architectures — nanowires, pillars, tubes, core-shell nanoparticles, and composite materials. The electrochemical processing technique is, in some cases, an alternative to other techniques like vapor-deposition methods, but it also finds an exclusive niche for the deposition of nanostructured materials of high aspect ratio geometries. This chapter discusses a variety of nanomaterials for industrial applications in order to demonstrate the vast richness promised by electrochemistry.

16.1 INTRODUCTION

Electrochemical deposition of metals is an ancient art that has emerged as an integral process for the fabrication of nanosize features. Electrodeposition, electroless deposition, and displacement reactions are used to deposit metals, alloys, and metal-matrix composite materials, governed by electrochemical reactions. Electrochemically prepared nanomaterials, characterized by at least one dimension in the nanometer range, include nanostrutured thin-film multilayers, nanowires, nanowires with nanometric

layers, nanotubes, nanosize particles embedded into metal matrices, and discrete or pressed nanoparticles with metal shells. Owing to the nanometric nature of the structure, the physical properties of nanomaterials can be significantly different from bulk materials having the same composition.

Electrodeposition refers to the reduction of metal ions with an impressed current (or potential). In contrast, electroless and displacement processes occur without an impressed current (or potential). Magnetic compositionally modulated multilayered thin films and nanowires are typical examples of electrodeposited nanostructured materials, while coatings around nanoparticles and lining nanoporous walls have been carried out by displacement and electroless processes. Electrochemical deposition has emerged not only as a cost-effective alternative to vapor-deposition methods for thin films, but also finds a niche in nanotechnology as a preferred method to deposit nanostructured layers onto irregular substrates and into deep recesses, enabling unique materials such as nanotubes and wires to be fabricated.

16.2 COMPOSITIONALLY MODULATED MULTILAYER

Compositionally modulated multilayer (CMM) materials are synthesized by deposition of alternate layers having different compositions in a sandwich-like fashion. One of the first examples of CMMs was demonstrated by Blum in 1921, when alternate Cu and Ni layers, tens of microns thick, were deposited from two different electrolytes. The resulting Cu/Ni multilayer improved the tensile strength of the electrodeposit compared to elemental copper deposits.[1] Today, CMM materials of interest in other systems include not only mechanical properties[2,3] (e.g., fracture and tensile strength, hardness) but also magnetic properties.[4,5] Magnetic multilayers separated by paramagnetic layers on the nanoscale give rise to giant magnetoresistance (GMR), characterized by a decrease in resistance ($>1\%$) with an applied magnetic field, as the magnetic domains change from an anti-ferromagnetic alignment to one that is in the direction of the magnetic field. Cobalt—copper, multilayer, Co/Cu, is one example that has been thoroughly examined, both in the form of a thin film[6–12] and nanowire.[13–15]

Figure 16.1 shows the MR response of an electrodeposited Co/Cu multilayer film with 1000 repeat bilayers, deposited from a pH 3 electrolyte containing 0.005 *M* $CuSO_4$, 0.5 *M* $CoSO_4$, and 0.54 *M* boric acid. The copper was deposited with a low-current density of $-0.2\,mA/cm^2$ and the cobalt at a high-current density of $20\,mA/cm^2$, under quiescent conditions. The current flow during the

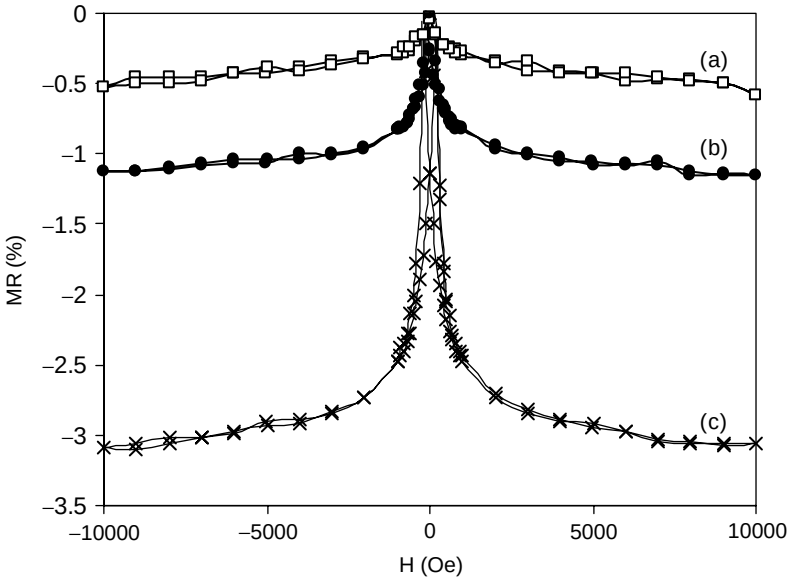

FIGURE 16.1 Co/Cu multilayers having 1000 bilayers, deposited on (111) Si, with 2.5 nm Co layer thickness and variable Cu layer thicknesses at room temperature: (a) 1 nm, (b) 1.5 nm, (c) 2 nm.

MR measurement was parallel to the multilayers, commonly referred to as current-in-plane (CIP) MR. The magnetic field in this example was perpendicular to the current flow (i.e., transverse). Repeating the experiment with the magnetic field aligned parallel to the layers and current flow (i.e., longitudinal) has been used to assess the quantity of the MR that arises from anisotropic magnetoresistance, which is typically less than 1%. However, such experimental probing assumes that GMR is isotropic. Recent theoretical and experimental evidence, however, has questioned this assumption.[16,17]

The decrease in resistance is dependent upon a variety of factors, including the choice of electrolyte, bilayer number and layer sizes, as depicted in Figure16.1. Larger room temperature GMR-percentage changes have been reported with thinner electrodeposited films having less than 100 bilayers,[6–8,18–22] although the values are still 2–4 times lower than vapor-deposited counterparts.[23]

Electrodeposition on multilayers can be carried out using a single or dual bath approach. Dual-bath electrodeposition requires that either the substrate or electrolyte be transferred during the deposition of each layer. To simplify the process, a single bath is more desirable and compositional modulation of the layers can be achieved by pulsing the current (or potential), as used to deposit the Co/Cu example in Figure 16.1.

Figure 16.2 shows the steady-state partial current densities of two depositing metals, M_1 and M_2 at the working electrode from a single electrolyte, where represents the more noble metal. The total polarization is shown as the dotted line. At point A, the reduction of M_1 occurs. At more negative potentials, such as at point B, both M_1 and M_2 deposit simultaneously. At point B, the rate of deposition of M_2 is larger than that of M_1, as a result of which the deposit is rich in the second component. In order to obtain layers with the highest purity, it is desireable for the rate of deposition of M_1 to be as small as possible, while depositing the M_2-rich layer. The trade-off, however, is that the low M_1 rate extends the processing time. Either the potential or current can be modulated in a square-wave pulse to fabricate the multilayers. Scanning tunneling microscopy of cleaved cross-sections of lead–thallium–oxygen nanometer size deposits showed that potentiostatic pulses resulted in more discrete layers than galvanostatic pulses.[24] However, no single method, pulsed-potentiostatic vs. pulsed-galvanostatic control, has been shown to exhibit superior GMR, including a potentiostatic/ galvanostatic scheme.[9]

In order to limit the reaction rate of the more noble species, its concentration in the electrolyte is maintained at a value that is orders of magnitude lower than the other metal ion species. In the example given in Figure 16.1, the electrolyte composition of Cu(II), M_1, is 100 times lower than Co(II), M_2, which permits a layered deposit when the current is pulsed. Thus, at point B, the reaction rate of M_1 reaches a mass-transport-limiting current density, i_{lim}. At steady state, an estimate of the limiting current density can be readily determined, assuming that diffusion is the dominant mode of transport with a Nernstian boundary layer approximation,

$$i = i_{lim} = \frac{-nFDC^b}{\delta} \tag{16.1}$$

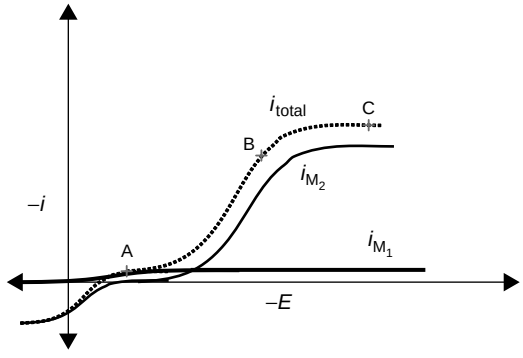

FIGURE 16.2 Sketch of two electrodepositing metals with disparate reaction rates.

where D (cm^2/sec) is the diffusion coefficient of the reacting species, C^b (mol/cm^3) its bulk concentration, δ (cm) the mass transport boundary layer thickness, n (equiv/mol) the number of electrons transferred, fixed by the reaction under consideration, and F (A s/equiv) the Faraday's constant (96485 C/equiv). The boundary layer thickness is the most difficult to ascertain as it is dependent on the hydrodynamic environment surrounding the electrode. In initially quiescent conditions, δ is typically several hundred microns, while it is only tens of microns in vigorously well-mixed electrolytes. A comprehensive list of limiting current correlations for different electrode shapes and hydrodynamic conditions has been tabulated by Selman and Tobias.[25]

The less noble reactant, M_2, is in excess in the electrolyte, and generally deposits under kinetic control during multilayer fabrication. Deposition far from equilibrium can be approximated by a Tafel equation, according to

$$i = -i_0 \exp\left(\frac{-\alpha_c F}{RT}\eta_s\right) \tag{16.2}$$

which requires knowledge of two kinetic parameters, the exchange-current density, i_0 (A/cm^2) and the cathodic-transfer coefficient, α_c- (dimensionless). These values have been reported for a wide variety of reactions; however, i_0 is dependent on the species' activity, i.e., concentration, and is highly specific to a particular electrolyte. The surface overpotential, η_s- (V), is the polarization away from the equilibrium potential, when no concentration gradients occur. If the polarization is large, kinetic control of the M_2 reaction gives way to a transport control as described by Equation (16.1), and depicted at point C in Figure 16.2. Deposition, however, is typically not desirable at this region, where both species are dominant by mass transport, due to the development of rough-surface deposits and excess-side reactions from the solvent (not shown in Figure 16.2) that contributes to a loss in efficiency.

Kinetic behavior is characterized by a uniform concentration distribution of reactants near the electrode surface. During the multilayer fabrication, if the more noble species, M_1, is deposited below point A (Figure 16.2), under kinetic control, and then is co-deposited at point B (Figure 16.2), under mass transport control, there will be a change in the noble metal-concentration gradient that is time-dependent, resulting in a compositional gradient within the alloy layer. Classical descriptions of a single reacting species under a time-dependent diffusion control for a galvanostatic or potentiostatic pulse have been developed by Sands and Cottrell.[26] Owing to the enhanced compositional gradient of a reactant during pulsing, its limiting current is subsequently enhanced during the pulse. An expression for the larger pulse limiting current density, i_p, compared with the DC, unpulsed, counterpart (Equation [16.1]) for a galvanostatic pulse, has been elegantly described by Cheh[27,28]

$$i = i_p = i_{lim}\left(1 - \frac{8}{\pi^2}\left(\frac{r-1}{r}\right)\sum_{k=1}^{\infty}\frac{1}{2(k-1)^2}\,\frac{\exp[(2k-1)^2 a\theta_2]-1}{\exp[(2k-1)^2 a\theta]-1}\right)^{-1} \tag{16.3}$$

where r is the ratio of the first current-density pulse (point A, Figure 16.2) to the second value (point B, Figure 16.2), a ($=\pi^2 D/4\delta^2$) the diffusion parameter, θ_2 the second period duration, and θ the cycle time. Equation (16.3) predicts that for the CoCu/Cu system, the amount of Cu co-deposited with Co in the alloy layer of a multilayer will be larger than Cu co-deposited with Co as a DC plated bulk alloy. An analogous equation for potentiostatic-pulse deposition onto a rotating disk electrode has also been presented by Viswanathan and Cheh.[29]

In the lower left-hand corner of Figure 16.2, a portion of the anodic component of the partial-current density of the less noble metal species is shown. Depending on the kinetics of this reaction, there can be a simultaneous displacement of M_2 deposited metal by the more noble species, M_1, occurring at the start of the M_1 pulse during multi-layer electrodeposition. For the CoCu/Cu system, the displacement involves the following reactions:

$$\mathrm{Co(s)} \rightarrow \mathrm{Co(II)} + 2\mathrm{e}^- \tag{16.4}$$

$$Cu(II) + 2e^- \rightarrow Cu(s) \tag{16.5}$$

Note that the net current is controlled, so that even when the impressed current is cathodic (negative), there can still be a small anodic contribution, given by the following general expression:

$$i = i_0 \exp\left(\frac{\alpha_a F}{RT}\eta_s\right) \tag{16.6}$$

where α_a is the anodic transfer coefficient. The consequence of displacement reactions occurring during the processing of the multilayer not only results in a change in the composition, but can also exaggerate the concentration gradients at the layer interfaces. To suppress displacement reactions, strategies such as adding additives to alter the kinetic parameters in Equation (16.6) or alloying the magnetic layer with a corrosion resistance material can be considered. Chassaing[30] has shown that saccharin can inhibit the dissolution of cobalt in multilayer deposition, consistent with the alloy results of Kelly et al.[31] However, the GMR value of CoCu/Cu multilayers decreased by half. Jyoko et al.[32] found that adding a small amount of CrO_3 to a cobalt–copper electrolyte resulted in a thin-film GMR of over 18%, which could be attributed to the decrease in the displacement reaction. Similarly, large GMR values in cobalt–copper multilayers that contain Ni have also been reported by Schwarzacher and colleagues.[18–22,33–36] Our group found, from studies carried out on rotating-disk electrodes, that the addition of Ni(II) into a pH 5 boric acid electolyte decreased both the Cu-reduction reaction and the alloy-dissolution reaction.[37] Larger GMR values were observed with a small amount of Ni incorporated into the Co-alloy layer (Figure 16.3), consistent with earlier works of Schwarzacher and colleagues.

The partial-current density equations (16.1)–(16.3) and (16.6) are vitally important to the design and prediction of the layer at composition, x,

$$x_j = \frac{i_j/n_j F}{\sum_k i_k/n_k F} \tag{16.7}$$

and thickness, Δ, in conjunction with Faraday's law, which relates the mass plated to the charge passed,

$$\Delta = \sum_j \frac{M_j i_j t}{n_j \rho_j F} \tag{16.8}$$

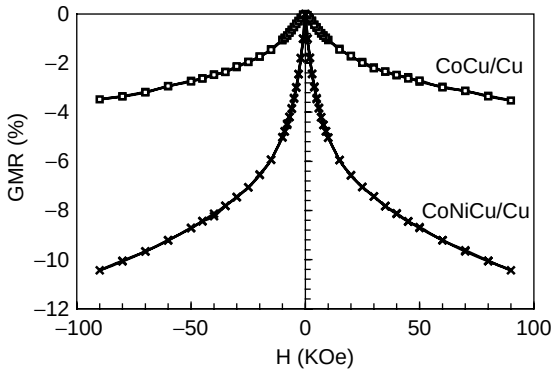

FIGURE 16.3 Giant magnetoresistance of two comparable electrodeposited multilayer films with one film containing 3.5 wt% Ni in the Co alloy layers, with 2000 bilayers, deposited at $-1.8\,mA/cm^2$, 1.54 sec, and $-353\,mA/cm^2$, 12.5 msec, onto a rotating-disk electrode (0.6 cm diameter) at 400 rpm.

for species j with atomic weight M, density ρ, and time of deposition, t. In the case of electrolytes containing mixtures of iron group (Co, Ni, Fe) ions, the kinetic information should be ascertained from the alloy electrolyte rather than from elemental, single-metal deposition, on account of the anomalous-co-deposition behavior. Anomalous co-deposition refers to the preferential deposition of the less noble metal species, and has been widely reviewed with regard to bulk alloy electrodeposition.[38–40] The behavior complicates the prediction of the alloy composition during multilayer fabrication. A mathematical model was developed by Huang and Podlaha,[41] that combined the nonsteady-state mass transport with an anomalous co-deposition kinetic mechanism, to simulate compositional gradients in an alloy multilayer of CoNiFeCu/Cu. The model shows that the composition gradients at the layer interface can be minimized by reducing displacement reactions and maximizing the mass transport boundary layer thickness.

16.3 NANOWIRES, PILLARS, AND TUBES

16.3.1 NANOWIRES

Deposition into recessed geometries is inherently amenable to improved electrodeposits from the point of view of minimizing concentration gradients within a multilayer. A number of templated nanostructured-electrodeposit examples are given in this section, although the most widely studied are nanowires. Template synthesis in nanoporous membranes have been carried out in anodic-aluminum oxide, polycarbonate, and diblock-copolymer membranes. Nanodimensional layers within a nanowire are of particular interest for GMR studies when the current flow is perpendicular to the plane of the layers, referred to as CPP-GMR. In contrast, current-in-plane giant magnetoresistance (CIP-GMR) is the preferred mode of measurement for thin-film multilayers because of the extremely small values of resistance in the perpendicular direction, which preclude accurate and easy analysis. In CIP-GMR, the characteristic scaling length is the electron mean-free path, typically a few nanometers. However, for CPP-GMR, the critical length scale is the spin-diffusion length, which is generally larger than 10 nm, and thus larger multilayer sizes can be tolerated. For example, GMR has been observed in multilayer nanowires with a layer size of 12 nm NiFeCu/4 nm Cu[44] and 5 nm CoCu/8 nm Cu — larger than typical thin-film multilayers.

Figure 16.4 shows a transmission electron micrograph (TEM) of a CoNiFeCu/Cu nanowire showing multilayers that are evident near the edge of a 200-nm-diameter wire. The layer sizes of the Co-rich alloy and Cu layers are 4 and 2 nm, respectively. The CPP-GMR of an array of nanowires is compared with a thin-film CIP-GMR with comparable layer sizes and chemical composition. While the GMR value is about the same (–5%), the magnetic field sensitivity clearly differs. Nanowires of multilayers have also been investigated for a variety of other systems. For example, room-temperature CPP-GMR of Co/Cu multilayer nanowires was reported to be 14–15%[44,45] and 20%.[14] CoNi/Cu nanowires have been reported[46,47] as possessing significantly larger GMR, 55% at room temperature. At low temperatures, such as those achieved by cooling in liquid helium, the coercivity of the material increases and two peaks develop in the GMR response with the applied magnetic field. A reduction in the coercivity is helpful in achieveing large-resistance changes in a low field and led to the development of NiFe/Cu electrodeposited multilayers.[45,48]

A variety of metallic, unlayered nanowires have been electrodeposited, following the seminal work of Whitney et al.[49] Elemental Ni and Co wires exihibiting perpendicular magnetization, a direct consequence of the nanowire geometry, have been deposited into polycarbonate membranes. In addition, the coercivity was enhanced as the wire diameter decreased. These features render magnetic nanowires of interest for high-density magnetic recording. Earlier work with Fe deposition into alumina-nanoporous templates also reported similar findings with an easy axis parallel to the wires with enhanced coercivity.[50,51] Magnetic-alloy nanowires that are not layered have been reported for CoFe,[52,53] CoNi,[54] NiFe,[55] and CoNiFe.[43]

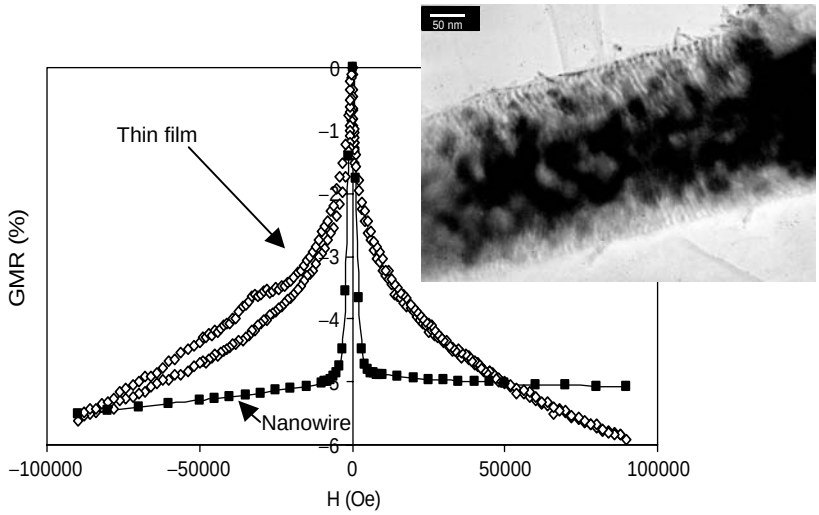

FIGURE 16.4 CoNiFeCu/Cu 200 nm nanowire CPP-GMR and CIP-GMR in a thin film. Inset, nanowire TEM exhibited. (From Huang, Q. et al., *J. Appl. Electrochem*., 2005. With permission.)

16.3.2 PILLARS

A disadvantage of nanowire deposition of multilayers is with the difficulty of measuring a single nanowire and the random array of the nanowires. An alternative architecture is micro-size pillars that still render GMR to be measured in the CPP mode. The resulting GMR pillars can thus be used as sensors for high-density magnetic storage.

The fabrication of CPP-GMR pillars has been demonstrated by vapor-deposition techniques etching through thin films of multilayers. For example, Gijs et al.[56] employed optical lithography and reactive-ion-etching techniques to fabricate pillars of vacuum-sputtered Fe/Cr multilayers, and molecular beam epitaxy evaporation deposition of Co/Cu multilayers. The samples had a height of 0.5 μm and a width ranging between 3 and 10 μm. Over 50% CPP-GMR was observed and the researchers showed that the CPP-GMR mode measurements were often larger than measurements in the CIP mode. Similarly, Spallas et al.[57] sputtered Co/Cu multilayer thin films and subsequently patterned an array of 0.4-μm-diameter circles. Electron-beam lithography was used to pattern a negative resist over the multilayer film. The pillars were formed by a dry etch of the multilayer having a height of 0.9-μm. A CPP-GMR of 13% was reported compared with the CIP-GMR for the same film of only 6%.

Electrodepostion of the multilayered material into a lithographic pattern, rather than by etching it, can offer a cost-effective alternative. In addition, the deposition of materials into deep recesses is problematic with vapor deposition, line-of-site type of techniques. The advantage of using electrodeposition for pillar fabrication is the same as for nanowire generation; it can offer conformal deposition in deep recesses. One notable early attempt of electrodeposited-multilayered pillars was carried out by Davail et al.[58] NiFe/Cu-multilayered nanopillars with a height of 0.3 μm and diameter of 0.1 μm were deposited, exhibiting a relatively low MR of 0.3% at temperature of 4.2 K. In our recent work, we combined x-ray lithography with electrodeposition to deposit CoCu/Cu multilayers into a deep recess with a height of 500 μm and a cross section of 183×183 μm. An array of representative posts is shown in Figure 16.5. A single pillar exhibits ~4% CPP-GMR with saturation-magnetic field <1 T at room temperature.

Typical diffusion layer thicknesses, δ, on planar electrodes in unagitated electrolytes are of the order of 100 μm. Thus, electrodeposition into deep recesses >100 μm, will extend the nonsteady-state regime for diffusion-controlled reactions, compared with planar electrodes. The convective hindrance of the recess further increases the diffusion boundary layer thickness by roughly the size

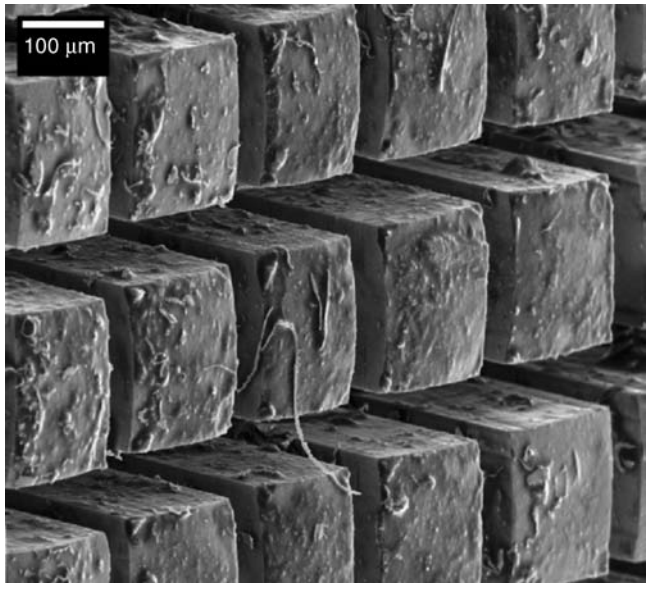

FIGURE 16.5 Array of CoCu microposts fabricated by x-ray lithography.

of the recess depth. An estimate of the change of the limiting-current density with time of a species inside a recess, where the outside pore-mouth region of the recess is well mixed, is given in two limits.[63] A short-time approximation for a reduction reaction follows

$$i = -nFc^b\left(\frac{D}{\pi t}\right)^{1/2}\left[1 + 2\exp\left\{\frac{-\pi^2 Dt}{L^2}\right\} + 2\exp\left\{\frac{-4\pi^2 Dt}{L^2}\right\} + \ldots\right] \tag{16.9}$$

where L is the recess depth. The leading term describes the Cottrell behavior on an unrecessed surface. At long times, the limiting current density is given as

$$i = \frac{-nFc^bD}{L}\left[1 + 2\exp\left\{\frac{-\pi^2 Dt}{L^2}\right\} + 2\exp\left\{\frac{-4\pi^2 Dt}{L^2}\right\} + \ldots\right] \tag{16.10}$$

and at steady state this reduces to Equation (16.1) where $\delta = L$.

Inspection of Equation (16.10) reveals that for typical metal ions, the time to achieve steady state in a recess hundreds of microns deep, can be several seconds to minutes. During multilayer pulse plating, the diffusion-controlled species, often Cu, is depositing under a nonsteady regime at the start of deposition, during both the magnetic alloy deposition layer and the elemental Cu layers. As the deposition proceeds, the limiting-current density of the transport-controlled species (e.g., Cu) will increase, due to a shortened boundary-layer thickness. In addition, the transient change in its concentration near the electrode surface is also altered so that steady state is achieved sooner. The consequence of this dynamic effect will result in more of the transport-controlled species in the second, magnetic layer, regardless of how the deposition is controlled, galvanostatically or potentiostatically.

16.3.3 NANOTUBES

Another type of nanometric architecture fabricated inside nanoporous membranes is nanotubes for advanced catalytic and sensory materials. Martin pioneered the use of electro-less deposition to create nanotubes in an experiement in which robust Au nanotubes with wall sizes only a few nanometers thick, in polycarbonate and alumina templates.[60,61]

Electro-less deposition of metals inside the pores of membranes requires use of a chemical reducing agent to deposit the metal onto a surface from solution. A sensitizer which binds to the pore wall is first used. The sensitized surface is activated by exposure to a catalyst, resulting in the formation of discrete nanoscopic-catalyst particles. Finally, the catalyst-covered surface is immersed in the electrolyte containing the ions of the metal to be deposited and the reducing agent, for a surface-constrained deposition on the pore walls. Therefore, at the pore surface, the cathodic reaction (metal deposition) is equal to the anodic reaction (oxidation of the reducing agent) without any external power supply. Dissolution of the membrane can release an array of deposited tubes if needed. Nanowires can also be achieved in this fashion by immersing the nanoporous membrane for longer periods of time. Unlike electrochemical deposition, electro-less deposition cannot control the length of the nanowires or the nanotubes. Also, the electro-less method provides no control over modulating composition for alloy deposition.

The rate of electro-less deposition is determined by knowing the rates of each reaction. Figure 16.6 shows schematically the partial current density of the cathode-deposition reaction ($M^{n+} + ne^- \rightarrow M$), and the anodic reaction of the reducing agent ($Red \rightarrow Ox + ne^-$). The equilibrium reduction/oxidation potential of the metal deposition, equilibrium potential, E_1, must be more noble, thus larger, than the reducing agent equilibrium potential, E_2, thus $E_1 > E_2$. The schematic in Figure 16.6 is often referred to as an Evan's diagram, depicting the absolute value of the partial current density with potential in order to view both the anodic and cathodic reactions in the same quandrant of the graph. A logarithm scale is used for the current-density axis, since kinetic expressions are exponential in nature (i.e., Equations [16.2] and [16.6]), and thus these regions will appear as potential-dependent straight lines. Potential-independent regions identify mass-transport control. The intersection of the two partial-current densities provides the resulting reaction rate, or current density of the electro-less process at a potential intermediate between the two equilibrium half-cell potentials. The Evan's diagram illustrates this concept of the "mixed-potential theory," where the resulting current density and potential of the electroless process depends on the kinetics or transport limitations involved in both the "mixed" anodic and cathodic systems.

Electrodeposition of Pt and Ni tubes and wires has been observed in aluminum oxide membranes by Yoo and Lee.[62] The tube formation was a result of a nonuniform electric field concentrated at the pore wall. Davis and Podlaha[63] showed that the generation of the tube could be controlled by selection of an electrolyte with low-current efficiency. A typical example of a tube released from a nanoporous membrane is shown in Figure 16.7. CoNiCu tubes were deposited from a boric acid electrolyte at a constant potential at current efficiencies $<50\%$. An increase in the current efficiency, by a change in the electrolyte composition, resulted in the wire formation. Thus, gas-evolving side reactions are suspected to be an additional controlling feature of tube formation.

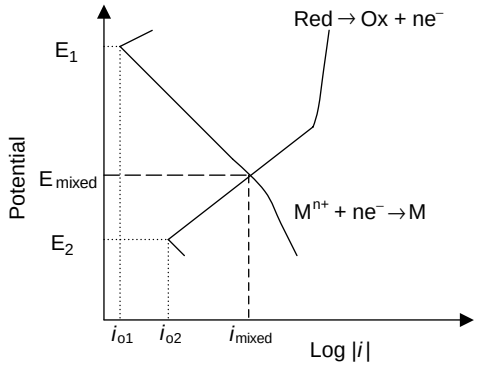

FIGURE 16.6 Schematic of the Evan's diagram showing the electroless process.

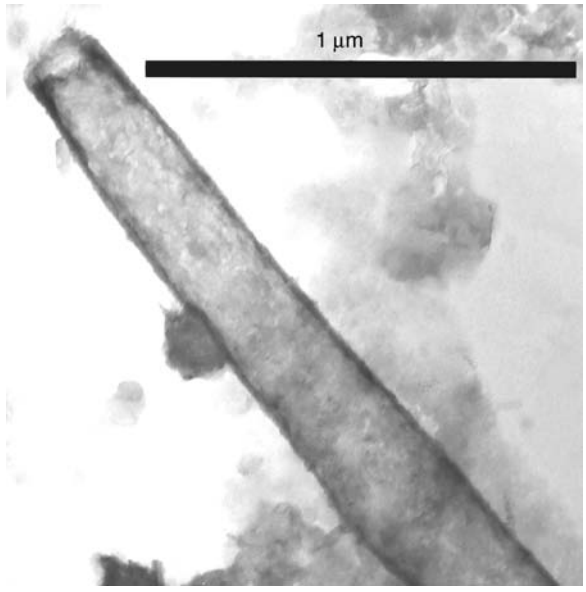

FIGURE 16.7 CoNiCu tubes electrodeposited from AAO membranes.

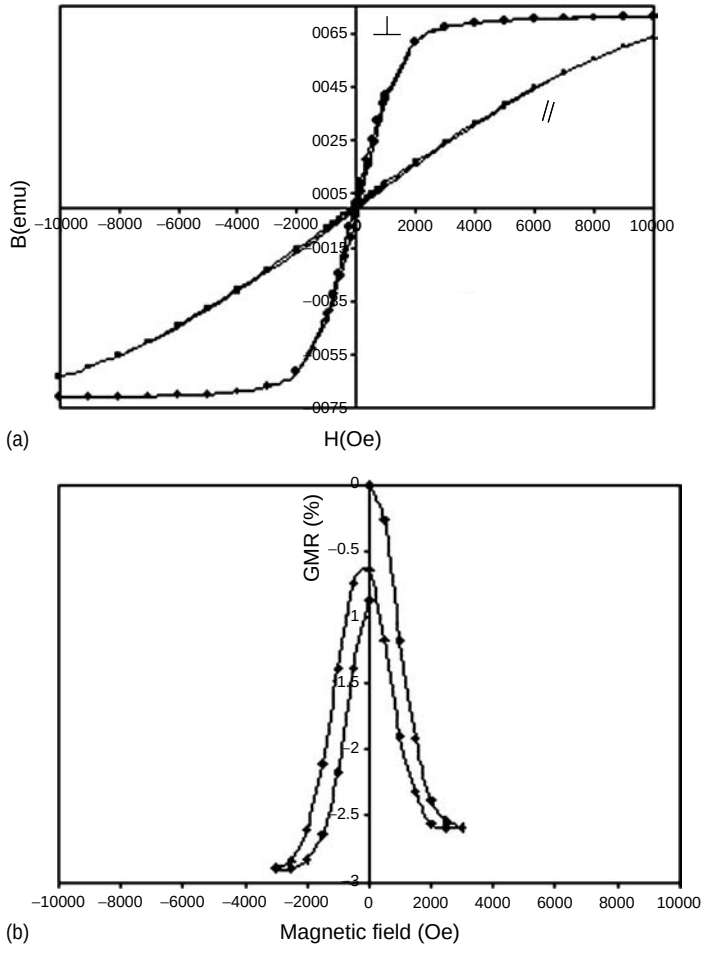

FIGURE 16.8 (a) CoNiCu/Cu room-temperature magnetization and (b) magnetoresistance in the CPP mode.

The properties of the nanotubes depend on the material being deposited. For magnetic materials, such as CoNiCu alloy tubes, magnetic anisotropy can occur. Modulating the applied potential or current will lead to layered tubes. Figure 16.8 shows a hysteresis plot and MR response of an array of CoNiCu/Cu nanotubes, deposited from an electrolyte containing $CoSO_4$ (50 m*M*), $NiSO_4$ (18 m*M*), $CuSO_4$ (1 m*M*), potassium tartrate (27 m*M*) and boric acid (5 m*M*) at pH 4. A double potentiostatic electrodeposition scheme was used: Cu layer (–0.325 V vs. SCE)/CoNi layer (–2 V vs. SCE) in 200-nm-diameter AAO membranes. Perpendicular anisotropy of the nanotubes is demonstrated in Figure 16.8(a); a small MR is shown in Figure 16.8(b). Although electrochemical deposition has the advantage of providing a versatile means to control composition of an alloy, its adaptation to nanotube formation is still in its infancy.

16.4 NANOPARTICULATE MATERIALS

16.4.1 NANOPARTICLES

Using template synthesis methods, such as alumina-porous membranes and track-etched polycarbonate porous membranes, to electrochemically deposit metal nanoparticles inside the pores has become popular in the recent years. These deposits have been studied in the context of a wide spectrum of scientific goals ranging from catalysis[64] to magnetic properties and magnetic-data storage.[65] Attention has also been focused on the application of small metal particles in surface-enhanced spectroscopy,[66] photocatalysis,[67,68] and selective solar absorbers.[69,70] Studies with atomic absorption have shown that iron, nickel, cobalt, and gold particles have equivalent areas per volume, with particle radii in the range 3 to 5 nm. Magnetic measurements on iron, nickel, and cobalt films reveal them to be highly anisotropic with magnetization perpendicular to the surface of the film. The unusual optical absorption of noble-metal nanoparticles such as copper, silver, and gold embedded in a dielectric medium such as alumina renders them of interest for optical applications. Electrochemical nucleation also plays a role in nanoparticle fabrication of metal nanoparticles at templated liquid/liquid interfaces.[71,73]

Iron, cobalt, and nickel nanoparticles have attracted much attention due to the enhanced magnetic properties such as coercivity[74,75] and magnetic moment.[76] The facile oxidation and dissolution in acidic environments limit their potential applications. Noble-metal shells such as gold and silver around nanoparticles can protect the nanoparticle core. Expensive catalytic materials (e.g., Pt) can also be used sparingly to coat inexpensive nanoparticles (e.g., Ni) to provide a cost-effective way to reduce the quantity of catalytic material needed for heterogenous reactions. To fabricate a metallic shell around a nanoparticle a variety of methods, such as the reverse micelle,[77–81] thermal-decomposition method,[82,83] photo-decomposition method,[84] and electrochemical displacement have been reported.[85–87] The displacement reaction can be carried out in neutral organic solutions[85,86] or in an aqueous electrolyte,[87] through the use of hydrophilic surfactant groups extending from the metal core. The resulting magnetic core-shell nanoparticles have potential applications in magnetic storage and as drug-delivery systems.

Core-shell nanoparticles generated by an electrochemical-displacement reaction (also referred to as immersion) is distinguished from electro-less deposition by the role of the substrate and the source of reducing agents. In electro-less deposition, the deposition reaction is driven by a reducing agent in the electrolyte and takes place on a catalytic substrate, whereas a displacement process results from the oxidation of the substrate surface without additional reducing agents, similar to the reactions in Equations (16.4) and (16.5). Electro-less and displacement depositions have one basic characteristic in common: no power supply is necessary to drive the deposition reaction. In brief, the displacement-reaction deposition can be carried out with noble-metal ions reduced by the nanoparticle. Table 16.1 shows the order of nobility of several relevant redox couples (in ascending order of nobility). According to the order of the equilibrium-standard potentials, a copper shell will form around a Co nanoparticle but an iron shell will not. In addition, the

TABLE 16.1
Selected Standard Potentials in Aqueous Solutions at 25°C vs. NHE[78]

Species	Fe/Fe^{2+}	Co/Co^{2+}	Cu/Cu^{2+}	$Pt/PtCl_4^{2-}$	Ag/Ag^{+}	Pd/Pd^{2+}	Pt/Pt^{2+}	Au/Au^{3+}
E^0(V)	−0.44	−0.277	0.340	0.758	0.7991	0.915	1.188	3.19

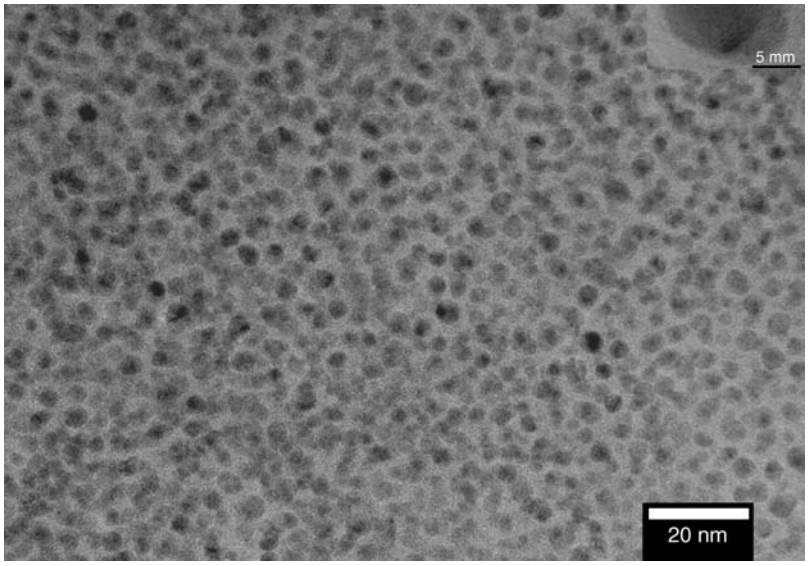

FIGURE 16.9 TEM micrograph of Co–Cu core-shell nanoparticles (inset shows the HRTEM image.) (Adapted from Guo, Z. et al., *J. Electrochem. Soc*., 152, D1–D5, 2005.)

standard-potential values also depend on the type of ion being reduced, as illustrated for the different values of Pt in Table 16.1.

Figure 16.9 shows a TEM micrograph of Co–Cu core-shell nanoparticles fabricated from a displacement reaction between Co nanoparticles and Cu(II) from a cupric sulfate–citrate electrolyte.[87] The cobalt-core nanoparticles were synthesized by a wet chemicalreduction method with superhydride as the reducing agent and 3-(*N*, *N*-dimethyldodecylammonio) propanesulfonate (SB-12) as stabilizer, following the procedure given by Boennemann et al.[89] The inset shows an expanded view of one nanoparticle revealing the (200) crystalline structure. It was observed that the cobalt nanoparticles with the copper shell have a higher blocking temperature compared with the cobalt precursor nanoparticles.

16.4.2 Metal-Matrix Nanocomposites

Metal-matrix composite electrodeposition refers to electrolysis in which nanoparticulates are suspended in the electrolyte and are subsequently embedded in the electro-formed solid phase. The particle deposition rate is affected by several interrelated parameters: the electrolyte concentration of the metal ions and particles, pH, current density (or potential), agitation, organic additives used to promote suspension, and particle size. The resulting composite possesses properties that differ from the bulk, depending on the degree and type of particle incorporation. Several reviews[90–93] have documented the wide variety of metal–matrix-particle systems, exhibiting enhanced properties such as corrosion and wear resistance, micro-hardness, and strength. Nanocomposites may also have a unique niche in the development of microdevices and micro-electromechanical systems (MEMS),

where the structural elements of the device are of the micron size, thus constraining the second phase particle to the nanoregime.

The models in the literature can be divided into two groups: those that predict the co-deposition behavior of large (micron size) particles[94] and those that are concerned with small (submicron size) particles.[95,96] The difference between the two is the mass-transport depiction of the particles. When particle size is large, of the order of microns, a Lagrangian approach can be used. Brownian motion is neglected and the particle trajectory can be determined by Newton's second law of motion. Brownian motion is most important for small particle sizes ($<1\,\mu m$), in which case a Eulerian method is applicable. Small particles may also be susceptible to electrokinetic effects if the potential field is high. However, in plating electrolytes where there is a high salt concentration, electrokinetic transport should be relatively small and can be neglected.

In both cases, the kinetics controlling particle incorporation requires that the particles reside at the electrode surface for a certain length of time. Guglielmi[97] was the first to propose an adsorption mechanism, which holds the particle at the electrode surface so that it is engulfed in the depositing metal. The adsorption was due to a loose and strong adsorption at the electrode surface. While many particles may be loosely adsorbed to the electrode surface, not all of them are strongly adsorbed and thus incorporated into the deposit. Only the second step (strong adsorption) was considered to be potential-dependent. Consequently, this mechanism supported experimental results showing that the particle concentration in the deposit increased with an increase in particles in the electrolyte and applied current density. This has been verified for micron and submicron particles in the case of the codeposition of SiC and TiO_2 with nickel[97] and alumina with copper.[98] Some limitations to Guglielmi's model are that hydrodynamic effects and the infuluence of particle size, which are two important parameters when plating into deep microstructures, were not considered.

Celis et al.[99] have proposed an alternative concept. They postulated statistically that there is a certain probability that a particle will become incorporated into a growing metal deposit. This idea is similar to the Guglielmi concept, recognizing that only a fraction of particles reaching the electrode surface is incorporated into the metal matrix. Additionally, the Celis, Roos, and Buelens' model included the important effect of hydrodynamics that was absent previously. They assumed that an adsorbed layer of ionic species occurs around the inert particles and that the reduction of these ionic species at the electrode surface is a requirement for particle incorporation. The particle thus travels from the bulk solution to the electrode surface with the adsorbed ions through convective–diffusion transport. The particle–ion complex then adsorbs onto the electrode surface, ions are reduced, and the particle is embedded into the electrodeposited metal.

Valdes and Cheh's model[100] also incorporated the mass transport of the particle and metal ion and presented three kinetic variations describing how the particle is influenced by the surrounding ions. One case was a "perfect sink" model, where all the particles that reach the electrode surface are embedded. This situation is perhaps unrealistic, but it gives a theoretical upper limit to the number of particles that are able to be codeposited at a given applied potential. More realistic approaches were the surface force boundary layer approximation and the electrode-ion-particle electron transfer models. In the former case, due to surface forces close to the electrode surface not all particles are co-deposited with the metal. Both attractive-and repulsive-surface force interactions were considered and described in terms of an energy-potential function at the electrode surface. The latter kinetic formulation is the most useful since it includes the effect of applied potential (or current) on the particle incorporation rate. The electroactive metal ion is assumed to be adsorbed onto the particle surface, and so the incorporation rate is directly linked with the metal deposition rate, as in the Celis, Roos, and Buelens' model. In agreement with experimental findings, the model predicts an increase in particle deposit concentration with applied current density up to a maximum and then decrease. The reason for the decrease in particle deposit concentration was the switch from a kinetic to diffusion control particle rate. Once the particle was diffusion-controlled, its rate remained the same as the current density increased. However, the rate of the metal deposition (still kinetically controlled) further increased with current density, resulting in a deposit with a lower particle content.

Fine particles have also been found to affect the metal-deposition rate. Inhibition of the metal reaction rate occurred when nanometric-size particles were present in the electrolyte. This feature has been observed by Webb and Robertson[101] for a nickel composite with nanometric alumina particles, and by Podlaha and Landolt[102] when alumina was co-deposited with copper. Webb and Robertson pointed out that if a blocking effect of the electrode surface by the particles is hypothesized to explain the metal inhibition, a very high particle coverage is necessary, even when a small amount of particles are found in the deposit. Therefore, some of the adsorbed particles at the electrode surface are not incorporated in the metal, consistent with the earlier kinetic models.[97,99] The effect of nanometric γ-Al_2O_3 particles (average diameter of 50 nm) on copper electrodeposition from a sulfuric acid electrolyte using a rotating-cylinder electrode has also been reported by Stojak and Talbot.[103] The current density decreased with the addition of particles in the kinetically limited region. Furthermore, Lozano-Morales and Podlaha[104] identified regions of copper inhibition and enhancement in the kinetic regime, with little change in the mass transport limiting-current density of copper when studying the effect of low amounts of γ-Al_2O_3 nanopowder in the electrolyte ($<$60 g/L).

In the mass-transport region of Cu deposition, Stojak and Talbot[103] observed an enhancement in the limiting-current density with a large particle loading in the electrolyte (e.g., 158 g/L), suggesting that the particles affected the boundary-layer thickness around the electrode. Panda and Podlaha[105] also observed an increase in the limiting-current density of Cu during co-deposition of γ-Al_2O_3 in a NiCu matrix into deep-recessed electrodes. Figure 16.10 shows the resulting copper fraction measured by a wavelength-dispersive microprobe analysis along the length of a micropost, similar to the size shown in Figure 16.5. The concentration of the Cu(II) in the electrolyte was 0.04 *M* with an excess of Ni(II), 1.0 *M* in a sodium citrate electrolyte (0.3 *M*) with ammonia hydroxide to maintain pH 8, and the deposition was carried out with pulsed current, 10 mA/cm^2, with 10 sec "on" or applied current and with a 70 sec "off" or relaxation time. Since the concentration of the Cu(II) ion is much smaller than the Ni(II), its deposition was ensured to occur under mass-transport control inside the recess so that the concentration of the deposit reflects the change in its rate. Other reports of metal-matrix composites into recess structures for MEMS type of applications, include that of Jakob et al.[106] regarding the co-deposition of nanometric TiO_2 and Al_2O_3 into Ni microstructures and Wang and Kelly[107] on the electrodeposition of submicron SiC–Ni and Al_2O_3–Ni composites. However few investigations have examined the unique features that result from the constrained deposition into patterned substrates.

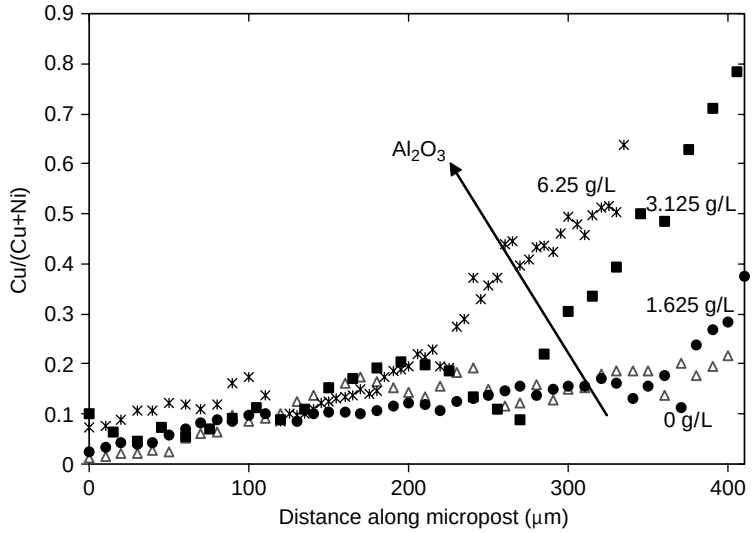

FIGURE 16.10 Fractional Cu content in a micro-post with variable alumina concentration in the electrolyte.

Nanoparticle inclusion into deposits and its presence in the electrolyte during the deposition of metals and alloys can affect the morphology of the deposit. Figure 16.11 demonstrates a case in point. A microfabricated Ni-rich NiCu alloy is electrodeposited without (a) and with (b) the addition of 3.125 g/L of alumina nanoparticles, under the same conditions. The addition of the particles resulted in a smoother deposit. A similar result was also observed in Cu thin-film electrodeposition onto a rotating-disk electrode from an acid electrolyte.[104] Figure 16.12 shows the morphology change from a rough elemental Cu deposit to a smoother deposit obtained with 60 g/L particles in the electrolyte, deposited under the same current density of 60 mA/cm^2. Intermediate particle loading concentrations imparted a rougher surface than the elemental Cu morphology and the number of particles in the deposit increased with the amount in the electrolyte.

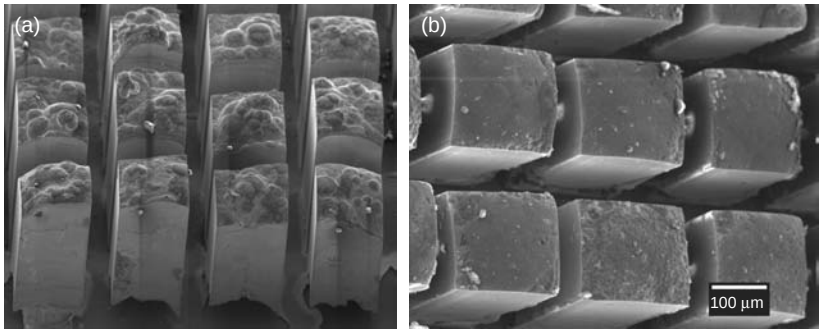

FIGURE 16.11 SEM micrographs of NiCu micro-posts (a) without and (b) with the addition of alumina nanoparticles.

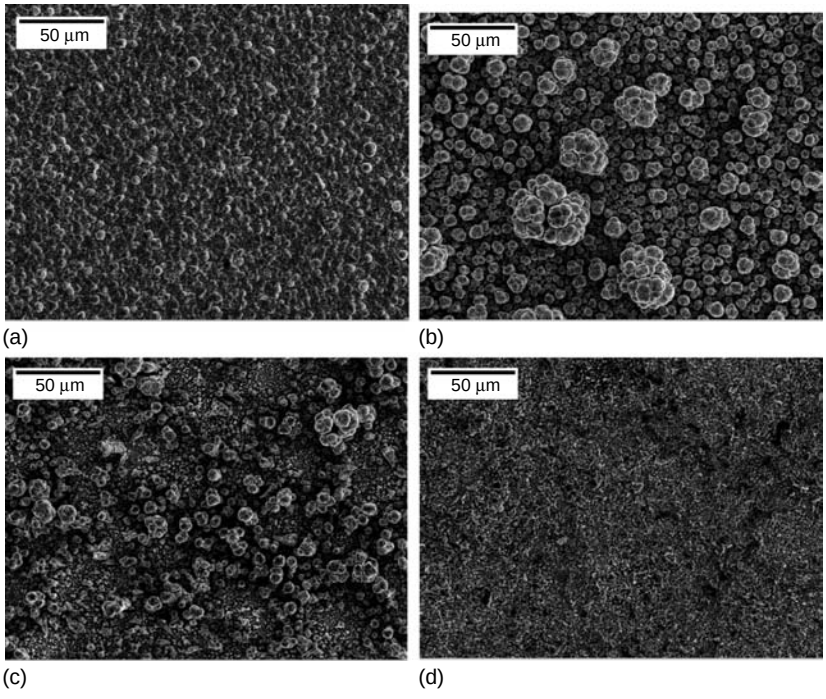

FIGURE 16.12 SEM micrographs of an (a) elemental copper deposit, and γ-Al_2O_3-Cu composites obtained from (b) 12.5, (c) 39, and (d) 60 g/L particle loadings. (From Lozano-Morales, A. and Podlaha, E.J., *J. Electrochem. Soc*., 151, C478–C483, 2004.)

Without the use of a stabilizer or surfactant around the nanoparticles in electrolytes used for electrodeposition, which often are high-ionic strength solutions, there may be agglomeration of the particles. Interpretation of the particle influence on the electrodeposition process may then be marred by the varying particle sizes in the electrolyte. In addition, commercially available nanoparticles often have a wide distribution of particle size. One method attempted for the selective deposition of particles of a maximum size is the use of pulse reverse deposition.[108] A cathodic pulse is used to deposit metal and a collection of particles from the electrolyte, albeit particles of varying sizes. A pulse with a reverse polarity is then used to dissolve the metal and particles down to a characteristic size. The remaining material is a collection of particles below a certain size. The method has recently been presented by the authors and much room for improvement and understanding of the pulse-reverse deposition remains.

16.5 SUMMARY

Electrochemical fabrication of nanomaterials is a wide area, and a short overview has been presented to familiarize the reader with some of the leading topics and challenges in this field. Emphasis has been placed on CMMs and nanoparticulate systems as both areas are of industrial interest for a wide variety of applications. Compositionally modulated multilayers, having nanosize dimensions, can be deposited as thin films, nanowires, pillars, and nanotubes and are governed by the electrodeposition process. Compositional control of the process requires knowledge of the kinetic and mass-transport regions of the depositing metals. Nanoparticles used as discrete particles may rely on electroless fabrication methods for the generation of shells around the nanoparticle core. Metal-matrix nanocomposite materials comprise encapsulated nanoparticules into the electrodepositing metal. The particles not only impart unique properties to the metal matrix but can also affect the metal deposition rate and morphology.

ACKNOWLEDGMENTS

The authors thank Professor Dave Young and Dr. Monica Moldovan of Physics and Astronomy Department at Louisiana State University for their help in conducting the magnetic measurements; Ms. Margaret Henk at Socolofsky Electron Microscopy Facility for assisting in TEM analysis, and Dr. X. Xie of Microscopy Characterization Facility at the Department of Geology and Geophysics at LSU for helpful direction in SEM analysis.

Support by the National Science Foundation under Grant No. 9984775 and No. 0210832 is gratefully acknowledged.

REFERENCES

1. W. Blum, The structure and propeties of alternately deposited metals, *Trans. Am. Electrochem. Soc*., 40: 307–320 (1921).
2. T. Foecke and D. Lashmore, Mechanical-behavior of compositionally modulated alloys, *Scr. Metall. Mater.*, 27: 651–656 (1992).
3. S. Menezes and D. Anderson, Wavelength-property correlation in electrodeposited ultrastructured Cu-Ni multilayers, *J. Electrochem. Soc*., 137: 440–444 (1990).
4. W. Schwarzacher and D.S. Lashmore, Giant magnetoresistance in electrodeposited films, *IEEE Trans. Magn*., 32: 3133–3153 (1996).
5. A. Fert and L. Piraux, Magnetic nanowires, *J. Magn. Magn. Mater*., 200: 338–358 (1999).
6. S. Lenczowski, C. Schonenberger, M. Gijs, and W. Dejonge, Giant magnetoresistance of electrodeposited Co/Cu multilayers, *J. Magn. Magn. Mater*., 148: 455–465 (1995).
7. Y. Jyoko, S. Kashiwabara, and Y. Hayashi, Preparation of giant magnetoresistance Co/Cu multilayers by electrodeposition, *J. Electrochem. Soc*., 144: L5–L8 (1997).

8. E. Chassaing, A. Morrone, and J.E. Schmidt, Nanometric Cu-Co multilayers electrodeposited on indium-tin oxide glass, *J. Electrochem. Soc*., 146: 1794 (1999).
9. V. Weihnacht, L. Peter, J. Toth, J. Padar, Z. Kerner, C.M. Schneider, and I. Bakonyi, Giant magnetoresistance in Co-Cu/Cu multilayers prepared by various electrodeposition control modes, *J. Electrochem. Soc*., 150: C507–C515 (2003).
10. L. Peter, A. Cziraki, L. Pogany, Z. Kupay, I. Bakonyi, M. Uhlemann, M. Herrich, B. Arnold, T. Bauer, and K. Wetzig, Microstructure and giant magnetoresistance of electrodeposited Co-Cu/Cu multilayers, *J. Electrochem. Soc*., 148: C168 (2001).
11. M. Shima, L. Salamanca-Riba, R.D. McMichael, and T.P. Moffat, Magnetic properties of ultrathin laminated Co/Cu films prepared by electrodeposition, *J. Electrochem. Soc*., 149: C439–C444 (2002).
12. A. Yamada, T. Houga, and Y. Ueda, Magnetism and magnetoresistance of Co/Cu multilayer films produced by pulse control electrodeposition method, *J. Magn. Magn. Mater*., 239: 272–275 (2002).
13. T. Ohgai, X. Hoffer, A. Fabian, L. Gravier, and J.P. Ansermet, Electrochemical synthesis and magnetoresistance properties of Ni, Co and Co/Cu nanowires in a nanoporous anodic oxide layer on metal.lic aluminium, *J. Mater. Chem*., 13: 2530–2534 (2003).
14. B. Voegeli, A. Blondel, B. Doudin, and J.P. Ansermet, Electron transport in multilayered Co/Cu nanowires, *J. Magn. Magn. Mater*., 151: 388–395 (1995).
15. K. Liu, K. Nagodawithana, P.C. Searson, and C.L. Chien, perpendicular giant magnetoresistance of multilayered Co/Cu nanowires, *Phys. Rev. B*, 51: 7381–7384 (1995).
16. A.B. Granovskii, A.V. Vedyaev, A.V. Kalitsov, Anisotropy of giant magnetoresistance in magnetic multilayered structures and granular films, *Fiz. Tverdogo Tela*, 37: 337–343 (1995).
17. B. Dieny, C. Cowache, A. Nossov, P. Dauguet, J. Chaussy, and P. Gandit, Anisotropy and angular variation of the giant magnetoresistance in magnetic multilayers, *J. Appl. Phys*., 79: 6370–6375 (1996).
18. M. Alper, K. Attenborough, R. Hart, S.J. Lane, D.S. Lashmore, C. Younes, and W.S. Schwarzacher, Giant magnetoresistance in electrodeposited superlattices, *Appl. Phys. Lett*., 63: 2144–2146 (1993).
19. S.Z. Hua, D.S. Lashmore, W. Schwarzacher, L.J. Swartzenruber, R.D. McMichael, L.H. Bennett, and R. Hart, Giant magnetoresistance peaks in CoNiCu/Cu multilayers grown by electrodeposition, *J. Appl. Phys*., 76: 6519–6521 (1994).
20. M. Alper, W. Schwarzacher, S.J. Lane, The effect of pH changes on the giant magnetoresistance of electrodeposited superlattices, *J. Electrochem. Soc*., 144: 2346–2352 (1997).
21. M. Alper, K. Attenborough, V. Baryshev, R. Hart, D.S. Lashmore, and W. Schwarzacher, Giant magnetoresistance in electrodeposited Co-Ni-Cu/Cu superlattices, *J. Appl. Phys*., 75: 6543–6545 (1994).
22. O.I. Kasyutich, W. Schwarzacher, V.M. Fedosyuk, P.A. Laskarzhevskiy, and A.I. Masliy, Comparison of the structure and magnetotransport properties of Co-Ni-Cu/Cu multilayers electrodeposited on n-GaAs(001) and (111), *J. Electrochem. Soc*., 147: 2964–2968 (2000).
23. S.S.P. Parkin, Giant magnetoresistance in magnetic nanostructures, *Ann. Rev. Mater. Sci*., 25: 357–388 (1995).
24. J.A. Switzer, R.P. Raffaelle, R.J. Phillips, C.J. Hung, and T.D. Golden, Scanning tunneling microscopy of electrodeposited ceramic superlattices, *Science*, 258: 1918–1921 (1992).
25. J.R. Selman and C.W. Tobias, *Adv. Chemical Eng.*, 10: 212 (1978).
26. D. Landolt, *Corrosion et chimie de surfaces des métaux*, vol 12 de *Traité des matériaux*, ed., Lausanne Presses Polytechniques et Universitaires Romandes, Lausanne, Switzerland, 1993.
27. H.Y. Cheh, Electrodeposition of gold by pulsed current, *J. Electrochem. Soc*., 118: 551–557 (1971).
28. C.C. Yang, H.Y. Cheh, Pulsed electrodeposition of copper/nickel multilayers on a rotating disk electrode, *J. Electrochem. Soc*., 142: 3034–3043 (1995).
29. K. Viswanathan and H.Y. Cheh, The application of pulsed potential and pulsed current on a rotating disc electrode system, *J. Appl. Electrochem*., 9: 537–543 (1995).
30. E. Chassaing, Effect of organic additives on the electrocrystallization and the magnetoresistance of Cu-Co multilayers, *J. Electrochem. Soc*., 148: C690–C694 (2001).
31. J. Kelly, P. Kern, and D. Landolt, Additive effects during pulsed deposition of Cu-Co nanostructures, *J. Electrochem. Soc*., 147: 3725–3729 (2000).
32. Y. Jyoko, S. Kashiwabara, and Y. Hayashi, Characterization of electrodeposited Co/Cu ultrathin films and multilayers, *J. Magn. Magn. Mater*., 165: 280–283 (1997).
33. A. O'Keeffe, O. Kasyutich, W. Schwarzacher, L. de Oliveira, and A. Pasa, Giant magnetoresistance in multilayers electrodeposited on n-Si, *Appl. Phys. Lett*., 73: 1002–1004 (1998).

34. A. Pasa and W. Schwarzacher, Electrodeposition of thin films and multilayers on silicon, *Phys. Stat. Sol.*, 173: 73–84 (1999).
35. G. Nabiyouni, O.I. Kasyutich, S. Roy, W. Schwarzacher, Co-Ni-Cu/Cu multilayers electrodeposited using a channel flow cell, *J. Electrochem. Soc*., 149: C218–C222 (2002).
36. G. Nabiyouni, W. Schwarzacher, Z. Rolik, and I. Bakonyi, Giant magnetoresistance and magnetic properties of electrodeposited Ni-Co-Cu/Cu multilayers, *J. Magn. Magn. Mater*., 253: 77–85 (2002).
37. J. Zhang, M. Moldovan, D.P. Young, and E.J. Podlaha, CoNi/Cu multilayers by electrochemical deposition, *Proceedings of the 205th Meeting of the Electrochemical Society on Electrochemical Processing in ULSI and MEMS*, San Antonio, TX, 2004.
38. A. Brenner, *Electrodeposition of Alloys*, Academic Press, New York (1963).
39. P.C. Andricacos, L.T. Romankiw, Magnetically soft materials: their properties and electrochemistry, in *Advances in Electrochemical Science and Engineering*, Vol. 3, Gerischer, H. and Tobias, C.W., Eds., Wiley-VCH, NY, 1990, pp. 227–321.
40. D. Landolt, Electrochemical and materials science aspects of alloy deposition, *Electrochim. Acta*, 39: 1075–1090 (1994).
41. Q. Huang and E.J. Podlaha, Simulation of pulsed electrodeposition for GMR FeCoNiCu/Cu multilayers, *J. Electrochem. Soc*., 151: C119–C126 (2004).
42. S. Dubois, C. Marchal, J.M. Beuken, L. Piraux, J.L. Duvail, A. Fert, J.M. George, and J.L. Maurice, Perpendicular giant magnetoresistance of NiFe/Cu multilayered nanowires, *Appl. Phys. Lett*., 70: 396–398 (1997).
43. Q. Huang, D. Davis, and E.J. Podlaha, Electrodeposition of FeCoNiCu nanowires, *J. Appl. Electrochem*., 2005, in press.
44. L. Piraux, J.M. George, J.F. Despres, C. Leroy, E. Ferain, R. Legras, K. Ounadjela, and A. Fert, Giant magnetoresistance in magnetic multilayered nanowires, *Appl. Phys. Lett*., 65: 2484–2486 (1994).
45. A. Blondel, J.P. Meier, B. Doudin, and J.-Ph. Ansermet, Giant magnetoresistance of nanowires of multilayers, *Appl. Phys. Lett*., 65: 3019–3021 (1994).
46. A. Blondel, J. Meier, B. Doublin, J.-Ph. Ansermet, K. Attenborough, P. Evens, R. Hart, G. Nabiyouni, and W. Schwarzacher, Wire-shaped magnetic mutilayers for 'current perpendicular to plane' magnetoresistance measurements, *J. Magn. Magn. Mater*., 148: 317–318 (1995).
47. W. Schwarzacher, O.I. Kasyutich, P.R. Evans, M.G. Darbyshire, Y. Ge, V.M. Fedosyuk, F. Rousseaux, E. Cambril, and D. Decanini, Metal nanostructures prepared by template electrodeposition, *J. Magn. Magn. Mater*., 185: 198–199 (1999).
48. S. Dubois, J.M. Beuken, L. Piraux, J.L. Duvail, A. Fert, J.M. George, and J.L. Maurice, Perpendicular giant magnetoresistance of NiFe/Cu and Co/Cu multilayered nanowires, *J. Magn. Magn. Mater*., 165: 30–33 (1997).
49. T.M. Whitney, J.S. Jiang, P.C. Searson, and C.L. Chien, Fabrication and magnetic-properties of arrays of metallic nanowires, *Science*, 261: 1316–1319 (1993).
50. N. Tsuya, Y. Saito, H. Nakamura, S. Hayano, A. Furugohri, K. Ohta, Y. Wakui, and T. Tokushima, A perpendicular magnetic recording medium by alumite, *J. Magn. Magn. Mater*., 54: 1681–1682 (1986).
51. D. Almawlawi, N. Coombs, and M. Moskovits, Magnetic-properties of Fe deposited into anodic aluminum-oxide pores as a function of particle-size, *J. Appl. Phys*., 70: 4421–4425 (1991).
52. H.R. Khan and K. Petrikowski, Magnetic and structural properties of the electrochemically deposited arrays of Co and CoFe nanowires, *J. Magn. Magn. Mater*., 249: 458–461 (2002).
53. H.R. Khan and K. Petrikowski, Synthesis and properties of the arrays of magnetic nanowires of Co and CoFe, *Mater. Sci. Eng. C*, 19: 345–348 (2002).
54. H. Zhu, S. Yang, G. Ni, D. Yu, and Y. Du, Fabrication and magnetic properties of Co67Ni33 alloy nanowire array, *Scr. Mater*., 44: 2291–2295 (2001).
55. H.R. Khan and K. Petrikowski, Anisotropic structural and magnetic properties of arrays of Fe26Ni74 nanowires electrodeposited in the pores of anodic, *J. Magn. Magn. Mater*., 215: 526–528 (2000).
56. M.A.M. Gijs, S.K.J. Lenczowski, J.B. Giesbers, R.J.M. van de Veerdonk, M.T. Johnson, and R.M. Jungblut, Perpendicular giant magnetoresistance using microlithography and substrate patterning techniques, *J. Magn. Magn. Mater*., 151: 333–340 (1995).

57. J.P. Spallas, Y. Huai, S. Vernon, B. Fuchs, B. Law, and D. R. Kania, Perpendicular current giant magnetoresistance in 0.4 mu m diameter Co-Cu multilayer sensors, *IEEE Trans. Magn.*, 32: 4710–4712 (1996).
58. J.L. Davail, S. Dubois, L. Piraux, A. Vaurès, A. Fert, D. Adam, M. Champagne, F. Rousseaux, and D. Decanini, Electrodeposition of patterned magnetic nanostructures, *J. Appl. Phys*., 84: 6359–6365 (1998).
59. A. Bond, D. Luscombe, K. Oldham, and C. Zoski, A comparison of the chronoamperometric response at inlaid and recessed disc microelectrodes, *J. Electroanalyt. Chem*., 249: 1–14 (1988).
60. C.R. Martin, Nanomaterials — a membrane-based synthetic approach, *Science*, 266: 1961–1966 (1994).
61. M.N.C.R. Martin, K. Jirage, and M. Kang, Investigations of the transport properties of gold nanotubule membranes, *J. Phys. Chem. B*, 105: 1925–1934 (2001).
62. W.C. Yoo and J.K. Lee, Field-dependent growth patterns of metals electroplated in nanoporous alumina membranes, *Adv. Mater*., 16: 1097–1101 (2004)..
63. D. Davis and E.J. Podlaha, CoNiFeCu nanotube electrodeposition, *Electrochem. Solid-State Lett.*, 8: D1–D4 (2005).
64. D. Miller and M. Moskovits, Separate pathways for oxygenate and hydrocarbon synthesis in the Fischer-Tropsch reaction, *J. Am. Chemical Soc*., 111: 9250–9252 (1989).
65. D. Almawlawi, N. Coombs, and M. Moskovits, Magnetic-properties of Fe deposited into anodic aluminum-oxide pores as a function of particle-size, *J. Appl. Phys*., 70: 4421–4425 (1991).
66. M. Moskovits, Surface-enhanced spectroscopy, *Rev. Mod. Phy*., 57: 783–826 (1985).
67. A. Heller, D.E. Aspnes, J.D. Porter, T.T. Sheng, and R.G. Vadimsky, Transparent metals — preparation and characterization of light-transmitting platinum films, *J. Phys. Chem*., 89: 4444–4452 (1985).
68. D. Franzke and A. Wokaun, Photochemistry of azo-compounds on silver island films studied by surface enhanced Raman-spectroscopy, *J. Phys. Chem*., 96: 6377–6381 (1992).
69. A. Andersson, O. Hunderi, and C.G. Granqvist, Nickel pigmented anodic aluminum-oxide for selective absorption of solar-energy, *J. Appl. Phys*., 51: 754–764 (1980).
70. G.A. Niklasson, Co-Al_2O_3 selective solar absorbing films — structure and effective medium theory for the optical-properties, *Solar Energy Mater*., 17: 217–226 (1988).
71. M. Platt, R.A.W. Dryfe, and E.P.L. Roberts, Structural and electrochemical characterisation of Pt and Pd nanoparticles electrodeposited at the liquid/liquid interface, *Electrochim. Acta*, 49: 3937–3945 (2004).
72. M. Platt, R.A.W. Dryfe, and E.P.L. Roberts, Controlled deposition of nanoparticles at the liquid-liquid interface, *Chem. Commn*., 20: 2324–2325 (2002).
73. C. Johans, K. Konturri, and D.J. Schiffrin, Nucleation at liquid vertical bar liquid interfaces: galvanostatic study, *J. Electroanalyt. Chem*., 526: 29–35 (2002).
74. S.P. Gubin and Y.A. Koksharov, Preparation, structure, and properties of magnetic materials based on Co-containing nanoparticles, *Inorg. Mater*., 38: 1085–1099 (2002).
75. J.P. Chen, C.M. Sorensen, K.J. Klabunde, and G.C. Hadjipanayis, Enhanced magnetization of nanoscale colloidal cobalt particles, *Phys. Rev. B: Condens. Matter*., 51: 11527–11532 (1995).
76. I.M.L. Billas, A. Chatelain, and W.A. de Heer, Magnetism from the atom to the bulk in iron, cobalt, and nickel clusters, *Science*, 265: 1682–1684 (1994).
77. B. Ravel, E.E. Carpenter, and V.G. Harris, Oxidation of iron in iron/gold core/shell nanoparticles, *J. Appl. Phys*., 91: 8195–8197 (2002).
78. J. Lin, W. Zhou, A. Kumbhar, J. Wiemann, J. Fang, E.E. Carpenter, and C.J. O'Connor, Gold-coated iron (Fe@Au) nanoparticles: synthesis, characterization, and magnetic field-induced self-assembly, *J. Solid State Chem*., 159: 26–31 (2001).
79. W.L. Zhou, E.E. Carpenter, J. Lin, A. Kumbhar, J. Sims, and C.J. O'Connor, Nanostructures of gold coated iron core-shell nanoparticles and the nanobands assembled under magnetic field, *Eur. Phys. J. D: At., Molecular Optical Phys*., 16: 289–292 (2001).
80. E.E. Carpenter, J.A. Sims, J.A. Wienmann, W.L. Zhou, and C.J. O'Connor, Magnetic properties of iron and iron platinum alloys synthesized via microemulsion techniques, *J. Appl. Phys*., 87: 5615–5617 (2000).
81. G. Salazar-Alvarez, M. Mikhailova, M. Toprak, Y. Zhang, and M. Muhammed, Fabrication and properties of self-assembled nanosized magnetic particles, *Materials Research Society 2001 Fall Meeting Symposium Proceedings*, Vol. 707, 2002, pp. 263–268.

82. D.A. Fleming, M. Napolitano, and M.E. Williams, Chemically functional alkanethiol derivitized magnetic nanoparticles, *Materials Research Society 2002 Fall Meeting Symposium Proceedings*, Vol. 746, 2003, pp. 207–212.
83. S.U. Son, Y. Jang, J. Park, H.B. Na, H.M. Park, H.J. Yun, J. Lee, and T. Hyeon, Designed synthesis of atom-economical Pd/Ni bimetallic nanoparticle-based catalysts for sonogashira coupling reactions, *J. Am. Chem. Soc*., 126: 5026–5027 (2004).
84. J. Rivas, R.D. Sanchez, A. Fondado, C. Izco, A.J. Garcia-Bastida, J. Garcia-Otero, J. Mira, D. Baldomir, A. Gonzalez, I. Lado, M.A.L. Quintela, S.B. Oseroff, Structural and magnetic characterization of Co particles coated with Ag, *J. Appl. Phys*., 76: 6564–6566 (1994).
85. J.-I. Park and J. Cheon, Synthesis of solid solution and core-shell type cobalt-platinum magnetic nanoparticles via transmetalation reactions, *J. Am. Chemical Soc*., 123: 5743–5746 (2001).
86. J.-I. Park, M.G. Kim, Y.-W. Jun, J.S. Lee, W.-R. Lee, and J. Cheon, Characterization of superparamagnetic "core-shell" nanoparticles and monitoring their anisotropic phase transition to ferromagnetic "solid solution" nanoalloys, *J. Am. Chem. Soc*., 126: 9072–9078 (2004).
87. Z. Guo, C.S.S.R. Kumar, L.L. Henry, E.E. Doomes, J. Hormes, and E.J. Podlaha, Electroless synthesis of Cu shells surrounding Co nanoparticles, *J. Electrochem. Soc*., 152: D1–D5 (2005).
88. A.J. Bard, R. Parsons, and J. Jordan, Eds., *Standard Potentials in Aqueous Solution*, Marcel Dekker, New York, 1985, pp. 790–795.
89. H. Boennemann, G. Braun, G. Brijoux, G. Braun, R. Brinkman, A. Tilling, A. Schulze, K. Seevogel, and K. Siepen, Nanoscale colloidal metals and alloys stabilized by solvents and surfactants. Preparation and use as catalyst precursors, *J. Organomet. Chem*., 520: 143–162 (1996).
90. A. Hovestad and L. Janssen, Electrochemical codeposition of inert particles in a metallic matrix, *J. Appl. Electrochem*., 25: 519–527 (1995).
91. M. Musiani, Electrodeposition of composites: arm expanding subject in electrochemical materials science, *Electrochim. Acta*, 45: 3397–3402 (2000).
92. J.P. Celis, J.R. Roos, C. Buelens, and J. Fransaer, Mechanism of electrolytic composite plating — survey and trends, *Trans. Inst. Met. Finish*., 69: 133–139 (1991).
93. C. Kerr, D. Barker, F. Walsh, and J. Archer, The electrodeposition of composite coatings based on metal matrix-included particle deposits, *Trans. Inst. Met. Finish*., 78: 171–178 (2000).
94. J. Fransaer, J.P. Celis, and J.R. Roos, Analysis of the electrolytic codeposition of non-brownian particles with metals, *J. Electrochem. Soc*., 139: 413–425 (1992).
95. J.L. Valdes and H.Y. Cheh, Deposition of colloidal particles in electrochemical systems *J. Electrochem. Soc*., 133: C322–C322 (1986).
96. P.M. Vereecken, I. Shao, P.C. Searson, Particle codeposition in nanocomposite films, *J. Electrochem. Soc*., 147: 2572–2575 (2000).
97. N. Guglielmi, Kinetics of deposition of inert particles from electrolytic baths, *J. Electrochem. Soc*., 119: 1009–1012 (1972).
98. J.P. Celis and J.R. Roos, Kinetics of deposition of alumina particles from copper-sulfate plating baths, *J. Electrochem. Soc*., 124: 1508–1511 (1977).
99. J.P. Celis, J.R. Roos, and C. Buelens, A mathematical-model for the electrolytic codeposition of particles with a metallic matrix, *J. Electrochem. Soc*., 134: 1402–1408 (1987).
100. J.L. Valdes and H.Y. Chen, Deposition of colloidal particles in electrochemical systems, *J. Electrochem. Soc*., 133: C322 (1986).
101. P. Webb and N. Robertson, Electrolytic codeposition of Ni-gamma-Al_2O_3 thin-films, *J. Electrochem. Soc*., 141: 669–673 (1994).
102. E.J. Podlaha and D. Landolt, Pulse-reverse plating of nanocomposite thin films, *J. Electrochem. Soc*., 144: L200–L202 (1997).
103. J. Stojak and J. Talbot, Effect of particles on polarization during electrocodeposition using a rotating cylinder electrode, *J. Appl. Electrochem*., 31: 559–564 (2001).
104. A. Lozano-Morales and E.J. Podlaha, The effect of Al_2O_3 nanopowder on Cu electrodeposition, *J. Electrochem. Soc*., 151: C478–C483 (2004).
105. A. Panda and E.J. Podlaha, Nanoparticles to improve mass transport inside deep recesses, *Electrochem. Solid-State Lett*., 6: C149–C152 (2003).

106. F. Erler, C. Jakob, H. Romanus, L. Spiess, B. Wielage, T. Lampke, and S. Steinhauser, Interface behaviour in nickel composite coatings with nano-particles of oxidic ceramic, *Electrochim. Acta*, 48: 3063–3070 (2003).
107. T. Wang and K. Kelly, Particulate strengthened Ni-Al_2O_3 microcomposite HARMs for harsh-environmental micromechanical applications, *J. Micromech. Microeng*., 15: 81–90 (2005)
108. E.J. Podlaha, Selective electrodeposition of nanoparticulates into metal matrices, *Nano Lett*., 1: 413–416 (2001).

17 Mechanical Behavior of Nanocrystalline Metals

Mingwei Chen
Tohoku University, Sendai, Japan

En Ma and Kevin Hemker
Johns Hopkins University, Baltimore, Maryland

CONTENTS

17.1 INTRODUCTION

One of the most notable properties of nanostructured materials is their extremely high hardness and strength, which makes them attractive for structural applications where strength and weight are critical. The widespread enthusiasm for research on the mechanical behavior of nanocrystalline materials is driven by both scientific curiosity and this technological promise. A key tenant for nanoscale research involves the search for new physics arising from length-scale effects that result in unusual properties at the nanoscale. In the case of mechanical behavior, it would be interesting to know if dislocation activity, the dominant deformation mode in coarse-grained ductile materials, still plays an important role as grain sizes approach tens of nanometers, and if novel deformation modes that cannot be activated in coarse-grained materials emerge. From the application point of view, with the increasing number of applications of nanocrystalline materials in microelectromechanical systems (MEMS), micro/nano devices, precise cutting tools, surface coating, and high-performance structural applications, it is important to develop a detailed understanding of the intrinsic mechanical behavior and underlying deformation mechanisms that govern the mechanical response of nanocrystalline materials. This fundamental knowledge is needed to be able to model and predict mechanical performance and to design for the use of nanocrystalline materials in devices. In this chapter, we present a brief overview of our current understanding of deformation behavior, focusing on experimental findings that are accepted by the community as representative of the general deformation response of nanocrystalline metals, and on the underlying deformation mechanisms that have been proposed to explain these results. The picture is far from complete, and we have made an effort to highlight outstanding questions and critical issues that appear to warrant further investigation.

17.2 CHARACTERIZATION TECHNIQUES

17.2.1 Mechanical Behavior

17.2.1.1 Microindentation

As a general rule, whether prepared by electrodeposition, vapor deposition, mechanical alloying, or gas-phase condensation and consolidation, nanocrystalline materials are only available in limited quantities and have limited sizes in at least one of the three dimensions. Measurements of mechanical properties using conventional tensile or compressive tests are often restricted by the small sizes of samples. As an alternative, micro-hardness tests have been widely used to evaluate the mechanical properties of nanocrystalline materials because no special sample preparation is required, and because tests of small samples or thin foils can be performed quickly and inexpensively. Hardness is defined for ductile materials as the resistance to penetration of a hard indenter or the resistance to plastic deformation. Since the strength of materials also reflects the resistance to plastic deformation, hardness has an intrinsic relation to the strength of materials. However, the complex stress/strain distribution around the hardness indent greatly complicates derivation of a straightforward relationship between the hardness and material strength. Numerical calculations are normally required to reveal the yield or flow strength from hardness measurements. In practice, a simple empirical relationship, with flow stress taken as one-third of the hardness, is widely used to estimate the material strength.[1]

17.2.1.2 Nanoindentation

Nanoindentation testing is similar to conventional hardness techniques, but is performed on a much smaller scale using special equipment that provides very precise measurements of load and displacement. The load is applied and measured with a magnetic coil, and tip displacement is

measured with parallel plate capacitors. The force required to press a sharp diamond indenter into a material is recorded as a function of indentation depth. By using this displacement-sensitive indentation technique both elastic modulus and hardness can be extracted from the nanoindentation curve.[2] In addition, with controllable loading and unloading, several types of mechanical tests including constant strain rate, constant loading rate, cyclic loading, adjustable maximum load, and displacement can be performed. By changing the testing parameters, strain rate sensitivity and work hardening of materials have been systematically investigated. Figure 17.1 illustrates an example in which the difference in loading rate sensitivity between ultrafine-grained and nanocrystalline Ni is revealed by systematic nanoindentation measurements.[3]

17.2.1.3 Tensile Testing

An increasing number of tensile tests of nanocrystalline materials have been conducted in recent years. The availability of ultrafine-grained and nanocrytstalline materials produced by electrodeposition and severe plastic deformation have resulted in samples with sufficient size to allow for traditional tensile testing.[4] Other researchers have employed microsample tensile testing to characterize micro-tensile specimens with dimensions of the order of hundreds of micrometers.[5,6] More recently, the development of MEMS-inspired thin film tensile samples has allowed for the tensile testing of vapor-deposited nanocrystalline thin films.[7,8] In addition to providing the full stress–strain response of the materials, these experiments have also been used to probe the transient behavior of the material and to extract fundamental parameters such as the strain rate sensitivity and activation volume. Cyclic tension–tension loading provides an opportunity for high-cycle fatigue testing, although specimen geometry still precludes fully reversed loading and fatigue crack growth experiments on microsamples. High-cycle fatigue and fatigue crack growth experiments have been conducted on nanocrystalline ED Ni.[9,10]

17.2.2 Microstructural Characterization

17.2.2.1 X-Ray Diffraction

Considering that grain size is the most important microstructural parameter to describe the nanocrystalline materials, various techniques have been proposed to experimentally measure the grain size, which include transmission electron microscopy (TEM), scanning probe microscopy (SPM), scanning electron microscopy (SEM), and x-ray diffraction (XRD). Among them, XRD has unique advantages in simple sample preparation and information from a large area and has been widely used to determine an averaged grain size. Various theoretical modes including Scherrer equation, integral breadth analysis, and methods derived by Warrant and Averbach, and Williamson and Hall, have been developed to attain the average grain size from the Bragg peak broadening.[11] For nanocrystalline materials, the microstructure has been shown to be inhomogeneous with a wide distribution in grain sizes. The single parameter of the average grain sizes appears to be insufficient to describe the microstructure features of nanocrystalline materials. The distribution range of grain size is especially important when considering the mechanical properties of nanocrystalline materials. A modified Warrant–Averbach and Williamson–Hall peak profile analysis method has been suggested recently to estimate grain size distributions of nanocrystalline materials.[12] The importance of measuring the grain size distribution experimentally should not be overlooked.

In addition tograin size measurements, XRD technique has been recently developed to measure the density and type of crystal defects in nanocrystalline metals and thereby can provide valuable information on the deformation mechanisms of nanocrystalline materials. This will be discussed in Section 17.4.

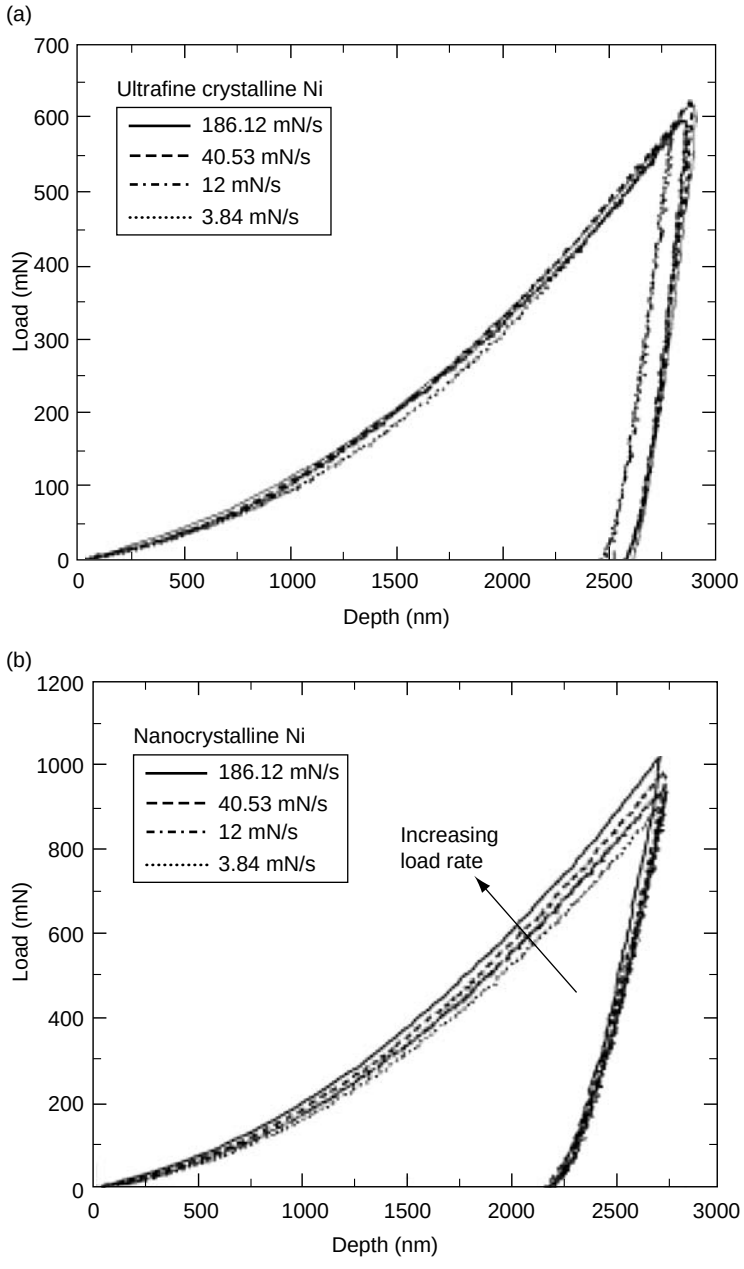

FIGURE 17.1 Load–displacement curves of (a) ultrafine-grained Ni (320 nm grain size) and (b) nanocrystalline Ni (40 nm grain size). These curves are averages of ten and five indentations, respectively, and four different load rates are shown. (From Schwaiger, R. et al., *Acta Mater*., 51, 5159–5172, 2003.)

17.2.2.2 Transmission Electron Microscopy

The use of TEM, which has proven to be extremely useful in the characterization of microcrystalline materials, is also very powerful for the characterization of nanocrystalline materials. TEM thin foils of nanocrystalline metals and alloys can be prepared in much the same way as their microcrystalline counterparts: electropolishing, ion milling, and focused ion beam machining are all

viable preparation routes. In some cases, the preparation of nanocrystalline thin films with thickness of the order of hundreds of nanometers allows for direct TEM observations without specimen preparation. Conventional (bright- and dark-field) imaging techniques can be used to characterize the grain size and presence of defects (dislocations, stacking faults, twins) and impurities. The overlapping of grains in the foil can make it difficult to identify individual grains in bright field, but the use of dark-field TEM has proven to be an effective way of imaging and characterizing grain size. Detailed titling experiments have been extremely effective for characterizing dislocation densities, Burger's vectors, and dislocation organization in microcrystalline alloys, but difficulties in obtaining diffraction patterns of, and setting up diffraction conditions for, nanosized grains have largely precluded such experiments in nanocrystalline alloys. Moreover, while postmortem observations of deformed nanocrystalline materials indicate that the dislocation content in these specimens is very low,[5,13] it is worth noting that the absence of dislocations cannot be taken as proof that they did not participate in the deformation process since the dislocations may have been absorbed into the grain boundaries either during or after the deformation process. In regions where the thickness of the TEM foil is less than the grain size, the use of high-resolution electron microscopy (HREM) has proven to be useful for the characterization of both intergranular grain boundaries and intragranular defects.[14,15]

The absence of dislocations in postmortem samples and the possibility of grain boundary-related relaxation processes have resulted in considerable interest in the use of *in situ* straining techniques to capture the deformation processes that govern plasticity in these materials. Techniques for specimen preparation and loading are now fairly common, and novel techniques such as the use of an in-column indenter[16] are also emerging. Single- and double-tilt strain holders are commercially available and, in principle, the use of bright field (BF), dark field (DF), and HREM imaging modes should allow for direct observations of dislocation activity, grain rotation, grain boundary sliding, twining, cracking, and even dynamic interaction between deformation processes. In practice, the implementation of such techniques requires considerable expertise as limitations of thin foil geometry and difficulties in specimen manipulation must be overcome.

17.3 MECHANICAL RESPONSE

17.3.1 STRENGTH

It is well known that the yield strength of coarse-grained metals follows, almost without exception, the Hall–Petch relationship between grain size and strength

$$\sigma = \sigma_o + kD^{-1/2} \tag{17.1}$$

where σ is the yield strength, D the average grain size in diameter, σ_o the "friction stress" representing the overall resistance of the crystal lattice to dislocation movement, and the Hall–Petch slope k is a constant that depends on the material. On the basis of an extrapolation of Equation (17.1), the advent of nanocrystalline materials naturally raise the expectation of superstrong materials. The mechanical properties documented in the literature for nanocrystalline metals with grain size well below 100 nm are mostly for face-centered-cubic (fcc) metals (e.g., Cu, Ni, and Pd). These data have been primarily derived from uniaxial tension/compression tests and micro- or nano indentation tests.[13] Typical tensile engineering stress–strain curves obtained at several strain rates are shown for electrodeposited nanocrystalline Ni in Figure 17.2.

Typically, these nanocrystalline metals exhibit yield strength of the order of 1 GPa, an order of magnitude higher than their coarse-grained counterparts. The strength has been found to increase with decreasing grain size, approximately following the Hall–Petch relationship (17.1). As examples, the Hall–Petch plots for Ni and Cu, obtained by compiling data from a number of experiments,

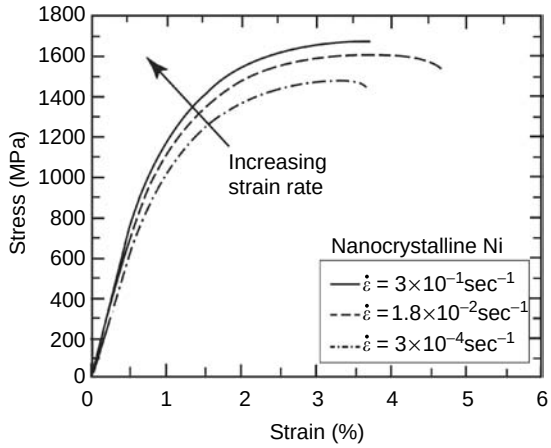

FIGURE 17.2 Engineering stress–strain curves of an electrodeposited nanocrystalline Ni with an average grain size of 40 nm, obtained in tensile tests at several strain rates. (From Schwaiger, R. et al., *Acta Mater*., 51, 5159–5172, 2003.)

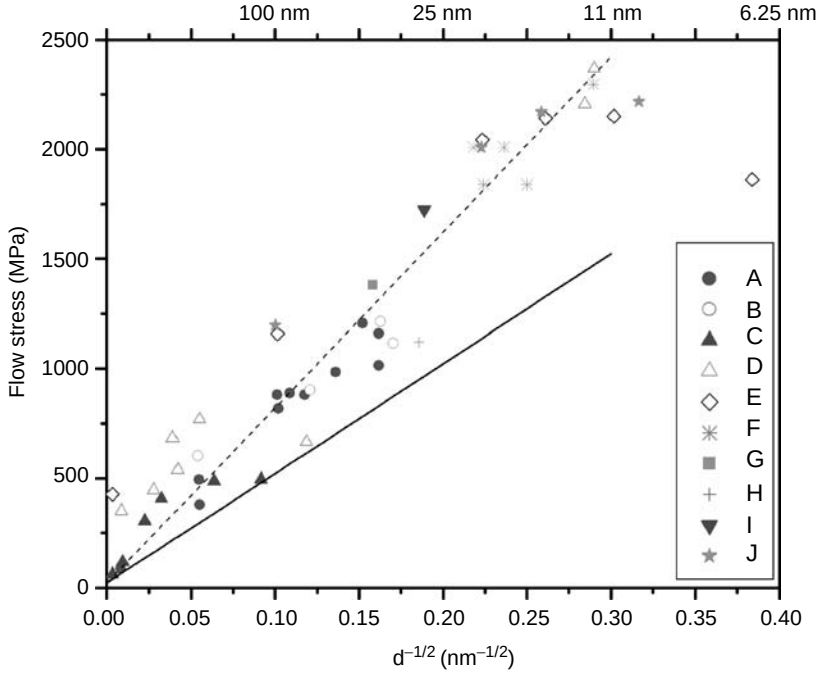

FIGURE 17.3 Hall–Petch plot summarizing experimental data from the literature for Ni, showing the grain size dependence of room-temperature flow stress (the stress at 1% plastic strain, or hardness divided by 3 to approximate the flow stress). A – tensile test;[18] B – hardness divided by 3;[18] C – tensile test;[19] D – hardness divided by 3;[20] E – hardness divided by 3;[21] F – tensile and hardness data;[22] G – tensile test;[3] H – tensile test;[23] I – tensile results;[5] J – hardness divided by 3.[24] The solid line is the Hall–Petch relationship for Ni with grain sizes ranging from 0.12 to 130 μm given by Thompson.[25]

are shown in Figure 17.3 and Figure 17.4, respectively. In the case of Ni, the slope of a linear fit to the data (e.g., the broken line in Figure 17.3) is higher than the Hall–Petch slope of conventional Ni. For Cu, in Figure 17.4, the Hall–Petch line given by Meyers and Chawla[17] goes through the data for reported grains sizes of >20 nm and seems to represent the data fairly well.

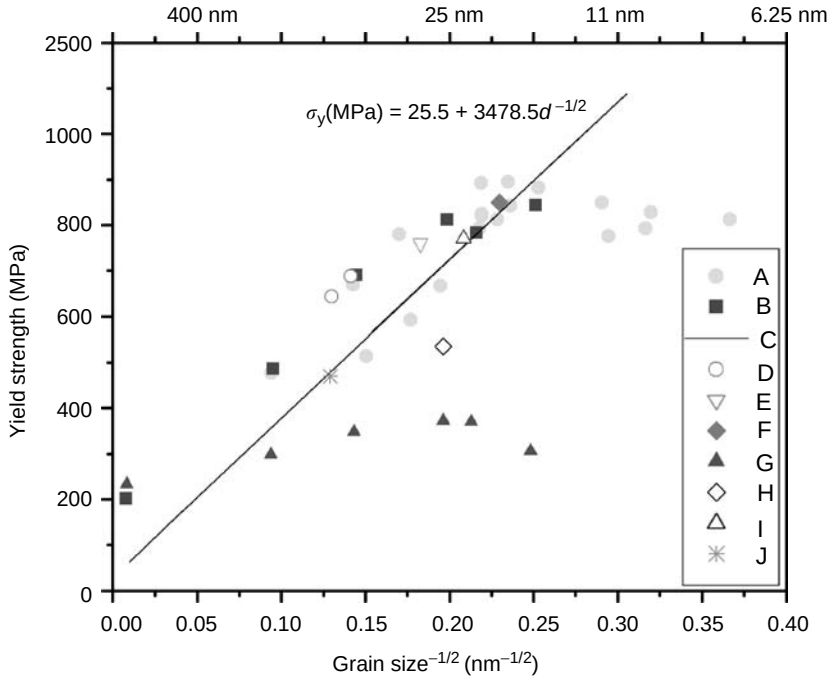

FIGURE 17.4 Summary of experimental data from the literature on the grain size dependence of strength for Cu. The equation for the solid line is the Hall–Petch relationship (C) given in Ref. 17. Note that all these data were reported in studies of nanocrystalline Cu (average d well below 100 nm), including some reference samples made in these studies to compare with nanocrystalline samples. The grain boundaries are mostly of the general high-angle varieties. Other studies on Cu with ultrafine grains ($d > \sim$100 nm), or Cu that has nanoscale features but of other types (such as nanoscale domain/cell/twin structures), are not included. A – hardness divided by 3;[33] B – hardness divided by 3;[34] C – Hall–Petch relationship;[17] D – tensile yield strength;[35] E – tensile yield strength;[6] F – compressive yield strength[34] G – tensile yield strength;[34] (these early tensile data showed rather low tensile strength due to sample porosity); H – tensile yield strength;[5] I – yield strength by miniaturized disk bend test;[36] J – compressive yield strength.[37]

Grain refinement leading to strengthening has traditionally been explained by the concept of pileup of dislocations at grain boundaries[25] (see Section 17.4). The reasons for the continued Hall–Petch type strengthening down to nanoscale grain sizes are not fully understood, because dislocation sources are not expected to operate within the tiny nanocrystalline grains and there is no experimental confirmation of dislocation pileups in deformed nanocrystalline specimens. Indeed, while the strengthening continues with decreasing grain size, Figure 17.3 (e.g., data set E) and Figure 17.4 seem to suggest a decrease in the Hall–Petch slope k in the nanocrystalline regime when d becomes very small. In other words, there is a flattening of the curves in the nanocrystalline regime.

Several reports[26–28] claim that below a grain size of ~10 nm, strength decreases with further grain refinement (the so-called "inverse Hall–Petch" relationship). There is thus a "strongest grain size" where the yield stress peaks, and this appears to occur at an average grain size in the range of 10 to 20 nm. An inverse Hall–Petch behavior was in fact reported very early in the 1980s,[29] but was later found to be an artifact due to sample porosity: the hardness increases for samples with a larger d because they were fabricated by thermally coarsening the as-prepared nanocrystalline material, resulting in densification and therefore an increase in the hardness.[11] In later studies, a couple of electrodeposited, full-density nanocrystalline samples have also shown the transition into a negative Hall–Petch slope; one example is seen in Figure 17.3 (data set E).[21] But the experimental evidence

pointing to such unusual deformation responses remains so limited that a verdict is still difficult to reach at present. The challenge comes from the fact that nanocrystalline samples with d of the order of a few nanometers and suitable for reliable mechanical tests are very difficult to achieve. They have to be of full density, free of contaminations, preferably in bulk form, and the grains should be equiaxed with uniform sizes. One would hope to obtain high-quality samples via vacuum vapor deposition. But deposited metals tend to grow columnar grains and the films are usually too thin for conventional mechanical property tests. For example, a recent nanoindentation test suggests that a single Hall–Petch slope would apply for grain sizes all the way from several micrometers down to 10 nm, but the hardness data were obtained for very thin (as thin as 70 nm) Ni films on a hard (silica) substrate, such that finite-element (FE) method modeling had to be used to deconvolute the data.[30] The hardness derived as such for the nanocrystalline film (not included in Figure 17.3) was higher than those shown in Figure 17.3. There are some experimental indications, however, that grain boundary sliding and grain rotation may become operative at grain sizes below 10 nm,[15,31] and thus could substantially contribute to deformation especially if very large stresses are applied. These suggest that the softening behavior or the controversial "inverse Hall–Petch relationship," predicted by molecular dynamics (MD) simulations and models,[32] is at least a possibility for extremely small grain sizes.

17.3.2 Tensile Ductility

A literature survey indicates that the vast majority of nanocrystalline metals have tensile elongation to failure (percent elongation) below ~10%, sometimes even exhibiting or bordering "brittle" behavior.[38] The elongation observed for nanocrystalline Ni in Figure 17.2 is in fact typical for nanocrystalline metals in this regard. As examples, the ductility data measured for various nanocrystalline metals ($d < 100$ nm) over the years are summarized in Figure 17.5. Recent summaries such as this

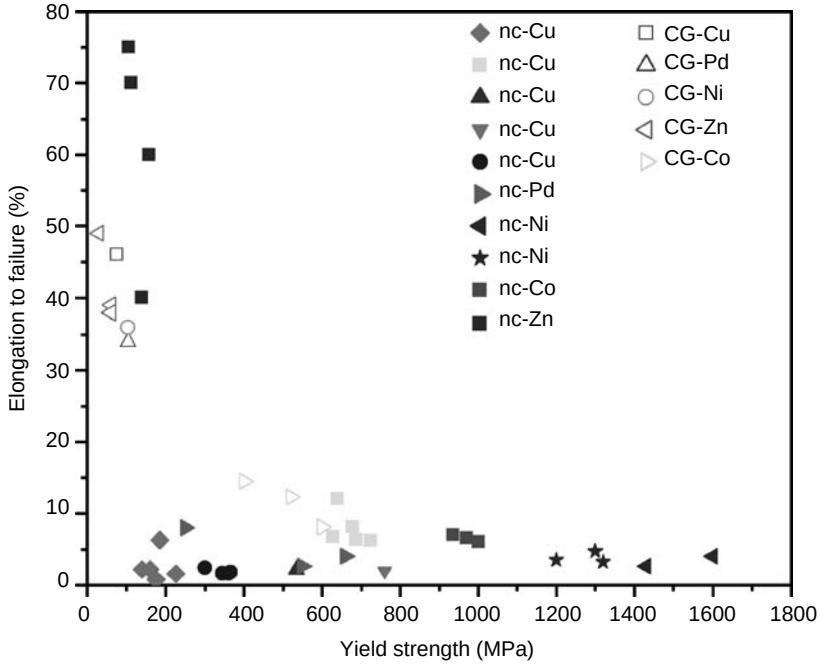

FIGURE 17.5 Tensile elongation to failure of various nanocrystalline metals (average $d < 100$ nm) in the literature, plotted against their yield strength. Note that almost all the nano-metals show a rather low tensile ductility (< ~10%) compared with their coarse-grained (CG) counterparts. The exceptions are nano-Co and nano-Zn, which showed a ductility not very different from CG-Co and CG-Zn. For Zn, however, room temperature is already a high homologous temperature.

indicate that the tensile elongation to failure of fcc metals ($d < 100$ nm) is usually much lower than their conventional coarse-grained counterparts (in Figure 17.5, the coarse-grained metals cluster on the upper-left corner). There are, however, exceptions. An electroplated Co ($d = 12$ nm) showed a respectable ~7% plastic strain at room temperature, a ductility not much lower than the hcp Co of normal grain sizes.[4]

In extreme cases, some nanocrystalline metals fail with little or no visible plastic strains (see Figure 17.5). Some also fail at rather low stresses (see bottom of Figure 17.5). It is now generally accepted that such an early and premature fracture, sometimes in the elastic regime even before yielding has a chance to start, is due to the processing flaws and artifacts.[11,39] This is especially true when the bulk sample is consolidated from loose nanoparticles, leaving pores inside the samples that trigger failure under the large tensile stresses the nanocrystalline material is subjected to. The residual porosity (of which the last 1% is extremely difficult to eliminate when consolidation has to be done at low temperatures to preserve the nanosized grains), insufficient interparticle bonding (even when full density is reached), impurities, large internal stresses, etc., can all promote the brittle behavior. The nanoscale pores and segregated impurities, particularly contaminations from H, S, O, etc., are also suspected to be detrimental to ductility in samples deposited through electrodeposition from complicated plating baths.[40]

The failure at small plastic strains can sometimes be due to a form of plastic instability, such as shear banding or necking in the early stage of straining.[39] The concentrated strains due to localization cause crack formation in the otherwise ductile metals. The observations of macroscopic chisel-tip fracture in tensile tests of electrodeposited nano-Ni that showed little tensile elongation to fracture also support the localized deformation hypothesis.[18] This tendency for the plastic deformation in nanocrystalline metals to become unstable and severely localized early upon straining originates from the lack of an effective mechanism to sustain sufficiently high rates of work hardening, as discussed below.

Intrinsically, the nanocrystalline metals appear to be ductile, at least for grain sizes above 10 nm. This is shown by the dimple features on the fracture surface (Figure 17.6) and the microscopic

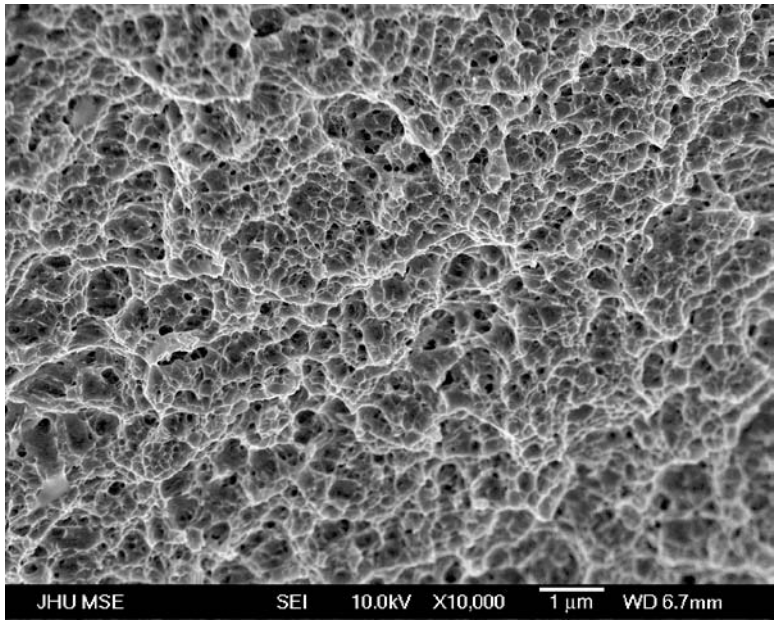

FIGURE 17.6 Scanning electron micrograph of the fracture surface of electroplated nanocrystalline Ni (d = ~30 nm) after tensile test to failure, showing dimpled rupture features indicative of ductile behavior.

necking features seen before fracture. Some recent tests on samples with low content of impurities and porosity, including nanocrystalline Ni alloys and nanocrystalline Cu, showed elongations at least >6%.[35,36,41] While this is still rather low compared with their coarse-grained counterparts, such a decent ductility is adequate for many engineering applications.

17.3.3 Work Hardening

The lack of effective strain hardening in nanocrystalline metals upon plastic deformation is perhaps to be expected because the extremely small grains cannot store dislocations to increase defect density by orders of magnitude, as normally possible in coarse-grained metals. Experimentally, stress–strain curves of nanocrystalline metals become flat quickly after the first few percent of plastic strain, with a high work-hardening rate only in the early stage of deformation (e.g., Figure 17.2).[3] This is seen in the tensile curves such as the one shown in Figure 17.2. There appears to be rather fast strain hardening at small strains (1 to 3%), immediately after yielding for nanocrystalline Ni and Cu.[13] This observation is not well understood. One possibility is that this is an initial transition period during which nanograins with different sizes gradually get involved in plastic deformation (either dislocation-based or via grain boundary sliding), since there is always a grain size distribution in nanocrystalline materials. The conventional mechanisms for high work-hardening rates in fcc metals, including the formation of dislocation locks such as the Lomer–Cottrell locks, formation of dipoles, and significant pinning due to dislocation intersections, have not been experimentally observed for nanocrystalline metals. These mechanisms, however, may be possible at very high strains and strain rates, as demonstrated in computer simulations of nanocrystalline Cu ($d = 50$ nm).[42]

17.3.4 Strain Rate Sensitivity

It has been hypothesized that nanocrystalline metals may show "low-temperature superplasticity" at or near room temperature due to grain boundary deformation mechanisms (such as grain boundary sliding and Coble creep). These grain boundary diffusion-mediated processes would lead to a high strain rate sensitivity of the flow stress, m, in the range 0.5 to 1. So far, such large m values have been reported only for creep tests, where the slow diffusional processes associated with grain boundary deformation mechanisms can largely accommodate the very slow strain rate. At ordinary strain rates, large m values have been observed only in nanocrystalline Zn,[43] for which room temperature is already a high homologous temperature.

Although far from the magnitude required for superplasticity, for fcc nanocrystalline metals, the m values are noticeably higher than those for their coarse-grained counterparts.[44] There has been evidence showing that the mechanical response of fcc nanocrystalline metals becomes more strain-rate-sensitive than coarse-grained counterparts. For nanocrystalline Ni ($d = 30$ to 40 nm), Schwaiger et al.[3] and Dalla Torre et al.[22] found an m of the order of 0.02 using depth-sensing instrumented indentation and tensile testing at various strain rates. Their tensile test results, in the range 3×10^{-3} to 3×10^{-1} sec^{-1}, have been included in Figure 17.2. The flow stress of nanocrystalline Ni increases noticeably with strain rates. Experimental results from several laboratories are summarized in Figure 17.7 for Cu and Ni. Clearly, nanocrystalline fcc metals exhibit a noticeably more pronounced strain rate sensitivity, up to a factor of ~4 at room temperature, compared to their larger grained counterparts. The mechanisms underlying the unusual rate sensitivity of deformation of fcc nanocrystalline metals and alloys are not fully understood at this time.

17.3.5 Localized Deformation

In the absence of adequate work-hardening mechanisms, local softening caused by thermal or geometrical fluctuations triggers the localization of plastic deformation. One possibility is the concentration of large deformation in narrow shear bands similar to those in amorphous materials,[51] although the exact flow mechanisms can be quite different. In addition, the simple force instability

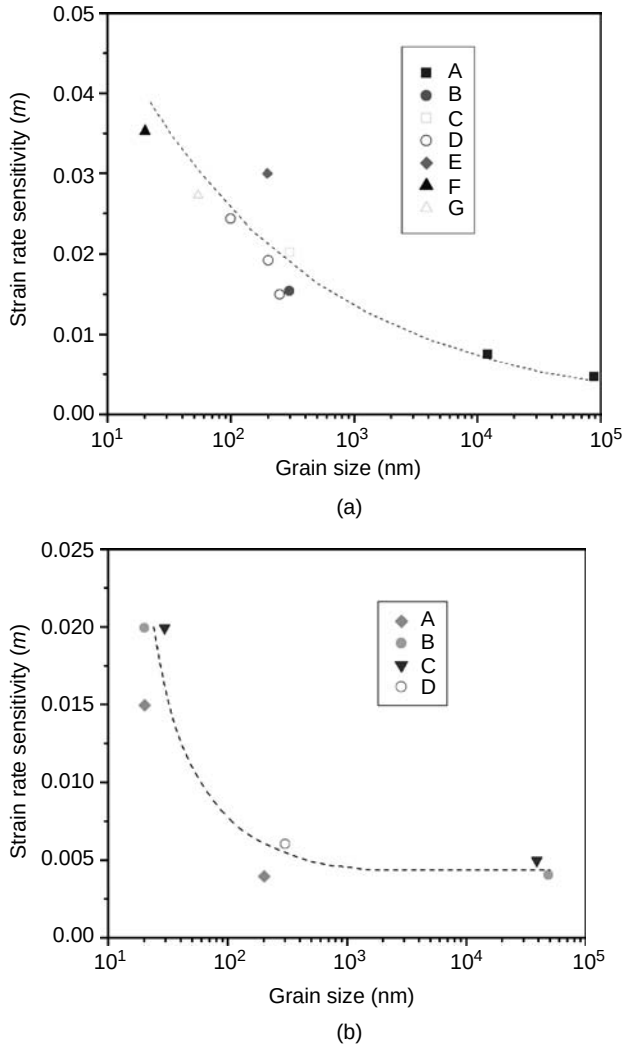

FIGURE 17.7 Summary of room-temperature strain rate sensitivity m vs. grain size d for Cu (a) and Ni (b) from the literature. Note that these figures include data not only for nanocrystalline Cu and Ni but also for ultrafine- and coarse-grained references to cover the entire d range. For both Cu and Ni, there is a clear trend of increasing m with decreasing d. The dashed curves are used to serve as a guide to the eye. In (a), A – from Ref. 45; B – from Ref. 46; C – from Ref. 47; D – from Ref. 44; E – from Ref. 48; F – from Ref. 49; G – from Ref. 35. A strain rate sensitivity m quoted as high as 0.14[50] was left out in the Cu graph because no data were presented for its measurement and it is apparently at odds with all other data. In (b), A – from Ref. 3; B – from Ref. 22; C – from Ref. 23; D – from Ref. 46.

in a tensile test, necking, can easily develop as predicted by the Considére criterion.[52] The lack of adequate strain hardening renders a high-strength nanocrystalline material very susceptible to these plastic instabilities, severely limiting the desirable uniform strain. A perfectly plastic material without strain hardening would neck right away after the plastic flow commences.

In this context, Jia et al.[53] have shown the formation of localized shear bands during compression deformation of nanocrystalline body-centered-cubic (bcc) Fe at quasi-static strain rates at room temperature; they further noted that the width of the band increased with increasing strain and increasing grain size. Figure 17.8 shows that shear bands develop in consolidated Fe ($d \sim 100$ nm)

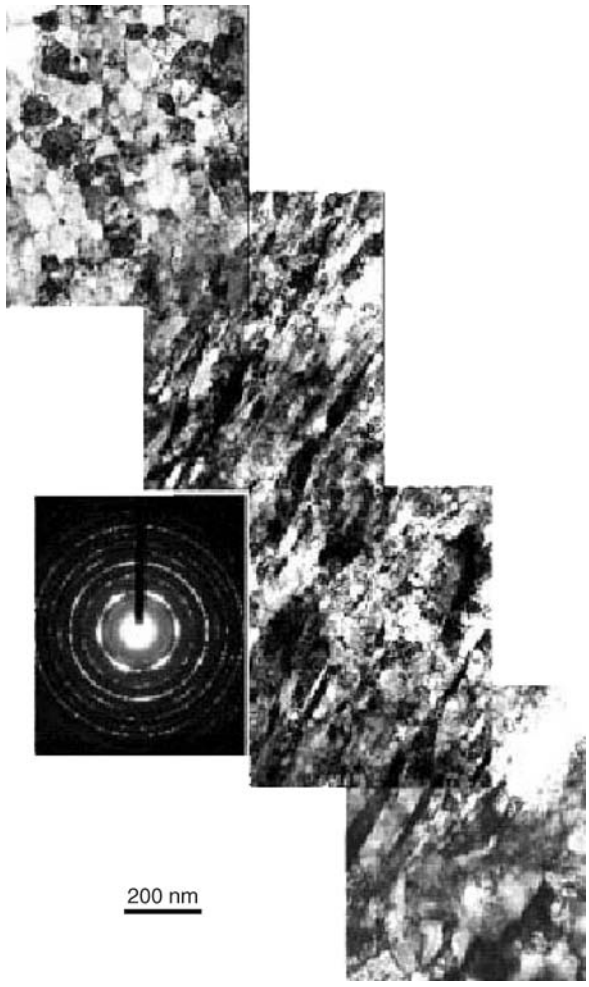

FIGURE 17.8 A collage of TEM micrographs across a shear band formed in nano-Fe ($d \sim 100$ nm), showing the elongated grains with dislocations inside the shear band, and the equi-axed grains outside the shear band (top and bottom corners). The electron diffraction pattern taken inside the shear band reveals texturing. (From Wei, Q. et al., *Appl. Phys. Lett.*, 81, 1240–1242 (2002).)

in a manner similar to that reported earlier in ultrafine-grained nanocrystalline Fe–10% Cu alloy in compression and in tension.[51] As seen in Figure 17.8, the grains within the shear band show large elongations along the direction of shearing, while the grains outside the band remain equiaxed. The elongated grains inside the shear band appear to contain high densities of dislocations, suggesting a dislocation-based mechanism of plastic flow. The lack of recovery/recrystallization and the sharp boundaries of the bands seem to suggest that the shear banding is not adiabatic in nature.[54] Signs of shear banding have also been reported in compression testing of nanocrystalline Pd[33] and in fatigue testing of nanocrystalline Cu,[55] but shear banding has not been found to be a prevalent mode of deformation for all nanocrystalline materials.

17.3.6 Cryogenic Behavior

Figure 17.9 shows the large increase in strength when nanocrystalline Ni is deformed at 77 K (liquid nitrogen temperature) when compared with that at room temperature.[23] The strength ratio is clearly higher than that for reference Ni (coarse-grained) shown in the inset, for which this

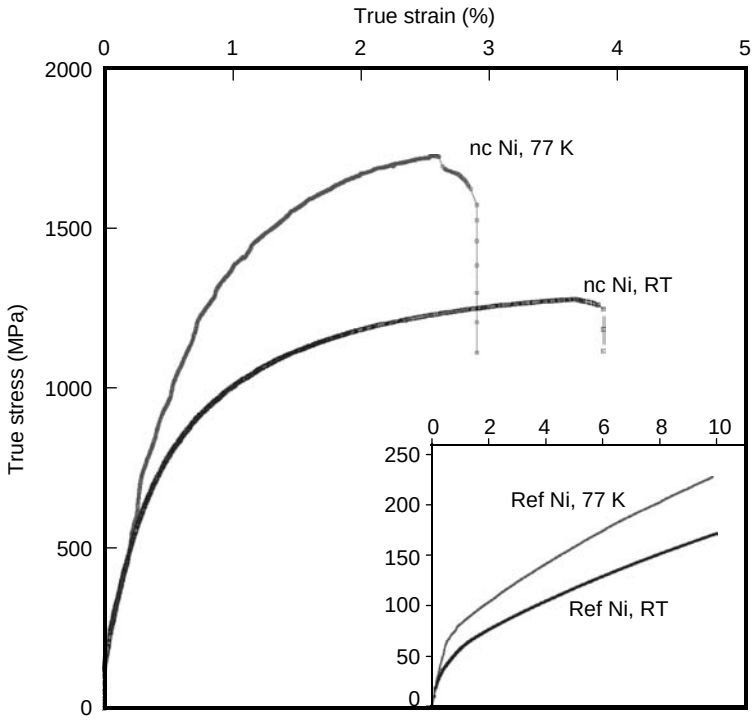

FIGURE 17.9 Tensile stress–strain curves of nanocrystalline Ni ($d = 30$ nm) tested at room temperature and 77 K. The inset shows the corresponding curves for the reference coarse-grained Ni for comparison. (From Wang, Y and Man, E., *Appl. Phys. Lett.*, 85, 2750–2752 (2004).)

(Cottrell–Stokes) ratio is approximately a constant of 1.2 for annealed Ni or Ni subjected to different amounts of cold work. This behavior is consistent with the increased strain rate dependence discussed above, and has also been observed in nanocrystalline Cu and nanocrystalline Co as well.[23,56]

17.3.7 Creep and Superplasticity

A number of studies have been performed to investigate whether creep mediated by grain boundary diffusion, which is dominant in coarse-grained metals at elevated temperatures (0.4 to $0.6T_m$, where T_m is the melting temperature), can become significant at low temperatures in nanocrystalline metals (e.g., room temperature). The possibly large contribution from grain boundary diffusional creep, due to the large fraction of grain boundary atoms and their unusual diffusion rates, has been hypothesized for many years, but existing data in the literature are conflicting. Creep rates consistent with Coble creep or long-range diffusion-mediated grain boundary sliding were indeed reported for electroplated nanocrystalline Ni ($d = 6$, 20, and 40 nm) and Au,[58,59] but not in Cu and Pd prepared using inert gas condensation (IGC) that showed creep rates similar to their coarse-grained counterparts.[60] The total creep strain range examined was usually small, less than 1%, making it difficult to judge if a steady-state creep rate has indeed been attained. As summarized in a review by Mohamed and Li,[61] data obtained by different investigators are either not consistent in trend, or too limited in scope. Some of the inconsistency may be due to the specific microstructural features in the samples studied, e.g., the appreciable number of twin boundaries and low-angle boundaries in the IGC samples could be resisting sliding.

Although there is no superplasticity established for nanocrystalline metals at room temperature, there are a small number of observations of superplastic deformation at moderately elevated temperatures. This has upheld the predictions of the advantage of nanocrystalline materials in low-temperature

superplastic deformation. Using electrodeposited nanocrystalline nickel ($d = 20$ nm), nanocrystalline 1420-Al ($d = 100$ nm), and nanocrystalline Ni_3Al ($d = 50$ nm) prepared via severe plastic deformation, McFadden et al.[57] conducted tensile tests at constant strain rates and elevated temperatures. In the case of nickel, a transition in deformation behavior occurred above 280°C; this is indicated by the curve for deformation at 350°C in Figure 17.10, which shows yielding and strong strain hardening with a large plastic deformation in the superplastic regime of >200% elongation. This onset of superplasticity coincided with the onset of grain growth. For Ni_3Al, the conventional material has a yield-stress maximum around 650°C, referred to in the literature as a "yield-stress anomaly," but this strength maximum is accompanied by a ductility minimum, around 20% total elongation. In contrast, in nanocrystalline Ni_3Al, the tensile ductility is as high as 350% at this temperature. As for nanocrystalline 1420-Al, in addition to lower superplastic temperatures, it also demonstrated high-strain-rate superplasticity, defined by superplastic strain rates greater than $10^{-2}\,sec^{-1}$. Samples before and after deformation are shown in Figure 17.11, which demonstrates the large uniform elongation representative of superplasticity.

After deformation at 350°C, the average grain size in the deformed gage section of Ni was 1.3 μm along the tensile axis and 0.64 μm transverse to the tensile axis. Although significant grain growth occurred during deformation, these grain sizes were still much smaller than those obtainable using conventional refinement techniques. After finishing testing on 1420-Al at 250°C, the

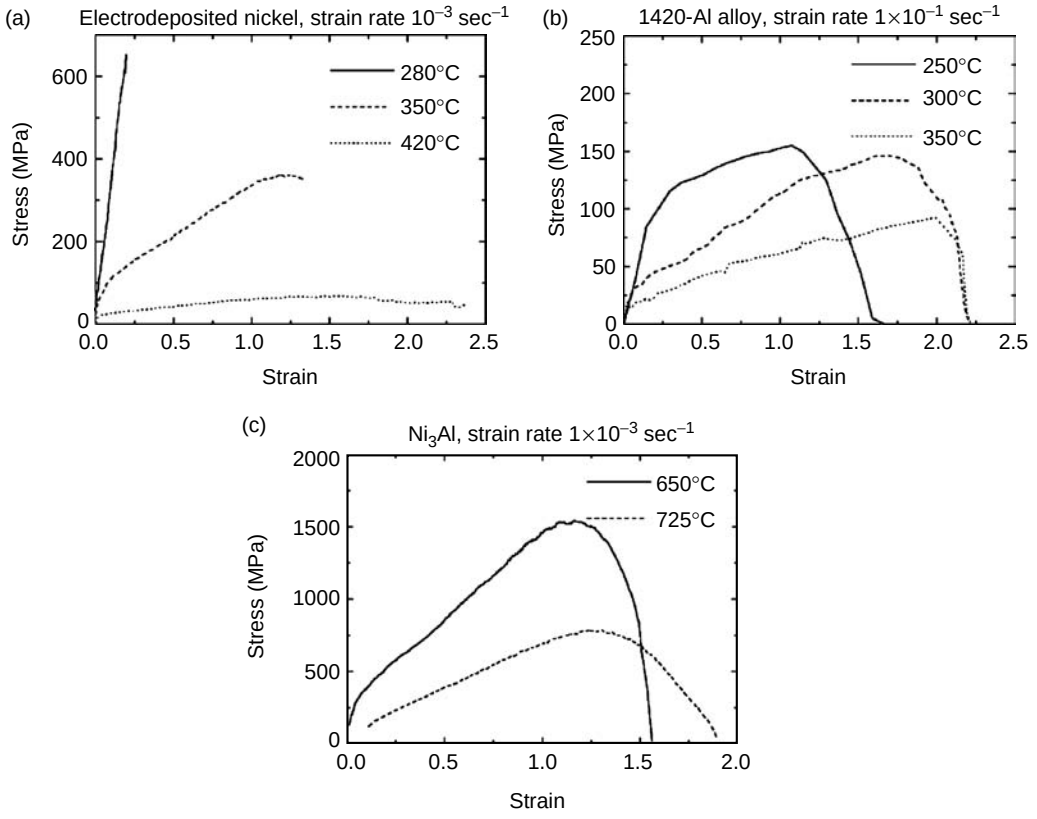

FIGURE 17.10 Stress–strain curves obtained at constant strain rates and temperatures, for (a) electrodeposited nano-Ni (a), nanocrystalline aluminium alloy 1420-Al processed by severe plastic deformation (b), and nanocrystalline Ni_3Al processed by severe plastic deformation (c). Note the transition from low plasticity to superplasticity in (a) between 280 and 350°C, the high strain rates in (b), and the very high flow stresses in (c). (From McFadden, S.X. et al., *Nature*, 398, 684–686, 1999.)

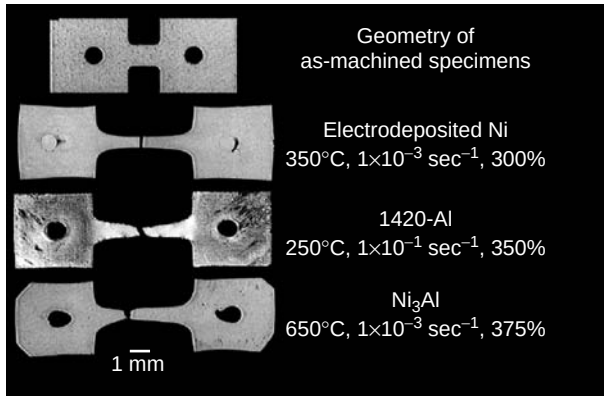

FIGURE 17.11 Tensile specimens in the as-machined geometry and after deformation, showing superplastic deformation (to elongations well beyond 100%). (From McFadden, S.X. et al., *Nature*, 398, 684–686, 1999.)

grain size in the deformed gage section was 0.22 μm. For the Ni_3Al that was tested at 650°C, the grain size in the deformed gage section was still nanocrystalline at 100 nm. Note that the high flow stresses and significant work hardening observed in Ni_3Al and 1420-Al suggest that the details of superplasticity may be fundamentally different in nanostructured materials.

17.3.8 Fatigue and Fracture

Many attractive features of nanocrystalline metals, such as high strength, high hardness, and improved resistance to wear and corrosion damage, would likely be rendered nonviable if the damage tolerance of these materials does not meet certain acceptable levels for specific applications. An understanding of the damage tolerance would require comprehensive knowledge of the resistance to fracture initiation and growth, and of stress- and strain-based total fatigue life and subcritical crack growth. However, only limited information is presently available in the literature. This lack of information can be attributed to the fact that the processing methods used to produce fully dense nanocrystalline materials with uniform purity and uniformly small grain sizes typically yield only thin foils. Although these methods can provide material with large in-plane dimensions, the small specimen thickness poses considerable experimental difficulties in performing a valid test to extract fracture toughness, resistance curve (R curve) or fatigue properties. A review of several very recent experiments in this area, including discussion on fracture mechanisms, has been published by Kumar et al.[13]

Mirshams et al.[62] studied the quasi-static fracture toughness of thin sheets of nanocrystalline nickel ($d = 19$ to 48 nm) produced by electrodeposition by investigating their R curve response. In this approach, the stress intensity factor or strain energy release rate is plotted against the increment in crack length with the objective of assessing the resistance of the material to quasi-static crack growth in a subcritical manner, usually for specimens in a state of plane stress. Mirshams et al. studied subcritical growth resistance by monitoring R curves with small compact tension specimens where a clip gage was used to monitor crack extension along with optical microscopy. They reported plane stress, steady-state, quasi-static fracture toughness values in the range 20 to 120 $MPa\,m^{1/2}$, and a strong negative influence of annealing temperature and carbon doping on the toughness value. Independent experimental studies of fracture resistance in fatigue precracked 100-μm-thick electrodeposited Ni sheets with $d = 20$ to 40 nm, also reveal that the plane stress fracture toughness in laboratory air is at least about 25 $MPa\,m^{1/2}$.[13] The nanocrystalline Ni as such has a reasonable fracture toughness considering its relatively high strength and low ductility compared with conventional Ni. However, further experimental studies of fracture toughness in nanocrystalline metals and alloys are critically needed so as to develop a fundamental framework with which their fracture mechanisms can be systematically assessed.

It is widely recognized from the wealth of experimental information available in the literature[63] on conventional metals and alloys that a reduction in grain size generally results in an elevation in strength which engenders an increase in fatigue endurance limit during stress-controlled cyclic loading of initially smooth-surfaced laboratory specimens. Since the total fatigue life under such conditions is dominated by crack nucleation and since fatigue cracks generally nucleate at the free surface, grain refinement here is considered to result in improvements in fatigue life as well as endurance limit. On the other hand, a coarser grain structure with lower strength and enhanced ductility generally plays a more beneficial role in the strain-controlled fatigue response of metals and alloys. Here, low-cycle fatigue properties generally improve with grain coarsening.

While several studies have examined the total fatigue life of ultrafine crystalline metals produced by equal channel angular pressing, where severe plastic deformation was used for grain refinement,[64] little is known about the fatigue characteristics of nanocrystalline metals. In a recent report[9] of the fatigue life and fatigue crack growth characteristics of a well-characterized electrodeposited nanocrystalline Ni with $d = 20$ to 40 nm, Hanlon et al.[9] compared its stress-life (S-N) fatigue response with that of a similarly produced ultrafine crystalline ($d = 300$ nm) Ni and of a conventional Ni. Figure 17.12 shows that grain refinement has a significant effect on the S-N fatigue response of pure Ni. Nanocrystalline Ni has a slightly higher, but reproducible increase in the tensile stress range needed to achieve a fixed life and in the endurance limit (defined at 2 million fatigue cycles) compared with the 300 nm Ni. A significantly higher fatigue endurance limit than the conventional microcrystalline metal is evident. Hanlon et al.[9] also conducted fatigue crack growth experiments on nanocrystalline Ni using edge-notched specimens. They found that the rate of fatigue crack growth is significantly increased with decreasing grain size in this intermediate regime of fatigue fracture. Such trends are fully consistent with the mechanistic expectations of fatigue fracture based on results available for conventional alloys.

Recently, Aktaa et al.[10] reported results for high-cycle tension–tension ($R = 0.1$) fatigue testing of electrodeposited ultrafine-grained LIGA Ni. The as-measured S–N data suggested that the ultrafine-grained samples were more fatigue resistant than bulk Ni, but Aktaa and co-authors[10] showed that using the Basquin relation as modified by Morrow[65] to account for the effect of mean stress (the LIGA tests were conducted with $R = 0.1$ while the literature data for bulk Ni was obtained using

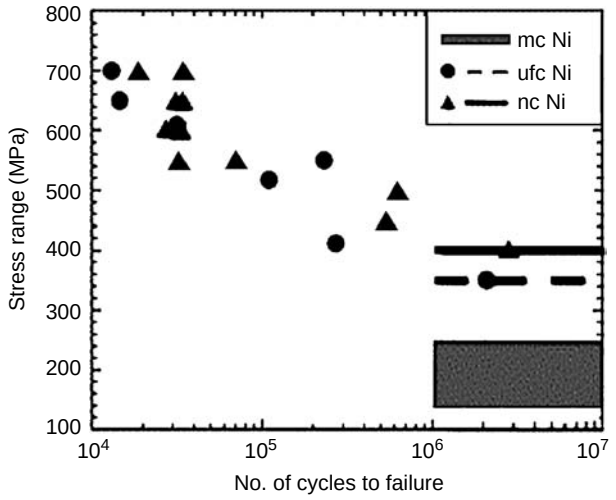

FIGURE 17.12 S-N fatigue response of nanocrystalline Ni ($d = 20$–40 nm) compared with that of an ultrafine crystalline Ni (ufc, $d \sim 300$ nm) at frequency of 1 Hz in air environment of the laboratory. Also shown for comparison are the literature values of the range of endurance limits for conventional microcrystalline (mc) pure Ni. (From Hanlon, T. et al., *Scr. Mater.*, 49, 675–680, 2003.)

fully reversed loading [$R = -1$]) indicated otherwise. Extended to the condition of fully reversed loading, the fatigue behavior of the ultrafine-grained LIGA Ni samples was found to be comparable with literature values for conventionally processed bulk Ni. Aktaa et al. also showed that final fracture of the ultrafine-grained LIGA Ni samples corresponded to a fracture toughness of ~50 MPa $m^{1/2}$.

17.4 DEFORMATION MECHANISMS

As described in Section 17.3, nanocrystalline materials often exhibit greatly enhanced mechanical properties; ultra-high strength, hardness, and superplasticity at relatively low temperatures and high strain rates, have all been reported. Numerous theoretical and experimental studies have been undertaken, but to date the underlying mechanisms responsible for these unusual properties have not been fully identified. In this section, we summarize the results and understanding that have been gleaned from studies aimed at describing the unusually high strength and limited ductility that nanocrystalline metals and alloys exhibit. While the overall ductility of metals is clearly diminished when grain size is reduced to the nanocrystalline regime (Figure 17.5), it is important to note that nanocrystalline metals and alloys do plastically deform. Identification of the physical mechanisms responsible for this plasticity is needed to model both the enhanced strength and the reduced plasticity. The picture is currently far from complete, but significant progress has been made and general trends and moderate levels of understanding appear to be emerging.

17.4.1 Extensions of Microscale Deformation Mechanisms

In undertaking to describe how nanocrystalline materials deform, it seems prudent to first establish to what scale microscale deformation mechanisms are operative. Plasticity on the microscale is well described in the framework of dislocation activity, and detailed models of the effect that lattice friction, strain hardening, and microstructural obstacles (precipitates, dispersiods, grain boundaries) have on dislocation mobility have been developed to depict the attendant mechanical behavior of numerous microcrystalline alloys. Time-dependent deformation of microcrystalline materials may also occur by diffusive processes, and the strain rates associated with processes such as Herring–Nabarro creep and Coble creep are known to be strongly grain-size-dependent. Here, we discuss the physical processes associated with both Hall–Petch strengthening and Coble creep and consider their applicability to nanocrystalline metals.

17.4.1.1 Hall–Petch Relationship

The empirical Hall–Petch relationship (17.1) for the effect of grain size on strength has been shown to hold for a remarkably wide range of microcrystalline grain sizes and it was first thought that extrapolation to smaller grain sizes might provide a measure of the changes that occur in the underlying deformation mechanism.

The composite Hall–Petch plots for Ni and Cu that are shown in Figure 17.3 and Figure 17.4 are similar to those that have been published elsewhere in that they indicate that the Hall–Petch relation holds for grain sizes of less than 100 nm. Closer inspection of the data in these plots indicates that the Hall–Petch slope is lower in the nanocrystalline domain than it is in the microcrystalline range. In some cases, a zero or even negative Hall–Petch slope has been reported.[26–28] Experimental evidence for the existence of a negative Hall–Petch slope is, however, not conclusive and has been the focus of considerable debate. This point aside, schematic representations of the variation of yield strength as a function of grain size have been constructed by several authors[13,32] and an example is shown in Figure 17.13. The following three different regions are identifiable:

1. A region from micro-scale to about 100 nm, where strengthening with grain refinement follows the traditional Hall–Petch relationship.

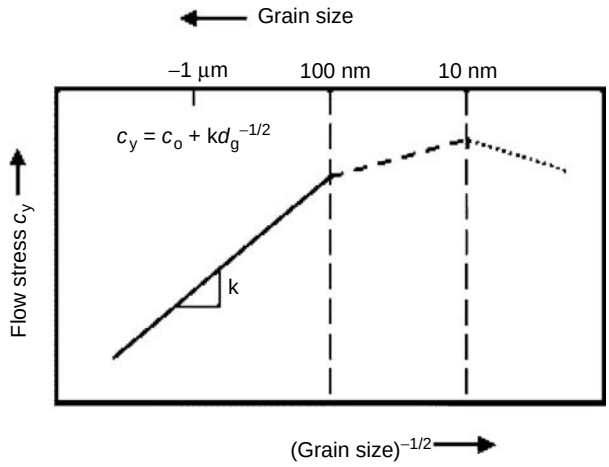

FIGURE 17.13 A schematic representation of the variation of yield stress as a function of grain size in microcrystalline, ultrafine-grained, and nanocrystalline metals and alloys. (From Kumar, K.S. et al., *Acta Mater.*, 51, 5743–5774, 2003.)

2. A region for grain sizes ranging from approximately 100 to 10 nm, where the linear relationship between σ_y and $D^{-1/2}$ appears to hold, but the slope (efficacy of grain boundaries as dislocation obstacles) and intercept (intrinsic strength) are different than for the microcrystalline region.
3. A region corresponding to grain sizes of 10 nm or smaller, where loss of the Hall–Petch exponent and potential grain boundary softening may occur.

This continuum level description of changes in the flow behavior of nanocrystalline metals can be related to changes in the underlying deformation mechanisms by considering the physical basis of the Hall–Petch relationship. To date, three models with different microscopic mechanisms have been proposed. It is useful to revisit these models and to consider the extent to which they would be valid in the nanocrystalline regime.

17.4.1.1.1 Dislocation Pileup Model

The original and most cited dislocation explanation for the Hall–Petch relationship is based on the concept that grain boundaries act as barriers to dislocation motion. As a result of this, dislocations gliding on the same slip plane can be expected to form a dislocation pileup at the edge of the grain (at the grain boundary). This piledup array of dislocations concentrates and magnifies the applied shear stress at the boundary (Figure 17.14). If there are n dislocations in the pileup, the effective shear stress at the boundary will be $n\tau_i$, where τ_i is the resolved shear stress.[66] The number of dislocations (n) in a pileup scales with the grain diameter D and is given by[67,68]

$$n = \frac{\kappa\pi\tau_i D}{4Gb} \tag{17.2}$$

where $\kappa = (1-\nu)$ for edges and 1 for screws and b is the magnitude of the Burger's vector. When the stress at the tip of the pileup exceeds a critical stress τ_c, dislocations are nucleated in the neighboring grain and slip continues. Macroscopic plastic deformation is thought to be associated with the spreading of dislocation activity throughout the specimen and the stress at which this occurs is given as

$$\tau_c = n\tau_i = \frac{\kappa\pi\tau_i^2 D}{4Gb} \tag{17.3}$$

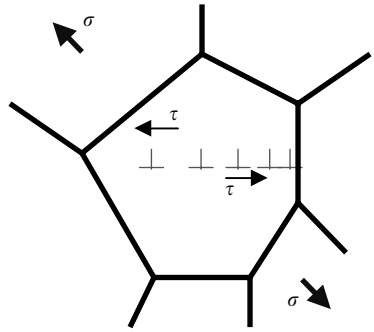

FIGURE 17.14 Schematic of the dislocation pileup model.

The resolved shear stress required to overcome the influence of the grain boundary can be taken as the applied stress τ less the friction stress to overcome intrinsic resistance τ_o, i.e.,

$$\tau_i = \tau - \tau_o \tag{17.4}$$

Substituting Equation (17.3) gives

$$\tau_c = n\tau_i = \frac{\kappa\pi(\tau - \tau_o)^2 D}{4Gb} \tag{17.5}$$

and rearranging yields

$$\tau = \tau_o + \left(\frac{4\tau_c Gb}{\pi D}\right)^{1/2} = \tau_o + k'D^{-1/2} \tag{17.6}$$

Expressing Equation (17.6) in terms of the normal stress, σ, results in Equation (17.1).

17.4.1.1.2 Grain Boundary Ledge Model

The fact that dislocation pileups are primarily observed in low stacking fault energy metals and alloys and observations of dislocation generation at grain boundaries in microcrystalline alloys suggest that dislocation pileups may not be the only micromechanism that leads to the Hall–Petch relationship. An alternative grain boundary dislocation model was proposed by Li.[69] In this model, the grain size effect is considered to come from dislocation emission at grain boundary ledges and the ability of a grain boundary to emit dislocations is defined by the parameter

$$\mu = \frac{L_{total}}{S} \tag{17.7}$$

where L_{total} is the total length of dislocation line emitted from a grain boundary and S the area of the grain boundary. μ is intrinsically related to the dislocation density ρ within the grain and at the yield point, the dislocation density is approximately expressed as

$$\rho = \frac{3\mu}{D} \tag{17.8}$$

If the yield stress depends on the dislocation density, according to the Taylor relation,

$$\sigma = \sigma_o + \alpha Gb\sqrt{\rho} \tag{17.9}$$

and the Hall–Petch relationship can be obtained from Equations (17.8) and (17.9)

$$\sigma = \sigma_o + \sqrt{3}\alpha G b \mu^{1/2} D^{-1/2} \tag{17.10}$$

17.4.1.1.3 Composite Model

Adopting the idea that the effect of grain size is associated with the generation of dislocations from grain boundaries, Meyers and Ashworth[70] suggested that the grain-size dependence of strength may be related to elastic incompatibility at grain boundaries. In this view, yielding of a polycrystalline metal can be described in three stages. In the first stage, the difference in elastic response between adjacent grains is responsible for the generation of incompatibility stresses at the grain boundaries, which reinforce the resolved shear stress and initiate plastic flow at the grain boundaries prior to grain interiors. In the second stage, the localized deformation results in a work-hardened grain boundary layer and a softer core ($\sigma_{fGB} > \sigma_{fB}$). In the third stage, the dislocation density in grain interiors and grain boundary regions equilibrate, both regions reach the same flow stress and the plastic incompatibility diminishes (Figure 17.15). In this way, a grain can be treated as a composite with a hard shell (grain boundary region) and soft core (grain interior). A "rule-of-mixtures" expression for the yield strength gives

$$\sigma_y = A_B \sigma_{fB} + A_{GB} \sigma_{fGB} \tag{17.11}$$

where A_{GB} and A_B are the area fractions of the grain boundary shell and of the core. With the assumptions that (1) the grains are spheres with diameter D and grain boundary thickness t and (2) that $t = kD^{1/2}$ (where k is constant), one obtains

$$\sigma_y = \sigma_{fB} + 8k(\sigma_{fGB} - \sigma_{GB})D^{-1/2} - 16k^2(\sigma_{fGB} - \sigma_{GB})D^{-1} \tag{17.12}$$

This equation yields the classical Hall–Petch relationship ($\sigma_y \propto D^{-1/2}$) for large grain sizes but the D^{-1} term becomes more important for smaller grain sizes, which is qualitatively consistent with the grain-size dependence illustrated in Figure 17.13.

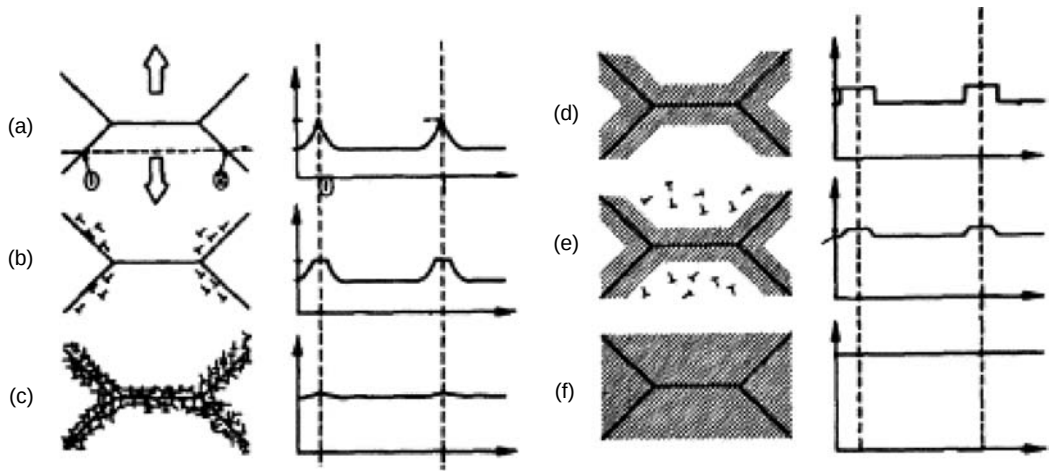

FIGURE 17.15 Sequence of stages in polycrystalline deformation, starting with (a,b) localized plastic flow in the grain-boundary regions, (c,d) formation of a work-hardened grain-boundary layer that leads to (e,f) macro-yielding in which the grain interiors undergo plastic deformation. (From Meyers, M.A. and Ashworth, E., *Phil. Mag. A*, 46, 737–759, 1982.)

17.4.1.1.4 Limitations in the Extension of Hall–Petch Models to Nanocrystalline Metals

There is a growing body of evidence to indicate that all three dislocation-based mechanisms used to describe the Hall–Petch relation in microcrystalline metals break down as the grain size is reduced from hundreds to several tens of nanometers. As discussed below, it is generally acknowledged that dislocation pileups become impractical and that Frank–Read and other traditional dislocation sources cease to operate at these reduced grain sizes. It is also important to recognize that postmortem TEM observations have failed to uncover any evidence of dislocation pileups or dislocation tangles in deformed nanocrystalline metals[71] and that *in situ* x-ray peak broadening experiments[72] also point to the absence of dislocation storage in these materials.

Nieh and Wadsworth[73] considered the absolute limit (a dislocation pileup composed of only two edge dislocations) and calculated the equilibrium distance between these two dislocations from an estimate of the lower bound repulsive force (f) per unit length, e.g.,

$$f = \frac{Gb^2}{2\pi(1-\nu)l} \tag{17.13}$$

where l is the distance between the dislocations. By balancing this repulsive force with the externally applied shear force $\tau_{app}b$, where τ_{app} is the applied shear stress and is taken to be $\tau_{app} = \sigma/2$, they predicted the critical distance between dislocations at yielding to be

$$l_c = \frac{Gb}{\pi(1-\nu)\sigma} \tag{17.14}$$

Using this relation, Nieh and Wadsworth calculated the critical size of a two dislocation pileup to be in the range of several nanometers to tens of nanometers for a variety of metals.[73] The strength predicted by the pileup model becomes increasingly discontinuous for pileups with limited numbers of dislocations (<20).[32,74] Given the discreteness of the model for small numbers of dislocations, it is reasonable to assume that the dislocation pileup model breaks down at considerably larger grain sizes.

Other researchers have considered the stress required to activate a Frank–Read source and have shown that for the strengths that have been measured in which such a source, the limiting source size and therefore the limiting grain size, could operate is of the order of 30 to 50 nm.[71] This estimate can be realized by considering the strength of a nano-Ni sample and comparing that strength with the stress required for operating a Frank–Read source:

$$\tau = \frac{\sigma}{2} = \frac{Gb}{l_{FR}} \tag{17.15}$$

Given the lack of intragranular dislocation sources, the required dimensions of a dislocation pileup and the absence of experimental evidence for such pileups, extension of the Hall–Petch dislocation pileup model to nanocrystalline grain sizes would be highly questionable.

For both the Li grain boundary edge model and the Meyer's composite model the grain size effect on strength is derived from localized work hardening that involves generation and tangling of dislocations in the near grain boundary regions. The absence of any evidence for dislocation storage in nanocrystalline metals suggests that these classic work-hardening models are not appropriate for nanocrystalline metals. Even if dislocation-based plasticity were to occur in nanocrystalline grains, the gradients in intragranular plasticity described in these models would be very hard to envision. Instead, the consensus building up seems to be that dislocation activity is fundamentally different in nanocrystalline metals than it is in microcrystalline metals.

17.4.1.2 Coble Creep

Given the absence of traditional dislocation activity in nanocrystalline metals, Chokshi et al.[29] proposed a model for room-temperature deformation that is based on increased efficiency of Coble

creep at relatively modest temperatures. Given the extremely high volume fraction of grain boundaries in nanocrystalline metals, enhanced diffusion and creep rates may be predicted to occur by the transport of vacancies along grain boundaries, and deformation that is enhancedby grain boundary behavior. For such diffusive processes, the deformation or creep rate ε can be expressed as[75]

$$\varepsilon = \frac{150\Omega\delta D_{GB}\sigma}{\pi\, kTD^3} \tag{17.16}$$

where Ω is the atomic volume, δ the grain boundary width, D_{GB} the grain boundary diffusion coefficient, k the Boltzmann's constant, and T the absolute temperature. Because of the very high dependence on grain size, the strain rate is predicted to be as high as $10^{-3}\,\text{sec}^{-1}$ for nanocrystalline Cu with 10 nm grains, which would be comparable with that required for quasi-static deformation. For this reason, Coble creep was originally thought to be a viable mechanism for the plastic deformation of nanocrystalline metals.[29]

Nieh and Wadsworth[73] have, however, pointed out that the functional dependence of stress on grain size assumed in the original work of Chokshi is not consistent with the theoretical model of Coble creep,

$$\sigma = \sigma_0 + \alpha D^3 \tag{17.17}$$

where σ_0 is the threshold stress for Coble creep and α a constant. This criticism seems to be supported by the fact that this relationship has not been found experimentally in other nanocrystalline metals. Weertman and colleagues[60] have shown that experimentally measured creep rates of nanocrystalline Cu and Pt are two to four orders of magnitude smaller than the values predicted by the equation for Coble creep. Thus, simple Coble creep cannot be the factor controlling the plastic deformation of nanocrystalline metals.

17.4.1.3 Mixture Model

Masumura et al.[32] suggested a mixture model that accounts for the distribution of grain sizes that occurs in most nanocrystalline materials. In this model, grains larger than a certain critical value are thought to deform by dislocation plasticity and their strength is predicted by Hall–Petch, while grains smaller than the critical value are modeled using descriptions for Coble creep. The yield stress corresponding to a material with a given average grain size is calculated using a simple weighted average of super- and subcritical grains. This description has been used to model the dependence of strength on grain size and the deviation from Hall–Petch behavior that have been reported for nanocrystalline Cu, e.g., Figure 17.3.[29] The physical basis for this mixture model is, however, less than clear. The Hall–Petch and Coble creep models were derived to explain intergranular behavior of a collection of grains; using them to describe the behavior of individual grains is not physically sound and seems less than satisfactory.

17.4.2 Observed Deformation Mechanisms for Nanocrystalline Metals

17.4.2.1 Molecular Dynamics Simulations

The recent development of large-scale atomistic simulation techniques provides an opportunity to observe atomic level processes associated with the deformation of nanocrystalline metals at a level of atomic detail that is inaccessible to experiments. Limitations associated with the computational complexity of these simulations preclude direct identification of exact deformation mechanisms, but the availability of MD simulations can and has been used to deduce possible deformation processes and to inspire mechanistic-based modeling of mechanical behavior in polycrystalline samples of nanocrystalline materials. Comprehensive reviews on the MD simulations of nanocrystalline metals

can be found in the literature[13,76] and the reader is referred to these references for a complete discussion of the merits and limitations of the MD studies. In this chapter, our purpose is to highlight results of MD simulations that can be compared with experimental observations and used to inspire future experiments and models aimed at increasing our fundamental understanding of deformation mechanism in nanocrystalline metals.

17.4.2.1.1 Grain Boundary Activity

Schiotz et al.[77] have reported MD simulations of uniaxial deformation in nanocrystalline Cu, which indicate that plastic deformation occurs predominantly in the grain boundaries (Figure 17.16). Temporal snapshots of the deformation suggest that such deformation comprises of a large number of small local sliding events, where only a few atoms (or at most a few tens of atoms) move with respect to each other. The simulations further suggest that reducing the grain size and increasing the fraction of the grain boundary atoms leads to enhanced grain boundary sliding and softening of the material, as would be consistent with reported reverse Hall–Petch behavior. The grain boundary sliding predicted by the simulation is similar in nature to the thermally assisted grain boundary sliding that occurs during superplastic deformation. However, in the simulations, the grain boundary sliding occurs at room temperature and at extremely fast strain rates. If thermal assistance is absent, the grain boundary sliding simulated in the nanocrystalline materials appears to be driven by the high stresses that accrue in the absence of dislocation plasticity. Extensive intragranular dislocation activity was not observed in the simulations, but a small number of partial dislocations were observed to nucleate at a grain boundary and traverse quickly through the adjacent grain. These partial dislocations were responsible for only a minor part of the total deformation, but in the absence of diffusion they are required for reshaping of the grains, as they slide past each other.

Van Swygenhoven et al.[78] reported similar atomic-scale processes in MD studies of tensile loaded 3-D nanocrystalline Ni. Again, no evidence of intragranular dislocation plasticity was uncovered, but grain boundary sliding was observed and associated with discrete atomic activity, either through uncorrelated shuffling of individual boundary atoms or by shuffling of correlated groups of boundary atoms. In both cases, the excess free volume present in the grain boundaries appeared to play an important role in determining the response of the boundaries. In addition to shuffling, hopping sequences involving several grain boundary atoms and, in many instances, the nucleation of partial dislocations was also observed. These atomic-level grain boundary processes

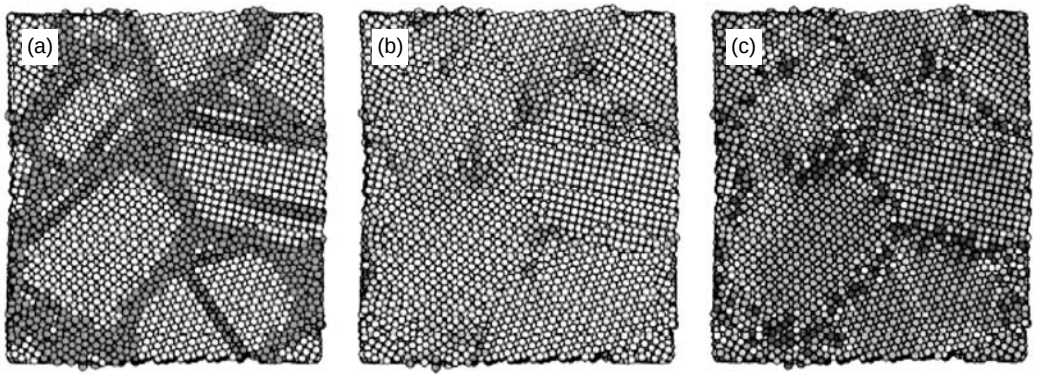

FIGURE 17.16 A simulated snapshot of the grain structure, displacements, and stresses in a nano-Cu sample after 8% deformation. (a) The grain boundaries are shown in blue and the stacking faults in red. (b) The relative motion of the atoms (green atoms move up, red atoms move down, in the plane of the paper) during the preceding 0.4% deformation highlights the concentration of slip at the grain boundaries. (c) The associated stress field indicates that highest tensile (red) and compressive (blue) stresses occur in the boundaries but vary dramatically on the atomic scale. (From Schiotz, J. et al., *Nature*, 391, 561–563, 1998.)

are needed to relieve the accommodation stresses that build up during the sliding of atomically rough grain boundaries. The resultant change in the structure of the grain boundary causes a redistribution of these stresses and is needed to facilitate further sliding. The MD simulations suggest that these grain boundary processes require short-range atomic motion and stress-assisted free-volume migration and may involve dislocation emission but do not involve long-range diffusive processes like Coble creep.

Yamakov et al.[79] investigated the room-temperature plastic deformation of 2-D columnar networks of nanocrystalline Al with MD simulations and reported a transformation in the dominant deformation process — plasticity being accommodated by grain boundary processes at relatively lower strain rates and stresses, and partial dislocation activity and twinning at relatively higher strain rates and stresses (Figure 17.17). It should be noted that the strain rates used in these MD simulations are all orders of magnitude higher than are realized in experiments, and the importance of dislocation activity at the highest strain rates may be over-exaggerated. Nevertheless, the importance of the grain boundary process and the fact that dislocation nucleation was observed in all of the MD studies suggests that grain boundary sliding and associated dislocation emission both play an important role in governing the plastic deformation of nanocrystalline metals. It is important to note that the role of dislocations in nanocrystalline metals is predicted to be fundamentally different from that for microcrystalline metals.

17.4.2.1.2 Dislocation Nucleation at Nanocrystalline Grain Boundaries

The MD simulations of deformation in nanocrystalline Cu, Ni, and Al samples all point to grain boundary sliding as the dominant strain accommodation mechanism, and also illustrate the importance of atomic shuffling and free-volume migration in the nucleation of partial dislocations at the grain boundaries and the subsequent propagation of these dislocations in the grain interiors. The dislocations generated by this process can be shown to make a relatively minor contribution to the overall strain, but they have a dramatic influence on the internal stresses that develop during plastic deformation.

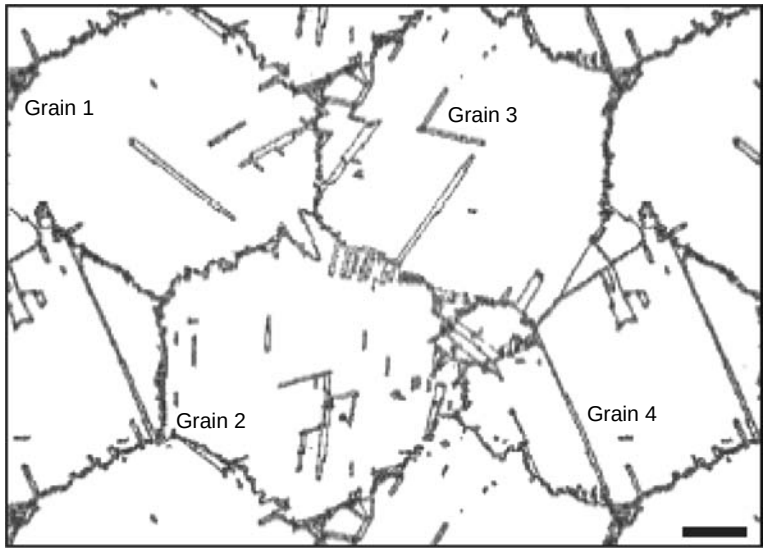

FIGURE 17.17 Simulated snapshot at 11.9% plastic strain for a nano-Al sample with an average grain diameter of 45 nm. A variety of processes involving dislocation–dislocation and dislocation–GB interactions have occurred. The blue dots highlight the grain boundaries while the red dots denote atoms associated with stacking faults or twins. (From Yamakov, V. et al., *Nat. Mater.*, 1, 45–48, 2002.)

The observation of partial dislocations was originally rationalized by the fact that partial dislocations are easier to nucleate than unit dislocations[80] and by the realization that the stress in the boundary would be immediately reduced by the generation of the first partial dislocation, thereby greatly decreasing the impetus for the second that would be needed to complete the unit dislocation. More recently, Van Swygenhoven[78] has argued that the overwhelming observation of partial dislocations is skewed by the geometry and subnanosecond time constraints employed in the MD simulations. She has argued that the formation of both unit and partial dislocations is possible and that the propensity for one or the other is governed by the ratio of the stacking fault and unstable stacking energies of the material. In either case, it is important to note that dislocation activity in nanocrystalline materials is significantly different than that observed in microcrystalline metals; it involves nucleation at a grain boundary, transmission across the adjoining nanometer-sized grain, and absorption into the opposing grain boundary. The time of flight across the grain is expected to be extremely short and the probability of two dislocations interacting and tangling within the grain is exceedingly low. This can be used to explain the lack of dislocation storage and low rate of strain hardening typically associated with nanocrystalline metals.

Another practical consequence of the low probability of dislocation–dislocation interactions in nanocrystalline metals is that it would be virtually impossible to image unit dislocations with postmortem TEM observations. By contrast, partial dislocations leave behind stacking faults and deformation twins that can be associated with their presence and activity. *In situ* TEM observations provide an opportunity for observing unit dislocations, but as is described below, these observations are extremely difficult to conduct.

17.4.2.2 Experimental Observations

17.4.2.2.1 Absence of Dislocation Substructure in Deformed Nanocrystalline Samples

Postmortem TEM studies have failed to provide evidence for the existence of unit dislocations in deformed nanocrystalline samples.[13,71] The absence of individual unit dislocations in deformed nanocrystalline samples cannot be taken as proof that they were not involved in the deformation process; they may have passed through the grain and been absorbed into the opposing grain boundary. Moreover, individual dislocations that stop in the grain interiors might be expected to relax into a nearby grain boundary when the stress is removed. It is, however, important to note that the observed absence of dislocation debris does indicate that dislocation interactions and tangling do not occur in nanocrystalline samples in the same way that they do in microcrystalline metals. This finding is important because it can be used to eliminate localized strain hardening as a source of Hall–Petch strengthening and because it is consistent with the general description of dislocation activity that has emerged from the MD simulations.

X-ray diffraction profile analysis has also been used for indirect characterization of dislocation substructures. Peak broadening can be related to both limited scattering volumes and the presence of inhomogeneous lattice strains.[81] In microcrystalline metals, broadening caused by inhomogeneous strains is often related to dislocation storage, and the shapes of x-ray peaks have been used as indirect measures of dislocation densities, arrangement parameters, dipole polarization, and dislocation character.[12] Budrovic et al.[72] have studied peak broadening associated with the *in situ* plastic deformation of nanocrystalline Ni samples in the Swiss Light Source and reported that the peak broadening that occurs upon loading is fully recovered upon unloading. This finding points to an absence of dislocation storage and is in good agreement with the TEM observations that report a lack of dislocation debris in deformed nanocrystalline samples. Taken together, these experimental results suggest that dislocation activity is fundamentally different for nanocrystalline metals than for microcrystalline metals.

17.4.2.2.2 Partial Dislocation Emission from Grain Boundaries

The MD simulations described above all suggest that partial dislocation emission from grain boundaries accompanies grain boundary sliding during the plastic deformation of nanocrystalline Cu, Ni, and Al. The motion of these partial dislocations would naturally result in the formation of stacking faults or deformation twins, which should be observable in postmortem TEM observations.

Twins are commonly observed in nanocrystalline Ni and Cu samples, but the formation of growth twins during the processing of these materials makes it hard to correlate the observation of twinning with deformation processes. Twinning in nanocrystalline Al, as predicted by MD simulations,[79] is an interesting case because the high stacking fault energy of Al greatly inhibits growth twins and deformation twins have not been seen in coarse-grained pure Al. For this reason, recent TEM observations of deformation twins and stacking faults in heavily deformed nanocrystalline pure aluminum by Chen et al. can be taken as direct evidence of partial dislocation-mediated plasticity. Twins and faults were not observed in the as-deposited films, but were formed by micro-indentation and manual grinding. Twins were observed in a significant fraction but not all of the grains. When observed, the twins were associated with the smallest grains and found to propagate across the whole grain (Figure 17.18) — observations which are in consistent with MD simulations.

Following the discovery of partial dislocation-mediated twinning in deformed nanocrystalline Al, TEM observations of deformation twins and partial dislocations have also been reported in ball-milled aluminum,[82,83] severely deformed Cu under high-pressure torsion,[35] nanocrystalline Cu,[84] and cold-rolled nanocrystalline Pd.[85] It is also worth noting that Ungar et al.[12] characterized deformed inert-gas-condensed nanocrystalline Cu with x-ray peak broadening experiments and found the character of the crystal defects to be twin-like in nature. On the whole, these experimental findings clearly suggest that partial dislocation activity plays an active role in the plastic deformation of nanocrystalline materials.

The preference for twinning and partial dislocation activity in nanocrystalline fcc metals can be rationalized by comparing the critical resolved shear stress needed to move a normal dislocation ($1/2\langle 110\rangle$) between lateral grain boundaries (τ_N) with that required to move a Shockley partial dislocation ($1/6\langle 112\rangle$) that generates stacking faults and deformation twins, τ_p. This comparison can be made using formulations given by classical dislocation theory,[67] assuming the dislocation is made to move through a grain of diameter, D. The critical stresses can be expressed as

$$\tau_N = \frac{2\alpha\mu b_N}{D} \tag{17.18}$$

and

$$\tau_p = \frac{2\alpha\mu b_p}{D} + \frac{\gamma}{b_p} \tag{17.19}$$

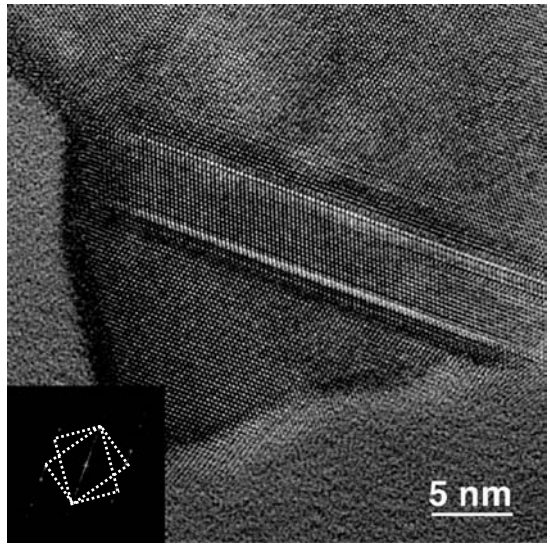

FIGURE 17.18 A deformation twin in a micro-indented nanocrystalline Al film and an FFT pattern showing the mirror symmetry between the twin and the matrix. (From Chen, M.W. et al., *Science*, 300, 1275–1277, 2003.)

where μ is the shear modulus, γ the stacking fault energy, and b_N and b_P are the magnitudes of the Burger's vectors of the perfect dislocations and the Shockley partial dislocations, respectively. The parameter α reflects the character of the dislocation ($\alpha = 0.5$ and 1.5 for edge and screw dislocations, respectively), and contains the scaling factor between the grain size and the length of the dislocation source. For coarse-grained materials with a large D, the line-tension term ($2\alpha\mu b_p/D$) is smaller, and τ_p is dominated by the stacking fault energy term γ. For smaller grain sizes, the line-tension term is much larger than (γ/b_p), and τ_p is determined by the grain size. Since b_p is smaller than b_N, τ_p will be smaller than τ_N for grains smaller than a critical value. The critical grain size for the transition from perfect dislocation slip to partial dislocation assisted twining and stacking faults formation can be obtained by equating Equations (17.1) and (17.2):

$$D_c = \frac{2\alpha\mu(b_N - b_P)b_P}{\gamma} \tag{17.20}$$

For Al, the critical grain size D_c is approximately 10 nm, while for Cu and Ni, the estimated values are 20 to 30 nm. Thus, predictions given by this simple model can shed light on the underlying physical mechanism of the preference of partial dislocation-related deformation in nanocrystalline metals.

17.4.2.2.3 In Situ *TEM Observations of Dislocation Activity in Nanocrystalline Metals*

Several attempts[86–88] have been made to explore the deformation processes of nanocrystalline metals by *in situ* straining TEM technique. It has been found that uniform plastic deformation is extremely difficult to achieve in nanocrystalline samples and crack formation is prevalent during *in situ* observations. Contrast changes around crack tips have been observed. These contrasts appear to be dislocations.[87] However, due to the disappearance of these contrasts upon unloading, the characteristics such as Burger's vectors have not been determined and evidence to support the dislocation behavior remains equivocal.

17.4.2.2.4 In Situ *TEM Observations of Nanocrystalline Grain Rotation*

Nano-grain rotation via grain boundary sliding has been predicted to be an important deformation mode in nanocrystalline materials as the grain size is reduced to less than 10 nm.[42,77,89] Definitive experimental evidence, however, is difficult to achieve. Through *in situ* straining HREM observations of nanocrystalline Au films with a grain size of 10 nm and a film thickness of 10 to 20 nm, Ke et al.[15] first claimed that grain rotation was observed by measuring the changes in the angular relationship between the lattice fringes of different grains during deformation at low strain rates. The strain tensor was calculated by measuring the relative displacements of three material points, and using an analysis similar to that for strain gage rosettes. Relative grain rotation of up to 15°, along with effective plastic strains of the order of 30%, was measured. However, because the film thickness is almost identical to the grain size, whether this deformation behavior is a result of the two-dimensional sample geometry needs to be clarified.

More recently, Shan et al.[31] reported *in situ* straining dark-field transmission electron microscope observations of grain rotation in nanocrystalline Ni. Continuous grain contrast change was viewed and it was claimed that the plastic deformation of nanocrystalline Ni is mediated by the grain rotation, which results from the misorientation dependence of the energy of the grain boundaries that delineate a given grain from its neighbors. However, the grain rotation and the associated contrast changes reported by Shan et al. can also be interpreted as nano-grain growth facilitated by electron beam irradiation and applied stresses.[90] Therefore, it is unclear if the observed grain rotation plays an important role in plastic deformation.

In situ TEM observations have evidenced dynamic deformation processes, such as dislocation motion and grain boundary sliding,[15,87,88] but questions remain as to whether the localized plastic deformation in the thin TEM foils under electron beam irradiation can faithfully represent the

macroscopic deformation behavior of three-dimensional nanocrystalline materials. Separate modeling based on collective response may be required to completely explain these observations.

17.4.3 Collective Response

The previous discussion highlights descriptions and models of specific deformation mechanisms for nanocrystalline metals. However, the link between atomic-scale deformation processes and macroscopic mechanical response remains to be established. Multi-scale models, spanning from the atomic scale to individual grains and grain boundaries and then encompassing the collective behavior of large numbers of nanocrystalline grains are needed to comprehensively describe the mechanical behavior of nanocrystalline materials. Kumar et al.[13] (Figure 17.19) have proposed a model that qualitatively links atomic-scale TEM observations of dislocation processes with micro-scale SEM observations of fracture surfaces of nano-Ni and suggests that localized plasticity and grain boundary sliding lead to void nucleation and the development of a fracture surface with dimples that encompass a number of individual grains. Similarly, MD simulations[91] suggest that packets of hard grains often bind together and result in rather inhomogeneous deformation in polycrystalline samples with grain sizes of the order of tens of nanometers. While very useful in providing insight into how deformation proceeds and in highlighting the importance of considering the collective nature of nanocrystalline grains, computational requirements severely limit the number of grains and amount of deformation that can be studied with MD.

Morita et al.[100] have developed a micromechanical model to investigate the influence of grain size variations on the yielding behavior of nanocrystalline metals. This model assumes a log-normal distribution of grains. The strength of each grain is determined from a relationship between grain size and the stress required to nucleate dislocations at a grain boundary. The model, which extends the Mori–Tanaka equations to the case of a finite solid containing many spherical inclusions that have different plastic strains and internal stresses, indicates that plasticity proceeds from large to small grains. The simulated results confirmed that both average grain size and grain size distribution play an important role in determining macroscopic stress–strain behavior of nanocrystalline metals.

The use of FE analysis provides unique opportunities for studying the statistical aspects and collective nature of deformation in nanocrystalline materials with large numbers of grains. The use of FE requires that the underlying physics be properly identified and implicitly input into the model, but the numerical efficiency of these codes allows for the study of microstructural variables, e.g., grain size distributions, and the activation and interaction of concomitant deformation processes. For nanocrystalline metals, the interplay of grain boundary sliding, intragranular plasticity, and intergranular voiding and fracture all warrant investigation. Grain boundary sliding and de-cohesion can both be modeled using cohesive elements, but the constitutive laws governing these processes are hard to measure experimentally. Sansoz and Molinari[92,93] have employed the quasi-continuum methods of Tadmor et al.[94] to deduce constitutive laws for grain boundary sliding and de-cohesion. Conventional crystal plasticity models[96–98] allow for intragranular plasticity and have been used in preliminary studies of deformation in nanocrystalline metals,[99,100] but the fact that dislocation processes are fundamentally different in nanocrystalline and microcrystalline metals places serious limitations on the utility of such efforts. Novel crystal plasticity models must be developed to take into account the discrete nature of plasticity in nanocrystalline metals and the nonlocal deformation behavior that involves dislocation emission and absorption from grain boundaries. Once developed, the use of these advanced FE techniques can be expected to provide a much-needed bridge between atomic-scale deformation processes and the continuum-scale properties of nanocrystalline structures.

17.5 CONCLUDING REMARKS

Nanocrystalline materials possess unusual mechanical properties and their deformation behavior has attracted intense activity in recent years. In this chapter, we have attempted to summarize the

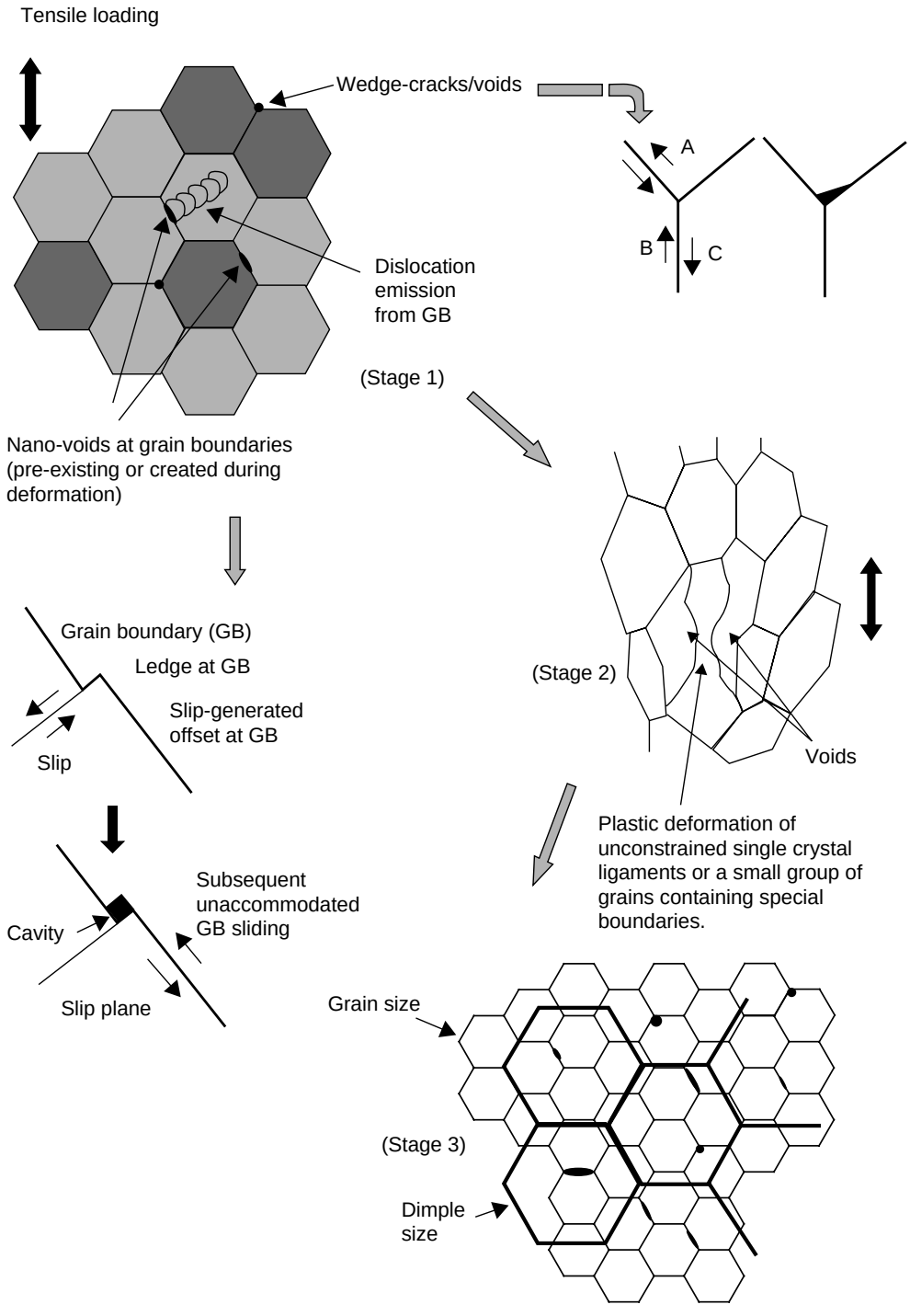

FIGURE 17.19 A schematic illustration depicting how deformation evolves in nanocrystalline nickel, based on experimental observations (i) during *in situ* deformation in the TEM, and (ii) of resulting fracture surfaces in the SEM. Dislocation motion, void formation/growth at grain boundaries and triple junctions, the formation of partially unconstrained ligaments that deform plastically, and the interaction of these various features to produce the eventual fracture morphology are all synthesized in this figure. (From Kumar, K.S. et al., *Acta Mater.*, 51, 5743–5774, 2003.)

reported mechanical behavior of nanocrystalline metals and to highlight recent progress in developing an understanding of the underlying deformation mechanisms for these metals. The value of reliable mechanical testing of well-characterized nanocrystalline metals is now universally appreciated, and efforts to measure the full suite of properties and to characterize grain size distributions and detailed deformation mechanisms are slowly being realized. There is strong physical evidence to indicate that the extension of Hall–Petch models to nanocrystalline grain sizes cannot be justified. The importance of intergranular grain boundary sliding, and de-cohesion and intragranular processes involving grain boundary nucleation and absorption of dislocations that do not interact with other dislocations have been highlighted by both MD simulations and experimental observations. The relative importance of these processes, the individual or collective rotation of grains, and the composite-like response of polycrystalline nanostructured metals remain to be elucidated and represent an exciting area for continued research.

REFERENCES

1. D. Tabor, *The Hardness of Metals*, Clarendon Press, Oxford, 1951, p. 174.
2. A.C. Fischer-Cripps, *Nanoindentation*, Mechanical Engineering Series, Springer, Berlin, 2002.
3. R. Schwaiger, B. Moser, M. Dao, N. Chollacoop, and S. Suresh, Some critical experiments on the strain-rate sensitivity of nanocrystalline nickel, *Acta Mater*., 51, 5159–5172 (2003).
4. A.A. Karimpoor, U. Erb, K.T. Aust, and G. Palumbo, High strength nanocrystalline cobalt with high tensile ductility, *Scr. Mater.*, 49, 651–656 (2003).
5. M. Legros, B.R. Elliott, M.N. Rittner, J.R. Weertman, and K.J. Hemker, Microsample tensile testing of nanocrystalline metals, *Phil. Mag. A*, 80, 1017–1026 (2000).
6. Y.M. Wang, K. Wang, D. Pan, K. Lu, K.J. Hemker, and E. Ma, Microsample tensile testing of nanocrystalline copper, *Scr. Mater.*, 48, 1581–1586 (2003).
7. M.A. Haque and M.T.A. Saif, Mechanical behavior of 30–50 nm thick aluminum films under uniaxial tension, *Scr. Mater.*, 47, 863–867 (2002).
8. D. Gianola, K.J. Hemker, M. Legros, and W.N. Sharpe, Experimental techniques for uncovering deformation mechanisms in nanocrystalline Al thin films, *TMS Lett.*, 1, 149–150 (2004).
9. T. Hanlon, Y.N. Kwon, and S. Suresh, Grain size effects on the fatigue response of nanocrystalline metals, *Scr. Mater.*, 49, 675–680 (2003).
10. J. Aktaa, J.Th. Reszat, M. Walter, K. Bade, and K.J. Hemker, High cycle fatigue and fracture toughness of LIGA nickel, *Scr. Mater*., 52, 2117–2121 (2005).
11. J.R. Weertman, *Mechanical Behavior of Nanocrystalline Metals in Nanostructured Materials: Processing, Properties, and Potential Applications*, William Andrew Publishing, Norwich, 2002, pp. 397–421.
12. T. Ungár, S. Ott, P.G. Sanders, A. Borbély, and J.R. Weertman, Dislocations, grain size and planar faults in nanostructured copper determined by high resolution X-ray diffraction and a new procedure of peak profile analysis, *Acta Mater.*, 46, 3693–3699 (1998).
13. K.S. Kumar, H. Van Swygenhoven, and S. Suresh, Mechanical behavior of nanocrystalline metals and alloys, *Acta Mater.*, 51, 5743–5774 (2003).
14. M.W. Chen, E. Ma, K.J. Hemker, H.W. Sheng, Y.M. Wang, and X.M. Cheng, Deformation twinning in nanocrystalline aluminum, *Science*, 300, 1275–1277 (2003).
15. M. Ke, S.A. Hackney, W.W. Milligan, and E.C. Aifantis, Observation and measurement of grain rotation and plastic strain in nanostructured metal thin films, *Nanostruct. Mater.*, 5, 689–697 (1995).
16. E. Stach, unpublished results.
17. M.A. Meyers and K.K. Chawla, *Mechanical Metallurgy: Principles and Applications*, Prentice-Hall, Englewood Cliffs, NJ, 1984.
18. F. Ebrahimi, G.R. Bourne, M.S. Kelly, and T.E. Matthews, Mechanical properties of nanocrystalline nickel produced by electrodeposition, *Nanostruct. Mater.*, 11, 343–350 (1999).
19. A.W. Thompson, Effect of grain-size on work-hardening in nickel, *Acta Metall.* 25, 83–86 (1977).
20. G.D. Hughes, S.D. Smith, C.S. Pande, H.R. Johnson, and R.W. Armstrong, Hall–Petch strengthening for the microhardness of 12 nanometer grain diameter electrodeposited nickel, *Scr. Metall.*, 20, 93–97 (1986).

21. U. Erb, Electrodeposited nanocrystals: synthesis, properties and industrial applications, *Nanostruct. Mater.*, 6, 533–538 (1995).
22. F. Dalla Torre, H. Van Swygenhoven, and M. Victoria, Nanocrystalline electrodeposited Ni: microstructure and tensile properties, *Acta Mater.*, 50, 3957–3970 (2002).
23. Y.M. Wang and E. Ma, *Appl. Phys. Lett*., 85, 2750–2752 (2004).
24. A.M. ElSherik, U. Erb, G. Palumbo, and K.T. Aust, Deviations from Hall–Petch behavior in as-prepared nanocrystalline nickel, *Scr. Metall.*, 27, 1185–1188 (1992).
25. A.W. Thompson, Yielding in nickel as a function of grain or cell size, *Acta Metall.* 23, 1337–1342 (1975).
26. C. Schuh, T.G. Nieh, and T. Yamasaki, Hall–Petch breakdown manifested in abrasive wear resistance of nanocrystalline nickel, *Scr. Mater.*, 46, 735–740 (2002).
27. C. Schuh, T.G. Nieh, and H. Iwasaki, The effect of solid solution W additions on the mechanical properties of nanocrystalline Ni, *Acta Mater.*, 51, 431–443 (2003).
28. D.H. Jeong, U. Erb, K.T. Aust, and G. Palumbo, The relationship between hardness and abrasive wear resistance of electrodeposited nanocrystalline Ni–P coatings, *Scr. Mater.*, 48, 1067–1072 (2003).
29. A.H. Chokshi, A. Rosen, J. Karch, and H. Gleiter, On the validity of the Hall–Petch relationship in nanocrystalline materials, *Scr. Metall.*, 23, 1679–1683 (1989).
30. J.A. Knapp and D.M. Follstaedt, Hall Petch relationship in pulsed-laser deposited nickel films, *J. Mater. Res.*, 19, 218–227 (2004).
31. Z.W. Shan, E.A. Stach, J.M.K. Wiezorek, J.A. Knapp, D.M. Follstaedt, and S.X. Mao, Grain boundary mediated plasticity in nanocrystalline nickel, *Science*, 305, 654–657 (2004).
32. R.A. Masumura, P.M. Hazzledine, and C.S. Pande, Yield stress of fine grained materials, *Acta Mater.*, 46, 4527–4534 (1998).
33. P.G. Sanders, J.A. Eastman, and J.R. Weertman, Elastic and tensile behavior of nanocrystalline copper and palladium, *Acta Mater.*, 45, 4019–4025 (1997).
34. C.J. Youngdahl, P.G. Sanders, J.A. Eastman, and J.R. Weertman, Compressive yield strengths of nanocrystalline Cu and Pd, *Scr. Mater.*, 37, 809–813 (1997).
35. S. Cheng, E. Ma, Y.M. Wang, L.J. Kecskes, K.M. Youssef, C.C. Koch, U.P. Trociewitz and K. Han, Tensile properties of in situ consolidated nanocrystalline Cu, *Acta Mater*., 53, 1521–1533 (2005).
36. K.M. Youssef, R.O. Scattergood, K.L. Murty, and C.C. Koch, *Appl. Phys. Lett.*, 85, 929 (2004).
37. Y. Champion, S. Guérin-Mailly, J.L. Bonnentien, and P. Langlois, Fabrication of bulk nanostructured materials from metallic nanopowders: structure and mechanical behaviour, *Scr. Mater.*, 44, 1609–1603 (2001).
38. C.C. Koch, Optimization of strength and ductility in nanocrystalline and ultrafine grained metals, *Scr. Mater.*, 49, 657–662 (2003).
39. E. Ma, Instabilities and ductility of nanocrystalline and ultrafine-grained metals, *Scr. Mater.*, 49, 663–668 (2003).
40. Y.M. Wang, S. Cheng, Q.M. Wei, E. Ma, T.G. Nieh, and A. Hamza, Effects of annealing and impurities on tensile properties of electrodeposited nanocrystalline Ni, *Scr. Mater*., 51, 1023–1028 (2004).
41. H.Q. Li and F. Ebrahimi, Transition of deformation and fracture behaviors in nanostructured face-centered-cubic metals, *Appl. Phys. Lett.*, 84, 4307–4309 (2004).
42. J. Schiotz and K.W. Jacobsen, A maximum in the strength of nanocrystalline copper, *Science*, 301, 1357–1359 (2003).
43. X. Zhang, H. Wang, R.O. Scattergood, J. Narayan, and C.C. Koch, Evolution of microstructure and mechanical properties of in situ consolidated bulk ultra-fine-grained and nanocrystalline Zn prepared by ball milling, *Mater. Sci. Eng. A*, 344, 175–181 (2003).
44. Q. Wei, S. Cheng, K.T. Ramesh, and E. Ma, Effect of nanocrystalline and ultrafine grain sizes on the strain rate sensitivity and activation volume: fcc versus bcc metals, *Mater. Sci. Eng. A*, 381, 71–79 (2004).
45. R.P. Carreker and W.R. Hibbard, Tensile deformation of high-purity copper as a function of temperature, strain rate, and grain size, *Acta Metall.*, 1, 656–658 (1953).
46. G.T. Gray, T.C. Lowe, C.M. Cady, R.Z. Valiev, and I.V. Alexandrov, Influence of strain rate and temperature on the mechanical response of ultrafine-grained Cu, Ni, and Al-4Cu-0.5Zr, *Nanostruct. Mater.*, 9, 477–480 (1997).
47. A.A. Elmustata, M.F. Tambwe, and D.S. Stone, *MRS Symp. Proc*., 750 Y.8.14.1 (2003).

48. Y.M. Wang, T. Jiao, and E. Ma, Dynamic processes for nanostructure development in Cu after severe cryogenic rolling deformation, *Mater. Trans.*, 44, 1926–1934 (2003).
49. L. Lu, S.X. Li, and K. Lu, An abnormal strain rate effect on tensile behavior in nanocrystalline copper, *Scr. Mater.*, 45, 1163–1169 (2001).
50. R.Z. Valiev, I.V. Alexandrov, Y.T. Zhu, and T.C. Lowe, Paradox of strength and ductility in metals processed by severe plastic deformation, *J. Mater. Res.*, 17, 5–8 (2002).
51. J.E. Carsley, A. Fisher, W.W. Milligan, and E. Aifantis, Mechanical behavior of a bulk nanostructured iron alloy, *Metall. Mater. Trans. A*, 29, 2261–2271 (1998).
52. Y.M. Wang, M.W. Chen, F.H. Zhou, and E. Ma, High tensile ductility in a nanostructured metal, *Nature*, 419, 912–915 (2002).
53. D. Jia, K.T. Ramesh, and E. Ma, Effects of nanocrystalline and ultrafine grain sizes on constitutive behavior and shear bands in iron, *Acta Mater.*, 51, 3495–3509 (2003).
54. Q. Wei, D. Jia, K.T. Ramesh, and E. Ma, Evolution and microstructure of shear bands in nanostructured Fe, *Appl. Phys. Lett*., 81, 1240–1242 (2002).
55. A. Vinogradov and S. Hashimoto, Fatigue of severely deformed metals, *Adv. Eng. Mater*., 5, 351–358 (2003).
56. Z. Huang, L.Y. Gu, and J.R. Weertman, Temperature dependence of hardness of nanocrystalleve copper in low-temperature range, *Scr. Mater.*, 37, 1071–1075 (1997).
57. S.X. McFadden, R.S. Mishra, R.Z. Valiev, A.P. Zhilyaev, and A.K. Mukherjee, Low-temperature superplasticity in nanostructured nickel and metal alloys, *Nature*, 398, 684–686 (1999).
58. N. Wang, Z. Wang, K.T. Aust, and U. Erb, Room temperature creep behavior of nanocrystalline Ni produced by an electrodeposition technique, *Mater. Sci. Eng. A*, 237, 150–158 (1997).
59. H. Tanimoto, S. Sakai, and H. Mizubayashi, Mechanical properties of high density nanocrystalline Au prepared by gas deposition method, *Nanostruct. Mater.*, 12, 751–756 (1999).
60. P.G. Sanders, M. Rittner, E. Kiedaisch, J.R. Weertman, H. Kung, and Y.C. Lu, Creep of nanocrystalline Cu, Pd, and Al-Zr, *Nanostruct. Mater*., 9, 433–440 (1997).
61. F.A. Mohamed and Y. Li, Creep and superplasticity in nanocrystalline materials: current understanding and future prospects, *Mater. Sci. Eng. A*, 298, 1–15 (2001).
62. R.A. Mirshams, C.H, Xiao, S.H. Whang, and W.M. Yin, R-Curve characterization of the fracture toughness of nanocrystalline nickel thin sheets, *Mater. Sci. Eng. A*, 315, 21–27 (2001).
63. S. Suresh, *Fatigue of Materials*, 2nd ed., Cambridge University Press, Cambridge, UK, 1998.
64. H. Mughrabi and H.W. Höppel, *Mater. Res. Symp. Proc*., 634 B2.1.1 (2001).
65. J.D. Morrow, *Fatigue Design Handbook — Advances in Engineering*, Society of Automotive Engineers, Warrendale, PA, Vol. 4, Sec. 3.2, 1968, pp. 21–29.
66. F.A. McClintock and A.S. Argon, *Mechanical Behavior of Materials*, Addison-Wesley Publishing Company, Inc., Reading, MA, 1966.
67. J.P. Hirth and J. Lothe, *Theory of Dislocations*, 2nd ed., Krieger Publishing, Malabar, UK, 1992.
68. J.C.M. Li and Y.T. Chou, Role of dislocation in flow stress grain size relationships, *Metall. Trans*., 1, 1145–1148 (1970).
69. J.C.M. Li, Petch relation and grain boundary sources, *Trans. Metall. Soc. AIME*, 227, 239 (1963).
70. M.A. Meyers and E. Ashworth, A model for the effect of grain-size on the yield stress of metals, *Phil. Mag. A*, 46, 737–759 (1982).
71. M. Legros, K.J. Hemker, A. Gouldstone, S. Suresh, R.M. Keller-Flaig, and E. Arzt, Microstructural evolution in passivated Al films on Si substrates during thermal cycling, *Acta Mater.*, 50, 3435–3452 (2002).
72. Z. Budrovic, H. Van Swygenhoven, and P.M. Derlet, Plastic deformation with reversible peak broadening in nanocrystalline nickel, *Science*, 304, 273–276 (2004).
73. T.G. Nieh and J. Wadsworth, Hall–Petch relation in nanocrystalline solids, *Scr. Met. Mat.*, 25, 955–958 (1991).
74. R.W. Armstrong, Y.T. Chou, R.M. Fisher, and N. Louat, Limiting grain size dependence of strength of a polycrystalline aggregate, *Phil. Mag.*, 14, 943–951 (1966).
75. R.L. Coble, A model for boundary diffusion controlled creep in polycrystalline materials, *J. Appl. Phys.*, 34, 1679–1682 (1963).
76. W.W. Milligan, S.A. Hackney, M. Ke, and E.C. Aifantis, In situ studies of deformation and fracture in nanophase materials, *Nanostruct. Mater.*, 2, 267–276 (1993).

77. J. Schiotz, F.D. Di Tolla, and K.W. Jacobsen, Softening of nanocrystalline metals at very small grain sizes, *Nature*, 391, 561–563 (1998).
78. H. Van Swygenhoven, D. Farkas, and A. Caro, Grain-boundary structures in polycrystalline metals at the nanoscale, *Phy. Rev. B*, 62, 831–838 (2000).
79. V. Yamakov, D. Wolf, S.R. Phillpot, A.K. Mukherjee, and H. Gleiter, Dislocation processes in the deformation of nanocrystalline aluminium by molecular-dynamics simulation, *Nat. Mater.*, 1, 45–48 (2002).
80. J.R. Rice, Dislocation nucleation from a crack tip- an analysis based on the peierls concept, *J. Mech. Phys. Solids*, 40, 239–271 (1992).
81. H.P. Klug and L.E. Alexander, *X-Ray Diffraction Procedures for Polycrystalline and Amorphous Materials*, Wiley, New York, 1974.
82. X.Z. Liao, F. Zhou, E.J. Lavernia, S.G. Srinivasan, M.I. Baskes, D.W. He, and Y.T. Zhu, A new deformation mechanism in nanocrystalline Al: particle dislocation slip. *Appl. Phys. Lett.*, 83, 632–634 (2003).
83. Y.T. Zhu, X.Z. Liao, S.G. Srinivasan, Y.H. Zhao, M.I. Baskes, F. Zhou, and E.J. Lavernia, Nucleation and growth of deformation twins in nanocrystalline aluminum, *Appl. Phys. Lett.*, 85, 5049–5051 (2004).
84. X.Z. Liao, Y.H. Zhao, S.G. Srinivasan, Y.T. Zhao, R.H. Valiev, and D.V. Gunderov, Deformation twinning in nanocrystalline copper at room temperature and low strain rate, *Appl. Phys. Lett.*, 84, 592–594 (2004).
85. H. Rosner, J. Markmann, and J. Weissmuller, Deformation twins in nanocrystalline Pd, *Phil. Mag. Lett.*, 84, 321–334 (2004).
86. C.J. Youngdahl, J.R. Weertman, R.C. Hugo, and H.H. Kung, Deformation behavior in nanocrystalline copper, *Scr. Mater.*, 44, 1475–1478 (2001).
87. R.C. Hugo, H. Kung, J.R. Weertman, R. Mitra, J.A. Knapp, and D.M. Follstaedt, In-situ TEM tensile testing of DC magnetron sputtered and pulsed laser deposited Ni thin films, *Acta Mater.*, 51, 1937–1943 (2003).
88. K.S. Kumar, S. Suresh, M.F. Chisholm, J.A. Horton, and P. Wang, Deformation of electrodeposited nanocrystalline nickel, *Acta Mater.*, 51, 387–405 (2003).
89. H. Van Swygenhoven, Polycrystalline materials — grain boundaries and dislocations, *Science*, 296, 66–67 (2002).
90. M.W. Chen and X.Q. Yan, Comment on "Grain boundary mediated plasticity in nanocrystalline nickel," *Science*, 308, 356C (2005).
91. A. Hasnaoui, H. Van Swygenhoven, and P.M. Derlet, *Science*, 300, 1550 (2003).
92. F. Sansoz and J.F. Molinari, Incidence of atom shuffling on the shear and decohesion behavior of a symmetric tilt grain boundary in copper, *Scr. Mater.*, 50, 1283–1288 (2004).
93. F. Sansoz and J.F. Molinari, Mechanical behavior of sigma tilt grain boundaries in nanoscale Cu and Al, *Acta Mater.*, 53, 1931–1944 (2005).
94. E.B. Tadmor, M. Ortiz, and R. Phillips, Quasicontinuum analysis of defects in solids, *Phil. Mag. A*, 73, 1529–1563 (1996).
95. R. Hill and J.R. Rice, Constitutive analysis of elastic-plastic crystals at arbitrary strain, *J. Mech. Phys. Solids*, 20, 401–413 (1972).
96. R.J. Asaro, Micromechanics of crystals and polycrystals, *Adv. Appl. Mech.*, 23, 1–115 (1983).
97. A.M. Cuitino and M. Ortiz, Computational modeling of single crystals. *Model. Simul. Mater. Sci. Eng.*, 1, 225–263 (1992).
98. Y.J. Wei and L. Anand, Grain-boundary sliding and separation in polycrystalline metals: application to nanocrystalline fcc metals, *J. Mech. Phys. Solids*, 52, 2587–2616 (2004).
99. D.H. Warner and J.F. Molinari, Atomistic-based continuum modeling of nanocrystalline copper, *TMS Lett.*, 1, 147–148 (2004).
100. T. Morita, R. Mitra, and J.R. Weertman, Micromechanics model concerning yield behavior of nanocrystalline materials, *Mater. Trans.*, 45, 502–508 (2004).

18 Grain Boundaries in Nanomaterials

I.A. Ovid'ko
Institute of Problems of Mechanical Engineering,
Russian Academy of Sciences, Moscow, Russia

C.S. Pande and R.A. Masumura
Naval Research Laboratory, Washington, D.C.

CONTENTS

ABSTRACT

This chapter gives a brief overview of theoretical models describing the structure and behavior of grain boundaries (GBs) in nanocrystalline materials. The specific structural peculiarities of GBs in nanocrystalline materials, which are related to the nanoscale effects and nonequilibrium methods of their fabrication, are discussed. Also, focus is placed on the specific deformation mechanisms conducted via GBs and grain growth processes that control, respectively, the unique mechanical properties and structural stability of nanocrystalline materials.

18.1 INTRODUCTION

Nanostructured solids (nanocrystalline bulk materials, films and coatings, nanocomposites, semiconductor quantum dots and wires, nanoparticles, carbon and noncarbon nanotubes, fullerenes,

nanoscale multilayers, etc.) represent the subject of rapidly growing fundamental and applied research efforts because of their outstanding physical, mechanical, and chemical properties (see, e.g., Refs. [1–5]). These outstanding properties are due to the interface and nanoscale effects associated with structural peculiarities of nanostructured materials, where the volume fraction of the interfacial phase is extremely high, and the crystallite size d does not exceed 100 nm. Of special importance from both fundamental and applied viewpoints are the unique mechanical properties of nanocrystalline materials, one of the basic classes of nanostructured materials (see, e.g., [5–10]. Nanocrystalline materials are solids consisting of approximately equiaxed nanocrystallites (grains) divided by GBs (Figure 18.1). GBs cruicially influence the mechanical properties of nanocrystalline materials are crucially influenced. These properties are essentially different from those of conventional coarse-grained polycrystalline materials with the same chemical compositions. In particular, nanocrystalline materials exhibit the superhardeness, superstrength, and enhanced tribological characteristics [5–11] highly desirable for applications. In many ways, the superhardeness, superstrength and high wear resistance of nanocrystalline materials are related to the role of GBs as effective obstacles for lattice dislocation slip, the dominant deformation mechanism in conventional coarse-grained polycrystals. Also, the image forces acting in nanometer-sized crystallites of nanocrystalline materials cause the difficulty in forming lattice dislocations in such nanocrystallites [12,13]. With these GB and nanoscale effects, the conventional lattice dislocation slip is hampered in nanocrystalline materials. At the same time, GBs in nanocrystalline materials provide the effective action of deformation mechanisms being different from the conventional lattice dislocation slip. As a corollary, the crystallite refinement leads to competition between the lattice dislocation slip and deformation mechanisms associated with the active role of GBs.

The competition between different deformation mechanisms is seen as being responsible for the unique mechanical properties of nanocrystalline solids [6–10,14–24] and represents a manifestation of both the GB and nanoscale effects in such materials. In general, the GB effect comes into play because a large fraction of atoms of nanocrystalline material are located at GBs, where

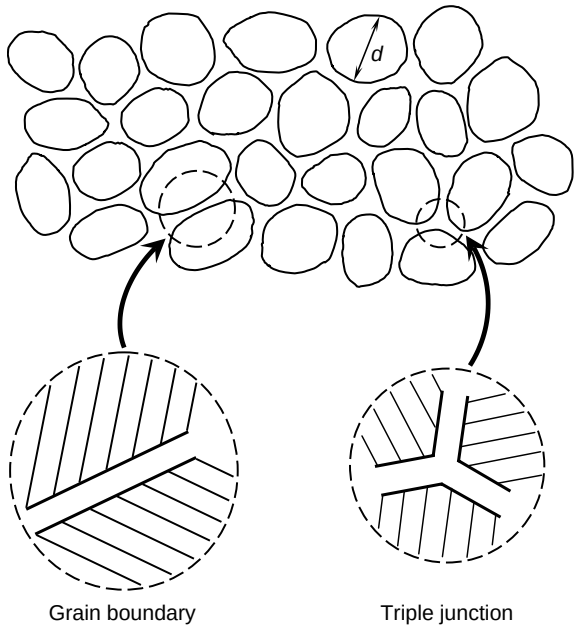

FIGURE 18.1 Nanocrystalline material consists of tentatively equiaxed grains (crystallites) of the same phase and grain size $d < 100$ nm. Large-scale views of typical structural elements of nanocrystalline material — short grain boundaries and their triple junctions are shown in the bottom portion of the figure.

their behavior is different from that seen in the bulk. The nanoscale effect occurs because many fundamental processes in crystals are associated with length scales of around a few nanometers.

Identification of GB structures and their contribution to plastic flow is very important for understanding the specific structural features and the unique mechanical behavior of nanocrystalline materials. However, in many cases, the structure and deformation mechanisms in nanocrystalline materials cannot be unambiguously identified with the help of contemporary experimental methods because of high precision demands on experiments at the nanoscale. Under these circumstances, theoretical modeling of GB structures and plastic deformation processes represents a very important part of both fundamental and applied research on nanocrystalline materials. In this chapter, we give a brief overview of theoretical models that describe GBs and their effects on plastic flow in nanocrystalline materials (see Sections 18.2 to 18.5). For brevity, we will concentrate on final results of theoretical models, and their mathematical details will be omitted.

The outstanding physical, mechanical, and chemical properties of nanocrystalline materials are highly sensitive to their structural stabilty. Grain growth processes that destroy the nanocrystalline state are capable of causing a dramatic degradation of these properties. In particular, the strength, hardness, and other mechanical characteristics of a material rapidly degrade with the increase in the mean grain size from nanometers to micrometers [6,7]. In this context, an adequate description of grain growth processes in nanocrystalline materials is very important for the design and control of their structure and unique properties. In Section 18.6, we will discuss theoretical models addressing grain growth processes in nanocrystalline and polycrystalline materials with special attention being paid to the nanoscale effects on these processes.

18.2 SPECIFIC STRUCTURAL FEATURES OF GRAIN BOUNDARIES IN NANOCRYSTALLINE MATERIALS

Nanocrystalline materials are solids consisting of approximately equiaxed nanoscale grains (nanocrystallites) divided by GBs (Figure 18.1). Grains are characterized by grain size $d<100$ nm and have the crystalline structure. Crystal lattices of grains are misoriented relative to each other. Therefore, neighboring grains are divided by GBs, narrow regions (with thickness being around 1 nm) that carry a geometric mismatch between adjacent misoriented crystalline grains (Figure 18.1). With the nanoscale range of grain sizes, the volume fraction of the GB phase is exteremely high in nanocrystalline materials, which is one of the definitive structural features of nanocrystalline materials.

Generally speaking, GBs are also typical structural elements of conventional coarse-grained polycrystals, where the volume fraction of the GB phase is low ($<1\%$). GBs in polycrystalline materials are subjects of traditional experimental and theoretical studies in materials science and solid-state physics (see, e.g., [25,26]). In these studies, it is well recognized that both the structure and properties of GBs in polycrystalline materials are essentially different from those of the bulk phase (crystalline grain interiors). Atoms in the bulk phase form equilibrium crystal lattices corresponding to the minimum free energy or another relevant thermodynamic potential of infinite crystal. Atoms in GBs are arranged in a more complicated and disordered manner (Figure 18.2) because there are restrictions on their arrangement, imposed by the adjacent crystal lattices of misoriented grains.

GB structures in coarse-grained polycrystals can be divided into the following key categories: low-angle periodic boundaries (Figure 18.2a) [26], high-angle periodic boundaries (Figure 18.2b) [26], nonequilibrium grain boundaries containing high-density ensembles of defects (Figure 18.2c) [27,28], and amorphous grain boundaries (Figure 18.2d) (see [29] and references therein). Low-angle periodic grain boundaries are characterized by low misorientation angles (tentatively < 15) between the adjacent grains and represent periodic arrays of lattice dislocations [26]. For illustration, a low-angle tilt boundary is shown as a periodic wall of edge lattice dislocations in Figure 18.2a. High-angle periodic boundaries represent narrow regions with thickness of around 1 nm and atomic structure very different from that of the adjacent crystalline grains [26–28] (Figure 18.2b).

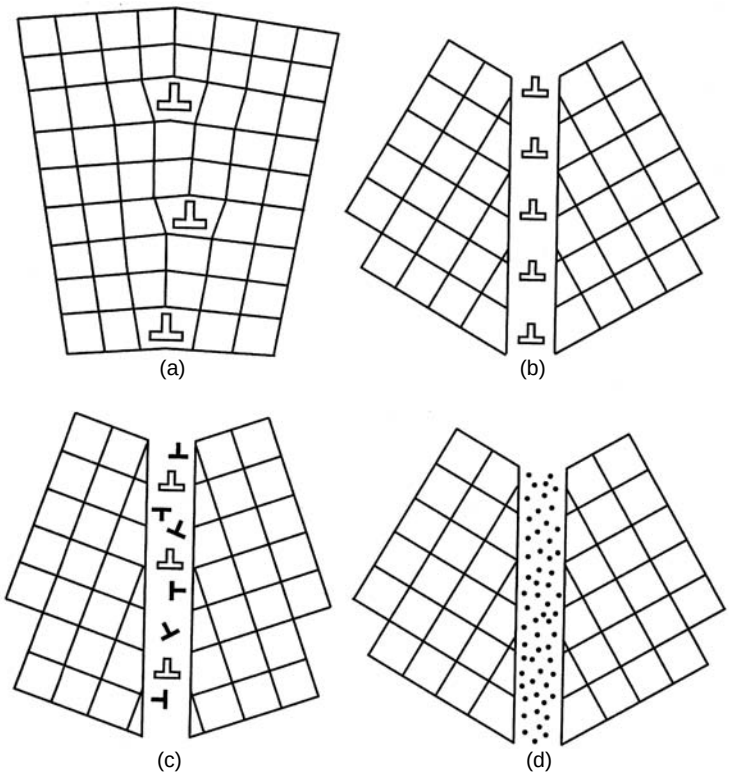

FIGURE 18.2 Types of grain boundaries: (a) low-angle periodic boundaries; (b) high-angle periodic boundaries; (c) nonequilibrium grain boundaries containing high-density ensembles of defects; and (d) amorphous grain boundaries.

High-angle periodic boundaries commonly contain periodic arrays of GB dislocations (with small Burgers vectors being displacement-shift-complete lattice vectors, which characterize GB translation symmetries) (Figure 18.2b). These GB dislocations are called "equilibrium" or, in other terms, intrinsic GB dislocations and are associated with the misorientation mismatch between the adjacent grains. Nonequilibrium GBs are often formed in coarse-grained polycrystalline materials under high-strain deformation, in which case GBs intensively absorb lattice dislocations [27,28]. Besides intrinsic GB dislocations, high-density ensembles of extrinsic GB dislocations (resulting from splitting of absorbed lattice dislocations) and other defects are present in nonequilibrium GBs (Figure 18.2c). Extrinsic GB dislocations, after some relaxation time interval, disappear via annihilation of dislocations with opposite Burgers vectors and other transformations. As a result of the relaxation process whose intensity is controlled by temperature, nonequilibrium GBs (Figure 18.2c) transform into their equilibrium states (Figure 18.2b). Amorphous GBs (Figure 18.2d) frequently exist in covalently bonded ceramic materials, where their chemical composition is different from that of the adjacent crystalline grains (see [29] and references therein).

The fact that the structure and behavior of GBs are very different from those of the bulk phase has been used by Gleiter and coworkers in 1984 in their pioneering paper [30], reporting on the fabrication of nanocrystalline materials and defining them as a new state of matter. Gleiter et al. [30] assumed that GBs with their very specific structural and behavioral features give rise to specific nanocrystalline materials defined as polycrystals with finest grains and exteremely high volume fraction of the GB phase. In early studies, the characteristic grain size range of the nanocrystalline matter was defined to be from 3 to 20 nm [30,31]. Later, the notion of nanocrystalline materials was extended to include diverse solids — nanocrystalline materials, nanocomposites, semiconductor

quantum dots and wires, nanoparticles, carbon and noncarbon nanotubes, fullerenes, nanoscale multilayers, and others — with structural elements (commonly crystallites), having at least one dimension smaller than 100 nm [2]. In this context, besides GBs, interphase boundaries and free surfaces represent interfaces and cause specific interface effects in diverse nanostructured materials. This chapter deals with GBs in nanocrystalline materials — a widely diverse class of nanostructured materials — that have unique properties highly desirable in current and future high technologies.

In general, GBs in nanocrystalline materials have specific structural features which are responsible for their specific behavior and properties. We distinguish the following key specific features of GBs in nanocrystalline materials, differentiating them from GBs in conventional coarse-grained polycrystals:

1. The volume fraction of the GB phase is extremely high in nanocrystalline materials.
2. GBs are very short; the boundary length does not exceed 100 nm.
3. The volume fraction of triple junctions of GBs is extremely high in nanocrystalline solids.
4. The structure of GBs in nanocrystalline materials in many cases is nonequilibrium with high densities of nonperiodically arranged GB defects.

Following is a brief general discussion of these structural features and their effects on the behavior of GBs and properties of nanocrystalline materials. The fact that nanocrystalline materials contain high-density ensembles of GBs is, in general, responsible for their crucial influence on the properties of nanocrystalline materials. The fact that GBs are very short in nanocrystalline materials has several consequences for their structural geometry and behavior. First of all, nanosized GBs in nanocrystalline materials with the finest grains are characterized by length values close to those of periods that characterize periodic GB structures in coarse-grained polycrystals. Under these circumstances, nanosized GBs in their equilibrium (low-energy) state in nanocrystalline materials often cannot be defined as periodic; they are either quasiperiodic [32] or have the structure with inhomogeneities of the GB dislocation distribution in vicinities of triple junctions [33]. Also, nanosized GBs easily undergo structural transformations related to changes in their length and form. In particular, the enhanced local migration of GBs facilitates grain growth and GB sliding processes in nanocrystalline materials. On the other hand, however, there is a strong elastic interaction between neighboring nanosized GBs, because (extremely short) distances between them are close to the characteristic scales of their stress fields. With this interaction, GB structures are formed that minimize the elastic energy of GB ensembles in nanocrystalline materials. The low-energy ensembles exhibit a certain structural stability, because there is an energy barrier needed to destroy low-energy GB structures. This factor hampers grain growth and other processes associated with structural transformations of GBs in nanocrystalline materials.

High-density ensembles of triple junctions of GBs also contribute to the structural stability of the nanocrystalline matter, because they serve as effective drag centers for GB migration and grain growth processes [34]. In general, triple junctions have both structure and properties different from those of GBs that they adjoin (see, e.g., [35]). In particular, triple junctions often contain defects that influence the structure of adjacent GBs [10] and, as shown in experiments [36,37] and theoretical models [38,39], are capable of enhancing the structural and chemical transformations in vicinities of triple junctions. Also, the diffusion along triple junction tubes is much faster than the diffusion along GB planes and bulk diffusion [40]. In this context, the effects of triple junctions are essential in nanocrystalline materials, where their volume fraction is very high [31].

Parallel with nanosized geometry and triple junctions, conditions of fabrication of nanocrystalline materials strongly affect the structure and behavior of GBs in these materials. More precisely, nanocrystalline materials are commonly fabricated by highly nonequilibrium methods, causing the formation of so-called extrinsic GB defects, that is, defects which are not geometrically

necessary at GBs. Under these circumstances, the density of nonequilibrium GBs (Figure 18.2c) in nanocrystalline materials is much higher than that in conventional coarse-grained polycrystals. Nonequilibrium GBs with high densities of extrinsic defects (Figure 18.2c) exhibit specific properties which are different from those of equilibrium GBs containing intrinsic defects only [27,28]. It is believed that the nonequilibrium GBs are responsible for the very unusual diffusional and mechanical properties of nanocrystalline materials produced by severe plastic deformation [27,41–43].

To summarize, GBs in nanocrystalline materials are characterized by specific geometric and structural features (1)–(4) that strongly affect their behavior and, as a corollary, their functional properties. In particular, these features essentially influence deformation and grain growth processes in the nanocrystalline matter. The role of GBs in plastic deformation and grain growth in nanocrystalline materials will be discussed in next sections.

18.3 EFFECTS OF GRAIN BOUNDARIES ON PLASTIC FLOW IN NANOCRYSTALLINE MATERIALS: GENERAL VIEW

Let us consider the effects of GBs on plastic deformation in nanocrystalline materials. Generally nanocrystalline materials show very high strength and specific deformation behavior [5–10]. In particular, their specific deformation behavior is exhibited by the so-called abnormal Hall–Petch effect which manifests itself as either the saturation or decrease in the yield stress of a nanocrystalline material with reduction in the grain size d in the range of very small grains (see, e.g., [6,7,44,45]). Most of the theoretical models relate the abnormal Hall–Petch dependence to the competition between deformation mechanisms in nanocrystalline materials (for a review, see [10,20]). In the framework of this approach, the conventional dislocation slip dominates in crystalline materials with the grain size in the range of $d > d_c$. The critical value d_c of the grain size is between 10 and 30 nm, depending on material and structural parameters. With the well-known strengthening effect of GBs [26], the yield stress and associated mechanical characteristics of these materials grow with diminishing grain size in the range of $d > d_c$. The deformation mechanisms associated with the active role of GBs dominate in nanocrystalline materials in the range of very small grains ($d < d_c$). These deformation mechanisms provide either saturation or a decrease of the yield stress (or strength) with diminishing grain size d in the range of $d < d_c$. In Section 18.4, we will consider in detail the situation where the competition between the lattice dislocation slip and GB diffusional creep (Coble creep) is responsible for the abnormal Hall–Petch relationship.

In general, according to contemporary representations on plastic flow processes in nanocrystalline matter [6–10,14–24,44–60], the following deformation mechanisms operate:

- Lattice dislocation slip
- GB sliding
- GB diffusional creep (Coble creep)
- Triple junction diffusional creep
- Rotational deformation occurring via movement of GB disclinations
- Twin deformation arising owing to by partial dislocations emitted from GBs

As noted previously, conventional dislocation slip dominates in crystalline materials in the mean grain size range $d > d_c$, where the critical grain size d_c is about 10 to 30 nm, depending on material and structural parameters. At the same time, with grain refinement, the lattice dislocation slip shows some specific features due to the GB and nanoscale effects. In particular, following the dislocation model of Pande and Masumura [46], though the lattice dislocation slip is still dominant in nanocrystalline solids in a wide range of the grain size, the number of dislocations within a grain cannot be very large. As a corollary, a contribution of the lattice dislocation slip to plastic flow gradually decreases with diminishing grain size.

Recently, Cheng et al. [23] have suggested a very interesting classification of polycrystalline and nanocrystalline materials, based on the specific features of the lattice dislocation slip and the role of GBs in the lattice dislocation generation. Following Chang et al. [23], materials are divided into four categories:

1. *Traditional materials with grain size d being larger than about 1 μm.* In these materials, the lattice dislocation slip is dominant with carriers — perfect lattice dislocations — being generated by dislocation sources (like Frank–Read sources) located in grain interiors.
2. *Fine-grained materials with grain size d being in the range from about 30 nm to 1 μm.* In these materials, the lattice dislocation slip is dominant with carriers — perfect lattice dislocations — being generated by dislocation sources located at GBs.
3. *Nano II materials with grain size d being in the range from about 10 to 30 nm.* In Nano II materials, the basic carriers of plastic flow are partial lattice dislocations generated by dislocation sources located at GBs. Movement of these partial dislocations is accompanied by the formation of stacking faults and deformation twins in grain interiors.
4. *Nano I materials with grain size d being lower than about 10 nm.* In these materials, GB sliding and other deformation mechanisms conducted by GBs are dominant.

Cheng et al. [23] emphasized that the grain size ranges used in their classification scheme are very approximate; they can be different in different materials. At the same time, the classification [23] attempts to describe the key tendency in the grain size effects on deformation mechanisms operating in polycrystalline and nanocrystalline materials. In this, the most intriguing mechanical behavior is exhibited by Nano I materials, that is, nanocrystalline materials with very small grains. In these materials, plastic flow occurs mostly through GB-conducted deformation mechanisms, in particular, GB diffusional creep and GB sliding that will be discussed in next sections.

18.4 COMPETITION BETWEEN LATTICE DISLOCATION SLIP AND GRAIN BOUNDARY DIFFUSIONAL CREEP (COBLE CREEP) IN NANOCRYSTALLINE MATERIALS

The relationship between yield stress τ and grain size d is described by the classic Hall–Petch relationship [61,62], namely,

$$\tau = \tau_0 + kd^{-1/2} \tag{18.1}$$

where τ_0 is the friction stress, and k a constant often referred to as the Hall–Petch slope that varies from material to material. This equation holds well for grain sizes larger than about a micron. Masumura et al. [14] have plotted (see Figure 18.3) some of the available data in a Hall–Petch plot (Ref. [14] contains detailed list of materials and references). It is seen that the yield stress-grain size exponent for relatively large grains appears to be very close to $-1/2$ and generally this trend continues until the very fine grain regime (~100 nm) is reached. With the advent of nanocrystalline materials whose grain sizes are of nanometer (nm) dimensions, the applicability and validity of Equation (18.1) becomes of interest [63].

A close analysis of experimental Hall–Petch data in a variety of materials shows that the plot of τ vs. $d^{-1/2}$ forms a continuous curve. However, below a critical grain size, the Hall–Petch slope is nearly zero with no increase in strength with decreasing grain size or a the strength actually decreases with decreasing grain size [64].

For large grain sizes (region I) a number of models have been proposed to account for the grain size dependence of the stress, τ, in Equation (18.1), most of which can be rationalized in terms of a dislocation pile-up model [65]. In deriving the Hall–Petch relation, the role of grain boundaries as a barrier to dislocation model is considered in various models. In one type of model [66–68], the

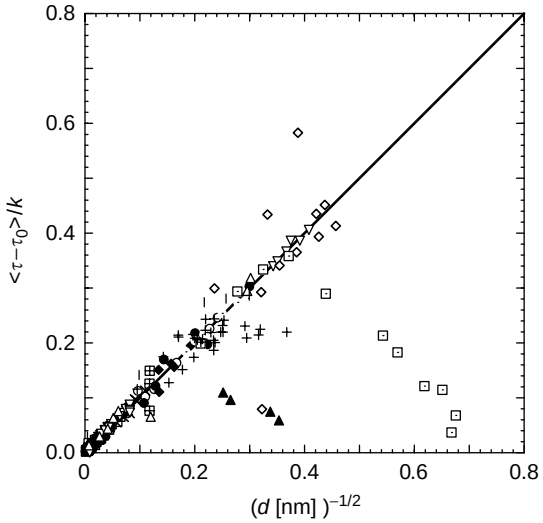

FIGURE 18.3 Compilation of yield stress data of materials whose behavior is in agreement with the Hall–Petch formulation. Deviation from the Hall–Petch slope may be due to Coble creep.

grain boundary acts as a barrier to pile up dislocations, causing stresses to concentrate and activate dislocation sources in the neighboring grains, thus initiating slip from grain to grain. In other models [69,70] the grain boundaries are regarded as dislocation barriers limiting the mean free path of the dislocations, thereby increasing strain hardening, resulting in a Hall–Petch type relation. (For a survey, see Lasalmonie and Strudel [71].) It is clear that a variety of processes, both dislocation and nondislocation based, could be postulated. Pande and Masumura [46], by considering the conventional Hall–Petch model, showed that a dislocation theory for the Hall–Petch effect only gives a linear dependence of τ on $d^{-1/2}$ when there are large number of dislocations in a pile-up. This model assumes that the classical Hall–Petch dislocation pile-up model is still dominant with the sole exception that the analysis must take into account the nanometer size of grains whereby the number of dislocations within a grain cannot be very large. Further, at still smaller grain sizes, this mechanism should cease when there are only two dislocations in the pile-up. When the number of dislocations falls to one, no further increase in the yield stress is possible and it should saturate.

Pande and Masumura [46] have modified the classical Hall–Petch dislocation model to include this effect. Their model recovers classical Hall–Petch at large grain sizes but for smaller grain sizes the τ levels decrease. This model therefore cannot explain a drop in τ for very fine-grained materials. One can of course assume that dislocation sources must operate in each grain, and so an additional component of the yield stress *GB/d* exists. However, as shown by Yamakov et al. [72], such a possibility is not probable.

There are other dislocation models such as Valiev et al. [73], Malygin [74], and Gryaznov et al. [75]. Gryaznov et al. proposed a generalization of the of Hall–Petch relationship. By making judicious assumptions and approximations, they were able to develop a formulation that can account for yield stress for any grain sizes.

Clearly, at sufficiently small grain sizes, the Hall–Petch model based upon dislocations may not be operative. However in this region it is believed that a new mechanism of deformation may be operative, called Coble creep or grain boundary diffusional creep. It is a deformation process that leads to homogeneous elongation of grains along the tensile direction.

Chokshi et al. [76] have proposed room-temperature Coble creep as the mechanism to explain their results. Certainly, there is an order of magnitude agreement and the trend is correct; however, the functional dependence of τ on d is incorrect as pointed out by Nieh and Wadsworth [77].

Conventional Coble creep requires that $\dot{\varepsilon} \propto d^3 \propto (d^{1/2})^{-6}$, i.e., the τ vs. $d^{-1/2}$ curve falls very steeply as $d^{-1/2}$ increases. This is not found experimentally [76].

A plausible explanation for this experimental fact was suggested by Masumura et al. [14]. In their model it is assumed that polycrystals with a relatively large average grain size obey the classical Hall–Petch relation. For very small grain sizes, it is assumed that Coble creep is active. If all the grains in the polycrystal are of the same size, the slope of the plot of the yield stress vs. $d^{-1/2}$ will change discontinuously at some critical grain size at which the mechanism changes. However, the statistical nature of the grain sizes in a polycrystal has to be taken into consideration by using an analysis similar to Kurzydlowski [78]. The volume of the grains is assumed to be log-normally distributed.

Finally, it is assumed that a grain size d^* exists, where the value of grain size in the classical Hall–Petch mechanism switches to the Coble creep mechanism, i.e., $\tau_{hp} = \tau_C$ at $d = d^*$. This model gives an analytical expression for τ as a function of the inverse square root of d in a simple and approximate manner that could be compared with experimental data over a whole range of grain sizes. A major consideration in this approach is which explicit expression is to be used for Coble creep.

In the model of Masumura et al. [14] the τ vs. d relationship used for Coble creep is given by

$$\tau_c = A/d + Bd^3 \tag{18.2}$$

where B is both temperature and strain-rate dependent. This threshold term A/d can be large if d is in the nanometer range. For intermediate grain sizes, both mechanisms might be active if the specimen has range of grain size distributions. Others (e.g., Sastry [79]) have also proposed a threshold of the form A/d. The term $p = (A/d^*)/(B(d^*)^3)$ is defined as the ratio of Coble threshold stress to conventional stress evaluated at d^* where the transition from Coble creep to Hall–Petch strengthening occurs,

$$p = \frac{A/d^*}{B(d^*)^3} \tag{18.3}$$

and yields a universal curve obtained with the form and shape of the curve similar to experimental data. In a recent publication, Yamakov et al. [72] have obtained a slightly different relation of Coble creep for small grain sizes.

Figure 18.4 and Figure 18.5 give the expression of the normalized yield stress as a function of normalized grain size raised to $-1/2$ for copper and palladium, respectively, and compared with experiments. In those figures, σ is the width of the grain size distribution, p and p' are measures of the Coble creep to Hall–Petch strengthening based on the formulation of Masumura et al. [14] and Yamakov et al. [72], respectively. The Coble creep expression developed with a threshold stress gives a better fit unless the values of d^* are relatively small. It should however be noted that the experimental result of Chokshi et al. [76] is controversial (see Refs. [80,81]) and hence further experimental results are needed to obtain a definite choice of the Coble creep expression.

18.5 GRAIN BOUNDARY SLIDING AND HIGH-STRAIN-RATE SUPERPLASTICITY IN NANOCRYSTALLINE MATERIALS

High-strain-rate superplasticity of nanocrystalline materials (Ni_3Al, Al-, and Ti-based alloys) [82–89] is a remarkable phenomenon which is different from both superplasticity of microcrystalline solids and conventional low tensile ductulity of nanocrystalline materials. In particular, nanocrystalline materials exhibit superplastic behavior at higher strain rates and lower temperatures compared with their micro-grained counterparts. Also, high-strain-rate superplasticity in nanocrystalline materials is characterized by very high flow stresses with the essential strengthening taking place at the extensive stage of deformation [82–89]. It is different from both superplasticity of microcrystalline materials at low flow stresses [90,91] and conventional low tensile ductility of most nanocrystalline materials [6].

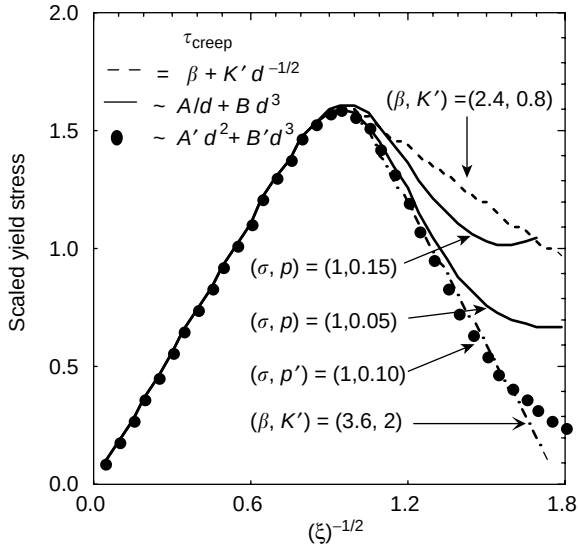

FIGURE 18.4 Normalized yield stress as a function of $\xi^{-1/2}$ (ξ is scaled grain size) comparing the various formulations of creep response for copper. The parameters β and K' are obtained from experimental data.

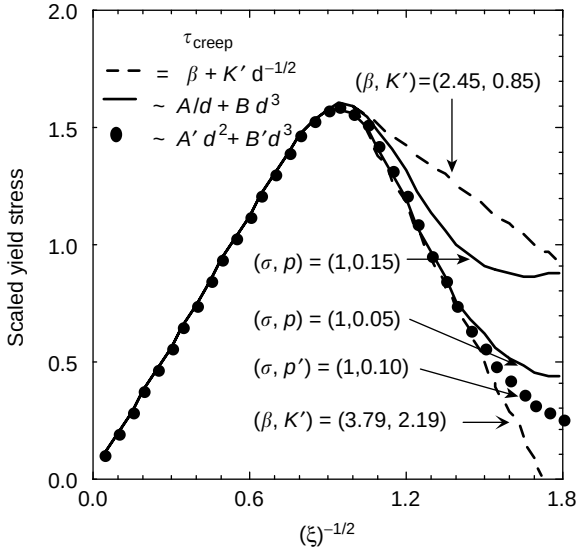

FIGURE 18.5 Normalized yield stress as a function of $\xi^{-1/2}$ (ξ is scaled grain size) comparing the various formulations of creep response for palladium. The parameters β and K' are obtained from experimental data.

In this context, recent experimental observations of high-strain-rate superplasticity [82–89] (and similar data on good tensile ductility [92–96]) of nanocrystalline materials give exciting evidence for the unusual deformation behavior of such materials. Following reviews [88,89] of experimental data on high-strain-rate superplasticity of nanocrystalline materials, GB sliding is the dominant mode of superplastic deformation in such materials. In this context, it is highly interesting to understand the specific features of GB sliding and its role in high-strain-rate superplasticity in nanocrystalline matter. These aspects are the subject of growing fundamental interest motivated by a range of new commercial applications based on the use of superplasticity of nanocrystalline materials.

In general, GB sliding is well-known as the dominant deformation mechanism in conventional microcrystalline materials exhibiting superplasticity (see, e.g., [90,91]). Carriers of GB sliding are treated as GB dislocations with small Burgers vectors being temporarily parallel to GB planes [26]. In the theory of superplasticity of conventional microcrystalline materials, characteristics of superplastic flow are caused by mechanisms that accommodate GB sliding (see, e.g., [97]). The same is true for the situation with nanocrystalline materials deformed through GB sliding, in which case, however, the GB and nanoscale effects modify the action of GB sliding and its accommodating mechanisms.

Hahn and coworkers [48,49] have suggested a model describing GB migration as the accommodation mechanism whose combined action with GB sliding gives rise to plastic flow localization in nanocrystalline bulk materials and materials. The model [48,49] suggests that GB migration occurs during plastic deformation and results in the formation of a zone where all GB planes are approximately parallel to each other (Figures 18.6a and b). The GB sliding is enhanced in this zone which, therefore, develops into a shear band where plastic flow is localized (Figure 18.6b). At the same time, however, the model [48,49] does not identify a mechanism for specific GB migration, which makes GB planes to be parallel to each other.

Representations of the model [48,49] have been recently extended in two ways. First, the formation of a zone where all GB planes are approximately parallel to each other has been recently described as that resulting from the movement of partial cellular dislocations (Figure 18.6c), defects in arrays of nanograins (cells) of a deformed nanocrystalline sample [53]. It is a large-scale description of plastic flow localization at the grain ensemble level.

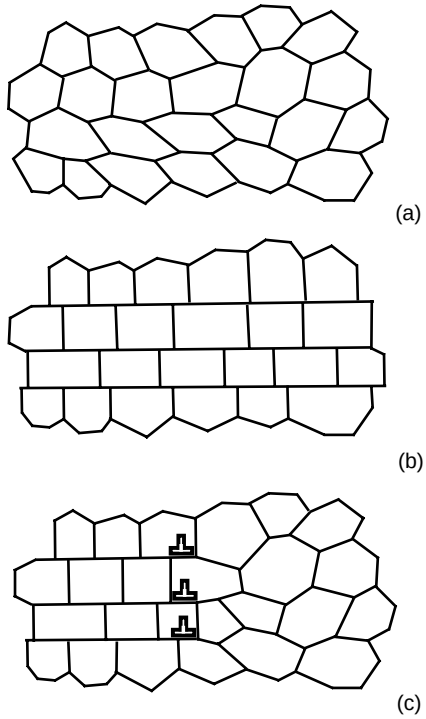

FIGURE 18.6 Plastic flow localization. (a) Nondeformed state of a nanocrystalline specimen modeled as a two-dimensional array of nanograins. (b) Local migration of grain boundaries gives rise to the formation of a local zone where grain boundaries are parallel to each other and intensive plastic shear through grain boundary sliding occurs. (c) The formation of a local zone where grain boundaries are parallel to each other results from movement of partial cellular dislocations.

Second, a theoretical model [60] has been suggested describing nanoscale peculiarities of GB sliding and transformations of defect structures near triple junctions of GBs. With results of the nanoscale analysis, the model [10] also describes the experimentally detected [82–89] strengthening and softening phenomena in nanocrystalline materials under high-strain-rate superplastic deformation. In the framework of this model, superplastic deformation, occurring mostly by GB sliding in nanocrystalline materials, is characterized by both strengthening due to transformations of gliding GB dislocations at triple junctions and softening due to local migration of triple junctions and adjacent GBs (Figures 18.7a–g). A theoretical analysis [60] of the energy characteristics of the transformations indicates that the transformations of GB dislocations at triple junctions are energetically favorable in certain ranges of parameters of the defect configuration. The corresponding flow stress is highly sensitive to both the level of plastic strain and the triple junction geometry. Sessile dislocations at triple junctions elastically interact with gliding GB dislocations. This interaction hampers GB sliding [60]. Thus, the storage of sessile GB dislocations at triple junctions (Figure 18.7) causes a strengthening effect that dominates at the first long stage of superplastic deformation. At the same time, the movement of GB dislocations across triple junctions can be accompanied with either GB migration (Figures 18.7a–g) [60] or the formation of a triple junction nanocrack (Figures 18.7h and i) [98], depending on parameters of the defect system. Let us consider the former route of defect structure evolution, that is, the action of GB migration as the accommodation mechanism for GB sliding (Figures 18.7a–g). As a result of numerous acts of movement of GB dislocations across triple junctions and the accompanying GB migration, the GB planes approximately become parallel to each other at the shear surface (Figures 18.7a–g). Under these circumstances, triple junctions stop being geometric obstacles for the movement of new GB dislocations, which, therefore, is enhanced along the shear surface (Figure 18.7h). This scenario quantitatively explains the softening effect experimentally observed [88,89] at the second stage of superplastic deformation in nanocrystalline materials. The discussed representations [60] on the softening mechanism related to local migration of GBs are supported by experimental observation [99,100] of plastic flow localization in nanocrystalline materials. Following electron microscopy experiments [99,100], shear bands where superplastic flow is localized in nanocrystalline Fe contain brick-like grains with GBs being parallel and perpendicular to the shear direction. It is effectively and naturally interpreted as a result of GB migration (Figures 18.7a–g) accompanying GB sliding across triple junctions.

Thus, in nanocrystalline solids deformed through GB sliding, there are both strengthening and softening effects occurring due to transformations of GB dislocations at triple junctions and accompanying local migration of GBs, respectively. The competition between the strengthening and softening effects is capable of crucially influencing the deformation behavior of nanocrystalline materials. In particular, superplastic deformation regime is realized if the strengthening dominates over the softening during the first extensive stage of deformation. This strengthening is responsible for an increase in the flow stress that drives the movement of GB dislocations and prevents plastic flow localization. With rising plastic strain, local GB migration (Figures 18.7a–h) makes GB planes roughly parallel to each other in some local regions of a loaded sample. As a result, local softening becomes substantial, which causes gradual macroscopic softening of nanocrystalline material. At some level of plastic strain, the softening becomes dominant over the strengthening. At this point, movement of new GB dislocations is dramatically enhanced along the shear surfaces where GB planes approximately become parallel to each other due to movement of previous GB dislocations across their junctions. As a corollary, the softening effect leads to plastic flow localization often followed by failure.

Notice that GB sliding is enhanced in deformed nanocrystalline materials due to lattice dislocation slip. Lattice dislocations moving in grain interiors come to GBs where they split into GB dislocations that carry intense GB sliding [27,28]. This kind of interaction between deformation modes is well known in the theory of superplasticity of conventional microcrystalline materials and definitely plays a significant role in nanocrystalline materials with grain size $d > 30$ nm, in which lattice dislocation slip is intense.

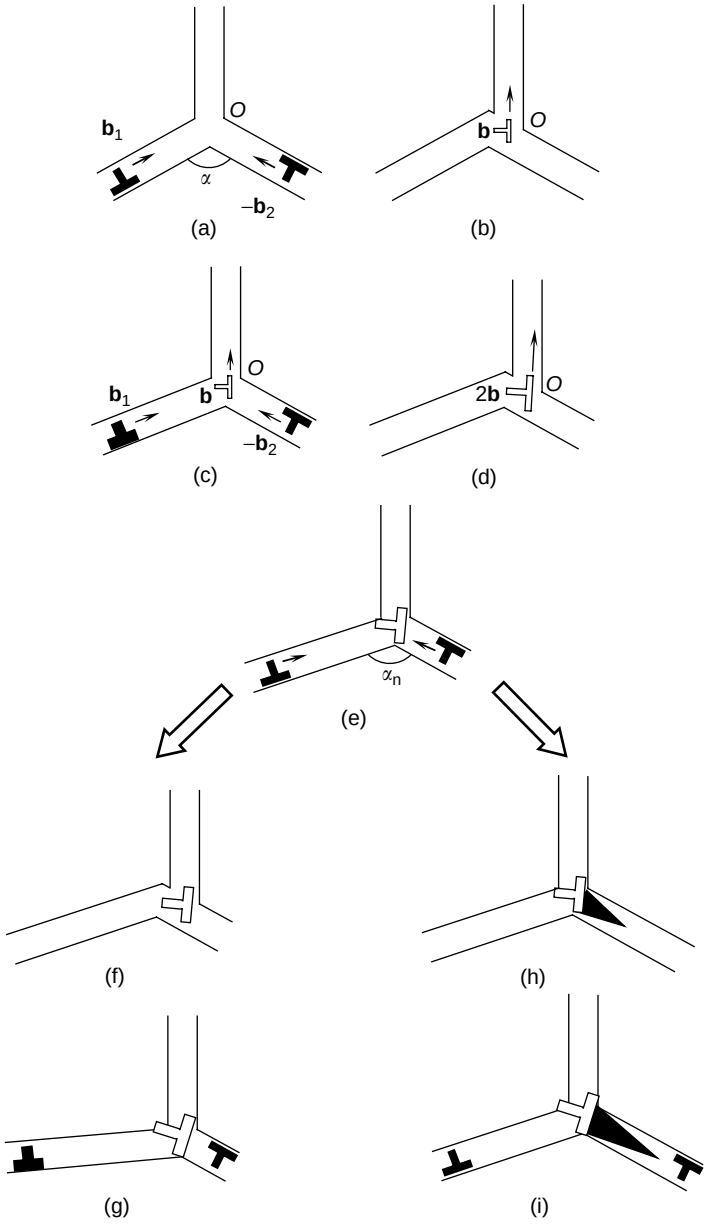

FIGURE 18.7 Grain boundary sliding and transformations of defect structures near a triple junction of grain boundaries. (a) Initial state of defect configuration in a deformed nanocrystalline material. Two gliding grain boundary dislocations with Burger's vectors b1 and b2 move towards the triple junction O. (b) Sessile dislocation (open dislocation sign) with the Burgers vector b is formed. Triple junction is displaced by the vector b2 from its initial position as shown in Figure 18.7(a). (c) Generation of two new gliding grain boundary dislocations that move towards the triple junction. (d) Convergence of two gliding dislocations results in increase in magnitude of sessile dislocation of Burger's vector. Also, the triple junction is transferred by the vector 2b2 from its initial position shown in Figure 18.7(a). (e) Generation of two new gliding grain boundary dislocations that move towards the triple junction. (f and g) Numerous acts of transfer of grain boundary dislocations across a triple junction and accompanying local migration of grain boundaries cause grain boundary planes (adjacent to the triple junction) to be approximately parallel to each other. This process enhances grain boundary sliding across the triple junction. An alternative way in which defect structures evolve involves (h) generation and (i) growth of a triple junction nanocrack in the stress field of the sessile dislocation.

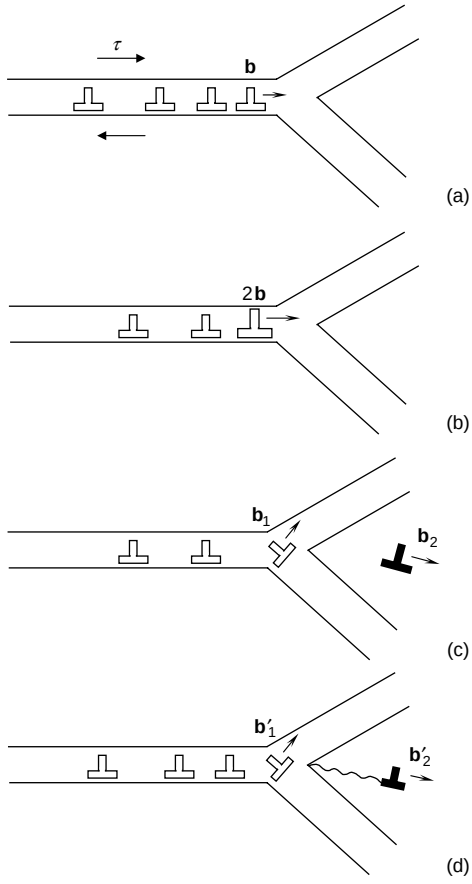

FIGURE 18.8 Emission of lattice dislocations from triple junction of grain boundaries in deformed nanocrystalline materials. (a) Grain boundary dislocations glide toward triple junction. (b) Two head grain boundary dislocations converge. (c) Perfect lattice dislocation is emitted from dislocated triple junction. (d) Partial lattice dislocation is emitted from dislocated triple junction. Stacking fault (wavy line) is formed behind the moving partial dislocation.

In nanocrystalline materials characterized by a high volume fraction of the GB phase, GBs not only absorb but also intensively emit lattice dislocations. This phenomenon has been observed in direct experiments [88,89,93] and indirectly confirmed by experimental data [54–58], indicating twin deformation conducted by partial lattice dislocations in nanograins. The theoretical model [52] describes emission of perfect and partial lattice dislocations as a process induced by the preceding GB sliding or rotational deformation as follows. A pile-up of GB dislocations is generated under the action of mechanical load in a GB in a plastically deformed nanocrystalline sample. Mechanical-load-induced motion of the GB dislocation pile-up is stopped by a triple junction of GBs. There are several ways of evolution of the GB dislocation pile-up, including emission of either perfect (Figure 18.8a) or partial (Figure 18.8b) dislocations from the triple junction [52]. In the second case, stacking faults are formed behind the moving partial dislocations (Figure 18.8b).

18.6 GRAIN GROWTH PROCESSES IN NANOCRYSTALLINE MATERIAL

In this section, we consider grain growth in nanocrystalline materials. We first review our current understanding of the phenomena in general and then apply these results to the growth of

nanocrystalline materials. For such systems it is shown that the mobility of the triple junctions may play a significant role.

Grain growth in general terms is the well-known phenomenon of an increase in average grain size during annealing due to grain boundary migration. This movement of grain boundaries is due to annealing at a certain temperature for some time. The driving force for this growth is the reduction in grain boundary area and, hence, the total grain boundary energy of the system. Grain growth is a cooperative process simultaneously involving many individual grains of various sizes and shapes [101–105]. Importance of grain boundary area/length reduction with time, motion by curvature, and the role of dihedral angles is now considered central to this understanding. Many properties of materials such as yield stress in metals and critical currents in superconductors depend on grain size. Therefore, a theoretical understanding of grain size [101] is expected to provide further insight into future applications in nanosystems as well.

The main features of grain growth described in great detail by Kurtz and Carpay [102] are briefly:

1. *Time exponent*: During growth, the average grain size increases as ~ $(\text{time})^{1/2}$.
2. *Independent of initial distribution*: The final grain size distribution is generally insensitive to the initial distribution.
3. *Scaling*: During growth, after sufficient time, the distribution of grain sizes remains self-similar if all sizes are scaled to average grain size.
4. Size distribution: After sufficient time in grain growth, the distribution approaches approximately a log-normal form.

For nanocrystalline materials experimental data are absent as far as these properties are concerned.

Owing to the complexity of the grain structure of the individual grain and the involvement of a large number of grain boundaries in the process, developing a realistic model of grain growth is a formidable challenge, and consequently, many conceptual and mathematical simplifications are made. Further simplification is possible by first considering grain growth in two dimensions only. This is possible owing to the von Neumann law [106] whose applicability to grain growth was proved by Mullins [107].

If $A_n(t)$ is the area of the grain with n sides at any instant t, and M is a constant, then under the assumptions mentioned above and further discussed later, the following relation is deduced [106,107]:

$$\frac{dA_n(t)}{dt} = M(n - 6) \tag{18.4}$$

This relation has played an important role in the development of the theory of grain growth.

In obtaining von Neumann–Mullins law (Equation [18.4]), Mullins used the following three basic assumptions of grain growth process:

1. All the grain boundaries during grain growth move with a velocity proportional to its curvature.
2. The triple junctions of the grain boundaries have infinite mobility during any change in the number of sides of the grain, etc.
3. When equilibrated, the boundaries meet at grain boundaries at an angle of 120°.

It should be realized that all the three assumptions are in accord with the von Neumann–Mullins law of grain growth, and so the use of this law is equivalent to accepting these assumptions. This law may have to be modified for nanocrystalline materials (see below).

Almost all grain growth models are based on an idealized univariate system where the grain size is characterized by its radius, R, and all the grain boundaries are assumed to have the same energy.

The grain size distribution is then expressed in terms of R only. With this starting point, a mean field model was developed [108,109], and subsequently more sophisticated stochastic models were constructed [110–116] for deriving the distribution function alluded to above and its time evolution.

A solution for grain size distributions, etc. using this formulation, is discussed by Pande and his co-workers [112–115]. By assuming a certain form for the drift and diffusion terms, the following results were deduced by Pande and Rajagopal [116]: (1) scaling; (2) nondependence of the long time solution from the initial distribution; (3) kinetics; and (4) the grain size distribution. Table 18.1 lists a comparison among the several mean field and stochastic models. Only the stochastic formulation is capable of describing all four of the required attributes for grain growth.

In case of nanocrystalline materials two additional factors need to be taken into account:

1. Grain rotation (increases grain growth)
2. Finite triple junction mobility (retards grain growth)

These two mechanisms will operate in addition to curvature-driven grain growth. Grain rotation has been considered in detail by Li [117] from theory and by Haslam et al. [118] using simulation. We will not consider grain rotation any further except to state that in nanocrystalline materials this mode is quite possible if the grain growth is retarded by triple junction finite mobility. We will consider the effect of finite mobility in detail below.

Gottstein and Shvindlerman [119] have shown that λ, defined as

$$\lambda = \frac{(\text{grain size})(\text{triple junction mobility})}{\text{grain boundary mobility}} \tag{18.5}$$

which involves the ratio of the mobilites of the triple junction to the grain boundary can be expressed as

$$\lambda = \frac{\ln \sin\theta}{2\cos\theta - 1} \text{ for } n > 6 \text{ and } \lambda = \frac{2\theta}{2\cos\theta - 1} \text{ for } n < 6 \tag{18.6}$$

where 2θ is the triple junction angle and n is the number sides. This relation is illustrated in Figure 18.9. It is seen that if the mobility is finite, the triple junction angle will always be different from 120° and the von Neumann–Mullins law is partially obeyed.

When the triple junction mobility is infinite, then λ is infinite and the triple junction angle, 2θ, is equal to 120°. However, when λ is finite, the triple junction can deviate from 120° and the von Neumann–Mullins law requires modification. Using the above results, we plot dA_n/dt as a function of λ for various values of n in Figure 18.10. It is seen that for $\lambda < 1.43$, $dA_n/dt > 0$, hence all of the grains grow, which is not possible since the total area of the polycrystal (for a two-dimensional system) is conserved. Grain growth is only possible if some grains decrease in size and disappear. Therefore a

TABLE 18.1
Comparison between the Mean Field and Stochastic Approaches

Grain Growth Attributes	Mean Field			Stochastic
	Hillert [108]	Lücke et al. [121]	Mullins [109]	
Time exponent	Yes	Yes	No	Yes
Initial distribution independence	No	No	No	Yes
Scaling	No	No	No	Yes
Correct distribution	No	No	No	Yes

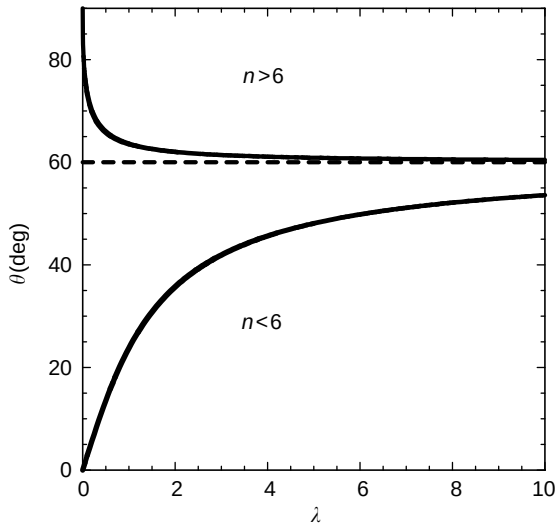

FIGURE 18.9 Triple junction angle dependence on λ.

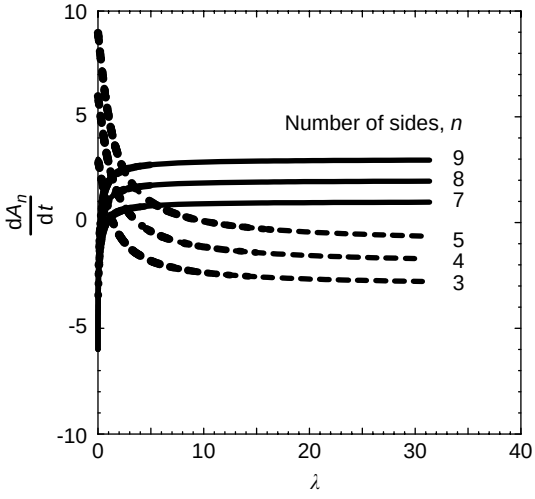

FIGURE 18.10 Growth rates for n-sided grains.

sufficiently small λ will retard grain growth. For $1.43 < \lambda < 3.79$, grains with $n \geqslant 4$ will grow and for $3.79 < \lambda < 10.73$, grains with five sides or more will grow. For values of $\lambda < 10.73$, the growth mechanism is considerably altered and becomes slower since there will be relatively fewer grains to shrink in size and ultimately disappear. Since λ depends on the grain size, the smaller grain sizes will have relatively smaller λ. Thus, in nanocrystalline materials, grain growth could be retarded. This conclusion is strictly true for two-dimensional systems only; however, since three-dimensional systems usually behave, at least qualitatively, in a similar fashion, it may be valid for these cases as well. Experimental evidence for grain retardation has been provided by Okuda et al. [120] for thin films.

18.7 CONCLUDING REMARKS

Thus, GBs in nanocrystalline materials are characterized by the specific structural and geometric features which are as follows: The volume fractions occupied by GBs and their triple junctions are

extremely high in nanocrystalline materials. GBs are very short and often contain high-density ensembles of extrinsic defects. With these specific features, GBs strongly contribute to the unique properties of nanocrystalline materials. In particular, GBs cause the action of the specific deformation mechanisms in nanocrystalline materials whose deformation behavior is very different from that of conventional coarse-grained polycrystalline materials. Such GB-conducted deformation mechanisms as GB sliding and GB diffusional creep (Coble creep) are capable of effectively operating and causing plastic flow of nanocrystalline materials with finest grains having the size $d < d_c$. Here the critical value of the grain size d_c is between 10 and 30 nm, depending on material and structural parameters. Similar to coarse-grained polycrystals, nanocrystalline materials having mean grain size $d > d_c$ are deformed mostly through lattice dislocation slip. However, the lattice dislocation slip in such nanocrystalline materials is strongly affected by high-density ensembles of GBs modifying its action compared to the conventional situation with coarse-grained polycrystals. In particular, GBs, on the one hand, obstruct movement of lattice dislocations and, on the other, emit perfect and partial lattice dislocations into grain interiors. The specific behavioral features of GBs in deformed nanocrystalline materials are responsible for their extremely high strength characteristics and, in most cases, low tensile ductility. Nevertheless, in several cases, high-density ensembles of GBs are capable of causing a good ductility and even superplasticity of nanocrystalline materials at relatively low temperatures and high strain rates. The fundamentals of this remarkable phenomenon in nanocrystalline materials are under intense discussion based on the idea of the specific structural and behavioral features of GBs.

Grain growth can break the nanocrystalline structure and thereby is very essential for performance of nanomaterials. Grain growth processes in nanocrystalline materials occur by migration of GBs and triple junctions sensitive to their specific structural and geometric features. In particular, two additional factors operate in nanocrystalline materials apart from curvature-driven grain growth, which is dominant in coarse-grained polycrystals. These factors are nanoscale grain rotation (increases grain growth) and finite triple junction mobility (retards grain growth).

To summarize, GBs in nanocrystalline materials are characterized by the specific structural, geometric and behavioral features which strongly contribute to the outstanding properties of nanocrystalline matter. These features, in particular, are exhibited in plastic deformation and grain growth processes and definitely should be taken into account in further experimental and theoretical studies of nanocrystalline materials.

ACKNOWLEDGMENTS

This work was supported, in part (for I.A.O.) by the Office of Naval Research, INTAS (grant 03-51-3779), Russian Science Support Foundation, Russian Academy of Sciences Program "Structural Mechanics of Materials and Construction Elements" and St. Petersburg Scientific Center. C.S. Pande and R.A. Masumura also gratefully acknowledge the support of the Office of Naval Research.

REFERENCES

1. Nalwa, H.S., Ed., *Handbook of Nanocrystalline Materials and Nanotechnology*, Vols. 1–5, Academic, San Diego, 1999.
2. Roco, M.C., Williams, R.S., and Alivisatos, P., Eds., *Nanotechnology Research Directions*, Kluwer, Dordrecht, 2000.
3. Berndt, C.C., Fischer, T., Ovid'ko, I.A., Skandan, G., and Tsakalakos, T., Eds., *Nanomaterials for Structural Applications, MRS Symposium Proceedings*, Vol. 740, MRS, Warrendale, 2003.
4. Tsakalakos, T., Ovid'ko, I.A., and Vasudevan, A.K., Eds., *Nanostructures: Synthesis, Functional Properties and Applications of Nanostructures, NATO Science Series*, Kluwer, Dordrecht, 2003.
5. Ovid'ko, I.A., Pande, C.S., Krishnamoorti, R., Lavernia, E., and Skandan, G., Eds., *Mechanical Properties of Nanocrystalline Materials and Nanocomposites, MRS Symposium Proceedings*, Vol. 791, MRS, Warrendale, 2004.

6. Mohamed, F.A. and Li, Y., Creep and superplasticity in nanocrystalline materials: current understanding and future prospects, *Mater. Sci. Eng. A*, 298, 1, 2001.
7. Kumar, K.S., Suresh, S., and Swygenhoven, H., Mechanical behavior of nanocrystalline metals and alloys, *Acta Mater*., 51, 5743, 2003.
8. Veprek, S. and Argon, A., Towards the understanding of mechanical properties of super- and ultrahard nanocomposites, *J. Vac. Sci. Tehcnol. B*, 20, 650, 2002.
9. Zhang, X., Wang, H., and Koch, C.C., Mechanical behavior of bulk ultrafine-grained and nanocrystalline Zn, *Rev. Adv. Mater. Sci*., 6, 53, 2004.
10. Gutkin, M.Yu. and Ovid′ko, I.A., *Plastic Deformation in Nanocrystalline Materials*, Springer, Berlin, 2004.
11. Patscheider, J., Nanocomposite hard coatings for wear protection, *MRS Bull.* 28, 180, 2003.
12. Gryaznov, V.G., Polonsky, I.A., Romanov, A.E., and Trusov, L.I., Size effects of dislocation stability in nanocrystals, *Phys. Rev. B*, 41, 42, 1991.
13. Romanov, A.E., Continuum theory of defects in nanoscale materials, *Nanostruct. Mater*., 6, 125, 1995.
14. Masumura, R.A., Hazzledine, P.M., and Pande, C.S., Yield stress of fine grained materials, *Acta Mater*., 46, 4527, 1998.
15. Van Swygenhoven, H., Spavzer, M., Caro, A., and Farkas, D., Competing plastic deformation mechanisms in nanophase metals, *Phys. Rev. B*, 60, 22, 1999.
16. Van Swygenhoven, H., Spaczer, M., and Caro, A., Microscopic description of plasticity in computer generated metallic nanophase samples: a comparison between Cu and Ni, *Acta Mater*., 47, 3117, 1999.
17. Kim, H.S., Estrin, Y., and Bush, M.B., Plastic deformation behaviour of fine-grained materials, *Acta Mater*., 48, 493, 2000.
18. Fedorov, A.A., Gutkin, M.Yu., and Ovid'ko, I.A., Triple junction diffusion and plastic flow in fine-grained materials, *Scripta Mater*., 47, 51, 2002.
19. Ovid'ko, I.A., Deformation of nanostructures, *Science*, 295, 2386, 2002.
20. Gutkin, M.Yu., Ovid'ko, I.A., and Pande, C.S., Physical mechanisms of plastic flow in nanocrystalline materials, in *Nanoclusters and Nanocrystals*, Nalwa, H.S., Ed., American Sci. Publ., California, 2003, p. 225.
21. Gutkin, M.Yu., Ovid'ko, I.A., and Skiba, N.V., Crossover from grain boundary sliding to rotational deformation in nanocrystalline materials, *Acta Mater*., 51, 4059, 2003.
22. Koch, C.C., Optimization of strength and ductility in nanocrystalline and ultrafine grained metals, *Scr. Mater*., 49, 657, 2003.
23. Cheng, S., Spencer, J.A., and Milligan, W.W., Strength and tension/compression asymmetry in nanostructured and ultrafine-grain metals, *Acta Mater*., 51, 4505, 2003.
24. Van Swygenhoven, H., Derlet, P.M., Hasnaoui, A., and Samaras, M., Impact of grain boundaries on structural and mechanical properties, in *Nanostructures: Synthesis, Functional Properties and Applications of Nanostructures*, Tsakalakos, T., Ovid'ko, I.A., and Vasudevan, A.K., Eds., NATO Science Series, Kluwer, Dordrecht, 2003, p. 155.
25. Ankem, S., Pande, C.S., Ovid'ko, I.A., and Ranganathan, S., Eds., *Science and Technology of Interfaces, Proceedings of International Symposium in Honor of Dr. Bhakta Rath.*, TMS, Warrendale, 2002.
26. Sutton, A.P. and Balluffi, R.W., *Grain Boundaries in Crystalline Materials*, Oxford Science Publications, Oxford, 1996.
27. Chuvildeev, V.N., *Non-Equilibrium Grain Boundaries in Metals*, Fizmatlit, Moscow, 2004 (in Russian).
28. Valiev, R.Z., Islamgaliev, R.K., and Alexandrov, I.V., Bulk nanostructured materials from severe plastic deformation, *Prog. Mater. Sci*. 45, 103, 2000.
29. Clarke, D.R., On the equilibrium thickness of intergranular glass phases in ceramic materials, *J. Am. Ceram. Soc.* 70, 15, 1987.
30. Birringer, R., Gleiter, H., Klein, H.P., and Marquardt, P., Nanocrystalline materials an approach to a novel solid structure with gas-like disorder, *Phys. Lett. A*, 102, 365, 1984.
31. Gleiter, H., Nanocrystalline materials, *Prog. Mater. Sci*., 33, 223, 1989.
32. Ovid'ko, I.A., Quasiperiodic interfaces and tilt boundaries of finite extent, *Mater. Sci. Eng. A*, 280, 355, 2000.
33. Nazarov, A.A., Bachurin, D.V., Shenderova, O.A., and Brenner, On the origin and energy of triple junction defect due to the finite length of grain boundaries, *Interf. Sci*., 11, 417, 2003.

34. Gottstein, G., King, A.H., and Shvindlerman, L.S., The effect of triple junction drag on grain growth, *Acta Mater*., 48, 397, 2000.
35. King, A.H., The geometric and thermodynamic properties of grain boundary junctions, *Interf. Sci*., 7, 251, 1999.
36. Palumbo, G. and Aust, K.T., Triple-line corrosion in high-purity nickel, *Mater. Sci. Eng. A*, 113, 139, 1989.
37. Yin, K.M., King, A.H., Hsieh, T.E., Chen, F.R., Kai, J.J., and Chang, L., Segregation of bismuth to triple junctions in copper, *Microscopy Microanal.*, 3, 417, 1997.
38. Osipov, A.V. and Ovid'ko, I.A., Diffusion-induced decay of disclinations and solid state amorphization in mechanically alloyed materials, *Appl. Phys. A*, 54, 517, 1992.
39. Gutkin, M.Yu. and Ovid'ko, I.A., Disclinations, amorphization and microcrack generation at grain boundary junctions in polycrystalline solids, *Phil. Mag. A*, 70, 561, 1994.
40. Bokstein, B., Ivanov, V., Oreshina, O., Peteline, A., and Peteline, S., Direct experimental observation of accelerated Zn diffusion along triple junctions in Al, *Mater. Sci. Eng. A*, 302, 151, 2001.
41. Kolobov, Yu.R., Grabovetskaya, G.P., Ratochka, I.V., and Ivanov, K.V., Diffusion-induced creep of polycrystalline and nanostructured metals, *Nanostruct. Mater*., 12, 1127, 1999.
42. Kolobov, Yu.R., Grabovetskaya, G.P., Ivanov, K.V., and Ivanov, M.B., Grain boundary diffusion and mechanisms of creep of nanostructured metals, *Interf. Sci*., 10, 31, 2002.
43. Ovid'ko, I.A. and Sheinerman, A.G., Grain boundary dislocations and enhanced diffusion in nanocrystalline bulk materials and films, *Philos. Mag*., 83, 1551, 2003.
44. Weertman, J.R. and Sanders, P.G., Plastic deformation of nanocrystallinemetals, *Solid State Phenom*., 35, 249, 1994.
45. Volpp, T., Göring, E., Kuschke, W.-M., and Arzt, E., Grain size determination and limits to Hall–Petch behavior in nanocrystalline NiAl powders, *Nanostruct. Mater*., 8, 855, 1997.
46. Pande, C.S. and Masumura, R.A., A model for flow stress dependence on grain size for nanocrytalline solids, in *Processing and Properties of Nanocrystalline Materials*, Suryanarayana, C., Singh, J., and Froes, F.H., Eds., TMS, Warrendale, 1996, p. 387.
47. Ke, M., Milligan, W.W., Hackney, S.A., Carsley, J.E., and Aifantis, E.C., Observation and measurement of grain rotation and plastic strain in nanostructured metal thin films, *Nanostruct. Mater*., 5, 689, 1995.
48. Hahn, H., Mondal, P., and Padmanabhan, K.A., Plastic deformation of nanocrystalline materials, *Nanostruct. Mater*., 9, 603, 1997.
49. Hahn, H. and Padmanabhan, K.A., A model for the deformation of nanocrystalline materials, *Philos. Mag. B*, 76, 559, 1997.
50. Konstantinidis, D.A. and Aifantis, E.C., On the "anomalous" hardness of nanocrystalline materials, *Nanostruct. Mater*., 10, 1111, 1998.
51. Murayama, M., Howe, J.M., Hidaka, H., and Takaki, S., Atomic-level observation of disclination dipoles in mechanically milled nanocrystalline Fe, *Science*, 295, 2433, 2002.
52. Fedorov, A.A., Gutkin, M.Yu., and Ovid'ko, I.A., Transformations of grainboundary dislocation pile-ups in nano- and polycrystalline materials, *Acta Mater*., 51, 887, 2003.
53. Ovid'ko, I.A., Nanodefects in nanostructures, *Philos. Mag. Lett*. 83, 611, 2003.
54. Chen, M., Ma, E., Hemker, K.J., Sheng, H., Wang, Y., and Cheng, X., Deformation twinning in nanocrystalline aluminum, *Science*, 300, 1275, 2003.
55. Liao, X.Z., Zhou, F., Lavernia, E.J., Srinivasan, S.G., Baskes, M.I., He, D.W., and Zhu, Y.T., Deformation mechanism in nanocrystalline Al: partial dislocation slip, *Appl. Phys. Lett*., 83, 632, 2003.
56. Liao, X.Z., Zhou, F., Lavernia, E.J., He, D.W., and Zhu, Y.T., Deformation twins in nanocrystalline Al, *Appl. Phys. Lett*., 83, 5062, 2003.
57. Liao, X.Z., Zhao, Y.H., Srinivasan, S.G., Zhu, Y.T., Valiev, R.Z., and Gunderov, D.V., Deformation twinning in nanocrystalline copper at room temperature and low strain rate, *Appl. Phys. Lett*., 84, 592, 2004.
58. Liao, X.Z., Srinivasan, S.G., Zhao, Y.H., Baskes, M.I., Zhu, Y.T., Zhou, F., Lavernia, E.J., and Hu, H.F., Formation mechanism of wide stacking faults in nanocrystalline Al, *Appl. Phys. Lett*., 84, 3564, 2004.
59. Gutkin, M.Yu., Ovid'ko, I.A., and Pande, C.S., Yield stress of nanocrystalline materials: role of grain boundary dislocations, triple junctions and Coble creep, *Philos. Mag*., 84, 847, 2004.
60. Gutkin, M.Yu., Ovid'ko, I.A., and Skiba, N.V., Strengthening and softening mechanisms in nanocrystaline materials under superplasti deformation, *Acta Mater*., 52, 1711, 2004.

61. Hall, E.O., The deformation and ageing of mild steel 3. Discussion of results. *Proc. Phys. Soc. London*, B64, 747, 1951.
62. Petch, N.J., The cleavage strength of polycrystals, *J. Iron Steel Inst*., 174, 25, 1953.
63. Pande, C.S., Masumura, R.A., and Armstrong, R.W., Pile-up based Hall–Petch relation for nanoscale materials, *Nanostruct. Mater*., 2, 323, 1993.
64. Sanders, P.G., Eastman, J.A., and Weertman, J.R., Elastic and tensile behavior of nanocrystalline copper and palladium, *Acta Mater*., 45, 4019, 1997.
65. Li, J.C.M. and Chou, Y.T., Role of dislocations in flow stress grain size relationships, *Met. Trans*, 1, 1145, 1970.
66. Mitchell, T.E., Hecker, S.S., and Smialek, R.L., Dislocation pile-ups in anisotropic crystals, *Phys. Stat. Sol*., 11, 585, 1965.
67. Armstrong, R.W. and Head, A.K., Dislocation queueing and fracture in an elastically anisotropic material, *Acta Met*., 13, 759, 1965.
68. Pande, C.S. and Masumura, R.A., Effect of elastic anisotropy on the brittle fracture of a polycrystalline solid, in *Proceedings of Sixth International Conference on Fracture*, Valluri, S.R., Taplin, D.M.R., Rama Rao, P., Knott, J.F., and Dubey, R., Eds., Pergamon, Oxford, 1984, p. 857.
69. Louat, N., Alloys, strong at room and elevated temperatures from powder metallurgy, *Acta Met.*, 33, 59, 1985.
70. Evans, A.G. and Hirth, J.P., Deformation of nanoscale cermets, *Scr. Met.*, 26, 1675, 1992.
71. Lasalmonie, A and Strudel, J.L., Influence of grain size on the mechanical behaviour of some high strength materials, *J. Mat. Sci.*, 21, 1837, 1986.
72. Yamakov, V., Wolf, D., Phillpot, S.R., and Gleiter, H., Grain-boundary diffusion creep in nanocrystalline palladium by molecular-dynamics simulation, *Acta Mater*., 50, 61, 2002.
73. Valiev, R.Z., Kozlov, E.V., Ivanov, Yu.F., Lian, J., Nazarov, A.A., and Baudelet B., Deformation behaviour of ultra-fine-grained copper, *Acta Mater*., 42, 2467, 1994.
74. Malygin, G.A., Breakdown of the Hall–Petch law in micro- and nanocrystalline materials, *Phys. Solid State*, 37, 1248, 1995.
75. Chokshi, A.H., Rosen, A., Karch, J., and Gleiter, H., On the yield stress of nanocrystals, *J. Mater. Sci*., 28, 4359, 1993.
76. Chokshi, et al., On the validity of the Hall-Petch relationship in nanocrystalline materials, *Scr. Met*., 23, 1679, 1989.
77. Nieh, T.G. and Wadsworth, J., Hall–petch relation in nanocrystalline solids, *Scr. Met*., 25, 955, 1991.
78. Kurzydlowski, K.J., A model for the flow stress dependence on the distribution of grain size in polycrystals, *Scr. Met*., 24, 879, 1990.
79. Sastry, S.M.L., private communication, 1997.
80. Van Swygenhoven, H., and Derlet, P.M., Grain-boundary sliding in nanocrystalline fcc metals, *Phys. Rev. B*., 64, 224105, 2001.
81. Van Swygenhoven, H. and Caro, A., Plastic behavior of nanophase metals studied by molecular dynamics, *Phys. Rev. B*, 58, 11246, 1998.
82. McFadden, S.X., Misra, R.S., Valiev, R.Z., Zhilyaev, A.P., and Mukherjee, A.K., Low-temperature superplasticity in nanostructured nickel and metal alloys, *Nature*, 398, 684, 1999.
83. Mishra, R.S., Valiev, R.Z., McFadden, S.X., Islamgaliev, R.K., and Mukherjee, A.K., High-strain-rate superplasticity from nanocrystalline Al alloy 1420 at low temperatures, *Phil. Mag. A*, 81, 37, 2001.
84. Islamgaliev, R.K., Valiev, R.Z., Mishra, R.S., Mukherjee, A.K., Enhanced superplastic properties in bulk metastable nanostructured alloys, *Mater. Sci. Eng. A*, 304–306, 206, 2001.
85. Mishra, R.S., Stolyarov, V.V., Echer, C., Valiev, R.Z., and Mukherjee, A.K., Mechanical behavior and superplasticity of a severe plastic deformation processed nanocrystalline Ti-6Al-4V alloy, *Mater. Sci. Eng. A*, 298, 44, 2001.
86. Valiev, R.Z., Song, C., McFadden, S.X., Mukherjee, A.K., and Mishra, R.S., TEM/HREM observations of nanostructured superplastic Ni3Al, *Phil. Mag. A*., 81, 25, 2001.
87. Valiev, R.Z., Alexandrov, I.V., Zhu, Y.T., and Lowe, T.C., Paradox of strength and ductility in metals processed by severe plastic deformation, *J. Mater. Res*., 17, 5, 2002.
88. Mukherjee, A.K., Elevated temperature crystalline plasticity at diminishing length scales, in *Creep Deformation: Fundamentals and Applications*., Mishra, R.S., Earthman, J.C., and Raj, S.V., TMS, Eds., Warrendale, 2002, p. 3.

89. Mukherjee, A.K., An examination of the constitutive equation for elevated temperature plasticity, *Mater. Sci. Eng. A*, 322, 1, 2002.
90. Padmanabhan, K.A. and Davies, G.J., *Superplasticity*, Springer, Berlin, 1980.
91. Pilling, J. and Ridley, N., *Superplasticity in Crystalline Solids*, The Institute of Metals, London, 1989.
92. Wang, Y., Chen, M., Zhou, F., and Ma, E., High tensile ductility in a nanostructured metal, *Nature*, 419, 912, 2002.
93. Kumar, K.S., Suresh, S., Chisholm, M.F., Norton, J.A., and Wang, P., Deformation of electrodeposited nickel, *Acta Mater*., 51, 387, 2003.
94. Wang, Y., Ma, E., Valiev, R.Z., and Zhu, Y., Tough nanostructured metals at cryogenic temperatures, *Adv. Mater*., 16, 328, 2004.
95. Zhu, Y.T. and Liao, X., Nanostructured metals retaining ductility, *Nature Mater*., 31, 361, 2004.
96. Youssef, K.M., Scattergood, R.O., Murty, K.L., and Koch, C.C., Ultratough nanocrystalline copper with a narrow grain size distribution, *Appl. Phys. Lett*., 85, 929, 2004.
97. Zelin, M.G. and Mukherjee, A.K., Geometrical aspects of superplastic flow, *Mater. Sci. Eng. A*, 208, 210, 1996.
98. Ovid′ko, I.A. and Sheinerman, A.G., Triple junction nanocracks in deformed nanocrystalline materials, *Acta Mater*., 52, 1201, 2004.
99. Wei, Q., Jia, D., Ramesh, K.T., and Ma, E., Evolution and microstructure of shear bands in nanostructured Fe, *Appl. Phys. Lett*., 81, 1240, 2002.
100. Jia, D., Ramesh, K.T., and Ma, E., Effects of nanocrystalline and ultrafine grain sizes on constitutive behavior and shear bands in iron, *Acta Mater*., 51, 3495, 2003.
101. Atkinson, H.V., Theories of normal grain growth in pure single phase systems, *Acta Metall.*, 36, 469, 1988.
102. Kurtz, S.K. and Carpay, F.M.A., Microstructure and normal grain growth in metals and ceramics. I. Theory, *J. Appl. Phys.*, 51, 5725, 1980.
103. Smith, C.S., The shape of metal grains, with some other metallurgical applications of topology, *Transactions AIME*, 175, 15, 1948.
104. Williams W.M. and Smith, C.S., A study of grain shape in an aluminum alloy and other applications of stereoscopic microradiograpy, *Trans. AIME*, 194, 755, 1949.
105. Smith, C.S., Further notes on the shape of metal grains: space-filling polyhedra with unlimited sharing of corners and faces, *Acta Metall.*, 1, 295, 1953.
106. von Neumann, J., in *Metal Interfaces*, American Society for Metals, Cleveland, OH, 1952, p. 108.
107. Mullins, W.W., Two-dimensional motion idealized grain boundaries, *J. Appl. Phys.*, 27, 900, 1956.
108. Hillert, M., On the theory of normal and abnormal grain growth, *Acta Metall.*, 13, 227, 1965.
109. Mullins, W.W., Grain growth of uniform boundaries with scaling, *Acta Metall.*, 1998, 46, 6219.
110. Pande, C.S., On a stochastic theory of grain growth, *Acta Metall.*, 35, 2671, 1980.
111. Chen, I.W., A stochastic theory of grain growth, *Acta Metall.*, 35, 1723, 1987.
112. Pande, C.S. and Dantsker, E., On a stochastic theory of grain growth—II, *Acta Metall*., 38, 945, 1990.
113. Pande, C.S. and Dantsker, E., On a stochastic theory of grain growth—III, *Acta Metall*., 39, 1359, 1991.
114. Pande, C.S. and Dantsker, E., On a stochastic theory of grain growth—IV, *Acta Metall*., 42, 2899, 1994.
115. Pande, C.S., Masumura, R.A., and Marsh, S.P., Stochastic analysis of two-dimensional grain growth, *Phil. Mag.*, 81, 1229, 2001.
116. Pande, C.S. and Rajagopal, A.K., Uniqueness and self similarity of size distributions in grain growth and coarsening, *Acta Metall*., 49, 1805, 2001.
117. Li, J.C.M., Possibility of subgrain rotation during recrystallization, *J. Appl. Phys.*, 33, 2958, 1962.
118. Haslam, A. J., Phillpot, S.R., Wolf, D., Moldovan, D., and Gleiter, H., Mechanisms of grain growth in nanocrystalline fcc metals by molecular-dynamics simulation, *Mat. Sci. Eng.*, 318, 293, 2001.
119. Gottstein, G. and Shvindlerman, L.S., Triple junction dragging and von Neumann–Mullins relation, *Scr. Mater*., 38, 1541, 1998.
120. Okuda, S., Kobiyama, M., Inami, T., and Takamura, S., Thermal stability of nanocrystalline gold and copper prepared by gas deposition method, *Scr. Mater*., 44, 2009, 2001.
121. Lücke, K., Abbruzzase, G., and Heckelmann, I., Proceedings of recrystallization, Chandra, T., Ed., Warrendale, PA, 90, 51, 1990.

19 Nanofiber Technology

Frank K. Ko
Department of Materials Science and Engineering,
Drexel University, Philadelphia, Pennsylvania

CONTENTS

19.1 INTRODUCTION

Nanofiber technology is a branch of nanotechnology whose primary objective is to create materials in the form of nanoscale fibers in order to achieve superior functions. The unique combination of high specific surface area, flexibility, and superior directional strength makes such fibers a preferred material form for many applications ranging from clothing to reinforcements for aerospace structures. Although the effect of fiber diameter on the performance and processibility of fibrous structures has long been recognized, the practical generation of fibers at the nanometer scale was not realized until the rediscovery and popularization of the electrospinning technology by Professor Darrell Reneker almost a decade ago [1]. The ability to create nanoscale fibers from a broad range of polymeric materials in a relatively simple manner using the electrospinning process, coupled with the rapid growth of nanotechnology in recent years have greatly accelerated the growth of nanofiber technology. Although there are several alternative methods for generating fibers in a nanometer scale, none matches the popularity of the electrospinning technology due largely to the simplicity of the electrospinning process. Electrospinning can be carried out from polymer melt or solution. A majority of the published work on electrospinning has been focused on solution-based electrospinning rather than on melt electrospinning due to higher capital investment requirements and the difficulty in producing submicron fibers by melt electrospinning. We will concentrate on solution-based electrospinning in this chapter. Specifically, after an introduction to the processing principles the relative importance of the various processing parameters in solution electrospinning is discussed. The structure and properties of the fibers produced by the electrospinning process are then examined. Recognizing the enormous increase in specific fiber surface, bioactivity, electroactivity, and enhancement of mechanical properties, numerous applications have been identified, including filtration, biomedical, energy storage, electronics, and multifunctional structural composites.

19.2 THE ELECTROSPINNING PROCESS

Electrostatic generation of ultrafine fibers or ''electrospinning'' has been known since the 1930s [2]. The rediscovery of this technology has stimulated numerous applications including high-performance filters [3] and as scaffolds in tissue engineering [4],which utilize the unique characteristics of surface area as high as 10^3 m^2/g provided by nanofibers. In this nonmechanical, electrostatic technique, a high electric field is generated between a polymer fluid contained in a glass syringe with a capillary tip and a metallic collection target. When the voltage reaches a critical value, the electric field strength overcomes the surface tension of the deformed droplet of the suspended polymer solution formed on the tip of the syringe, and a jet is produced. The electrically charged jet undergoes a series of electrically induced bending instabilities during its passage to the fiber collection screen or drum that results in the hyperstretching of the jet. This stretching process is accompanied by the rapid evaporation of the solvent molecules that reduces the diameter of the jet, in a cone-shaped volume called the ''envelope cone.'' The dry fibers are accumulated on the surface of the collection screen resulting in a nonwoven random fiber mesh of nano- to micron diameter fibers. The process can be adjusted to control the fiber diameter by varying the electric field strength and polymer solution concentration. By proper control of the electrodes, aligned fibers can also be produced. A schematic drawing of the electrospinning process and the random and aligned nanofibers are shown in Figure 19.1.

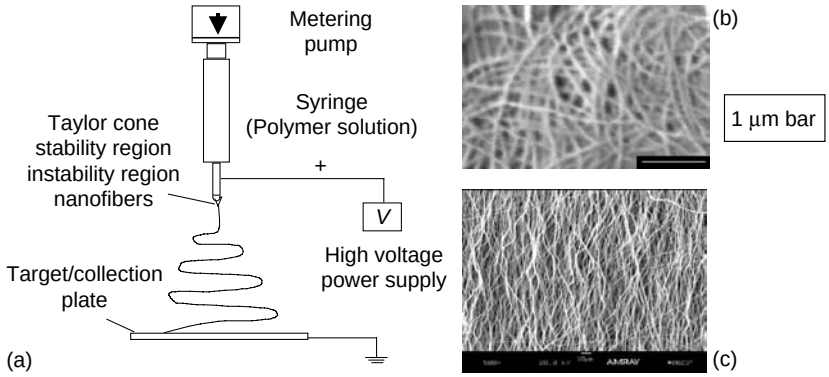

FIGURE 19.1 (a) Schematic drawing of the electrospinning process. (b) (top) random; (c) (bottom) aligned.

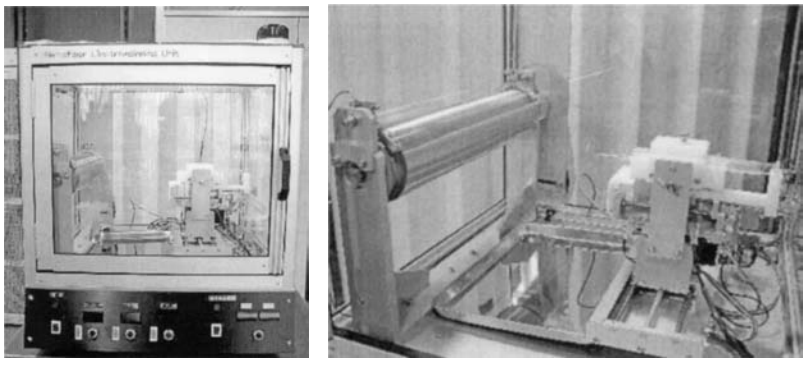

FIGURE 19.2 (a) The first commercially available nanofiber electrospinning unit (NEU) produced by the Kato-Tech Co. (b) Close-up of the NEU system including a metering pump, a syringe containing the spinning dope, the syringe needle is connected to a power supply (not shown), and a fiber collection drum connecting to the electrical ground.

Figure 19.2 shows a commercial nanofiber electrospinning unit known as NEU produced by the Kato-Tech Co. The NEU system consists of a metering pump, which controls the volume flow rate of the spinning dope in a syringe. An electrical potential is applied by a power supply between the steel syringe needle and the fiber collection ground in the form of a metallic screen or a drum. The temperature and humidity of the spinning chamber can be controlled.

19.3 KEY PROCESSING PARAMETERS

A key objective in electrospinning is to generate fibers of nanometer diameter consistently and reproducibly. Considerable effort has been devoted to understand the parameters affecting the spinnability and more specifically the diameter of the fibers resulting from the electrospinning process. Many processing parameters have been identified, which influence the spinnability and the physical properties of nanofibers. These parameters include electric field strength, polymer concentration, spinning distance, and polymer viscosity.
According to Rutledge et al. [5], the diameter of electrospun fibers is governed by the following equation:

$$d = \left[\gamma \varepsilon \frac{Q^2}{I^2} \frac{2}{\pi (2\ln\chi - 3)} \right]^{1/3}$$

where d is the fiber diameter, γ the surface tension, ε the dielectric constant, Q the flow rate, I the current carried by the fiber, and χ the ratio of the initial jet length to the nozzle diameter.

One can control the fiber diameter by adjusting the flow rate, the conductivity of the spinning line, and the spinneret diameter. Fiber diameter can be minimized by increasing the current carrying capability of the fiber through the introduction of a conductive filler such as carbon black, carbon nanotube, metallic atoms, or mixing with an inherently conductive polymer. For example, an increase of current carrying capability, I, of the fiber by 32 times will bring about 10-fold decrease in fiber diameter. Alternatively, if the current I is kept constant, one can bring about a 10-fold decrease in the fiber diameter by reducing the flow rate by 32 times. Reducing the spinneret nozzle diameter can also bring about a reduction in fiber diameter. When the value of χ is increased from 10 to 1000, the diameter of the fiber will decrease by approximately 2 times.

Experimental evidence has shown that the diameter of the electrospun fibers is influenced by molecular conformation that is related to the molecular weight and the concentration of the polymer in the spinning dope [6]. It was found that the diameter of fibers spun from dilute polymer solutions can be expressed in terms of the Berry number B, a dimensionless parameter and a product of intrinsic viscosity η, and polymer concentration, C. This relationship has been observed in a large number of polymers. An example for this relationship is illustrated using polylactic acid (PLA). The relationship between polymer concentration and fiber diameter of a PLA of different molecular weight in chloroform are shown in Figure 19.3. It can be seen that fiber diameter increases as polymer concentration increases. The rate of increase in fiber diameter is greater at higher molecular weight. Accordingly, one can tailor the fiber diameter by proper selection of polymer molecular weight and polymer concentrations.

Expressing fiber diameter as a function of B, as shown in Figure 19.4, a pattern emerges illustrating four regions of B vs. diameter relationships. At region (I), $B<1$, characterizing a very dilute polymer solution with molecular chains barely touching each other. It is almost impossible to form fibers by electrospinning of such solution, since there is not enough chain entanglement to form a continuous fiber, and the effect of surface tension will make the extended conformation of a single molecule unstable. As a result, only polymer droplets are formed. In region (II), $1<B<3$, fiber diameter increases slowly as B increases within the range ~100 to ~500 nm. In this region, the degree of molecular entanglement is just sufficient for fiber formation. The coiled macromolecules of the dissolved polymer are transformed by the elongational flow of the polymer jet into orientated

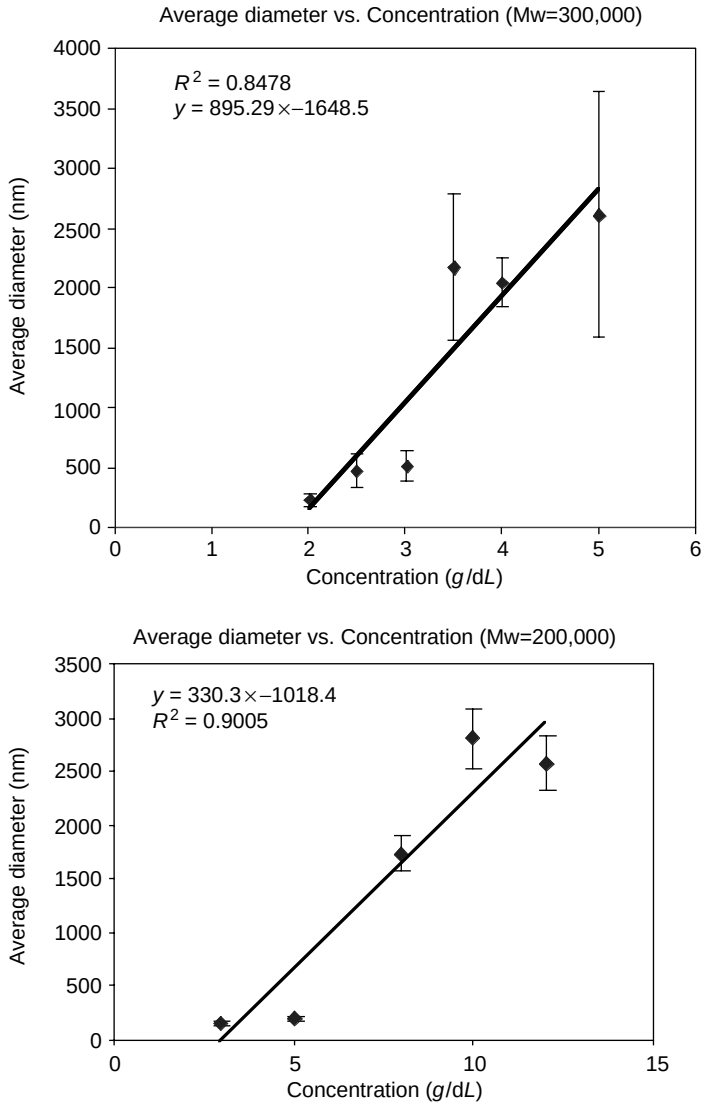

FIGURE 19.3 Relationship of fiber diameter and concentrations of polymer with different molecular weights.

molecular assemblies with some level of inter- and intramolecular entanglement. These entangled networks persist as the fiber solidifies. In this region, some bead formations are observed as a result of polymer relaxation and surface tension effect. In region (III), $3<B<4$, fiber diameter increases rapidly with B in the range from ~1700 to ~2800 nm. In this region, the molecular chain entanglement becomes more intensive, contributing to an increase in polymer viscosity. Because of the intense level of molecular entanglement, it requires a higher level of electric field strength for fiber formation by electrospinning. In region (IV), $B>4$, the fiber diameter is less dependent on B. With a high degree of inter- and intramolecular chain entanglement, other processing parameters such as electric field strength and spinning distance become dominant factors affecting fiber diameter. A schematic illustration of the four Berry regions is shown in Table 19.1, showing the corresponding relationship between fiber morphology and Berry numbers.

More recently, we further demonstrated, as shown in Figure 19.5, that the diameter, d, of electrospun fibers is related to the Berry number B for three amorphous polymers with different molec-

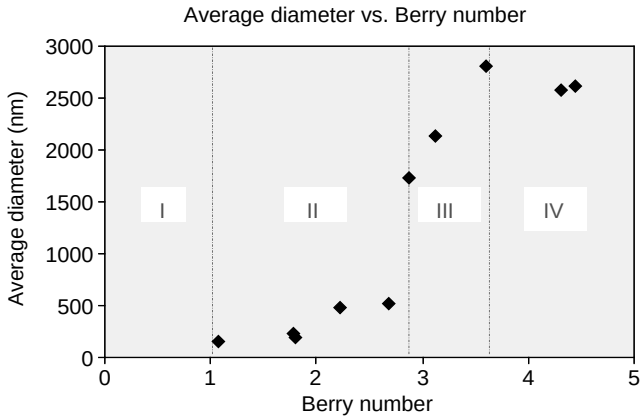

FIGURE 19.4 The relationship between Berry number and fiber diameter.

TABLE 19.1
Schematic of Polymer Chain Conformation and Fiber Morphology Corresponding to Four Regions of Berry Number

	Region I	Region II	Region III	Region IV
Berry Number	**B<1**	**1<B<2.7**	**2.7B<3.6**	**B>3.6**
Polymer chain conformation in solution		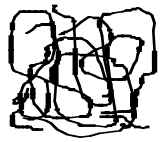		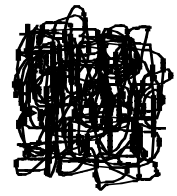
Fiber morphology	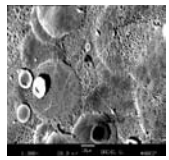	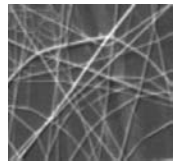	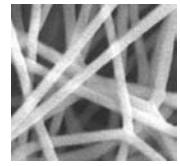	
Average fiber diameter	(Only droplets formed)	~100–500 nm	1700–2800 nm	~2500–3000 nm

ular weights. It was shown that the relationship of fiber diameter to Berry number can be expressed by $d = a\,B^c$, where a and c are experimental coefficients. The molecular weight of the three polymers polystyrene, polybutadiene, and SBS are 48,000, 60,000, and 100,000 dalton, respectively. It is of interest to note that the slope of the diameter vs. Berry number curves are approximately the same, with a value of 5, reflecting the degree of crystallinity of the polymer. The coefficient q is thought to be related to the molecular weight, radius of gyration of molecular chains, and entanglement of the molecular chains. From this relationship, the polymer concentration necessary to produce nanofiber can be predicted.

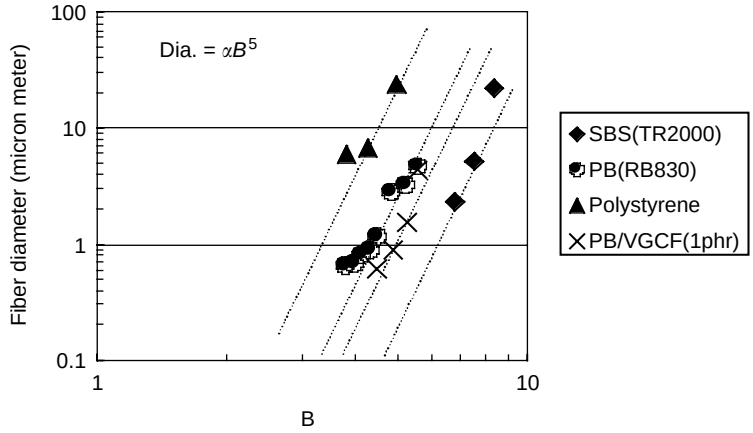

FIGURE 19.5 The relationship between fiber diameter and the Berry number.

19.4 NANOFIBER YARNS AND FABRICS FORMATION

In order to translate nanoeffect to the macroscopic structural level, the nanofibers must be organized into linear, planar, and 3-D assemblies. The formation of nanofiber assemblies provides a means to connect nanofiber effect to macrostructure performance. Electrospun fiber structures can be assembled by direct fiber-to-fabric formation to create a nonwoven assembly and by the creation of a linear assembly or a yarn from which a fabric can be woven, knitted, or braided. Linear fiber assemblies can be aligned mechanically or by electrostatic field control. Alternatively, a self-assembled continuous yarn can be formed during electrospinning by proper design of the ground electrode. Self-assembled yarn can be produced in continuous length with appropriate control of electrospinning parameters and conditions. The fibers are allowed to accumulate until a tree-like structure is formed. Once a sufficient length of yarn is formed, the accumulated fibers attach themselves to the branches and continue to build up. A device such as a rotating drum can be used to spool up the self-assembled yarn in continuous length as shown in Figure 19.6. This method produces partially aligned nanofibers yarn bundles of continuous length.

19.5 POTENTIAL APPLICATIONS OF ELECTROSPUN FIBERS

The Donaldson Company was the first to realize the commercial value of electrospinning taking advantage of the enormous availability of the specific surface of electrospun fibers and the ultrafine nature of the fibers. They introduced the Ultra-Web® cartridge filter for industrial dust collection in 1981 and more recently the Hollingsworth & Vose Company introduced the Nanoweb® for automotive and truck filter applications. To date, industrial filter remains the primary commercial use of electrospun fibers. The rediscovery and popularization of the electrospinning process in the 1990s have changed the dynamics of the field of nanofiber technology. Electrospinning has been transformed from an obscure technology to a word common in academia and one gradually being recognized by industry and government organizations. This was most evident in the Polymer Nanofiber Symposium held in New York at the American Chemical Society (ACS) in September 2003, wherein 75 papers and posters were presented [7]. On the basis of the papers presented in the ACS symposium and the rapidly growing number of publications, one can categorize the potential applications of electrospun fibers into (1) biomedical applications — tissue engineering scaffolds, wound care, superabsorbent media, drug delivery carrier, etc. [8,9]; (2) electronic applications — electronic packaging, sensors, wearable electronics, actuators, fuel cells, etc. [10,11]; (3) industrial applications — filtration, structural toughening/reinforcement, chemical/bio-protection, etc.

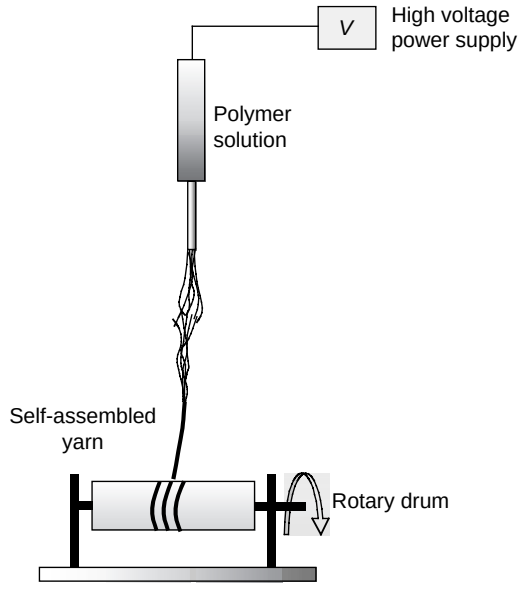

FIGURE 19.6 Schematic illustration of the formation of self-assembled yarns by the electrospinning process.

[12,13]. It is of interest to note that these applications invariably made use of the large surface area created by the fineness of the fibers. A few examples will be used herein to illustrate the potential applications of nanofibers.

19.5.1 Nanofibers for Tissue Engineering Scaffolds

It is well recognized, as articulated by Vacanti and Mikos [14], that the key challenges in tissue engineering are the synthesis of new cell adhesion-specific materials and the development of fabrication methods to produce reproducible three-dimensional synthetic or natural biodegradable polymer scaffolds with tailored properties. These properties include porosity, pore size distribution and connectivity, mechanical properties for load-bearing applications, and rate of degradation. Of particular interest in tissue engineering is the surface adhesion of the cells to the scaffold. Considering the importance of surfaces for cell adhesion and migration, experiments were carried out in our laboratory using osteoblasts isolated from neonatal rat calvarias and grown to confluence in Ham's F-12 medium (GIBCO), supplemented with 12% sigma fetal bovine on PLAGA-sintered spheres, 3-D-braided 20 μm filament bundles, and nanofibrils. Four matrices were fabricated for the cell culture experiments. These matrices include (1) 150–300 μm PLAGA-sintered spheres, (2) unidirectional bundles of 20 μm filaments, (3) 3-D-braided structure consisting of 20 bundles of 20 μm filaments, and (4) nonwoven consisting of nanofibrils. The cell proliferation, as shown in Figure 19.7, is expressed in terms of the amount of [^{3}H]-thymidine uptake as a function of time. It can be seen that there is a consistent increase in cell population with time for all the matrices. However, the nanofibrous structures demonstrated the most proliferate cell growth, whereas the cell growth in the structures consisting large diameter fibers and spheres were the least proliferate. Taking advantage of this cell-friendly characteristic of nanofiber scaffolds, nanofibers are being evaluated for the regeneration of skin, vascular grafts, ligament, cartilage, bone, and many other tissues and organs.

19.5.2 Nanofibers for Chemical/Bio Protective Membranes

Nanofiber assemblies are excellent structure barrier systems for dust filtration [12] and for the prevention of the penetration of chemical and biological agents [13]. Considering the various barrier concepts shown in Figure 19.8, it is concluded that neither the impermeable nor the permeable

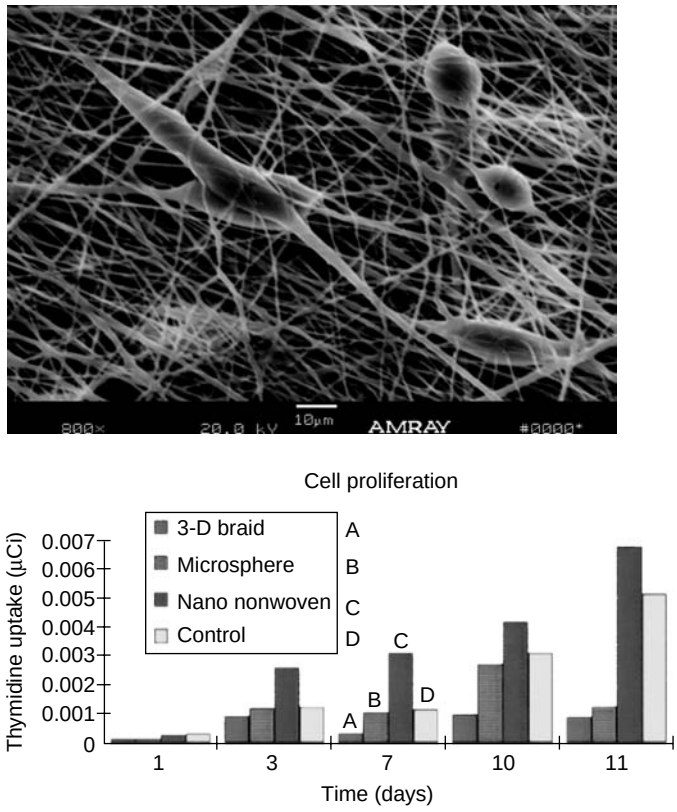

FIGURE 19.7 Directed cell growth (top) and cell proliferation (bottom) behavior in PLA nanofiber scaffold.

barrier systems are suitable because of the unacceptable level of heat generation in the impermeable barriers and the porous nature of the permeable systems. The semi-permeable barrier provides incremental improvement but the addition of the sorptive layer may serve as a reservoir for bacteria growth as well as adding bulk to the garment. Accordingly, the current design favors a system that is carbon-free with selective permeable capability and which has the multiple functions of repelling CB agents while allowing the body moisture vapor to escape. As an example, we illustrate the feasibility of using the electrospinning process to construct a selective permeable membrane using the polymers formulated and provided by Utility Development Cooperation (UDC).

An example of an solvent-based electrospun polymer is shown in Figure 19.9 showing a three dimensional interconnected fiber network. The morphology of the polymer was found to be controllable by varying polymer concentration.

The electrospun membranes were tested at UDC for moisture vapor transmission by using the Thwing Albert permeation cups. The testing was performed at 110°F to simulate hot weather conditions. The moisture vapor transmission results of dip-coated nylon fabric with the same polymer as the electrospun polymer formulation were compared to uncoated nylon fabric. These dip-coated fabrics were about 6 mil thick compared to electrospun membrane at 10 mil thick. As shown in Table 19.2, moisture vapor transmission through electrospun membrane was equivalent to uncoated nylon fabric and there was no detectable moisture vapor transmission through the dip-coated nylon fabric. The test duration was 5 h. Considering that the water vapor permeability of the state-of-the-art protective membranes are of the order of 0.1 to 0.25 g/cm^2, these results indicated that the electrospun membranes meet the requirements for wearing comfort over an extended period. This favorable comparison with the performance of the state-of-the-art membranes appears to be consistent with the findings

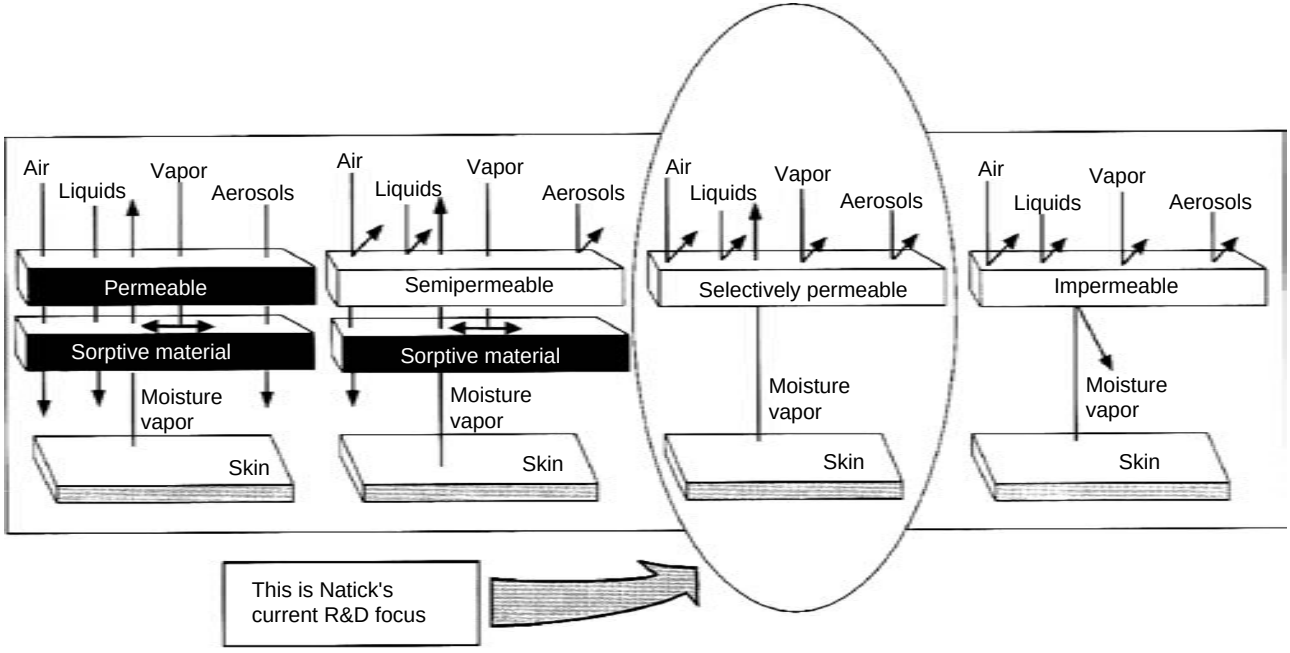

Selectively semipermeable barrier construction, Source: Wilusz, 1998.

FIGURE 19.8 Concepts of barrier systems for chemical/biological agent protection.

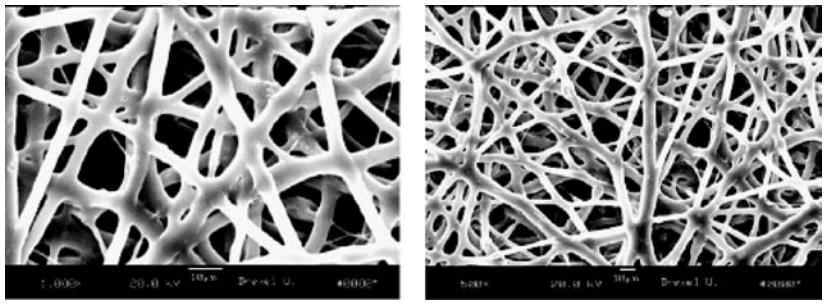

FIGURE 19.9 Electrospun UDC843A polymer showing an interconnected fiber network.

TABLE 19.2
Water Vapor Loss of Various Membranes (g/cm^2)

Uncoated Nylon	Electrospun Membrane on Nylon Cloth	Dip Coated Nylon Cloth
0.402	0.348	0.055
0.323	0.105	0.012
0.478	0.235	0.035

of Gibson et al. [15], who showed that the water-transport properties of electrospun nonwovens are superior to that of the state-of-the-art commercial membranes.

Chemical agent testing was performed at Geomet Technology using HD chemical agents for these tests in accordance with MIL-STD-282 static diffusion test. As indicated in the report from Geomet, the UDC-formulated product has more than 24 h of HD chemical agent resistance exceeding the performance requirement for state-of-the-art chemical/bio protective membranes.

19.5.3 Nanocomposite Fibers for Structural Applications

Carbon nanotubes (CNTs) [16] are seamless graphene tubule structures with nanometer-size diameters and high aspect ratios. This new class of one-dimensional material is shown to have exceptional mechanical, thermal, and novel electronic properties. The elastic moduli of the CNTs are in the range of 1 to 5 TPa [17–19] and fracture strains of 6 to 30%—both parameters about an order of magnitude better than those of commercial carbon fibers, which typically have 0.1 to 0.5 TPa elastic moduli and 0.1 to 2% fracture strains [20]. The factor of 10 enhancement in strength implies that, for the same performance, replacing or augmenting commercial carbon fibers with CNTs will lead to significant reduction in the volume and weight of the structural composites currently used in space applications.

Studies carried out in our laboratory have demonstrated that composite nanofibers containing 1 to 10 wt% single wall nanotube (SWNT) can be produced by electrospinning [21,22]. Fiber diameters in the range of 40 to 300 nm have been obtained by varying the solution concentration and electrospinning parameters. The alignment of SWNT in the nanofibers was confirmed by Raman spectroscopy and TEM. Bulk mechanical properties of the green (as-spun) composite nanofibers were characterized in the random mat form. With proper dispersion of SWNT and preparation of the spinning dope, a twofold increase in strength and modulus is observed for the polyacrylonitrile (PAN)/SWNT fiber assemblies containing 1 wt% SWNT. In addition, a continuous process for the conversion of nanofibers into continuous yarn has also been successfully demonstrated. These continuous yarns provide an effective means to translate the properties of the SWNT to higher order textile structures suitable for advanced composites and numerous other applications.

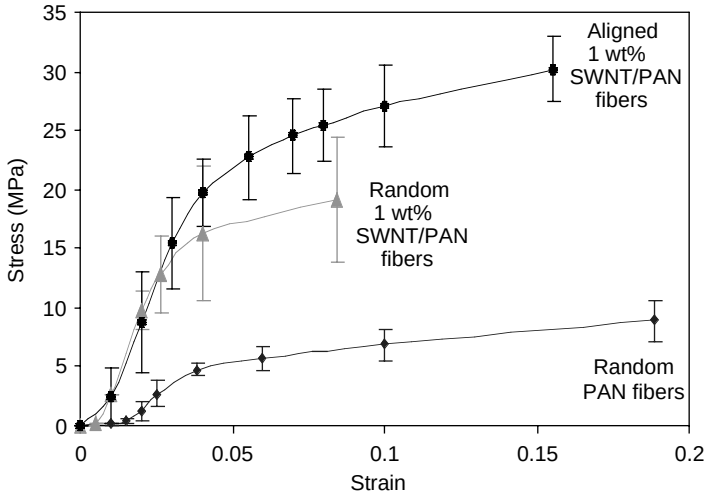

FIGURE 19.10 Tensile properties of electrospun pristine PAN and 1 wt% SWNT/PAN fibers in random and aligned.

Figure 19.10 shows the stress–strain properties of electrospun pristine PAN and 1 wt% SWNT/PAN nanofibers. As can be seen in the random fiber mats, a more than twofold increase in tensile strength and elastic modulus was obtained with the addition of 1 wt% SWNT. For the aligned 1 wt% SWNT/PAN, a 33% increase in tensile strength and almost double strain were obtained as compared with the random composite nanofibers. However, the increase in elastic modulus is not significant. A large increase in the area under the stress–strain curve of SWNT/PAN indicates the effectiveness of SWNT in toughening and strengthening the fibers. Fibril as well as SWNT alignments play an important role in maximizing properties translation from the nanoscopic level to higher order structure. Even without any posttreatment, remarkable improvement in properties was achieved in the electrospun composite nanofibrils. It is anticipated that posttreatment such as mechanical drawing further aligns the SWNT in the fiber axis. Drawing of the fibers also induces molecular orientation resulting in much higher properties. Furthermore, heat treatment enhances interaction between the reinforcement and matrix leading to better load transferring across reinforcement–matrix interface.

The stress–strain behavior of the SWNT-loaded PAN suggested toughening and strengthening of the fiber with the incorporation of 1 wt % SWNT.

19.6 SUMMARY AND CONCLUSIONS

The combination of high-specific surface area, flexibility, and superior directional strength makes fiber a preferred material form for many applications ranging from clothing to reinforcements for aerospace structures. The availability of fibers in nanoscale will greatly expand the performance limit of materials and thus create new marketing opportunities leading to the birth of a new nanofiber-based industry. Of the processing methods capable of fabricating nanofibers, electrospinning has received the most intensive attention due to its simplicity and the potential for generating continuous nanofiber assemblies. With the enormous increase in available surface area per unit mass, nanofibers provide a remarkable capacity for the attachment or release of functional groups, absorbed molecules, ions, catalytic moieties, and nanometer scale particles of many kinds. As a result, these nanofiber assemblies provide favorable conditions for cell adhesion and cell migration for bioactive nanofibers thus creating new opportunities for nanofiber-based scaffolds for tissue engineering and for ultra-sensitive biosensors. Other areas expected to be impacted by nanofiber-based technology

include drug delivery systems, wires, capacitors, transistors, and diodes for information technology, systems for energy transport, conversion and storage, such as batteries and fuel cells, and structural composites for aerospace structures. In order to capitalize on these new opportunities new processing technology is needed, precise characterization tools for single nanofibers are required, and nanoscale manipulation machines must be developed. These technologies must be supported by well-verified engineering design tools and analytical methods. It is expected that nanofiber technology will provide a critical link between nanoscale effect and macroscopic phenomena and become the enabling pathway for the conversion of nanomaterials into practical large-scale applications.

REFERENCES

1. Reneker, D.H. and Chun, I., *Nanotechnology*, 7, 216, 1966.
2. Formhals, A., US Patent 1,975,504, October 2, 1934.
3. Donaldson Co., US Patent 6,716,274; 6,673,136.
4. Ko, F.K., Laurencin, C.T., Borden, M.D., and Reneker, D., *Proceedings, Annual Meeting*, Biomaterials Research Society, San Diego, April 1998.
5. Rutledge, G., Fridrikh, S. et al., Texcomp 6, Philadelphia, PA, September 2002.
6. Ko, F.K., Nanofiber technology: bridging the gap between nano and macro world, in *NATO ASI on Nanoengineeered Nanofibrous Materials*, Guceri, S., Gogotsi, Y. and Kuznetsov, V., NATO Series II, Vol. 169, 2004.
7. Reneker, D.H. and Fong, H., Eds., Polymer nanofibers, *Polymer Preprints*, 44, September 2003, American Chemical Society.
8. Li, W.J., Laurencin, C.T., Caterson, E.J., Tuan, R.S., and Ko, F.K., Electrospun nanofibrous structure: a novel scaffold for bioengineering, *J. Biomed. Mater. Res.*, 58, 613–621, 2002.
9. Boland, E.D., Simpson, D.G., Wnek, G. E., and Bowlin, G.L., Electrospinning of biopolymers for tissue engineering scaffolds, *Polymer Pre-preprints*, 44, 92, 2003.
10. Kwoun, J., Lec, R.M., Han, B., and F. Ko. K., A novel polymer nanofiber interface for chemical sensor applications, *Proceedings of the IEEE International Frequency Control Symposium*, May 7–9, 2000, Kansas City, MS, pp. 52–57.
11. MacDiarmid, A.G., Jones, W.E., Jr., Norris, I.D., Gao, J., Johnson, A.T., Jr., Pinto, N.J., Hone, J., Han, B., Ko, F.K., Okusaki, H., and Llanguno, M., Electrostatically-generated nanofibers of electronic polymers, *Synth. Met.*, 119, 27–30, 2001.
12. Lifshutz, N. and Binzer, J.C., Nanofiber coated filter materials for automotive and other applications, *Proceedings of First International Congress on Nanofiber Science and Technology*, June 28, 2004, The Society of Fiber Science and Technology, Tokyo, Japan, pp. 54–62.
13. Ko, F. K., Yang, H., Argawal, R., and Katz, H., Electrospinning of improved CB protective fibrous materials, *Proceedings*, March 30–31, 2004, Techtextil, Atlanta.
14. Vacanti, C.A. and Mikos, A.G., Letter from the editors, *Tiss. Eng.*, 1, 1, 1995.
15. Gibson, P.W., Schreuder-Gibson, H.L., and Rivin, D., Electrospun fiber mats:transport properties, *AIChE J.*, 45, 190–195, 1999.
16. Ijimi, S., Helical microtubules of graphitic carbon, *Nature*, 354, 53–58, 1991.
17. Treacy, M.M., Ebbesen, T.W., and Gibson, J.M., *Nature*, 381,67–80, 1996.
18. Wang, E.W., Sheehan, P.E., and Lieber, C.M., Nanobeam mechanics: elasticity, strength and toughness of nanorods and nanotubes, *Science*, 277, 1971–1975, 1997.
19. Lu, J.P., Elastic properties of single and multilayered nanotubes. *Phys. Rev. Lett.*, 179, 1297, 1997.
20. Peebles, L.H., *Carbon Fibers: Formation, Structure, and Properties*. CRC Press, Boca Raton, FL, 1995.
21. Ko, F., Gogotsi, Y., Ali, A., Naguib, N., Ye, H., Yang, G., Li, C., and Willis, P., Electrospinning of continuous carbon nanotube-filled nanofiber yarns, *Adv. Mater.*, 15, 1161–1165, 2003.
22. Ko, F.K., Lam, H., Titchenal, N., Ye. H., and Gogotsi, Y., Co-electrospinning of carbon nanotube reinforced nanocomposite fibrils, in *Science and Technology of Electrospinning*, Reneker, D. and Fong, H., Eds., Wiley, New York, chapter X, in press.

20 Nanotubes in Multifunctional Polymer Nanocomposites

Fangming Du
Department of Chemical and Biomolecular Engineering,
University of Pennsylvania, Philadelphia, Pennsylvania

Karen I. Winey
Department of Material Science and Engineering,
University of Pennsylvania, Philadelphia, Pennsylvania

CONTENTS

20.1 INTRODUCTION

Polymer nanocomposites have attracted great attention due to the unique properties introduced by nanofillers, which typically refer to carbon blacks, silicas, clays, or carbon nanotubes (CNT). The polymer matrix acts as a supporting medium and the improvement in the properties of the nanocomposites generally originates from the nature of these nanofillers. Compared to other nanofillers, the unique structures of CNT potentially provide superior mechanical, electrical, and thermal properties. There are two types of CNT with high structural perfection, single-walled nanotubes (SWNT) and multi-walled nanotubes (MWNT) (Figure 20.1). SWNT can be considered as a single graphite sheet seamlessly wrapped into a cylindrical tube. MWNT comprise an array of such nanotubes that are concentrically nested. Theoretical and experimental results[1] on individual CNT have shown extremely high elastic modulus, greater than 1TPa, and their reported strength is many times higher than the strongest steel at a fraction of the weight. The fiber-like structure of CNT with low density makes them particularly attractive for reinforcement of composite materials. The nearly one dimensional (1D) electronic structure of CNT allows electrons to be transported along the nanotubes without scattering, enabling them to carry high current with essentially no heating. Phonons also propagate easily along the nanotubes, such that the measured room temperature thermal conductivity for an individual MWNT[2] (>3000 W/m K) is greater than that of natural diamond (~2000 W/m K). The thermal

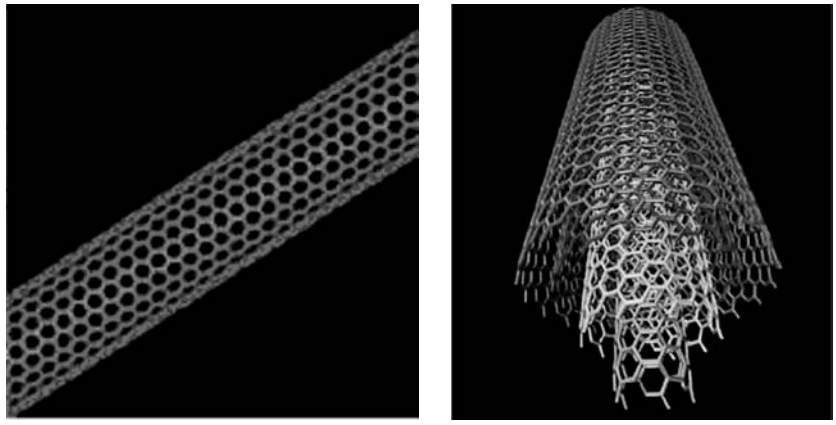

(a) (b)

FIGURE 20.1 (a) Image of SWNT. (Copyright, Dr. Smalley Group, Rice University, 2004; (b) Image of MWNT. (Copyright, Rochefort, Nano-CERCA, University of Montreal, Canada, 2004.)

conductivity of an individual SWNT is expected to be even higher.[3] The high aspect ratio (length/diameter) of CNT suggests lower percolation thresholds for both electrical and thermal conductivity in their nanocomposites. Therefore, CNT have considerable potential in multifunctional polymer nanocomposites for structural, electrical, and thermal applications.

To date this potential has not yet been fully realized, although many researchers are devoting much attention to developing CNT/polymer nanocomposites. One significant challenge is to obtain uniform nanotube dispersion within the polymer matrix. CNT have diameters on the nanoscale and substantial van der Waals attractions between them, so CNT tend to agglomerate. As shown in Figure 20.2, these SWNT (synthesized by a high-pressure carbon monoxide method at Rice University)[4] are highly entangled and the diameter of the nanotube bundles is tens of nanometers, indicating hundreds of individual nanotubes in one bundle. Unfortunately, the nanotube bundles have significantly lower aspect ratios and inferior mechanical (due to slipping of nanotubes inside the bundles)[5] and electrical properties. Lower aspect ratios are likely to lead to higher percolation thresholds for both electrical and thermal conductivity in these nanocomposites. Therefore, uniformly dispersed nanotubes within the polymer matrix is critical for improved properties at the minimal CNT content. Various nanotube processing procedures and nanocomposite fabrication methods have been used toward this goal.[6–8] The second challenge is to understand the effect of nanotube alignment on nanocomposite properties because the nanotubes have asymmetric structures and properties. For example, nanotube alignment increases the elastic modulus[6] and increases the electrical conductivity[9] of the nanocomposites along the nanotube alignment direction. The third challenge is to create strong physical or chemical bonds between the nanotubes and the polymer matrix. These bonds can efficiently transfer load from the polymer matrix to the nanotubes, which is important for mechanical reinforcement. Covalent bonds can also benefit phonon transferring between the nanotubes and the polymer matrix, which is a key factor for improving thermal conductivity of the nanocomposites. Therefore, various surfactants and chemical functionalization procedures have been adopted to modify the surface of nanotubes, so as to enable more adhesion to the polymer matrix.

It is to be noted that nanotubes are synthesized by a variety of methods that give rise to different mean lengths, mean diameters, distributions in lengths and diameters, relative amounts of conductive nanotubes, and concentrations and types of impurities.[10] Furthermore, we have found important differences between different batches of nanotubes produced by seemingly equivalent synthetic processes. Added to this complexity are the observations that nanotube distribution and alignment significantly influence properties and is expected that the physical properties of

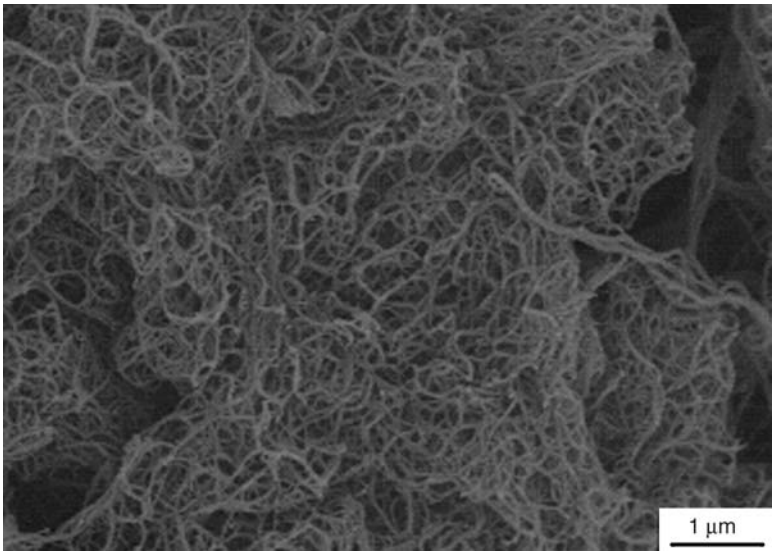

FIGURE 20.2 SEM image of as-produced SWNT, showing that nanotube bundles are highly entangled. (Copyright, Winey group.)

nanotube/polymer composites will vary dramatically in the published literature. Thus, this chapter focuses on trends rather than absolute values for elastic modulus, electrical percolation, and so forth, because the nanotubes and composite processing methods employed by different researchers are substantially different. After reviewing various methods for producing nanotube/polymer nanocomposites, the mechanical, rheological, electrical, and thermal conductivities will be discussed separately.

20.2 NANOCOMPOSITE FABRICATION AND NANOTUBE ALIGNMENT

Solvent casting and melt mixing are two common fabrication methods for the nanotube-based nanocomposites. Solvent casting involves preparing a suspension of nanotubes in a polymer solution and then allowing the solvent to evaporate to produce a nanotube/polymer nanocomposite. Qian et al.[11] cast a MWNT/polystyrene (PS)/toluene suspension after sonication into a dish to produce the nanocomposites with enhanced elastic modulus and break stress. Benoit et al.[7] obtained electrically conductive nanocomposites by dispersing SWNT and poly(methyl methacrylate) (PMMA) in toluene, followed by drop casting the mixture on substrates. Nanocomposites with other thermoplastic matrices with enhanced properties have also been fabricated by solvent casting,[12] but nanotubes tend to agglomerate during solvent evaporation, which leads to inhomogeneous nanotube distribution in the polymer matrix. Unlike solvent casting methods, in which nanotubes are typically dispersed by sonication, melt mixing uses elevated temperatures and high shear forces to disrupt the nanotube bundles. Bhattacharyya et al.[13] made a 1 wt% SWNT/polypropylene (PP) nanocomposite by melt mixing, but found that melt mixing alone did not provide uniform nanotube dispersion. A subsequent processing step, namely passing the 1 wt% nanocomposite through a stainless-steel filter at 240°C, removed the larger SWNT agglomerates and reduced the nanotube loading to 0.8 wt%.

Some researchers use combined methods, such as solvent casting in conjunction with sonication, followed by melt mixing. For example, Haggenmueller et al.[6] first demonstrated the combination of solvent casting and melt mixing for SWNT/PMMA composites with considerable improvement in nanotube dispersion. They dissolved PMMA in dimethylformamide that was also used to disperse SWNT by sonication and the resulting suspension was then cast into a dish. After drying, the

nanocomposite film exhibited heterogeneous nanotube dispersion when subjected to optical microscopy. These SWNT/PMMA films prepared by solvent casting alone contained micron-scale nanotube agglomerates due to reaggregation during solvent evaporation. Thus, the nanocomposite films were broken into pieces, stacked together, and then hot pressed. This hot pressing procedure was repeated for up to 20 times and the state of dispersion steadily improved with each additional melt mixing cycle. This combination of solvent casting and melt processing produced superior SWNT dispersion.

As seen above, solvent casting can allow CNT to agglomerate during solvent evaporation. There have been some attempts to reduce the solvent evaporation time by spin casting or drop casting.[7,14,15] Spin casting, also called spin coating, involves putting a nanotube/polymer suspension on a rotating substrate, so that the solvent evaporates within seconds. Drop casting involves dropping a nanotube/polymer suspension on a hot substrate, so that the solvent can evaporate very quickly. To better eliminate nanotube reagglomeration, Du et al.[8] developed a coagulation method to produce nanotube-based nanocomposites with uniform dispersion. Optical microscopy (Figure 20.3a) shows that there are no obvious agglomerations of the nanotubes in a 1 wt% SWNT/PMMA nanocomposite fabricated by the coagulation method, indicating that the nanotubes are uniformly distributed within the polymer matrix. Scanning electron microscopy (SEM) of a 7 wt% nanocomposite (Figure 20.3b) shows that the nanotubes are also uniformly distributed on a sub-micrometer scale. This coagulation method begins with a nanotube/polymer suspension in which the nanotubes have been well dispersed by sonication, and then poured into an excess of a nonsolvent, causing the polymer to precipitate and entrap the nanotube bundles. This precipitation process is rapid, so the nanotubes apparently do not aggregate or flocculate during the coagulation process.[16] Therefore, the coagulation method provides better nanotube dispersion.

In addition to the solvent casting, melt mixing, and coagulation methods, which combine nanotubes with high molecular weight polymers, *in situ* polymerization method have also been used to make nanotube-based nanocomposites starting with nanotubes and monomers. The most common *in situ* polymerization methods involve epoxy in which the resins (monomers) and hardeners are combined with SWNT or MWNT prior to curing (polymerizing).[17,18] Epoxy is the most commonly used thermoset polymer. Its resin can be crosslinked after mixing with a hardener of an appropriate ratio (resin/hardener) based on the number of functional groups on them. In addition to thermoset matrixes, a few examples of thermoplastic nanocomposites have been prepared by *in situ* polymerization. Park et al.[19] performed *in situ* polymerization of polyimide while sonicating to keep the nanotubes dispersed in the reaction medium. The role of sonication during polymerization is to disperse the SWNT in the low-viscosity monomer solution. As polymerization progresses, the

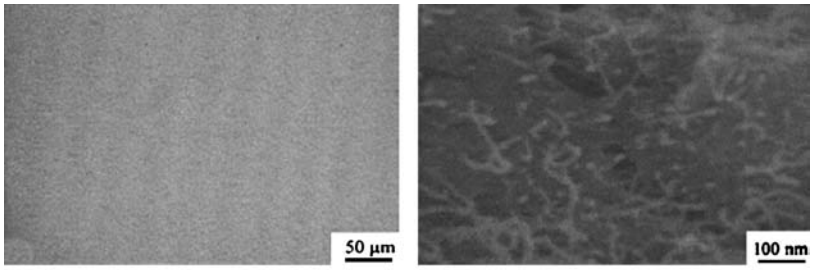

FIGURE 20.3 (a) Optical micrograph of a 1wt% SWNT/PMMA nanocomposite thin film illustrating the absence of nanotube agglomerates; (b) SEM image of a 7wt% SWNT/PMMA nanocomposite. These nanocomposites were fabricated by the coagulation method and show uniform nanotube distribution. (Adapted from Du, F. et al.[8] *J. Poly. Sci.: Part B: Poly. Phys*. 41, 3333–3338, 2003.)

high-molecular-weight polymer increases the solution viscosity, restricts Brownian motion and sedimentation of the nanotubes, and stabilizes the nanotube dispersion against agglomeration.

Many of the fabrication methods described above require nanotubes to be well dispersed in solvents. The nanotube dispersion in the polymer matrix largely depends on the state of nanotube dispersion in a solvent, assuming that the following processing procedures effectively avoid nanotube flocculation. However, the chemical structure of CNT makes dissolving long CNT in common solvents to form true solutions virtually impossible. Most nanotube/solvent systems are suspensions of nanotube bundles where the size and concentration of the bundles dictate how long the suspensions persist before flocculation. To date, large fractions of individual nanotubes have only been achieved either by functionalizing the nanotubes or by surrounding the nanotubes with dispersing agents, such as surfactants and polymers. The improved nanotube suspensions resulting from functionalization or dispersing agents can be employed in many of the methods described above to make nanotube nanocomposites with improved nanotube dispersion. Furthermore, functionalized CNT might also allow covalent bonds between the nanotubes and the polymer matrix.

Nanotube functionalization typically begins with oxidative conditions, such as refluxing in nitric acid, to attach carbonoxylic acid moieties to the defect sites on the nanotubes surface.[20,21] These acid moieties can be further transformed to more reactive groups, like –COCl, or $–CORNH_2$. These reactive groups allow CNT to chemically bond with the polymer chains through certain chemical reactions. Hill et al.[22] showed that SWNT and MWNT could be chemically bonded to a PS copolymer based on esterification. Lin et al.[23] also reported that the carbonoxylic acid on the surface of MWNT could attach aminopolymers via the formation of amide linkages. As functionalization chemistries advance, those interested in nanocomposites will continue to adapt these methods for the preparation of nanotube/polymer nanocomposites. One caveat in this regard is the degradation of properties, particularly aspect ratio and electrical conductivity, as the bonding of the CNT is disrupted by attaching functional groups to the nanotubes. There is likely to be an optimal level and type of nanotube functionalization that captures the advantages of better nanotube dispersion while minimizing the disadvantages of reduced nanotube performance.

The addition of dispersing agents, particularly surfactants, to nanotube/solvent systems has also shown improved dispersion.[24] Islam et al.[24] reported that sodium dodecylbenzene sulfonate was an effective surfactant to solubilize high-molecular-weight SWNT fractions in water by sonication. Their atomic force microscopy (AFM) showed that ~63 ± 5% of SWNT bundles exfoliated into single tubes even at 20 mg(SWNT)/ml(H_2O). Barrau et al.[25] used palmitic acid as a surfactant to disperse SWNT into the epoxy resin, followed by a curing procedure in the presence of the hardener. In comparison with nanocomposites not using palmitic acid, the use of palmitic acid lowers the threshold of the electrical conductivity percolation, indicating better SWNT dispersion in the epoxy. Polymers can also solubilize nanotubes in water by a noncovalent association. O'Connell et al.[26] first reported improved nanotube dispersion in water associated with modest concentration of polyvinyl pyrrolidone and also found that the nanotubes can be disassociated by changing the solvent system. Star et al.[27] discovered that starch improves the dispersion of SWNT in water and Barisci et al.[28] found that DNA could disperse SWNT well in water. Many groups investgating the interactions between nanotubes and polymers describe the mechanism by which nanotubes show improved dispersion as "polymer wrapping."[26,27] While there might be a few examples in which a polymer chain finds it energetically favorable to assume a periodic helical conformation about an isolated nanotube, it is far more likely that the improved nanotube solubility is accomplished with a more random association between the polymers and nanotubes. Regardless of the polymer conformations and mechanisms, improved nanotube solubility with the addition of surfactants and polymers provides a means to improve the nanotube dispersion in nanocomposites by improving the initial state of dispersion and by hindering the reaggregation during solvent casting and other fabrication methods.

Nanotubes can be aligned by magnetic force[29–31] (Figure 20.4a) and by polymer flow introduced by mechanical stretching,[32] spin casting,[33] or melt fiber spinning,[6,8] (Figure 20.4b). Magnetic fields have been used to align nanotubes in low-viscosity suspensions based on the anisotropic magnetic susceptibility of nanotubes. While magnetic alignment has shown some promise in the preparation of nanotube samples or buckypapers, this method is less appealing in nanotube/polymer composites due to the higher viscosities of the nanotube/polymer suspensions. Alternatively, polymer flow elongates and orients polymer molecules along the flow direction and the frictional forces of this process align nanotubes within the polymer matrix. Of the mechanical methods used to align nanotubes in a polymer matrix, melt fiber spinning methods exhibit the greatest degree of alignment.

The characterization of dispersion and alignment requires special attention in nanotube/polymer nanocomposites, because the physical properties are quite sensitive to these morphological attributes. Transmission electron microscopy (TEM) is a direct method to characterize MWNT/polymer composites, although there has been little success with SWNT/polymer composites due to the small size of the filler. Figure 20.5 is an aligned 5 wt% MWNT/PS nanocomposite film made by melt mixing and the MWNT were further aligned by drawing the nanocomposite in the molten state.[34] It shows that the nanocomposite has quite good dispersion and the nanotubes are well aligned along the polymer flow direction. In contrast to the qualitative measurements by TEM, polarized Raman spectroscopy and x-ray scattering provide quantitative descriptions of the degree of nanotube alignment in the nanocomposites. Besides detecting nanotube alignment, Raman spectroscopy can also be used to measure quantitatively nanotube dispersion in the polymer matrix.[16]

Nanotubes show a resonance-enhanced Raman scattering effect when a visible or near-infrared laser is used as the excitation source, while most polymers do not. By taking advantage of this scattering effect, polarized Raman spectra are recorded for the nanocomposites with the nanotube alignment direction at some angles with respect to the incident polarization axis. In the recorded spectra, the intensity

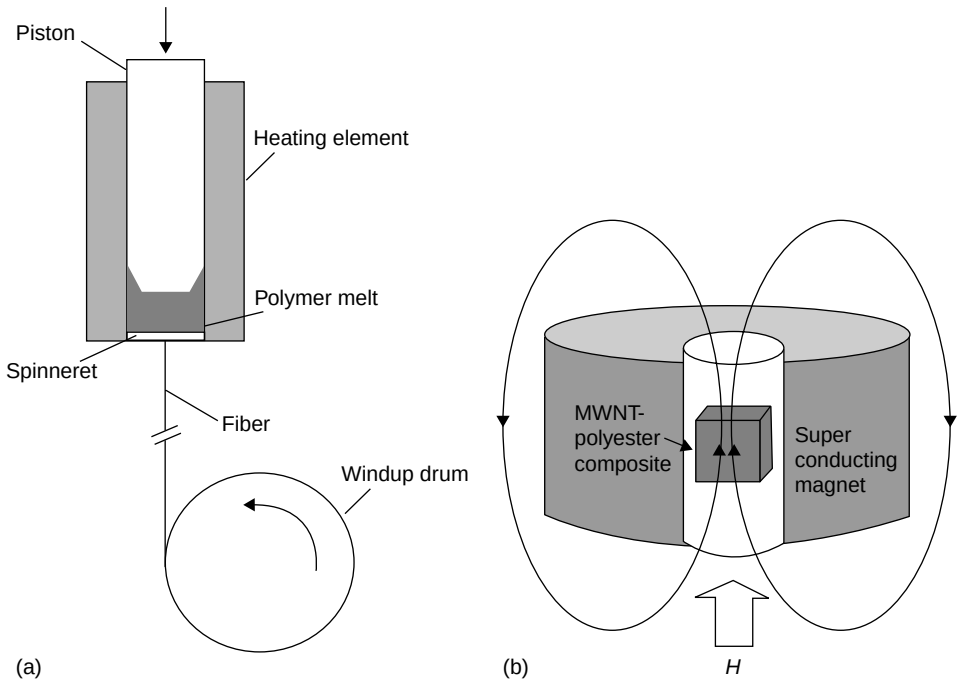

FIGURE 20.4 Schematics for aligning nanotubes in nanocomposites (a) by melt fiber spinning using extensional polymer flow and (b) by a magnetic field. (Adapted from Kimura, T.et al., *Adv. Mater.*, 14, 1380–1383, 2002.)

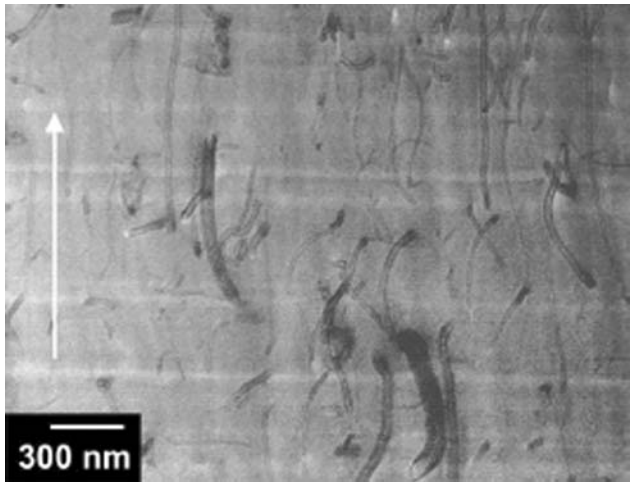

FIGURE 20.5 TEM image of a 5wt% MWNT/PS nanocomposite film showing strong nanotube alignment after mechanical stretching. The arrow indicates the stretch direction. (Adapted from Thostenson, E.T. et al., *Compos. Sci. Technol*., 61, 1899–1912, 2001.)

of the unique nanotube scattering mode as a function of angle can be fitted by a Lorentzian or a Gaussian function whose full-width at half-maximum (FWHM) can quantitatively determine the extent of nanotube alignment. For example, Haggenmueller et al.[35] obtained the degree of nanotube alignment for their SWNT/polyethylene (PE) fibers aligned by melt spinning with polarized Raman spectroscopy.

However, Raman spectroscopy is surface sensitive because the penetration depth of the incident beam is generally no more than several micrometers, depending on the nanotube loading. This problem can be solved by x-ray scattering, which is a bulk measurement for the nanocomposite in transmission and can describe the degree of nanotube alignment. Jin et al.[32] aligned nanotubes in a 50% MWNT/polyhydroxyaminoether nanocomposite film by mechanical stretching. Wide-angle x-ray scattering patterns that were dominated by a strong Bragg peak resulting from the intershell of MWNT ((002) peak) were collected from both unstretched and stretched samples. The 2D scattering intensity, I, was then integrated along the 2θ axis and plotted as I vs. azimuth, f, after subtracting the background intensity, as shown in Figure 20.6 for the unstretched and stretched samples, respectively. The scattering intensity from the unstretched sample is essentially a constant over the whole f range, as shown in Figure 20.6a, indicating random nanotube orientation. The spectrum in Figure 20.6b was fitted by 2D Lorentzian function with a FWHM of 46.4°, corresponding to a mosaic angle of ±23.2° around the stretching direction. Du et al.[8] used small-angle x-ray scattering to characterize the degree of nanotube alignment in the SWNT/PMMA nanocomposites, in which SWNT were aligned by melt spinning. X-ray intensity from SWNT nanocomposites in the small-angle range (0.01 Å < q < 0.1 Å) was mainly from the form factor scattering of SWNT and SWNT bundles. They observed that the aligned 1 wt% SWNT/PMMA had a FWHM of 16°, indicating that SWNT were highly aligned.

20.3 MECHANICAL PROPERTIES

Nanotubes were first considered as reinforcing fillers in polymer matrices due to their fiber-like structure and their exceptionally high axial strengths and axial Young's moduli. To date, the mechanical properties of various polymer matrices have shown only moderate improvements with the addition of either SWNT or MWNT.

Qian et al.[11] measured mechanical properties of MWNT/PS nanocomposites. With the addition of only 1 wt% MWNT the nanocomposite exhibited a 36–42% increase in the elastic stiffness and

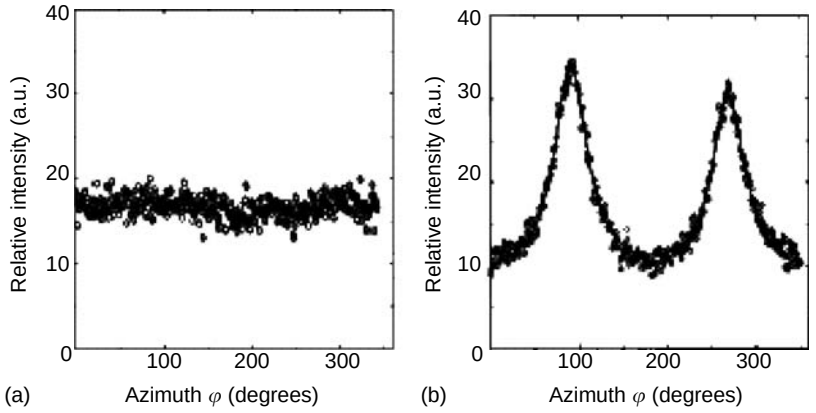

FIGURE 20.6 Integrated x-ray intensity (along the 2θ axis) vs. the azimuth for (a) an as-cast 50% MWNT/polyhydroxyaminoether nanocomposite film, and (b) the nanocomposite after being mechanically stretched. The solid line is a fit to the data by two Lorentzian functions and a constant background. (Adapted from Jin, L. et al., *Appl. Phys. Lett*., 84, 2660–2669, 2002.)

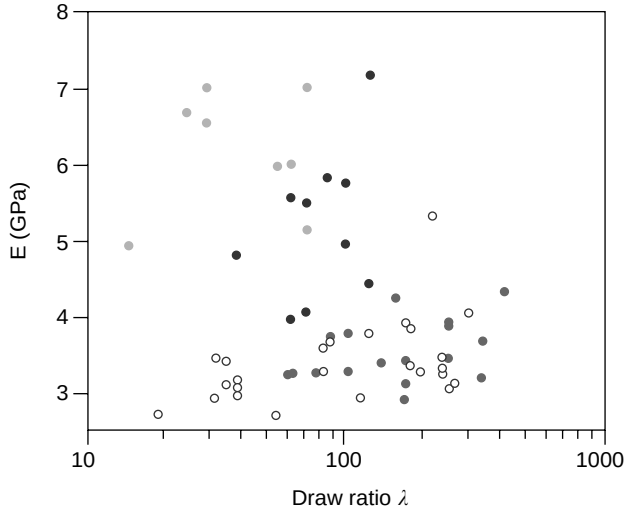

FIGURE 20.7 Elastic modulus as a function of draw ratio λ for the SWNT/PMMA nanocomposites melt spun fibers containing 0wt% (white), 1wt% (blue), 5wt% (red), or 8wt% (green) of SWNT. (Adapted from Haggenmueller, R. et al., *Chem. Phys. Lett*., 330, 219–225, 2000.)

a 25% increase in the tensile strength. Haggenmueler et al.[6] investigated the effect of both nanotube loading and nanotube alignment on the elastic modulus of SWNT/PMMA nanocomposite fibers. Nanotube alignment was achieved by melt fiber spinning and characterized by polarized resonant Raman spectroscopy. The elastic modulus of the nanocomposite fibers increased with nanotube loading and nanotube alignment, as shown in Figure 20.7. Note that the x-axis in Figure 20.7 is the draw ratio, where higher draw ratios correspond to better nanotube alignment. Andrews et al.[36] also reported that the tensile strength and modulus of a 5 wt% SWNT/pitch nanocomposite fiber were enhanced by ~90 and ~150%, respectively, as compared to pure pitch fiber.

To enhance mechanical properties, mechanical load has to be efficiently transferred from the polymer matrix to the nanotubes. Lordi and Yao[37] suggest that the strength of the interface might

result from molecular-level entanglement of pristine nanotubes and polymer chains. Thus, many researchers have investigated the interactions and load transfer between nanotubes and polymer matrices in nanocomposites. Lourie et al.[38] collected TEM images showing good epoxy-nanotube wetting and significant nanotube-epoxy interfacial adhesion, and concluded SWNT-epoxy interfacial affinity. This group also performed *in situ* deformation studies within the TEM and followed the rupture of SWNT, another indication of strong nanotube/epoxy interfaces. Wagner and co-workers[39] performed reproducible nano-pullout experiments using AFM to measure the force required to separate a CNT from poly(ethylene-co-butene) and found a separation stress of 47 MPa. In comparison, composite materials containing fiber reinforcements with weak fiber/polymer interactions typically have separation stresses of <10 MPa.[39] Simulating nanotube pullout in a CNT/PS nanocomposite, Liao and Li[40] obtained an interfacial shear stress of ~160 MPa, corresponding to a strong interface. These results from TEM, AFM, and simulation indicate that CNT can form strong interfaces with various polymer matrices.

Stress transfer can be most directly investigated by Raman spectroscopy, because the second-order (disorder-induced) Raman peak for nanotubes shifts with applied strain. If nanotubes within a nanocomposite carry part of the mechanical strain, then the Raman peak shifts with increasing applied strain. Cooper et al.[41] observed that when their SWNT/epoxy nanocomposite was mechanically strained the G′ Raman band (2610 cm^{-1}) shifted to a lower wave number. This shift in the G′ Raman band corresponds to strain in the nanotube graphite structure, indicating stress transfer between the epoxy matrix and nanotubes, and hence reinforcement by the nanotubes.

In addition to the publications showing improvements in mechanical properties along with good interfacial adhesion and load transfer, other reports have been less promising and highlight the sensitivity of nanotube/polymer composites to all aspects of materials and fabrication. Fisher et al.[42] used a combined finite element and micromechanical approach and found that the nanotube waviness significantly reduced the effective reinforcement when compared to straight nanotubes. Cooper et al.[43] investigated the detachment of MWNT from an epoxy matrix using a pullout test for individual MWNT. Observed values for the interfacial shear strength ranged from 35 to 376 MPa, and the authors attribute this variability to differences in structure, morphology, or surface properties of the nanotubes. This structural variety in nanotubes occurs during their synthesis, but can also be introduced during purification and other processing procedures.[10] Defects to the nanotube structure are expected to reduce significantly the mechanical properties of nanotubes.[44] Some methods of handling nanotubes, including acid treatments and high- as well as low-power sonication for extended periods of time, are known to shorten nanotubes.[10] Shorter nanotubes and thereby reduced aspect ratios are detrimental to mechanical properties. In contrast, some purification and processing steps might also introduce functional groups, such as carboxylic acid to the nanotube surface that subsequently form secondary bonds, such as hydrogen bonds, between the nanotubes and polymer matrices. Such functional groups might improve interfacial strength and promote nanotube compatibility and composite properties. Given the complexity of the starting materials (raw nanotubes), the range of chemical and physical processing methods and the breadth of polymer matrices being explored, variability in the mechanical properties in nanotube/polymer composites will persist.

Although improvements in mechanical properties have been reported for various nanotube/polymer nanocomposites, the gains are modest and fall far below simple estimates. Haggenmueller et al.[35] applied the Halpin–Tsai composite theory to their SWNT nanocomposites and found their experimental elastic modulus more than an order of magnitude smaller than predicted. They attribute this large difference mainly to the lack of perfect load transfer from the nanotube to the matrix, but other sources of uncertainty in the model include the aspect ratio and modulus of the nanotubes.

20.4 THERMAL AND RHEOLOGICAL PROPERTIES

The glass transition temperature (T_g) is a measure of the thermal energy required to allow polymer motion involving 10 to 15 monomeric units and corresponds to the softening of a polymer. Park

et al.[19] reported that T_g did not change for their *in situ* polymerized SWNT/polyimide nanocomposites. The SWNT/PMMA nanocomposites produced by the coagulation method have the same T_g over a wide range of nanotube loadings.[16] The addition of nanotubes does not change the glass transition temperature in nanotube/polymer nanocomposites, because in the absence of strong interfacial bonds and at low nanotube loadings, the majority of polymers are locally constrained only by other polymers.

In contrast, at larger length scales, nanotubes do impede the motion of polymer molecules as measured by rheology. Rheological (or dynamic mechanical) measurements at low frequencies probe the longest relaxation times of polymers that correspond to time required for an entire polymer molecule to change conformation. Du et al.[16] found that although it has little effect on polymer motion at the length scales comparable to or less than an entanglement length, the presence of nanotubes has a substantial influence at large length scales corresponding to an entire polymer chain. The storage modulus, G′, at low frequencies becomes almost independent of the frequency as nanotube loading increases (Figure 20.8a). These data show a transition from liquid-like behavior (short relaxation

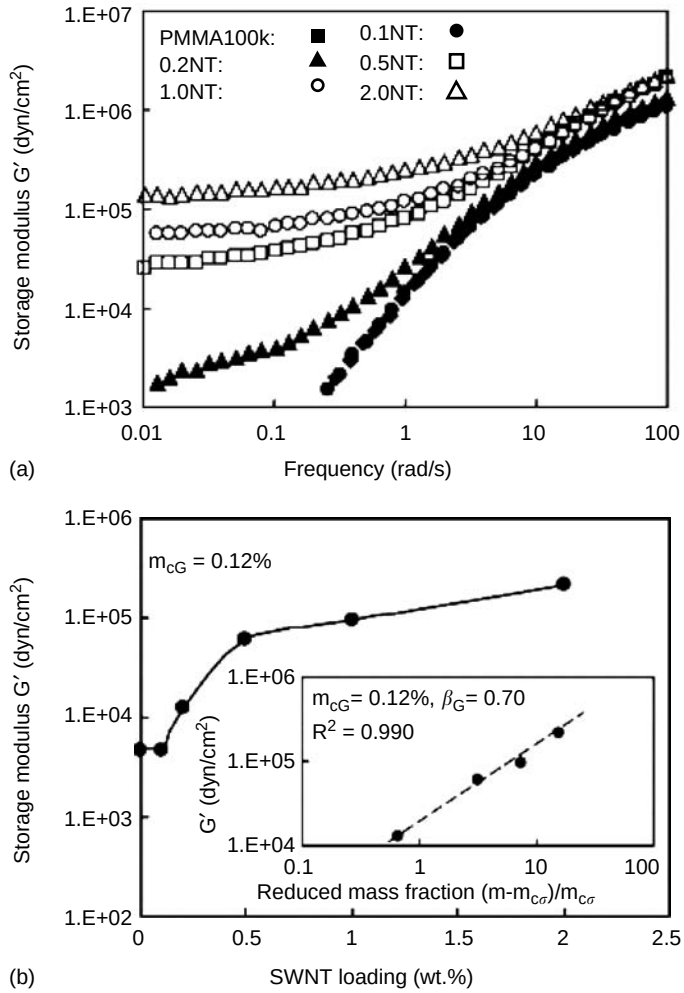

FIGURE 20.8 (a) Storage modulus (G') vs. shear frequency for SWNT/PMMA nanocomposites with various nanotube loadings; (b) G' as a function of the nanotube loading for SWNT/PMMA nanocomposites at a fixed frequency, 0.5rad/sec. The inset is a power law plot of G′ of the nanocomposites vs. reduced mass fraction on a logarithmic scale. (Adapted from Du, F. et al., *Macromolecules*, 37, 9048–9055, 2004.)

times) to solid-like behavior (infinite relaxation times) with increasing nanotube loading. By plotting G' versus nanotube loading and fitting with a power law function, the rheological threshold of these nanocomposites is ~0.12 wt% (Figure 20.8b). This rheological threshold can be attributed to a hydrodynamic nanotube network that impedes the large-scale motion of polymer molecules. This phenomenon has previously been reported in polymer nanocomposites filled with nanoclays by Krishnamoorti et al.[45] A network of nanoscale fillers restrains polymer relaxations, leading to solid-like or nonterminal rheological behavior. Therefore, any factor that changes the morphology of the nanotube network will influence the low-frequency rheological properties of the nanocomposites.

Du et al.[16] found that better nanotube dispersion, less nanotube alignment, and longer polymer chains result in more restraint on the mobility of the polymer chains; i.e., the onset of solid-like behavior occurs at low nanotube concentrations. In addition to the loading, dispersion and alignment of the nanotubes, the size, aspect ratio, and interfacial properties of the nanotubes are expected to influence the rheological response in nanocomposites. For example, at a fixed loading, nanotubes with smaller nanotube diameters and larger aspect ratios will produce a network with smaller mesh size and larger surface area/volume, which might restrain polymer motion to a greater extent. Experimental results support this hypothesis. Lozano et al.[46] observed a rheological threshold of 10–20 wt% in carbon nanofiber/PP nanocomposites in which the diameter of the carbon nanofiber is ~150 nm. The rheological threshold is ~1.5 wt% in MWNT/polycarbonate nanocomposites,[47] and only 0.12 wt% for the SWNT/PMMA system.[16] Although these three systems have different polymer matrices and their states of dispersion are unclear, the diameters of carbon nanofibers, MWNT, and SWNT differ by orders of magnitude. As the filler size decreases, the filler loading required for solid-like behavior increases substantially.

The constraints imposed by nanotubes on polymers in nanocomposites are also evident in the polymer crystallization behavior. Bhattacharyya et al.[13] studied crystallization in 0.8 wt% SWNT/PP nanocomposites using optical microscopy (with cross-polars) and differential scanning calorimetry (DSC) (Figure 20.9). The spherulite size in PP is much larger than in SWNT/PP nanocomposites. DSC results show that upon cooling, the SWNT/PP nanocomposites begins crystallizing at ~11°C higher than PP, suggesting that nanotubes act as nucleating sites for PP crystallization. They also observed that both melting and crystallization peaks in the nanocomposite are narrower than in pure PP. The authors proposed that higher thermal conductivity of the CNT as compared to that of the polymer, at least in part may be responsible for the sharper but narrower crystallization and melting peaks, as heat will be more evenly distributed in the samples containing the nanotubes.

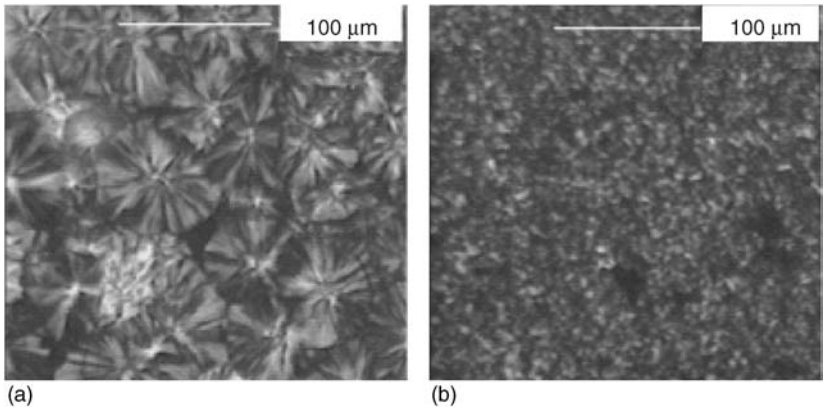

FIGURE 20.9 Optical micrographs using cross-polarizers of (a) pure PP and (b) a 0.8wt% SWNT/PP nanocomposite, showing that the nanocomposite has much smaller spherulite size compared to pure PP. (Adapted from Bhattacharyya, A.R. et al., *Polymer*, 44, 2373–2377, 2003.)

20.5 ELECTRICAL CONDUCTIVITY

A variety of applications are being pursued using electrically conductive nanotube/polymer nanocomposites including electrostatic dissipation, electromagnetic interference shielding, printable circuit wiring, and transparent conductive coatings. For example, charge buildup can lead to explosions in automotive gas lines and filters, and carbon black is typically added to plastics to dissipate the charge. Nanotube/polymer composites also dissipate charge and have the added advantage that the barrier properties against fuel diffusion are superior to composites made with carbon black.[48] Compared to carbon black's globular shape and micron-scale size, nanotubes are cylindrical in shape and with diameter in nanometer-scale. The larger aspect ratios and smaller diameters of nanotubes led to improved electrical conductivity in polymers at lower filler concentrations as compared to carbon black, so that a polymer's other desired performance aspects, such as mechanical and permeability properties, can be preserved.

Figure 20.10a shows the conductivity of SWNT/PS nanocomposites as a function of nanotube loading measured by Ramasubramaniam et al.[49] The conductivity of the nanocomposite increases sharply between 0.02 and 0.05 wt% SWNT loading, indicating the formation of a conductive nanotube network; this behavior is typical of percolation. According to percolation theory, the conductance should follow the following power law close to the threshold concentration: $\sigma \sim (v\text{-}v_c)^{\beta}$, where v is the volume fraction of the conductive component and β is the critical exponent for the conductivity. Most

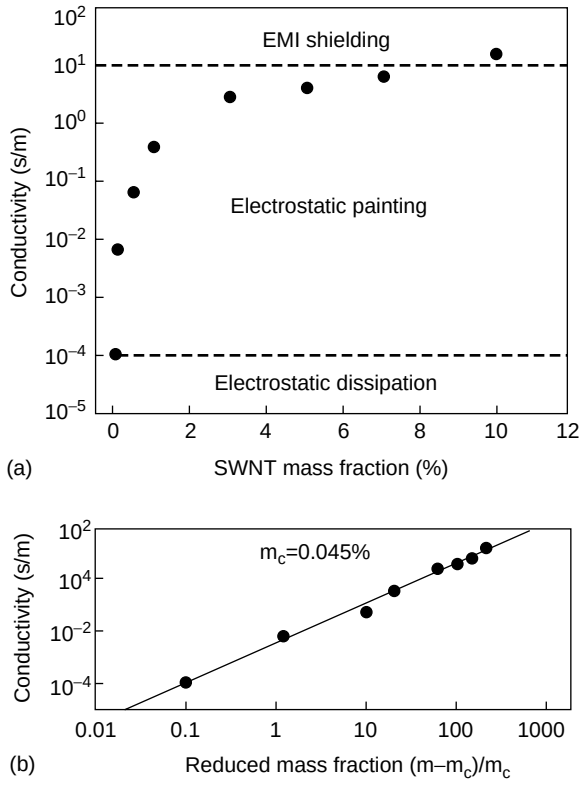

FIGURE 20.10 (a) Electrical conductivity of SWNT/PS nanocomposites as a function of nanotube loading, showing a typical percolation behavior. Dashed lines represent the lower limits of electrical conductivity required for the specified applications, (b) Electrical conductivity as a function of reduced mass fraction of nanotubes, showing a threshold of 0.045wt%. (Adapted from Ramasubramaniam, R. et al., *Appl. Phys. Lett.*, 83, 2928–2930, 2003.)

researchers assume that the nanotube volume fraction is comparable to the nanotube mass fraction, because the densities of nanotubes and polymers are similar. The power law expression for percolation fits the conductivity data for SWNT/PS nanocomposites giving a low percolation threshold, 0.045 wt%. Ounaies et al.[50] also observed percolation behavior for electrical conductivity in SWNT/polyimide nanocomposites with a percolation threshold of 0.1 vol%. Their current–voltage measurements exhibited nonohmic behavior, which is most likely due to a tunneling conduction mechanism. Conduction probably occurs by electron hopping between adjacent nanotubes when their separation distance is small. At concentrations greater than the percolation threshold, conductive paths are formed through the whole nanocomposite, because the distance between the conductive filler (nanotubes or nanotube bundles) is small enough to allow efficient electron hopping. Ounaies et al.[50] developed an analytical model and numerical simulation using high aspect ratio and rigid spherocylinders in a unit cube to mimic SWNT/polymer nanocomposites to aid in understanding these results. The predictions from both the analytical model and the numerical simulation were in good agreement with the experimental results.

As presented earlier, a hydrodynamic nanotube network forms upon increasing nanotube loading and leads to the nonterminal rheological behavior. Similarly, a conductive nanotube network turns polymers from insulating to conducting. Du et al.[16] have compared the hydrodynamic and the conductive nanotube networks. In their SWNT/PMMA nanocomposites, the rheological percolation threshold, 0.12 wt%, is significantly smaller than the percolation threshold for electrical conductivity, 0.39 wt%. They understand this difference in the percolation threshold in terms of the smaller nanotube–nanotube distance required for electrical conductivity as compared to that required to impede polymer mobility. Specifically, the proposed electron hopping mechanism requires tube–tube distance of less than ~5 nm, while for rheological percolation the important length scale is comparable to the size of the polymer chain, which is ~18 nm for PMMA (M = 100 kDa). Thus, they conclude that a less dense nanotube network can restrict polymer motion than can conduct electricity.

Three main factors that influence the percolation threshold for the electrical conductivity are nanotube dispersion, aspect ratio, and alignment. Barrau et al.[25] used palmitic acid as a surfactant to improve the nanotube dispersion in SWNT/epoxy nanocomposites and reduced the threshold concentration for electrical conductivity from ~0.18 to ~0.08 wt%. Bai and Allaoui[51] pretreated MWNT to alter their aspect ratios before preparing MWNT/epoxy nanocomposites and found that the threshold concentration for electrical conductivity varied from 0.5 to >4 wt% with decreasing aspect ratio. This observation is consistent with the predictions from Balberg's model.[52] As the quality of nanotube dispersion improves and the aspect ratios of nanotubes increase, lower nanotube loadings are required to increase the electrical conductivities and these loadings are smaller than the loading required, obtaining comparable conductivities by adding other conductive fillers, like carbon black and graphite.[53]

Owing to their highly anisotropic shape the alignment of nanotubes must be considered when studying the properties, including electrical conductivity of nanotube/polymer nanocomposites. Du et al.[8] found that the electrical conductivity of a 2 wt% SWNT/PMMA nanocomposite decreased significantly (from ~10^{-4} to ~10^{-10}S/cm) when the SWNT were highly aligned (FWHM=20° as measured by x-ray scattering as described above). This decrease in electrical conductivity is the result of fewer contacts between nanotubes when they are highly aligned as compared to having an isotropic orientation. In contrast, Choi et al.[9] observed that nanotube alignment increased the conductivity of a 3 wt% SWNT/epoxy nanocomposite from ~10^{-7} to ~10^{-6} S/cm. Note that nanotubes in the SWNT/PMMA systems[8] were aligned by melt spinning, while they were aligned in the SWNT/epoxy[9] by magnetic force during fabrication. Although Choi et al. did not quantify the degree of alignment, it is reasonable to assume that SWNT are better aligned by the extensional flow of melt fiber spinning. More recently, we found an optimal degree of nanotube alignment that yields a maximum electrical conductivity.[63] The degree of nanotube alignment was varied by controlling the melt fiber spinning conditions and was characterized by x-ray scattering. In all cases, the SWNT/PMMA nanocomposites with isotropic nanotube orientation have greater electrical conductivity than the nanocomposites with highly aligned nanotubes. Furthermore, at low nanotube

concentrations, there are intermediate levels of nanotube alignment with higher electrical conductivities than the isotropic condition. We attribute the maximum electrical conductivity at an intermediate nanotube alignment observed in the competition between the number of tube–tube contacts and the distance between these contacts.

The electrical properties of nanocomposites made from electrically conductive conjugated polymers have also been studied.[14,54] Tchmutin et al.[55] compared the electrical conductivity behavior of SWNT/polyanaline (PA) and SWNT/PP nanocomposites produced by the same method. The nanocomposites prepared with PA have a lower threshold for electrical conductivity than SWNT/PP nanocomposites, specifically ~2 vol% compared to ~ 4 vol%. They attribute this lower threshold to a "double percolation," involving both the nanotubes and the conjugated polymer matrix, where the PA becomes conductive when injected with charge carriers from the nanotubes. In SWNT/PA composites, the nanotubes are surrounded by PA domains of higher conductivity that increase the effective volume of conductive nanotubes and thereby reduce the concentrations required for percolation in these nanocomposites.

20.6 THERMAL CONDUCTIVITY AND FLAMMABILITY

Nanotube/polymer nanocomposites are expected to have superior thermal conductivity due to the exceptionally high thermal conductivities reported for nanotubes. Biercuk et al.[56] first reported the improvement in thermal conductivity for SWNT/polymer nanocomposites; their 1 wt% SWNT/epoxy nanocomposite showed a 70% increase in thermal conductivity at 40 K, increasing to 125% at room temperature. Choi et al.[9] reported a 300% increase in thermal conductivity at room temperature with 3 wt% SWNT in epoxy. The thermal conductivity of individual nanotube is –approximately four orders of magnitude higher than that of typical polymers (~0.2 W/m K), so these reported enhancements are smaller than expected if one assumes perfect phonon transfer between nanotubes in the composite. A more appropriate benchmark for thermal conductivities in nanotube/polymer composites is the thermal conductivity of nanotube buckypaper (a low-density felt or mat of nanotubes typically made via filtration of nanotube suspensions) so as to account for the thermal resistance between nanotubes. Hone et al.[17] used a comparative method to measure the thermal conductivity of an unaligned SWNT buckypaper at room temperature and found it to be ~30 W/m K. In the absence of thermal resistance between nanotubes, this value would be expected to be less of the order of 10^3 W/m K. Researchers are currently exploring the extent, to which substantial interfacial thermal resistance is intrinsic to nanotubes.

A comparison of the electrical and thermal conductivity behaviors in nanotube-based nanocomposites provides some insight to heat transport. A 2 wt% SWNT/PMMA nanocomposite is well above the threshold concentration for electrical conductivity (~0.4 wt%),[16] but has the thermal conductivity of pure PMMA.[64] In other words, the electrically conductive nanotube network in the 2 wt% SWNT/PMMA is not thermally conductive. This can be explained by the different transport mechanisms for electrons and phonons. As we discussed above, an electron hopping mechanism has been applied to nanotube-based nanocomposites, which requires close proximity (but not direct contact) of the nanotubes or nanotube bundles in the composites. However, heat transport inside nanotube-based nanocomposites proceeds by phonon transfer. The nanotubes and polymer matrix are coupled only by a small number of low-frequency vibrational modes in the absence of covalent bonds at the interface. Thus, thermal energy contained in high-frequency phonon modes within the CNT must first be transferred to low frequencies through phonon–phonon couplings before being exchanged with the surrounding medium.[57] This is the origin of the high interfacial thermal resistance in nanotube/polymer composites. Huxable et al.[57] used picosecond transient absorption to measure the interface thermal conductance of CNT suspended in surfactant micelles in water, a system comparable to polymer-based composites. They estimated that the thermal resistance posed by the nanotube–polymer interface was equivalent to the resistance of a 20-nm-thick layer of polymer. This finding indicates that heat transport in a

nanotube-based nanocomposite material will be limited by the exceptionally small interface thermal conductance and is in marked contrast to the findings regarding electrical conduction in these composites. Thus, the thermal conductivity of nanotube/polymer nanocomposite will be much lower than the value estimated from the intrinsic thermal conductivity of nanotubes. Improvements in thermal conductivity will require strategies for overcoming the interfacial thermal resistance, perhaps by interfacial covalent bonding.

In addition to interfacial bonding, nanotube dispersion, alignment, and aspect ratio are expected to influence the thermal conductivity of the nanocomposites. There are a limited number of reports on thermal conductivity of nanotube-based nanocomposites, due at least in part to the difficulty of the experiments. Thus, only an incomplete view of how these parameters influence thermal conductivity is available. Choi et al.[9] showed that the thermal conductivity of the magnetically aligned 3 wt% SWNT/epoxy was 10% higher than that of the unaligned nanocomposite with the same loading.

Like silica[58] and clay,[59,60] nanotubes also improve the thermal stability of polymer matrices in nanocomposites. In these nanocomposites, the filler particles absorb a disproportionate amount of thermal energy, thereby retarding the thermal degradation of the polymer. Du et al.[8] showed that the temperature of the maximum weight loss peak shifts from 300°C for pure PMMA to 370°C for the 0.5 wt% SWNT/PMMA nanocomposite, as determined by thermal gravimetric analysis. Similar results were also found using MWNT in various polymer matrices.[12,61]

Nanotubes have also proven to be effective flame-retardant additives. Kashiwagi et al.[12,31] reported that small amount of MWNT greatly improve flammability of PP, as measured both by cone calorimetery and radiant gasification in nitrogen. Mass loss rates decrease with increasing MWNT concentration (Figure 20.11a) indicating that the addition of MWNT effectively prolongs the burning of PP. The sample residue collected after nitrogen gasification (Figure 20.11b) is nearly the same shape as the original sample and is a low-density, self-supporting structure of nanotubes, a nanotube network. Kashiwagi et al.[62] attribute the improvement in flammability to nanotube networks spanning the nanocomposite that dissipate heat and thereby reduce the external radiant heat transmitted to the PP in the sample. A recent study[62] of SWNT/PMMA nanocomposites also shows similar flame retardancy effectiveness with lower concentrations of SWNT.

Kashiwagi et al.[31] compared MWNT/PP and carbon black/PP nanocomposites. With the same carbon loading, 1 wt%, carbon black is much less flame retardant than MWNT. The residue of the 1 wt% carbon black/PP nanocomposite after nitrogen gasification contains discrete aggregates and granular particles in contrast to the residue from the MWNT/PP composites having a MWNT network. The presence of the nanotube network is critical to improving the flame retardancy, because this morphology provides efficient heat dissipation. A similar network was observed in clay/PP nanocomposites with 5 wt% filler,[59] but the residue was brittle. At only 0.5 wt% loading, intact nanotube networks form in both SWNT and MWNT nanocomposites, indicating that nanotubes are more potent flame-retardant additives than nanosilicates. As with other properties of nanotube/polymer composites, the flame-retardant performance will depend on nanotube dispersion,[62] aspect ratio, and alignment.

20.7 CONCLUSIONS

Polymers are frequently modified to improve their physical properties for specific applications. Among the additives now available are CNT that provide unique opportunities to improve mechanical, electrical, and thermal properties of a variety of polymer matrices. We have summarized the current state of this field, though each month brings new publications that expand the understanding of nanotube/polymer nanocomposites. The published literature, as presented above, is only a fraction of the current activity as companies pursue research and development on nanotube/polymer materials. Upon review of the available literature the following generalizations are evident:

1. In addition to nanotube concentration, the properties of nanotube/polymer composites strongly depend on the nanotube dispersion within the matrix, the aspect ratio of the

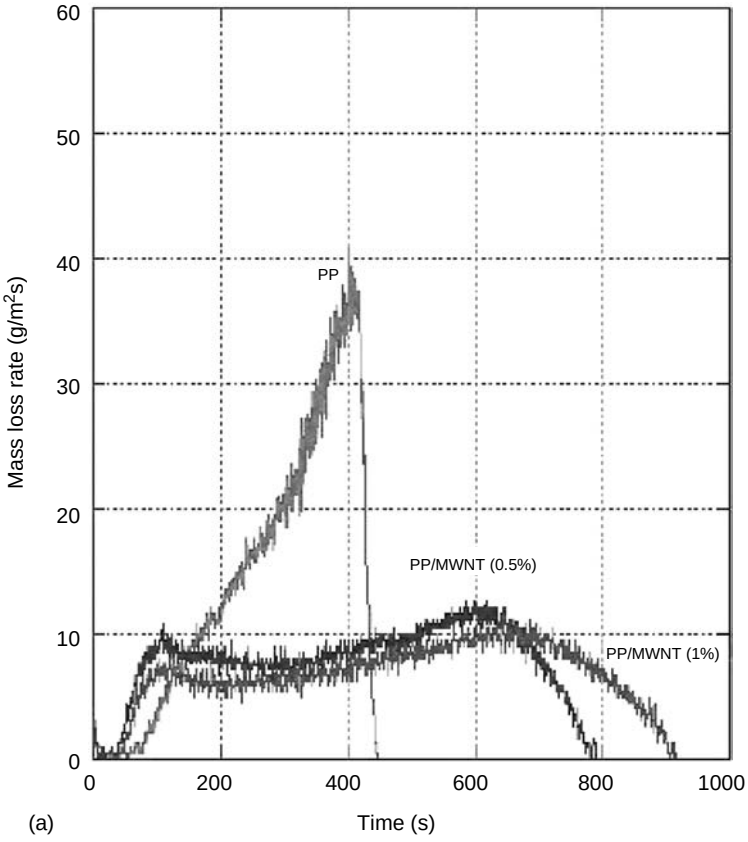

(a)

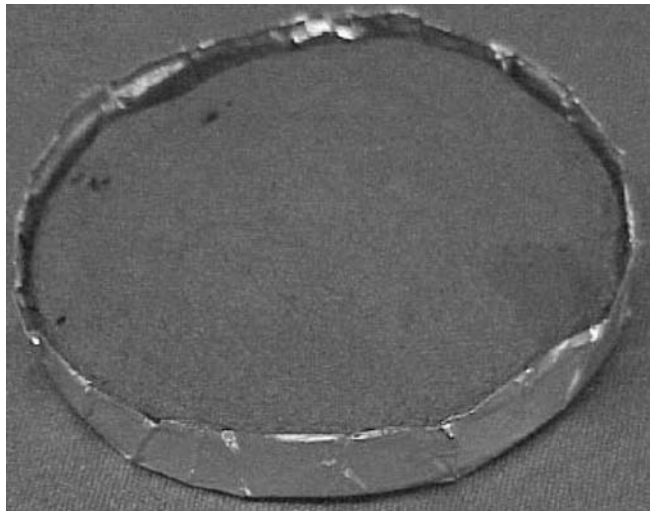

(b)

FIGURE 20.11 (a) Mass loss rate for PP and MWNT/PP nanocomposites in nitrogen gasification, showing that the addition of MWNT slows the thermal degradation of the polymer matrix; (b) highly porous residue of the 1wt% MWNT/PP nanocomposite after nitrogen gasification suggesting the presence of a nanotube network in the nanocomposite. (Adapted from Kashiwagi et al.[31])

nanotubes and the alignment of the nanotubes within the polymer matrix. These traits, dispersion, aspect ratio, and alignment, are difficult and tedious to determine, and many publications fail even to attempt a qualitative description of these characteristics of their composites. As these traits are not independent (e.g., shorter nanotubes are easier to disperse) control experiments are challenging. Nanotube dispersion in a nanocomposite must be explored over a range of length scales from nm to mm. The aspect ratios of nanotubes depend on the synthetic route of the nanotubes with batch-to-batch variations that are considerable. In addition, postsynthesis processing to increase purity and improve dispersion can alter the distribution of aspect ratios. The high aspect ratios of nanotubes make them prone to alignment by even modest applied forces (e.g., during solvent casting gravity is sufficient to bias the spatial distribution of nanotubes to be preferentially horizontal). These nuances are important to nanotube/polymer composites and their properties and serve to caution researchers in the field.

2. The concept of networks of nanotubes provides strong correlations between nanocomposite morphology and properties. Nanotube networks are structures in which interconnected nanotubes form an open and irregular framework of nanotubes that span across the nanocomposites. Such nanotube networks are readily detected by dynamic mechanical (rheological) or electrical conductivity measurements. In fact, the detection of a nanotube network provides a reliable, though indirect and qualitative, measure of the relative nanotube dispersion and aspect ratio. For example, the presence of solid-like behavior indicates better dispersion than a comparable nanocomposite with the same nanotube loading and aspect ratio having liquid-like behavior. The presence of nanotube networks in nanocomposites provides a framework for discussing rheological, electrical, and flame-retardant properties. This framework is inappropriate for properties such as mechanical and thermal properties in which the interfacial properties of the nanotube/ polymer nanocomposite are dominant.
3. Nanotubes are certainly capable of improving the physical properties of polymers. As with any filler, there will be a balance of advantages and disadvantages. The higher electrical conductivity available at low nanotube loadings will be balanced with the onset of solid-like behavior that will make the nanocomposite more difficult to process. The current cost of nanotubes is such that loadings as small as l wt% could be prohibitive over the next few years, except in highly selective markets. Because the cost of nanotubes will continue to drop, research with available nanotube materials should continue in earnest. At the moment, improvements in the electrical and thermal properties are perhaps the most promising, although mechanical properties of nanotube/polymer composites will benefit substantially from the emerging availability of all nanotube fibers.

In conclusion, nanotube/polymer nanocomposites have demonstrated their promise as multifunctional materials. Attention to the challenges detailed above will maximize their potential as a new class of nanocomposites for a variety of applications in the coming decades.

ACKNOWLEDGMENTS

The authors thank the Office of Naval Research (N00014-3-1-0890) for funding and Dr. Fischer, Dr. Kashiwagi, Dr. Lukes, R. Haggenmueller, and C. Guthy for helpful discussions.

REFERENCES

1. Thostenson, E.T., Ren, Z., and Chou, T.W., *Comp. Sci. Technol.,* 61, 1899–1912, 2001.
2. Kim, P., Shi, L., Majumdar, A., and McEuen, P.L., *Phys. Rev. Lett.,* 87, 21550201–21550204, 2001.
3. Maruyama, S., *Physica B,* 323, 193–195, 2002.
4. Bronilowski, M.J., Willis, P.A., Colbert, D.T., Smith, K.A., and Smalley, R. E., *J. Vac. Sci. Technol. A,* 19, 1800–1805, 2001.

5. Salvetat, J.P., Andrew, G., Briggs, D., Bonard, J.M., Bacsa, R.R, Kulik, A. J., Stockli, T., Burnham, N.A., and Forro, L., *Phys. Rev. Lett.*, 82, 944–947, 1999.
6. Haggenmueller, R., Commans, H.H., Rinzler, A.G., Fischer, J.E., and Winey, K.I., *Chem. Phys. Lett.*, 330, 219–225, 2000.
7. Benoit, J.M., Corraze, B., Lefrant, S., Blau, W., Bernier, P., and Chauvet, O., *Synth. Met.*, 121, 1215–1216, 2001.
8. Du, F., Fischer, J.E., and Winey, K.I., *J. Polym. Sci.: Part B: Polym. Phys.* 41, 3333–3338, 2003.
9. Choi, E.S., Brooks, J.S., Eaton, D.L., Al-Haik, M.S., Hussaini, M.Y., Garmestani, H., Li, D., and Dahmen, K., *J. Appl. Phys.*, 94, 6034–6039, 2003.
10. Furtado, C.A., Kin, U.J., Gutierrez, H.R., Pan, L., Dickey, E.C., and Eklund, P.C., *J. Am. Chem. Soc.*, 126, 6095–6105, 2004.
11. Qian, D., Dickey, E.C., Andrews, R., and Rantell, T., *Appl. Phys. Lett.*, 76, 2868–2870, 2000.
12. Kashiwagi, T., Grulke, E., Hilding, J., Harris, R., Awad, W., and Douglas, J., *Macromol. Rapid Commun.*, 23, 761–765, 2002.
13. Bhattacharyya, A.R., Sreekumar, T.V., Liu, T., Kumar, S., Ericson, L. M., Hauge, R.H., and Smalley, R.E., *Polymer*, 44, 2373–2377, 2003.
14. Coleman, J.N., Curran, S., Dalton, A.B., Davey, A.,P., McCarthy, B., Blau, W., and Barklie, R.C., *Phys. Rev. B*, 58, 57–60, 1998.
15. Benoit, J.M., Corraze, B., and Chauvet, O., *Phys. Rev. B*, 65, 24140501–24140504, 2002.
16. Du, F., Scogna, R.C., Zhou, W., Brand, S., Fischer, J.E., and Winey, K.I., *Macromolecules*, 37, 9048–9055, 2004.
17. Hone, J., Batlogg, B., Benes, Z., Llaguno, M.C, Nemes, N.M., Johnson, A.T., and Fischer, J.E., *Mater. Res. Soc. Symp. Proc.*, 633, A17.ll.ll–A17.ll.12, 2001.
18. Ajayan, P.M., Schadler, L.S., Giannaris, C., and Rubio, A., *Adv. Mater.*, 12, 750–753, 2000.
19. Park, C., Ounaies, Z., Watson, K.A., Crooks, R.E., Smith J., Jr. Lowther, S.E., Connell, J.W., Siochi, E.J., Harrison, J.S., and Clair, T.L.S., *Chem. Phys. Lett.*, 364, 303–308, 2002.
20. Sun, Y., Fu, K., Lin, Y., and Huang, W., *Acc. Chem. Res.*, 35, 1096–1104, 2002.
21. Chen, J., Hamon, M.A., Hu, H., Chen, Y., Rao, A.M., Eklund, P.C., and Haddon, R.C., *Science*, 282, 95–98, 1998.
22. Hill, D.E., Lin, Y., Rao, A.M., Allard, L.F., and Sun, Y., *Macromolecules*, 35, 9466–9471, 2002.
23. Lin, Y., Rao, A.M., Sadanadan, B., Kenik, E.A., and Sun, Y, *J. Phys. Chem. B*, 106, 1294–1298, 2001.
24. Islam, M.F., Rojas, E., Bergey, D.M., Johnson, A.T., and Yodh, A.G, *Nano Lett.*, 3, 269–273, 2003.
25. Barrau, S., Demont, P., and Perez, E., *Macromolecules*, 36, 9678–9680, 2003.
26. O'Connell, M.J., Boul, P., Ericson, L.M., Huffman, C., Wang, Y., Haroz, E., Kuper, C., Tour, J., Ausman, K.D., and Smalley, R.E., *Chem. Phys. Lett.*, 342, 265–271, 2001.
27. Star, A., Steuerman, D.W., Heath, J.R., and Stoddart, J.F., *Angew. Chem. Int. Ed*, 41, 2508–2512, 2002.
28. Barisci, J.N., Tahhan, M., Wallace, G.G., Badaire, S., Vaugien, T., Maugey, M., and Poulin, P., *Adv. Funct. Mater.*, 14, 133–138, 2004.
29. Kimura, T., Ago, H., Tobita, M., Ohshima, S., Kyotani, M., and Yumura, M., *Adv. Mater.*, 14, 1380–1383, 2002.
30. Walters, D.A., Casavant, M.J., Qin, X.C, Huffman, C.B., Boul, P.J., Ericson, L.M., Haroz, E.H., O'Connell, M.J., Smith, K., Colbert, D.T., and Smalley, R.E, *Chem. Phys. Lett.*, 338, 14–20, 2001.
31. Kashiwagi, T., Grulke, E., Hilding, J., Groth, K., Harris, R., Shields, J., Kathryn, B., Kharchenko, S., and Douglas, J, *Polymer*, 45, 4227–4239, 2004.
32. Jin, L., Bower, C, and Zhou, O., *Appl. Phys. Lett.*, 73, 1197–1199, 1998.
33. Safadi, B., Andrews, R., and Grulke, E.A., *J. Appl. Poly. Sci.*, 84, 2660–2669, 2002.
34. Thostenson, E.T., and Chou, T.-W., *J. Phy. D: Appl. Phy.*, 35, 77–80, 2002.
35. Haggenmueller, R., Zhou, W., Fischer, J.E., and Winey, K.I., *J. Nanosci. Nanotechnol.*, 3, 104–108, 2003.
36. Andrews, R., Jacques, D., Rao, A.M., Rantell, T., Derbyshire, F., Chen, Y., Chen, J., and Haddon, R.C., *Appl. Phys. Lett.*, 75, 1329–1331, 1999.
37. Lordi, N., and Yao, V., *J. Mater. Res.*, 15, 2770–2779, 2000.
38. Lourie, O., and Wagner, H.D., *Appl. Phys. Lett.*, 73, 3527–3529, 1998.
39. Barber, A.H., Cohen, S.R., and Wagner, H.D., *Appl. Phys. Lett.*, 82, 4140–4142, 2003.
40. Liao, K., and Li, S., *Appl. Phys. Lett.*, 79, 4225–4227, 2001.
41. Cooper, C.A., Young, R.J., and Halsall, M., *Comp. Part A: Appl. Sci. Manuf.*, 32, 401–411, 2001.

42. Fisher, F.T., Bradshaw, R.D., and Brinson, L.C., *Appl. Phys. Lett.*, 80, 4647–4649, 2002.
43. Cooper, C.A., Cohen, S.R., Barber, A.H., and Wagner, H.D., *Appl. Phys. Lett*., 81, 3873–3875, 2002.
44. Wagner, H.D., *Chem. Phys. Lett*., 361, 57–61, 2002.
45. Krishnamoorti, R., and Giannelis, E.P., *Macromolecules*, 30, 4097–4102, 1997.
46. Lozano, K., Bonilla-Rios, J., and Barrera, E.V., *J. Appl. Poly. Sci.*, 80, 1162–1172, 2000.
47. Cumings, J., and Zettl, A., *Science*, 602, 289–291, 2000.
48. Baughman, R.H., Zakhidov, A.A., and deHeer, W.A., *Science*, 297, 787–792, 2002.
49. Ramasubramaniam, R., Chen, J., and Liu, H. *Appl. Phys. Lett*., 83, 2928–2930, 2003.
50. Ounaies, Z., Park, C., Wise, K.E., Siochi, E.J., and Harrison, J.S., *Comp. Sci. Technol*, 63, 1637–1646, 2003.
51. Bai, J.B., and Allaoui, A., *Comp. Part A: Appl. Sci. Manuf*., 34, 689–694, 2003.
52. Balberg, I., and Binenbaum, N., *Phys. Rev., B*, 28, 3799–3812, 1983.
53. Lau, K., Shi, S., and Cheng, H., *Comp. Sci, Technol*., 63, 1161–1164, 2003.
54. Kymakis, E., Alexandou, I., and Amaratunga, G.A.J., *Synthetic Metals*, 127, 59–62, 2002.
55. Tchmutin, I.A., Ponomarenko, A.T., Krinichnaya, E.P., Kozub, G.I., and Efimov, O.N., *Carbon*, 41, 1391–1395, 2003.
56. Biercuk, M.J., Llaguno, M.C., Radosavljevic, M., Hyun, J.K., Johnson, A.T., and Fischer, J.E., *Appl. Phys. Lett.*, 80, 2767–2739, 2002.
57. Huxtable, S.T., Cahill, D.G., Shenogin, S., Xue, L., Ozisik, R., Barone, P., Usrey, M., Strano, M.S., Siddons, G., Shim, M., and Keblinski, P., *Nat. Mater*., 2, 731–734, 2003.
58. Morgan, A.B., Antonucci, J.M., VanLandingham, M.R., Harris, R.H., and Kashiwagi, T., *Polym. Mater. Sci. Eng*., 83, 57–58, 2000.
59. Marosi, G., Marton, A., SZep, A., Csontos, I., Keszei, S., Zimonyi, E., Toth, A., Almeras, X., and Le Bras, M., *Polym. Degrad. Stabil*., 82, 379–385, 2003.
60. Qin, H., Su, Q., Zhang, S., Zhao, B., and Yang, M., *Polymer*, 44, 7533–7538, 2003.
61. Pötschke, P., Fornes, T.D., and Paul, D.R., *Polymer,* 43, 3247–3255, 2002.
62. Kashiwagi, T., Du, F., Winey, K.I., Groth, K.M., Shields, J.R., Bellayer, S.P., Kim, H., and Douglas, J.F., *Polymer*, 46, 471–481, 2005.
63. Du, F., Fischer, J.E., and Winey, K.I., *Phys. Rev. B*, 72, 12140401–12140404, 2005.
64. Du, F., Guthy, C., Kashiwagi, T., Fischer, J.E., and Winey, K.I., In preparation.

21 Nanoporous Polymers — Design and Applications

Vijay I. Raman and Giuseppe R. Palmese
Department of Materials Science and Engineering,
Drexel University, Philadelphia, Pennsylvania

CONTENTS

ABSTRACT

This chapter deals with the methods used for designing nanoporous polymers and the potential applications of nanoporous polymers. There are innumerable reviews and books on the topic of designing

porous polymers where the average pore sizes are generally greater than 1μm. In this chapter, our objective is to review only those methods that have been shown to be useful in designing nanoporous polymers where the pore sizes are in the range of 1 to 100 nm. Methods of designing nanoporous polymers are broadly classified in this review as (1) methods with no pore-generating agents (porogen) — track etching, (2) methods that use templates — micellar imprinting, nanotemplates, molecular imprinting, self-assembled nanostructures, and hyper-branched polymers, and (3) methods that use a solvent as porogen — thermally induced, diffusion-induced, and polymerization-induced phase separations, and microemulsion and miscible systems. This review presents the basic principles behind each of these methods and in doing so classifies these methods into three general categories and summarizing some of the relevant literature. Furthermore, the potential applications of nanoporous polymers such as (1) polymer electrolytes in fuel cells, (2) separation membranes, (3) templates for nanostructures/nanomaterials synthesis, and (4) nanocomposites are also discussed.

21.1 INTRODUCTION

Porous materials have a heterogeneous distribution of atoms in three-dimensional space (3D) i.e., they have regions of no or few atoms which are called pores/voids, interspersed within regions of more atoms. Materials with pores/voids in the size range of 1 to 100 nm are called *nanoporous*. Generally, inorganic materials such as ceramics and metals, and organic materials such as *polymers* are used to design nanoporous materials. Polymers are widely used for this purpose because of the ease of their synthesis and the large number of controllable properties. For example, polymeric material can range from insulating to conducting, from hydrophobic to hydrophilic, and from soft to hard. Alongside this, the recent interest in material design at nanoscopic level to obtain advanced and smarter materials with improved functionality has precipitated the usefulness of nanoporous polymers. In general, the presence of pores and voids results in materials with low density or materials with the capability of transporting permeants through the pore channels (if they are interconnected). These aspects form the basis of the applications of nanoporous polymers such as templates for nanostructures and nanomaterials synthesis,[1] polymer electrolytes in electrochemical cells,[2,3] separation membranes,[4] and nanocomposites.[5] Depending upon the final application, nanoporous polymers with specific structural and geometric attributes, such as pore size, shape, porosity, etc. and specific pore interface chemistry and activity, such as hydrophilicity, bioactivity, proton conductivity, etc., are required. For example, in the application of nanoporous polymers as substrates for synthesizing nanowires a controlled cylindrical pore shape with narrow pore size distribution (PSD) is required, whereas in applications such as polymer electrolytes in fuel cells pore interfaces with ionic groups that favor proton transport mechanisms are essential. Thus, the ability to tailor the geometric and structural attributes of the pores and chemistry and activity of the pore interface are important in designing nanoporous polymers for the applications mentioned above. The objective of this chapter is to review different methods reported in the literature for the design of nanoporous polymers and to discuss the potential applications of nanoporous polymers. Specifically, the goal here is to mention the basic principles on which these methods are based, thus giving the reader a general sense of the design attributes, such as pore shapes, sizes, interconnectedness, porosity, and pore interface chemistry and activity that can be obtained from these methods; and finally to show how these aspects can be used in the potential applications of nanoporous polymers.

21.2 DESIGN OF NANOPOROUS POLYMERS

Both physical and synthetic methods have been used to design nanoporous polymers. These methods are broadly classified into three main categories: (1) methods with no pore-generating agents (porogen), (2) methods that use templates, and (3) methods that use solvent as porogen, as shown schematically in Figure 21.1. These categories are further subdivided into sections which are systematically discussed below.

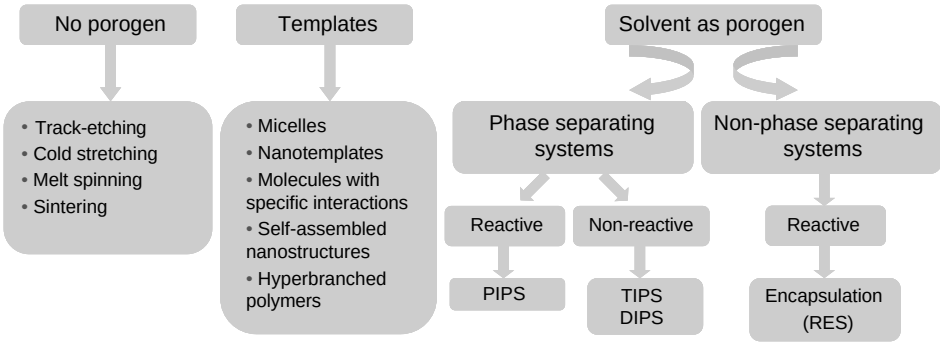

FIGURE 21.1 The classification of the methods used to design nanoporous polymers.

21.2.1 No Porogen

These methods employ thermal, mechanical, or radiation processing of the polymer to obtain porous structure. The methods that fall under this category are melt extrusion and processing, stretching, sintering, and track etching. Methods like melt extrusion and processing, stretching, and sintering generally yield dense polymeric membranes.[6] In addition, these methods are restricted in the range of pore sizes and porosity. In this category of methods, only track etching has been widely used to obtain nanoporous polymers and will be discussed in detail.

21.2.1.1 Track Etching

This technique[7–11] involves two important steps: (1) track formation — producing latent tracks by irradiation with high-energy beams and (2) etching process — where the latent tracks are removed to form the pore channel. Track etching offers distinct advantages over other methods due to its ability to produce ordered and oriented nanopores with controlled characteristics such as *pore size, shape, porosity (or density), and separation distances between pores*. The polymers that are widely used in this technique are polyethylene terephthalate (PET) and polycarbonate (PC).

Apel[7] has summarized the work undertaken until recently in the field of using track-etching technique to design nanoporous polymers. This work mentions the origin and the development of track etching as an industrial technology. The major advances as reported are new particle sources (accelerators), new polymeric materials, new applications, and the development of modification methods, i.e., tailoring pore interface interactions. The first step in the design of nanoporous polymers using this technique involves creating latent tracks. The two basic methods employed to produce latent tracks are (1) irradiation with fission fragments of heavy nuclei and (2) irradiation with ion beams from accelerators. Apel summarized the literature instrumental in the development of these two methods and mentioned their salient features and limitations. The radiation treatment step is followed by a chemical-etching process. The etching process determines the size and shape of the pores. The two important factors that influence the size and shape during this step are the bulk- and track-etch rates. The track-etch rate is the rate of dissolution along the latent track and bulk-etch rate is the rate of dissolution of the surfaces, i.e., the etched surface and the interior surface of the etched track. Cylindrical pores are usually obtained if the track-etch rate is significantly greater than bulk-etch rate. Apel et al.[8,9] have shown that the etching rates and hence the pore shapes can be controlled by adsorbtion of surfactants to the pore walls during the etching process. As shown in Figure 21.2[7] pore shapes like cylinder, cone, cigar, and bow tie are obtained by changing the irradiation and chemical treatment methods. Apel[7] discussed the research efforts carried out to obtain track-etched membranes (TMs) with the PET, PC, polypropylene (PP), polyvinylidene fluoride (PVDF), polyimides (PI), CR-39, polysulfones, polyetheretherketones, and polyethylene naphthalate systems.

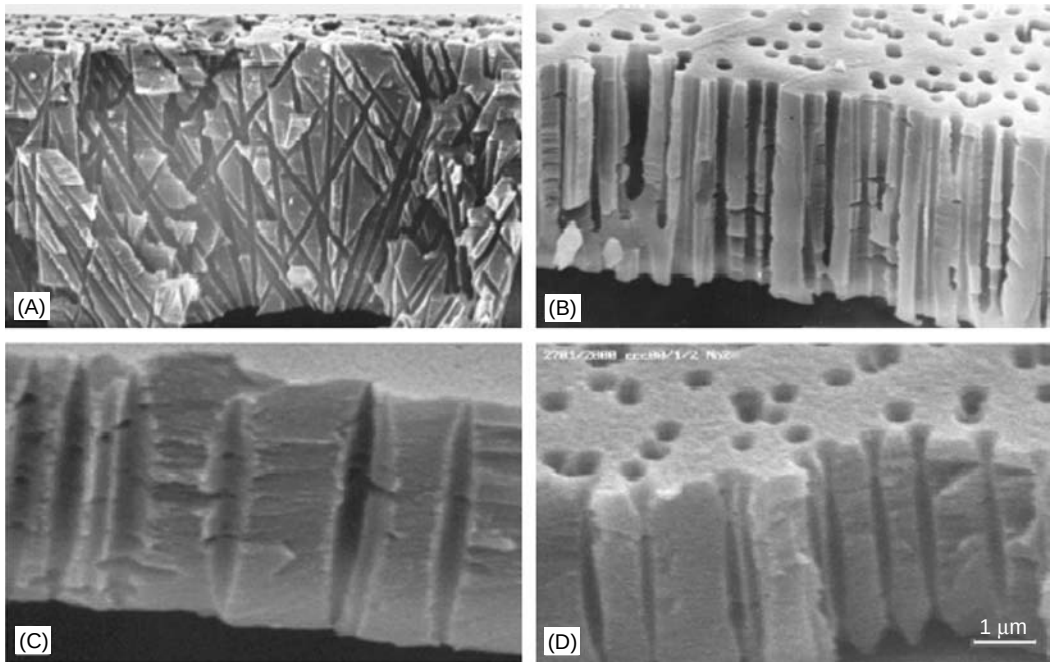

FIGURE 21.2 Different pore shapes that could be obtained by track etching: (A) cylinder; (B) cone; (C) cigar; and (D) bow tie. From Apel, P., *Radiat. Measure.*, 34, 559–566, 2001. With permission.

The uniqueness of TM is that the number of pores (or porosity) and the pore size can be tuned independently. In addition, a narrow PSD can be obtained. Track-etched membranes with pores in the range of 10 nm to 10µm and a pore density of 1 to $10^{10}\,cm^{-2}$ have been reported. In general, the pore channels and their distribution can be precisely tailored using this method. However the pore density and porosity obtained are generally low and this limits the permeant throughput that can be achieved.

The modification procedures to tailor the pore interface activity and interaction effects to impart new functionality on the TMs have also been reported.[7] Modification procedures such as (1) physical adsorption of small or large molecules on the surface, (2) plasma treatment, (3) grafting using covalent reactions, and (4) radiation-induced grafting have been used for this purpose.

21.2.2 TEMPLATES

In these methods, a template is used to design the nanoporous attributes of the polymer. Templates are defined as a molecule, a phase, or any nanostructure around which the polymer is formed. Generally, the templates are leached out to obtain the nanoporous polymer. Alternatively, in some cases, templates with inherent nanopores are used. This section is further divided on the basis of the type of template, i.e., into systems that use micelles, molecules with nanopores (nanotemplates), molecules with specific interactions (molecular imprinting), self-assembled nanostructures, and hyperbranched polymers.

21.2.2.1 Micellar Imprinting

In this technique,[12–14] nanoporous polymers are prepared by forming reverse micelles in a mixture of monomers, cross-linkers and water. The reverse micelles are formed by stabilizing the organic phase (continuous) and aqueous phase (dispersed) using surfactants.

One such system was used by Zhu et al.[12,13] with styrene and divinylbenzene as the monomer and cross-linker and sodium *bis*(2-ethylhexyl) sulfosuccinate (AOT) as the surfactant. The schematic representation of this system and the steps involved in this method are shown in Figure 21.3. The size of the micelles here was controlled by varying the water to surfactant molar ratio. Subsequently, the monomers were cross-linked to form a polymer matrix around these micellar structures. The reverse micelles are then leached and extracted from this matrix to get the nanoporous polymer. The micelle size directly influenced the pore size, surface area, porosity, and PSD of the final matrix.[12,13] Figure 21.4[12] shows the PSD for the nanoporous polymers synthesized using different water to surfactant ratio. As seen in this figure, increasing the water content (R2>R1) increases the overall pore sizes.

21.2.2.2 Nanotemplates

Ma and Li[15] synthesized nanoporous polymers by reacting cyclodextrins (CDs) with di-isocyanato compounds. CD has a characteristic toroidal shape, which forms a well-defined cylindrical nanocavity. The di-isocyanato compounds used were hexamethylene di-isocyanate (HDI) and toluene 2,6-di-isocyanate (TDI). Three-dimensional cross-linked structures interconnected with CD nanochannels were formed. Nanoporosities of these networks were determined by solute rejection methods using molecules of different structures and sizes. A PSD of 0.7 to 1.1 nm was reported based on this method. Ma and Li[16,17] in some of their other works showed that such nanoporous networks can be used to remove traces of organic contaminants from water.[15–18]

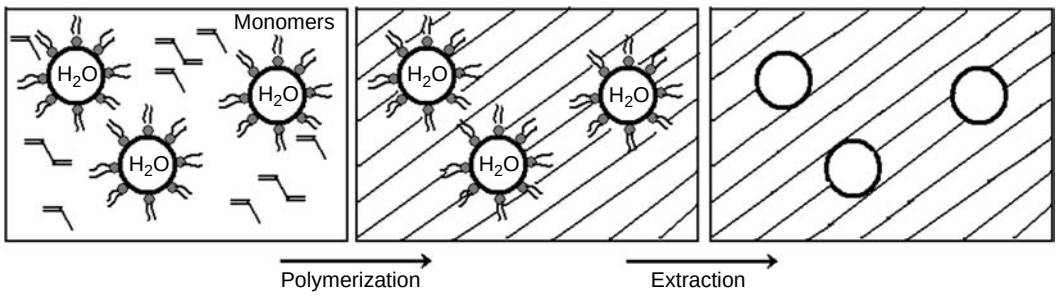

FIGURE 21.3 Schematic of the micellar imprinting technique.

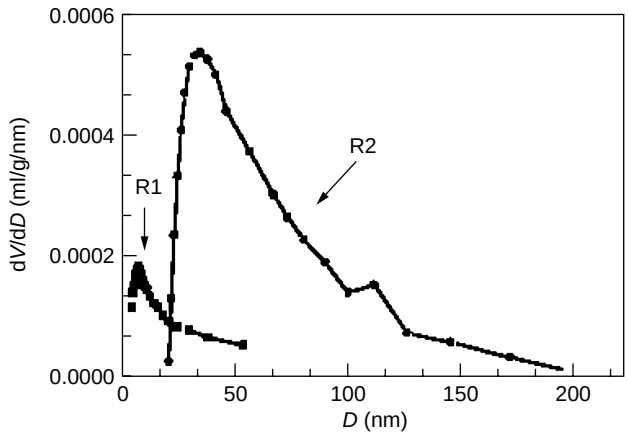

FIGURE 21.4 Distribution of pore diameters (BET method), showing that increasing the water to surfactant ratio (R2>R1) increases the size of the micelles and thereby increases the pore sizes. From Zhu, X.X., Banana, K., and Yen, R., *Macromolecules*, 30, 3031–3035, 1997. With permission.

21.2.2.3 Molecular Imprinting

The molecular-imprinting technique[19–27] involves formation of template–monomer complexes followed by subsequent polymerization. During polymerization, the geometry of the self-assembled template–monomer complex is captured in the growing polymer matrix. Removal of the templates leaves behind cavities possessing a shape and an arrangement of functional groups similar to that of the template. Thus, molecular imprinting is an effective way to introduce specific selectivity and molecular recognition in the polymer matrix. Piletsky et al.[19] have comprehensively reviewed the work in this field. Molecularly imprinted polymers find wide-spread applications in the field of separation membranes[20] and biosensors.[21,22] Sometimes, the molecular-imprinting technique is used in conjunction with phase-separation techniques (discussed later)[23,24] to obtain porous materials with specific recognition sites.

21.2.2.4 Self-Assembly of Diblock Copolymers

A di-block copolymer[28–32] consists of two dissimilar homopolymers covalently linked together at one end. The thermodynamic incompatibility of the di-block copolymer causes self-assembly into ordered, periodic arrays of spheres, cylinders, or lamellae depending on the volume fraction of the components. These self-assembled domains form the nanostructures that are used as templates. The nanoporous polymers are obtained by selectively leaching these self-assembled nanostructures.

Zalusky et al.[28] used the polystyrene (PS)–polylactide (PLA) copolymer that self-assembled into hexagonally packed nanocylinders of PLA in a PS matrix. Figure 21.5[28] shows the steps involved in designing nanoporous polymers using this method. The self-assembled structures are usually aligned through reciprocating shear or shear flow. Other methods such as extrusion, oscillatory shear, roll casting, electric fields, and temperature gradients are also reported for microstructural alignment. The resulting cylindrical PLA domains are hydrolytically degraded using 0.5 M sodium hydroxide water and methanol solution to obtain the nanoporous polymer.

The domain sizes of the original block copolymer dictate the pore size characteristics of the nanoporous polymer. The domain sizes can be directly modified by changing the block copolymer

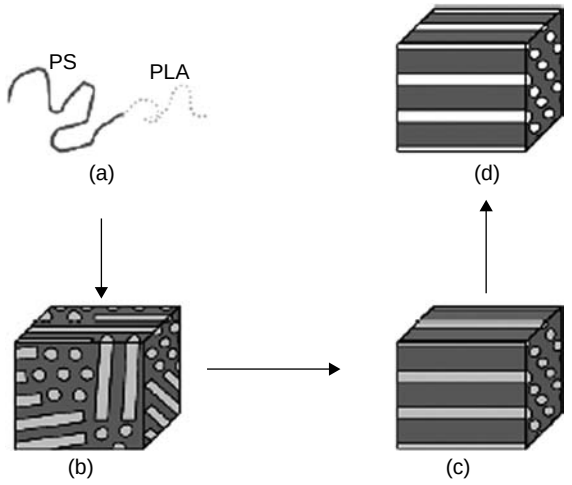

FIGURE 21.5 Schematic showing the methodology used to design nanoporous polymers: (a) PS-PLA di-block copolymer; (b) self-assembled cylindrical morphology; (c) cylindrical morphology after shear alignment; and (d) nanoporous polymers obtained after hydrolytic removal of PLA. From Zalusky, A.S., Olayo-Valles, R., Wolf J. H., and Hillmyer, M.A., *J. Amer. Chem. Soc.*, 124, 12761–12773, 2002. With permission.

molecular weights. An alternative method of blending a homo-polymer to tailor the pore sizes was also reported by Zalusky et al.[28] In this method, the PS-PLA di-block copolymer is blended with hydroxyl terminated PS (PSOH). The homo-polymer (PSOH) swells the domains and thereby influences the pore sizes. Figure 21.6[28] shows how the pore sizes of the nanoporous polymers were tailored in these systems. In this figure, a, b, and c show the influence of molecular weight on the nanoporous morphology and d shows the influence of blending PSOH into these systems. Pore sizes in the range of 15 to 45 nm were reported for these systems.

Xu et al.[30] used an asymmetric di-block copolymer of PS and poly (methylmethacrylate) (PMMA) to obtain such nanoporous morphologies. Cylindrical domains of PMMA in PS matrix were obtained. These domains were aligned by controlled interfacial interactions and applied electric fields. Exposure to deep UV radiation degraded the PMMA domains and cross-linked the PS matrix. After rinsing with a selective solvent, a nanoporous film was obtained. The pore sizes were controlled by changing the molecular weight of the polymer. Nanoporous films with hexagonal arrays of pores with diameters ranging from 14 to 50 nm and separation distances from 24 to 89 nm were reported. Similarly, Drzal et al.[29] synthesized nanoporous polymers using a blend of semicrystalline di-block compolymer of ethylene and ethylene-propylene and 1,4-polyisoprene homopolymer. Wolf and Hillmyer[31] used a hydrogenated form of PS, polycyclohexylethylene (PCHE) and PLA di-block copolymer.

Zalusky et al.[28] delineated the following common features and limitations of this method: (1) preparation procedure is generally restricted to thin films ($<10\,\mu m$) and (2) identity and accessibility

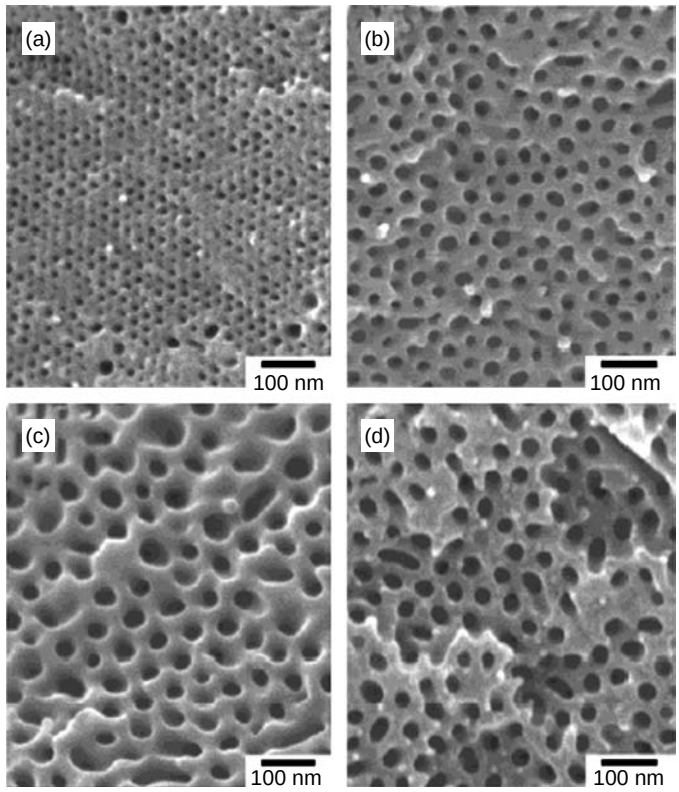

FIGURE 21.6 SEM micorgraphs showing that the pore size can be tailored by changing the molecular weight of the di-block copolymer and by blending a homopolymer (PSOH). (a)–(c) represent the nanoporous morphology obtained with increasing molecular weights and d represents the morphology obtained by blending PSOH. From Zalusky, A.S., Olayo-Valles, R., Wolf J.H., and Hillmyer, M.A., *J. Amer. Chem. Soc.*, 124, 12761–12773, 2002. With permission.

of the functionality in the pore wall has not been established, or in other words, the pore interface chemistry and activity is difficult to control.

21.2.2.5 Hyperbranched Polymers or Dendrimers

Hyper-branched polymers or dendrimers are also used as templates.[33–35] In this method, nanoporous materials are synthesized by preparing a nanophase mixture of organic and inorganic compounds, such as functionalized hyper-branched polymers in low-molecular-weight silsesquioxanes (SSQ). The organosilicate precursor (SSQ) is subsequently vitrified around these dendrimeric templates that are thermally decomposed (~450°C) to form the nanoporous material.[33] Generally, these systems would be expected to phase-separate due to the incompatibility of organic and inorganic phases. Such phase separations would result in random nanoporous morphologies, unlike, the ordered morphologies that are usually formed in these techniques. It is believed that in hyper-branched systems phase-separation effects are hindered due to the limited mobility and low chain entanglement characteristics as well as the increased number of end groups and functionality of branched architectures. This method of inducing nanoporosity is being explored to design low-dielectric ($\kappa < 2$) nanoporous poly(methylsilsesquioxane) for the microelectronics industry. [34]

21.2.3 Solvent As Porogen

In this method, solvent is used as a pore-generating agent (porogen). The solvent is the component present in the system that influences the final porous morphology by its solubility and diffusivity. The primary role of the solvent is to induce phase-separation mechanisms in the system. Such phase-separation mechanisms usually form the final nanoporous morphology. In this category of methods, a polymer–solvent or monomer–polymer–solvent system phase separates to form a polymer and a solvent-rich phase. The polymer-rich phase forms the matrix of the nanoporous material and the solvent-rich phase forms the pores. Conventionally such phase-separation techniques are used to obtain polymers with pore sizes greater than 1 μm.[36–38] In this chapter, we discuss some of the research efforts where phase-separation techniques are used to obtain nanoporous polymers and briefly describe the principles of phase separation on which these systems are based. The two important parameters that influence the final porous morphologies in this technique are the solvent quality (solubility) and quantity (solvent content). The systems in this category are further divided into nonreactive and reactive systems.

21.2.3.1 Nonreactive Systems

These systems depend upon controlled phase separation of a polymer solution to form nanoporous morphologies. On the basis of the method of inducing phase separation these systems are further divided into thermally induced phase separation (TIPS) and diffusion induced phase separation (DIPS). Van de Witte et al.[39] extensively reviewed the experimental and theoretical research in understanding the mechanisms of pore formation. Generally, the final porous morphology depends upon the mechanisms of phase separation and phase transitions as well as diffusion and mass transfer characteristics of the system. Van de Witte et al. reviewed various phase transitions including liquid–liquid de-mixing, crystallization, gelation and vitrification, and diffusion mechanisms such as coalescence and Ostwald ripening, that could occur in these systems. In addition, this review discusses how an extensive knowledge of phase transitions and coarsening phenomena is required to understand and optimize the porous morphologies obtained using this technique.

21.2.4 TIPS

TIPS technique is based on the principle that the solvent thermodynamic quality (solubility) depends upon temperature, i.e., heat is utilized as a latent solvent to induce phase separation.

Solvent quality can be decreased by either decreasing the temperature (UCST) or by increasing the temperature (LCST). Mostly, UCST systems are used in this technique.

Tsai and Torkelson,[40,41] showed that under certain conditions nanoporous polymers with pore sizes $<0.1\,\mu m$ (100 nm) can be formed using a solution of poly(methylmethacrylate) (PMMA)-sulfolane. They compared and contrasted the morphologies obtained via two distinct phase-separation mechanisms namely bi-nodal decomposition (nucleation and growth) and spinodal decomposition. The temperature–composition plot for a polymer solution with UCST as shown in Figure 21.7 could be used to understand these mechanisms that form the porous morphologies. Points A, B, C, and D in Figure 21.7 represent homogeneous solutions with increasing polymer concentration. The region under the bi-nodal curve (thick curve in Figure 21.7) represents a two-phase region where the homogeneous polymer solution phase separates into polymer-rich and polymer-lean phase (miscibility gap) upon decreasing the temperature. The dotted curve is the spinodal curve that divides the two-phase region into metastable and unstable states. The region under the spinodal curve represents the unstable state and region between spinodal and bi-nodal curve represents the metastable state. The significance of the metastable and unstable states is that the mechanisms by which phase separation takes place are different. The initial compositions and the temperatures through which the system passes determine the mechanism of phase separation in these systems. For example, when the temperature of the polymer solution of composition A is reduced to induce phase separation, the system undergoes de-mixing in metastable region by bi-nodal decomposition via nucleation and growth of polymer-rich phase as shown on the left-hand side of Figure 21.7. Similarly, the de-mixing of polymer solution of composition D takes place by bi-nodal decomposition via nucleation and growth of polymer-lean phase. In contrast, the polymer solution of critical composition C when quenched passes through the critical point and the phase separates purely by spinodal decomposition, which usually results in an interconnected morphology. Thus by varying the temperature and composition of the polymer solution, de-mixing can be carried out via different phase-separation mechanisms that form the nanoporous morphologies.

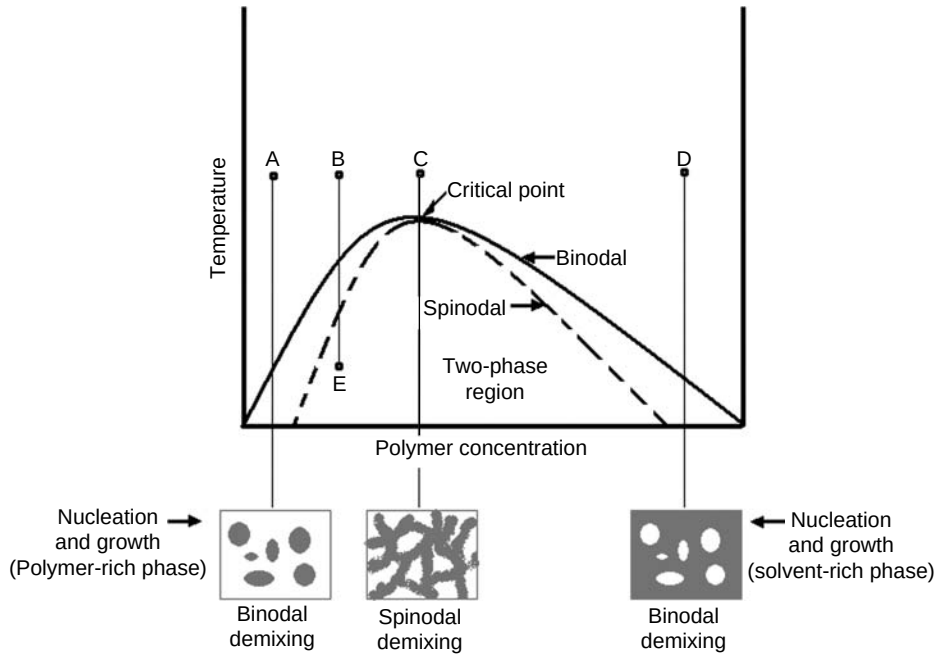

FIGURE 21.7 Phase diagram for a binary polymer–solvent system, showing the two primary phase separation mechanisms (i) bi-nodal de-mixing (A, D) and (ii) spinodal de-mixing (C).

Point B represents a typical polymer solution used in the synthesis of nanoporous polymers using the above technique. This solution when cooled along the path BE, passes through both the metastable region where de-mixing takes place by bi-nodal decomposition, and then through the unstable region where de-mixing takes place by spinodal decomposition. Thus, the cooling rate would be an important parameter in determining the final porous morphology. If the cooling rate is high, phase separation would be predominately by spinodal decomposition. In contrast, if the cooling rate is slow enough for the formation of a nucleus, phase separation would be dominated by bi-nodal decomposition. Figure 21.8[40] compares the porous morphologies that were obtained using bi-nodal and spinodal decompositions. The sample phase separated by bi-nodal decomposition (top, Figure 21.8) showed a beaded structure, whereas the sample phase separated by spinodal decomposition (bottom, Figure 21.8) showed a characteristic interconnected or bi-continuous structure.

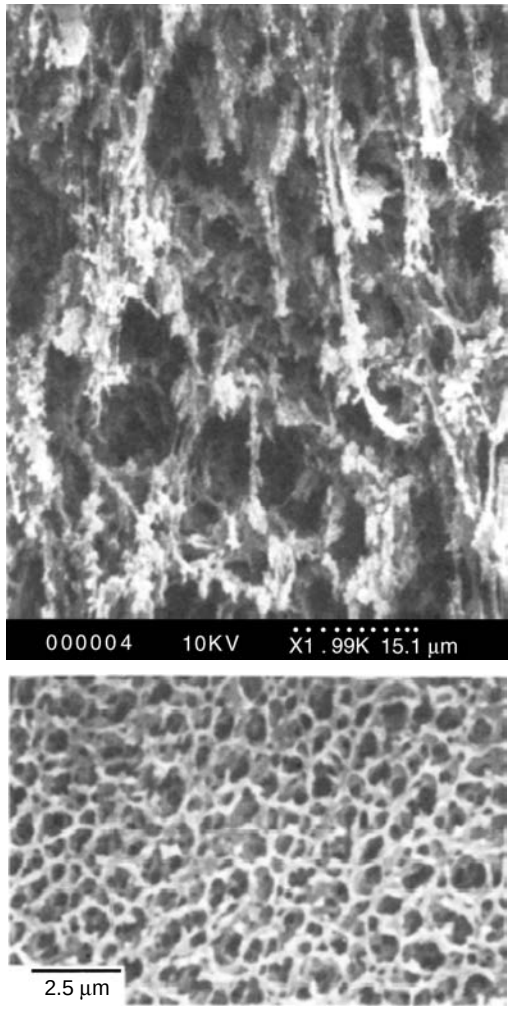

FIGURE 21.8 SEM micrographs of porous morphology obtained by bi-nodal (top) and spinodal (bottom) decomposition. Bi-nodal decomposition yields a beaded structure whereas spinodal decomposition yields a characteristic interconnected or bi-continuous structure. From Tsai F. and Torkelson, J.M., *Macromolecules*, 23, 775–784, 1990. With permission.

The other important factor is the quenching period, i.e., the amount of time allowed to attain equilibrium conditions. During this period, diffusion mechanisms like ripening and coalescence that result in the densification of these morphologies become important.

21.2.5 DIPS

In the DIPS technique,[42–43] diffusion of nonsolvent into the polymer–solvent system or diffusion of solvent out of the polymer–solvent–nonsolvent system induces the phase separation. In the former case, the nonsolvent diffusing into and in the latter the solvent diffusing out of the system cause the reduction in solubility necessary for phase separation. Similar to the binary-phase diagram in TIPS, a ternary-phase diagram can be used to understand the phase-separation mechanisms that form the porous morphologies in these systems.

Stephan and Teeters[42] showed the influence of the chemical structure and diffusion characteristics of the nonsolvent on the nanoporous morphologies obtained using the DIPS technique. The polymer poly(vinylidene fluoride-co-hexafluoropropylene) (PVdF-HFP) was used in this work. Acetone was the solvent and was more volatile than the nonsolvents such as pentane or 1-butanol. The resulting solutions of PVdF–acetone–pentane and PVdF–acetone–1-butonal were cast as films on a glass substrate and the solvent was allowed to evaporate under ambient conditions. As acetone evaporates, phase separation of the polymer from the solution takes place. It was reported that a homogeneous phase with uniformly sized pores was obtained when the linear aliphatic nonsolvent, pentane, was used. In contrast, flaky surfaces with unevenly- sized pores were reported for systems with 1-butanol. An average pore size of 12 nm and specific surface area of 120 m^2/g were obtained using pentane as the nonsolvent, whereas an average pore size of 40 nm and specific surface area of 48 m^2/g were reported for systems with 1-butanol. Thus, Stephan and Teeters demonstrated that the nanoporous morphologies can be tailored by changing the type of non-solvent used. It is speculated that the difference in the interaction effects between the polymer and the nonsolvents (pentane and 1-butanol) and the difference in the diffusion characteristics of the nonsolvent caused the morphological differences observed.

21.2.6 Carbon Dioxide Foaming

Foaming of polymers using blowing agents has been widely used to synthesize closed cell foams with pore sizes $>1\,\mu m$.[44] Krause et al.[45–47] used such foaming techniques to design interconnected nanoporous structures. The basic steps involved in this technique were summarized by Krause et al.[45] as follows: (1) saturation of the polymer with a gaseous penetrant (blowing agent), usually supercritical or gaseous carbon dioxide (CO_2), at high pressure, (2) followed by quenching of the polymer and gas mixture into a supersaturated state by either reducing the pressure or increasing the temperature, and finally (iii) nucleation and growth of gas cells dispersed throughout the polymer sample as forces driving the mass transport mechanisms vanish. In this method, supercritical or gaseous CO_2 plays the role of a solvent. The advantage of this method is that the final nanoporous polymers obtained do not have potentially toxic and volatile residues in contrast to other phase-separation techniques that are based on organic solvents. Krause et al.[45] foamed thin extruded poly(ether imide) (PEI) and poly(ether sulfone) (PES) films with CO_2 to obtain bi-continuous nanoporous polymers. SEM micrograph of one such structure is shown in Figure 21.9.[46] The pore sizes of this sample were reported to be in the range 20 to 50 nm.

Krause et al.[46] also showed that blends of polysulfone and polyimide can be used to obtain similar nanoporous structures.

21.2.6.1 Reactive Systems

In these systems, the monomers are dissolved in a solvent and subsequently polymerized. The polymers formed are usually insoluble in the solvent and thus phase separate to form the porous structure. This method is also known as polymerization-induced phase separation (PIPS) technique.

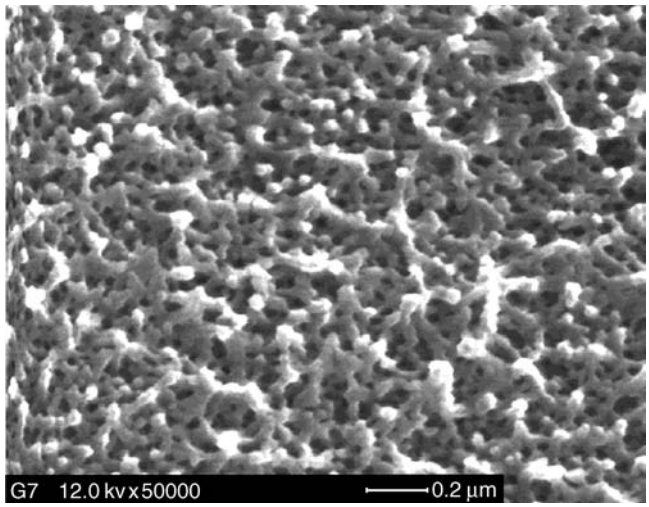

FIGURE 21.9 The bi-continuous nanoporous structure of poly(ether imide) obtained by carbon dioxide foaming. From Krause, B., Sijbesma, H.J.P., Munuklu, P., van der Vegt, N.F.A., and Wessling, M., *Macromolecules*, 34, 8792–8801, 2001. With permission.

21.2.7 PIPS

In this category, conventionally porous polymers were synthesized by suspension polymerization. As a result, the porous materials obtained were in the form of spherical beads, which in turn are formed by aggregated interconnected globules. Distributions of voids and pores are obtained using this method. In general, the voids located between beads are macroporous (>50 nm), those between the globules of a given bead are mesoporous (2 to 50 nm) and those within the globules themselves are microporous (<2 nm).[48] There is some equivocalness in this literature about the usage of the word "macroporous." Macroporous as used here might mean materials that remain porous even in their dry state and may not refer to the pore sizes of these materials.

Svec and Frechet[48] used a reactive system to obtain nanoporous polymers in the form of monoliths having bi-modal distribution of pores with large channels (1000 nm) and more conventional diffusive nanopores. Such monoliths were used for chromatographic applications. In this work, Svec and Frechet compared the systems that form monoliths with those that form beads (suspension polymerization) for the same processing conditions. It was observed that the PSD and the median pore size of the beads and monoliths were significantly different. Such observed differences in the porous morphologies were attributed to the differences in the mechanisms of pore formation. Generally, the final nanoporous morphologies are formed by the fundamental mechanisms of phase separation and polymerization that take place in these systems. Thus, both the thermodynamic and kinetic parameters such as the quality of porogenic solvent, solvent composition, polymerization temperature, and the amount of cross-linking agent, etc. influence the nanoporous structures and morphologies in these systems. Svec and Frechet[48] synthesized porous monoliths using glycidyl methacrylate and ethylene dimethacrylate as monomers and a mixture of cyclohexanol and dodecanol as the solvent. The polymerization reaction in these systems was based on thermally initiated free-radical mechanisms. In their work, they discuss the influence of porogenic solvent and polymerization temperature on the PSD of the monoliths. In an effort to show the influence of the structure of monomeric units on the porous morphology, Svec et al.[49] carried out work comparing two monomer pairs, styrene–divinylbenzene and glycidyl methacrylate–ethylene dimethacrylate, for synthesizing monoliths. They discussed how the variables, such as temperature, composition of the porogenic solvent, and the extent of cross-linking allow for the facile tailoring of average pore sizes in

these monoliths. In their other work, Svec et al.[50] showed that nanoporous monoliths could be synthesized using photoinitiated reaction mechanisms.

Cooper and Holmes[51] synthesized nanoporous monoliths by polymerizing ethylene glycol dimethacrylate (EDMA) or trimethylolpropane trimethacrylate (TRM) in the presence of supercritical carbon dioxide (SCO_2) as the porogenic solvent. An attractive alternative as a solvent is SCO_2 as its diffusivity and solubility can be tuned over a wide range by simply changing the pressure. In addition, SCO_2 reverts to the gaseous state upon de-pressurization, simplifying separation of solvent from the polymer and eliminating solvent residues. Cooper and Holmes[51] reported materials with median pore sizes of <100 nm for monomer concentrations of 50 vol% and above. Cooper et al.[52, 53] also used 1,1,1,2-tetrafluoroethane (R134a) as the porogenic solvent instead of SCO_2 to synthesize such monoliths.

The resorcinol–formaldehyde[54–57] (RF) and melamine–formaldehyde[58] (MF) systems that are based on simultaneous addition and condensation polymerization mechanisms form a class of its own. In these systems, the accepted mechanisms of pore formation are based on simultaneous microphase separation and polymerization. And depending upon the extent of microphase separation, these systems are classified into "polymeric" and "colloidal" RF gels.[54] Both aqueous and organic solvents are used in these systems. In general, RF- and MF-based gels are supercritically dried after gelation. The resulting materials, called organic aerogels, find wide-spread applications due to their physical,[59] and optical properties. In some cases, these organic aerogels are pyrolyzed to get nanoporous carbon aerogels,[60] Al-Muhtaseb and Ritter[54] have reviewed the literature on RF gels extensively and explained how the nanostructures of these gels can be controlled by adjusting the synthesis and processing conditions. The important parameters in these systems are catalyst concentration, initial pH, and monomer concentration.

Kabra et al.[61] synthesized nanoporous hydroxypropyl cellulose (HPC) gels, where they subjected the reacting system to a temperature cycle above and below the LCST. In doing so, they were able to control the extent of phase separation in this system. Thus, they have integrated the principles of TIPS and PIPS techniques for designing nanoporous structures.

21.2.8 Microemulsion Systems

In microemulsion systems,[62–65] instead of a homogeneous monomer solution, a microemulsion of monomers, a solution of water and surfactant is used as the precursor solution. microemulsions are thermodynamically stable, transparent, isotropic liquids consisting of water and oil (monomers) phases stabilized by a surfactant or a combination of surfactant and co-surfactant.[62] The final porous morphology formed in this system usually depends upon the microstructure of the micro-emulsion and any phase separation that occurs during polymerization. In a sense, the principles of templating (microstructure of the micro-emulsion) and phase-separation techniques are simultaneously used in these systems to control the final nanoporous morphology.

Gan and Chew[63] used micro-emulsion systems based on water, methyl methacrylate, 2-hydroxyethyl methacrylate, and surfactants. They used two different types of surfactants: ones that are polymerizable and those that are nonpolymerizable. With the nonpolymerizable surfactants like sodium dodecyl sulfate (SDS) or n-alkyltrimethyl-ammonium bromide (C_nTAB), opaque polymer composites showing phase separation during polymerization were obtained. In these systems, porous morphologies ranging from globular to bi-continuous structures were observed. Gan and Chew[63] showed the influence of water, surfactant, and monomer concentrations on these morphologies. For cationic C_nTAB microemulsions, the effect of alkyl chain length of C_nTAB ($n = 12$, 14, and 16) was found to be significant. Figure 21.10[63] shows this effect where the pore-volume distribution curves for systems with surfactants of increasing chain lengths, $n = 12$, 14, and 16 are plotted. PSDs were found to be in the range of 5 to 20 nm (in radius) for a sample containing C_{12}TAB, 5 to 50 nm for the one containing C_{14}TAB, and 10 to 100 nm for the C_{16}TAB-based system, thus showing that changing the alkyl chain length of the surfactant provides a facile way of tailoring the median pore sizes and PSD in these systems.

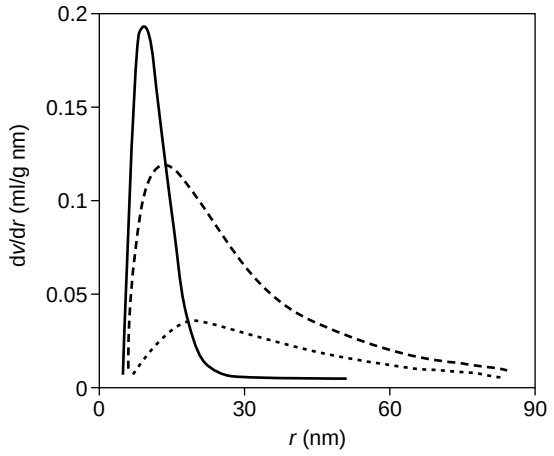

FIGURE 21.10 Effect of alkyl chain length of cationic nonpolymerizable surfactant (C_nTAB) on the pore sizes and PSDs of nanoporous materials synthesized using microemulsion systems:——, C_{12}TAB; −−−−, C_{14}TAB; and, ·····C_{16}TAB. From Gan, L.M. and Chew, C.H., *Colloids and Surfaces A: Physicochem. Eng. Aspects*, 123–124, 681–693, 1997. With permission.

Gan et al.[63,64] also worked with polymerizable surfactants to obtain transparent polymers i.e., systems with reduced phase separation during polymerization. In such systems, the final porous morphologies would primarily depend upon the micro-structure of the precursor solution. Four different types of surfactants such as anionic, cationic, zwitter-ionic, and nonionic systems were studied; mostly bi-continuous structures were reported for these systems. Palani Raj et al.[65] and Gan et al.[62] are some of the other works in which micro-emulsion systems were used.

21.2.9 Miscible Systems

Until now, the systems in which the solvent is used as a porogen, where it affects the final nanoporous morphology by influencing the phase-separation mechanisms, polymerization kinetics (reactive), and diffusion characteristics of system have been discussed. In our laboratory, we designed nanoporous polymers using a homogenous system by carrying out the polymerization without any micro- and macroscopic phase separation.[66–67] This was possible because the polymer formed could interact favorably with the solvent (negative ΔH_{mix}) and remain miscible throughout the polymerization. Thus for a cross-linking system, the growing polymer network would encapsulate the solvent and form nanoporous gels, whose typical pore dimensions can be tailored by changing the solvent content. Controlling the pore size is much more straightforward in this case where the final morphology does not depend upon phase-separation mechanisms. Instead, they are primarily governed by polymerization kinetics. A system based on cross-linking epoxy-amine monomers in the presence of tetrahydrofuran (THF) as the miscible and inert solvent was used. The polymer network in this system is formed by step-growth polymerization unlike most phase-separating systems that are based on free-radical polymerization. Generally, the step-growth mechanisms result in homogenous network structures, which could be important in a miscible system like ours where the solvent would influence the molecular connectivity of the polymer network and thereby affect the nanoporous structures formed in this system. In effect, this method can be perceived as a transition in the role of the solvent from being a porogen (i.e., by phase separating in the system) to being a template. The nanoporous gels synthesized using this method were supercritically dried and the nanoporous structures of the resulting organic aerogels were analyzed using SEM. Figure 21.11 shows the SEM micrographs of epoxy-amine samples synthesized using increasing THF content: 0:1, 4:1, 6:1, and 8:1 solvent to monomers by weight, respectively. These micrographs show that the pore size and porosity of these aerogels can be tailored

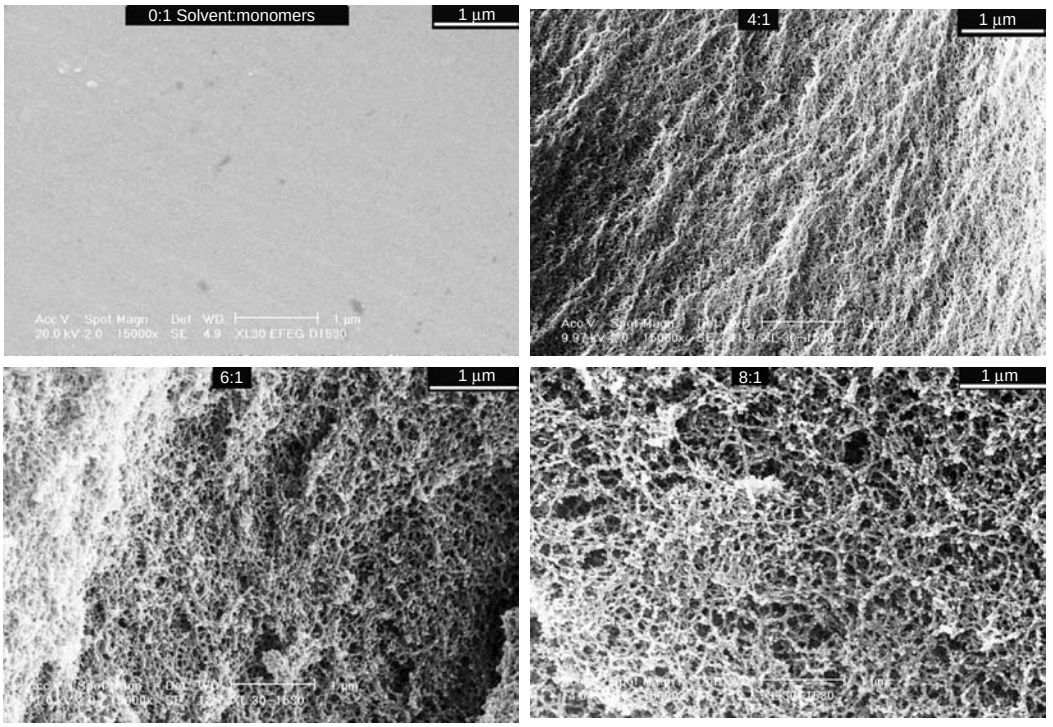

FIGURE 21.11 SEM micrographs of epoxy amine samples synthesized using increasing solvent content, (0:1, 4:1, 6:1, and 8:1 solvent to monomers by weight), showing that solvent content influences nanoporous structures by changing the pore sizes and porosity (15,000×). From Raman, V.I. and Palmese, G.R., *Langmuir,* 21: 1539–1546 (2005). With permission.

by changing the solvent content. Furthermore, bi-continuous or interconnected morphologies are observed in this system. Nanoporous organic aerogels with average pore sizes ranging from 1 to 50 nm and porosities of 0 to 80% were obtained using this technique.

21.3 POTENTIAL APPLICATIONS FOR NANOPOROUS POLYMERS

21.3.1 POLYMER ELECTROLYTE MEMBRANES FOR FUEL CELLS

A fuel cell is an electrochemical device that converts chemical energy of a fuel-oxidation reaction directly into electrical energy with high efficiency. Thus, fuel cells can potentially replace combustion engines due to their cleanliness and high-energy efficiency. Nanoporous polymers find a potential application as an electrolyte between the electrodes in fuel cells, akin to a liquid electrolyte used in a conventional electrochemical cell. The polymer electrolyte provides the mechanical integrity and chemical stability required for these applications; in contrast, the transport properties of the polymer electrolytes are much lower when compared with liquid electrolytes. Thus, design of polymer electrolytes for fuel cell application entails designing nanoporous polymers with pore channels that would facilitate the desired transport mechanisms, i.e., high proton (H^+) transfer while reducing the amount of fuel transfer. Apart from the pore size and structure of the pore channels, the H^+ transport through nanoporous polymer depends on the ionic groups present at the pore interface that can exchange H^+ ions with the solution present in the pore channel. The proton transport in such membranes is usually based on sulfonic acid group electrolyte chemistry with water as the medium of transport in the pore channel. Peled et al.[2] have used one such nanoporous proton-conducting membrane for fuel cell application. Vorrey and Teeters[68] designed polymer electrolytes by confining PEO to the nanoporous

channels of track-etched polycarbonates. Similar to proton conduction principles in nanoporous channels, Liu et al.[3] showed that nanoporous polymers can be used for Li^+ ion transport for lithium battery applications. The nanostructures of these materials were designed using phase-separation techniques.

21.3.2 Separation Membranes

The membrane separation processes are more energy- and time efficient than conventional separation techniques. The general principles on which membrane separation processes work are shown in Figure 21.12. As shown, a mixture of permeants with different sizes can be separated using a nanoporous membrane by sieving effect, whereas a mixture of permeants with different thermodynamic activity, for example molecules with charged group, can be separated based on their interactions with the nanoporous membrane. In most applications, both of these principles are used simultaneously to get the desired selectivity in separation. Polymeric membranes have been developed for industrial applications such as microfiltration, ultrafiltration, reverse osmosis, and gas separation.[39] Depending upon the application, specific requirements are imposed on the structural and thermodynamic attributes of nanoporous polymer. For example, in microfiltration and ultrafiltration applications the efficiency of separation depends upon the controlled pore size and porosity of the membrane, whereas for gas separation the selectivity and the thermodynamic interactions between the permeants and pore interface determines the efficacy of separation.[39] The nanoporous membranes used for these applications are usually obtained by phase-separation techniques. A system based on micro-emulsion was used by Li et al.[69] to design ultrafiltration membranes.

21.3.3 Template for Nanostructures/Nanomaterials Synthesis

Nanoporous polymers are used as templates and substrates for synthesizing nanostructured materials.[1,70] Such materials find applications in the field of optical, mechanical, and chemical devices. The underlying principle of synthesizing nanomaterials using nanoporous polymers as templates is akin to that of producing components using replication, e.g., die-casting or mold casting.[1] Generally, controlled pore sizes and shapes are required to obtain nanostructured material with desired structure and property. Ferain and Legras[71] used track-etched polyimide membrane as templates for the fabrication of polymeric nanowires and tubules, as shown in Figure 21.13.[71]

21.3.4 Nanocomposites

Another potential application of nanoporous polymers is in designing functional nanocomposites. The advantages of such composite systems lie in the fact that improved properties could be obtained by forming composites of two significantly different materials (for example, organic and inorganic[5] and hydrophobic and hydrophilic) at the nanoscopic level. Figure 21.14 shows the design of such nanocomposites by infusing incompatible materials into nanoporous polymers.

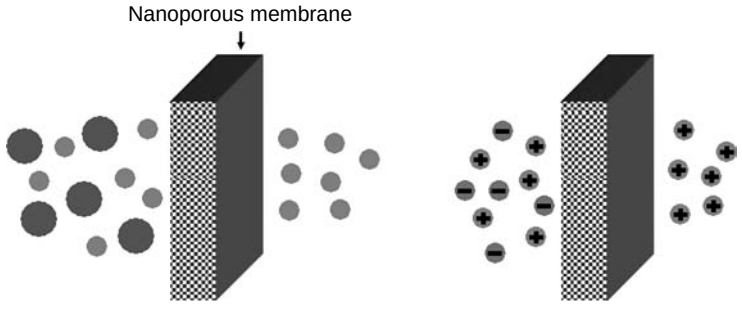

FIGURE 21.12 Separation of permeants based on sieving effect (left) and interaction effect (right), demonstrating the principles involved in separation.

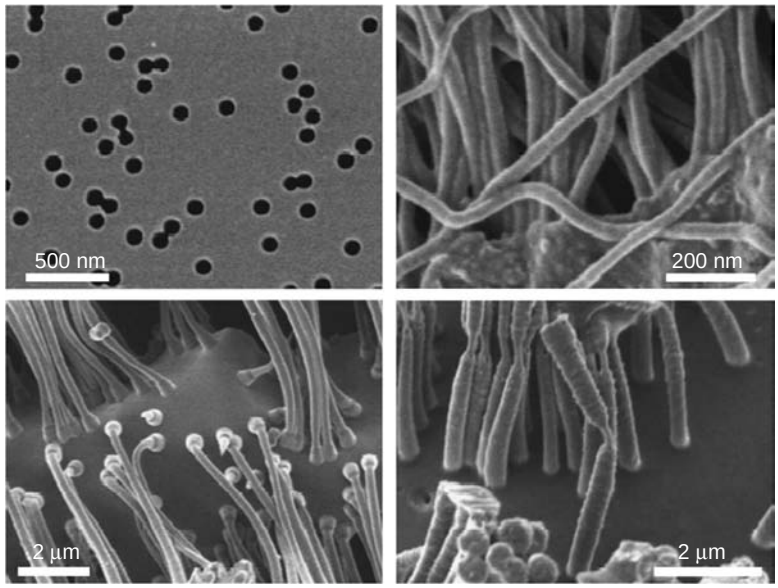

FIGURE 21.13 Nanoporous polyimide track-etch template (upper left). Templates similar to these were used to synthesize cylindrical polypyrrole nanowires (upper right), and templates obtained with specific treatment prior to track etching resulted in new wire shapes (down left and right). From Ferain, E. and Legras, R., *Nucl. Intstr. Meth. Phys. Res.*, B 208, 115–122, 2003. With permission.

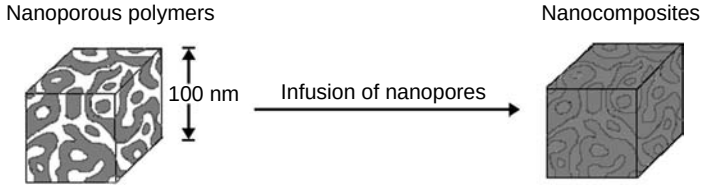

FIGURE 21.14 The application of nanoporous polymers as substrates for nanocomposites design.

Nanoporous polymers for such applications should have specific molecular attributes at the polymer–permeant interface within the pore to facilitate the infusion of dissimilar material. This can be done by tailoring the pore interface interactions by grafting methods. In our laboratory, we have shown that chemical grafting techniques based on Michael's addition of acrylamide and sulfonation of aromatic rings can be used to improve the hydrophilicity of epoxy-amine networks synthesized using a miscible system.[67] Currently, efforts are being carried out to infuse hydrophilic-electroactive materials into this grafted nanoporous substrates for sensing applications. In some cases, the materials infused are monomers that are subsequently polymerized in the nanopores to form the final nanocomposite. In these cases, the nanopores are used as nanoreactors. Baradie et al.[5] synthesized a polymer and inorganic nanocomposite by infusing tetraethyloxysilane (TEOS) into the nanoporous polymer and hydrolyzing TEOS within the nanopores.

21.4 CONCLUSIONS AND FUTURE DIRECTION

In this chapter, methods of designing nanoporous polymers were classified into three main categories: (1) methods with no pore-generating agents (porogen) — track etching; (2) methods that use templates – micellar imprinting, nanotemplates, molecular imprinting, self-assembled nanostructures, and

hyperbranched polymers; and (3) methods that use solvent as porogen — TIPS, DIPS, PIPS, microemulsion systems and miscible systems. The general principles and nanostructure and morphology obtained from each of these methods along with their salient features and limitations were discussed. In general, it is observed that phase-separation techniques have been widely used for designing nanoporous polymers. The use of super-critical carbon dioxide as a solvent in these techniques provides an environmentally safe alternative. Recent advancements are in developing nanoporous polymers using solvent-free techniques such as carbon dioxide foaming and track etching. Furthermore, the miscible systems as discussed in this chapter represent an interesting subset of the methods that use solvent as porogen. Potential applications for nanoporous polymers, such as polymer electrolytes in fuel cells, separation membranes, templates for nanostructures and nanomaterials synthesis, and nanocomposites were also discussed. An important future application of nanoporous polymers would be in nanomaterials and nanostructures design. Oriented and ordered pore structures with narrow PSD are generally required for this application. Track-etching technique, with its ability to provide controlled pore structures with well-defined PSD, is a suitable technique for this application. It can be generally observed that designing nanostructure and morphology has been the primary focus of most research efforts in this field, whereas the design of pore interface chemistry and activity of nanoporous polymers is still not possible with most of these techniques. A future direction would be to tailor the pore interface chemistry and activity of these controlled nanoporous structures for specific applications as discussed above.

REFERENCES

1. S.K. Chakaravarti and J. Vetter, *Radiat. Measure.* 29: 149–159 (1998).
2. E. Peled, V. Livshits, and T. Duvdevani, *J. Power Sources* 106: 245–248 (2002).
3. Y. Liu, J.Y. Lee, E.T. Kang, P. Wang, and K.L. Tan, *React. Funct. Polym.* 47: 201–213 (2001).
4. T.D. Li, L.M. Gan, C.H. Chew, W.K. Teo, and L.H. Gan, *Langmuir* 12: 5863–5868 (1996).
5. B. Baradie, J.P. Dodelet, and D. Guay, *J. Electroanal. Chem.* 489: 101–105 (2000).
6. R.E. Kesting, *Synthetic Polymeric Membranes: A Structural Perspective*, 2nd ed., Wiley, New York, 1985.
7. P. Apel, *Radiat. Measure.* 34: 559–566 (2001).
8. P. Apel, I.V. Blonskaya, A. Didyk, S.N. Dmitriev, O.L. Orelovitch, D. Root, L.I. Samoilova, and V.A. Vutsadakis, *Nucl. Intstrum. Meth. Phys. Res. B* 179: 55–62 (2001).
9. P. Apel, I.V. Blonskaya, O.L. Orelovitch, D. Root, V.A. Vutsadakis, and S.N. Dmitriev, *Nucl. Intstrum. Meth. Phys. Res. B* 209: 329–334 (2003).
10. P. Apel, I.V. Blonskaya, O.L. Orelovitch, D. Root, V. Vutsadakis, and S.N. Dmitriev, *Nucl. Instrum. Meth. Phys. Res. B-Beam Interactions with Materials and Atoms* 209: 329–334 (2003).
11. L.D.D. Pra, E. Ferain, R. Legras, and S. Demoustier-Champagne, *Nucl. Instrum. Meth. Phys. Res. B-Beam Interactions with Materials and Atoms* 196: 81–88 (2002).
12. X.X. Zhu, K. Banana, and R. Yen, *Macromolecules* 30: 3031–3035, 1997.
13. X.X. Zhu, K. Banana, H.Y. Liu, M. Krause, and M. Yang, *Macromolecules* 32: 277–281 (1999).
14. X. X. Zhu, K. Banana, and R. Yen, *Polymer. Mater. Sci. Eng.* 74: 418–19 (1996).
15. M. Ma and D. Li, *Chem. Mater.* 11: 872–874 (1999).
16. D. Li and M. Ma, *Filtrat.Separat.* 36: 26–28 (1999).
17. D. Li and M. Ma, *CHEMTECH* 29: 31–37 (1999).
18. J. Yim, J. Seon, H. Jeong, L.S. Pu, M.R. Baklanov, and D.W. Gidley, *Adv. Funct. Mater.* 14: 277–282 (2004).
19. S.A. Piletsky, T.L. Panasyuk, E.V. Piletskaya, I.A. Nicholls, and M. Ulbricht, *J. Membrane Sci.* 157: 263–278 (1999).
20. M. Yoshikawa, J. Izumi, T. Kitao, and S. Sakamoto. *Macromolecules* 29: 8197–8203, 1996.
21. J. Steinke, I.R. Dunkin, and D.C. Sherrington, *Macromolecules* 29: 407–415 (1996).
22. S.A. Piletetsky, E. Piletskaya, T. Panasyuk, A.V. El'skaya, R. Levi, I. Karube, and G. Wulff, *Macromolecules* 31: 2137–2140 (1998).
23. J. Matsui, T. Kato, T. Takeuchi, M. Suzukit, K. Yokoyama, E. Tamiya, and I. Karube, *Anal. Chem.* 65: 2223–2224 (1993).

24. H.Y. Wang, T. Kobayashi, T. Fokaya, and N. Fujii, *Langmuir* 13: 5396–5400 (1997).
25. M. Yoshikawa, J. Izumi, T. Kitao, S. Koya, and S. Sakamoto, *J. Membrane Sci.* 108: 171–175 (1995).
26. M. Yoshikawa, J. Izumi, and T. Kitao, *React. Funct. Polym.* 42: 93–102 (1999).
27. M. Yoshikawa, T. Ooi, and J. Izumi, *Euro. Polym. J.* 37: 335–342 (2001).
28. A.S. Zalusky, R. Olayo–Valles, J. H. Wolf, and M.A. Hillmyer, *J. Amer. Chem. Soc.* 124: 12761–12773 (2002).
29. P.L. Drzal, A.F. Halasa, and P. Kofinas, *Polymer* 41: 4671–4677 (2000).
30. T. Xu, H. Kim, J. DeRouchey, C. Seney, C. Levesque, P. Martin, C.M. Stafford, and T.P. Russell, *Polymer* 42: 9091–9095 (2001).
31. J.H. Wolf and M.A. Hillmyer, *Langmuir* 19: 6553–6560 (2003).
32. J.H. Wolf and M.A. Hillmyer, *Polym. Preprints* 44: 984 (2003).
33. A. Heise, C. Nguyen, R. Malek, J.L. Hedrick, C.W. Frank, and R.D. Miller, *Macromolecules* 33: 2346–2354 (2000).
34. C. Nguyen, C.J. Hawker, R.D. Miller, E. Huang, J.L. Hedrick, R. Gauderon, and J.G. Hilborn, *Macromolecules* 33: 4281–4284 (2000).
35. S. Jahromi and B. Mostert, *Macromolecules* 37: 2159–2162 (2004).
36. T. Tanaka and D. R. Lloyd, *J. Membrane Sci.* 238: 65–73 (2004).
37. F.J. Hua, T.G. Park, and D.S. Lee, *Polymer* 44: 1911–1920 (2003).
38. Y.S. Nam and T.G. Park, *Biomaterials* 20: 1783–1790 (1999).
39. P. van de Witte, P.J. Dijkstra, J.W.A. van den Berg, and J. Feijen, *J. Membrane Sci.* 117: 1–31 (1996).
40. F. Tsai and J.M. Torkelson, *Macromolecules* 23: 775–784 (1990).
41. F. Tsai and J.M. Torkelson, *Macromolecules* 23: 4983–4989 (1990).
42. A.M. Stephan and D. Teeters, *Electrochim. Acta* 48: 2143–2148 (2003).
43. A.M.W. Bulte, M.H.V. Mulder, C.A. Smolders, and H. Strathmann, *J. Membrane Sci.* 121: 37–49 (1996).
44. L. Singh, V. Kumar, and B.D. Ratner, *Biomaterials* 25: 2611–2617 (2004).
45. B. Krause, H.J.P. Sijbesma, P. Munuklu, N. F. A. van der Vegt, and M. Wessling, *Macromolecules* 34: 8792–8801 (2001).
46. B. Krause, K. Diekmann, N. F. A. van der Vegt, and M. Wessling, *Macromolecules* 35: 1738–1745 (2002).
47. B. Krause, N.F.A. van der Vegt, and M. Wessling, *Desalination* 144: 5–7 (2002).
48. F. Svec and J.M.J. Frechet, *Chem. Mater.* 7: 707–715 (1995).
49. C. Viklund, F. Svec, J.M.J. Frechet, and K. Irgum, *Chem. Mater.* 8: 744–750 (1996).
50. C. Viklund, E. Ponten, B. Glad, K. Irgum, P. Horstedt, and F. Svec, *Chem. Mater.* 9: 463–471 (1997).
51. A.I. Cooper and A.B. Holmes, *Adv. Mater.* 11: 1270–1274 (1999).
52. A.K. Hebb, K. Senoo, and A.I. Cooper, *Compos. Sci. Tech.* 63: 2379–2387 (2003).
53. C.D. Wood and A.I. Cooper, *Polymer. Mater. Sci. Eng.* 84: 125–126 (2001)
54. S.A. Al-Muhtaseb and J.A. Ritter, *Adv. Mater.* 15: 101–114 (2003).
55. E.J. Zanto, S.A. Al-Muhtaseb, and J.A. Ritter, *Ind. Eng. Chem. Res.* 41: 3151–3162 (2002).
56. R.W. Pekala and D.W. Schaefer, *Macromolecules* 26: 5487–5493 (1993).
57. D.W. Schaefer, R. Pekala, and G. Beaucage, *J. Non-Crystal. Solid.* 186: 159–167 (1995).
58. G.C. Ruben and R.W. Pekala, *J. Non-Crystal. Solid.* 186: 219–231 (1995).
59. X. Lu, M.C. Arduini-Schuster, J. Kuhn, O. Nilsson, J. Fricke, and R.W. Pekala, *Science* 255: 971–972 (1992).
60. C.I. Merzbacher, S.R. Meier, J.R. Pierce, and M.L. Korwin, *J. Non-Crystal. Solid.* 285: 210–215 (2001).
61. B.G. Kabra, S.H. Gehrke, and R.J. Spontak, *Macromolecules* 31: 2166–2173 (1998).
62. T.H. Chieng, L.M. Gan, C.H. Chew, and S.C. Ng, *Polymer* 36: 1941–1946 (1995)
63. L.M. Gan and C.H. Chew, *Colloids and Surfaces A: Physicochem. Eng. Aspects* 123–124: 681–693 (1997).
64. T.H. Chieng, L.M. Gan, C.H. Chew, S.C. Ng, and K.L. Pey, *Langmuir*, 12: 319–324 (1996).
65. W.R. Palani Raj, M. Sasthav, and H.M. Cheung, *Langmuir*, 7: 2586–2591 (1991).
66. V.I. Raman and G.R. Palmese, *Colloids Surfaces A: Physicochem. Eng. Aspects* 241: 119–125 (2004).
67. V.I. Raman and G.R. Palmese, *Langmuir*, 21: 1539–1546 (2005).
68. S. Vorrey and D. Teeters, *Electrochim. Acta* 48: 2137–2141 (2003).
69. T.D. Li, L.M. Gan, C.H. Chew, W.K. Teo, and L.H. Gan, *Langmuir*, 12: 5863–5868 (1996).
70. L.M. Bronstein, *Encycl. Nanosci. Nanotech.* 7: 193–206 (2004).
71. E. Ferain and R. Legras, *Nucl. Intstr. Meth. Phys. Res. B* 208: 115–122 (2003).

22 Nanotechnology and Biomaterials

J. Brock Thomas and Nicholas A. Peppas
University of Texas, Austin, Texas

Michiko Sato and Thomas J. Webster
Purdue University, West Lafayette, Indiana

CONTENTS

22.1 INTRODUCTION

Biomaterials have received a considerable amount of attention over the last 30 years as a means of treating diseases and easing suffering. The focus of treatment is no longer a conventional pharmaceutical formulation but rather a combination of device-integrated biomaterial and the necessary therapeutic

treatment. Biomaterials have found applications in approximately 8000 different kinds of medical devices [1], which have been used in repairing skeletal systems, returning cardiovascular functionality, replacing organs, and repairing or returning senses [2]. Even though biomaterials have had a pronounced impact in medical treatment, a need still exists to be able to design and develop better polymer, ceramic, and metal systems [3].

Polymeric biomaterials originated as off-the-shelf materials that clinicians were able to use in solving a problem, for example, dialysis tubing was originally made of cellulose acetate, vascular grafts were fabricated from Dacron, and artificial hearts were molded from polyurethanes (PUs) [2]. However, these materials did not possess the chemical, physical, and biological properties necessary to prevent further complications. Recent advances in synthetic techniques have allowed these properties to be imparted on polymeric biomaterials, which help to alleviate accompanying biocompatibility issues. Nanotechnology, as this chapter will describe, further adds to the ability of chemically tailoring polymeric materials to provide more opportunities for revolutionary breakthroughs in the science and technology associated with developing novel devices. Undoubtedly, nanoscale science and engineering has the potential to have a profound impact on medical science and technology, which will lead to improved diagnostics and enhanced therapeutic methods [4].

For ceramics and metals, similar advancements through the use of nanotechnology can be envisioned. For example, bioimplants, administered to humans over the past nine decades, have mostly been synthetic prostheses consisting of ceramic or metal particles and grain sizes with conventional dimensions (of the order of 1 to 10^4 μm). But the lack of sufficient bonding of these synthetic implants to surrounding body tissues has, in recent years, led to the investigation of novel material formulations. One such category of materials, nanophase ceramics and metals (or materials with constituent components less than 100 nm in at least one direction), can be used to synthesize implants with surface roughness similar to that of natural tissues. Natural tissues have numerous nanometer features available for cellular interactions since they are composed of many nanostructures (specifically, proteins). Several nanophase ceramic and metal biomedical implants are currently being investigated, and are likely to gain approvals for clinical use in the near future.

One area in which nanophase polymers, ceramics, and metals are being heavily investigated involves orthopedic/dental applications and this is for a good reason. Since 1990, the total number of hip replacements, which is the replacement of the femoral and hip bones, has been steadily increasing [5–11]. In fact, in the United States alone in 2000 there were 152,000 total hip replacements — a 33% increase from the number performed in 1990 and a little over half of the projected number of total hip replacements (272,000) by the year 2030 [5–8]. However, in 1997, 12.8% of the total hip arthroplasties were simply due to revision surgeries of previously implanted failed hip replacements [5–8].

The fact that such a high percentage of hip replacements performed every year are revision surgeries is not surprising when you consider the life expectancy of the implant versus that of the patient receiving the implant. Consistently, over 30% of those requiring total hip replacements have been below the age of 65 and even those at the age of 65 have a life expectancy of 17.9 years [9–11]. Females, who comprise a majority of those receiving total hip replacements, have a life expectancy of 19.2 years at the age of 65. Since the longevity of implants ranges only from about 12 to 15 years, even the majority of those who receive bone implants at the age of 65 will require at least one revision surgery before the end of their lives [9–11].

For the dental community the story is not any better. Since dental implants may be necessary for the young and old alike, it is imperative that they are able to last for the duration of the patient's life. Recent studies have found that dental implants which have been used in over 300,000 cases in the United States, have up to a 96% success rate (meaning that the implant was not mobile and was noninflamed) after 5 years, 80% after 10 years, and less than 75% after 15 years [5–11].

The above information strongly suggests that the longevity of the current prostheses is a reoccurring problem for the orthopedic/dental community that has to be dealt with since current approaches clearly fail. Orthopedic implant failure can be due to numerous reasons, including poor initial bonding of the implant to juxtaposed bone, generation of wear debris that lodges between the

implant and surrounding bone to cause bone cell death, and stress and strain imbalances between the implant and surrounding bone causing implant loosening and eventual failure [12]. Although there are many reasons why implants fail, a central one is the lack of sufficient bone regeneration around the implant immediately after insertion [12]. Shockingly, about a quarter of dental implant failures (of those that failed between 3 and 6 months) are attributed to incomplete healing of the implant to juxtaposed bone [5–11]. Importantly, this leads to eventual implant loosening and regions for possible wear debris to situate between the implant and surrounding bone, further complicating bone loss [12–15].

Nanotechnology is playing an important role in decreasing this failure. This is because, in order to improve biomaterial performance and hence extend the lifetime of bone implants, it is essential to design surface characteristics that interface optimally with select proteins and subsequently with pertinent bone cell types. That is, immediately after implantation, proteins will adsorb from plasma to biomaterial surfaces to control cell attachment and eventual tissue regeneration (Figure 22.1) [16,17]. Initial protein interactions that mediate cell function depend on many biomaterial properties, including chemistry, charge, wettability, and topography [16,17]. Of significant influence for protein interactions is surface roughness and energy [18–22], and this represents the promise of nanophase materials in bone implant applications.

The critical factor for the merging of nanotechnology with medicine is the increasingly documented, special, biologically improved material properties of nanophase implants compared to conventional formulations of the same material chemistry. This chapter will highlight a novel property of nanophase materials that makes them attractive for use as implants: increased tissue regeneration. Work is ongoing in the domains of orthopedic, dental, bladder, neurological, vascular, cartilage, and cardiovascular applications. However, only orthopedic applications, which are the closest to clinical applications, will be emphasized here. This contribution will briefly articulate the seeming revolutionary changes and the potential gains nanostructured materials can make for bone implant technology.

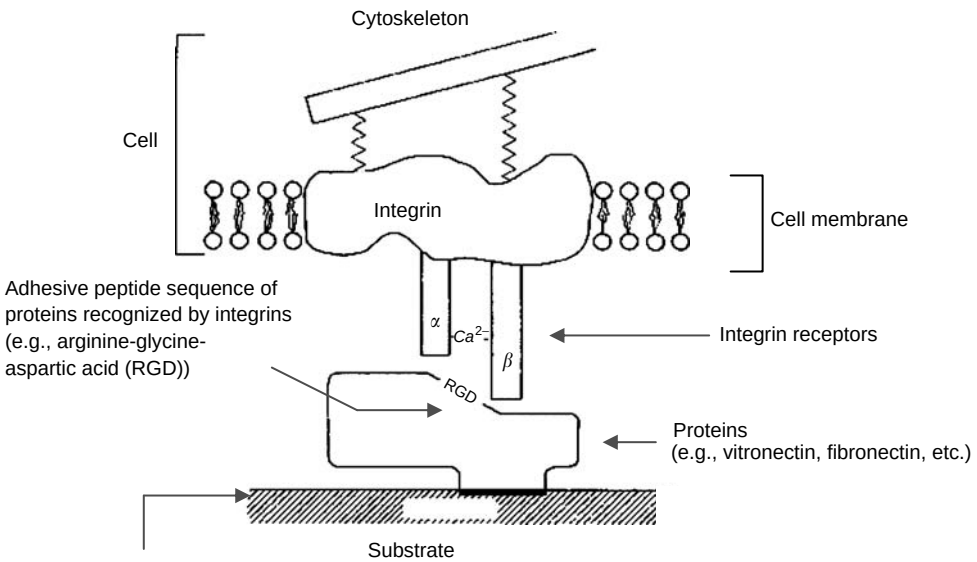

FIGURE 22.1 Cell recognition of biomaterial surfaces controlled by initial protein interactions. Initial protein interactions can influence cell adhesion and, thus, degree of bone tissue formation on biomaterials. Changing material properties will alter protein interactions and influence subsequent cell function. (Adapted and redrawn from Schakenraad, J.M., in *Biomaterials Science: An Introduction to Materials in Medicine*, Ratner, B.D., Hoffman, A.S., Schoen, F.S., and Lemmons, J.E., Eds., Academic Press, New York, 1996, pp. 133–140. With permission.)

22.2 NANOTECHNOLOGY IN BIOMATERIALS SCIENCE

The emergence of micro- and nanoscale science and engineering has provided new avenues for engineering materials with macromolecular and even down to molecular-scale precision, leading to diagnostic and therapeutic technologies that will revolutionize the way health care is administered. Biomaterials have evolved from off-the-shelf products (e.g., Dacron for vascular grafts) to materials that have been designed with molecular precision to exhibit the desired properties for a specific application, often mimicking biological systems [2,3].

Controlling interactions at the level of natural building blocks, from proteins to cells, facilitates the novel exploration, manipulation, and application of living systems and biological phenomena. Nanostructured tissue scaffolds and biomaterials are being applied for improved tissue design, reconstruction, and reparative medicine [23–26]. Nano- and micro-arrays have been established as the preferred method for carrying out genetic and other biological (e.g., drug discovery) analysis on a massive scale [27]. Natural nanopores [28,29] and synthetic nanopores of tailored dimensions [30,31] are probing, characterizing, and sequencing biological macromolecules and have demonstrated the possibility to analyze the structure of individual macromolecules faster and cheaper [32]. Self-assembly is being applied to create new biomaterials with well-ordered structures at the nanoscale, such as nanofiber peptide and protein scaffolds [33]. In addition, polymer networks with precisely engineered binding sites have been created via molecular imprinting, where functional monomers are preassembled with a target molecule and then the structure is locked with network formation [34].

In medical diagnostics, the speed and precision with which a condition is detected directly impacts the prognosis of a patient. Point-of-care (POC) diagnostic devices, which enable diagnostic testing (*in vivo* or *ex vivo*) at the site of care, can enhance patient outcomes by substantially abbreviated analysis times as a result of the intrinsic advantages of the miniature device and by eliminating the need for sample transport to an on-site or off-site laboratory for testing. The development of micro or miniaturized total analysis systems (μ-TAS), also referred to as lab-on-a-chip devices, has profoundly impacted the corresponding development of POC diagnostic devices. These μ-TAS devices integrate microvalves, micropumps, micro-separations, microsensors, and other components to create miniature systems capable of analysis that typically requires an entire laboratory of instruments. Since being introduced as a novel concept for chemical sensing devices [35], μ-TAS devices have been applied as innovative biological devices [36] and POC diagnostic devices [37,38]. With the further development of micro- and nanosensors, POC diagnostic devices will provide for improved medical management, leading eventually to self-regulated POC diagnostic devices that intermittently or continuously monitor the biological molecule of interest and deliver the therapeutic agents as required.

Additionally, nanoscale science and engineering have accelerated the development of novel drug delivery systems and led to enhanced control over how a given pharmaceutical is administered, helping biological potential to be transformed into medical reality [39]. Micro- and nanoscale devices have been fabricated using integrated circuit processing techniques and have been demonstrated to allow for strict control over the temporal release of the drug. Silicon microchips that can provide controlled release of single or multiple chemical substances on demand via electrochemical dissolution of the thin anode membranes covering microreservoirs have been created [40]. The advantages of this microdevice are that it has a simple release mechanism, very accurate dosing, ability to have complex release patterns, potential for local delivery, and possible biological drug stability enhancement by storing in a microvolume that can be precisely controlled. More recently, multi-pulse drug delivery from a resorbable polymeric microchip device was demonstrated [41].

In particular, the development of polymer systems that are able to interact with their environment in an "intelligent" manner has led to novel materials and applications. These intelligent materials are attractive options as functional components in micro- and nanodevices, due to the ease with which their recognition and actuation properties can be precisely tailored. In this section, neutral and intelligent polymers and networks based on environmentally responsive hydrogels and bio-mimetic polymer networks will be discussed for application as sensing/recognition elements in novel diagnostic

devices, such as microsensors and microarrays, and therapeutic devices, for tailoring loading and release properties.

In addition to advances in polymer nanotechnology for sensing and recognizing changes in micro-environments, advances have been made concerning tissue regeneration on ceramic and metallic nanomaterials. Broadly speaking, nanotechnology embraces a system whose core of materials is in the range of nanometers (10^{-9} m) [42–52]. The application of nanomaterials for medical diagnosis, treatment of failing organ systems, or prevention and cure of human diseases can generally be referred to as nanomedicine [51,52]. The branch of nanomedicine devoted to the development of biodegradable or nonbiodegradable prostheses fall within the purview of nanobiomedical science and engineering [51,52]. Although various definitions are attached to the word "nanomaterial" by different experts, the commonly accepted concept refers nanomaterials as that material with the basic structural unit in the range 1 to 100 nm (nanostructured), crystalline solids with grain sizes 1 to 100 nm (nanocrystals), individual layer or multilayer surface coatings in the range 1 to 100 nm (nanocoatings), extremely fine powders with an average particle size in the range 1 to 100 nm (nanopowders) and, fibers with a diameter in the range 1 to 100 nm (nanofibers) [42,43].

Since nature itself exists in the nanometer regime, especially tissues in the human body [53], it is clear that nanotechnology can play an integral role in tissue regeneration. Specifically, bone is composed of numerous nanostructures — like collagen and hydroxyapatite (HA) that, most importantly, provide a unique nanostructure for protein and bone cell interactions in the body (Figure 22.2) [50]. Although the ability to mimic constituent components of bone is novel in itself, there are additional reasons to consider nanomaterials for tissue regeneration such as in orthopedic applications: their special surface properties compared to conventional (or micron constituent component structured) materials [47–50]. For example, a nanomaterial has increased numbers of atoms at the surface, grain boundaries or material defects at the surface, surface area, and altered electron distributions compared to conventional materials (Figure 22.3) [50]. In summary, nanophase material surfaces are more reactive than their conventional counterparts. In this light, it is clear that proteins which influence cell interactions that lead to tissue regeneration will be quite different on nanophase compared with conventional implant surfaces (Figure 22.1).

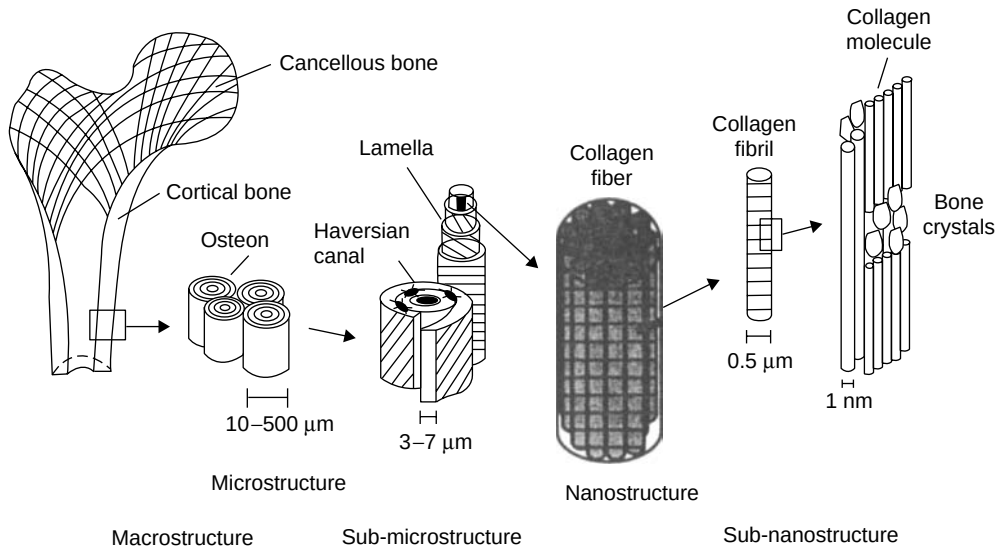

FIGURE 22.2 Nanocomponents of bone provide a high degree of nanostructured surface roughness for bone cells. (Adapted and redrawn from Cowin, R., *Handbook of Bioengineering*, McGraw-Hill, New York, 1987. With permission.)

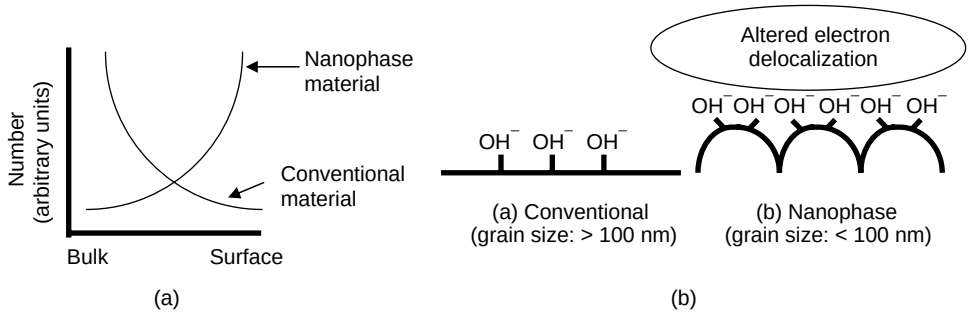

FIGURE 22.3 Special surface properties of nanophase materials. (a) Higher number of atoms at the surface for nanophase compared to conventional materials. (b) Nanophase materials have higher surface areas, possess greater numbers of material defects at the surface, and altered electron delocalization. Such special properties will influence protein interactions for controlling cell functions. (Adapted and redrawn from Klabunde, K.J. et al., *J. Phys. Chem.*, 100, 12141, 1996. With permission.)

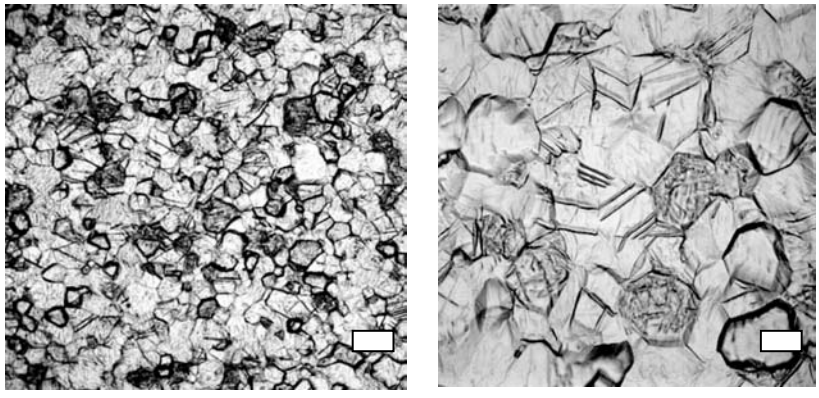

Ti (Medical grade 2) at a magnification of ×100

Ti (Medical grade 2) at a magnification of ×400

FIGURE 22.4 Conventional grain size of currently used orthopedic implants. Bar = 10 and 1 μm for the left and right micrograph, respectively.

Despite this, the evolution of tissue engineering has centered on the use of materials with non-biologically inspired micron surface features [55,56], mostly changing in chemistry or micron roughness but not degree of nanometer roughness (Figure 22.4). In this context, it should not be surprising why the optimal tissue engineering material (in particular, to regenerate bone) has not been found.

22.3 CURRENT RESEARCH EFFORTS TO IMPROVE BIOMEDICAL PERFORMANCE AT THE NANOSCALE

Nanoscale materials currently being investigated for bone tissue engineering applications can be placed in the following categories: ceramics, metals, polymers, and composites thereof. Each type of material has distinct properties that can be advantageous for specific bone regrowth applications. For example, HA, a ceramic mineral present in bone (Figure 22.2), can also be made synthetically. Ceramics, though, are not mechanically tough enough to be used in bulk for large-scale bone fractures. However, they have found applications for a long time as bioactive coatings due to their ionic bonding mechanisms favorable for osteoblast (or bone-forming cells) function [57].

Unlike ceramic materials, metals are not found in the body. Due to their mechanical strength and relative inactivity with biological substances, metals (specifically, Ti, Ti6Al4V, and CoCrMo) have been the materials of choice for large bone fractures [55,56]. Polymers exhibit unique properties (such as viscosity, malleability, moldability) and possess mechanical strength that is comparable with many soft (not hard) tissues in the body [54]. To date, because of their excellent friction properties, polymers (like ultra-high-molecular-weight polyethylene) have been primarily used as articulating components of orthopedic joint replacements [58]. Additionally, some polymers (particularly the polyester family) can be resorbed or degraded in the body, which opens the window for controllable repair of damaged bone that is actively being investigated in tissue engineering circles. Lastly, composites of any or all of the above, can be synthesized to provide a wide range of material properties to increase bone implant performance [59]; such ability to tailor composite properties to specific orthopedic applications makes them attractive.

Owing to the numerous materials currently being used and investigated in orthopedics, this review will cover select efforts to create nanoscale surfaces in all of these categories: ceramics, metals, polymers, and composites. Several current and potential materials that have shown promise in nanotechnology for bone biomedical applications as well as needed future directions, will be emphasized.

22.4 SOFT BIOMATERIALS

Polymers are only one of the four major classes of biomaterials; however, polymeric biomaterials have a significant advantage over metals, ceramics, and natural materials in that they can be chemically synthesized or modified according to the desired application. Hydrogels, hydrophilic, and cross-linked polymeric structures, have received considerable attention for use in biomedical applications due to the biocompatible nature of their physical properties [60–62]. Poly(hydroxyethyl methacrylate) [63] is the most widely used hydrogel, and the cross-linked variant has been frequently used in soft contact lenses [64,65]. Hydrogels are also widely used in pharmaceutical applications especially for the oral delivery of therapeutic proteins [66]. This class of materials is also capable of responding to changes in the external pH (Figure 22.5), temperature, ionic strength, nature and composition of the swelling agent, enzymatic or chemical reaction, and electrical or magnetic stimuli [67].

Much consideration must be given when designing a material for a specific application. Certain properties of the material must be controlled so as to perform the necessary function and elicit the

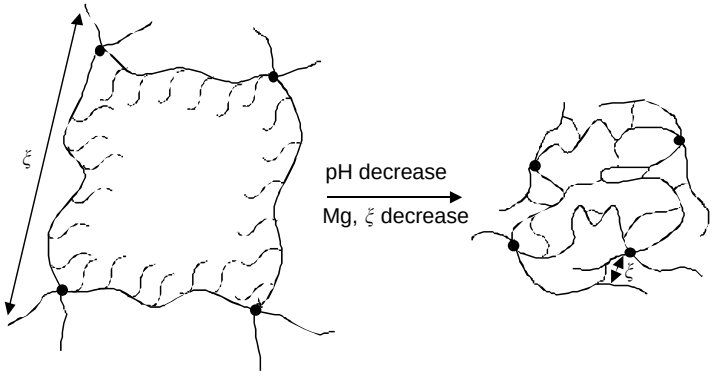

FIGURE 22.5 Network structural changes due to variations on environmental pH. Higher pHs disrupt the interpolymer complexes and ionic moieties deprotonize leading to extensive swelling (left). As pH is decreased, interactions between the tethered grafts with the protonized ionic moieties increase leading to the formation of interpolymer complexes.

appropriate response. These properties can be tailored to the specific need by carefully controlling structural characteristics, modifying the surface properties, and employing biomimesis in the material design. Hydrogels are a suitable material for biomedical devices because their properties can be controlled during or after the chemical synthesis, providing a significant amount of flexibility to aid in need-specific design applications.

22.4.1 Structural Characteristics

Hydrogel networks are prepared via chemical cross-linking, photopolymerization, or irradiative cross-linking [68] with the behavior of the materials dependent on their equilibrium and dynamic swelling behavior in water. Flory [69] was the first to develop the theory to explain the swelling behavior of cross-linked polymers based upon a Gaussian distribution of the polymer chains. Various parameters have been employed to define the equilibrium-swelling behavior. The volume degree of swelling, Q, is the ratio of the actual volume of a sample in the swollen state divided by its volume in the dry state and q, the weight degree of swelling, is the ratio of the weight of the swollen sample to that of the dry sample [62]. The basic structure of the hydrogel is described by the molecular weight between cross-links, $\overline{M}_c$, and the cross-linking density, ρ_x and can be calculated from Equations (22.1) and (22.2), respectively. The structural characteristics influence the diffusion coefficient of solutes through the network, optical properties, mechanical properties, and surface mobility:

$$\frac{1}{\overline{M}_c} = \frac{2}{\overline{M}_c} - \frac{\frac{\overline{\upsilon}}{V_1}[1n(1-\upsilon_{2,S})+\upsilon_{2,S}+\chi\upsilon_{2,S}^2]}{\left(\upsilon_{2,S}^{1/3}-\frac{\upsilon_{2,S}}{2}\right)} \tag{22.1}$$

$$\rho_x = \frac{1}{\overline{\upsilon M}_c} \tag{22.2}$$

These key properties of the hydrogel are typically determined during initial synthesis of the biomaterial and are representative of the bulk structure of the material. Advances in nanotechnology have afforded the ability to refine further the structure by molecularly engineering the hydrogel to impart a recognitive capacity. Domains within the molecularly designed hydrogel are able to recognize specific molecules through highly select noncovalent interactions between the building blocks of both the hydrogel network and the recognizable molecule [70].

22.4.2 Surface Properties

In addition to the bulk structural characteristics of the biomaterial, the surface plays a key role in the ability of the material to function as designed. A surface provides a low-energy barrier to mobility, a high accessibility for reaction, enhanced reaction turnover rates, and ultimately allows for molecular recognition [71]. As the first biomaterials were developed (intraocular lenses, hip joint replacements, and blood-contacting devices), the importance of the surface properties, protein–surface interaction, and surface modification was evident to researchers [72,73]. Baier et al. [74] introduced methods with the ability to determine the driving mechanisms behind bioreactions. Hoffman [75] demonstrated that materials could be engineered so as to provide the desired biological responses necessary for effective biomaterial functionality.

In this light, poly(ethylene glycol) (PEG) has received considerable attention for its use at the biomaterial–host interface to prevent protein fouling [76–78]. Castner and Ratner [71] list other strategies in addition to PEG that have been employed in biomaterials to prevent protein adsorption. However, possessing the ability to design surface properties has not been able to fully solve the issues

associated with the biocompatibility of the material. True biocompatibility will be achieved when absorbing proteins are able to maintain their conformation, eliminating the detrimental foreign body reaction to this newly formed unnatural layer of denatured proteins [71]. The surface of the material must be designed so as to provide components inherent to the natural wound healing process. This is an important contribution nanotechnology can make to improve biomaterial performance.

22.4.3 Biomimetics

The design and development of biomaterials have primarily been focused on the biocompatibility of the device with its surroundings, overlooking the biomolecular interactions that occur. The paradigm for biomaterial characterization has shifted from one focusing on broad design parameters to one that focuses on eliciting specific molecular responses from the physiological environment. Biomimetic materials emulate nature and mimic biological architecture to elicit a desired cellular response [79,126]. Because of their hydrophilic structure, hydrogels inherently possess the characteristics of natural tissue; however, these materials in device form are much larger than individual cells. The major thrust of biomimesis is to design structures that have the ability to interact on a sub-cellular basis.

In designing biomaterials one must understand the mechanisms by which cells interact for efficient biological mimicking. Three specific interactions that are crucial in material development include cell adhesion, morphogenic stimuli signaling, and endocytosis [79]; since all of these are events controlled at the nanoscale, biomimetics is a critical field in nanotechnology.

22.4.4 Nanoscale Biopolymer Carriers

Polymer nanoparticle and nanosphere carriers (Figure 22.6 and Figure 22.7) are very attractive for biomedical and pharmaceutical applications, due to their unique and tailorable properties. In the case of polymer networks, the release profile can be precisely controlled through the design of its molecular structure, such as degree of cross-linking and ionic characteristics of the pendent functional groups [80,81].

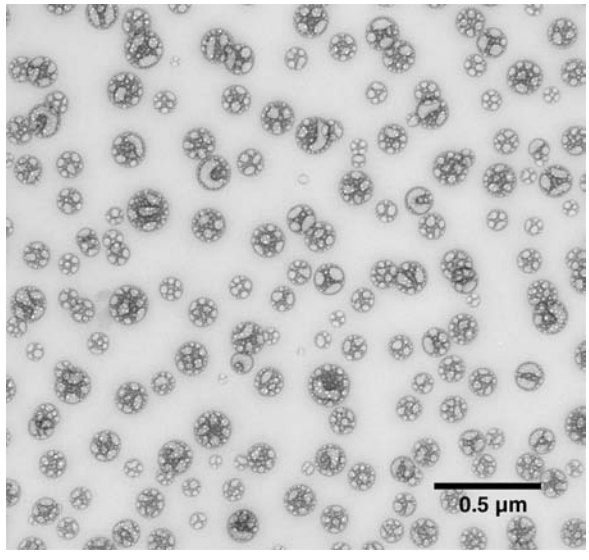

FIGURE 22.6 TEM image of P(MAA-g-EG) nanospheres prepared from a MAA/EG molar feed ratio of 1:1. The P(MAA-g-EG) nanospheres were stained with uranyl acetate at pH 4.0.

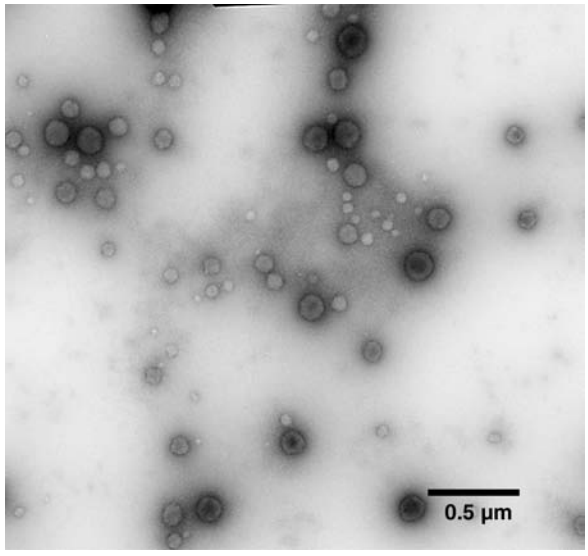

FIGURE 22.7 TEM image of P(MAA-g-EG) nanospheres prepared from a MAA/EG molar feed ratio of 1:1. The P(MAA-g-EG) nanospheres were stained with phosphotugstic acid pH 7.2.

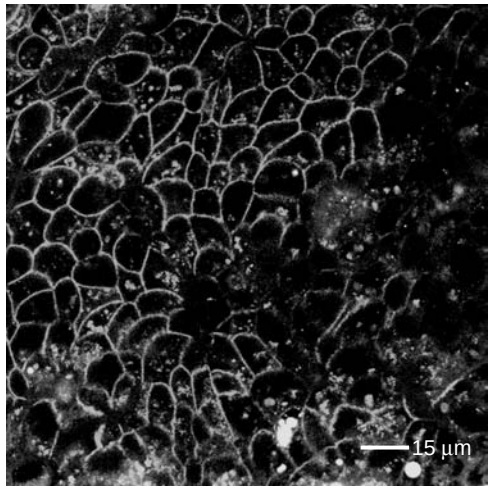

FIGURE 22.8 Optical section of a Caco-2 cell monolayer grown on microporous Transwell® plates obtained with a confocal microscope. FITC-labeled insulin (green) was added to the apical chamber of the cell monolayer in the presence of poly(methacrylic acid-grafted-ethylene glycol) microparticles for 120 min, and images were taken after fixing the cells with 3.7% formaldehyde.

Polymer nanospheres have been molecularly designed to be responsive to the pH of their environment, enabling the protection of fragile therapeutic peptides (Figure 22.8) and proteins in the harsh, acidic stomach environment and then releasing them in the more amiable environment of the upper small intestine [82–84]. In addition, nanoparticle carriers have been designed to have stealth properties, allowing extended residence time without being recognized by the immune system [85,86]. In other efforts, synthetic delivery systems, including polymeric nanoparticles, have been developed for application in gene delivery [87,88]. By creating polymer drug delivery systems that are biodegradable, the need for removal of the system postdelivery is eliminated, since the polymer

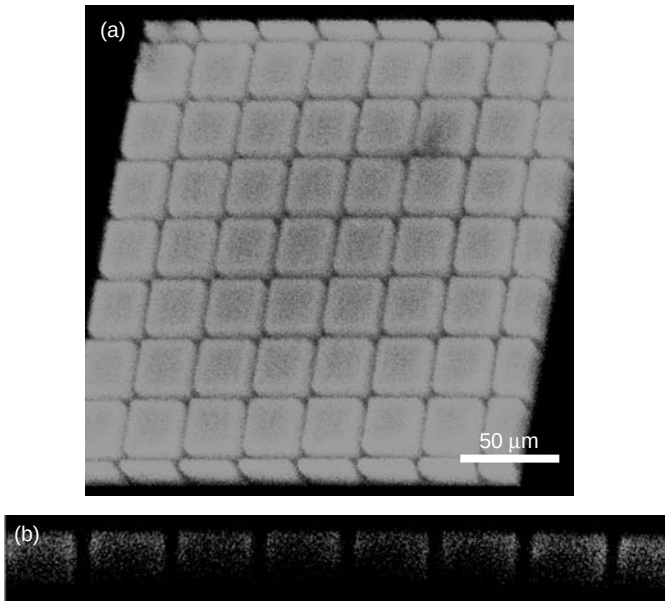

FIGURE 22.9 (a) 3-D projection of a micropatterned square array of a biomimetic polymer network based on a cross-linked polyacrylamide obtained utilizing a confocal microscope. (b) A slice of the square array.

can be naturally resorbed by the body [89]. Also, a number of companies are reformulating insoluble drugs as nanoparticles and nanocrystals to control uptake through cellular membranes.

Microchips (Figure 22.9) have been created for the storage and then delivery of multiple drugs in a controlled manner. For instance, a solid-state silicon microchip that can provide controlled release of single or multiple chemical substances on demand was fabricated and demonstrated [40,90]. The release is achieved via electrochemical dissolution of the thin anode membranes covering the micro-reservoirs filled with chemicals in solid, liquid, or gel form. The advantages of this microdevice include a simple release mechanism, very accurate dosing, ability to have complex release patterns, potential for local delivery, and possible biological drug stability enhancement by storing in a micro-volume that can be precisely controlled. Recently, multi-pulse drug delivery from a resorbable polymeric microchip device was demonstrated [41].

The aforementioned microdevices demonstrate only a few examples of the wide variety of novel applications that exist for integration of micro- and nanofabrication technologies in drug delivery, revealing the immaturity of the field. These novel drug delivery devices can enable efficient delivery that was unattainable with conventional drug delivery techniques, resulting in the enhancement of the therapeutic activity of a drug.

22.5 CERAMIC NANOMATERIALS

Perhaps slightly more mature, is the application of nanophase ceramics in bone tissue engineering applications. The next series of sections will highlight the improvement in bone regeneration that can be obtained through the use of ceramic nanotechnology.

22.5.1 INCREASED OSTEOBLAST FUNCTIONS

The first report correlating increased bone cell function with decreased material grain or particulate size into the nanometer regime dates back to 1998 and involves ceramics [91]. Such reports described how *in vitro* osteoblast (bone-forming cell) adhesion, proliferation, differentiation (as measured by intracellular and extracellular matrix protein synthesis such as alkaline phosphatase), and calcium

deposition were enhanced on ceramics with particulate or grain sizes less than 100 nm [91–100]. Specifically, this was first demonstrated for a wide range of ceramic chemistries including titania (Figure 22.10), alumina, and HA [93]. For example, four, three, and two times the amount of calcium-mineral deposition was observed when osteoblasts were cultured for up to 28 days on nanophase compared with conventional alumina, titania, and HA, respectively [95]. It is important to note that for each respective nanophase and conventional ceramic mentioned in these first reports, similar chemistry and material phase were studied [91–100]. That is to say, only the degree of nanometer surface features were altered between respective nanophase and conventional alumina, titania, and HA. This is important since as previously discussed it is well known that alterations in surface chemistry will influence bone cell function [12,55–59], but this was the first time changes in the degree of nanometer roughness alone were reported to enhance bone cell responses [91].

Although these studies provided preliminary evidence that osteoblast functions can be promoted on nanostructured materials compared with conventional materials regardless of ceramic chemistry, Elias et al. [101] further described a study where the topography of compacted carbon nanometer fibers were transferred to poly-lactic-glycolic acid (PLGA) using well-established silastic mold techniques. The same procedure was followed for compacts composed of conventional carbon fibers. The successful transfer of nanometer surface features in compacted carbon nanometer fibers and micron surface features in conventional fiber compacts were compared and is illustrated in Figure 22.11 [101]. Importantly, osteoblast adhesion increased on PLGA molds made from nanometer fibers compared to conventional carbon fibers [101]. Increased osteoblast functions were also observed on the original nanometer fiber material compared with conventional carbon fiber compacts [101]. In this manner, this study provided further evidence of the importance of nanometer surface features (and not chemistry) in promoting functions of bone-forming cells.

Equally interesting, a step-function increase in osteoblast performance has been reported at distinct ceramic grain sizes, specifically at alumina and titania spherical grain sizes below 60 nm [93]. This is intriguing since when creating alumina or titania ceramics with average grain sizes below 60 nm, a drastic increase in osteoblast function was observed compared to respective ceramics with grain sizes just 10 nm higher (i.e., those with average grain sizes of 70 nm) [93]. This critical grain size for improving osteoblast function is also of paramount importance since numerous other special properties (such as mechanical, electrical, catalytic) of materials have been reported when grain size is specifically reduced to below 100 nm [42–50]. With this information, evidence has been provided to show for the first time that the ability of nanophase ceramics to promote bone cell function is indeed limited to grain sizes (or subsequent surface features) below 100 nm, specifically below 60 nm [93]. Thus, another novel size-dependent property of nanostructured ceramics has been elucidated by these studies.

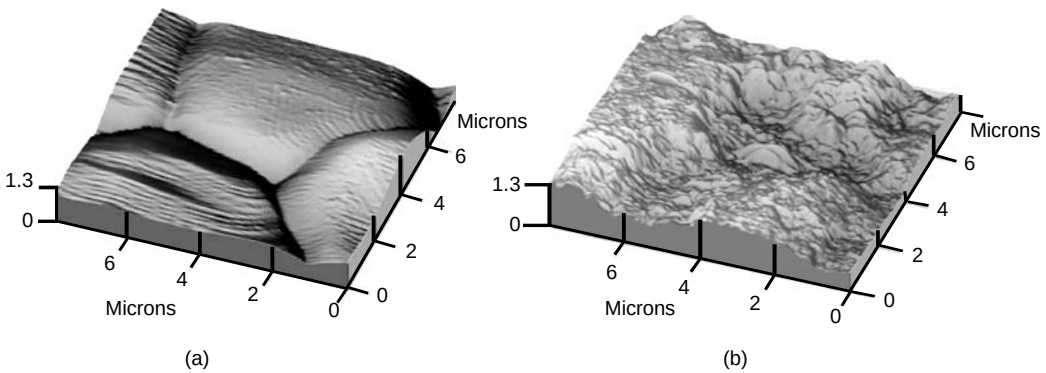

FIGURE 22.10 (a) Conventional and (b) nanophase titania. One of the first studies correlating increased osteoblast function with decreasing ceramic grain size was carried out on titania as pictured here. (From Webster, T.J. et al., *Biomaterials*, 20, 1221, 1999. With permission.)

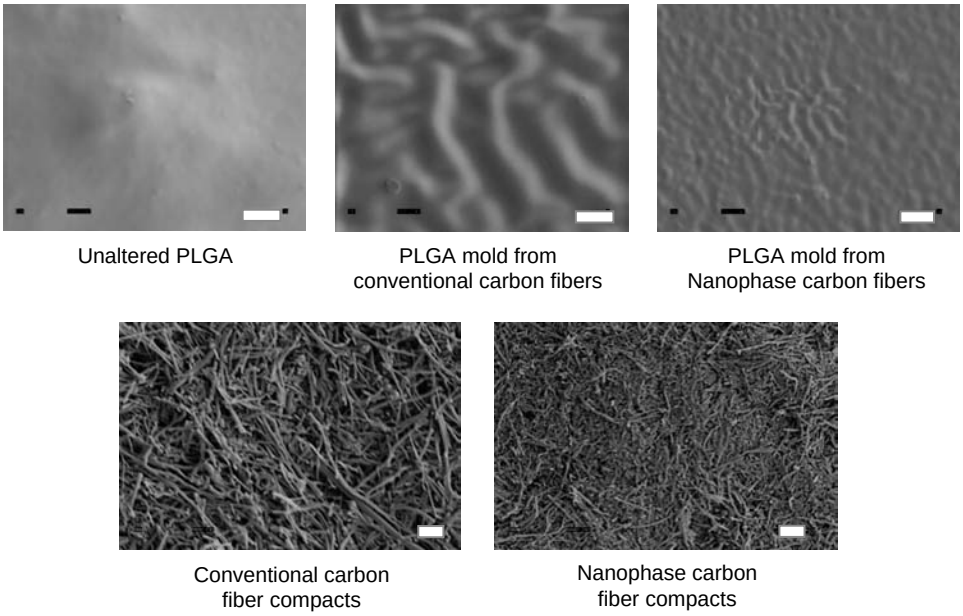

FIGURE 22.11 Poly-lactic-glycolic acid (PLGA) molds of conventional and nanophase carbon fiber compacts. To highlight the importance of nanometer surface roughness regardless of substrate chemistry, studies have shown increased functions of osteoblasts on PLGA molds of nanophase compacts compared to conventional carbon compacts. Studies have also shown increased functions of osteoblasts on compacts composed of nanometer fibers compared to conventional carbon fibers. Bar = 1 μm. (From Elias, K.L. et al., *Biomaterials*, 23, 3279–3287, 2002. With permission.)

Although an exact explanation as to why greater bone regeneration is observed on smaller grain size ceramics in the nanometer regime is not known to date, it is believed that the importance of this specific grain size in improving osteoblast function is connected with interactions of vitronectin (a protein known to mediate osteoblast adhesion with linear dimensions remarkably similar to the critical grain size of 60 nm mentioned above) [94,99]. Moreover, as mentioned previously, several studies have indicated that vitronectin and other proteins important for osteoblast adhesion are more well spread and thus expose amino acid sequences to a greater extent when interacting with nanometer ceramics compared with conventional ceramics [94,99]. It is also intriguing to note that numerous investigators have confirmed that the minimum distance between protein ligands (such as arginine-glycine-aspartic acid or RGD) necessary for cell attachment and spreading is in the nanometer regime (specifically from 10 to 440 nm depending on whether the study was completed with full proteins, protein fragments, or single RGD units) [102–107]. Therefore, an underlying substrate surface that mediates protein spreading (as opposed to protein folding) to expose such ligands, coupled with a nanometer surface roughness to further project such ligands to the cell, may promote cell adhesion due to this optimal ligand spacing.

22.5.2 Increased Osteoclast Functions

In addition to studies highlighting enhanced osteoblast function on nanophase ceramics, increased functions of osteoclasts (bone-resorbing cells) have been reported on nanospherical compared with larger grain size alumina, titania, and HA [100]. Specifically, osteoclast synthesis of tartrate-resistant acid phosphatase (TRAP) and subsequent formation of resorption pits was up to two times greater on nanophase compared to conventional ceramics such as HA. Coordinated functions of osteoblasts and osteoclasts are imperative for the formation and maintenance of healthy new bone

juxtaposed to an orthopedic implant [12]. Frequently, newly formed bone juxtaposed to implants is not remodeled by osteoclasts and thus becomes unhealthy or necrotic [57]. At this time, the exact mechanism of greater functions of osteoclasts on nanophase ceramics is not known, but it may be tied to the well-documented increased solubility properties of nanophase compared with conventional materials [48]. In other words, due to larger numbers of grain boundaries at the surface of smaller grain size materials, increased diffusion of chemicals (such as TRAP) may be occurring to subsequently result in the formation of more resorption pits.

Collectively, results of promoted functions of osteoblasts coupled with greater functions of osteoclasts imply increased formation and maintenance of healthy bone juxtaposed to an implant surface composed of nanophase ceramics. In fact, although not compared with conventional grain size apatite-coated metals, some studies have indeed demonstrated increased new bone formation on metals coated with nanophase apatite [108]. As shown in Figure 22.12, bone formation can be clearly seen on the surface of metals coated with nano-apatite, whereas there is no indication of new bone formation on the underlying metal without the coating [108]. Incidentally, coating metals with nanophase HA has been problematic [109]. For example, owing to their small grain size, techniques

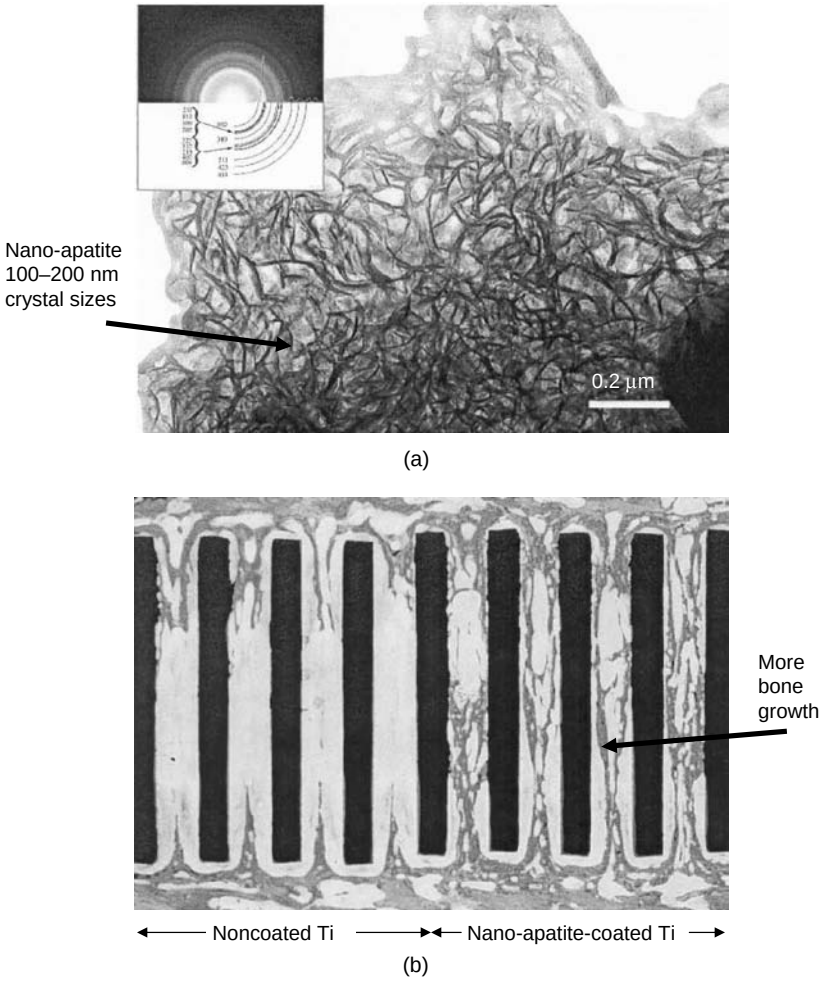

FIGURE 22.12 Increased *in vivo* bone regeneration on titanium coated with nanophase apatite. Scanning electron micrograph of nanometer-dimensioned apatite (specifically, between 100–200 nm in size) is depicted in (a). Increased bone regeneration in titanium cages when coated with nano-apatite is depicted in (b). (From Li, P., *J. Biomed. Mater. Res*., 66, 79–85, 2003. With permission.)

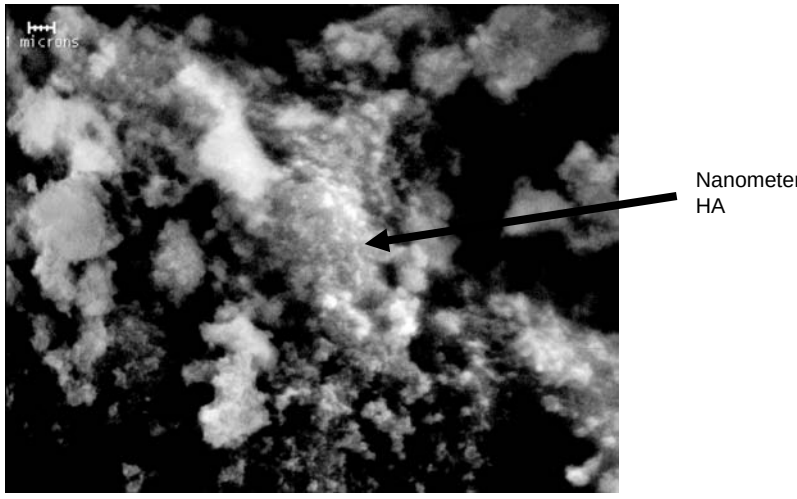

FIGURE 22.13 Nanophase hydroxyapatite coated on titanium. Owing to elevated temperatures, traditional coating techniques, like plasma spray deposition, cannot be used to coat metals with nanophase ceramics. This process developed by Spire Biomedical (Bedford, MA) uses high pressure at low temperatures so as to not allow for grain growth. Bar = 1 μm (upper left).

which use high temperatures (like plasma spray deposition) are not an option since they will result in HA grain growth into the micron regime [109]. To circumvent such difficulties, some investigators have allowed nanophase HA to precipitate on metal surfaces; this can be time consuming and not very controllable [108]. In contrast, others have developed novel techniques which use high-pressure-based processes that do not significantly create elevated temperatures to coat nanophase ceramics on metals so as to retain their bioactive properties (Figure 22.13) [110].

22.5.3 Decreased Competitive Cell Functions

Importantly, it has also been shown that competitive cells do not respond in the same manner to nanophase materials as osteoblasts and osteoclasts do [94,101,111]. In fact, decreased functions of fibroblasts (cells that contribute to fibrous encapsulation and callus formation events that may lead to implant loosening and failure [12] and of endothelial cells [cells that line the vasculature of the body]) have been observed on nanophase compared with conventional ceramics [94]. In fact, the ratio of osteoblast to fibroblast adhesion increased from 1:1 on conventional alumina to 3:1 on nanophase alumina [94].

Previously, such selectivity in bone cell function on materials has only been observed through delicate surface chemistry (e.g., through the immobilization of peptide sequences like Lys-Arg-Ser-Arg or KRSR) [112]. It has been argued that immobilized delicate surface chemistries may be compromised once implanted due to macromolecular interactions that render such epitopes non-functional *in vivo*. For these reasons, it is important to note that studies demonstrating select enhanced osteoblast and osteoclast functions with decreased functions of competitive cells on nanophase materials have been conducted on surfaces that have not been chemically modified by the immobilization of proteins, amino acids, peptides, or other entities [94,101,111]. Rather it is the unmodified, raw material surface that is specifically promoting bone cell functions.

Fibroblast function was also investigated in the same study that was previously mentioned in which Elias et al. transferred the topography of compacted carbon nanometer fibers compared to conventional fibers to PLGA using well-established silastic mold techniques (Figure 22.11) [102]. Similar to the observed greater osteoblast adhesion already noted, decreased fibroblast adhesion was measured on PLGA molds synthesized from carbon nanometer fibers compared to conventional fibers [102]. Again, this was the same trend observed on the starting material of carbon nanometer

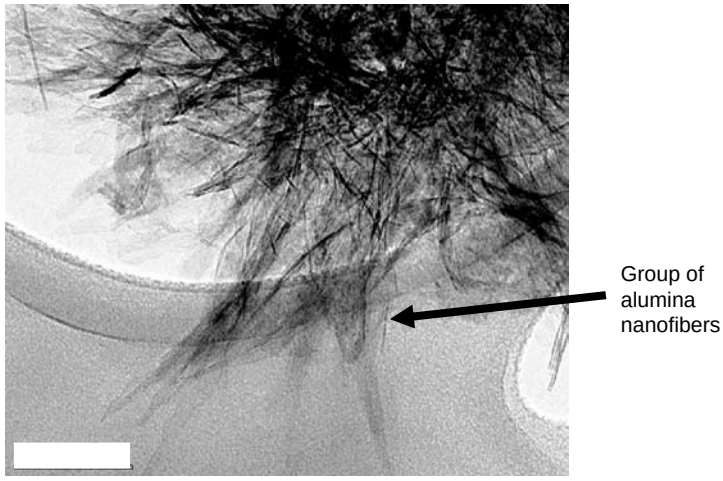

FIGURE 22.14 Transmission electron microscope image of alumina nanofibers. Compared to spherical conventional alumina, increased functions of osteoblasts have been reported on nanophase fibrous alumina. Scale bar = 10 nm. (From Price, R.L. et al., *J. Biomed. Mater. Res.*, 67, 1284, 2003. With permission.)

fiber compacts compared to conventional fiber compacts [102]. Thus, this study demonstrated the importance of a nanometer surface roughness (and not chemical composition of the material) in decreasing functions of fibroblasts that may lead to undesirable fibrous encapsulation and callus formation events inhibiting osseointegration of orthopedic implants with surrounding bone.

22.5.4 Increased Osteoblast Functions on Nanofibrous Materials

Recently, researchers have further modified nanophase ceramics to simulate not only the nanometer dimension but also the aspect ratio of proteins and HA crystals found in the extra-cellular matrix of bone [111]. For example, consolidated substrates formulated from nanofibrous alumina (diameter = 2 nm, length > 50 nm; Figure 22.14) increased osteoblast functions in comparison with similar alumina substrates formulated from the aforementioned nanospherical particles [111]. Specifically, Price et al. [111] determined a twofold increase in osteoblast cell adhesion density on nanofiber vs conventional nanospherical alumina substrates, following only a 2-h culture. Greater subsequent functions leading to new bone synthesis has also been reported on nanofibrous compared to nano- and conventional spherical alumina [111]. Thus, perhaps not only is the nanometer grain size of components of bone important to mimic in materials, but the aspect ratio may also be key to simulate in synthetic materials to optimize bone cell response.

Another class of novel biologically inspired nanofiber materials that have been investigated for orthopedic applications are self-assembled helical rosette nanotubes [113]. These organic compounds are composed of guanine and cytosine DNA pairs that self-assemble when added to water to form unique nanostructures (Figure 22.15). These nanotubes have been reported to be 1.1 nm wide and up to several millimeters wide [113]. Compared to currently used titanium, recent studies have indicated that osteoblast function is increased on titanium coated with helical rosette nanotubes (Figure 22.15) [113]. Although in these studies it has not been possible to separate the influence of nanometer dimensions from the effects of nanotube chemistry on cell functions, it is clear that these nanotubes are another category of novel nanostructured materials that can be used to promote bone formation. It is also intriguing to consider what role self-assembled nanofibers may play in orthopedics since bone itself is a self-assembled collection of nanofibers.

In this context it is important to mention that only nanophase materials can mimic the unique aspect ratio of HA and proteins found in the extracellular matrix of bone; it is not possible for micron-sized

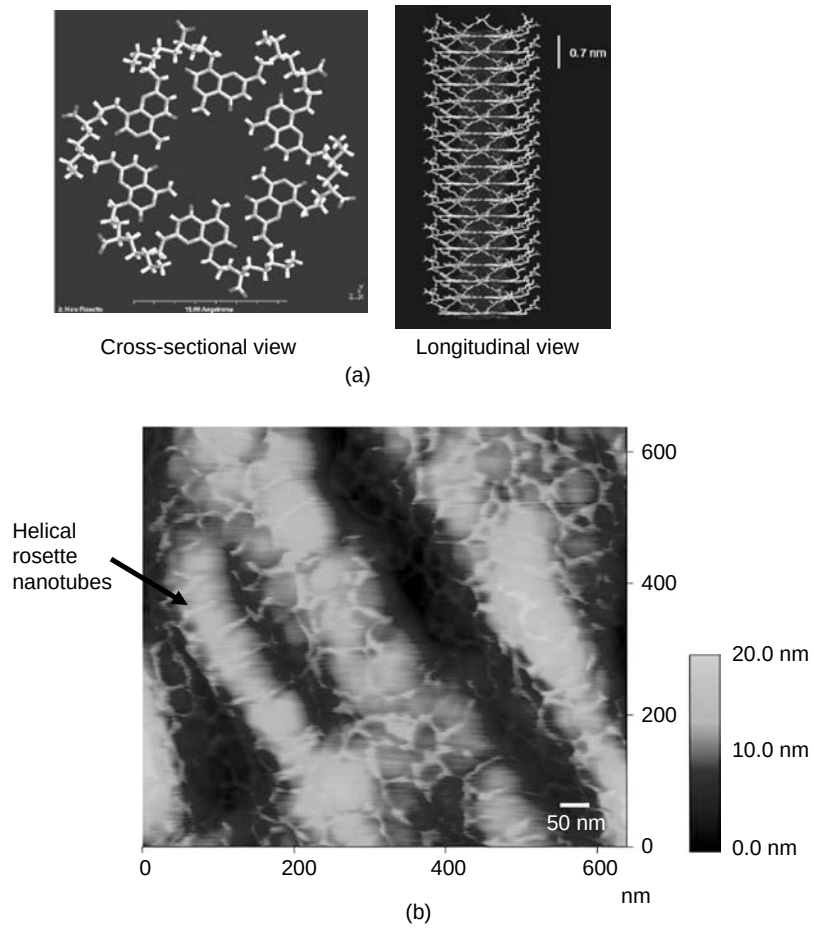

FIGURE 22.15 Helical rosette nanotubes. Drawing of the cross-sectional (left) and longitudinal (right) view of self-assembled helical rosette nanotubes is depicted in (a) while helical rosette nanotubes coated on titanium is depicted in (b). Note the nanophase dimension of these organic tubes. Increased osteoblast function has been observed on helical rosette nanotubes coated on Ti. (From Chun, A. et al., *Nanotechnology*, 15, S234, 2004. With permission.)

materials to simulate the unique nanometer constituent components of bone. As mentioned previously, results concerning the importance of nanofibrous materials in promoting functions of osteoblasts have been reported for carbon and polymer molds of carbon nanofibers (Figure 22.11) [101]. These findings consistently testify to the unprecedented ability to create nanomaterials to mimic the dimensions of components of physiological bone to promote new bone formation.

22.6 METAL NANOMATERIALS

Although much work has been conducted on nanophase ceramics for orthopedic applications to date, several recent studies have focused on the analysis of bone regeneration on nanophase metals. Metals investigated to date include titanium, Ti6Al4V, and CoCrMo [114]. While many have attempted to create nanostructured surface features using chemical etchants (such as HNO_3) on titanium, results concerning increased bone synthesis have been mixed [58]. Moreover, through the use of chemical etchants it is unclear what the cells may be responding to — changes in chemistry or changes in topography. For this reason, as was done for the ceramics in this chapter, it is important

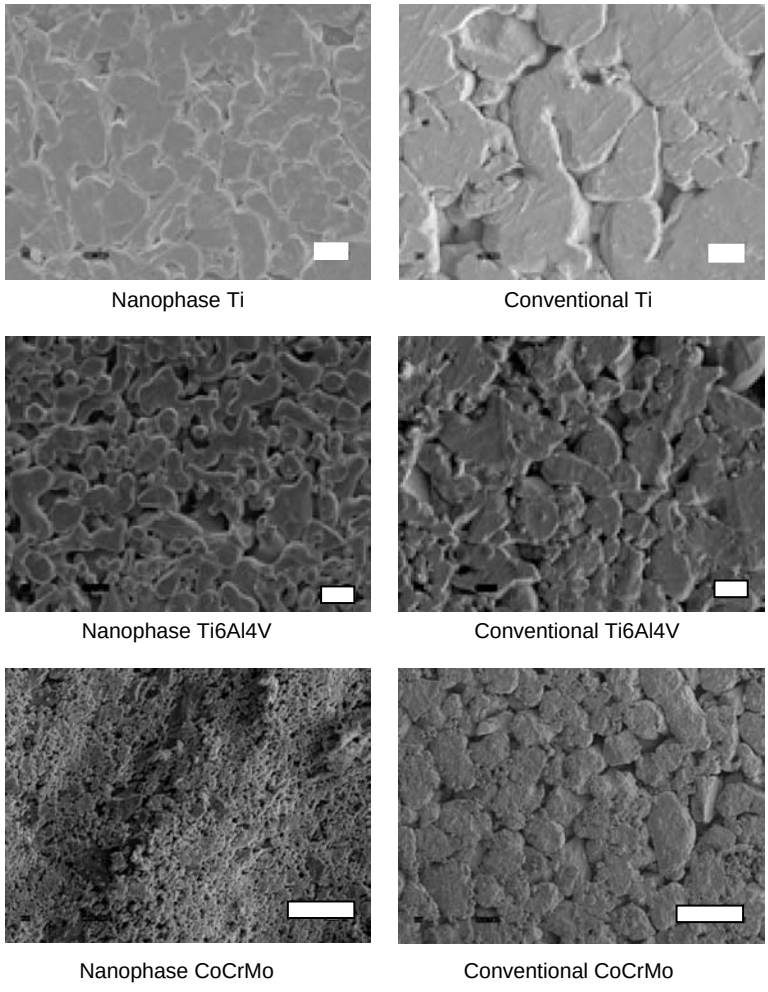

FIGURE 22.16 Scanning electron micrographs of nanophase metals. Increased functions of osteoblasts have been observed on nanophase compared to conventional c.p. Ti, Ti6Al4V, and CoCrMo. Scale bar = 1 μm for nanophase Ti/Ti6Al4V and 10 μm for conventional Ti/Ti6Al4V. Scale bar = 10 μm for nanophase and conventional CoCrMo. (From Ejiofor, J.U. and Webster, T.J., *ASM Conference*, Las Vegas, NV, 2004. With permission.)

to focus on studies that have attempted to minimize large differences in material chemistry and focus only on creating surfaces that alter in their degree of nanometer roughness.

One such study by Ejiofor et al. [114] utilized traditional powder metallurgy techniques without the use of heat to avoid changes in chemistry to fabricate different particle size groups of Ti, Ti6Al4V, and CoCrMo (Figure 22.16). Increased osteoblast adhesion, proliferation, synthesis of extracellular matrix proteins (like alkaline phosphatase and collagen), and deposition of calcium-containing mineral was observed on respective nanophase compared to conventional metals [114]. This was the first study to demonstrate that the novel enhancements in bone regeneration previously seen in ceramics by decreasing grain size can be achieved in metals.

Interestingly, when Ejiofor et al. [114] examined spatial attachment of osteoblasts on the surfaces of nanophase metals, they observed directed osteoblast attachment at metal grain boundaries (Figure 22.17). Because of this, the authors speculated that the increased osteoblast adhesion may be due to more grain boundaries at the surface of nanophase compared to conventional metals. As was the case with nanophase ceramics [94,99], it is plausible that protein adsorption and

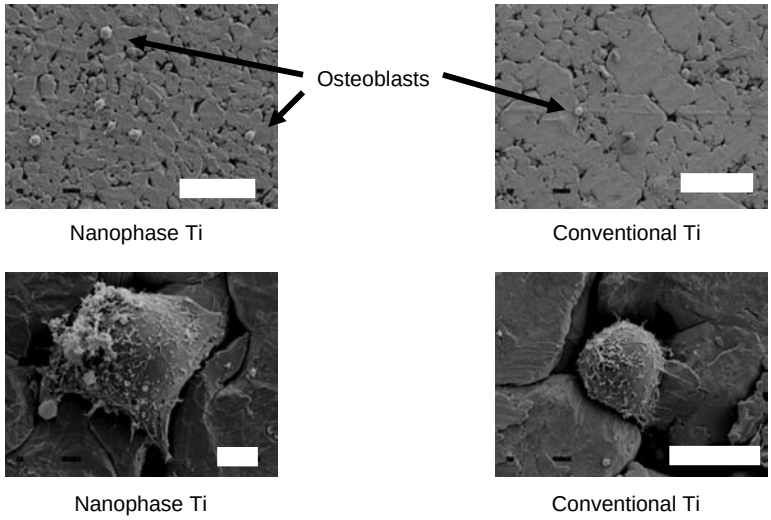

FIGURE 22.17 Scanning electron micrographs of adherent osteoblasts on nanophase c.p. Ti. Directed osteoblast adhesion on nanophase metal grain boundaries has been reported. Scale bar = 100 μm for top and 10 μm for bottom. Adhesion time = 30 min. (From Ejiofor, J.U. and Webster, T.J., *ASM Conference*, Las Vegas, NV, 2004. With permission.)

conformation at nanophase metal grain boundaries may be greatly altered compared to nongrain boundary areas and conventional grain boundaries; in this manner, protein interactions at grain boundaries may be key for osteoblast adhesion.

22.7 POLYMERIC NANOMATERIALS

For ceramics and metals, most studies conducted to date have created desirable nanometer surface features by decreasing the size of constituent components of the material, e.g., a grain, particle, or fiber. However, due to the versatility of polymers, many additional techniques exist to create nanometer surface roughness values. In addition, polymers contribute even further to rehabilitating damaged tissue by possibly providing a degradable scaffold that dissolves within a controllable time while the native tissue reforms. Techniques utilized to fabricate nanometer features on polymers include e-beam lithography, polymer de-mixing, chemical etching, cast-mold techniques, and the use of spin-casting [114–122]. For those that have been applied to bone regeneration, chemical etching followed by mold casting and polymer de-mixing techniques have received the most attention [115,116].

For chemical etching techniques, polymers investigated to date include PLGA (Figure 22.18), PU, and polycaprolactone [116,118–120]. The idea proposed by Kay et al. has been to treat acidic polymers with basic solutions (i.e., NaOH) and basic polymers with acidic solutions (i.e., HNO_3) to create nanosurface features [116]. Kay et al. observed greater osteoblast adhesion on PLGA treated with increasing concentrations and exposure times of NaOH only on two-dimensional films. As expected, data were also provided indicating larger degrees of nanometer surface roughness with increased concentrations and exposure times of NaOH on PLGA. Park et al. [118] took this one step further and fabricated three-dimensional tissue engineering scaffolds by NaOH treatment of PLGA. When comparing osteoblast functions on such scaffolds, even though similar porosity properties existed between nontreated and NaOH-treated PLGA (since similar amounts and sizes of NaCl crystals were used to create the pores through salt-leaching techniques), greater numbers of osteoblasts were counted on and in NaOH-treated PLGA [118]. Unfortunately, due to these fabrication techniques, it is unclear whether the altered PLGA chemistry or nano-etched surface promoted osteoblast adhesion; however, in light

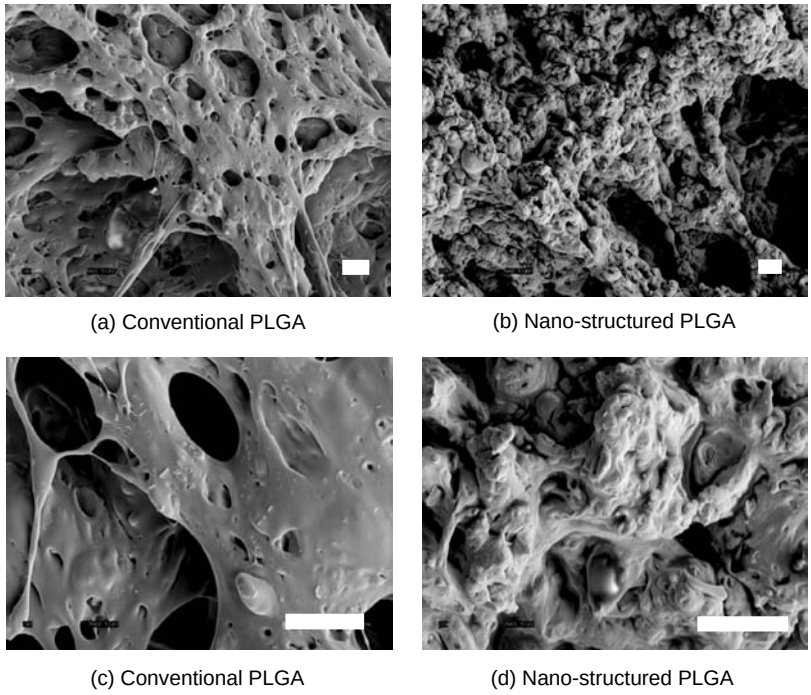

(a) Conventional PLGA (b) Nano-structured PLGA

(c) Conventional PLGA (d) Nano-structured PLGA

FIGURE 22.18 Scanning electron micrographs of conventional and nanophase PLGA scaffolds. Increased osteoblast functions have been demonstrated on nanophase PLGA scaffolds. Scale bar = 10 μm. (From Park, G.E. et al., *Biomaterials*, 26, 3075–3082, 2005. With permission.)

of the previous studies mentioned in this chapter, the authors of Ref. [118] suggested that the nanometer surface roughness of the NaOH-treated PLGA played an important role [118].

Studies have also been conducted on cell responses to polymers with changes in nanometer surface roughness without changes in chemistry. Specifically, Li et al. utilized polymer de-mixing techniques to create well-controlled nanometer islands of polystyrene and polybromo-styrene [121]. Although osteoblast functions have not been tested on these constructs to date, fibroblast morphology was significantly influenced by incremental nanometer changes in polymer island dimensions (Figure 22.19). Again, this study points to the unprecedented control that can be gained over cell functions by synthesizing materials with nanometer surface features.

Although not related to orthopedic applications, vascular and bladder cell responses have also been promoted by altering the topography of polymeric materials in the nanometer regime [116,118,120,122]. In these studies, chondrocytes [116], bladder [120], and vascular smooth muscle cell [119] adhesion and proliferation were greater on two-dimensional nanometer surfaces of biodegradable polymers such as PLGA, PU, and polycaprolactone; similar trends have recently been reported on three-dimensional PLGA scaffolds [122].

22.8 COMPOSITE NANOMATERIALS

Owing to the previous information of increased osteoblast function on ceramics [100] and polymers [111], bone cell function on nanophase ceramic polymer composites have also been determined. Specifically, studies conducted to date show promoted osteoblast responses on composites of PLGA combined separately with nanophase alumina, titania, and HA (30:70 wt% PLGA/ceramic) (Figure 22.20) [123]. For example, up to three times more osteoblasts adhered to PLGA when it contained nanophase compared to conventional titania particles [116]. Since similar porosity

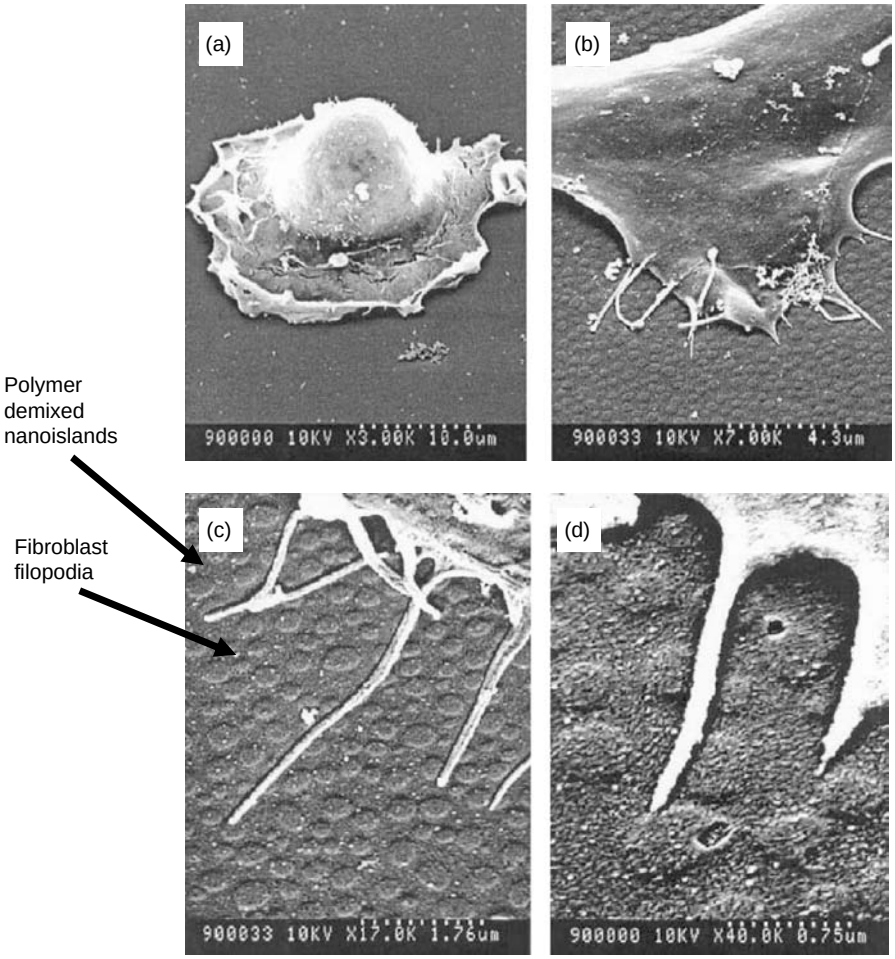

FIGURE 22.19 Polymer nanoislands created by de-mixing polystyrene and polybromo-styrene. Altered cell functions have been observed on polymer nanoislands compared to conventional polymer topographies. (a) through (d) represents increased magnification. (From Dalby, M.J. et al., *Biomaterials*, 23, 2945, 2002. With permission.)

(both percentages and diameters) existed between PLGA with conventional titania compared to nanophase titania, another novel property of nanophase ceramic composites was elucidated in this study: increased osteoblast functions. This is in addition to numerous reports in the literature highlighting greater toughness of nanophase compared to conventional ceramic/polymer composites [44–46].

Moreover, promoted responses of osteoblasts have also been reported when carbon nanofibers were incorporated into polymer composites; specifically, three times the number of osteoblasts adhered on PU with increasing weight percentages of nanometer carbon fibers when compared with conventional dimension carbon fibers (Figure 22.21) [124]. As mentioned, reports in the literature have demonstrated higher osteoblast adhesion on nanophase carbon fibers in comparison with conventional carbon fibers (or titanium [ASTM F-67, Grade 2] [124]), but this study demonstrated greater osteoblast adhesion with only a 2 wt% increase of carbon nanofibers in the PU matrix. Up to three and four times the number of osteoblasts that adhered on the 100:0 PU/CN wt%, adhered on the 90:10 and the 75:25 PU/CN wt% composites, respectively [124]. This exemplifies the unprecedented ability of nanophase materials to increase functions of bone cells whether used alone or in polymer composite form.

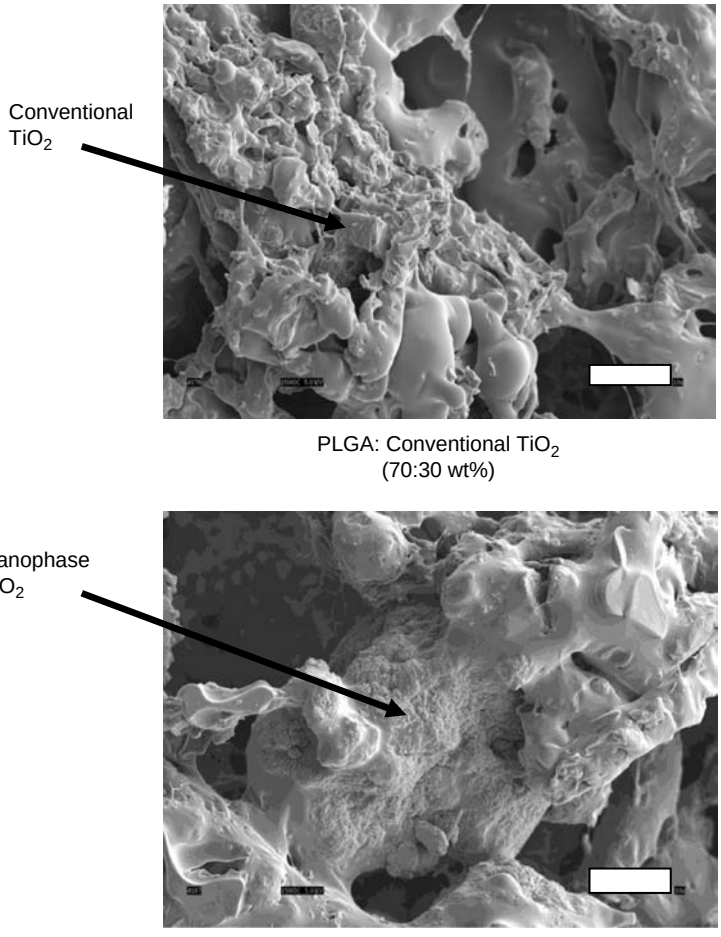

FIGURE 22.20 Scanning electron micrographs of poly-lactic-glycolic acid (PLGA): titania composites. Increased osteoblast function has been observed on polymer composites containing nanophase compared to conventional ceramics. Scale bar = 10 μm. (From Webster, T.J. and Smith, T.A., *J. Biomed. Mater. Res.*, 74, 677–686, 2004. With permission.)

22.9 AREAS OF APPLICATION

While there has already been some effort on incorporating nanotechnology into orthopedic applications, it is clear that this is only the beginning for the incorporation of nanotechnology into biology. In the following sections some additional avenues are highlighted.

22.9.1 DRUG DELIVERY

Polymers have found a significant role in the development of novel drug delivery systems. Biomaterials for muco-adhesive drug delivery applications have been improved through the addition of PEG as an adhesion promoter [126–129]. Additionally, smart hydrogel drug carriers have been molecularly designed to carry safely proteins and peptides to the duodenum region, avoiding the harsh, acidic conditions of the stomach and the proteolytic enzymes present along the gastrointestinal tract [130–132]. Drug delivery systems composed of degradable polymers, such as

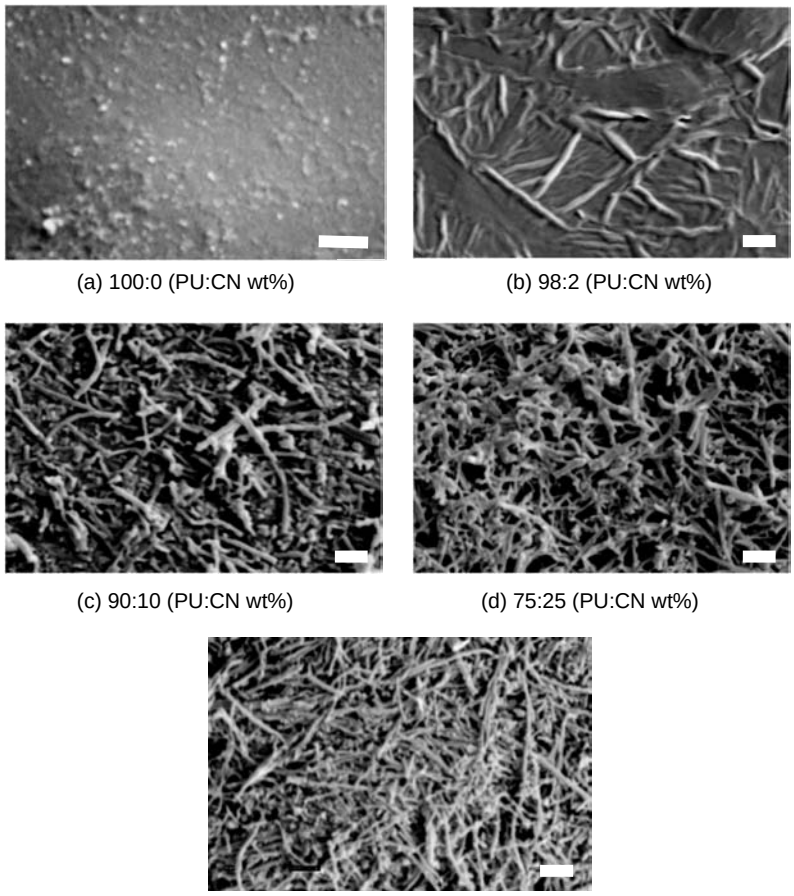

FIGURE 22.21 Scanning electron micrographs of poly-ether-urethane (PU): carbon nanofibers (wt.%) composites. Increased functions of osteoblasts have been observed on polymer composites containing carbon nanofibers. Scale bar = 1 μm. (From Price, R.L. et al., *Biomaterials*, 24, 1877, 2003. With permission.)

polyanhydrides [133–136], polyorthoesters [137,138], and PLGA [139,140], have been implemented in chemically controlled drug delivery.

Lu and Chen [141] have highlighted recent developments in the nanofabrication of biodegradable drug delivery systems, and Leoni and Desai [142] have offered a review of the abilities to create nanoporous structures containing an optimal pore size and distribution. Nanoporous structures [143] have the ability to allow mass transport of desirable compounds but limit those that are undesirable. An example given in the aforementioned review is the nanoporous encapsulation of pancreatic islet cells. The controlled pore size could allow certain molecules such as glucose transport but significantly hinder the diffusion of molecules responsible for causing immune response-mediated device failure such as immunoglobulin G and M molecules (IgG and IgM).

Nanodrug delivery systems are quickly evolving in their ability to integrate biologically complex components into a functional nanodevice. Lee et al. [144] offer the bacmid process as an object-oriented approach for designing novel nanosystems and outline the possibility of using this type of design process for effective delivery of vaccines. Santini et al. [40] have demonstrated the ability to deliver nanoliter quantities of therapeutics on demand from an array of sealed reservoirs. Drug discovery and delivery are becoming sciences that encompass skills in nanotechnology,

microtechnology, and biology to design systems effectively more capable of achieving efficient and effective therapeutic treatments [145].

Much effort has been dedicated to engineering nanoparticulate drug delivery systems [146,147]. Surface modification allows the specific targeting of particles and enhances their ability to interact with certain types of cells [148]. Size plays a key role in the ability of particles to participate in intracellular uptake, and biodegradable nanoparticles can be used as sustained-release delivery systems once inside the cytoplasm [149].

22.9.2 Tissue Engineering

Tissue engineering strives to create living tissue and organs through the use of synthetic, hybrid, or natural materials that have been designed or fabricated in a way to elicit a desirable cellular response from the scaffold [150]. The major thrust of developing materials for tissue engineering is providing the cells an environment in which they can continue their normal functionality. Biodegradable and resorbable materials are favorable due to the lack of necessity of a material structure to be present once the matrix has been formed. Poly(lactic acid), poly(glycolic acid), and their copolymers (PLGA) were first utilized in the development of biodegradable materials for tissue engineering applications, followed by other types of materials that include PUs [151], polyanhydrides [152,153], and, more recently, poly(ether anhydrides) [154].

This chapter has provided some nanotechnology-based examples of tissue engineering advances in orthopedics. In addition, Tsang and Bhatia [155] offer an extensive review into the fabrication techniques developed to aid in the development of novel tissue scaffolds. Significant advances in fabrication using heat, light, adhesives, and molding are elaborated upon. The use of cells to self-assemble native cellular matrices and cell/scaffold hybrids are also highlighted. Biomimetic materials are actively being pursued as integral components of novel tissue engineering biomaterials [156,157]. Various techniques are being employed to take advantage of the ability to modify the surface of tissue engineering materials, with RGD modification receiving the most attention [158].

Synthetic hydrogels have traditionally been employed in the development of tissue engineering scaffolds due to their high biocompatibility, hydrophilicity, and tissue-like properties. The molecular design of these materials affords the engineer the ability to impart certain physical properties into the device to obtain the necessary physiological response. Poly(lactic acid)-g-poly(vinyl alchol) (PLA-g-PVA) have been developed for heart valves [159], and PVA/poly(vinyl pyrrolidone) (PVA/PVP) blends have been proposed for nucleus pulposus replacement [160]. Natural materials that have been developed for tissue engineering applications include collagen, hyaluronic acid, alginate, and chitosan [161].

Hybrid materials are being utilized to take advantage of the ability to synthesize polymeric materials with specific properties combined with a bioactive entity that helps elicit a particular biological response. Chondroitin sulfate, a biological polymer and PVA, a synthetic polymer, have been used to synthesize hydrogels that promote chondrogenesis [162]. Mixtures of peptides and synthetic polymers are combined in order to mimic extracellular matrix proteins to enable natural wound healing and reduce the formation of fibrous encapsulation. RGD has been used frequently to impart these properties into a biomaterial [158].

22.9.3 Biological Micro-Electro-Mechanical Systems

Most research focusing on biological micro-electro-mechanical systems (BioMEMS) is for their use in diagnostic devices and for the detection of DNA, viruses, proteins, and other biologically derived molecules [163]. Nanoscale BioMEMS could allow for the real-time detection and analysis of signaling pathways, which would further our knowledge and understanding of the basic mechanisms and functions of the cell. While nanoscale BioMEMS is at its infancy, it is clear that nanotechnology will play an important role in its development.

22.10 CONSIDERATIONS AND FUTURE DIRECTIONS

Although preliminary attempts to incorporate nanotechnology into biomedical applications seem promising, numerous urgent questions still remain with regard to this new field. First and foremost, the question of safety of nanoparticles once in the human body remains largely unanswered both from a manufacturing point of view and when used in full or as a components of an implantable device. Since such particles are smaller than many pores of biological tissues, it is clear that this information will have to be obtained before further consideration of implantable nanomaterials is undertaken. Such nanoparticles can easily become dislodged from implants during surgical implantation or by fragmentation of articulating components of a joint prosthetic composed of nanophase materials. Although preliminary *in vitro* studies highlight a less adverse influence of nanometer compared to micron particulate wear debris on bone cell viability [164,165], many more experiments are needed, especially *in vivo* to evaluate their efficacy.

Specifically for orthopedic applications, additional questions remain. For example, once exact optimal nanometer surface features are elucidated for increasing bone regeneration, inexpensive tools that can be used in industry will be required. In this context, if the only nanofabrication devices that can be used to synthesize desirable nanometer surface features for bone regeneration are e-beam lithography or other equally expensive techniques, industry may not participate in this boom of nanotechnology at the intersection of tissue engineering. Inexpensive but effective nanometer synthesis techniques must continually be a focus of many investigators.

The direction of the nanotechnology should be and is geared toward dealing with these issues. For example, according to the U.S. government's research agenda, current and future broad interests in nanobiomedical activity can be categorized into three broad related fronts [51,52]:

1. development of pharmaceuticals for inside-the-body applications — such as drugs for anti-cancer and gene therapy
2. development of diagnostic sensors and lab-on-a-chip techniques for outside-the-body applications — such as biosensors to identify bacteriological infections in biowarfare
3. development of prostheses and implants for inside-the-body uses

Whereas the European governments emphasize commercial applications in all the three fronts mentioned above, according to Marsch [52], the U.S. government tends to lean toward fundamental research on biomedical implants and biodefense, leaving commercial applications to industry. Both classifications identify nanophase biomedical implants as a potential interest. The biological and biomimetic nanostructures to be used as orthopedic implants involve some sort of an assembly in which smaller materials later on assume the shape of a body part, such as hip bone. These final biomimetic, bulk nanostructures can start with a predefined nanochemical (like an array of large reactive molecules attached to a surface) or nanophysical (like a small crystal) structure. It is believed that by using these fundamental nanostructured building blocks as seed molecules or crystals, a larger bulk material will self-assemble or keep growing by itself.

In summary, it is now believed that significant evidence exists that highlights the promise nanotechnology has for biological applications, particularly in the bone arena. Clearly, nanomaterials as mentioned here are at their infancy and require much more testing before their full potential can be realized. However, even if nanophase materials never make it to the marketplace due to safety concerns, we have already learned much about how cells interact with surfaces through their application in the orthopedic environment.

ACKNOWLEDGMENTS

JBT is supported through a Department of Homeland Security graduate research fellowship. JBT and NAP thank NIH and NSF for support of the research summarized here. MS and TJW thank the NSF and NIH for funding part of the research summarized here through the Bio-Nanotechnology National Initiative.

REFERENCES

1. Ratner, B.D., Biomaterials science: a multidisciplinary endeavor, in *Biomaterials Science: An Introduction to Materials in Medicine*, 2nd ed., Ratner, B.D., Hoffman, A.S., Schoen, F.J., and Lemons, J.E., Eds., Academic Press, San Diego, 2004, pp. 1–9.
2. Langer, R. and Peppas, N.A., Advances in biomaterials, drug delivery, and dionanotechnology, *AIChE J.*, 49, 2990, 2003.
3. Peppas, N.A. and Langer, R., New challenges in biomaterials, *Science*, 263, 1715, 1994.
4. Hilt, J.Z., Nanotechnology and biomimetic methods in therapeutics: molecular scale control with some help from nature, *Adv. Drug Delivery Rev.*, 56, 1533, 2004.
5. http://www.aaos.org/wordhtml/press/arthropl.htm
6. http://www.azcentral.com/health/0617newhips17/html
7. http://www.aaos.org/wordhtml/press/joinrepl.htm
8. http://www.aaos.org/wordhtml/press/hip_knee.htm
9. Minino, A.M. and Smith, B.L., Vital statistics, *National Vital Statistics Reports*, Vol. 49, 2001, p. 12.
10. http://www.cdc.gov/nchs/fastats/lifexpec.htm
11. Dowson, D., New joints for the millennium: wear control in total hip replacement hip joints, *Proc. Inst. Mech. Eng. Part H- J. Eng. Med.*, 215, 335, 2001.
12. Kaplan, F.S., Hayes, W.C., Keaveny, T.M., Boskey, A., Einhorn, T.A., and Ianotti, J.P., in *Bone in Orthopedic Basic Science*, Simon, S.P., Ed., American Academy of Orthopedic Surgeons, Columbus, OH, 1994, p. 127.
13. Oparaugo, P.C., Clarke, I.C., Malchau, H., and Herberts, P., Correlation of wear debris-induced osteolysis and revision with volumetric wear-rate of polyethylene: a survey of 8 reports in literature, *Acta Orthopaed. Scand.*, 72, 22, 2001.
14. Urban, R.M., Jacobs, J.J., Tomlinson, M.J., Gavrilovic, J., Black, J., and Peoc'h, M., Dissemination of wear particles to the liver, spleen, and abdominal lymph nodes of patients with hip or knee replacement, *Am. J. Bone Jt. Surg.*, 82, 457, 2000.
15. Lerouge, S., Huk, O., Yahia, L.H., and Sedel, L., Characterization of in vitro wear debris from ceramic-ceramic total hip arthroplastics, *J. Biomed. Mater. Res.*, 32, 627, 1996.
16. Horbett, T.A., Proteins: structure, properties and adsorption to surfaces, in *Biomaterials Science: An Introduction to Materials in Medicine*, Ratner, B.D., Hoffman, A.S., Schoen, F.S., and Lemmons, J.E., Eds., Academic Press, New York, 1996, p. 133.
17. Schakenraad, J.M., Cell: their surfaces and interactions with materials, in *Biomaterials Science: An Introduction to Materials in Medicine*, Ratner, B.D., Hoffman, A.S., Schoen, F.S., and Lemmons, J.E., Eds., Academic Press, New York, 1996, p. 133.
18. Brunette, D.M., The effects of implant surface topography on the behavior of cells, *Int. J. Oral Max. Implants*, 3, 231, 1988.
19. Martin, J.Y., Schwart, Z.Z., Hummert, T.W., Schraub, D.M., Simpson, J., Lankford, J.J., Dean, D.D., Cochran, D.L., and Boyan, B.D., Effect of titanium surface roughness on proliferation, differentiation, and protein synthesis of human osteoblast-like cells (MG63), *J. Biomed. Mater. Res.*, 29, 389, 1995.
20. Wen, H.B., Cui, F.Z., and Zhu, X.D., Microstructural features of non-union of human humeral shaft fracture, *J. Struct. Biol.*, 119, 239, 1997.
21. Larsson, C., Thomsen, P., Aronsson, B.O., Rodal, M., Lausmaa, J., Kasemo, B., and Ericson, L.E., Bone response to surface modified titanium implants: studies on electropolished implants with different oxide thicknesses and morphology, *Biomaterials*, 15, 1062, 1994.
22. Bordji, K., Jouzeau, J.Y., Mainard, D., Payan, E., Wetter, P., Rie, K.T., Stucky, T., and Hage-Ali, M., Cytocompatibility of Ti-6Al-4V and Ti-5Al-2.5Fe alloys according to three surface treatments, using human fibroblasts and osteoblasts, *Biomaterials*, 17, 929, 1996.
23. Lalan, S., Pomerantseva, I., and Vacanti, J.P., Tissue engineering and its potential impact on surgery, *World J. Surg.*, 25, 1458, 2001.
24. Andersson, H. and van den Berg, V., Microfabrication and microfluidics for tissue engineering: state of the art and future opportunities, *Lab On A Chip*, 4, 98, 2004.
25. Saltzman, W.M. and Olbricht, W.L., Building drug delivery into tissue engineering, *Nat. Rev. Drug Discov.*, 1, 177, 2002.
26. Tirrell, M., Kokkoli, E., and Biesalski, M., The role of surface science in bioengineered materials, *Surf. Sci.*, 500, 61, 2002.

27. Gershon, D., Microarray technology an array of opportunities, *Nature*, 416, 885, 2002.
28. Meller, A., Nivon, L., Brandin, E., Golovchenko, J., and Branton, D., Rapid nanopore discrimination between single polynucleotide molecules, *Proc. Natl. Acad. Sci. USA*, 97, 1079, 2000.
29. Bayley, H. and Cremer, P., Stochastic sensors inspired by biology, *Nature*, 413, 226, 2001.
30. Li, J.L., Gershow, M., Stein, D., Brandin, E., and Golovchenko, J.A., DNA molecules and configurations in a solid-state nanopore microscope, *Nat. Mater.*, 2, 611, 2003.
31. Storm, A.J., Chen, J.H., Ling, X.S., Zandbergen, H.W., and Dekker, C., Fabrication of solid-state nanopores with single-nanometre precision, *Nat. Mater.*, 2, 537, 2003.
32. Wang, H. and Branton, D., Nanopores with a spark for single-molecule detection. *Nat. Biotechnol.*, 19, 622, 2001.
33. Zhang, S., Fabrication of novel biomaterials through molecular self-assembly, *Nat. Biotechnol.*, 21, 1171, 2003.
34. Byrne, M.E., Park, K., and Peppas, N.A., Molecular imprinting within hydrogels, *Adv. Drug Delivery Rev.*, 54, 149, 2002.
35. Manz, A., Graber, N., and Widmer, H., Miniaturized total chemical analysis systems: a novel concept for chemical sensing, *Sensors Actuators B – Chem.*, 1, 244, 1990.
36. Jakeway, S., de Mello, A., and Russell, E., Miniaturized total analysis systems for biological analysis, *Fresen. J. Anal. Chem.*, 366, 525, 2000.
37. Tudos, A., Besselink, G., and Schasfoort, R., Trends in miniaturized total analysis systems for point-of-care testing in clinical chemistry, *Lab On A Chip*, 1, 83, 2001.
38. Liu, Y., Garcia, C., and Henry, C., Recent progress in the development of μTAS for clinical analysis, *Analyst*, 128, 1002, 2003.
39. LaVan, D., Lynn, D., and Langer, R., Moving smaller in drug discovery and delivery, *Nat. Rev. Drug Discov*., 1, 77, 2002
40. Santini, S., Jr., Cima, M., and Langer, R., A controlled-release microchip, *Nature*, 397, 335, 1999.
41. Grayson, A.C.R., Choi, I.S., Tyler, B.M., Wang, P.P., Brem, H., Cima, M.J., and Langer, R., Multi-pulse drug delivery from a resorbable polymeric microchip device. *Nat. Mater*., 2, 767, 2003.
42. Siegel, R.W. and Fougere, G.E., Mechanical properties of nanophase materials, in *Nanophase Materials: Synthesis-Properties Applications*, Hadjipanayis, G.C. and Siegel, R.W., Eds., Kulwer, Dordrecht, 1994, p. 233.
43. Roco, M.S., Williams, R.S., and Alivisatos, P., Nano-Technology Research Directions, IWGN Workshop Report, 1999.
44. Siegel, R.W. and Fougere, G.E., Mechanical properties of nanophase metals, *Nanostruct. Mater.*, 6, 205, 1995.
45. Siegel, R.W., Creating nanophase materials, *Sci. Amer.*, 275, 42, 1996.
46. Siegel, R.W., Hu, E., and Roco, M.C., *Nano-Structure Science and Technology*, Kluwer Academic Press, Boston, MA, 1999.
47. Baraton, M.I., Chen, X., and Gonsalves, K.E., FTIR study of nanostructured alumina nitride powder surface: determination of the acidic/basic sites by CO, CO_2, and acetic acid adsorptions, *Nanostruct. Mater.*, 8, 435, 1999.
48. Klabunde, K.J., Strak, J., Koper, O., Mohs, C., Part, D., Decker, S., Jiang, Y., Lagadic, I., and Zhang, D., Nanocrystals as stoichiometric reagents with unique surface chemistry, *J. Phys. Chem.*, 100, 12141, 1996.
49. Wu, S.J., DeJong, L.C., and Rahaman, M.N., Sintering of nanophase γ-Al_2O_3 powder, *J. Am. Ceramic Soc.*, 79, 2207, 1996.
50. Martyanov, I.N. and Klabunde, K.J., Photocatalytic oxidation of gaseous 2-chloroethyl ethyl sulfide over TiO_2, *Environ. Sci. Technol.*, 37, 3448, 2003.
51. Malsch, I., Biomedical applications of nanotechnology, *Ind. Phys.*, June/July 15, 2002.
52. Malsch, I., The nano-body: sense and non-sense on biomedical applications of nanotechnology, *Lecture for COST and NanoSTAG Conference*, Leuven, Oct. 29, 2001.
53. Ayad, S., Boot-Handford, R., Humphries, M.J., Kadler, K.E., and Shuttleworth, A., *The Extracellular Matrix Factsbook*, Academic Press, San Diego, CA, 1994, p. 29.
54. Cowin, R., *Handbook of Bioengineering*, McGraw Hill, New York, 1987.
55. Brunette, D., The effect of surface topography of cell migration and adhesion, in *Titanium in Medicine*, Brunette, D.M., Tengvall, P., Textor, M., and Thomsen, P., Eds., Springer, New York, 2001, pp. 486–512.

56. Buser, D., Nydegger, T., Oxland, T., Cochran, D.L., Schenk, R.K., Hirt, H.P., Snetivy, D., and Nolte, L.P., Interface shear strength of titanium implants with a sandblasted and acid-etched surface: a biomechanical study in the maxilla of miniature pigs, *J. Biomed. Mater. Res.*, 45, 75, 1999.
57. Hench, L.L. and Paschall, H.A., Histochemical responses at a biomaterial's interface, *J. Biomed. Mater. Res.*, 8, 49, 1974.
58. Litsy, A.S. and Spector, M., Biomaterials, in *Orthopedic Basic Science*, Simon, S.P., Ed., American Academy of Orthopedic Surgeons, Columbus, OH, 1994, p. 482.
59. Nikolovski, J. and Mooney, D.J., Smooth muscle cell adhesion to tissue engineering scaffolds, *Biomaterials*, 21, 2025, 2000.
60. Peppas, N.A., *Hydrogels in Medicine and Pharmacy*, CRC Press, Boca Raton, FL, 1987.
61. Peppas, N.A., Gels for drug delivery, in *Encylcopedia of Materials: Science and Technology*, Elsevier, Amsterdam, 2001, p. 3492.
62. Peppas, N.A., Hydrogels, in *Biomaterials Science: An Introduction to Materials in Medicine*, 2nd ed., Ratner, B.D., Hoffman, A.S., Schoen, F.J., and Lemons, J.E., Eds., Academic Press, San Diego, CA, 2004, p. 100.
63. Wichterle, O. and Lim, D., Hydrophilic gels for biological use, *Nature*, 185, 117, 1960.
64. Tighe, B.J., The design of polymers for contact lens applications, *Br. Polym. J.*, 8, 71, 1976.
65. Peppas, N.A. and Yang, W.H.M., Properties-based optimization of the structure of polymers for contact lens applications, *Contact Intraocular Lens Med. J.*, 7, 300, 1981.
66. Peppas, N.A, Wood, K.M., and Blanchette, J.O., Hydrogels for oral delivery of therapeutic proteins, *Expert Opinion Bio. Ther.*, 4, 881, 2004.
67. Peppas, N.A., Fundamentals of pH- and temperature-sensitive delivery systems, in *Pulsatile Drug Delivery*, Gurny, R., Junginger, H.E., and Peppas, N.A., Eds., Wissenschaftliche Verlagsgesellschaft, Stuttgart, 1993, pp. 41–56.
68. Peppas, N.A. et al., Physicochemical foundations and structural design of hydrogels in medicine and biology, *Ann. Rev. Biomed. Eng.*, 2, 9, 2000.
69. Flory, P.J., *Principles of Polymer Chemistry*, Cornell University Press, Ithaca, NY, 1953.
70. Hilt, J.Z. and Byrne, M.E., Configurational biomimesis in drug delivery: molecular imprinting of biologically significant molecules, *Adv. Drug Delivery Rev.*, 56, 1599, 2004.
71. Castner, D.G. and Ratner, B.D., Biomedial surface science: foundations to frontiers, *Surf. Sci.*, 500, 28, 2002.
72. Vroman, L., Effects of hydrophobic surfaces upon blood coagulation, *Thrombos. Diathes. Haemorth.*, 10, 455, 1964.
73. Vroman, L. and Adams, A.L., Findings with the recording ellipsomoter suggesting rapid exchange of specific plasma proteins at liquid/solid interfaces, *Surf. Sci.*, 16, 438, 1969.
74. Baier, R.E. et al., Surface properties determine bioadhesive outcomes: methods and results, *J. Biomed. Mater. Res.*, 18, 337–355, 1984.
75. Hoffman, A.S., Principles governing biomolecule interactions in foreign interfaces, *J. Biomed. Mater. Res. Symp.*, 5, 77, 1974.
76. Lopez, G.P. et al., Plasma deposition of ultrathin films of poly(2-hydroxy-ethyl methacrylate): Surface analysis and protein adsorption measurements, *Macromolecules*, 26, 3247, 1993.
77. Merrill, E.W., Pol(ethylene oxide) blood contact, in *Poly(ethylene glycol) Chemistry: Biotechnical and Biomedical Applications*, Harris, J.M., Ed., Plenum Press, New York, 1992, pp. 199–220.
78. Mar, M.N., Ratner, B.D., and Yee, S.S., An intrinsically protein-resistant surface plasmon resonance biosensor based upon a RF-plasma-deposited thin film, *Sensors Actuators B*, 54, 125, 1999.
79. Drotleff, S. et al., Biomimetic polymers in pharmaceutical and biomedical sciences, *Eur. J. Pharm. Biopharm.*, 58, 385–407, 2004.
80. Peppas, N. and Khare, A., Preparation, structure and diffusional behavior of hydrogels in controlled release, *Adv. Drug Delivery Rev.*, 11, 1–35, 1993.
81. Peppas, N.A. et al., Hydrogels in pharmaceutical formulations, *Eur. J. Pharm. Biopharm.*, 50, 27, 2000.
82. Torres-Lugo, M. and Peppas, N.A., Preparation and characterization of p(MAA-g-EG) nanospheres for protein delivery applications, *J. Nanoparticle Res.*, 4, 73, 2002.
83. Donini, C. et al., Preparation of poly(methacrylic acid-g-poly(ethylene glycol)) nanospheres from methacrylic monomers for pharmaceutical applications, *Int. J. Pharm.*, 245, 83, 2002.
84. Robinson, D. and Peppas, N.A., Preparation and characterization of pH-resonsive poly(methacrylic acid-g-ethylene glycol) nanospheres, *Macromolecules*, 35, 3668, 2002.

85. Gref, R. et al., Biodegradable long-circulating polymeric nanospheres, *Science*, 263, 1600, 1994.
86. Peracchia, M.T., Stealth nanoparticles for intravenous administration, S*TP Pharma Sci.*, 13, 155, 2003.
87. Cohen, H. et al., Sustained delivery and expression of DNA encapsulated in polymeric nanoparticles, *Gene Ther*., 7, 1896, 2000.
88. Luo, D. and Saltzman, W., Synthetic DNA delivery systems, *Nat. Biotechnol.*, 18, 33, 2000.
89. Brannon-Peppas, L., Recent advances on the use of biodegradable microparticles and nanoparticles in controlled drug delivery, *Int. J. Pharm.*, 116, 1, 1995.
90. Santini, J., Jr. et al., Microchips as controlled drug-delivery devices, *Angew. Chem. Int. Ed*., 39, 2396–2407, 2000.
91. Webster, T.J., Siegel, R.W., and Bizios, R., An in vitro evaluation of nanophase alumina for orthopaedic/dental applications, in *Bioceramics 11: Proceedings of the 11th International Symposium on Ceramics in Medicine*, LeGeros, R.Z. and LeGeros, J.P., Eds., World Scientific, New York, 1998, p. 273.
92. Webster, T.J., Siegel, R.W., and Bizios, R., Design and evaluation of nanophase alumina for orthopaedic/dental applications, *Nanostruct. Mater.*, 12, 983, 1999.
93. Webster, T.J., Siegel, R.W., and Bizios, R., Osteoblast adhesion on nanophase ceramics, *Biomaterials*, 20, 1221, 1999.
94. Webster, T.J., Ergun, C., Doremus, R.H., Siegel, R.W., and Bizios, R., Specific proteins mediate enhanced osteoblast adhesion on nanophase ceramics, *J. Biomed. Mater. Res.*, 51, 475, 2000.
95. Webster, T.J., Siegel, R.W., and Bizios, R., Enhanced functions of osteoblasts on nanophase ceramics, *Biomaterials*, 21, 1803, 2000.
96. Webster, T.J., Siegel, R.W., and Bizios, R., Enhanced surface and mechanical properties of nanophase ceramics for increased orthopaedic/dental implant efficacy, in *Bioceramics 13: Proceedings of the 13th International Symposium on Ceramics in Medicine*, Giannini S. and Moroni, A., Eds., World Scientific, New York, 2000, p. 321.
97. Webster, T.J., The future of orthopedic and dental implant materials, in *Advances in Chemical Engineering Vol. 27*, Ying J.Y., Ed., Academic Press, New York, 2001, p. 125.
98. Webster, T.J., Schadler, L.S., Siegel, R.W., and Bizios, R., Mechanisms of enhanced osteoblast adhesion on nanophase alumina involve vitronectin, *Tissue Eng.*, 7, 291, 2001.
99. Webster, T.J., Ergun, C., Doremus, R.H., Siegel, R.W., and Bizios, R., Enhanced functions of osteoclast-like cells on nanophase ceramics, *Biomaterials*, 22, 1327, 2001.
100. Webster, T.J., Siegel, R.W., and Bizios, R., Nanoceramic surface roughness enhances osteoblast and osteoclast functions for improved orthopaedic/dental implant efficacy, *Scr. Mater.*, 44, 1639, 2001.
101. Elias, K.L., Price, R.L., and Webster, T.J., Enhanced functions of osteoblasts on nanometer diameter carbon fibers, *Biomaterials*, 23, 3279, 2002.
102. Danilov, Y.N. and Juliana, R.L., (Arg-Gly-Asp)n-albumin conjugates as a model substratum for integrin-mediated cell adhesion, *Exp. Cell Res.*, 182, 186, 1989.
103. Hughes, R.C., Pena, S.D.J., Clark, J., and Dourmashkin, R.R., Molecular requirements for adhesion and spreading of hamster fibroblasts, *Exp. Cell Res.*, 121, 307, 1979.
104. Humphries, M.J., Akiyama, S.K., Komoriya, A., Olden, K., Yamada, and K.M., Identification of an alternatively spliced site in human plasma fibronectin that mediates cell type-specific adhesion, *J. Cell Biol*., 103, 2637, 1986.
105. Singer, I.I., Kawka, D.W., Scott, S., Mumford, R.A., and Lark, M.W., Cell surface distribution of fibronectin and vitronectin receptors depends on substrate composition and extracellular matrix accumulation, *J. Cell Biol*., 104, 573, 1987.
106. Underwood, P.A. and Bennett, F.A., A comparison of the biological activities of the cell-adhesive proteins vitronectin and fibronectin, *J. Cell Sci.*, 93, 641, 1989.
107. Massia, S.P. and Hubbell, J.A., Human endothelial cell interactions with surface-coupled adhesion peptides on a nonadhesive glass substrate and two polymeric biomaterials, *J. Cell Biol.*, 14, 1089, 1991.
108. Li, P., Biomimetic nano-apatite coating capable of promoting bone ingrowth, *J. Biomed. Mater. Res.*, 66, 79, 2003.
109. Thull, R. and Grant, D., Titanium surface modification, in *Titanium in Medicine*, Brunette, D.M., Tengvall, P., Textor, M., and Thomsen P., Eds., Springer, New York, 2001, p. 284.
110. Sato, M., Slamovich, E.B., and Webster, T.J., Novel nanophase hydroxyapatite coatings on titanium, *29th International Conference on Advanced Ceramics and Composites*, Cocoa Beach, FL, 2005.

111. Price, R.L., Gutwein, L.G., Kaledin, L., Tepper, F., and Webster, T.J., Osteoblast function on nanophase alumina materials: influence of chemistry, phase, and topography, *J. Biomed. Mater. Res.*, 67, 1284–1293, 2003.
112. Dee, K.C., Andersen, T.T., Rueger, D.C., and Bizios, R., Conditions which promote mineralization at the bone-implant interface: a model in vitro study, *Biomaterials*, 17, 209, 1996.
113. Chun, A., Moralez, J., Fenniri, H., and Webster, T.J., Helical rosette nanotubes: a more effective orthopaedic implant material, *Nanotechnology*, 15, S234, 2004.
114. Ejiofor, J.U. and Webster, T.J., Increased osteoblast functions on nanostructured metals, *ASM Conference*, Las Vegas, NV, 2004.
115. Dalby, M.J., Riehle, M.D., Johnstone, H., Affrossman, S., and Curtis, A.S.G., In vitro reaction of endothelial cells to polymer demixed nanotopography, *Biomaterials*, 23, 2945, 2002.
116. Kay, S., Thapa, A., Haberstroh, K.M., and Webster, T.J., Nanostructured polymer: nanophase ceramic composites enhance osteoblast and chondrocyte adhesion, *Tissue Eng.*, 8, 753, 2002.
117. Zhang, R. and Ma, P.X., Porous poly(L-lactic acid)/apatite composites created by biomometic process, *J. Biomed. Mater. Res.*, 45, 285, 1999.
118. Park, G.E., Park, K., and Webster, T.J., Accelerated chondrocyte functions on NaOH-treated PLGA scaffolds, *Biomaterials*, 26, 3075, 2005.
119. Miller, D.C., Thapa, A., Haberstroh, K.M., and Webster, T.J., Endothelial and vascular smooth muscle cell function on poly(lactic-co-glycolic acid) with nano-structured surface features, *Biomaterials*, 25, 53, 2004.
120. Thapa, A., Webster, T.J., and Haberstroh, K.M., Nano-structured polymers enhance bladder smooth muscle cell function, *J. Biomed. Mater. Res.*, 67, 1374, 2003.
121. Li, W.-J., Laurencin, C., Caterson, E.J., Tuan, R.S., and Ko, F.K., Electrospun nanofibrous structure: a novel scaffold for tissue engineering, *J. Biomed. Mater. Res.*, 60, 613–621, 2002.
122. Pattison, M., Webster, T.J., and Haberstroh, K.M., Three-dimensional, nano-structured PLGA scaffolds for bladder tissue replacement applications, *Biomaterials*, 26, 3075–3082, 2005.
123. Webster, T.J., and Smith, T.A., Improved osteoblast functions on polymer: nanophase ceramic composites, *J. Biomed. Mater. Res.*, 74, 677–686, 2005.
124. Price, R.L., Waid, M.C., Haberstroh, K.M., and Webster, T.J., Select bone cell adhesion on formulations containing carbon nanofibers, *Biomaterials*, 24, 1877, 2003.
125. Tu, R. and Tirrell, M., Bottom-up design of biomimetic assemblies, *Adv. Drug Delivery Rev.*, 56, 1537, 2004.
126. Huang, Y.B., Leobandung, W., Foss, A., and Peppas, N.A., Molecular aspects of muco- and bioadhesion: tethered structures and site-specific surfaces, *J. Controlled Release*, 65, 63, 2000.
127. Huangs, Y., Szleifer, I., and Peppas, N.A., Gel-gel adhesion by tethered polymers, *J. Chem. Phys.*, 114, 3809, 2001.
128. Efremova, N.V., Huang, Y., Peppas, N.A., and Leckband, D.E., Direct measurement of interactions between tethered poly(ethylene glycol) and adsorbed mucin layers, *Langmuir*, 18, 836, 2002.
129. Peppas, N.A. and Huang, Y., Nanoscale technology of mucoadhesive interactions, *Adv. Drug Delivery Rev.*, 56, 1675, 2004.
130. Oral, E. and Peppas, N.A., Responsive and recognitive hydrogels using star polymers, *J. Biomed. Materer. Res.*, 68A, 439, 2004.
131. Nakamura, K., Murray, R.J., Joseph, J.I., Peppas, N.A., Morishita, M., and Lowman, A.M., Oral insulin delivery using P(MAA-g-EG) hydrogels: effect of network morphology on insulin delivery characteristics, *J. Controlled Release*, 95, 589, 2004.
132. Donini, C., Robinson, D.N., Colombo, P., Giordano, F., and Peppas, N.A., Preparation of P(MAA-g-EG) nanospheres for pharmaceutical applications, *Int. J. Pharm.*, 245, 83, 2002.
133. Quick, D.J., Macdonald, K.K., and Anseth, K.S., Delivering DNA from photocrosslinked, surface eroding polyanhydrides, *J. Controlled Release*, 97, 333, 2004.
134. Gopferich, A. and Tessmar, J., Polyanhydride degradation and erosion, *Adv. Drug Delivery Rev.*, 54, 911, 2002.
135. Burkoth, A.K., Burdick, J., and Anseth, K.S., Surface and bulk modifications to photocrosslinked polyanhydrides to control degradation behavior, *J. Biomed. Mater. Res.*, 51, 352, 2000.
136. Dang, W.B. and Saltzman, W.M., Controlled-release of macromolecules from a degradable polyanhydride matrix, *J. Biomater. Sci. Polym. Edn.*, 6, 297, 1994.

137. Shi, M., Yang, Y.Y., Chaw, C.S., Goh, S.H., Moochhala, S.M., Ng, S., and Heller, J., Double-walled POE/PLGA microspheres: encapsulation of water-soluble and water-insoluble proteins and their release properties, *J. Controlled Release*, 89, 167, 2003.
138. Merkli, A., Heller, J., Tabatabay, C., and Gurny, R., Synthesis and characterization of a new biodegradable semisolid poly(ortho ester) for drug-delivery systems, *J. Biomater. Sci. Polym. Edn.*, 4, 505, 1993.
139. Cegnar, M., Kos, J., and Kristi, J., Cystatin incorporated in poly(lactide-co-glycolide) nanoparticles: development and fundamental studies on preservation of its activity, *Eur. J. Pharm. Sci.*, 22, 357, 2004.
140. Kempen, D.H.R., Lu, L.C., Zhu, X., Kim, C., Jabbari, E., Dhert, W.J.A., Currier, B.L., and Yaszemski, M.J., Development of biodegradable poly(propylene fumarate)/poly(lactic-co-glycolic acid) blend microspheres: I. Preparation and characterization, *J. Biomed. Mater. Res. Part A*, 70A, 283, 2004.
141. Lu, Y. and Chen, S.C., Micro and nano-fabrication of biodegradable polymers for drug delivery, *Adv. Drug Delivery Rev.*, 56, 1621, 2004.
142. Leoni, L. and Desai, T.A., Micromachined biocapsules for cell-based sensing and delivery, *Adv. Drug Delivery Rev.*, 56, 211–229, 2004.
143. Desai, T.A., West, T., Cohen, M., Boiarski, T., and Rampersaud, A., Nanoporous microsystems for islet cell replacement, *Adv. Drug Delivery Rev.*, 56, 1661, 2004.
144. Lee, S.C., Bhalerao, K., and Ferrari, M., Object-oriented design tools for supramolecular devices and biomedical nanotechnology, *Ann. NY Acad. Sci*, 1013, 110, 2004.
145. LaVan, D.A., Lynn, D.M., and Langer, R., Moving smaller in drug discovery an delivery, *Nat. Rev. Drug Discov.*, 1, 77, 2002.
146. Crommelin, D.J.A., Storm, G., Jiskoot, W., Stenekes, R., Mastrobattista, E., and Hennink, W.E., Nanotechnological approaches for the delivery of macromolecules, *J. Controlled Release*, 87, 81, 2003.
147. Brannon-Peppas, L. and Blanchette, J.O., Nanoparticle and targeted systems for cancer therapy, *Adv. Drug Delivery Rev.*, 56, 1649, 2004.
148. Gupta, A.K and Curtis, A.S.G., Surface modified superparamagnetic nanoparticles for drug delivery: Interaction studies with human fibroblasts in culture, *J. Mater. Sci. Mater. Med.*, 18, 493, 2004.
149. Panyam, J. and Labhasetwarm, V., Biodegradable nanoparticles for drug and gene delivery to cells and tissue, *Adv. Drug Delivery Rev.*, 55, 329, 2003.
150. Griffith, L.G., Emerging design principles in biomaterials and scaffolds for tissue engineering, *Ann. NY Acad. Sci.*, 961, 83, 2002.
151. Buma, P., Ramrattan, N.N., van Tienen, T.G., and Veth, R.P.H., Tissue engineering of the meniscus, *Biomaterials*, 25, 1523, 2004.
152. Burkoth, A.K. and Anseth, K.S., A review of photocrosslinked polyanhydrides: in situ forming degradable networks, *Biomaterials*, 21, 2395, 2000.
153. Muggli, D.S., Burkoth, A.K., and Anseth, K.S., Crosslinked polyanhydrides for use in orthopedic applications: degradation behavior and mechanics, *J. Biomed. Mater. Res.*, 46, 271, 1999.
154. Kim, B.S., Hrkach, J.S., and Langer, R., Synthesis and characterization of novel degradable photocrosslinked poly(ether-anhydride) networks, *J. Polym. Sci. Part A Polym. Chem.*, 38, 1277, 2000.
155. Tsang, V.L. and Bhatia, S.N., Three-dimensional tissue fabrication, *Adv. Drug Delivery Rev.*, 56, 1635, 2004.
156. Shin, H., Jo, S., and Mikos, A.G., Biomimetic materials for tissue engineering, *Biomaterials*, 24, 4353, 2003.
157. Hacker, M., Tessmar, J., Neubauer, M., Blaimer, A., Blunk, T., Gopferich, A., and Schulz, M.B., Towards biomimetic scaffolds: anydrous scaffold fabrication from biodegradable amine-reactive diblock copolymers, *Biomaterials*, 24, 4459, 2003.
158. Hersel, U., Dahmen, C., and Kessler, H., RGD modified polymers: biomaterials for stimulated cell adhesion and beyond, *Biomaterials*, 24, 4385, 2003.
159. Nuttelman, C.R., Henry, S.M., and Anseth K.S., Synthesis and characterization of photocrosslinkable, degradable poly(vinyl alcohol)-based tissue engineering scaffolds, *Biomaterials*, 23, 3617, 2002.
160. Thomas, J., Lowman, A., and Marcolongo, M., Novel associated hydrogels for nucleus pulposus replacement, *J. Biomed. Mater. Res. Part A*, 67A, 1329, 2003.
161. Drury, J.L. and Mooney, D.J., Hydrogels for tissue engineering: scaffold design variables and applications, *Biomaterials*, 24, 4337, 2003.

162. Bryant, S.J., Davis-Arehart, K.A., Luo, N., Shoemaker, R.K., Arthur, J.A., and Anseth, K.S., Synthesis and characterization of photopolymerized multifunctional hydrogels: water-soluble poly(vinyl alcohol) and chondroitin sulfate macromers for chondrocyte encapsulation, *Macromolecules*, 37, 6726, 2004.
163. Bashir, R., BioMEMS: state-of-the-art in detection, opportunities and prospects, *Adv. Drug Delivery Rev.*, 56, 1565, 2004.
164. Gutwein, L.G. and Webster, T.J., Osteoblast and chrondrocyte proliferation in the presence of alumina and titania nanoparticles, *J Nanoparticle Res.*, 4, 231, 2002.
165. Price, R.L. and Webster, T.J., Increased osteoblast viability in the presence of smaller nano-dimensioned carbon fibers, *Nanotechnology*, 15, 892, 2004.

23 Nanoparticles for Drug Delivery

Meredith L. Hans and Anthony M. Lowman
Department of Materials Science and Engineering,
Drexel University, Philadelphia, Pennsylvania

CONTENTS

23.1 INTRODUCTION

Polymer nanoparticles are particles of less than 1 μm diameter that are prepared from natural or synthetic polymers. Nanoparticles have become an important area of research in the field of drug delivery because they have the ability to deliver a wide range of drugs to different areas of the body for sustained periods of time. The small size of nanoparticles is integral for systemic circulation. Natural polymers (i.e., proteins or polysaccharides) have not been widely used for this purpose since they vary in purity, and often require crosslinking that could denature the embedded drug. Consequently, synthetic polymers have received significantly more attention in this area. The most widely used polymers for nanoparticles have been poly-ε-caprolactone (PCL), poly(lactic acid) (PLA), poly(glycolic acid) (PGA), and their co-polymers, poly(lactide-co-glycolide) (PLGA) [1–3]. In addition, block co-polymers of PLA and poly(ethylene glycol) (PEG) and poly(amino acids) have been used to make nanoparticles and micelle-like structures [4,5]. These polymers are known for both their biocompatibility and resorbability through natural pathways. Additionally, the degradation rate and accordingly the drug release rate can be manipulated by varying the ratio of PLA or PCL, increased hydrophobicity, to PGA, and increased hydrophilicity.

During the 1980s and 1990s, several drug delivery systems were developed to improve the efficiency of drugs and minimize toxic side effects [6]. The early nano- and microparticles were mainly formulated from poly(alkylcyanoacrylate) [6]. Initial promise of microparticles was dampened by the fact that there was a size limit for the particles to cross the intestinal lumen into the lymphatic system following oral delivery. Likewise, the therapeutic effect of drug-loaded nanoparticles was relatively poor due to rapid clearance of the particles by phagocytosis postintravenous administration. In recent years, headway has been made in solving this problem by the addition of surface modifications to nanoparticles. Nanoparticles, such as liposomes, micelles, worm-like micelles, polymersomes, and vesicles have also been proposed recently in the literature as promising drug delivery vehicles because of their small size and hydrophilic outer shell.

In recent years, significant research has been done on nanoparticles as oral drug delivery vehicles. For this application, the major interest is in lymphatic uptake of the nanoparticles by the Peyer's patches in the gut associated lymphoid tissue (GALT). There have been many reports on the optimum size for Peyer's patch uptake ranging from <1 to <5 μm [7,8]. It has been shown that microparticles remain in the Peyer's patches while nanoparticles are disseminated systemically [9].

Nanoparticles have a further advantage over larger microparticles because they are better suited for intravenous (IV) delivery. The smallest capillaries in the body are 5 to 6 μm in diameter. The size of particles being distributed into the bloodstream must be significantly smaller than 5 μm, and should not form aggregates, to ensure that the particles do not form an embolism.

Clearly, a wide variety of drugs can be delivered using nanoparticulate carriers via a number of routes. Nanoparticles can be used to deliver hydrophilic drugs, hydrophobic drugs, proteins, vaccines, biological macromolecules, etc. [10–13]. They can be formulated for targeted delivery to the lymphatic system, brain, arterial walls, lungs, liver, spleen, or made for long-term systemic circulation. Therefore, numerous protocols exist for synthesizing nanoparticles based on the type of drug used and the desired delivery route. Once a protocol is chosen, the parameters must be tailored to create the best possible characteristics of the nanoparticles. Four of the most important characteristics of nanoparticles are their size, encapsulation efficiency, zeta potential (surface charge), and release characteristics. In this chapter, we intend to summarize many of the types of nanoparticles available for drug delivery, the techniques used for preparing polymeric nanoparticles, including the types of polymers and stabilizers used, and how these techniques affect the structure and properties of the nanoparticles. Additionally, we will discuss advances in surface modifications, targeted drug delivery applications, and release mechanisms and characteristics.

23.2 SYNTHESIS OF SOLID NANOPARTICLES

As stated previously, there are several different methods for preparing nanoparticles. Additionally, numerous methods exist for incorporating drugs into the particles. For example, drugs can be entrapped in the polymer matrix, encapsulated in a nanoparticle core, surrounded by a shell-like polymer membrane, chemically conjugated to the polymer, or bound to the particle's surface by adsorption. Many of the previously mentioned nanoscale carriers such as micelles and polymersomes are synthesized via self-assembly mechanisms. The following section will deal primarily with the production of solid nanoparticles. A summary of these methods including the types of polymer, solvent, stabilizer, and drugs used is given in Tables 23.1 and 23.2.

The most common method used for the preparation of solid, polymeric nanoparticles is the emulsification–solvent evaporation technique. This technique has been successful for encapsulating hydrophobic drugs, but has had poor results in incorporating bioactive agents of a hydrophilic nature. Briefly, solvent evaporation is carried out by dissolving the polymer and the compound in an organic solvent. Frequently, dichloromethane is used for PLGA copolymers. The emulsion is prepared by adding water and a surfactant to the polymer solution. In many cases, nano-sized polymer droplets are induced by sonication or homogenization. The organic solvent is then evaporated and the nanoparticles are usually collected by centrifugation and lyophilization [7,14–17].

A modification on this procedure has led to the protocol favored for encapsulating hydrophilic compounds and proteins, the double or multiple emulsion technique. First, a hydrophilic drug and a stabilizer are dissolved in water. The primary emulsion is prepared by dispersing the aqueous phase into an organic solvent containing a dissolved polymer. This is then re-emulsified in an outer aqueous phase also containing a stabilizer [8,9,15,18–20]. From here, the procedure for obtaining the nanoparticles is similar to the single emulsion technique for solvent removal. The main problem with trying to encapsulate a hydrophilic molecule like a protein or a peptide drug is the rapid diffusion of the molecule into the outer aqueous phase during the emulsification. This can result in poor encapsulation efficiency, i.e., drug loading. Therefore, it is critical to have an immediate formation of a polymer membrane during the first water-in-oil emulsion. Song et al. [15] were able to accomplish this by dissolving a high concentration of high-molecular-weight PLGA in the oil phase consisting of 80/20 wt% dichloromethane/acetone solution. Additionally, the viscosity of the inner aqueous phase was increased by increasing the concentration of the stabilizer, bovine serum albumin (BSA). The primary emulsion was then emulsified with Pluronic F68 resulting in drug-loaded particles of approximately 100 nm [15].

Another method that has been used to encapsulate insulin for oral delivery is phase inversion nanoencapsulation (PIN) [15,21]. In one example, Zn–insulin is dissolved in Tris-HCl and a portion of that is recrystallized by the addition of 10% $ZnSO_4$. The precipitate is added to a polymer solution of PLGA in methylene chloride. This mixture is emulsified and dispersed in 1 L of petroleum ether, which results in the spontaneous formation of nanoparticles [21].

All of the techniques mentioned previously use toxic, chlorinated solvents that could degrade certain drugs and proteins if they come into their contact during the process. Consequently, an effort has been made to develop other techniques in order to increase drug stability during the synthesis. One such technique is the emulsification–diffusion method. This method uses a partially water-soluble solvent like acetone or propylene carbonate. The polymer and bioactive compound are dissolved in the solvent and emulsified in the aqueous phase containing the stabilizer. The stabilizer prevents the aggregation of emulsion droplets by adsorbing the surface of the droplets. Water is added to the emulsion to allow the diffusion of the solvent into the water. The solution is stirred leading to the nanoprecipitation of the particles. They can then be collected by centrifugation or the solvent can be removed by dialysis [22,23].

One problem with this technique is that water-soluble drugs tend to leak out of the polymer phase during the solvent diffusion step. To improve this process for water-soluble drugs, Takeuchi

TABLE 23.1
Comparison of Methods for Nanoparticle Preparation

Method	Polymer	Solvent	Stabilizer	Size	References
Solvent diffusion	PLGA	Acetone	Pluronic F-127	200 nm	[88]
	PLGA	Acetone/DCM	PVA	200–300 nm	[58]
	PLA-PEG	MC	PVA/PVP	~130 nm	[114]
	PHDCA	THF	—	150 nm	[98]
	PLGA	Acetone	Sodium cholate	161 nm	[96]
	PLGA	Propylene carbonate	PVA or DMAB	~100 nm	[53]
Solvent displacement	PLA	Acetone/MC	Pluronic F68	123 ± 23 nm	[106]
	SB-PVA-g-PLGA	Actone/Ethyl acetate	Poloxamer 188	~110 nm	[87]
Nanoprecipitation	PLGA/ PLA/ PCL	Acetone	Pluronic F68	110–208 nm	[59]
	PLGA	Acetonitrile	—	157.1 ± 1.9 nm	[57]
Solvent evaporation	PLA-PEG-PLA	DCM	—	193–335 nm	[129]
	PLGA	DCM	PVA	800 nm	[47]
	PLGA	DCM	TPGS	>300 nm	[67]
Multiple emulsion	PLGA	Ethyl acetate	—	>200 nm	[97]
	PEG-PLGA	DCM	PVA	~300 nm	[93]
	PLGA	Ethyl acetate/MC	PVA	335–743 nm	[92]
	PLGA-mPEG	DCM	—	133.5±3.7–163.3±3.6	[130]
	PLGA	DCM	PVA	213.8 ± 10.9 nm	[51]
	PLGA	DCM/Acetone	PVA	100 nm	[46]
	PLGA	Ethyl acetate	PVA	192±12 nm	[49]
	PLGA	Ethyl acetate	PVA	300–350 nm	[55]
	PLGA	DCM	PVA	380±40–1720±110 nm	[50]
Salting out	PLA	Acetone	PVA	300–700 nm	[60]
Ionic gelation	Chitosan	TPP	—	278±03 nm	[106]
Interfacial deposition	PLGA	Acetone	—	135 nm	[103]
Phase inversion nanoencapsulation	PLGA	MC	—	>5 μm	[52]
Polymerization	CS-PAA	—	—	206±22 nm	[64]
	PECA	—	Pluronic F68	320±12 nm	[66,85]
	PE-2-CA	—	—	380±120 nm	[84]
Modified microemulsion	PolyoxStyl 20-stearyl ether	—	Emulsifying wax	~67 nm	[106]

DCM, dicloromethane; MC, methylene chloride; PVP, polyvinylpyrrolidone; PHDCA, poly(hexadecylcyanoacrylate); THF, tetrahydrofuran; SB-PVA-g-PLGA, sulfobutylated PVA-graft-PLGA; PCL, poly(epsilon-caprolactone); TPP, sodium tripolyphosphate; PAA, poly(acrylic acid); PECA, polyethylcyanoacrylate; PE-2-CA, polyethyl-2-cyanoacrylate.

TABLE 23.2
Comparison of Nanoparticle Size for Different Drug-Loaded Particles

Polymer	Drug	Size	References
PLGA	Doxorubicin	200 nm	[88]
PLGA/PLA/PCL	Isradipine	110–208 nm	[59]
PLGA	U-86983	144 ± 37–88 ± 41 nm	[46]
PLGA	Rose Bengal	150 nm	[103]
PLGA	Triptorelin	335–743 nm	[92]
PLGA	Procaine hydrochloride	164 ± 1.1–209.5 ± 2.7 nm	[57]
PLGA-mPEG	Cisplatin	133.5 ± 3.7–163.3 ± 3.6 nm	[130]
PLGA	Insulin	>1 μm	[52]
PLGA	Hemagglutinin	~250 nm	[6]
PLGA	Haloperidol	800 nm	[47]
PLGA	Estrogen	~100 nm	[53]
PEO-PLGA	Paclitaxel	150 ± 25 nm	[45]
PLA	Tetnus toxoid	>200 nm	[97]
PLA	Savoxepine	~300–700 nm	[60]
PLA	PDGFRβ tyrphostin inhibitor	123 ± 23 nm	[106]
PLA-PEG-PLA	Progesterone	193–335 nm	[129]
PECA	Amocicillin	320 ± 12 nm	[85]
Poly(butyl cyanoacrylate)	Dalargin	250 nm	[83]
Chitosan	Cyclosporin A	283 ± 24–281 ± 05 nm	[119]
PLGA	Paclitaxel	>300 nm	[67]
PLGA	Paclitaxel	< 200 nm	[94]
PLA	N^6-cyclopentyladenosine	210 ± 50–390 ± 90 nm	[91]

et al. [23] changed the dispersing medium from an aqueous solution to a medium chain triglyceride and added a surfactant, Span® 80, to the polymer phase. The nanoparticles were collected from the oily suspension by centrifugation. A double emulsification solvent diffusion technique has also been demonstrated to increase encapsulation efficiency of water-soluble drugs and maintenance of protein activity [24]. Protein activity during the fabrication process is a delicate balance between energy input (mechanical stirring, homogenization, and sonication) and particle size. A synergistic effect between mechanical stirring and ultrasound was shown to produce nanoparticles of 300 nm in diameter, while maintaining 85% of the starting activity of the cystatin protein [10]. Table 23.3 shows the changes in particle size with varied stirring rates. The addition of protein protectants, such as BSA or sugars, was also found to be essential in maintaining the biologically active, three-dimensional structure of cystatin [10]. These protectants may serve to shield proteins from interfaces during nanoparticle formation and lyophilization.

Several parameters can also be changed to benefit the encapsulation of hydrophilic molecules. Govender et al. [2] found that increasing the aqueous phase pH to 9.3 and incorporating pH-responsive excipients, such as poly(methyl methacrylate-co-methacrylic acid) (PMMA-MAA) and lauric and caprylic acid, increased hydrophilic drug encapsulation without affecting the particle size, morphology, or yield. Murakami et al. [25] effectively modified the solvent diffusion technique by using two water-miscible solvents, one with more affinity for PLGA and the other with more affinity for the stabilizer, PVA, such as acetone and ethanol.

Nanoparticles can also be synthesized by the nanoprecipitation method. Briefly, the polymer and drug are dissolved in acetone and added to an aqueous solution containing a surfactant/stabilizer. The acetone is evaporated under reduced pressure and the nanoparticles remain in the suspension resulting in particles from 110 to 208 nm [26]. The salting-out process is another method, which does not require the use of chlorinated solvents. Using this technique, a water-in-oil emulsion is formed

TABLE 23.3
The Effect of Combination of Stirring and Bath Sonication on Size of Particles Made from Polymer RG® 503H (Mean ± S.D., *n*=3)

Organic Solvent	Particle Size (nm)		
	10,000 rpm[a]	7500 rpm[a]	5000 rpm[a]
Ethyl acetate	254±16	254±30	331±25
Dichloromethane/acetone	235±19	318±14	314±28

[a] Stirring rate.

Source: Reprinted from Cegnar, M. et al., *Eur. J. Pharm. Sci*., 22, 357–364, 2004.

containing polymer, acetone, magnesium acetate tetrahydrate, stabilizer, and the active compound. Subsequently, water is added until the volume is sufficient to allow for diffusion of acetone into water, which results in the formation of nanoparticles. This suspension is purified by cross-flow filtration and lyophilization [27]. However, one disadvantage to this procedure is that it uses salts that may be incompatible with many bioactive compounds.

In most published techniques, nanoparticles are synthesized from biocompatible polymers. However, it is possible to make biodegradable nanoparticles from monomers or macromonomers by polycondensation reactions [28,29]. These processes also result in sizes ranging from 200 to 300 nm. Nanoparticles can also be made from hydrophilic polysaccharides like chitosan (CS). CS nanoparticles can be formed by the spontaneous ionic gelatin process [18,30]. CS-poly(acrylic acid) nanoparticles have also been made by polymerization of acrylic acid and the "dropping method" [31]. The resulting nanoparticles have small sizes and positive surface potentials. This technique is promising as the particles can be prepared under mild conditions without using harmful organic solvents.

23.3 PROCESSING PARAMETERS

The method of producing polymeric nanoparticles has several independent variables. Consequently, total drug loading, nanoparticle stability, and release characteristics may vary with slight changes in processing parameters. First, one must consider the selection of the components used in the nanoparticle production, including the polymer, molecular weight of the polymer, the surfactant, the drug, and the solvent [32]. For example, different surfactants may produce particles of different sizes [33]. An increase in polymer molecular weight will cause an impact on the release rate from the particles causing slower pore formation within the particles and therefore slower release [9,34]. Other processing variables include the time of emulsification, the amount of energy input, and the volume of the sample being emulsified. As energy input into an emulsion increases, the resulting particle size decreases [35]. In addition, there are four separate concentrations that can be altered: the polymer, drug, surfactant, and solvent. Often, a low concentration of surfactants will result in a high degree of polydispersity and aggregation [36]. Finally, the recovery of the particles can be changed depending on the method of lyophilization or centrifugation.

23.3.1 SURFACTANT/STABILIZER

One key parameter is the type of surfactant/stabilizer to be used. A wide range of synthetic and natural molecules with varying properties has been proposed to prepare nanoparticles. Feng and Huang [17] have investigated the use of phospholipids as natural emulsifiers. In their study, dipalmitoylphosphatidylcholine (DPPC) improved the flow and phagocytal properties due to a denser packing of DPPC molecules on the surface of the nanoparticles leading to a smoother surface than particles made with the synthetic polymer, poly(vinyl alcohol) (PVA). DPPC also improved the encapsulation

efficiency compared to PVA using the emulsification–solvent evaporation method. In a different study conducted by Kwon et al. [22], PLGA nanoparticles prepared using didodecyl dimethyl ammonium bromide (DMAB) were smaller than particles prepared with PVA. Lemoine and Preat [8] found that the presence of PVA in the inner aqueous phase produced smaller particles than Span® 40 [7]. When Pluronic is used as a stabilizer, the grade used can have a distinct effect on the size of the nanoparticles. For example, particles prepared with Pluronic F68 were smaller than particles prepared with Pluronic F108 [37].

A promising stabilizer for nanoparticles is the amphiphile D-α-tocopheryl polyethylene glycol 1000 succinate vitamin E (TPGS). TPGS has high emulsification efficiency, can increase incorporation efficiency when used as a matrix component, and can be used as a cellular adhesion enhancer. TPGS can be used at a concentration as low as 0.015% (w/v); in fact a lower concentration decreases particle size and polydispersity [38]. Figure 23.1 shows scanning electron micrographs of PLGA particles made with PVA and TPGS. Moreover, the addition of TPGS dramatically reduced the release rate of paclitaxel from PLGA nanoparticles compared to those made with PVA (Figure 23.2). Using TPGS as an emulsifier, uptake by Caco-2 cells was greater than that of PVA-coated particles [33]. In addition, only TPGS-coated particles were found to be taken up in the nucleus [33].

The amount of stabilizer used will also have an effect on the properties of the nanoparticles. Most importantly, if the concentration of the stabilizer is too low, aggregation of the polymer droplets will occur and little if any nanoparticles will be recovered. Alternatively, if too much of the stabilizer is used, the drug incorporation could be reduced due to interaction between the drug and the stabilizer. However, when the stabilizer concentration is between the "limits," adjusting the concentration can be a means of controlling nanoparticle size. For example, in using the solvent evaporation technique, increasing the PVA concentration will decrease the particle size [8,15]. However, when using the emulsification–diffusion method, Kwon et al. [22] found that a PVA concentration from 2 to 4% was ideal for creating smaller nanoparticles, ~100 nm in diameter.

23.3.2 Type of Polymer

Biodegradable polymers retain their properties for a limited period of time *in vivo* and then gradually degrade into materials that can become soluble or are metabolized and excreted from the body. In order to be used for *in vivo* applications, the polymers used for such systems must have favorable properties for biocompatibility, processability, sterilization capability, and shelf life. In the past, polystyrene or gold nanoparticles were used to investigate particle distribution and uptake. However, biodegradable polymer particles have several properties, such as hydrophobicity, surface charge, particle size distribution, density, or protein adsorption, which are different from polystyrene and gold

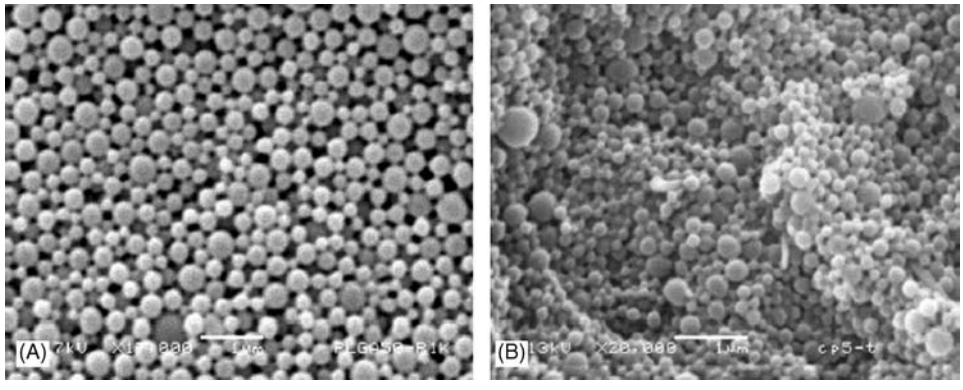

FIGURE 23.1 SEM images of coumarin 6-loaded PLGA particles coated with PVA (A) and vitamin E TPGS (B) (scale bar = 1 μm). (Reprinted from Yin Win, K. and Feng, S. S., *Biomaterials*, 26, 2713–2722, 2005.)

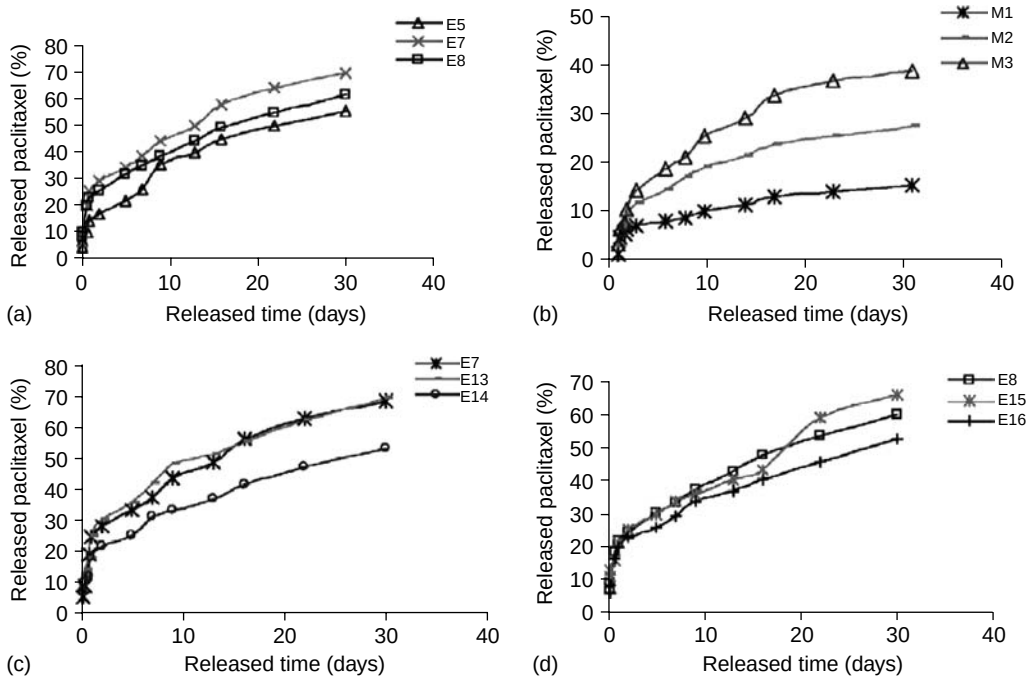

FIGURE 23.2 *In vitro* release curves of paclitaxel-loaded nanoparticles prepared under various experiment parameters (a) E5: PLA, E7: PLGA (75:25), E8: PLGA (50:50); (b) ratio for PLGA–TPGS: M1 (2:1), M2 (1:1), M3 (1:2); (c) PLGA (75:25) concentration — E7: 0.125, E13: 0.188, E14: 0.25; (d) PLGA (50:50) concentration — E8: 0.125, E15: 0.188, E16: 0.25. (Reprinted from Mu, L. and Feng, S. S., *J. Control. Release*, 86, 33–48, 2003.)

that might have an impact on results of these studies [39]. Figure 23.3 and Figure 23.4 show examples of physical internalization of PLGA nanoparticles by vascular smooth muscle cells (VSMCs).

23.3.2.1 Poly(lactide-co-glycolide)

Many biodegradable systems rely on the random co-polymers of PLGA. These classes of polymers are highly biocompatible and have good mechanical properties for drug delivery applications [40]. In addition, PLA and PLGA have been approved by the FDA for numerous clinical applications, such as sutures, bone plates, abdominal mesh, and extended-release pharmaceuticals. PLGA degrades chemically by hydrolytic cleavage of the ester bonds in the polymer backbone. Its degradation products, lactic acid and glycolic acid, are water-soluble, nontoxic products of normal metabolism that are either excreted or further metabolized to carbon dioxide and water in the Krebs cycle [41,42]. The composition of the PLGA random co-polymer, that is the relative amount of lactic acid and glycolic acid monomeric units, determines the degradation rate [34,43]. Since PGA is more hydrophilic than PLA a higher proportion of PGA incorporated into the co-polymer will increase the degradation rate by allowing more biological fluids to penetrate and swell the polymer matrix.

23.3.2.2 Poly(lactic acid)

Poly(lactic acid) occurs naturally as the pure enantiomeric poly(L-lactic acid) (LPLA) with a semicrystalline structure. However, most types of PLA used for biological applications exist in the racemic D,L form (DLPLA) and are amorphous polymers. PLGA is also an amorphous polymer; both DLPLA and PLGA have glass transition temperatures above body temperature. The biomedical uses

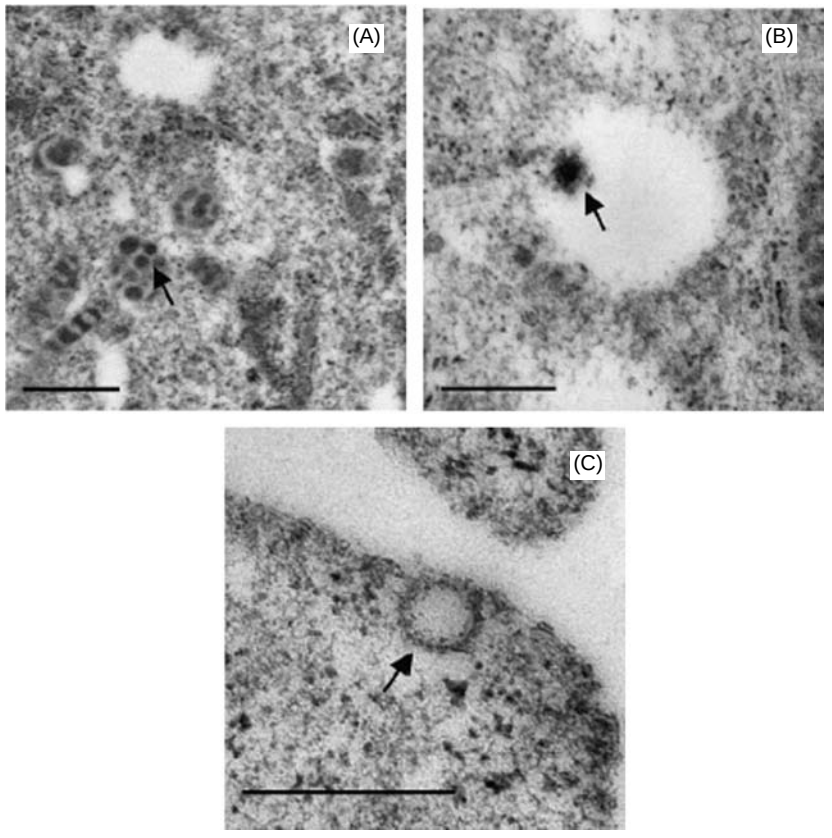

FIGURE 23.3 TEM images showing (A) nanoparticles (indicated by arrow) present in cytoplasm (×16,900), (B) a nanoparticle (indicated by arrow) interacting with vesicular membrane (×21,000), and (C) control vascular smooth muscle cells (VSMCs) (untreated cells) with nanoparticle-like vesicles of approximately 100 nm (indicated by arrow) (×38,000). Scale bars, 500 nm. (Reprinted from Panyam, J. et al., *Int. J. Pharm.*, 262, 1–11, 2003.)

of PLA have been reported since the 1960s [44]. Numerous systems already utilize PLGA and PLA, including several micro- and nanoparticle systems as well as devices to control thyrotropin-releasing hormone in controlling metabolism [42], L-dopa to treat Parkinson's disease [45], and naltrexone in treating narcotic addiction [46] to successfully achieve long-term delivery. Several intraocular systems, including Vitrasert® (Bausch and Lomb), offer biocompatible delivery systems with controlled release drug therapy for periods ranging from several days up to 1 year [47].

23.3.2.3 Poly-ε-caprolactone

Poly-ε-caprolactone is another biodegradable and nontoxic polyester. PCL is polymerized similarly to PLA and PLGA, by ring-opening polymerization [48,49]. PCL is a semicrystalline polymer owing to its regular structure. The melting temperature of PCL is above body temperature, but its T_g is −60°C; so in the body, the semicrystalline structure of PCL results in high toughness, because the amorphous domains are in the rubbery state [50]. Hydrolysis of PCL yields 6-hydroxycaproic acid, which enters the citric acid cycle and is metabolized. Degradation of PCL occurs at a slower rate than PLA. PCL has also been used in blends and co-polymers with other biodegradable polymers [51]. Combinations of polymers allow the user to tailor mechanical properties and degradation kinetics, among other characteristics, to suit the needs of a specific application.

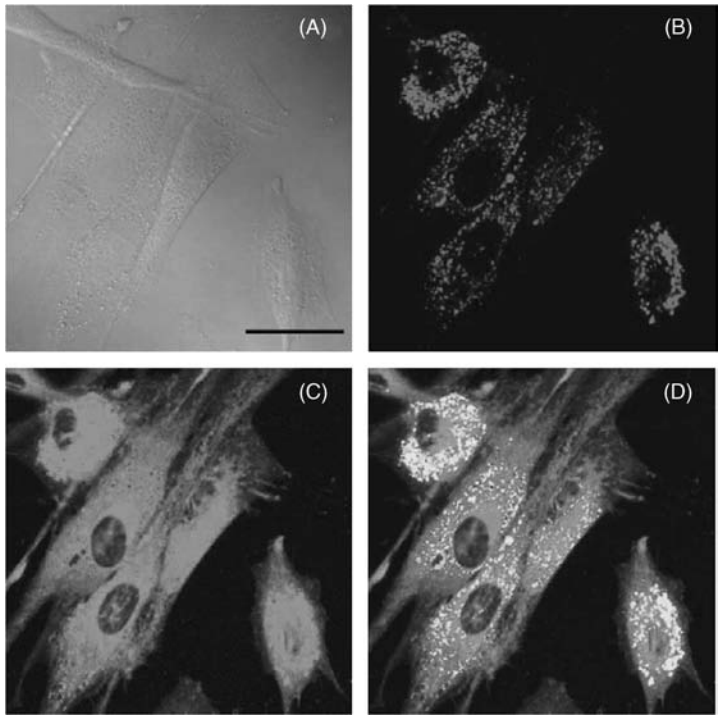

FIGURE 23.4 Confocal microscopic images demonstrating the intracellular distribution of 6-coumarin-loaded nanoparticles in VSMCs. (A) Differential interference contrast image showing the outline of the cells. (B) Cells stained with LysoTracker® Red and visualized using RITC filter. (C) Uptake of green fluorescent 6-coumarin-loaded nanoparticles in VSMCs visualized using FITC filter. (D) Overlay of (B, C) showing the co-localization of nanoparticles with endolysosomes. Scale bar, 25 μm. (Reprinted from Panyam, J. et al., *Int. J. Pharm.*, 262, 1–11, 2003.)

The amorphous regions of a semicrystalline polymer degrade prior to the crystalline domains [52]. This can lead to a change in the release profile. Thus, polymers that have a higher percent crystallinity are more impervious to water and therefore degrade at a slower rate. The drug entrapped in the amorphous region is released first and at a faster rate than the drug entrapped by the crystalline domains. The percent crystallinity in a polymer depends on the type of polymer used in the application, the polymer's composition, and the processing conditions for the polymer system. PCL typically has the highest percent crystallinity and the slowest degradation rate. This is evident by comparing PCL and LPLA versus PGA and PEG.

23.3.3 Polymer Choice

The polymer chosen to formulate the nanoparticles will strongly affect the structure, properties, and applications of the particles. As stated previously, PLGA has been the most common polymer used to make biodegradable nanoparticles, however, these are clearly not the optimal carrier for all drug delivery applications. For each application and drug, one must evaluate the properties of the system (drug and particle) and determine whether or not it is the optimal formulation for a given drug delivery application. For example, poly(butyl cyanoacrylate) nanoparticles have been successful in delivering drugs to the brain [53]. Other cyanoacrylate-based nanoparticles, such as polyalkylcyanoacrylate (PACA) and polyethylcyanoacrylate (PECA), have also been prepared. They are considered to be promising drug delivery systems due to their muco-adhesive properties and ability to entrap a variety of biologically active compounds. These polymers are biodegradable, biocompatible, as well as compatible

with a wide range of compatible drugs [37,54]. Furthermore, these polymers have a faster degradation rate than PLGA, which in some cases may be more desirable. PECA nanoparticles have been prepared by emulsion polymerization in the presence and absence of different molecular weights PEGs, using Pluronic F68 as the stabilizer [55].

pH-sensitive nanoparticles made from a poly(methylacrylic acid and methacyrlate) co-polymer can increase the oral bioavailability of drugs like cyclosporin A by releasing their load at a specific pH within the gastrointestinal tract. The pH sensitivity allows this to happen as close as possible to the drug's absorption window through the Peyer's patches [56].

Other groups have successfully prepared nanoparticles from functionalized PLGA polymers. In one study, Jung et al. [57] synthesized nanoparticles made of a branched, biodegradable polymer, poly(2-sulfobutyl-vinyl alcohol)-g-PLGA. The purpose of using sulfobutyl groups attached to the hydrophilic backbone was to provide a higher affinity to proteins by electrostatic interactions that would favor adsorptive protein loading. Adjustments can be made to the characteristic nanoparticles by differing degrees of substitution of sulfobutyl groups. In another case, a carboxylic end group of PLGA was conjugated to a hydroxyl group of doxorubicin and formulated into nanoparticles [58]. This modification produced a sustained release of the drug that was approximately six times longer than the unconjugated drug [59]. The presence of the carboxylic end group on PLGA may also help in preserving cystatin activity in PLGA particles [10]. However, the carboxylic acid end group may also increase the overall release rate of drug from particles, so in some cases, a methyl-capped PLGA carboxylic acid end group can be utilized.

23.3.4 Polymer Molecular Weight

Polymer molecular weight, being an important determinant of mechanical strength, is also a key factor in determining the degradation rate of biodegradable polymers. Low-molecular-weight polymers degrade faster than high-molecular-weight polymers thereby losing their structural integrity more quickly. As chain scission occurs over time, the small polymer chains that result become more soluble in the aqueous environment of the body. This introduces "holes" into the polymer matrix. Consequently, lower molecular weight polymers release drug molecules more quickly [9,15]. This can be used to further engineer a system to control the release rate. A combination of molecular weights might be used to tailor a system to meet the demands of specific release profiles.

23.3.5 Collection Method

Another factor that can affect the properties of nanoparticles is the final freeze-drying process. It has been reported that additives such as saccharides are necessary for cryoprotection of nanoparticles in the freeze-drying process [60]. These saccharides may act as a spacing matrix to prevent particle aggregation. Because of the possibility of aggregation, freeze-drying procedure can affect the "effective" nanoparticle size, and consequently, their release behavior and accordingly the drug pharmacokinetics [61].

Nanoparticles can also be collected by dialysis, ultracentrifugation, and gel filtration. While gel filtration has shown decreased encapsulation efficiency and total drug incorporation, it is thought that this collection method may remove drug adsorbed onto the particle surface, which may cause a dangerous release of drug immediately upon immersion in body fluid [62]. Figure 23.5 shows the difference in particle size and morphology in particles collected by gel filtration and ultracentrifugation. This burst effect will be discussed later in more detail.

23.4 CHARACTERIZATION

23.4.1 Size and Encapsulation Efficiency

When considering a particular polymeric nanoparticle for a given drug delivery application, particle size and encapsulation efficiency are two of the most important characteristics. It is necessary

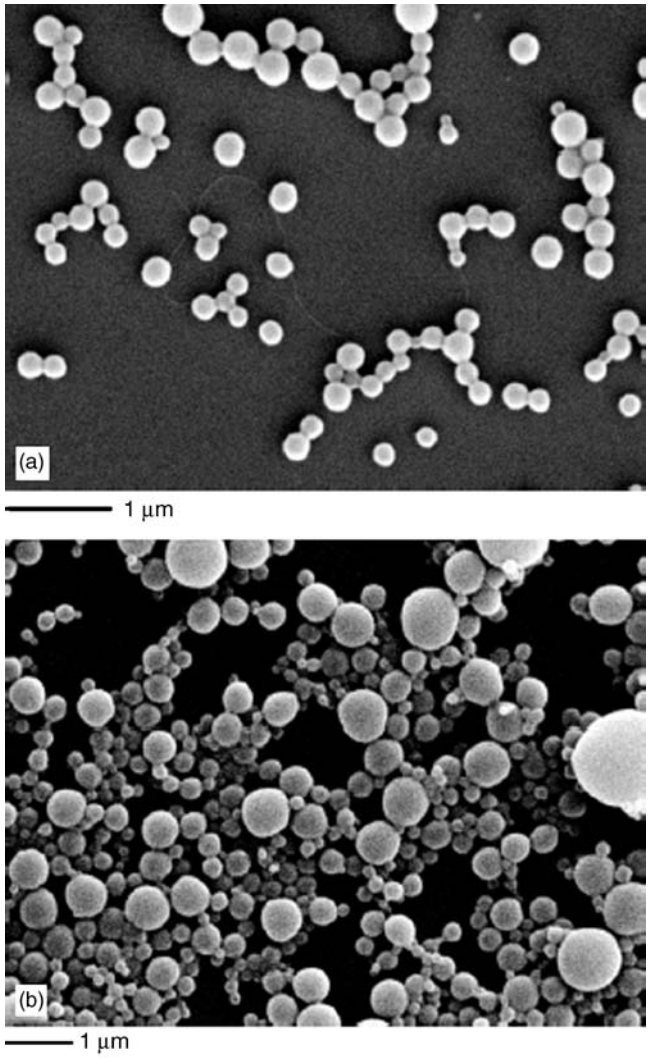

FIGURE 23.5 SEM of Oct-CPA-loaded nanospheres prepared by nanoprecipitation method: (a) II-Oct-CPA sample recovered by gel filtration and (b) IV-Oct-CPA sample recovered by ultracentrifugation. (Reprinted from Dalpiaz, A. et al., *Biomaterials*, 26, 1299–1306, 2005.)

to determine first what the goal of the nanoparticle delivery system is before determining the size desired. For example, if the goal is rapid dissolution in the body or arterial uptake, then the size of the nanoparticles should be ~100 nm or less. If prolonged dissolution is required, or targeting the mononuclear phagocytic system (MPS), larger particles around 800 nm, or particles engineered to have a stealth quality would be preferable. A comparison of various drugs encapsulated and the resulting sizes of the particles are summarized in Table 23.2. From examination of these data, it appears that the encapsulation efficiency increases with the diameter of the nanoparticles. In one study, the encapsulation efficiency was maximized in the double-emulsion solvent evaporation technique when the pH of the internal and the external aqueous phases were brought to the isoelectric point of the peptide being encapsulated, methylene chloride was used as a solvent, and the PLGA was rich in free carboxylic end groups [63]. It has also been found that by adding a freeze-thaw step during the primary emulsion of a double-emulsion process, there is an increase in overall protein incorporation by inducing the polymer phase to precipitate around the primary emulsion [35].

The molecular weight of the polymer has opposite effects on nanoparticle size and encapsulation efficiency. Smaller size nanoparticles, ~100 nm, can be prepared with lower molecular weight polymer however, at the expense of reduced drug encapsulation efficiency. On the other hand, an increase in polymer concentration increases encapsulation efficiency and the size of the nanoparticles [9,15,22].

The synthesis method can also have a profound effect on the encapsulation efficiency. In loading paclitaxel into PLGA nanoparticles using the nanoprecipitation method, when the drug and polymer were mixed first and then solubilized in the organic solvent prior to fabrication, encapsulation efficiency was 15% [3]. However, when a solution of drug was used to dissolve the polymer prior to fabrication, nearly 100% encapsulation efficiency was achieved.

23.4.2 Zeta Potential

Another characteristic of polymeric nanoparticles that is of interest is zeta potential. The zeta potential is a measure of the charge of the particle, the relation being that the larger the absolute value of the zeta potential, the larger the amount of charge of the surface. In a sense, the zeta potential represents an index for particle stability. In the case of charged particles, as the zeta potential increases, the repulsive interactions will be larger leading to the formation of more stable particles with a more uniform size distribution. A physically stable nanosuspension solely stabilized by electrostatic repulsion will have a minimum zeta potential of ± 30 mV [64]. This stability is important in preventing aggregation. When a surface modification like PEG is added, the negative zeta potential is lowered, increasing the nanoparticles stability [18].

23.4.3 Surface Modification

Before deciding which of the techniques to be used for synthesizing nanoparticles, one must consider what is the nature of the drug as well as the means and duration desired for the delivery. That will determine not only how the particles are synthesized, but also what the nature of the particles should be. In particular, the body recognizes hydrophobic particles as foreign and thus they are rapidly taken up by the MPS. However, if sustained systemic circulation is required then the surface of the hydrophobic nanoparticles must be modified in order to prevent phagocytosis [65].

Following intravenous administration, hydrophobic nanoparticles are rapidly cleared from the systemic circulation by the MPS, ending in the liver or the spleen [27]. If the goal is to treat a condition in the liver, then the proper choice for the application would be a hydrophobic nanoparticle. While it would appear that the hydrophobic nature of most biodegradable particles would limit the applicability of these carriers in many drug delivery applications, one may overcome concerns of clearance by the MPS through surface modification techniques. The goal of these modification techniques is to produce a particle that is not recognized by the MPS due to the hydrophilic nature of the surface [65,66].

Several types of surface-modified nanoparticles that have been described in recent literature are summarized in Table 23.4. The most common moiety used for surface modification is PEG [65,66]. PEG is a hydrophilic, non-ionic polymer that has been shown to exhibit excellent biocompatibility. PEG molecules can be added to the particles via a number of different routes including covalent bonding, mixing in during nanoparticle preparation, or surface adsorption [4,20,65–68]. The presence of a PEG brush on the surface of nanoparticles can serve other functions besides increasing residence time in the systemic circulation. For one, PEG tethers on the particle surface can reduce protein and enzyme adsorption on the surface, which for PLGA-based particles will retard degradation [68]. The degree of protein adsorption can be minimized by altering the density and molecular weight of PEG on the surface [65]. The stability of PLA particles has been shown to increase in simulated gastric fluid (SGF) with the addition of PEG on the particle surface. After 4 h in SGF, 9% of the PLA nanoparticles converted into lactate versus 3% conversion for PEG–PLA particles [68]. PEG is also believed to facilitate transport through the Peyer's patches of the GALT [18].

TABLE 23.4
Nanoparticle Sizes after Surface Modifications

Polymer	Surface Modification	Size (nm)	References
PLGA	Poloxamine 908	~160	[103]
PLGA	Poloxamer 407	~160	[103]
PLGA	Chitosan	500± 29	[49]
PLGA-mPEG	mPEG	133.5 ± 3.7–163.3 ± 3.6	[130]
PLGA-mPEG	mPEG	113.5 ± 14.3	[100]
PLGA-PEG	PEG	198.1 ± 11.1	[51]
PLA	PEG	164–270	[96]
PLA	PEG 6000	295	[60]
PLA-PEG	PEG	>200	[97]
PLA-PEG	PEG	~130	[114]
PHDCA	PEG	~150	[98]
PECA	PEG	220 ± 10–280 ± 8	[85]
PBCA	Polysorbate 80	250	[83]
PEG-PLGA	PEG	~300	[93]
Polyoxyl 20-stearyl ether	Thiamine	67	[105]
PEG-PACA	Transferrin	101.4 ± 7.2	[108]
PLA	Polysorbate 80	~160	[104]
PEI-b-PLGA	PEG	~100	[24]
PLA	Neutravidin™	~270	[111]
Glycoprotein-liposomes	Lectin	100	[19]

As stated previously, the primary reason for interest in preparing PEG-functionalized particles is to improve the long-term systemic circulation of the nanoparticles [65,66]. The PEG-functionalized particles are not seen as a foreign body and in combination with the nanoscale size of the particles, are not taken up by the body, allowing them to circulate longer providing for a sustained systemic drug release. Because of their behavior, these PEG-functionalized nanoparticles are often called “stealth nanoparticles” [66]. Furthermore, it has been determined that PEG MW is important with respect to MPS uptake. For example, Leroux et al. [27] showed that an increase in PEG molecular weight in PLGA nanoparticles was associated with less interaction with the MPS and longer systemic circulation. Also, PEG-containing PLGA nanoparticles synthesized by Li et al. [20] were able to extend the half-life of BSA in a rat model from 13.6 min to 4.5 h [69]. Another study compared the dosages of PLGA nanoparticles versus PEG–PLGA nanoparticles. The PLGA nanoparticle pharmacokinetics seemed to depend on MPS saturation. However, the pharmacokinetics of PEG–PLGA dosages did not exhibit the same dependence on dosage/MPS saturation due to their stealth nature [70]. PEG may also benefit nanoparticle interaction with blood constituents. PLGA nanoparticles were shown to cause damage to red blood cells; PEGylated nanoparticles caused less damage [71]. It should be noted that the red blood cell damage was also concentration dependent.

Another way to prevent nanoparticles from becoming sequestered and eliminated by the spleen is by noncovalent adhesion of particles on to erythrocyte membranes [72]. This adhesion is controlled by van der Waals, electrostatic, hydrophobic, and hydrogen-bonding forces. The adhesion did not change the morphology of the red blood cells, and the particles were retained on their membranes for 24 h and beyond. This technology improved the circulation time of nanoparticles 10-fold.

Poloxamer and poloxamines have also been shown to reduce capture by macrophages and increase the time for systemic circulation. Similarly, PLGA particles coated with poloxamer 407 and poloxamine 908 extended the half-life of rose bengal, a hydrophilic model drug, with ~30% left in the bloodstream after 1 h postnanoparticle administration, as opposed to 8% present after 5 min postfree drug administration [73].

Another polymer used for surface modification is CS. The addition of CS to the surface of PLGA nanoparticles resulted in increased penetration of macromolecules in mucosal surfaces [30]. CS-coated PLGA particles were able to increase the positive zeta potential of the particles and increase the efficiency of tetanus toxoid protein encapsulation. Radiolabeled tetanus toxoid was used to show enhanced transport across nasal and intestinal epithelium using CS-coated particles versus uncoated particles, with a higher percentage of ^{125}I present in the lymph nodes for CS-coated particles [18].

23.5 NANOPARTICULATE DELIVERY SYSTEMS

23.5.1 LIPOSOMES

Lipid bilayers occur throughout science and nature — cells use them to regulate chemical species within and outside of cells. Liposomes serve as excellent mimics of naturally occurring cell membranes [74]. Investigations with liposomes mimicking natural cell functions, especially those involving chemical transport, has led to their use as vehicles for drug delivery [75–78]. A primary advantage of liposomes is their high level of biocompatibility. Liposomes now constitute a mainstream technology for drug delivery; clinical approval has been given to liposomal formulations of anticancer drugs, doxorubicin (Doxil®/Caelyx® and Myocet®) and daunorubicin (Daunosome®) [79]. Another advantage of liposomes is their ability to transport a wide diversity of drugs that can be hydrophilic, lipophilic, or amphiphilic. This relates to the amphiphilic nature of phospholipid molecules themselves, which self-assemble in water to form bilayers that enclose an aqueous interior. Hydrophilic drugs can therefore be entrapped within the aqueous core, whereas hydrophobic drugs partition into the hydrocarbon-rich region of the bilayer. Loading techniques, such as the ammonium sulfate method [80] and the pH gradient method [81], can be used to place amphiphilic drugs (e.g., doxorubicin and vincristine, respectively) at the inner-phospholipid-monolayer/water interface [79].

A major disadvantage of liposomes as drug delivery vehicles is their rapid clearance from blood via the MPS, or reticuloendothelial system. This limitation was overcome by the advancement of 'PEGylated Stealth®' liposomes, which avoid protein adsorption, and hence subsequent recognition and uptake, via a surface coating of PEG [80–82]. Incorporation of PEG into ordinary liposomes increases their circulation half-life from minutes to hours [79,83]. In addition to conveying this stealth quality, PEG also increases the susceptibility of liposomes to ultrasound-induced leakage [84]. This quality might prove useful in the development of a targeted, localized drug delivery system using external ultrasound as a remote mechanical stimulus to trigger drug release. Liposomes can also be decorated with glycoproteins and sugar chains to target specific cells [85].

23.5.2 POLYMERIC MICELLES

Polymeric micelles can be assembled from block co-polymers composed of hydrophilic and hydrophobic segments. The hydrophobic segment creates the inner core of the micelle, while the hydrophilic segment creates the outer shell in an aqueous media [86]. Polymeric micelles can be used as a drug delivery device by either physically entrapping the drug in the core (i.e., hydrophobic drugs can be trapped inside the micelle by hydrophobic interactions), or by chemically conjugating the drug to the hydrophobic block prior to micelle formation [87,88]. Drugs either physically or chemically trapped in the hydrophobic core are protected from chemical degradation, causing unwanted side effects [87,88]. Micelles have several benefits as drug delivery vehicles. Their hydrophilic outer shell and small size (<100 nm) renders these particles nearly invisible to the reticuloendothelial system, allowing for long-term circulation in the bloodstream. Furthermore, micelle stability is relatively high due to the fact that, unlike other aggregates for drug delivery such as vesicles, they are a thermodynamically equilibrium aggregate. Micelles spontaneously form when the concentration of

the amphiphile composing them (lipids, surfactants, or block copolymers) is higher than a critical concentration called the critical micelle concentration (CMC). The CMC is significantly lower for higher molecular weight polymers as opposed to surfactants or lipids. Micelle stability is further enhanced by crystallization or rigidity in the polymer core, which prevents rapid dissolution of block co-polymer micelles *in vivo*.

Triblock copolymers such as poly(ethylene oxide)-block-poly(propylene oxide)-block-poly(ethylene oxide) (PEO-b-PPO-b-PEO) or Pluronics® have frequently been studied to create block co-polymer micelles. Pluronics® conjugated to brain-specific antibodies or insulin have been used to solubilize haloperidol and other small compounds, such as FITC [89].

Polyethylenimine (PEI)-block-PLGA have been used to form micelles for cellular uptake [90]. Figure 23.6 shows size, polydispersity, and morphology of these micelles using transmission electron microscopy. Using confocal laser scanning microscopy (CLSM), PEI–PLGA micelles were shown to be absorbed onto human keratinocyte cell surfaces and translocated into the cytoplasm.These particles were not cytotoxic to the cells for up to 2 days at a concentration of 50 μg/mL. By comparison there was limited cellular internalization of PLGA particles [90].

Poly(ethylene oxide)-Poly(amino acid) (PEO-PAA) block co-polymers have received a great deal of attention, because the biodegradable amino acid core has free functional groups for chemical modification [88]. To achieve this, PEO-PBLA (Poly(β-benzyl L-aspartate)) is synthesized from β-benzyl *N*-carboxy L-aspartate anhydride (BLA-NCA) and α-methyl-ω-aminopoly(oxyethylene). PEO-P(Asp) is then prepared by debenzylation under alkaline conditions of the PEO-PBLA. Following this step, ADR is conjugated via amide bond formation [91]. Micelles prepared from drug conjugates have the added advantage that extended drug release will still be possible in the

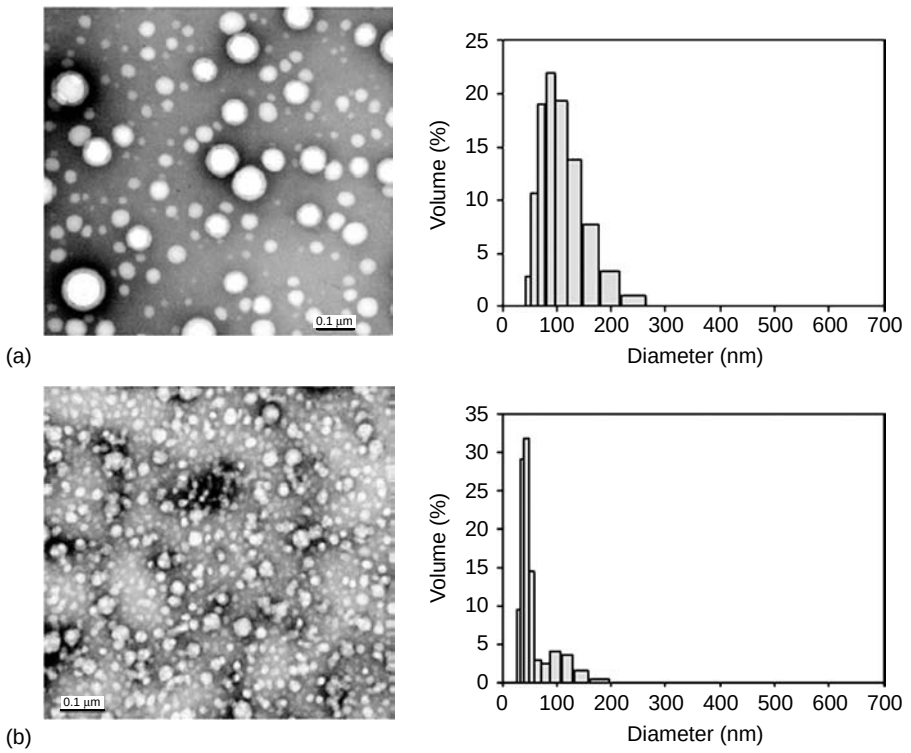

FIGURE 23.6 TEM pictures and size distributions of PEI–PLGA aggregates formed in (a) pure water, (b) 30 m*M* HCl (aqueous solution) (scale bar = 100 nm).(Reprinted from Nam, Y.S. et al., *Biomaterials*, 24, 2053–2059, 2003.)

event of dissociation of the micelle as the drug must still be cleaved from the polymer chain. Stability of these PEO-P(Asp(ADR)) micelles has been shown to be dependent on a longer chain of PEO in comparison to the chain length of P(Asp) and ADR content. PEO-PBLA could also be synthesized with free hydroxyl groups on the outer core of the micelle for further conjugation to a targeting moiety (i.e., antibody, glucose) [87].

23.5.3 Worm-Like Micelles

Cylindrical worm micelles [92] are a promising new class of supermolecular drug/dye carriers [93] to explore for a number of reasons. First, even if microns long, they can "worm" through small pores, including gels, and circulate for perhaps weeks. Second, targeted worms can cooperatively zip up — binding with high affinity — to surfaces or cells that bear suitable receptors. And third, once bound, internalization by the cell leads to delivery of a relatively large amount of drug all at once [94].

It is of central importance that several system characteristics be elucidated, including polymer molecular weight versus worm diameter, worm stability, and flexibility [93]. The first issue has already been addressed with vesicles [95]. Nanoscale worm micelles can be very stable; they appear similar to filamentous phages that have been used with great success *in vivo* for phage display of targeting ligands (including tumors) [96]. Unlike phages that carry nucleic acids, worm micelles can carry lipophilic drugs.

23.5.4 Polymersomes

Recently, interest has been focused on polymeric vesicles, composed of hydrophobic–hydrophilic diblock co-polymers, as drug delivery vehicles [95,97–100]. The advantages of these polymersomes, as compared to liposomes, include enhanced mechanical stability and greater flexibility to tailor bi-layer characteristics, such as thickness and chemical composition [98,101–104]. Moreover, it has been speculated that protein interactions with the polymeric bilayers will greatly differ from their interactions with lipid ones, thereby affecting drug delivery characteristics, such as circulation time *in vivo*. Indeed, Photos et al. [105] have shown that the circulation time of polymersomes *in vivo* increases with the bilayer thickness. Pata and Dan [106] have found that the characteristics of the polymeric bi-layer, when compared to the lipid bi-layer, are quite different and can be used for tailoring the carrier properties. Recently, Meng et al. [107] have synthesized biodegradable polymersomes from block co-polymers of PEG-PLA.

Finally, polymeric vesicles have been synthesized from multiblock co-polymers of Pluronic F27 with a PLA block on either end [108]. The vesicle structure is characterized by a hydrophilic core with hydrophobic layers, and can form several conformations such as bilayer or onion-like vesicles. The PLA-F27-PLA co-polymers exhibit a decrease in T_g and T_m values, which indicate an increased permeability and chain mobility in aqueous solutions. This may explain the high burst release from these vesicles, but does not eliminate this class of particles as a drug delivery system [108].

23.6 TARGETED DRUG DELIVERY USING NANOPARTICLES

23.6.1 Oral Delivery

Oral delivery of nanoparticles has focused on uptake via the Peyer's patches in the GALT. Peyer's patches are characterized by M cells that overlie the lymphoid tissue and are specialized for endocytosis and transport into intraepithelial spaces and adjacent lymphoid tissue. There have been several differing opinions as to the ease of nanoparticle transport through the M cells, and the method by which this occurs [109,110]. One theory is that nanoparticles bind the apical membrane of the M cells, followed by a rapid internalization and a "shuttling" to the lymphocytes [110,111]. The size and surface charge of the nanoparticles are crucial for their uptake. However, there have only been two published phase 1 clinical trials examining the oral uptake of PLGA nanoparticles encapsulating

Escherichia coli antigens, with no clear benefit determined [109]. There is some promise in identifying M cell receptors and targeting them on the surface of nanoparticles. The carbohydrate epitope, sialytated Lewis antigen A (SLAA), has been identified on human M cells [109]. This application of targeted nanoparticles in oral delivery holds tremendous promise for the development of oral vaccines and in cancer therapy.

23.6.2 Brain Delivery

Another exciting application of surface-modified particles is targeted drug delivery to cells or organs. Kreuter et al. [53] were able to deliver several drugs successfully through the blood–brain barrier using polysorbate 80-coated poly(butylcyanoacrylate) nanoparticles. It is thought that after administration of the polysorbate 80-coated particles, apolipoprotein E (ApoE) adsorbs onto the surface coating. The ApoE protein mimics low-density lipoprotein (LDL) causing the particles to be transported via the LDL receptors into the brain. The effects of polysorbate-80 on endocytosis by the blood–brain barrier were confirmed by Sun et al. [112] with PLA nanoparticles. Nanoparticles made from emulsifying wax and polyoxyl 20-stearyl ether linked to a thiamine surface ligand, fabricated using microemulsion precursors and had an average final diameter of 67 nm [113]. These particles are able to associate with the blood–brain barrier thiamine transporters and thereby increase the unidirectional transfer coefficient for the particles into the brain.

23.6.3 Arterial Delivery

There are other specific areas, where nanoparticle administration may have an advantage over microparticulate-based drug delivery systems. One area that has been of recent interest is in prevention of restenosis [15,114]. Restenosis is a major postoperative concern following arterial surgery. In order to inhibit VSMC proliferation, drugs must be delivered at a high concentration over a long period of time. Nanoparticles offer an advantage, because the medication would not have to be delivered systemically as they are small enough for cellular internalization and connective tissue permeation. Several types of drugs including antiproliferative agents have been used to test this method of delivery. PLA nanoparticles were loaded with platelet-derived growth factor receptor β tyrphostin inhibitor and delivered intra-lumenally to an injured rat carotid artery [115]. The drug had the desired effect of preventing restenosis, but of significance was the absence of drug in other areas of the arteries and systemic circulation. Song et al. [15] found that specific additives after nanoparticles formation, such as heparin, DMAB, or fibrinogen, could enhance arterial retention of the particles. Suh et al. [14] created PEO–PLGA nanoparticles, which had an initial burst release of 40% of the antiproliferative drug in the first 3 days. However, a total of 85% of the drug was released after 4 weeks. This shows that nanoparticles have a great potential for long-term arterial drug delivery.

23.6.4 Tumor Therapy

One of the most common targeting applications for nanoparticles is of chemotheraputic agents against cancerous cells and tumor sites. Figure 23.7 shows the cellular internalization of PLGA nanoparticles into MCF-10A neoT cells. Oral delivery of chemotherapy is of high interest, because chemotheraputic agents are eliminated by the first-pass effect with cytochrome p450 [33]. Another reason is that it has attracted attention is due to the phenomena known as the enhanced permeation and retention (EPR) effect. The vasculature around tumor sites is inherently leaky due to the rapid vascularization necessary to serve fast-growing tumors [116]. Much attention has also been given to lymphatic targeting using nanoparticles. In addition, poor lymphatic drainage at the site prevents elimination of the particles from the tumor tissue. Another benefit of tumor targeting is the fact that many cancer cells over-express specific antigens. Coating or binding the ligands on nanoparticulate surfaces can exploit this property. One example is covalently attaching sugar chains to nanoparticles.

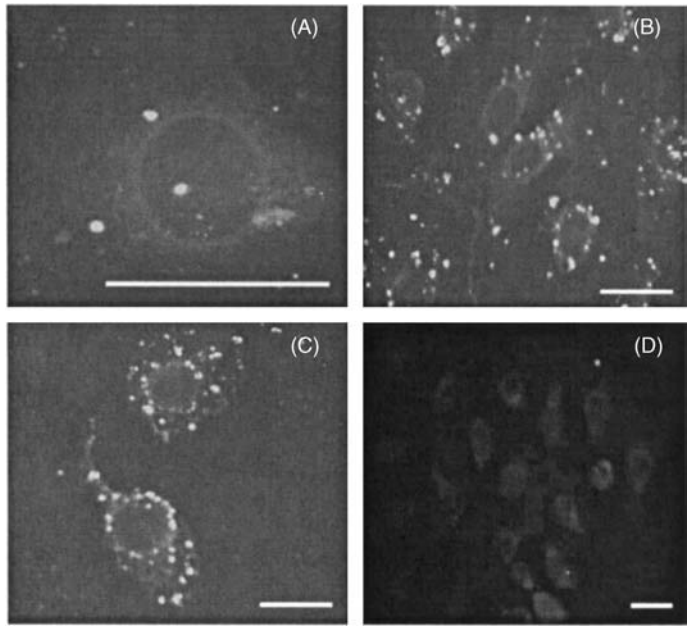

FIGURE 23.7 Internalization of NPs loaded with Alexa Fluor 488-labeled cystatin into MCF-10A neoT cells. (A) 10 min incubation, concentration = 100 μg NP/mL; (B) 30 min incubation, concentration = 100 μg NP/mL; (C) 45 min incubation, concentration = 100 μg NP/mL; (D) free Alexa Fluor 488-labeled cystatin, 45 min incubation, concentration = 0.1 μ*M*. Scale bar, 20 μm. All the images are representative of at least two independent experiments. (Reprinted from Cegnar, M. et al., *Exp. Cell Res.*, 301, 223–231, 2004.)

Yamazaki et al. [85] used sugar chain remodeled glycoprotein–liposome conjugates for binding to E-selectin. These particles showed uptake by solid tumor tissue. Cancer cells overexpress transferrin, which is normally used for iron uptake. Paclitaxel-loaded PACA nanoparticles with a PEG linker chain conjugated to transferrin were shown to have a decreased burst release over nontargeted particles and were able to increase the lifespan in tumor-bearing mice with a decreased weight loss compared to mice given conventional paclitaxel [117]. The decreased burst may be due to the removal of surface-associated drug during the activation process and the decreased weight loss may point to a reduction in paclitaxel-associated side effects.

Yokoyama et al. [91,118–121] have conducted numerous studies on the chemical conjugation as well as physical entrapment of adriamycin (ADR, also known as doxorubicin), an anticancer drug, in PEO–Poly(aspartic acid) micelles (PEO–P(Asp)). It was found that polymer micelles with conjugated ADR alone or physically entrapped ADR alone did not have anti-tumor activity. However, high amounts of both chemically conjugated and physically entrapped ADR were necessary for antitumor activity [121]. Other anticancer drugs have been used in block co-polymer micelles. Cisplatin has been bound to P(Asp) using the same block co-polymer PEO-P(Asp) [122]. Methotrexate (Mtx) esters of PEO-block-poly(2-hydroxyethyl-L-aspartimide) (PEO-PHEA) were found to form stable micelles with a sustained release profile, dependent on the amount of Mtx substitution [123].

One method for targeting that is attracting attention is by exploiting the high noncovalent binding of biotin and avidin. Each avidin molecule binds four biotin molecules. Using the multifunctionality of this technology, drugs and homing molecules for cancer cells can be combined [124]. By using biotinylated PEG–PCL and associating that with avidin-bound lectin, the amount of nanoparticles associated with Caco-2 cells is increased dramatically [1]. NeutrAvidin™ has been covalently attached to the surface of PLA nanoparticles via sulfhydrl groups [125]. These thiol

groups are bound via a carbodiimide reaction with cystamine. Using this technology, biotinylated antibodies or ligands can be attached to the particle surface. Biotinylated worm-like micelles have also been found to be stable in an aqueous solution for at least a month, and have the potential for the delivery of large quantities of hydrophobic drugs or dyes [94].

23.6.5 Lymphatic System and Vaccines

The lymphatic absorption of a drug via the GALT has an advantage over a portal blood route since it avoids any liver presystemic metabolism, known as the first-pass effect. This could be beneficial for anticancer treatment, mucosal immunity, as well as having the potential for staining the lymph nodes prior to surgery [126]. Nanoparticles can also be used to carry antisense oligonucleotides and plasmid DNA that can be used to treat some forms of cancer and viral infections, as well as a new vaccination approach. Antisense oligionucleotides normally have poor stability and cannot easily penetrate cells, but are easily encapsulated in nanoparticles [13,127]. High doses of antibiotics and antiparasitics are given to treat gastrointestinal bacteria and parasites because only 10 to 15% of the drug administered is absorbed [64]. The increased muco-adhesivity of nanoparticles could be effective in treating these pathogens with lower doses of drugs.

Nanoparticles have also had some success as a new delivery vehicle for vaccines. CS nanoparticles have been successful as a nasal vaccine in some animal studies producing significant IgG serum responses and superior IgA secretory responses when used in influenza, pertussis, and diphtheria vaccines [128]. Another option for vaccine delivery is the delivery of PLGA nanoparticles to dendritic cells [12]. Dendritic cells initiate an antigen-specific immune response. The co-delivery of antigens and immunomodulators in the same particles helps to overcome peripheral tolerance against self-antigens. This technology can potentially be used for cancer vaccines or hepatitis antigens.

23.6.6 Pulmonary Delivery

The lungs owing to their large surface area, good mucosal permeation, well-developed vascular system, thin alveolar walls, and low activity of drug-metabolizing enzymes are another target area for nanoparticles. Direct administration to the lungs is beneficial because of the decreased systemic side effects, the availability for increased dose levels at the site, and the lack of first-pass metabolism. The tracheo-bronchial region is protected by a mucosal barrier, which can be cleared by nanoparticle technology. One obstacle for the inhalation of nanoparticles is their inappropriate mass median aerodynamic diameter. They do not have sufficient size for sedimentation or impaction deposition mechanisms and would be exhaled postinhalation [129]. Carrier particles have been proposed, which after deposition in the carrier matrix dissolve, while the nanoparticles are released.

When CS-coated nanoparticles were administered via the lungs, there were detectable blood levels of the drug 24 h after administration, as opposed to 8 h for the noncoated particles [23]. PACA nanoparticles have been found to be cytotoxic to airway epithelial cells, but gelatin and human serum albumin nanoparticles of ~200 nm in diameter were taken up by bronchial epithelial cells with no evidence of cytotoxicity or inflammation [130].

Nanoparticles have been used to target other mucosal surfaces. Long-term extra-ocular (cornea and conjunctiva) drug delivery with nanoparticles provides an improvement in conventional drug delivery in this region. It was possible to deliver drug-loaded CS nanoparticles to the extra-ocular structures over the course of 48 h at higher levels than with free drug, without exposing the inner ocular structures (iris and aqueous humour) to the drug [131].

Nanoparticles may be used for skin delivery to prolong the residence time of sunscreen agents in the stratum corneum or to deliver vitamin A to the upper layers of the skin [132]. CLSM demonstrates nanoparticles accumulating in the follicular openings, with higher percentages of smaller diameter nanoparticles accumulating.

23.7 DRUG RELEASE

23.7.1 MECHANISMS

Biodegradable polymers release drug in one of the two ways: erosion and diffusion. Release from biodegradable polymers *in vivo* is governed by a combination of both mechanisms, which depends on the relative rates of erosion and diffusion. Erosion is defined as the physical dissolution of a polymer as a result of its degradation [133]. Most biodegradable polymers used for drug delivery are degraded by hydrolysis. Hydrolysis is a reaction between water molecules and bonds in the polymer backbone, typically ester bonds, which repeatedly cuts the polymer chain until it is returned to monomers. Other biodegradable polymers are enzymatically degradable, which is also a type of chain scission. As water molecules break chemical bonds along the polymer chain, the physical integrity of the polymer degrades and allows drug to be released.

There are two possible mechanisms of erosion. When water is confined to the surface of the matrix, as in the case of a hydrophobic polymer, chain scission will occur only on the surface and the drug will be released as the surface of the polymer matrix erodes. If the water penetrates the polymer matrix faster than it hydrolyzes the bonds on the surface, then erosion will occur throughout the entire material — this is also called bulk erosion. In many cases, the erosion of a polymer matrix *in vivo* is some combination of these mechanisms. Degradation by surface erosion alone may be preferred, because the degradation rate can be controlled through the surface area of the matrix [134].

In the case of diffusion-controlled release, the drug's concentration gradient in the polymer matrix is the driving force for the molecules to diffuse into the surrounding medium. The diffusion of a drug molecule through the polymer matrix is dependent upon the solubility of the drug in the polymer matrix and the surrounding medium, the diffusion coefficient of the drug molecule, the molecular weight of the drug, its concentration throughout the polymer matrix, and the distance necessary for diffusion. Drugs can be either distributed evenly throughout the matrix or encapsulated as a reservoir [135]. The release rate for the reservoir system also factors in the membrane thickness and area. Practically, reservoir systems often have a lag period after placement *in vivo*, as opposed to the burst release present for most other systems. However, these systems need to be carefully engineered to prevent premature membrane rupture that might release a toxic amount of drug into the body.

When a drug is dissolved in the matrix and the mechanism for delivery is diffusion, then the driving force for release is the concentration gradient and release predictions can be made based on Fick's laws of diffusion [134]. Cumulative release from diffusion-controlled matrix devices is inversely proportional to the square root of time [136]. This presents an engineering challenge because surface area becomes smaller due to degradation, with a resulting decrement in the release rate.

Frequently, diffusion-controlled release is important in the early stages of drug release. For many of the polymeric delivery systems, there is some concentration of drug molecules entrapped near the surface of the matrix and adsorbed onto the surface of the matrix. Upon immersion into a medium, the release of these drug molecules is controlled by the rate of diffusion of the drug into the surrounding environment. This can cause a problem referred to as the "burst effect," which can potentially release a toxic amount of drug in some geometries (frequently 50% or more of the incorporated drug) into the body within the first 24 h [137]. This burst release is part of what is frequently referred to as a biphasic release profile [3]. During the first phase, the burst release, the structural integrity of the nanoparticles is maintained. The second phase, or the linear release, is characterized by pore formation, particle deformation, and fusion [138]. One method for eliminating the burst release is by tailoring the collection of the nanoparticles to remove the drug attached to the surface. By collecting PLA nanoparticles through gel filtration, the antiischemic drug N^6-cyclopentyladenosine near the surface was removed, which decreased the overall encapsulation efficiency, and eliminated the burst release from the particles [62].

The specific chemical and biological characteristics of the drug and the polymer are crucial in designing a polymeric delivery system. For example, drugs with greater hydrophilicity can increase the overall release rate by promoting polymer swelling and degradation which in turn increases drug

diffusion, and certain drug molecules may potentially react with the polymer matrix [139]. The drug's molecular weight, solubility in biological fluids as well as its miscibility in the polymer matrix will influence the drug's diffusivity from the system and the concentration profile of the drug throughout the matrix. Since polymeric delivery systems are rarely homogenous throughout the entire matrix, the drug's diffusivity, and therefore release rate, can change with the local polymer composition and structure. One example of this phenomenon showing the effect of drug polymer interaction is the release of the prodrug, 3-methoxyxanthone and its active form xanthone, from PLGA nanocapsules [140]. Incorporation into nanocapsules was significantly higher than that of solid nanoparticles. The release profile of these drugs suggest a physical interaction of the drug with the polymer when given the nanocapsule structure [140].

23.7.2 Release Characteristics

The release characteristics of polymeric nanoparticles are among the most important features of the drug/polymer formulations because of the possible applications in sustained drug delivery. There are several factors that affect the release rate of the entrapped drug. Larger particles have a smaller initial burst release and longer sustained release than smaller particles. In addition, the greater the drug loading, the greater the burst and faster the release rate. For example, PLA nanoparticles containing 16.7% savoxepine released 90% of their drug load in 24 h, as opposed to particles containing 7.1% savoxepine, which released their content over 3 weeks [27]. The initial burst release is thought to be caused by poorly entrapped drug, or drug adsorbed onto the outside of the particles. When using polymers, which interact with a drug, like PLGA with a free COOH group and proteins, the burst release is lower and in some cases absent, and drug release is prolonged [9,63].

The addition of other polymers to PLA-based polymers can also be used to control drug release. For example, PEG has been polymerized into a PLA homopolymer creating a PLA-PEG-PLA co-polymer [141]. The amount of the drug (in this case progesterone) released increased with the PEG content and the molecular weight of the co-polymers. The drug release continued to increase as the total molecular weight of the co-polymers decreased. The initial burst was decreased in the absence of lower molecular weight polymers. The content of PEG in the co-polymer affected the size of the particles as well as the degradation of the polymers. Similar effects were seen with PLGA-mPEG nanoparticles loaded with cisplatin [142]. Consequently, it would be possible to alter the release rate of the drug by changing the amount of PEG in the co-polymer as well as the molecular weights of the polymers.

ACKNOWLEDGMENTS

We thank the Nanotechnology Institute of Southeastern Pennsylvania and IGERT Grant # DGE-0221664 for support.

REFERENCES

1. R. Gref, P. Couvreur, G. Barratt, and E. Mysiakine, Surface-engineered nanoparticles for multiple ligand coupling, *Biomaterials*, 24, 4529–4537, 2003.
2. T. Govender, S. Stolnik, M. C. Garnett, L. Illum, and S. S. Davis, PLGA nanoparticles prepared by nanoprecipitation: drug loading and release studies of a water soluble drug, *J. Control. Release*, 57, 171–185, 1999.
3. C. Fonseca, S. Simoes, and R. Gaspar, Paclitaxel-loaded PLGA nanoparticles: preparation, physiochemical characterization and *in vitro* anti-tumoral activity, *J. Control. Release*, 83, 273–286, 2002.
4. Y. Dong and S. Feng, Methoxy poly(ethylene glycol)-poly(lactide) (MPEG-PLA) nanopartiocles for controlled drug delivery of anticancer drugs, *Biomaterials*, 25, 2843–2849, 2004.
5. X. Zhang, Y. Li, X. Chen, X. Wang, X. Xu, Q. Liang, J. Hu, and X. Jing, Synthesis and characterization of the paclitaxel/MPEG-PLA block copolymer conjugate, *Biomaterials*, 26, 2121–2128, 2005.

6. M. Aprahamian, C. Michel, W. Humbert, J.-P. Devissaguet, and C. Damge, Transmucosal passage of polyalkylcyanoacrylate nanocapsules as a new drug carrier in the small intestine, *Biol. Cell*, 61, 69–76, 1987.
7. A.-M. Torche, H. Jouan, P. L. Corre, E. Albina, R. Primault, A. Jestin, and R. L. Verge, *Ex vivo* and *in situ* PLGA microspheres uptake by pig ileal Peyer's patch segment, *Int. J. Pharm.*, 201, 15–27, 2000.
8. D. Lemoine and V. Preat, Polymeric nanoparticles as delivery system for influenza virus glycoproteins, *J. Control. Release*, 54, 15–27, 1998.
9. M. D. Blanco and M. J. Alonso, Development and characterization of protein-loaded poly(lactide-co-glycolide) nanospheres, *Eur. J. Pharm. Biopharm.*, 43, 287–294, 1997.
10. M. Cegnar, J. Kos, and J. Kristl, Cystatin incorporated in poly(lactide-co-glycolide) nanoparticles: development and fundamental studies on preservation of its activity, *Eur. J. Pharm. Sci.*, 22, 357–364, 2004.
11. J. Barichello, M. Morishita, K. Takayama, and T. Nagai, Encapsulation of hydrophilic and lipophilic drugs in PLGA nanoparticles by the nanoprecipitation method, *Drug Dev. Indus. Pharm.*, 25, 471–476, 1999.
12. P. Elamanchili, M. Diwan, M. Cao, and J. Samuel, Characterization of poly(D,L-lactic-co-glycolic acid) based nanoparticulate system for enhanced delivery of antigens to dendritic cells, *Vaccine*, 22, 2406–2412, 2004.
13. C. Perez, A. Sanchez, D. Putnam, D. Ting, R. Langer, and M. J. Alonso, Poly(lactic acid)-poly(ethylene glycol) nanoparticles as new carriers for the delivery of plasmid DNA, *J. Control. Release*, 75, 211–224, 2001.
14. H. Suh, B. Jeong, R. Rathi, and S. W. Kim, Regulation of smooth muscle cell proliferation using paclitaxel-loaded poly(ethylene oxide)-poly(lactide/glycolide) nanospheres, *J. Biomed. Mater. Res.*, 42, 331–338, 1998.
15. C. X. Song, V. Lanhasetwar, H. Murphy, X. Qu, W. R. Humphrey, R. J. Shebuski, and R. J. Levy, Formulation and characterization of biodegradable nanoparticles for intravascular local drug delivery, *J. Control. Release*, 43, 197–212, 1997.
16. Y.-H. Cheng, L. Illum, and S. S. Davis, A poly(D,L-lactide-co-glycolide) microsphere depot system for delivery of haloperidol, *J. Control. Release*, 55, 203–212, 1998.
17. S.-S. Feng and G. Huang, Effects of emulsifiers on the controlled release of paclitaxel (Taxol) from nanopsheres of biodegradable polymers, *J. Control. Release*, 71, 53–69, 2001.
18. A. Vila, A. Sanchez, M. Tobio, P. Calvo, and M. J. Alonso, Design of biodegradable particles for protien delivery, *J. Control. Release*, 78, 15–24, 2002.
19. H. Rafati, A. G. A. Coombes, J. Adler, J. Holland, and S. S. Davis, Protein-loaded poly(DL-lactide-co-glycolide) microparticles for oral administration: formulation, structural and release characteristics, *J. Control. Release*, 43, 89–102, 1997.
20. Y.-P. Li, Y.-Y. Pei, X.-Y. Zhang, Z.-H. Gu, Z. H. Zhou, W.-F. Yuan, J.-J. Zhao, J.-H. Zhu, and X.-J. Gao, PEGylated PLGA nanoparticles as protein carriers: synthesis, preparation and biodistribution in rats, *J. Control. Release*, 71, 203–211, 2001.
21. G. P. Carino, J. S. Jacob, and E. Mathiowitz, Nanosphere based oral insulin delivery, *J. Control. Release*, 65, 261–269, 2000.
22. H.-Y. Kwon, J.-Y. Lee, S.-W. Choi, Y. Jang, and J.-H. Kim, Preparation of PLGA nanoparticles containing estrogen by emulsification–diffusion method, *Colloids Surfaces*, 182, 123–130, 2001.
23. H. Takeuchi, H. Yamamoto, and Y. Kawashima, Mucoadhesive nanoparticulate systems for peptide drug delivery, *Adv. Drug Del.*, 47, 39–54, 2001.
24. M. Cegnar, A. Premzl, V. Zavasnik-Bergant, J. Kristl, and J. Kos, Poly(lactide-co-glycolide) nanoparticles as a carrier system for delivering cysteine protease inhibitor cystatin into tumor cells, *Exp. Cell Res.*, 301, 223–231, 2004.
25. H. Murakami, M. Kobayahi, H. Takeuchi, and Y. Kawashima, Preparation of poly(DL-lactide-co-glycoide) nanoparticles by modified spontaneous emulsification solvent diffusion method, *Int. J. Pharm.*, 187, 143–152, 1999.
26. M. L.-L. Verger, L. Fluckiger, Y. Kim, M. Hoffman, and P. Maincent, Preparation and characterization of nanoparticles containing an antihypertensive agent, *Eur. J. Pharm. Biopharm.*, 46, 137–143, 1998.
27. J.-C. Leroux, E. Allemann, F. D. Jaeghere, E. Doelker, and R. Gurny, Biodegradable nanoparticles — from sustained release formulations to improved site specific drug delivery, *J. Control. Release*, 39, 339–350, 1996.

28. S. Sakuma, M. Hayashi, and M. Akashi, Design of nanoparticles composed of graft copolymers for oral peptide delivery, *Adv. Drug Del.*, 47, 21–37, 2001.
29. N. Behan, C. Birkinshaw, and N. Clarke, Poly *n*-butyl cyanoacrylate nanoparticles: a mechanistic study of polymerisation and particle formation, *Biomaterials*, 22, 1335–1344, 2001.
30. K. A. Janes, P. Calvo, and M. J. Alonso, Polysaccharide colloidal particles as delivery systems for macromolecules, *Adv. Drug Del.*, 47, 83–97, 2001.
31. Y. Hu, X. Jiang, Y. Ding, H. Ge, Y. Yuan, and C. Yang, Synthesis and characterization of chitosan–poly(acrylic acid) nanoparticles, *Biomaterials*, 23, 3193–3201, 2002.
32. H. Rafati, E. C. Lavelle, A. G. Coombes, S. Stolnik, J. Holland, and S. S. Davis, The immune response to a model antigen associated with PLG microparticles prepared using different surfactants, *Vaccine*, 15, 1888–1897, 1997.
33. K. Yin Win and S. S. Feng, Effects of particle size and surface coating on cellular uptake of polymeric nanoparticles for oral delivery of anticancer drugs, *Biomaterials*, 26, 2713–2722, 2005.
34. M. J. Dorta, O. Manguia, and M. Llabres, Effects of polymerization variables on PLGA properties: molecular weight, composition, and chain structure, *Int. J. Pharm.*, 100, 9–14, 1993.
35. T. D. Dziubla, A. Karim, and V. R. Muzykantov, Polymer nanocarriers protecting active enzyme cargo against proteolysis, *J. Control. Release*, 102, 427–439, 2005.
36. S. K. Sahoo, J. Panyam, S. Prabha, and V. Labhasetwar, Residual polyvinyl alcohol associated with poly (D,L-lactide-co-glycolide) nanoparticles affects their physical properties and cellular uptake, *J. Control. Release*, 82, 105–114, 2002.
37. G. Fontana, G. Pitarresi, V. Tomarchio, B. Carlisi, and P. L. S. Biagio, Preparation, characterization and *in vitro* antimicrobial activity of ampicillin-loaded polyethylcyanoacrylate nanoparticles, *Biomaterials*, 19, 1009–1017, 1998.
38. L. Mu and S. S. Feng, A novel controlled release formulation for the anticancer drug paclitaxel (Taxol): PLGA nanoparticles containing vitamin E TPGS, *J. Control. Release*, 86, 33–48, 2003.
39. J. Panyam, S. K. Sahoo, S. Prabha, T. Bargar, and V. Labhasetwar, Fluorescence and electron microscopy probes for cellular and tissue uptake of poly(D,L-lactide-co-glycolide) nanoparticles, *Int. J. Pharm.*, 262, 1–11, 2003.
40. J. P. Kitchell and D. L. Wise, Poly(lactic/glycolic acid) biodegradable drug-polymer matrix systems, *Methods Enzymol.*, 112, 436–448, 1985.
41. H. Curtis, *Biology*, Worth Publishers Inc., New York, 1983.
42. H. Okada and H. Toguchi, Biodegradable microspheres in drug delivery, *Crit. Rev. Ther. Drug Carrier Syst.*, 12, 1–99, 1995.
43. K. Sung, R. Han, O. Hu, and L. Hsu, Controlled release of nalbuphine prodrugs from biodegradable polymeric matrices: influence of prodrug hydrophilicy and polymer composition, *Int. J. Pharm.*, 172, 17–25, 1998.
44. R. K. Kulkarni, K. C. Pani, C. Neuman, and F. Leonard, Polylactic acid for surgical implants, *Arch. Surg.* 93, 839–843, 1966.
45. B. A. Sabel, P. Dominiak, W. Hauser, M. J. During, and A. Freese, Levodopa delivery from controlled-release polymer matrix: delivery of more than 600 days *in vitro* and 225 days of elevated plasma levels after subcutaneous implantation in rats, *J. Pharmacol. Exp. Ther.*, 255, 914–922, 1990.
46. A. C. Sharon and D. L. Wise, Development of drug delivery systems for use in treatment of narcotic addiction, *NIDA Res. Monogr.* 28, 194–213, 1981.
47. S. J. Siegel, K. I. Winey, R. E. Gur, R. H. Lenox, W. B. Bilker, D. Ikeda, N. Gandhi, and W.-X. Zhang, Surgically implantable long-term antipsychotic delivery systems for the treatment of schizophrenia, *Neuropsychopharmacology*, 26, 817–823, 2002.
48. H. Qian, J. Bei, and S. Wang, Synthesis, characterization and degradation of ABA block copolymer of -lactide and -caprolactone, *Polym. Degrad. Stab.*, 68, 423–429, 2000.
49. P. Dubois, M. Krishnan, and R. Narayan, Aliphatic polyester-grafted starch-like polysaccharides by ring-opening polymerization, *Polymer*, 40, 3091–3100, 1999.
50. C. G. Pitt, Poly-ε-caprolactone and its copolymers, in *Biodegradable Polymers as Drug Delivery Systems*, Vol. 2, M. Chasin and R. Langer, Eds., Marcel Dekker, New York, 1990, pp. 71, chapter 3.
51. Y. Lemmouchi, E. Schacht, and C. Lootens, In vitro release of trypanocidal drugs from biodegradable implants based on poly(ε-caprolactone) and poly(D,L-lactide), *J. Control. Release*, 55, 79–85, 1998.
52. M. Miyajima, A. Koshika, J. Okada, M. Ikeda, and K. Nishimura, Effect of polymer crystallinity on papaverine release from poly(lactic acid) matrix, *J. Control. Release*, 49, 207–215, 1997.

53. J. Kreuter, Nanoparticulate systems for brain delivery of drugs, *Adv. Drug Del.*, 47, 65–81, 2001.
54. J. L. Arias, V. Gallardo, S. A. Gomez-Lopera, R. C. Plaza, and A. V. Delgado, Synthesis and characterization of poly(ethyl-2-cyanoacrylate) nanoparticles, *J. Control. Release*, 77, 309–321, 2001.
55. G. Fontana, M. Licciardi, S. Mansueto, D. Schilaci, and G. Giammona, Amoxicillin-loaded polyethylcyanoacrylate nanoparticles: influenece of PEG coating on the particle size, drug release rate and phagocytic uptake, *Biomaterials*, 22, 2857–2865, 2001.
56. J. Dai, T. Nagai, X. Wang, T. Zhang, M. Meng, and Q. Zhang, pH-sensitive nanoparticles for improving the oral bioavailability of cyclosporine A, *Int. J. Pharm.*, 280, 229–240, 2004.
57. T. Jung, A. Breitenbach, and T. Kissel, Sulfobutylated poly(vinyl alcohol)-graft-poly(lactide-co-glycolide)s facilitate the preparation of small negatively charged biodegradable nanospheres, *J. Control. Release*, 67, 157–169, 2000.
58. H. S. Yoo, J. E. Oh, K. H. Lee, and T. G. Park, Biodegradable nanoparticles containing doxorubicin-PLGA conjugate for sustained release, *Pharm. Res.*, 16, 1114–1118, 1999.
59. H. S. Yoo, K. H. Lee, J. E. Oh, and T. G. Park, *In vitro* and *in vivo* anti-tumor activities of nanoparticles based on doxorubicin-PLGA conjugates, *J. Control. Release*, 68, 419–431, 2000.
60. M. Chacon, J. Molpeceres, L. Berges, M. Guzman, and M. R. Aberturas, Stability and freeze-drying of cyclosporine loaded poly (D,L lactide-glycolide) carriers, *Eur. J. Pharm. Sci.*, 8, 99–107, 1999.
61. A. Saez, M. Guzman, J. Molpeceres, and M. R. Aberturas, Freeze-drying of polycarolactone and poly(D,L-lactic-glycolic) nanoparticles induces minor particle size changes affecting the oral pharmacokinetics of loaded drugs, *Eur. J. Pharm. Biopharm.*, 50, 379–387, 2000.
62. A. Dalpiaz, E. Leo, F. Vitali, B. Pavan, A. Scatturin, F. Bortolotti, S. Manfredini, E. Durini, F. Forni, B. Brina, and M. A. Vandelli, Development and characterization of biodegradable nanospheres as delivery systems of anti-ischemic adenosine derivatives, *Biomaterials*, 26, 1299–1306, 2005.
63. S. Nicoli, P. Santi, P. Couvreur, G. Couarraze, P. Colombo, and E. Fattal, Design of triptorelin loaded nanospheres for transdermal iontophoretic administration, *Int. J. Pharm.*, 214, 31–35, 2001.
64. R. H. Muller, C. Jacobs, and O. Kayser, Nanosuspensions as particulate drug formulations in therapy. Rationale for development and what we can expect for the future, *Adv. Drug Del.*, 47, 3–19, 2001.
65. R. Gref, M. Luck, P. Quellec, M. Marchand, E. Dellacherie, S. Harnisch, T. Blunk, and R. H. Muller, Stealth corona-core nanoparticles surface modified by polyethylene glycol (PEG): influeneces of the corona (PEG chain length and surface density) and of the core composition on phagocytic uptake and plasma protein adsorption, *Colloids Surfaces B: Biointerfaces*, 18, 301–313, 2000.
66. M. T. Peracchia, E. Fattal, D. Desmaele, M. Besnard, J. P. Noel, J. M. Gomis, M. Appel, J. d'Angelo, and P. Couvreur, Stealth PEGylated polycyanoacrylate nanoparticles for intravenous administration and splenic targeting, *J. Control. Release*, 60, 121–128, 1999.
67. P. Calvo, B. Gouritin, I. Brigger, C. Lasmezas, J. Deslys, A. Williams, J. P. Andreux, D. Dormont, and P. Couvreur, PEGylated polycyanoacrylate nanoparticles as vector for drug delivery in prion diseases, *J. Neurosci. Methods*, 11, 151–155, 2001.
68. M. Tobio, A. Sanchez, A. Vila, I. Soriano, C. Evora, J. L. Vila-Jato, and M. J. Alonso, The role of PEG on the stability in digestive fluids and *in vivo* fate of PEG-PLA nanoparticles following oral administration, *Colloids Surfaces B: Biointerfaces*, 18, 315–323, 2000.
69. J. E. Blackwell, N. M. Daglia, B. Dickerson, E. L. Berg, and D. J. Goetz, Ligand coated nanosphere adhesion to E- and P-Selectin under static and flow conditions, *Ann. Biomed. Eng.*, 29, 523–533, 2001.
70. Z. Panagi, A. Beletsi, G. Evangelatos, E. Livaniou, D. S. Ithakissios, and K. Avgoustakis, Effect of dose on the biodistribution and pharmacokinetics of PLGA and PLGA-mPEG nanoparticles, *Int. J. Pharm.*, 221, 143–152, 2001.
71. D. Kim, H. El-Shall, D. Dennis, and T. Morey, Interaction of PLGA nanoparticles with human blood constituents, *Colloids Surfaces B Biointerfaces*, 40, 83–91, 2005.
72. E. Chambers and S. Mitragotri, Prolonged circulation of large polymeric nanoparticles by non-covalent adsorption on erythrocytes, *J. Control. Release*, 100, 111–119, 2004.
73. H. M. Redhead, S. S. Davis, and L. Illum, Drug delivery in poly(lactide-co-glycolide) nanoparticles surface modified with poloxamer 407 and poloxamine 908: *in vitro* characterization and *in vivo* evaluation, *J. Control. Release*, 70, 353–363, 2001.
74. E. Kisak, B. Coldren, and J. Zasadinski, Nanocompartments enclosing vesicles, colloids, and macromolecules via interdigitated lipid bilayers, *Langmuir*, 18, 284–288, 2002.
75. T. Allen, Liposomal drug delivery, *Curr. Opin. Colloid Interfaces Sci.*, 1, 645–651, 1996.
76. D. Lasic, *Liposomes: From Physics to Applications*, Elsevier, Amsterdam, 1993.

77. D. Lasic and D. Papahadjopoulos, Liposomes and biopolymers in drug and gene delivery, *Curr. Opin. Solid State Mater. Sci.*, 1, 392–400, 1996.
78. D. Papahadjopoulos, T. Allen, A. Gabizon, E. Mayhew, K. Matthay, S. Huang, K. Lee, M. Woodle, D. Lasic, and C. Redemann, Sterically stabilized liposomes: improvements in pharmacokinetics and antitumor therapeutic efficacy, *Proc. Natl. Acad. Sci.*, 88, 11460–11464, 1991.
79. P. Sapra and T. Allen, Ligand-targeted liposomal anticancer drugs, *Prog. Lipid Res.*, 42, 439–462, 2003.
80. T. Allen and A. Chonn, Large unilamellar liposomes with low uptake into the reticuloendothelial system, *FEBS Lett.*, 223, 42–46, 1987.
81. A. Gabizon and D. Papahadjopoulos, Liposome formulations with prolonged circulation time in blood and enhanced uptake by tumors, *Proc. Natl. Acad. Sci. U.S.A.*, 85, 6949, 1988.
82. Papahadjopoulos and A. Gabizon, Liposomes designed to avoid the reticuloendothelial system, *Prog. Clin. Biol. Res.*, 343, 85–93, 1990.
83. T. Allen and C. Hansen, Pharmacokinetics of stealth versus conventional liposomes: effect of dose, *Biochim. Biophys. Acta*, 1068, 133–141, 1991.
84. H. Lin and J. Thomas, PEG-lipids and oligo(ethylene glycol) surfactants enhance the ultrasonic permeabilizability of liposomes, *Langmuir*, 19, 1098–1105, 2003.
85. N. Yamazaki, S. Kojima, and H. Yokoyama, Biomedical nanotechnology for active drug delivery systems by applying sugar-chain molecular functions, *Curr. Appl. Phys.*, 5, 112–117, 2005.
86. G. S. Kwon and K. Kataoka, Block copolymer micelles as long-circulating drug vehicles, *Adv. Drug Del. Rev.*, 16, 295–309, 1995.
87. S. Cammas-Marion, T. Okano, and K. Kataoka, Functional and site-specific macromolecular micelles as high potential drug carriers, *Colloids Surfaces B: Biointerfaces*, 16, 207–215, 1999.
88. A. Lavasanifar, J. Sammuel, and G. S. Kwon, Poly(ethylene oxide)-block-poly(L-amino acid) micelles for drug delivery, *Adv. Drug Del.*, 54, 169–190, 2002.
89. A. V. Kabanov, E. V. Batrakova, N. S. Melik-Nubarov, N. A. Fedoseev, T. Y. Dorodnich, V. Y. Alakhov, V. P. Chekhonin, I. R. Nazarova, and V. A. Kabanov, A new class of drug carriers: micelles of poly(oxyethylene)-poly(oxypropylene) block copolymers as microcontainers for drug atrgeting from blood in brain, *J. Control. Release*, 22, 141–158, 1992.
90. Y. S. Nam, H. S. Kang, J. Y. Park, T. G. Park, S. H. Han, and I. S. Chang, New micelle-like polymer aggregates made from PEI-PLGA diblock copolymers: micellar characteristics and cellular uptake, *Biomaterials*, 24, 2053–2059, 2003.
91. M. Yokoyama, G. S. Kwon, T. Okano, Y. Sakurai, T. Seto, and K. Kataoka, Preparation of micelle-forming polymer-drug conjugates, *Bioconjugate Chem.*, 3, 295–301, 1992.
92. Y. Won, H. Davis, and F. Bates, Giant wormlike rubber micelles, *Science*, 283, 960–963, 1999.
93. P. Dalhaimer, F. Bates, H. Aranda-Espinoza, and D. Discher, Synthetic cell elements from block copolymers — hydrodynamic aspects, *Comptes Rendus d'Academie Sci. — Serie IV Phys.*, 4, 251–258, 2003.
94. P. Dalhaimer, A. J. Engler, R. Parthasarathy, and D. E. Discher, Targeted worm micelles, *Biomacromolecules*, 5, 1714–1719, 2004.
95. H. Bermudez, A. Brannan, D. Hammer, F. Bates, and D. Discher, Molecular weight dependence of polymersome membrane structure, elasticity, and stability, *Macromolecules*, 35, 8203–8208, 2002.
96. W. Arap, R. Pasqualini, and E. Ruoslahti, Chemotherapy targeted to tumor vasculature, *Curr. Opin. Oncol.*, 10, 560–565, 1998.
97. Z. G. Gao, K. H. Oh, and C. K. Kim, Preparation and characterization of sustained-release microspheres of chlorpromazine, *J. Microencapsul.*, 15, 75–83, 1998.
98. B. Discher, Y.-Y. Won, D. Ege, J. Lee, D. Discher, and D. Hammer, Polymersomes: tough vesicles made from diblock copolymers, *Science*, 284, 1143–1146, 1999.
99. C. Dufes, A. Schatzlein, L. Tetley, A. Gray, D. Watson, J. Olivier, W. Couet, and I. Uchegbu, Niosomes and polymeric chitosan based vesicles bearing transferrin and glucose ligands for drug targeting, *Pharm. Res.*, 17, 1250–1258, 2000.
100. B. Discher, D. Hammer, F. Bates, and D. Discher, Polymer vesicles in various media, *Curr. Opin. Colloids Interfaces Sci.* 5, 125–131, 2000.
101. J. C.-M. Lee, H. Bermudez, B. M. Discher, M. A. Sheehan, Y.-Y. Won, F. S. Bates, and D. E. Discher, Preparation, stability, and *in vitro* performance of vesicles made with diblock coploymers, *Biotechnol. Bioeng.*, 73, 135–145, 2001.
102. D. Discher and A. Eisenberg, Polymer vesicles, *Science*, 297, 967–973, 2002.

103. R. Dimova, U. Seifert, B. Pouligny, S. Forster, and H. Dobereiner, Hyperviscous diblock copolymer vesicles., *Eur. Phys. J.*, 7, 241–250, 2002.
104. D. Discher, P. Photos, F. Ahmed, R. Parthasarathy, and F. Bates. Polymersomes: a new platform for drug targeting, in *Biomedical Aspects of Drug Targeting*, V. Torchilinand and V. Muzykantov, Eds., Springer, Philadelphia, 2002.
105. P. Photos, B. Discher, L. Bacakova, F. Bates, and D. Discher, Polymersomes *in vivo*: increased stealth with both PEG density and molecular weight, *J. Control. Release*, 90, 323–334, 2003.
106. V. Pata and N. Dan, The effect of chain length on protein solubilization in polymer-based vesicles (polymersomes), *Biophys. J.*, 85, 2111–2118, 2003.
107. F. Meng, C. Hiemstra, G. Engbers, and J. Feijen, Biodegradable polymersomes, *Macromolecules*, 36, 3004–3006, 2003.
108. X. Xiong, K. Tam, and L. Gan, Release kinetics of hydrophobic and hydrophilic model drugs from pluronic F127/poly(lactic acid) nanoparticles, *J. Control. Release*, 103, 73–82, 2005.
109. D. J. Brayden and A. W. Baird, Apical membrane receptors on intestinal M cells: potential targets for vaccine delivery, *Adv. Drug Deliv. Rev.*, 56, 721–726, 2004.
110. A. T. Florence, The oral absorption of micro- and nanopariculates: neither exceptional nor unusual, *Pharm. Res.*, 14, 259–266, 1997.
111. A. T. Florence and N. Hussain, Transcytosis of nanoparticle and dendrimer delivery systems: evolving vistas, *Adv. Drug Deliv. Rev.*, 50, S69–S89, 2001.
112. W. Sun, C. Xie, H. Wang, and Y. Hu, Specific role of polysorbate 80 coating on the targeting of nanoparticles to the brain, *Biomaterials*, 25, 3065–3071, 2004.
113. P. R. Lockman, M. O. Oyewumi, J. M. Koziara, K. E. Roder, R. J. Mumper, and D. D. Allen, Brain uptake of thiamine-coated nanoparticles, *J. Control. Release*, 93, 271–282, 2003.
114. C. Song, V. Labhasetwar, X. Cui, T. Underwood, and R. J. Levy, Arterial uptake of biodegradable nanoparticles for intravascular local drug delivery: results with an acute dog model, *J. Control. Release*, 54, 201–211, 1998.
115. I. Fishbein, M. Chorny, L. Rabinovich, S. Banai, I. Gati, and G. Golomb, Nanoparticulate delivery system of a tyrphostin for the treatment of restenosis, *J. Control. Release*, 65, 221–229, 2000.
116. L. Brannon-Peppas and J. O. Blanchette, Nanoparticle and targeted systems for cancer therapy, *Adv. Drug Deliv. Rev.*, 56, 1649–1659, 2004.
117. Z. Xu, W. Gu, J. Huang, H. Sui, Z. Zhou, Y. Yang, Z. Yan, and Y. Li, *In vitro* and *in vivo* evaluation of actively targetable nanoparticles for paclitaxel delivery, *Int. J. Pharm.*, 288, 361–368, 2005.
118. M. Yokoyama, A. Satoh, Y. Sakurai, T. Okano, Y. Matsumura, T. Kakizoe, and K. Kataoka, Incorporation of water-insoluble anticancer drug into polymeric micelles and control of their particle size, *J. Control. Release*, 55, 219–229, 1998.
119. M. Yokoyama, T. Okano, Y. Sakurai, and K. Kataoka, Improved synthesis of adriamycin-conjugated poly (ethylene oxide)-poly(aspartic acid) block copolymer and formation of unimodal micellar structure with controlled amount of physically entrapped adriamycin, *J. Control. Release*, 32, 269–277, 1994.
120. M. Yokoyama, G. S. Kwon, T. Okano, Y. Sakurai, M. Naito, and K. Kataoka, Influencing factors on *in vitro* micelle stability of adriamycin-block copolymer conjugates, *J. Control. Release*, 28, 59–65, 1994.
121. M. Yokoyama, S. Fukushima, R. Uehara, K. Okamoto, K. Kataoka, S. Sakurai, and T. Okano, Characterization of physical entrapment and chemical conjugation of adriamycin in polymeric micelles and their design for *in vivo* delivery to a solid tumor, *J. Control. Release*, 50, 79–92, 1998.
122. M. Yokoyama, T. Okano, Y. Sakurai, S. Suwa, and K. Kataoka, Introduction of cisplatin into polymeric micelles, *J. Control. Release*, 39, 351—356, 1996.
123. Y. Li and G. S. Kwon, Methotrexate esters of poly (ethylene oxide)-block-poly(2-hydroxyethyl-L-aspartamide). Part I: effects of the level of methotrexate conjugation on the stabiliy of micelles and on drug release, *Pharm. Res.*, 17, 607–611, 2000.
124. T. Ouchi, E. Yamabe, K. Hara, M. Hirai, and Y. Ohya, Design of attachment type of drug delivery system by complex formation of avidin with biotinyl drug model and biotinyl saccharide, *J. Control. Release*, 94, 281–291, 2004.
125. L. Nobs, F. Buchegger, R. Gurny, and E. Allemann, Poly(lactic acid) nanoparticles labeled with biologically active Neutravidin for active targeting, *Eur. J. Pharm. Biopharm.*, 58, 483–490, 2004.
126. Y. Nishioka and H. Yoshino, Lymphatic targeting with nanoparticulate system, *Adv. Drug Deliv.*, 47, 55–64, 2001.

127. G. Lambert, E. Fattal, and P. Couvreur, Nanoparticulate systems for the delivery of antisense oligonucleotides, *Adv. Drug Deliv.*, 47, 99–112, 2001.
128. L. Illum, I. Jabbal-Gill, M. Hinchcliffe, A. N. Fisher, and S. S. Davis, Chitosan as a novel nasal delivery system for vaccines, *Adv. Drug Deliv. Rev.*, 51, 81–96, 2001.
129. J. O. Sham, Y. Zhang, W. H. Finlay, W. H. Roa, and R. Lobenberg, Formulation and characterization of spray-dried powders containing nanoparticles for aerosol delivery to the lung, *Int. J. Pharm.* 269, 457–467, 2004.
130. M. Brzoska, K. Langer, C. Coester, S. Loitsch, T. O. Wagner, and C. Mallinckrodt, Incorporation of biodegradable nanoparticles into human airway epithelium cells — in vitro study of the suitability as a vehicle for drug or gene delivery in pulmonary diseases, *Biochem. Biophys. Res. Commun.*, 318, 562–570, 2004.
131. A. DeCampos, A. Sanchez, and M. Alonso, Chitosan nanoparticles: a new vehicle for the improvement of the delivery of drugs to the ocular surface. Application to cyclosporin A, *Int. J. Pharm.*, 224, 159–168, 2001.
132. R. Alvarez-Roman, A. Naik, Y. N. Kalia, R. H. Guy, and H. Fessi, Skin penetration and distribution of polymeric nanoparticles, *J. Control. Release*, 99, 53–62, 2004.
133. U. Edlund and A. C. Albertsson, Degradable polymer microspheres for controlled drug delivery, *Degrad. Aliph. Polyest.: Adv. Polym. Sci.*, 157, 67–112, 2002.
134. M. Maeda, S. Moriuchi, A. Sano, and T. Yoshimine, New drug delivery system for water-soluble drugs using silicone and its usefulness for local treatment: application of GCV-silicone to GCV/HSV-tk gene therapy for brain tumor, *J. Control. Release*, 84, 15–25, 2002.
135. J. J. Kim and K. Park, Modulated insulin delivery from glucose-sensitive hydrogel dosage forms, *J. Control. Release*, 77, 39–47, 2001.
136. D. S. Hsieh, W. D. Rhine, and R. Langer, Zero-order controlled-release polymer matrices for micro- and macromolecules, *J. Pharm. Sci.*, 72, 17–22, 1983.
137. X. Huang and C. S. Brazel, On the importance and mechanisms of burst release in matrix-controlled drug delivery systems, *J. Control. Release*, 73, 121–136, 2001.
138. J. Panyam, M. M. Dali, S. K. Sahoo, W. Ma, S. S. Chakravarthi, G. L. Amidon, R. J. Levy, and V. Labhasetwar, Polymer degradation and in vitro release of a model protein from poly(D,L-lactide-co-glycolide) nano- and microparticles, *J. Control. Release*, 92, 173–187, 2003.
139. F. I. Liu, J. H. Kuo, K. C. Sung, and O. Y. Hu, Biodegradable polymeric microspheres for nalbuphine prodrug controlled delivery: *in vitro* characterization and *in vivo* pharmacokinetic studies, *Int. J. Pharm.*, 257, 23–31, 2003.
140. M. Texeira, M. Alonso, M. Pinto, and C. Barbosa, Development and characterization of PLGA nanospheres and nanocapsules containing xanthone and 3-methoxyxanthone, *Eur. J. Pharm. Biopharm.*, 59, 491–500, 2005.
141. J. Matsumoto, Y. Nakada, K. Sakurai, T. Nakamura, and Y. Takahashi, Preparation of nanoparticles consisted of poly (L-lactide)-poly(ethylene glycol)-poly(L-lactide) and their evolution *in vitro*, *Int. J. Pharm.*, 185, 93–101, 1999.
142. K. Avgoustakis, A. Beletsi, Z. Panagi, P. Klepetsanis, A. G. Karydas, and D. S. Ithakissios, PLGA-mPEG nanoparticles of cisplatin: *in vitro* nanoparticle degradation, *in vivo* drug release and *in vivo* drug residence in blood properties, *J. Control. Release*, 79, 123–135, 2002.

24 Nanostructured Materials for Field Emission Devices

J.D. Carey and S.R.P. Silva
Advanced Technology Institute, University of Surrey,
Guildford, United Kingdom

CONTENTS

ABSTRACT

In this review, the state of the art in the use of thin film nanomaterials for use as electron sources is described. We first begin with a discussion of the phenomena of electron field emission and a discussion of the minimum specifications required for practical device fabrication. The bulk of the review concentrates on what is known about thin film emitters, based on amorphous carbon. The concept and importance of dielectric inhomogeneity is discussed. Extensions to other nanomaterial systems are also presented and examples of the use of amorphous silicon and excimer laser-processed amorphous silicon for the fabrication of thin film cold cathodes will also be introduced. Finally, we describe how external treatments can be used to improve the field emission characteristics.

24.1 INTRODUCTION TO FIELD EMISSION AND CRITERIA FOR PRACTICAL ELECTRON SOURCES

The ability to extract electrons from a material has a ready number of applications ranging from field emission based displays (FEDs) to electron sources for microwave applications. Such

applications are generally considered as being within the realm of vacuum micro- and nanoelectronics. (For a comprehensive review of the physics and applications of amorphous carbon-thin films, see [1].) Field-induced electron emission from a surface is primarily determined by the strength of the *local* electric field and the potential barrier to emission. In a metal, the barrier would correspond to the work function of the material. The other key aspect in the discussion of FE is the concept of the local field, which differs from the applied macroscopic field. In the usual two-terminal experimental set-up, described in Figure 24.1, an anode at a potential V is separated by a distance D from a grounded cathode. The applied field is then V/D. The local field is enhanced relative to the applied field and this increase is characterized by the field enhancement factor or field magnification factor β. For tip-based emitters such as Spindt tips or carbon nanotubes, the enhancement factor usually depends on the geometric properties of the emitter tip, such as height and radius. For example, the field-enhancement factor for a single-grounded hemisphere is calculated to be 3. The enhancement factor may also depend on the location of the anode plane if the anode–cathode separation becomes comparable with the anode-tip separation. In the case of semiconductors, field penetration becomes an important consideration when compared with metallic emitters, where no penetration into the cathode is present.

The application of an electric field to the surface of an emitter can have several effects and they are summarized in Figure 24.2. As the electric field is increased, thermionic emission over the top of the surface barrier occurs. This is followed by emission over the field-reduced barrier (Schottky emission). Emission will then occur partly over and partly through the barrier if the temperature is high enough. As the temperature is lowered, emission will result from electrons tunneling through the barrier from electron states at the Fermi level. This is known as Fowler–Nordheim (FN) tunneling. Finally, at very high fields, emission occurs from electron states below the Fermi level (ballistic electron emission). In Figure 24.2, the simple triangular potential can be taken to be of the form

$$V(z) = h - eEz \tag{24.1}$$

where h is the surface barrier height (eV), often regarded as the work function (Φ) of the material.

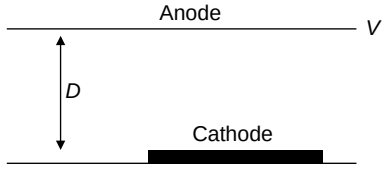

FIGURE 24.1 Two terminal field emission arrangement in which the anode, at potential V, is separated from a grounded cathode by a distance D. The macroscopic electric field is V/D.

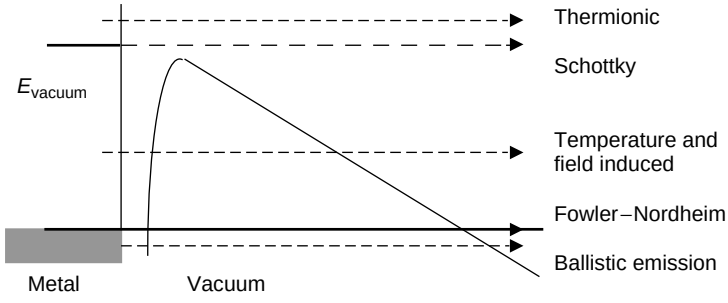

FIGURE 24.2 Electron emission processes that can occur in the presence of an electric field.

The second rounded potential in Figure 24.2 incorporates the image charge effects and adds an additional term to Equation (24.1) to give

$$V(z) = h - eEz - \frac{e^2}{16\pi\varepsilon\varepsilon_0 z} \tag{24.2}$$

The effect of this additional term is to round off the overall potential barrier and lower the overall barrier height by an amount

$$\Delta h = 3.975 \times 10^{-5} E^{1/2}, \tag{24.3}$$

where the field E is measured in V/m. For a field of 20 V/μm the barrier lowering due to image charge effects is approximately 0.17 eV. It is evident from Figure 24.2 that the emission of electrons is a quantum mechanical tunneling process and various forms of the FN theory and equation have been employed. Indeed, the FN theory has been applied to explain the emission from gated emitter arrays, chemical vapor deposition (CVD) grown diamond films incorporating grain boundaries, atomically smooth amorphous carbon thin films and carbon nanotubes, both single and multiwall, and as such its application to these structures is somewhat remarkable when considering the assumptions on which the theory is based. The standard FN theory makes the following assumptions [2]:

1. The emitter is an atomically smooth and clean metal surface.
2. The metal has a free electron band structure and the electrons in the metal obey Fermi–Dirac statistics.
3. Emission occurs at 0 K and the barrier to emission (work function) is uniform and independent of applied electric field.
4. Electron tunneling can be described in terms of the Wentzel–Kramers–Brillouin approximation.
5. The barrier to emission can be represented by a triangular potential onto which a classical image potential is superimposed.

It is useful to examine the final form(s) of the FN equation and discuss its application to FE data. Representing the applied electric field by E and the barrier height by Φ, the emission current I can be expressed as

$$I = \frac{aA(\beta E)^2}{\Phi} \exp\left[\frac{-b\Phi^{3/2}}{\beta E}\right] \tag{24.4}$$

where a and b are constants with values of 1.54×10^{-6} A eV/V^2 and 6.8×10^9 eV$^{-3/2}$ V/m, respectively, and A is the emission area. Here, βE represents the local electric field and in this context β represents the enhancement of the applied electric field. FE measurements are usually performed in either a diode arrangement in which an anode, either a parallel plate or spherical ball electrode, is located above a grounded cathode or in a triode arrangement in which a gated electrode is located nearby. Analysis of FE I–V characteristics using the FN equation can be performed by plotting $\log(I/E^2)$ against $1/E$, the slope being $-b\,\Phi^{3/2}/\beta$. It is not possible from an FE measurement to determine both β and Φ independently, although the latter can be determined via other methods. Armed with a knowledge of the work function, considerable attention has been paid to the significance of the value and origin of the enhancement factor. However, some care must be exercised in the interpretation of enhancement factors since complications arise in comparing theory with experiment. The levels of sophistication that have been developed in understanding the application of an electric field to a clean metal surface (or other material) are often masked by experimental factors such as the presence of

absorbates on the cathode surface. For example, different atoms can induce dipoles on the surface, which can change the work function of a metal, or the work function itself may possess a dependence on the electric field and nano-protrusions on the surface may act to increase the local electric field.

Finally, it is worth noting that FE from semiconductors is complicated by the possibility of emission from either the conduction or valence bands, from the Fermi level or from surface states. In addition, the effects of band bending, field penetration, and internal FE, particularly in wide-gap semiconductors, as well as the possibility of negative electron affinity, need to be taken into account. There is also the issue of "conditioning" of the cathode, in which the onset of stable and reproducible emission is sometimes only observed after several cycles of the voltage, a process that will be discussed later. Despite these potential complications in understanding the mechanism of emission, because of their inherently simpler fabrication process and ability to scale up production, semiconductor thin film emitters have a number of advantages over tip-based arrays. First, electron emission from a thin film comes from a much larger area than from a tip array. This results in a low current density at emission points for a given emission current. Second, the absence of highly focused electric fields reduces the ion bombardment and sputter erosion of the thin film. With these advantages in mind, we now discuss some common nano-material cold cathodes based on amorphous carbon.

For a practical flat panel display, it is necessary to have typically 100 Cd/m^2 brightness but with FE most devices will exceed 300 Cd/m^2. In general, emission current densities of 10 mA/cm^2 will be sufficient to give suitable output from conventional phosphor cathodes with ideally emission sites in excess of 10^6 cm^{-2} in order to obtain uniform emission from a high-density display without correction optics.

24.2 CARBON NANOMATERIAL BASED COLD CATHODES

Nanomaterials based on amorphous carbon have attracted particular attention since it is possible to deposit thin films over large areas and at low temperatures [1]. The latter point is of notable importance since it is possible to deposit films onto organic or plastic substrates. In addition, the softening temperature of most common display glass is around 400°C and as a result deposition processes which significantly exceed this temperature are not compatible with current technology. Fortunately, the low-temperature deposition of amorphous carbon makes it an ideal candidate as a potential cathode material. Early interest in carbon films as cold cathodes was driven by the hope that these films possessed negative electron affinity (NEA) [3] in the same way that certain H-terminated diamond films can possess an NEA surface. As a result, once electrons were injected into the conduction band of the film, there would be a steady supply of electrons which could emerge at the film/vacuum interface. However, it is important to realize at this stage that there are many different types of amorphous carbon films that are possible, based upon different configurations of bonding hybridizations that are available to carbon. These include tetrahedral sp^3 bonds, trigonal sp^2 bonds, and linear sp^1 bonds as shown in Figure 24.3. As in the crystalline case, each of these bond variations is available to its amorphous counterpart, and this enables the unique and large variation in the physical and material properties to be extended to amorphous carbon (a-C) thin films. The sp^3 phase in low density a-C films tends to be found in aliphatic chains, whereas the sp^2 phase tends to cluster into olephinic chains or aromatic rings. Amorphous carbon is the generic term used here to describe most disordered carbon films. Although there is no long-range order present, both short-and medium-range order is preserved, which gives rise to physical properties that can mimic those found in the crystalline material. In these materials, by examining the nearest neighbor distance and the next-nearest-neighbor distance, it is clear that the short-/medium-range order is very close to its crystalline counterpart. It is generally the bond angle, not bond length, that is different from that of the crystalline case which gives a-C no long-range order. Such bond angle disorder can also give rise to the narrowing of the band gap by virtue of it creating highly localized states within the band gap [4].

The description of a-C films can be broken down into two distinct categories; hydrogenated and non-hydrogenated films. Whenever a hydrocarbon source gas or plasma system is used to deposit

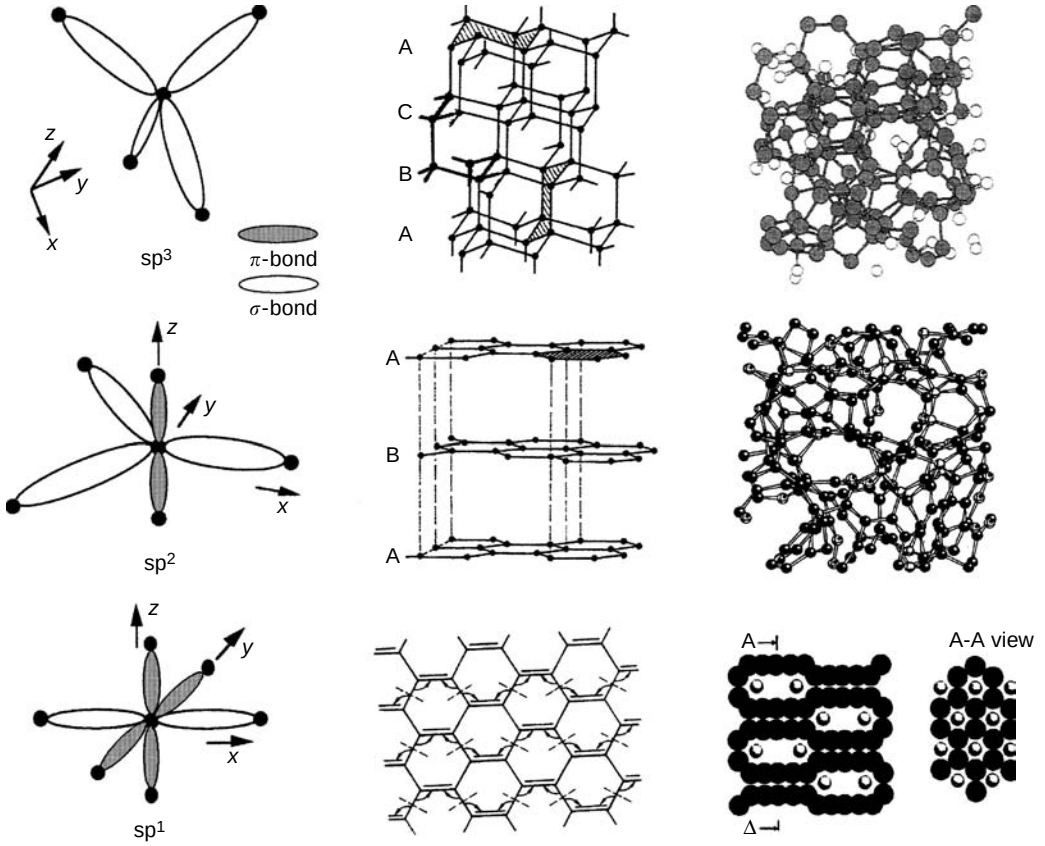

FIGURE 24.3 A schematic representation of sp^1-, sp^2-, and sp^3-hybridized bonds and the resultant crystalline and model amorphous structures.

films, some quantity of hydrogen gets incorporated within its microstructure [1]. Since hydrogen prefers to bond in an sp^3 hybridized manner by terminating single bonds, they tend to enhance the sp^3 or tetrahedral nature within the films. Using techniques such as the plasma beam source, an sp^3 content as high as 80% has been recorded in the presence of 30% hydrogen within these highly tetrahedral hydrogenated a-C (ta-C:H) films [5]. This is in contrast to the more usual 40–60% sp^3 bonding found in the diamond-like carbon (DLC) films deposited using radio frequency plasma-enhanced chemical vapor deposition (r.f. PECVD) with ion bombardment (and H contents of ~30–40 at.%). When no ion bombardment is used, as in the case of film growth on the earthed electrode of a r.f. PECVD systems, highly polymer-like a-C:H (PAC) films are deposited [6]. These films have an sp^3 content between 60 and 80% (but mostly in the form of C–H bonds with little sp^3 C–C bonds) and high hydrogen contents (H content up to 55 at.%). At the high end of the hydrogen content, thin films deposited are more similar to hydrocarbon polymers such as polythene which possesses 66 at.% H. Tetrahedral amorphous carbon (ta-C) can also be produced, which tends to have a high sp^3 content and is grown by arc or laser ablation methods. The different types of films are summarized in the ternary phase diagram presented in Figure 24.4. We will use this classification to describe the a-C films below.

Polymer-like films tend to be grown under low-energy conditions, such as those found with low negative self-bias in r.f. PECVD, whereas DLC films tend to be grown under higher deposition self-bias (energy) conditions. Examples of DLC films are those deposited on the driven electrode of an r.f. PECVD system, where during the growth process there is also ion beam "subplantation" of growth species involved. In other deposition systems such as sputtering, a similar result could be

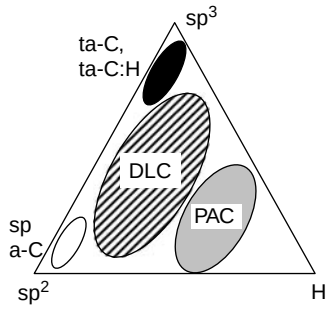

FIGURE 24.4 Ternary phase diagram for amorphous carbon system. Not shown is sp^1 bonding which is considered not to be present in sufficient quantities.

achieved by either having a second ion source that is used purely to ion-bombard the growth surface or by the application of a negative self-bias to the growth substrate. Graphite-like a-C (GAC) are also possible with very high-energy C ion sources. It is worth highlighting that it is imperative that to understand the FE characteristics of these nanomaterials, detailed knowledge of the film's electronic properties is required. For example, the films deposited by Gröning et al. [7] have been compared by a number of authors to films deposited by Amaratunga and Silva [8] using rf PECVD. A closer examination of the material properties shows that Gröning's films are graphite-like GAC films with no optical band gap while the DLC films by Amaratunga and Silva have an optical band gap close to 2 eV. Therefore, few parallels can be made in terms of FE models and transfer of experimental results for films that have material properties that are dissimilar.

It is worth categorizing several types of a-C films for the analysis of their electron field emission process. Progressing with ascending energies required for the growth of the films, we will consider emission from PAC, DLC, ta-C, GAC, as well as nanocomposite amorphous carbon (NAC) films. It is also worth discussing that in the case of a-C films that do not possess large numbers of defect states within the films or graphitic or conducting regions in its microstructure, a conditioning process is often required before the emission of electrons takes place. Subsequent to the initiation voltage required in the conditioning, emission takes place at successively lower threshold fields which reaches a minimum value after about four cycles. The hysteresis observed in this process of conditioning is shown clearly in Figure 24.5, and is non-reversible, i.e., once a cathode has been conditioned, it will remain conditioned despite being exposed to atmospheric condition for several days. This points to the fact that surface termination or the front surface dipole effects may play less of a role than originally thought for these types of film. Other types of both carbon- and noncarbon-based nanomaterials will also be considered.

Since there are different types of a-C and a-C:H film possible with very different properties, it is not surprising that there is more than one possible emission mechanism. One immediate feature for the need of different models concerns the application of an electric field to the surface of a semiconductor. It is well known that the degree of field penetration into a semiconductor film depends on the conductivity of the sample. The higher the conductivity, the smaller the extent that the externally applied field will penetrate into the film. In the ultimate limit of a metallic conductor, there will be no penetration of the field into the film. As the sp^2 phase is associated with the more conductive clusters within the film, the field lines from the anode will terminate on these clusters. As a result there is an immediate link between the emission mechanism and the extent of field penetration. In some cases, field penetration will extend to the film/substrate interface, where the emission mechanism will be referred to as a "back contact" controlled emission. Such an emission mechanism differs in films for which there is little field penetration and where the emission is controlled by the properties at or near to the front of the film/vacuum interface, referred to as the "front surface" controlled mechanism. The origin of these two different types of mechanism will be explored in detail below.

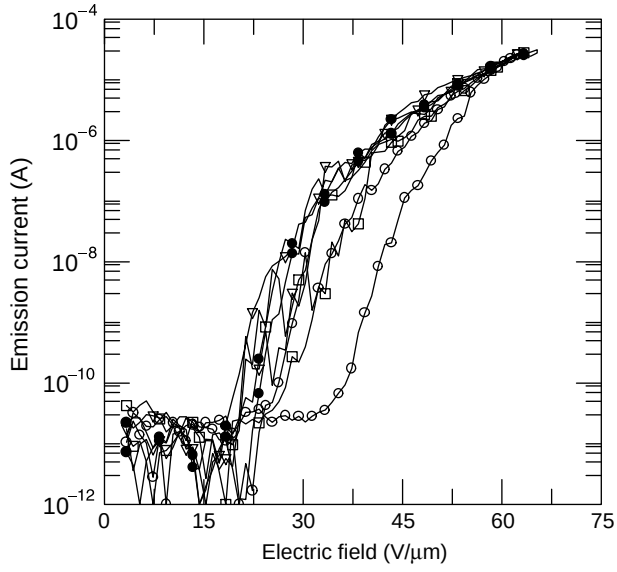

FIGURE 24.5 Emission current vs. macroscopic electric field for a 67-nm-thick polymer-like a-C:H film. The applied field is cycled up and down four times: (○) run 1; (□) run 2; (●) run 3; (▽) run 4.

Finally, to produce a satisfactory model for electron emission, three fundamental questions are worth addressing before continuing the discussion of the mechanisms that are responsible for emission from these materials. First, what is the source of the electrons? Second, how are the electrons transported through the film? Finally, how are the electrons emitted into vacuum?

24.3 FIELD EMISSION FROM DIFFERENT TYPES OF AMORPHOUS CARBON

24.3.1 Polymer-Like Amorphous Carbon Films

There are a number of reports of electron field emission properties of these types of films [9,10]. These films have low defect densities and often require a high initiation electric field for emission to take place. Significant hysteresis is often observed in the first cycle after initiation (as shown in Figure 24.5). Subsequent to the initiation process, the threshold field for electron emission has been shown to vary between 10 and 70 V/μm by changing the thickness of the undoped films by Forrest et al. [9] (Figure 24.6). Despite some of these films being subject to very high electric fields of the order of 70 V/μm, no surface morphological change was observed with a scanning electron microscope after emission. The data show a very strong dependence of the conditioned threshold field on film thickness, with the required field showing a minimum turning point at a film thickness close to 60 nm. The threshold field needed for emission increases on either side of this optimum thickness, with the surface of the films not exhibiting any morphological changes when examined by an atomic force microscope (AFM), as a function of film thickness.

As will be described later, the degree of sp^2 clustering is shown to be a major factor in the control of FE from a-C films. However, the growth conditions in the study of Forrest et al. have been kept constant throughout the deposition process and so no changes in the microstructure of the film is expected. The observed variations with film thickness in these films were explained using the inter-layer model based on space-charge-induced band bending. In this model, the a-C films act as an interlayer with the true cathode being the underlying Si or metal substrate, with the crucial factor being the heterojunction (or in other materials if formed, the Schottky barrier) that is formed at the back contact. This model, proposed by Amaratunga and Silva [8], is based on

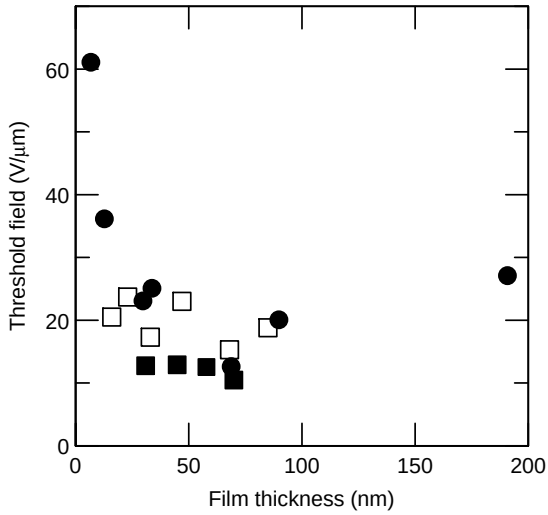

FIGURE 24.6 Variation of threshold field as a function of thickness for a polymer-like film (●) and for DLC films deposited at −90 V (□) and –265 V (■) self-bias.

assuming that the a-C thin film is n-doped and has an electron affinity close to 2.5 eV, a Fermi level of 0.5 eV as shown in Figure 24.7a.

When a bias is applied to the heterojunction and the anode becomes positive, and the applied field is large enough to fully deplete the carbon thin film, it was shown [8,9] that the field experienced by the electrons that tunnel through the heterojunction barrier into the conduction band is larger than the applied electric field, due to space charge considerations. This field decreases parabolically within the film, as it traverses toward the surface of the semiconductor (Figure 24.7b). According to the band diagram, the pool of electrons gathered at the n-Si/a-C interface has a built-in barrier that prevents the tunneling/thermal excitation of electrons into the conduction band of the a-C layer before the interlayer band bending is large enough for the electrons to overcome the energy barrier for emission into the vacuum. The electrons can now lose up to 3 eV in phonon scattering and still retain sufficient kinetic energy to enter the vacuum level in the a-C thin films and thus emit into the vacuum. In the case of electrons that do not have enough energy to reach the vacuum, they will collect at the front surface of the a-C thin film and decrease the band bending in the space charge layer as shown in Figure 24.7c. Until the total band bending is lost, there will be some electrons emitted from the a-C thin films. This is an example of a back contact controlled mechanism. Similar arguments may be applied to any material which allows field penetration and this includes wide-gap semiconductor materials.

24.3.2 Diamond-Like Amorphous Carbon Films

The higher energy deposition found in DLC films produces more defect states near the Fermi level. In the a-C system, the defect states are those associated with the conductive sp^2 clusters, which themselves may be distorted or undistorted. The location of the sp^2 clusters in the energy gap depends on two factors: whether they consist of even or odd numbers of carbon atoms and whether they are distorted. Undistorted even-numbered clusters will give rise to states near the Fermi level (E_F) only if they are sufficiently large. This differs from the case of odd-numbered clusters which can give rise to gap states even if composed of a small number of atoms. In general, distorted clusters gives rise to a state that is closer to E_F than undistorted clusters. In this way, electron spin resonance (ESR) can give a measure of the density of sp^2 states at the Fermi level, provided that a majority of these states have a net unpaired electron spin present. Note that measurements of ESR spin densities do not themselves measure the sp^2 content [11].

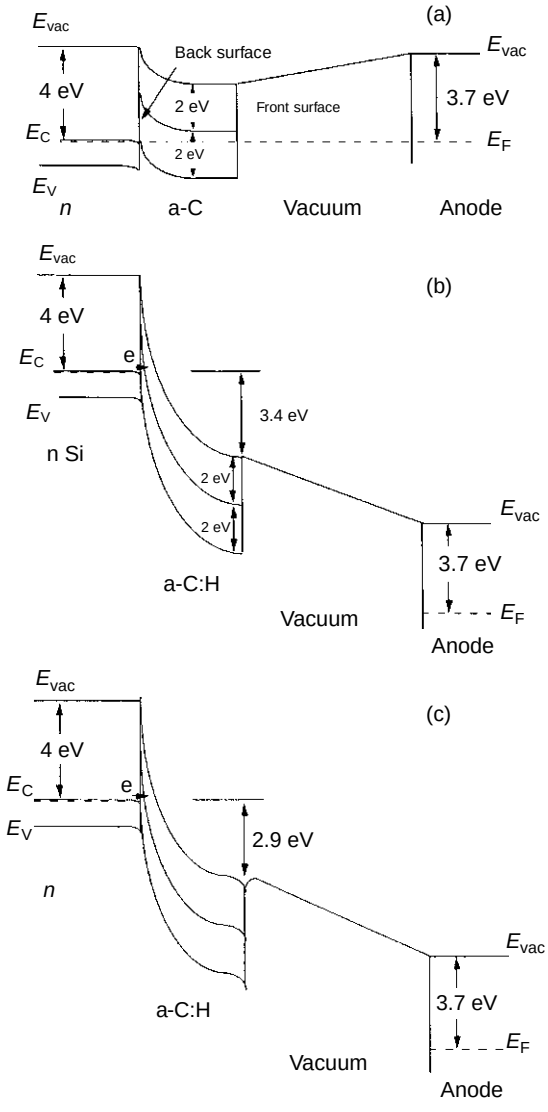

FIGURE 24.7 Space-charge-induced band bending for field emission in low defect density materials for zero bias (a) and two different levels of bias (b, c).

Films were deposited using a standard capacitively coupled rf PECVD system with feed gases of CH_4 and He. The negative DC self-bias developed across the plasma sheath was varied in the range -50 to -265 V at a fixed pressure of 200 mT. The films were deposited on n^{++}-Si substrates, which were degreased and then Ar (He) plasma-cleaned prior to deposition. The variation of (a) threshold field and (b) spin density with negative self-bias is shown in Figure 24.8. As the self-bias is increased from -50 to -90 V, the threshold field increases from a value of 18 V/μm to a value close to 26 V/μm. For bias values above -90 V, the threshold field decreases to around 12 V/μm, where it remains approximately constant in this bias regime. The measured spin density, N_s, of these films rises rapidly from 3×10^{17} to 1.1×10^{20} cm^{-3} at -125 V. At higher biases, N_s increases only very gradually, finally reaching 1.6×10^{20} cm^{-3}. The Tauc gap, which is a measure of the π–π^* separation, falls rapidly from 2.6 (-50 V bias) to 1.3 eV (-125 V), and then falls gradually to about 1.1 eV at the highest bias voltages, as shown in Figure 24.9. In the case of the peak-to-peak ESR

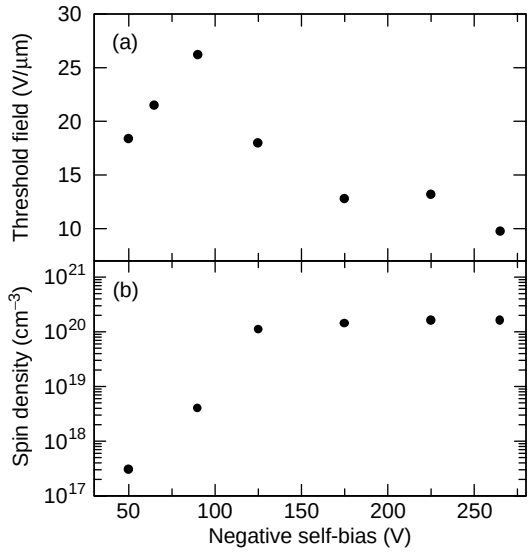

FIGURE 24.8 Variation of (a) threshold field and (b) spin density for a-C:H films as a function of negative self-bias. Increasing the bias results in a change from polymer-like films to DLC films.

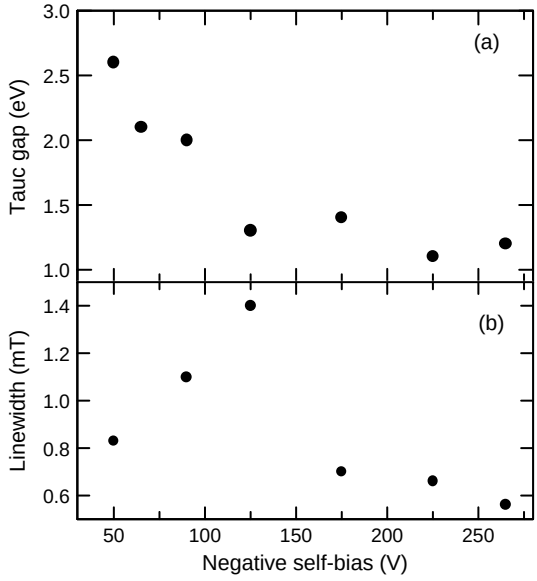

FIGURE 24.9 Variation of (a) Tauc gap and (b) ESR linewidth for a-C:H films as a function of negative self-bias. Increasing the bias results in a change from polymer-like films to DLC films.

linewidth, ΔB_{pp}, there is an initial increase in the linewidth, reaching a maximum of 1.4 mT at −125 V bias followed by a rapid decrease to 0.7 mT, which continues to decrease to 0.56 mT at −265 V bias. These results suggest the existence of two regimes, above and below −125 V bias, and it is therefore convenient to discuss the results from the two regimes separately.

For the sample deposited at −125 V bias, the measured spin density is 1.1×10^{20} cm^{-3} and the observed linewidth is 1.4 mT. The Lorenzian line shape can be explained using dipolar broadening. Above −125 V, it is thought that the narrowing of the linewidth is due to rapid exchange of spins as the sp^2 clusters increase in size [12]. This is consistent with the narrowing of the band gap,

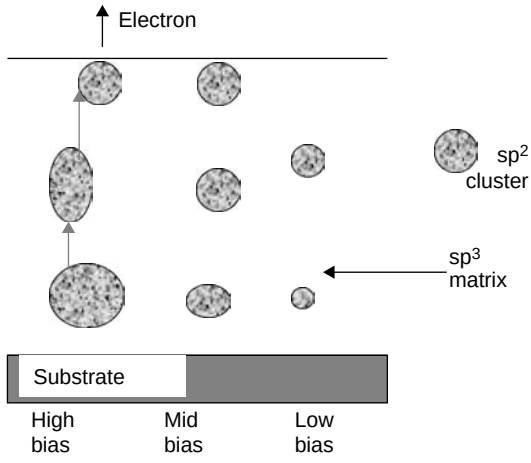

FIGURE 24.10 Cluster arrangements in low-, mid-, and high-bias samples showing the variation of density and size of the clusters present. As the cluster size gets larger, hopping between clusters becomes easier which contributes to the conduction in the material. The higher the cluster density, the lower the extent of field penetration.

and the reason for the convergence of the threshold field to a limiting value close to 12 V/μm for these films. These films have a high sp^2 content (>65%) as well as a high band gap (>2 eV) and as a consequence the wave function overlap of the clusters will result in electron delocalization or enhanced hopping between the clusters that will enhance the connectivity, as shown in Figure 24.10. Application of an external electric field results in extraction of electrons from the film surface. Replenishment of the emitted electrons to the surface layer is accomplished due to the good connectivity between the clusters. Emission from these high sp^2-rich films would be characterized as a "front surface"-type emission. The high conductivity of these samples means the films would not be able to sustain any form of space charge. As the films have a high concentration of defect states (10^{20} cm^{-3}), it would not be possible to form a "leak-free" barrier (Schottky or heterojunction) at the back contact to the film. As a result the emission process will not be controlled by the back contact as described earlier for PAC films.

Reducing the self-bias to −90 V decreases the spin density by about two orders of magnitude and gives rise to an increase in the Tauc gap. The rise in the Tauc gap shows that major structural changes in the film are occurring at low bias voltages with the films likely to have a lower sp^2 content due to C–H bonding. At low self-biases, a low concentration of small isolated sp^2 clusters form. Initially, the number of C atoms in each cluster is small (as inferred from the large Tauc gap), but the greater energy available at higher biases allows the formation of a greater number of larger, but still isolated, clusters. This results in a reduction in the Tauc gap and an increase in the spin density, although the electron delocalization in the cluster or hopping between clusters is kept to a minimum. This leads to poor connectivity and explains why the threshold field is higher at the lower bias voltages when compared with the films deposited at higher biases. The subsequent drop in threshold field for the film at the lowest bias voltages indicates that another emission mechanism is also present in these low defect, polymer-like, wide energy gap films. The low concentration of sp^2 clusters is unable to screen the field at the front surface. In this way, emission from these low bias deposited films would be more correctly described as being determined by the "back contact" model discussed earlier rather than being a "front surface"-dominated process. This view is further supported by the lack of a significant variation in the threshold field as a function of film thickness for two series of films grown under higher bias (see Figure 24.6).

24.3.3 Tetrahedral Amorphous Carbon Films

Tetrahedral amorphous carbon films can be produced using a filtered cathodic arc system. The films produced are highly tetrahedral in nature (>80% sp^3) and extremely hard (with hardnesses

approaching 60% of that of diamond and a Young's modulus close to 500 GPa). Their properties, such as sp^2 content, can be controlled by the ion energy of the carbon arc used for deposition and any negative bias applied to the substrate. It is well established that the sp^2 content in ta-C films is primarily controlled by the deposition ion energy [13], which also controls many of the microstructural [14] and electronic [15] properties. It should be noted at the outset that the ta-C films discussed here have a large defect concentration comparable to that found in DLC films. On the basis of the analysis by Ilie et al. [16], it was suggested that the clustering of sp^2 states plays an important role. As a result, emission from this type of nanomaterial will be front surface-dominated. Indeed, this was demonstrated by Hart et al. [17] for ~25 nm thick films deposited onto substrates of different metals (varying work functions). It was stated that several of these substrates (Ti, Mo, Si, and Cr) can form interfacial carbides which could lower the barrier at the back contact and possibly lead to the formation of an Ohmic contact. However, the authors noted that since there was a significant spread in the measured values of threshold field between the carbide and noncarbide forming substrates, the back contact does not play a significant role in determining the emission characteristics of ta-C films, as would be predicted from a front surface-controlled electron emission process. A forming process or initiation field is sometimes needed before stable emission could be observed from some of the films [18]. Once more no surface damage was observed after forming. Field emission studies on ta-C films have also been performed by Cheah et al. [19], with low threshold fields reported.

24.3.4 Graphite-Like Amorphous Carbon Films

Cluster beam growth of macro-aggregates having 500–2000 atoms loosely bound together are formed by an adiabatic expansion of evaporated material through a nozzle into a high-vacuum chamber. The advantages associated with the technique are due to the fact that any charge placed upon the cluster is equally distributed across each of the constituent atoms and thereby its use for ultra-shallow implants cannot be overemphasized. Each of the atoms imparts precisely the total ion energy given to the cluster divided by the size of the cluster upon impact with a surface. So the growth process possesses very low charge to mass ratios for the ionized cluster which prevents the build up of surface space charge. Electron emission has also been reported from polycrystalline graphite films produced by supersonic cluster beam assembly techniques [20,21]. Owing to the high sp^2 content the FN theory was applied since emission was assumed to originate for the Fermi level. Assuming a work function of 5 eV, a field-enhancement factor of 350 was obtained.

24.3.5 Nanocomposite Amorphous Carbon Films

Nanocomposite films consist of crystalline nanoparticles, in the form of multiwall carbon nanotubes, intentionally embedded into an amorphous carbon matrix [22]. The nanoparticles were formed by having a cathode striker in a high pressure of He or N_2. Low thresholds for emission of 4.5 V/μm were obtained, which could be reduced by etching of the front surface. The emission mechanism was explained in terms of FN tunneling and hot electron emission in which the matrix acts as an interlayer that moderates the emission. Amaratunga et al. [22] also used the interlayer model described earlier to explain successfully the variations of their films. In this case, the internal junctions of the particles and the a-C matrix allow for heating of electrons within the thin film, with the emission process at the outer end of the particle being purely due to FN tunneling.

24.3.6 Ultrananocrystalline Diamond Thin Films

It is interesting to compare the results obtained from the FE and scanning tunneling microscope (STM) studies from amorphous DLC film with those from ultrananocrystalline (UNCD) films carried out by Krauss et al. [23] Despite the difference in the long-and medium-range order, the bonding in the two materials can be described as mixed sp^2 and sp^3 phases. In the study by Krauss et al., it was shown that UNCD films have grain sizes between 2 and 5 nm in size and grain boundaries

$<$0.4 nm in thickness. It was observed that when UNCD films were deposited on Si micro tips there was little variation in the threshold field with either the film thickness or the Si tip radius. Furthermore, STM results showed that the emission sites from the UNCD films could not be related to any surface asperities. Both electrical and theoretical calculations show that the grain boundaries are the most probable path for conduction from the substrate. It is also worth noting that the tight binding calculations for UNCD showed the presence of a continuum density of states throughout the bulk diamond gap. Since the sp^2 grain boundary is less than 0.4 nm in thickness and surrounds a 2 to 5 nm size diamond sp^3 grain, this is similar to the situation encountered above in amorphous DLC type films. The study by Krauss et al. shows the importance of nanoscale inhomogeneities to the FE process. These studies also show the importance of understanding the nature of the cathode material at a nanometer level.

24.4 FIELD EMISSION AND DIELECTRIC INHOMOGENEITY

From the discussion in Section 24.3, it is apparent that the role of sp^2 clusters embedded in an sp^3 matrix plays an important role for a-C and a-C:H films. For films with a high sp^2 content and good inter-cluster interactions, FE is determined by the properties of the film near to the front surface. It is known from AFM images of DLC films that they are atomically flat with a typical RMS roughness of less than 1 nm. If an FN emission process is present then it is necessary to explain the large enhancement factors, typically several hundreds, required to lower a barrier by 4 eV. Since there are no surface features to aid the geometric enhancement of the electric field, we have examined the possibility of a non-geometric internal enhancement mechanism. The results of a high-resolution STM study of the DLC film deposited at –265 V are presented in Figure 24.11. It is apparent that the conductivity of the film is not uniform, with a number of localized high conductivity regions of a few nm in size surrounded by a more insulating matrix. The STM results can be interpreted as resulting from a series of closely spaced localized conductive sp^2 regions which, under the action of the applied field, allows electrons to hop from one spatially localized cluster to another, as in Figure 24.10. In the continuous limit, this would produce a conducting channel or filament which can extend through the bulk of the film. High-resolution electron microscopy studies of a-C films have never revealed such a feature, leading us to conclude that an alternative enhancement mechanism is present.

We propose that the enhancement is due to the different intrinsic dielectric and conductive properties of nanometer-sized sp^2 clusters embedded in the surrounding sp^3 insulating matrix. It is well

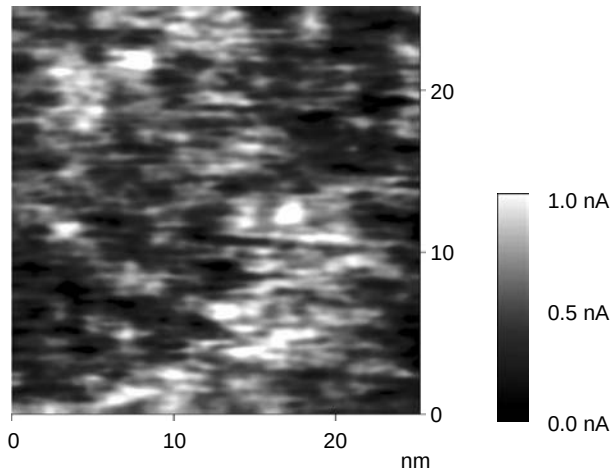

FIGURE 24.11 High resolution scanning tunneling microscopy measurement made on a DLC film showing regions of electrical nonuniformity.

known that the electric field near a single conductive dielectric sphere in an insulating matrix is increased by a factor of up to 2 due to the dielectric mismatch between the sphere and the matrix. It has been calculated that in the presence of two closely spaced spheres with the conductivity of gold, an enhancement of the electric field by a factor of 56 is possible if the spheres have a separation of 5 nm [24]. This enhancement increases as the separation between the spheres is reduced, reaching a factor of 400 for a sphere–sphere separation of 1 nm. Although the conductivity of the sp^2 clusters will not be as high as Au, these calculations demonstrate that high enhancement factors can be obtained by considering the effects of just two conductive spheres near the surface.

In this manner, the emission process for DLC films can be explained as follows: the high density of defects will act to localize and attract the field lines from the anode to a thin region near the surface of the film. High-field enhancement factors are present if two (or more) sp^2 conductive clusters are nearby. Once the electrons are emitted from the clusters near the surface of the film, they can be replaced by electrons from clusters deeper within the film. Such a description aids us in explaining the spotty nonuniform (on the nano- to microscale) nature of the emission across the surface of the film in which the *local* arrangement of the clusters below the surface is important.

Other nanomaterials for which dielectric inhomogeneity have been suggested to play a role include B-doped Si nanoparticles. A turn on field of 6 V/μm was reported for B-doped Si nanoparticles which is lower than that reported for undoped particles (9 V/μm) [25]. Tsang et al. [26] studied electron field emission from ion beam synthesized SiC layers. They reported that in as-implanted film the field enhancement was attributed to dielectric inhomogeneity; however, after annealing the surface morphology changed and nanoprotrusions aid in the observation of emission at low fields. The presence of large amount of N aids in the clustering of the sp^2 phase, which was reported as being important for a-CN_x film grown by excimer laser ablation [27]. Liao [28] reported that the inhomogeneous nature of HfN_xO_y films comprising nanoscale conductive hafnium nitride grains embedded in a matrix of dielectric oxide or oxynitride played an important role in the FE from these materials. Finally, another study has examined the electron field emission of radio frequency magnetron-sputtered CN_x films annealed at different temperatures and also concluded that the film's nanostructure is important [29].

In the case of excimer laser crystallized amorphous silicon a low turn on field of 10 V/μm without any hysteresis were reported [30]. Techniques for producing self aligned and gated FE device using a single mask process have also been shown to be possible [31]. Taking into account that in the case of active matrix liquid crystal displays, polysilicon driver circuitry can be produced on glass flat panel on the scale of 1 m^2, having fully integrating large areas, single mask technology comparable with current flat panel display (FPD) production lines makes this material system very valuable and technologically important. In the case of excimer laser produced materials, the aspect ratio for the enhancement factors cannot account for the observation of FE at low applied fields. The apparent discrepancy was reconciled with a FN type emission if nanoscale inhomogeneity also plays an important role.

24.5 FIELD EMISSION AS A FUNCTION OF CONDITIONING

We have discussed previously conditioning, i.e. the need to apply several voltage cycles before the onset of stable emission (cf. Figure 24.5) [32,33]. Similar conditioning treatments have also been reported necessary in ta-C [16,34] and in diamond films grown by chemical vapor deposition [35]. The exact nature of this conditioning step and the role of any damage-induced surface micro-protrusions is not fully understood, although conditioning may involve an increase in the concentration of threefold coordinated carbon atoms at the expense of fourfold coordinated atoms [36]. For practical a-C:H-based display applications, the values of the threshold field must be as reproducible as possible. Furthermore, to limit the spread in the drive voltages, the hysteresis in the current–voltage (*I–V*) characteristics should be kept to a minimum. Current stressing has been shown to overcome the need for a voltage-controlled conditioning cycle [37]. It should be noted that in improperly

conditioned films there may be significant differences in values of E_{th} depending on whether the current is recorded on the upward voltage cycle or on the downward cycle. As a measure of this "hysteresis effect," the difference in the applied fields between the upward and downward voltage cycles at a current of 1 nA is used. Current stressing of the films was performed by contacting the anode to the film and passing a current through the film up to a predetermined level [37]. Each film was tested before stressing by applying a field of up to 100 V/μm and only those samples which *did not* emit after this preliminary test were subject to current stressing. For the current stressing measurements, several identical films from the same deposition run were examined. For reference, the typical value of E_{th} for films which did emit after conventional conditioning is about 30 V/μm.

The three current stress levels chosen were $\times 10^{-8}$, 5.2×10^{-8}, and 2×10^{-7} A. The FE characteristics of the film stressed to $\times 10^{-8}$ A (not shown) exhibited emission but with an E_{th} of over 85 V/μm and a full width (at half maximum) of the first cycle hysteresis loop of over 20 V/μm. Subsequent voltage cycles resulted in a reduction of E_{th}, although the average threshold field obtained from the latter three cycles was 66 ± 4 V/μm. Stressing to a higher current of 5.2×10^{-8} A results in an initial emission at a field of 48 V/μm through a hysteresis width of 20 V/μm, as shown in Figure 24.12. The *I–V* characteristics of the film before stressing is also presented and shows that no emission had occurred from this film even up to fields of 90 V/μm. The threshold field continued to decrease after subsequent voltage cycles and finally reached 40 V/μm after the 4th cycle. The average value of E_{th} obtained from this film is 38 ± 10 V/μm, higher than that obtained from a film which underwent the conventional conditioning treatment. Since the width of the first cycle is 20 V/μm, the film is not fully conditioned.

The *I–V* characteristic of the film stressed to 2×10^{-7} A is shown in Figure 24.13, where the value of E_{th} for the 1st cycle was only 34 V/μm, which subsequently decreased to 30, 26, and 27 V/μm in the remaining three cycles. The average E_{th} of 28 ± 2 V/μm is comparable to the values of E_{th} for films which have undergone a conventional conditioning treatment. The width of the *I–V* hysteresis loop is about 2 V/μm in each run and no evidence of a conditioning cycle after current stressing is observed. Since the FE characteristics are different and are observed to improve with higher stress currents, the mechanical effects of contacting between the anode and film as the primary reason for the improvements were eliminated.

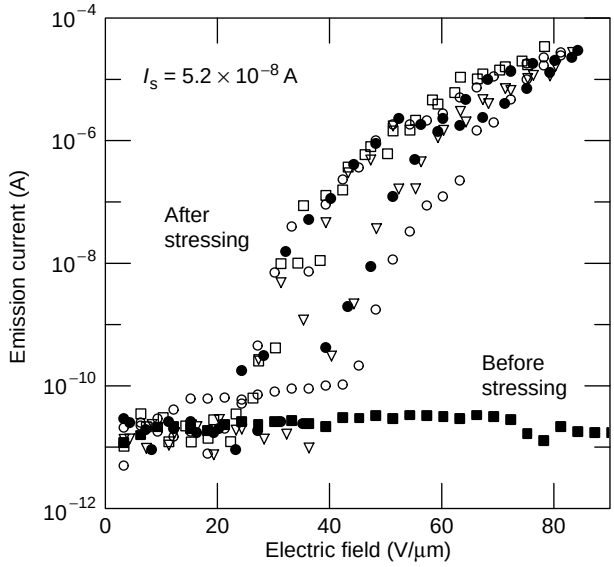

FIGURE 24.12 Emission current vs. electric field for films stressed to 5×10^{-8} A. The applied field is cycled up and down four times: (○) run 1; (□) run 2; (●) run 3; (▽) run 4. The emission current for the film before stressing is indicted by (■).

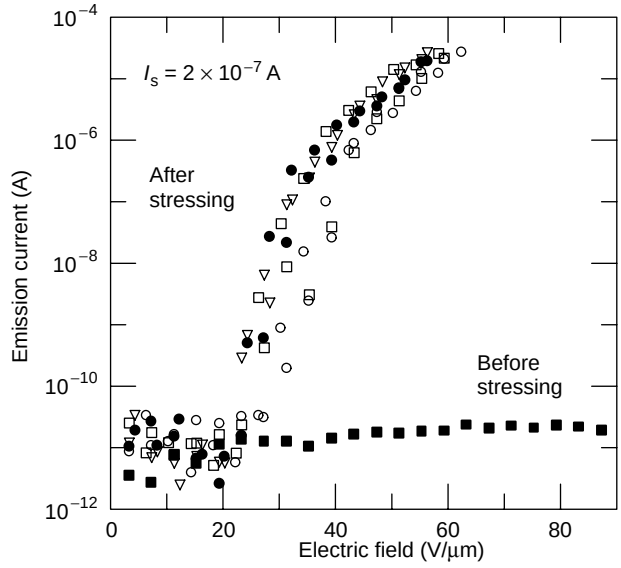

FIGURE 24.13 Emission current vs. electric field for films stressed to 2×10^{-7} A. The applied field is cycled up and down four times: (○) run 1; (□) run 2; (●) run 3; (▽) run 4. The emission current for the film before stressing is indicted by (■).

In order to examine whether the current-induced conditioning was permanent, the films were retested some hours after the initial stressing had been performed. In order to prevent any possible atmospheric contamination, the samples were kept held under vacuum during this period. Figure 24.14a shows that even after just 15 h in the sample that was stressed to 5.2×10^{-8} A, E_{th} had increased to about 50 V/μm, similar to the value obtained in the first cycle after this sample had just been stressed, indicating that some form of "healing" process had occurred. By contrast, Figure 24.14b shows that in the film stressed to 2×10^{-7} A, no evidence of a conditioning cycle is required 23 h after the original current stressing had occurred. Only the first two *I–V* characteristics are presented in Figure 24.14b and values of E_{th} obtained after 23 h are 30 and 32 V/μm with a hysteresis width of 2 to 3 V/μm. Testing after 87 h revealed similar results to those obtained after testing after 23 h, with the values of E_{th} for the first two cycles being 31 and 32 V/μm, again showing that the film remains conditioned.

In a study by Mercer et al. [36] an STM tip was used to effectively current stress ta-C films by generating a highly spatially localized electric field. They observed that after ramping the tip-sample bias and current, nanostructures of about 100 nm in the extent form is produced. By using high-resolution spatially resolved electron energy loss spectroscopy , they showed that the predominant bonding configuration changes from predominately four-fold coordinated C to three-fold coordinated. The net effect of the conditioning or the current stressing treatment may well be to generate conductive sp^2-rich areas either in the form of filaments or clusters through localized Joule heating. Missert et al. [38] proposed that the presence of conductive filaments is related to the deposition conditions under which the film was grown. Since the deposition conditions for the films in this study were kept the same, the current stressing may well increase the number of such filaments/clusters extending through the film.

24.6 SURFACE MODIFICATIONS

Shi et al. [39] and Hart et al. [17] have studied the effects of post-deposition surface treatments using ion beam bombardment and ion plasmas, respectively. In the study performed by Shi et al., undoped and n^+ doped ta-C deposited at 100 eV using the filtered cathodic vacuum arc (FCVA) method were subjected to H, O and Ar ion bombardment. Growth at 100 eV in undoped ta-C

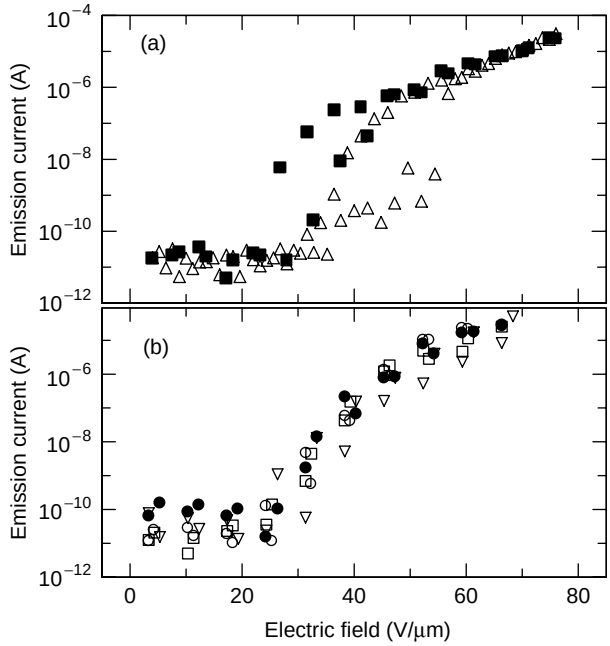

FIGURE 24.14 Emission current vs. electric field for films (a) stressed to 5×10^{-8} A and retested after 15 h (Δ, ■) and (b) stressed to 2×10^{-7} A and retested after 23 (○, □) and 87 h (●, ∇). Only the first two cycles of each retest are shown for clarity.

resulted in the maximum sp^2 content and n-type doping was achieved by the addition of N. They noted that the threshold field in the undoped films decreased from 18 to 14 V/μm after treatment with each of the ions and n^+-ta-C ion beam treatment resulted in a decrease from 12 to 8 V/μm. The saturated emission current density of the post-treated films was noted to improve by about an order of magnitude and appeared to be independent of the ion used. Shi et al. also measured the effects on the threshold field of undoped ta-C by varying the H ion energy from 50 to 800 eV. In this ion energy range, the threshold field increased from 14 to 22 V/μm. Hart et al. studied the effects of reactive ion etching using H_2, O_2 and Ar gases. By varying the etching time, it is possible to remove different thicknesses from the surface layer. Such a consideration is important since ta-C has a sp^2-rich surface layer extending about 1 nm from the surface. As-deposited films had a threshold field of 8 V/μm. Removal of 0.5 nm resulted in the threshold field reducing to 3.0 V/μm and removal of 2 nm resulted in the threshold field reducing to 3.9 V/μm. The former treatment corresponds to incomplete sp^2 surface layer removal whereas the latter corresponds to complete removal. For O_2 etching, the threshold field decreased to 5 V/μm for both 0.5 and 2 nm etch. Ar-plasma etching reduced the threshold field to 6 V/μm. Finally, emission maps using an ITO anode as a phosphor showed that the emission site density measured at 20 V/μm increased from about 50 to 100 cm^{-2} in as-deposited films to 1000 cm^{-2} for O_2-etched films, 2000 cm^{-2} for Ar-etched films, and 4000 cm^{-2} for H_2-etched films. Treatment with H_2 plasmas is predicted to increase the probability of C–H surface termination and, therefore, within the confines of the negative electron affinity model, would be expected to reduce the emission barrier at the front ta-C/vacuum interface. However, a reduction in the threshold field was also observed for O_2 plasma treatment which should raise the front surface barrier since the surface would be terminated with C–O bonds. Since Hart et al. used a parallel plate geometry to measure FE characteristics, the lowering of the threshold field is due to a higher emission site density and thus a greater distribution of sites with lower threshold fields. Atomic force microscopy showed that the RMS roughness of films did not change after plasma treatment and therefore surface features do not play a significant role.

24.7 SUMMARY AND OUTLOOK FOR THE FUTURE

In summary, there are a plethora of different carbon films from which electron emission has been obtained at relatively low threshold fields. Threshold fields below 30 V/μm can be integrated into gated structures using commercial CMOS technology, provided that any hysteresis is kept to a minimum. Amorphous carbon films appear to be unique in that most forms of carbon films give FE at low fields. Each of these films has a unique structure with some common features with the categorized a-C films discussed in this review. It is important that researchers first understand the basic microstructure of their a-C films before venturing into postulating a possible electron field emission mechanism in their films. There are a few more established emission models which can explain the electron emission from a number of these films as well as the variations with the physical properties. Extensions to noncarbon-based nanomaterials have also been presented.

In terms of future prospects, the scene is currently set with researchers having an excellent working knowledge of the emission characteristics of planar amorphous carbon cathodes. When this is coupled with high brightness that can be obtained from FED devices and the lifetime studies of FED prototype structures, it is a matter of time before these properties will be exploited in FE-type display applications.

REFERENCES

1. Silva, S.R.P., Carey, J.D., Khan, R.U.A., Gerstner, E.G., and Anguita, J.V., Amorphous carbon thin films, in *Handbook of Thin Film Materials*, Vol. 4, Nalwa, H.S., Ed.,Academic Press, Florida, USA, 2002, Chap. 9, pp. 403–506.
2. Ed by The Proceedings of the International Vacuum Microelectronics Conference; *J. Vac. Sci. Technol*.
3. Robertson, J., *Diamond Relat. Mater*., 5, 797, 1996.
4. Fanchini, G. and Taliaferro, A., *Appl. Phys. Lett.*, 85, 730, 2004.
5. Weiler, M., Sattel, S., Jung, K., Erhardt, H., Veerasamy, V.S., and Robertson, J., *Appl. Phys. Lett.*, 64, 2798, 1994.
6. Silva, S.R.P., Ed., *Properties of Amorphous Carbon*, EMIS Datareviews series no. 29, IEE, London, 2002.
7. Gröning, O., Küttel, O.M., Gröning, P., and Schlapbach, L., *Appl. Phys. Lett.*, 71, 2253, 1997.
8. Amaratunga, G.A.J. and Silva, S.R.P., *Appl. Phys. Lett.*, 68, 2529, 1996.
9. Forrest, R.D., Burden, A.P., Silva, S.R.P., Cheah, L.K., and Shi, X., *Appl.Phys. Lett.*, 73, 3784, 1998.
10. Burden, A.P., Forrest, R.D., and Silva, S.R.P., *Thin Solid Films*, 337, 257, 1999.
11. Carey, J.D., Forrest, R.D., Khan, R.U.A., and Silva, S.R.P., *Appl. Phys. Lett.*, 77, 2006, 2000.
12. Carey, J.D., Forrest, R.D., and Silva, S.R.P., *Appl. Phys. Lett.*, 78, 2339, 2001.
13. Silva, S.R.P., Xu, S., Tay, B.K., Tan, H.S., and Milne, W.I., *Appl. Phys. Lett.*, 69, 491, 1996.
14. Fallon, P.J., Veerasany, V.S., Davis, C.A., Robertson, J., Amaratunga, G.A.J., Milne, W.I., and Koskinen, J., *Phys. Rev. B*, 48, 4777, 1993.
15. Veerasamy, V.S., Yuan, J., Amaratunga, G.A.J., Milne, W.I., Gilkes, K.W.R., Weiler, M., and Brown, L.M., *Phys. Rev. B*, 48, 17954, 1993.
16. Ilie, A., Ferrari, A.C., Yagi, T., and Robertson, J., *Appl. Phys. Lett.*, 76, 2627, 2000.
17. Hart, A., Satyanarayana, B.S., Robertson, J., and Milne, W.I., *Appl. Phys. Lett.*, 74, 1594, 1999.
18. Satyanarayana, B.S., Hart, A., Milne, W.I., and Robertson, J., *Diam. Relat. Mater.*, 7, 656, 1998.
19. Cheah, L.K., Shi, X., Tay, B.K., Silva, S.R.P., and Sun, Z., *Diam. Relat. Mater.*, 7, 640, 1998.
20. Milani, P., Ferretti, M., Piseri, M., Bottani, C.E., Ferrari, A., Bassi, A.L., Guizzetti, G., and Patrini, M., *J. Appl. Phys.*, 82, 5793, 1997.
21. Ferrari, A.C., Satyanarayana, B.S., Robertson, J., Milne, W.I., Barborini, E., Piseri, P., and Milani, P., *Europhys. Lett.*, 46, 245, 1999.
22. Amaratunga, G.A.J., et al., *New Diam. Front. C. Technol.*, 9, 31, 1999.
23. Krauss, A.R., Auciello, O., Ding, M.Q., Gruen, D.M., Huang, Y., Zhirnov, V.V., Givargizov, E.I., Breskin, A., Chechen, R., Shefer, E., Konov, V., Pimenov, S., Karabutov, A., Rakhimov, A., and Suetin, N., *J. Appl. Phys.*, 89, 2958, 2001.

24. Chaumet, P.C. and Dufour, J.P., *J. Electrostat.*, 43, 145, 1998.
25. Tang, Y.H., Sun, X.H., Au, F.C.K., Liao, L.S., Peng, H.Y., Lee, C.S., Lee, S.T., and Sham, T.K., *Appl. Phys. Lett.*, 79, 1673, 2001.
26. Tsang, W.M., Wong, S.P., and Lindner, J.K.N., *Appl. Phys. Lett.*, 81, 3942, 2002.
27. Fogarassy, E., Szorenyi, T., Antoni, F., Pirio, G., Olivier, J., Legagneux, P., and Boher, P., *Appl. Phys.* A, 76, 15, 2003.
28. Liao, M.Y., Gotoh, Y., Tsuji, H., and Ishikawa, J., *Appl. Phys. Lett.*, 83, 1626, 2003.
29. Li, J.J., Zheng, W.T., Jin, Z.S., Wang, X., Bian, H.J., Gu, G.R., Zhao, Y.N., Meng, S.H., He, X.D., and Han, J.C., *J. Vac. Sci. Technol. B*, 21, 2382, 2003.
30. Tang, Y.F., Silva, S.R.P., and Rose, M.J., *Appl. Phys. Lett.*, 78, 186, 2001.
31. Forrest, R.D., Cox, D.C., Tang, Y.F., Shannon, J.M., and Silva, S.R.P., *J. Vac. Sci. Technol. B*, 21, 1560, 2003.
32. May, P.W., Hohn, S., Wang, W.N., and Fox, N.A., *Appl. Phys. Lett.*, 72, 2182, 1998.
33. Carey, J.D., Poa, C.H., Forrest, R.D., Burden, A.P., and Silva, S.R.P., *J. Vac. Sci. Technol. B*, 18, 1051, 2000.
34. Talin, A.A., Felter, T.E., Friedmann, T.A., Sullivan, J.P., and Siegal, M.P., *J. Vac. Sci. Technol. A*, 14, 1719, 1996.
35. Sowers, A.T., Ward, B.L., English, S.L., and Nemanich, R.J., *J. Appl. Phys.*, 86, 3973, 1999.
36. Mercer, T.W., DiNardo, N.J., Rothman, J.B., Siegal, M.P., Friedmann, T.A., Martinez Miranda, L.J., *Appl. Phys. Lett.*, 72, 2244, 1998.
37. Carey, J.D. and Silva, S.R.P., *Appl. Phys. Lett.*, 78, 347, 2001.
38. Missert, N., Friedmann, T.A., Sullivan, J.P., Copeland, R.G., *Appl. Phys. Lett.* 70, 1995, 1997.
39. Shi, X., Cheah, L.K., Tay, B.K., and Silva, S.R.P., *Appl. Phys. Lett.*, 74, 833, 1999.

25 Tribology of Nanostructured and Composite Coatings

Ali Erdemir and Osman Levent Eryilmaz
Argonne National Laboratory, Argonne, Illinois

Mustafa Urgen and Kursat Kazmanli
Istanbul Technical University, Istanbul, Turkey

Nikhil Mehta and Barton Prorok
Auburn University, Auburn, Alabama

CONTENTS

25.1 INTRODUCTION

In recent years, there has been an overwhelming interest in the production and widespread utilization of multifunctional, nanostructured, and composite coatings by various industries [1–4]. Specifically, increasing demands for greater power density, more compact design, better reliability,

lower fuel and material consumption in numerous advanced tribological systems have increasingly necessitated the use of such coatings to achieve greater performance, longer durability, and higher efficiency. For numerous applications, nanostructured and composite coatings can make a huge positive impact [5–7]. Because of their superior mechanical properties (in particular, superhardness and supertoughness) and high chemical inertness, these coatings can significantly lower friction and wear losses and at the same time increase resistance to fatigue, erosion, and corrosion, which have increasingly become the life-limiting factors for mechanical components in many industrial applications. Such coatings can also provide greater resistance to contact deformation and damage during heavily loaded rolling or rotating contacts [8]. Their isotropic, nanocrystalline structure may provide higher load-carrying capacity, greater fracture toughness, and hence better resistance to crack initiation and growth under both normal and tangential loads [9].

Production of bulk nanostructured or nanocomposite materials (metallic, ceramic, and polymeric types) was demonstrated a long time ago and the superior property and performance characteristics of these novel materials have been demonstrated under a wide range of application conditions [10–13]. In particular, ceramic-based nanostructured or composite materials have recently become very popular in applications that range from microelectronics to transportation. One particular concern has been the relatively high production cost of nanopowders used in the making of actual parts and components. Nevertheless, several kinds of nanostructured ceramics have recently been produced and offered for use in automotive, machining, and biomedical fields [10,11]. For example, production of high-strength springs, ball bearings, fuel injectors, and valve lifters for demanding automotive applications has been demonstrated and their superior chemical, mechanical, and tribological properties have been verified. In the near future, nanostructured ceramics are expected to find more application possibilities, especially in biomedical field, cutting tools, sensors, fuel cells, electronic substrates, wear-resistant coatings, optical materials, and catalysis.

Production of nanostructured and nanocomposite coatings is realized by using a wide range of vacuum deposition systems, which have been in existence for many decades [2,3]. These coatings are much cheaper to produce than the bulk nanocomposite materials. They can be applied on most ceramic and metallic substrates with strong bonding. In fact, with recent advances in surface engineering and coating technologies, the application of nanocomposite coatings on all kinds of substrates became very easy [3,14]. Some of the most recent nanostructured and composite coatings may combine superhardness with self-lubricating properties and they are extremely well suited for demanding tribological applications. For example, recently developed nanostructured carbon films, such as nanocrystalline diamond [15] and carbide-derived carbon [16] as well as nitride, carbide, and boride-based multicomponent nanocomposite coatings [1,2,17], can dramatically increase hardness and hence reduce wear under harsh sliding or machining conditions. These novel coatings can also offer superior mechanical, optical, magnetic, biomedical, electronic, catalytic, and surface acoustic properties that can be very useful in a wide range of advanced industrial applications [2,18,19].

In some of the current applications, the use of liquid lubricants is no longer desired, mainly because of increasingly tougher environmental regulations [20], whereas in others, steep variations in load, speed, and temperature have become a routine operating condition under which current materials or coatings fail rather rapidly or wear out quickly [21]. For example, dry machining and hot forming of machine parts and components are much desired practices in today's manufacturing operations, but they are currently very difficult to realize, mainly because of high friction and severe wear losses in current tool materials and coatings [19,22,23].

Nanostructured and composite coatings can be formulated in such a way that they can substantially increase the load-bearing capacity of sliding surfaces and hence improve their resistance to scuffing as well as adhesive or cohesive failures. Some of the innovative design considerations for multifunctional nanostructured coating architectures include nanograde, superlattice, or multilayer films, whose properties are specifically tailored to meet the stringent application conditions of advanced tribosystems [2,3,24–27]. It is also possible to design nanocomposite coatings that can form self-replenishing and self-lubricating tribofilms on their sliding surfaces and thus help in

increasing the overall lubricity of these surfaces [3,28]. One can also design a multicomponent, nanocomposite film that can adapt and follow the changing operating or environmental conditions of a specific application. For example, in such films, while one component provides lubricity, a second or third component may provide wear resistance; alternatively, while one phase is active and provides both lubricity and high wear resistance at room temperature, a second phase may become more active and provide lubricity at high temperatures [29]. Figure 25.1 schematically illustrates some of the design architectures that are possible for most popular nanostructured and composite films [3,30].

Recent experimental studies have shown that some of the key advantages of nanostructured coatings over conventional coatings for tribological applications are superior mechanical hardness, resilience and toughness, high resistance to fatigue, oxidation, and corrosion, lower friction, and greater tendency to produce lubricious tribofilms on dry or marginally lubricated sliding surfaces [1–3,7,17–19,26,27,30]. Some nanostructured coatings are specifically designed to promote the formation of such low-friction tribofilms on sliding surfaces [7,31]. Such nanocomposites are often referred to as self-lubricating and they are well suited for green machining and manufacturing applications.

Liquid lubricants have existed for centuries and have been perfected over the years to provide the levels of lubrication that we appreciate every day while we drive our cars. The additive package of these lubricants has also reached its limits and further optimization does not seem feasible or will not really make much difference in the friction and wear of those sliding surfaces that are subjected to heavy loading or high operating temperatures. However, it is possible to design new nanomaterials and coatings around the existing liquid lubricants or additives to achieve further improvements in lubrication [7]. These coatings can be regarded as smart or adaptive tribological coatings because of their excellent compatibility with, and favorable response to, the lubricated test environments. Such nanocomposite coatings may further be optimized to provide low friction and wear even in the near absence of ZDDP- and Mo-DTC-type additives in future liquid lubricants.

This chapter presents an overview of recent advances in the fields of superhard and low-friction nanostructured and nanocomposite coatings that have attracted a great deal of interest in recent years. When applied properly, these coatings can exert a huge positive impact on a wide range of industrial applications, including manufacturing, transportation, aerospace, information technology, and biomedical fields. Specific examples are given to demonstrate the superior performance and durability of such novel coatings under a very wide range of mechanical and tribological conditions. The major emphasis has been placed on recent developments in the production and uses of superhard and low-friction coatings. The fundamental tribological mechanisms that control their superior friction and wear behaviors are also discussed. It must be understood that the application conditions of future tribosystems will be much more challenging than in the past. To meet these challenges, researchers must develop more exotic coatings that can further improve durability and performance and at the same time self-adapt to the increasingly harsh and rapidly changing application conditions of future tribological systems. Ultimately, it will be extremely desirable to design or discover a universal nanostructured or composite coating that can work under any application conditions. However, the development of such a coating is still far in the future and perhaps is hard to realize with existing technological capabilities.

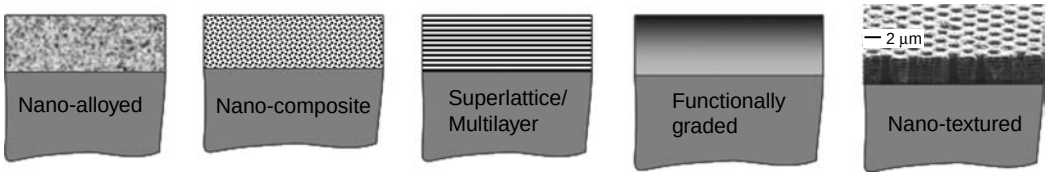

FIGURE 25.1 Schematic representation of various design architectures for nanostructured and composite coatings.

In the following section, we provide a short overview of recent advances in deposition technologies that are used in the production of nanostructured and composite coatings. These advances were essential for the design and development of several nanostructured or composite films. This will be followed by a review of structural and mechanical properties that are most relevant to and important for tribological improvements in various application fields. Tribological properties or performance characteristics of such coatings will be reviewed next. Finally, future prospects for such films will be discussed, with emphasis on the development of next-generation coatings that may combine supertoughness with superhardness and superlow friction.

25.2 RECENT ADVANCES IN DEPOSITION TECHNOLOGIES

Over the years, significant advances have been made in physical and chemical vapor deposition (PVD and CVD) of tribological coatings. Some of these developments have been covered extensively in several review articles in various technical journals, books and handbooks [32–38]. The increased versatility of PVD and CVD techniques (such as sputtering, ion plating, cathodic-arc PVD, pulse laser deposition [PLD], ion-beam-assisted deposition [IBAD], plasma-enhanced chemical vapor deposition [PECVD]) has in recent years enabled the production of novel coatings with complex microstructural architectures and chemical compositions [2,3,7,25,38]. In fact, today's deposition technologies offer enormous possibilities for the design and production of novel coatings that are very robust and truly multi-functional. In particular, reactive magnetron sputtering and cathodic-arc PVD methods are widely used by industry for the deposition of conventional, and nanostructured and composite coatings [14,17]. The techniques of PLD and IBAD are also used in the production of these coatings. In particular, PLD is favored as a convenient research tool and, with the introduction of femto-second laser sources, the control of the ablation process became even easier and the stream of ablated atomic species became cleaner and more stable [39]. Figure 25.2 is a schematic representation of two advanced PVD systems that are used to produce nanostructured or composite films with superlattice, multilayer, or multiphase architectures.

25.2.1 HYBRID DEPOSITION PROCESSES

Deposition technologies used in the production of nanostructured or composite coatings may combine two or more of the methods mentioned above. These methods are referred to as hybrid deposition processes [40–43]. Some of them can also be used for nitriding or carburizing substrate

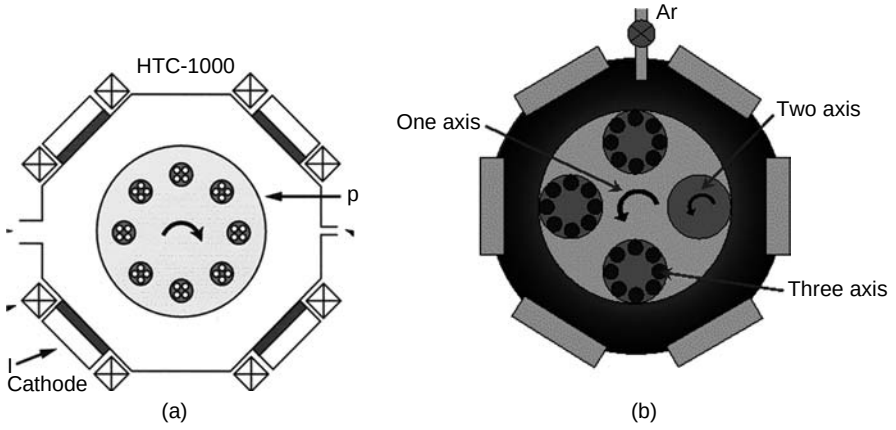

FIGURE 25.2 Schematic layout of multi-target (a) hybrid magnetron sputtering and cathodic-arc PVD system (courtesy of R. Dielis, Hauzer Techno Coating) and (b) closed-field magnetron sputter ion plating system (courtesy of D. Teer, Teer Coatings, Ltd).

materials before film deposition. The use of hybrid processes is most ideal for the production of duplex, multiplex, or superlattice coatings. In these processes, the physical shape or architecture of conventional deposition systems is not greatly changed, but additional targets and appropriate power sources are added to enable coating deposition by one of the methods alone, two or three of them in sequence, or altogether. For example, in the production of nanocomposite or multilayer Cr, Ti, or W, and carbon films, sputtering and arc-PVD techniques (see Figure 25.2) may be used alone or simultaneously [44,45]. In essence, the nanoscale Cr layers are alternated with those of carbon, (see Figure 25.3a) or Ti or W grains are imbedded in the amorphous matrix of diamond-like carbon (DLC) film, as shown in the transmission electron microscopy (TEM) images in Figures 25.3b and c [46,47], respectively.

In recent years, multilayer coating architectures have become very popular. Because of their layered structure, these coatings provide much better fracture toughness, higher mechanical hardness as well as excellent tribological properties to the coated parts and components [1,2,9,30]. By employing an innovative design approach, one can also produce a coating that may allow machining or manufacturing under application conditions that are dry or marginally lubricated. Elemental or chemical ingredients used in each layer may themselves become lubricious, thus enabling tools to operate without external lubrication [48,49]. These coatings may also have direct implications for other fields such as transportation and aerospace [7,29,30]. In the manufacturing and transportation sectors, the reduction or even complete elimination of some oils or oil additives is currently being considered (mainly because of environmental concerns) [50]. Coated machine elements with self-lubricating capability can certainly make a huge positive impact on such applications.

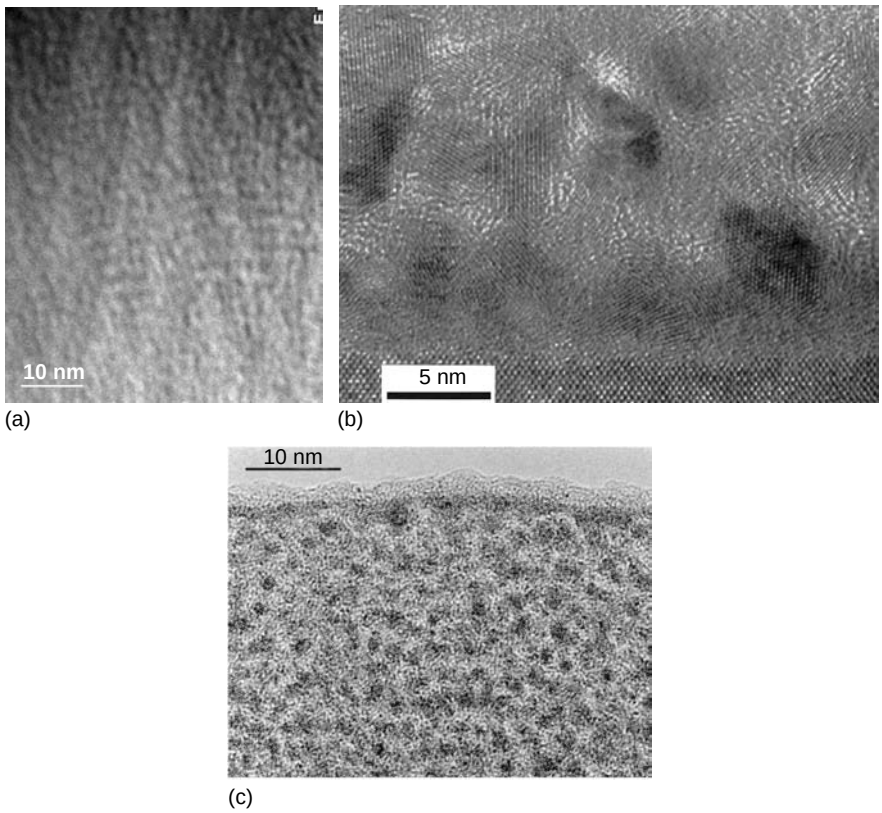

FIGURE 25.3 TEM images of (a) nanolayered Cr/C (from Hovsepian, P.Eh. et al., *Thin Solid Films*, 447–448, 7–13, 2004, with permission from Elsevier), (b) nanocomposite Ti/C (Reused from Meng, W.J. et al., *J. Appl. Phys.*, 88, 2415, 2000, Copyright (2000), American Institute of Physics), and (c) nanocomposite W/C:H films (courtesy of Hauzer Techno Coating).

25.2.2 Control of Process Parameters

Proper selection and control of several deposition parameters are critically important for the successful synthesis of multifunctional nanostructured or composite films [4,51,52]. Furthermore, close control of some of these parameters is essential for preserving chemical, structural, and mechanical integrity of the underlying substrates. For example, some of the major engineering materials, including machining tools or metal-forming dies may suffer from thermal softening if they are exposed to high temperatures or temperatures higher than their tempering points [53]. However, most deposition processes (CVD in particular) involve the creation of high temperatures, which can potentially soften these substrates by changing their microstructure and thus their mechanical properties. For certain high-speed steels, other heat-resistant alloys, and cemented carbides and ceramics, deposition temperatures as high as 450°C may be permissible. However, some of the nonferrous alloys, such as aluminum- and magnesium-based alloys, may not endure such high temperatures. Today, these alloys are highly sought after for use in all kinds of automotive applications (mainly due to their light weight) but application of a PVD or CVD coating on them may require special precautions. Another potential problem with the CVD method is that the precursor gases (such as $TiCl_4$, $SiCl_4$, or SiH_4) used in the synthesis of many hard coatings may pose health and fire hazards.

With increasing ionization efficiency and plasma current densities of advanced PVD systems in recent years, it is now possible to maintain substrate temperatures at very low levels and, at the same time obtain very dense and chemically stoichiometric hard nitride or carbide coatings. Cathodic-arc PVD and closed-field unbalanced magnetron sputter ion plating processes are well known for their high ionization efficiencies [31,54]. In recent years, high-power pulsed-magnetron sputtering processes have also been developed and very high ionization efficiencies and high plasma densities have been achieved [55,56]. Both processes may provide very effective plasma etching capability before coating deposition and thus ensure strong bonding between films and substrates and very dense film morphology.

25.2.3 Modern Coating Practices

Physical vapor deposition and CVD technologies available today are used in a large variety of industrial applications (ranging from magnetic hard disks to decorative coatings) [57–59]. Some of them are well suited for coating of planar workpieces such as magnetic hard disks and window glasses, whereas others can also coat complex three-dimensional (3-D) objects such as metal-cutting and metal-forming tools, automotive parts. Planar magnetron sputtering processes tend to be line of sight and thus are well suited for coating of flat workpieces and conformal tribological surfaces. Ion-beam-assisted deposition, ion-beam mixing, and PLD methods can also produce high-quality coatings on flat metallic or ceramic substrates [60,61]. Most CVD methods, ion plating, and multicathode arc-PVD, and unbalanced magnetron sputtering systems are well suited for the coating of fairly intricate 3-D workpieces. High ionization efficiency and very energetic particles produced in these methods ensure strong film-to-substrate adhesion, dense film morphology, and perfect or near-perfect chemical stoichiometry, even at relatively low deposition temperatures. Energetic ions produced by these processes increase ad-atom mobility, surface and bulk diffusivity that can positively influence nucleation and growth, and crystallographic growth orientation or texture of the coatings. Among others, deposition systems based on ion plating, multicathode arc-PVD, and magnetron sputtering have dominated the coating industry in recent years. Multistage and multirotational substrate holders further improved coating uniformity and chemical stoichiometry, even on very large workpieces.

Besides the advanced PVD processes mentioned above, plasma-activated or plasma-enhanced CVD processes have become very popular in recent years and are used to deposit a wide variety of functional coatings at very low to very high temperatures. Prime examples are the deposition of DLC films by PECVD at room temperature or at temperatures up to 300°C, and, at the other extreme, the deposition of crystalline diamond films by hot-filament or microwave CVD processes at high temperatures (i.e., 600 to 1000°C). Among others, PECVD is widely used to produce nanocomposite

carbon films in which carbon makes up the matrix while nanocrystalline phases of transition metal carbides are produced as dispersoids within the amorphous matrix [62]. Microwave CVD, which uses a hydrogen–methane plasma, is used for the synthesis of diamond films at very high temperatures. The same method is also used to produce nanocrystalline diamond films with grain sizes in the range of 2 to 6 nm; in this case, hydrogen is replaced with argon in the plasma [15].

Most of the PVD and CVD methods mentioned above can be scaled up and used to achieve large production volumes. However, extreme caution is needed to make sure that the quality of the coatings is repeatable from one production run to another, and that deposition rates and temperatures are very stable and fairly uniform across the workpieces being coated. With the use of hybrid deposition processes in one system, much greater flexibility has been achieved in the design and production of novel coating architectures. In particular, hybrid deposition systems based on cathodic-arc and magnetron sputtering have recently become very popular. These methods are used not only to clean substrate surfaces effectively but also to form a graded interface that can lead to strong bonding [56]. Multicathode hybrid deposition systems are currently used for the production of nano- or multilayered coatings that can provide very low friction as well as very high wear resistance in sliding bearing applications. Such coatings can also provide greater durability when used in machining or metal-forming applications [19,27,63].

25.3 STRUCTURE AND MECHANICAL PROPERTIES

With recent advances in surface engineering and deposition technologies, design and production of nanostructured and composite coatings have become relatively easy. Some of the most common design strategies for nanostructured coatings include the production of multilayer or nanocomposite architectures such as those illustrated in Figure 25.1 and Figure 25.3. In the case of multilayer coatings, the layer thickness may vary from a few atoms to several angstroms or nanometers [2,46,63,64]. Some of these are referred to as superlattice coatings and are shown in Figure 25.4 [65]. Such coatings may offer superhardness and toughness as well as high thermal stability [66]. Other design strategies are based on building up alternating very thin and very thick layers, nano-to-micro scale grading, disruptive or discontinued layering, etc. Success in achieving high-precision layer buildup depends on several factors, including the selection and effective control of process parameters during deposition. These parameters may play a major role in surface and bulk diffusion of impinging atoms, and ad-atom mobility, nucleation, and growth processes, and hence, layer uniformity or coverage of substrate materials.

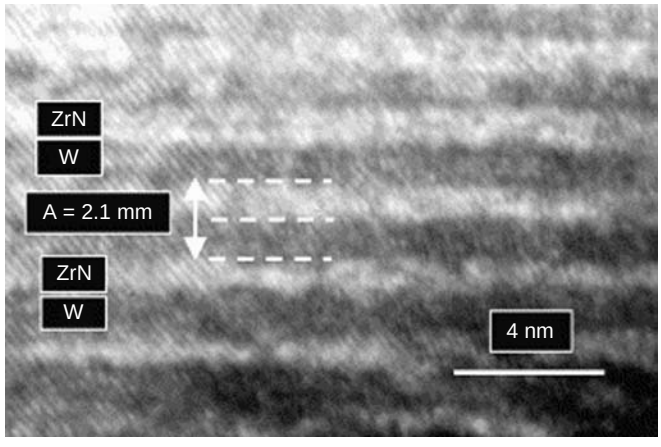

FIGURE 25.4 High-resolution TEM image of a W/ZrN nanolayer coating after annealing at 1000°C for 1 h. (From Barnett, S.A. and Madan, A., *Scr. Mater*., 50, 739–744, 2004, with permission from Elsevier.)

Another popular design strategy for nanostructured coatings has been the production of truly nanocomposite films by using a hybrid PVD or CVD system. A typical nanocomposite coating architecture includes a nanocrystalline phase surrounded by an amorphous carbon and ceramic or metallic phase [1,2,5,24]. The amorphous and metallic phases are kept at very small volumes and selected to have a strong chemical bonding to the hard crystalline phase. It is also possible to have more than one crystalline phase imbedded into the amorphous matrix, or both phases made of dissimilar crystalline phases. The yield strengths of such nanocomposite films may far exceed those observed in the bulk crystalline forms of either single component or even of their bulk composites. Some of the major factors that can influence mechanical and tribological properties of such nanocomposite coatings are size, shape, and orientation of nanograins; surface area and thickness of grain boundary phases; residual stresses; and stress gradient across the overall coating thickness.

In recent years, several theoretical models have been proposed for the many superior mechanical properties (in particular hardness and elastic modulus) of nanostructured and composite films. In one of the theories, Koehler has proposed that the dramatic increases in hardness of nanostructured coatings may largely be the result of the fact that dislocations are elastically repelled at grain boundaries and hence plastic deformation is hindered. In another theory, the Hall–Petch relationship has been proposed as the major reason for the superhardness of nanostructured coatings. According to the Hall–Petch equation (i.e., $H(d) = H_0 + Kd^{-1/2}$), the yield strength or hardness $H(d)$ of a polycrystalline solid is related to its average grain diameter d (while H_0 and K are material-specific constants). In general, the smaller the grains, the harder the material. In bulk materials or composites, this relationship may be valid down to $\approx 0.01\,\mu m$ grain size, but beyond this, the hardness may decrease (mainly because of increased grain boundary sliding). If the grain boundaries of a composite material or coating are engineered to be very strong, these materials or coatings should provide high hardness values, even at grain sizes less than $0.01\,\mu m$. Table 25.1 presents the chemical composition and mechanical properties of some of the nanocomposite coatings developed recently by various research groups.

At present, several nanostructured and nanocomposite films that can provide hardness values well above 40 GPa are available and they are referred to as superhard coatings. In this case, the grains are in nano domains (i.e., 3 to 5 nm) and the grain boundaries are decorated by a very thin (one or two atomic size), immiscible but strongly bonded phase [2]. The same effect or superhardness can be achieved by producing a nanocomposite film in which two or more crystalline phases may be present and strongly bonded to each other at the grain boundaries so that grain boundary sliding is very difficult.

TABLE 25.1
Chemical Composition and Mechanical Properties of Some of the Standard and Superhard Coatings Developed by Various Research Groups

Coating	Average Grain Size (nm)	% Cu (at.)	Hardness H (GPa)	$E^*(E/(1-\nu^2))$ (GPa)	Ref.
Zr-Cu-N	38	1–2	55	395	[67–69]
Zr-Ni-N	6	4.1 (Ni)	57	430	[70]
CrCu-N	70–90	1	35		[71]
Ti-Cu-N (J.L. He)	22	1, 5	30		[72]
Al-Cu-N	9, 5	8, 1	47	313	[69]
Zr-Cu-N	10–15	23	23	250	[67–69]
Ti-Cu-N (J.L. He)	5	12	10		[72]
ZrN	—	0	16		[68]
TiN (J.L. He)	22	0	23		[72]
nc-TiN/a-Si_3N_4			40–60	>500	[52,74]
nc-TiN/a-Si_4N_4/a-$TiSi_2$			>80		[52]

The unusual hardness properties of nanocomposite coatings are almost impossible to achieve by using simple rule of mixtures. For example, some of the recently developed nanocomposite coatings (such as TiN/Si_3N_4, Ni/ZrN, Cu/MoN) exhibit hardness values higher than 40 GPa [1–5] if each of the phases that make up such a composite coating was considered; it is obvious that the composite or combined hardness of these phases must have been much lower. However, it has been proved that these coatings exhibit hardness values two to three times higher than the phases of which they are composed. In general, it has been well established that, by the selection and proper use of metallic or ceramic phases, it is now possible to achieve very soft composite films that exhibit hardness values less than 10 GPa or coatings with hardness values greater than 50 GPa. Briefly, nanocomposite coatings can be designed to provide tunable mechanical properties.

In addition to superhardness, fracture toughness of a coating is very important, especially for tribological applications where high normal and shear forces are present [9]. Hardness alone may not provide the level of protection that one needs in a sliding contact or machining application. Sometimes, high levels of internal stresses within the films may partially be the reason for superhardness observed in thin coatings, and such a situation may be detrimental to the fatigue and wear resistance of such coatings. Recent experimental studies have confirmed that most nanostructured and composite coatings possess relatively high fracture toughness [5,75]. It is proposed that their nano-size grain morphology can provide an ideal condition for resisting crack initiation. Even if a crack has initiated within a grain, strong grain boundaries can arrest or deflect it back to the grain and hence prevent or retard crack growth. Overall, superhardness and toughness are quite achievable in nanostructured or composite coatings by producing high-strength grain boundaries and by controlling the surface and interface energy of nanograins, and the extent of texture, residual stress, and strain throughout the films.

In recent years, many researchers have concentrated on the design of a novel nanocomposite coating that can rival the hardness of diamond. To realize this quest, several complex coating systems that consist of more than two phases were explored. Most refractory nitrides with little or no miscibility with each other would satisfy this condition. Such a coating system was recently designed by Veprek in the form of a nanocrystalline TiN phase imbedded into an amorphous Si_3N_4 phase and in an amorphous and nanocrystalline $TiSi_2$ phase. The reported hardness value of this coating was more than 100 GPa [76,77]. Several other coating systems (such as (Ti,Al)N and VN) that exhibit superhardness were designed and produced in several PVD and CVD systems by similar approach.

Beside high hardness and toughness, strong adhesion between film and substrate materials is by far the most important prerequisite for most mechanical and tribological applications [78]. If adhesion is poor, coatings rapidly delaminate under the influence of high normal and shear forces of most tribological applications. Poor adhesion may often be the result of high residual stress or stress build-up at the film–substrate interface, inadequate physical and chemical intermixing, or poor mechanical interlocking at the interface. In most tribological applications, adhesion determines a film's endurance life, load-bearing capacity and, hence, effectiveness in such applications. With recent advances in the field, it is now possible to achieve very strong bonding between thin coatings and their substrates. Arc-PVD and high-power pulse magnetron sputtering can provide an atomically clean surface and promote high levels of inter-diffusion or mixing between coating and substrate atoms at the interface and thus ensure strong bonding. However, there are a few exceptions. Despite their superhardness and very attractive tribological properties, cubic boron nitride or some of the coatings based on B-C-N still suffer from poor adhesion and high internal stresses [79]. Therefore, these coatings are currently not widely available for commercial use.

In most tribological applications, operating conditions may involve high temperatures or aggressive environments. Therefore, tribological coatings are expected to be chemically and structurally benign to routine variations in ambient temperature and environment. In certain applications, high temperature is often generated by the high speed of the sliding or machining operations. Under the influence of repeated sliding passes, nanostructured and composite coatings may undergo some structural or chemical changes, which, in turn, lead to gradual degradation of their mechanical and tribological properties. During operation or use in open air or aggressive environments, some chemical changes are

expected to occur in certain coatings (especially at or near their sliding surfaces). Despite being somewhat inert or chemically stable, these coatings may oxidize. With increasing desires for dry machining and high-temperature metal-forming operations, chemical and thermal stability of coating systems is becoming much more important than before. Doping with Al, Y, Ce, etc. seems to help in retarding the oxidation process and hence increase wear-life of tools and dies used in such applications [79].

25.4 TRIBOLOGY OF NANOSTRUCTURED AND COMPOSITE FILMS

Although the physical, chemical, and mechanical aspects of sliding contacts between tribological surfaces are not well understood, previous research has shown that thin coatings can positively affect both the friction and wear properties of these surfaces. Nowadays, most tools and dies used in manufacturing operations are routinely coated with a protective film. With recent advances in PVD and CVD technologies, several novel coating systems have been developed and used to combat friction and wear in numerous industrial applications. In particular, the use of nanostructured and composite coatings has become increasingly popular.

As mentioned earlier, if a tribological coating is to affect a given application positively, it must meet several important requirements, including strong adhesion, high mechanical hardness and toughness, high thermal/chemical stability, uniform and adequate thickness, smooth surface finish, low friction, etc. Structurally, the coatings must also exhibit a dense morphology (i.e., no porosities or open columnar grain boundaries). Coatings with porous columnar structures tend to wear out rather quickly during tribological use. The result of repeated tilting or bending of columnar grains with poor inter-column cohesion is microfracture-dominated wear during sliding or machining operations. Therefore, a strong cohesive bonding among grains of a coating is extremely important. The adequacy and uniformity of coating thickness are also very important for improved performance. When all of these requirements are met, the tribological coatings can certainly make a significant positive impact on a given application. Specifically, they can increase durability and performance of those parts and components that are being used in an application.

When used on a sliding contact surface, nanostructured coatings will experience the same levels of nominal contact pressures as their conventional counterparts. If in a situation where the wear mechanism involves micro-fracture or plastic deformation, such coatings can resist crack initiation because of their high fracture toughness. If they are subjected to heavy loading in vertical directions, they may not fracture as easily as their conventional counterparts. As is known, most conventional coatings are highly anisotropic and hence exhibit a columnar micro-structure. The column boundaries may be relatively weak and hence very susceptible to deformation or fracture. However, in the case of nanostructured coatings, the grains are extremely small and the morphology is not necessarily anisotropic or columnar. Figure 25.5 shows the cross-sectional morphology of a conventional MoN film with columnar morphology and a superhard Cu/MoN film with a featureless morphology. Note that additional cracks are present away from the sectioned surface, along the columnar grains of the conventional MoN, but no such cracks are present in the case of the nanocomposite Cu/MoN coating. The average grain size of nanocomposite film is in a range that is not well suited for crack initiation and propagation. In other words, Griffith's criteria for crack growth are very difficult to meet in nanostructured and composite coatings [80]. Therefore, it is reasonable to claim that one of the main reasons why nanostructural coatings exhibit superior wear properties is that they are better able to prevent crack initiation and growth.

The superhardness and extreme stiffness of nanostructured and composite films ensure that during a tribological sliding situation the real areas of contact are very small. Coatings produced in a superlattice or multilayer fashion can also substantially increase the load-bearing capacity of sliding surfaces [8,44,63]. In general, when combined with high chemical inertness or stability, smaller contact areas on a sliding surface may often lead to low friction. Specifically, the adhesion component of the overall friction force is reduced on such highly chemically inert surfaces. When selected properly, one of the phases in a nanocomposite film can provide low shear and hence low friction during sliding contacts. Nanocomposite and multilayer coatings can also be designed in such a way that, when used in lubricated sliding applications, they lead to the formation of self-replenishing

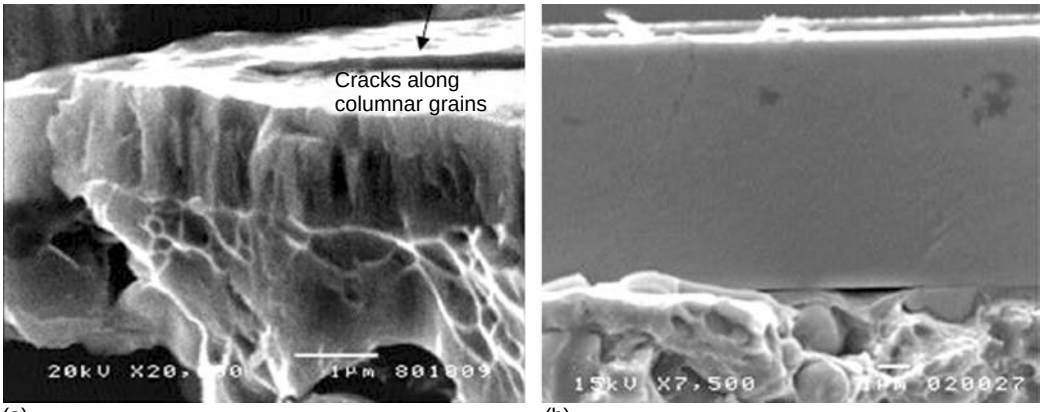

FIGURE 25.5 Fracture morphology of (a) conventional MoN and (b) nanocomposite Cu/MoN coating.

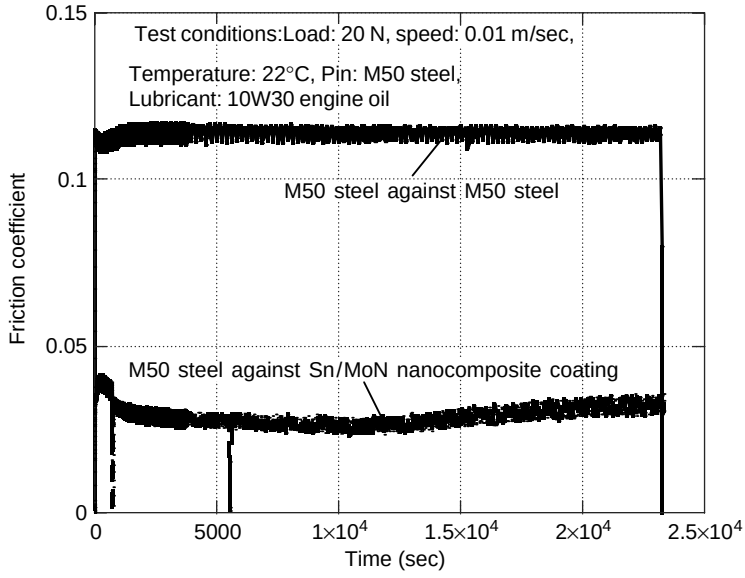

FIGURE 25.6 Friction coefficients of steel sliding against steel and steel sliding against Sn/MoN nanocomposite film under boundary-lubricated sliding conditions.

and self-lubricating secondary films on the sliding surfaces and thus provide much lower friction. Figure 25.6 shows the frictional behavior of a nanocomposite Sn/MoN film under boundary-lubricated sliding conditions. When compared with an uncoated steel surface, the Sn/MoN coating provided a much lower friction coefficient. It is possible that such a reduction in friction is due to the low-shear-strength Sn phase in the nanocomposite structure. Sn may have also reacted with additives in oil to produce a low-shear boundary film on the sliding surface.

25.4.1 Self-Lubricating Nanocomposite Coatings

The production and uses of self-lubricating composite materials and coatings for tribological applications are not new. For many years, metal, ceramic, and polymer-matrix composites with self-lubricating capabilities have been produced successfully and used to combat friction and wear in many mechanical applications [81–83]. Fairly thick (0.1 to 0.2 mm) plasma-sprayed self-lubricating

composite coatings were also produced on sliding surfaces of various engineering components and used to combat friction and wear, especially at high temperatures [84]. Several other composite coatings that consist of graphite, molybdenum disulfide, and hexagonal boron nitride (HBN) were also produced by plasma spraying or electroplating methods and used to achieve better mechanical and tribological properties [85]. The development and use of thin self-lubricating nanostructured and composite coatings are imperative. Nanoalloying of thin coatings with special metals may also lead to superior tribological properties for more demanding tribological applications (involving severe application conditions such as high speeds, loads, temperatures, vacuum, etc.).

In the past, a series of alloying ingredients was introduced into conventional coatings to improve their mechanical properties and environmental compatibilities. A prime example is self-lubricating MoS_2 films, which have found numerous applications in aerospace and a few other areas. Some of the alloying elements or compounds used in such coatings included Au, Ni, Ti, Pb, C, TiN, PbO, Sb_2O_3, etc. [86–89]. Tribological studies have demonstrated that when alloyed properly and tested under the right conditions, such alloying ingredients can substantially improve the mechanical and tribological properties of MoS_2 films. Alloying of MoS_2 with Pb, Ti, Ni, Fe, Au, and Sb_2O_3 leads to film amorphization or nanocrystalline structure, which, in turn, further reduces friction and substantially increases film wear life [86,90]. In recent years, electro-less nickel, chromium, and nickel–phosphorus coatings that contain small amounts of nanoscale graphite, MoS_2, PTFE, and diamond particles have also been developed and used to achieve relatively thick films with self-lubricating properties [91].

Since the early 1990s, interest has steadily shifted toward the production of self-lubricating thin nanostructured and composite coatings. It was felt that, with the design and realization of such coatings, greatly improved tribological performance may be feasible. Conceptually, the approach was similar to the conventional methods used in the production of bulk self-lubricating composite materials and coatings mentioned above. However, structurally, the individual grains that make up such coatings are on the nanoscale or mixed homogenously within the produced layers. Chemically, such coatings may consist of soft and hard nanoscale phases (such as metal carbides, amorphous or crystalline solid lubricant phases) that can provide high fracture toughness, high load-carrying capacity, low friction and high wear resistance in sliding contacts [3,29–31,92]. In such coating systems, the hard carbide and carbon phases may provide high hardness and hence wear resistance, whereas the relatively soft solid lubricant phase may provide low friction and high load-bearing capacity.

The soft solid lubricant phases in self-lubricating nanocomposite films may be selected from graphite, HBN, and transition metal dichalcogenides such as molybdenum, tungsten, and niobium disulfide or diselenide. These lubricants owe their lubricity to a layered crystal structure. As illustrated in Figure 25.7, the crystal structures of these solids are such that while the atoms lying in the same layer are closely packed and strongly bonded to each other, the layers themselves are relatively far apart, and the forces that bond them, e.g., van der Waals, are weak. When present between sliding surfaces, these layers can align themselves parallel to the direction of relative motion and slide over one another with relative ease to provide low friction. They are used extensively in various tribological applications. Among the dichalcogenides, WS_2 and MoS_2 have been used as single-component thick or thin coatings for solid lubrication purposes in aerospace mechanisms [29,89]. In inert gases or space-like environments, they can provide friction coefficients as low as 0.01. However, their friction may become high or fluctuate significantly at high temperatures and moist or oxidative environments. WS_2 is preferred over MoS_2 when applications involve relatively higher temperatures. Selenides of W, Nb, and Mo may provide higher temperature capabilities than their sulfide analogs, but they are very expensive for large-scale applications.

The dichalcogenides mentioned above have been used as self-lubricating components in nanoalloyed or multicomponent tribological coatings. One of the nanoalloyed films is based on the MoS_2 and Ti system and is produced by the closed-field unbalanced magnetron sputter ion plating technique [31]. Figure 25.8 shows the typical friction behavior of such a film in humid-air and dry-nitrogen environments. This film is much harder and more wear resistant than the single-component MoS_2 films that were used for a long time by industry for solid lubrication purposes. The friction coefficient

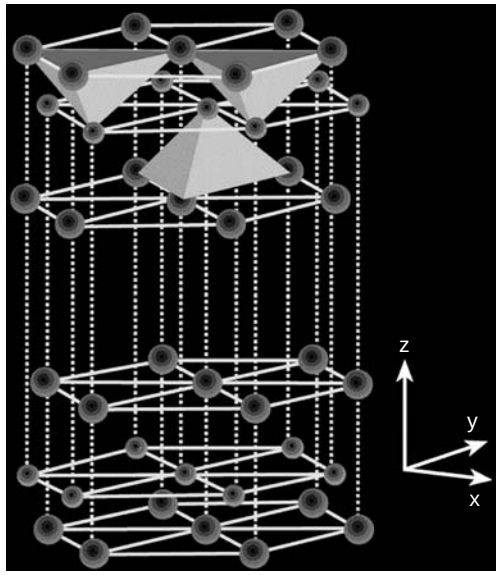

FIGURE 25.7 Layered lattice structure of MoS_2.

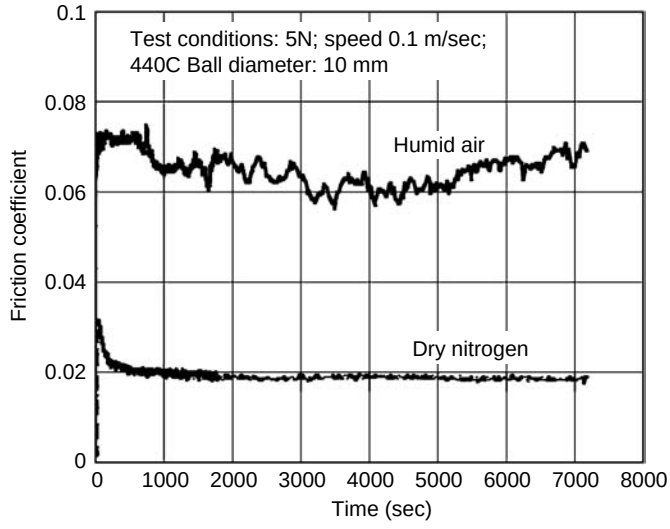

FIGURE 25.8 Friction behavior of MoS_2/Ti coating in humid air (40% R.H.) and dry nitrogen (less than 1% humidity). (MoS_2/Ti coating is from Teer Coatings, Ltd.)

of such an MoS_2/Ti film against steel or ceramic balls is below 0.1 in humid air and less than 0.05 in dry N_2; when compared with conventional MoS_2 films, its Vickers hardness is much higher and hence it lasts longer in tribological applications [93]. Furthermore, the frictional properties of this coating are not greatly affected by moisture in the test environment and it is proposed for use in various dry-sliding and machining applications (e.g., milling, drilling, tapping, cold-forming dies and punches, stamping, bearings, and gears for aerospace and vacuum applications) [31,93].

In more recent research activities, attempts have been made to produce self-lubricating nanocomposite films that consist of multilayers or discrete phases of a solid lubricant (such as MoS_2 or WS_2) and a metal, ceramic, or hard-metal nitride or carbide (i.e., Ti, Pb, Au, TiN, TiC) [3,28,89].

These coatings can be prepared by co-sputtering MoS_2 and TiN or TiB_2 targets or a single target composed of both TiN and MoS_2. The resultant coatings may consist of distinct nanolayers or phases of hard ceramic and soft dichalcogenide compounds. The hardness of these coatings could be as high as 20 GPa, while their friction coefficients are ≈0.1, even in open-air environments. Because of high hardness and low friction, they can be used in both sliding and machining applications [94]. Recently, researchers have also produced multi-layer MoS_x/Pb and MoS_x/Ti coatings (with individual layer thicknesses in the range of 4 to 100 nm) by magnetron sputtering at room temperature. Sliding wear tests in 50% relative humidity showed great improvement in wear-life over that of pure MoS_x coatings [95]. The 3-D design of adaptive coatings based on multicomponent MoS_2/TiC/DLC or WS_2/WC/DLC coating architectures led to improved tribological properties over broad ranges of environmental humidity and other test parameters [96]. Whereas the hard coatings of TiC and DLC provided high strength and resistance to wear, solid lubricants DLC and MoS_2 provided low friction at the sliding surface. The friction coefficients of the coatings were 0.15 in humid air and 0.02 in dry nitrogen, thus increasing the prospects for use in space mechanisms.

PbO/MoS_2- and ZnO/WS_2-based nanocomposite films have also been produced in recent years and tested for their lubricity and durability in various environments [97]. Composite films perform significantly better during tribotesting than films composed entirely of MoS_2 or PbO and ZnO. In addition, the composite films demonstrate the properties of "adaptive" lubricants. MoS_2 provides lubrication at room temperature; however, when the films are exposed to oxidizing environments at elevated temperatures, they adapt by forming $PbMoO_4$, a compound that has been noted to display low friction at high temperatures.

Other layered solid lubricants such as graphite and HBN can also provide low friction to sliding tribological interfaces, but they are not widely used as nanodispersoids in coatings to achieve low friction. In contrast to dichalcogenides, these solid lubricants work best in moist environments but fail in vacuum or under dry running conditions. It is generally agreed that no solid can provide very low friction and wear regardless of test environment and conditions. Furthermore, lifetimes of most solid lubricants tend to be very limited because of the finite film thickness and susceptibility to chemical or thermal degradation. In general, no single lubricant can provide reasonably low and consistent friction coefficients over broad test conditions, temperatures, and environments. Lubricants mentioned above function rather well under certain, but not all, test conditions.

25.4.2 Superhard Nanocomposite Films

As mentioned earlier, most of the superhard nanocomposite coatings consist of multilayers of hard nitride and carbide materials or a hard nanocrystalline phase (such as TiN) embedded in an amorphous (such as Si_3N_4) or metallic (such as Cu, Ag, Ni, etc.) phase [1,2,4]. Figure 25.9 shows a high-resolution TEM image of the TiN/Si_3N_4 system, together with its hardness profile with respect to the thickness of the grain boundary Si_3N_4 phase [98]. Other nitride phases that can provide superhardness may include VN, NbN, ZrN, and (TiAl)N, again embedded in an amorphous Si_3N_4 matrix [2,52,80,99]. Because of their superhardness, these coatings can provide excellent protection against wear and oxidation when used in high-speed machining or high-temperature metal-forming operations. Their friction coefficients are not very low, especially when used under dry-sliding conditions, but under lubricated-sliding conditions, they can also provide very low friction coefficients. From an application point of view, a combination of superhardness and superlow friction is most desirable but seldom achieved in the field of tribology. Superhardness is primarily needed for protection against wear, whereas low friction is good for energy-saving purposes. Multilayer superhard coatings have been studied extensively in recent years by several researchers for their mechanical and tribological properties. In particular, systems that consist of CrN/NbN and TiAlN/VN have been studied extensively for their friction and wear performance, and significant improvements have been reported [4,79,100].

In some of the recent machining trials, nanocomposite TiN/Si_3N_4 coatings exhibited much better performance than conventional hard coatings such as TiN, TiC, and (TiAl)N. Figure 25.10 shows the

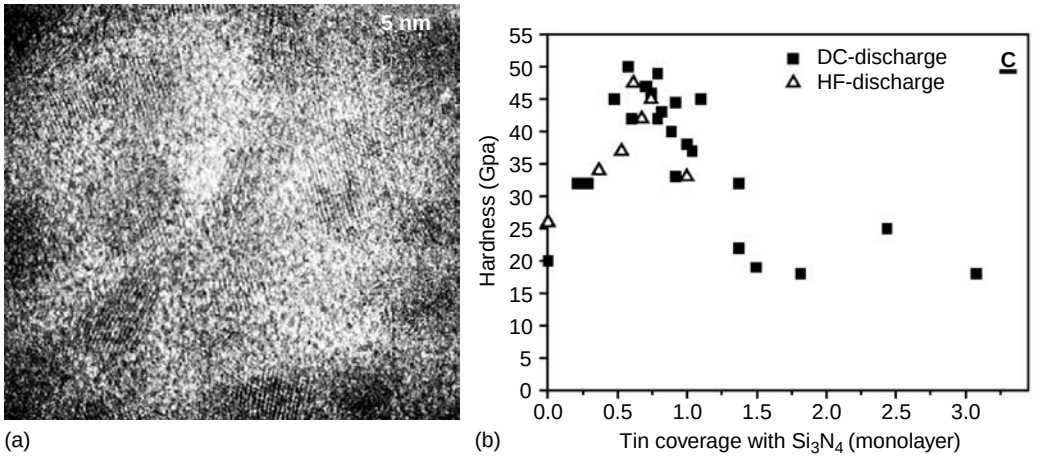

FIGURE 25.9 (a) Typical high-resolution TEM photomicrograph and (b) hardness dependence of TiN/Si_3N_4 nanocomposite coating on thickness of grain boundary Si_3N_4 phase. (From Veprek, S. et al., *Thin Solid Films*, 476, 1–29, with permission from Elsevier.)

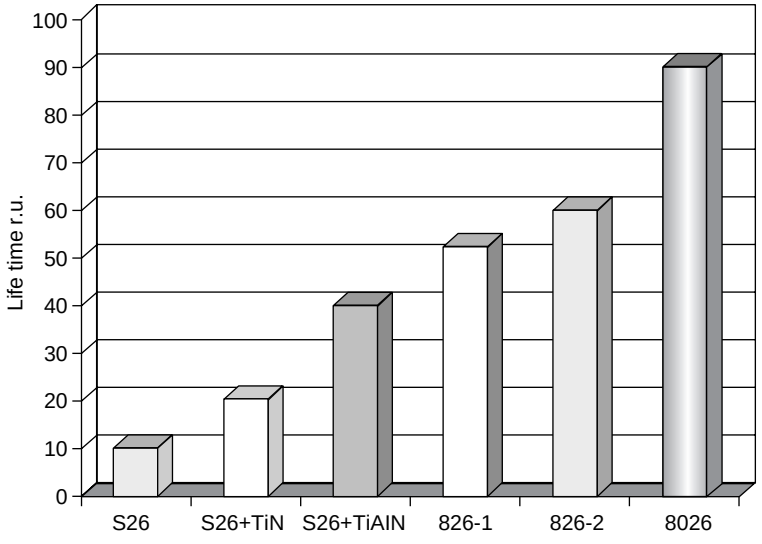

FIGURE 25.10 Cutting performance of various hard coatings while milling a CK45 steel (cutting conditions — feed rate, 0.23 mm/tooth; depth of cut, 2 mm; cutting speed, 179 m/min). S26, indexable uncoated insert; S26+TiN, TiN-coated; S26+TiAlN, (TiAl)N-coated; 826-1 and 826-2, same inserts coated with ($Ti_{1-x}Al_x$)N/a-Si_3N_4 nanocomposite coatings; and 8026: nc-($Ti_{1-x}Al_x$)N/a-Si_3N_4 multilayer nanocomposite coating. (From Veprek, S. and Jilek, M., *Pure Appl. Chem*., 74, 475–481, 2002, with permission from Elsevier.)

machining performance of some superhard coatings and conventional hard coatings [101]. With the use of novel lateral-rotating-arc cathodes during deposition, and virtual shutters for the precleaning of the cathodes, additional improvements have been achieved in the cutting performance of coated tools, particularly in dry machining. For example, when these nanocomposite coatings are used in dry drilling of hard steel, the lifetime of tools is increased by factors of 4 or more as compared to the state-of-the-art (AlTi)N-coated tools [4,101,102]. Under such machining conditions, the temperature of the cutting edge of tools may reach as high as 800°C. In addition to superhardness, these nanocomposite coatings are also expected to have very high thermal stability and high resistance to oxidation [102].

25.4.3 Nanostructured Carbon Films

Carbon as an element constitutes the building block of some of the hardest known materials (e.g., diamond, boron carbide, and transition metal carbides). It is also a key ingredient of some of the well-known nanomaterials, such as fullerenes, nanotubes, nano-onions, nanofibers, nanoscale carbon, and carbon nitride coatings [103]. Besides diamond and DLC, other carbon-based tribomaterials (such as graphite, graphite fluoride, glassy carbon, and carbon–carbon or carbon–graphite composites) have also been in use for quite some time for combating friction and wear. In particular, diamond and DLC coatings are very effective in reducing sliding friction and wear of machine elements and, hence, are used extensively by industry as solid lubricants. Carbon-based bulk composites are also an important class of tribomaterials, providing some of the lowest friction coefficients and high resistance to heat. The low-friction carbon composites are primarily used as seal materials by the rotating-equipment industry, whereas the high-friction carbon–carbon composites are used in the making of high-performance brakes for racing cars and various aircrafts.

In recent years, carbon has been used as a precursor for the production of several nanocomposite and nanocrystalline coatings. In particular, the production of nanostructured diamond and carbide-derived carbon films has been achieved and a series of carbon-based nanocomposite films were realized and offered for use in demanding tribological applications.

25.4.3.1 Nanocrystalline Diamond Films

As the hardest natural material known, diamond offers huge possibilities for combating friction and wear in numerous engineering applications. Because of its high chemical inertness, diamond also provides very low friction coefficients to sliding surfaces. Synthetic diamond films can be produced on tribological surfaces by several CVD methods [58,103]. However, the surface finish of most conventional diamond films is very rough. This roughness can cause severe wear losses on most sliding surfaces. In recent years, researchers have developed effective polishing methods (e.g., laser polishing) to achieve a smoother surface finish on diamond films. However, these polishing processes are rather expensive, and, in the case of complex geometries, they are impractical. During the past decade or so, new procedures have been developed for the deposition of very smooth (hence, less abrasive) nanocrystalline diamond films. Specifically, by using proper seeding techniques and plasmas based on Ar–C_{60} and Ar–CH_4 gas mixtures in microwave CVD systems, phase-pure nanocrystalline diamond films have been developed in our laboratory [15]. The grain size of these films is in the range of 2 to 5 nm, and their surface finish is 10 to 20 nm, RMS. Figure 25.11 shows structural details of a nanocrystalline diamond film. When used on sliding bearing surfaces, these films could provide friction coefficients of $\leq$0.05 [104–106]. Figure 25.12 summarizes the frictional performance of crystalline diamond films that exhibit varying degrees of roughness. This figure also shows the surface morphology of micro- vs. nanocrystalline diamond films. Because of their superhardness and low friction, nanocrystalline diamond films can be very useful in metal-cutting and -forming operations and in sliding or rotatingbearing applications (such as mechanical seals). In recent years [107], these diamond films have also been used in making various microelectromechanical systems (MEMS).

25.4.3.2 Nanostructured Carbide-Derived Carbon

Besides the nanocrystalline diamond films discussed above, carbide-derived carbon (CDC) films can also provide very low friction and wear coefficients to sliding contact surfaces [108]. These films are typically produced on the outer surfaces of carbide-based ceramics essentially by reacting them with chlorine or chlorine–hydrogen gas mixtures in a sealed reactor [16,108–110]. Unlike the plasma-based CVD and PVD methods that are necessary for the synthesis of diamond and other hard coatings, this new method require neither a high vacuum nor a gas discharge plasma. It is performed at atmospheric pressures in a tube furnace by simply passing chlorine or a mixture of chlorine and

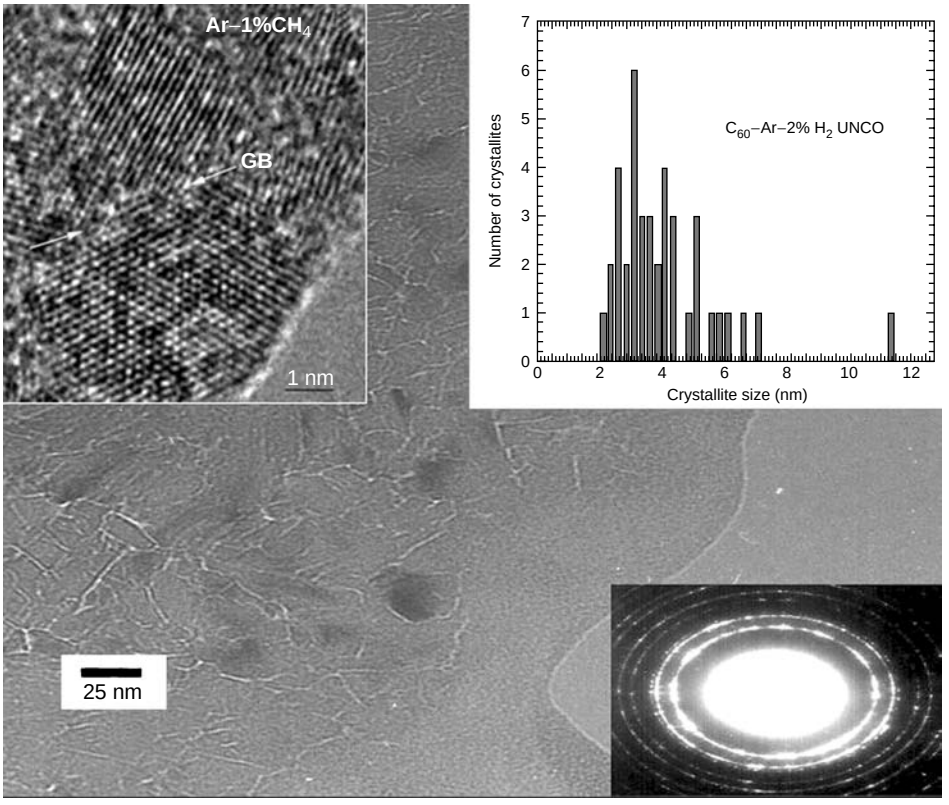

FIGURE 25.11 TEM image of nanocrystalline diamond film. (Left inset shows details of nanograins and grain boundaries; right inset shows grain size distribution.)

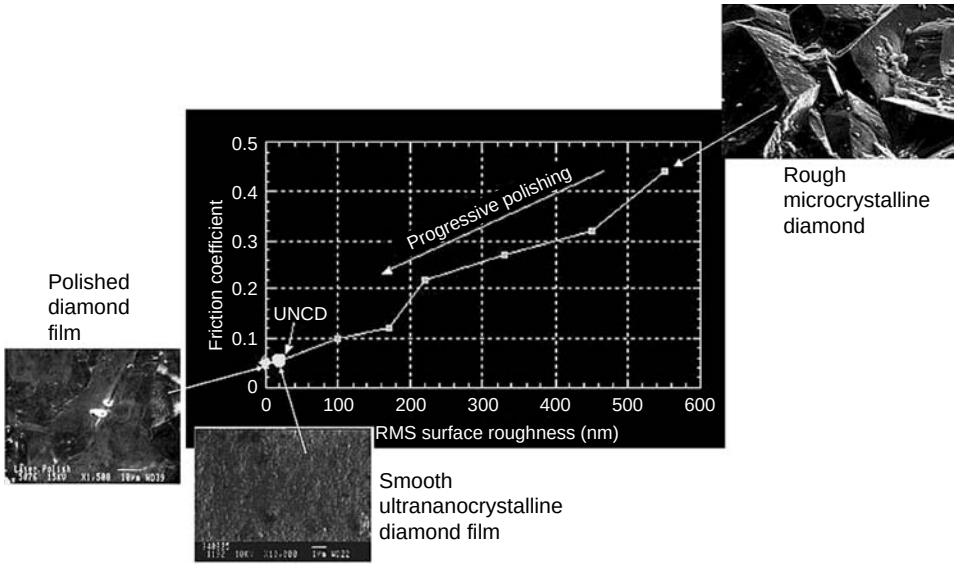

FIGURE 25.12 Frictional behavior of microcrystalline, nanocrystalline, and polished diamond films. Note that friction coefficient of microcrystalline diamond film is ten times higher.

hydrogen gases over the carbide-based substrates at temperatures of 600 to 1100°C. Chlorine in the gas mixture reacts preferentially with metal atoms and etches them away. In the case of SiC, the reaction product is $SiCl_4$, which is volatile and thus easily removed. The carbon atoms left behind on the surface rearrange themselves to form a truly nanostructured carbon film, which is composed of nanocrystalline diamond and graphite phases, carbon nanoonions, and amorphous carbon [16,108]. Figure 25.13 shows the typical microstructure of these coatings [16].

By controlling process parameters, the structure and properties of CDC films can easily be manipulated or fine-tuned to meet the specific application needs of a given tribological system. Recent experimental studies have shown that the friction properties of these films are quite sensitive to test environments [111,112]. In humid air, their friction coefficients are comparable to those of highly oriented pyrolitic graphite, whereas in dry nitrogen or vacuum, the friction values may vary greatly. Figure 25.14 shows the friction coefficient of CDC and SiC. Certain CDC films can provide friction coefficients less than 0.1 in dry nitrogen but others exhibit much higher friction (perhaps due to some structural or topographical differences). By exposing these films to post-deposition hydrogenation, their friction coefficients can be reduced to values in dry nitrogen of less than 0.05 [113]. These low-friction carbon films hold promise for applications that involve MEMS, electrical contacts, biomedical implants, and mechanical seals.

25.4.3.3 Nanocomposite Diamond-Like Carbon Films

Diamond-like carbon films are generally amorphous and made of a mixture of sp^2- and sp^3-hybridized carbon atoms. If they are derived from hydrocarbons or produced in a hydrogen-containing argon plasma, they may also contain some hydrogen in their structure. Tribologically, they can provide very low friction and high wear resistance to sliding surfaces. At present, they are used in a wide range of tribological applications that range from magnetic hard disks to various automotive parts and components. To improve further their tribological functionality, researchers have been introducing additional crystalline phases into these films. Such nanocomposite films are thought to provide even lower friction and wear and significantly higher load-carrying capacity.

Among others, recently developed multilayer DLC coatings have been studied extensively by several investigators for their mechanical and tribological properties. In particular, films of C/W and

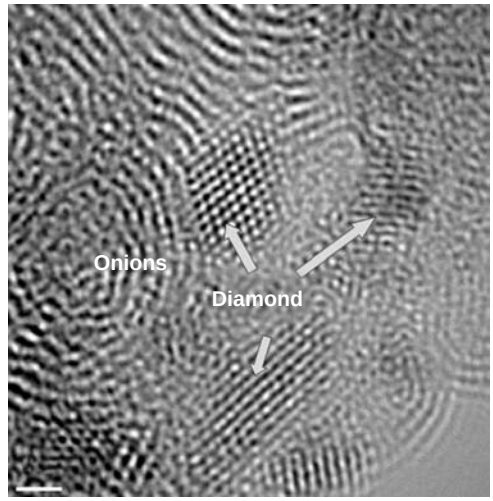

FIGURE 25.13 High-resolution TEM photomicrograph of nanostructured CDC film on SiC substrate. Sample was treated for 24 h at 1000°C in Ar/3.5% Cl_2. (From Gogotsi, Y. et al., *Nature*, 411, 283–287, 2001, with permission from Elsevier.)

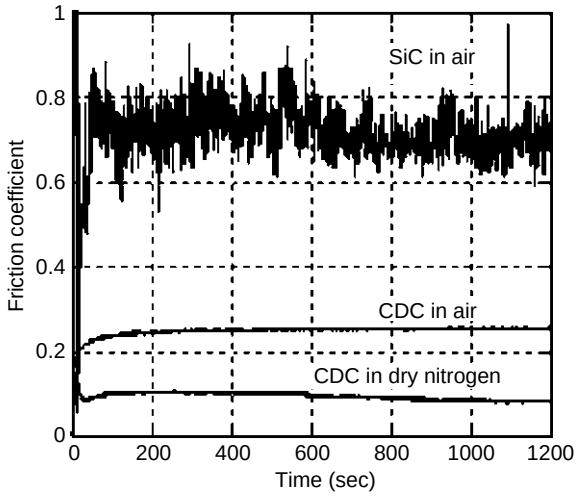

FIGURE 25.14 Friction performance of CDC against Si_3N_4 ball in humid air and dry nitrogen. For comparison, friction coefficient of SiC is also provided.

C/Cr multilayers have attracted the most attention [44,46,75]. These coatings have been produced on steel substrates and evaluated for their tribological properties under a wide range of dry- and lubricated-sliding conditions [114–116]. The results indicate that these coatings indeed possess superior load-carrying capacity and wear resistance not only in laboratory tests but also in actual applications.

Some of the nanostructured carbon films consisted of nanoscale carbide and other crystalline phases that are evenly dispersed or imbedded into the amorphous carbon matrix. Figure 25.3 shows a few examples of nanolayered and nanocomposite carbon films that are currently used for a wide range of tribological applications. Crystalline carbide grains in these films are measured on the nanometer scale and they are evenly distributed within the amorphous DLC films. When compared with conventional or monophase DLC films, these nanocomposite films possess an unusual combination of high mechanical hardness and toughness.

25.5 NOVEL DESIGN CONCEPTS FOR SELF-LUBRICATING NANOCOMPOSITE FILMS FOR HIGH-TEMPERATURE APPLICATIONS

Some of the critical tribological applications (such as forging, rolling, piston ring and cylinder liner assemblies, and turbomachines) involve harsh operating conditions in the form of high temperatures, high speeds, oxidizing environments, etc. Among other conditions, increasing operating temperatures of certain tribological systems are rendering most of the liquid and solid lubricants ineffective or essentially useless. One of the major degradation mechanisms in high-temperature applications is related to oxidation. Specifically, the sliding interfaces of tribo-systems are oxidizing, and the thin oxide films that are formed on these surfaces then dominate friction and wear. Most of the oxides are known to be very hard and hence abrasive, but certain oxides do soften and hence shear easily at high temperatures.

Advanced PVD and CVD systems available today can be used to formulate nanoalloyed or composite coatings that can lead to the formation of such low-shear-strength oxides, which are often referred to as lubricious oxides. Recent experimental studies have demonstrated that the oxides of Re, Ti, Ni, W, Mo, Zn, V, B, etc. are very lubricious and hence can provide fairly low friction at elevated temperatures [117,118]. When two or more alloying elements or phases are present in a nanocomposite film, mixed lubricious oxides (such as $CuO–Re_2O_7$, $CuO–MoO_3$, $PbO–B_2O_3$, $PbO–MoO_3$, $CoO–MoO_3$, $Cs_2O–MoO_3$, $NiO–MoO_3$) may form on sliding surfaces and provide low

friction coefficients (i.e., 0.1 to 0.4) [3,57]. The major drawbacks of oxide-based solid lubricants are that they are inherently brittle and thus may easily fracture and wear out quickly. Furthermore, most oxide-based lubricants do not provide lubrication down to room temperature. Potential applications for lubricious oxides include high-temperature seals, bearings, and gears, valves and valve seats, variable stator vanes, and foil bearings.

Recently, a crystal-chemical approach was introduced by Erdemir [119] to classify lubricious oxides on the basis of their lubrication performance and operational limits. This approach was proposed to serve as a guide for determining the kind(s) of lubricious oxides that are needed on a sliding surface at high temperatures. Apparently, the crystal chemistry of certain oxides that form on sliding surfaces relates strongly to their shear rheology and hence their lubricity at high temperatures.

The crystal-chemical approach is based essentially on the ionic potential of an oxide and is defined as Z/r, where Z is the cationic charge and r the radius of the cation. Apparently, ionic potential controls several key physical and chemical phenomena in oxides. In general, the higher the ionic potential, the greater the extent of screening of a cation in an oxide by surrounding anions. Oxides with highly screened cations (such as B_2O_3 or Re_2O_7) are generally soft and hence easily sheared at elevated temperatures. Their cations are well separated and completely screened by anions; hence, they participate in little or no chemical interactions with other cations in the system. Most of their bonding is with surrounding anions. As can be deduced from Figure 25.15, the higher the ionic potential, the lower the friction coefficient. This means that oxides with higher ionic potentials appear to shear more easily and thus exhibit lower friction at high temperatures.

In nanocomposite coatings, more than two chemically dissimilar solid phases are present. When such coatings are rubbed against another material or against themselves, then there is no doubt that there will be more than one kind of oxide on the sliding surface. The crystal-chemical approach may be used as a guide in the formulation of such nanocomposite films so that complex oxide layers that form on their sliding surfaces may have low shear, and hence, low friction. Figure 25.16 shows several cases in which two oxides ($CuO–Re_2O_7$, $CuO–MoO_3$, $PbO–B_2O_3$, $PbO–MoO_3$, $CoO–MoO_3$, and $NiO–MoO_3$, etc.) were either present at or purposely introduced to sliding interfaces to achieve low friction at high temperatures. As can be expected, there is a reasonable correlation between the

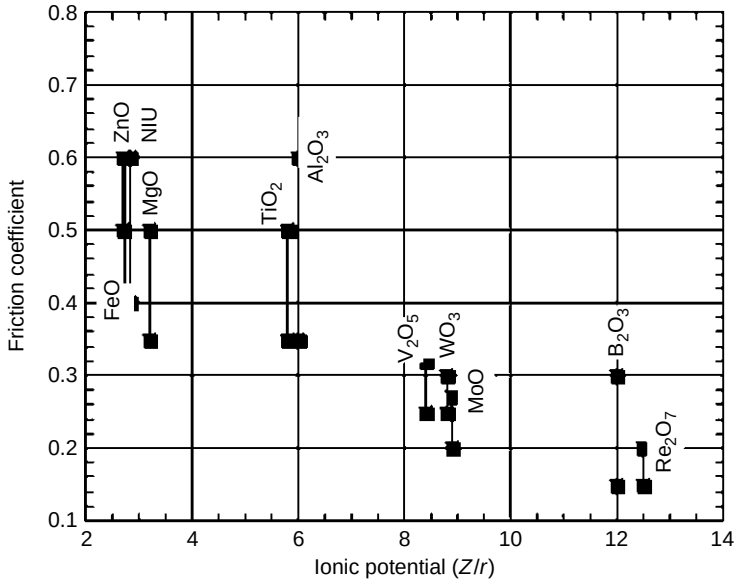

FIGURE 25.15 Relationship of friction coefficients of certain oxides to their ionic potentials. (From Erdemir, A., *Tribol. Lett.*, 8, 97–102, 2000.)

difference in ionic potentials of these oxides and the levels of friction coefficients measured at high temperatures [119].

The crystal-chemical approach presented above may have broad practical implications for the design or formulation of novel self-lubricating nanocomposite coatings. Such coatings may find applications in metal-cutting and metal-forming operations, wherein high temperature always exists and causes severe adhesive and oxidative wear of cutting- or forming-tool surfaces. The lubrication of such tools by traditional means (i.e., using metal-working fluids) is becoming more and more difficult, mainly because of increasingly more stringent environmental regulations. What will be very desirable is a tool that needs little or no external lubrication.

Most cutting and forming tools used by industry today are coated with a hard nitride or carbide film. Nowadays, they are increasingly coated with a nanocomposite coating that functions quite well when used in externally lubricated cutting or forming operations. However, when used under dry or marginally lubricated cutting operations, they fail rather quickly. By incorporating certain alloys or nanophases in these coatings, one can potentially improve the performance and durability of these tools. These alloying elements or phases must be selected in such a way that they promote the formation of lubricious oxides on cutting or forming surfaces of the tools during operation. Similar lubrication approaches may also be used in the formulation of novel thermal or plasma spray coatings that are already used in various engine components, and in rolls and dies that are used in high-temperature forging or metal-forming operations.

In recent years, several attempts have been made to incorporate lubricious oxides and oxide-forming elements into hard coating systems to achieve better performance and longer life in cutting tools and various tribological systems. In one of these attempts, researchers have incorporated tungsten and vanadium oxides into the coating systems and achieved reasonably low friction and wear coefficients at elevated temperatures [120]. In another study, vanadium was purposely added to TiAlN coatings with the hope that it would produce V_2O_5 as a lubricious oxide and thus enable dry machining. Dry-sliding tests showed that the friction coefficient of such a composite coating dropped from 0.6–0.8 to about 0.18 at 700°C. It was concluded that the addition of vanadium to hard coatings holds promise for achieving greater lubricity during dry machining, mainly because

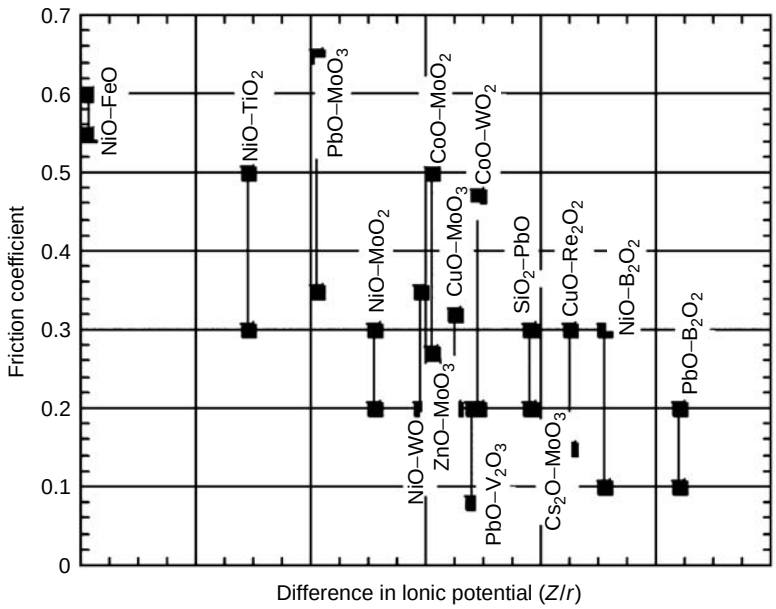

FIGURE 25.16 Relationship of friction coefficients of certain double oxides to differences in their ionic potentials. (From Erdemir, A., *Tribol. Lett.*, 8, 97–102, 2000.)

of the formation of V_2O_5 and other easily shearable lower oxidizes of vanadium [49]. As suggested by Figure 25.15, ionic potentials of V_2O_5 are high and hence the lubricity of this material at high temperatures is high.

Gulbinski et al. [121] studied the dry-sliding behavior of pure MoO_3 and V_2O_5 as well as composite phases that originate from Ag_2O–MoO_3, Cu–V_2O_5, and Ag–V_2O_5. All of these phases lowered friction, but the best results were obtained from surfaces that formed silver molybdate (Ag_2MoO_4) and silver–vanadium oxides (the reported friction coefficients were ≈0.2). Note that these complex oxides also exhibit low ionic potentials. In fundamental studies, researchers have also achieved low friction on certain oxides that form low-shear Magneli phases [22,122]. They mainly are the result of tribo-oxidation at sliding interfaces and once formed, they can dominate friction and wear.

25.6 SUMMARY

In this chapter, we provide an overview of recent advances in the production and uses of nanostructured and composite coatings in tribology. Unlike conventional coatings, nanostructured and composite coatings offer a combination of low friction and high wear resistance to sliding surfaces under a wide range of tribological conditions. Structurally, they consist of two or more phases that are mixed in a very special manner to provide a very dense structural morphology. These coatings may be super-hard and exhibit very low friction and wear coefficients. The type of grain-boundary phases seems to play a major role in their hardness and other properties. Multi-layer coatings, with layer thicknesses that range from a few atoms to several nanometers are also available and can provide superior mechanical and tribological properties. At present, several PVD and CVD techniques are available to reliably deposit nanostructured and composite coatings on several metallic and ceramic substrates. Some of the films (such as nanocrystalline diamond, CDC, and DLC) are self-lubricating and may provide friction coefficients of less than 0.1, even under very harsh sliding conditions. These films hold promise for a wide range of tribological applications (such as mechanical face seals, MEMS, engine and drivetrain components, and invasive or implantable medical devices). Another important development in the field is the design and production of self-lubricating nanocomposite and multilayered coatings on various tribological components. Because of their low friction, these coatings can be very useful in extreme tribological applications such as aerospace and green manufacturing. For applications that involve high temperatures, the development of thermally stable, self-lubricating coatings is essential. Recently, a crystal-chemical approach was introduced to understand better and classify lubricious oxides or oxide-forming nanocomposites on the basis of their lubrication performance and operational limits at high temperatures. This approach may serve as a basis for the design of novel nanocomposite coatings that can produce the kind(s) of lubricious oxides that are needed on sliding surface at high temperatures.

ACKNOWLEDGMENTS

This work is supported by the U.S. Department of Energy, Office of Energy Efficiency and Renewable Energy, Freedom Car & Heavy Vehicle Technologies Program, under Contract W-31-109-Eng-38. The authors thank R. Dielis of Hauzer Techno Coating and D. Teer of Teer Coatings, Ltd for providing some of the figures used in Figures 25.2 and 25.3.

This chapter has been created by the University of Chicago as Operator of Argonne National Laboratory (“Argonne”) under Contract No. W-31-109-ENG-38 with the U.S. Department of Energy. The U.S. Government retains for itself, and others acting on its behalf, a paid-up, nonexclusive, irrevocable worldwide license in said article to reproduce, prepare derivative works, distribute copies to the public, and perform publicly and display publicly, by or on behalf of the Government.

REFERENCES

1. Musil, J. (2005) *Physical and Mechanical Properties of Hard Nanocomposite Films Prepared by Magnetron Sputtering, Nanostructured Hard Coatings*, Kluwer Academic, New York, pp. 1–46.
2. Veprek, S. (2004) Superhard nanocomposites: design concept, properties, present and future industrial applications, *Eur. Phys. J. App. Phys.*, 28, 313–317.
3. Donnet, C. and Erdemir, A. (2004) Historical developments and new trends in tribological and solid lubricant coatings, *Surf. Coat. Technol*., 180–181, 76–84.
4. Jilek, M., Cselle, T., Holubar, P., Morstein, M., Veprek-Heijman, M.G.J., and Veprek, S. (2004) Development of novel coating technology by vacuum arc with rotating cathodes for industrial production of nc-$(Al_{1-x}Ti_x)$N/a-Si_3N_4 superhard nanocomposite coatings for dry, hard machining, *Plasma Chem. Plasma Process*., 24, 493–510.
5. Zhang, S., Sun, D., Fu, Y., and Du, H. (2003) Recent advances of superhard nanocomposite coatings: a review, *Surf. Coat. Technol*., 167, 113–119.
6. Holubar, P., Jilek, M., and Sima, M. (2000) Present and possible future applications of superhard nanocomposite coatings, *Surf. Coat. Technol.*, 133–134, 145–151.
7. Erdemir, A. (2005) Review of engineered tribological interfaces for improved boundary lubrication, *Tribol. Int.*, 38, 249–256.
8. Chen, Y-H., Polonsky, I.A., Chung, Y-W., and Keer, L.M. (2002) Tribological properties and rolling-contact-fatigue lives of TiN/SiN_x multilayer coatings, *Surf. Coat. Technol.*, 154, 152–161.
9. Leyland, A. and Matthews, A. (2000) On the significance of the *H*/*E* ratio in wear control: a nanocomposite coating approach to optimised tribological behaviour, *Wear*, 246, 1–11.
10. Ajayan, P. M., Schadler, L.S., and Braun, P.V. (2003) *Nanocomposite Science and Technology*, Wiley-VCH-Verlag GmbH, Weinheim, Germany.
11. Nalwa, H.S. (2003) Handbook of Organic-Inorganic Hybrid Materials and Nanocomposites, Vol. 1–2, Stevenson Ranch, CA, USA, American Scientific Publishers.
12. Lee, K.Y. and Goettler, L.A. (2004) Structure-property relationships in polymer blend nanocomposites, *Polym. Eng. Sci.*, 44, 1103–1111.
13. Vollath, D. and Szabo, D. V. (2004) Synthesis and properties of nanocomposites, *Adv. Eng. Mater*., 6, 117–127.
14. Karvankova, P., Veprek-Heijman, M.G.J., Zindulka, O., Bergmaier, A., and Veprek, S. (2003) Superhard nc-TiN/a-BN and nc-TiN/a-TiB_x/a-BN coatings prepared by plasma CVD and PVD: a comparative study of their properties, *Surf. Coat. Technol.*, 163–164, 149–156.
15. Gruen, D.M. (1999) Nanocrystalline diamond films, *Annu. Rev. Mater. Sci*., 29, 211–259.
16. Gogotsi, Y., Welz, S., Ersoy, D.A., and McNallan, M.J. (2001) Conversion of silicon carbide to crystalline diamond-structured carbon at ambient pressure, *Nature*, 411, 283–287.
17. Mitterer, C. and Mayrhofer, P.H. (2004) Design of nanostructured hard coatings for optimum performance, *Key Eng. Mater*., 264–268, 453–458.
18. Holleck, H., Leiste, H., Stuber, A., and Ulrich, S. (2003) Nanoscale protective coatings for highly stressed tools and components, *Z. Metallkunde*, 94, 621–627.
19. Lugscheider, E., Bobzin, K., Pinero, C., Klocke, F., and Massmann, T. (2004) Development of a superlattice (ti, hf, cr) n coating for cold metal forming applications, *Surf. Coat. Technol*., 177, 616–622.
20. Boyde, S. (2002) Green lubricants. Environmental benefits and impacts of lubrication, *Green Chem.*, 4, 293–307.
21. Gamulya, G.D., Ostrovskaya, E.L., and Yukhno, T.P. (2001) Tribological properties of materials for use under extreme conditions, *Powder Metall. Metal Ceram.*, 40, 135–143.
22. Kutschej, K., Mayrhofer, P.H., Kathrein, M., Polcik, P., and Mitterer, C. (2004) A new low-friction concept for $Ti_{1-x}Al_xN$ based coatings in high-temperature applications, *Surf. Coat. Technol*., 188–189, 358–363.
23. Schramm, B.C., Scheerer, H., Hoche, H., Broszeit, E., Abele, E., and Berger, C. (2004) Tribological properties and dry machining characteristics of PVD-coated carbide, *Surf. Coat. Technol.*, 188–189, 623–629.
24. Mitterer, C. and Mayrhofer, P.H. (2001) Some materials science aspects of pvd hard coatings, *Adv. Solid State Phys.*, 41, 263–274.
25. Hauert, R., Patscheider, J., Knoblauch, L., and Diserens, M. (1999) New coatings by nanostructuring, *Adv. Mater*., 11, 175–177.

26. Chung, Y-W. and Sproul, W.D. (2003) Superhard coating materials, *MRS Bulletin*, 28, 164–168.
27. Münz, W.D. (2000) Super lattice-structured hard coatings, in *Trends and Applications of Thin Films*, Vides, Nancy, pp. 12–16.
28. Wu, J.H., Rigney, D.A., Falk, M.L., Sanders, J.H., Voevodin, A.A., and Zabinski, J.S. (2004) Tribological behavior of WC/DLC/WS_2 nanocomposite coatings, *Surf. Coat. Technol.*, 188–189, 605–611.
29. Voevodin, A.A., O'Neill, J.P., and Zabinski, J.S. (1999) Nanocomposite tribological coatings for aerospace applications, *Surf. Coat. Technol.*, 119, 36–45.
30. Donnet, C. and Erdemir, A. (2004) Solid lubricant coatings: recent developments and future trends, *Tribol. Lett.*, 17, 389–397.
31. Teer, D.G. (2001) New solid lubricant coatings, *Wear*, 251, 1068–1074.
32. Bunshah, R.F. (2001) *Handbook of Hard Coatings*, William Andrew Publishing, Noyes, Park Ridge, NJ.
33. Mattox, D.M. (1998) *Handbook of Physical Vapor Deposition (PVD) Processing*, William Andrew Publishing, Noyes.
34. Seshan, K. (2002) Handbook of Thin-Film Deposition Processes and Techniques — Principles, Methods, Equipment and Applications, William Andrew Publishing, Noyes.
35. Choy, K.L. (2003) Chemical vapour deposition of coatings, *Prog. Mater. Sci.*, 48, 57–170.
36. Safaie, S., Pochet, L. F., and Howard, C. (1997) CVD coatings: From cutting tools to aerospace applications and their future potential, *Surf. Coat. Technol*., 94–95, 70–77.
37. Schneider, J. M., Rohde, S. L., Sproul, W. D., and Matthews, A. (2000) Recent developments in plasma assisted physical vapour deposition, *J. Phys. Appl. Phys*., 33, 173–186.
38. Bergmann, E., van der Kolk, G. I., Buil, B., and Hurkmans, T. (1999) The next generation of deposition equipment for wear protection coatings, *Surf. Coat. Technol*., 114, 101–107.
39. Loir, A.S., Garrelie, F., and Donnet, F. (2004) Toward the deposition of tetrahedral diamondlike carbon films on hip joints by femtosecond pulsed laser ablation, *Surf. Coat. Technol.*, 188–189, 728–734.
40. Jeon, J.H., Choi, S.R., and Chung, W.S. (2004) Synthesis and characterization of quaternary Ti-Si-C-N coatings prepared by a hybrid deposition technique, *Surf. Coat. Technol.*, 188–189, 415–419.
41. Goller, R., Torri, P., and Baker, M.A. (1999) The deposition of low-friction TiN-MoSx hard coatings by a combined arc evaporation and magnetron sputter process, *Surf. Coat. Technol*., 121, 453–457.
42. Celis, J.P., Drees, D., Huq, M.Z., Wu, P.Q., and De Bonte, M., (1999) Hybrid processes — a versatile technique to match process requirements and coating needs, *Surf. Coat. Technol*., 113, 165–181.
43. Renevier, N.M., Oosterling, H., Konig, U., Dautzenberg, H., Kim, B.J., Geppert, L., Koopmans, F.G.M., and Leopold, J. (2003) Performance and limitation of hybrid PECVD (hard coating) — PVD magnetron sputtering (MoS_2/Ti composite) coated inserts tested for dry high-speed milling of steel and grey cast iron, *Surf. Coat. Technol.*, 163, 659–667.
44. Hovsepian, P.E., Lewis, D.B., Constable, C., Luo, Q., Kok, Y.N., and Münz, W.D. (2003) Combined steered cathodic arc/unbalanced magnetron grown C/Cr nanoscale multilayer coatings for tribological applications, *Surf. Coat. Technol.*, 174, 762–769.
45. Strondl, C., Carvalho, N.M., De Hosson, J.T.M., and Van der Kolk, G.J. (2003) Investigation on the formation of tungsten carbide in tungsten-containing diamond like carbon coatings, *Surf. Coat. Technol.*, 162, 288–293.
46. Hovsepian, P.Eh., Kok, Y.N., Ehiasarian, A.P., Erdemir, A., Wen, J.G., and Petrov, I. (2004) Structure and tribological behaviour of nanoscale multilayer C/Cr coatings deposited by the combined steered cathodic arc/unbalanced magnetron sputtering technique, *Thin Solid Films*, 447–448, 7–13.
47. Meng, W.J., Tittsworth, R.C., Jiang, J.C., Feng, B., Cao, D.M., Winkler, K., and Palshin, V. (2000) Ti atomic bonding environment in Ti-containing hydrocarbon coatings, *J. Appl. Phys.*, 88, 2415–2422.
48. Gassner, G., Mayrhofer, P.H., Kutschej, K., Mitterer, C., and Kathrein, M. (2004) A new low-friction concept for high temperatures: lubricious oxide formation on sputtered VN coatings, *Tribol. Lett.*, 17, 751–756.
49. Mayrhofer, P.H., Hovsepian, P.E., Mitterer, C., and Münz, W.D. (2004) Calorimetric evidence for frictional self-adaptation of TiAlN/VN superlattice coatings, *Surf. Coat. Technol.*, 177, 341–347.
50. Canter, N.M. (2003) The possibilities and limitations of dry machining, *Tribol. Lubr. Technol.*, 11, 30–35.
51. Yau, B.S., Huang, J.L., Lii, D.F., and Sajgalik, P. (2004) Investigation of nanocrystal-(Ti,AI)N-x/amorphous-SiNy composite films by co-deposition process, *Surf. Coat. Technol.*, 177, 209–214.

52. Veprek, S., Niederhofer, A., Moto, K., Bolom, T., Mannling, H.D., Nesladek, P., Dollinger, G., and Bergmaier, A. (2000) Composition, nanostructure, and origin of the ultrahardness in nc-TiN/a-Si_3N_4/a- and nc-$TiSi_2$ nanocomposites with H-v = 80 to <= 105 GPa, *Surf. Coat. Technol.*, 133, 152–159.
53. Perry, A.J. and Teer, D.G. (1997) Surface technology for temperature-sensitive materials, *Surf. Coat. Technol*., 97, 244–249.
54. Knotek, O., Loffler, F., Kramer, G., and Stossel, C. (1992) Reproducible arc-pvd process management under various reactive gases source, *Vacuum*, 43, 567–571.
55. Sproul, W.D., Christie, D.J., Carter, D.C., Tomasel, F., and Linz, T. (2004) Pulsed plasmas for sputtering applications, *Surf. Eng.*, 20, 174–176.
56. Ehiasarian, A.P., Münz, W.D., Hultman, L., Helmersson, U., and Petrov, I. (2003) High-power pulsed-magnetron-sputtered CrNx films, *Surf. Coat. Technol*., 163, 267–272.
57. Quinto, D.T. (1996) Technology perspective on CVD- and PVD-coated metal-cutting tools, *Int. J. Refract. Metals Hard Mater*., 14, 7–20.
58. Erdemir, A. (2001) Solid Lubricants and Self-lubricating Films, Handbook of Modern Tribology, CRC Press, Boca Raton, FL, pp. 787–818.
59. Erdemir, A. (2002) Friction and wear of diamond and diamond-like carbon films, *Proc. Inst. Mech. Eng. Part J – J. Eng. Tribol.*, 216, 387–400.
60. Lackner, J.M., Waldhauser, W., Berghauser, R., Ebner, R., Major B., and Schoberl, T. (2004) Structural, mechanical and tribological investigations of pulsed-laser-deposited titanium nitride coatings, *Thin Solid Films*, 453–454, 195–202.
61. Erdemir, A., Busch, D.E., Erck, R.A., Fenske, G.R., and Lee, R.H. (1991) Ion-beam-assisted deposition of silver films on zirconia ceramics for improved tribological behavior, *Lubr. Eng.*, 47, 863.
62. Meng, W.J., Curtis, T.J., Rehn, L.E., and Baldo, P.M. (1998) Plasma-assisted deposition and characterization of Ti-containing diamondlike carbon coatings, *J. Appl. Phys*., 83, 6076–6081.
63. Yao, S.H., Kao, W.H., Su, Y.L., and Liu, T.H. (2004) On the tribology and micro-drilling performance of TiN/AlN nanolayer coatings, *Mater. Sci. Eng. A-Struct. Mater. Properties Microstruct. Process.*, 386, 149–155.
64. Zhou, Z., Rainforth, W.M., Rother, B., Ehiasarian, A.P., Hovsepian, P.Eh., and Münz, W.D. (2004) Elemental distributions and substrate rotation in industrial TiAlN/VN superlattice hard PVD coatings, *Surf. Coat. Technol.*, 183, 275–282.
65. Barnett, S.A. and Madan, A. (2004) Hardness and stability of metal–nitride nanoscale multilayers, *Scr. Mater*., 50, 739–744.
66. Hultman, L., Engström, C., and Odén, M. (2000) Mechanical and thermal stability of TiN/NbN superlattice thin films, *Surf. Coat. Technol.*, 133–134, 227–233.
67. Musil, J., Zeman, P., Hruby, H., Mayrhofer, P.H. (1999b) ZrN/Cu nanocomposite film — a novel superhard material, *Surf. Coat. Technol.*, 120–121, 179–183.
68. Zeman, P., Cerstvy, R., Mayrhofer, P.H., Mitterer, C., and Musil, J. (2000) Structure and properties of hard and superhard Zr-Cu-N nanocomposite coatings, *Mater. Sci. Eng*. A, 289, 189–197.
69. Musil, J., Hruby, H., Zeman, P., Zeman, H., Cerstvy, R., Mayrhofer, P.H., and Mitterer, C. (2001) Hard and superhard nanocomposite Al-Cu-N films prepared by magnetron sputtering, *Surf. Coat. Technol.*, 142–144, 603–609.
70. Musil, J. and Vlcek, J. (2001) Magnetron sputtering of hard nanocomposite coatings and their properties, *Surf. Coat. Technol.*, 142–144, 557–566.
71. Musil, J., Leipner, I., and Kolega, M. (1999) Nanocrystalline and nanocomposite CrCu and CrCu-N films prepared by magnetron sputtering, *Surf. Coat. Technol.*, 115, 32–37.
72. He, J.L., Setsuhara, Y., Shimizu, I., and Miyake, S. (2001) Structure refinement and hardness enhancement of titanium nitride films by addition of copper, *Surf. Coat. Technol.*, 137, 38–42.
73. Gogotsi, Y.G., Jeon, I.D., and McNallan, M.J. (1997) Carbon coatings on silicon carbide by reaction with chlorine-containing gases, *J. Mater. Chem*., 7, 1841–1848.
74. Veprek, S., and Reiprich, S. (1995) A concept for the design of novel superhard coatings, *Thin Solid Films*, 268, 64–71.
75. Czyzniewski, A. (2003) Deposition and some properties of nanocrystalline WC and nanocomposite WC/a-C:H coatings, *Thin Solid Films*, 433, 180–185.
76. Veprek, S. (2000) Ultra Hard Nanocomposite Coatings with Hardness of 80 to 105 GPa, Societe Francaise du Vide, pp. 185–192.

77. Nesládek, P. and Veprek, S. (2000) Superhard nanocrystalline composites with hardness of diamond, *Phys. Stat. Sol*. A, 177, 53–62.
78. Holmberg, K., Matthews, A., and Ronkainen, H. (1998) Coatings tribology-contact mechanisms and surface design, *Tribol. Int.*, 31, 107–120.
79. Münz, W.D., Lewis, D.B., Hovsepian, P.E., Schonjahn, C., Ehiasarian, A., and Smith, I.J. (2001) Industrial-scale manufactured superlattice hard PVD coatings, *Surf. Eng*., 17, 15–27.
80. Veprek, S., Nesládek, P., Niederhofer, A., Glatz, F., Jílek, M., and Šíma, M. (1998) Recent progress in the superhard nanocrystalline composites: towards their industrialization and understanding of the origin of the superhardness, *Surf. Coat. Technol.*, 108–109, 138–147.
81. Rohatgi, P.K., Ray, S., and Liu, Y. (1992) Tribological properties of metal matrix graphite particle composites, *Int. Mat. Rev*., 37, 129–149.
82. Prasad, S.V. and McConnell, B.D. (1991) Tribology of aluminum metal-matrix composites, lubrication by graphite, *Wear*, 149, 241–253.
83. Friedrich, K., Lu, Z., and Hager, A.M. (1995) Recent advances in polymer composites tribology, *Wear*, 190, 139–144.
84. DellaCorte, C. and Sliney, H.E. (1990) Tribological Properties of PM 212: A High-Temperature Self-Lubricating Powder Metallurgy Composite, NASA TM-102355.
85. Zimmerman, F., Clark, D.G., Aust, K.T., and Erb, U. (2002) Pulse electrodeposition of Ni–SiC nanocomposite, *Mater. Lett.*, 52, 85–90.
86. Zabinski, J.S., Donley, M.S., Dyhouse, V.J., and McDevitt, N.T. (1992) Chemical and tribological characterization of PbO-MoS_2 films grown by pulsed laser deposition, *Thin Solid Films*, 214, 156–163.
87. Zabinski, J.S., Donley, M.S., Walck, S.D., Schneider, T.R., and McDevitt, N.T. (1995) Effects of dopants on the chemistry and tribology of sputter-deposited MoS_2 films, *Tribol. Trans*., 38, 894–904.
88. Hilton M.R., Bauer, R., Didziulis, S.V., Dugger, M.T., Keem, J., and Scholhamer, J. (1992) Structural and tribological studies of MoS_2 solid lubricant films having tailored metal-multilayer nanostructures, *Surf. Coat. Technol*., 53, 13–23.
89. Lince, J.R. (2004) Tribology of co-sputtered nanocomposite Au/MoS_2 solid lubricant films over a wide contact stress range, *Tribol. Lett.*, 17, 419–428.
90. Wahl, K.J., Seitzman, L.E., Bolster, R.N., and Singer, I.L. (1995) Low-friction, high-endurance, ion-beam-deposited Pb-Mo-S coatings, *Surf. Coat. Technol.*, 73, 152–159.
91. Ghorbani, M., Mazaheri, M., Khangholi, K., and Kharazi, Y. (2001) Electro deposition of graphite-brass composite coatings and characterization of their tribological properties, *Surf. Coat. Technol.*, 148, 71–76.
92. Voevodin, A.A. and Zabinski, J.S. (2000) Supertough wear-resistant coatings with 'chameleon' surface adaptation, *Thin Solid Films*, 370, 223–231.
93. Teer, D.G., Hampshire, J., Fox, V., and Bellido-Gonzalez, V. (1997) The tribological properties of MoS_2/metal composite coatings deposited by closed-field magnetron sputtering, *Surf. Coat. Technol.*, 94–95, 572–578.
94. Gilmore, R., Baker, M.A., Gibson, P.N., and Gissler, W. (1998) Preparation and Characterization of low-friction TiB_2-based coatings by incorporation of C or MoS_2, *Surf. Coat. Technol.*, 105, 45–50.
95. Simmonds, M.C., Savan, A., Van Swygenhoven, H., Pfluger, E., and Mikhailov, S. (1998) Structural, morphological, chemical and tribological investigations of sputter-deposited MoS_x/metal multilayer coatings, *Surf. Coat. Technol.*, 108–109, 340–344.
96. Voevodin, A.A., Bultman, J., and Zabinski, J.S. (1998) Investigation into three-dimensional laser processing of tribological coatings, *Surf. Coat. Technol.*, 107, 12–19.
97. Walck, S.D., Zabinski, J.S., McDevitt, N.T., and Bultman, J.E. (1997) Characterization of air_annealed, pulsed laser deposited ZnO-WS_2 solid film lubricants by transmission electron microscopy, *Thin Solid Films*, 305, 130–143.
98. Veprek, S., Veprek-Heijman, M.G.J, Karvankova, P., and Prochazka, J. (2005) Different approaches to superhard coatings and nanocomposites, *Thin Solid Films*, 476, 1–29.
99. Veprek, S. and Jilek, M. (2002) Super- and ultrahard nanacomposite coatings: generic concept for their preparation, properties and industrial applications, *Vacuum*, 67, 443–449.
100. Münz, W.D., Lewis, D.B., Hovsepian, P.E., Schönjahn, C., Ehiasarian, A., and Smith I.J. (2000) Industrial-scale manufactured superlattice hard PVD coatings, *J. Vac. Sci. Technol. A: Vac. Surf. Films*, 18, 1681–1689.

101. Veprek, S. and Jilek, M. (2002) Superhard nanocomposite coatings. From basic science toward industrialization, *Pure Appl. Chem*., 74, 475–481.
102. Jilek, M., Holubar, P., Veprek-Heijman, M., and Veprek S. (2003) Toward the industrialization of superhard nanocrystalline composites for high speed and dry machining, *MRS Symp. Proc.*, 750, 393.
103. Erdemir, A. and Donnet, C. (2000) in *Tribology of Diamond, Diamondlike Carbon and Related Films, Modern Tribology Handbook*, Bhushan, B., Ed., CRC Press, Boca Raton, FL, pp. 871–899.
104. Erdemir, A., Bindal, C., Fenske, G.R., Zuiker, C., Krauss, A.R., and Gruen, D.M. (1996) Friction and wear properties of smooth diamond films grown in fullerene plus argon plasmas, *Diamond Relat. Mater*., 5, 923–931.
105. Erdemir, A., Bindal, C., Fenske, G.R., Zuiker, C., Csencsits, R., Krauss, A.R., and Gruen, D.M. (1996) Tribological characterization of smooth diamond films grown in Ar-C-60 and Ar-CH4 plasmas, *Diamond Films Technol.*, 6, 31–47.
106. Erdemir, A., Fenske, G.R., Krauss, A.R., Gruen, D.M., McCauley, T., and Csencsits R.T. (1999) Tribological properties of nanocrystalline diamond films, *Surf. Coat. Technol.*, 121, 565–572.
107. Krauss, A.R., Auciello, O., Gruen, D.M., Jayatissa, A., Sumant, A., Tucek, J., Mancini, D.C., Moldovan, N., Erdemir, A., Ersoy, D., Gardos, M.N., Busmann, H.G., Meyer, E.M., and Ding, M.Q. (2001) Ultrananocrystalline diamond thin films for MEMS and moving mechanical assembly devices, *Diamond Relat. Mater*., 10, 1952–1961.
108. Ersoy, D.A., McNallan, M.J., Gogotsi, Y., and Erdemir, A. (2000) Tribological properties of carbon coatings produced by high-temperature chlorination of silicon carbide, *Tribol. Trans.*, 43, 809–815.
109. Ersoy, D.A., McNallan, M.J., and Gogotsi, Y. (2001) Carbon coatings produced by high-temperature chlorination of silicon carbide ceramics, *Mater. Res. Innovations*, 5, 55–62.
110. Welz, S., Gogotsi, Y., and McNallan, M.J. (2003) Nucleation, growth, and graphitization of diamond nanocrystals during chlorination of carbides, *J. Appl. Phys.*, 93, 4207–4214.
111. Carroll, B., Gogotsi, Y., Kovalchenko, A., Erdemir, A., and McNallan, M.J. (2004) Tribological characterization of carbide-derived carbon layers on silicon carbide for dry friction applications, *Key Eng. Mater*., 264–268, 465–468.
112. Carroll, B., Gogotsi, Y., Kovalchenko, A., Erdemir, A., and McNallan, M.J. (2003) Effect of humidity on the tribological properties of carbide-derived carbon (CDC) films on silicon carbide, *Tribol. Lett.*, 15, 51–55.
113. Erdemir, A., Kovalchenko, A., and McNallan, M.J. (2004) Effects of high-temperature hydrogenation treatment on sliding friction and wear behavior of carbide-derived carbon films, *Surf. Coat. Technol.*, 188–189, 588–593.
114. Podgornik, B., Viintin, J., Jacobson, S., and Hogmark, S. (2004) Tribological behaviour of WC/C coatings operating under different lubrication regimes, *Surf. Coat. Technol.*, 177–178, 558–565.
115. Wänstrand, O., Larsson, M., and Hedenqvist, P. (1999) Mechanical and tribological evaluation of PVD WC/C coatings, *Surf. Coat. Technol.*, 111, 247–254.
116. Voevodin, A.A., Prasad, S.V., and Zabinski, J.S. (1997) Nanocrystalline carbide amorphous carbon composites, *J. Appl. Phys.*, 82, 855–858.
117. Kanakia, M., Owens, M.E., and Ling, F.F. (1984) in Proceedings of Workshop on Fundamentals of High Temperature Friction and Wear with Emphasis on Solid Lubrication for Heat Engines, Industrial Tribology Institute, Troy, NY, pp. 19–38.
118. Kanakia, M.D. and Peterson, M.B. (1987) Literature Review of the Solid Lubrication Mechanisms, Interim Report, BFLRF #213, Southwest Research Institute, San Antonio, TX, pp. 6–18.
119. Erdemir, A. (2000) A crystal-chemical approach to lubrication by solid oxides, *Tribol. Lett*., 8, 97–102.
120. Lugscheider, E., Knotek, O., Barwulf, S., and Bobzin, K., (2001) Characteristic curves of voltage and current, and phase generation and properties of tungsten- and vanadium-oxides deposited by reactive d.c.-MSIP-PVD-process for self-lubricating applications, *Surf. Coat. Technol.*, 142–144, 137–142.
121. Gulbinski, W., Suszko, T., Sienicki, W., and Warcholinski, B. (2003) Tribological properties of silver- and copper-doped transition metal oxide coatings, *Wear*, 254, 129–135.
122. Storz, O., Gasthuber, H., and Woydt, M. (2001) Tribological properties of thermal-sprayed Magnéli-type coatings with different stoichiometries (Ti_nO_{2n-1}), *Surf. Coat. Technol.*, 140, 76–81.

26 Nanotextured Carbons for Electrochemical Energy Storage

François Béguin
Centre de Recherche sur la Matière Divisée, CNRS-Université, Orléans, France

Elzbieta Frackowiak
Institute of Chemistry and Technical Electrochemistry, Poznań University of Technology, Poznań, Poland

CONTENTS

26.1 GENERAL PROPERTIES OF CARBONS FOR ENERGY STORAGE

The exponential growth of the portable electronic devices' market together with the development of electric vehicles has created a continuously increasing demand for lightweight and compact electric power sources of high energy and power density. Among the many topics under investigation in industry and academic laboratories, the development of new materials is one of the most important.

For many years, nanotextured carbons have been shown as a basic material for the realization of high-performance power sources, e.g., supercapacitors, lithium-ion accumulators, or fuel cells.

The key factors that dictate the selection of carbon for this target are its accessibility, low cost, easy processability, as well as the different forms attainable (powder, fibers, foams, fabrics, composites) [1], adaptable porosity [2,3], and surface functionality [4,5]. Carbon electrodes are well polarizable, chemically stable in different solutions (acidic, basic, aprotic) and in a wide range of temperatures. The amphoteric character of carbons, both electron donor/acceptor, and the simultaneous presence of acidic/basic surface groups allows the electrochemical properties of materials based on this element to be extensively varied. A wide variety of carbon materials, e.g., graphites, cokes, mesocarbon microbeads, activated carbons, aerogels, xerogels, carbon blacks, carbon nanotubes, carbons from templates, etc. have been extensively considered as electrode materials for energy storage.

The nanotextural and chemical properties of carbons determine their efficiency for electrochemical application as electrodes. A strict control of the carbonization process (time, temperature, gas flow), the kind of natural or synthetic precursor and/or chemical vapor deposition conditions allow carbons with almost defined nanotexture and surface functionality to be prepared. The modification of carbon by an activation process gives a further possibility of modifying the properties, especially by highly developing the specific surface area [2]. Oxygenated surface groups can be created by treatment with liquid oxidants (e.g., aqueous solutions of HNO_3, H_2O_2, NaOCl). Alternatively, heat treatment of carbons under neutral atmosphere up to 700 to 800°C strongly diminishes the concentration of surface groups. Various advanced forms of carbon can be designed and prepared by a careful selection of templates with different dimensionalities, in such a way that one-, two-, or three-dimensional carbons can be obtained easily [6]. Taking into account the versatility for preparing various forms, there is a great interest in designing carbons for different energy storage devices.

The main preferred characteristics of carbon for all electrochemical applications are a good conductivity and wettability. Wettability is generally improved by the presence of a rich surface functionality, whereas electrical conductivity depends mainly on the thermal treatment conditions, nanotexture, hybridization of carbon, and content of heteroatoms. However, the electrolyte may be also decomposed by reaction with the surface groups of carbon that causes performance fading during cycling of the energy-storage systems. Therefore, the type of surface functionality must be perfectly adapted to the kind of device developed. Moreover, each electrochemical application involves completely different nanotextural properties of carbon characterized by its specific surface area, the presence of micro- and mesopores, their ratio, pore shapes, and so on. It is well known, for example, that carbon materials used as catalyst support in fuel cells should have a moderate surface area. By contrast, a highly developed surface area is required for good performance of supercapacitors; also, pore size must be adapted to ion size in order to ensure quick charge propagation.

Finally, besides its role of catalyst support or active electrode material, carbon can be also used in power sources as a conductivity additive. The most widely applied percolators are carbon blacks because of their availability and low cost. Recently, carbon nanotubes have been shown to be more efficient than carbon black [7], allowing new kind of composite electrodes to be developed.

The use of carbons for anodes of lithium-ion batteries is extensively discussed in the literature [8–10]. Therefore, in this chapter, we prefer to describe only the new trends related to the use of carbons for energy storage and, consequently, to focus mainly on the application of carbons in supercapacitors and for electrochemical hydrogen storage. An additional reason for this choice is related to very close electrochemical concepts for both applications where highly porous carbon materials are generally required.

26.2 SUPERCAPACITORS

26.2.1 Performance of Supercapacitors

Electrochemical capacitors (often called supercapacitors or ultracapacitors) [11–13] are very attractive power sources for portable systems and automotive applications due to their high specific

power and very long durability. In most cases, being often associated to a battery, they are used to deliver a high power during a short time, which in turn provides a high specific energy. Some applications of supercapacitors are hybrid power sources for electrical vehicles, computers, UPS, pulse laser technique, starters for engines, etc.

In a true electrochemical capacitor the charges are accumulated in the electrical double layer at the electrode/electrolyte interface. In contrast with typical accumulators, this process occurs without any charge transfer (faradaic) reaction. As shown in the schematic representation of Figure 26.1, an electrochemical capacitor is constituted of two electrodes on which the ions are fixed, the positive one with electron deficiency and the second one with electron excess (negative). The capacitance C_n of one electrode is given by

$$C_n = \frac{\varepsilon S}{d} \tag{26.1}$$

where ε is the permittivity or dielectric constant of the solution, S the surface area of the electrode/electrolyte interface, i.e., the electrode surface, and d the thickness of the electrical double layer. Taking into account that d is generally less than 1 nm, Equation (26.1) shows immediately the technological advantage of supercapacitors over conventional capacitors, giving rise to specific capacitances of approximately $0.1\,\mathrm{F/m^2}$. Moreover, if high-specific surface area activated carbons are used as substrate for ion adsorption, high values of capacitance may be reached. For example, assuming a specific capacitance of $0.1\,\mathrm{F/m^2}$ and a specific surface area of $1000\,\mathrm{m^2/g}$, it gives a capacitance value of 100 F/g of carbon.

From Figure 26.1, it is noteworthy that the overall capacitance C of the device results from the series connection of two capacitors C_1 and C_2, according to

$$\frac{1}{C} = \frac{1}{C_1} + \frac{1}{C_2} \tag{26.2}$$

where C_1 and C_2 represent the capacitance of each electrode. Hence, in the case of a capacitor built from electrodes of different surfaces, or more generally of different capacitances, the component with the smallest capacitance contributes more to the total value C due to the inverse dependence in formula (26.2).

The capacitance is expressed in F, which is the charge (in C) accumulated in a defined voltage range ($1\,\mathrm{F} = 1\,\mathrm{C}/1\,\mathrm{V}$). Depending on the applied objective, the specific capacitance can be related to the electrode mass (F/g), to its volume ($\mathrm{F/cm^3}$), or to its surface area ($\mathrm{F/cm^2}$).

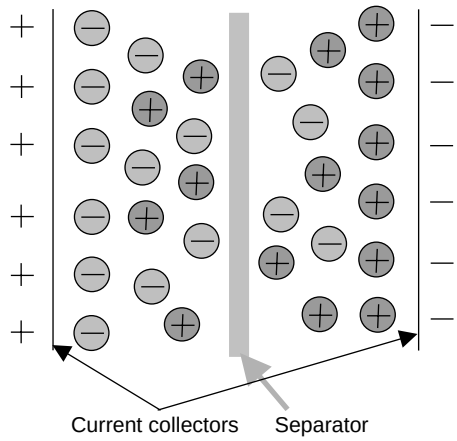

FIGURE 26.1 Schematic representation of an electrochemical capacitor: ⊕ cations of the electrolyte; ⊖ anions of the electrolyte.

The amount of electrical energy W accumulated in an electrochemical capacitor is proportional to capacitance C and square of voltage U

$$W = \frac{1}{2} CU^2 \tag{26.3}$$

The capacitance C depends essentially on the electrode material used, whereas the operating voltage is determined by the stability window of the electrolyte. Capacitors in an organic electrolyte can easily operate in the range 2 to 2.5 V, and using ionic liquids it is even possible to extend this range to 3.5–4 V [14], whereas in aqueous solution it is generally below 1 V. Hence, at least for symmetric systems, about one order of magnitude higher capacitance can be expected with organic electrolytes or ionic liquids compared to water medium.

Since the electrodes do not undergo any phase transformation as in accumulators, the main advantage of an electrochemical double-layer capacitor (EDLC) lies in its ability of high dynamic charge propagation that allows a rapid withdrawing of energy, i.e., a high power. The power P of a supercapacitor is given by

$$P = \frac{U^2}{4R_s} \tag{26.4}$$

where R_S is the internal resistance, i.e., commonly the equivalent series resistance (ESR). The ESR of the entire device is the sum of the resistances of all the materials between the external contacts, i.e., substrate, carbon, binder, separator, and electrolyte. Since the main function of supercapacitors is their use in high-power applications, it is essential to lower the series resistance R_S by using high-conductivity additives.

The electrochemical capacitors where carbon is an electrode component are of two types, depending on the charge-storage mechanism. In the EDLCs, a pure electrostatic attraction occurs between the ions and the charged surface of the electrode that is generally from activated carbon. The electrons involved in double-layer charging are the de-localized conduction-band electrons of the carbon electrode. The capacitance of activated carbons is limited both by their specific surface capacitance, close to 10 μF/cm^2 [11–13], and their specific surface area, which cannot be higher than 2500 to 3000 m^2/g. In the second type of capacitors, called pseudocapacitors, electrons are additionally involved in quick faradaic reactions and are transferred to or from the valence states of the redox cathode or anode reagent, although they may arrive in or depart from the conduction band of carbon [11,13]. In this case, contrary to a battery redox process, the charge transferred is proportional to voltage, as in a real capacitor, therefore it is called pseudocapacitance. Electrode materials with pseudocapacitance properties are generally metal oxides (RuO_2, MnO_2, etc.) [7,15–17] or conducting polymers [18–21]. Examples of pseudofaradaic reactions are illustrated by Equations (26.5) and (26.6) for polypyrrole (PPy) and ruthenium oxide, respectively,

$$[PPy^+A^-] + e^- \rightleftharpoons [PPy] + A^- \tag{26.5}$$

$$RuO_a(OH)_b + \delta H^+ + \delta e^- \rightleftharpoons RuO_{a-\delta}(OH)_{b+\delta} \tag{26.6}$$

Pseudocapacitance may also be realized through special doping of carbons via the presence of heteroatoms, e.g., oxygen or nitrogen [22,23]. The values of capacitance are strictly connected to the nature and surface of the electrode/electrolyte interface [24,25] as well as to the amount of pseudocapacitive additive.

The most useful techniques for investigating the performance of supercapacitors are galvanostatic charge/discharge and cyclic voltammetry. In the first case, a constant current — generally in the range of 1 mA/g of carbon to 1 A/g — is passed through the device, and the voltage is measured as a function of time. In the case of an ideal capacitor — where $Q = C \times V$ — the curve $V = f(t)$

should be perfectly triangular, as shown in Figure 26.2 for a carbon obtained by KOH activation of pitch mesophase [26]. In the case of the voltammetry technique, a linear variation of voltage is imposed in the limits of the electrolyte stability window — generally at scan rates between 1 to 100 mV/sec — and the charging current is measured. In the case of an EDLC with a low value of ESR, the curve $I = f(V)$ has a rectangular box-like shape, as shown in Figure 26.3 for activated carbon from pitch mesophase [26]. The value of capacitance C is easily evaluated either from the slope of the galvanostatic characteristics or from the current I measured on the voltammetry curve using

$$C = \frac{I}{\upsilon} \tag{26.7}$$

where υ represents the voltage scan rate. In general, the most reliable values are obtained from galvanostatic discharge measurements.

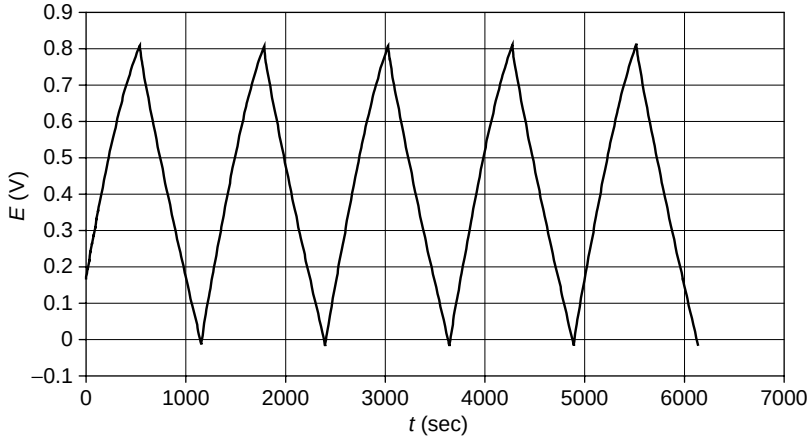

FIGURE 26.2 Galvanostatic ($I = 2$ mA) charge/discharge characteristics of a capacitor built with AC electrodes obtained by KOH activation of pitch mesophase. Electrolytic solution 1 mol/L H_2SO_4. (From Kierzek, K. et al., *Electrochim. Acta*, 49, 515, 2004.)

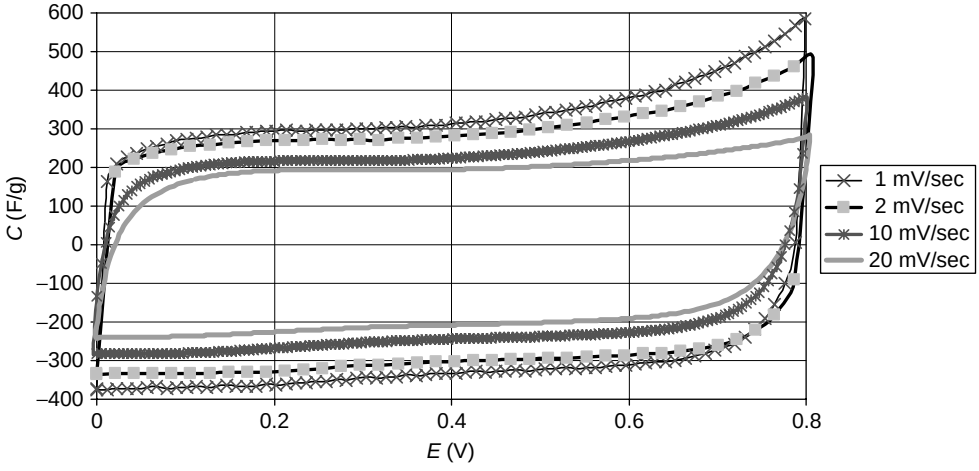

FIGURE 26.3 Cyclic voltammograms of a capacitor built with activated carbon electrodes obtained by KOH activation of pitch mesophase at different scan rates. Electrolytic solution 1 mol/L H_2SO_4. (From Kierzek, K. et al., *Electrochim. Acta*, 49, 515, 2004.)

26.2.2 Carbons for Pure Electrochemical Double-Layer Capacitors

26.2.2.1 Activated Carbons

A highly developed surface area of carbon is a crucial factor for trapping a high amount of ions in the electrode/electrolyte interface [12,13]. Generally, the more developed the specific surface area of carbon, the higher the ability for charge accumulation. However, this surface must be electrochemically accessible to ions. Therefore, apart from the high values of specific surface area determined by micropores (with a diameter less than 2 nm), where the ions are adsorbed forming the electrical double layer, the presence of mesopores (diameter from 2 to 50 nm) is essential for a quick transportation of ions in the bulk of the electrode material. The availability and wettability of pores, with dimensions adapted to the size of solvated anions and cations, which have to be transported from the electrolytic solution, is crucial for the high performance of the capacitor. Besides the maximum value of capacitance which can be realized with a given activated carbon/electrolyte interface, a quick charge transportation can fulfill the so-called frequency response, i.e., the ability for energy extraction at higher frequencies (e.g., 1 Hz).

Activated carbons prepared from different precursors and by different activation processes have been widely used in supercapacitors [24–26]. Natural precursors such as coal- and pitch-derived carbonaceous materials are of high interest due to their low cost and availability [26]. Among many physical (e.g., water, carbon dioxide) and chemical activation procedures, KOH activation seems to be the most adapted one for obtaining carbons with extensively developed porosity, where micropores efficiently contribute to the value of capacitance [26–29]. However, taking into account the low values of specific surface capacitance, which are generally reported in the literature ($10\,\mu F/cm^2$ when only charging of the double-layer is involved), one can assume that not all micropores are effective in charge accumulation. For this reason, it is easy to understand why capacitance is generally not proportional to the specific surface area [30,31]. Taking into account that most activated carbons are characterized by a relatively wide pore-size distribution, it is clear that the micropores not adapted to the size of the solvated ions do not take part in the double-layer charging [32]. Moreover, even if the pore size is high enough, the micropores may be filled at different rates, which will affect considerably the frequency dependence and power. Highly micro-porous carbons always pose some diffusion limitation. This effect can be observed at quick scan rates during voltammetry or impedance spectroscopy experiments. For example, for an activated carbon with a BET specific surface area of $2130\,m^2/g$, it has been shown by impedance spectroscopy in KOH medium that pores with a size larger that 1.1 nm can be reached by electrolyte ions within less than 0.1 sec, while 5 sec are necessary to access pores of size 0.6 nm [24]. An optimized material for EDLCs should be highly micro-porous to ensure a high capacity and should contain a high enough proportion of mesopores for quick dynamics of charge propagation reflected by a small time constant (RC). The clue for fulfilling both conditions is to design carbon materials with interconnected micropores and mesopores in well-balanced proportion as, for example the micro/meso-porous carbons prepared by the template techniques [33]. Nevertheless, even if such conditions are realized, due to the different size of solvated cations and anions, it is obvious that the efficiency of such optimized materials may be different for both electrodes. Therefore, asymmetric capacitors with electrodes of activated carbons with different distributions of pore diameters adapted to the size of both kinds of ions have been proposed to circumvent the size differences between cations and anions [34].

Although it is well demonstrated that nanotexture plays a key role in the determination of EDLCs' properties, the charging of the double layer remains a very complex process which, besides accessibility of micropores, depends also on a number of other parameters such as the affinity of the electrolyte ions for the electrode material, the hydrophobic–hydrophilic character, the particles' conductivity and their size. Among all, surface functionality is certainly an important parameter that should be taken into account for explaining the difficulties in establishing a direct relationship between the capacitance and the nanotextural parameters of the carbon material [29,31].

Though most of the fundamental work on carbon-based EDLCs focuses on obtaining high values of capacitance, the practical application of these devices is essentially determined by other important parameters. Generally, carbon materials are investigated with three-electrode cells, while using a limited potential range. When the same materials are applied in the real two-electrode cells, the results may be completely different. First, depending on the sizes of both cations and anions, the efficiency of porosity may be different at each electrode. Second, contrary to a three-electrode cell, the potential at which each electrode operates cannot be controlled, which imposes a limit of maximum cell voltage to 0.6 to 0.7 V in aqueous medium for avoiding electrolyte decomposition. Third, in an organic medium some different redox decomposition processes may occur at each electrode, depending on its polarity. Therefore, even if the preliminary investigation of activated carbons shows high capacitance values, other parameters must be investigated to demonstrate the applicability of a given system. To be applicable, a two-electrode supercapacitor must demonstrate a low-performance fading during cycling, a quick charge propagation at different loads, and a low self-discharge. The micropores are not easily wetted by the electrolyte and the exposed surface in micropores may not be utilized for charge storage. Moreover, even in the situation wherein the micropores are wetted by the electrolyte, ionic motion in such small pores may be so slow that the high rate capability, which is one of the advantages of EDLCs, may not be realized.

26.2.2.2 Porous Carbons Prepared by the Template Technique

As stated above, both charge storage and rate capability are further limited if the pores are randomly connected. Therefore, high-surface area carbon materials containing regularly interconnected micro- and mesopores are highly desirable for EDLC electrodes. Recently, many groups have synthesized ordered meso-porous silica which could be used later as a template for the preparation of carbons with well-sized pores [35–38], meeting the above-mentioned capacitor requirements. The templates are mesostructured silicas such as MCM48, MCM41, SBA15, whereas the carbon source is a liquid or gas phase, e.g., sucrose solution, polyfurfuryl alcohol, propylene, or pitch [33,39–41]. The steps of the preparation process are schematized in Figure 26.4. After its deposition inside the pores of the template, the carbon precursor is carbonized at temperatures close to 800°C. The last step is the removal of the silica template by dissolution in hydrofluoric acid.

In an attempt to correlate the electrochemical performance of template carbons with their nanotextural parameters, a perfect linear relationship has been found between the capacitance values in aqueous or organic medium and the micro-pore volume determined by CO_2 adsorption at 273 K (Figure 26.5) [33]. It clearly proves that, with this kind of porous carbon, the ions are essentially trapped in ultramicropores, i.e., pores with size <0.7 nm. Comparison of the measured value of capacitance in aqueous solution with the available volume of ultramicropores shows that most of them take part in trapping nonsolvated ions in the electrical double layer. In these template carbons, micro- and mesopores are perfectly interconnected, mesopores being the former walls of the silica matrix, whereas the carbonaceous walls are microporous. Under the application of an electrical polarization, the solvated ions easily diffuse in the mesopores (playing the role of corridors) for being finally trapped as nonsolvated in ultramicropores. In a typical microporous activated carbon, the situation is completely different. The pathway for solvated ions to reach the active surface is very tortuous and long, with several bottlenecks (gates). Therefore, the limiting pore size in this case is probably higher

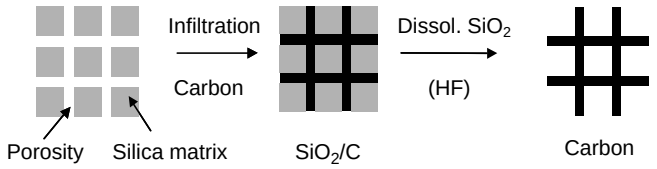

FIGURE 26.4 Schematic representation of the elaboration of porous carbon by the template technique.

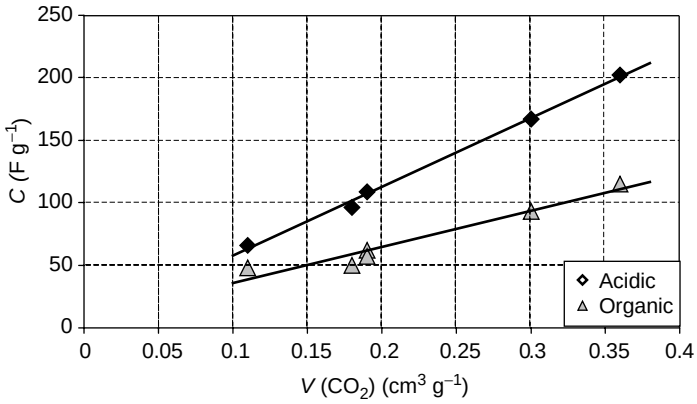

FIGURE 26.5 Capacitance values in aqueous and organic media of the nanotextured carbons synthesized with different carbon precursors and templates vs. their micro-pore volume determined by CO_2 adsorption. (From Vix-Guterl, C. et al., *Carbon*, 43, 1293, 2005.)

than the size of the pores where the ions are finally accumulated. Templated carbons, in spite of the difficulty in their preparation and relatively high cost, are certainly a good means for supplying important information about pore-size effects on electrical double-layer charging.

26.2.3 Electrochemical Capacitors from Carbons with Pseudocapacitance Properties

Many commercially available activated carbons already reach the theoretical value of specific surface area for a single graphene layer, i.e., 2600 m^2/g. Hence, according to formula (26.1), the only possibility of enhancing capacitance with this kind of material is by improving the access to micropores. However, high BET surface area-activated carbons possess a high number of active sites or surface groups, which considerably reduce the life cycle of supercapacitors due to side reactions [42]. Therefore, instead of developing the specific surface area largely, an alternative is to introduce pseudofaradaic properties by doping of carbon through foreign elements. The presence of different heteroatoms (oxygen, nitrogen) substituted for carbon in the graphene layers or occurring as functional groups has been considered for modifying the electronic properties which can further influence the electrochemical performance [43,44]. The foreign atoms modify the electron donor/acceptor properties of the graphene layers, and are consequently expected to affect the charging of the electrical double layer and to give pseudocapacitance faradaic reactions. The main dopant studied in literature is nitrogen [45–48]. A part of the nitrogen can be substituted to carbon ("lattice nitrogen"), and the other can be chemically bound to the edge carbon atoms ("chemical nitrogen").

The effect of substitutional nitrogen in the graphitic network on the pseudocapacitance properties has been studied recently. A series of nitrogen-enriched carbons has been prepared by carbonization of polyacrylonitrile (PAN) or oxidized poly (4-vinylpyridine) cross-linked with 25 wt% of divinylbenzene (PVPox) and of their blends with pitch (P). Then, they have been activated by steam to give activated carbons that were tested in two electrode capacitors [23,49]. The detailed nanotextural characteristics together with elemental composition expressed by N/C, O/C, and N/O atomic ratios and the potential of zero charge are presented in Table 26.1. The BET-specific surface area of the activated carbons ranges from 800 to 1400 m^2/g, and their nitrogen content from 1.9 to 7.2 wt%. It is also noteworthy that the higher the amount of nitrogen, the higher the basicity of carbon. The voltammetry characteristics for activated carbon from PAN (Figure 26.6) show a perfect rectangular shape at 2 mV/sec and a slight aggravation from 10 to 20 mV/s, supporting the hypothesis that faradaic reactions in the presence of nitrogen proceed with limitations at higher load. The galvanostatic charge/discharge curves for the

TABLE 26.1
Characteristics of the Activated Carbons from N-polymers and Their Blends with Pitch *P*

Sample	Porosity		Elemental Composition				pH_{PZC}
	S_{BET} (m^2/g)	V_μ/V_T	*N* (wt%)	$(N/C)_{at}$	$(O/C)_{at}$	$(N/O)_{at}$	
PAN	807	0.93	7.2	0.071	0.050	1.42	9.3
P/PAN 1:1	832	0.89	4.2	0.041	0.042	0.98	8.5
P/PAN 3:1	747	0.84	3.1	0.029	0.037	0.78	7.7
PVPox	1420	0.92	2.6	0.025	0.043	0.58	7.6
P/PVPox 1:1	889	0.87	1.9	0.018	0.033	0.55	7.4

Source: From Lota, G. et al., *Chem. Phys. Lett.*, 404, 53, 2005.

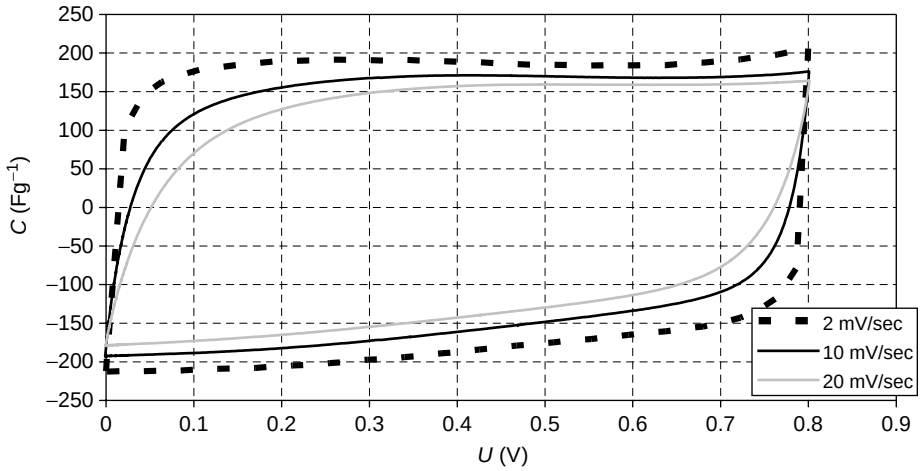

FIGURE 26.6 Voltammetry characteristics of a two-electrode capacitor built with the AC from PAN (electrolytic medium: 1 mol/L H_2SO_4) at three different scan rates. (From Frackowiak, E. et al., *Electrochim. Acta*, in press, 2005.)

nitrogenated material from PVPox, which contains roughly three times less nitrogen than that from PAN, are of the triangular shape typical of a good capacitor even at a high load of 1000 mA/g (Figure 26.7), demonstrating that upon reducing the amount of substitutional nitrogen, the faradaic perturbations are less visible. The capacitance values of nitrogenated carbons are strongly affected by the nature of the electrolyte and the electronic structure induced by nitrogen. A careful analysis of the results obtained for samples with comparable nanotextural properties, i.e., $S_{BET} \approx 800\ m^2/g$, shows no remarkable differences in organic medium, whereas capacitance is proportional to the N content and pH_{PZC} in acidic medium (Figure 26.8) [49]. The extrapolation to a nitrogen content of 0 wt% gives a capacitance of 85 F/g which is the order generally found for activated carbons with a specific surface area of 800 m^2/g. The enhancement of the capacitance values in H_2SO_4 medium was interpreted by pseudofaradaic reactions due to the nitrogen functionality, as illustrated by the following equations [49,50]:

$$C^* = NH + 2e^- + 2H^+ \rightleftharpoons C^*H - NH_2 \tag{26.8}$$

$$C^* - NHOH + 2e^- + 2H^+ \rightleftharpoons C^* - NH_2 + H_2O \tag{26.9}$$

where C^* stands for the carbon network. Figure 26.9 shows the capacitance vs. frequency dependence for capacitors built in 1 mol/L H_2SO_4 from the two activated carbons from PVPox and P/PAN

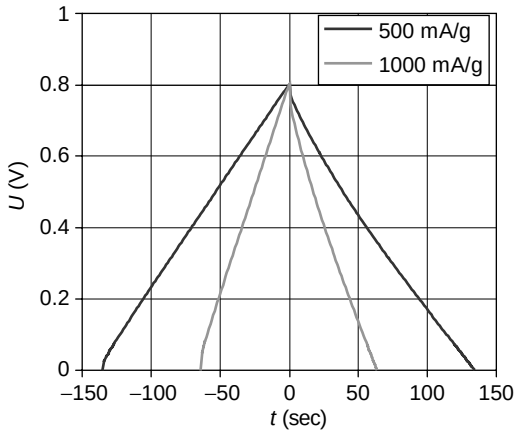

FIGURE 26.7 Galvanostatic charge/discharge of a two-electrode capacitor built with the AC from PVPox (electrolytic medium: 1 mol/L H_2SO_4) at two different current loads. (From Lota, G. et al., *Chem. Phys. Lett.*, 404, 53, 2005.)

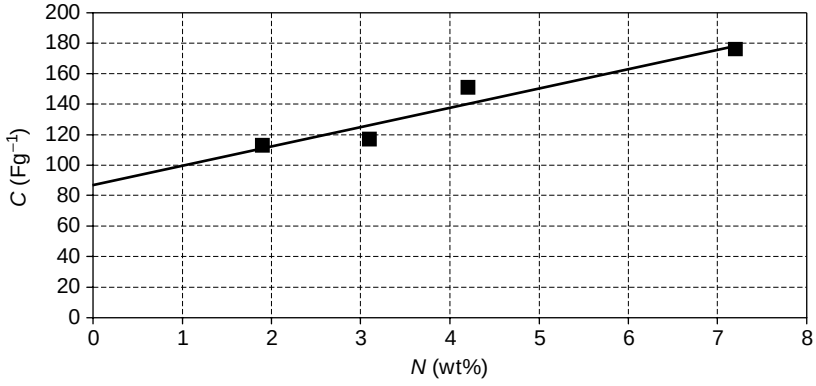

FIGURE 26.8 Capacitance values (F/g) in acidic medium vs. nitrogen content (wt%) for the ACs from PAN-A, P/PAN 1:1, P/PAN 3:1, P/PVPox 1:1. (From Frackowiak, E. et al., *Electrochim. Acta*, in press, 2005.)

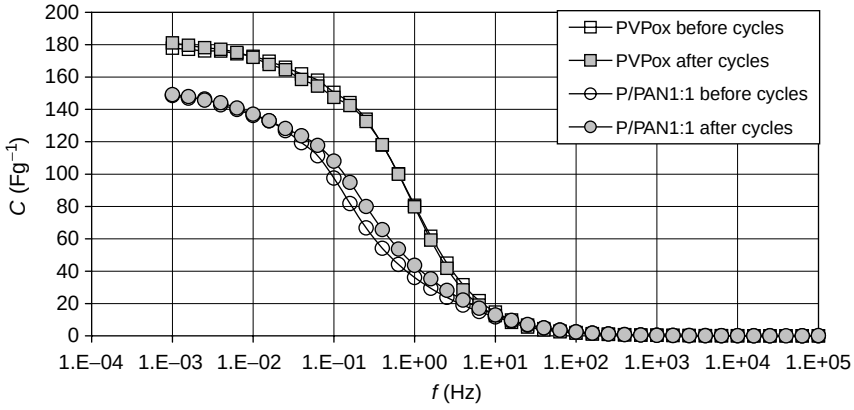

FIGURE 26.9 Capacitance values vs. frequency for two activated carbons from PVPox and P/PAN 1:1 before and after 3000 cycles at 500 mA/g current load. Electrolytic solution: 1 mol/L H_2SO_4. (From Frackowiak, E. et al., *Electrochim. Acta*, in press, 2005 .)

as 1:1, before and after 3000 cycles at 500 mA/g current load. The fact that the before and after cycling curves are almost superimposed proves that the pseudocapacitance effect introduced by nitrogen is stable with cycling. Moreover, capacitance only slightly decreases at low frequency, as it would be the case for an electrochemical double-layer capacitor.

Hence, it is clear that noticeable capacitance values can be obtained when heteroatoms are incorporated into the network of activated carbons, even if their specific surface area is quite moderate. These kinds of materials open new insights for the development of high-performance supercapacitors. It also confirms that the pseudofaradaic effects due to heteroatoms are an additional factor that apart from nanotextural parameters may contribute to the determination of capacitance [31].

26.2.4 Carbon Nanotubes as a Composite Component

As already explained in Section 26.2.1, materials with pseudocapacitance properties, such as oxides [16,17] or electronically conducting polymers (ECPs) [19,21] may be a promising alternative for the development of high-performance supercapacitors. However, in most reports, a very thin layer of the active material coats a metallic current collector — very often platinum — that is far from the requirements for an industrial application. Moreover, swelling and shrinkage may occur during doping/de-doping of the active film, which leads to mechanical degradation of the electrode and fading of the electrochemical performance during cycling. Such problems have been partly overcome in the case of ECPs by adding an insulating polymer with good mechanical properties such as poly-*N*-vinylalcohol [51], but as a result the electrical conductivity of the composite material is lower than in the pristine ECP. Adding carbon [52], and especially carbon nanotubes, is the most interesting solution that has been proposed to improve the mechanical and electrochemical properties of the electrodes [7,18]. Carbon nanotubes (CNTs), due to their unique morphology and extended graphitic layers, are characterized by exceptional conducting and mechanical properties which allow them to be used directly as three-dimensional support for active materials. With nanotubes, the percolation of the active particles is more efficient than with traditional carbon blacks, which are generally used for the manufacture of electrodes [7]. On the other hand, the open mesoporous network formed by the entanglement of nanotubes, allows the ions to diffuse easily to the active surface of the composite components. The two latter properties are essential to lower the ESR and consequently increase the power of the device. Finally, since nanotubular materials are characterized by a high resiliency, the composite electrodes can easily adapt to the volumetric changes during charge and discharge, which drastically improves the cycling performance. For all these reasons, composites incorporating a nanotubular backbone coated by an active phase with pseudocapacitive properties represent an interesting breakthrough for developing a new generation of supercapacitors.

Chemical and electrochemical polymerization of the monomer has been considered in order to get an ECP layer — the most investigated being polypyrrole (PPy) — on nanotubular materials. The TEM micrograph presented in Figure 26.10 for a material prepared by PPy electrochemical deposition shows a very uniform polymer coating [53]. Coating by a thin layer of polypyrrole has been realized on multiwalled nanotubes (MWNTs) [18,54,55], well-aligned MWNTs [56], and single-wall nanotubes (SWNTs) [57]. When MWNTs are oxidized, their surface is covered with oxygen-containing groups, which can be used as anionic dopant of a PPy film electrodeposited on the MWNTs [58]. These films are notably less brittle and more adhesive to the electrode than those formed using an aqueous electrolyte as a source of counterion. The electrochemical behavior of ECP/CNT composites has been studied either in two- or three-electrode cells. Comparison of the redox performance of PPy films on aligned MWNTs and on flat Ti and Pt surfaces shows a noticeable improvement in the case of the composites with MWNTs due to the high-accessible surface area of CNTs in the aligned arrays [56]. By contrast, the results found with SWNT/PPy nanocomposites [57] are probably of limited application because (1) the nickel foam used as a current collector supplies an additional capacity in the alkaline solution used for the study; and (2) PPy degrades quickly in alkaline solution. With the electrochemically obtained MWNTs/PPy

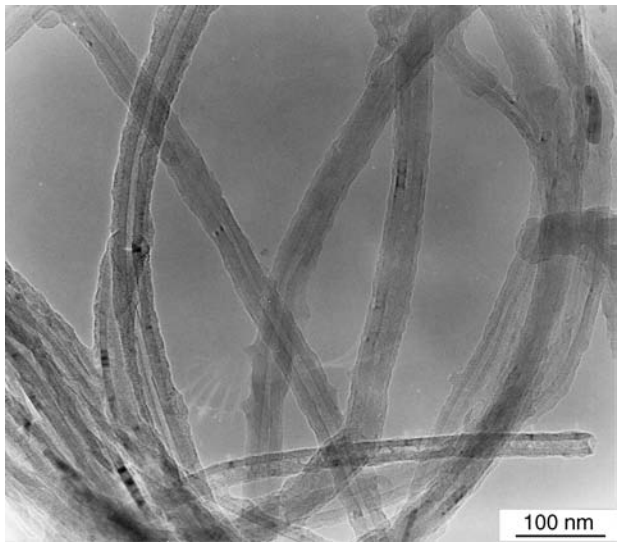

FIGURE 26.10 Multiwalled carbon nanotubes electrochemically coated by a thin layer of polypyrrole. The coating thickness is estimated to be 5 nm. (From Frackowiak, E. et al., *Polish J. Chem.*, 78, 1345, 2004.)

composite, the capacitance values reach ca. 170 F/g with a good cyclic performance over 2000 cycles [18]. In fact, it has been shown that the capacitance values for composites with polyaniline (PANI) and PPy strongly depend on the cell construction [59]. With chemically deposited ECPs, extremely high values of specific capacitance can be found — from 250 to 1100 F/g — using a three-electrode cell, whereas smaller values of 190 F/g for MWNTs/PPy and 360 F/g for MWNTs/PANI have been measured in a two-electrode cell. It highlights the fact that only two-electrode cells allow the material's performance to be estimated well in electrochemical capacitors. The applied voltage was found to be the key factor influencing the specific capacitance of ECP-based nanocomposites. Generally, it cannot exceed 0.6 to 0.8 V due to oxygen evolution in the positive range of potentials and switching to an insulating state in the negative values [59]. The high values of capacitance found with MWNT/ECP composites is due to the unique property of the entangled nanotubes that supply a perfect three-dimensional volumetric charge distribution and a well-accessible electrode/electrolyte interface. Comparing the results of the two coating techniques, the nonhomogeneous PPy layer deposited chemically is more porous and less compact than the electrochemically deposited one. Consequently, the diffusion of ions proceeds more easily, giving a better efficiency for charge storage [59]. Figure 26.11 illustrates the electrochemical performance obtained in a two-electrode capacitor with the chemically deposited PPy. The square shape of the voltammogram and linear galvanostatic charge/discharge demonstrate perfect capacitance behavior, even if pure PPy itself gives more irregular characteristics [59].

Carbon nanotubes can also be a perfect support for cheap transition metal oxides of poor electrical conductivity, such as amorphous manganese oxide (a-$MnO_2 \cdot nH_2O$) [7]. The a-MnO_2/MWNTs composite can be prepared by precipitation of a-MnO_2 from a $KMnO_4$ + $Mn(OAc)_2$ $4H_2O$ mixture which contains a predetermined amount of CNTs. The scanning electron microscopy (SEM) image presented in Figure 26.12 for an a-MnO_2/MWNT composite containing 15 wt% of nanotubes shows a remarkable template effect of the entangled nanotubes framework. Consequently, the composite electrodes have a good resiliency, and their porosity is high enough to favor the access of ions to the bulk of the active material. The other interesting property of this composite is an extremely good adhesion of the coating layer on the CNTs that is reflected by low values of electrical resistance. In order to demonstrate the advantage of this material, two-electrode capacitors were built in aqueous medium with two kinds of a-MnO_2-based composite

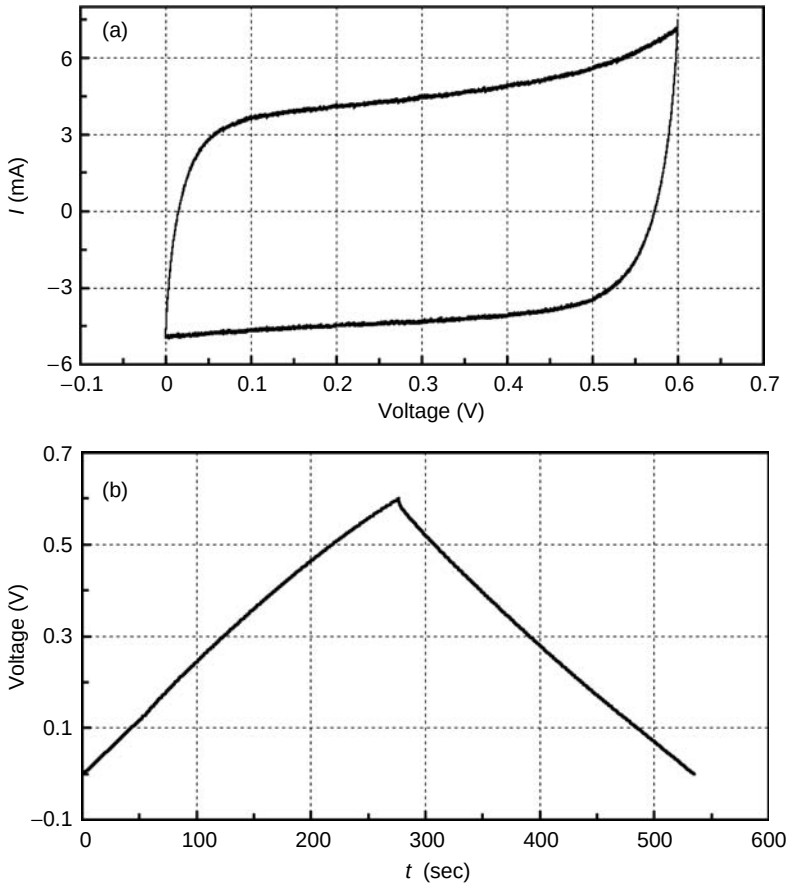

FIGURE 26.11 Electrochemical characteristics of a symmetric capacitor based on PPy/MWNTs composite electrodes (mass of each electrode = 8.6 mg). (a) cyclic voltammogram (5 mV/s); (b) galvanostatic charge/discharge at 2 mA. (From Khomenko, V. et al., *Electrochim. Acta*, 50, 2499, 2005.)

containing either 15 wt% of carbon black or 15 wt% of MWNTs. The shape of the characteristics in the presence of carbon black demonstrates a resistive behavior of the electrodes, whereas a perfectly rectangular voltammogram was observed with the a-MnO_2/MWNTs composite [7]; the corresponding values of ESR were 50 and 2 Ωcm^2, respectively. The a-MnO_2/MWNTs composite supplies a capacitance of 140 F/g with good cyclability and high dynamic of charge propagation. However, the voltage window of MnO_2-based capacitors is limited to 0.6 V, due to the irreversible reactions Mn(IV) to Mn(II) at the negative electrode and Mn(IV) to Mn(VII) at the positive. In order to circumvent this drawback, an asymmetric configuration has been proposed, where the positive electrode consists of a-MnO_2 and the negative is built from activated carbon [61–63]. When the a-MnO_2/MWNTs composite is used as the positive electrode, the supercapacitor demonstrates perfectly rectangular voltammograms (Figure 26.13) and it can be operated up to 2 V in aqueous medium with an extremely good cyclability [63]. High energy and power density can be reached in aqueous electrolyte, 10.5 Wh/kg and 123 kW/kg, respectively, due both to the large voltage window and to the presence of MWNTs [63]. While being environment-friendly, this system offers electrochemical characteristics comparable with EDLCs in organic electrolytes. Hence, it demonstrates perfectly that combining materials with pseudocapacitance properties in an asymmetric construction is a very promising direction for developing a new generation of high-performance supercapacitors.

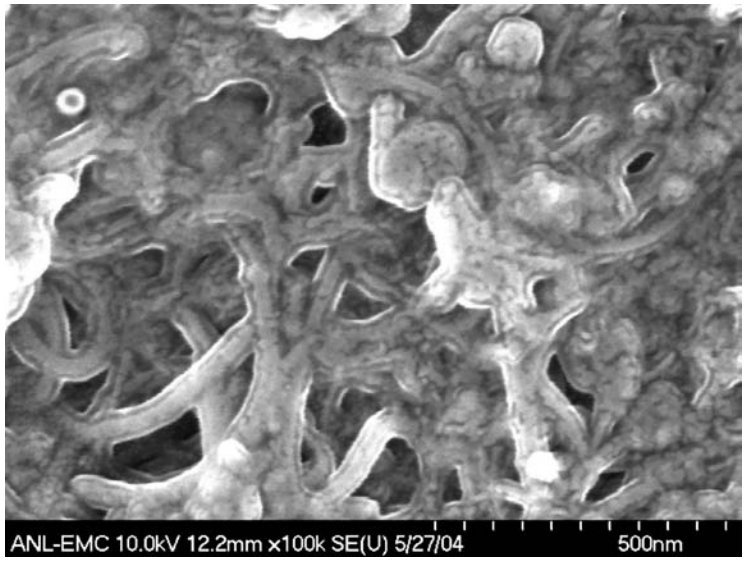

FIGURE 26.12 Scanning electron microscopy image of an a-MnO_2/MWNTs composite containing 15 wt% of nanotubes. (Courtesy of M. Thackeray, Argonne National Laboratory, USA.)

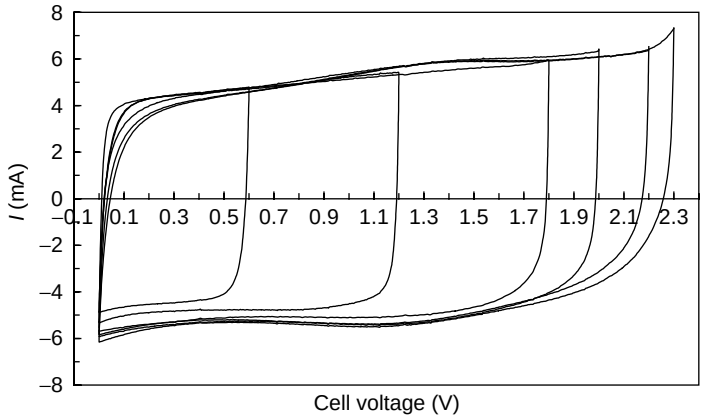

FIGURE 26.13 Voltammograms of an asymmetric capacitor in 2 mol/L KNO_3 where the positive electrode is from the a-MnO_2/MWNTs composite and the negative electrode is from AC. Scan rate 10 mV/sec. (From Khomenko, V. et al., *J. Power Sourc*., in press, 2005.)

26.3 ELECTROCHEMICAL HYDROGEN STORAGE

26.3.1 INTRODUCTION

In the last few decades, hydrogen has been recognized as an ideal fuel for many energy converters because of its high efficiency and nonpolluting nature. However, the major drawback for practical usage of hydrogen is the difficulty to store it safely and economically. Storage neither as compressed gas nor as a cryogenic liquid appears to be suitable for wide application. Hydrogen storage in metal alloys by absorption or electrodecomposition of a water solution [64] is an interesting alternative, but these materials are not cheap and their reversible capacity, ca. 1.5 wt%, is still far from the US Department of Energy benchmark (5 wt%), as far as powering of vehicles with a hydrogen

fuel-based system is considered. Therefore, the realization of economical and efficient hydrogen-storage techniques is a critical requirement for hydrogen-fueled transportation that stimulates ongoing search for new possibilities.

Although many papers have claimed that nanostructured carbons and nanotubes are able to store large amounts of hydrogen, there is a high discrepancy among all the values published [9,65–78]. Moreover, the factors that allow storage to be optimized are not clearly elucidated. As far as di-hydrogen adsorption is considered, it seems that high pressure (at least 10 MPa) or low temperature (77 K) are necessary for getting noticeable values. Especially in the case of SWNTs and MWNTs, the values of hydrogen capacity are very scarce and doubtful, ranging from 0.2 to 3.7 wt% [67–71]. The possible reasons for the fluctuations in the results may not only be due to experimental errors, but also a large amount of impurities in the samples (e.g., metallic particles and microporous carbon), and the use of additives for conductivity enhancement of the electrodes when an electrochemical technique is used. Investigating high-purity SWNTs and MWNTs, the storage capacity by electrodecomposition of water does not exceed 0.2–0.4 wt% [72]. This fits well also with the di-hydrogen adsorption studies in the gas phase on a number of carbon materials, which confirms the poor efficiency of CNTs for this process [73,74]. By contrast, using activated carbons, the values of reversible hydrogen sorption reach ca. 2 wt% by cathodic electrodecomposition of water at room temperature [72,75–77], and by adsorption of the gas, they range from 1 to 5 wt% depending on whether high pressure (up to 70 MPa) and low temperature (77 K) are applied together or not [65,66,79,80].

The accuracy of the techniques used for measuring the di-hydrogen uptake — volumetric and gravimetric methods, thermo-programmed desorption coupled to mass spectrometry — is quite doubtful. On the contrary, hydrogen storage by galvanostatic electrochemical decomposition of an aqueous basic medium, where the measured variable is the discharging time, is a very accurate method [67,75–77]. Moreover, this reversible process is attractive from the point of view of energy efficiency since it associates in a unique step the hydrogen production by water electrolysis and its simultaneous storage in the carbon substrate. The *in situ* produced hydrogen easily penetrates into the nanopores of carbon, where it is adsorbed due to the driving force of the negative polarization. By this process, higher pressures (approximately calculated from the Nernst law) than in the gas phase can be reached [77]. The overall charge/discharge phenomenon can be represented as

$$C + x\mathrm{H_2O} + x\mathrm{e}^- \rightleftharpoons \langle \mathrm{CH}x \rangle + x\mathrm{OH}^- \tag{26.10}$$

where $\langle \mathrm{CH}x \rangle$ stands for hydrogen inserted into the nanotextured carbon during charging and oxidized during discharging.

26.3.2 Mechanism of Reversible Hydrogen Insertion

The mechanism of electrochemical hydrogen storage in nanoporous activated carbon should be taken into account in order to detect the possible optimizations of this process. The electrochemical hydrogen capacities of carbons depend on various parameters such as their physicochemical properties, the nature of the electrolytic medium, and its concentration, the potential cutoff. The carbon sample should contain a noticeable amount of ultramicropores ($<$0.7 nm) [81], which are generally supposed to be highly efficient for hydrogen sorption [80,82].

Potentiodynamic cycling is a well-adapted electrochemical technique to obtain information on the mechanism and kinetics of reversible hydrogen storage. Examples of voltammetry experiments using an activated carbon (AC) cloth in 3 mol/L KOH and H_2SO_4, are shown in Figure 26.14 and Figure 26.15, respectively. The various curves have been recorded with a stepwise (100 mV) shift of potential cutoff to more negative values, it means towards hydrogen evolution. In both electrolytic media, it is obvious that the two phenomena of charging the electrical double layer and hydrogen adsorption during electrochemical decomposition of water are very much linked. When

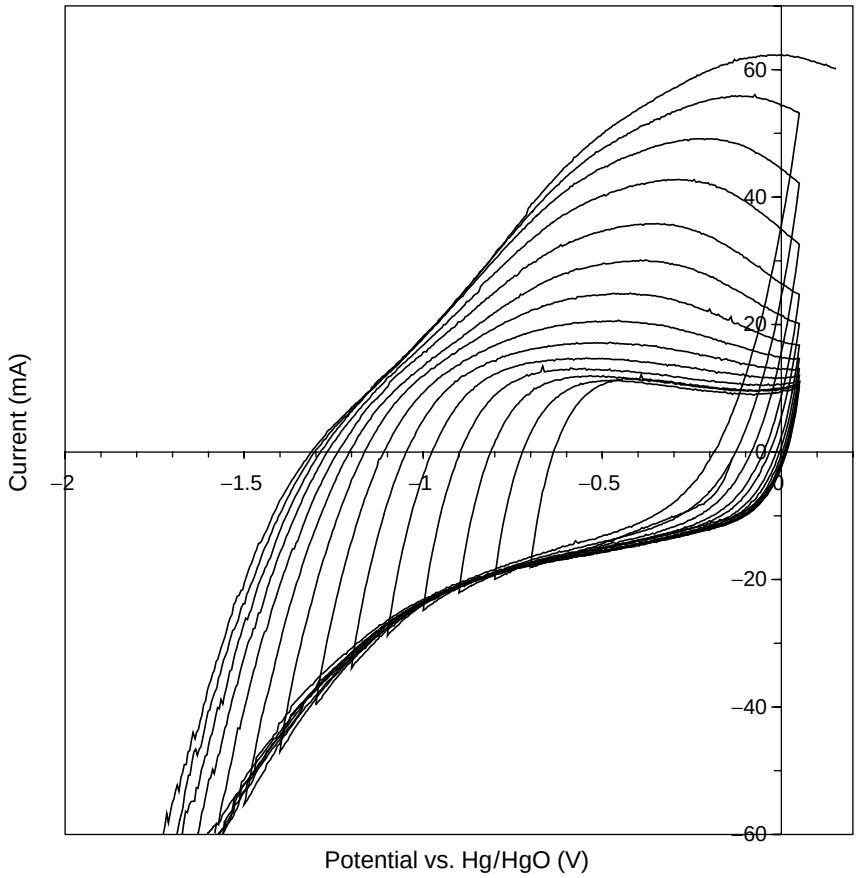

FIGURE 26.14 Dependence of the voltammetry characteristics of an activated cloth AC (15.2 mg) with the value of negative potential cutoff. Electrolyte: 3 mol/L KOH. Scan rate of potential: 5 mV/sec. The various loops are obtained by stepwise (100 mV) shifting of the potential cutoff to more negative values. (From Jurewicz, K. et al., *Appl. Phys. A*, 78, 981, 2004.)

the electrode potential is higher than the thermodynamic value that corresponds to water decomposition, only the electrical double layer is charged, whereas when it becomes lower than this value, not only the double layer is charged, but hydrogen is also adsorbed in the pores of carbon. In the latter case, the two processes contribute to the amount of electrical energy, which is reversibly stored [77].

26.3.2.1 Mechanism in Aqueous KOH Medium

In the case of the voltammetry experiment in aqueous KOH (Figure 26.14), the almost rectangular shape of the curves down to a potential cutoff of −0.8 V vs. Hg/HgO proves entirely the pure capacitive and reversible behavior of AC. The negative current reflects the number of hydrated potassium ions, K^+_{aq}, which are accumulated in the carbon/electrolyte interface during the negative polarization of AC, whereas the positive current corresponds to the desorption of K^+_{aq}. The faradaic water decomposition starts gradually to take place from the third loop when the potential cutoff is lower than the equilibrium potential (the theoretical value of the equilibrium potential in 3 mol/L KOH is −0.856 V vs. NHE, i.e., −0.908 V vs. Hg/HgO). The increase in positive current during the anodic scan is the proof that the hydrogen that was adsorbed in the pores as H_{ad} during water reduction is now electrooxidized when the potential is higher than the equilibrium value.

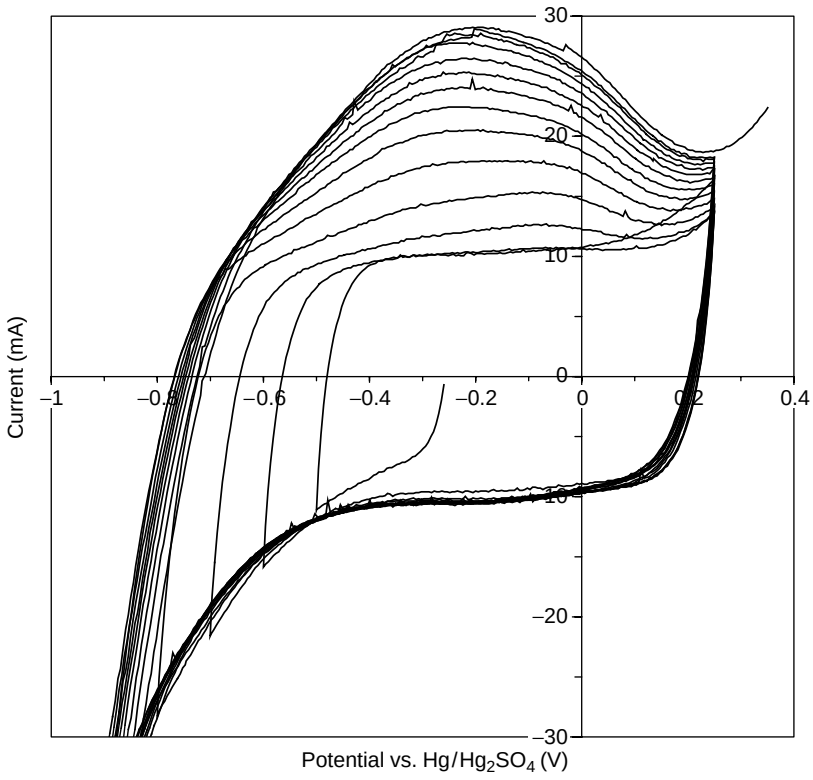

FIGURE 26.15 Dependence of the voltammetry characteristics of an activated cloth AC (14.1 mg) with the value of negative potential cutoff. Electrolyte: 3 mol/L H_2SO_4. Scan rate of potential: 5 mV/s. The various loops are obtained by stepwise (100 mV) shifting of the potential cutoff to more negative values. (From Jurewicz, K., et al., *Appl. Phys. A*, 78, 981, 2004.)

In alkaline solution, water is reduced according to

$$H_2O + e^- \rightarrow H + OH^- \tag{26.11}$$

The nascent hydrogen formed in the reaction (26.11) is adsorbed on the pores surface (reaction [26.12]):

$$C + H \rightarrow CH_{ad} \tag{26.12}$$

and/or it recombines to form H_2 molecules through one of the processes described in the following:

$$CH_{ad} + H_2O + e^- \rightarrow H_2 + OH^- + C \tag{26.13}$$

$$2H \rightarrow H_2 \tag{26.14}$$

$$CH_{ad} + CH_{ad} \rightarrow H_2 + 2C \tag{26.15}$$

These steps are often distinguished as Volmer (26.11), Heyrovsky (26.13) and Tafel (26.14) reactions. If the hydrogen adsorption energy is smaller than the energy released in the Tafel or Heyrovsky reactions, and if the activation barrier for one of these processes is low enough, then the

recombination of H_{ad} takes place and molecular hydrogen evolves by chemical or electrochemical processes, respectively. If not, the adsorbed hydrogen can further diffuse in the bulk of the carbon host occupying sites with higher adsorption energy; this process is strongly dependent on the sizes and shapes of the pores.

During the oxidation step, the above reactions run in opposite directions. When during charging the value of the cutoff potential is below −0.8 V vs. Hg/HgO, the hydrogen oxidation is well observed on the anodic part of the voltammetry characteristics. The positive current due to hydrogen oxidation increases with the decrease of potential cutoff and a more and more pronounced hump shifts towards more positive values of potential. When the negative potential cutoff reaches −2 V vs. Hg/HgO, the hump is located close to 0 V vs. Hg/HgO, i.e., +0.052 V vs. NHE. The latter value is very high compared with the equilibrium potential for reaction (26.11) in 3 mol/L KOH, i.e., −0.856 V vs. NHE. This high over-voltage required for hydrogen oxidation is a clear proof that hydrogen stored at very negative values of potential is strongly trapped in the porous carbon bulk. The high difference of positive and negative currents measured at 0 V vs. Hg/HgO indicates that a part of hydrogen remains irreversibly trapped in the carbon material. The dangling bonds present at the edge of the graphene layers may be responsible for trapping hydrogen more energetically than it can be the case for classical physisorption [83].

26.3.2.2 Mechanism in Aqueous H_2SO_4 Medium

In sulfuric acid, H_3O^+ is the available proton source for the initial charge transfer step according to

$$H_3O^+ + e^- \rightarrow H + H_2O \tag{26.16}$$

The theoretical value of the equilibrium potential for reaction (26.16) in 3 mol/L H_2SO_4 is 0.046 V vs. NHE, i.e., −0.566 V vs. Hg/Hg_2SO_4. Figure 26.15 presents the voltammetry characteristics of AC in H_2SO_4 with a stepwise shift (100 mV) of negative potential cutoff from −0.5 to −1.8 V vs. Hg/Hg_2SO_4. During the first cycle, the solvated H_3O^+ ions are accumulated in the electrical double layer during the cathodic sweep, and the anodic one corresponds to their repulsion. In Figure 26.15, one can see that the faradaic reaction according to (26.16) proceeds at more negative values than −0.6 V vs. Hg/Hg_2SO_4. It is noteworthy that the voltammetry response differs significantly from the alkali medium. The intermediate region where hydrogen adsorption takes place during the cathodic polarization is almost absent, and di-hydrogen evolution starts almost immediately after the region of pure capacitance behavior. It is clear that the Tafel recombination (Equation [26.14]) determines the process, i.e., is quicker than hydrogen diffusion and incorporation into the bulk of AC. Owing to this phenomenon, the oxidation current is lower in 3 mol/L H_2SO_4 (Figure 26.15) than in 3 mol/L KOH (Figure 26.14), which means 30 mA against 60 mA for equivalent masses of AC. Moreover, in contrast to the KOH medium, the oxidation hump locates at a constant position, ca. −0.2 V vs. Hg/Hg_2SO_4, i.e., +0.4 V vs. NHE. The latter value is only slightly higher than the equilibrium potential in 3 mol/L H_2SO_4 medium. In acidic medium, the hydrogen evolution as well as its oxidation proceed more easily, i.e., with a smaller polarization than in the KOH medium, because the protons are directly available in the electrode/electrolyte interface for the redox process. In conclusion, hydrogen is mainly trapped in a state close to physisorption when electrodecomposition is performed in aqueous H_2SO_4 medium.

26.3.2.3 Comparison of Galvanostatic Charge/Discharge in Acidic and Basic Media

The amount of hydrogen stored reversibly in both alkaline and acidic electrolytes is estimated quantitatively by galvanostatic charge/discharge (Figure 26.16). The hydrogen insertion into AC proceeds spontaneously during the decomposition of the electrolytic solution using a current load of −500 mA/g. After saturation of the samples using a charge excess, the system is allowed to relax for 1/2 to 1 h, and the amount of hydrogen reversibly stored in the AC is determined by measuring the time of galvanostatic discharge at a current load of 25 mA/g. Taking into account the Faraday law, 1 wt% of hydrogen corresponds to a charge of 270 mAh/g.

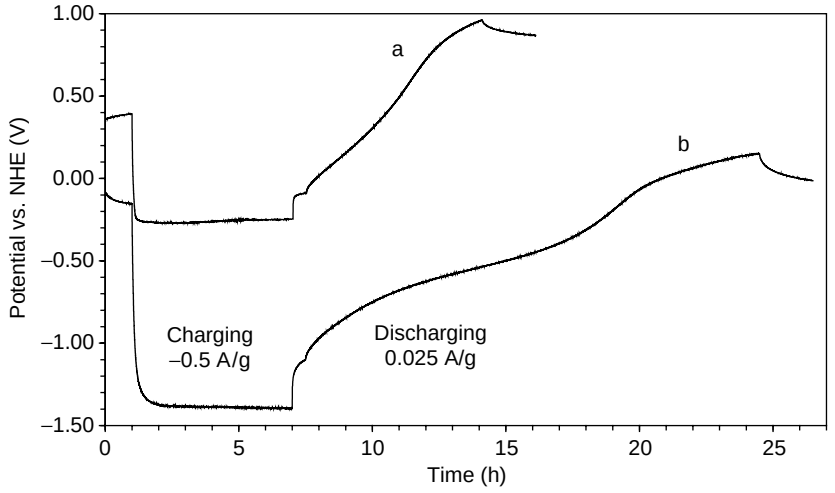

FIGURE 26.16 Galvanostatic charge/discharge of hydrogen in AC: (a) in 3 mol/L H_2SO_4 (mass of AC = 19.4 mg); (b) in 3 mol/L KOH (mass of AC = 20.0 mg). The system is first allowed to equilibrate for 1 h; then a negative current of −0.5 A/g is applied for 6 h. After a relaxation period of 30 min, a positive current of 0.025 A/g is applied in order to oxidize the inserted hydrogen. (From Jurewicz, K. et al., *Appl. Phys. A*, 78, 981, 2004.)

Considering the values of equilibrium potentials, a significant over-voltage η for di-hydrogen evolution is observed in basic and in acidic medium, i.e., 0.55 and 0.32 V, respectively. It confirms the previous observations from potentiodynamic investigations that hydrogen adsorption is favored in alkaline medium. The well-defined potential plateau at −0.55 V vs. NHE on the discharge curve in 3 mol/L KOH is a typical proof of hydrogen electro-desorption from the material. By contrast, in 3 mol/L H_2SO_4 there is almost a monotonic increase in potential with time, which demonstrates a lack of distinct energy sites in this medium (Figure 26.16). Hence, both potentiodynamic and galvanostatic experiments confirm that the storage conditions are better in KOH than in H_2SO_4, and that charging of the electrical double layer is the main contribution to charge storage in acidic medium.

Under appropriate conditions, the reversible capacity of AC in 6 mol/L KOH can reach 480 mAh/g [77], i.e., 1.8 wt%, which is quite interesting for battery application by comparison with metallic hydrides [64]. Moreover, this value is much better than that found when di-hydrogen is adsorbed in the same material under a pressure of 70 bar at 273 K, e.g., 0.4 wt% [75]. Such a difference between the two techniques is easily explained by an estimation of the local pressure during a galvanostatic charge. Activated carbon is first submitted to a prolonged galvanostatic charge in 6 mol/L KOH, and then the system is allowed to relax for 1 h before measuring the open circuit voltage (OCV). From the value of OCV, a local hydrogen pressure of 1.3×10^2 MPa is estimated by the application of the Nernst equation to reaction (26.11) [77]. This high value of pressure, which cannot be easily reached with conventional systems in the gas phase, justifies the better efficiency of the electrochemical process for hydrogen storage [75].

26.3.2.4 Relation between the Reversible Hydrogen Storage Capacity and the Nanotextural Characteristics of Porous Carbons

Taking into account that the part of hydrogen that can be reversibly recovered is in a state close to physisorption, the adsorption capacity should be influenced by the porous nanotexture of the carbon material. Therefore, in order to find the possible directions of optimization, some correlations were tentatively established with the nanotextural parameters of carbons.

The electrochemical storage capacity of various nanostructured carbons, including high-surface area graphites, ACs, SWNTs, and MWNTs, seems to slightly correlate with the BET specific surface area [72,84]. From the slope of the capacity vs. surface area plot (Figure 26.17), an uptake of

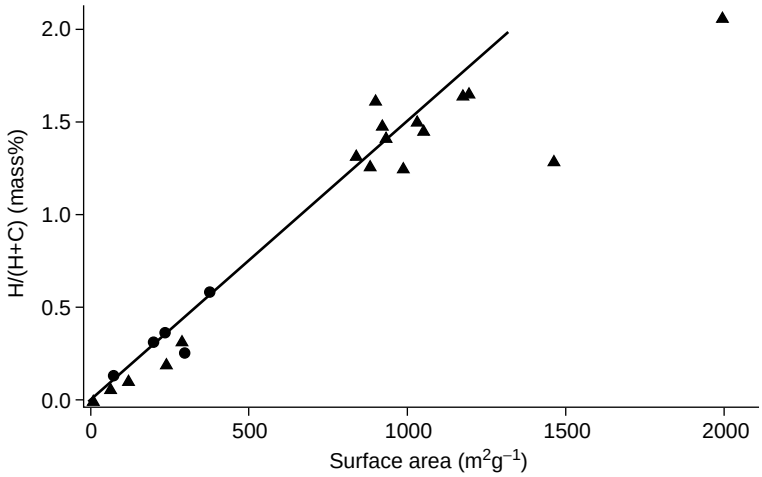

FIGURE 26.17 Desorbed amount of hydrogen vs. the BET specific surface area for carbon nanotubes and high surface area graphite samples. (From Züttel, A. et al., *Int. J. Hydrogen Energy*, 27, 203, 2002.)

1.5 wt% for 1000 m^2/g is estimated. However, Figure 26.17 shows clearly that it is only a trend, several points being quite out of linearity. A similar tendency vs. S_{BET} has been found under di-hydrogen pressures up to 12.5 MPa at room temperature, but most of the experimental points are quite scarce and the linear relationship is not so obvious [78]. The hydrogen adsorption under higher pressures of 10 and 70 MPa at room temperature was also tentatively correlated with the micro-pore volume measured by nitrogen adsorption at 77 K, showing a trend to proportionality, but for some carbons the values are quite out of the proposed correlation [79].

Although authors often propose a correlation of the electrochemical properties of nanoporous carbons with their BET area, this parameter does not take into account that in most cases only micropores with an appropriate size are efficient. Moreover, the total capacity, which is measured by galvanostatic cycling, includes also the capacity due to the charging of the double layer, which should be subtracted to get values typical of hydrogen uptake. The surface functionality may play an additional role in shifting the electrochemical behavior from a tight correlation with any nanotextural parameter. Recently, a significant effort has been undertaken to depict ideal nanotextured carbons for hydrogen storage. Experimental or theoretical studies have shown that the presence of ultramicropores, i.e., smaller than 0.7 nm [81], determines the hydrogen adsorption capacity. However, some discrepancy exists between the theoretical results regarding the optimal pore size for hydrogen adsorption. From Reference [82], the optimum pore size is close to 0.35 nm, which corresponds to a monolayer of adsorbed hydrogen; whereas Reference [85] indicates a size of 0.56 nm that is compatible with two layers of adsorbed hydrogen. The theoretical information obtained in Reference [85] seems to agree with the experimental results obtained either by nitrogen [79] or by CO_2 adsorption [80] on activated carbons.

Hence, a strict control of the pore size is strongly required if one wants to optimize the electrochemical hydrogen storage process. Additionally, as already explained above in the case of supercapacitors, besides the micropores, the presence of mesopores may be very useful to facilitate the diffusion of ions to the pores where they will be adsorbed and subsequently reduced. Unfortunately, most of the commercially available carbon adsorbents display a wide pore-size distribution and their adjustment to required values is not easy. Therefore, the reversible hydrogen capacity has been determined for a series of template carbons and correlated with the volume of ultramicropores measured by CO_2 adsorption at 273 K [33]. The tendency for the amount of hydrogen stored to increase with the total surface area is confirmed, but without any proportionality, in agreement with previous works carried out on CNTs or high surface area graphites [78]. By contrast, if the amount of hydrogen reversibly stored is plotted vs. $V(CO_2)$, a perfect linear relationship is observed (Figure 26.18),

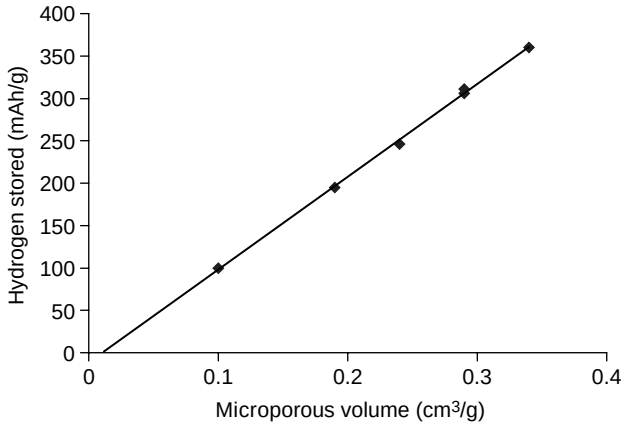

FIGURE 26.18 Hydrogen storage capacity of various nanotextured carbons prepared by a template technique vs. their ultramicropore volume determined by CO_2 adsorption. (From Vix-Guterl, C. et al., *Carbon*, 43, 1293, 2005.)

confirming the theoretical predictions that hydrogen adsorption is strongly related to the presence of ultramicropores [33]. Taking into account that such a perfect correlation with the ultramicropore volume is not so well observed for all kinds of porous carbons [86], it is obvious once more that the electrochemical performance for hydrogen storage is strongly controlled by the presence of mesopores connected to the micropores. The mesopores are essential to "feed" the micropores with ions or water molecules, which will be further reduced giving hydrogen the ability to be fixed in the ultramicropores.

26.4 CONCLUSIONS AND PERSPECTIVES

This chapter shows that all the electrochemical parameters related with capacitance properties and hydrogen storage are strongly correlated with nanotexture and surface functionality of carbons. In most of the literature reports, the effect of surface functionality is neglected, considering rather nanotextured carbons as hosts with inert pores, whose properties would be only dependent on pore volume development. The surface groups not only affect the wettability of porous carbons and their redox properties, but also the cycling performance. Therefore, for future developments, they should be taken more into account and strategies should be developed to efficiently control their nature and amount. Electrochemical grafting of carbon surfaces with well-defined functions would be certainly an adapted technique to reach such objectives.

The most used materials for electrochemical double-layer capacitors are ACs, because they are commercially available and cheap, and they can be produced with large specific surface area. However, many pores are not useful because they cannot be reached by ions. Therefore, the objective is not to develop high surface area carbons, but porous carbons with micropores of small size, which are perfectly connected to a framework of mesopores. A fundamental study establishing the respective sizes of pores and ions to reach optimal capacitance performance would be very useful. Also, it should not be neglected that an asymmetric construction where the pores of the positive and negative electrodes are adapted to the size of the ions to be trapped is preferable to a symmetric cell. Finally, as far as the energy density is concerned, the voltage window must be extended as much as possible. Substitutional heteroatoms in the carbon network might be profitable in shifting the operating potential range of each electrode, leading to a possible voltage increase without electrolyte decomposition.

One of the drawbacks of porous carbons is the poor volumetric capacity that can be reached with these materials. Carbons obtained by one-step pyrolysis of organic precursors are very interesting,

because they present a higher density than the ACs. In this case, the lack of porosity available for charging the electrical double layer must be compensated by pseudofaradaic properties. For this objective, the pyrolysis of nitrogen carriers seems to be very promising.

Another important use of carbon materials for supercapacitors and more generally for energy storage systems, is their presence as electrode component for improving both the electrical conductivity and mechanical properties. In this sense, CNTs are more efficient than carbon black, because they form a three-dimensional and interconnected framework on which the active material can be deposited. In this chapter, extremely interesting properties of composites incorporating nanotubes and an active material, such as electrically conducting polymers or a-MnO_2, have been shown. Taking into account that noticeable improvements cannot be expected with ACs, the nanotube-based composites probably represent an important breakthrough. It will be nevertheless necessary to have the ability to ensure their homogeneous dispersion in the composite materials in order to enhance their efficiency.

In the case of electrochemical hydrogen storage, knowledge is still in the state of seeking. During the last few years, the scientific aspect has been poorly considered, with many authors wishing to demonstrate the exceptional properties of CNTs, without any fundamental background that could justify the choice of this material. All the serious studies published in the last 3 to 4 years agree that the hydrogen uptake with nanotubes is less than 0.5 wt%, irrespective of the experimental conditions. Activated carbons, as cheap and versatile materials, offer definitely better performance and promises. Independent studies, in gas phase or by water decomposition, demonstrate that ultramicropores (<0.7 nm) are essential in this process. Further work should focus on designing carbon materials with a highly developed porosity in this range of size. Other probe molecules, such as CF_4, SF_6, should also be used to analyze more correctly the pore sizes. Finally, an important aspect would be to determine to which extent the pore shape affects the hydrogen adsorption properties. Presently, this is probably the most difficult task, because of the lack of an available technique for this kind of analysis. Nevertheless, without any optimization, carbon materials already demonstrate better gravimetric capacity than metallic alloys during the electrodecomposition of alkaline solutions; therefore they should be more extensively investigated as electrode materials for hydrogen storage.

REFERENCES

1. Inagaki, M., *New Carbons*: *Control of Structure and Functions*, Elsevier, Amsterdam, 2000.
2. Bansal, R.C., Donnet, J., and Stoeckli, F., *Active Carbon*, Marcel Dekker, New York, 1988.
3. Py, X., Guillot, A., and Cagnon, B., Activated carbon porosity tailoring by cyclic sorption/decomposition of molecular oxygen, *Carbon*, 41, 1533, 2003.
4. Boehm, H.P., Some aspects of the surface chemistry of carbon blacks and other carbons, *Carbon*, 32, 759, 1994.
5. Montes-Moran, M.A., Suárez, D., Menéndez, J.A., Fuente, E., Radovic, L.R., Cannon, F.S., and Strelko, V., On the nature of basic sites on carbon surfaces: an overview, *Carbon*, 42, 1219, 2004.
6. Huczko, A., Template-based synthesis of nanomaterials, *Appl. Phys. A*, 70, 365, 2000.
7. Raymundo-Piñero, E., Khomenko, V., Frackowiak, and E., Béguin, F., Performance of manganese oxide/CNTs composites as electrode materials for electrochemical capacitors, *J. Electrochem. Soc.*, 152, A229, 2005.
8. Zheng, T. and Dahn, J.R., Applications of carbon in lithium-ion batteries, in *Carbon Materials for Advanced Technologies*, Burchell, T.D., Ed., Elsevier, Oxford, 1999, p. 341.
9. Frackowiak, E. and Béguin, F., Electrochemical storage of energy in carbon nanotubes and nanostructured carbons, *Carbon*, 40, 1775, 2002.
10. Flandrois, S. and Simon, B., Carbon materials for lithium-ion rechargeable batteries, *Carbon*, 37, 165, 1999.
11. Conway, B.E., *Electrochemical supercapacitors — scientific fundamentals and technological applications*, Kluwer Academic/Plenum, New York, 1999.

12. Kötz, R. and Carlen, M., Principles and applications of electrochemical capacitors, *Electrochim. Acta*, 45, 2483, 2000.
13. Frackowiak, E. and Béguin, F., Carbon materials for the electrochemical storage of energy in capacitors, *Carbon*, 39, 937, 2001.
14. Balducci, A., Bardi, U., Caporali, S., Mastragostino, M., and Soavi, F., Ionic liquids for hybrid supercapacitors, *Electrochem. Commun.* 6, 566, 2004.
15. Toupin, M., Brousse, T., and Bélanger, D., Influence of microtexture on the charge storage properties of chemically synthesized manganese dioxide, *Chem. Mater*., 14, 3946, 2002.
16. Wu, N.L., Nanocrystalline oxide supercapacitors, *Mater. Chem. Phys.*, 75, 6, 2002.
17. Miller, J.M., Dunn, B., Tran, T.D., and Pekala, R.W., Morphology and electrochemistry of ruthenium/carbon/aerogel nanostructures, *Langmuir*, 15, 799, 1999.
18. Jurewicz, K., Delpeux, S., Bertagna, V., Béguin, F., and Frackowiak, E., Supercapacitors from nanotubes/polypyrrole composites, *Chem. Phys. Lett*., 347, 36, 2001.
19. Laforgue, A., Simon, P., Sarrazin, Ch., and Fauvarque, J.-F., Polythiophene-based supercapacitors, *J. Power Sourc*. 80, 142, 1999.
20. Arbizzani, C., Mastragostino, M., and Soavi, F., New trends in electrochemical supercapacitors, *J. Power Sourc*., 100, 164, 2001.
21. Mastragostino, M., Arbizzani, C., and Soavi, F., Conducting polymers as electrode materials in supercapacitors, *Solid State Ionics*, 148, 493, 2002.
22. Jurewicz, K., Babel, K., Ziolkowski, A., and Wachowska, H., Ammoxidation of active carbons for improvement of supercapacitor characteristics, *Electrochim. Acta*, 48, 1491, 2003.
23. Lota, G., Grzyb, B., Machnikowska, H., Machnikowski, J., and Frackowiak, E., Effect of nitrogen in carbon electrode on the supercapacitor performance, *Chem. Phys. Lett*., 404, 53, 2005.
24. Qu, D. and Shi, H., Studies of activated carbons used in double-layer capacitors, *J. Power Sourc*., 74, 99, 1998.
25. Gambly, J., Taberna, P. L., Simon, P., Fauvarque, J. F., and Chesneau, M., Studies and characterization of various activated carbons used for carbon/carbon supercapacitors, *J. Power Sourc*., 101, 109, 2001.
26. Kierzek, K., Frackowiak, E., Lota, G., Gryglewicz, G., and Machnikowski, J., Electrochemical capacitors based on highly porous carbons prepared by KOH activation, *Electrochim. Acta*, 49, 515, 2004.
27. Raymundo-Pinero, E., Cazorla-Amoros, D., Linares-Solano, A., Delpeux, S., Frackowiak, E., Szostak, K., and Béguin, F., High surface area carbon nanotubes prepared by chemical activation, *Carbon*, 40, 1614, 2002.
28. Frackowiak, E., Delpeux, S., Jurewicz, K., Szostak, K., Cazorla-Amoros, D., and Béguin, F., Enhanced capacitance of carbon nanotubes through chemical activation, *Chem. Phys. Lett*. 361, 35, 2002.
29. Lozano-Castelló, D., Cazorla-Amorós, D., Linares-Solano, A., Shiraishi, S., Kurihara H., and Oya, A., Influence of pore structure and surface chemistry on electric double layer capacitance in non-aqueous electrolyte, *Carbon*, 41, 1765, 2003.
30. Shi, H., Activated carbons and double layer capacitance, *Electrochim. Acta*, 41, 1633, 1996.
31. Guo, Y., Qi, J., Jiang, Y., Yang, S., Wang, Z., and Xu, H., Performance of electrical double-layer capacitors with porous carbons derived from rice husk, *Mat. Chem. Phys*., 80, 704, 2003.
32. Salitra, G., Soffer, A., Eliad, L., Cohen, Y., and Aurbach, D., Carbon electrodes for double-layer capacitors. I. Relations between ion and pore dimensions, *J. Electrochem. Soc*., 147, 2486, 2000.
33. Vix-Guterl, C., Frackowiak, E., Jurewicz, K., Friebe, M., Parmentier, J., and Béguin, F., Electrochemical energy storage in ordered porous carbon materials, *Carbon*, 43, 1293, 2005.
34. Okamura, M., Electric Double Layer Capacitor, U.S. Patent 6,064,562 and JP11067608, JEOL Ltd., 2000.
35. Kyotani, T., Control of pore structure in carbon, *Carbon*, 38, 269, 2000.
36. Ryoo, R., Joo, S.H., Kruk, M., and Jaroniec, M., Ordered mesoporous carbons, *Adv. Mater*., 13, 677, 2001.
37. Han, S., Lee, K.T., Oh, S.M., and Hyeon, T., The effect of silica template structure on the pore structure of mesoporous carbons, *Carbon*, 41, 1049, 2003.
38. Fuertes, A.B., Template synthesis of mesoporous carbons with a controlled particle size, *J. Mater. Chem*., 13, 3085, 2003.
39. Lee, J., Yoon, S., Hyeon, T., Oh, S. M., and Kim, K. B., Synthesis of a new mesoporous carbon and its application to electrochemical double-layer capacitors, *Chem. Comm*., 2177, 1999.

40. Jurewicz, K., Vix, C., Frackowiak, E., Saadallach, S., Reda, M., Parmentier, J., Patarin, J., and Béguin, F., Capacitance properties of ordered porous carbon materials prepared by a templating procedure, *J. Phys. Chem. Solids*, 65, 287, 2004.
41. Yoon, S., Lee, J., Hyeon, T., and Oh, S. M., Electric double-layer capacitor performance of a new mesoporous carbon, *J. Electrochem. Soc*., 147, 2507, 2000.
42. Pillay, B. and Newman, J., The influence of side reactions on the performance of electrochemical double-layer capacitors, *J. Electrochem. Soc*., 143, 1806, 1996.
43. Biniak, S., Świątkowski, A., and Pakuła, M., in *Chemistry and Physics of Carbon*, Vol. 27, Radovic, L.R., Ed., Marcel Dekker, New York, 2001, p. 125.
44. Laszlo, K., Tombacz, E., and Josepovits, K., Effect of activation on the surface chemistry of carbons from polymer precursors, *Carbon*, 39, 1217, 2001.
45. Pels, J.R., Kaptein, F., Moulijn, J.A., Zhu, Q., and Thomas, K.M., Evolution of nitrogen functionalities in carbonaceous materials during pyrolysis, *Carbon*, 33, 1641, 1995.
46. Kaptein, F., Moulijn, J.A., Matzner, S., and Boehm, H.P., The development of nitrogen functionality in model chars during gasification in CO_2 and O_2, *Carbon*, 37, 1143, 1999.
47. Grzyb, B., Machnikowski, J., Weber, J.V., Koch, A., and Heintz, O., Mechanism of co-pyrolysis of coal-tar pitch with polyacrylonitrile**,** *J. Anal. Appl. Pyrolysis*, 67, 77, 2003.
48. Grzyb, B., Machnikowski, J., and Weber, J.V., Mechanism of co-pyrolysis of coal-tar pitch with polyvinylpyridine, *J. Anal. Appl. Pyrolysis*, 72, 121, 2004.
49. Frackowiak, E., Lota, G., Machnikowski, J., Vix-Guterl, C., and Béguin, F., Optimisation of supercapacitors using carbons with controlled nanotexture and nitrogen content, *Electrochim. Acta*, on line, 2005.
50. Grimshaw, J., *Electrochemical Reactions and Mechanisms in Organic Chemistry*, Elsevier, Amsterdam, 2000, chapters 10 and 11.
51. Campomanes, R. S., Bittencourt, E., and Campos, J. S. C., Study of conductivity of polypyrrole-poly(vinyl alcohol) composites obtained photochemically, *Synth. Met*., 102, 1230, 1999.
52. Wampler, W.A., Wei, C., and Rajeshwar, K., Electrocomposites of polypyrrole and carbon black, *J. Electrochem. Soc*., 141, L13, 1994.
53. Frackowiak, E., Jurewicz, K., and Béguin, F., Development of new supercapacitor electrodes based on carbon nanotubes, *Polish J. Chem*., 78, 1345, 2004.
54. Frackowiak, E., Jurewicz, K., Delpeux, S., and Béguin, F., Nanotubular materials for supercapacitors, *J. Power Sourc*., 97–98, 822, 2001.
55. Xiao, Q. and Zhou, X., The study of multiwalled carbon nanotube deposited with conducting polymer for supercapacitor**,** *Electrochim. Acta*, 48, 575, 2003.
56. Chen, J. H., Huang, Z. P., Wang, D. Z., Yang, S. X., Li, W. Z., Wen, J. G., and Ren, Z. F., Electrochemical synthesis of polypyrrole films over each of well-aligned carbon nanotubes, *Synth. Met*., 125, 289, 2002.
57. An, K. H., Jeon, K. K., Heo, J. K., Lim, S. C., Bae, D. J., and Lee, Y. H., High-capacitance supercapacitor using a nanocomposite electrode of single-walled carbon nanotube and polypyrrole, *J. Electrochem. Soc*., 149, A1058, 2002.
58. Chen, G.Z., Shaffer, M.S.P., Coleby, D., Dixon, G., Zhou, W., Fray, D. J., and Windle, A.H., Carbon nanotube and polypyrrole composites: coating and doping, *Adv. Mater*., 12, 522, 2000.
59. Khomenko, V., Frackowiak, E., and Béguin, F., Determination of specific capacitance of conducting polymers/nanotubes composite electrodes using different cell configurations, *Electrochim. Acta*, 50, 2499, 2005.
60. Lee, H.Y. and Goodenough, J.B., Supercapacitor behavior with KCl electrolyte, *J. Solid State Chem*., 144, 220, 1999.
61. Hong, M.S., Lee, S.H., and Kim, S.W., Use of KCl aqueous electrolyte for 2 V manganese oxide/activated carbon hybrid capacitor, *Electrochem. Solid State Lett*., 5, A227, 2002.
62. Brousse, T., Toupin, M., and Bélanger, D., A hybrid activated carbon–manganese dioxide capacitor using mild aqueous electrolyte, *J. Electrochem. Soc*., 151, A614, 2004.
63. Khomenko, V., Raymundo-Piñero, E., and Béguin F., Optimisation of an asymmetric manganese oxide/activated carbon capacitor working at 2 V in aqueous medium, *J. Power Sourc*., in press, 2005.
64. Cuevas, F., Joubert, J.-M., Latroche, M., and Percheron-Guégan, A., Intermetallic compounds as negative electrodes of Ni/MH batteries, *Appl. Phys. A*, 72, 225, 2001.

65. Carpetis, C. and Peschka, W., A study on hydrogen storage by use of cryoadsorbents, *Int. J. Hyd. Energy*, 5, 539, 1980.
66. Agarwal, R.K., Noh, J.S., Schwarz, J.A., and Davini, P., Effect of surface acidity of activated carbon on hydrogen storage, *Carbon*, 25, 219, 1987.
67. Nützenadel, C., Züttel, A., Chartouni, D., and Schlapbach, L., Electrochemical storage of hydrogen in nanotube materials, *Electrochem. Solid State Lett.*, 2, 30, 1999.
68. Qin, X., Gao, X.P., Liu, H., Yuan, H.T., Yan, D.Y., Gong, W.L., and Song, D.Y., Electrochemical hydrogen storage of multiwalled carbon nanotubes, *Electrochem. Solid State Lett.*, 3, 532, 2000.
69. Rajalakshmi, N., Dhathathreyan, K.S., Govindaraj, A., and Satishkumar, B.C., Electrochemical investigation of single-walled carbon nanotubes for hydrogen storage, *Electrochim. Acta*, 45, 4511, 2000.
70. Kibria, A.K.M., Mo, Y.H., Park, K.S., Nahm, K.S., and Yun, M.Y., Electrochemical hydrogen storage behaviours of CVD, AD, and LA grown carbon nanotubes in KOH medium, *Int. J. Hydrogen Energy*, 26, 823, 2001.
71. Gundiah, G., Govindaraj, A., Rajalakshmi, N., Dhathathreyan, K.S., and Rao, C.N.R., Hydrogen storage in carbon nanotubes and related materials, *J. Mat. Chem.*, 13, 209, 2003.
72. Züttel, A., Sudan, P., Mauron, P., Kioyobayashi, T., Emmenegger, C., and Schlapbach, L., Hydrogen storage in carbon nanostructures, *Int. J. Hydrogen Energy*, 27, 203, 2002.
73. Tibbetts, G.G., Meisner, G.P., and Olk, C. H., Hydrogen storage capacity of carbon nanotubes, filaments, and vapor-grown fibres, *Carbon*, 39, 2291, 2001.
74. Hirscher, M., and Becher, M., Hydrogen storage in carbon nanotubes, *J. Nanosci. Nanotech.*, 3, 3, 2003.
75. Jurewicz, K., Frackowiak, E., and Béguin, F., Enhancement of reversible hydrogen capacity into activated carbon through water electrolysis, *Electrochem. Solid State Lett.*, 4, A27, 2001.
76. Jurewicz, K., Frackowiak, E., and Béguin, F., Electrochemical storage of hydrogen in activated carbons, *Fuel Process. Tech.*, 77–78, 415, 2002.
77. Jurewicz, K., Frackowiak, E., and Beguin, F., Towards the mechanism of electrochemical hydrogen storage in nanostructured carbon materials, *Appl. Phys. A*, 78, 981, 2004.
78. Ströbel, R., Jörissen, L., Schliermann, T., Trapp, V., Schütz, W., Bohmhammel, K., Wolf, G., and Garche, J., Hydrogen adsorption on carbon materials, *J. Power Sourc.*, 84, 221, 1999.
79. De la Casa-Lillo, M.A., Lamari-Darkrim, F., Cazorla-Amoros, D., and Linares-Solano, A., Hydrogen storage in activated carbons and activated carbon fibers, *J. Phys. Chem. B*, 106, 10930, 2002.
80. Texier-Mandoki, N., Dentzer, J., Piquero, T., Saadallah, S., David, P., and Vix-Guterl, C., Hydrogen storage in activated carbon materials: role of the nanoporous texture, *Carbon*, 42, 2744, 2004.
81. Cazorla Amorós, D., Alcañiz Monge, J., De la Casa Lillo, M.A., and Linares-Solano, A., CO_2 as an adsorptive to characterize carbon molecular sieves and activated carbons, *Langmuir*, 14, 4589, 1998.
82. Rzepka, M., Lamp, P., and De la Casa-Lillo, M.A., Physisorption of hydrogen on microporous carbons and carbon nanotubes, *J. Phys. Chem. B*, 102, 10894, 1998.
83. Béguin, F., Vix-Guterl, C., Dentzer, J., Friebe, M., Jurewicz, K., and Frackowiak, E., Mechanism of electrochemical hydrogen storage in nanotextured carbons, *Carbon*, submitted.
84. Nijkamp, M.G., Raaymakers, J.E.M.G., van Dillen, A.J., de Jong, K.P., Hydrogen storage using physisorption: materials demands, *Appl. Phys. A*, 72, 619, 2001.
85. Wang, Q. and Johnson, J.K., Molecular simulation of hydrogen adsorption in single-walled carbon nanotubes and idealized carbon slit pores, *J. Chem. Phys.*, 110, 577, 1999.
86. Béguin, F., Kierzek, K., Friebe, M., Jankowska, A., Machnikowski, J., Jurewicz, K., and Frackowiak, E., Effect of various porous nanotextures on the reversible electrochemical sorption of hydrogen in activated carbons, *Electrochim. Acta*, in press, 2005.

27 Low-Dimensional Thermoelectricity

Joseph P. Heremans
The Ohio State University, Columbus, Ohio

Mildred S. Dresselhaus
Massachusetts Institute of Technology,
Cambridge, Massachusetts

CONTENTS

ABSTRACT

This chapter reviews low-dimensional thermoelectricity in terms of the enhancement to the thermoelectric performance of materials in the form of quantum wells, quantum wires, or quantum dots, relative to their bulk counterparts. The nanometer-scale size effects on the thermopower, electrical, and thermal conductivity are discussed, and the ability of nanostructures to provide independent control of these variables is emphasized. Large-scale implementation of these concepts is also considered.

27.1 INTRODUCTION

The thermoelectric and thermomagnetic properties of materials are fundamental transport properties. Thermoelectric phenomena also have practical applications in energy conversion. Thermoelectric materials can generate electrical power from heat, and use electricity to function as heat pumps, thereby providing active cooling or heating. The working fluid in these energy converters consists of conduction electrons.

The classical aspects of this subject have a long and distinguished history. Since the discovery of the thermoelectric effects in the 1823–1836 period by Seebeck, Peltier, and Lenz, the field has

grown in spurts, benefiting from scientific breakthroughs over the centuries. The first period of rapid growth, in the years 1851–1887, resulted from the development of thermodynamics, leading to major new contributions to the field by Lord Kelvin, Boltzmann, and Nernst. Interest in the irreversible thermodynamic aspects of thermoelectric phenomena continued [1], but the applications were limited to thermocouple thermometry. The second growth spurt occurred in the period 1947–1960 when Telkes [2], Ioffe [3,4] and Goldsmid [5] applied the newly developed knowledge of transport in semiconductors to the problem. The technology developed at that time still dominates today [6], except for progress made in skutterudite materials [7–9]. We can hope that recent strides in nanotechnologies will lead to the third period of rapid growth in this field. In this context, it was recognized [10,11] in the 1990s that low-dimensional systems should result in materials with much better thermoelectric efficiencies than their bulk counterpart materials, through low-dimensional effects on both charge carriers and lattice waves. Such improvements in thermoelectric properties have been experimentally demonstrated on Bi_2Te_3/Sb_2Te_3 superlattices [12] and on PbTe/PbSeTe and PbSnTe/PbSnSeTe quantum dot superlattices [13] in the early 2000.

The basic material property governing the efficiency of thermoelectric generators, and the coefficient of performance of thermoelectric heat pumps, is the thermoelectric figure of merit [5]:

$$Z = S^2\sigma/\kappa \tag{27.1}$$

where S is the Seebeck coefficient, also called the thermoelectric power, σ the electrical conductivity and κ the thermal conductivity. Z is usually multiplied by the average temperature T to yield a number ZT, which is the dimensionless thermoelectric figure of merit. Conventional thermoelectric materials have been limited to $ZT = 1$ at $T = 300$ K; the new nanoscale materials have reached $ZT = 2$ at 300 K [13], and even $ZT = 3$ at 450 K [14] (see Section 27.5.2). This is significant as the value of $ZT = 2$ is the threshold [15] at which one can envision large-scale applications of thermoelectricity with performances comparable to those of conventional mechanical machines.

The three ingredients in the figure of merit, S, σ, and κ are interdependent, and this impedes the optimization of Z in conventional three-dimensional (3-D) systems. Indeed, most thermoelectric materials are semiconductors in which κ is in large part due to lattice conduction, with acoustic phonons as the dominant carriers. It is therefore usual to dissociate Z into a power factor $S^2\sigma$, dominated by charge carriers, and a thermal conductivity κ, dominated by phonons. The higher the density of electrons, the higher σ, but the lower S. Longer electron mean free paths will improve σ without detriment to S, but they usually also imply longer phonon mean free paths, and thus an increase in κ. Herein lies the advantage of being able to think in terms of the nanometer scale: the dimensionality of the system adds a new design parameter that can lift the interdependence between the transport coefficients. The resulting gain in ZT low-dimensional thermoelectricity comes through a combination of two mechanisms:

1. A reduction in the lattice thermal conductivity due to the scattering [12,16], or to the refraction [17] of phonons at the physical boundaries of the nanoscale structure.
2. An increase in the power factor $S^2\sigma$, or at least the avoidance of a decrease in $S^2\sigma$ with the decrease in κ, through size quantization [10,11] or through energy filtering [18,19] of the electrons.

It is convenient to view the problem of low-dimensional thermoelectricity in terms of the different length scales that enter the transport equations, and to compare these with the characteristic sample dimension or size d. Firstly, in the regime of diffusive transport, the electrical conductivity and the lattice thermal conductivity are typically dominated by the electron and the phonon mean free paths, l_e and l_ϕ, respectively, both of the order of tens to hundreds of nanometers. Since it is beneficial to increase the electrical conductivity and to decrease the thermal conductivity, one would want to work with samples with critical dimensions d so that d may influence l_ϕ but affect l_e much less. It was realized

earlier [4] in the example of the $PbSe_xTe_{1-x}$ alloy system that alloy scattering can induce a strong decrease in l_ϕ, accompanied by only a moderate decrease in l_e, and thus in the electrical conductivity, although this sets a condition on the system: $l_e < l_\phi$. In low-dimensional systems, an eventual decrease in l_e can be compensated by an increase in the Seebeck coefficient that results from size quantization [10,11]. For this to work, the system must be sufficiently free of disorder so that the band structure model holds. The density of electronic states is then a strong function of the dimensionality of the system, as can be seen in Figure 27.1. As we will show later, S is a function of the energy derivative of the density of states, and is thus enhanced when the latter is a sharply peaked function of energy, as is the case for lower dimensional crystals in Figure 27.1. Size quantization occurs when the size d becomes smaller or comparable to the electron wavelength λ. However, disorder in the solid broadens the peaks shown in the lower dimensional 0-D and 1-D systems in Figure 27.1. The smaller the diameter of a quantum wire, the higher the likelihood that one defect will localize the electron wave function to one section of the wire, impeding transport. The band structure picture then no longer holds and the conduction becomes dominated by localization effects, characterized by the phase coherence length L_p of the electrons in the system. Localization effects are typically identified by magnetoresistance measurements, in which L_p is compared with the sample dimension d and also to the magnetic length $l_H = \sqrt{\hbar/2eH}$, which represents the spatial extent of the wave function on a Landau level. Since L_p is the order of d only at low temperatures, localization effects are not encountered at room temperature in high-quality thermoelectric materials with $d > 5$ nm.

In this review, we start by outlining a few of the basic transport equations in 3-, 2-, and 1-dimensions, and show how low dimensionality can improve *ZT*. We then review the thermoelectric (TE) properties in quantum wells (2-D systems), in Bi and $Bi_{1-x}Sb_x$ quantum wires (1-D systems), and in nearly 0-D systems, such as segmented quantum wires, quantum dot superlattices, and quantum dots between quantum point contacts. We conclude by suggesting that the technological future for thermoelectric energy conversion devices lies in "bulk" low-dimensional systems: indeed, the nanostructures that have experimentally demonstrated the considerable increases in *ZT* that make the whole endeavor worthwhile are difficult to manufacture, and provide only a proof of principle. For the field of low-dimensional thermoelectricity to make economic sense, one must be able to produce kilograms or even tons of thermoelectric nanomaterials, which therefore must self-assemble. Several approaches have already yielded encouraging preliminary results: for instance, an increase in Seebeck coefficient is observed in sintered PbTe samples made of nanometer-sized grains [19] as well as in $CoSb_3$/fullerene composites [20]. We cite in this context a recent report on bulk AgSbPbTe alloys [21]; these materials exhibit a high-temperature performance of $ZT = 2$, and the

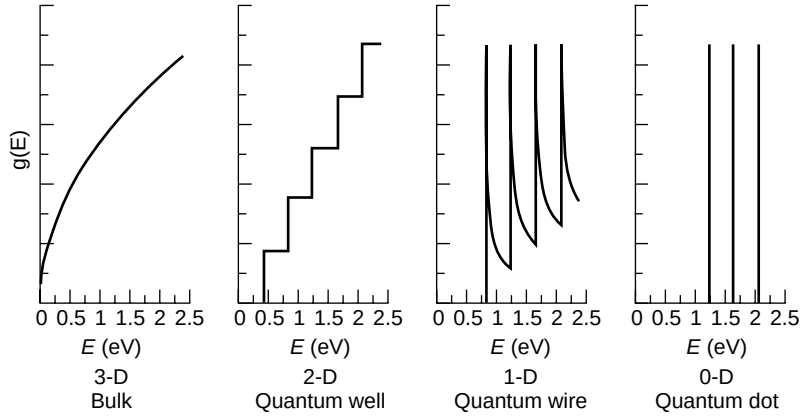

FIGURE 27.1 Electronic density of states $g(E)$ as a function of carrier energy E, for semiconductors of different dimensionality: (a) a bulk three-dimensional (3-D) crystal; (b) a 2-D crystal, or quntum well; (c) a 1-D crystal or quantum wire; (4) a 0-D crystal or quantum dot (see Table 27.1).

alloys contain nanometer-sized inclusions, although the precise role of these inclusions is not clear at present.

27.2 PHENOMENOLOGICAL THEORY FOR TRANSPORT IN DIFFERENT DIMENSIONALITIES

The first concepts related to low-dimensional thermoelectricity were introduced in the early 1990s in terms of theoretical predictions for enhanced thermoelectric performance in 2-D quantum well superlattices [10] and 1-D quantum wire systems [11] based on very elementary models. We start by reviewing the factors that affect *Z*.

The thermal conductivity is the sum of two terms [22], the lattice thermal conductivity κ_L and the electronic thermal conductivity κ_E:

$$\kappa = \kappa_L + \kappa_E \tag{27.2}$$

The lattice thermal conductivity is mostly due to the propagation of acoustic phonons in the solid, and can be described by the classical theory of transport in diffusive regimes:

$$\kappa_L = C_v v_s l_\phi \tag{27.3}$$

where C_v is the specific heat per unit volume, v_s is the sound velocity, and l_ϕ is the phonon mean free path. The dominant mechanism through which low-dimensional systems limit κ_L is by limiting $l_\phi \leqslant d$.

The electronic thermal conductivity is related to the electrical conductivity by the Wiedemann–Franz law [22]:

$$\kappa_E = L\sigma T \tag{27.4}$$

where L is the Lorenz number, a relatively complex transport parameter, but which we can approximate by its free electron value $L_0 = (\pi^2/3)(\kappa_B/e)$ when the charge carriers undergo only elastic collisions.

The electrical conductivity of a degenerate semiconductor is given by [22]

$$\sigma = ne\mu \tag{27.5}$$

where n is the density of charge carriers, each with charge e, and a mobility μ. The mobility is, in turn, related to the carrier's drift velocity per unit of electric field [22], and is therefore related to the electron mean free path l_e. Most thermoelectric materials are degenerately doped semiconductors, for which

$$l_e = v_F \tau = v_F \mu m^*/e \tag{27.6}$$

where v_F is the carrier Fermi velocity, τ the relaxation time and m^* the carrier effective mass.

The Mott [23] relation gives the Seebeck coefficient, irrespective of the transport mechanism, as a function of the energy-dependent electrical conductivity $\sigma(E)$ of the charge carriers of energy E:

$$S = \frac{k_B}{e}\int_0^\infty \sigma(E)\left(\frac{E - E_F}{\kappa_B T}\right)\left(\frac{\partial f_0}{\partial E}\right)\mathrm{d}E \tag{27.7}$$

where f_0 is the Fermi distribution function, with Fermi energy E_F. Equation (27.5) holds at each energy level E, and $\sigma(E) = n(E)e\mu(E)$, where $n(E)$ is the density of electrons at any given level E,

namely the density of states times the occupation probability. For degenerate semiconductors, Equation (27.7) simplifies to

$$S = \frac{\pi^2}{3}\frac{k_B^2 T}{3}\left\{\frac{\mathrm{d}[\ln(\sigma(\mathrm{E}))]}{\mathrm{d}E}\right\}_{E=E_F} \tag{27.8}$$

The electrical conductivity σ is given by

$$\sigma = \int_0^\infty \sigma(E)\left(-\frac{\partial f_0}{\partial E}\right)\mathrm{d}E \tag{27.9}$$

and, for degenerate semiconductors, $\sigma = \sigma(E_F)$. When the density of states is a rapidly varying function of E, such as is the case for 1-D and 0-D systems in Figure 27.1, Equation (27.8) implies that the Seebeck coefficient is much enhanced. This is one of the mechanisms through which low-dimensionality can preserve, or indeed enhance, the power factor.

Only the diffusion thermoelectric transport is considered in this review, ignoring such low-temperature effects as phonon drag. Strictly speaking, there is no diffusive transport in 0-D systems as there is no free electron wave vector, but the Mott relation holds irrespective of the transport mechanism. The early Hicks and Dresselhaus [10,11] theory for the diffusive transport in low-dimensional solids assumes for simplicity that the dispersion relation is parabolic, that the Fermi surfaces are ellipsoidal, and that acoustic phonon scattering dominates the scattering of electrons. While the detailed models that were developed later to describe actual low-dimensional systems are usually made using numeric simulations, we will derive here simple algebraic formulae to illustrate how the use of low dimensions gives rise to an increase in ZT.

In a 3-D bulk system, the process to determine the optimum ZT of a material has been known since the advent of semiconductor thermoelectric materials systems [5]. The dispersion relation for a single-carrier pocket is assumed to be

$$E = \frac{\hbar^2 k_x^2}{2m_x^*} + \frac{\hbar^2 k_y^2}{2m_y^*} + \frac{\hbar^2 k_z^2}{2m_z^*} \tag{27.10}$$

where the propagation vectors are k_x, k_y, and k_z along the three principal axes x, y, and z of the crystal. The effective mass tensor is diagonal and consists of components m_x^*, m_y^*, and m_z^*. The density of states is given as a function of carrier energy E, in Table 27.1: it follows a $E^{1/2}$ law for a 3-D system, as represented in Figure 27.1. Hicks and Dresselhaus [10] further derive equations for the transport integrals following the classical theory, and derive analytic expressions for σ, S, and κ_E also given in Table 27.l. In these integrals, the relaxation time τ and the mobility μ, which are related as shown in Equation (27.6), are taken to be along the direction x of the flow of charge and heat current. The transport properties are given as a function of integrals over the electron population, which are Fermi integrals defined as

$$F_n = \int_0^\infty \frac{x^n}{\exp(x - x_F) + 1}\mathrm{d}x \tag{27.11}$$

where x and x_F are the energy and the Fermi energy of the carriers, normalized to the thermal energy, $x = E/(k_B T)$. In Figure 27.2, we show as full lines the values of σ, S, and κ_E at 300 K for a hypothetical 3-D solid as a function of the Fermi energy. The value of $E_F = 0$ corresponds to a Fermi energy aligned with the band edge. We assumed, when calculating Figure 27.2, values of the masses and mobilities somewhat similar to those of the classical bulk Bi_2Te_3 material that is most commonly in practical use today, but projected onto an isotropic solid with $m_x^* = m_y^* = m_z^* = 0.1\ m_0$, where m_0 is the free electron mass. We also assume that $\mu = 1200\ \mathrm{cm^2/Vsec}$ and thus $\tau = 6.8 \times 10^{-13}$ sec. As

TABLE 27.1
The Density of States[a] and Transport Integrals[b] in 3-D, 2-D, and 1-D Systems for Transport along the *x* Direction

	3-D System Bulk	2-D System Quantum Well	1-D System Quantum Wire
$g(E)$	0 for $E < 0$ $\frac{\sqrt{m_x^* m_y^* m_z^* (2E)}}{\hbar^3 \pi^2}$; $E > 0$	0 for $E < E_i$ $\frac{\sqrt{m_x^* m_y^*}}{\hbar \pi d}$; $E > E_i$	0 for $E < E_{i,j}$ $\frac{\sqrt{2m_x^*}}{\hbar \pi d^2 \sqrt{E - E_{i,j}}}$; $E > E_{i,j}$
σ	$\frac{\sqrt{(2k_BT)^3 m_x^* m_y^* m_z^*}}{2\pi^2\hbar^3} F_{1/2} e\mu$	$\frac{k_BT\sqrt{m_x^* m_y^*}}{\pi\hbar^2 d} F_0 e\mu$	$\frac{\sqrt{2k_BTm_x^*}}{\pi\hbar d^2} F_{-1/2} e\mu$
S	$\frac{k_B}{e}\left(\frac{5F_{3/2}}{3F_{1/2}} - \frac{E_F}{k_BT}\right)$	$\frac{k_B}{e}\left(\frac{2F_1}{F_0} - \frac{E_F}{k_BT}\right)$	$\frac{k_B}{e}\left(\frac{3F_{1/2}}{F_{-1/2}} - \frac{E_F}{k_BT}\right)$
κ_E	$\frac{\tau k_B (2k_BT)^{5/2}\sqrt{m_y^* m_z^*}}{6\pi^2\hbar^3\sqrt{m_x^*}}$ $\times\left(\frac{7F_{5/2}}{2} - \frac{25F_{3/2}^2}{6F_{1/2}}\right)$	$\frac{\tau k_B (2k_BT)^2\sqrt{m_y^*}}{4\pi\hbar^2 d\sqrt{m_x^*}}$ $\times\left(3F_2 - \frac{4F_1^2}{F_0}\right)$	$\frac{\tau k_B (2k_BT)^{3/2}}{\pi^2\hbar d^2\sqrt{m_x^*}}$ $\times\left(\frac{5F_{3/2}}{2} - \frac{9F_{1/2}^2}{2F_{-1/2}}\right)$

[a] The density of states for 1-D and 2-D systems are a sum of the density of states contributions given in this table for each subband (see Figure 27.1).

[b] Transport integrals are expressed in terms of the Fermi integral defined in Equation (27.11).

the Fermi energy is increased, the Seebeck coefficient decreases, while σ and κ_E increase. Since the total thermal conductivity is given by Equation (27.2), these two conductivities do not cancel each other out in *ZT*, and the figure of merit itself, shown in the bottom frame of Figure 27.2, exhibits a maximum when plotted as a function of E_F. The doping level of the thermoelectric material must be optimized in such a way that the Fermi level aligns with this maximum, and this, in turn, depends on the exact value of the lattice thermal conductivity. In this plot, we assumed a constant $\kappa_L = 1.5$ W/m K, again compatible with conventional thermoelectric materials. With these assumptions, we see in Figure 27.2, that it is possible to achieve about $ZT \simeq 1$ in this 3-D material.

The 2-D structure that Hicks and Dresselhaus [10] consider next is a slab of the same semiconductor material of thickness *d*, where *x* and *y* are the in-plane dimensions and *z* denotes the quantum confined direction. When *d* is smaller than the de Broglie wavelength of the electron along *z* in the equivalent 3-D case, the finite dimensions of the sample are modeled by the existence of two infinite potential walls that confine the electron in a quantum well along *z*, while leaving the electron unconstrained along *x* and *y*. The resulting dispersion relation is:

$$E = \frac{\hbar^2 k_x^2}{2m_x^*} + \frac{\hbar^2 k_y^2}{2m_y^*} + E_i \tag{27.12}$$

where E_i are the quantum sublevels given by ($i = 1, 2, ...$)

$$E_i = \frac{\hbar^2 \pi_z^2}{2m_z^* d^2} i \tag{27.13}$$

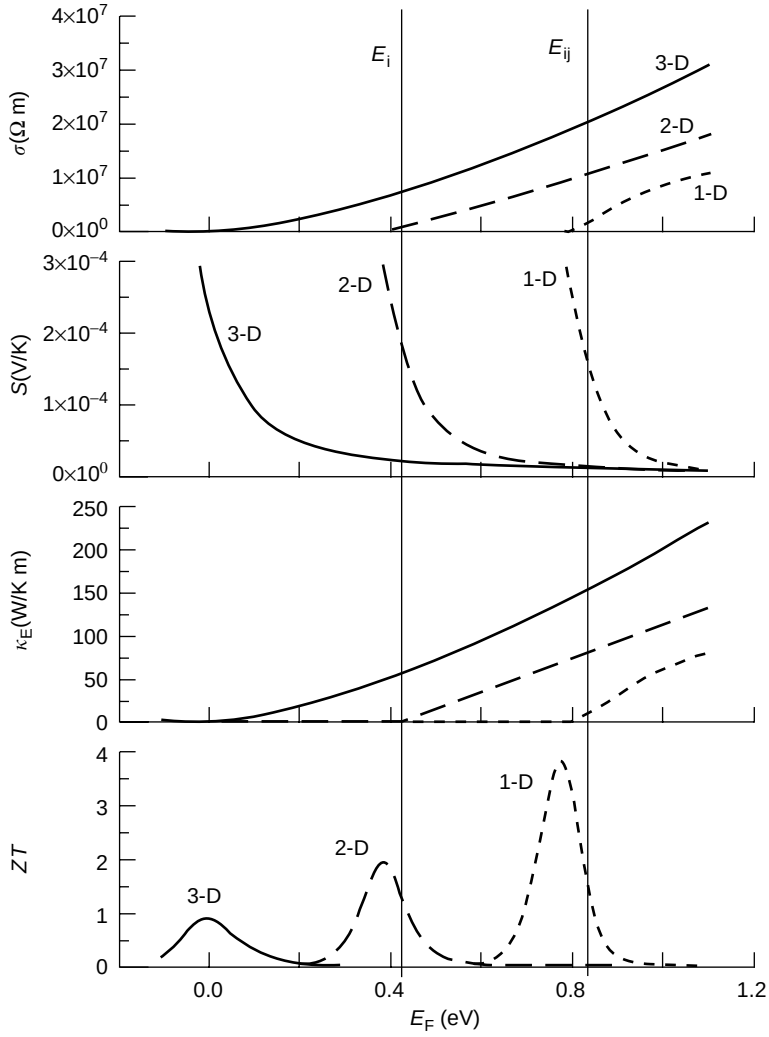

FIGURE 27.2 The transport properties for 3-D (full line), 2-D (long dashes), and 1-D (short dashes) solids as a function of the Fermi energy. The calculations are made at 300 K, and assume an isotropic Fermi surface with $m^* = 0.1m_0$. The thickness of the quantum well and the diameter of the quantum wire are $d = 3$ nm. The value of the first size-quantized subband edge, E_i for 2-D systems and $E_{i,j}$ for a 1-D system, are shown. The Fermi energy in each system has to be chosen by doping to maximize the value of ZT, and the location is different for the different dimensionalities. For the calcualtions of ZT, a constant $\kappa_L = 1.5$ W/m K was used. The maximum achievable ZT is improved as the dimensionality of the system is decreased.

The density of states in 2-D is a series of steps, given in Table 27.1 and represented in Figure 27.1. The resulting transport integrals, assuming that only the lowest sublevel E_i is occupied, are again in Table 27.1 and shown in Figure 27.2 as lines with long dashes, assuming that d is smaller than the de Broglie wavelength in the z direction. We also show in Figure 27.2 the position of the sublevel E_i $(i = 1)$. The procedure to find the optimum Fermi energy is the same as in the 3-D case, and we used the same value of $\kappa_L = 1$–5 W/m K. The best ZT is achieved when the Fermi level is near E_i. The maximum value of ZT that can be achieved in this 2-D system is $ZT \simeq 2$.

Moving on to the 1-D system, Hicks and Dresselhaus [11] consider a square wire of the same semiconductor material of cross-section $d \times d$, in the y and z directions, leaving the carrier motion free along the x direction. Once again, d is smaller than the de Broglie wavelength of the electron

along the *z* and *y* direction in the equivalent 3-D case, and the finite dimensions of the sample are modeled by the existence of infinite potential walls that confine the electron in a quantum well along *z* and *y*, while leaving the electron unconstrained along *x*. The structure is a "quantum wire," with a dispersion relation given by

$$E = \frac{\hbar^2 k_x^2}{2m_x^*} + E_{i,j} \tag{27.14}$$

where $E_{i,j}$ are the quantum sublevels given by ($i, j = 1, 2, ...$)

$$E_{i,j} = \frac{\hbar^2 \pi^2}{2m_y^* d^2} i + \frac{\hbar^2 \pi^2}{2m_z^* d^2} j \tag{27.15}$$

The density of states is a series of discontinuities, given in Table 27.1 and represented in Figure 27.1. The resulting transport integrals, assuming that only the lowest sublevel $E_{i,j}$ is occupied, are again in Table 27.1 and shown in Figure 27.2 as lines with short dashes, for $d = 3$ nm. Once again following the same procedure to find the optimum Fermi energy, we observe that the maximum value of *ZT* that can be achieved in this 1-D system is now almost 4. This is the effect of only the size quantization of the electrons, and comes on top of eventual reductions in lattice thermal conductivity which further increases *ZT*.

The energy levels of a perfect 0-D system, a quantum dot, are given by a set of three discrete quantum numbers. The density of states at 0-K of a perfect quantum dot is, as can be seen in Figure 27.1, a delta function, and thus one expects an extremely large Seebeck coefficient. However, since there is no free *k* vector, there is no transport of heat or charge. Connecting a quantum dot with effective electrical contacts perturbs the energy levels of the dot to the extent that the system is only quasi-zero-dimensional. The thermoelectric properties of quantum dots have been measured in several specific geometries, which we will review in the experimental section. In general, it can be stated that the Seebeck coefficient of these systems is related to the conductivity by the Mott relation, or, for nondegenerate systems, by Equation (27.7).

The above calculations do assume that the scattering rate is independent of dimension or sample size. Broido and Reinecke [24,25] did reconsider this hypothesis and suggest that the power factor is negatively affected when the carriers are confined to a 2-D structure due to an enhancement of the electron–phonon scattering rates. While this leads to a lesser improvement of the power factor in quantum well structures, quantum wires are still expected by these authors to be particularly attractive for thermoelectric applications.

Conversely, the argument can be made that in lower dimensional systems, there are fewer states that an electron can scatter into so that the mobility and the power factor could also possibly improve.

27.3 TWO-DIMENSIONAL THERMOELECTRIC MATERIALS: QUANTUM WELLS

One of the first reports of a material with $ZT > 2$ [12] was published on Bi_2Te_3/Sb_2Te_3 superlattices. The films were rather thin, so that the measurements of *ZT* were taken using a set of samples with different thicknesses, and then extrapolated to infinite thickness. The results are thus indirect. In these superlattices, the claimed increase in *ZT* comes from a strong decrease in κ_L. Comparing random $Bi_{2-x}Sb_xTe_3$ ($x = 0.5$) alloys with $\kappa_L = 0.49$ W/m K in the direction parallel to the *c*-axis to the value $\kappa_L = 0.22$ W/m K for a Bi_2Te_3/Sb_2Te_3 superlattice with 1 nm/5 nm layer thicknesses grown along the same direction, one observes a decrease of κ_L by a factor of 2.2. The decrease in thermal conductivity has been confirmed for $Bi_2Te_3/Bi_2(Se_xTe_{1-x})_3$ superlattices [26,27].

Lead salt films have been extensively studied in this context by numerous groups [28–31]. The decrease in thermal conductivity has been well documented, for instance for $PbTe/PbSe_{0.2}Te_{0.8}$

superlattices. Experimental proof of principle for the predictions of enhanced of *ZT* by a combination of thermal conductivity reduction and an enhancement of the power factor by quantum confinement effects was demonstrated in the PbTe/$Pb_{0.93}Eu_{0.07}Te$ quantum well system [31,32], and this work stirred interest in low-dimensional thermoelectric systems as a fruitful direction for new thermoelectric materials research. Figure 27.3(a) shows the structure (a) of a 2 nm/20 nm PbTe/$Pb_{0.93}Eu_{0.07}Te$ multiple quantum well, and Figure 27.3(b) shows as dots the in-plane Seebeck coefficient measured on the multiple quantum well as a function of doping density for p-type materials. The values of *S* for similarly doped bulk PbTe are also shown. The resulting power factor is shown again as a function of doping level in Figure 27.3(c). Both the bulk and the 2-D structures have a maximum, consistent with the simple theory in Figure 27.2. The maximum $S^2\sigma$ value achieved for quantum wells is four times higher than that for bulk and is shifted to higher doping levels; the measured values of the power factor are in good agreement with model calculations [34]. Using a value for lattice thermal conductivity of 2 W/m K for the wells alone, and ignoring the influence of the PbEuTe barrier layers, these values correspond to room temperature *ZT* values of 1.5 for p-type material (a *ZT* value of 1.2 was obtained for n-type material). Similar, although somewhat different results were reproduced by the Fraunhofer group for PbTe/PbSrTe [35] and PbTe/PbSeTe [26–28] quantum well structures. They too have a power factor that increases for well structures below 3 to 5 nm due to a strong increase in *S*, but the power factor of their quantum wells does not exceed that of their bulk material because the narrower wells have a reduced electron mobility. The *ZT* values reported for their PbTe/PbSrTe quantum wells are, in one case, in excess of 1, but this case is ascribed to a reduction of the lattice thermal conductivity to about 0.30 W/m K.

The subsequent development in the field of lead salt quantum structures focuses on quantum dot superlattices, which will be treated in Section 27.5.2.

Historically, the first thin-film materials on which size quantization effects were observed were bismuth thin films [36]. At 4.2 K and even at 77 K, Ogrin et al. [36] observed an oscillatory behavior of the resistivity and Hall coefficients of these films when these quantities were plotted as a function of film thickness. The authors modeled this behavior by the presence of size-quantized energy levels which modulate the density of states much like Landau levels do in Shubnikov–de Haas measurements. These results were repeated and extended to thermoelectric properties by Rogacheva et al. [37] recently; they observed an oscillatory behavior up to room temperature.

In the 2-D structures described so far, only the quantum wells were achive and the barrier material was not electrically conducting. Attempts to use both wells and barriers are labeled “carrier pocket engineering.” It was for the GaAs/AlAs system that the concept of carrier pocket engineering [39] was first developed. In this system, the whole GaAs/AlAs superlattice sample contributes to enhancing *ZT*. In the GaAs regions, the zone center carrier pockets contribute to transport and thermoelectricity, with the AlAs regions forming the energy barriers and thereby giving rise to quantum confinement transport conditions. However, in the AlAs regions of the sample, the *X* point carriers would also be contributing to the Seebeck coefficient and to thermoelectricity. Another prototype thermoelectric 2-D quantum well system was demonstrated in the Si–Ge superlattice system [38].

27.4 ONE-DIMENSIONAL THERMOELECTRIC MATERIALS: QUANTUM WIRES

The literature on 1-D thermoelectric materials is dominated by bismuth because it is an attractive material for low-dimensional effects in general and because it can be successfully fabricated in the form of a quantum wire. Bismuth has a band structure with multiple carrier pockets, comprising three electron and one hole pockets per unit cell. Carrier mobilities are very high. In bulk, Bi is a semimetal, with an energy overlap between the electron and hole extrema of about 38 meV. The electron and hole Fermi surfaces of bulk Bi and their locations within the Brillouin zone are shown as an inset in Figure 27.4(a). Having opposite signs, the electron and hole thermopowers partially compensate each other,

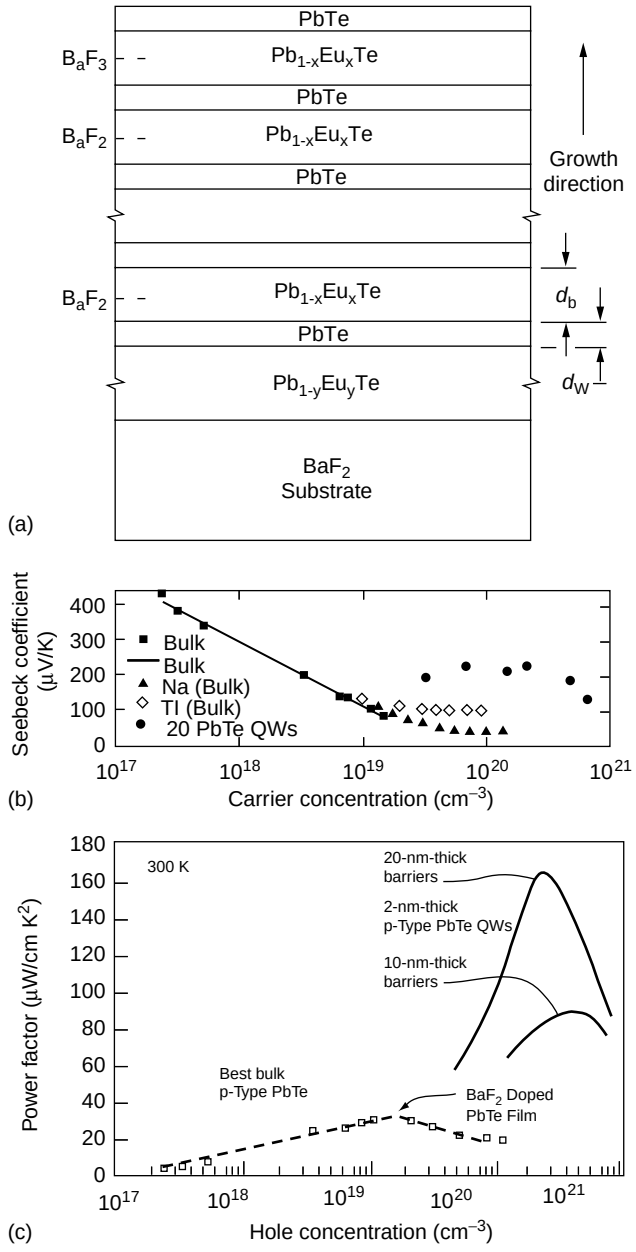

FIGURE 27.3 (a) Structure of a PbTe/$Pb_{1-x}Eu_xTe$ superlattice, typically with 2 nm thick PbTe wells d_W and 10- or 20-nm thick $Pb_{1-x}Eu_xTe$ barriers d_b. The $Pb_{1-y}Eu_yTe$ buffer layer is about 150 nm thick. (b) Seebeck coefficient S vs. hole carrier density in a superlattice with 2 nm p-type wells (dots), compared to the same quantity in bulk p-type PbTe doped with Na or Tl. (c) The resulting power factor $S^2\sigma$ vs. hole density shows a strong enhancement over the power factor of bulk PbTe in the high carrier concentration regime. S and σ are measured in the plane of the superlattice. (After Harman, T.C., et al., United States Patent No. 6452206 B1, 2002.)

so that the total thermopower is too low for bulk Bi to be useful as a thermoelectric. It was recognized early on [40] that if one could somehow suppress the holes, n-type Bi would have a ZT value as high as 1.7 at 300 K. The smallness of the electron effective masses results in very high size-quantization energies (see Equations (27.13) and (25.15)) so that the separation between the quantum sublevels exceeds the thermal energy k_BT at room temperature for wires of diameters in tens of

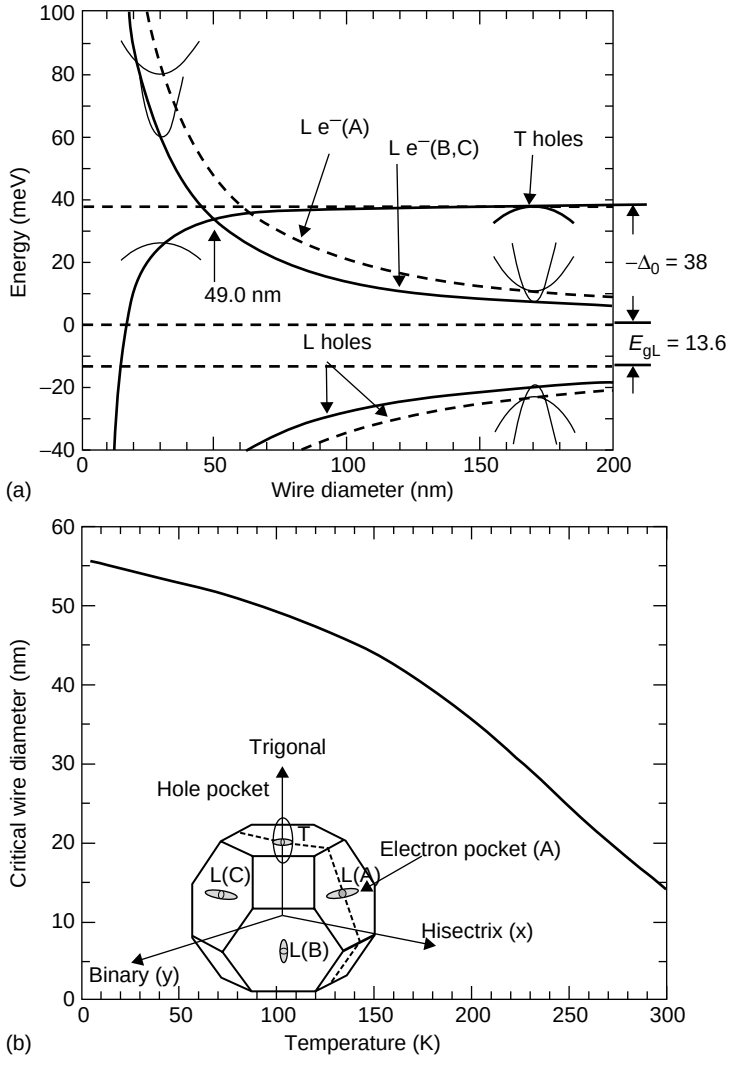

FIGURE 27.4 (a) Dependence on wire diameter of the shifts of the energies of the hole and electron subbands of bismuth nanowires oriented along the $[01\bar{1}2]$ crystalloprophic axis. The inset in (b) shows the Brillouin zone of Bi, with the Fermi surface consisting of one T-point hole pocket and three L-point electron pockets. With respect to the direction of the long axis of the wire $[\bar{0}1\bar{1}2]$, the electron pockets are not equivalent. The pocket labled A is along one of the mirror planes, and the two pockets labeled B and C are equivalent to each other, but inequivalent with respect to A. The value of the wire diameter where the electron and hole pockets cross (49 nm) is the critical wire diameter d_c. The temperature dependence of the critical wire diameter d_c is shown in frame (b). (After Lin, Y.-M. et al., *Phys. Rev. B*, 62, 4610–4623, 2000.)

nanometers. More importantly, it was predicted [41] that by introducing quantum confinement and going to systems of smaller size, nanowires of the semimetal Bi could undergo a transition to a semiconductor as the lowest conduction subband edge crossed the highest valence subband edge, as shown in Figure 27.4(b) [42]. In this way, semimetals such as bismuth, which are not good thermoelectric materials in bulk form, become attractive low-dimensional thermoelectric materials.

Detailed numerical band structure calculations [33] on bismuth nanowires assumed the simplest possible model for a 1-D quantum wire in which the carriers are confined inside a cylindrical potential well bounded by a barrier of infinite potential height. This is justified in view of the large band gap of the Al_2O_3 host material (3.2 eV) that has been used successfully as a barrier material for Bi

quantum wires [43]. The computational model produced the results shown in Figure 27.4. With decreasing wire diameter d_w, Figure 27.4(a) shows that the energies of the lowest lying electron subband edges decrease while the energy of the hole subband edge increases, resulting in a metal–insulator transition at a critical diameter d_c of ~49 nm at 77 K. The exact value of this critical diameter d_c depends on which crystallographic direction is aligned with the wire axis. Since the band structure parameters are temperature-dependent, so is the critical diameter, and this temperature dependence is shown in Figure 27.4(b).

The results of these numerical calculations have been experimentally confirmed. Bismuth nanowires of diameters in the range of ot 4 to 200 nm have been grown in a variety of porous host materials, typically based on alumina or silica. Much work has been done using porous anodic alumina as a host material for growing Bi nanowires [44]. In this host material, a layer of anodic Al_2O_3 is grown on metallic Al, and that layer contains a quasi-periodic array of ordered cylindrical pores that self-organize and grow normal to the layer. The $A1_2O_3$ layer can be chemically detached from the metal substrate to form a free-standing membrane with 7 to 200 nm diameter pores extending across the whole layer thickness. Other porous host materials, in which the pores form a random network, have been used [45], including porous Al_2O_3, silica gel, and porous vycor glass. Three different techniques have been used to grow Bi nanowires in these pores: electrochemical deposition [46,47], high-pressure liquid injection [44], and vapor-phase growth [48]. All three techniques produce highly crystalline wires and, in the case of oriented porous anodic alumina host, the liquid injection and vapor-phase growth techniques produce single-crystal wires along a preferred orientation. For vapor-grown wires the wire axis is preferentially in the $[01\bar{1}2]$ direction for which the calculations are shown in Figure 27.4(a).

Figure 27.5 shows a summary of the data from measurements of the electrical conductivity [45,48] and Seebeck coefficient [45,49] collected from various references. The exact number of wires connected between the measurement electrodes in these experiments is unknown, and so is the effective cross section of the sample. Therefore no absolute values of σ can be given, and for this reason the value of the resistance $R(T)$ normalized to the room-temperature value is plotted in Figure 27.5(a). This has the unfortunate consequence that neither the power factor nor the one-dimensional figure of merit can be measured. For a quantitative determination of $R(T)$ and ZT, single-wire measurements are needed, but these are not available to date. The Seebeck coefficient of oriented 200 nm-diameter semimetallic wires was measured first [49] and was shown to be very consistent with the partial electron and hole thermopowers calculated from the band structure and from the density of carriers, which were determined from Shubnikov–de Haas measurements on the same samples. The results of thermopower measurements [45] on wires of narrower diameters grown in alumina, silica, and vycor glass, three host materials with randomly oriented pores, is also shown in Figure 27.5(b). The resistance data (Figure 27.5[a]) show the semiconductor/semimetal transition as follows. At wire diameters above 50 nm, the low-temperature slope of $R(T)$ is positive since the carrier density in a semimetal is fixed by the energy overlap between the conduction and valence bands, and the carrier mobility decreases through phonon scattering. At $T > 100$ K, the density of both electrons and holes increases through thermal activation, and this gives a negative temperature coefficient to $R(T)$. In the semiconductor regime, the negative slope prevails over the entire temperature regime. The resistance of the 15 nm wires, and the high-temperature resistance of the 9 nm wires can be fit to a thermally activated behavior. The activation energies, given in Figure 27.5(a), correspond very well [15] to the value predicted by the theory shown in Figure 27.4(a) as the distance between the lowest lying conduction band edge and the highest lying valence band edge. The 4 nm wires and the 9 nm wires below 200 K have a resistance that follows a $T^{-1/2}$ law; magnetoresistance measurements [50] on small diameter wires show that this behavior is due to weak localization effects.

The thermopower of bulk Bi (along the binary direction) and of 200 nm wires are similar. In contrast, the thermopower of 15 nm wires has a very pronounced temperature dependence that has been attributed to two-carrier [15] conduction, with, as in the semimetallic case, a compensation between the electron and hole partial thermopowers. The thermopower of 9 nm wires is much enhanced over that of the bulk, and above 100 K follows a T^{-1} dependence shown as a dashed line, as expected from

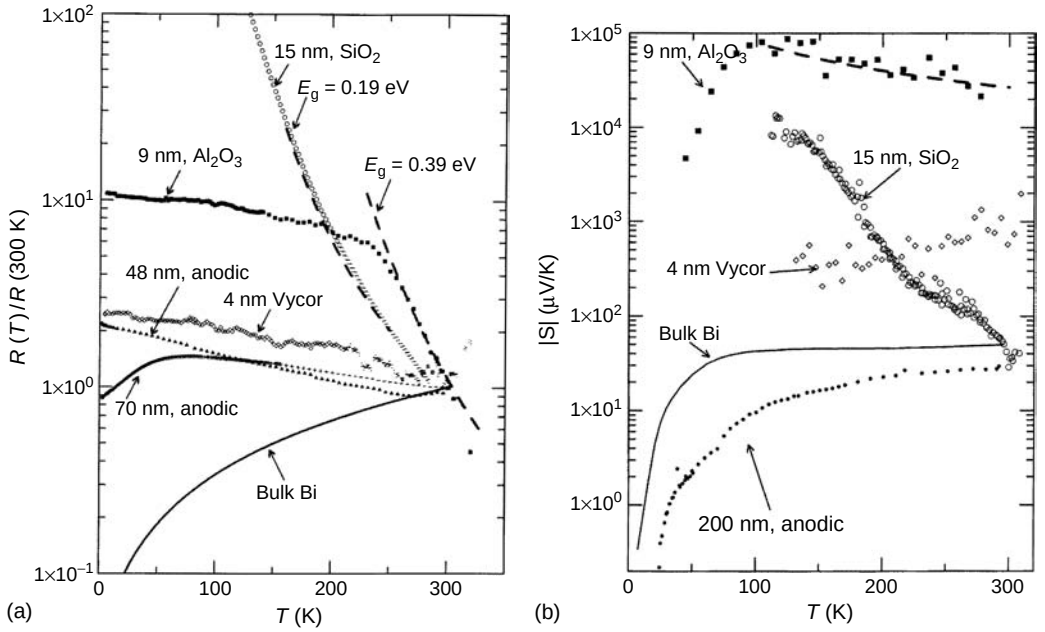

FIGURE 27.5 Temperature dependence of (a) the resistance ratio $R(T)/R(300\text{ K})$ (From Heremans, J.P. et al., *Phys. Rev. Lett.*, 88, 216801, 2002; Heremans, J. et al., *Phys. Rev. B*, 61, 2921–2930, 2000, with permission.) and (b) of the absolute value of the Seebeck coefficient (From Heremans, J.P. et al., *Phys. Rev. Lett.*, 88, 216801, 2002; Heremans, J. and Thrush, C.M., *Phys. Rev. B*, 59, 12579–12583, 1999, with permission.) of Bi nanowires of various diameters dW. The wires cover the transition from the semimetallic ($d_W > 50$ nm) to the semiconducting ($d_W < 50$ nm) regime. The solid curve denotes $S(T)$ for bulk Bi (From Gallo, C.F. et al., *J. Appl. Phys.*, 34, 144–152, 1963, with permission.). The semiconducting wires show an activated temperature dependence of $R(T)$, with the activation energy corresponding to the energy gap shown. The Seebeck coefficient of the 9 nm wires follows a $1/T$ law (dashed line) at high temperature.

an intrinsic semiconductor. Finally, the low-temperature Seebeck coefficient S of 9 nm wires and that of 4 nm wires (up to 300 K) is strongly decreased. This decrease in S is consistent with the onset of weak localization as the conduction mechanism. A similar experiment was conducted using Zn nanowires [51], in which no size-quantization effects and no enhancement in Seebeck coefficient are expected, but the effects of localization are expected to be present. Indeed, it [51] was shown to be the case and the Mott relation (27.9) holds, implying that the enhancement of the Seebeck coefficient only occurs when there is a strong (activated) temperature dependence of the resistivity, as is indeed observed in Figure 27.5. One can also conclude that localization dominates low-temperature transport in Bi nanowires at diameters substantially below 9 nm. In that case, the band-conduction model no longer applies, and the resulting size-quantization effects that are the basis for semiconductor–semimetal transition are not observed.

Having confirmed the validity of the theory, the optimum doping level that maximizes ZT for a 1-D system can be calculated as before, and in this context, we plot in Figure 27.6, ZT for n-type Bi as a function of the concentration of Te, a monovalent donor. In Figure 27.6(a), we show $Z_{1D}T$ vs. doping concentration for various diameters, assuming that the wire axis is oriented in the trigonal direction, the most promising direction for good thermoelectric performance. The influence of the crystallographic orientation of the longitudinal axis of the wires is shown in Figure 27.6(b), where it can be observed that the actual growth direction achieved in the vapor-grown or pressure-injected wires, $[01\bar{1}2]$ is considerably less desirable than that in the trigonal direction.

Similar calculations have been carried out [33] for p-type doped Bi (Sn and Pb are monovalent acceptors in Bi). The situation is unfortunately less favorable for p-type Bi, with a maximum

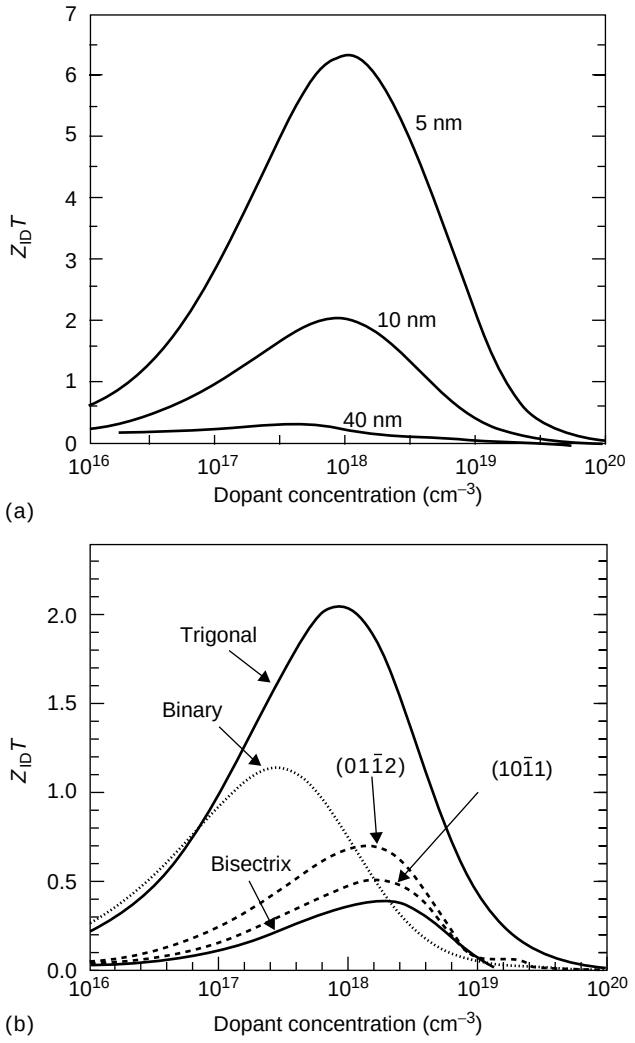

FIGURE 27.6 Calculated one-dimensional figure of merit at 77 K as a function of donor (Te) concentration for an n-doped Bi nanowire for: (a) three nanowires oriented along the trigonal direction with different diameters, (b) five different crystalline orientations for $d_w = 10$ nm. (From Lin, Y.-M. et al., *Phys. Rev. B*, 62, 4610–4623, 2000, with permission.)

one-dimensional figure of merit reaching $Z_{1D}T = 0.7$ for 10 nm wires oriented along the trigonal direction, which is also the most favorable crystalline direction for p-type Bi. It is further shown in Ref. [23] that this is due to the fact that the holes are located in fairly heavy mass bands at the T-point of the Brillouin zone. The influence of this hole band can be eliminated by alloying Bi with Sb, thus opening the possibility of obtaining favorable p-type thermoelectric properties in nanowires made from $Bi_{1-x}Sb_x$ alloys, which, in bulk form, are well known as good low-temperature thermoelectric materials [52].

Since Bi is isoelectronic with Sb, $Bi_{1-x}Sb_x$ nanowires can be prepared [53] using the same basic electrochemical and pressure-injection synthesis methods as described above for preparing bismuth nanowires. The vapor-phase method is less easy to apply because the vapor pressures of Bi and Sb are very different from one another at any given temperature. $Bi_{1-x}Sb_x$ nanowires (for $x < 0.2$) are predicted to have a better thermoelectric performance than pure Bi nanowires of the same diameter. As indicated above, Sb alloying is especially important for improving the thermoelectric capabilities for p-type bismuth.

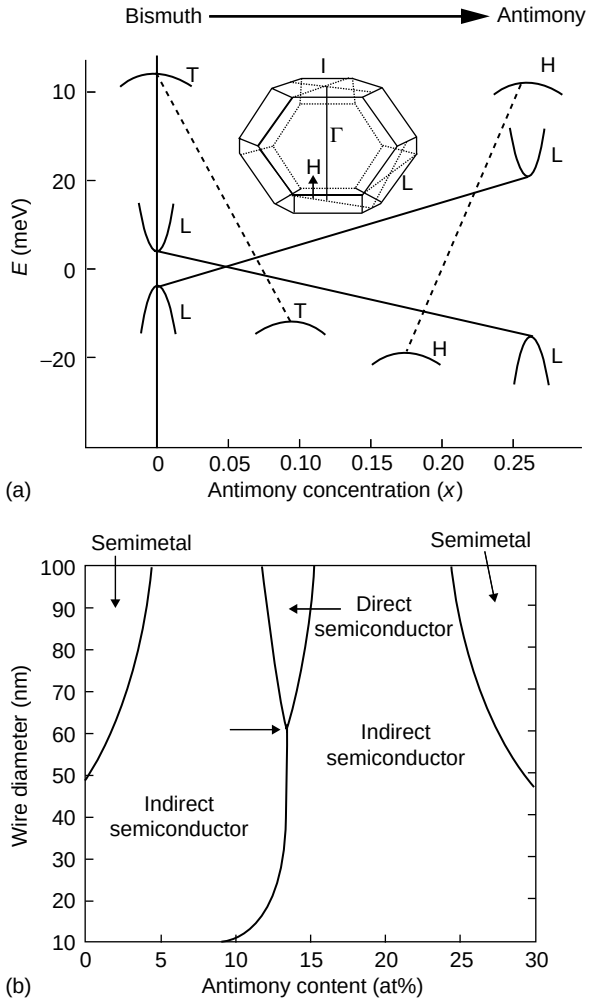

FIGURE 27.7 Phase diagram at 4.2 K of the electronic band structure of (a) bulk 3-D crystalline $Bi_{1-x}Sb_x$ and (b) $Bi_{1-x}Sb_x$ nanowires oriented along the trigonal direction; the inset in (a) shows the Brillouin zone and identifies points around which the Fermi surfaces are centered. Bulk $Bi_{1-x}Sb_x$ alloys are Bi-like semimetals for $x < 0.07$, and Sb-like semimetals for $x > 0.22$; they are direct-gap semiconductors for $0.08 < x < 0.17$, and indirect-gap semiconductors at other Sb concentrations. The semiconductor regime is dramatically expanded in the nanowires configuation at diameters below 50 nm. The bold arrow in the center of (b) points at the condition where the 10 hole pockets (about the T-point, the 3 L-points and the 6 H-points in the Brillouin zone) coalesce in energy. (From Rabin, O. et al., *Appl. Phys. Lett.*, 79, 81–83, 2001, with permission.)

Figure 27.7 shows the phase diagram for the $Bi_{1-x}Sb_x$ system as a function of Sb concentration for both 3-D bulk bismuth (a) and bismuth nanowires (b) as a function of nanowire diameter [54]. The phase diagram for the bulk crystal shows that addition of a small amount of Sb lowers the energy of the T-point valence band, crossing the L-point valence band at $x \simeq 0.07$. With further addition of Sb, the H-point hole valence band rises and crosses the L-point valence band at $x \simeq 0.18$. Comparison of Figures 27.7(a) and (b) shows the dramatic effect of the nanowire diameter on the phase diagram of the $Bi_{1-x}Sb_x$ system. The phase diagram, Figure 27.7(b), was calculated [54] using the same assumptions as for pure Bi nanowires, and by further assuming that the periodic potential within a unit cell of the alloy nanowires is similar to that in the bulk alloy of the same composition, since the crystal structure and lattice constants for nanowires down to 40 nm and below are equal to those of the bulk parent material. The extrema of the first subband of the carrier pockets at two different points in the Brillouin zone

coalesce in energy along the solid lines in this phase diagram. The phase diagram in Figure 27.7(b) identifies one regime where Bi nanowires are predicted to be in a direct gap semiconducting phase, with both electrons and holes at the L points. It predicts two semimetal regimes, one Bi-like with holes at the T point and one Sb-like with holes at the H point, and two indirect gap semiconducting regimes with band gaps between L-point electrons and either T- or H-point holes. There is one singular point, shown with a bold arrow in the center of Figure 27.7(b), denoting the condition where the ten hole pockets (about the T point, the three L points and the six H points in the Brillouin zone) coalesce in energy. At this point (wire diameter $d_w = 60$ nm, and $x = 0.13$) the electronic density of states is particularly high, which is beneficial for increasing the magnitude of the Seebeck coefficient. The alloying effect thus shows how low dimensionality can be used to increase the carrier pocket degeneracy which is very important for enhancing the figure of merit for thermoelectrics. The diagram in Figure 27.7(b) also predicts an increase in the critical diameter at which the overlap between the L-point electron subbands and the T-point hole subbands vanishes (semimetal-to-semiconductor transition) as Sb is added to pure Bi. We therefore expect to obtain better thermoelectric performance in $Bi_{1-x}Sb_x$ ($x \sim 0.2$) when compared to pure Bi nanowires of the same diameter.

The phase diagram for $Bi_{1-x}Sb_x$ nanowires has been confirmed by experimental observations [41]. In this context, we compare, in Figure 27.8, the temperature dependence of the resistance (normalized to 300 K) of pure Bi nanowires (a) of different diameters ranging from 7 to 200 nm to the resistance (b) (normalized to 270 K) of nanowires of $d_w = 65$ nm, but prepared from $Bi_{1-x}Sb_x$ alloys of different compositions. Figure 27.8(a) includes some of the data shown in Figure 27.5(a), but displays more data on a larger number of oriented wires housed in an anodic alumina template. Figure 27.8(a) illustrates the behavior of nanowires as one that follows a vertical line at the $x = 0$ position in the phase diagram Figure 27.7(b), while Figure 27.8(b) follows a horizontal line in the same diagram at an ordinate value of 65 nm. The similarities between the families of curves in Figures 27.8(a) and (b) suggest a common origin: a change in band structure. As already outlined for Figure 27.5, the nonmonotonic temperature dependence in Figure 27.8(a) is associated with semimetallic behavior, and the monotonic temperature dependence with semiconducting behavior: in the semimetallic regime, the resistance ratio of the semimetallic wires rises as x increases due to the decreased band overlap between the conduction and valence bands, giving rise to a decrease in carrier concentration of the nanowires. In contrast, in the semiconducting regime, the resistance ratio for the nanowires decreases due to the increasing dominance of extrinsic carriers. A more quantitative analysis of the resistance ratio R(10 K)/R(100 K) has been made in Ref. [54]. The maximum in the value of the ratio R(10 K)/R(100 K) corresponds to the metal–semiconductor transition, which is expected to occur at $d_w = 50$ nm in pure Bi (Figure 27.4[a]) and at $x = 0.02$ for $d_w = 65$ nm from the phase diagram Figure 27.7(b). Indeed, experimentally, the maximum occurs for 48 nm $< d_w <$ 70 nm in Figure 27.8(a) and for $0 < x < 0.05$ in Figure 27.8(b). The value of the ratio R(10 K)/(100 K) of the three samples of $d_w = 65$ nm in Figure 27.8(b) is similar to that of the samples of pure Bi at $x = 0$ as follows: ($x = 0$, $d_w = 65$ nm) compared to ($x = 0$, $d_w = 70$ nm); ($x = 0.05$, $d_w = 65$ nm) compared to ($x = 0$, $d_w = 48$ nm); ($x = 0.1$, $d_w = 65$ nm) compared to ($x = 0$, $d_w = 28$ nm). This concurs with the predictions of the phase diagram Figure 27.7(b).

The Seebeck coefficient of $Bi_{1-x}Sb_x$ nanowires of different diameters, embedded in porous anodic alumina, has also been measured [41] as a function of temperature. The results are shown in Figure 27.9. As expected, the magnitude of $|S|$ increases as x increases or as d_w decreases. The increase is not as large as in Figure 27.5(b) because the diameters used are much larger, and the Bi samples in Figure 27.5(b) have much larger energy gaps.

Model calculations, once again validated experimentally, have been used [55] to outline the regions of optimal one-dimensional figure of merit for the quantum wires, $Z_{1D}T$. The values of optimum $Z_{1D}T$ contours have been plotted as a function of Sb content and wire diameter, in Figure 27.10(a) and (b) for n- and p-type $Bi_{1-x}Sb_x$ alloys. $Z_{1D}T$ values of 2 are predicted for n-type material for $x = 0.25$ at $d_w = 30$ nm, a diameter value that is much larger than in pure Bi, and where the effects of carrier localization are minimal. A much better performance is predicted for p-type

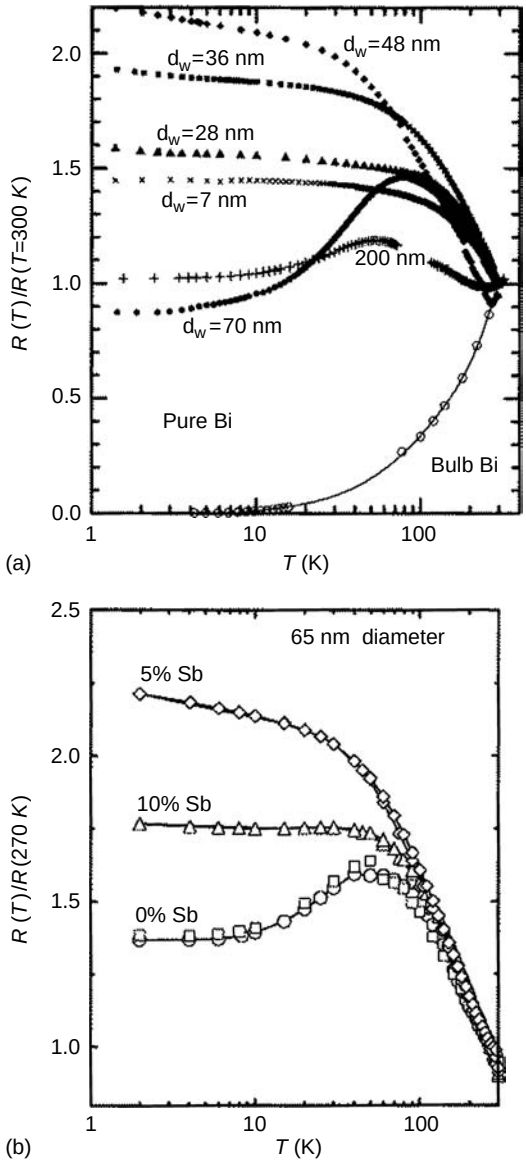

FIGURE 27.8 (a) Measured temperature dependence of the resistance ratio $R(T)/R(300\ \text{K})$ of Bi nanowires of various wire diameters going from the semimetal regime (for $d_w > 50$ nm) to the semiconducting regime (for $d_w < 50$ nm) (From Heremans, J., in *Thermoelectric Materials 2003 — Research and Applications*: *MRS Symposium Proceedings, Boston, December 2003*, Nolas, G.S. et al., Eds., Materials Research Society Press, Pittsburg, PA, 2004, pp. 3–14.). (b) Measured temperature dependence of the resistance $R(T)$ normalized to the $R(270\ \text{K})$ of $d_w = 65$ nm $Bi_{1-x}Sb_x$ nanowires with different Sb concentrations. (From Lin, Y.-M. et al., *Appl. Phys. Lett.*, 81, 2403–2405, 2002, with permission.)

$Bi_{0.13}Sb_{0.87}$ nanowires at $d_w = 40$ nm than for pure Bi ($x = 0$) p-type nanowires, due to the effect of the high degeneracy of the carrier pockets.

In addition to their promise for thermoelectric applications, Bi and $Bi_{1-x}Sb_x$ nanowires constitute an attractive model system more generally for the study of transport behavior in low-dimensional structures, due to their tunable band structures, small electron effective masses, and long carrier mean free paths. The ability to prepare bismuth in semiconducting form through the growth of nanowires with diameters less than 50 nm opens up many new opportunities to study a material (semiconducting

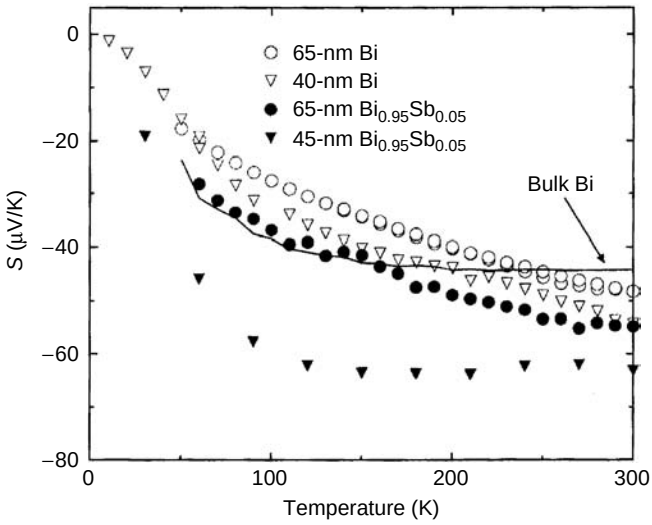

FIGURE 27.9 Measured Seebeck coefficient vs. T for Bi (open symbols) and $Bi_{0.95}Sb_{0.05}$ (full symbols) nanowires with different diameters (From Lin, Y.-M. et al., *Appl. Phys. Lett*., 81, 2403–2405, 2002, with permission.). The solid curve denoted $S(T)$ for bulk Bi. (From Gallo, C.F. et al., *J. Appl. Phys*., 34, 144–152, 1963, with permission.)

bismuth) with an unusual electronic structure under a variety of new conditions, thereby providing new possibilities for interesting applications to thermoelectricity and nanotechnology [41].

27.5 QUASI-ZERO-DIMENSIONAL THERMOELECTRIC MATERIALS

Since the enhancement in ZT is expected to be more pronounced as the dimensionality decreases, one might expect from Figure 27.2 that 0-D structures might possess thermoelectric properties that are even more promising than those of 1-D systems, resulting from the highly singular electronic density of states of quantum dots. However, unlike 1-D or 2-D systems, where at least one of the directions is not quantum-confined and thus able to provide an electrical conduction pathway, 0-D structures, such as quantum dots, are quantum confined in all directions. In order to utilize the unique properties of quantum dots for transport applications, it is therefore necessary to devise some means of electron conduction pathways between individual quantum dots. Transport in 0-D thermoelectric materials is thus different from that in other low-dimensional structures (1-D and 2-D) in the sense that certain unconventional or non-band conduction behavior (e.g., through quantum point contacts [56], tunneling or hopping) is necessary to utilize the special electronic band structure of 0-D systems to produce good thermoelectric materials in the transport direction. In this section, we will discuss some quasi-zero-dimensional systems, such as segmented nanowires [57], a quantum dot [58] located between two quantum point contacts, and quantum-dot superlattices [59,60]. The theoretical section is presented first to gain an understanding of some of the fundamental issues, and is followed by several different examples of experimental quantum-dot systems for which unusual thermoelectric behaviors have been observed. Of particular interest are the quantum-dot superlattices, which hold the record for the highest ZT, with a value of $ZT \simeq 3$ at 450 K [14]. It remains to be determined which conduction mechanism between the quantum dots provides the optimal thermoelectric performance from a theoretical standpoint. However, the major mechanism contributing to the enhancement of ZT in these experimental quantum-dot systems is the reduction of the lattice thermal conductivity through the strong interface scattering of phonons.

27.5.1 SEGMENTED SUPERLATTICE QUANTUM WIRES

A quantum-dot nanostructure that is of interest as a model system for 0-D thermoelectricity [57] is the superlattice nanowire (SLNW) structure shown in Figure 27.11(a), which consists of a series of

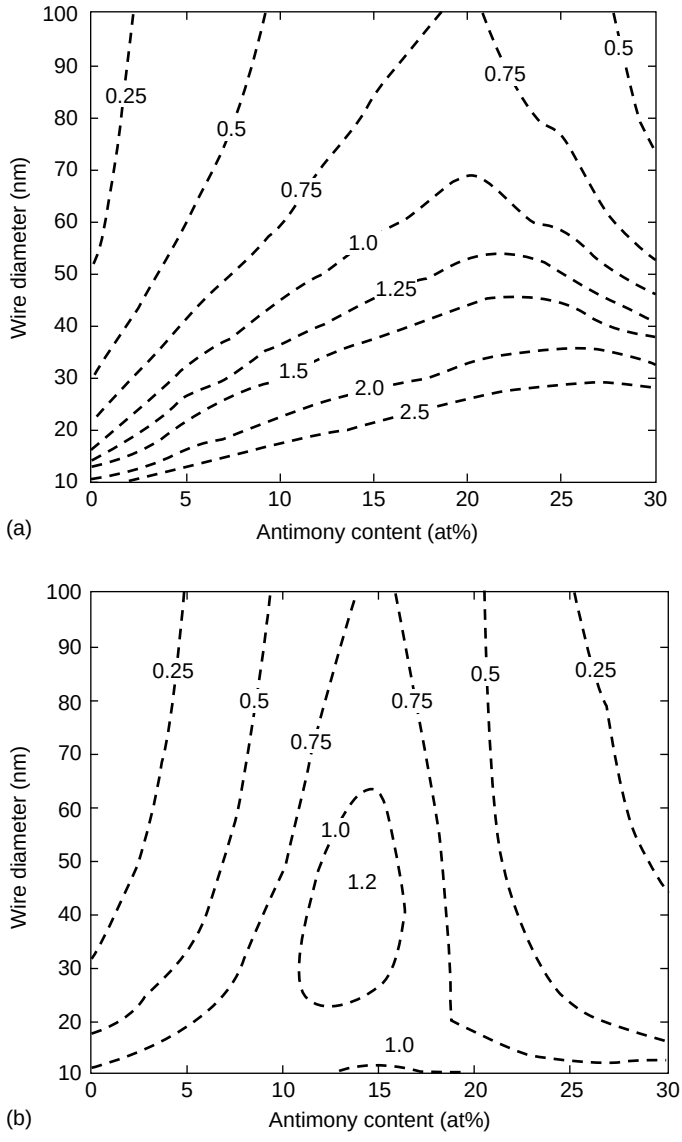

FIGURE 27.10 Contours of constant $Z_{1D}T$ at 77K as a function of wire diameter an antimony concentration for (a) n-type and (b) p-type $Bi_{1-x}Sb_x$ nanowires. (From Rabin, O. et al., *Appl. Phys. Lett.*, 79, 81–83, 2001, with permission.)

interlaced nanodots of two different materials A and B, with segment lengths L_A and L_B. Tunneling between adjacent quantum dots makes electronic transport along the wire axis possible in this SLNW structure. The 0-D characteristics of each quantum dot are maintained by the energy difference of the conduction (or valence) bands between the different A and B materials (see Figure 27.11[b]). The band offset energy ΔE_{nm} provides a limited quantum confinement and creates a periodic potential for carriers moving along the wire axis, which may result in the formation of minibands that yield a sharper density of electronic states than is present in ordinary 1-D systems. Note that the band offset in the SLNW ΔE_{nm} is in general different from the band offset $(E_C^A - E_C^B)$ between the bulk materials due to the quantum confinement energies $(\varepsilon_{nm}^A - \varepsilon_{nm}^B)$ resulting from the quantum wire geometry. This periodic potential also results in the presence of many interfaces, which strongly block the phonon conduction of heat along the wire axis [61], reducing the lattice thermal

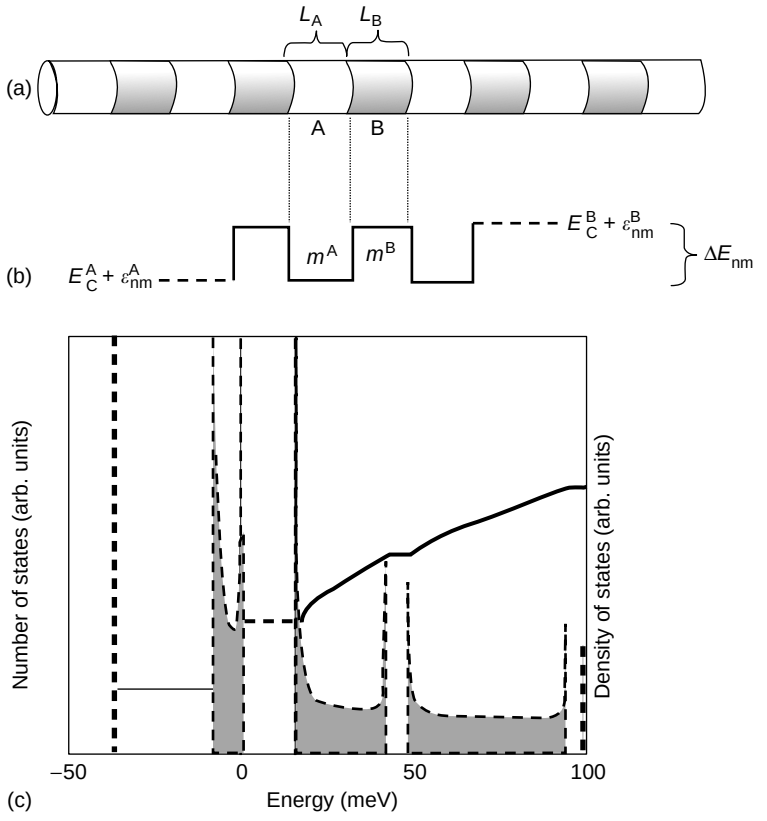

FIGURE 27.11 (a) Schematic diagram of a superlattice nanowire consisting of interlaced nanodots A and B. (b) Schematic potential profile of one conduction subband in a quantum-dot superlattice nanowire. (c) Calculated density of states and the number of states of a 1-D subband in a periodic potential with segment lengths $L_A = L_B = 5$ nm, assuming a potential barrier height of 50 meV and effective mases of 0.5 m_0. The zero in energy is chosen to be at the top of the potential barrier. (From Lin, Yu.M. and Dreselhaus, M.S., *Phys. Rev. B*, 68, 075304S(1–14), 2003, with permission.)

conductivity, and is a major factor in increasing the thermoelectric figure of merit of this 0-D system.

The synthesis of such superlattice nanowire structures has been achieved in different material systems. Piraux et al. [62] fabricated superlattice nanowires in Co/Cu system using electrochemical deposition in nanoporous templates. A nanowire synthesis technique known as vapor–liquid–solid growth (VLS) has been used to extend this work to produce high-quality semiconductor SLNWs of the type shown in Figure 27.11(a) in systems such as Si/SiGe [63], GaAs/GaP [64], and InP/InAs [65]. Calculations of the thermal conductivity reduction in these systems have been published [61], and preliminary thermal conductivity measurements have been made on Si/SiGe superlattice nanowires [66] in comparison with SiGe alloy nanowires of the same average composition.

The electronic band structure of superlattice nanowires can, under specific circumstances, exhibit dramatically different features from that of a simple 1-D nanowire of either of the bulk materials A and B or of an alloy of A and B that forms individual superlattice segments of the nanowires. Figure 27.11(c) shows the results of the model calculations for the density of states of quantum-dot systems based on the SLNWs shown in Figure 27.11(a). The calculations take into account the cylindrical boundary conditions of the nanowires, the diameter-dependent band offsets for the periodic potential along the wire axis, and the multiple anisotropic carriers that may contribute to thermal and electrical transport [57]. It is assumed that each quantum dot consists of a sufficient number

of atoms so that the effective mass theorem is valid to describe the local electronic properties of a quantum-dot by the band structure parameters of the bulk material. Results for a generic superlattice structure show that for very short superlattice periods (L_A = l nm), the electronic band structure approaches that of an alloy system (alloy limit) with an effective band edge equal to the average of the periodic potentials of the two constituents A and B. For long segment lengths ($L_A > 60$ nm), minibands arising from the superlattice come so close to each other in energy that they may be approximated by a continuum, and the density of states of the superlattice nanowire is approximately equivalent to the averaged density of states of the two constituent materials (classical limit). The classical limit is reached when the thermal energy, $k_B T$, is larger than the miniband separation. The range of greatest interest for superlattice nanowires is the range in which the nanowires exhibit clearly different features from simple 1-D nanowires either of AB alloys or of A or B constituents. This range occurs when only a few minibands span the band gaps of the parent materials A and B as shown in Figure 27.11(c). Two conditions must be satisfied for the structure to exhibit transport properties characteristic of this quasi-1-D band structure: the segmented nanowire must be designed so that the electron wave functions exceed the alloy limit and yet avoid the classical limit.

Assuming that $L_A = L_B = L$, the energy separation between minibands (in Figure 27.11[c]) is of the order of $E \simeq (\pi\hbar/L)\sqrt{\Delta E_{nm}/2m_z^A}$, where m_z^A is the effective mass of the carriers moving along the nanowire axis z, and increases as L decreases. However, one cannot decrease L too much. The electron de Broglie wavelength near the effective potential barrier ΔE_{nm} is approximately $\Lambda_e \approx (2\pi\hbar)\sqrt{2\Delta E_{nm} m_z^A}$. When the de Broglie wavelength is much longer than the segment length, it covers multiple superlattice periods and the electron wave functions do not probe the details of the periodic potential: this is the alloy limit. Combining both requirements implies that, for the minibands to be observable, one must have $2k_B T < \Delta E_{nm}$ and $L \leq (2\pi\hbar)\sqrt{2\Delta E_{nm} m_z^A}$.

The lattice thermal conductivity is also expected to be much reduced in SLNWs based on its dependence on the mean free path (see Equation [27.3]), and ignoring any changes in the heat capacity or sound velocity between nanowires and their bulk counterparts. In this very simple model [57,61], we can define an effective phonon mean free path for segment A for example, limited by two additional scattering terms, $3L_A/4$ for interface scattering and d_w for wire boundary scattering:

$$l_{A,eff}^{-1} = l_A^{-1} + \frac{4}{3} L_A^{-1} + \frac{1}{\beta_A} d_w^{-1} \tag{27.16}$$

where l_A^{-1} is the phonon mean free path in bulk material A and β_A is a dimensionless geometrical factor that includes the specularity of the wire boundary. The thermal conductivity of segment A is then reduced by a factor $l_{A,eff}/l_A$, and the lattice thermal conductivity of the segmented quantum dot wire κ_{QD} is expressed in terms of the contributions of both constituents by connecting the segments in series:

$$\frac{2L}{\kappa_{QD}} = \frac{L_A}{\kappa_A}\frac{l_A}{l_{A,eff}} + \frac{L_B}{\kappa_B}\frac{l_B}{l_{B,eff}} \tag{27.17}$$

where κ_A and κ_B are the bulk lattice thermal conductivities of materials A and B, respectively, and $2L = L_A + L_B$.

The concepts described above were applied [57] to segmented superlattice wires in the lead chalcogenide family (PbTe, PbSe, PbS) because their electronic properties [67] are better known at high temperature that those of the $Bi_{1-x}Sb_x$ system, and because lead salts are technologically important thermoelectric materials and have been shown experimentally to have desirable quantum dot properties [13,14]. The calculated Seebeck coefficient and electrical conductivity of n-type doped PbSe/PbS SLNWs are shown in Figure 27.12(a) as a function of the electron Fermi energy at 77 K. They are compared to the same properties in a uniform nanowire of an $PbSe_{0.5}S_{0.5}$ alloy. A striking difference is the fact that the SLNW shows regions in which the Seebeck coefficient is positive. This can be understood in terms of the energy dependence of the conductivity and the Mott formula Equation (27.8). The energy dependence of the conductivity, in turn, is strongly non monotonic due to the particular structure of the density of states (Figure 27.11[b]) and the presence of minibands. The figure of merit is then

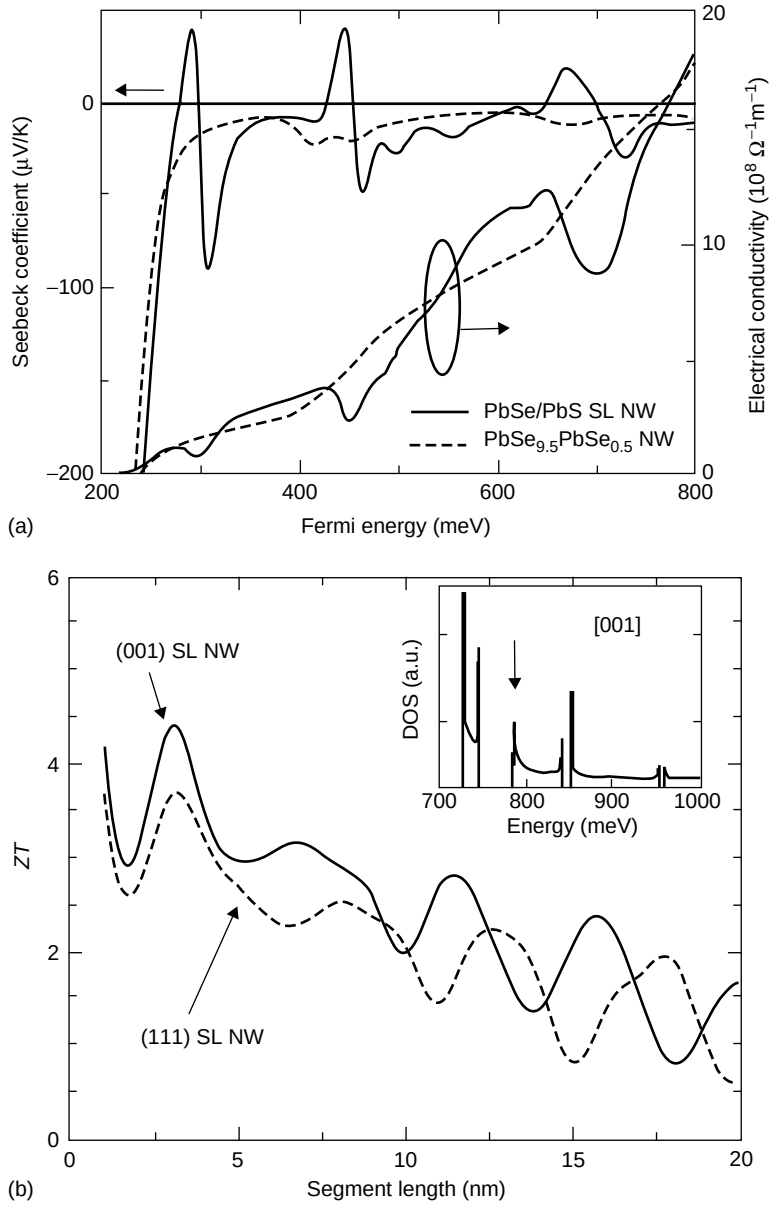

FIGURE 27.12 (a) Calculated electrical conductivity and Seebeck coefficient as a function of the Fermi energy in an n-type doped PhSe(5 nm)/PbS(5 nm) superlattice nanowire with d_w = 10 nm (full lines). These quantities are compared with those (dashed lines) in a uniform 10 nm diameter wire of $PbSe_{0.5}S_{0.5}$ alloy. (b) Calculated optimized *ZT* of the a PbSe/PbS superlattice nanowire with d_w = 5 nm, as a function of segment length $L_A = L_B$ for [001] (full line) and [111] (dashed line) orientations. The inset shows the density of states of this wire, and the arrow indicates the Fermi energy at which *ZT* is optimal (T = 77 K). (After Lin, Yu.M., and Dresselhaus, M.S., *Phys. Rev. B*, 68, 075304S(1–14), 2003.)

optimized in the familiar way, and the optimal figure of merit is shown in Figure 27.12(b). The inset identifies the Fermi energy at which this optimum is achieved. The SLNWs offer an enhancement in *ZT* over alloy nanowires. The second maximum in *ZT* corresponds to a positive Seebeck coefficient, whereas the first and third peaks correspond to negative Seebeck values. This raises the possibility of using a single donor impurity to manufacture both the n and the p leg of a Peltier couple.

The lead salts have valence band structures that are quite similar to their conduction band structures, and the model calculations were extended [57] to include p-type doped material. The calculations suggest that the thermoelectric performance of p-type segmented nanowires is slightly better than that of n-type wires in the PbSe/PbS system, due to the fact that holes have smaller effective masses than electrons in both PbSe and PbS. n-Type PbTe/PbSe segmented nanowires also have a somewhat higher optimum *ZT* than their PbTe/PbS counterpart.

To our knowledge, there are no experimental data on SLNWs in the lead–salt systems available today. Bjork and coworkers [65] have prepared InP/InAs SLNWs with atomically sharp interfaces by chemical beam epitaxy with segment lengths as short as 1.5 nm, showing that it may be possible to test the above-mentioned concepts experimentally.

27.5.2 Quantum-Dot Superlattices

Springholz and coworkers [68,69] developed a technique to grow self-organized PbSe islands by molecular beam epitoxy (MBE) spontaneously in a PbSe/PbEuTe superlattice, forming a three-dimensional array of quantum dots. In fact, self-assembled PbSe quantum dots can be grown by MBE [70] on a 4 μm thin PbTe layer on Si (111), with a very narrow (3nm) CaF_2 buffer layer, with a uniformity in size distribution of better than 2%. Harman and coworkers [13,59,60], at the MIT Lincoln Laboratory, realized the implication of this work on low-dimensional thermoelectrics. The Harman group was successful in showing that periodic MBE growth of PbTe and $PbSe_{1-x}Te_x$ layers formed a quantum-dot superlattice (QDSL), as small quantum-dots with a high Se content grew at the interface between the PbTe regions and the alloy regions. The structure of a PbTe/$PbSe_{1-x}Te_x$ QDSL is shown in Figure 27.13, along with a plan-view scanning electron micrograph showing the quantum dots [13,32]. When viewed from a 3-D standpoint, these quantum-dot superlattices can be interpreted as a PbTe host into which PbSeTe quantum dots are introduced in a periodic way in all three (*x*, *y*, *z*) directions. Systematic improvements of the growth procedures and the substitution of quaternary Pb_{1-y} Sn_ySe_{1-x} Te_x alloys for the $PbSe_{1-x}$ Te_x alloys in the quantum dots have led to dramatic enhancements in *ZT* and, most recently, values of $ZT > 3$ at elevated temperatures were reported [14]. The device performance potential of Harman's quantum-dot superlattices has also attracted a great deal of attention.

Some of the properties of n- and p-type quantum-dot superlattices described in Ref. [13] and its supplemental on-line material are presented in Table 27.2. The room temperature values of *ZT* reported in Table 27.2, which were record-breaking at that time, are measured on free-standing films of the QDSL system, with the current in the plane of the film, and the reported results are thus expected to be very reliable. The authors deduce the thermal conductivity for the n-type PbSeTe/PbTe QDSL to be of the order of 5.8 to 6.2 mW/cm K. Subtracting an estimate for κ_E from the electrical conductivity, leaves $\kappa_L = 3.3$ mW/cm K, with possibly lower values yet for the

TABLE 27.2
Properties of Quantum-Dot Superlattices at 300 K

Sample Units	*ZT*	*S* (μ*V*/*K*)	*n*,*p* (10^{19} cm^{-3})	*μ* cm^2/Vsec	*ρ* (10^{-3} Ω cm)
n-Type (Bi-doped) $PbSe_{0.98}Te_{0.02}$/PbTe	1.6	−219	1.2	370	1.4
n-Type (Bi-doped) $PbSe_{0.98}Te_{0.02}$/PbTe	1.3	−208	1.1	300	1.9
n-Type (Bi-doped) $Pb_{0.84}Sn_{0.16}Se_{0.98}Te_{0.02}$/PbTe	1.6	−228	1.3	320	1.5
n-Type (Bi-doped) $Pb_{0.84}Sn_{0.16}Se_{0.98}Te_{0.02}$/PbTe	2.0	−241	0.89	540	1.3
n-Type (Tl-doped) $PbSe_{0.98}Te_{0.02}$/PbTe	0.8	248	0.27	440	5.3
nType (Tl-doped) $PbSe_{0.98}Te_{0.02}$/PbTe	0.9	165	1.8	260	1.3

Compiled from Harman, T.C., et al., *Science*, 297, 2229–2232, 2000 and its supplemental on-line material.

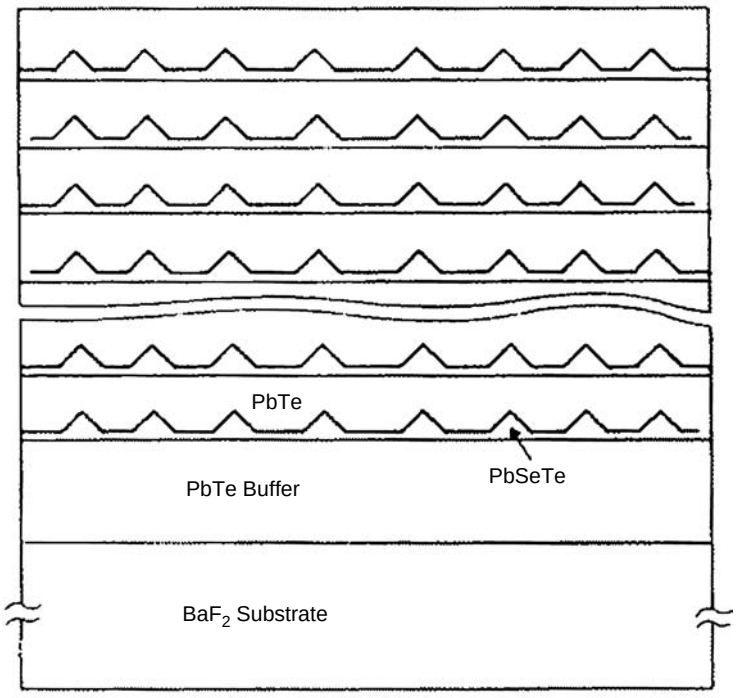

(a)

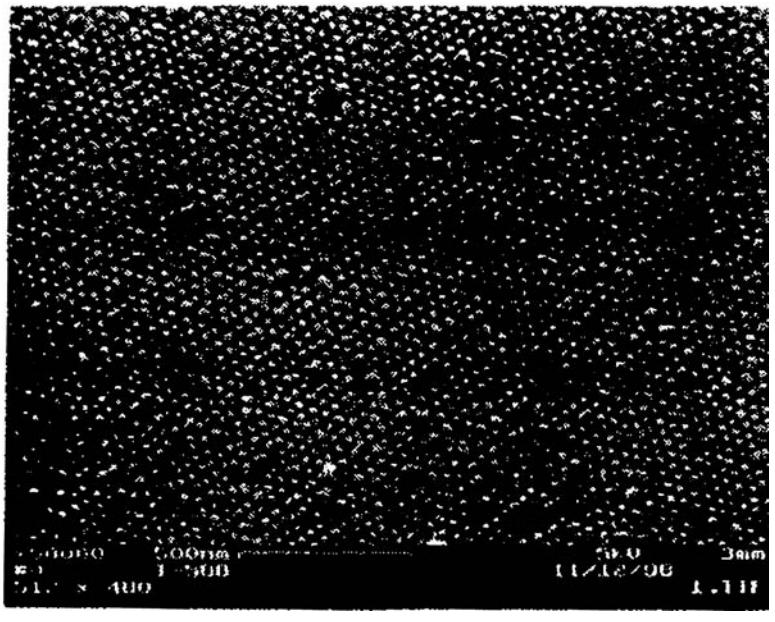

(b)

FIGURE 27.13 Structure (a), and plan-view scanning electron micrograph (b) of a PhTe/$PbSe_{1-x}Te_x$ quantum-dot superlattice. (After Harman, T.C. et al., United States Patent No. 6452206 B1, 2002.)

quaternary $Pb_{0.84}Sn_{0.16}Se_{0.98}Te_{0.02}$/PbTe QDSLs. The average composition of the latter is $Pb_{0.98}Sn_{0.02}Se_{0.13}Te_{0.87}$; the lattice thermal conductivity of an equivalent 16% alloy in the PbSeTe system is 12.5 mW/cm K, so that the first effect of the quantum dots is to reduce κ_L by a factor of almost 4. On the other hand, the electron mobility of a similar PbSeTe alloy at a very low doping

level is 1000 cm^2/Vsec [3,4], and the 300 K mobility in lead salts [71] is not very sensitive to doping levels up to $2 \times 10^{19}\,cm^{-3}$. Compared to the ternary n-type QDSLs, the mobility reduction is only of the order of 3 or somewhat less. This is the first mechanism through which quantum dots improve *ZT*. There is, however, the second mechanism for improvement in the power factor, similar to that described in Figure 27.3 for the PbTe quantum well structures.

Figure 27.14 shows the absolute value of the Seebeck coefficient of the samples described in Ref. [13] (full diamonds) as a function of the carrier density, along with data for bulk samples (open circles) and other samples that will be described later. This plot is similar to that in Figure 27.3(b), and shows that the thermopower is considerably enhanced in the QDSLs compared to bulk samples, as it was in 2-D PbTe-based structures. Also as in 2-D structures, the optimum doping level in QDSLs is shifted toward higher carrier concentrations. The exact physical mechanism that leads to this enhancement has not been clearly identified, but is likely to be attributable to either quantization effects or perhaps scattering effects, as will be discussed in Section 27.6.

27.5.3 Quantum Dots between Quantum-Point Contacts

A third example of quasi-zero-dimensional system is a system consisting of a quantum-dot [58] enclosed between two quantum-point contacts [56]. Such structures can exhibit transport properties in the Coulomb blockade regime and, at very low temperatures show universal conductance fluctuations. In all cases, we observe that the Mott relation, Equation (27.8) (or Equation [27.7] for nondegenerate samples), explains the Seebeck coefficient. The thermoelectric properties of such quantum dots as well as those of single quantum point contacts, are given [72] as a function of the electrical conductances of the quantum structures.

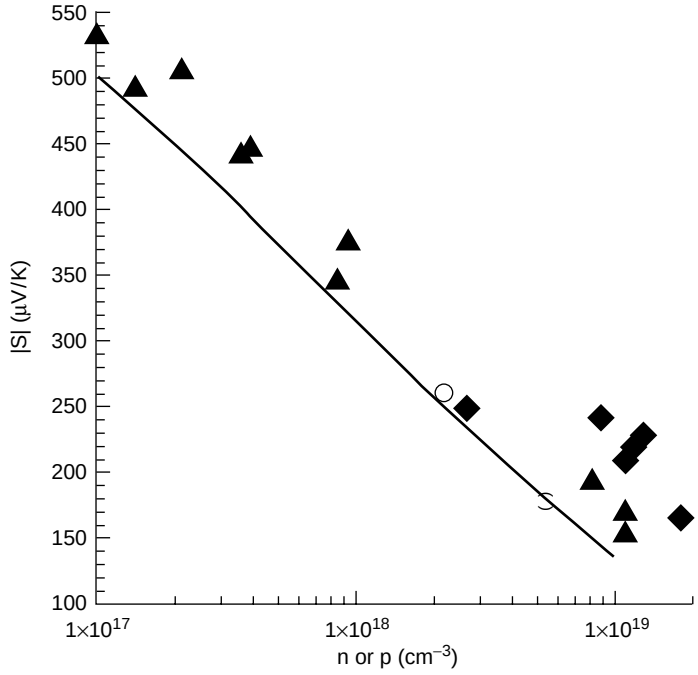

FIGURE 27.14 Seebeck coefficient vs. carrier concentration for n- or p-type PbTe. The bottom solid line represents a fit to literature data on bulk samples in which acoustic phonon scattering dominates. A few data on bulk samples (from Heremans, J.P. et al., *Phys. Rev. B*, 70, 115334, 2004, with permission.) are shown as open circles. The Seebeck coefficient of quantum-dot PbSeTe/PbTe and PbSnSeTe/PbTe superlattices (From Harman, T.C. et al., *Science*, 297, 2229–2232, 2002, with permission.) are indicated by (◆) and exhibit a strong enhancement; a similar, though weaker, enhancement is observed in nanogranular PbTe samples (▲).

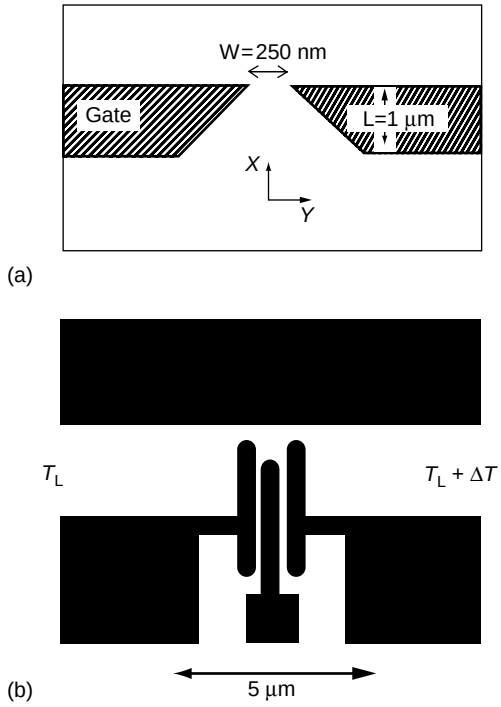

FIGURE 27.15 (a) The geometry of a quantum point contact formed in a 2-D electron gas at the interface of GaA1As/GaAs heterostructures. The figure shows a plan-view of two gate electrodes deposited on the imulating GaAlAs layer. The 2-D gas lies at the interface between this layer and the underlying GaAs. The point contact itself is formed in a constriction that is electrostatically induced in the 2-D gas by the two gates shown. (After van Wees, B.J. et al., *Phys. Rev. Lett*., 60, 848, 1988.) The conductance through the channel is a step-like fucntion of the gate voltage. (b) A quantum-dot device defined by four gate electrodes (dark) on top of a 2-D electron gas in AlGaAs/GaAs. (After Dzurak, A.S. et al., *Phys. Rev. B*, 55, R10197, 1997.)

An example of a quantum-point contact formed in a 2-D electron gas in a GaAs/AlGaAs heterostructure is shown in Figure 27.15(a). Two gates, shaped as shown, define a constriction through which conductance paths are established between the top and the bottom areas of the 2-D gas. The width W of the constriction is changed by varying the voltage between the gate and the GaAs substrate. At 0 K, the conductance G through this constriction is quantized as [56]

$$G = \frac{e^2}{\pi\hbar}\sum_{i=1}^{N_c} t_i \tag{27.18}$$

where N_c is the largest integer that is smaller than $k_F W/\pi$, while k_F is the Fermi wave vector of the 2-D carriers in the plane and, using the Landauer [73] formulation, t_i is the transmission coefficient through the constriction. The wider the constrictions, the larger the N_c, and the number of "channels" of index i, so that each can contribute a factor $(2e^2/h)$ to the conductance. When plotted as a function of W, the conductance exhibits a series of steps of amplitude $(2e^2/h)$. The width W is a function of the difference between the electrochemical potential μ and the applied gate voltage V_o, so that the conductance, when plotted as a function of $(\mu - V_o)$ follows a series of steps. Such steps are also seen in the resistance, shown in Figure 27.16, where the effect of thermal smearing is also shown.

A quasi-zero-dimensional system consists of a quantum dot contacted by two tunneling contacts. An example of such a system is shown in Figure 27.15(b). As in Figure 27.15(a) the actual device is constructed in a 2-D electron gas at the interface of an AlGaAs/GaAs heterojunction using gate electrodes. The gate electrodes are the dark features in Figure 27.15(b). The quantum dot itself resides in the 2-D gas in the white space above the middle electrode. Two electron reservoirs reside under the

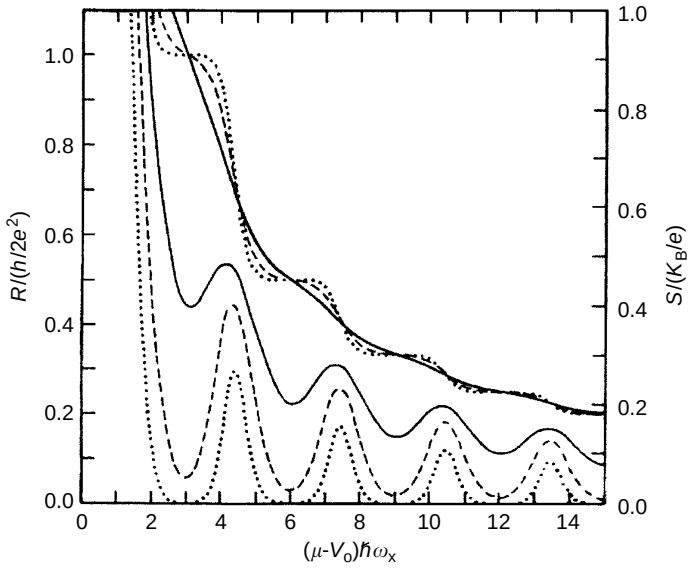

FIGURE 27.16 Resistance (left) and Seebeck coefficient (right) of quantum point contacts as a function of the normalized chemical potential for different temperatures ($T_{\text{full-line}} > T_{\text{dashed-line}} > T_{\text{dotted-line}}$). The abscissa axis is the gate voltage V_o referred to the electrochemical potential of the electrons, μ, divided by the thermal smearing energy. (After Proetto, C.R., *Phys. Rev. B*, 44, 9096, 1991.)

white spaces labeled T_L and $T_L + \Delta T$, and the electrical contact to the dot occurs by tunneling between the reservoirs and the dot.

The conductance through the quantum dot is determined at low temperatures by a combination of confinement and charging effects [58]. The Coulomb blockade [74] regime is one in which a finite number *N* of electrons reside in the quantum-dot and the contacts represent only a slight perturbation to the quantum-dot system. The *N*-particle system occupies discrete energy levels. Under a bias voltage between the left and right electrodes, tunneling occurs between the electron reservoir at the left and right of the quantum dots, with a larger tunneling current observed when the reservoirs are aligned electrostatically with the discrete energy levels within the dots; this results in conductance spikes when the differential conductance is plotted as a function of bias voltage.

The Seebeck coefficient of both low-dimensional systems can be deduced [72] from the conductance by the Mott relation (27.8) for degenerate systems, or from Equation (27.7) for nondegenerate systems, and results for *S* are shown in Figure 27.16 as the gate voltage V_o is varied. These theoretical predictions have been verified experimentally in several transport regimes of quantum-dot structures, for instance, in the Coulomb blockade regime [58].

27.6 OTHER RELATED TOPICS

In this final section, we present a brief summary of several topics closely related to low-dimensional thermoelectric materials, namely bulk materials containing nanostructured constituents, low-dimensional thermionic materials operating on an energy filtering mechanism, and recent advances in measurement techniques with important implications on low-dimensional thermoelectricity.

For thermoelectric materials engineered to the nanometer scale to have a practical impact, one must be able to produce bulk quantities of them through some bulk-like production scheme such as self-assembly. We note, in this regard, that many industrial materials such as precipitation-hardened aluminum [75,76] owe their properties to some feature or inclusion at the nanometer scale. In the field of bulk thermoelectric alloys, the recently reported $AgPb_m$ $SbTe_{2+m}$ bulk alloys [21], with

$ZT = 2.1$ at 800 K (at $m = 0.18$), have nanoscale inclusions, although the role of these inclusions is not yet quite clear metallurgically, these bulk alloys can be viewed [77] as solid-state solutions of PbTe and $AgSbTe_2$, much like TeAgGeSb (TAGS) alloys [78], which are alloys of GeTe and $AgSbTe_2$. The latter compound has long been known to have nanometer inclusions [79]. A more recent review [80] has attributed the hiphz to a decreased in k_L, compiled with an increase in S itself due to resonant electronic states attributed to the Ag and Sb nanostructure.

One approach to increasing the thermoelectric power factor $S^2\sigma$ that has a long history [81] has been to induce an enhancement in the energy dependence of the relaxation time or mobility. This results in a stronger energy dependence of the conductivity which, via the Mott relation again, results in an increase in the Seebeck coefficient for a system with a given carrier concentration. In the case of PbTe-based materials, one then expects the effect of this increased energy dependence of the scattering to yield Seebeck coefficient values that will fall further above the solid line in Figure 27.14. If this result can be obtained without decreasing the carrier mobility too much, it should result in an increase in power factor. The idea was first suggested [4,5] in the context of lead-salt materials using ionized impurity scattering as the scattering mechanism, because its relaxation time is expected to follow an $E^{3/2}$ law, which has a much stronger energy dependence than the $E^{-1/2}$ dependence that is expected for acoustic phonon scattering; unfortunately, the decrease in mobility due to this additional scattering is too high [82] for lead salts. We note that this problem is not present in counterdoped Bi, a material in which ionized impurity scattering does indeed result in an increased power factor [83]. Nanoscale inclusions do present a new opportunity to revisit the concept, and this has recently been achieved in both skutterudites and lead salts [19,20]. Figure 27.14 shows, as full triangles, the Seebeck coefficient of several sintered bulk PbTe samples that have grains in the 30 nm scale. The Seebeck coefficient shows an enhancement of the same order as those shown by the QDSL samples, in which indeed the same mechanism might contribute. Using Nernst effect measurements, in conjunction with the resistivity, Hall and Seebeck effects, the authors [19] identified the mechanism of the enhancement as indeed being due to an increased energy dependence of μ; unfortunately, as in the case of Ref. [82], the decrease in mobility was too strong in these nanocomposites to obtain a satisfactory thermoelectric performance.

A different approach to direct thermal-to-electrical energy conversion is thermionic emission, originally proposed in vacuum devices [84]. In vacuum thermionic emitters, electrons that leave a metal plate under the influence of a bias voltage carry a thermal energy with them, and thus cool the plate. Several authors have more recently realized that similar structures can be made from semiconducting heterojunctions [85,86], and thus a brief discussion is warranted here. In essence, these thermionic devices aim to induce a strong energy dependence of the electrical conductivity, and thus an enhanced Seebeck coefficient, by departing from the regime of linear transport on which the entire discussion has been based until now, and entering a regime in which the current/voltage curves deviate from linear behavior. A good review of thermoelectricity under conditions of nonlinear transport in semiconductors is given in Tauc's classic monograph [87]. Device optimization calculations [18] show that conceptually, values of ZT up to 5 could be achieved in very specific heterostructures, which have been labeled heterojunction integrated thermionic (HIT) coolers. The basic element of HIT devices consists of two quantum well layers of strongly degenerate semiconductors separated by relatively wide-gap energy barriers, which, in turn, are thick enough to prevent tunneling. This basic element can be repeated into a superlattice. As a specific example [18], consider the case of a superlattice consisting of 50 layers of the basic structural unit consisting of the two constituent segments, 10 nm $Hg_{0.8}Cd_{0.2}Te$/20 nm $Hg_{0.2}Cd_{0.8}Te$. The electrons in the quantum well layers are size-quantized to energy levels E_i, and those levels are filled up to the Fermi energy E_F. The electrons are confined by the band offset E_b between the wells and the barriers. The superlattice is subjected to a bias voltage applied across the film thickness, the z direction. Electrons, whose total energy is a function of the Fermi energy, the bias potential, and the thermal energy, are transported over the barrier when their energy exceeds the barrier energy E_b, and these electrons develop a momentum vector k_z. When the bias voltage is appropriately selected, the potential barrier selects only the electrons with the highest

thermal energy, thus skewing the electron energy distribution. The Seebeck coefficient of the resulting structure is then enhanced compared with that of the same semiconductor in the linear transport regime. The overall gain in *ZT* with respect to a conventional thermoelectric material operating in the linear transport regime (current linear with voltage) can be substantial. While the thermoelectric *ZT* of bulk HgCdTe is less than 0.2, values of *ZT* up to 3.5 are calculated [18] to be possible under the HIT conditions described above. This calculation, however, depends on a number of factors. The first important question [18] is whether or not the in-plane momentum, k_x and k_y of the electrons that propagate along k_z is conserved. This affects the total number of electrons that participate in the process, and thus also affects the conductivity and *ZT*. Optimum values of *ZT* are only reached if the transverse momentum is not conserved. Second, Vashaee and Shakouri [18] show that the value of *ZT* results from an optimization process of the doping levels, as it does in all thermoelectric devices (see Figure 27.2). They further show that the final *ZT* value is much more sensitive to the doping level than in bulk thermoelectric devices, and that the optimum *ZT* occurs at much higher doping levels than in bulk. These properties are, in fact, shared by all low-dimensional thermoelectric devices, as is also schematically illustrated in Figure 27.2. Finally, we introduce a note of caution in the context of thermoelectric phenomena in nonlinear systems. The idea of developing solid-state thermoelectric devices that work in a nonlinear transport regime was proposed long before the advent of heterojunction physics using, for example, p–n junctions [88]. It was proven theoretically [89] that the efficiency of any semiconductor device in which minority carriers play a significant role must be lower than that of a structure without minority carriers. The degenerately doped HIT systems described by Vashaee and Shakouri [18], are not subject to minority-carrier recombination mechanisms.

Recently, major advances have been made in the development of a scanning thermoelectric probe which allows measurements of the spatial profiles of the thermoelectric voltage, the carrier concentration and electron band energy of a p–n junction to 2 nm resolution, as shown in Figure 27.17 [90]. Such an instrument will not only allow thermoelectric measurements to be made on individual

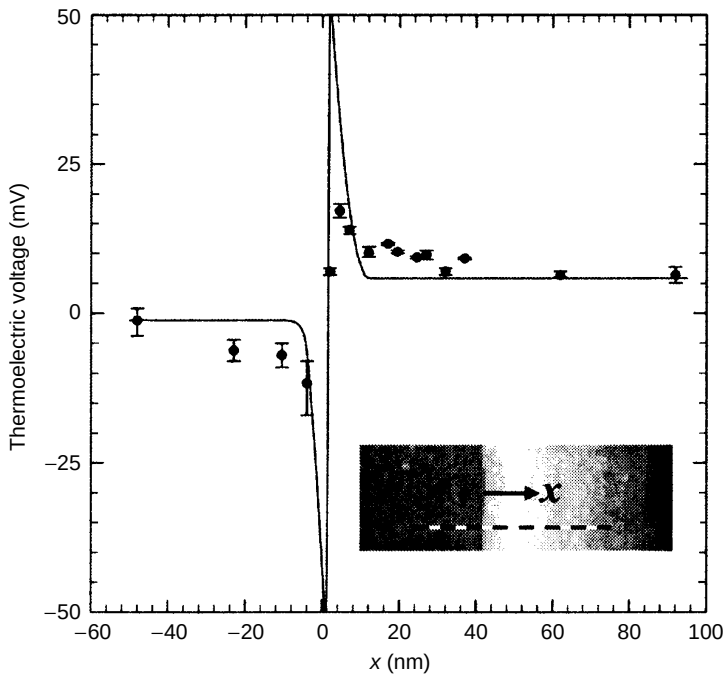

FIGURE 27.17 Thermoelectric voltage profile across a p–n junction with a 2 nm resolution. (Reprinted with permission from Lyeo, H.-K. et al., *Science*, 303, 816, 2004, ©AAAS, 2004.)

nanosystems, but will also provide a sensitive tool for the measurement of the electron and hole concentrations to high spatial resolution. This advance has important implications for characterizing nanoelectronic and optoelectronic devices. Likewise, the development of nanoscale thermal sensors [91,92] is enabling measurement of the thermal conductivity of individual nanowires [90,91] or multiwall nanotubes [93].

The field of bulk nanoscale thermoelectric composite materials, devices based on these materials, and measurement techniques for thermal transport on the nanoscale are all in their infancy. The above observations provide encouraging early results. It is therefore quite possible that nanotechnologies will indeed provide the basis for the next period of bloom in the development of thermoelectric technologies, just as thermodynamics and semiconductor physics have done in the past century and a half.

ACKNOWLEDGMENTS

JPH gratefully acknowledges support from the Delphi Corporation for this work and from Dr. D. T. Morelli for critical reading of the manuscript. MSD was supported by NASA, contract NAS 3-03108.

REFERENCES

1. Onsager, L., *Phys. Rev*., 37, 405, 1930; 38, 2265, 1931.
2. Telkes, M., *J. Appl. Phys.*, 18, 1116, 1947.
3. Ioffe, A. F., *Semiconductor Thermoelements and Thermoelectric Cooling*, Infosearch Ltd, London, 1957.
4. Ioffe, A. F., *Physics of Semiconductors*, Academic, New York, 1960.
5. Goldsmid, H. J., *Applications of Thermoelectricity*, Methuen, London, 1969.
6. Nolas, G. S., Sharp. J., and Goldsmid, H. J., in *Thermoelectricity*, Springer-Berlin, 2000.
7. Fleurial, J.-P., Borshchevsky, A., Caillat, T., Morelli, D. T., and Meisner, G. P., *Proceedings of the 15th IEEE International Conference on Thermoelectrics*, Caillat, T., Fleurial, J.-P., and Borshchevsky, A., Eds., IEEE, Pasadena, CA, 1996., p. 91. IEEE Catalogue Number 96TH8169.
8. Sales, B. C., Mandrus, D., and Williams, R. K., *Science*, 22, 1325–1328, 1996.
9. Morelli, D. T., Caillat, T., Fleurial, J.-P., Borshchevsky, A., Vandersande, J., Chen, B., and Uher, C., *Phys. Rev. B*, 51, 9622–9628, 1995.
10. Hicks, L. D., and Dresselhaus, M. S., *Phys. Rev. B*, 47, 12727–12731, 1993.
11. Hicks, L. D., and Dresselhaus, M. S., *Phys. Rev. B*, 47, 16631, 1993.
12. Venkatasubramanian, R., Siivola, E., Colpitts, and O'Quinn, B., *Nature*, London, 413, 597, 2001.
13. Harman, T. C., Taylor, P. J., Walsh, M. P., and LaForge, B. E., *Science*, 297, 2229–2232, 2002.
14. Harman, T., Oral report at invited talk at the MRS Symposium on Thermoelectric Materials, Boston, MA, December 2003.
15. Heremans, J., in *Thermoelectric Materials 2003 — Research and Applications: MRS Symposium Proceedings, Boston, December 2003*, Nolas, G. S., Yang, J., Hogan, T. P., Johnson, and D. C., Eds., Materials Research Society Press, Pittsburgh, PA, 2004, pp. 3–14.
16. Simkin, N. V., and Mahan, G. D., *Phys. Rev. Lett.*, 84, 927–930, 2000.
17. Dames, C., Dresselhaus, M. S. and Chen, G., in *Thermoelectric Materials 2003 — Research and Applications: MRS Symposium Proceedings, Boston, December 2003*, Nolas, G. S., Yang, J., Hogan, T. P., and Johnson, D. C., Materials Research Society Press, Pittsburgh, PA, 2004, pp. 15–20.
18. Vashaee, D., and Shakouri, A., *Phys. Rev. Lett.*, 92, 106103, 2004.
19. Heremans, J. P., Thrush, C. M., and Morelli, D. T., *Phys. Rev. B*, 70, 115334, 2004.
20. Shi, X., Chen, L., Yang, J., and Meisner, G. P., *Appl. Phys. Lett.*, 84, 2301–2303, 2004.
21. Hsu, K. F., Loo, S., Guo, F., Chen, W., Dyck, J. S., Uher, C., Hogan, T., Polychroniadis, E. K., and Kanatzidis, M. G., *Science*, 303, 818, 2004.
22. Blatt, F. J., *Physics of Electronic Conduction in Solids*, McGraw-Hill, New York, 1968.
23. Mott, N. F., and Davis, E. A., *Electronic Processes in Non-crystalline Materials*, Oxford University, Oxford, 1979.
24. Broido, D. A., and Reinecke, T. L., *Phys. Rev, B*, 64, 045324(1–10), 2001.

25. Broido, D. A., and Reinecke, T. L., in *Semiconductors and Semimetals, Recent Trends in Thermoelectric Materials Research III*, Tritt, T. L., Ed., Academic Press, San Diego, CA, 2001, Chap. 2, pp. 123–155.
26. Beyer, H., Nurnus, J., Böttner, H., Lambrecht, A., Wagner, E., and Bauer, G., *Physica E*, 13, 965–968, 2002.
27. Lambrecht, A., Beyer, H., Nurnus, J., Kiinzel, C., and Bottner, H., *Proceedings of the 20th International Conference on Thermoelectricity*, Beijing, China, 2001.
28. Beyer, H., Nurnus, J., Böttner, H., Lambrecht, A., Roch, T., and Bauer, G., *Appl. Phys. Lett.*, 80, 1216, 2002.
29. Dauscher, A., Lenoir, B., Jacquot, A., Bellouard, C., and Dinescu, M., *MRS Symp*., 691, G8.3.1, 2001.
30. Beyer, H., Nurnus, J., Böttner, H., Lambrecht, A., Schmitt, L., and Voelklein F., *MRS Symp*., 626, Z2.5.1, 2000.
31. Hicks, L. D., Harman, T. C., Sun, X., and Dresselhaus, M. S., *Phys. Rev. B*, 53, R10493–R10496, 1996.
32. Harman, T. C., Dresselhaus, M. S., Spears, D. L., Walsh, M. P., Cronin, S. B., Sun, X., and Koga, T., United States Patent No. 6452206 B1, 2002.
33. Lin, Y.-M., Sun, X., and Dresselhaus, M. S., *Phys. Rev. B*, 62, 4610–4623, 2000.
34. Cassian, A., Sur, I., Scherrer, H., and Dashevsky, Z., *Phys. Rev. B*, 61, 15965, 2000.
35. Beyer, H., Lambrecht, A., Nurmus, J., Böttner, H., Greissmann, H., Hein-rich, A., Schmitt, L., Blumers, M., and Völklein, F., *The 18th International Conference on Thermoelectrics: ICT Symposium Proceedings, Baltimore*, Institute of Electrical and Electronics Engineers, Inc., Pis-cat-away, NJ 09955–1331, 1999, pp. 687–708.
36. Ogrin, Yu. F., Lutskii, V. N., and Elinson, M. I., *Sov. Phys. JETP Lett.*, 3, 71–73, 1966.
37. Rogacheva, E. I., Grigorov, S. N., Nashchekina, O. N., Lyubchenko, S., and Dresselhaus, M. S., *Appl. Phys. Lett*., 82, 2628–2630, 2003.
38. Koga, T., Cronin, S. B., Dresselhaus, M. S., Liu, J. L., and Wang, K. L., *Appl. Phys. Lett.*, 77, 1490–1492, 2000.
39. Koga, T., Sun, X., Cronin, S. B., and Dresselhaus, M. S., *Appl. Phys. Lett*., 73, 2950–2952, 1998.
40. Gallo, C. F., Chandrasekhar, B. S., and Sutter, P. H., *J. Appl. Phys.*, 34, 144–152, 1963.
41. Lin, Y.-M., Rabin, O., Cronin, S. B., Ying, J. Y., and Dresselhaus, M. S., *Appl. Phys. Lett.*, 81, 2403–2405, 2002.
42. Hicks, L. D., Harman, T. C., and Dresselhaus, M. S., *Appl. Phys. Lett.*, 63, 3230, 1993.
43. Rabin, O., Bismuth Nanowire and Antidot Array Studies Motivated by Thermoelectricity. Ph.D. thesis, Massachusetts Institute of Technology, Department of Chemistry, June 2004.
44. Dresselhaus, M. S., Lin, Yu-M., Cronin, S. B., Rabin, O., Black, M. R., Dresselhaus, G., and Koga, T., in *Semiconductors and Semimetals: Recent Trends in Thermoelectric Materials Research III*, Tritt, T. M., Ed., Academic Press, San Diego, CA, 2001. Chap. pp. 11–121.
45. Heremans, J. P., Thrush, C. M., Morelli, D. T., and Wu, M.-C., *Phys. Rev. Lett.*, 88, 216801, 2002.
46. Rabin, O., Herz, P. R., Lin, Y.-M., Cronin, S. B., Akinwande, A. I., and Dresselhaus, M. S., *The 21st International Conference on Thermoelectricssssss: ICT Symposium Proceedings*, Long Beach, CA, 2002, pp. 276–279.
47. Rabin, O., Lin, Y.-M., Cronin, S. B., and Dresselhaus, M. S., in *Thermoelectric Materials 2001 — Research and Applications: MRS Symposium Proceedings, Boston, December 2001*, Nolas, G. S., Johnson, D. C., Mandus, D. G., Eds., Materials Research Society Press, Pittsburgh, PA, 2002, G8.20.
48. Heremans, J., Thrush, C. M., Lin, Yu-M., Cronin, S., Zhang, Z., Dresselhaus, M. S., and Mansfield, J. F., *Phys. Rev. B*, 61, 2921–2930, 2000.
49. Heremans, J., and Thrush, C. M., *Phys. Rev. B*, 59, 12579–12583, 1999.
50. Heremans, J., Thrush, C. M., Zhang, Z., Sun, X., Dresselhaus, M. S., Ying, J. Y., and Morelli, D. T., *Phys. Rev. B Rapid*, 58, R10091–R10095, 1998.
51. Heremans, J., Thrush, C. M., Morelli, D. T., and Wu, M.-C., *Phys. Rev. Lett*., 91, 076804, 2003.
52. Lenoir, B., Cassart, M., Michenaud, J. P., Scherrer, H., and Scherrer, S., *J. Phys. Chem. Solids*, 57, 89–99, 1996.
53. Lin, Yu-M., *Thermoelectric Properties of $Bi_{1-x}Sb_x$ and Superlattice Nanowires.* Ph.D. thesis, Massachusetts Institute of Technology, Department of Electrical Engineering and Computer Science, June 2003.

54. Rabin, O., Lin, Yu-M., and Dresselhaus, M. S., *Appl. Phys. Lett*., 79, 81–83, 2001.
55. Lin, Yu-M., Cronin, S. B., Rabin, O., Ying, J. Y., and Dresselhaus, M. S., *Appl. Phys. Lett.*, 79, 677–679, 2001.
56. Van Wees, B. J., Van Houten, H., Beenakker, C. W. J., Williamson, J. G., Kouwenhoven, L. P., Van der Marel, D., and Fonon, C. T., *Phys. Rev. Lett*., 60, 848, 1988.
57. Lin, Yu-M., and Dresselhaus, M. S., *Phys. Rev. B*, 68, 075304S(l–14), 2003.
58. Dzurak, A. S., Smith, C. G., Barnes, C. H. W., Pepper, M., Martin-Moreno, L., Liang, C. T., Ritchie, D. A., and Jones, G. A. C., *Phys. Rev. B*, 55, R10197, 1997.
59. Harman, T. C., Spears, D. L., and Walsh, M. P., *J. Electron. Mater. Lett*., 28, LI, 1999.
60. Harman, T. C., Taylor, P. J., Walsh, M. P., and Spears, D. L., *J. Electron. Mater*., 29, L1–L4, 2000.
61. Dames, C., and Chen, G., *J. Appl. Phys.*, 95, 682–693, 2004.
62. Piraux, L., George, J. M., Despres, J. F., and Leroy, C., *Appl. Phys. Lett*., 65, 2484, 1994.
63. Wu, Y., Fan, R., and Yang, P., *Nanoletters*, 2, 83–86, 2002.
64. Gudiksen, M. S., Lauhon, L. J., Wang, J., Smith, D., and Lieber, C. M., *Nature*, 415, 617–620, 2002.
65. Bjork, M. T., Ohlsson, B. J., Sass, T., Persson, A. I., Thelander, C., Magnusson, M. H., Deppert, K., Wallenberg, L. R., and Samuelson, L., *Nanoletters*., 2, 87–89, 2002.
66. Li, D., Wu, F. R., Yang, P., and Majumdar, A., *J. Appl. Phys*., 83, 3186–3188, 2003.
67. Dalven, R., *Infrared Phys*., 9, 141, 1969.
68. Springholz, G., Holy, V., Pinczolits, M., and Bauer, G., *Science*, 282, 734–737, 1998.
69. Springholz, G., Pinczolits, M., Mayer, P., Holy, V., Bauer, G., Kang, H. H., and Salamanca-Riba, L., *Phys. Rev. Lett*., 84, 4669–4672, 2000.
70. Alchalabi, K., Zimin, D., Kostorz, G., and Zogg, H., *Phys. Rev. Lett*., 90, 026104(1–4), 2003.
71. Ravich, Yu. I., Efimova, B. A., and Tamarchenko, V. I., *Phys. Stat. Sol*. (b), 43, 453–469, 1971.
72. Proetto, C. R., *Phys. Rev. B*, 44, 9096, 1991.
73. Landauer, R., *IBM J. Res. Dev*., 1, 223, 1957.
74. Wharam, A., Thornton, T. J., Newbury, R., Pepper, M., Ahmed, H., Frost, J.E.F., Hasko, D. G., Peacock, D. C., Ritchie, D. A., and Jones, G. A. C., *J. Phys. C*, 21, L209, 1988.
75. Guinier, A., *Nature*, 142, 569, 1938
76. Preston, G. P., *Nature*, 142, 570, 1938.
77. Irie, T., Takahama, T., and Ono, T., *Japanese J. Appl. Phys*., 2, 72–82, 1963.
78. Rosi, F. D., Dismukes, J. P., and Hockings, E. F., *Elect. Eng.*, 79, 450–459, 1960.
79. Armstrong, R. W., Faust, J. W., and Tiller, W. A., *J. Appl. Phys*., 31, 1954–1959, I960.
80. Bilc, D., Mahanti, S.D., Quarez, E., Hsu, K.-F., Pcionek, R., and Kanatzidis, M.G., *Phys. Rev. Lett*., 93, 146403-1, 2004.
81. Ravich, Y. I., *CRC Handbook of Thermoelectrics*, Rowe, D. M., Ed., CRC Press, New York, 1995, pp. 67–73.
82. Stavitskaya, T. S., and Stilbans, L. S., *Sov. Phys. Solid State*, 2, 1868–1870, 1961.
83. Issi, J. P., Michenaud, J. P., and Heremans, J., *Phys. Rev. B*, 14, 5156–5160, 1976.
84. Hatsopoulos, G. N., and Welsh, J. A., *Thermoelectric Materials and Devices*, Pergamon Press, New York, l960, p. 47.
85. Shakouri, A., and Bowers, J. D., *Appl. Phys. Lett*., 71, 1234, 1997.
86. Mahan, G., and Woods, L. M., *Phys. Rev. Lett*., 80, 4016, 1998.
87. Tauc, J., *Photo and Thermoelectric Effects in Semiconductors*, Pergamon Press, New York, 1962.
88. Lehovec, K., Accardo, C. A., and Jamgonichian, E., *Phys. Rev*., 89, 20, 1953.
89. Hall R. N., *Solid-State Electronics*, 2, 115, 1958.
90. Lyeo, H.-K., Khajetoorians, A. A., Shi, L., Pipe, K. P., Ram, R. J., Shakouri, A., and Shih, C. K., *Science*, 303, 816, 2004.
91. Majumdar, A., *Science*, 303, 777–778, 2004.
92. Kim, P., Shi, A., Majumdar, L., and McEuen, P. L., *Phys. Rev. Lett*., 87, 215502, 2001.
93. Small, J. P., Shi, L., and Kim, P., *Solid State Commun*., 127, 181–186, 2003.